Aeronomy of the Middle Atmosphere

Chemistry and Physics of the Stratosphere and Mesosphere

Third revised and enlarged Edition

Guy P. Brasseur and Susan Solomon

Atmospheric and Oceanographic Sciences Library

Springer

Aeronomy of the Middle Atmosphere

ATMOSPHERIC AND OCEANOGRAPHIC SCIENCES LIBRARY

VOLUME 32

Aeronomy of the Middle Atmosphere

Chemistry and Physics of the Stratosphere and Mesosphere

Third revised and enlarged edition

Guy P. Brasseur

Max Planck Institute for Meteorology,
Hamburg, Germany
and
National Center for Atmoshpheric Research,
Boulder, CO, U.S.A.

and

Susan Solomon

NOAA Aeronomy Laboratory,
Boulder, CO, U.S.A.

Springer

A C.I.P. Catalogue record for this book is available from the Library of Congress.

ISBN-10 1-4020-3284-6 (HB)
ISBN-13 978-1-4020-3284-4 (HB)
ISBN-10 1-4020-3824-0 (e-book)
ISBN-13 978-1-4020-3824-1 (e-book)

Published by Springer,
P.O. Box 17, 3300 AA Dordrecht, The Netherlands.

www.springeronline.com

Printed on acid-free paper

Printed in the Netherlands.

Contents

Preface ix

1. THE MIDDLE ATMOSPHERE AND ITS EVOLUTION 1

1.1 Introduction 1
1.2 Evolution of the Earth's Atmosphere 2
1.3 Anthropogenic Perturbations 4

2. CHEMICAL CONCEPTS IN THE ATMOSPHERE 11

2.1 Introduction 11
2.2 Energy Levels of Molecules 12
2.3 Thermodynamic Considerations 21
2.4 Elementary Chemical Kinetics 24
2.5 Heterogenous and Multiphase Reactions 34
2.6 Photolysis Processes 40
2.7 Excited Species in the Middle Atmosphere 44

3. DYNAMICS AND TRANSPORT 51

3.1 Introduction 51
3.2 Structure of the Atmosphere and Some Observed Dynamical Characteristics 53
3.3 Fundamental Description of Atmospheric Dynamics 59
3.4 Atmospheric Waves 74
3.5 Effects of Dynamics on Chemical Species: Transport . . . 84
3.6 Dynamics and Meridional Transport in Two Dimensions: A Conceptual View 92
3.7 The Importance of Wave Transience and Dissipation . . 112
3.8 Vertical Transport above the Mesopause 125
3.9 Models of the Middle Atmosphere 129

4. RADIATION 151

4.1 Introduction 151
4.2 Definitions 156
4.3 Extraterrestrial Solar Radiation 159
4.4 The Attenuation of Solar Radiation in the Atmosphere . 169
4.5 Radiative Transfer 180
4.6 The Thermal Effects of Radiation 206
4.7 Photochemical Effects of Radiation 218

5. COMPOSITION AND CHEMISTRY 265

5.1 General 265
5.2 Oxygen Compounds 271
5.3 Carbon Compounds 292
5.4 Hydrogen Compounds 307
5.5 Nitrogen Compounds 327
5.6 Halogen Compounds 358
5.7 Stratospheric Aerosols and Clouds 386
5.8 Generalized Ozone Balance 401

6. OZONE PERTURBATIONS 443

6.1 Introduction 443
6.2 The Photochemically-Controlled Upper Stratosphere and Mesosphere: 25-75 km 444
6.3 Lower Stratospheric Ozone Depletion: Observations and Explanations 459
6.4 Summary and Outlook 501

7. THE IONS 533

7.1 Introduction 533
7.2 Formation of Ions in the Middle Atmosphere 539
7.3 Positive Ion Chemistry 552
7.4 Negative Ion Chemistry 570
7.5 Effect of Ionic Processes on Neutral Constituents 581
7.6 Radio Waves in the Lower Ionosphere 586

APPENDICES 599

Appendix 1: Physical Constants and Other Data 599
Appendix 2: Conversion Factors and Multiplying Prefixes . . 603

Appendix 3: Rate Coefficients for Second-Order Gas-Phase Reactions 607
Appendix 4: Rate Coefficients for Gas-Phase Associating Reactions 611
Appendix 5: Surface Reaction Probability 613
Appendix 6: Atmospheric Profiles 615

Figure Acknowledgements 625

Color Section 627

Index 637

Preface

Since the industrial revolution, the chemical composition of the atmosphere has changed at a rate unprecedented in recent history. The concentration of carbon dioxide has increased by about 25% during the 20^{th} century as a result of fossil fuel combustion, and is expected to further increase substantially over the next several decades. The level of methane is more than a factor 2 higher than a century ago, due in large part to agricultural practices. The aerosol load of the atmosphere has been perturbed by such practices as the intensive use of coal as a primary energy source. The release of nitrogen oxides, carbon monoxide and hydrocarbons, as a result of fossil fuel and biomass burning has led to enhanced abundances of ozone and other oxidants in the troposphere. Organic halogenated compounds including the industrially manufactured chlorofluorocarbons have become a dominant source of ozone-depleting chlorine and bromine in the stratosphere. The science of the ozone layer and its interactions with halogenated chemicals are the focus of this book.

These human-induced changes have led to significant perturbations in the Earth's global environment, and will further affect it in the decades ahead. Among these perturbations are the degradation of air quality with associated health effects, the acidification of precipitation with potential consequences for ecosystems, changes in the oxidizing power of the atmosphere and hence on the ability of the atmosphere to eliminate pollutants, changes in the Earth's climate in response to modified absorption and emission of radiation by atmospheric trace constituents, and stratospheric ozone depletion leading to enhanced levels of harmful solar ultraviolet radiation at the Earth's surface.

Ozone plays a central role in the Earth's environment. By absorbing DNA damaging ultraviolet light originating from the Sun, it protects living organisms including humans from lethal effects. It also strongly affects the thermal structure of the atmosphere, and maintains a dynamically stable layer, –the stratosphere–, between approximately 10 and 50 km altitude. Ozone, a greenhouse gas and a powerful oxidant, also influences the Earth's climate and plays a key role in the ability

of the atmosphere to destroy several chemical compounds, including many primary or secondary pollutants.

The depletion of the stratospheric ozone layer captured the attention of scientists, policy makers, and the public, particularly in the 1970s, 1980s, and 1990s. Active research quickly provided an improved understanding of the mechanisms involved in the formation and fate of stratospheric ozone. Ozone depletion emerged as one of the most important environmental issues of the 20^{th} century as the evidence grew for substantial human influences on the ozone abundances over much of the globe. An international environmental agreement (The Montreal Protocol and its amendments and adjustments) now governs the global use of ozone-depleting halocarbons. In the 21^{st} century, interest remains strong in the science, the history, and the future of the stratospheric ozone layer.

The purpose of this volume is to provide to graduate students and research scientists a comprehensive view of the chemical, dynamical and radiative processes that affect ozone and other chemical compounds in the middle atmosphere. The title of this volume –Aeronomy of the Middle Atmosphere– has been chosen to highlight the topics covered in this book. The word "Aeronomy" is defined as the science dealing with planetary atmospheres with reference to their chemical composition, physical properties, relative motions and reactions to radiation from outer space (Chambers Dictionary). The field of aeronomy is therefore highly interdisciplinary, drawing on the fields of chemistry, physics, fluid dynamics, meteorology, statistics, mathematics, engineering, etc. The middle atmosphere is defined as the region extending from the tropopause (approximately 12 km) to the homopause (about 100 km altitude).

The book is intended to provide an overview in a manner understandable to persons familiar with college level chemistry and physics. After a general introduction presented in Chapter 1, Chapter 2 reviews basic concepts from physical chemistry, which are of relevance to atmospheric studies. Chapter 3 presents a highly simplified view of dynamical and transport processes above the tropopause, and Chapter 4 summarizes important aspects of radiative transfer in relation to the energy budget and photolytic processes in the middle atmosphere. Chapter 5 presents an overview of the key chemical processes, which influence the chemical composition of the middle atmosphere, while Chapter 6 discusses human-induced perturbations affecting ozone and other compounds. The chapter also presents a detailed discussion of ozone depletion, particularly the formation of the spectacular Antarctic

ozone hole is provided in this chapter. Finally, Chapter 7 provides an overview of ionization processes in the mesosphere and stratosphere. Although the discussion focuses on the atmospheric layers ranging from 10 to 100 km, we have sometimes found it necessary to discuss processes occurring in the troposphere (surface to about 12 km altitude) and thermosphere (region above 100 km) in order to explain the roles of these neighboring regions.

Due to the large number of topics to be addressed in the present volume, we have found it impossible to provide a complete review of the available literature. We anticipate that the interested reader will regard the discussions as a starting point and find additional references by consulting publications cited here. The periodic international assessments of the state of the ozone layer, published by the World Meteorological Organization and the United Nations Environment Program, provide additional information.

When we wrote the first edition of this book in the early 1980's, we did not anticipate that the question of stratospheric ozone would soon receive so much scientific attention. The discovery of the Antarctic ozone hole sparked the rapid development of exciting scientific programs and new research understanding. Since the publication of the early editions of this book, new measurement techniques (including space platforms and instruments), more accurate laboratory methods, and more sophisticated atmospheric models have become available. Our understanding of the middle atmosphere, including the role of chemical transformations on the surfaces of liquid or solid particles and the complexity of the air motions, has improved dramatically. More importantly, the discovery and explanation of the Antarctic ozone hole has shown that human activities can lead to major changes in the chemical composition of the atmosphere not just locally and regionally, but at the global scale. The new edition of the present volume attempts to synthesize some of the most recent findings.

The review of critical portions of the manuscript by colleagues has certainly improved the quality of this volume. Material provided to us has also been of great help. We particularly thank S. Chabrillat, D. Edwards, R. Garcia, M. Giorgetta, H. Graf, C. Granier, M. Hagan, J. Holton, I. Karol, K. Kodera, E. Kopp, S. Madronich, E. Manzini, D. Marsh, M. Mlynczak, J. Orlando, T. Peter, W. Randel, A. Smith, Stan Solomon, X. Tie, G. Tyndall, S. Walters, X. Zhu. We deeply appreciate the assistance of R. Terrell Bailey, Paula Fisher, and Debe Fisher for the preparation of the camera-ready manuscript, of C. Granier for her proofreading of the manuscript, and of the Imaging and Design Center

at the National Center for Atmospheric Research (NCAR) for their expert figure drafting. We also acknowledge the Atmospheric Chemistry Division at NCAR for supporting the preparation of this book.

Guy P. Brasseur
Susan Solomon
Boulder, Colorado
March, 2005

Chapter 1

THE MIDDLE ATMOSPHERE AND ITS EVOLUTION

1.1 Introduction

Our atmosphere is the medium for life on the surface of the planet, and the transition zone between Earth and space. Humankind has always been interested in the characteristics, manifestations and perturbations of the atmosphere — in its changing weather patterns, and its brilliant sunsets, rainbows, and aurorae.

The lower part of the atmosphere has been continuously studied over many years through meteorological programs. The development of rocket and satellite technology during the past 40 years has also led to the investigation of the upper atmosphere, establishing a new field of research.

The intermediate region which extends from about 10 to 100 km altitude is sometimes called the *middle atmosphere*. This region is somewhat less accessible to observation and has only been systematically studied for the past 25 to 30 years. The purpose of this volume is to outline some of the factors which control the behavior of this layer of the atmosphere, a region which is particularly vulnerable to external perturbations such as solar variability and volcanic eruptions or the emission of anthropogenic material, either at the surface or at altitude.

One of the most important chemical constituents in the middle atmosphere is *ozone*, because it is the only atmospheric species that effectively absorbs ultraviolet solar radiation from about 250-300 nm, protecting plant and animal life from exposure to harmful radiation. Therefore, the stability of the ozone layer (located near 15 to 25 km) is a central part of the study of the middle atmosphere.

In the study of planetary atmospheres it has been customary to distinguish between thermodynamic and dynamic aspects, which constitute a portion of the field of *meteorology*, and the chemical and photochemical aspects, which are part of the domain of *aeronomy*. However, the interactions between these different disciplines play an

important role, particularly in the altitude region which we shall address here, so that an effort to examine the coupled dynamical, chemical, and radiative problem must be made in order to understand the observed variations in atmospheric chemical constituents.

1.2 Evolution of the Earth's Atmosphere

The terrestrial atmosphere has evolved considerably over the course of time. The details of this evolution, however, are not well established, and not all scholars agree on how it occurred. Reviews of our current understanding of the atmospheric evolution are given, for example, by Walker (1977) and Kasting (1993).

The universe was created some 15-20 billion years ago when an enormous explosion of a dense center of matter took place (the *big bang*). The Earth was formed approximately 4.6 billion years ago by accretion of small celestial bodies (planetisimals) that had condensed from the solar nebula during its cooling. The gases present at the early stage of the Earth's formation, which could have formed the primordial atmosphere, rapidly dissipated before they could be retained by a strong gravitational field. Instead, a secondary atmosphere was produced by the gradual release of gases from the Earth's interior (which was extremely warm due to radiative decay of uranium, thorium, and potassium contained in the planetisimals). Support for this idea stems in part from the depletion of inert gases such as He, Ne, Ar, and Kr on Earth, relative to their observed abundance in the solar system. Since there is no known process which could remove these very unreactive species from the atmosphere, their low abundance suggests that they never represented as large a fraction of our atmosphere as they do elsewhere in our solar system (*e.g.*, Moulton, 1905).

It is believed that the secondary atmosphere contained large quantities of carbon dioxide (CO_2), water vapor (H_2O), nitrogen (N_2) and perhaps hydrogen chloride (HCl) and trace amounts of other substances. As the planet cooled, water vapor condensed, initiating a vigorous hydrological cycle and producing large oceans. The sediments of the early Earth were probably produced by weathering of the primordial igneous rock minerals by dissolved carbon, nitrogen, chlorine, and sulfur acidic rain water.

An important question related to the evolution of the Earth's climate is the so-called "faint young sun paradox". Like other stars, the Sun evolves with time, so that the radiative energy it provides was probably 25-30% smaller 4 billion years ago than it is today. In spite of the small

energy available, the planet's average temperature was always higher than the water frost point (based on the analysis of geological records). It is probably the presence of high quantities of CO_2 in the atmosphere (on the order of 100 times the present value) and perhaps of other greenhouse gases (*i.e.*, methane, ammonia) at the early stage of the Earth's evolution that prevented the planet from being frozen (a condition required for life to develop).

As time evolved and the energy provided by the sun increased, the gradual removal of carbon dioxide from the atmosphere became critical to avoid a "runaway greenhouse effect" (with extremely high surface temperatures) as observed on Venus. This removal of CO_2 was accomplished by weathering of calcium silicate ($CaSiO_3$) minerals by acidic CO_2-rich rainwater, leading to the formation of limestone ($CaCO_3$).

The evolution of atmospheric CO_2 on geological time scales became regulated by the storage of limestone (and of dead organic carbon which appeared later as life developed) in the interior of the Earth's crust (as a result of plate tectonic motions) and the volcanic ejection of CO_2 produced by metamorphism in the Earth's sediments (chemical activation of limestone and dead organic carbon in high pressure and high temperature environments).

The first atmospheric molecules of oxygen (O_2) were probably formed as a result of water vapor photolysis. This source, however, is insufficient to account for the large percentage of oxygen found in the present atmosphere. The evolution of oxygen was rather closely tied to the evolution of life. Several hypotheses have been presented to describe the emergence of life on the planet some 3.5-4.0 billion years ago. One of them, supported by the historical laboratory experiment of Miller (1953) and Miller and Urey (1959), suggests that organic molecules such as amino acids and sugar (which may be the precursors of living matter) could have been formed by spark discharges (*i.e.*, lightning flashes) in a mixture of gases containing methane, ammonia, hydrogen, and water molecules. Organic molecules could also have been injected from space by bombardment of micro-meteorites which include molecules containing carbon, hydrogen, oxygen, and nitrogen. A more plausible hypothesis is that life began in specialized regions of the ocean (*e.g.*, in volcanic vents) where high concentrations of sulfide may have favored the formation of organic molecules. Some of the first living creatures survived by fermentation. These were followed by chemoautotrophs which obtained energy from chemical reactions, and finally photosynthetic organisms began to produce oxygen in much larger amounts, eventually increasing the oxygen content to contemporary levels. The evolution from an oxygen-free, reducing atmosphere to an oxidizing atmosphere (one that

can sustain life for higher organisms) has been a special characteristic of the Earth. Today, the most abundant gases in the atmosphere of our neighboring planets, Mars and Venus, are not nitrogen (N_2) and oxygen (O_2) as on Earth, but carbon dioxide (CO_2).

Present photosynthetic life is protected from harmful solar radiation by oxygen and ozone. Thus we must ask how these original creatures survived and evolved to the present state even as they formed the protective shield which their descendants would enjoy. It is possible that they were a form of algae, protected by liquid water from the sun's rays. It has also been suggested that primitive microbes could have been protected by layers of purine and pyrimidine bases, which absorb in the ultraviolet range (Sagan, 1973).

In conclusion, it is clear that the evolution of the Earth's atmosphere depended on many factors, including its albedo, the biosphere (plant and animal life), the oceans, the sun, and the composition of the solid Earth. Physical processes such as volcanic eruptions together with biological activity at the surface have contributed to the evolution of the composition of the terrestrial atmosphere and of the Earth's climate over geological time. Lovelock and Margulis (1974), for example, have argued that the Earth's environment is controlled primarily by the biota in a way that is favorable to life. Thus, the stability of our atmosphere is a complex function of both organic and inorganic processes. Today, many of these processes are disrupted by the human species. In the rest of this chapter and throughout this volume, we discuss the natural processes which control the present atmosphere, and assess the possible impact which human activities may have upon it.

1.3 Anthropogenic Perturbations

The possible modification of the chemical composition of the atmosphere, and the attendant climatic effects, is a problem which attracts the attention of the international scientific community, decision makers, and the public. Some of the processes which may produce these modifications will be briefly identified in this section. A more detailed analysis will be presented in Chapter 6.

We first consider the effects of the agricultural revolution and ask whether the modification of the Earth's ecosystems may influence the atmosphere. In tropical regions, for example (Brazil, Central Africa, Southeast Asia), large regions of forest and savannah are burned for agricultural reasons. It has been estimated that 160000 km^2 of wooded land are destroyed each year (*e.g.*, Kandel, 1980). The combustion

produces numerous chemical species, such as CO_2, CO, CH_4 (and many other organic compounds), H_2, N_2, N_2O, NO, NO_2, COS, CH_3Cl, CH_3Br, CH_3I, HCN, CH_3CN, as well as aerosol particles (*e.g.*, black carbon; see Crutzen *et al.*, 1979; Andreae and Merlet, 2001). Some of these compounds eventually reach the middle atmosphere, where they can influence the budgets of several minor species, particularly ozone. Further, the introduction of modern agricultural techniques, especially the intensive use of nitrogen fertilizers, has altered the natural nitrogen cycle by increasing the fixation of this element in the form of ammonia, amino acids, and nitrates. During nitrification and denitrification, part of the nitrogen is emitted to the atmosphere in the form of N_2O rather than N_2. N_2O provides the principal source of NO in the middle atmosphere and accelerates the destruction of ozone in the stratosphere (see Chapter 5).

The rate of nitrogen fixation on the Earth's surface is not known with great accuracy. The contributions of natural biological fixation, as well as the effects of lightning and combustion must be considered. It is estimated, however (Vitousek, 1994), that the annual amount of nitrogen fixed naturally by the biosphere is between 50 to 200 Tg N/yr, while fixation by combustion represents about 20 to 40 Tg/yr. The contribution from nitrogen fertilizers probably exceeds 80 Tg N/yr, and the fixation by legume crops is of the order of 30-50 Tg N/yr. An additional 2-20 Tg N/yr are fixed by lightning in thunderstorms and 20 Tg N/yr in internal combustion engines. Since human-induced nitrogen fixation has increased with time, the effect of this artificial source on the ozone layer (pointed out by Crutzen, 1974, and McElroy *et al.*, 1976) could become significant in the future.

The possible effects of nitrogen oxides on the middle atmosphere have been very actively studied since Crutzen (1970) and Johnston (1971) indicated that the injection of large quantities of these species in aircraft exhaust might alter the protective ozone layer. Later, calculations showed that the effect introduced by such aircraft depends directly on the flight altitude: An injection of nitrogen oxide could contribute to ozone production at altitudes below about 15 km (Brasseur *et al.*, 1998; IPCC, 1999), but to ozone destruction if the craft flew at higher altitudes. It is estimated that current commercial aircraft release approximately 0.5 Tg N/yr (a third of which is being released in the stratosphere) and that the fleet of 500 high-speed civil transport aircraft projected in the early 1970s would have injected 0.1 Tg N/yr (mostly as NO) near 15-22 km altitude. Another source of nitrogen oxides which perturbed the atmosphere in the 1950s and 1960s is the explosion of powerful atomic bombs. Approximately 0.15 to 0.55 Tg N were injected into the stratosphere during the Soviet tests in the fall of 1962. This

figure is a significant fraction of the 1 Tg N produced naturally from N_2O oxidation.

The effects of industrial activities, especially the emission of gaseous effluents and their possible effects on climate, have also attracted considerable attention. The most well known problem is certainly that of CO_2, but the cycling of this gas between the atmosphere, biosphere, hydrosphere (clouds and oceans), and the lithosphere (solid Earth) remains insufficiently well quantified. The emission of CO_2 as a result of combustion of fossil fuels (coal, oil) appears to be responsible for the increase in the CO_2 concentration which has been observed in the atmosphere. Between 1960 and 1990 the total amount of CO_2 in the atmosphere increased from 2.53 to 2.81×10^{12} tons. Such an increase influences the thermal budget of the atmosphere, both by cooling of the upper layers due to an increase in the emission of infrared radiation to space, and through heating in the lower layers due to absorption of the infrared emission from the Earth's surface and lower atmosphere (the so-called greenhouse effect). Global models indicate that the globally averaged surface temperature of the Earth should increase by 1.4 to 5.8°C over the period 1990-2100, depending on the adopted scenario for future emissions (IPCC, 2001). Such changes would greatly influence the polar ice caps and global precipitation processes. The exact magnitude of the effect of increased greenhouse gas emissions is difficult to establish because of the complicated feedbacks that exist between the atmosphere, oceans, and biosphere. Observations indicate that a systematic increase in the Earth's mean surface temperature has occurred in the twentieth century. Since the secular temperature variation is also dependent on the aerosols released by combustion processes and perhaps on solar variability, this trend cannot be unambiguously attributed entirely to CO_2 and other greenhouse gases.

Changes in the atmospheric temperature alter the rates of many photochemical processes and therefore the concentrations of minor species. For example, the increase in CO_2 between 30 and 50 km should lead to a small increase in the ozone content, according to current models. Thermal perturbations can also influence atmospheric dynamics (see Chapter 3).

The emission of chlorine and bromine compounds also is a matter of interest, because stratospheric ozone is easily destroyed by these halogen species (Stolarski and Cicerone, 1974; Molina and Rowland, 1974; Wofsy *et al.*, 1975). Chlorine and bromine atoms are present in a variety of industrial products dispersed in the atmosphere, but many of these are rapidly destroyed at low altitudes and therefore do not reach the middle atmosphere where the bulk of the atmospheric ozone layer resides. Some industrial compounds do, however, have sufficiently long

lifetimes to represent a potential perturbation. This is the case, for example, for halogenated hydrocarbons such as the chlorofluorocarbons (CFCs), and specifically for trichlorofluoromethane ($CFCl_3$ or CFC-11), dichlorodifluoromethane (CF_2Cl_2 or CFC-12), carbon tetrachloride (CCl_4), and methylchloroform (also called trichloroethane or CH_3CCl_3). CFCs are very stable compounds and, hence, have been used as refrigerants, solvents, foam-blowing agents and, until the late 1970s, as aerosol spray propellants. Methyl chloride (CH_3Cl) is the major natural chlorocarbon of relevance for the stratosphere; it is produced in seawater and released by biomass burning. As these long-lived organic molecules penetrate into the stratosphere, they are photodecomposed and release ozone-destroying agents. It is estimated that in the early 1990s when the emissions of industrially produced CFCs represented approximately 1 Tg/yr, about 85% of the stratospheric chlorine was of anthropogenic origin. There is strong evidence today that the ozone depletion observed in the 1980s and 1990s, and specifically the formation of a large "ozone hole" in Antarctica each spring since about the early 1980s, has been caused by the rapid increase in the chlorine load of the stratosphere. The CFCs are also believed to be responsible for the ozone depletion recorded in the Arctic during many winters since the early 1990s.

International agreements (Montreal Protocol in 1987 and subsequent amendments), as well as national regulations, have strongly limited the production and the use of the CFCs. These chemical compounds have been gradually replaced by partially halogenated hydrocarbons, and specifically by hydrochlorofluorocarbons (HCFCs) and hydrofluorocarbons (HFCs). These alternative products are relatively easily destroyed in the troposphere and hence their lifetimes are substantially shorter than those of the CFCs (typically 1-10 yrs as opposed to 10-100 yrs). The ozone depletion potential of the HCFCs is about an order of magnitude smaller than that of the fully halogenated halocarbons. HFCs are not a threat to ozone because they do not contain any chlorine or bromine atoms.

Bromine, whose potential to destroy ozone (per atom) is about 50 times higher than that of chlorine, is released in the stratosphere by photodecomposition of methyl bromide and other brominated organic compounds, including the so-called halons (*e.g.*, CF_2ClBr or Halon-1211, and CF_3Br or Halon-1301). CH_3Br is produced by biological activity in the ocean, biomass burning, automobile exhaust, and agricultural usage (*i.e.*, as a pre-planting and post-harvesting fumigant). The anthropogenic source of CH_3Br represents about 40% of the total emission. Halons, whose lifetime is several decades, are used in fire extinguishers. Their production is now banned owing to their harmful effects on stratospheric ozone.

Numerical models have been used to predict the potential ozone depletion in response to the emission of halocarbons, based on different plausible scenarios. All of these models indicate that the time required for the middle atmosphere to respond to surface emissions of these halocarbons is very long (several decades). In particular, even with the measures taken to reduce or phase-out the emissions of the CFCs and other halocarbons, it is expected that the Antarctic ozone hole will be observed each spring (September-October) at least until the year 2040. It should also be noted that the halocarbons are active in the infrared, and contribute to the greenhouse effect.

The analysis of perturbations to the middle atmosphere must also include natural processes, such as the effects of volcanic eruptions, which produce large quantities of fine particles as well as water vapor and SO_2, which eventually produces H_2SO_4 and sulfate aerosols. The amount of gas injected, the composition and the maximum altitude of injection vary with the intensity of the eruption. Such events can alter the budgets of some atmospheric constituents and are clearly reflected in the middle atmospheric aerosol content. Particles also provide sites for surface reactions to occur. Such heterogeneous reactions may activate chlorine and enhance the depletion of ozone by industrially manufactured halocarbons.

We have also noted the important role of the sun in establishing the thermal and photochemical conditions in the Earth's environment. Variations in the solar output are caused by its 27-day rotation period, the 11-year solar cycle, and by solar flares. Each of these processes may account for part of the natural variability of the atmosphere.

The effects of human activities on the composition of the atmosphere have been clearly detected on local, regional, and global scales. Agricultural development and industrial activities are likely to influence terrestrial ecosystems as well as the climate system. It is therefore important to understand the behavior of the atmosphere, which is so vulnerable to external perturbations and so essential to the climatic and photochemical environment on Earth.

References

Andreae, M.O., and P. Merlet, Emission of trace gases and aerosols from biomass burning. *Glob Biogeochem Cycles: 15*, 955, 2001.

Brasseur, G.P., R.A. Cox, D. Hauglustaine, I. Isaksen, J. Lelieveld, D.H. Lister, R. Sausen, U. Schumann, A. Wahner, and P. Wiesen, European scientific assessment of the atmospheric effects of aircraft emissions. *Atmos Env: 32*, 2327, 1998.

Crutzen, P.J., The influence of nitrogen oxide on the atmospheric ozone content. *Quart J Roy Met Soc: 96*, 320, 1970.

Crutzen, P.J., Estimates of possible variations in total ozone due to natural causes and human activity. *Ambio: 3*, 201, 1974.

Crutzen, P.J., L.E. Heidt, J.P. Krasnec, W.H. Pollock, and W. Seiler, Biomass burning as a source of the atmospheric gases CO, H_2, N_2O, NO, CH_3Cl, and COS. *Nature: 282*, 253, 1979.

IPCC (Intergovernmental Panel on Climate Change), *Aviation and the Global Atmosphere*. J. Penner *et al.* (eds.), Cambridge University Press, 1999.

IPCC (Intergovernmental Panel on Climate Change), *Climatic Change 2001: The scientific basis*. J.T. Houghton, Y. Ding, D.J. Griggs, M. Noguer, P.J. Van de Linden, X. Da, K. Maskell, and C.A. Johnson (eds.), Cambridge University Press, 2001.

Johnston, H.S., Reduction of stratospheric ozone by nitrogen oxide catalysts from supersonic transport exhaust. *Science: 173*, 517, 1971.

Kandel, R.S., *Earth and Cosmos.* Pergamon Press, 1980.

Kasting, J.F., Earth's early atmosphere. *Science: 259*, 920, 1993.

Lovelock, J.E., and L. Margulis, Atmospheric homeostatis by and for the atmosphere: The gaia hypothesis. *Tellus: 26*, 2, 1974.

McElroy, M.B., J.W. Elkins, S.C. Wofsy, and Y.L. Yung, Sources and sinks for atmospheric N_2O. *Rev Geophys Space Phys: 14*, 143, 1976.

Miller, S.L., A production of amino acids under possible primitive earth conditions. *Science: 117*, 528, 1953.

Miller, S.L., and H.C. Urey, Organic compound synthesis on the primitive earth. *Science: 130*, 245, 1959.

Molina, M.J., and F.S. Rowland, Stratospheric sink for chlorofluoromethanes: Chlorine atom catalyzed destruction of ozone. *Nature: 249*, 810, 1974.

Moulton, F.R., On the evolution of the solar system. *Astrophys J: 22*, 165, 1905.

Sagan, C., Ultraviolet selection pressure on the earliest organisms. *J Theo Bio: 39*, 195, 1973.

Stolarski, R.S., and R.J. Cicerone, Stratospheric chlorine: A possible sink for ozone. *Can J Chem: 52*, 1610, 1974.

Vitousek, P.M., Beyond global warming: Ecology and global change. *Ecology: 75*, 1861, 1994.

Walker, J.C.G., *Evolution of the Atmosphere.* McMillan Pub., 1977.

Wofsy, S.C., M.B. McElroy, and Y.L. Yung, The chemistry of atmospheric bromine. *Geophys Res Lett: 2*, 215, 1975.

Chapter 2

CHEMICAL CONCEPTS IN THE ATMOSPHERE

2.1 Introduction

Almost all of the constituents that are present in the middle atmosphere undergo chemical and photochemical processes, which greatly affect their spatial and temporal distributions. Chemical reactions can occur in the gas phase, in the condensed phase, or at the interface between these phases. The energy provided by the Sun can break the chemical bonds of many species, producing reactive fragments which interact with other compounds. Most of these fragments are *free radicals* (particles containing one or more unpaired electrons). Gas phase reactions typically involve at least one "free radical" species, while condensed phase reactions can include molecules only. Reactions occurring in the middle atmosphere are discussed in detail in Chapter 5. Rate constants for chemical reactions are measured in the laboratory. Quantitative values of these rate constants are regularly compiled by the Jet Propulsion Laboratory (see *e.g.*, JPL, 2002). The absorption of solar energy also plays an important role in the thermal budget and dynamical properties of the middle atmosphere. To understand the aeronomy of the middle atmosphere, we must first understand some of the basic principles of spectroscopy, photochemistry, kinetics and thermodynamics. In this chapter, we attempt to outline how these enter into the chemistry of the middle atmosphere, and present examples of their use. The discussion presented here will be very elementary; the reader may wish to examine the bibliography for detailed treatments. See, for example, the comprehensive textbook by Finlayson-Pitts and Pitts (1999). Some useful definitions are provided in Box 2.1.

2.2 Energy Levels of Molecules

The motions of molecules can be decomposed into translational, rotational and vibrational motions. Radiation, once absorbed by a molecule, affects only its rotational and vibrational states. Therefore, translation motions will not be further considered here, even though we should note that once absorbed, the incoming energy can be converted into translational energy (kinetic energy) and hence transformed into heat through collisions with the medium. The absorption of radiation can also lead to changes in the electron distribution and hence in the electronic state of the molecules. Transitions between rotational, vibrational and electronic states are quantified, and obey certain selection rules, which can be derived from quantum mechanics principles (*e.g.*, Steinfeld, 1978). These selection rules describe the ease with which transitions occur. It is common to refer to transitions as "forbidden" or "allowed". In practice, even highly "forbidden" transitions occur under certain circumstances, although much more slowly than "allowed" transitions. Therefore, we will refer to transitions here as "unfavorable" or "allowed".

The energy associated with transitions between electronic states is relatively large, of the order of electron-volts (eV), and the photons capable of inducing such transitions are generally in the ultraviolet and the visible. The energy associated with vibrational transitions is significantly smaller, and corresponds to the near-infrared (wavelengths of typically 10 μm). In the case of rotational transitions, the energy involved is even smaller, and corresponds to the far-infrared and microwave regions (wavelengths of the order of 10 mm).

Box 2.1 Some Useful Definitions
(Adapted from Ebbing, 1990)

Photon	Quantum of electromagnetic radiation with energy proportional to the observed frequency ν of the light: $E = h\nu$ (where h is Planck's constant).
Atom	An extremely small particle of matter that retains its identity during chemical reactions.
Nucleus	Central core of an atom containing one or more positive charges.
Proton	A particle found in the nucleus of an atom. Its electric charge is equal in magnitude, but opposite in sign, to that of an electron and its mass is 1836 times that of the electron.
Neutron	A particle found in the nucleus of an atom. Its mass is almost identical to that of a proton. It has no electric charge.

Box 2.1 (Continued)

Electron	A light particle (mass = 9.1096×10^{-31}kg) that carries a unit negative charge (1.6022×10^{-19}C) and exists in the region around the positively-charged nucleus.
Element	A substance that cannot be decomposed by any chemical reaction into simpler substances. A type of matter composed of one kind of atom.
Molecule	A group of atoms that are tightly connected by attractive forces (that are chemically bonded together).
Isomers	Compounds of the same molecular formula but with different arrangements of atoms.
Covalent Bond	A chemical bond formed by the sharing of a pair of electrons between atoms in a molecule.
Free Radical	Highly reactive species (*e.g.*, H, OH, NO, NO_3, Cl) with one or more unpaired electrons
Mole	The quantity of a given substance that contains as many molecules as the number of atom in exactly 12g of carbon –12. The amount of substance containing 6.0222137×10^{23} molecules.
Compound	A substance composed of two or more elements chemically combined in fixed proportions.
Ion	An electrically-charged particle obtained from an atom or a chemically-bonded group of atoms by adding or removing one or more electrons.
Plasma	An electrically neutral gas made up of ions and electrons.
Gas	The form of matter that is an easily compressible fluid.
Vapor	The gaseous state of matter.
Liquid	The form of matter that is a relatively incompressible fluid; it has a fixed volume, but no fixed shape.
Solid	The form of matter that is characterized by rigidity; it is relatively incompressible and has a fixed shape and volume.
Condensation	The changing of a gas to either the liquid or the solid state.
Vaporization	The changing of a solid or a liquid to the vapor state.
Sublimation	The changing of a solid to the vapor state.
Fusion	The changing of a solid to the liquid state.
Aerosols	Liquid droplets or solid particles dispersed throughout a gas.
Nucleation	The formation of particles in a supersaturated vapor (or in the air).
Coagulation	A process in which particles grow by collisions.
Diffusion	A process whereby a gas spreads out through another gas to occupy the space with uniform partial pressure.
Chemical Reaction	A change in which one or more kinds of matter are transformed into a new kind of matter or several new kinds of matter. It consists of the rearrangement of atoms present in the reacting substances to give new chemical combinations characterizing the substances formed by the reaction.

Box 2.1 (Continued)

Chemical Equilibrium	The state reached by a reaction mixture when the rate of forward reaction becomes equal to the rate of reverse reaction.
Exothermic Process	A chemical reaction or physical change in which heat is released.
Endothermic Process	A chemical reaction or physical change in which heat is absorbed.
Internal Energy (U)	The sum of the kinetic and the potential energies of the particles making up a system.
Enthalpy (H)	An extensive property of a substance that can be used to obtain the heat absorbed or released by a chemical reaction or physical change at constant pressure. It is defined as the sum of the internal energy (U) and the product of the pressure and the volume of the system (PV) H = U + PV.
Entropy (S)	A thermodynamic quantity that is a measure of the randomness or disorder of a system.
Free Energy (G)	A thermodynamic quantity defined by G = H – TS where H is the enthalpy, S the entropy, and T the absolute temperature.
Oxidation	A chemical reaction in which a compound or a radical loses electrons.
Reduction	A chemical reaction in which a compound or a radical gains electrons.
Catalyst	A substance that increases the rate of reaction without being consumed in the overall reaction.

Figure 2.1.a presents a typical potential energy diagram for a hypothetical diatomic molecule XY. The bond between the two atoms X and Y can be viewed as an oscillating spring, in which the internuclear distance varies with a frequency that is determined by the strength of the bond and the masses of the atoms. In the idealized case of a harmonic oscillator, the restoring force acting on the atoms is proportional to the displacement from the equilibrium position located at the minimum of the potential energy curve, which is represented by a parabola. Quantum mechanics (Schrödinger's equation solved for the harmonic oscillator) shows that, in this case, the vibrational energy is quantized with energy levels equally spaced. The corresponding quantum numbers v are equal to 0 (fundamental state), 1, 2, 3, etc. Transitions can only modify the energy level by one quantum at the time. The selection rule for the harmonic oscillator is therefore $\Delta v = \pm 1$. For a non-idealized oscillator, the curve representing the potential energy becomes asymmetric and is

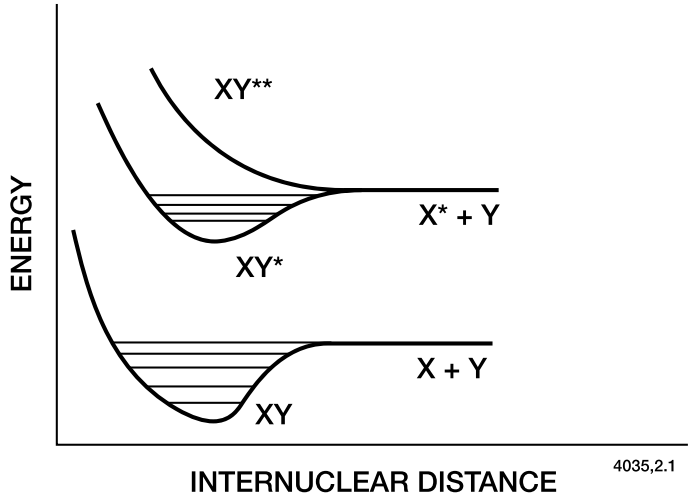

Figure 2.1.a. Typical potential energy diagram for a hypothetical diatomic molecule XY. The lower curve corresponds to an anharmonic oscillator, showing a strong repulsive branch for small internuclear distances and an attractive branch allowing, however, the dissociation of the molecule, when the molecular bond is stretched beyond a given internuclear distance. Electronic states corresponding to XY and XY* exhibit maximum stability at the minimum of the potential energy curve, so that this state represents a stable bound configuration of the molecule. In these bound states, vibrational levels (v=0, 1, 2, etc.) are represented by horizontal lines. Rotational levels are not shown. The electronically excited XY** state, represented by the uppermost curve, is repulsive for all values of the internuclear distance, and is thus unstable.

often called the Morse curve (see Figure 2.1.a). The potential energy increases sharply towards smaller internuclear distances, as charge repulsion becomes more intense. For large internuclear distances, the molecular bond is stretched and can break; in this case, the molecule dissociates. In the non-idealized case, weak overtone transitions with $\Delta v = \pm 2, \pm 3$, etc. are possible and the vibrational energy levels are not equidistant anymore, but are more closely spaced with increasing quantum number v. Note, in addition, that vibrational transitions occur only if the electric field of the radiation can interact with an oscillating electric field produced by the dipole moment of the vibrating molecule. Only heteronuclear diatomic molecules such as NO or CO produce such an oscillating dipole moment, while homonuclear species like O_2 and N_2 do not undergo vibrational transitions. Since the energy corresponding to a vibrational transition is relatively large compared to the thermal energy, most molecules present in the atmosphere are found to be in their lowest vibrational state ($v = 0$). Vibrationally excited species can be produced by photon absorption, collision with an atom or a

molecule, or as a result of a chemical reaction (see *e.g.*, reaction 2.95). De-excitation can result from a collision or from spontaneous radiative emission from level u to level ℓ. The probability of this latter process is provided by the Einstein coefficient $A_{u,\ell}$, whose value is determined in the laboratory. Vibrational energy transitions play a particularly important role in the thermal balance of the middle atmosphere, because they are the fundamental processes responsible for most of the infrared cooling occurring there (see Chapter 4).

Diatomic molecules with a permanent dipole moment (*i.e.*, heteronuclear molecules) produce an oscillating electric field during their rotation, resulting in light absorption and rotational transitions. These transitions occur between quantified energy levels (with the corresponding quantum numbers J equal to 0, 1, 2, 3, etc.). In the case of an idealized rigid rotor, the selection rule for such transitions is given by $\Delta J = \pm 1$. Since the energy corresponding to rotational transitions is small compared to that of vibrational transitions, and to the thermal energy of the molecules, the population of the rotational energy is not confined to the fundamental state, but is generally significant for levels above $J = 0$.

Since molecules vibrate and rotate simultaneously, combined vibration-rotation transitions (and spectra) need to be considered. In the idealized harmonic oscillator, rigid rotor case, the only significant processes to be considered are the transitions between vibrational level $v = 0$ and level $v = 1$, together with a number of rotational transitions. An example of such system is shown in Figure 2.1.b. The intensity of the corresponding lines observed in the absorption spectra reflects the relative population of the rotational energy levels. The transitions associated with the selection rule $\Delta J = +1$ (*i.e.*, found on the high energy side of the spectrum) produce the so-called R branch, while the transitions associated with $\Delta J = -1$ (low energy side of the spectrum) lead to the so-called P branch.

In the case of polyatomic molecules, such as CO_2, H_2O, O_3, etc., the principles discussed above still apply, but the spectra become more complex. Polyatomic molecules do not rotate only about one single axis, but about three mutually perpendicular axes. In addition, the number of vibrational degrees of freedom is also increased.

Vibrational quanta are distributed among the available vibrational modes of the molecule, which correspond physically to stretching and bending the chemical bonds of the molecule. These are conventionally referred to as ν_1, ν_2, etc.

Figure 2.2 presents a schematic diagram of the possible vibrational modes for diatomic, linear triatomic, and bent triatomic molecules. The vibrational term symbol provides an ordered list of quantum numbers

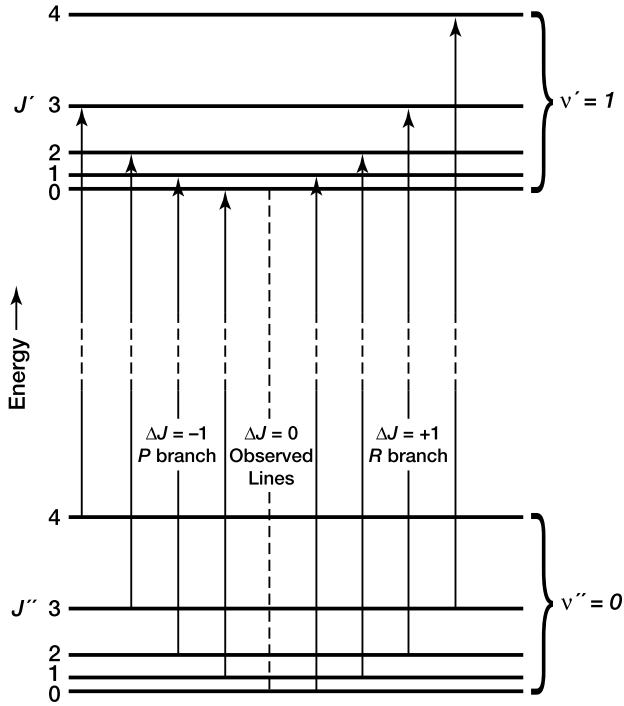

Figure 2.1.b. Schematic diagram of the energy levels and vibration-rotation transitions (after Herzberg, 1950). The lower lines ($v'' = 0$) correspond to the fundamental vibrational state with different rotational states ($J'' = 0, 1, 2, 3, 4$). The first vibrationally excited state ($v' = 1$) with related rotational states ($J' = 0$ to 4) are shown by the upper lines. The transitions corresponding to the P and R branches are indicated. Transition $\Delta J = 0$ is not allowed in the case of the idealized rigid rotor, harmonic oscillator for a linear molecule, but can be observed (Q-branch) in other cases. The notations are from Herzberg (1950).

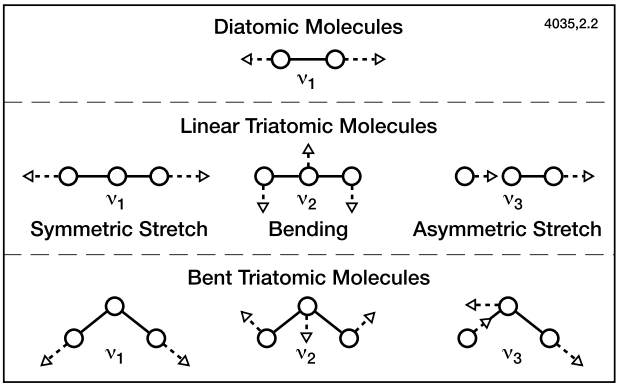

Figure 2.2. Vibrational modes of diatomic and triatomic molecules.

for each mode. For example, (010) means that the quantum number is zero for ν_1, one for ν_2 and zero for ν_3. As we shall see in Chapter 4, the 15μm ν_2 band of CO_2 plays a dominant role in cooling throughout the middle atmosphere.

The absorption of visible and ultraviolet radiation can lead to electronic transitions. The curves labelled XY^* and XY^{**} in Figure 2.1.a correspond to electronically excited states of the hypothetical molecule XY considered earlier. Electronically excited states may be repulsive at any internuclear distance (as in the case of XY^{**}), or may have a stable bound configuration (XY^*) like the ground state, with associated vibrational and rotational levels. If an electronic transition occurs along with simultaneous vibrational and rotational transitions, the selection rules are not as restricted as those described above. Transitions from the fundamental vibrational level v = 0 to high levels (v > 1) becomes possible. Rotational transitions with unchanged quantum number J (ΔJ = 0) are observed and produce a Q-branch in the corresponding spectrum.

The electronic states of molecules and atoms are expressed by quantum numbers, which represent the total orbital angular momentum and the net spin of the electrons. The corresponding symbols and the selection rules for electronic transitions are discussed in Sections 2.2.1 and 2.2.2, respectively. Different electronic configurations of the same particle generally have very different reactive properties; for example, the excited O^1D atom behaves very differently upon collision with a water molecule than does the ground O^3P atom. Photochemical processes involving absorption and emission of photons induce transitions from one state to another, and these occur more readily between certain electronic states than others. The transitions between electronic states, which result from absorption of relatively high energy photons, serve two important purposes in the middle atmosphere. They represent the major source of heating, as will be discussed in Chapter 4, and they initiate photochemical processes (*e.g.*, photodecomposition or *photolysis* and photoionization) which play a major role in establishing the distributions of minor constituents (this is described in detail in Chapters 5 and 7).

2.2.1 Term Symbols

In general, term symbols indicate both spin angular momentum (S for atoms, Σ for diatomic molecules) and orbital angular momentum (L for atoms, Λ for diatomic molecules). The term symbol is written ^{2S+1}L for atoms and $^{2\Sigma+1}\Lambda$ for molecules. We will not concern ourselves here

with the derivation of L and Λ. Part of the reason for this is the fact that the selection rules involving orbital angular momentum are often not strictly followed in actual transitions; the restrictions regarding spin are the ones which tend to be most rigidly followed in practice, and we shall concentrate only on these. For increasing L from 0 to 6, the term takes on the values S, P, D, F, G, H. For increasing Λ, the Greek symbols Σ, Π, Δ, and Φ are used. See, for example, Karplus and Porter (1970).

The spin terms can be readily evaluated given knowledge of basic atomic and molecular orbital theory (see Moore, 1962; Karplus and Porter, 1970). The ground state of the oxygen atom is conventionally described as

$$(1s)^2(2s)^2(2p_1)^2(2p_2)^1(2p_3)^1$$

The superscripts denote the number of electrons in each atomic orbital. Electrons must be paired (*i.e.*, of equal and opposite spin) in atomic orbitals containing two electrons. Paired electrons do not contribute to the atomic or molecular spin angular momentum. Hund's rule of maximum multiplicity states that in the lowest energy configuration, the electrons must be spread over as many available orbitals of equal energy as possible, in order to maximize the spin multiplicity. Since three 2p orbitals are available in which 4 electrons must be distributed, the lowest electronic state therefore has two unpaired electrons in each of two 2p orbitals. Each unpaired electron contributes $\frac{1}{2}$ to the spin angular momentum. Thus $2S + 1 = 3$ for the oxygen atom, and the term symbol is ^3P.

The oxygen molecule has the ground configuration

$$(\sigma_g 1s)^2(\sigma_u 1s)^2(\sigma_g 2s)^2(\sigma_u 2s)^2(\sigma_g 2p)^2(\pi_u 2p)^4(\pi_g 2p)^2$$

The two $\pi_g 2p$ electrons are unpaired, so that $2\Sigma + 1 = 3$, and the ground state is $X^3\Sigma_g^-$. The X is used to denote that this is the ground state of the molecule; first and second excited states are indicated by A, B, or a, b, etc. The subscripts "g" (from the German "gerade" = even) and "u" ("ungerade" = uneven) used for homonuclear diatomic molecules (*e.g.*, O_2) refer to cases where the wavefunction representing the molecular state keeps the same sign or changes sign, respectively, through the center of symmetry of the molecule. The superscripts "+" and "–" apply only to Σ states. Symbol "+" is used when the wavefunction is unaltered by reflection through a plane passing through the 2 nuclei of the molecule. Symbol "–" is used if the wavefunction changes sign. More details regarding the significance of the term symbols can be obtained, for example, in Herzberg (1950).

Polyatomic molecules have different term symbols, but again the spin multiplicity is given by the left-hand superscript. For example, the ground state of the ozone molecule is denoted by the term $^1A_1$. Note that these terms should not be confused with the excited states of diatomic molecules, which can also contain A, B, etc. in their term symbols.

2.2.2 Selection Rules for Electronic Radiative Processes

The importance of the term symbols lies in their use in predicting the ease with which photon absorption

$$A + h\nu \rightarrow A^* \tag{2.1}$$

and radiative decay can occur.

$$A^* \rightarrow A + h\nu \tag{2.2}$$

The selection rules for radiative processes permit us to evaluate the ease or difficulty with which a particular transition can proceed. The basic rules are as follows:

* Spin is unchanged in an allowed transition, for both atoms and molecules. This is generally the most important consideration in establishing the transition probability.
* L or Λ changes of 1 or zero are allowed, except in the case of atoms if $0 \rightarrow 0$ ($S \rightarrow S$). Changes of L or Λ of more than one (*i.e.*, $D \rightarrow S$) are unfavorable.
* For molecules with g and u subscripts, $g \rightarrow u$ transitions are allowed, but $u \rightarrow u$ or $g \rightarrow g$ transitions are difficult.
* For Σ states, $\Sigma^+ \rightarrow \Sigma^+$ and $\Sigma^- \rightarrow \Sigma^-$ transitions are allowed, while $\Sigma^+ \rightarrow \Sigma^-$ transitions are unfavorable.

Examples of transitions which are of importance in the middle atmosphere are, for example,

$$O_2\,(^1\Delta_g) \rightarrow O_2\,(^3\Sigma_g^-) + h\nu \tag{2.3}$$

This process is unfavorable because it involves a change in spin, a change in Λ of two, and a $g \rightarrow g$ transition. Thus its probability is relatively low, which is reflected in a time constant for radiative decay of almost an hour. Similarly, the cross section for production of O_2 $(^1\Delta_g)$ by photon absorption from the ground state

$$O_2\,(^3\Sigma_g^-) + h\nu \rightarrow O_2\,(^1\Delta_g) \tag{2.4}$$

is small.

2.3 Thermodynamic Considerations

2.3.1 Enthalpy, Entropy, and Free Energy

The basic principles governing the reactivity of chemical substances lie in the thermodynamic properties of these species. In order to evaluate the feasibility of chemical processes, the enthalpy of reaction must be examined. The *enthalpy* of formation of chemical constituents or "heat content" represents the energy required to make and break the chemical bonds which compose that substance, starting only from the elements in their most stable form (*e.g.*, O_2, N_2, S, etc.), which are conventionally assigned an enthalpy of formation of zero. Consider, for example, the formation of two ground state oxygen atoms, starting from an oxygen molecule. The energy required to break the O_2 bond is about 120 kcal/mole at room temperature, so that the enthalpy of formation of each atom is about 60 kcal/mole (see Table 2.1). Let us examine a general reaction:

$$A + B \rightarrow C + D \tag{2.5}$$

The enthalpy change associated with such a reaction is given by the difference between the enthalpy of formation of the products and the enthalpy of formation of the reactants:

$$\Delta H^0_R = \Delta H^0_f(C) + \Delta H^0_f(D) - \Delta H^0_f(A) - \Delta H^0_f(B) \tag{2.6}$$

where the superscript 0 refers to the standard state, which is 298.15 K by convention. If ΔH^0_R is negative, heat is liberated by the reaction, and it is called *exothermic.* If ΔH^0_R is positive, heat must be supplied in order for the reaction to proceed, and it is then called *endothermic.* Exothermic reactions can proceed spontaneously in the atmosphere, while endothermic processes require additional energy, and this necessary external energy may not be available. Exothermic reactions may nevertheless be non-spontaneous.

It must be noted that ΔH is a function of temperature. Tabulations of ΔH generally refer to $\Delta H_{298.15K}$. The temperature dependence of ΔH is given by

$$\Delta H_T = \Delta H^0_{298.15K} + \int_{298.15K}^{T} C_p dT \tag{2.7}$$

where T is the temperature and C_p is the heat capacity at constant pressure (cal/deg mol). This correction is generally small over the range of atmospheric temperatures so that the tabulated values can be applied as a first approximation.

Entropy may also influence the spontaneity of chemical reactions. In general terms the entropy represents the disorder or randomness associated with a particular process. The *Gibbs free energy* of reaction includes both the enthalpy and entropy associated with chemical processes, and is defined as

$$\Delta G^0 = \Delta H^0 - T\Delta S^0 \tag{2.8}$$

and the ΔG^0_R is defined similarly to ΔH^0_R:

$$\Delta G^0_R = \Delta G^0_f(C) + \Delta G^0_f(D) - \Delta G^0_f(A) - \Delta G^0_f(B) \tag{2.9}$$

In the case of an elementary reaction (*i.e.*, reaction without energy barrier associated with the formation of an intermediate complex), if ΔG^0_R is negative, then the reaction can proceed spontaneously at the temperature under consideration. Values of ΔG^0, ΔH^0, S^0 and C^0_p for most atmospheric species can be found in chemical handbooks.

One of the most important uses of thermodynamic data is the evaluation of the feasibility of proposed chemical reactions, which have perhaps never been studied in the laboratory. Let us imagine, for example, that the reaction of NO_3 with H_2O might be an important source of HNO_3:

$$NO_3 + H_2O \rightarrow HNO_3 + OH \tag{2.10}$$

Is this reaction possible? This question can be answered immediately by examining the Gibbs free energy of reaction:

$$\Delta G^0_R = \Delta G^0_{HNO_3} + \Delta G^0_{OH} - \Delta G^0_{NO_3} - \Delta G^0_{H_2O} \tag{2.11}$$

which equals +17.8 kcal/mole. Therefore, the reaction is thermodynamically impossible without an external source of energy; we need not await laboratory studies to rule out the possibility of its occurrence in the atmosphere.

Another important use of thermodynamic data in atmospheric applications is the evaluation of the exothermicity of chemical reactions which may play a role in the thermal budget of the atmosphere. Consider, for example, the addition of atomic oxygen to molecular oxygen:

$$O + O_2 + M \rightarrow O_3 + M \tag{2.12}$$

where M can be any arbitrary atom or molecule (see the discussion of termolecular reactions below). We may write

$$\begin{aligned} \Delta H^0_R &= \Delta H^0_{O_3} + \Delta H^0_M - \Delta H^0_O - \Delta H^0_{O_2} - \Delta H^0_M \\ \Delta H^0_R &= \Delta H^0_{O_3} - \Delta H^0_O \end{aligned} \tag{2.13}$$

Adopting numerical values from thermodynamic tables, one finds ΔH^0_R = 34.1 – 59.5 = –25.4. Thus this reaction is exothermic, liberating

25.4 kcal per mole. We shall see later in Chapter 4 that this process can serve as an important source of heat in the upper part of the middle atmosphere.

An endothermic reaction can proceed if the required energy is provided by some external source, such as a photon. The energy of a photon of wavelength λ is given by

$$\mathrm{E} = \frac{\mathrm{hc}}{\lambda} \tag{2.14}$$

where $\mathrm{h} = 6.62 \times 10^{-34}\mathrm{J}s$ is Planck's constant, and $\mathrm{c} = 2.998 \times 10^{8}$ m s^{-1} is the speed of light in a vacuum. Other commonly used units are the frequency, ν, which is related to λ by

$$\nu = \frac{\mathrm{c}}{\lambda} \tag{2.15}$$

and the wavenumber $\bar{\nu}$, given by

$$\bar{\nu} = \frac{1}{\lambda} = \frac{\nu}{\mathrm{c}} \tag{2.16}$$

Thus consider, for example, for the photolysis of molecular oxygen to form two $\mathrm{O}^3\mathrm{P}$ atoms:

$$\mathrm{O_2} + \mathrm{h}\nu \rightarrow 2\mathrm{O}(^3\mathrm{P}) \tag{2.17}$$

$$\Delta\mathrm{H_R} = 2(59.55) - \frac{\mathrm{hc}}{\lambda} = 119.10 \text{ kcal/mole} - \frac{\mathrm{hc}}{\lambda} \tag{2.18}$$

This process requires that at least 119.10 kcal/mole, or 8.27×10^{-19}J/molecule, be provided by the photon. This corresponds to a wavelength $\lambda \leq 240$ nm.

2.3.2 Solubility of Gases in Liquid Particles

The atmosphere is not only a mixture of gases. It also contains a variety of tiny liquid or solid particles, commonly referred to as *aerosols*. Atmospheric particulate matter may consist of a large variety of species; in the lower stratosphere, however, the most abundant aerosol particles are composed of highly concentrated aqueous sulfuric acid droplets. In polar regions during winter, very sparse clouds, called *polar stratospheric clouds* (PSCs) are also observed.

The chemical composition of stratospheric particles at a given altitude is governed by local thermodynamic conditions, and specifically is a complex function of temperature and water vapor concentration. The solubility of gas-phase compounds into liquid aerosol particles

$$\mathrm{X(gas)} \rightleftharpoons \mathrm{X(aqueous)} \tag{2.19}$$

is governed by an equilibrium usually expressed as

$$\mathcal{H}_x = \frac{[\mathrm{X(aqueous)}]}{p_x} \tag{2.20}$$

where [X(aqueous)] is the concentration (moles per liter) of X dissolved in the aqueous phase and p_x (atm) is the partial pressure of X in the gas-phase. The equilibrium constant $\mathcal{H}_x$ is called *Henry's law constant* and is usually expressed in M atm^{-1}, where M (= mole/ℓ) is the molarity. Henry's law constants are measured in the laboratory for different temperatures. It can be shown that the solubility of gases increases with decreasing temperature. If a dissolved compound dissociates in water (*e.g.*, acids), the total solubility of the gas is increased above what would result from the physical solubility alone. In this case, the solubility is usually expressed as an *effective* Henry's law constant which varies with the pH of the solution and the equilibrium constants associated with the dissociation mechanisms involved.

2.4 Elementary Chemical Kinetics

The preceding section describes the thermodynamics associated with determining whether a reaction can proceed spontaneously at a given temperature. The next question one might wish to pose is how fast such a reaction will occur. That is the concern of chemical kinetics. The concentrations of almost all atmospheric chemical species depend critically on reaction kinetics, which determines the rates at which these constituents are produced or destroyed. The observed density of most chemical species in the atmosphere is dependent on the balance between the rates of photochemical production and destruction, and the rate of atmospheric transport processes. The rate at which a chemical reaction occurs varies considerably from one reaction to another and must be determined in the laboratory. For a reaction between species A, B, C, ..., expressed as

$$\mathrm{aA} + \mathrm{bB} + \mathrm{cC} + \ldots \rightarrow \mathrm{mM} + \mathrm{nN} + \ldots \tag{2.21}$$

where coefficients a, b, c, etc. are the smallest possible integers that provide the correct stoichiometry, the reaction rate R can be expressed by the general expression

$$\mathrm{R} = \mathrm{f}\left[(\mathrm{A}), (\mathrm{B}), (\mathrm{C}), \ldots\right] \tag{2.22}$$

where (A) represents the concentration of species A. As shown by experimental studies, this function may be complex, but may often be of the form

$$\mathrm{R} = \mathrm{k}(\mathrm{A})^{\alpha}(\mathrm{B})^{\beta}(\mathrm{C})^{\gamma}\ldots \tag{2.23}$$

where k is the *rate coefficient* or *rate constant* for this particular reaction. For many chemical processes, factor k varies with temperature. Exponents $\alpha, \beta, \gamma \ldots$ are independent of concentration and time, and are referred to as the *order* of the reaction with respect to reactants A, B, C, ..., respectively. The *overall order* of the reaction is given by the sum $\alpha + \beta + \gamma + \ldots$ Note that $\alpha, \beta, \gamma, \ldots$ are not always the stoichoimetric coefficients a, b, c, ... as shown by laboratory experiments. Different experimental methods have been developed to derive reaction rates, but will not be presented here. The parameters describing the kinetics of the reactions are generally derived by measuring the concentration of the reactants or products as a function of time. The rate of change of a reactant or of a product is related to the rate of reaction R (molec $cm^{-3}s^{-1}$) by

$$R = -\frac{1}{a}\frac{d(A)}{dt} = -\frac{1}{b}\frac{d(B)}{dt} = \ldots = \frac{1}{m}\frac{d(M)}{dt} = \frac{1}{n}\frac{d(N)}{dt} + \ldots \qquad (2.24)$$

For example, for reaction

$$(k); \qquad O + O \rightarrow O_2$$

where k is the corresponding rate constant, the reaction rate is $R = k(O)^2$ and the changes with time in the concentration of O and O_2 are given by

$$\frac{d(O)}{dt} = -2k(O)^2 \qquad (2.25a)$$

$$\frac{d(O_2)}{dt} = k(O)^2 \qquad (2.25b)$$

Reactions involving decomposition of a single particle are called *first order* or *unimolecular*; reactions involving the collision between two particles are *second order, two body*, or *bimolecular*; processes involving the collision between three particles are referred to as *third order, three body*, or *termolecular*.

For the special case of a unimolecular (first order) process:

$$(k_u); \qquad A \rightarrow C + D \qquad (2.26)$$

the rate is given by

$$R = -\frac{d(A)}{dt} = k_u(A) \qquad (2.27a)$$

where k_u is the reaction rate constant (expressed in s^{-1} for a unimolecular process) and (A) denotes the concentration of species A (molec cm^{-3}). Rearranging this equation, we can write

$$\frac{d(A)}{(A)} = -k_u\, dt \qquad (2.27b)$$

or

$$\ln(\mathrm{A}) = -\mathrm{k_u}\,\mathrm{t} + \mathrm{C} \tag{2.27c}$$

where C is the constant of integration. Assuming that initially $(\mathrm{A}) = (\mathrm{A})_\mathrm{o}$ at time $\mathrm{t} = 0$, the evolution with time of number density (A) can be expressed as

$$(\mathrm{A}) = (\mathrm{A})_\mathrm{o}\, \mathrm{e}^{-\mathrm{k_u}\,\mathrm{t}} \tag{2.27d}$$

The time required for the concentration of A to decrease to 1/e of its initial value, if this were the only reaction process occurring, is therefore equal to $1/\mathrm{k_u}$. This defines the *chemical lifetime* (or *e-folding lifetime*) of species A. The concept of lifetime is an important one in atmospheric applications. If, for example, we wish to know whether an atmospheric species is likely to be directly affected by transport processes, we can compare its chemical lifetime to the time scale appropriate to transport. If chemistry is much faster than transport for that particular species, then the direct effects of transport can be neglected to a first approximation. This will be discussed in more detail in Chapters 3 and 5.

Referring to the general bimolecular equation A + B → products, the rate at which such a reaction proceeds is described by

$$\mathrm{R} = -\frac{\mathrm{d(A)}}{\mathrm{dt}} = -\frac{\mathrm{d(B)}}{\mathrm{dt}} = \mathrm{k_b(A)\,(B)} \tag{2.28}$$

where $\mathrm{k_b}$ represents the reaction rate constant (expressed in $\mathrm{cm^3\ molec^{-1}s^{-1}}$ for a two body reaction).

In the case of a termolecular process

$$\mathrm{A + B + C \rightarrow products} \tag{2.29}$$

the reaction rate is expressed as

$$\mathrm{R} = -\frac{\mathrm{d(A)}}{\mathrm{dt}} = \mathrm{k_t(A)(B)(C)} \tag{2.30}$$

where the rate coefficient is now expressed in $\mathrm{cm^6 molec^{-2} s^{-1}}$. Very often, one of the reactants is not directly involved in forming the reaction products, but assists in promoting the reaction by transferring energy through collisions with the other reactants. This reactant, conveniently termed M, is called the *third body* and in most cases represents an $\mathrm{O_2}$ or $\mathrm{N_2}$ molecule.

Second and third order reactions (A + B → products and A + B + C → products are commonly reduced to a pseudo first order form to examine the chemical lifetime. For example,

$$(\mathrm{A}) \approx (\mathrm{A})_\mathrm{o}\, \mathrm{e}^{-\mathrm{k_b(B)t}} \text{ or } (\mathrm{A}) \approx (\mathrm{A})_\mathrm{o}\, \mathrm{e}^{-\mathrm{k_t(B)(C)t}} \tag{2.31}$$

and the lifetime is:

$$\tau_A = \frac{1}{k_b(B)} \text{ or } \frac{1}{k_t(B)(C)} \ . \tag{2.32}$$

These expressions can be used only if the concentrations of species B and C can be considered constant over the time τ_A. This is not always the case, since B and C may also be undergoing production and destruction reactions that introduce a time dependence in their densities over the time τ_A.

In a system like the atmosphere, in which numerous gases are interacting simultaneously, chemical change usually occurs through a network of interacting steps (*reaction mechanism*). In this case, examination of the lifetime and the rate of change of a species (*e.g.*, species A) must involve the sum of all of its possible production and loss processes, *i.e.*, assume the following reactions

$$(k_1); \qquad A + B \rightarrow \text{Products} \tag{2.33a}$$

$$(k_2); \qquad A + C + M \rightarrow \text{Products} \tag{2.33b}$$

$$(k_3); \qquad A + F \rightarrow \text{Products} \tag{2.33c}$$

$$(k_4); \qquad G + H \rightarrow A + \text{Products} \tag{2.33d}$$

$$\frac{d(A)}{dt} = -k_1(A)(B) - k_2(A)(C)(M) - k_3(A)(F) + k_4(G)(H) \tag{2.34}$$

$$\tau_A = \frac{1}{k_1(B) + k_2(C)(M) + k_3(F)} \tag{2.35}$$

If this lifetime is short compared to transport times and if the densities of B, C, F, G, and H are not changing over the time scale considered, then photochemical stationary state (also called *steady state*) can be assumed; this implies that A is in instantaneous balance as determined by its sources ($\sum_i P_i$) and sinks ($\sum_i L_i$):

$$\frac{d(A)}{dt} = 0 = \sum_i P_i - \sum_i L_i(A) \tag{2.36}$$

$$(A) = \frac{\sum_i P_i}{\sum_i L_i} \tag{2.37}$$

In the particular case described by mechanism (2.33),

$$(A) = \frac{k_4(G)(H)}{k_1(B) + k_2(C)(M) + k_3(F)} \tag{2.38}$$

In some cases, the effective rate of a reaction can be increased by a so-called catalytic cycle of intermediate reactions. Such a cycle is

initiated by a substance that is not consumed in the overall process, but is constantly regenerated. This is the case, for example, for the destruction of ozone

$$O_3 + O \rightarrow 2\ O_2 \tag{2.39}$$

which is accelerated in the presence of a catalytic agent X (which can be H, OH, NO, Cl, Br) through the following *catalytic cycle*

$$\begin{array}{rll} X + O_3 & \rightarrow XO + O_2 & (2.40a) \\ XO + O & \rightarrow\ X + O_2 & (2.40b) \\ \hline \text{Overall:}\quad O_3 + O & \rightarrow\quad 2\ O_2 & \end{array}$$

Other cycles including more than two reactions are known to destroy ozone efficiently (see Chapter 5). Catalytic cycles can be very efficient, even if the concentration of the catalyst X is several orders of magnitude smaller than that of ozone. The efficiency of such a cycle regarding the destruction of ozone is given by the number of times the cycle repeats itself before the catalyst is eventually lost, usually by conversion to a stable reservoir species (*e.g.*, NO and NO_2 are converted into HNO_3). The *rate limiting step* for the destruction of ozone in a cycle like (2.40) is provided by the reaction that ultimately determines the rate at which ozone is destroyed. Such a step can be identified, provided that all reactions involved are known.

2.4.1 Collision Theory of Bimolecular Reactions

Simple collision theory provides a useful conceptual framework to understand two body reactions. It cannot be applied to first and third order reactions without considerable modifications.

Let us again examine the reaction of A and B. Clearly the reaction cannot occur more rapidly than the rate at which A and B collide. If we assume that the particles behave as hard spheres, then the collision rate constant between these two particles is defined by

$$k_{AB} = \sigma v_r \tag{2.41}$$

where σ is the collision cross section and v_r is the relative particle speed (thermal velocity). In the hard sphere approximation, the collision cross section is given by

$$\sigma = \pi\ (r_A + r_B)^2 \tag{2.42}$$

where r_A and r_B are the radii of particles A and B. For typical molecular radii, the value of σ is about 10^{-15}cm^2. The mean relative speed, v_r is

$$v_r = \left(\frac{8kT\,(m_A + m_B)}{\pi m_A m_B} \right)^{\frac{1}{2}} \tag{2.43a}$$

where m_A and m_B are the respective molecular masses of A and B, and k is Boltzmann's constant. For typical masses, the mean relative speed is about $4 \times 10^4 \text{cm s}^{-1}$, and the value of k_{AB} is about $4 \times 10^{-11} \text{cm}^3 \text{molec}^{-1} \text{s}^{-1}$. We can also see that the temperature dependence of the rate constant thus defined is $T^{\frac{1}{2}}$. Note that if the mass of one of the colliding particles is much larger than that of the other particle (*e.g.*, $m_B \gg m_A$), the velocity v_r can be approximated as

$$v_r = \left[\frac{8kT}{\pi\, m_A} \right]^{\frac{1}{2}} \tag{2.43b}$$

This expression is typically used to describe the collisions between molecules (mass m_A) with aerosol particles (mass m_B).

Unfortunately, the actual interactions between reacting gases are considerably more complex than this and not all two-body rate constants are equal to 4×10^{-11} (in fact few of them do conform to this simple description). The reasons for this lie in the differences between the actual interactions between reacting molecules and the "hard sphere" assumption made above. In general, particles form an intermediate species during reaction, and this intermediate is often called an *activated complex*. Indeed, several detailed theories of chemical interactions achieve successful descriptions of certain processes simply by considering the energy modes available to the activated complex (*e.g.*, RRK theory, see Rice and Ramsperger, 1927; Weston and Schwarz, 1972). Here we simply note that formation of such a complex generally involves an enthalpy of reaction, such that the overall process can be crudely represented as shown in Figure 2.3. In general, a certain "*energy of activation*" is associated with forming the activated complex. If the reactants have sufficient energy to surmount the barrier involved in complex formation, then products will be formed.

The energy distribution of particles is often expressed as a Maxwell-Boltzmann distribution:

$$\frac{dn^*}{n_o} = 4\pi \left(\frac{m}{2\pi kT} \right)^{3/2} c^2\, e^{-(mc^2/2 + \epsilon_p)/kT}\, dc \tag{2.44}$$

(see, *e.g.*, Castellan, 1971) where ϵ_p is the potential energy of the particle, and where dn^* is the number of particles per cubic centimeter, which have velocities from c to c + dc, and m is the particle mass. Here k is the Boltzmann constant. The exponential term accounts for both the kinetic and potential energies of the particle. For a given potential energy, the kinetic energy distribution depends only on temperature T.

Given the form of this expression and the reaction barrier discussed above, it is not surprising that the experimentally derived kinetic rate expression for many processes is:

$$k_{reaction} = A\, e^{(-E_{act}/RT)} \tag{2.45}$$

In this expression, called the Arrhenius equation, E_{act} represents the activation energy, R is the gas constant, and A is the "pre-exponential" factor (assumed to be constant over a limited temperature range). In this case, we would then expect the exponential term to denote the fraction of colliding molecules which have the energy required to surmount the barrier, while A represents roughly the collision rate constant, k_{AB} as presented in Equation (2.41). Once again, we find experimentally that this is not always the case. One simple explanation for this is that only certain orientations are conducive to reactions, especially for complex molecules. Thus we can introduce a "steric factor" to represent the probability that the molecules will be in the proper geometric arrangement when they collide. Finally, another area of possible failure in the hard sphere model lies in the true nature of the approaching particles: They are not hard spheres, rather, they exert attractive forces on one another. In the case of ion-molecule reactions, the attractive forces are coulombic, and exert an influence even at relatively large distances. Therefore these reactions often proceed very much faster than values derived from simple hard sphere collision theory. Even for neutral unpolarized molecules, London forces produce an interaction potential. Thus the interactions between particles become multi-dimensional and quite complex. Molecular scattering experiments, in which reaction kinetics are examined as functions of energy and orientation, have led to considerable progress in our study of these processes. See, for example, Johnston (1966), Weston and Schwarz (1972) and Smith (1980).

2.4.2 Unimolecular Reactions

The special case of a unimolecular reaction

$$(k_u); \qquad A \rightarrow B + C \tag{2.46}$$

deserves a brief discussion. Under what circumstances does a molecule decompose into its constituent parts? Clearly this type of process cannot be understood in the context of collision theory as discussed above for bimolecular processes.

The first successful theory of unimolecular reactions (2.46) was proposed by Lindemann in 1922. He introduced the idea that apparently unimolecular reactions were really the result of the following processes:

$$(k_{act}); \qquad A + M \rightarrow A^* + M \text{ activation} \tag{2.47a}$$

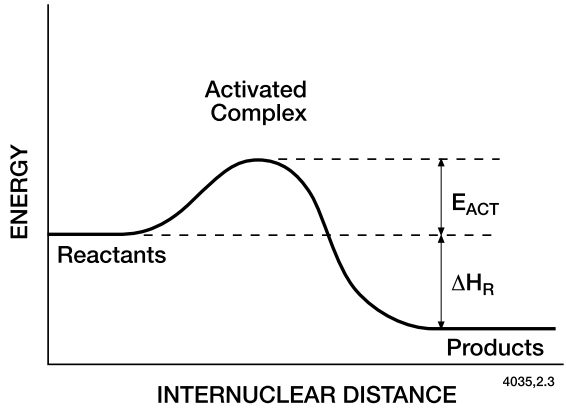

Figure 2.3. Enthalpy variation during an exothermic reaction. E_{ACT} represents the activation energy of the reaction and ΔH_R the enthalpy or heat released by the reaction.

$$(k_d); \qquad A^* + M \rightarrow A + M \text{ deactivation} \tag{2.47b}$$

$$(k_r); \qquad A^* \rightarrow B + C \text{ reaction of energized molecule} \tag{2.47c}$$

The rate of decomposition of A (which is equal to the rate of formation of B or C) is

$$-\left(\frac{d(A)}{dt}\right) = k_r(A^*) \tag{2.48}$$

The steady state concentration of A^* is derived as follows:

$$\frac{d(A^*)}{dt} = 0 = k_{act}(A)(M) - [k_d(M) + k_r]\,(A^*) \tag{2.49}$$

$$(A^*) = \frac{k_{act}(A)(M)}{k_r + k_d(M)} \tag{2.50}$$

so that

$$\frac{d(A)}{dt} = -\left(k_r \frac{k_{act}(A)(M)}{k_r + k_d(M)}\right) \tag{2.51}$$

and the effective first order reaction rate k_u (sec^{-1}) is given by

$$k_u = k_{act}(M)\ \frac{k_r}{k_r + k_d(M)} \tag{2.52}$$

Thus A is conceived to be transformed to an "energized" state, A^*, by collision. A^* can then be deactivated by collision, or it may decompose. At sufficiently high pressures (high pressure limit), the rate of deactivation is much greater than the rate of decomposition; the rate limiting step is then Equation (2.47*c*) and the reaction will be found to

be independent of pressure.

$$k_d(M) >> k_r; \qquad \frac{d(A)}{dt} = -k_r \frac{k_{act}(A)}{k_d} \tag{2.53}$$

At very low pressures (low pressure limit), the observed rate is proportional to the pressure, since the rate limiting step is given by the production of the energized molecules by Equation (2.47*a*).

$$k_d(M) << k_r; \qquad \frac{d(A)}{dt} = -k_{act}(A)(M) \tag{2.54}$$

Between these two extremes, the reaction is neither first nor second order, and the pressure dependence must be carefully parameterized. The thermal decomposition of N_2O_5,

$$N_2O_5 \rightarrow NO_2 + NO_3 \tag{2.55}$$

is an important stratospheric reaction which is of intermediate order at stratospheric pressures.

2.4.3 Termolecular Reactions

Reactions involving three particles

$$(k_t); \qquad A + B + M \rightarrow C + M \tag{2.56}$$

do not generally occur via a single collision involving all three particles at once; indeed, the probability of such an event is quite small. In general a termolecular reaction can be understood in the context of activated complex theory as discussed earlier. The initial step involves an interaction of two particles:

$$(k_{act}); \qquad A + B \rightarrow C^* \tag{2.57a}$$

which must be followed by deactivation

$$(k_d); \qquad C^* + M \rightarrow C + M \tag{2.57b}$$

in order that the energized molecule not decompose back to reactants:

$$(k_{uni}); \qquad C^* \rightarrow A + B \tag{2.57c}$$

Thus this type of process is the reverse of unimolecular decay. The rate of formation of the product, C, is given by

$$\frac{d(C)}{dt} = k_d(M)(C^*) = k_d(M)\frac{k_{act}(A)(B)}{k_d(M) + k_{uni}} \tag{2.58}$$

(in which steady state is assumed for C^* as shown above). Thus, the effective rate constant can be expressed in terms of the elementary steps

$$k_t = k_{act}\ \frac{k_d(M)}{k_d(M) + k_{uni}} \tag{2.59}$$

If $k_0 = k_{act}k_d/k_{uni}$ is the termolecular rate coefficient at low pressure (expressed in cm^6 $molecule^{-2}$ s^{-1}) and $k_\infty = k_{act}$ is the bimolecular high pressure limiting rate coefficient (expressed in $cm^3 molecule^{-1} s^{-1}$), the effective rate constant can be expressed as

$$k_t = \frac{k_\infty k_0\ (M)}{k_0(M) + k_\infty} \tag{2.60}$$

At low pressure when $k_{uni} \gg k_d\ (M)$ (*e.g.*, in most of the stratosphere), the apparent kinetic rate depends linearly on pressure (third-order reaction)

$$k_t = k_0(M) \tag{2.61a}$$

while at high-pressure when $k_{uni} \ll k_d\ (M)$ (*e.g.*, in the troposphere), it becomes independent of pressure (second-order reaction)

$$k_t = k_\infty \tag{2.61b}$$

As in the case of unimolecular processes, it is certainly possible for a reaction to be neither second nor third order, and a more detailed model of the pressure dependence must be used. For example, the apparent rate constant can be expressed as a function of the air density (M) and the temperature T by the empirical Troe's relation (Troe, 1979)

$$k_t = \frac{k_\infty k_0\ (M)}{k_0\ (M) + k_\infty} F_c^{\left\{1+[\log_{10}(k_0(M)/k_\infty)]^2\right\}^{-1}} \tag{2.62}$$

where k_0 and k_∞ can be expressed as a function of temperature by

$$k_0(T) = k_0\,(300K)\left(\frac{T}{300}\right)^{-n} \tag{2.63a}$$

$$k_\infty(T) = k_\infty\,(300K)\left(\frac{T}{300}\right)^{-m} \tag{2.63b}$$

Parameters k_0 and k_∞ at 300 K as well as n and m are derived from laboratory data. The broadening factor F_c is often taken as equal to 0.6.

Since k_{uni} is generally larger than $k_d\ (M)$, termolecular processes often are found to exhibit negative energies of activation. Physically, this may be thought of as related to the degree of energization of C^*. At higher temperatures, the C^* intermediate will be formed with higher mean internal energy, and fewer of them will live long enough for the rate limiting stabilizing reaction, k_d, to occur.

2.5 Heterogeneous and Multiphase Reactions

Reactions taking place on the surface of solid or liquid particles and inside liquid droplets play an important role in the middle atmosphere, especially in the lower stratosphere where sulfate aerosol particles and polar stratospheric clouds (PSCs) are observed. The nature, properties and chemical composition of these particles are described in Chapters 5 and 6. Several parameters are commonly used to describe the uptake of gas-phase molecules into these particles: (1) the *sticking coefficient s* which is the fraction of collisions of a gaseous molecule with a solid or liquid particle that results in the uptake of this molecule on the *surface* of the particle; (2) the *accommodation coefficient* α which is the fraction of collisions that leads to incorporation into the *bulk* condensed phase, and (3) the *reaction probability* γ (also called the *reactive uptake coefficient*) which is the fraction of collisions that results in reactive loss of the molecule (chemical reaction). Thus, the accommodation coefficient α represents the probability of reversible physical uptake of a gaseous species colliding with a surface, while the reaction probability γ accounts for reactive (irreversible) uptake of trace gas species on condensed surfaces. This latter coefficient represents the transfer of a gas into the condensed phase and takes into account processes such as liquid phase solubility, interfacial transport or aqueous phase diffusion, chemical reaction on the surface or inside the condensed phase, etc.

The loss rate of an atmospheric molecule resulting from the uptake by liquid or solid particles is generally expressed by a pseudo-first-order equation

$$\frac{\mathrm{d(X)}}{\mathrm{dt}} = -\mathrm{k_X(X)} \tag{2.64}$$

if (X) is the atmospheric concentration of molecule X. Neglecting gas-phase diffusion, the rate coefficient $\mathrm{k_X(s^{-1})}$ is given by the product of the collision frequency (between a gas-phase molecule and a particle), and the reaction probability γ

$$\mathrm{k_X} = \frac{\gamma \overline{c_X} \mathrm{A}}{4} \tag{2.65}$$

where A is the surface area density (expressed, for example, in $\mathrm{cm^2\ cm^{-3}}$) provided by the particles present in the atmosphere and $\overline{\mathrm{c}}_\mathrm{X}$ is the mean thermal velocity of the molecule (see Eq. (2.43b)), with

$$\overline{\mathrm{c_X}} = \left[\frac{8k\mathrm{T}}{\pi \mathrm{m_X}}\right]^{\frac{1}{2}} \tag{2.66}$$

if T is the temperature, $\mathrm{m_X}$ the mass of molecule X, k the Boltzmann constant and $\pi = 3.14159$. Box 2.2 provides more information on the methods used to calculate $\mathrm{k_X}$.

Box 2.2 Modeling Heterogeneous Processes in the Stratosphere

Liquid and solid particles observed in the atmosphere are generally a mixture of water, sulfuric acid and nitric acid with potentially the presence of traces of other chemical compounds like HCl (see Table 5.9 in Section 5.7). The determination of the pseudo first-order rate coefficient k_X (see Eq. (2.65)) for uptake by such particles in the stratosphere requires an accurate estimate of the surface area density available and of the reaction probability involved.

The mean surface area density A can be calculated if the size distribution of the particles present in the atmosphere is known. For spherical particles

$$A = \int_0^\infty 4\pi r^2 \frac{dn}{dr}\, dr$$

if dn represents the number of particles whose radius is in the range [r, r + dr]. Typical values of A are 1 μm^2 per cm^3 of air in the case of background sulfuric aerosols (10 to 100 times more after a large volcanic eruption), 1 μm^2 per cm^3 in the case of nitric acid trihydrates, 10 μm^2 cm^{-3} for liquid ternary solutions and 10-100 μm^2 per cm^3 in the case of ice particles.

The reaction probability γ depends in general on the physical nature and chemical composition of the particle and on temperature. The composition of the liquid or solid particles is derived from thermodynamic considerations. The value of γ for different conditions is determined in the laboratory. In the case of liquid sulfuric acid aerosols, for most reactions, γ depends on the weight percentage W (wt%) of H_2SO_4 in the aerosol. W can be expressed as a function of temperature T(K) and water vapor pressure p_{H_2O} (hPa) by (Steele and Hamill, 1981; Hanson *et al.*, 1994)

$$W\,(\%\text{wt}\,H_2SO_4) = \frac{(-14.458 + 0.62456Z)\,T + 3565}{44.777 + 1.3204Z - 0.19988T}$$

with

$$Z = \ln p_{H_2O}$$

When HCl molecules are dissolved in the aerosol, they can contribute to the uptake take of other molecules, and the γ coefficient is modified as a function of the concentration of HCl dissolved in the solution [HCl](M) and hence of the partial pressure of HCl in the atmosphere p_{H_2O} and temperature T(K) since

$$[HCl] = \mathcal{H}_{HCl}\, p_{HCl}$$

if $\mathcal{H}_{HCl}$(M atm^{-1}) is the Henry's law constant which can be expressed as

$$\mathcal{H}_{HCl} = 10^{(15.514 - 0.1791W)}$$

Box 2.2 (Continued)

Heterogeneous reaction rates on particles in polar stratospheric clouds (PSCs) are more difficult to estimate because of the uncertainties in the type of PSC particles present in the lower stratosphere. The particle composition, volume density and radius must be derived from a thermodynamic model (*e.g.*, Carslaw *et al.*, 1994; 1997). Condensation of HNO_3 occurs when the partial pressure of nitric acid in air exceeds the equilibrium vapor pressure $p^{eq}_{HNO_3}$. For example, in the case of nitric acid trihydrates (NAT), if partial pressures are expressed in Torr and the temperature T in Kelvin, we have (Hanson and Mauersberger, 1988)

$$\log p^{eq}_{HNO_3} = (-2.7836 - 0.00088T) \log p_{H_2O} + 38.9855 - 11397/T + 0.009179T$$

if p_{H_2O} is the partial pressure of water vapor in the atmosphere.

Similarly, ice particles may form when the partial pressure of atmospheric water vapor becomes supersaturated relative to ice (*i.e.*, as temperatures drop below the freezing point). $p^{eq}_{H_2O}$ (here in hPa) over ice can be expressed as a function of temperature T (in Kelvin) as

$$\log p^{eq}_{H_2O} = -2663.5/T + 12.537$$

Sedimentation of PSC particles can be an effective process for removing water and nitrogen compounds from the atmosphere (dehydration and denitrification), and has to be taken into account when modeling PSC effects. The velocity at which particles sediment increases with the size of these particles. If the size distribution of the particles follows a log-normal law, the sedimentation flux for a given chemical compound can be expressed as (Considine *et al.*, 2000)

$$\Phi = n\, w_0 \exp\left(8 \ln^2 \sigma\right)$$

where n is the number density of the sedimenting molecules in the condensed phase, w_0 is the fall velocity derived for a radius equal to the median radius of the size distribution, and σ is the standard deviation of the log-normal distribution.

Different expressions relating the reaction probability γ to other parameters of the system have been proposed in the case of *liquid* particles (see *e.g.*, Schwartz, 1986; Hanson and Ravishankara, 1994; Hu *et al.*, 1995; Hanson, 1997a, b; Seinfeld and Pandis, 1998). Adopting the scheme shown in Figure 2.4 to account for the transfer of molecules from the gas phase to the surface (adsorption with a corresponding transfer coefficient noted k_{ads}), from the surface to the gas phase (desorption noted k_{des}), from the surface into the bulk of the particle (solvation noted k_{sol}), and from the bulk to the surface ($k_{\ell s}$), Hanson (1997b) has

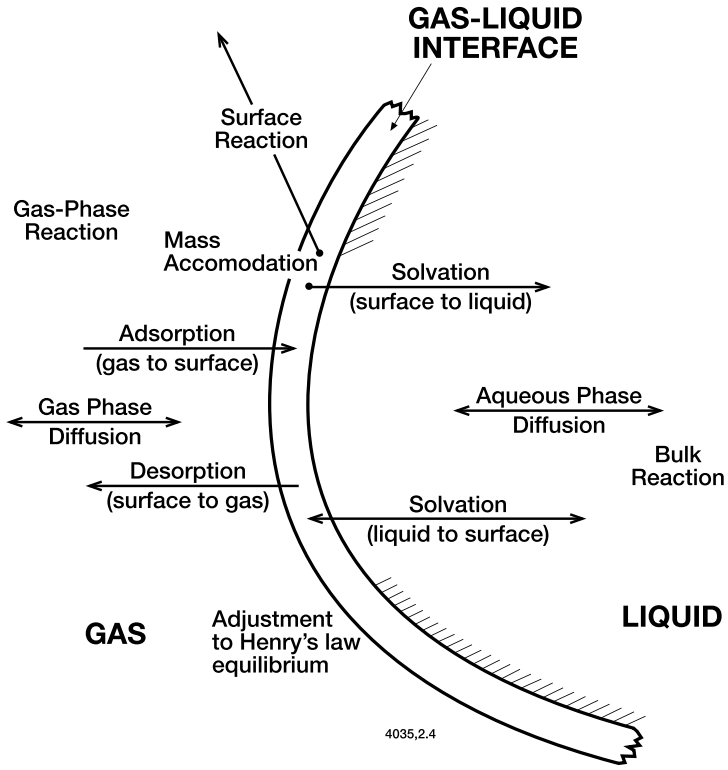

Figure 2.4. Reactive uptake of a gas-phase molecule by a liquid particle.

derived the following expression

$$\frac{1}{\gamma} = \frac{1}{\mathrm{s}} + \frac{1}{\Gamma_{\mathrm{bulk}} \frac{\mathrm{k}_{\ell \mathrm{s}}}{\mathrm{k}_{\ell \mathrm{s}} + (\mathrm{k}_{\mathrm{R}} \mathrm{D}_{\mathrm{L}})^{0.5}} + \Gamma_{\mathrm{surf}}} \tag{2.67}$$

in which s represents the sticking coefficient, $\mathrm{D_L}$ is the diffusion coefficient in the solution, $\mathrm{k_R}$ is the first order reactive loss coefficient in the bulk of the particle, and

$$\Gamma_{\mathrm{bulk}} = \frac{4\mathrm{RT}\mathcal{H}_{\mathrm{X}} \left(\mathrm{k_R D_L}\right)^{0.5}}{\overline{\mathrm{c_X}}} \mathrm{f}\left[\mathrm{a}\left(\frac{\mathrm{k_R}}{\mathrm{D_L}}\right)^{0.5}\right] \tag{2.68a}$$

$$\Gamma_{\mathrm{surf}} = \frac{4\mathrm{k_s}}{\overline{\mathrm{c_X}}} \frac{\mathrm{k_{ads}}}{\mathrm{k_{des}}} \tag{2.68b}$$

represent the effects of bulk and surface reactions, respectively. In these expressions, $\mathcal{H}_{\mathrm{X}}$ is the Henry's law coefficient which relates the equilibrium concentration of molecule X in the gas phase to the concentration of the same species in the liquid phase. R is the gas constant, T is the temperature, and $\mathrm{k_s}$ is the first-order loss rate coefficient for molecule X on the surface of the particle. Factor

$\mathrm{f}\left[\mathrm{a}\left(\mathrm{k_R}/\mathrm{D_L}\right)^{0.5}\right]$, where a is the radius of the particles, accounts for the sphericity of the particles. The value of this function is given by

$$\mathrm{f}\left(\zeta\right) = \coth\left(\zeta\right) - \zeta^{-1} \tag{2.69}$$

where $\zeta = \mathrm{a}\left(\mathrm{k_R}/\mathrm{D_L}\right)^{0.5}$ is a dimensionless parameter which describes the relative rates of chemical reaction and diffusion.

Assuming that the transfer rates between the surface and the bulk of the particles are fast, and noting that the sticking coefficient s is related to the accommodation coefficient α by

$$\alpha = \mathrm{s}\,\frac{\mathrm{k_{sol}}}{\mathrm{k_{sol}} + \mathrm{k_{des}}} \tag{2.70}$$

the expression for the reaction probability becomes (Hanson and Ravishankara, 1994)

$$\frac{1}{\gamma} = \frac{1}{\alpha} + \frac{1}{\Gamma_{\mathrm{bulk}} + \Gamma_{\mathrm{surf}}} \tag{2.71}$$

By analogy with an electrical circuit, the resistance to uptake $(1/\gamma)$ can thus be represented by 2 resistors in series $1/\alpha$ and $1/(\Gamma_{\mathrm{bulk}} + \Gamma_{\mathrm{surf}})$.

In the case of *solid* particles (*e.g.*, ice), reactive uptake is driven primarily by chemical reactions at the surface since bulk diffusion is generally too slow to allow for solubility in the condensed phase.

Recent laboratory studies have shown that the reaction probability γ can depend strongly on the physical nature, the chemical composition of the aerosols, and hence on the atmospheric temperature and concentration of water vapor and other chemical compounds (*e.g.*, HCl). Figure 2.5 shows the reaction probability as a function of temperature (and equivalently of the weight percentage of sulfuric acid) for the following key stratospheric heterogeneous processes on liquid sulfate aerosols:

$$\mathrm{N_2O_5\,(g) + H_2O\,(\ell) \rightarrow 2\,HNO_3} \tag{2.72}$$

$$\mathrm{ClONO_2\,(g) + H_2O\,(\ell) \rightarrow HOCl}(g) + \mathrm{HNO_3} \tag{2.73}a$$

$$\mathrm{ClONO_2\,(g) + HCl\,(\ell) \rightarrow Cl_2}(g) + \mathrm{HNO_3} \tag{2.73}b$$

$$\mathrm{HOCl\,(g) + HCl\,(\ell) \rightarrow Cl_2}(g) + \mathrm{H_2O} \tag{2.74}a$$

$$\mathrm{BrONO_2\,(g) + H_2O\,(\ell) \rightarrow HOBr + HNO_3} \tag{2.74}b$$

where g and ℓ refer to the gas and liquid phases, respectively. The values of γ displayed in Figure 2.5 refer to conditions characteristic of the lower stratosphere (JPL, 2000). Such reactions, which also occur in the presence of other types of particles (including PSC particles) convert relatively inert halogen compounds such as HCl and $\mathrm{ClONO_2}$ into gaseous products ($\mathrm{Cl_2}$, HOCl, etc.) which are rapidly photolyzed into

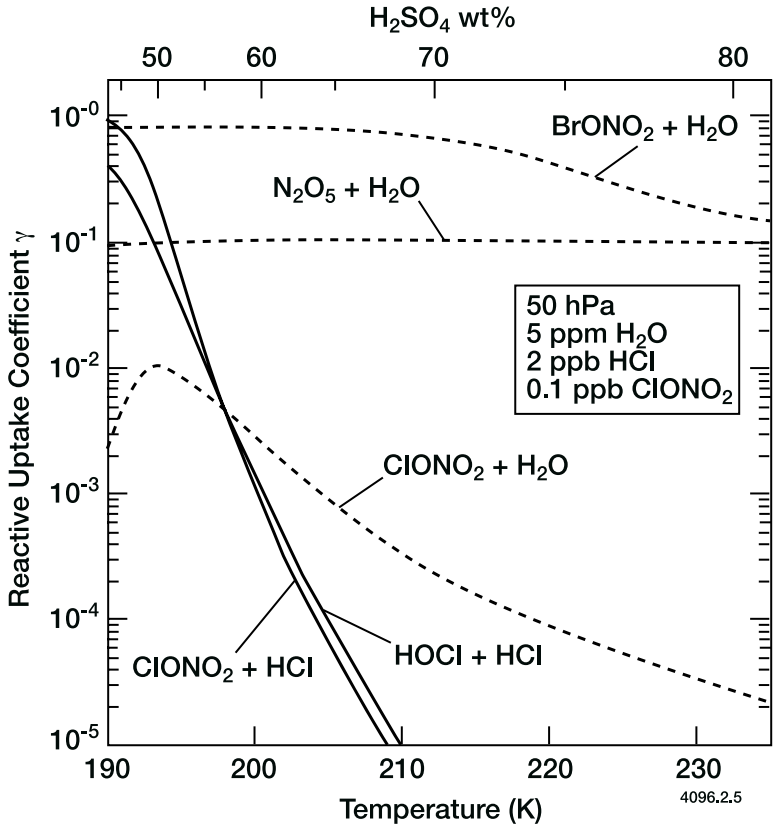

Figure 2.5. Reactive uptake coefficient (γ) for several stratospheric heterogeneous processes as a function of temperature and aerosol sulfuric acid weight percentage. Values established for atmospheric conditions representative of the lower stratosphere: pressure of 50 hPa, 5 ppmv H_2O, 2 ppbv HCl and 0.1 ppbv $ClONO_2$. Aerosol diameter of 10^{-5}cm. After JPL (2000).

reactive halogen radicals that efficiently destroy ozone (see Chapters 5 and 6).

Heterogeneous reactions are often complex and nonlinear processes. For example, in the case of the heterogeneous conversion of $ClONO_2$, the total (observed) reaction probability is determined by reactions with water molecules (Reaction 2.73*a*) and with HCl (Reaction 2.73*b*). The total reactive uptake coefficient γ varies, therefore, with the amount of HCl dissolved in the particles, and hence with the concentration of gaseous HCl present in the atmosphere (Hanson and Ravishankara, 1994). Figure 2.6 shows the contribution of the two reactions as a function of the atmospheric HCl partial pressure, and specifically

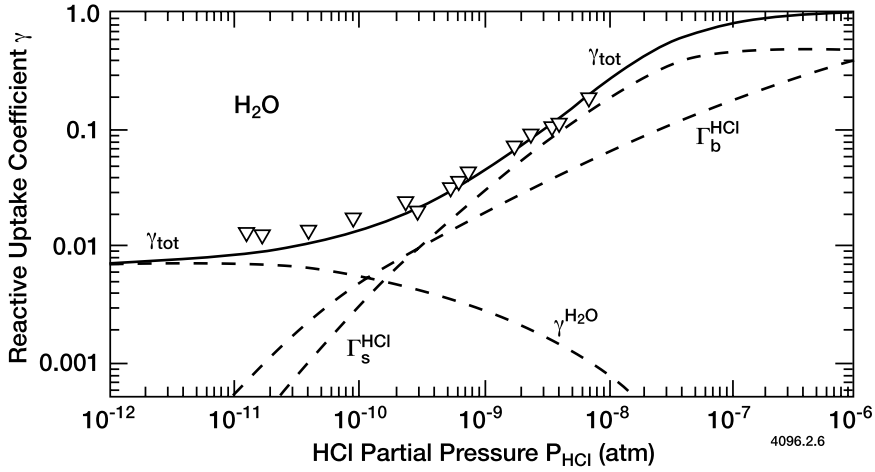

Figure 2.6. Reactive uptake coefficient (γ) for the heterogeneous conversion of $ClONO_2$ on 55.6 wt% sulfuric acid aerosol particles. The triangles represent the measurements of Hanson and Ravishankara (1994). The solid line represents the parameterization of γ as a function of the atmospheric partial pressure of HCl. The dashed lines represent the fraction of $ClONO_2$ reacting with water molecules (γ^{H_2O}), with HCl in the bulk of the aerosol (Γ_b^{HCl}), and with HCl on the surface of the particles (Γ_s^{HCl}). A HCl mixing ratio of 2 ppbv at a pressure level of 50 hPa (lower stratosphere) corresponds to a HCl partial pressure of 10^{-10}atm. From Peter (1997).

the fraction of $ClONO_2$ reacting with HCl in the bulk (Γ_b^{HCl}) and on the surface (Γ_s^{HCl}) of a sulfate aerosol particle (see Eq. 2.71). Note that the reaction pathway with H_2O dominates for low concentrations of HCl, but drops as the reaction with HCl becomes dominant. In this latter case, the probability for the reaction to occur on the surface of the aerosol is often larger than in the bulk of the particle. As expected, the total γ coefficient tends to saturate at a value close to unity for high values of the HCl partial pressure.

2.6 Photolysis Processes

Photochemical processes in the atmosphere are initiated by the absorption of a photon (quantum of electromagnetic energy) by a molecule XY, leading to promotion of the molecule to an electronically-excited state (conventionally denoted by the superscript *):

$$XY + h\nu \rightarrow XY^* \tag{2.75}$$

The excited state is usually unstable, and is therefore followed by *dissociation*

$$XY^* \rightarrow X + Y \tag{2.76a}$$

by *ionization*

$$XY^* \rightarrow XY^+ + e^- \tag{2.76b}$$

by *fluorescence*

$$XY^* \rightarrow XY + h\nu \tag{2.76c}$$

or by *intramolecular energy transfer*

$$XY^* \rightarrow XY^{**} \tag{2.76d}$$

The excited state molecule can also be *quenched* by a third body M

$$XY^* + M \rightarrow XY + M \tag{2.77a}$$

or react with a molecule AB with *intermolecular energy transfer*.

$$XY^* + AB \rightarrow \text{products} \tag{2.77b}$$

The quantum yield of a given pathway following the light absorption is defined as the number of reactant molecules which decompose along this pathway relative to the number of photons absorbed. The sum of quantum yields for all possible pathways is then unity. In this section, we focus on photodissociation processes (also called *photolysis*), as described by Reactions (2.75) and (2.76a).

Figure 2.7 presents a typical potential energy diagram for a diatomic molecule, where possible photon-induced transitions are indicated. At atmospheric temperatures, most molecules are in their ground vibrational state. Possible transitions are represented by the vertical lines labeled 1 and 2, for example. Transition 1 leads from the ground state to an unbound state, and thus a continuum of wavelengths near the energy of 1 are possible. The spectrum should therefore consist of a smooth continuum at wavelengths above the dissociation limit. Transition 2, on the other hand requires that absorption into a specific vibrational level of the upper electronic state occur. It is therefore quantized at nearly the energy defined by 2 (differences in rotational energy levels, which are too small to show in the figure, will lead to a band of possible energies about 2). The spectrum corresponding to these transitions will be banded at discrete wavelengths. Such spectra are exhibited by oxygen in the Herzberg continuum and Schumann-Runge bands and continuum. An approximate potential energy diagram for O_2 is shown in Figure 2.8, where these transitions are indicated. The Schumann-Runge bands correspond to transitions from the ground $^3\Sigma_g^-$ to the bound portion of the $B^3\Sigma_u^-$ state, and the Schumann-Runge continuum involves the same electronic states, but at shorter

wavelengths above the dissociation limit. The Herzberg continuum involves excitation from the ground state to the repulsive $A^3\Sigma_u^+$ state.

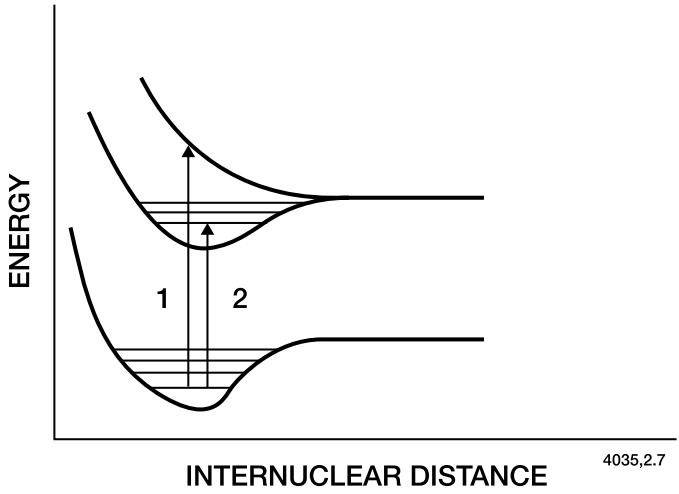

Figure 2.7. Typical potential energy curves for a diatomic molecule.

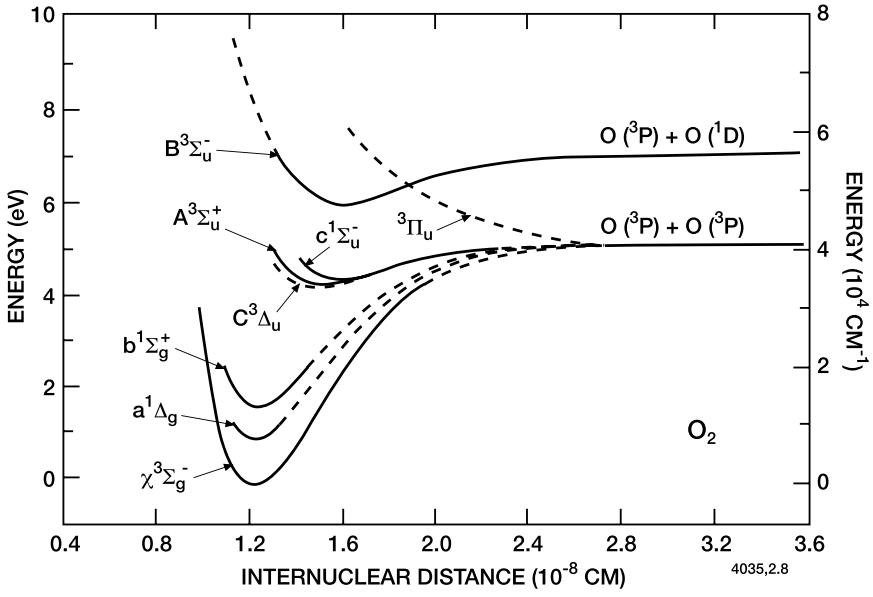

Figure 2.8. Potential energy diagram for the principal states of the oxygen molecule. Adapted from Gilmore (1964).

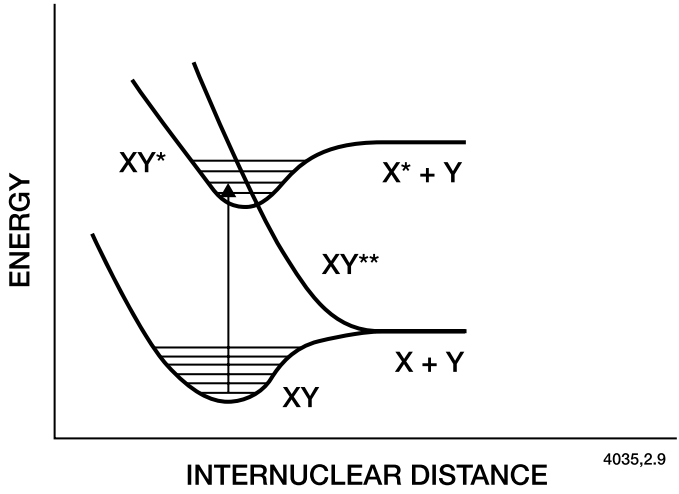

Figure 2.9. Potential energy curves for a predissociative process in a diatomic molecule.

If the upper state is bound, as it is for transition 2 in Figure 2.7, can such a transition lead to dissociation? Dissociation can often occur in such a case through curve crossing onto a *predissociating state*. Figure 2.9 presents a corresponding potential energy curve showing this phenomenon. The excited state, XY^*, which is initially produced, can cross into XY^{**} by a non-radiative transition or by collision-induced crossing. From the predissociating state, ground state atoms are eventually produced. The indicated transition for the Schumann-Runge bands as depicted in Figure 2.8 involves crossing into the repulsive $^3\Pi_u$ state leading to dissociation. Nitric oxide photolysis in the middle atmosphere occurs largely through predissociation. Polyatomic molecules have more complex potential surfaces in three or more degrees of freedom, and an increased probability of possible predissociating surfaces.

The rate at which molecule XY is photodecomposed is expressed as

$$\frac{\mathrm{d}\,(\mathrm{XY})}{\mathrm{dt}} = -\mathrm{J_{xy}}\ (\mathrm{XY}) \tag{2.78}$$

where $\mathrm{J_{xy}}$ is the unimolecular rate constant for photolytic loss of XY. $\mathrm{J_{xy}}$, which is also called the *photolysis frequency* (expressed in $\mathrm{s^{-1}}$), is determined by the number of photons available (the solar actinic flux), the ability of the molecule to absorb these photons (the absorption cross-section), and the probability that the photon absorption leads to the decomposition of the molecule (quantum yield for photodissociation). The product of these 3 factors is integrated over all wavelengths contributing to the photolysis of the molecule (see Chapter 4 for

more details). The absorption cross sections and quantum yields are determined in the laboratory. In many cases, these quantities vary with temperature. In some cases, the quantum yield is a function of pressure.

2.7 Excited Species in the Middle Atmosphere

Photolysis reactions produce a number of *electronically excited* species, (*e.g.*, $O(^1D)$) which play an important role in the middle atmosphere. Some of these constituents are important because they are very reactive and can initiate chains of important free radical chemistry. Examples of such processes include

$$O_3 + h\nu \rightarrow O_3^* \rightarrow O\,(^1D) + O_2\,(^1\Delta_g) \tag{2.79}$$

$$O\,(^1D) + H_2O \rightarrow 2OH \tag{2.80}$$

which provides the major source of reactive hydrogen containing radicals in the stratosphere and troposphere. This will be discussed in much more detail in Chapter 5. Another excited species, $N(^2D)$, produces large amounts of NO in the lower thermosphere (see Chapters 5 and 7) via

$$N\,(^2D) + O_2 \rightarrow NO + O \tag{2.81}$$

A significant aspect of excited state chemistry, especially in the mesosphere and lower thermosphere, is the importance of fluorescence and chemiluminescence. *Fluorescence* is the rapid re-emission of absorbed photons:

$$A + h\nu \rightarrow A^* \tag{2.82}$$

$$A^* \rightarrow A + h\nu \tag{2.83}$$

In the process of *chemiluminescence*, the emitting particle is excited by chemical reactions rather than direct photon absorption:

$$A + B \rightarrow C^* + D \tag{2.84}$$

$$C^* \rightarrow C + h\nu \tag{2.85}$$

Excited species can lose their energy by collision (or *quenching*) with other molecules. However, in the upper atmosphere, where the density of air molecules is relatively small and more high energy photons are available to produce excited species, many constituents fluoresce or chemiluminesce. Thus, photons of specific wavelengths are released, producing characteristic *airglow* emissions. Many of these emissions can also be used to deduce information about the concentrations of atmospheric species. Table 2.1 presents a summary of some of the more

Table 2.1 Emissions of Some Excited Species in the Middle Atmosphere

Lower state	*Excited state*	*Radiative* lifetime* (s)	λ (nm)	*Name*
O (^{3}P)	O (^{1}D)	110	630	Red line
O (^{1}D)	O (^{1}S)	0.74	557.7	Green line
O_2 ($X^3\Sigma_g^-$)	O_2 ($a^1\Delta_g$)	2.7 (3)	1270	Infrared atmospheric bands
O_2 ($X^3\Sigma_g^-$)	O_2 ($b^1\Sigma_g^+$)	12	761.9	Atmospheric bands
O_2 ($X^3\Sigma_g^-$)	O_2 ($A^3\Sigma_u^+$)	1	260-380	Herzberg bands
OH $(X^2\Pi)_{v=0,1,..}$	OH $(X^2\Pi)_{v=9,8,..}$	6 (–2)	< 2800.7	Meinel bands
N (^{4}S)	N (^{2}D)	9.36 (4)	520	
N (^{4}S)	N (^{2}P)	12	346.6	
N_2 ($X^1\Sigma_g^+$)	N_2 ($A^3\Sigma_u^+$)	2	200-400	Vegard-Kaplan bands
NO ($X^2\Pi$)	NO ($A^2\Sigma^+$)	2 (–7)	200-300	γ bands

* read 2.7 (3) as 2.7×10^3.

important emitting species in the middle atmosphere. Plate 1 shows an aurora produced by the radiative emission of excited oxygen atoms (green and red light).

Note the very long radiative lifetimes of O (^{1}D), O_2 ($^1\Delta_g$), and N (^{2}D). Transitions of these species to their respective ground states involve violation of the spin conservation rule, and are therefore relatively slow. The O (^{1}S) $\rightarrow$ O (^{1}D) transition, which produces the green line, is spin allowed, but corresponds to ΔL of 2, and is therefore somewhat unfavorable. In contrast, the NO ($A^2\Sigma^+$) $\rightarrow$ NO ($X^2\Pi$) transition is fully allowed and the radiative lifetime of this state is correspondingly short.

The green line of atomic oxygen is believed to arise mainly through the reaction

$$O + O + M \rightarrow O_2^* + M \tag{2.86}$$

followed by

$$O_2^* + O \rightarrow O\,(^1S) + O_2 \tag{2.87}$$

and finally

$$O\,(^1S) \rightarrow O\,(^1D) + h\nu\,(557.7\ nm) \tag{2.88}$$

commonly referred to as the Barth mechanism (Barth and Hildebrand, 1961; see the review by Bates, 1981). Here the symbols O and O_2 refer to oxygen atoms and molecules in their fundamental states ^3P and $^3\Sigma$, respectively. The green line emission provides a useful means of deducing the atomic oxygen density near 100 km, as shown for example by Slanger and Black (1977).

O_2 ($^1\Delta_g$) is produced in the sunlit mesosphere principally via

$$O_3 + h\nu \rightarrow O\,(^1D) + O_2\,(^1\Delta_g) \tag{2.89}$$

and to a lesser extent from

$$O\,(^1D) + O_2 \rightarrow O_2(^1\Sigma_g^+) + O \tag{2.90}$$

or

$$O_2 + h\nu \rightarrow O_2(^1\Sigma_g^+) \tag{2.91}$$

followed by

$$O_2(^1\Sigma_g^+) + M \rightarrow O_2(^1\Delta_g) + M \tag{2.92}$$

O_2 ($^1\Delta_g$) is in turn destroyed either by radiative decay (1.27μm),

$$O_2\left(^1\Delta_g\right) \rightarrow O_2\left(^3\Sigma_g^-\right) + h\nu\,(1.27\mu m) \tag{2.93}$$

or by quenching:

$$O_2(^1\Delta_g) + O_2 \rightarrow 2O_2 \tag{2.94}$$

If the rates of all of these processes are known, then ozone densities can be derived from measurements of the infrared atmospheric volume emission rate (*e.g.*, Evans *et al.*, 1968; Thomas *et al.*, 1983). This provides a useful means of measuring mesospheric ozone abundances (Mlynczak and Olander, 1995). Dayglow production mechanisms by oxygen compounds are shown schematically in Figure 2.10 (Mlynczak *et al.*, 1993).

The OH Meinel bands are generated between 80 and 100 km altitude by the reaction between atomic hydrogen and ozone

$$H + O_3 \rightarrow OH^\dagger(v = 9, 8, 7, 6) + O_2 \tag{2.95}$$

followed by chemiluminescence (radiative emission)

$$OH^\dagger\,(v') \rightarrow OH^\dagger\,(v'') + h\nu \tag{2.96}$$

or by quenching with M (N_2, O_2 or O)

$$OH^\dagger + M \rightarrow OH + M \tag{2.97}$$

of the *vibrationally excited* hydroxyl radical (v is the vibrational quantum number). The Einstein A-coefficients associated with the $OH^\dagger$ vibrational emissions (and hence the corresponding radiative lifetimes) have been measured in the laboratory (Nelson *et al.*, 1990).

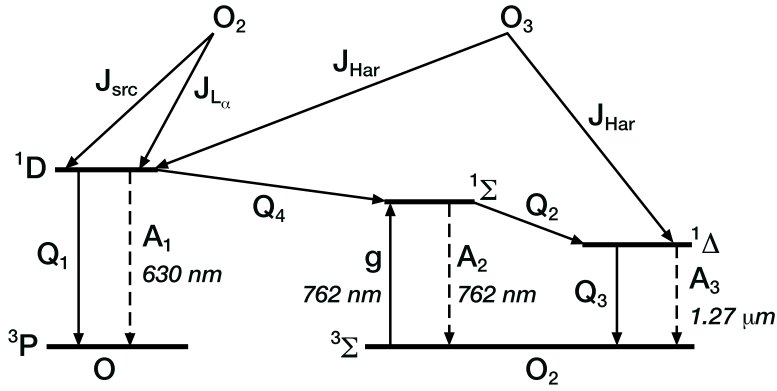

Figure 2.10. Oxygen dayglow production mechanism in the middle atmosphere. The photolysis of ozone (J_{Har}) in the Hartley band ($\lambda < 320$ nm) leads to the formation of the excited oxygen atom O (^{1}D) and molecule O_2 ($^1\Delta$g). The photolysis of molecular oxygen in the Schumann-Runge continuum (J_{SRC} at $\lambda < 175$ nm) and at Lyman α ($J_{L\alpha}$ at $\lambda = 121.6$ nm) leads to the formation of 2 electronically excited oxygen atoms O (^{1}D). De-activation is associated with radiative emissions (A_i) and quenching (Q_i). The emission A_1 produces a red line at 630 nm (see Table 2.1), A_2 produces atmospheric bands at wavelengths near 762 nm, and A_3 (Reaction 2.93) produces infrared bands at 1.27μm. The quenching processes correspond to the following reactions: 2.90 for Q_1 and Q_4, 2.92 for Q_2, and 2.94 for Q_3. Radiative excitation (g) at 762 nm is represented by reaction 2.91 (from Mlynczak *et al.*, 1993).

Uncertainties regarding the quenching lifetimes and the rate constants for reactions of $OH^\dagger$ with atomic oxygen remain fairly large (Mlynczak *et al.*, 1998), and make the interpretation of the airflow feature difficult (Llewellyn *et al.*, 1978). Note that the hydroxyl airglow reduces the amount of energy potentially available for heat from the exothermic reaction between ozone and atomic hydrogen. Measurements of the hydroxyl airglow can be used to derive the atomic hydrogen concentration (if the ozone concentration is known, see Mlynczak *et al.*, 1998) and the (OH rotational) temperature near the mesopause (Viereck and Deehr, 1989; Lowe and Turnbull, 1995).

Emissions from N (^{2}D) and N (^{2}P) are particularly important in the aurora, where they are produced primarily through photoelectron impact on N_2 (see Chapter 5 and 7). As mentioned above, the reactions of N (^{2}D) or N (^{2}P) provide an important source of NO in the lower thermosphere, and this emission feature can indicate the yield of excited nitrogen production in auroral processes (see, for example, Frederick and Rusch, 1977; Zipf *et al.*, 1980).

The fluorescence of NO in the γ bands represents a useful method of NO measurement in the lower thermosphere, as first pointed out by Barth (1966).

Excited state chemistry is one of the most important aspects of classical chemistry as applied to the middle atmosphere. Indeed, as shown in Figures 2.7, 2.9, and 2.10, all photolysis reactions involve at least temporary production of electronically excited species; thus the photochemistry of the atmosphere is closely tied to the excited states of a number of important species. More detail regarding the chemistry of some of these states will be presented in Chapter 5.

References

Barth, C.A., and A.F. Hildebrand, The 5577 Å airglow emission mechanism. *J Geophys Res: 66*, 985, 1961.

Barth, C.A., Nitric oxide in the upper atmosphere. *Ann Geophys: 22*, 198, 1966.

Bates, D.R., The green light of the night sky. *Planet Space Sci: 29*, 1061, 1981.

Carslaw, K.S., B.P. Luo, S.L. Clegg, T. Peter, P. Brimblecombe, and P.J. Crutzen, Stratospheric aerosol growth and HNO_3 gas phase depletion from coupled HNO_3 and water uptake by liquid particles. *Geophys Res Lett: 21*, 2479, 1994.

Carslaw, K.S., T. Peter, and S. L. Clegg, Modeling the composition of liquid stratospheric aerosols. *Rev Geophys: 35*, 125, 1997.

Castellan, G.W., *Physical Chemistry.* Addison-Wesley, 1971.

Considine, D.B., A.R. Douglass, P.S. Connell, D.K. Kinnison, and D.A. Rotman, A polar stratospheric cloud parameterization for the global modeling initiative three-dimensional model and its response to stratospheric aircraft. *J Geophys Res: 105*, 3955, 2000.

Ebbing, D.D., *General Chemistry.* 3rd ed. Houghton Mifflin Co., 1990.

Evans, W.F.J., D.M. Hunten, E.J. Llewellyn, and A. Vallance-Jones, Altitude profile of the infrared atmospheric system of oxygen in the dayglow. *J Geophys Res: 73*, 2885, 1968.

Finlayson-Pitts, B.J., and J.N. Pitts, Jr., *Chemistry of the Upper and Lower Atmosphere, Theory, Experiments, and Applications.* Academic Press, 1999.

Frederick, J.E., and D.W. Rusch, On the chemistry of metastable atomic nitrogen in the F-region deduced from simultaneous satellite measurements of the 5200 Å airglow and atmospheric composition. *J Geophys Res: 82*, 3509, 1977.

Gilmore, F.R., *Potential energy curves for N_2, NO, O_2, and corresponding ions.* RAND corporation memorandum R-4034-PR, June, 1964.

Hanson, D.R., and K. Mauersberger, Laboratory studies of the nitric acid trihydrate: Implications for the south polar stratosphere. *Geophys Res Lett: 15*, 855, 1988.

Hanson, D.R., and A.R. Ravishankara, Reactive uptake of $ClONO_2$ onto sulfuric acid due to reaction with HCl and H_2O. *J Phys Chem: 98*, 5728, 1994.

Hanson, D.R., A.R. Ravishankara, and S. Solomon, Heterogeneous reactions in sulfuric acid aerosols: A framework for model calculations. *J Geophys Res: 99*, 3615, 1994.

Hanson, D.R., Reaction of N_2O_5 with H_2O on bulk liquids and on particles and the effect of dissolved HNO_3, *Geophys Res Lett: 24*, 1087, 1997a.

Hanson, D.R., Surface-specific reactions on liquid. *J Phys Chem: 101*, 4998, 1997b.

Herzberg, G., *Spectra of Diatomic Molecules.* D. Van Nostrand Co., 1950.

Hoffman, D.J., and S. Solomon, Ozone destruction through heterogeneous chemistry following the eruption of El Chichón. *J Geophys Res: 94*, 5029, 1989.

Hu, J.H., Q. Shi, P. Davidovits, D.W. Worsnop, M.S. Zahniser, and C.E. Kolb, Reactive uptake of Cl_2 (g) and Br_2 (g) by aqueous surfaces as a function of Br^- and I^- ion concentrations: The effect of chemical reaction at the interface. *J Phys Chem: 99*, 8768, 1995.

Jet Propulsion Laboratory (JPL), *Chemical Kinetics and Photochemical Data for Use in Atmospheric Studies*, Evaluation 14: NASA Jet Propulsion Laboratory Publication 02-25, 2002.

Johnston, H. S., *Gas Phase Reaction Rate Theory.* Ronald Press, 1966.

Karplus, M., and R.N. Porter, *Atoms and Molecules: An Introduction for Students of Physical Chemistry.* W.A. Benjamin, Inc., 1970.

Llewellyn, E.J., B.H. Long, and B.H. Solheim, The quenching of OH^* in the atmosphere. *Planet Space Sci: 26*, 525, 1978.

Lowe, R.P., and D.N. Turnbull, Comparison of ALOHA-93, ANLC-93 and ALOHA-90 observations of the hydroxyl rotational temperature and gravity wave activity. *Geophys Res Lett: 22*, 2813, 1995.

Mlynczak, M.G., S. Solomon, and D.S. Zaras, An updated model for the O_2 ($a^1\Delta_g$) concentrations in the mesophere and lower thermosphere and implications for remote sensing of ozone at 1.27μm. *J Geophys Res: 98*, 18,639, 1993.

Mlynczak, M.G., and D.S. Olander, On the utility of the molecular oxygen dayglow as proxies for middle atmosphere ozone. *Geophys Res Lett: 22*, 1377, 1995.

Mlynczak, M.G., D.K. Zhou, and S.M. Adler-Golden, Kinetic and spectroscopic requirements for the inference of chemical heating rates and atomic hydrogen densities from OH Meinel band measurements. *Geophys Res Lett: 25*, 647, 1998.

Moore, W.J., *Physical Chemistry.* Prentice Hall, 1962.

Mozurkiewicz, M., and J.G. Calvert, Reaction probability of N_2O_5 on aqueous aerosols. *J Geophys Res: 93*, 15,889, 1998.

Nelson, D.D., Jr., A. Schiffman, D.J. Nesbitt, J.J. Orlando, and J.B. Burkholder, H + O_3 Fourier-transform infrared emission and laser absorption studies of OH ($X^2\pi$) radical: An experimental dipole moment function and state-to-state Einstein A coefficients. *J Chem Phys: 93*, 7003, 1990.

Peter, T., Microphysics and heterogeneous chemistry of polar stratospheric clouds. *Ann Rev Phys: 48*, 785, 1997.

Rice, O.K., and H.C. Ramsperger, Theories of unimolecular gas reactions at low pressures. *J Am Chem Soc: 49*, 1617, 1927.

Schwartz, S.E., Mass transport considerations pertinent to aqueous-phase reactions of gases in liquid-water clouds, in *Chemistry of Multiphase Atmospheric Systems.* W. Jaeschke, ed. Springer-Verlag, 1986.

Seinfeld, J.H., and S.N. Pandis, *Atmospheric Chemistry and Physics — From Air Pollution to Climate Change.* J. Wiley and Sons, 1998.

Slanger, T.G., and G. Black, O^1S in the lower thermosphere — Chapman vs. Barth. *Planet Space Sci: 25*, 79, 1977.

Smith, I.W.M., *Kinetics and Dynamics of Elementary Gas Reactions.* Butterworths, 1980.

Steele, H.M., and P. Hamill, Effects of temperature and humidity on the growth and optical properties of sulfuric acid-water droplets in the stratosphere. *J Atmos Sci: 12*, 517, 1981.

Steinfeld, J.I., *Molecules and Radiation: An Introduction to Modern Molecular Spectroscopy.* MIT Press, 1978.

Thomas, R.J., C.A. Barth, G.J. Rottman, D.W. Rusch, G.H. Mount, G.M. Lawrence, R.W. Sanders, G.E. Thomas, and L.E. Clemens, Ozone density in the mesosphere (50-90 km) measured by the SME limb scanning near infrared spectrometer. *Geophys Res Lett: 10*, 245, 1983.

Troe, J., Predictive possibilities of unimolecular rate theory. *J Phys Chem: 83*, 114, 1979.

Viereck, R.A., and C.S. Deehr, On the interaction between gravity waves and the OH Meinel (6-2) and the O_2 atmospheric (0-1) bands in the polar night airglow. *J Geophys Res: 94*, 5397, 1989.

Weston, R.E., and H.A. Schwarz, *Chemical Kinetics.* Prentice Hall, 1972.

Zipf, E.C., P.J. Espy, and C.F. Boyle, The excitation and collisional deactivation of metastable N^2P atoms in auroras. *J Geophys Res: 85*, 687, 1980.

Chapter 3

DYNAMICS AND TRANSPORT

3.1 Introduction

The distribution of most chemical species in the middle atmosphere results from the influences of both dynamical and chemical processes. In particular, when the rates of formation and destruction of a chemical compound are comparable to the rate at which it is affected by dynamical processes, then transport plays a major role in determining the constituent distribution. In an environment like the Earth's atmosphere, air motions, and hence transport of chemical species, are strongly constrained by density stratification (gravitational force) which resists vertical fluid displacements, and the Earth's rotation (Coriolis force) which is a barrier against meridional displacements. Geophysical fluid dynamics describes how atmospheric motions are produced within these constraints.

Transport occurs at a variety of spatial and temporal scales. In atmospheric models, it is customary to distinguish between motions that can be resolved on the numerical grid of the model (often called large-scale *advection*) and sub-grid scale processes (such as molecular diffusion or turbulent *mixing*) that are often parameterized by diffusion coefficients. In turn, the distributions of certain chemical species, particularly ozone, can influence the radiative budget of the atmosphere, affecting temperatures and flow patterns. Therefore the study of atmospheric chemistry intersects greatly with those of fluid dynamics and meteorology. In this chapter, the structure of the middle atmosphere will be discussed, and the transport processes in the stratosphere, mesosphere, and lower thermosphere will be described. In our description of atmospheric motions, we have not sought to provide a detailed account of the dynamic meteorology of the middle atmosphere. For a comprehensive description of middle atmosphere dynamics, the reader is referred to the excellent books by Andrews *et al.* (1987), Holton (1992) and James (1994). See also the chapter by Garcia *et al.* in the book by Brasseur *et al.* (1999) and the papers by Shepherd (2000; 2003).

The present chapter is directed towards an understanding of the effects of atmospheric dynamics on chemical constituents.

The sections of this chapter deal with the following elements of atmospheric dynamics: vertical structure of the atmosphere (Section 3.2), fundamental equations of atmospheric motions (Section 3.3), transport of chemical constituents and the relative importance of dynamical and chemical effects on photochemical species (Section 3.4), atmospheric waves (Section 3.5), the mean meridional circulation and the use of the transformed Eulerian formalism to illustrate the roles of mean meridional and eddy transports (Section 3.6), the important role of wave transience and dissipation (Section 3.7), vertical transport by molecular diffusion in the thermosphere (Section 3.8), and finally, models of the middle atmosphere (Section 3.9).

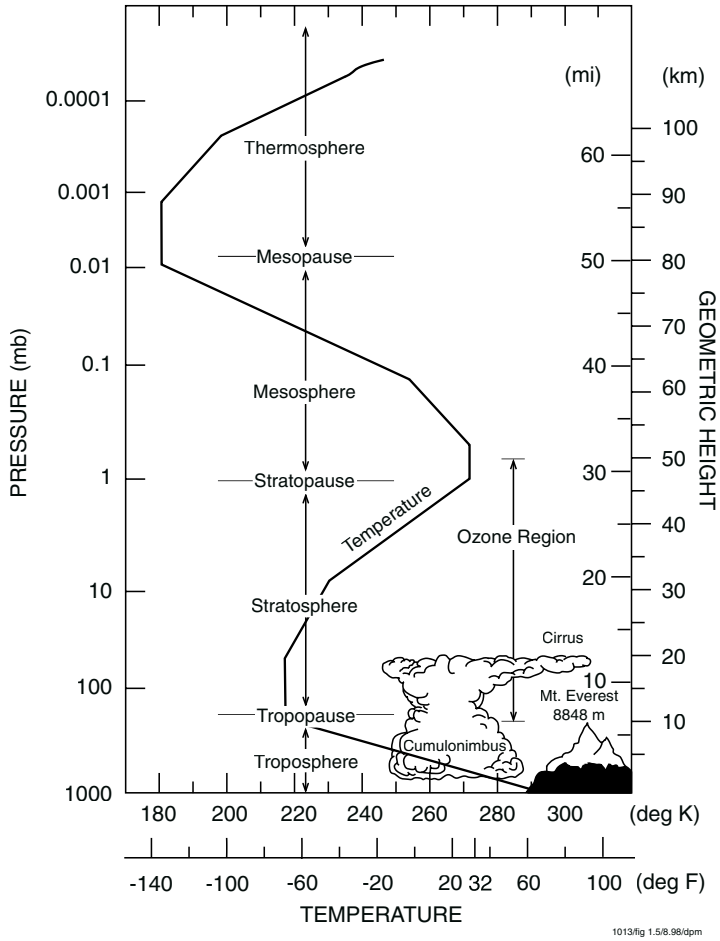

Figure 3.1. Schematic representation of the thermal structure of the atmosphere with its different layers.

3.2 Structure of the Atmosphere and Some Observed Dynamical Characteristics

The Earth's atmosphere is commonly described as a series of layers defined by their thermal characteristics (Figure 3.1). Specifically, each layer is a region where the change in temperature with respect to altitude has a constant sign. The layers are called "spheres" and the boundary between connecting layers is the "pause". The lowest layer, called the *troposphere,* exhibits generally decreasing temperatures with increasing altitudes up to a minimum called the *tropopause.* The temperature and location of the tropopause vary with latitude and season (see Box 3.1). At the equator, its mean altitude is located near 16 km, and the corresponding temperature is about 190 K, while in polar regions its elevation is only about 8 km, and the mean temperature roughly 220 K (see Figure 3.2). Above the tropopause, the *stratosphere* exhibits increasing temperatures with altitude up to a maximum of about 270 K at the level of the *stratopause* located near 50 km. At still higher altitudes, the temperature again decreases up to 85-100 km, where another temperature minimum is found. This layer is called the *mesosphere* and its upper boundary is the *mesopause* (see Box 3.2). In all these layers, the major constituents, N_2 and O_2, make up about 80 and 20%, respectively, of the total number density, so that the mean molecular weight of air varies little with altitude. Because of this common feature, the three layers are collectively referred to as the *homosphere.* Figure 3.2 presents a contour plot of the observed meridional distribution of the zonal mean temperature in the homosphere in January, showing some of these features in more detail.

The region located above the mesopause is called the *thermosphere.* The temperatures there increase very rapidly with altitude and can reach 500 to 2000 K above 500 km, depending on the level of solar activity. The composition of the thermosphere is very different from that of the lower regions due to diffusive separation between light and heavier compounds (see Section 3.8). As a result, the relative abundance of atomic oxygen increases substantially with height and becomes comparable to and even greater than those of O_2 and N_2 above about 130 km. The abundances of O_2 and N_2 decrease as a result of rapid photodissociation. Atomic hydrogen (the lightest chemical element) becomes the most abundant compound in the upper thermosphere. In contrast to the homosphere, the mean molecular weight of air in this region varies with altitude; for this reason the region above 100 km is also called the *heterosphere.*

As was mentioned in Chapter 2, the major source of heat in the middle atmosphere is provided by absorption of ultraviolet radiation, particularly by ozone and to a lesser extent by molecular oxygen

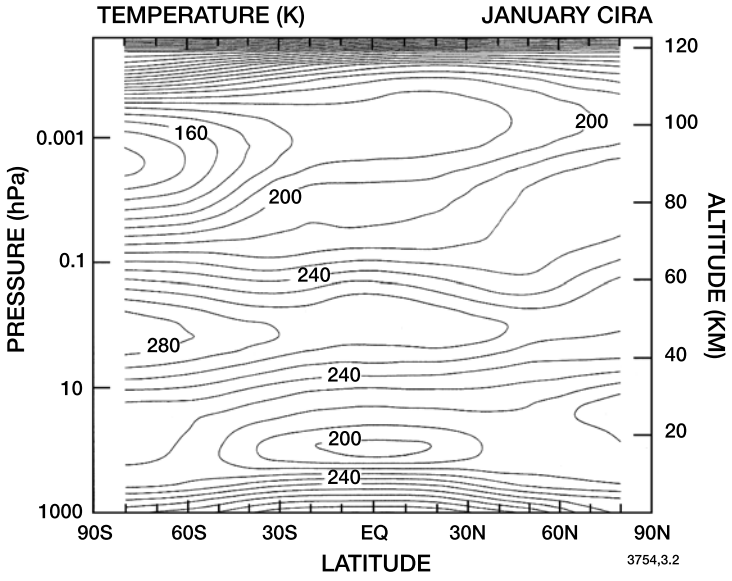

Figure 3.2. Zonally averaged temperature (K) from the surface to approximately 120 km altitude in January, based on Fleming *et al.* (1988). Note the temperature minimum (less than 200 K) at the tropical tropopause, the temperature maximum (280 K) at the summer stratopause and the temperature minimum (less than 140 K) at the summer mesopause. The height of the mesopause increases from approximately 90 km in summer to 100 km in winter.

(see Chapter 4). Radiative cooling occurs through infrared emission associated with the vibrational relaxation of CO_2, H_2O, and O_3. Figure 3.3 presents a model estimate of the rate of net radiative heating in the middle atmosphere. The large radiative heating rates found in the stratosphere are due primarily to the large amounts of ozone found there. The observed increase in temperature with altitude in the stratosphere is a result of heating by ozone, illustrating the important relationship of atmospheric chemical composition to the radiation budget and the thermal structure of the atmosphere.

Comparison of Figures 3.2 and 3.3 reveals several interesting features. For example, although the radiative heating rate at the *summer* mesopause is large, the temperatures observed there (120-160 K) are much lower than those found in the winter hemisphere (200-240 K). The tropical tropopause, as we have already noted, is much colder than its counterpart at middle and high latitudes, although no dramatic variation in the radiative heating rate occurs there. Both cases illustrate the importance of dynamical effects in establishing the temperature structure of the middle atmosphere. Specifically, an air parcel displaced adiabatically upward undergoes expansion and cooling while adiabatic

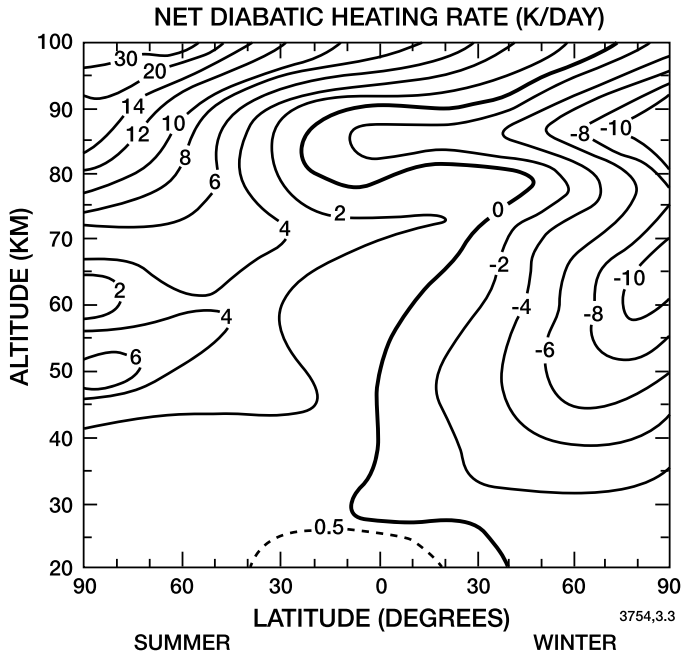

Figure 3.3. Net radiative heating rate associated with (1) absorption of ultraviolet radiation by molecular oxygen in the upper mesosphere and thermosphere, and by ozone in the stratosphere and mesosphere, and (2) emission of infrared radiation by atmospheric CO_2, O_3, and H_2O. Values given in K/day and positive in the summer hemisphere (net diabatic heating) and negative (net diabatic cooling) in the winter hemisphere. From London (1980).

compression and heating accompanies downward displacements. These principles will be described in more detail below in connection with the thermodynamic and momentum equations, but we note at this point that mean upward motions are characteristic of the summer mesopause and of the tropical tropopause.

One of the most important atmospheric dynamical quantities is the *zonal* wind (wind speed in the *longitudinal* direction). Wind velocities are conventionally positive for eastward winds (also called westerlies) and negative for westward winds (easterlies). They are mostly derived from the observed thermal structure of the atmosphere, although local values can be provided by radiosonde and radar measurements. To date, very few attempts have been made to directly measure the atmospheric wind components from space. The High Resolution Doppler Imager (HRDI) on board the Upper Atmosphere Research Satellite (UARS) has provided information on horizontal winds in the mesosphere/lower thermosphere (50-115 km) and in the stratosphere (10-40 km) by observing the Doppler shifts in the emission lines of an O_2 atmospheric

band (Hays *et al.*, 1993; Ortland *et al.*, 1996; Burrage *et al.*, 1996). Figure 3.4 shows the wind fields recovered from HRDI at an altitude of 25 km on March 8, 1994 (Ortland *et al.*, 1996). The Wind Imaging Interferometer (WINDII) on the same satellite has provided the neutral winds in the 80-300 km altitude range from measurements of the Doppler shift in the O(^{1}S) green line emission (Shepherd *et al.*, 1993; Gault *et al.*, 1996).

Figure 3.5 presents a typical latitude height distribution of mean zonal winds, averaged over longitude and time. In the lower stratosphere, the zonal circulation is an extension of the tropospheric flow characterized by the two jets centered at 30-40 degrees latitude, with wind speeds almost twice as large in winter as in summer. In most parts of the stratosphere (above 20 km) and the mesosphere, the prevailing mean zonal winds are directed eastward (westerlies) during winter and westward (easterlies) during summer, with maximum velocities of the order of 60-75 m/s near 70 km. Above this altitude the zonal flow becomes less intense and its direction even reverses in the extratropics above 85-95 km. Note also the strong westerly winds in the winter polar stratosphere which form the so-called *polar vortex* and partly isolate the polar region from low latitude influences. The zonal mean flow is strongly influenced by the seasonal variation in the solar heating.

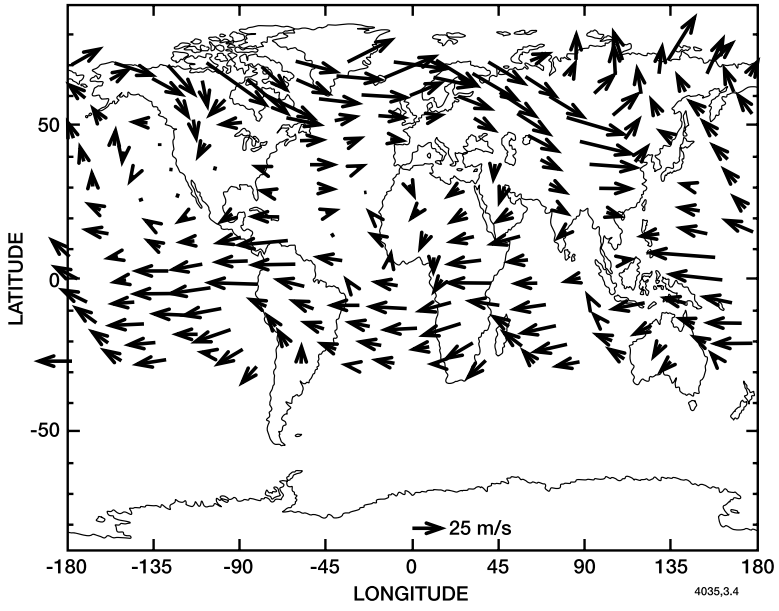

Figure 3.4. Horizontal wind field at 25 km altitude measured by the UARS/HRDI instrument on 8 March 1994. From Ortland *et al.* (1996).

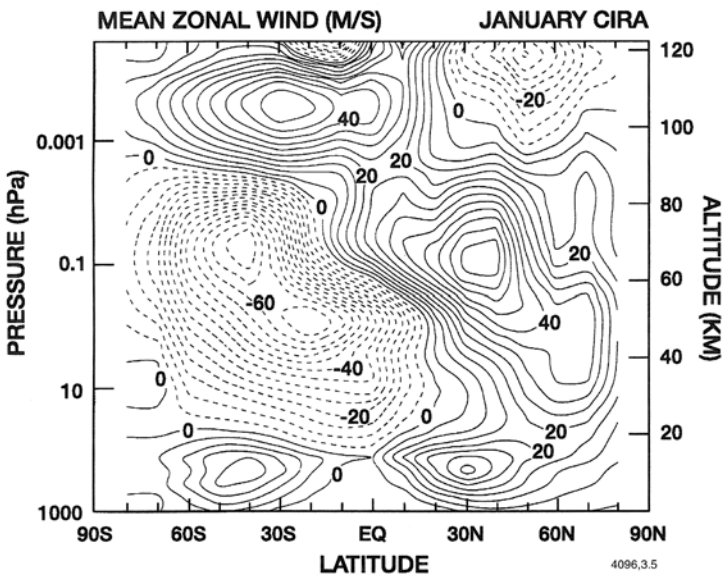

Figure 3.5. Longitudinally averaged zonal wind (m/s) from the surface to approximately 120 km altitude in January, based on Fleming *et al.* (1988). Positive winds are blowing eastwards (westerlies) and negative winds are blowing westwards (easterlies). Note the presence of the 2 tropospheric subtropical jets. Stratospheric winds are primarily westerlies in winter and easterlies in summer. A reversal of the winds is observed above approximately 90 km altitude.

Vertical and *meridional* winds in the stratosphere can be estimated from theoretical studies, which are usually based on solutions to the equations of atmospheric dynamics, as will be described below. In the mesosphere, however, the *meridional* wind (wind speed in the *latitudinal* direction) has been measured at particular points, usually with radar techniques (see Figure 3.6 from Nastrom *et al.*, 1982) and derived from space observations (see, *e.g.*, Lieberman *et al.*, 2000). Meridional winds are denoted by a positive velocity when they are directed from the south to the north. In the vertical, wind speeds are positive when they are directed upwards.

It should be emphasized that Figure 3.5 presents *the mean zonal wind,* that is, the wind speed averaged over longitude and time. In addition, local variations in the wind speed and direction are observed. These dynamical disturbances are associated with the presence of *atmospheric waves* (see Section 3.4). The propagation of these waves through the atmospheric medium is determined by the basic state of the atmospheric fluid; at the same time, the dissipation of the waves tends to modify the basic state itself. Beside radiatively forced seasonal variations,

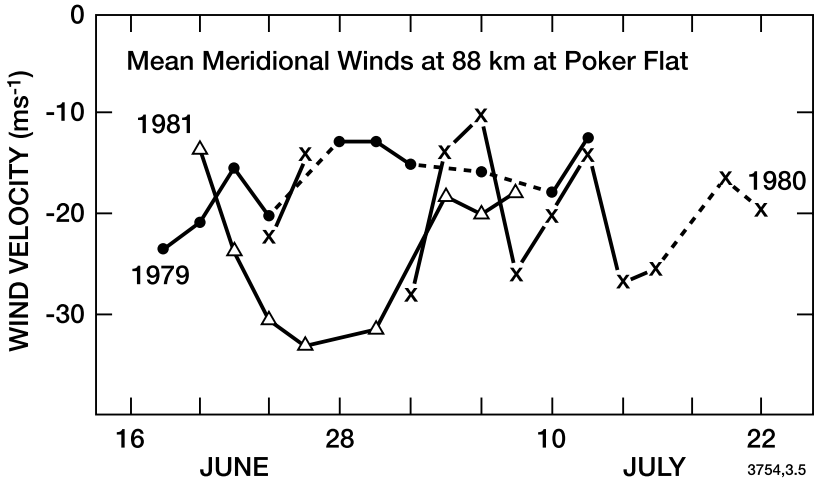

Figure 3.6. Velocity of meridional winds observed in the mesosphere at Poker Flat, Alaska (m s^{-1}). The air flow at 88 km is directed southwards during summertime. From Nastrom *et al.* (1982).

the atmosphere exhibits periodic or quasi-periodic cycles resulting from the interactions of atmospheric waves with the mean flow; examples are provided by the quasi-biennial oscillation (QBO) in the lower stratospheric equatorial zonal wind (whose period varies from 22 to 34 months), and of the semi-annual osciallation (SAO) which is observed near the equatorial stratopause and mesopause.

In addition to large-scale advection, another possible mechanism for transport of chemical species is provided by *irreversible mixing*, sometimes referred to as eddy diffusion. The only true diffusion in the atmosphere occurs at the molecular level, via the random motion of atoms and molecules (see Section 3.8). This becomes important as a transport process only in the thermosphere. At lower altitudes, all transport results from motions of parcels of air rather than individual particles. However, the concept of *eddy diffusion* is a useful way to describe the mixing effects of fluid motions occurring on time and spatial scales much smaller than advection. This process is formally represented as turbulent mixing, modeled after the behavior of diffusion. In this chapter we are primarily interested in gradients of photochemical constituents which occur over spatial scales of the order of kilometers in the vertical, and thousands of kilometers in the horizontal directions. Motions which occur over spatial scales much smaller than these may be understood as mixing processes rather than organized motion over the relevant distance.

3.3. Fundamental Description of Atmospheric Dynamics

3.3.1 The Primitive Equations

To describe the theoretical dynamical and thermal behavior of the atmosphere, the fundamental equations of fluid mechanics must be employed. In this section these equations are presented in a relatively simple form. A more conceptual view will be presented in Section 3.6. The circulation of the Earth's atmosphere is governed by three basic principles: Newton's laws of motion, the conservation of energy, and the conservation of mass. Newton's second law describes the response of a fluid to external forces. In a frame of reference which rotates with the Earth, the first fundamental equation, called the *momentum* equation, is given by:

$$\frac{\mathrm{d}\vec{\mathrm{v}}}{\mathrm{dt}} + \frac{1}{\rho}\vec{\nabla}\mathrm{p} + 2\vec{\Omega}\,\mathrm{x}\vec{\mathrm{v}} = \vec{\mathrm{g}} + \vec{\mathrm{F}} \tag{3.1}$$

where $\vec{\mathrm{v}}$ represents the velocity vector of an air parcel, p is pressure, ρ is the mass per unit volume, $\vec{\Omega}$ is the angular rotation rate of the Earth, $\vec{\mathrm{g}}$ is the effective gravitational acceleration (including the centrifugal acceleration owing to the rotation of the Earth), $\vec{\mathrm{F}}$ is the frictional force, and t is time. The terms in the above equation each correspond to a different force acting on the fluid; these are the pressure gradient force $(1/\rho\vec{\nabla}\mathrm{p})$, the Coriolis force (expressed by the vector product $2\vec{\Omega}\,\mathrm{x}\vec{\mathrm{v}}$), the gravitational $(\vec{\mathrm{g}})$ and frictional $(\vec{\mathrm{F}})$ forces (these conventionally represent the force per unit mass in meteorological studies). d/dt is the total derivative (following the motion). Note that the Coriolis force is an apparent force which arises because the frame of reference used to describe the motion is rotating. See, for example, Holton (1992) and Andrews *et al.* (1987) for a detailed physical explanation of each of these terms.

The second fundamental equation expresses *conservation of energy* (first law of thermodynamics):

$$\mathrm{c_p}\frac{\mathrm{dT}}{\mathrm{dt}} - \frac{1}{\rho}\frac{\mathrm{dp}}{\mathrm{dt}} = \mathrm{Q} \tag{3.2}$$

where T is the temperature (K), $\mathrm{c_p}$ represents the specific heat of air at constant pressure and Q is the net heating rate per unit mass (due to physical processes such as radiative effects or release of latent heat). The first two terms express the relationship between pressure and temperature, which describes expansion cooling or compression heating associated with *adiabatic* (energy conserving) processes taking place in a compressible fluid. The remaining term on the right-hand side of the

equation represents *diabatic* processes involving heating or cooling of the parcel. In the stratosphere and mesosphere, this rate is principally due to the difference between two terms: i) heating by absorption of solar ultraviolet radiation by ozone and, in the upper mesosphere and lower thermosphere by molecular oxygen, and ii) cooling by infrared emission by carbon dioxide, ozone, water vapor, and other radiatively active molecules. It therefore depends strongly on the atmospheric distributions of these minor constituents. A detailed account of the radiation and thermal budgets is presented in Chapter 4.

The third fundamental equation expresses *conservation of mass* (and is called the continuity equation):

$$\frac{\mathrm{d}\rho}{\mathrm{dt}} + \rho\vec{\nabla}\cdot\vec{\mathrm{v}} = 0 \tag{3.3a}$$

In equations (3.1), (3.2) and (3.3), the total time derivative (also called the *material derivative* along the flow) can be written:

$$\frac{\mathrm{d}}{\mathrm{dt}} = \frac{\partial}{\partial \mathrm{t}} + \vec{\mathrm{v}}\cdot\vec{\nabla} \tag{3.4}$$

The material derivative is the total time rate of change following the motion. By combining (3.3) and (3.4) one finds an alternative form of the continuity equation

$$\frac{\partial\rho}{\partial \mathrm{t}} + \vec{\nabla}\cdot(\rho\vec{\mathrm{v}}) = 0 \tag{3.3b}$$

The first term on the left-hand side of this equation represents the local time rate of change (at a fixed point in space) and the second term describes the advective transport of mass by the velocity $\vec{\mathrm{v}}$.

The net radiative heating (Q) is the only source of external forcing in the energy conservation equation. If we assume that $\mathrm{Q} = 0$ and consider a frame of reference which moves with a moving air parcel, we can examine the thermodynamics of *adiabatic* air parcel displacements. In this case, equation (3.2) becomes

$$\mathrm{c_p}\frac{\mathrm{dT}}{\mathrm{dt}} = \frac{1}{\rho}\frac{\mathrm{dp}}{\mathrm{dt}} \tag{3.5}$$

The *ideal gas law* (also called *the equation of state*) can be used to relate p and T:

$$\mathrm{p} = \rho\mathrm{RT} \tag{3.6}$$

where R is the gas constant for air. Substituting for ρ using (3.6), we obtain

$$\frac{\mathrm{dT}}{\mathrm{T}} = \frac{\mathrm{R}}{\mathrm{c_p}}\frac{\mathrm{dp}}{\mathrm{p}} \tag{3.7}$$

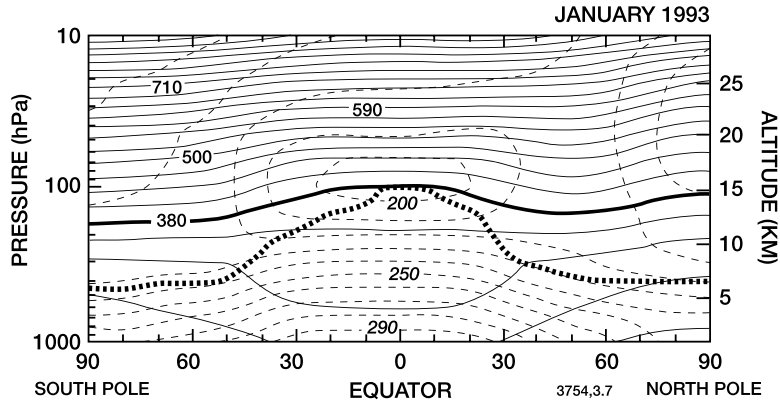

Figure 3.7. Zonally averaged distribution of the potential temperature (unbroken lines, in K) from the surface to approximately 30 km altitude (10 hPa). The isolines for the absolute temperature (dashed lines, in K) are also shown. The tropopause is represented by the dotted line. Note that isentropes corresponding to potential temperatures larger than 380 K are located exclusively in the stratosphere (an area called the *overworld*). Air parcels located in the lowermost stratosphere between the tropopause and the 380 K isentrope (an area called the *middle world*) are susceptible to crossing the tropopause when adiabatically transported, and entering the troposphere (also called the *underworld*). From Holton *et al.* (1995), based on Appenzeller (1994).

which can be integrated to yield

$$T = Ap^{\kappa} \tag{3.8}$$

where A is a constant and $\kappa = R/c_p = 2/7 \equiv 0.286$ for dry air. Noting that the ratio T/p^{κ} remains constant under adiabatic conditions, one can define the *potential temperature* Θ

$$\Theta = T\,[p_0/p]^{\kappa} \tag{3.9}$$

which represents the temperature that would be attained by an air parcel if it were adiabatically compressed or expanded starting from a temperature T and pressure p to a nominal pressure p_0. p_0 is usually taken as 1000 hPa, representative of the pressure at sea level. Θ is therefore a conservative quantity in any dry adiabatic air parcel displacement, and is sometimes used to evaluate air parcel trajectories (see, *e.g.*, Danielsen, 1961). Figure 3.7 shows the zonally averaged distribution of the potential temperature along with temperature contours. From Equation (3.9) it can be seen that in an isothermal atmosphere the potential temperature varies with height as $p^{-\frac{2}{7}}$.

The thermodynamic equation (3.2) can be expressed using the potential temperature Θ rather than the absolute temperature T:

$$\frac{d\Theta}{dt} = \left[\frac{p_o}{p}\right]^{\kappa} \frac{Q}{c_p} \equiv q \tag{3.10}$$

This form allows for ready evaluation of the influence of external heating (Q) on Θ, and expresses that, in the absence of heat input or loss [Q = 0], the potential temperature is conserved.

Newton's second law, relation (3.1), is generally written as three scalar equations, often expressed in spherical coordinates. Given the independent variables:

λ the longitude in the easterly direction
ϕ the latitude in the northerly direction
z_g the geometric altitude

we define

$r = a + z_g$ as the distance from the center of the Earth (a is the Earth's radius).
$u = r \cos\phi \, d\lambda/dt$ as the zonal component of the wind velocity $\vec{v}$ measured towards the east.
$v = r \, d\phi/dt$ as the meridional component of $\vec{v}$ measured towards the north.
$w = dz_g/dt$ as the vertical component of $\vec{v}$.

These components of motion are the scalar products of $\vec{v}$ with the unit vectors in the zonal, meridional, and vertical directions, respectively.

$$\vec{i} = \frac{\vec{\Omega} \times \vec{r}}{|\vec{\Omega} \times \vec{r}|}$$
$$\vec{j} = \vec{k} \times \vec{i}$$
$$\vec{k} = \frac{\vec{r}}{r}$$

In the *spherical coordinate system*, the components of the acceleration $d\vec{v}/dt$ are not simply given by the derivatives of the components of $\vec{v}$ because the derivatives of the Cartesian unit vectors $\vec{i}, \vec{j}$, and $\vec{k}$ must be considered. Figure 3.8 shows a schematic representation of the adopted coordinate system.

The equations of motion then become:

$$\frac{du}{dt} = \frac{\tan\phi}{r} uv - \frac{1}{r} uw + 2\Omega v \sin\phi - 2\Omega w \cos\phi - \frac{1}{\rho r \cos\phi} \frac{\partial p}{\partial \lambda} + F_\lambda \qquad (3.11a)$$

$$\frac{dv}{dt} = -\frac{\tan\phi}{r} u^2 - \frac{1}{r} uw - 2\Omega u \sin\phi - \frac{1}{\rho r} \frac{\partial p}{\partial \phi} + F_\phi \qquad (3.11b)$$

$$\frac{dw}{dt} = \frac{1}{r} u^2 + \frac{1}{r} v^2 + 2\Omega u \cos\phi - g - \frac{1}{\rho} \frac{\partial p}{\partial z_g} + F_z \qquad (3.11c)$$

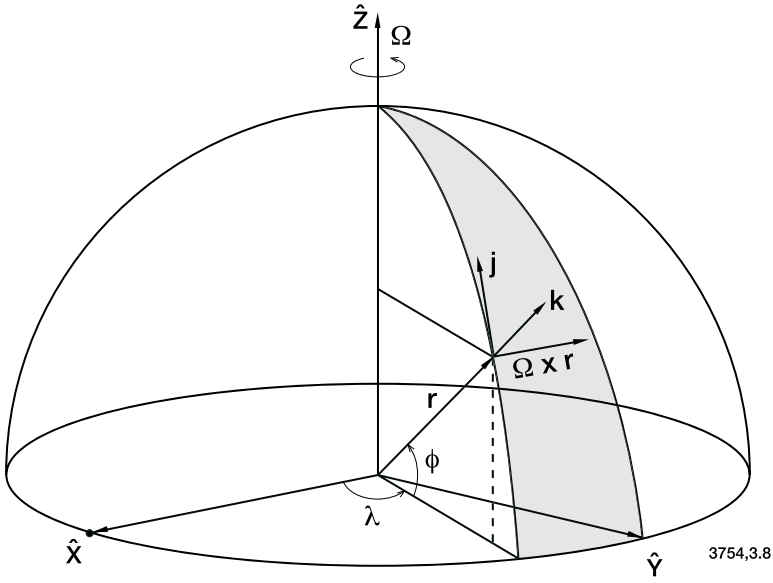

Figure 3.8. Representation of the adopted coordinate system.

with the material derivative (or derivative following the motion) defined as

$$\frac{\mathrm{d}}{\mathrm{dt}} = \frac{\partial}{\partial \mathrm{t}} + \frac{\mathrm{u}}{\mathrm{r}\,\cos\phi}\,\frac{\partial}{\partial\lambda} + \frac{\mathrm{v}}{\mathrm{r}}\,\frac{\partial}{\partial\phi} + \mathrm{w}\frac{\partial}{\partial z_{\mathrm{g}}} \tag{3.11d}$$

and where F_λ, F_ϕ, and F_z are the 3 components of the dissipative force $\vec{\mathrm{F}}$.

The last of these three momentum equations can be greatly simplified by retaining only the two dominant terms:

$$\frac{1}{\rho}\,\frac{\partial \mathrm{p}}{\partial \mathrm{z_g}} + \mathrm{g} = 0 \tag{3.12}$$

This simplification is commonly called the *hydrostatic approximation.* The approximation states that, in the vertical direction, the most important forces acting on a parcel of air are the vertical pressure gradient and gravity. This approximation is common in dynamical models, although it neglects some phenomena such as sound waves, and is not appropriate for high resolution models. The ideal gas law can be used to substitute for ρ in the above equation to obtain

$$\frac{\mathrm{dp}}{\mathrm{p}} = -\frac{\mathrm{dz_g}}{\mathrm{H_g}} \tag{3.13}$$

where $\mathrm{H_g}$ is called the atmospheric *scale height.* $\mathrm{H_g}$ is given by

$$\mathrm{H_g} = \frac{\mathrm{RT}}{\mathrm{g}} = \frac{\mathrm{kT}}{\mathrm{mg}} \tag{3.14}$$

if m is the molecular mass of air and k is the Boltzmann's constant.

Relation (3.13) can be used to characterize the vertical structure of the atmosphere in a convenient form. For example, the vertical distributions of the pressure and air density can be represented by, respectively

$$p\,(z_g) = p_o \exp\left[-\int_{z_{g,o}}^{z_g} \frac{dh}{H_g\,(h)}\right] \qquad (3.15a)$$

and

$$n\,(z_g) = \frac{n_o T_o}{T(z)} \exp\left[-\int_{z_{g,o}}^{z_g} \frac{dh}{H_g\,(h)}\right] \qquad (3.15b)$$

where the subscript o denotes that the corresponding value is defined at some reference altitude $z_{g,0}$. If the scale height (and the temperature) vary little with altitude, one can write

$$p\,(z_g) \approx p_o \exp\left[-\frac{z_g - z_{g,o}}{H_g}\right] \qquad (3.16a)$$

and

$$n\,(z_g) \approx n_o \exp\left[-\frac{z_g - z_{g,o}}{H_g}\right] \qquad (3.16b)$$

The atmospheric scale height is roughly 7 ± 1 km in the homosphere. It represents the altitude which corresponds to a reduction by 1/e in the pressure or the air concentration. The distribution of any atmospheric constituent i can also be characterized by its concentration, $n_i(z_g)$, or its scale height, $H_i(z_g)$. When the scale height of a minor species is equal to the atmospheric scale height, H_g (z), the constituent is well mixed and its mixing ratio (or mole fraction) $X_i = n_i/n$ is constant with altitude (n is the total air density). It can be shown that H_g represents twice the distance through which atoms or molecules having the equipartition of translational energy, 1/2 kT, can rise in the vertical direction against the force of gravity (Campbell, 1977). Table 3.1 presents a possible reference atmosphere for mid-latitudes, illustrating the variation of temperature, pressure, air density, potential temperature, and scale height with geometric altitude.

The decrease of temperature with increasing altitude is called the *lapse rate.* Combining the hydrostatic equation and the expression for potential temperature, we can evaluate the dry adiabatic lapse rate (Γ_d), *i.e.*, the temperature decrease which would be associated with a vertical adiabatic displacement. Logarithmic differentiation of equation (3.9)

Table 3.1 Example of typical values of physical parameters below 120 km at middle latitudes. From the U. S. Standard Atmosphere (1976)

Altitude (km)	*Temperature* (K)	*Scale Height* (km)	*Pressure* (hPa)	*Concentration* (cm^{-3})	*Potential Temperature*[2] (K)
0	288	8.4	1013.3	2.55 (19)[1]	288
5	256	7.5	540.5	1.53 (19)	307
10	223	6.5	265.0	8.61 (18)	327
15	217	6.4	121.1	4.04 (18)	398
20	217	6.4	55.3	1.85 (18)	498
25	222	6.5	25.5	8.33 (17)	636
30	227	6.6	12.0	3.83 (17)	807
35	237	6.9	5.7	1.74 (17)	1043
40	250	7.3	2.3	6.67 (16)	1426
45	264	7.7	1.5	4.12 (16)	1702
50	271	7.9	8.0 (-1)	2.14 (16)	2091
55	261	7.6	4.3 (-1)	1.19 (16)	2405
60	247	7.2	2.2 (-1)	6.45 (15)	2757
65	233	6.8	1.1 (-1)	3.42 (15)	3170
70	220	6.4	5.2 (-2)	1.71 (15)	3709
75	208	6.1	2.4 (-2)	8.36 (14)	4374
80	198	5.8	1.1 (-2)	4.03 (14)	5205
85	189	5.5	4.5 (-3)	1.72 (14)	6416
90	187	5.5	1.8 (-3)	6.98 (13)	8250
95	188	5.5	7.6 (-4)	2.93 (13)	10613
100	195	5.7	3.2 (-4)	1.19 (13)	14098
105	209	6.1	1.5 (-4)	5.20 (12)	18767
110	240	7.0	7.1 (-5)	2.14 (12)	26690
115	300	8.8	4.0 (-5)	9.66 (11)	39313
120	360	10.5	2.5 (-5)	5.03 (11)	53963

[1] read 2.55 (19), for example, as 2.55×10^{19}.
[2] calculated with $p_0 = 1013$ hPa.

holding Θ constant yields:

$$\frac{1}{T}\frac{dT}{dz_g} = \frac{\kappa}{p}\frac{dp}{dz_g} \tag{3.17}$$

Substituting for dp/dz_g from equation (3.13), one obtains

$$\Gamma_d = -\frac{dT}{dz_g}\bigg|_{\Theta=ct} = \frac{g}{c_p} = 10\text{K/km} \tag{3.18}$$

If potential temperature varies with height, then the actual lapse rate ($\Gamma = -\frac{dT}{dz_g}$) will differ from the dry adiabatic lapse rate. This difference

indicates the importance of diabatic processes, such as the absorption of ultraviolet radiation by ozone, for example. The difference between the actual and the dry adiabatic lapse rates provides a measure of the tendency of a displaced air parcel to return to its original position. The static stability of the atmosphere is often characterized by the *buoyancy* or *Brunt-Väisälä frequency* N defined as

$$N^2 = \frac{-g}{T}\left[\Gamma - \Gamma_d\right] \tag{3.19a}$$

or, in terms of potential temperature,

$$N^2 = g\,\frac{\partial\left(\ln\Theta\right)}{\partial z_g} \tag{3.19b}$$

If $N^2 > 0$ $(\Gamma < \Gamma_d)$, *i.e.*, if the actual temperature T increases with height or decreases less rapidly than the adiabatic lapse rate, the atmosphere is stably stratified. Such conditions apply in most regions of the atmosphere and specifically in the stratosphere where the temperature increases with height. Therefore, an air parcel lifted from its equilibrium position tends to sink back to its original position. N can be regarded as the frequency of the oscillation movement produced by the Archimedean restoring force that applies to the air parcel. Typical values of the buoyancy period (1/N) are 5 minutes in the stratosphere and 10 minutes in the troposphere. The occasional breakdown of static stability in the troposphere (for example, when the Earth's surface is becoming warm during summer months) generates convection with rapid vertical exchanges of heat and mass.

As can be seen from the hydrostatic equation (3.12), there exists a single-valued monotonic relationship between pressure and geometric height in a static atmosphere. Therefore, meteorologists often use the pressure (rather than the altitude) as the independent vertical coordinate. It is also convenient to use the *log-pressure altitude*

$$z = -H\ln\left(\frac{p}{p_s}\right) \tag{3.20}$$

as the vertical coordinate because it scales nearly linearly with geometric height z_g. (It would scale exactly in an isothermal atmosphere). In this expression, H is a *constant* scale height, often chosen to be 7 km, and p_s a reference pressure, often chosen to be 1000 hPa. When this definition is adopted, the equations of motion as well as the thermodynamic and continuity equations assume simpler forms, and their solution is facilitated.

It is also convenient to introduce the *geopotential,* Φ, defined as the work required to raise a unit mass from mean sea level to height z_g

$$\Phi = \int_0^{z_g} g dz \tag{3.21}$$

Using the hydrostatic approximation, one derives the following expression

$$d\Phi = g dz_g = -RT d\ln p = \frac{RT}{H_g} dz_g = \frac{RT}{H} dz \tag{3.22}$$

which states that the rate of change of the geopotential relative to the log-pressure altitude is proportional to temperature.

By neglecting minor terms and noting that the depth of the atmosphere is small compared to the radius of the Earth ($r \simeq a$), the equations of motion become in spherical log-pressure coordinates:

$$\frac{du}{dt} - \left[f - \frac{u \tan\phi}{a}\right] v + \frac{1}{a\cos\phi}\frac{\partial\Phi}{\partial\lambda} = F_\lambda \tag{3.23a}$$

$$\frac{dv}{dt} + \left[f + \frac{u \tan\phi}{a}\right] u + \frac{1}{a}\frac{\partial\Phi}{\partial\phi} = F_\phi \tag{3.23b}$$

$$\frac{\partial\Phi}{\partial z} - \frac{RT}{H} = 0 \tag{3.23c}$$

where $f = 2\Omega\sin\phi$ is the *Coriolis parameter* (vertical component of the Earth rotation vector with the angular velocity $\Omega = 7.292 \times 10^{-5} s^{-1}$). Equations (3.23a) and (3.23b) are statements of Newton's second law of motion applied to a fluid continuum. They are often referred to as the momentum equations because they describe the change of momentum per unit mass along the two horizontal coordinate directions. Equation (3.23c) is the hydrostatic equation expressed in terms of the geopotential and in log pressure coordinates, and is equivalent to equation (3.12). The law of conservation of energy is given by

$$\frac{dT}{dt} + w\frac{\kappa T}{H} = \frac{Q}{c_p} \tag{3.24a}$$

or equivalently by

$$\frac{d\Theta}{dt} = q \tag{3.24b}$$

where, as stated in (3.10),

$$q \equiv \left[\frac{p_0}{p}\right]^\kappa \frac{Q}{c_p}$$

Mass conservation (continuity) is expressed by

$$\frac{1}{\mathrm{a}\cos\phi}\frac{\partial \mathrm{u}}{\partial\lambda}+\frac{1}{\mathrm{a}\cos\phi}\frac{\partial(\mathrm{v}\cos\phi)}{\partial\phi}+\frac{1}{\rho_0}\frac{\partial\rho_0\mathrm{w}}{\partial \mathrm{z}}=0 \tag{3.25}$$

where $\rho_0=\rho_\mathrm{s}\exp(-\mathrm{z}/\mathrm{H})$, and ρ_s is a reference density at the surface ($\mathrm{z}=0$). The operator $\mathrm{d}(\ )/\mathrm{dt}$ in spherical coordinates is again defined by (3.11*d*). Equations (3.23) through (3.25) are called the *primitive equations* because they contain almost no approximations, except for those of hydrostatic balance, the neglect of Coriolis acceleration terms due to the horizontal component of the Earth's rotation vector, and the substitution of the Earth's radius a for variable r.

These equations define the basis for a theoretical treatment of the atmospheric circulation. Together with suitable boundary and initial conditions they are used in primitive equation models of the atmosphere (see Section 3.9).

It can be easily deduced from equations (3.10) and (3.20) that the potential temperature increases with the pressure-altitude z as

$$\Theta=\mathrm{T}\ \exp\left(\frac{\kappa \mathrm{z}}{\mathrm{H}}\right) \tag{3.26}$$

Because, in a stably stratified atmosphere, the potential temperature increases monotonically with height, it is often used as "the vertical coordinate" in atmospheric problems. Such a system is called the *isentropic coordinate system* because a constant Θ surface corresponds to a surface of constant entropy $\mathrm{S}(\Theta)=\mathrm{c_p}\ln\Theta+\text{constant}$. In this framework, the vertical velocity

$$\dot{\Theta}=\frac{\mathrm{d}\Theta}{\mathrm{dt}}=\mathrm{q} \tag{3.27}$$

is proportional to the diabatic heating rate Q. The "horizontal" momentum equations are expressed by

$$\frac{\mathrm{d}_\Theta \mathrm{u}}{\mathrm{dt}}-\left[\mathrm{f}+\frac{\mathrm{u}\tan\phi}{\mathrm{a}}\right]\mathrm{v}+\frac{\partial\Psi}{\mathrm{a}\cos\phi\partial\lambda}=\mathrm{F}_\lambda \tag{3.28a}$$

$$\frac{\mathrm{d}_\Theta \mathrm{v}}{\mathrm{dt}}+\left[\mathrm{f}+\frac{\mathrm{u}\tan\phi}{\mathrm{a}}\right]\mathrm{u}+\frac{\partial\Psi}{\mathrm{a}\partial\phi}=\mathrm{F}_\phi \tag{3.28b}$$

where $\Psi=\mathrm{c_pT}+\Phi$ is the *Montgomery stream function*, and where the material derivative is now expressed as

$$\frac{\mathrm{d}_\Theta}{\mathrm{dt}}=\frac{\partial}{\partial \mathrm{t}}+\frac{\mathrm{u}}{\mathrm{a}\cos\phi}\frac{\partial}{\partial\lambda}+\frac{\mathrm{v}}{\mathrm{a}}\frac{\partial}{\partial\phi}+\dot{\Theta}\frac{\partial}{\partial\Theta} \tag{3.29}$$

The hydrostatic relation takes the form

$$\frac{\partial\Psi}{\partial\Theta}=\mathrm{c_p}\frac{\mathrm{T}}{\Theta} \tag{3.30}$$

and the mass conservation equation is given by

$$\frac{\partial \sigma}{\partial \mathrm{t}} + \frac{\partial (\sigma \mathrm{u})}{\mathrm{a} \cos\phi \partial \lambda} + \frac{1}{\mathrm{a}\cos\phi}\frac{\partial}{\partial \phi}(\sigma \mathrm{v}\cos\phi) + \frac{\partial}{\partial \Theta}\left(\sigma \dot{\Theta}\right) = 0 \qquad (3.31)$$

where

$$\sigma = -\frac{1}{\mathrm{g}}\frac{\partial \mathrm{p}}{\partial \Theta} \qquad (3.32)$$

is called the *pseudodensity*.

The conceptual advantage of the isentropic system is that, in the absence of diabatic heating ($\dot{\Theta} = 0$), the motion becomes two-dimensional: it has no "vertical" component and air parcels are displaced along "horizontal" isentropic surfaces. In this case, isopleths (surfaces of constant mixing ratios) for long-lived tracers tend to be parallel to isentropic surfaces. In the presence of diabatic processes with "cross isentropic" motions, these isopleths tend to slope slightly across the isentropes. In the stratosphere, diabatic processes are sufficiently slow that air parcels remain close to their isentropes for typically 1-2 weeks. Isentropic coordinates are therefore convenient to analyze motions and tracer transport over such time scales. In the interpretation of the results, however, it should be remembered that isentropic surfaces move (often significantly) relative to geometric or pressure height.

3.3.2 The Geostrophic Approximation

Scale analysis of the primitive momentum equations, (3.23a,b), reveals that, for typical wind speeds and spatial scales observed in the atmosphere, the time derivative and curvature terms in these equations are small compared to the pressure gradient and Coriolis accelerations (see Holton, 1992, for details). In particular, if we scale the time derivative term in equation (3.23a) as follows:

$$\frac{\mathrm{du}}{\mathrm{dt}} \approx \frac{\mathrm{U}}{(\mathrm{L/U})} \approx \frac{\mathrm{U}^2}{\mathrm{L}} \qquad (3.33)$$

where U is a typical zonal wind speed (order of 10-100 m/s for the stratosphere) and L is a typical length scale (order of 1000-10,000 km), the Coriolis acceleration is

$$2\Omega \sin\phi \, \mathrm{u} \approx \mathrm{fU} \qquad (3.34)$$

where f is the Coriolis parameter (roughly 10^{-4} s^{-1} except near the equator). The ratio of the inertial (du/dt) to Coriolis accelerations

defines the *Rossby number* (R_o) *of the flow,* given by

$$R_o = \frac{U^2/L}{fU} = \frac{U}{fL} \tag{3.35}$$

Substituting the numbers given above, we obtain $R_o \approx 10^{-1}$, indicating that the inertial term (du/dt) is significantly smaller than the Coriolis acceleration in the momentum equation for the case considered here. It can be shown that for this case, the only term in equation (3.23a) which is of comparable magnitude to the Coriolis term is the one representing the horizontal pressure gradient force, $1/(a \cos \phi)\ \partial\Phi/\partial\lambda$, and indeed these two terms are nearly in balance with one another. It can also be shown that $R_o \leq 0.1$ is a good assumption for all scales of motion larger than about 1000 km, except very near the equator, where $f \rightarrow 0$.

Retaining only the Coriolis and pressure gradient terms in (3.23a) and (3.23b), we obtain the *geostrophic* wind equations:

$$fu = -\frac{1}{a}\frac{\partial\Phi}{\partial\phi} \tag{3.36a}$$

$$fv = \frac{1}{a \cos\phi}\frac{\partial\Phi}{\partial\lambda} \tag{3.36b}$$

These equations show that stratospheric winds blow approximately parallel to the contours of the geopotential field. An alternative version of the geostrophic balance can be obtained by substituting the hydrostatic approximation as given in (3.23c) into (3.36a,b), after differentiating with respect to z:

$$f\frac{\partial u}{\partial z} = -\frac{R}{H}\frac{1}{a}\frac{\partial T}{\partial\phi} \tag{3.37a}$$

$$f\frac{\partial v}{\partial z} = \frac{R}{H}\frac{1}{a \cos\phi}\frac{\partial T}{\partial\lambda} \tag{3.37b}$$

These are the *thermal wind equations,* which state that the vertical shear of the horizontal wind field is proportional to the horizontal temperature gradient. These equations illustrate that the wind structure is strongly coupled to the temperature gradient, underscoring the close relationship between thermodynamic conditions and advective motion. Note, for example, that the zonal wind, u, as shown in Figure 3.4, increases with altitude in the presence of an equatorward temperature gradient (Figure 3.2) in both the northern and southern hemispheres. It decreases for a poleward temperature gradient. Thus the region of maximum zonal wind (the "jet") near the polar night region can be understood to be a manifestation of geostrophic balance as expressed by the thermal wind equation.

Although the geostrophic wind equations are an excellent approximation of the horizontal wind field in atmospheric motion systems of scales greater than about 1000 km, they do not contain time derivatives (tendencies), and are thus diagnostic, not prognostic (predictive) equations. However, by performing a more detailed scale analysis, it is possible to derive a system of prognostic equations which still embody the geostrophic balance as the lowest order approximation, but include in certain terms the possibility of departures from geostrophy. These are known as the *quasi-geostrophic* equations. There is no single quasi-geostrophic system, since the form of the equations depends, among other things, on the horizontal scale of the motions of interest compared to the Earth's radius.

3.3.3 The Potential Vorticity

For a large class of scale of motions, the primitive equations (which are rather expensive to solve numerically) can be replaced by approximate equations for the vorticity or the potential vorticity. *Relative vorticity* can be thought of as a measure of the rotation of the fluid with respect to a coordinate sytem fixed to the Earth. Its vertical component is defined in spherical coordinates as

$$\xi = \frac{1}{\mathrm{a}\cos\phi}\frac{\partial \mathrm{v}}{\partial \lambda} - \frac{1}{\mathrm{a}\cos\phi}\frac{\partial\left(\mathrm{u}\cos\phi\right)}{\partial\phi} \tag{3.38}$$

By cross-differentiating and combining the primitive equations (3.23*a* and 3.23*b*) and using the continuity equation (3.25), one obtains the vorticity equation

$$\frac{\mathrm{d}\left(\xi+\mathrm{f}\right)}{\mathrm{dt}} = \left(\xi+\mathrm{f}\right)\left[\frac{1}{\mathrm{a}\cos\phi}\frac{\partial \mathrm{u}}{\partial\lambda} + \frac{1}{\mathrm{a}\cos\phi}\frac{\partial\left(\mathrm{v}\cos\phi\right)}{\partial\phi}\right] + \frac{1}{\mathrm{a}\cos\phi}\frac{\partial \mathrm{F}_\phi}{\partial\lambda} - \frac{1}{\mathrm{a}\cos\phi}\frac{\partial\left(\mathrm{F}_\lambda\cos\phi\right)}{\partial\phi} \tag{3.39}$$

The sum $\xi + \mathrm{f}$ is called the *absolute vorticity*. It represents the spin of air parcels relative to a coordinate system fixed to the Earth and of the planetary vorticity (represented by the Coriolis parameter f), which accounts for the fact that the coordinate system is rotating at angular vorticity Ω. As shown by equation (3.39), even in the absence of frictional forces, the absolute vorticity is not a conserved quantity. Its tendency is proportional to the horizontal component of the wind convergence. If this component is positive, absolute vorticity filaments will gather closer together, increasing the magnitude of the air parcel

spin by decreasing the cross-sectional area of the vortex tubes (see *e.g.*, Pedlosky, 1987).

A more general form of the vorticity is provided by Ertel's *potential vorticity* (Rossby, 1940; Ertel, 1942). In the log-pressure coordinate system, this quantity is defined by

$$\mathrm{P} = \frac{1}{\rho_\mathrm{s}} \left(\xi + \mathrm{f}\right) \frac{\partial \Theta}{\partial \mathrm{z}} \tag{3.40a}$$

and is therefore the product of the absolute vorticity and the vertical gradient of the potential temperature. The potential vorticity is a measure of the vertical component of angular momentum of fluid elements. In the stratosphere, the value of P on an isentropic surface increases monotonically from the South Pole to the North Pole as the Coriolis factor f increases with latitude. The value of P is generally negative in the Southern hemisphere and positive in the Northern hemisphere. In the vicinity of the tropopause (where the vertical gradient of the potential temperature is large), a strong vertical gradient is also observed in the potential vorticity.

As indicated earlier, atmospheric motions are often advantageously represented in an isentropic coordinate system. In this case, Ertel's potential vorticity is defined by

$$\mathrm{P} = \frac{1}{\sigma} \left(\xi + \mathrm{f}\right) \tag{3.41}$$

where σ is the "pseudo-density" (see expression (3.32)). Starting from the primitive equations (3.28a-b), one can show that P satisfies the following equation

$$\frac{\mathrm{d}_\Theta \mathrm{P}}{\mathrm{dt}} = \frac{1}{\sigma \mathrm{a} \cos\phi} \left[-\frac{\partial \left(\mathrm{F}_\lambda \cos\phi\right)}{\partial \phi} + \frac{\partial \mathrm{F}_\phi}{\partial \lambda} - \frac{\partial \mathrm{Q}}{\partial \lambda} \frac{\partial \mathrm{v}}{\partial \Theta} + \frac{\partial \mathrm{Q}}{\partial \phi} \frac{\partial \mathrm{u}}{\partial \Theta} \cos\phi \right] + \mathrm{P} \frac{\partial \mathrm{Q}}{\partial \Theta} - \mathrm{Q} \frac{\partial \mathrm{P}}{\partial \Theta} \tag{3.42}$$

where the material derivative in the isentropic system is defined by (3.29). This expression shows that for frictionless and adiabatic conditions ($\mathrm{F}_\lambda = \mathrm{F}_\phi = 0$; $\mathrm{Q} = 0$), Ertel's potential vorticity is a conserved quantity following the motion.

Apart from the absolute vorticity (ξ+f), the Ertel's potential vorticity varies in the vertical as $\Theta^{9/2}$ (see Lait, 1994). It is therefore useful to define a modified potential vorticity

$$\Pi = \mathrm{P} \left(\frac{\Theta}{\Theta_0} \right)^{-9/2} \tag{3.40b}$$

which removes the quasi-exponential variation with height while preserving the conservation properties of P. (Θ_0 is a reference potential temperature chosen, for example, as 420 K, see Lait, 1994). Figure 3.9

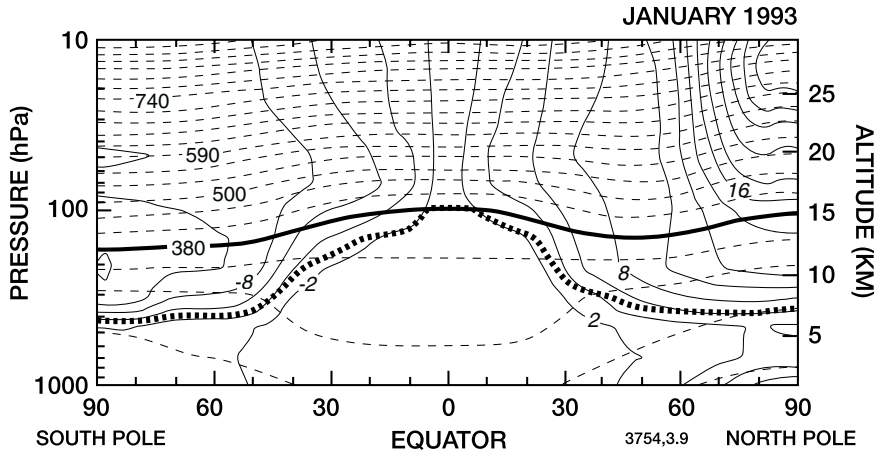

Figure 3.9. Zonally averaged distribution of the modified potential vorticity (unbroken lines in 10^{-4}K m^{2}s^{-1}kg^{-1}) from the surface to approximately 30 km altitude (10 hPa). The potential temperature (K) is represented by dashed lines and the tropopause by a dotted line. From Appenzeller (1994).

shows the zonally averaged distribution of the modified potential vorticity superimposed on the potential temperature for January.

The concept of potential vorticity is of central importance in fluid dynamics and in meteorology. When the powerful constraint of vorticity conservation can be applied, the physical interpretation of atmospheric motions becomes more accessible (Hoskins *et al.*, 1985). The fact that in many situations dissipative processes do not play a major role on advective time scales makes this quantity very useful as a tracer of atmospheric motions (see Danielsen, 1961; McIntyre and Palmer, 1983). Figure 3.10 presents an example of an observationally derived potential vorticity distribution on the 850 K isentropic surface. Potential vorticity is often expressed in 10^{-6}K m^{2}kg^{-1}s^{-1}, referred to as PV units (Holton *et al.*, 1995). This figure shows that, as expected, the potential vorticity tends to increase with latitude. Potential vorticity contours, however, are affected by planetary-scale waves. The behavior of long-lived chemical tracers is very similar to that of potential vorticity. Knowledge of potential vorticity distributions from meteorological analyses can therefore be used to extrapolate limited observations of chemical tracers to a broad region of the atmosphere (see *e.g.*, Coffey *et al.*, 1999). Potential vorticity has, however, an important property not shared by chemical tracers: It is not only advected by the flow, but it actually determines the distribution of the flow itself. Changes in potential vorticity, therefore, induce changes in the wind and temperature fields.

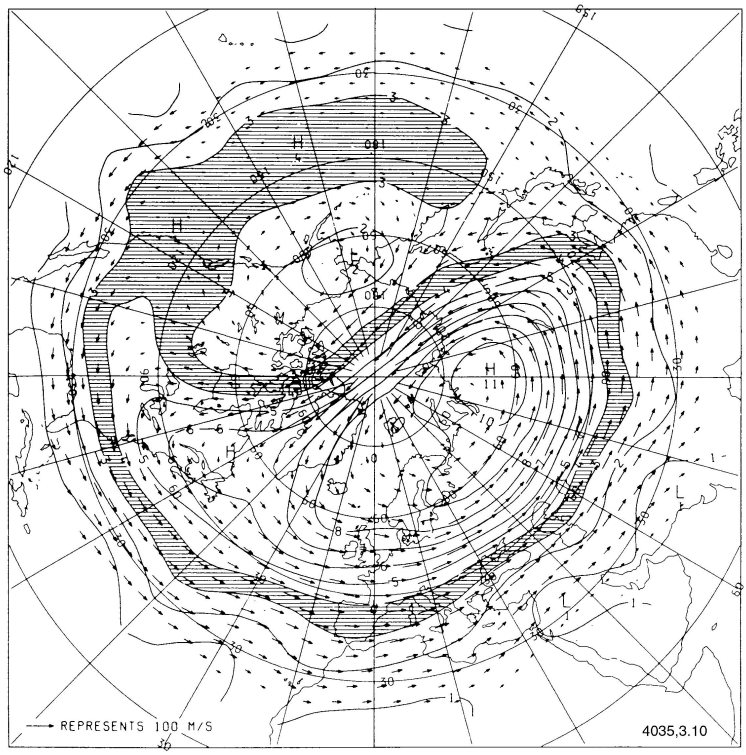

Figure 3.10. Global distribution of the potential vorticity on the 850 K isentropic surface during a wintertime planetary wave event. The shaded region over the Pacific ocean with a weak gradient is characterized by nonlinear wave dissipation and strong quasi-horizontal mixing. This region is referred to as the "surf zone". Wind vectors are also indicated and provide information about large-scale transport. Courtesy of A. O'Neill, University of Reading, UK.

Finally, it is interesting to note that, since potential vorticity is a conserved quantity, air parcels that are displaced to an area with different PV values develop a differential motion which tends to restore them to their original PV area. Thus, strong PV gradients act as *dynamical barriers* to transport. Barriers against horizontal mixing are observed in the lower stratosphere near the polar vortex and at the boundary between tropical and extratropical air masses. Wave events distort PV surfaces often leading to the formation of thin filaments which are pulled away from the barriers.

3.4 Atmospheric Waves

Waves are key dynamical features of the atmosphere. They can be defined as propagating disturbances of material contours whose

acceleration is balanced by a restoring force. This force can be produced by buoyancy in a stably stratified fluid (*e.g.*, gravity waves) or by the Coriolis force (*e.g.*, inertial waves). In the first case, the force acts to oppose vertical displacements, while in the second case, it opposes horizontal displacements.

Different types of waves can be distinguished: resonant modes produced by small random forcing are referred to as *free modes*. The observed 2, 5, and 16-day large-scale atmospheric waves belong to this category. Waves excited at the Earth's surface, for example by air flow over topography, by land/ocean temperature contrasts or by convective systems, are called *forced modes*. Some such waves can propagate to high altitudes where they dissipate and transfer momentum to the atmospheric circulation. Waves are often refracted in the atmosphere, and a refractive index which determines the ray path along which the wave propagates can be defined. Large-scale waves that propagate vertically as well as horizontally are called *global modes*, while waves that remain trapped in the tropics and propagate only in the zonal and vertical directions are referred to as *equatorial modes*. If the waves propagate over several scale heights in the vertical direction, they are said to be *internal modes*. Conversely, if they are rapidly attenuated as they propagate upwards, they are called *external modes*.

Waves are characterized by their amplitudes and their phases, as well as by their phase speeds (which describe the rates at which the crest and the trough of the waves propagate) and their group speeds (which are a measure of the rate at which the energy of the disturbance propagates).

The evolution of disturbances on a given basic atmospheric state is described by the wave momentum, continuity, and thermodynamic equations. These are obtained by replacing all fields ψ in the primitive equations by the sum of the basic state $\overline{\psi}$ and a wave perturbation of ψ' (see Section 3.6.1), and by subtracting the equations applied to the basic state. The basic state is often taken to be the zonally averaged state of the atmosphere. For small-amplitude disturbances, second-order terms can be neglected and waves are approximated as linear. In the case of large disturbances, the nonlinear terms in the wave equations become significant and nonlinear wave-wave interactions become important. The solution of the wave equations leads to dispersion equations which express the conditions under which a wave can propagate in the atmosphere.

Gravity waves are oscillations with relatively short horizontal wavelengths (typically 10-1000 km) that arise in a stably stratified fluid when air parcels are being displaced vertically. These waves are produced by air flow over mountains (orographic waves) or by other (not well identified) non-orographic sources such as thunderstorms, frontal

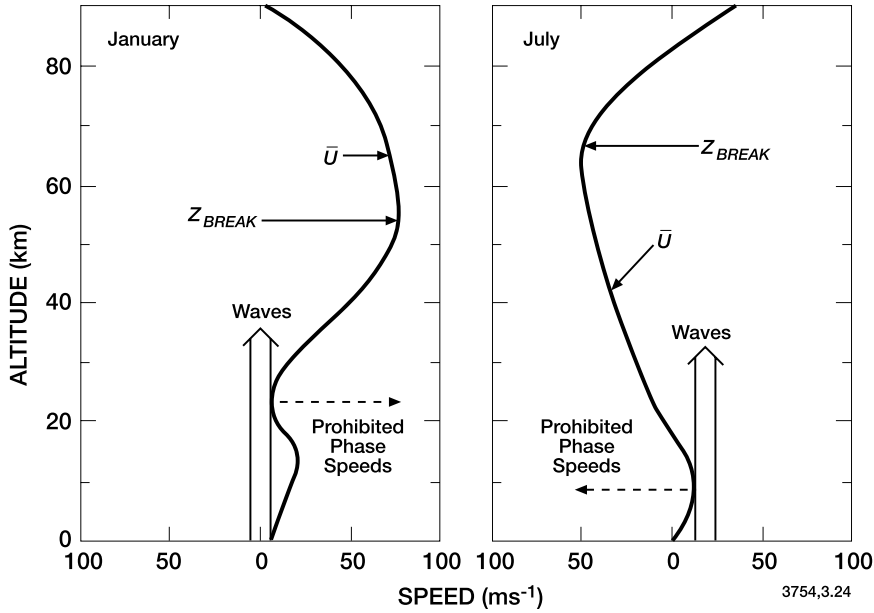

Figure 3.11. Approximate altitude profiles of the mean zonal winds in winter (left panel) and summer (right panel). The permitted phase speeds for the propagation of gravity waves and their breaking levels are also shown. Adapted from Lindzen (1981).

systems or instabilities. The propagation of gravity waves through the atmosphere depends on the wind distribution and thermal structure, which varies markedly with season and the static stability. Specifically it can be shown that, when the phase speed c of a wave is equal to the zonal wind speed $\overline{\mathrm{u}}$, the wave is absorbed. The point where this occurs is referred to as the *critical level* for that particular wave. Figure 3.11 shows how this absorption effect influences gravity wave propagation at mid-latitudes for different seasons. Specifically, owing to the strong filtering by passage through the stratosphere, mesospheric gravity waves are predominantly westward propagating waves in winter and eastward propagating waves in summer. In the absence of dissipation, the amplitude of gravity waves grows as the inverse square of the density. This can be understood by considering that for kinetic energy

$$E = \frac{1}{2}\rho_{\mathrm{o}} \left|\mathrm{v}'(\mathrm{z})\right|^2 \tag{3.43}$$

to remain constant, the amplitude of the wave must grow as

$$\left|\mathrm{v}'(\mathrm{z})\right| = \mathrm{A}\left[\rho_0\,(\mathrm{z})\right]^{-\frac{1}{2}} \tag{3.44a}$$

where A is a constant. Since $\rho_0(z)$ varies with altitude as $\rho_s \exp(-z/H)$, then

$$|v'(z)| = \frac{A}{\rho_s} \exp\left(\frac{z}{2H}\right) \qquad (3.44b)$$

i.e., the wave amplitude grows exponentially with height. At some altitude, the gravity wave will have grown so large that its temperature perturbation will produce a superadiabatic lapse rate and become convectively unstable. At this point, the wave is said to "break". Note that if, in addition to buoyancy, the Coriolis force acts as a restoring force, the waves are referred to as *inertia-gravity waves*. This effect becomes significant if the horizontal wavelength of the waves is larger than approximately 300 km.

Gravity waves provide the major source of dynamical variability in the mesosphere. The presence of gravity waves has been inferred from oscillations observed in airglow emissions (Walterscheid *et al.*, 1987; Makhlouf *et al.*, 1995; 1998; Swenson and Gardner, 1998). Lidar observations (see Figure 3.12 and also Hauchecorne *et al.*, 1987) also show, for example, that such waves can create alternating layers with near adiabatic lapse rate temperature profiles and strong temperature inversions. These waves can also affect some chemical species, particularly in the mesosphere and lower thermosphere. In addition, as first pointed out by Leovy (1966), photochemistry can damp or enhance the amplitude of gravity waves and even destabilize them in the vicinity of the mesopause (see also Xun Zhu and Holton, 1986; Xu, 1999).

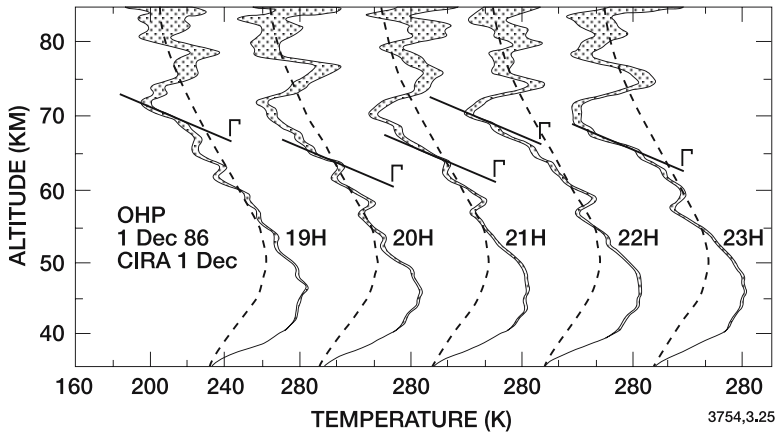

Figure 3.12. Sequence of temperature profiles measured by Lidar at Bicarosse, France (from 19:00 to 23:00) showing the presence of gravity waves in the mesosphere. From Hauchecorne *et al.* (1987).

Rossby waves are planetary-scale waves that owe their existence to meridional gradients in potential vorticity. These waves are westward propagating relative to the mean flow. The waves with the largest amplitudes, however, are quasi-stationary because they are produced by stationary sources including large-scale orography and land-sea contrasts. These Rossby waves propagate upwards and equatorwards in the middle atmosphere. It can be shown, however, that upward propagation requires that the zonal wind be westerly (from west to east) with a velocity smaller than a critical value. This critical value is a function of the horizontal wavenumber of the wave and is typically 100 m/s in the case of wavenumber 1. On the basis of this criterion (called the Charney-Drazin criterion), Rossby waves propagate into the stratosphere primarily during winter, which explains the quasi-zonal symmetric nature of the dynamical fields during summer, when wave propagation is much reduced. Figure 3.13 shows the seasonal difference in stratospheric meteorological fields. Note, however, that free Rossby waves with smaller amplitudes do propagate in the summer and may cause substantial mixing in the lower stratosphere at high latitudes (see Wagner and Bowman, 2000). The presence of such waves could explain the variability of ozone observed at mid- to high latitudes during the summer in the altitude range of 20-30 km (see Hoppel *et al.*, 1999). In practice, the Charney-Drazin criterion is satisfied only for wavenumbers 1-3, so that only the longest Rossby waves penetrate in the extratropical winter stratosphere. An extension of the tropospheric weather systems (wavenumbers 5 to 15) can, however, be observed in the lower stratosphere.

When the planetary waves reach environments for which nonlinear effects can no longer be neglected, wave breaking may occur. In this case, the reversible undulation of material contours (mixing ratios, PV) described by linear wave theory is replaced by rapid and irreversible deformation of these contours with the generation of small-scale motions in situ. A simple mathematical treatment of the wave equation for the quasi-geostrophic potential vorticity shows that this situation occurs in the vicinity of a *critical surface* along which the phase velocity of the wave is equal to the zonal mean wind ($\overline{u} = c$). When wave breaking occurs, considerable deformation of material contours (potential vorticity, trace constituents) takes place, producing a cascade of gradually smaller scale motions, and eventually irreversible mixing of air parcels along isentropic surfaces. Regions where large scale mixing associated with Rossby wave breaking is observed (mid-latitude winter hemisphere) are referred to as the "*surf zone*" (McIntyre and Palmer, 1983; 1984) and are characterized by weak horizontal gradients in conservative tracers. The surf zone is bounded by narrow regions of

strong PV gradients which act as dynamical barriers: the polar vortex and the subtropical barrier. The existence of a surf zone between 25 and 45°S is refected in the distribution of nitrous oxide shown in Figure 3.25. The surf zone is also apparent over the Pacific Ocean in Figure 3.10 where the potential vorticity is very uniform.

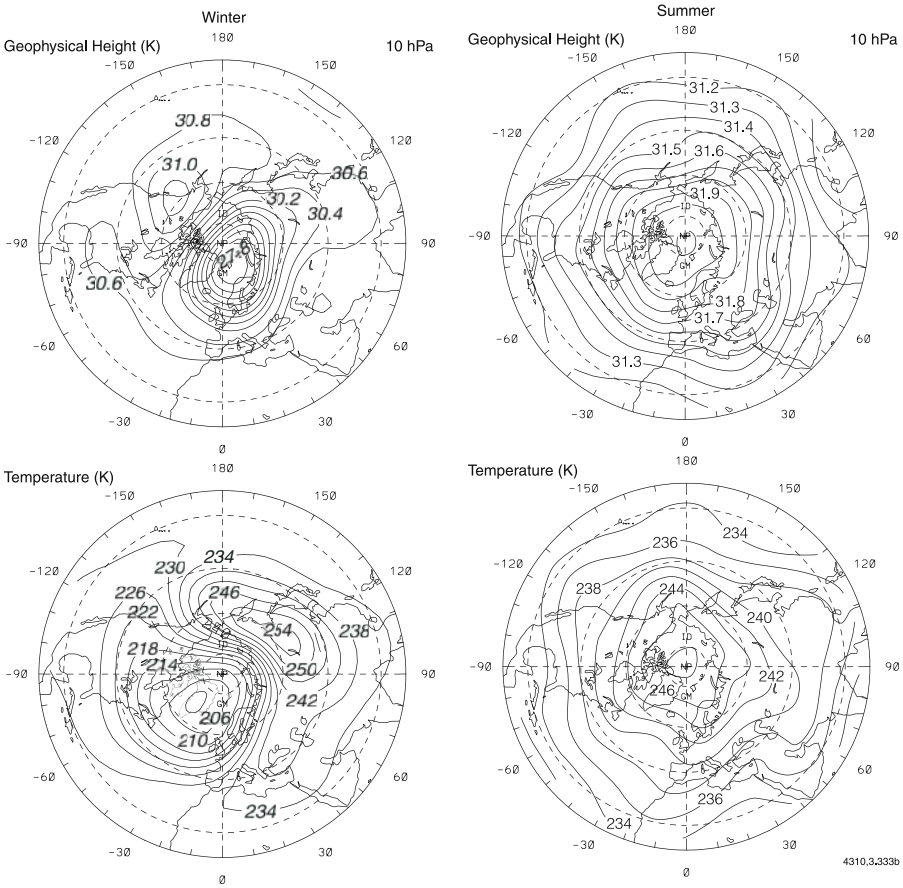

Figure 3.13. Geopotential height (km) and temperature (K) on the 10 hPa surface in the stratosphere during Northern Hemisphere winter (18 February 1999 — left) and summer (9 July 1999 — right). Planetary-scale waves are visible in the winter hemisphere with the polar vortex displaced towards northern Europe and a "high" visible over Western Canada and the Aleutian Islands. The temperature is lowest over the north Atlantic and is highest over Siberia. This situation is representative of a wavenumber 1 event. In the summer hemisphere, planetary-scale wave activity is low and the geopotential height and temperature fields are nearly symmetric around the North Pole (Courtesy of W. Randel, NCAR, 2001).

The change of sign of the Coriolis parameter at the equator leads to a specific class of large-scale waves that are generally trapped laterally in the tropics, but propagate vertically and zonally. *Kelvin waves*, which propagate eastward with a phase velocity of typically 30 m s^{-1}, are characterized by a vertical wavelength of typically 10 km and wavenumbers of 1-3. *Mixed Rossby-gravity* waves propagate westward, with vertical wavelengths of the order of 6-8 km, and with 4-5 wavenumbers in the zonal direction. The horizontal structure of these types of waves (geopotential and winds) is shown in Figure 3.14.

In the equatorial upper stratosphere and lower mesosphere, low zonal wavenumber "pancake" structures have frequently been observed (Hitchman *et al.*, 1987), and are suggestive of *inertially unstable motions*. The sources and dynamics of such disturbances need to be elucidated.

Finally, the *tides* observed in the mesosphere and thermosphere should be mentioned. Atmospheric solar tides are global-scale waves with periods that are harmonics of a 24-hour day. These oscillations are

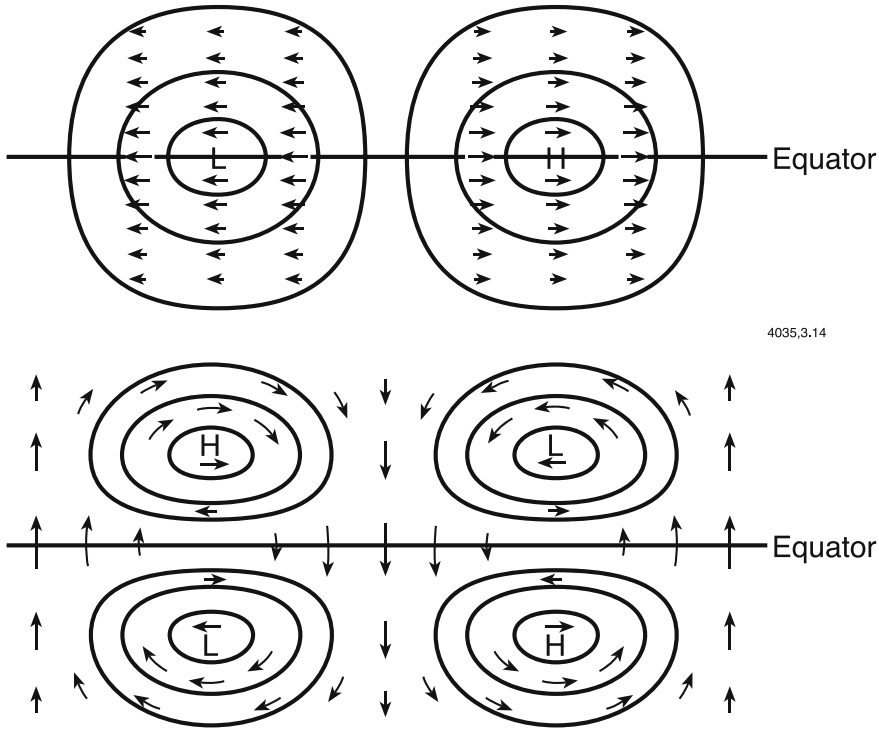

Figure 3.14. Geopotential and wind structure of an equatorial Kelvin wave (upper panel) and mixed Rossby-gravity wave (lower panel).

driven primarily by the periodic absorption of solar ultraviolet energy by ozone in the middle atmosphere and of solar infrared energy by water vapor in the troposphere. An additional thermal driver is provided by latent heat which is stored as water vapor, transported within the troposphere and released when the vapor precipitates.

Migrating tides are those waves which propagate westward with the apparent motion of the Sun. They have significant diurnal and semi-diurnal components. Non-migrating tidal components are also harmonics of the solar day, but they may be stationary, or propagate either eastward or westward. Their dominant source is provided by latent heat release in the troposphere, and thus related to meteorological processes in the lower atmosphere. A small semi-diurnal tide is also forced by the gravitational attraction of the Moon.

The propagation of atmospheric tides has been described by Lindzen (1967), Chapman and Lindzen (1970), Lindzen and Blake (1970), Forbes (1982a, b), Hagan (2000) and many others. These waves have also been observed from space instruments such as HRDI and WINDII on board the Upper Atmosphere Research Satellite (UARS; see *e.g.*, Hays *et al.*, 1994). Figures 3.15a-b show the signature of the tides in the zonally averaged winds measured at 12:00 h local solar time (McLandress *et al.*, 1996). Tide ampitudes increase with height in the mesosphere due to decreasing air density. Figure 3.15c shows the amplitude of the diurnal tide in the meridional wind at 95 km and 20°N between 1992 and 1995 (Burrage *et al.*, 1996). There is some indication that the tide amplitude is modulated by the quasi-biennial oscillation (see Section 3.7). Large tidal variations are also observed in the temperature (1 K at 80 km, 10 K at 100-120 km, and 100 K at 150 km). The tidal oscillation in the vertical wind produces strong variations in the concentration of chemical species that exhibit large vertical concentration gradients (*e.g.*, atomic oxygen, nitric oxide).

The amplitude of the diurnal tide is largest around 30° latitude in the case of the horizontal wind components. In the case of temperature, pressure and the vertical wind component, the tidal perturbation is largest at the equator. Figure 3.15d shows the diurnal vertical wind perturbation (migrating tide) in April, when the tidal amplitude is largest. The semi-diurnal component is observed at all latitudes above 80 km altitude. Ground-based and satellite instruments, as well as dynamical models, show that tides often govern the dynamics of the upper mesosphere and lower thermosphere. For example, numerical experiments (see, *e.g.*, Liu and Hagan, 1998) show that the tidal wind may have a strong impact on gravity wave breaking and hence on local heating/cooling of the mesosphere. Tidal dampening occurs above 80 km altitude, where it provides a source of momentum and causes turbulence.

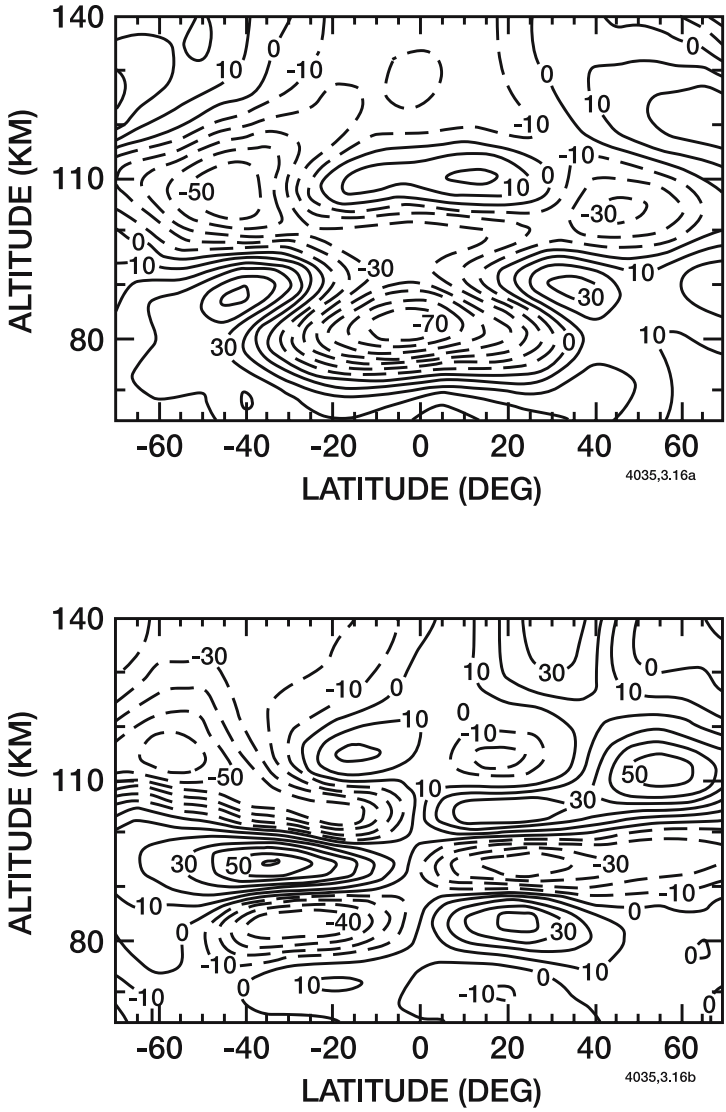

Figure 3.15a,b. Zonally averaged wind velocities for the equinox period (February 12 to May 3, 1993) at 12:00 h local solar time derived from the combined observations of HRDI and WINDII on board the UARS satellite. Zonal (a) and meridional (b) wind velocities (m/s) are shown between 65 and 140 km altitude. Dashed lines correspond to westward winds (easterlies) for the zonal component and to southward winds for the meridional component. The signature of solar tides is visible. Adapted from McLandress *et al.*, 1996.

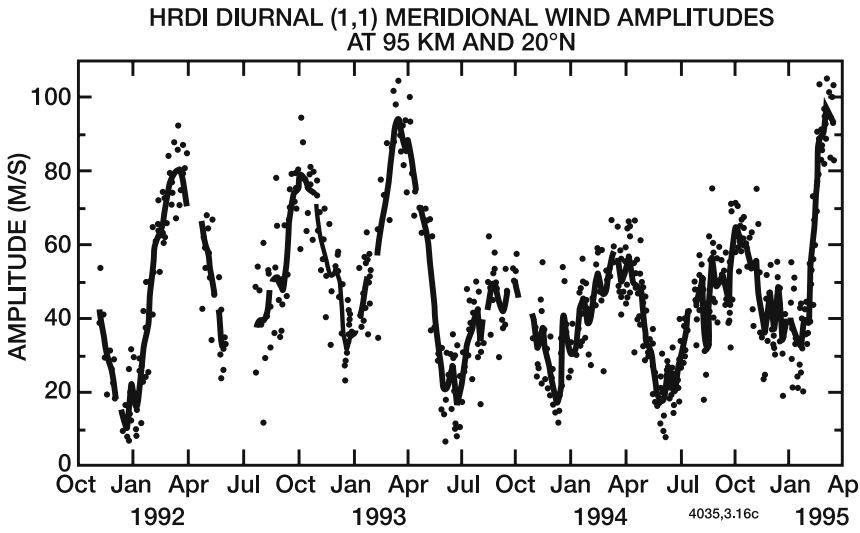

Figure 3.15c. Amplitude of the meridional wind variation at 95 km and 20°N between October 1991 and April 1995 produced by the diurnal component of the migrating tides. From Burrage *et al.*, 1996.

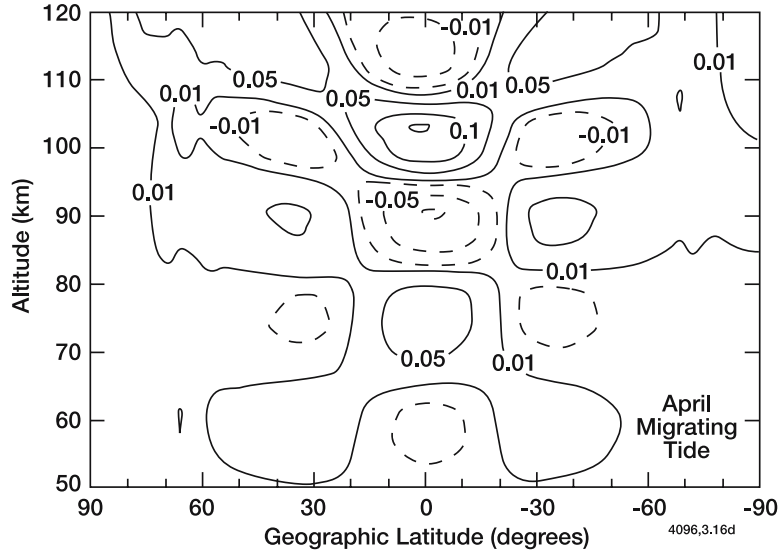

Figure 3.15d. Calculated diurnal vertical wind perturbation (m/s) at 12 LT associated with the migrating tide in April. Courtesy of M. Hagan, NCAR, 2001.

3.5 Effects of Dynamics on Chemical Species: Transport

3.5.1 The Continuity Equation

The density of a chemical compound at a given point of the atmosphere is derived from the *continuity equation*. The equation can be understood by noting that the change in concentration results from local sources (*e.g.*, chemical reactions) and from transport processes. The tendency associated with transport is given by the convergence (or divergence) of the concentration of this chemical compound within an infinitely small volume element surrounding the point under consideration. Thus, for a chemical species i, the *mass density* ρ_i at time t is governed by the following equation

$$\frac{\partial \rho_\mathrm{i}}{\partial \mathrm{t}} + \vec{\nabla} \cdot (\rho_\mathrm{i} \vec{\mathrm{v}}) = \widetilde{\mathrm{S}}_\mathrm{i} \qquad (3.45a)$$

Note that the source term $\widetilde{\mathrm{S}}_\mathrm{i}$ (expressed here in mass per unit volume and time) is often expressed as the difference between rates of photochemical production $\mathrm{P_i}$ and loss $\mathrm{L_i}$. Introducing the *mass fraction* or *mass mixing ratio* $\mu_\mathrm{i} = \rho_\mathrm{i}/\rho$ where ρ is the air mass density, and making use of the mass conservation equation for air (3.3b), it is easy to show that equation

$$\frac{\mathrm{d}\mu_\mathrm{i}}{\mathrm{dt}} = \frac{\widetilde{\mathrm{S}}_\mathrm{i}}{\rho} \qquad (3.45b)$$

is equivalent to (3.45a). Relation (3.45b) expresses that, in the absence of chemical processes, the mixing ratio of a chemical tracer in an air parcel is conserved along the parcel trajectory. Just as in the case of the potential temperature and potential vorticity, tracer mixing ratios can be used to characterize air motions in the atmosphere if dissipative (chemical) processes are weak.

The continuity equations can also be expressed in terms of *number density* $\mathrm{n_i} = \rho_\mathrm{i}/\mathrm{m}$ and *mole fraction* or *volume mixing ratio* $\mathrm{X_i} = \mathrm{n_i}/\mathrm{n}$, where $\mathrm{n} = \rho/\mathrm{m}$ is the air number density, $\mathrm{m} = \mathrm{M}/\mathrm{N_A}$ is the molecular mass of air, $\mathrm{N_A}$ is Avogadro's number (6.02×10^{26} molecules per mol) and M is the molar mass of air. In the homosphere, where $\mathrm{M} \simeq 29$ kg/mol is approximately constant,

$$\frac{\partial \mathrm{n_i}}{\partial \mathrm{t}} + \vec{\nabla} \cdot (\mathrm{n_i} \vec{\mathrm{v}}) = \mathrm{S_i} \qquad (3.45c)$$

or

$$\frac{\mathrm{dX_i}}{\mathrm{dt}} = \frac{\mathrm{S_i}}{\mathrm{n}} \qquad (3.45d)$$

where the chemical source term S_i is now expressed in particles per unit volume and time ($m^{-3}s^{-1}$ or $cm^{-3}s^{-1}$), with the total air number density n expressed in m^{-3} (or cm^{-3}).

In spherical coordinates, these equations are expressed as

$$\frac{\partial n_i}{\partial t} + \frac{1}{a\cos\phi}\frac{\partial (n_i u)}{\partial \lambda} + \frac{1}{a\cos\phi}\frac{\partial (n_i v\cos\phi)}{\partial \phi} + \frac{\partial (n_i w)}{\partial z} = S_i \quad (3.46a)$$

and

$$\frac{\partial X_i}{\partial t} + \frac{u}{a\cos\phi}\frac{\partial X_i}{\partial \lambda} + \frac{v}{a}\frac{\partial X_i}{\partial \phi} + w\frac{\partial X_i}{\partial z} = \frac{S_i}{n} \quad (3.46b)$$

3.5.2 Time Constants for Transport

In Chapter 2, the time constant appropriate to photochemical processes (τ_{chem}) was discussed, and it was shown that this time constant can be readily derived from knowledge of the rate of loss of chemical species. The time constants for dynamical effects on chemical species are somewhat more difficult to evaluate.

If we consider only the effects of advection and chemistry, the continuity equation for a chemical species i can be written as:

$$\frac{\partial n_i}{\partial t} = S_i - \frac{\partial}{\partial z}(n_i w) - \frac{\partial}{\partial y}(n_i v) - \frac{\partial}{\partial x}(n_i u) \quad (3.47)$$

where n_i is the number density of species i, and where, for simplicity, we have used Cartesian coordinates. To derive the time constant for dynamical processes (τ_{dyn}), some assumption must be made regarding the gradient of compound i. If we assume, for example, that the vertical distribution of chemical species i can be described by a scale height, H_i:

$$n_i = n_{i,o}\exp(-z/H_i) \quad (3.48)$$

where z is the altitude and $n_{i,o}$ is the density of i at a reference altitude, then

$$\frac{\partial n_i}{\partial z} = -\frac{1}{H_i}\, n_{i,o}\exp(-z/H_i) = -\frac{1}{H_i}\, n_i \quad (3.49)$$

Consider, for the purpose of illustration, transport only by vertical winds:

$$\frac{\partial n_i}{\partial t} = -\frac{\partial}{\partial z}(n_i w) = \frac{w}{H_i}\, n_i \quad (3.50)$$

(assuming that w is constant over the spatial distance H_i). By integration,

$$n_{i,t} = n_{i,t_o}\exp\left(\frac{w}{H_i}t\right) \quad (3.51)$$

so that the time required for species i to change by 1/e relative to its initial value, n_{i,t_o} is given by H_i/w. This defines a time constant for transport by the vertical winds. Assuming a scale height of about 5 km for chemical constituents and approximate values for the zonally averaged mean vertical winds as derived from models, the time constant for vertical exchanges is of the order of months in the stratosphere and days in the upper mesosphere.

Time constants for transport by the meridional and zonal winds can be derived in similar fashion, but in these directions it is somewhat more difficult to characterize the typical gradients of chemical species. Assuming for these horizontal changes a typical length scale of about 1000 km in the zonal and meridional directions, the time constant for transport by the zonal winds is of the order of days throughout the middle atmosphere, while that for mean meridional transport is of the order of months in the stratosphere and days in the upper mesosphere.

When considering the formulation adopted in a simple one-dimensional model, in which the mean vertical flux is represented by "eddy diffusivity"

$$\frac{\partial n_i}{\partial t} = S_i - \frac{\partial}{\partial z}\left[-K_z \frac{\partial (n_i/n)}{\partial z}\right] \tag{3.52}$$

(where K_z is the one-dimensional diffusion coefficient), the time constant associated with vertical exchanges is given by H^2/K_z, where H is the atmospheric scale height. It is of the order of months to years in the lower stratosphere, and days in the mesosphere. Figure 3.16 presents an altitude profile of the approximate time constant for one-dimensional eddy diffusion, as well as the chemical time constants of the O_x ($O + O_3$), HO_x ($H+OH+HO_2$), and NO_y ($N + NO + NO_2 + NO_3 + HNO_4 + 2\times N_2O_5 + HNO_3$) chemical families, and water vapor. As a general rule, wherever the time constant for the dynamical process under consideration is comparable to the chemical time constant, then the effects of transport and chemistry will both be important in determining the constituent's density. For example, in the one-dimensional framework, we can see that vertical eddy transport would be important for NO_y at all the altitudes shown, but not for HO_x below about 85 km. This is discussed more explicitly below.

Three different cases can be identified to characterize the effects of the competition between dynamics and chemistry in determining constituent distributions:

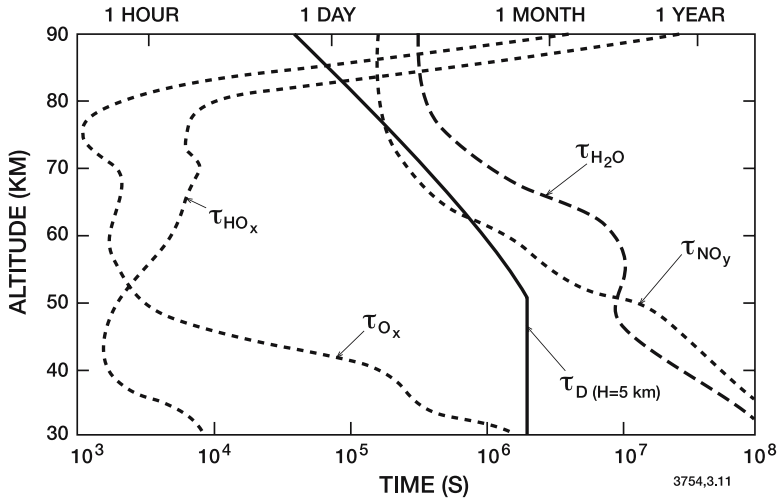

Figure 3.16. Vertical profiles of the chemical lifetimes of O_x, HO_x, H_2O, and NO_y. Typical constants for vertical exchanges (τ_D) are also shown.

- $\tau_{chem} << \tau_{dyn}$. Under these circumstances, the species in question will be in photochemical equilibrium (see Eq. 2.30), and the effects of dynamical processes will not be directly important. Strong spatial gradients often characterize the distribution of photochemically-driven species. Dynamics may still be important in an indirect fashion through the effects of temperature or coupling between chemical species. For example, a very short lived species, such as HO_x can be produced or destroyed by reaction with a longer lived species which does depend on transport (for example, H_2O, see Figure 3.16). Thus an indirect coupling can be important even for very short-lived species.

- $\tau_{chem} >> \tau_{dyn}$. In this case the effect of dynamics is to reduce substantially the gradient in the mixing ratio of chemical compounds. For example, the chemical lifetime of N_2O is of the order of years in the lower stratosphere, while the dynamical time constant associated with the zonal wind is of the order of days. Thus the effect of the zonal wind is to make the N_2O mixing ratio very uniform in longitude. Moderate perturbations to the zonal wind speed will not dramatically influence the constituent density. The major species, O_2 and N_2, are so long lived in the middle atmosphere that they are thoroughly mixed by atmospheric motions, and typical spatial and temporal variations in transport do not influence them. This is not the case in the thermosphere, where their chemical lifetimes are much shorter.

- $\tau_{\text{chem}} \approx \tau_{\text{dyn}}$. Under these circumstances, the effect of dynamics can be quite large, and the species distribution depends critically on both dynamics and chemistry. Chemical processes tend to introduce or enhance spatial gradients in the distribution of the tracers, while dynamics (*e.g.*, mixing) tends primarily to reduce these gradients. The time constants for meridional and vertical transport, are, for example, comparable to the photochemical lifetime of N_2O in the stratosphere, so that transport in the meridional plane is expected to be quite important in determining its density, in contrast to zonal transports, as discussed above.

The special case of zonal asymmetries should also be mentioned. The vector wind is generally aligned along latitude circles in summer, but in winter the influence of planetary waves can cause the vector wind to flow across latitude lines (see Figure 3.13). Under these zonally asymmetric conditions, the local wind speed in the meridional direction is much greater than the *mean* meridional wind. Indeed, winds of zonal speeds (tens of meters per second) can flow across latitude lines, and any species exhibiting a latitude gradient will be affected.

3.5.3 The Age of Air

Long-lived trace gases of tropospheric origin penetrate into the stratosphere, primarily in the tropics. If the mixing ratio of an inert tracer increases with time at the tropical tropopause, its mixing ratio at any point of the middle atmosphere will also increase, but with a certain time lag. An estimate of this lag provides information on the rate at which transport takes place. Observations of tracers such as CO_2, SF_6, and chlorofluorocarbons, whose concentration has been systematically increasing with time, have shown that the time required to transport air parcels from the equatorial tropopause to the mid- and high latitude stratosphere is typically 3-7 years (Bischof *et al.*, 1985; Schmidt and Khedim, 1991; Pollock *et al.*, 1992; Boering *et al.*, 1996; Elkins *et al.*, 1996, etc.).

If large-scale advection alone was responsible for the transport of air parcels from the tropopause to any location in the middle atmosphere, the calculation of the transit time between these two locations would be straightforward. Air parcels, however, do not maintain their integrity over long time scales, because they are rapidly distorted by wave-induced mixing processes into many smaller-scale components. Therefore, the transit time from any point P_0 to point P in the atmosphere cannot

be characterized by a single quantity, but rather by the statistical distribution of the transit times for all material elements that comprise the air parcel. Thus, for conserved tracers that enter the stratosphere at the equatorial tropopause (point P_0) with a time-varying mixing ratio X (P_0, t), the mixing ratio at some point P can be expressed by adding the contributions of all irreductible material elements which reach point P at time t after having traversed different paths with different transit times. Therefore (see Hall and Plumb, 1994)

$$X(P, t) = \int_0^t X(P_0, t - t')\, G(P, P_0, t')\, dt' \tag{3.53}$$

where G represents the Green's function of the differential operator governing the transport from P_0 to P. The Green's function can be interpreted as the distribution of transit times and is therefore called the *age spectrum* (Kida, 1983; Hall and Plumb, 1994; Hall and Waugh, 1997). Its value cannot be directly measured, but it can be estimated as a function of time at any point P by applying a pulse ($X(P_0, t) = \delta(t)$ in Eq. (3.53)) in the tracer mixing ratio at the equatorial tropopause. The mean *age* $\widetilde{\Gamma}$ of middle atmosphere air is defined as the first moment of the age spectrum:

$$\widetilde{\Gamma}(P, P_0) = \int_0^\infty t\ G(P, P_0, t) dt \tag{3.54}$$

Figure 3.17 shows an estimate of the mean age of air as a function of altitude and latitude as derived from aircraft observations of CO_2 and SF_6. It suggests that the mean age in the tropics, which increases with height, exhibits little vertical variation above 25 km altitude, where it can be 4 or more years. At mid-latitudes, $\widetilde{\Gamma}$ increases monotonically from the tropopause to the upper stratosphere and reaches 7 or more years about 30 km altitude.

It is straightforward to show that, for purely advective motions (without mixing), the age of air at a given point is simply the time by which the mixing ratio at this point lags the value of the mixing ratio at the equatorial tropopause. In a more general case, when advection and mixing take place, the equivalence between age and lag time does not hold, except in the long-term limit ($t \to \infty$) when the mixing ratio of the tracer at the equatorial tropopause increases *linearly* with time (see Hall and Prather, 1993; Hall and Plumb, 1994). The measurement of time lags for species such as CO_2 or SF_6, whose mixing ratios increase quasi-linearly in time (neglecting seasonal variations), provides a good estimate of the age of middle atmosphere air.

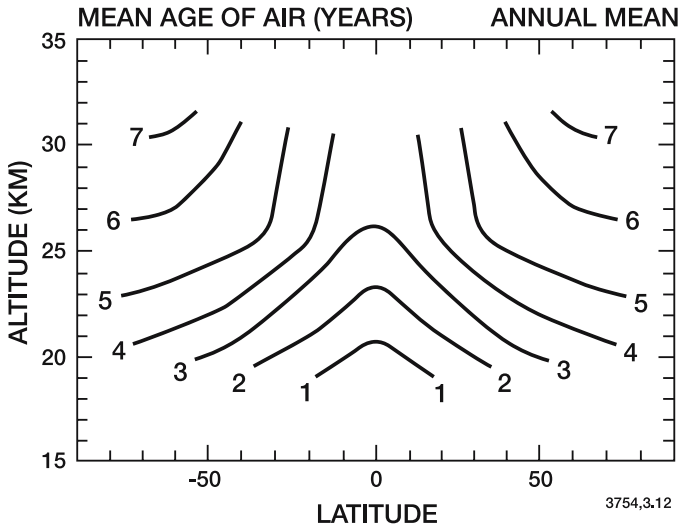

Figure 3.17. Meridional distribution of the mean age of stratospheric air (schematic representation of the annual mean expressed in years). From Hall *et al.*, (1999).

3.5.4 Tracer Correlations

As indicated earlier (see Section 3.3), in the absence of strong dissipative processes (*i.e.*, diabatic heating, friction), quantities such as the potential temperature Θ and the potential vorticity P are often sufficiently conserved to act as tracers of atmospheric motions. Long-lived chemical compounds such as nitrous oxide (N_2O), methane (CH_4), chlorofluorocarbons (CFCs), and even, under many circumstances, ozone (O_3), can also be regarded as excellent tracers of motion, especially in the lower stratosphere. Because of its long photochemical lifetime, nitrous oxide is a suitable reference for comparing measurements of a variety of trace gases (Lowenstein *et al.*, 1989; Chang *et al.*, 1996a; 1996b).

Observations made in the lower stratosphere have shown many cases of strong quasi-linear correlations between the mixing ratio of different long-lived species. These correlations are represented by scatter plots as shown in Figure 3.18 (Chang *et al.*, 1996a; 1996b). Such diagrams suggest that, if the observed mixing ratios of 2 compounds collapse to a compact curve, it is possible to deduce the mixing ratio of one of them from the measurement of the mixing ratio of the other. Furthermore, the departure from the correlation curve is an indication that chemical processes have affected the corresponding airmass during its displacement in the atmosphere. Such departure is clearly seen in the

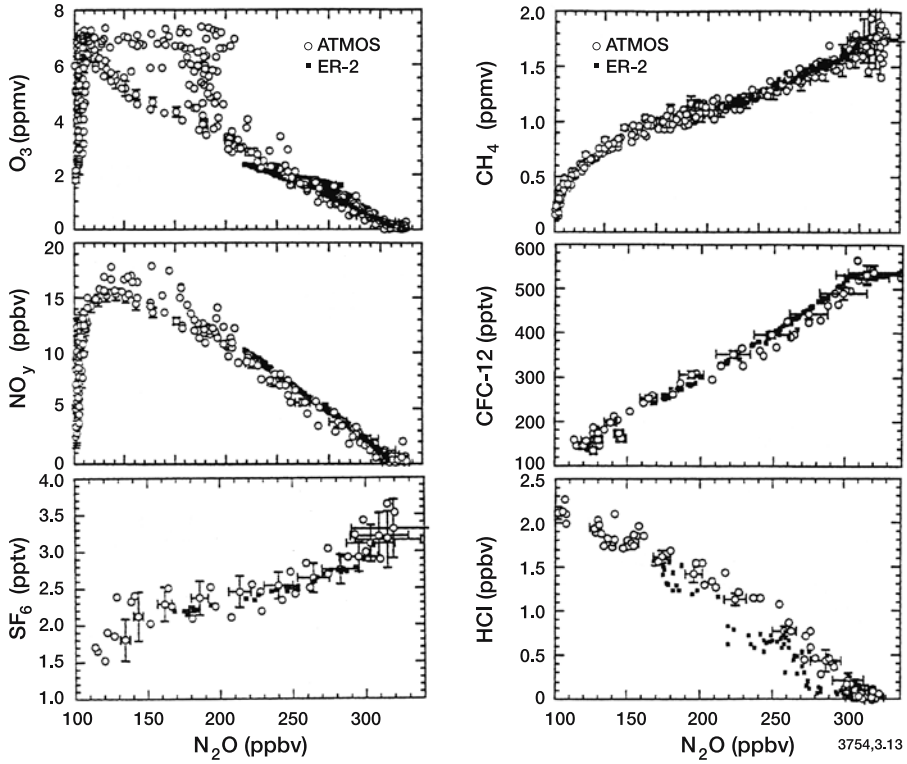

Figure 3.18. Observed mixing ratio of several chemical compounds (O_3, NO_y, SF_6, CH_4, CFC-12, HCl) represented as a function of the observed mixing ratio of N_2O. These scatterplots are established with measurements made from the ER-2 high altitude aircraft and during the spaceborne ATMOS experiment. From Chang *et al.* (1996a, 1996b).

case of ozone if measurements are performed in air masses that have been travelling in the polar regions during springtime when massive ozone destruction takes place (*e.g.*, Antarctic ozone hole). The compactness of the correlations also breaks down for many species in the tropical upper stratosphere (where lifetimes become short) and for ozone in the middle and upper stratosphere.

Plumb and Ko (1992) have shown that, for two chemical compounds whose local photochemical lifetimes are longer than the quasi-horizontal transport time constant, the slope of the correlation curve is provided by the ratio between the net fluxes of the two species through their respective mixing ratio isopleths (see also Murphy and Fahey, 1994). In addition, they calculated that for two long-lived source gases (*e.g.*, N_2O, CH_4, etc.) that are emitted at the surface and are photochemically

destroyed in the stratosphere, the slope dX_2/dX_1 of the correlation curve is related to the ratio of the atmospheric photochemical lifetimes τ_1/τ_2 of the 2 species. For steady-state conditions:

$$\frac{\tau_1}{\tau_2} \simeq \frac{dX_2}{dX_1} \cdot \frac{X_1(0)}{X_2(0)} \tag{3.55}$$

where $X_1(0)$ and $X_2(0)$ represent the mixing ratio of compounds 1 and 2 in the very low stratosphere (or in the troposphere). Measurements of correlations between chemical species provide a powerful analysis tool to establish the origin and fate of air masses in the stratosphere and in the troposphere.

3.6 Dynamics and Meridional Transport in Two Dimensions: A Conceptual View

3.6.1 Zonal Means and Eddies

The description of dynamical processes is often facilitated by distinguishing between zonal mean motions and fluctuations about the zonal mean (called the *eddies*). As indicated in Section 3.4, these fluctuations can be of varied spatial scale — from a few meters to thousands of kilometers. In the stratosphere, observed wave structure indicates that most of the waves are of large scales, of zonal wavenumber 3 or less, as discussed earlier. Note that the use of the word "eddy" in the context of atmospheric dynamics is thus rather different than the idea of a whirlwind, which is probably a more common usage of the same word (Oxford English Dictionary). Any atmospheric quantity $\psi(\lambda, \varphi, z)$ can be expressed as the sum of the zonal mean:

$$\overline{\psi}(\varphi, z; t) = \frac{1}{2\pi} \int_0^{2\pi} \psi\ (\lambda, \varphi, z; t)\ d\lambda \tag{3.56}$$

and the eddy term, ψ', as follows:

$$\psi\ (\lambda, \varphi, z; t) = \overline{\psi}(\varphi, z; t) + \psi'\ (\lambda, \varphi, z; t) \tag{3.57}$$

where λ, φ, z, and t represent longitude, latitude, height, and time, respectively. Using (3.56) and (3.57), one can derive from the primitive equations (3.23a), (3.25) and (3.24b), the zonal mean momentum equation

$$\begin{aligned} &\frac{\partial \overline{u}}{\partial t} + \frac{\overline{v}}{a \cos\phi} \frac{\partial (\overline{u} \cos\phi)}{\partial \phi} + \overline{w} \frac{\partial \overline{u}}{\partial z} - f\overline{v} \\ &\quad = \overline{F}_\lambda - \frac{1}{a \cos^2\phi} \frac{\partial}{\partial \phi} \left(\overline{u'v'} \cos^2\phi \right) - \frac{1}{\rho_0} \frac{\partial}{\partial z} \left(\rho_0 \overline{u'w'} \right) \end{aligned} \tag{3.58}$$

the continuity equation

$$\frac{1}{\mathrm{a}\cos\phi}\frac{\partial\left(\overline{\mathrm{v}}\cos\phi\right)}{\partial\phi}+\frac{1}{\rho_0}\frac{\partial}{\partial \mathrm{z}}\left(\rho_0\overline{\mathrm{w}}\right)=0 \tag{3.59}$$

and the thermodynamic equation

$$\begin{aligned}&\frac{\partial\overline{\Theta}}{\partial \mathrm{t}}+\frac{\overline{\mathrm{v}}}{\mathrm{a}}\frac{\partial\overline{\Theta}}{\partial\phi}+\overline{\mathrm{w}}\frac{\partial\overline{\Theta}}{\partial \mathrm{z}}\\&\quad=\overline{\mathrm{q}}-\left[\frac{1}{\mathrm{a}\cos\phi}\frac{\partial}{\partial\phi}\left(\overline{\mathrm{v}'\Theta'}\cos\phi\right)+\frac{1}{\rho_0}\frac{\partial}{\partial \mathrm{z}}\left(\rho_0\overline{\mathrm{w}'\Theta'}\right)\right]\end{aligned} \tag{3.60}$$

where

$$\overline{\mathrm{q}}=\left[\frac{\mathrm{p}_0}{\mathrm{p}}\right]^{\kappa}\frac{\overline{\mathrm{Q}}}{\mathrm{c_p}}$$

is proportional to the zonally averaged net heating rate $\overline{\mathrm{Q}}$.

The zonally averaged continuity equation for chemical species i expressed in mixing ratio $\mathrm{X_i}$ becomes

$$\begin{aligned}&\frac{\partial\overline{\mathrm{X}}_\mathrm{i}}{\partial \mathrm{t}}+\frac{\overline{\mathrm{v}}}{\mathrm{a}}\frac{\partial\overline{\mathrm{X}}_\mathrm{i}}{\partial\phi}+\overline{\mathrm{w}}\frac{\partial\overline{\mathrm{X}}_\mathrm{i}}{\partial \mathrm{z}}\\&\quad=\overline{\mathrm{s}}_\mathrm{i}-\left[\frac{1}{\mathrm{a}\cos\phi}\frac{\partial}{\partial\phi}\left(\overline{\mathrm{v}'\mathrm{X}'_\mathrm{i}}\cos\phi\right)+\frac{1}{\rho_0}\frac{\partial}{\partial \mathrm{z}}\left(\rho_0\overline{\mathrm{w}'\mathrm{X}'_\mathrm{i}}\right)\right]\end{aligned} \tag{3.61}$$

where

$$\overline{\mathrm{s}}_\mathrm{i}=\frac{\overline{\mathrm{S}}_\mathrm{i}}{\mathrm{n}} \tag{3.62}$$

is the chemical source term ($\mathrm{m^{-3}s^{-1}}$) divided by the total air density n ($\mathrm{m^{-3}}$). The eddy terms in the right-hand side of the momentum, thermodynamic, and chemical continuity equations are known as the eddy flux divergences. Note that equations (3.58) to (3.60) do not constitute a closed system; they contain products of eddy quantities (such as $\overline{\mathrm{v}'\Theta'}$) which are not calculated within this system. These eddy terms can be an important part of the heat and momentum budgets. For example, Figure 3.19 shows the relative magnitudes of the most important terms in the thermodynamic equation as a function of latitude at 10 hPa. Note that the terms $\overline{\mathrm{w}}\partial\overline{\Theta}/\partial \mathrm{z}$ and $1/\mathrm{a}\cos\phi\;\partial/\partial\phi(\overline{\mathrm{v}'\Theta'})\cos\phi$ are larger than the diabatic heating rate and are nearly in balance with one another.

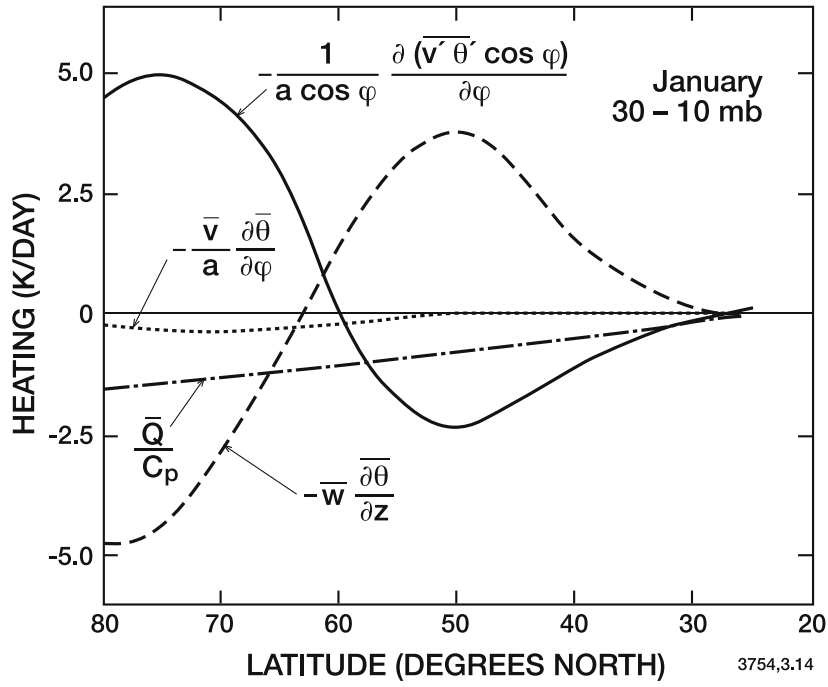

Figure 3.19. Magnitude of the terms in the thermodynamic equation as a function of latitude at 10-30 hPa during winter. Note that the largest contributions to the heat budget are provided by adiabatic compression and wave driven meridional heat transport. From O'Neill (1980).

3.6.2 Description of the Mean Meridional Stratospheric Circulation

Some of the earliest proposed descriptions of stratospheric transport were based on observations of chemical species. The first observations of stratospheric water vapor densities showed that the stratosphere was extremely dry, exhibiting mixing ratios of the order of a few parts per million by volume, in marked contrast to the troposphere, where water vapor abundance reaches a few percent. Brewer (1949) suggested that the dryness of the stratosphere was determined primarily by condensation and that the water vapor content of an air parcel rising from the troposphere to the stratosphere would therefore be determined by the lowest temperature experienced by the parcel, which would normally correspond to the tropopause. He also noted that the tropopause temperatures in the tropics were low enough to yield stratospheric water vapor densities as low as those observed, while the

middle and high latitude tropopause was much too warm to explain the observed dryness. Thus he suggested a circulation exhibiting rising motion only in the tropics, and descending motion at extra-tropical latitudes. Dobson (1956) suggested a qualitatively similar transport pattern based on observations of stratospheric ozone.

Murgatroyd and Singleton (1961) presented the first calculated mean circulation for the middle atmosphere by using an analysis of radiative heating rates. They derived a circulation much like the one suggested by the tracer studies discussed above. However, they noted that discrepancies existed in the angular momentum budget of the derived circulation, which were presumably due to eddy transport processes. The meridional circulation derived from that study is shown in Figure 3.20.

A few years later, observational studies using the angular momentum and/or heat budgets led to mean circulations of the lower stratosphere based on meteorological data, (specifically, observations of the dominant eddy terms in Eqs. 3.58 and 3.60; *e.g.*, Reed *et al.*, 1963; Julian and Labitzke, 1965; Vincent, 1968). These studies produced circulations which were quite different from the one derived by Murgatroyd and Singleton or those deduced from tracer studies (see *e.g.*, Figure 3.21). In particular, the existence of *rising motion*s (the "Ferrell cell") was suggested as occurring during winter at high latitudes (60°) in the troposphere and lower stratosphere.

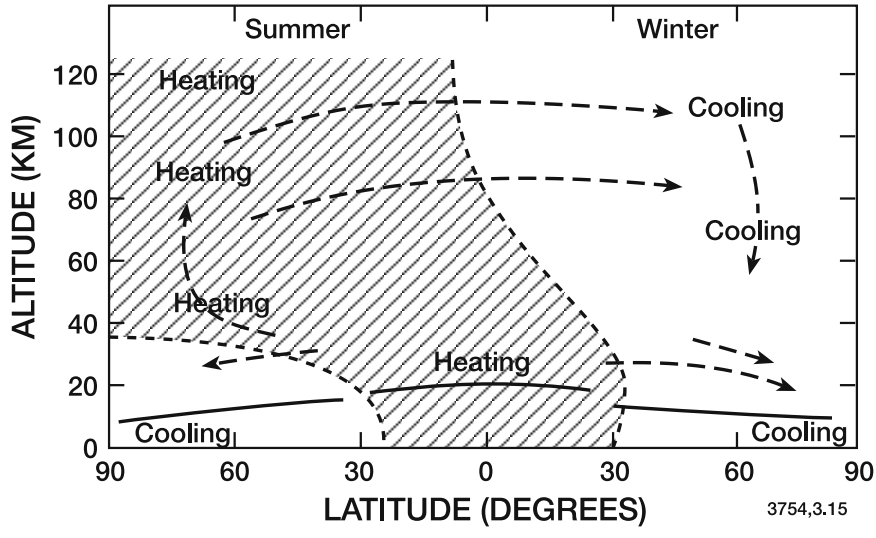

Figure 3.20. Meridional circulation based on the study of Murgatroyd and Singleton (1961). From Murgatroyd (1971).

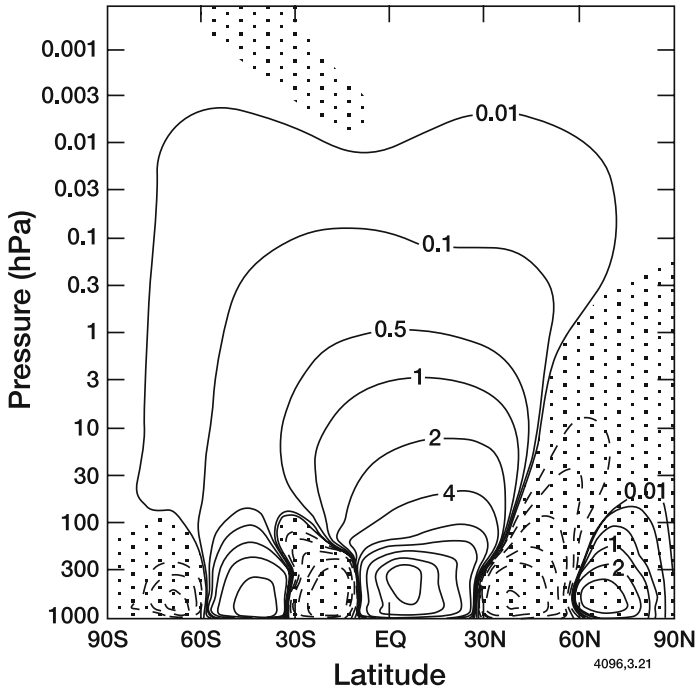

Figure 3.21. Mass streamfunction representing the Eulerian mean circulation in January calculated by Becker and Schmitz (2002). Values are expressed in 10^9kg/s.

Which depiction of the mean meridional circulation is correct, Figure 3.20 or Figure 3.21? The answer is that they both are, but that they represent different quantities. To a first approximation, Figure 3.20 represents the zonally averaged motion of air parcels (net transport in the meridional plane) while Figure 3.21 represents the transport by the zonally averaged circulation. As we will show below, the net motion in the case described by Murgatroyd and Singleton is the sum of the zonal mean circulation shown in Figure 3.21 and the transport by eddy motions. The differences between the two circulations are a result of the zonal averaging procedure applied in the presence of wave disturbances (the "eddies"). It can be shown that, for waves that are steady (no change in amplitude with time) and conservative (no dissipation or wave breaking), the mean meridional eddy heat transport and the adiabatic heating/cooling associated with the mean vertical motion cancel exactly (Boyd, 1976; Andrews and McIntyre, 1976; see also Figure 3.19). This property of Eulerian zonal averages is known as the *non-acceleration theorem* and is of great importance in understanding the evolution of zonally averaged fields of wind and temperature in the presence of wave motions.

A physical understanding of how the cancellation between the eddy heat transport and the wave induced mean meridional circulation arises can be gained from Figure 3.22. This figure depicts in schematic form the structure of a vertically propagating planetary wave which is assumed to be steady and conservative. Streamlines of the flow in the latitude-longitude plane are shown as solid lines that meander north and south. Horizontal velocity vectors (heavy arrows) and vertical velocity vectors (dashed lines) are shown at selected points along the streamlines. Temperature perturbations T' associated with the wave are denoted by the letters W (warm) and C (cold). The projection onto the height-latitude plane of the parcel trajectories following a given streamline are shown as ellipses, with the arrows indicating the sense of the parcel motion (it may be useful to imagine these projections as those of a three-dimensional elliptical corkscrew). Note, first of all, that for the wave depicted here the horizontal velocity and the temperature perturbations are in phase (*i.e.*, positive velocities coincide with positive temperature perturbations, and vice versa). Thus, the average heat flux, $\overline{v'T'}$ taken along any of the latitude circles $\phi_{1,3,5}$ is positive. It is largest at ϕ_3 because the wave has maximum amplitude in mid-latitudes. As a result, there is a *divergence* of zonally averaged eddy heat flux, $\overline{v'T'}$ at ϕ_2 and a *convergence* at ϕ_4. These are balanced by compression heating (sinking motion) and expansion cooling (rising motion), respectively, and so one obtains negative $\overline{w}$ at ϕ_2 and positive $\overline{w}$ at ϕ_4 (dashed

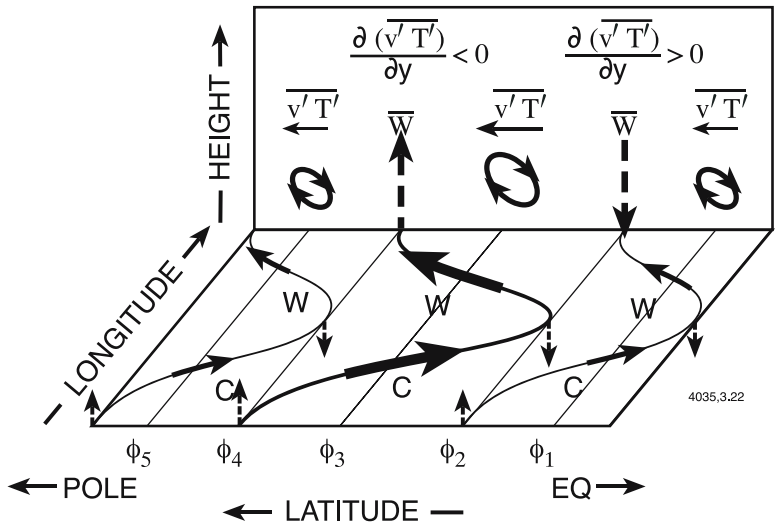

Figure 3.22. Schematic diagram of the idealized planetary wave structure and the resulting eddy transport of heat. Adapted from Matsuno (1980).

arrows). This is the "Ferrell cell" pattern characteristic of the Eulerian meridional circulation in winter. However, since the projections of the parcel trajectories are closed ellipses, there is in fact no net parcel motion in the latitude-height plane as a result of these processes, and the Ferrell cell arises purely as a result of the zonal averaging procedure at the fixed points $\phi_{1,3,5}$. This is essentially the state of affairs described by the non-interaction theorem. A detailed explanation of the relationship between Eulerian eddy heat fluxes, meridional circulations, and parcel trajectories is given by Matsuno (1980).

The foregoing arguments demonstrate qualitatively that as long as wave motion is steady and conservative, a *net* meridional mass circulation takes place only when the zonally averaged diabatic heating ($\overline{\mathrm{q}}$ in Eq. 3.60) is different from zero. The large-scale planetary waves, which dominate the wave structure of the stratosphere probably conform to this description at least in part. Therefore no net transport is produced in the meridional plane through the effects of these eddies. Thus the apparent discrepancy between the mean circulations derived by Brewer, Dobson, and Murgatroyd and Singleton, versus those computed by the later studies is reconciled when it is understood that the former studies represent *net* transport, while the latter correspond to a mean circulation only. The meridional transport produced by this latter circulation is cancelled to a large degree by eddy transports, when these terms are evaluated in the standard fashion using a reference frame which is fixed in latitude and height.

The eddy-mean flow cancellation represents a difficulty for two-dimensional descriptions of stratospheric transport. Perhaps most importantly, it suggests that in the Eulerian framework, the mean and eddy transports are intimately coupled, and that a proper representation of atmospheric transport must employ a consistent set (see, *e.g.*, Harwood and Pyle, 1975; Rood and Schoeberl, 1983). Further, it suggests that the use of eddy diffusion coefficients to characterize all types and scales of eddy processes must be questioned, since the stratospheric eddies appear to be at least partly steady and conservative (*i.e.*, non-diffusive in character, see *e.g.*, Matsuno, 1980).

3.6.3 Lagrangian Mean, Diabatic, and Transformed Eulerian Mean Circulations

The difficulties associated with the eddy-mean flow cancellation have motivated the search for a mathematical formalism to describe the zonally averaged structure of the atmosphere in such a way as to

provide a more meaningful separation between the eddies and the mean meridional circulation. Andrews and McIntyre (1978) introduced the so-called *Lagrangian mean averaging*, wherein horizontal averages are computed not along latitude circles, but along a path that follows the wave trajectory in latitude and longitude. Referring again to Figure 3.22, it should be clear that if v' is evaluated along any of the wave streamlines shown, then no eddy fluxes appear. Although the Lagrangian mean formalism is mathematically elegant and physically meaningful, it suffers from technical problems that limit its applicability to situations where wave amplitudes are very large (McIntyre, 1980).

A more practical approach is simply to derive the net mean circulation directly from the diabatic heating rate, $\overline{\mathrm{q}}$, as suggested by Dunkerton (1978). From the thermodynamic equation (3.60) in which it is assumed that $\partial\overline{\Theta}/\partial\mathrm{t}$ and $(\overline{\mathrm{v}}/\mathrm{a})(\partial\overline{\Theta}/\partial\phi)$ are small (see Figure 3.19), and that the vertical eddy heat fluxes are negligibly small, one can deduce that

$$\overline{\mathrm{w}}\,\frac{\partial\overline{\Theta}}{\partial\mathrm{z}} \simeq \overline{\mathrm{q}} - \frac{1}{\mathrm{a}\,\cos\phi}\,\frac{\partial}{\partial\phi}\left(\overline{\mathrm{v}'\Theta'}\,\cos\phi\right) \tag{3.63}$$

This expression reveals that for small diabatic effects ($\overline{\mathrm{q}} \simeq 0$), the eddy heat flux divergence is in close balance with the vertical advection of the mean potential temperature (non-acceleration theorem).

A transformation can be introduced to represent the net mean meridional and vertical velocities $\overline{\mathrm{v}}^{\,*}$ and $\overline{\mathrm{w}}^{\,*}$

$$\overline{\mathrm{v}}^{\,*} = \overline{\mathrm{v}} - \frac{1}{\rho_0}\,\frac{\partial}{\partial\mathrm{z}}\left(\frac{\rho_0\overline{\mathrm{v}'\Theta'}}{\partial\overline{\Theta}/\partial\mathrm{z}}\right) \tag{3.64a}$$

$$\overline{\mathrm{w}}^{\,*} = \overline{\mathrm{w}} + \frac{1}{\mathrm{a}\,\cos\phi}\,\frac{\partial}{\partial\phi}\left(\frac{\overline{\mathrm{v}'\Theta'}\,\cos\phi}{\partial\overline{\Theta}/\partial\mathrm{z}}\right) \tag{3.64b}$$

It defines the *transformed Eulerian mean* (TEM) or *residual circulation*. When these definitions are applied to the simplified form (3.63) of the thermodynamic equation, the resulting circulation is called the *diabatic circulation* and the meridional and vertical velocities will be noted $(\overline{\mathrm{v_D}}, \overline{\mathrm{w_D}})$ rather than $(\overline{\mathrm{v}}^{\,*}, \overline{\mathrm{w}}^{\,*})$. In this case, the simplified thermodynamic equation and the steady state approximation for the continuity equation become

$$\overline{\mathrm{w}}_\mathrm{D}\,\frac{\partial\overline{\Theta}}{\partial\mathrm{z}} = \overline{\mathrm{q}} \tag{3.65}$$

$$\frac{1}{\mathrm{a}\,\cos\phi}\,\frac{\partial}{\partial\phi}\left(\overline{\mathrm{v}}_\mathrm{D}\,\cos\phi\right) + \frac{1}{\rho_0}\,\frac{\partial}{\partial\mathrm{z}}\left(\rho_0\overline{\mathrm{w}}_\mathrm{D}\right) = 0 \tag{3.66}$$

Note that the eddy heat flux does not appear in the transformed thermodynamic equation (3.65). From these equations, $\overline{\mathrm{v}}_\mathrm{D}$ and $\overline{\mathrm{w}}_\mathrm{D}$ may be derived directly from a knowledge of the diabatic heating rate. We

emphasize that this is, in fact, just what Murgatroyd and Singleton (1961) did when they ignored the eddy heat flux. See also Dunkerton (1978).

It is important to note that the diabatic circulation can be estimated from the thermodynamic and continuity equations only if the temperature distribution is known *a priori*. However, a fully self-consistent mean meridional circulation can be obtained when the momentum budget is considered together with the thermodynamic and continuity equations. When transformations (3.64a, b) are applied to the zonal mean equations (3.53-3.60), the solution of the following momentum, continuity, and thermodynamic equations defines the transformed Eulerian mean (TEM) or residual circulation (here expressed in log-pressure coordinates):

$$\frac{\partial \overline{\mathrm{u}}}{\partial \mathrm{t}} + \frac{\overline{\mathrm{v}}^{\,*}}{\mathrm{a}\,\cos\phi}\,\frac{\partial \overline{\mathrm{u}}\,\cos\phi}{\partial\phi} + \overline{\mathrm{w}}^{\,*}\frac{\partial \overline{\mathrm{u}}}{\partial \mathrm{z}} - \mathrm{f}\overline{\mathrm{v}}^{\,*} = \frac{\nabla\cdot\vec{\mathrm{E}}}{\rho_0 \mathrm{a}\,\cos\phi} + \overline{\mathrm{F}}_\lambda \equiv \overline{\mathrm{G}}_\mathrm{u} \quad (3.67)$$

$$\frac{1}{\mathrm{a}\,\cos\phi}\,\frac{\partial \overline{\mathrm{v}}^{\,*}\,\cos\phi}{\partial\phi} + \frac{1}{\rho_0}\,\frac{\partial}{\partial \mathrm{z}}\,(\rho_0 \overline{\mathrm{w}}^{\,*}) = 0 \quad (3.68)$$

$$\frac{\partial \overline{\Theta}}{\partial \mathrm{t}} + \frac{\overline{\mathrm{v}}^{*}}{\mathrm{a}}\,\frac{\partial \Theta}{\partial\phi} + \overline{\mathrm{w}}^{\,*}\,\frac{\partial \overline{\Theta}}{\partial \mathrm{z}} = \overline{\mathrm{q}} + \overline{\mathrm{G}}_\Theta \quad (3.69)$$

where

$$\overline{\mathrm{G}}_\Theta = -\frac{1}{\rho_0}\,\frac{\partial}{\partial \mathrm{z}}\left[\rho_0\left(\overline{\mathrm{v}'\Theta'}\frac{\partial\overline{\Theta}/\mathrm{a}\partial\phi}{\partial\overline{\Theta}/\partial \mathrm{z}} + \overline{\mathrm{w}'\Theta'}\right)\right] \quad (3.69a)$$

represents the contribution of the eddies to the temperature tendency. This term is generally small and often ignored (although the contribution involving $\overline{\mathrm{w}'\Theta'}$ can be important for gravity waves). The forcing term $\overline{\mathrm{G}}_\mathrm{u}$ appearing in the zonal momentum equation includes the divergence of the Eliassen flux $\vec{\nabla}\cdot\vec{\mathrm{E}}$ as well as any additional dissipative force (F_λ). The components of the *Eliassen-Palm* (EP) *flux* are

$$\mathrm{E}_\phi = -\rho_0 \mathrm{a}\,\cos\phi\left[\overline{\mathrm{u}'\mathrm{v}'} - \frac{\partial \overline{\mathrm{u}}}{\partial \mathrm{z}}\,\frac{\overline{\mathrm{v}'\Theta'}}{\partial\overline{\Theta}/\partial \mathrm{z}}\right] \quad (3.70a)$$

$$\mathrm{E}_\mathrm{z} = \rho_0 \mathrm{a}\,\cos\phi\left[\left(\mathrm{f} - \frac{1}{\mathrm{a}\,\cos\phi}\,\frac{\partial \overline{\mathrm{u}}\,\cos\phi}{\partial\phi}\right)\frac{\overline{\mathrm{v}'\Theta'}}{\partial\overline{\Theta}/\partial \mathrm{z}} - \overline{\mathrm{u}'\mathrm{w}'}\right] \quad (3.70b)$$

For planetary waves in the stratosphere, quasi-geostrophic scaling can be applied, in which case expressions (3.70a) and (3.70b) reduce to

$$\mathrm{E}_\phi = -\rho_0 \mathrm{a}\,\cos\phi\,\overline{\mathrm{u}'\mathrm{v}'} \quad (3.71a)$$

and

$$\mathrm{E_z} = \rho_0 \mathrm{a}\, \cos\phi\, \mathrm{f}\, \frac{\overline{\mathrm{v}'\Theta'}}{\partial\overline{\Theta}/\partial \mathrm{z}} \qquad (3.71b)$$

Thus, the meridional component of the EP flux is proportional to the momentum flux $\overline{\mathrm{u}'\mathrm{v}'}$ while the vertical component is proportional to the meridional heat flux $\overline{\mathrm{v}'\Theta'}$.

Note that, aside from the contribution of $\overline{\mathrm{G}}_\Theta$ in the thermodynamic equation, which vanishes exactly for steady conservative waves (Andrews and McIntyre, 1978), wave forcing in the TEM system is limited to the Eliassen-Palm divergence in the zonal momentum equation (assuming $\mathrm{F}_\lambda \simeq 0$). The important role played by the momentum budget will be discussed in more detail in Section 3.7. Figure 3.23 shows the transformed Eulerian mean streamlines from the model of Becker and Schmitz (2002). As the transformed Eulerian mean circulation is very similar to the diabatic circulation, upward transport by TEM motions occurs primarily where the net diabatic heating (Q) is positive, while downward transport is found in regions where Q is negative. A

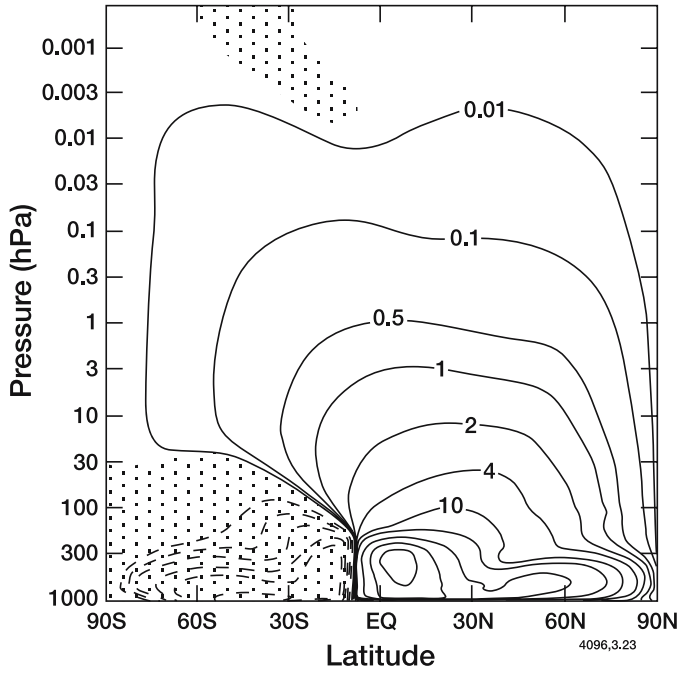

Figure 3.23. Mass streamfunction for the transformed Eulerian mean circulation (10^9kg/s) calculated by Becker and Schmitz (2002) for the month of January. Compare this residual circulation with the Eulerian mean circulation shown in Figure 3.21.

generalization of the TEM circulation which describes the mass flux across an arbitrary iso-surface (provided that this quantity defining this iso-surface varies monotonically with height) is given by Juckes (2001).

As in the case of the potential temperature, the Eulerian mean and eddy components of meridional transport for the mixing ratio of chemical species tend to cancel, and the continuity equation for species i, written as a function of the TEM winds becomes

$$\frac{\partial \overline{\mathrm{X}}_\mathrm{i}}{\partial \mathrm{t}} + \frac{\overline{\mathrm{v}}^*}{\mathrm{a}} \frac{\partial \overline{\mathrm{X}}_\mathrm{i}}{\partial \phi} + \overline{\mathrm{w}}^* \frac{\partial \overline{\mathrm{X}}_\mathrm{i}}{\partial \mathrm{z}} = \overline{\mathrm{s}}_\mathrm{i} + \overline{\mathrm{G}}_\mathrm{X} \tag{3.72}$$

where $\overline{\mathrm{G}}_\mathrm{X}$ expresses the contribution of the eddies through the correlations between the wave components of the mixing ratio and wind velocities. It is written as

$$\overline{\mathrm{G}_\mathrm{X}} = \frac{1}{\mathrm{a}\cos\phi} \frac{\partial}{\partial \phi} \left(\overline{\mathrm{v}'\mathrm{X}'}^* \cos\phi \right) + \frac{1}{\rho_0} \frac{\partial}{\partial \mathrm{z}} \left(\rho_0 \, \overline{\mathrm{w}'\mathrm{X}'}^* \right)$$

where the net eddy flux components are expressed by (Garcia and Solomon, 1983)

$$\overline{\mathrm{v}'\mathrm{X}'}^* = \overline{\mathrm{v}'\mathrm{X}'} - \frac{\overline{\mathrm{v}'\Theta'}}{\partial\overline{\Theta}/\partial \mathrm{z}} \frac{\partial \overline{\mathrm{X}}}{\partial \mathrm{z}}$$

$$\overline{\mathrm{w}'\mathrm{X}'}^* = \overline{\mathrm{w}'\mathrm{X}'} + \frac{\overline{\mathrm{v}'\Theta'}}{\partial\overline{\Theta}/\partial \mathrm{z}} \frac{\partial \overline{\mathrm{X}}}{\partial \mathrm{y}}$$

For inert tracers, and for conservative and steady waves, the $\overline{\mathrm{G}}_\mathrm{X}$ term vanishes identically, and the zonally averaged distribution $\overline{\mathrm{X}}$ is determined solely by the residual circulation $(\overline{\mathrm{v}^*}, \overline{\mathrm{w}^*})$. If the chemical lifetime of the chemical compound is comparable to the physical scale of the wave, and if that lifetime is comparable to the time it takes for an air parcel to move through the wave, then the effects of production and loss along wave trajectories cannot be ignored. Under these special circumstances, the wave can move air parcels into different photochemical environments (regions of different chemical lifetimes), introducing *chemical eddy transport*. This effect can be parameterized in terms of wave structure and the photochemical lifetime of the species considered (see Plumb, 1979). The importance of this effect has been shown, for example, by Garcia and Hartmann (1980), Pyle and Rogers (1980), Matsuno (1980), Hartmann (1981), Strobel (1981), and Kawahira (1982). In practical applications, the net eddy flux

components are often written as

$$\overline{v'X'}^{*} = -\left\{ K_{yy} \frac{\partial \overline{X}}{\partial y} + K_{yz} \frac{\partial \overline{X}}{\partial y} \right\}$$

$$\overline{w'X'}^{*} = -\left\{ K_{zy} \frac{\partial \overline{X}}{\partial y} + K_{zz} \frac{\partial \overline{X}}{\partial z} \right\}$$

where the eddy diffusion coefficients K_{ij} can be expressed as a function of the chemical lifetime of the trace constituents and of the time needed for an air parcel to move through a disturbance. One of the species most strongly influenced by chemical eddy transports is stratospheric ozone in high latitude winter. Figure 3.24 shows an estimate of the influence of chemical eddy transport on ozone as calculated with the model of Garcia and Solomon (1983).

The conceptual advantage of the diabatic or transformed Eulerian mean circulations is that the eddy-mean flow cancellation is avoided, and a first approximation to the net meridional and vertical transport needed for atmospheric studies is therefore readily obtained. The most important features of this transport description are that air generally enters the lower stratosphere in the tropics and exits at middle and high latitudes in both hemispheres. In the upper stratosphere and mesosphere, air flows from the summer hemisphere to the winter hemisphere, and downward near the winter pole. This transport description is qualitatively very similar to that proposed by Brewer based

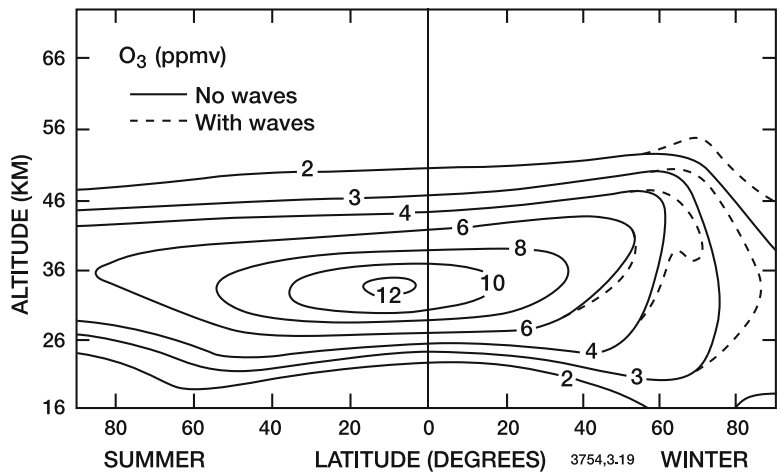

Figure 3.24. Calculated ozone distribution (in ppmv) for Northern Hemisphere winter solstice with and without chemical eddy transport. From Garcia and Solomon (1983).

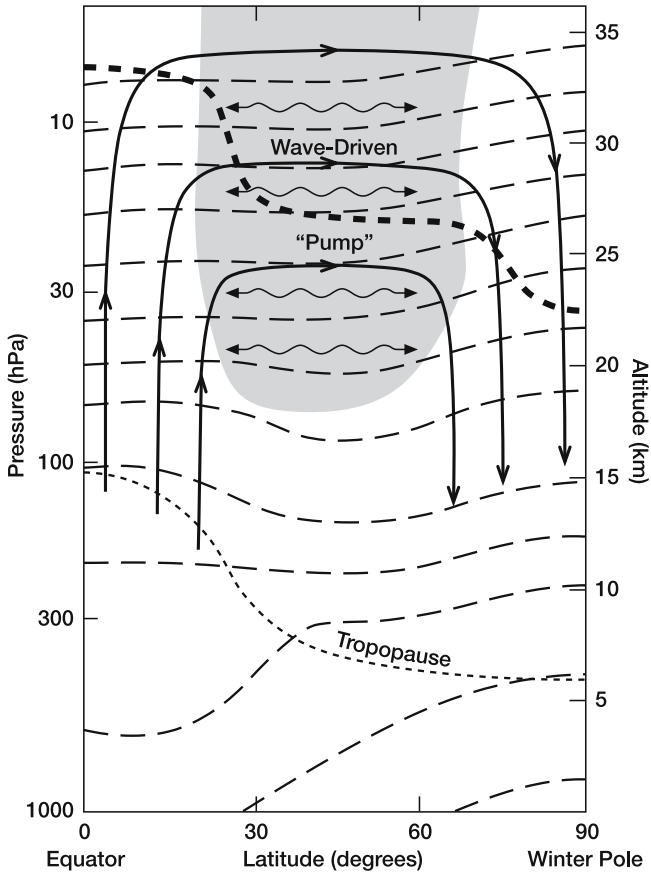

Figure 3.25. Schematic representation of the wave-driven transport circulation (solid lines with arrows) in the winter stratosphere. The shaded area represents the surf zone where meridional mixing associated with wavebreaking is taking place. Light dashed lines represent isentropes. The heavy dashed line shows a constant mixing ratio surface of a long-lived tracer. The dotted line represents the tropopause. Adapted from Holton and Alexander (2000).

on early observations of water vapor. Indeed, this very simple picture provides a reasonable qualitative description of transport of chemical species, at least in the monthly or seasonal mean, and can successfully explain many of the observed features of the distributions of chemical constituents.

The formalism of the transformed Eulerian mean circulation shows that meridional transport in the middle atmosphere is generated primarily by non-local momentum forcing associated with wave dissipation. This forcing, represented by the Eliassen-Palm flux divergence in equation (3.67), acts as an *extratropical pump* producing strong upward air motions in the tropics and downward "return"

flows at high latitudes (Figure 3.25). This circulation is most intense in winter when planetary waves are penetrating in the stratosphere (see Section 3.4). In the mesosphere, the meridional flow generated primarily by gravity wave breaking is directed from the summer to the winter pole. By continuity, the flow is directed upward in the summer hemisphere and downward in the winter hemisphere (see Figure 3.33 in Section 3.7). Such cross-isentropic motions are accompanied by diabatic heating/cooling and tend to steepen the slope of atmospheric tracers.

At the same time, mixing is produced as a result of planetary wave dissipation, primarily along quasi-horizontal isentropic surfaces. This process tends to reduce the slope of quasi-inert atmospheric tracers. The balance between these two competing processes affects the compact relationship between the mixing ratio of two long-lived species noted in some of the scatterplots in Figure 3.18. The slope of the mixing ratio isopleths for different long-lived constituents is determined essentially by transport processes, and is therefore nearly the same for all these compounds.

The relative importance of slope-steepening diabatic motions and slope-flattening quasi-horizontal mixing can be deduced from the examination of Figure 3.26 (see also Plate 2). Figure 3.26 represents the zonally averaged distribution of hydrogen fluoride (HF) as measured from space. The source region of this long-lived compound is located in

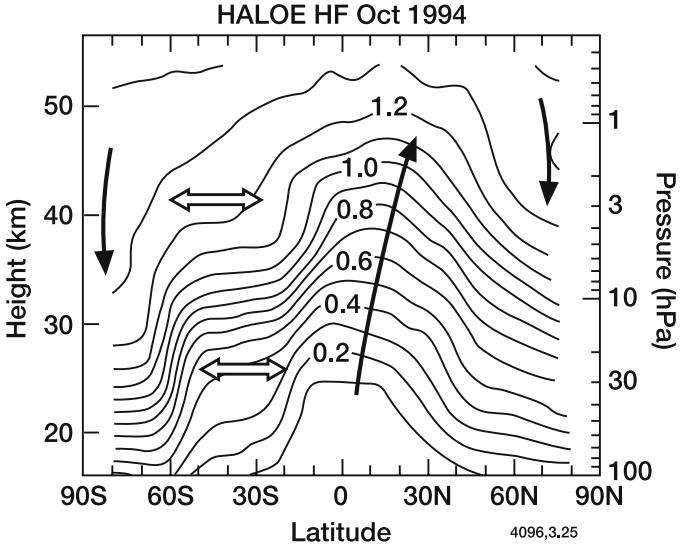

Figure 3.26. Zonally averaged distribution of hydrogen fluoride (HF) mixing ratio (in ppbv) measured by the HALOE instrument on UARS. The heavy solid arrows denote the mean meridional transport and the horizontal arrows show the location of strong quasi-horizontal mixing by planetary waves. Courtesy of W. Randel, NCAR, 2001.

the stratosphere, and its mixing ratio below 50 km therefore increases with height. The minimum mixing ratio in the tropics is associated with strong upward motions while the high concentrations at high latitudes result from downwelling, primarily inside the wintertime polar vortex. Quasi-horizontal mixing at mid-latitude in the winter hemisphere explains the nearly flat mixing ratio isopleths observed between 30°S and 50°S.

3.6.4 Dynamical Barriers against Meridional Transport

Observations of numerous tracers reveal sharp horizontal concentration gradients near 30° latitude in both hemispheres, suggesting that the tropical stratosphere is fairly isolated from extratropical regions (McIntyre, 1990). Plumb and Ko (1992) noted that the compactness of the tracer relationships depicted in the scatterplots (Figure 3.18) breaks down when considering mixing ratios observed in the tropical upper stratosphere. The classic picture of stratospheric transport has been, therefore, significantly refined in recent years, and, for example, Plumb (1996) proposed replacing the notion of a global diffuser model by a "tropical pipe model" represented by the lower panel of Figure 3.27. In this model, the abundance of chemical compounds within the "tropical pipe" is determined primarily by a balance between upwelling and local chemical destruction or production.

Several observations confirm the quasi-isolation of the tropical stratosphere (in addition to the sharp meridional gradients affecting long-lived tracers near 20-30° latitude). These include the formation of a tropical reservoir of radioactive material after nuclear explosions in the atmosphere (Feely and Spar, 1960) and of aerosols after volcanic eruptions (Trepte and Hitchman, 1994; Grant *et al.*, 1996). Another indication is provided by the annual variation in tropical water vapor in the lower stratosphere, specifically the *tape recorder* effect (Mote *et al.*, 1995; see Figure 5.24b). Because air passing through the equatorial tropopause tends to be "freeze dried" to a water saturation mixing ratio corresponding to the tropopause temperature ("cold trap"), and since this temperature is affected by a strong annual cycle, the water influx (and hence the H_2O mixing ratio near the equator) is minimum during the Northern Hemisphere early spring (February-March) and maximum six months later. The fact that this water vapor signal is pulled upward by rising motions and remains confined within the tropical pipe provides evidence for the existence of strong dynamical barriers against meridional mixing at the edge of the tropical region.

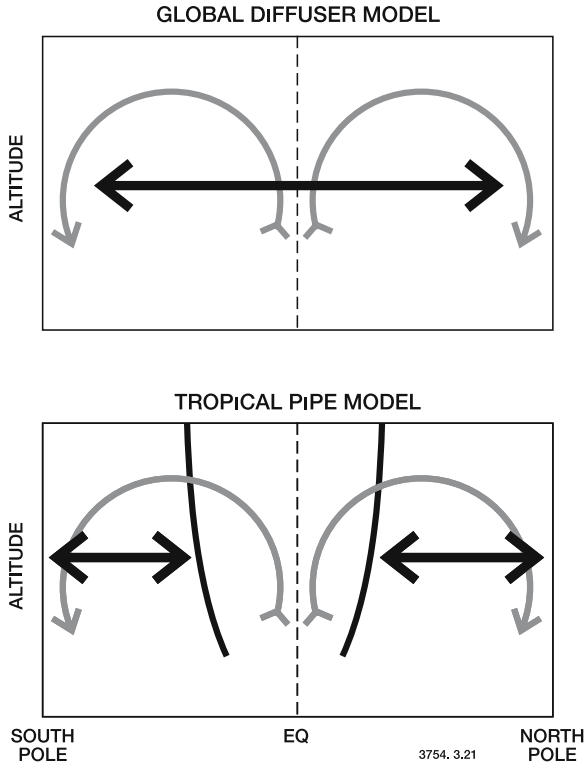

Figure 3.27. Schematic representation of the global diffuser model (upper panel) and tropical pipe model (lower panel). Gray arrows denote meridional transport by the transformed Eulerian mean circulation while the heavy solid arrows show quasi-horizontal mixing by large scale waves. The vertical lines in the lower panel represent dynamical barriers against meridional transport in the tropics. From Plumb and Ko (1992).

Randel *et al.* (1993) have shown that planetary-scale deformations of the barrier, shaped as tongues of tropical air can extend out deep into the mid-latitudes (Figure 3.28 and Plate 3). Occasionally, such tongues become unstable and break, implying subsequent irreversible mixing in the extratropics. This process provides a potential mechanism for quasi-isentropic transport of chemical compounds across the tropical barrier (Boering *et al.*, 1996). The timescale for detrainment from the tropics is estimated to be less than 6 months in the lower stratosphere (Volk *et al.*, 1996). Similarly, studies that have attempted to assess the degree of isolation of the tropics suggest that the timescale for mixing into the tropics (from mid-latitudes) is close to 1 year.

The polar vortex (near 60° latitude, above approximately 16 km) is another dynamical barrier against meridional transport. The isolation of the polar regions, and specifically of the Antarctic lower stratosphere

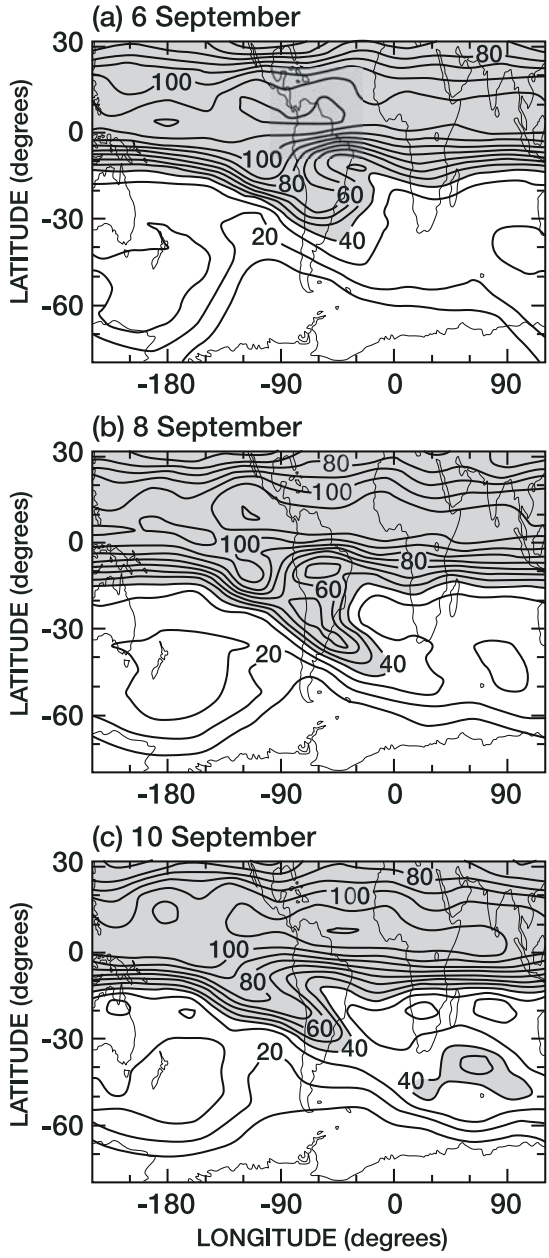

Figure 3.28. Sequence showing the evolution of a tongue of nitrous oxide extending from the tropics into mid-latitude regions and subsequent irreversible mixing. Nitrous oxide mixing ratio (ppbv) is shown on the 1100 K isentropic surface (near 38 km altitude or a pressure surface of 5 hPa) for 6-10 September, 1992, based on the measurements of UARS/CLAES. From Randel *et al.* (1993).

during winter, is an important factor in explaining the formation of the ozone hole in spring. Limited mixing of air across the vortex occurs primarily when large-scale Rossby waves irreversibly pull filaments of polar air from the edge of the winter vortex (See Plate 4). Air is stripped from the vortex edge, eroding the vortex and steepening the potential vorticity gradient at the edge of the vortex (Juckes and McIntyre, 1987). Modeling studies (Waugh and Plumb, 1994; Waugh *et al.*, 1994) suggest that air is ejected from the vortex as long and narrow filaments (see Figure 3.29). These fine-scale structures, also observed in the lower stratosphere from high altitude aircraft (Newman *et al.*, 1996), are stretched around the polar vortex and progressively mixed (after typically 20-25 days) with surrounding mid-latitude air. Below approximately 16 km (potential temperature of 400 K), the vortex edge barrier becomes weaker, and mixing reaches high latitudes. As Rossby waves are generally less intense in the Southern Hemisphere, the Antarctic polar vortex is more stable than the Arctic vortex, and Antarctic air is considerably more isolated from mid-latitude influences than Arctic air. The large planetary wave disturbance and the associated weak ozone hole observed in Antarctica during September 2002 correspond to an exceptional situation. Meridional transport out of the polar vortex regions is thought to affect significantly the mid-latitude ozone budget in the lower stratosphere.

Figure 3.30 presents a schematic view of the meridional circulation in the lower stratosphere, including the roles of the tropical and polar dynamical barriers. This figure also shows that extratropical cross-tropopause exchanges (Box 3.1) involve wave-driven cross-isentropic diabatic descent from the "overworld" (the region where isentropic surfaces lie entirely in the stratosphere) to the "lowermost stratosphere" (the region where isentropes cross the tropopause). Once air and chemical constituents have reached the lowermost stratosphere following diabatic descent, they can be adiabatically transported along isentropes (followed by irreversible mixing) into the troposphere ("the underworld"; see Haynes *et al.*, 1991; Holton *et al.*, 1995). Thus, on the average, the rate at which a stratospheric inert tracer is transported through the tropopause is equal to the rate at which it is transported by the "extratropical pump" across the upper boundary of the lowermost stratosphere. The tropopause exchanges are often linked to strong disturbances (*e.g.*, "cutoff lows") leading to the formation of tongues of stratospheric air (with high PV and high ozone concentrations) which can penetrate deep into the troposphere.

The details of such mass exchanges involve dynamical processes at medium and small scales. For example, in the vicinity of extratropical cyclones (spatial scale of typically 1000 km), cold stratospheric air is

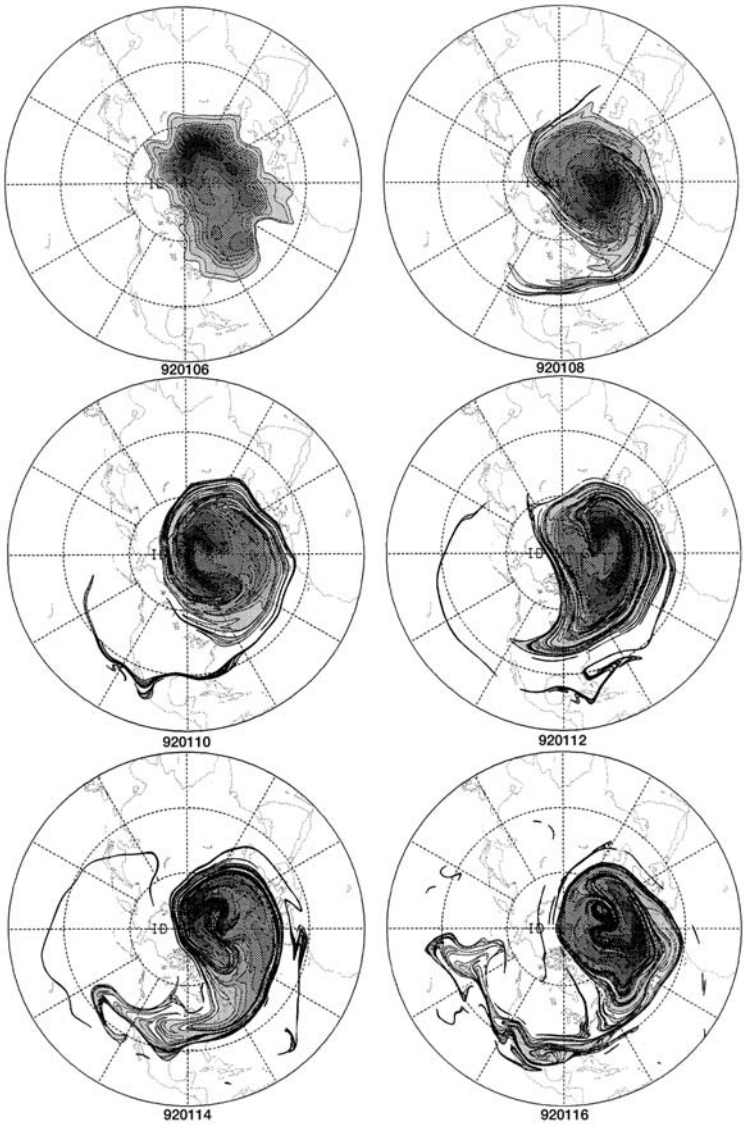

Figure 3.29. Fine-scale structure of a tracer in the vicinity of the polar vortex from 6 January to 16 January 1992 on the 850 K isentropic surface. The calculation made with NMC-analyzed winds show that, as a result of Rossby wave breaking, air is ejected from the polar vortex as long filamentary structures. This process transfers vortex air into mid-latitudes. From Waugh *et al.*(1994).

transported equatorwards at the west side of the depression (within tropopause folds) and is gradually mixed with tropospheric air as a

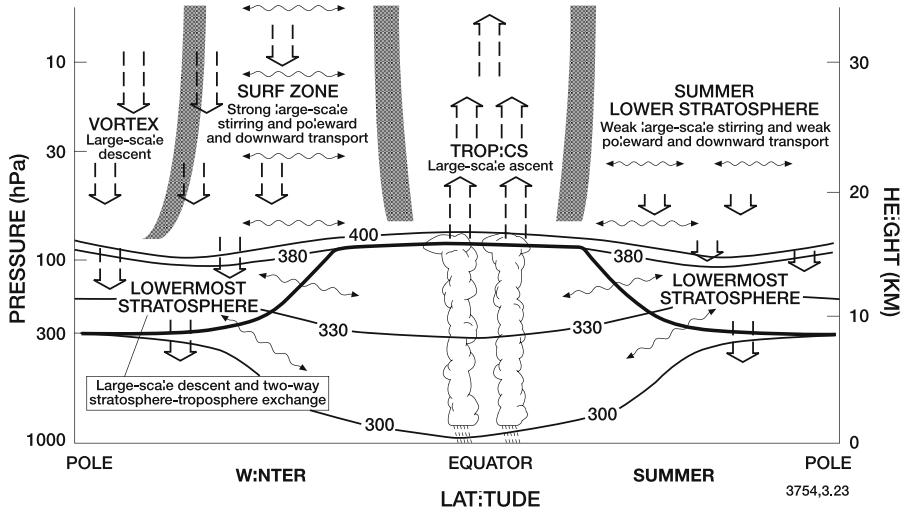

Figure 3.30. Schematic representation of the atmospheric circulation (arrows) and associated quasi-horizontal mixing between the surface and the middle stratosphere. Mixing processes leading to stratosphere-troposphere exchanges are also represented. The heavy vertical lines denote dynamical barriers against meridional transport. Note the large-scale ascent in the tropical stratosphere above intense convective systems in the tropical troposphere, and large scale descent associated with the polar vortex during winter (WMO, 1999).

result of mechanical and radiative dissipation (turbulence and irregular distribution of ozone and water vapor). Part of the descending air may return to the stratosphere, so that the net stratosphere to tropospheremass flux is not straightforward to quantify. Convective activity in the vicinity of such storms, which tend to mix tracers in the vicinity of the tropopause, makes this estimate even more difficult. At smaller spatial scales (typically 100 km), turbulence and mixing caused by gravity wave breaking events or strong wind shear (*e.g.*, clear air turbulence) also contribute to cross-tropopause exchanges.

Transport from the troposphere to the stratosphere occurs primarily in the tropics and is associated with the upward branch of the Brewer-Dobson circulation. Folkins *et al.* (1999) argue that the top of the tropospheric Hadley circulation in the tropics occurs at 14 km, *i.e.*, well below the tropopause, and that a barrier to vertical mixing therefore exists in the *tropical tropopause layer* (TTL) 2 or 3 km below the thermal tropopause. Air injected above this barrier subsequently participates in generally slow vertical ascent into the stratosphere. Small-scale exchanges also take place at mid-latitudes through filamentary structures that are drawn poleward in relation with anticyclonic circulation in the upper troposphere (Chen, 1995).

Box 3.1 The Tropopause

The surface separating the troposphere from the stratosphere is called the *tropopause*. It is associated with the minimum in the vertical temperature profile observed near 7-16 km altitude. The World Meteorological Organization (WMO) defines the tropopause level as the lower boundary of a layer in which the vertical decrease in temperature is less than 2 K/km for a depth of at least 2 km.

The stratosphere is characterized by a rapid increase with height of the potential temperature in response to the strong heating produced by ozone absorption of solar ultraviolet radiation. As a result, the stratosphere is stably stratified with very slow vertical exchanges. At the same time, the troposphere, especially in the tropics, is easily subject to destabilization caused primarily by the solar heating of the Earth's surface, producing powerful deep convection. The transition between these two regions is complex and not fully understood. The temperature minimum at the tropical tropopause (located near 16 km altitude) is believed to be produced by the wave-driven upward motion in this region. In the extratropics, the tropopause is located at considerably lower altitudes (12 km at mid- latitudes and 8 km in the polar regions). Its height is determined primarily by the dynamical heating associated with baroclinic waves and cyclonic activity.

Rather than being an infinitely thin surface, the tropopause should be regarded as a highly dynamic layer over which the mixing ratios of chemical compounds (such as water vapor or ozone) change rapidly from their tropospheric to their stratospheric values. This layer behaves as a quasi-material entity: in the tropics, it nearly coincides with the isentropic surface of 380 K. In the extratropics, it corresponds to the iso-surface of 2-4 potential vorticity units, and includes a mixture of air with tropospheric and stratospheric characteristics (*e.g.*, tracer mixing ratios).

3.7 The Importance of Wave Transience and Dissipation

Equations (3.67) to (3.69) show that, in a hypothetical case where the effects of wave transience and dissipation are ignored ($\overline{G}_u$ and $\overline{G}_\Theta = 0$) in both the thermodynamic and momentum equations and steady state is assumed, the atmosphere would eventually reach a *radiative equilibrium*, corresponding to a temperature distribution similar to that displayed in Figure 3.31. In this case, the residual circulation (v^*, w^*) would vanish and the temperatures would be quite different from those observed, particularly at the tropical tropopause and in the mesosphere. At the same time, zonal winds would be considerably faster than are observed with a particularly strong polar vortex during winter.

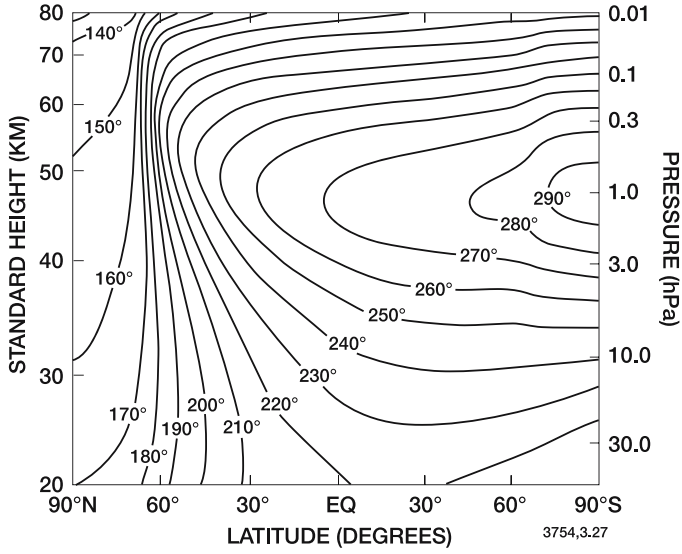

Figure 3.31. Meridional distribution of the radiative equilibrium temperature calculated by Fels *et al.* (1985).

What is lacking in this picture is the mechanism for deceleration of the zonal winds provided by the Eliassen-Palm divergence or any other dissipation force (Leovy, 1964; Schoeberl and Strobel, 1978; Holton and Wehrbein, 1980). Assuming that wave transience and dissipation can be neglected in the thermodynamic (but not the zonal momentum) equation, and considering the dominant terms in the momentum equation (3.67), we can write

$$-\mathrm{f}\overline{\mathrm{v}}^{*} = \overline{\mathrm{G}}_{\mathrm{u}} \tag{3.73}$$

if $\overline{\mathrm{G}}_{\mathrm{u}}$ accounts for momentum forcing produced by wave breaking and other dissipative effects. The TEM circulation as well as the related meridional transport in the middle atmosphere is therefore driven primarily by wave dissipation. Our ability to derive the strength of the mean meridional circulation in a rotating frame of reference depends consequently on the accuracy to which transient and dissipative eddies (and specifically the Eliassen-Palm flux divergence $\vec{\nabla}\vec{\mathrm{E}}$) are determined. From equation (3.73), from the continuity equation (3.45), and for an upper boundary condition $\rho_0\overline{\mathrm{w}} \to 0$ as $\mathrm{z} \to \infty$, one easily derives

$$\overline{\mathrm{w}}^{*}(\phi, \mathrm{z}) = \frac{-1}{\rho_0(\mathrm{z})\, \mathrm{a}\cos\phi} \frac{\partial}{\partial\phi}\left[\frac{1}{\mathrm{f}}\int_{\mathrm{z}}^{\infty} \rho_0(\mathrm{z}')\, \overline{\mathrm{G}}_{\mathrm{u}}(\phi, \mathrm{z}') \cos\phi\, \mathrm{dz}'\right] \tag{3.74}$$

This expression describes the so-called *downward control principle* (Haynes *et al.*, 1991). It shows that in the extratropics ($\mathrm{f} \neq 0$), the vertical velocity $\overline{\mathrm{w}}^{*}$ (and hence the vertical transport) at a given

altitude is determined only by wave dissipation *above* this height. Thus, as suggested by the concept of the extratropical fluid pump described earlier, the TEM circulation at a given atmospheric level is driven by the zonal momentum force associated with wave dissipation above this level. Specifically, the strength of the mass exchanges between the stratosphere and the troposphere can be explained by nonlocal wave forcing in the middle atmosphere rather than local dynamical or thermodynamical processes.

An accurate representation of wave drag is essential for chemical modeling because chemical species are advected by the mean meridional circulation and are also transported by the irreversible mixing which accompanies wave drag. Modeling studies (*e.g.*, Schoeberl and Strobel, 1978; Holton and Wehrbein, 1980) sometimes use a "Rayleigh" coefficient to crudely parameterize the effects of wave dissipation. In this case, a deceleration is assumed to act linearly on $\overline{\mathrm{u}}$, and is substituted for the wave drag term $\overline{\mathrm{G}}_u$ as follows:

$$\frac{\partial \overline{\mathrm{u}}}{\partial \mathrm{t}} - \mathrm{f}\overline{\mathrm{v}}^{\,*} = \overline{\mathrm{G}}_{\mathrm{u}} \equiv -\mathrm{k}_{\mathrm{r}}\overline{\mathrm{u}} \tag{3.75}$$

where k_{r} is the *Rayleigh friction coefficient.* Although the formulation in equation (3.75) must be regarded as no more than a crude parameterization, the dynamic and thermal structure obtained by models that include Rayleigh friction is in broad agreement with observations as long as $\mathrm{k}_{\mathrm{r}}^{-1}$ is of the order of 100 days in the stratosphere and a few days in the mesosphere. The higher values of k_{r} required for the mesosphere as compared to the stratosphere highlights the importance of gravity wave dissipation above the stratopause.

In the thermosphere, where ions (charged particles) represent a substantial fraction of the atmospheric fluid, dissipative forces involve the effects of the electromagnetic field and of momentum transfer between ions and neutral particles. As a result, the dissipative forces cannot be expressed anymore by a simple Rayleigh friction coefficient, but by a tensor λ_{ij} (Dickinson *et al.*, 1975; 1977; Hong and Lindzen, 1976; Kasting and Roble, 1981) characterizing an anisotropic drag:

$$\overline{\mathrm{G}}_{\mathrm{u}} = -\left(\lambda_{\mathrm{xx}}\,\overline{\mathrm{u}} + \lambda_{\mathrm{xy}}\overline{\mathrm{v}}\right) \tag{3.76a}$$

$$\overline{\mathrm{G}}_{\mathrm{v}} = -\left(\lambda_{\mathrm{yx}}\,\overline{\mathrm{u}} + \lambda_{\mathrm{yy}}\overline{\mathrm{v}}\right) \tag{3.76b}$$

Two effects must be considered: At altitudes sufficiently high for the collisions between ions and neutral particles to become infrequent, and

hence the ions and the neutrals to behave as two independent fluids (ions move preferentially along magnetic field lines), neutral particles that cross field lines suffer momentum loss: this dissipation is called *ion drag*. Hong and Lindzen (1976) have shown that the ion drag coefficients can be expressed as

$$\lambda_{xx} = \alpha_i\,(z)$$
$$\lambda_{xy} = \alpha_i\,(z)\sin^2 I$$

where factor $\alpha_i\,(z)$ can be expressed as a function of the ion number density $N_i(z)$ by

$$\alpha_i\,(z) = \frac{5 \times 10^{-10} N_i\,(z)}{1 + (\nu_i/\omega_i)^2}\left(s^{-1}\right)$$

where ν_i/ω_i is the ratio between the ion/neutral collision frequency ν_i and the ion gyrofrequency ω_i.

The second effect to be considered is the deflection of the weakly charged air flow by the electromagnetic field through the Lorentz force. The corresponding drag coefficients are (Hong and Lindzen, 1976)

$$\lambda_{xy} = \lambda_{yx} = \alpha_i\,(z)\left(\frac{\nu_i}{\omega_i}\right)\sin I\ .$$

In the above expressions, I is the dip angle of the magnetic field. For magnetic poles coincident with the geographic poles, $\tan I = -2 \tan \phi$, where ϕ is the geographic latitude. λ_{ij} coefficients become significant only above 100 km altitude. The time constant $(1/\lambda_{xx})$ associated with ion drag is typically 1 day at 120 km and about 1 hour at 250 km. The Lorentz effect (λ_{xy}) plays a role only in the lower thermosphere (110 to 150 km).

At lower altitudes, except at the tropical tropopause and in the winter hemisphere, the stratosphere may be considered to be approximately in radiative equilibrium, while the mesosphere is very far from these conditions. The most dramatic manifestation of the importance of meridional motions for the temperature structure of the middle atmosphere occurs at the summer polar mesopause, where the temperature (about 130 K) is the lowest observed anywhere on Earth, even though the region receives substantially more solar radiation than does the winter mesopause (Box 3.2).

Box 3.2 The Mesopause

The transition between the mesosphere and the thermosphere, called the *mesopause*, is characterized by a temperature minimum whose location varies significantly with latitude and season (see Figure 3.32). In the tropics during all seasons, and in the winter mid- and high-latitudes, this transition takes place at approximately 100 km altitude. At the winter pole, the mesopause temperature is typically 180–200 K. At mid- and high latitudes during summer, the mesopause is located near 85 km, and the temperature at the pole reaches values as low as 120-140 K (coldest place in the Earth's atmosphere where polar mesospheric clouds are occasionally observed).

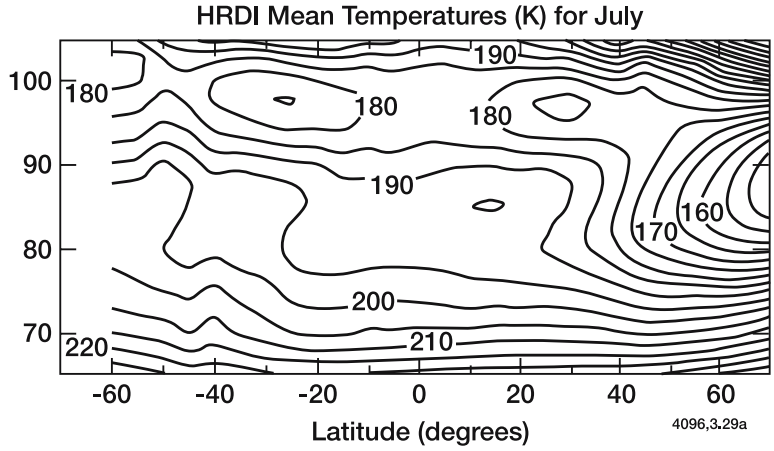

Figure 3.32. Zonally averaged temperature in the vicinity of the mesopause (65 to 105 km) observed in July by the HRDI instrument on board the Upper Atmosphere Research Satellite (UARS). From Ortland *et al.*, 1997.

The structure of the mesopause (see Smith, 2004) depends on a complex interplay between dynamics, radiative transfer, and photochemistry. Although, on the average, radiative processes dominate the energy budget in the region surrounding the mesosphere, adiabatic heating and cooling mechanisms associated with large scale advection by the general circulation, transport of heat by molecular diffusion and by turbulence, energy deposition by gravity waves and occasionally heat transport resulting from convective instability must be taken into account. Heat release by exothermic reactions (chemical heating) as well as energy loss to space by radiative emissions, primarily by carbon dioxide, also play key roles in the energetics of the region.

Box 3.2 (Continued)

Interestingly, the mesopause can be regarded as a layer separating two distinct dynamical regions of the atmosphere: the thermosphere, where atmospheric processes are governed primarily by external solar influences, and the mesosphere, which is influenced primarily by internal variability produced by upward propagating waves.

Recent studies have suggested that the mesopause may have been perturbed in response to human-induced emissions of chemical compounds, including carbon dioxide and methane. Although a cooling of the mesosphere has been reported, not enough data is currently available to quantify any change that could have occurred in the vicinity of the mesopause during recent decades.

It has long been suspected that wave drag in the mesosphere results from the dissipation of gravity waves (*e.g.*, Lindzen, 1967). Radar observations (*e.g.*, Fritts and Vincent, 1987) support the view that the momentum flux associated with these waves accounts for the momentum budget of the mesosphere. Several parameterizations to represent these effects have been developed (Lindzen, 1981; Weinstock, 1982; Fritts and Lu, 1993; Medvedev and Klaasen, 1995; Hines, 1997a,b) and used in atmospheric models. Lindzen (1981), for example, assumes that, above the breaking level, gravity waves produce strong turbulent diffusion and further growth of their amplitude is prevented. This assumption leads to expressions for the wave drag and the turbulent diffusion that are strong functions of the Doppler shift, $\overline{u} - c$, the difference between the zonally averaged wind ($\overline{u}$) and the phase speed (c) of the wave:

$$\overline{G}_u = -\frac{k(\overline{u} - c)^3}{2HN} \tag{3.77}$$

$$K_z = \frac{k(\overline{u} - c)^4}{2HN^3} \tag{3.78}$$

In these expressions, k is the horizontal wavenumber of the gravity wave, H is the atmospheric scale height, and N is the Brunt-Vaisala frequency (see *e.g.*, Eqs. 3.19a-b, and Holton, 1992). Equation (3.77) is a more satisfactory description of the effect of wave drag in the mesosphere than is the simple Rayleigh friction used in Equation (3.75), since it is based on a simple but physically motivated description of the wave breaking process. Equation (3.77) can produce positive or negative acceleration of the zonal wind, depending on the sign of $\overline{u} - c$. Figure 3.33 shows a typical meridional distribution of the forcing produced on the zonal mean velocity as a result of gravity wave breaking. The resulting meridional circulation consists of a single cell directed from the summer to the

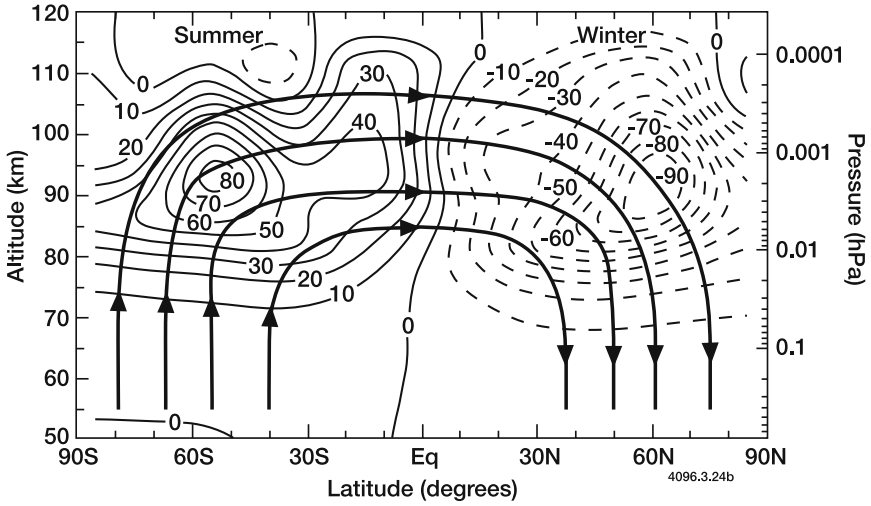

Figure 3.33. Meridional distribution of the zonal momentum forcing associated with gravity wave breaking (m s^{-1}/day) as calculated by the 2-D model of Brasseur *et al.* (2000). The forcing is positive in the summer hemisphere and negative in the winter hemisphere, so that gravity wave breaking tends to decelerate the zonal flow in both seasons. The pole-to-pole wave driven circulation in the mesosphere (solid lines with arrows) is schematically represented.

winter poles. Air is therefore drawn upward toward the mesopause in summer and downward away from the mesopause in winter. As a result, the mesosphere is kept away from thermodynamic equilibrium, with very low temperatures at the summer mesopause (130 K) and relatively high temperature at the winter mesopause (210 K).

It should be noted that, since the zonal wind distribution varies considerably with season, equations (3.77)-(3.78) introduce the possibility of seasonal variability of wave drag and diffusion. Holton (1982; 1983) has shown that the filtering produced by stratospheric winds (see Section 3.4 and Figure 3.11) does indeed result in seasonal differences in mesospheric wave drag. Wave breaking produces a westward force in winter and an eastward force in summer, leading in both seasons to a deceleration of the zonal wind in good agreement with observations. Clearly, if wave drag varies seasonally, so too must the mixing produced by wave breaking, a phenomenon that has consequences on the vertical transport of chemical species (like water vapor) in the mesosphere (see Garcia and Solomon, 1985; Holton and Schoeberl, 1988).

Gravity wave breaking also affects the heat budget of the mesosphere indirectly through changes in the meridional circulation induced by momentum deposition. Direct thermal effects have also the potential to

play a significant role (see *e.g.*, Huang and Smith, 1991; Lieberman *et al.*, 2000) through conversion of turbulent energy to heat (see Eq. 3.69a)

$$\mathrm{G}_{\Theta}^{(1)} = \frac{1}{\rho_0}\frac{\partial}{\partial \mathrm{z}}\left(\rho_0 \overline{\mathrm{w}'\Theta'}\right)$$

and, above the gravity wave breaking level, by transport of heat through induced turbulence

$$\mathrm{G}_{\Theta}^{(2)} = \frac{1}{\rho_0}\frac{\partial}{\partial \mathrm{z}}\left(\rho_0 \, \mathrm{K_h} \, \frac{\partial \overline{\Theta}}{\partial \mathrm{z}}\right)$$

In these expressions, $\mathrm{G}_{\Theta}^{(1)}$ and $\mathrm{G}_{\Theta}^{(2)}$ represent additional dissipative terms to be added to the thermodynamic equation (3.69). $\mathrm{K_h}$ represents the vertical eddy diffusion coefficient for heat, which is related to the vertical eddy diffusion coefficient for momentum and tracers (Eq. 3.78) by the Prandtl number Pr:

$$\mathrm{K_h} = \frac{\mathrm{K_z}}{\mathrm{Pr}}$$

Strobel *et al.* (1985) and Strobel (1989) showed that tracer and heat transport in the mesosphere were best reproduced for a Prandtl number of 3. Huang and Smith (1991) suggested the choice of a Prandtl number of 10, which implies that gravity wave breaking has a small direct effect on the thermal budget of the mesosphere. Gavrilov and Roble (1994) showed that gravity wave dissipation $\mathrm{G}_{\Theta}^{(1)}$ and turbulent heating $\mathrm{G}_{\Theta}^{(2)}$ are nearly in equilibrium near 100 km altitude.

The origin and magnitude of wave drag in the stratosphere is also an important question for stratospheric dynamics. Geller (1983) suggested that gravity wave breaking may provide much of the frictional dissipation in the stratosphere as well as in the mesosphere. However, Rossby wave transience and dissipation must also be important, at least in winter. Figure 3.34 shows a climatological view of the Eliassen-Palm (EP) flux and its divergence produced by the absorption of Rossby waves during the month of January. The EP flux is directed upward and equatorward. Wave propagation into the stratosphere is observed primarily in the winter hemisphere and the momentum forcing on the mean flow is largest between 30°N and 70°N. As indicated earlier (McIntyre and Palmer, 1983; 1984), Rossby waves tend to break in the vicinity of the critical surface ($\mathrm{u} = \mathrm{c}$), where a substantial EP flux convergence and hence a strong wave-mean flow interaction take place (see Figure 3.34). Such a situation is accompanied by strong quasi-horizontal mixing on isentropic surfaces over distances of typically several thousands of kilometers (see also Figure 3.10). The mechanism leading to Rossby wave instability is not, as in the case of gravity waves, the presence of vertical static

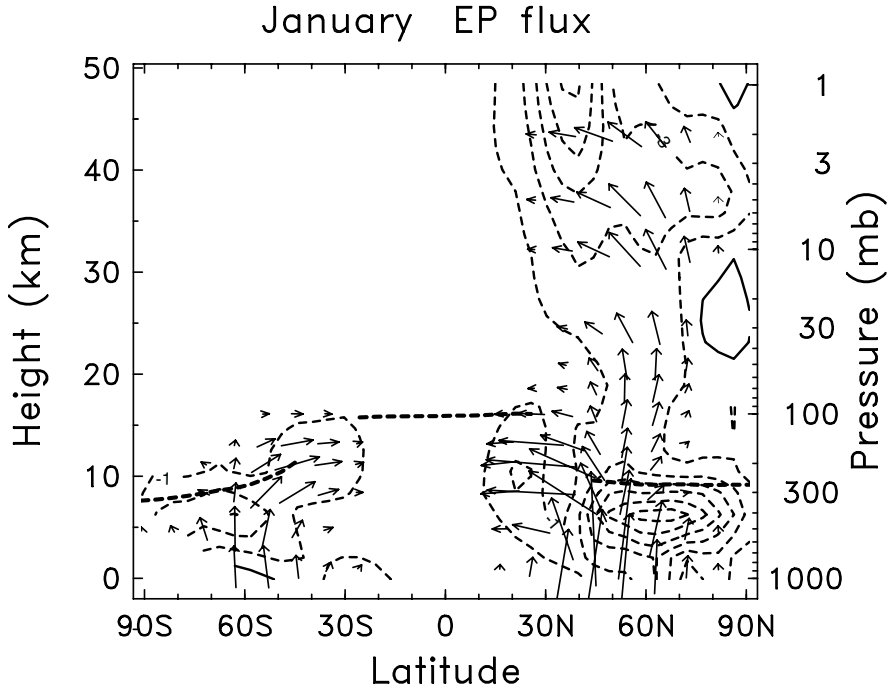

Figure 3.34. Eliassen-Palm (EP) flux (arrows) and its divergence (dashed lines) represented as a function of altitude and latitude for January. The EP flux propagates in the stratosphere only during winter. The EP flux divergence is associated with Rossby wave transience and dissipation. Courtesy of W. Randel, NCAR (2001).

instability, but a reversal of the potential vorticity gradient on an isentropic surface.

In late winter and spring within the space of a few days, large temperature increases are occasionally observed to occur in the lower stratosphere, accompanied by cooling in the mesosphere and upper stratosphere (*e.g.*, Labitzke, 1980). Under these circumstances, the stratopause may be found to be as low as 35 km altitude. The polar night jet decreases in strength and on certain occasions even reverses (breakdown of polar vortex). Matsuno (1971) and Holton (1976) have simulated such *sudden stratospheric warmings* by considering the interaction of large scale waves that propagate from the troposphere with winds in the stratosphere and mesosphere. Matsuno (1971), Matsuno and Nakamura (1979), Dunkerton *et al.* (1981), and Palmer (1981), have further emphasized that sudden warmings are caused by strong

planetary wave drag due to wave transience and critical level absorption. As a result of the decelerated flow, the propagation of planetary waves is modified and produces an even stronger deceleration of the mean zonal wind at a lower altitude. At the same time, a mean meridional circulation is induced with strong downward motion at high latitude and upward motion in the tropics, producing the observed high latitude warming as a result of adiabatic compression. Sudden warmings have significant effects on the annual cycle of total ozone, and on many other constituents. Observations (*e.g.*, Naujokat and Labitzke, 1993) show that the wind deceleration associated with momentum convergence often starts in the upper stratosphere and propagates downward. A sudden warming is considered to be major when the zonal wind reverses in the region poleward of 60° and above the height corresponding to 10 hPa. Extreme warming events are occasionally observed in the upper stratosphere where the temperature (which is typically 240 K at 40 km in January) can reach more than 320 K at certain locations near the pole (see *e.g.*, von Zahn *et al.*, 1998).

In the tropics, where the dynamics is determined by the vanishing Coriolis force and its maximum change with latitude, the zonal mean circulation in the middle atmosphere is characterized by oscillatory equatorial zonal wind systems, including super-rotating westerly jets, and a spectrum of transient vertically propagating waves, some of them equatorially trapped. At these latitudes, the zonal forces exerted by dissipating equatorial eastward and westward waves can efficiently accelerate (decelerate) zonal currents or jets and indirectly cause secondary meridional circulations. Existing zonal jets in turn alter the propagation and dissipation conditions for waves emerging from the troposphere, leading to a strong vertically varying wave mean-flow interaction and dynamical vertical coupling of the atmospheric layers.

The most prominent examples of oscillatory low latitude wind systems are the quasi-biennial oscillation (QBO) in the equatorial stratosphere and the semi-annual oscillation (SAO) at the equatorial stratopause (Figure 3.35). The *quasi-biennial oscillation* (QBO) (Veryard and Ebdon, 1961; Reed et al., 1961) is characterized by the downward propagation of westerly and easterly jets from the upper stratosphere to the lower stratosphere near 70 hPa, almost without loss in amplitude, at a rate of typically 1 km per month (Figure 3.36). The period of the QBO varies between 22 and 34 months (28 months on average), and the amplitude of the westerly and easterly jets is typically 15 m/s and -30 m/s, respectively. The QBO is the main cause of interannual variance of the zonal wind in the equatorial stratosphere. Detailed reviews are given by Dunkerton and Delisi (1985) and Baldwin et al. (2001).

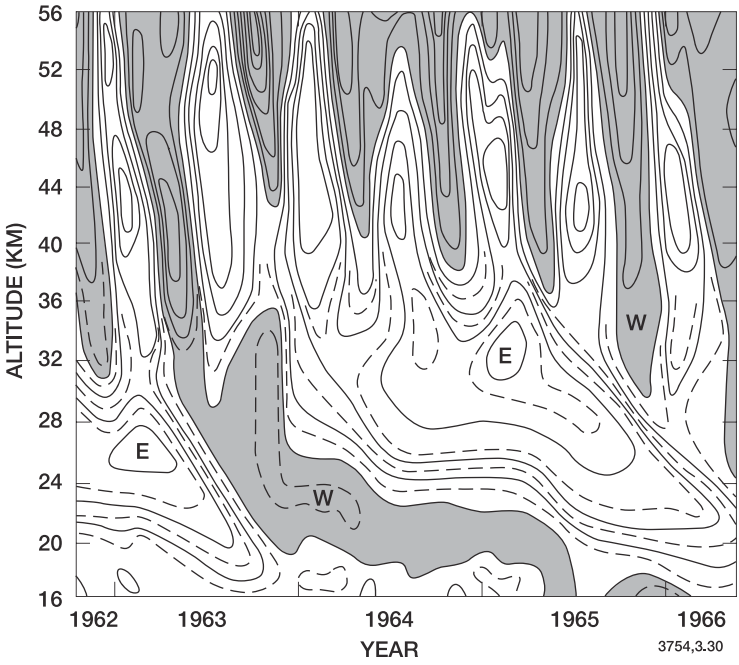

Figure 3.35. Time-height cross section of the zonal wind near the equator highlighting the quasi-biennial oscillation between 16 and 36 km and the semi-annual oscillation in the vicinity of the stratopause. Solid lines are drawn at intervals of 10 ms^{-1}. Shaded areas denote flow from west to east (westerlies). Other areas correspond to westward winds. The mean value of the wind has been filtered out. From Wallace (1973).

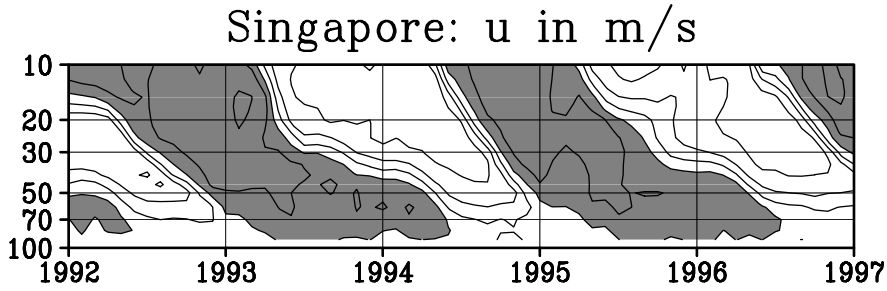

Figure 3.36. Time height cross-section of the zonal wind at Singapore between 1992 and 1997 with the quasi-biennial oscillation between the pressure levels of 100 and 10 hPa. Contour intervals 10 m/s. Shaded areas represent eastward (or westerly) winds. Courtesy of B. Naujokat, Free University of Berlin.

Theoretical studies (Lindzen and Holton, 1968; Holton and Lindzen, 1972; Dunkerton, 1997) as well as laboratory simulations of the analogue of large scale geophysical flows (Plumb and McEwan, 1978) suggest that the origin of the QBO lies in the vertical transport of momentum by certain types of equatorial waves and by gravity waves. Although the QBO is primarily a tropical phenomenon, it has substantial impact in the extratropics, including on the breakdown of the polar vortices in spring (Holton and Austin, 1991; O'Sullivan and Young, 1992). By filtering tropical waves that propagate upward, the QBO also affects the variability of the mesosphere. Atmospheric tracers including water vapor, methane, and ozone respond to the circulation changes (see Plate 5). The importance of the coupling between the QBO anomalies in ozone concentration, stratospheric heating rates, temperature and winds has been reviewed by Hasebe (1994).

The *semi-annual oscillation* (SAO), which is observed in the zonal mean flow near the equatorial stratopause with maximum westerlies at the equinox and maximum easterlies at the solstices (see Figure 3.35), is also believed to be of dynamical (rather than radiative) origin. Unlike the QBO, the SAO is locked to the annual cycle. The westerly accelerations in March and September are believed to be caused by Kelvin and high frequency gravity waves, while the easterly acceleration in June and December is produced by the advection of easterly momentum across the equator from the summer hemisphere and involve EP flux convergence produced by Rossby wave breaking. The QBO signal is evident below 36 km, while the SAO signal is dominant in the upper stratosphere. A separate SAO observed near the mesopause is probably caused by gravity wave breaking with alternate easterly and westerly forcing around 80-90 km altitude. The signal of the SAO is also observed in the concentrations of chemical compounds.

Finally, increasing attention has recently been given to an important circulation anomaly observed in the Northern Hemisphere (see Box 3.3) and characterized by a nearly symmetric oscillation in temperature, wind, and pressure between the Arctic and mid-latitudes (Thompson and Wallace, 1998). This annular mode of oscillation in the climate system is called the *Arctic oscillation* (AO), and extends from the surface to the upper stratosphere. The AO affects the strength and location of the Arctic vortex, with associated effects on stratospheric ozone (Wallace and Thompson, 2002).

Box 3.3 Stratospheric Dynamics, Weather, and Climate

There have been long debates in the scientific community regarding the possible influence of stratospheric dynamics on weather and climate at the Earth's surface. Dynamical links between the stratosphere and the troposphere were suggested by Charney and Drazin (1961) and Matsuno (1970) several decades ago, and more recent investigations have provided strong evidence of the relationship between the tropospheric and stratospheric circulations, and specifically between the strength of the stratospheric winter vortex and the structure of tropospheric planetary waves (Boville, 1984; Kodera, *et al.*, 1991; 1996; Baldwin *et al.*, 1994; Perlwitz and Graf, 1995; Perlwitz *et al.*, 2000). Links between stratospheric and tropospheric circulations have been studied in relation with large volcanic eruptions (Graf *et al.*., 1993; 1994; Kodera, 1994), solar-terrestrial relationships (Geller and Alpert, 1980; Labitzke and van Loon, 1988; Kodera and Yamazaki, 1990), and middle atmosphere cooling (Kodera and Yamazaki, 1994; Shindell *et al.*, 2001.) The discovery of certain recurrent spatial patterns in the dynamics of the atmosphere, called *modes of variability*, provides some evidence for dynamical couplings between the middle and lower atmosphere. These modes can often be regarded as the signature of dynamical interactions and feedback mechanisms in the Earth system.

One of the patterns that has recently received wide attention is the Northern Hemisphere annular mode (NAM), also called the *Arctic Oscillation* (AO), a distinctive annular feature in the sea-level pressure deviation near 55°N (Thompson and Wallace, 1998; 2000). A similar mode (SAM) is also observed in the Southern Hemisphere. These patterns correspond to the annular modes provided by a set of empirically determined orthogonal functions (EOF) that can be derived from the observed dynamical fields. The NAM's index is a normalized value of the NAM expansion coefficient: a positive value corresponds to below-normal sea-level surface pressures in the Arctic with strong eastward winds around 50-60°N, especially across the North Atlantic, and higher than normal temperatures in the Northern Hemisphere. Under those conditions, Northern Europe during wintertime is subject to precipitations, while the southern part of the continent is sunny. A negative index is suggestive of weak surface eastward winds over the Atlantic, with slowly propagating weather systems; winter cold air masses are expanding from Russia towards Northern Europe (with occasionally extremely cold conditions), and storms are developing in the Mediterranean. As the contrasts in meteorological variables appear to be most coherent over the Atlantic sector, the Northern Hemisphere annular mode is often referred to as the *North Atlantic Oscillation* (NAO). Fragmentary evidence of this oscillation was already appearing in the beginning of the 20th century (Exner, 1913; Walker, 1924; Walker and Bliss, 1932).

Box 3.3 (Continued)

Analyses of meteorological fields by Baldwin and Dunkerton (1999, 2001) have highlighted a statistically significant relationship between the strength of the stratospheric winter polar vortex and the Northern Hemisphere annular mode: a strengthening of the polar vortex tends to be associated with a positive NAM index at the Earth's surface, while a weakening of the polar night jet induces negative NAM indices. A statistical analysis based on several wintertime events shows that the signal produced by a reduction in the strength of the polar vortex at 30 km propagates down and reaches the troposphere with a time lag of several weeks (Baldwin and Dunkerton, 2001). Although downward propagation (within a timeframe of 5-10 days) of middle atmosphere planetary-scale perturbations (such as those resulting from stratospheric warming events) to the lower stratosphere and perhaps the upper troposphere are well-known features (see *e.g.*, Matsuno, 1971; Kodera and Kuroda, 2000a, b), the recent analyses of Baldwin and Dunkerton (2001) suggest that the stratospheric signal penetrates as far down as the surface, and with a phase delay of typically 30-40 days. Links between stratospheric dynamics and tropospheric weather patterns offer therefore hope for improved long-range weather forecasts (Wallace and Thompson, 2002).

Trends in the past 30 years toward higher positive NAM indices (Thompson *et al.*, 2000) have favored milder and wetter winters in Northern Europe together with a strengthening of the polar night jet and reduced ozone abundances in the stratosphere at high latitudes. Stratospheric zonal wind anomalies produced by changes in solar activity, by the equatorial QBO, by volcanic eruptions, by stratospheric ozone depletion and by the increase in carbon dioxide concentration could trigger or modulate internal modes of stratospheric variability and generate similar patterns that propagate downward into the troposphere.

The observed trends in the NAM towards higher indices may have resulted from human-induced changes in the temperature structure of the lower stratosphere in response to greenhouse gas emissions and ozone depletion (Shindell *et al.*, 2001). The radiative effects of solar activity and of volcanic eruptions may also have produced NAM- like signatures detectable at the Earth's surface. The response of the Earth system to climate forcing may therefore involve changes in particular dynamical modes, and hence the human influence on climate at the Earth surface may occur in part by way of the stratosphere.

3.8 Vertical Transport above the Mesopause

Above the mesopause (85-95 km altitude), the air density starts to decrease more slowly with height than at lower altitudes, suggesting that

the atmospheric scale height is progressively increasing. This change results primarily from a dramatic temperature increase in the lower thermosphere as well as a simultaneous decrease with height in the mean molecular mass of air. In the vicinity of the homopause (transition between the homosphere and the heterosphere near 100 km), vertical mixing (which leads to a uniform mixing ratio of major gases such as N_2 or O_2 below 100 km) is gradually replaced by diffusive separation of atmospheric constituents according to their molecular mass. As a result, the lightest compounds (such as the hydrogen and helium atoms) are transported upward and their relative abundances increase with altitude. Conversely, the heaviest species (such as N_2 or O_2) are transported downwards and, as a result, their mixing ratio decreases very rapidly with height. Figure 3.37 shows an example of the vertical profiles derived for several compounds between the surface and 1000 km altitude.

The thermosphere is also characterized by large molecular viscosity (which affects the circulation of the air) and by rapid thermal conduction (which is the principal transport process for thermal energy above 100 km altitude). Under these conditions, the momentum and thermodynamic equations ((3.1) and (3.2)) need to be slightly modified by the inclusion of additional terms. For a mixture of gases, they can

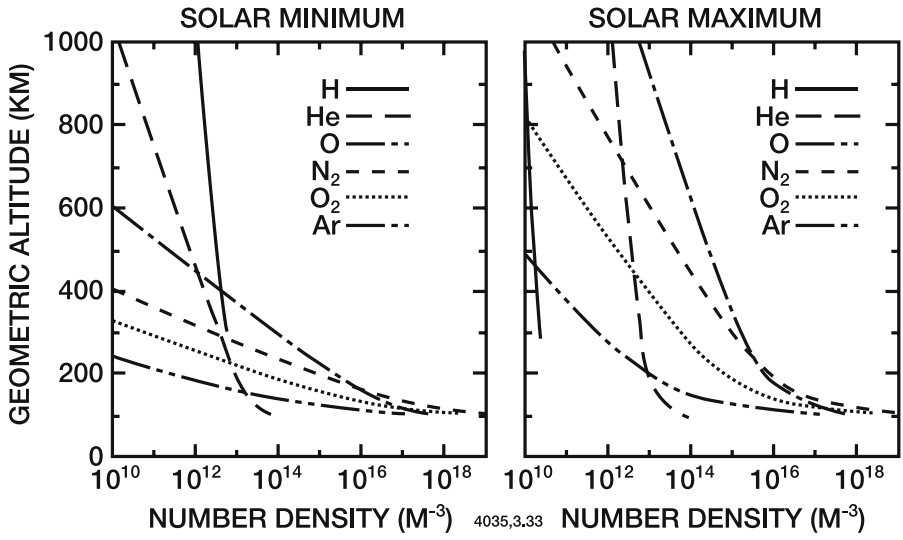

Figure 3.37. Vertical distribution of the concentration of several chemical species in the thermosphere. The importance of diffusive separation is visible. From Richmond (1983).

be expressed as

$$\frac{d\vec{v}}{dt} + \frac{1}{\rho}\vec{\nabla}p + 2\vec{\Omega} \times \vec{v} = \vec{g} + \frac{\mu}{\rho}\nabla^2\vec{v} + \sum_i F_i$$

and

$$c_p \frac{dT}{dt} - \frac{1}{\rho}\frac{dp}{dt} + \frac{1}{\rho}\vec{\nabla} \cdot \vec{E} = Q$$

with most of the symbols defined in Section 3.3.1. In the above expressions, μ is the viscosity coefficient and F_i accounts for the external forces (*e.g.*, ion drag) applying to i-type particles. $\vec{E}$ is the heat flow vector, which is proportional to the temperature gradient

$$\vec{E} = -\lambda \vec{\nabla} T$$

where λ is the thermal conductivity coefficient. Expressions for μ and λ can be derived from the gas kinetics theory. Semi-empirical expressions of the form

$$\mu = A\,T^s$$
$$\lambda = B\,T^s + CT + D$$

can also be applied for a mixture of gases (see *e.g.*, Banks and Kockarts, 1973), with s usually chosen as equal to 0.69, and A, B, C, and D varying with the relative abundance of the major thermospheric compounds.

Vertical transport of chemical compounds in the thermosphere is governed primarily by molecular diffusion. The vertical flux of chemical species associated with molecular diffusion can be derived from the momentum equations applied to thermospheric conditions (Gombosi, 1998). Considering elastic collisions between particles, but ignoring all reactive collisions, and taking into account the effect of thermal diffusion, the vertical "molecular diffusion velocity" for species i at geometric altitude z_g can be expressed as (Banks and Kockarts, 1973)

$$w_{D,i} = -D_i \left[\frac{1}{n_i}\frac{dn_i}{dz_g} + (1 + \alpha_T)\,\frac{1}{T}\frac{dT}{dz_g} + \frac{1}{H_i} \right] \tag{3.79}$$

where n_i is the concentration of minor constituent i, $H_i = kT/m_i g$ is the scale height of this species and m_i its molecular mass. α_T is the thermal diffusion factor (–0.40 for helium, –0.25 for hydrogen, 0 for heavier particles) and D_i the molecular diffusion coefficient. This coefficient is related to the collision frequency between species i and all other molecules and atoms. Its value can be derived from the classic gas kinetic theory (Chapman and Cowling, 1970). An approximate expression for D_i (in $cm^2 s^{-1}$) is provided by Banks and Kockarts (1973):

$$D_i = 1.52 \times 10^{18} \left[\frac{1}{m_i} + \frac{1}{m} \right]^{\frac{1}{2}} \frac{T^{\frac{1}{2}}}{n} \tag{3.80}$$

where the molecular mass of species i (m_i) and the mean molecular air mass (m) are expressed in amu, the temperature (T) is expressed in Kelvin and the total air density (n) is expressed in cm^{-3}. Since it is inversely proportional to the air density, the molecular diffusion coefficient D_i increases quasi-exponentially with height with values of the order of (1-5) $\times$ $10^4 cm^2 s^{-1}$ at 80 km and (1-5) $\times$ $10^7 cm^2 s^{-1}$ at 120 km.

As indicated earlier, vertical exchanges associated with turbulent mixing such as that caused by gravity wave breaking below the homopause are often represented as eddy diffusion. When expressed in terms of number density in an atmosphere following hydrostatic equilibrium conditions, the effective vertical "eddy diffusion velocity" becomes

$$w_{E,i} = -K_z \left[\frac{1}{n_i} \frac{dn_i}{dz_g} + \frac{1}{T} \frac{dT}{dz_g} + \frac{1}{H_g} \right] \tag{3.81}$$

where K_z is the vertical eddy diffusion coefficient and H_g is the atmospheric scale height. In the vicinity of the homopause, the effects of both eddy and molecular diffusion have to be taken into account, and the total vertical diffusion velocity is

$$w_i = w_{E,i} + w_{D,i} \tag{3.82}$$

In the absence of significant chemical production or destruction mechanisms, a chemical compound follows diffusive equilibrium conditions ($w_i = 0$), and the vertical profile of its density can be expressed as (Banks and Kockarts, 1973)

$$n_i^{eq}(z_g) = n_{i,0} \frac{T_0}{T(z_g)} \exp\left[- \int_{z_{g,0}}^{z_g} \left(\frac{1}{H_i(z')} + \frac{\Lambda_i(z')}{H_g(z')} \right) \frac{dz'}{1+\Lambda_i(z')} - \int_{z_{g,0}}^{z_g} \frac{\alpha_T}{1+\Lambda_i(z')} \frac{1}{T(z')} \frac{dT}{dz'} dz' \right] \tag{3.83}$$

where $n_{i,0}$ and T_0 are the number density of species i and temperature at altitude $z_{g,0}$, respectively, and $\Lambda_i = K_z/D_i$ is the ratio between eddy and molecular diffusion coefficients. In the homosphere where $\Lambda_i \to \infty$, the vertical profile of an inert gas follows the hydrostatic law (corresponding to perfect mixing)

$$n_i^{eq}(z_g) = n_{i,0} \frac{T_0}{T(z_g)} \exp\left[- \int_{z_{g,0}}^{z_g} \frac{dz'}{H_g(z')} \right] \tag{3.84a}$$

while in the heterosphere, where $\Lambda_i \rightarrow 0$, the diffusive equilibrium condition becomes

$$n_i^{eq}(z_g) = n_{i,0}\left[\frac{T_0}{T(z_g)}\right]^{1+\alpha_T} \exp\left[-\int_{z_{g,0}}^{z} \frac{dz'}{H_i(z')}\right] \qquad (3.84b)$$

In both cases, the number density of inert (or quasi-inert) species i decreases exponentially with height. However, in the homosphere, the rate of decrease is characterized by the atmospheric scale height H_g (and is therefore identical for all inert gases), while in the heterosphere, it is related to the scale height H_i and hence the mass m_i of species i (and is therefore specific to each compound). As a result, the density of the lightest particles decreases the least rapidly with height (see Figure 3.37). Note that in numerical models of the middle atmosphere, the upper boundary condition is often prescribed by the maximum diffusion flux $\Phi_i^{max} = n_i w_i^{max}$ where w_i^{max} is given by (Banks and Kockarts, 1973; Gombosi, 1998)

$$w_i^{max} = \frac{D_i}{H_g}\left(1 - \frac{m_i}{m}\right) \qquad (3.85)$$

In the case of the hydrogen atom ($m_i = 1$) whose density is of the order of $10^8 cm^{-3}$ at 100 km, the upward vertical flux at this height is typically a few times $10^8 cm^{-2} s^{-1}$. The diffusive velocity w_i^{max} increases with height. Above 500 km, the mean free path of atoms become so long that collisions can be ignored: particles follow individual balistic trajectories. If the kinetic energy of atoms becomes larger than the potential energy required for these particles to be lifted out of the Earth's gravitational fields, these atoms escape to space. The probability that an atom reaches the escape velocity (typically 11 km s^{-1} at 500 km) is, however, extremely low, except in the case of hydrogen and, to a lesser extent, helium. The loss of hydrogen to space is compensated by the continuous production of H by water vapor photolysis above 60-70 km altitude.

3.9 Models of the Middle Atmosphere

3.9.1 General Circulation Models

Three-dimensional models which provide solutions to some form of the primitive equations outlined in Section 3.3 are called *general circulation models* (GCMs). These models can provide insight on the coupling between dynamical and radiative processes in the atmosphere. They resolve large-scale waves and synoptic eddies, and include state-of-the-

art parameterizations to represent unresolved (small-scale) processes. Deficiencies in model simulations often lead to the identification of key processes that have been omitted or inadequately treated in numerical models. In the most recent climate system models, atmospheric GCMs coupled to ocean circulation models, ice models, and continental surface models attempt to simulate the evolution of the entire Earth system and its response to various types of climate forcings. A long-term objective of GCMs is to quantify natural variability in the atmosphere and to assess the response of the atmosphere and to perturbations of natural or of human origin.

Ideally, the solution of the primitive equations for specified external constraints (*e.g.*, the solar irradiance at the top of the atmosphere) and appropriate boundary conditions (*e.g.*, observed sea-surface temperature) should provide a comprehensive representation in space and time of the atmospheric dynamical system. In practice, however, limitations in computer capabilities impose limits on the spatial resolution of these models, so that small-scale processes, rather than being explicitly reproduced, must be parameterized. The uncertainties associated with these physical parameterizations (*e.g.*, boundary layer exchanges, convection, clouds, gravity wave breaking, etc.) often limit the overall accuracy in the model results.

General circulation models of the middle atmosphere cannot ignore the dynamical and other physical processes occuring in the troposphere, due to the strong coupling between these two atmospheric regions. Middle atmosphere GCMs generally extend therefore down to the Earth's surface. An exception is provided by the so-called middle atmosphere *mechanistic models* in which the effects of tropospheric processes are represented by lower boundary conditions in the vicinity of the tropopause (*e.g.*, 200 or 300 hPa). These models are suitable for performing sensitivity tests and studying specific physical or chemical processes in the stratosphere and mesosphere.

The first general circulation model extending to the stratosphere was developed by Smagorinsky *et al.* (1965) at the Geophysical Fluid Dynamics Laboratory (GFDL) (Princeton, New Jersey, USA). This model covered only the Northern Hemisphere and included 9 vertical levels, among which 3 were in the stratosphere. Manabe and Hunt (1968) used a similar model, but included 18 levels up to the altitude of 37.5 km. After these early attempts to represent dynamical fields above the tropopause, many other middle atmosphere GCMs were developed and used to address scientific questions (Fels *et al.*, 1980; Simmons and Strüfing, 1983; Mechoso *et al.*, 1985; Déqué *et al.*, 1994; Boville, 1995; Hamilton *et al.*, 1995; Kitoh *et al.*, 1995; Chiba *et al.*, 1996; Beagley *et al.*, 1997; Langematz and Pawson, 1997; Manzini *et al.*, 1997; Rind

et al., 1998; Swinbank *et al.*, 1998). Many middle atmosphere models extend to the mesopause, or to even higher altitudes.

The three-dimensional equations of atmospheric dynamics are generally solved using different numerical approaches: In *grid point models* (see *e.g.*, Arakawa, 1966), the variables are defined by their values at particular points spaced in longitude, latitude, and altitude (model grid). The derivatives appearing in the equations are replaced by finite differences. The stability and accuracy generally depends on the spatial resolution of the model (size of the spacing between grid points) and on a time step chosen to solve the equations (typically 10-30 minutes in most models). In *spectral models* (see *e.g.*, Bourke, 1972), the horizontal distribution of the meteorological fields is expressed in terms of truncated spherical harmonic expansions (which can be regarded as the superposition of atmospheric waves). This method has the advantage of allowing exact calculation of the horizontal derivatives. The horizontal resolution of the model is provided by the number of waves retained in the harmonic expansions. This number is typically 21, 30, or 42 in most current middle atmosphere spectral models.

Figure 3.38 shows the zonal mean wind velocity calculated for January conditions by a number of middle atmosphere GCMs (Pawson *et al.*, 2000), together with a reference climatology (Randel, 1992). The degree of success in reproducing the observed winds depends strongly on the formulation of dissipative processes including diabatic heating (radiative transfer) and momentum deposition (gravity wave parameterization). In the case of gravity waves, the simplest parameterization is provided by the introduction of a Rayleigh friction term in the momentum equation (see Eq. (3.75)). More elaborate approaches are based on the recent parameterizations of Lindzen (1981), Medvedev and Klaasen (1995), or Hines (1997a,b), which account for orographic (zero phase speed) and non-orographic (nonzero phase speed) gravity waves (see Section 3.4). In some models, the temperature calculated in the polar winter stratosphere is colder than observed, and hence the polar jet is too strong. This cold polar bias is significantly reduced in the lower stratosphere when the effects of orographic gravity waves are included in the model (Boville, 1995).

3.9.2 Chemical-Transport Models

Chemical-transport models (CTMs) simulate the formation, transport, and destruction of chemical compounds in the atmosphere. These models can be directly coupled to the general circulation models

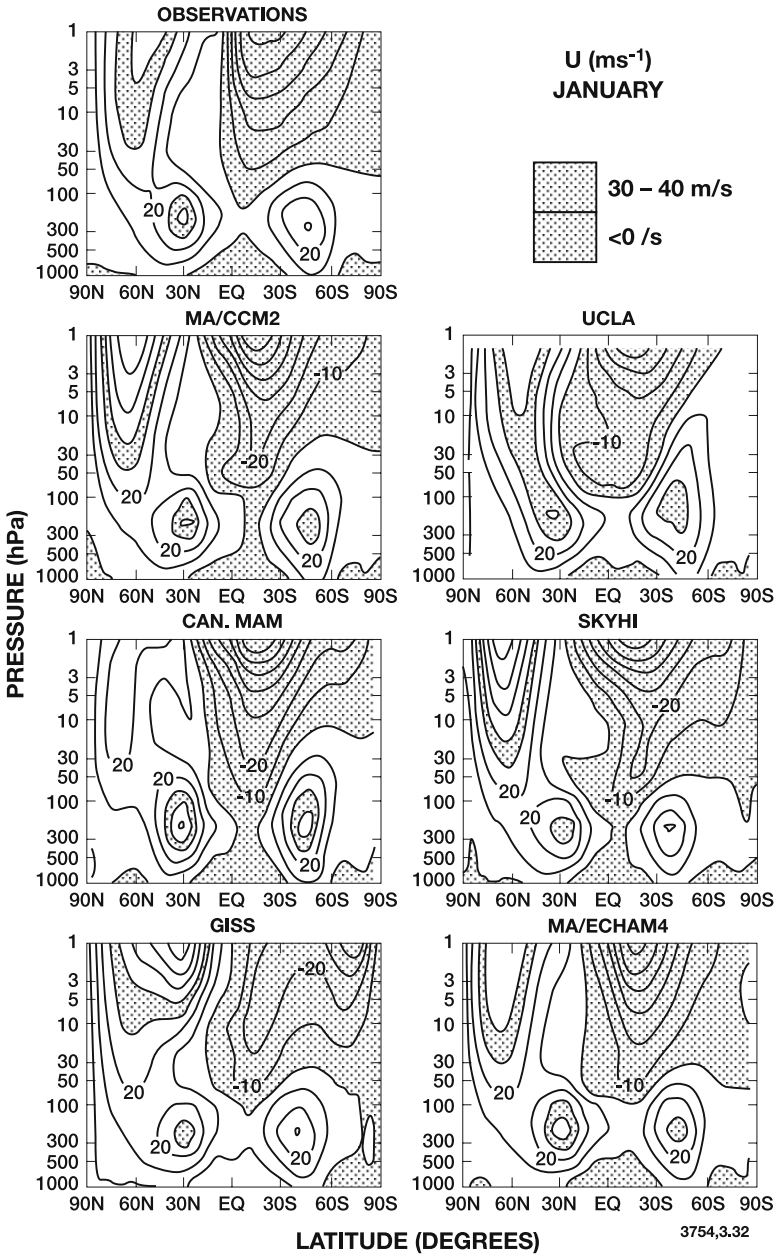

Figure 3.38. Comparison of the zonal wind calculated for January by several general circulation models of the middle atmosphere with climatological values. From Pawson *et al.* (2000).

described in the previous section and run "on-line". In this case, the three-dimensional transport of chemical tracers is calculated using the

winds derived at each timestep by the GCM, and diabatic heating and cooling rates calculated in the GCM make use of the calculated distributions of radiatively active compounds (ozone, water vapor, carbon dioxide, etc.) in the CTM. "Off-line" chemical-transport models are uncoupled from the GCMs. The winds and temperature required to calculate the distribution of chemical species are provided at regular time intervals (*e.g.*, every 6 or 12 hours) from pre-calculated dynamical fields or from meteorological analyses based on observations. In the latter case, the distributions of calculated chemical tracers can be compared to the distributions observed during specific time periods.

The first attempts to simulate the three-dimensional global distribution of chemically active species in the stratosphere have been based on the "on-line" approach. Hunt (1969) introduced ozone in the early GCM developed at GFDL, and studied the transport of this compound, using a simple parameterization for its photochemistry. Somewhat more sophisticated coupled models for ozone and related compounds have been developed by Cunnold *et al.* (1975) and Schlesinger and Mintz (1979).

The role of dynamics in controlling the distribution of idealized tracers (with extremely simple chemistry) has been investigated in some detail by Mahlman and Moxim (1978), Levy *et al.* (1979), Mahlman and Umscheid (1983), Sassi *et al.* (1993), and many others. Levy *et al.* (1979), for example, studied the behavior of a long-lived compound like N_2O, including its zonal mean concentration and the longitudinal deviation in the concentration. More recent chemical-transport models (*e.g.*, Grose *et al.*, 1987; Rose and Brasseur, 1989; Austin *et al.*, 1992; Pitari *et al.*, 1992; Chipperfield *et al.*, 1993; Lefèvre *et al.*, 1994; Rasch *et al.*, 1995; de Grandpré *et al.*, 1997; Brasseur *et al.*, 1997) have included relatively comprehensive representations of the photochemistry in the middle atmosphere. State-of-the-art CTMs account typically for 150-250 chemical (gas phase and heterogeneous) reactions affecting 50-100 chemical species.

Resolved transport by the atmospheric circulation (advection) is simulated through different numerical methods (see Box 3.4). The performance of transport algorithms is measured by evaluating their accuracy, stability, and computational efficiency. In addition, important properties for the adopted method are its ability to conserve mass, to preserve the shape of the solution (by avoiding overshoots or undershoots near regions of strong gradients), to be local (so that the solution at a given point is not strongly influenced by the field far from this point), and to advect any perturbation downwind only. Spectral transport methods, for example, are computationally efficient, but non-local. Most Eulerian algorithms require small timesteps. In Lagragian schemes (where a

Box 3.4 Numerical Algorithms to Solve the Transport Equation

Advective transport is described by partial differential equations. In the simple one-dimensional (1-D) case where the wind u is directed along direction x, the evolution with time of a conserved quantity ψ (*e.g.*, tracer mixing ratio, potential temperature, potential vorticity) is expressed as

$$\frac{\partial \psi}{\partial \mathrm{t}} + \frac{\partial \left(\mathrm{u}\psi\right)}{\partial \mathrm{x}} = 0 \tag{1}$$

If the wind velocity u is a constant and the initial distribution of the transported quantity at time t = 0 is $\psi_0(\mathrm{x})$, the analytic solution of (1) at location x and time t is provided by:

$$\psi\left(\mathrm{x},\mathrm{t}\right) = \psi_0\left(\mathrm{x} - \mathrm{ut}\right) \tag{2}$$

In the more general case where the wind velocity varies with space and time, the solution of (1) is derived by numerical algorithms. Rood, (1987) has reviewed several practical methods. None of these algorithms can be regarded as the single universal method that is recommended in all cases. The choice of the method will usually result from a compromise between different requirements (*e.g.*, accuracy, efficiency, etc.). These include the accuracy of the solution, the stability of the method (which often imposes a restriction on the timestep), and the efficiency of the algorithm (limited computer resources). Additional criteria should be met: conservation (no mass gain or loss), transportivity (perturbations should be advected only downwind), locality (solutions at a given point should not be substantially affected by the field far from the point), monotonicity (no overshoots or undershoots should be produced by the algorithm). If ψ represents the concentration of a tracer, it should remain positive in the entire model domain.

In *Eulerian schemes*, the solution of (1) is provided on fixed grid points $(\mathrm{i}-1, \mathrm{i}, \mathrm{i}+1, \ldots)$ at time intervals $(\mathrm{n}-1, \mathrm{n}, \mathrm{n}+1, \ldots)$. In this case, Equation (1) is replaced by a discretized form such as

$$\psi_{\mathrm{i}}^{\mathrm{n}+1} = \psi_{\mathrm{i}}^{\mathrm{n}} - \frac{\Delta \mathrm{t}}{\Delta \mathrm{x}}\left[\left(\mathrm{u}\psi\right)_{\mathrm{i}+\frac{1}{2}} - \left(\mathrm{u}\psi\right)_{\mathrm{i}-\frac{1}{2}}\right] \tag{3}$$

where the flux $(\mathrm{u}\psi)$ is evaluated at the right $(\mathrm{i} + \frac{1}{2})$ and left $(\mathrm{i} - \frac{1}{2})$ boundaries of the numerical box. Methods differ by the way these fluxes are evaluated. Some of them are diffusive (*e.g.*, the upstream scheme) or produce noise near strong gradients in the advected field (*e.g.*, the leapfrog scheme). In order to overcome these limitations Smolarkiewicz (1983) introduced an "antidiffusion velocity" in the upstream algorithm and Bott (1989), rather than considering the value of ψ to be constant over individual grid-boxes, fitted the function by a polynomial within each box. Prather (1986) represented ψ by a second-order polynomial and assumed

Box 3.4 (Continued)

that the zeroth order moment (mean value of ψ within the grid cell), first order moment (slope of ψ) and second-order moment (curvature of ψ) are conserved during an advective step. His method provides very little numerical diffusion, but requires considerable amounts of computer memory to store various moments.

A practical limitation of the Eulerian schemes is that the convergence of the numerical integration is achieved only if the adopted timestep $\Delta t \leq C\Delta x/u$, where the constant C is generally equal to unity. This criterion, called the Courant-Fredrichs-Lewy (CFL) condition, imposes timesteps that are generally much smaller than the physical timescales of interest.

In *Lagrangian algorithms*, the displacement of distinct air parcels (in which the tracer is assumed to be homogeneously mixed) is calculated as a function of time. If a sufficiently large number of parcels are considered, the evolution of a tracer over a global or regional domain can be determined. The accumulation of errors in the determination of the parcel location and the lack of mixing allowed between neighboring parcels provides a major limitation of the method, especially if the integration is carried on over long periods of time. Lagrangian methods are, however, often used in conjunction with field observations to assess the evolution of chemical species within a limited number of air parcels along their trajectory during a few days.

The *semi-Lagrangian method* (Robert, 1981; Staniforth and Coté, 1991) determines through a backward Lagrangian trajectory calculation the origin at time $t - \Delta t$ of air parcels which have reached the model grid points at time t. The value of ψ at these original points is determined by interpolation of the solution at the grid points at time $t - \Delta t$. The accuracy of the method depends greatly on the type of interpolation used. A major limitation of the method is that it is intrinsically nonconservative. The flux-form algorithm of Lin and Rood (1996) is a combination of semi-Lagrangian and finite volume methods. It is mass conservative. Advantages of the semi-Lagrangian method are the circumvention of the CFL stability condition and, at the same time, the convenience of a regular mesh discretization.

large number of distinct air parcels with prescribed mixing ratios are followed along the wind trajectories), the accumulation of errors in the determination of the parcel trajectory over long periods of time introduces a limitation when applied to chemical-transport models. The semi-Lagrangian approach (Robert, 1981), in which the trajectory of air parcels is derived over 1 time-step and interpolations are made on the Eulerian grid of the model, is not mass-conserving. Conservative flux-form semi-Lagrangian methods, however, have been recently developed (Lin and Rood, 1996).

Unresolved transport, such as mixing processes associated with gravity wave breaking in the mesosphere, is generally expressed as vertical eddy diffusion (see Eq. (3.52)) with the corresponding coefficient being determined through parameterization algorithms.

A large aspect of model development is the *evaluation* and *verification* of the results, mainly through extensive comparisons with observations. Global distributions of chemical species observed from space have been very useful in testing these models. Models are also used increasingly to "*assimilate*" observational data. The purpose is to combine our "a priori" knowledge of the atmosphere (model) with observations that are usually irregularly distributed in space and time to obtain an optimal representation of the atmospheric system.

In many cases, a full three-dimensional treatment may not be necessary to resolve many of the important features of the distributions of chemical species. The time constant associated with transport by the zonal wind is relatively rapid, of the order of days. Many chemical species with which we shall be concerned have time constants much longer than this, and may therefore be considered to be "well mixed" in the zonal direction. In view of the computational limitations associated with global three-dimensional models, and the relatively small impact of zonal transport on longer lived species, two-dimensional (zonally averaged) models are often used to describe the global distribution of chemical species in the middle atmosphere, and the response of the atmosphere to external perturbations. Different approaches can be used to derive the zonal mean of the quantities involved. As shown in Section 3.5.3, it is often advantageous to write the zonal mean primitive equations and continuity equations in the Transformed Eulerian Mean (TEM) framework. Most current models (*e.g.*, Garcia and Solomon, 1983; Brasseur *et al.*, 1990; Fleming *et al.*, 1999) use this formulation.

References

Andrews, D.G., and M.E. McIntyre, Planetary waves in horizontal and vertical shear: The generalized Eliassen-Palm relation and the zonal mean acceleration. *J Atmos Sci: 33*, 2031, 1976.

Andrews, D.G., and M.E. McIntyre, An exact theory of nonlinear waves on a Lagrangian mean flow. *J Fluid Mech: 89*, 609, 1978.

Andrews, D.G., J.R. Holton, and C.B. Leovy, *Middle Atmosphere Dynamics.* Academic Press, 1987.

Appenzeller, C., *Wave developments on surface fronts and stratospheric intrusions.* Ph.D. thesis, 1117 pp., ETH, Zurich, Switzerland, 1994.

Arakawa, A., Computational design for long-term numerical integration of the equations of fluid motions: Two-dimensional incompressible flow. *J Comput Phys: 1*, 119, 1966.

Austin, J., N. Butchard, and K.P. Shine, Possibility of an Arctic ozone hole in a doubled-CO_2 climate. *Nature: 360*, 221, 1992.

Baldwin, M.P., X. Cheng, and T.J. Dunkerton, Observed correlations between winter-mean tropospheric and stratospheric circulation anomalies. *Geophys Res Lett: 2*, 1141, 1994.

Baldwin, M.P., and T.J. Dunkerton, Propagation of the Arctic Oscillation from the stratosphere to the troposphere. *J Geophys Res: 104*, 30,937, 1999.

Baldwin, M.P., and T.J. Dunkerton, Stratospheric harbingers of anomalous weather regimes. *Science: 294*, 581, 2001.

Baldwin, M.P., L.J. Gray, T.J. Dunkerton, K. Hamilton, P.H. Haynes, W.J. Randal, J.R. Holton, M.J. Alexander, I. Hirota, T. Horinouchi, D.B.A. Jones, J.S. Kinnersley, C. Marquardt, K. Sato, and M. Takahashi, The quasi-biennial oscillation. *Rev Geophys: 39*, 179, 2001.

Banks, P.M., and G. Kockarts, *Aeronomy*. Academic Press, 1973.

Beagley, S.R., J. de Grandpré, J.N. Koshyk, N.A. McFarlane, and T.G. Shepherd, Radiative-dynamical climatology of the first-generation Canadian middle atmosphere model. *Atmos Ocean: 35*, 293, 1997.

Becker, E., and G. Schmitz, Energy deposition and turbulent dissipation owing to gravity waves in the mesosphere. *J Atmos Sci: 59*, 54, 2001.

Bischof, W., R. Borchers, P. Fabian, and B.C. Kruger, Increased concentration and vertical distribution of carbon dioxide in the stratosphere. *Nature: 316*, 708, 1985.

Boering, K.A., S.C. Wofsy, B.C. Daube, H.R. Schneider, M. Loewenstein, J.R. Podolske, and T.J. Conway, Stratospheric mean ages and transport rates from observations of atmospheric CO_2 and N_2O. *Science: 274*, 1340, 1996.

Bott, A., A positive definite advection scheme obtained by nonlinear normalization of the advective fluxes. *Mon Weath Rev: 117*, 1006, 1989

Bourke, W., An efficient, one-level primitive equation spectral model. *Mon Weath Rev: 100*, 683, 1972.

Boville, B.A., The influence of the polar night jet on the tropospheric circulation in a GCM. *J Atmos Sci: 41*, 1132, 1984.

Boville, B.A., Middle atmosphere version of CCM2 (MACCM2): Annual cycle and interannual variability. *J Geophys Res: 100*, 9017, 1995.

Boyd, J.P., The noninteraction of waves with the zonally-averaged flow on a spherical Earth, and the interrelationship of eddy fluxes of energy, heat and momentum. *J Atmos Sci: 33*, 2285, 1976.

Brasseur, G.P., M.H. Hitchman, S. Walters, M. Dymek, E. Falise, and M. Pirre, An interactive chemical dynamical radiative two-dimensional model of the middle atmosphere. *J Geophys Res: 95*, 5639, 1990.

Brasseur, G.P., X.X. Tie, P.J. Rasch, and F. Lefèvre, A three-dimensional simulation of the Antarctic ozone hole: Impact of anthropogenic chlorine on the lower stratosphere and upper troposphere. *J Geophys Res: 102*, 8909, 1997.

Brasseur, G.P., J.J. Orlando, and G.S. Tyndall, *Atmospheric Chemistry and Global Change*. Oxford University Press, 1999.

Brasseur, G.P., A.K. Smith, R. Khosravi, T. Huang, and S. Walters, Natural and human-induced perturbations in the middle atmosphere: A short tutorial, in:

Atmospheric Science Across the Stratopause, *Geophys Monograph 123: 7*. American Geophysical Union, 2000.

Brewer, A.W., Evidence for a world circulation provided by measurements of helium and water vapor distribution in the stratosphere. *Quart J Roy Meteorol Soc: 75*, 351, 1949.

Burrage, M.D., W.R. Skinner, D.A. Gell, P.B. Hays, A.R. Marshall, D.A. Ortland, A.H. Manson, S.J. Franke, D.C. Fritts, P. Hoffman, C. McLandress, R. Niciejewski, F.J. Schmidlin, G.G. Shepherd, W. Singer, T. Tsuda, and R.A. Vincent, Validation of mesosphere and lower thermosphere winds from the high resolution Doppler images on UARS. *J Geophys Res: 101*, 10,365, 1996.

Campbell, I.M., *Energy and the Atmosphere*. John Wiley and Sons, 1977.

Chang, A.Y., R.J. Salawitch, H.A. Michelsen, M.R. Gunson, M.C. Abrams, R. Zander, C.P. Rinsland, M. Loewenstein, J.R. Podolske, M.H. Proffitt, J.J. Margitan, D.W. Fahey, R.-S. Gao, K.K. Kelly, J.W. Elkins, C.R. Webster, R.D. May, K.R. Chan, M.M. Abbas, A. Goldman, F.W. Irion, G.L. Manney, M.J. Newchurch, and G.P. Stiller, A comparison of measurements from ATMOS and instruments aboard the ER-2 aircraft: Tracers of atmospheric transport. *Geophys Res Lett: 23*, 2389, 1996a.

Chang, A.Y., R.J. Salawitch, H.A. Michelsen, M.R. Gunson, M.C. Abrams, R. Zander, C.P. Rinsland, J.W. Elkins, G.S. Dutton, C.M. Volk, C.R. Webster, R.D. May, D.W. Fahey, R.-S. Gao, M. Loewenstein, J.R. Podolske, R.M. Stimpfle, D.W. Kohn, M.H. Proffitt, J.J. Margitan, K.R. Chan, M.M. Abbas, A. Goldman, F.W. Irion, G.L. Manney, M.J. Newchurch, and G.P. Stiller, A comparison of measurements from ATMOS and instruments aboard the ER-2 aircraft: Halogenated compounds. *Geophys Res Lett: 23*, 2393, 1996b.

Chapman, S., and T.G. Cowling, *The Mathematical Theory of Non-uniform Gases*. 3rd ed., Cambridge University Press, 1970.

Chapman, S., and R.S. Lindzen, *Atmospheric Tides*. D. Reidel, The Netherlands, 1970.

Charney, J.G., and P.G. Drazin, Propogation of planetary-scale disturbances from the lower into the upper atmosphere. *J Geophys Res: 66*, 83, 1961.

Chen, P., Isentropic cross-tropopause mass exchange in the extratropics. *J Geophys Res: 100*, 16,661, 1995.

Chiba, M., K. Yamazaki, K. Shibata, and Y. Kuroda, The description of the MRI atmospheric spectral GCM (MRI-GSPM) and its mean statistics based on a 10-year integration. *Pap Meteorol Geophys: 47*, 1, 1996.

Chipperfield, M.P., D. Cariolle, P. Simon, R. Ramaroson, and D.J. Lary, A three-dimensional modeling study of trace species in the Arctic lower stratosphere during winter 1989-1990. *J Geophys Res: 98*, 7199, 1993.

Coffey, M.T., W.G. Mankin, and J.W. Hannigan, A reconstructed view of polar stratospheric chemistry. *J Geophys Res: 104*, 8295, 1999.

Crutzen, P.J., A two-dimensional photochemical model of the atmosphere below 55 km: Estimates of natural and man-caused perturbations due to NO_x, in *Proc Fourth Conf on CIAP*, DOT-TSC-OST-38, 1975.

Cunnold, D.M., F. Alyea, N. Phillips, and R.G. Prinn, A three-dimensional dynamical-chemical model of atmospheric ozone. *J Atmos Sci: 32*, 170, 1975.

Danielsen, E.F., Trajectories: Isobaric, isentropic, and actual. *J Meteorol: 18*, 479, 1961.

de Grandpré, J., J.W. Sandilands, J.C. McConnell, S.R. Beagley, P.C. Croteau, and M.Y. Danilin, Canadian middle atmosphere model: Preliminary results from the chemical transport module. *Atmos Ocean: 35*, 385, 1997.

Déqué, M., C. Dreveton, A. Braun, and D. Cariolle, The ARPEGE/IFS atmospheric model: A contribution to the French community climate modelling. *Clim Dyn: 10*, 249, 1994.

Dickinson, R.E., E.C. Ridley, and R.G. Roble, Meridional circulation in the thermosphere, I. Equinox conditions. *J Atmos Sci: 32*, 1737, 1975.

Dickinson, R.E., E.C. Ridley, and R.G. Roble, Meridional circulation in the thermosphere. *J Atmos Sci: 34*, 178, 1977.

Dobson, G.M.G., Origin and distribution of polyatomic molecules in the atmosphere. *Proc Roy Soc Lond A: 236*, 187, 1956.

Dunkerton, T., On the mean meridional mass motions of the stratosphere and mesosphere. *J Atmos Sci: 35*, 2325, 1978.

Dunkerton, T., C.P.F. Hsu, and M.E. McIntyre, Some Eulerian and Lagrangian diagnostics for a model stratospheric warming. *J Atmos Sci: 38*, 819, 1981.

Dunkerton, T.J., The role of gravity waves in the quasi-biennial oscillation. *J Geophys Res: 102*, 26,053, 1997.

Dunkerton, T. J., and D. P. Delisi, Climatology of the equatorial lower stratosphere. *J Atmos Science: 42*, 376, 1985.

Elkins, J.W., D.W. Fahey, J.M. Gilligan, G.S. Dutton, T.J. Baring, C.M. Volk, R.E. Dunn, R.C. Myers, S.A. Montzka, P.R. Wamsley, A.H. Hayden, J.H. Butler, T.M. Thompson, T.H. Swanson, E.J. Dlugokencky, P.C. Novelli, D.F. Hurst, J.M. Lobert, S.J. Ciciora, R.J. McLaughlin, T.L. Thompson, R.H. Winkler, P.J. Fraser, L.P. Steele, and M.P. Lucarelli, Airborne gas chromatograph for in situ measurements of long-lived species in the upper troposphere and lower stratosphere. *Geophys Res Lett: 23*, 347, 1996.

Ertel, H., Ein neuer hydrodynamischer Wirbelsatz. *Meteorol Z: 59*, 271, 1942.

Exner, F.M., *Sitzungberichte der Mathematisch-Naturwissenschaftlichen Klasse der Akad. Wissenschaften*, 122 Abt. 2a, 2. Halbband 6(10), 1165, 1913.

Feely, H.W., and J.S. Spar, Tungsten-185 from nuclear bomb tests as a tracer for stratospheric meteorology. *Nature: 188*, 1062, 1960.

Fels, S.B., J.D. Mahlman, M.D. Schwarzkopf, and R.W. Sinclair, Stratospheric sensitivity to perturbations in ozone and carbon dioxide: Radiative and dynamical response. *J Atmos Sci: 37*, 2265, 1980.

Fels, S.B., Radiative-dynamical interactions in the middle atmosphere. *Adv Geophys: 28A*, 277, 1985.

Fleming, E.L., S. Chandra, M.R. Schoeberl, and J.J. Barnett, *Monthly mean global climatology of temperature, wind, geopotential height, and pressure for 0-120 km.* NASA Tech Memo 100687, 85 pp., 1988.

Fleming, E.L., C.H. Jackman, R.S. Stolarski, and D.B. Considine, Simulation of stratospheric tracers using an improved empirically-based two-dimensional model transport formulation. *J Geophys Res: 104*, 23,911, 1999.

Folkins, I., M. Loewenstein, J. Podolske, S. Oltmans, and M. Proffitt, A barrier to vertical mixing at 14 km in the tropics: Evidence from ozonesondes and aircraft measurements. *J Geophys Res: 104*, 22,095, 1999.

Forbes, J.M., Atmospheric tides: 1. Model description and results for the solar diurnal tides. *J Geophys Res: 87*, 5222, 1982a.

Forbes, J.M., Atmospheric tides: 2. Solar and lunar semidiurnal components. *J Geophys Res: 87*, 5241, 1982b.

Fritts, D.C., and R.A. Vincent, Mesospheric momentum flux studies at Adelaide, Australia: Observations of gravity wave/tidal interaction model. *J Atmos Sci: 44*, 605, 1987.

Fritts, D.C., and W. Lu, Spectral estimates of gravity wave energy and momentum fluxes, II. Parameterization of wave forcing and variability. *J Atmos Sci: 50*, 3695, 1993.

Garcia, R.R., and D.L. Hartmann, The role of planetary waves in the maintenance of the zonally averaged ozone distribution of the upper stratosphere. *J Atmos Sci: 37*, 2248, 1980.

Garcia, R.R., and S. Solomon, A numerical model of the zonally averaged dynamical and chemical structure of the middle atmosphere. *J Geophys Res: 88*, 1379, 1983.

Garcia, R.R., and S. Solomon, The effect of breaking gravity waves on the dynamics and chemical composition of the mesosphere and lower thermosphere. *J Geophys Res: 90*, 3850, 1985.

Gault, W.A., G. Thuillier G.G. Shepherd, S.P. Zhang, R.H. Wiens, W.E. Ward, C. Tai, B.H. Solheim, Y.J. Rochon, C. McLandress, C. Lathuillere, V. Fauliot, M. Hersé, C.H. Hersom, R. Gattinger, L. Bourg, M.D. Burrage, S.J. Franke, G. Hernandez, A. Manson, R. Niciejewski, and R.A. Vincent, Validation of O(^{1}S) wind measurements by WINDII: The wind imaging interferometer on UARS. *J Geophys Res: 101*, 10,405, 1996.

Gavrilov, N.M., and R.G. Roble, The effect of gravity waves on the global mean temperature and composition structure of the upper atmosphere. *J Geophys Res: 99*, 25,773, 1994.

Geller, M.A., and J.C. Alpert, Planetary wave coupling between the troposphere and the middle atmosphere as a possible sun-weather mechanism. *J Atmos Sci: 37*, 1197, 1980.

Geller, M.A., Dynamics of the middle atmosphere. *Space Sci Rev: 34*, 359, 1983.

Gombosi, T.I., *Physics of the Space Environment*. Cambridge University Press, 1998.

Graf, H.-F., I. Kirchner, A. Robock, and I. Schult, Pinatubo eruption winter climate effects: Model versus observations. *Climate Dyn: 9*, 81, 1993.

Graf, H.-F., J. Perlwitz, and I. Kirchner, Northern hemisphere tropospheric midlatitute circulation after violent volcanic eruptions. *Contrib Atmos Phys: 67*, 3, 1994.

Grant, W.B., E.V. Browell, C.S. Long, L.L. Stowe, R.G. Grainger, and A. Lambert, Use of volcanic aerosols to study the tropical stratospheric reservoir. *J Geophys Res: 101*, 3973, 1996.

Grose, W.L., J.E. Nealy, R.E. Turner, and W.T. Blackshear, Modeling the transport of chemically active constituents in the stratosphere, in *Transport Processes in the Middle Atmosphere*. G. Visconti, and R. Garcia, eds., 229, D. Reidel, Massachusetts, 1987.

Hagan, M.E., Modeling atmospheric tidal propagation across the stratopause, in: *Atmospheric Science Across the Stratopause. Geophysical Monograph: 123*, 177, American Geophysical Union, 2000.

Hall, T.M., and M.J. Prather, Simulations of the trend and annual cycle in stratospheric CO_2. *J Geophys Res: 98*, 10,573, 1993.

Hall, T.M., and R.A. Plumb, Age as a diagnostic of stratospheric transport. *J Geophys Res: 99*, 1059, 1994.

Hall, T.M., and D.W. Waugh, Timescales for the stratospheric circulation derived from tracers. *J Geophys Res: 102*, 8991, 1997.

Hall, T.M., *et al.*, 2. Transport experiments, in *Models and Measurements Intercomparison II.* J.H. Park, M.K.W. Ko, C.H. Jackman, R.A. Plumb, J.A. Kaye, and K.H. Sages, eds., NASA/TM-1999-209554, 1999.

Hamilton, K., R.J. Wilson, J.D. Mahlman, and L.J. Umscheid, Climatology of the GFDL SKYHI general circulation model. *J Atmos Sci: 52*, 44, 1995.

Hare, F.K., and B.W. Boville, *The Polar Circulation.* Tech. Note 70, World Meteorological Organization, Geneva, 1965.

Harwood, R.S., and J.A. Pyle, A two-dimensional mean circulation model for the atmosphere below 80 km. *Quart J Roy Meteorol Soc: 101*, 723, 1975.

Hartmann, D.L., Some aspects of the coupling between radiation, chemistry, and dynamics in the stratosphere. *J Geophys Res: 86*, 9631, 1981.

Hasebe, F., Quasi-biennial oscillations of ozone and diabatic circulation in the equatorial stratosphere. *J Atmos Sci: 51*, 729, 1994.

Hauchecorne, A., M.L. Chanin, and R. Wilson, Mesospheric temperature inversion and gravity wave breaking. *Geophys Res Lett: 14*, 933, 1987.

Haynes, P.H., C.J. Marks, M.E. McIntyre, T.G. Shepherd, and K.P. Shine, On the "downward control" of extratropical diabatic circulation by eddy-induced mean zonal forces. *J Atmos Sci: 48*, 651, 1991.

Hays, P.B., V.J. Abreu, M.E. Dobbs, D.A. Gell, H.J. Grassl, and W.R. Skinner, The high-resolution Doppler imager on the Upper Atmosphere Research Satellite. *J Geophys Res: 98*, 10,713, 1993.

Hays, P.B., D.L. Wu, and the HRDI Science Team, Observations of the diurnal tide from space. *J Atmos Sci: 51*, 3077, 1994.

Hines, C.O., Doppler spread parameterization of gravity wave momentum deposition in the middle atmosphere, Part 1: Basic formulation. *J Atmos Solar Terr Phys: 59*, 371, 1997a.

Hines, C.O., Doppler spread parameterization of gravity wave momentum deposition in the middle atmosphere, Part 2: Broad and qausi-monochromatic spectra and implementation. *J Atmos Solar Terr Phys: 59*, 387, 1997b.

Hitchman, M.H., C.B. Leovy, J.C. Gille, and P.L. Bailey, Quasi-stationary zonally assymmetric circulations in the equatorial lower mesosphere, *J Atmos Sci: 44*, 2219, 1987.

Holton, J.R., and R.S. Lindzen, An updated theory for the quasi-biennial cycle of the tropical stratosphere. *J Atmos Sci: 29*, 1076, 1972.

Holton, J.R., A semi-spectral numerical model for wave, mean flow interactions in the stratosphere: Application to sudden stratospheric warmings. *J Atmos Sci: 33*, 1639, 1976.

Holton, J.R., and W.M. Wehrbein, The role of forced planetary waves in the annual cycle of the zonal mean circulation of the middle atmosphere. *J Atmos Sci: 37*, 1968, 1980.

Holton, J.R., The role of gravity wave induced drag and diffusion in the momentum budget of the mesosphere. *J Atmos Sci: 39*, 791, 1982.

Holton, J.R., The influence of gravity wave breaking on the general circulation of the middle atmosphere. *J Atmos Sci: 40*, 2497, 1983.

Holton, J.R., and M.R. Schoeberl, The role of gravity wave generated advection and diffusion in transport of tracers in the mesosphere. *J Geophys Res: 93*, 11,075, 1988.

Holton, J.R., and J. Austin, The influence of equatorial QBO on sudden stratospheric warmings. *J Atmos Sci: 48*, 607, 1991.

Holton, J.R., *Introduction to Dynamic Meteorology.* 3rd ed. Academic Press, 1992.

Holton, J.R., P.H. Haynes, M.E. McIntyre, A.R. Douglass, R.B. Rood, and L. Pfister, Stratosphere-troposphere exchange. *Rev Geophys: 33*, 403, 1995.

Holton, J.R., and M.J. Alexander, The role of waves in the transport circulation of the middle atmosphere, in: *Atmospheric Science Across the Stratopause, Geophys Monograph: 123*, 21, American Geophysical Union, 2000.

Hong, S.-S., and R.S. Lindzen, Solar semi-diurnal tide in the thermosphere. *J Atmos Sci: 33*, 135, 1976.

Hoppel, K.W., K.P. Bowman, and R.M. Bevilacqua, Northern hemisphere summer ozone variability observed by POAMII. *Geophys Res Lett: 26*, 827, 1999.

Hoskins, B.J., M.E. McIntyre, and A.W. Robertson, On the use and significance of isentropic potential vorticity maps. *Quart J Roy Meteorol Soc: 111*, 877, 1985.

Huang, T.Y.W., and A.K. Smith, The mesospheric diabatic circulation and the parameterized thermal effect of gravity wave breaking on the circulation. *J Atmos Sci: 48*, 1093, 1991.

Hunt, B.G., and S. Manabe, Experiments with a stratospheric general circulation model, II. Large scale diffusion of tracers in the stratosphere. *Mon Weath Rev: 96*, 503, 1968.

Hunt, B., Experiments with a stratospheric general circulation model, III. Large scale diffusion of ozone including photochemistry. *Mon Weath Rev: 97*, 287, 1969.

James, I.N., *Introduction to Circulatory Atmospheres*, Cambridge University Press, 1994.

Juckes, M.N., and M.E. McIntyre, A high-resolution, one layer model of breaking planetary waves in the stratosphere. *Nature: 328*, 590, 1987.

Juckes, M., A generalization of the transformed Eulerian-mean meridional circulation. *Quart J Roy Meteorol Soc: 127*, 147, 2001.

Julian, P.R., and K.B. Labitzke, A study of atmospheric energetics during the January-February 1963 stratospheric warming. *J Atmos Sci: 22*, 597, 1965.

Kasting, J.F., and R.G. Roble, A zonally averaged chemical-dynamical model of the lower thermosphere. *J Geophys Res: 86*, 964l, 1981.

Kawahira, K., A two-dimensional model for ozone changes by planetary waves in the stratosphere, I. Formulation and the effect of temperature waves on the zonal mean ozone concentration. *J Meteorol Soc Japan: 60*, 1058, 1982.

Kida, H., General circulation of air parcels and transport characteristics derived from a hemispheric GCM, Part 1. A determination of advective mass flow in the lower stratosphere. *J Meteorol Soc Japan: 61*, 171, 1983.

Kitoh, A., Y. Noda, Y. Nikaidou, T. Ose, and T. Tokioka, AMIP simulations of the MRI GCM. *Pap Meteor Geophys: 45*, 121, 1995.

Kodera, K., and K. Yamazaki, Long-term variation of upper stratospheric circulation in the Northern hemisphere in December. *J Meteorol Soc Japan: 68*, 101, 1990.

Kodera, K., M. Chiba, K. Yamazaki, and K. Shibata, A possible influence of the polar night stratospheric jet on the subtropical tropospheric jet. *J Meteorol Soc Japan: 69*, 715, 1991.

Kodera, K., Influence of volcanic eruptions on the troposphere through stratospheric dynamical processes in the Northern hemisphere winter. *J Geophys Res: 99*, 1273, 1994.

Kodera, K., and K. Yamazaki, A possible influence of recent polar stratospheric coolings on the troposphere in the Northern hemisphere winter. *Geophys Res Lett: 21*, 809, 1994.

Kodera, K., M. Chiba, H. Koide, A. Kitoh, and Y. Nikaidou, Interannual variability of the winter stratosphere and troposphere in the Northern hemisphere. *J Meteorol Soc Japan: 74*, 365, 1996.

Kodera, K., and Y. Kuroda, Tropospheric and stratospheric aspects of the Arctic oscillation. *Geophys Res Lett: 27*, 3349, 2000a.

Kodera, K., and Y. Kuroda, A mechanistic model study of slowly propagating coupled stratosphere-troposphere variability. *J Geophys Res: 105*, 12,361, 2000b.

Lait, L., An alternative form of potential vorticity. *J Atmos Sci: 12*, 1754, 1994.

Labitzke, K., Climatology of the stratosphere and mesosphere. *Philos Trans R Soc London: 296*, 7, 1980.

Labitzke, K., and H. van Loon, Association between the 11-year solar cycle, the QBO and the atmosphere, Part I: The troposphere and the stratosphere in the northern hemisphere in winter. *J Atmos Terr Phys: 50*, 197, 1988.

Langematz, U., and S. Pawson, The Berlin troposphere-stratosphere-mesosphere GCM: Climatology and annual cycle. *Quart J Roy Meteorol Soc: 123*, 1075, 1997.

Lefèvre, F., G.P. Brasseur, I. Folkins, A.K. Smith, and P. Simon, The chemistry of the 1991-92 stratospheric winter: Three-dimensional model simulation. *J Geophys Res: 99*, 8183, 1994.

Leovy, C., Simple models of thermally driven mesospheric circulation. *J Atmos Sci: 21*, 327, 1964.

Leovy, C., Photochemical de-stabilization of gravity wave near the mesopause. *J Atmos Sci: 23*, 223, 1966.

Levy, H., J.D. Mahlman, and W.J. Moxim, A preliminary report on the numerical simulation of the three-dimensional structure and variability of atmospheric N_2O. *Geophys Res Lett: 6*, 155, 1979.

Lieberman, R.S.,A.K. Smith, S.J. Franke, R.A. Vincent, J.R. Isler, A.H. Manson, C.E. Meek, G.J. Fraser, A. Fahrutdinova, T. Thayaparan, W. Hocking, J. MacDougall, T. Nakamura, and T. Tsuda, Comparison of mesospheric and lower thermospheric residual wind with High Resolution Doppler Imager, medium frequency, and meteor radar winds. *J Geophys Res: 105*, 27,023, 2000.

Lin, S.J., and R.B. Rood, Multidimensional flux-form semi-Lagrangian transport schemes. *Mon Weath Rev: 124*, 2046, 1996.

Lindzen, R.S., Thermally driven diurnal tide in the atmosphere. *Quart J Roy Meteorol Soc: 93*, 18, 1967.

Lindzen, R.S., and J.R. Holton, A theory of the quasi-biennial oscillation. *J Atmos Sci: 22*, 341, 1968.

Lindzen, R.S., and D. Blake, Mean heating of the thermosphere by tides. *J Geophys Res: 75*, 6868, 1970.

Lindzen, R.S., Turbulence and stress owing to gravity wave and tidal breakdown. *J Geophys Res: 86*, 9707, 1981.

Liu, H.L., and M.E. Hagan, Local heating/cooling of the mesosphere due to gravity wave and tidal coupling. *Geophys Res Lett: 25*, 2941, 1998.

Loewenstein, M., J.R. Podolske, K.R. Chan, and S.E. Strahan, Nitrous oxide as a dynamical tracer in the 1987 Airborne Antarctic Ozone Experiment. *J Geophys Res: 94*, 11,598, 1989.

London, J.L., Radiative energy sources and sinks in the stratosphere and mesosphere, *Proc NATO Advanced Study Institute on Atmospheric Ozone* FAA-EE-80-20, NTIS, Springfield, Va., 1980.

Mahlman, J.D., and W.J. Moxim, Tracer simulation using a global general circulation model: Results from a mid-latitude instantaneous source experiment. *J Atmos Sci: 35*, 1340, 1978.

Mahlman, J.D., and L.J. Umscheid, Dynamics of the middle atmosphere: Successes and problems of the GFDL "SKIHI" general circulation model, in *Proc of the U.S.-Japan Seminar on Middle Atmosphere Dynamics,* Terra Scientific Pub., Tokyo, 1983.

Makhlouf, U.B., R.H. Picard, and J.R. Winick, Photochemical-dynamical modeling of the measured response of airglow to gravity waves, 1. Basic model for OH airglow. *J Geophys Res: 100*, 11,289, 1995.

Makhlouf, U.B., R.H. Picard, J.R. Winick, and T.F. Tuan, A model for the response of the atomic oxygen 557.7 nm and the OH Meinal airglow to atmospheric gravity waves in a realistic atmosphere. *J Geophys Res: 103*, 6261, 1998.

Manabe, S., and B.G. Hunt, Experiments with a stratospheric general circulation model, I. Radiative and dynamic aspects. *Mon Weath Rev: 96*, 477, 1968.

Manzini, E., N.A. McFarlane, and C. McLandress, Impact of the Doppler-spread parameterization on the simulation of the middle atmosphere circulation using the MA/ECHAM4 general circulation model. *J Geophys Res: 102*, 25,751, 1997.

Matsuno, T., Vertical propagation of stationary planetary waves in the Northern hemisphere. *J Atmos Sci: 27*, 871, 1970.

Matsuno, T., A dynamical model of the stratospheric sudden warming. *J Atmos Sci: 28*, 1479, 1971.

Matsuno, T., and K. Nakamura, The Eulerian and Lagrangian mean meridional circulations in the stratosphere at the time of a sudden warming. *J Atmos Sci: 36*, 640, 1979.

Matsuno, T., Lagrangian motion of air parcels in the stratosphere in the presence of planetary waves. *Pure Appl Geophys: 118*, 189, 1980.

Matsuno, T., Quasi-geostrophic motions in the equatorial area. *J Meteorol Soc Japan: 44*, 25, 1986.

McIntyre, M.E., Towards a Lagrangian mean description of stratospheric circulations and chemical transports. *Philos Trans R Soc London: 296*, 129, 1980.

McIntyre, M.E., and T.N. Palmer, Breaking planetary waves in the stratosphere. *Nature: 305*, 593, 1983.

McIntyre, M.E., and T.N. Palmer, The "surf zone" in the stratosphere. *J Terr Phys: 46*, 825, 1984.

McIntyre, M.E., Middle atmosphere dynamics and transport: Some current challenges to our understanding, in *Dynamics, Transport, and Photochemistry of the Southern Hemisphere*, A. O'Neill (ed.), Kluwer, Dordrecht, 1990.

McLandress, C., G.S. Shepherd, B.H. Solheim, M.D. Burrage, P.B. Hays, and W.R. Skinner, Combined mesosphere/thermosphere winds using WINDII and HRDI data from the Upper Atmosphere Research Satellite. *J Geophys Res: 101*, 10,441, 1996.

Mechoso, C.R., K. Yamazaki, A. Kitoh, and A. Arakawa, Numerical forecasts of atmospheric warming events during the winter of 1979. *Mon Weath Rev: 113*, 1015, 1985.

Medvedev, A.S., and G.P. Klaassen, Vertical evolution of gravity wave spectra and the parameterization of associated wave drag. *J Geophys Res: 100*, 25,841, 1995.

Mote, P.W., K.H. Rosenlof, J.R. Holton, R.S. Harwood, and J.W. Waters, Seasonal variations of water vapor in the tropical lower stratosphere. *Geophys Res Lett: 22*, 1093, 1995.

Murgatroyd, R.J., and F. Singleton, Possible meridional circulations in the stratosphere and mesosphere. *Quart J Roy Meteorol Soc: 87*, 125, 1961.

Murgatroyd, R.J., Dynamical modelling of the stratosphere and mesosphere, in *Mesospheric Models and Related Experiments.* G. Fiocco, ed., Reidel Publishing Co., Dordrecht, 1971.

Murphy, D.M., and D.W. Fahey, An estimate of the flux of stratospheric reactive nitrogen and ozone into the troposphere. *J Geophys Res: 99*, 5325, 1994.

Nastrom, G.D., B.B. Balsley, and D.A. Carter, Mean meridional winds in the mid and high latitude mesosphere. *Geophys Res Lett: 9*, 139, 1982.

Naujokat, B., and K. Labitzke (eds.), *Collection of Reports on the Stratospheric Circulation during Winters 1974-75 to 1991-92.* Report 1, Sci Comm on Sol Terr Phys, University of Illinois, 1993.

Newman, P.A., L.R. Lait, M.R. Schoeberl, M. Seablom, L. Coy, R. Rood, R. Swinbank,M. Profitt, M. Loewenstien, J.R. Podolske, J.W. Elkins, C.R. Webster, R.D. May, D.W. Fahey, G.S. Dutton and K.R. Chan, Measurement of polar vortex air in the midlatitudes. *J Geophys Res: 101*, 12,879, 1996.

O'Neill, A., Dynamical processes in the stratosphere: Wave motion, in *Proc NATO Advanced Study Institute on Atmospheric Ozone*, FAA-EE-80-20, NTIS, Springfield, Va., 1980.

Ortland, D.A., W.R. Skinner, P.B. Hays, M.D. Burrage, R.S. Lieberman, A.R. Marshall, and D.A. Gell, Measurement of stratospheric winds by the high resolution Doppler imager. *J Geophys Res: 101*, 10,351, 1996.

Ortland, D.A., P.B. Hays, W.R. Skinner, and J.-H. Yee, Remote sensing of mesosphere temperature and O_2 ($^1\Sigma$) band volume emission rates with the higher resolution Doppler imager. *J Geophys Res: 103*, 1821, 1997.

O'Sullivan, D., and R.E. Young, Modeling the quasi-biennial oscillation effect on the winter stratospheric circulation. *J Atmos Sci: 49*, 2437, 1992.

Palmer, T. N., Diagnostic study of a wavenumber 2 stratospheric sudden warming in a transformed Eulerian mean formalism. *J Atmos Sci: 38*, 544, 1981.

Pawson, S., K. Kodera, K. Hamilton, T.G. Shepherd, S.R. Beagley, B.A. Boville, J.D. Farrara, T.D.A. Fairlie, A. Kitoh, W.A. Lahoz, U. Langematz, E. Manzini, D.H. Rind, A.A. Scaife, K. Shibata, P. Simon, R. Swinbank, L. Takacs, R.J. Wilson, J.A. Al-Saadi, M. Amodei, M. Chiba, L. Coy, J. de Grandpré, R.S. Eckman, M. Fiorino, W.L. Grose, H. Koide, J.N. Koshyk, D. Li, J. Lerner, J.D. Mahlman, N.A. McFarlane, C.R. Mechoso, A. Molod, A. O'Neill, R.B. Pierce, W.J. Randel, R.B. Rood, and F. Wu, The GCM-reality intercomparison project for SPARC (GRIPS): Scientific issues and initial results. *Bull Amer Meteorol Soc: 81*, 781, 2000.

Pedlosky, J., *Geophysical Fluid Dynamics,* Springer-Verlag, 1987.

Perlwitz, J., and H.-F. Graf, The statistical connection between tropospheric and stratospheric circulation of the Northern hemisphere in winter. *J Clim: 8*, 2281, 1995.

Perlwitz, J., H.-F. Graf, and R. Voss, The leading variability mode of the coupled troposphere-stratosphere winter circulation in different climate regimes. *J Geophys Res: 105*, 6915, 2000.

Pitari, G.S., S. Palermi, G. Visconti, and R. Prinn, Ozone response to a CO_2 doubling: Results from a stratospheric circulation model with heterogeneous chemistry. *J Geophys Res: 97*, 5953, 1992.

Plumb, R.A., and A.D. McEwan, The instability of a forced standing wave in a viscous stratified fluid: A laboratory analogue of the quasi-biennial oscillation. *J Atmos Sci: 35*, 1827, 1978.

Plumb, R.A., Eddy fluxes of conserved quantities by small amplitude waves. *J Atmos Sci: 36*, 1699, 1979.

Plumb, R.A., and M.K.W. Ko, Interrelationships between mixing ratios of long-lived stratospheric constituents. *J Geophys Res: 97*, 10,145, 1992.

Plumb, R.A., A "tropical pipe" model of stratospheric transport. *J Geophys Res: 101*, 3957, 1996.

Pollock, W.A., L.E. Heidt, R.A. Lueb, J.F. Vedder, M.J. Mills, and S. Solomon, On the age of stratospheric air and ozone depletion potentials in the polar regions. *J Geophys Res: 97*, 12,993, 1992.

Prather, M.J., Numerical advection by conservation of second order moments. *J Geophys Res: 91*, 6671, 1986.

Pyle, J. A., and C. F. Rogers, Stratospheric transport by stationary planetary waves — The importance of chemical processes. *Quart J Roy Meteorol Soc: 106*, 421, 1980.

Randel, W.J., *Global Atmospheric Circulation Statistics, 1000-1 mb.* NCAR Tech Note, TN-366+STR, 1992.

Randel, W.J., J.C. Gille, A.E. Roche, J.B. Kumer, J.L. Mergenthaler, J.W. Waters, E.F. Fishbein, and W.A. Lahoz, Stratospheric transport from the tropics to middle latitudes by planetary-wave mixing. *Nature: 365*, 533, 1993.

Rasch, P.J., B.A. Boville, G.P. Brasseur, A three-dimensional general circulation model with coupled chemistry for the middle atmosphere. *J Geophys Res: 100*, 9041, 1995.

Reed, R.J., W.J. Campbell, L.A. Rasmusson, and D.G. Rogers, Evidence of a downward propagating annual wind reversal in the equatorial stratosphere. *J Geophys Res: 66*, 813, 1961.

Reed, R.J., J.L. Wolfe, and H. Nishimoto, A spectral analysis of the energetics of the stratospheric sudden warming of early l957. *J Atmos Sci: 20*, 256, 1963.

Reed, R.J., The quasi-biennial oscillation of the atmosphere between 30 and 50 km over Ascension Island. *J Atmos Sci: 22*, 331, 1965.

Reed, R.J., and K.E. German, A contribution to the problem of stratospheric diffusion by large scale mixing. *Mon Weath Rev: 93*, 313, 1965.

Richmond, A.D., Thermospheric dynamics and electrodynamics, in *Solar Terrestrial Physics*, R.L. Corovilano and J.M. Forbes, eds. D. Reidel, Dordrecht, 1983.

Rind, D., R. Suozzo, N.K. Balachandran, A. Lacis, and G. Russell, The GISS global climate-middle atmosphere model, Part I: Model structure and climatology. *J Atmos Sci: 45*, 329, 1988.

Rind, D., D. Shindell, P. Lonergan, and N.K. Balachandran, Climate change in the middle atmosphere, Part III. The doubled CO_2 climate revisited. *J Clim: 11*, 876, 1998.

Robert, A., A stable numerical integration scheme for the primitive meteorological equations. *Atmos Ocean: 19*, 35, 1981.

Rood, R.B., and M.R. Schoeberl, A mechanistic model of Eulerian, Lagrangian mean, and Lagrangian ozone transport by steady planetary waves. *J Geophys Res: 88*, 5208, 1983.

Rood, R.B., Numerical advection algorithms and their role in atmospheric transport and chemistry models. *Rev Geophys: 25*, 71, 1987.

Rose, K., and G. P. Brasseur, A three-dimensional model of chemically active trace species in the middle atmosphere during disturbed winter conditions. *J Geophys Res: 94*, 16,387, 1989.

Rossby, C.-G., Planetary flow patterns in the atmosphere. *Quart J Roy Meteorol Soc: 66*, Suppl 68, 1940.

Sassi, F., R.R. Garcia, and B.A. Boville, The stratopause semiannual oscillation in the NCAR Community Climate Model. *J Atmos Sci: 50*, 3608, 1993.

Schlesinger, M.E., and Y. Mintz, Numerical simulation of ozone production, transport and distribution with a global atmospheric general circulation model. *J Atmos Sci: 36*, 1325, 1979.

Schmidt, U., and A. Khedim, In situ measurements of carbon dioxide in the winter Arctic vortex and at mid-latitude: An indicator of the age of stratospheric air. *Geophys Res Lett: 18*, 763, 1991.

Schoeberl, M.R., and D.F. Strobel, The zonally averaged circulation of the middle atmosphere. *J Atmos Sci: 35*, 577, 1978.

Shepherd, T.G., The middle atmosphere. *J Atmos Sol-Terr Phys: 62*, 1587, 2000.

Shepherd, T.G., Large-scale atmospheric dynamics for atmospheric chemists. *Cehm Rev: 103*, 4509, 2003.

Shepherd, G.G., G. Thuillier, W.A. Gault, B.H. Solheim, C. Hersom, J.M. Alunni, J.-F. Brun, S. Brune, P. Charlot, L.L. Cogger, D.-L. Desaulniers, W.F.J. Evans, R.L. Gattinger, F. Girod, D. Harvie, R.H. Hum, D.J.W. Kendall, E.J. Llewellyn, R.P. Lowe, J. Ohrt, F. Pasternak, O. Peillet, I. Powell, Y. Rochon, W.E. Ward, R.H. Wiens, and J. Wimperis, WINDII, the wind imaging interferometer on the upper atmosphere research satellite. *J Geophys Res: 98*, 10,725, 1993.

Shindell, D.T., G.A. Schmidt, M.E. Mann, D. Rind, and A. Waple, Solar forcing of regional climate change during the Maunder minimum. *Science: 294*, 2149, 2001.

Simmons, A.J., and R. Strüfing, Numerical forecasts of stratospheric warming events using a model with a hybrid vertical coordinate. *Quart J Roy Meteorol Soc: 109*, 81, 1983.

Smagorinsky, J., S. Manabe, and J.L. Holloway, Numerical results from a nine-level general circulation model of the atmosphere. *Mon Weath Rev: 93*, 727, 1965.

Smith, A.K., Physics and chemistry of the mesopause region. *J Atm Sol Terr Phys: 66*, 839, 2004.

Smolarkiewicz, P.K., A simple positive definite advection scheme with small implicit diffusion. *Mon Weath Rev: 111*, 479, 1983.

Staniforth, A., and J. Coté, Semi-Lagrangian integration schemes for middle atmosphere models—A review. *Mon Weath Rev: 119*, 2206, 1991.

Strobel, D.F., Parameterization of linear wave chemical transport in planetary atmospheres by eddy diffusion. *J Geophys Res: 86*, 9806, 1981.

Strobel, D.F., J.P. Apruzese, and M.R. Schoeberl, Energy balance constraints on gravity wave induced eddy diffusion in the mesophere and lower thermosphere. *J Geophys Res: 90*, 13,067, 1985.

Strobel, D.F., Constraints on gravity wave induced diffusion in the middle atmosphere. *Pure Appl Geophys: 130*, 533, 1989.

Swenson, G.R., and C.S. Gardner, Special section: The 1993 airborne lidar and observations of Hawaiian airglow airborne noctilucent cloud campaigns–preface. *J Geophys Res: 103*, 6249, 1998.

Swinbank, R., W.A. Lahoz, A. O'Neill, C.S. Douglas, A. Heaps, and D. Podd, Middle atmosphere variability in the UK Meteorological Office Unified Model. *Quart J Roy Meteorol Soc: 124*, 1485, 1998.

Thompson, D.W.J., and J.M. Wallace, The Arctic oscillation signature in the winter geopotential height and temperature fields. *Geophys Res Lett: 25*, 1297, 1998.

Thompson, D.W.J., and J.M. Wallace, Annular modes in the extratropical circulation, Part I. Month-to-month variability. *J Clim: 13*, 1000, 2000.

Thompson, D.W.J., J.M. Wallace, and G.C. Hegerl, Annular modes in the extratropical circulation, Part II. Trends. *J Clim: 13*, 1018, 2000.

Trepte, C.R., and M.H. Hitchman, Tropical stratospheric circulation deduced from satellite aerosol data. *Nature: 335*, 626, 1992.

U.S. Standard Atmosphere 1976. National Oceanic and Atmospheric Administration, National Aeronautics and Space Administration, and United States Air Force, Washington, D.C., 1976.

Veryand, R.G., and R.A. Ebdon, Fluctuations in tropical stratospheric winds. *Meteorol Mag: 90*, 125, 1961.

Vincent, D.G., Meridional circulation in the northern hemisphere lower stratosphere during 1964 and 1965. *Quart J Roy Meteorol Soc: 94*, 333, 1968.

Volk, C.M., J.W. Elkins, D.W. Fahey, R.J. Salawitch, G.S. Dutton, J.M. Gilligan, M.H. Proffitt, M. Loewenstein, J.R. Podolske, K. Minschwaner, J.J. Margitan, and K.R. Chan, Quantifying transport between the tropical and mid-latitude stratosphere. *Science: 272*, 1763, 1996.

von Zahn, U., J. Friedler, B. Naujokat, V. Langematz, and K. Krüger, A note on record-high temperature at the northern polar stratopause in winter 1997-98. *Geophys Res Lett: 25*, 4169, 1998.

Vupputuri, R.K., The structure of the natural stratosphere and the impact of chlorofluoromethanes on the ozone layer investigated in a 2-D time dependent model. *Pure Appl Geophys: 117*, 448, 1979.

Wagner, R.E., and K.P. Bowman, Wavebreaking and mixing in the Northern hemisphere summer stratosphere. *J Geophys Res: 105*, 24,799, 2000.

Walker, G.T., Correlations in seasaonal variations of weather. *Mem Ind Meteorol Dept: 25*, 275, 1924.

Walker, G.T., and E.W. Bliss, World weather, *Mem Roy Meteorol Soc: 4*, 53, 1932.

Wallace, J.M., General circulation of the tropical lower stratosphere. *Rev Geophys Space Phys: 11*, 191, 1973.

Wallace, J.M., and D.W.J. Thompson, Annular modes and climate prediction. *Phys Today: 28*, 2002.

Walterscheid, R.-L., G. Schubert, and J.M. Straus, A dynamical-chemical model of wave-driven fluctuations in the OH nightglow. *J Geophys Res: 92*, 1241, 1987.

Waugh, D.W., and R.A. Plumb, Contour advection with surgery: A technique for investigating fine scale structure in tracer transport. *J Atmos Sci: 51*, 530, 1994.

Waugh, D.W., R.A. Plumb, R.J. Atkinson, M.R. Schoeberl, L.R. Lait, P.A. Newman, M. Loewenstein, D.W. Toohey, L.M. Avallone, C.R. Webster, and R.D. May, Transport out of the lower stratospheric Arctic vortex by Rossby wave breaking. *J Geophys Res: 99*, 1071, 1994.

Weinstock, J., Nonlinear theory of gravity waves: Momentum deposition, generalized Rayleigh friction, and diffusion. *J Atmos Sci: 39*, 1698, 1982.

World Meteorological Organization (WMO), *Scientific Assessment of Ozone Depletion: 1998, Global Ozone Research and Monitoring Project- Report No. 44*, Geneva, 1999.

Xu, J., The influence of photochemistry on gravity waves in the middle atmosphere. *Earth Planets Space: 51*, 855, 1999.

Xun, Z., and J.R. Holton, Photochemical damping of inertio-gravity waves. *J Atmos Sci: 43*, 2578, 1986.

Chapter 4

RADIATION

4.1 Introduction

The atmosphere can be considered to be a mixture of gases and particles exposed to the electromagnectic energy of the sun. An understanding of the dynamical and photochemical processes that occur in this environment requires evaluation of atmospheric radiative transfer. For example, the rate of reaction between two constituents often depends on the local temperature (see Chapter 2), which is affected by absorption, scattering, and emission of solar and terrestrial radiation. Further, solar radiation of particular energies can dissociate and ionize atmospheric molecules, producing reactive ions and radicals which, in turn, participate in many important chemical processes.

Radiation is characterized by a *spectrum* of energies. Spectral variables can be wavelength λ, frequency $\nu = c/\lambda$ (where $c = 3 \times 10^8$m s^{-1} is the speed of light in vacuum), or wavenumber $\overline{\nu} = 1/\lambda$ (see Figure 4.1). The energy E of a photon is given by

$$\mathrm{E} = \mathrm{h}\nu = \frac{\mathrm{hc}}{\lambda} = \mathrm{hc}\overline{\nu} \tag{4.1}$$

where h $= 6.626 \times 10^{-34}$ J s is the Planck constant. Table 4.1 presents the nomenclature associated with various parts of the electromagnetic spectrum. In the region of X-rays, ultraviolet (UV), and visible, wavelength λ is usually expressed in *nanometers* (1 nm $= 10^{-9}$m), while, in the infrared (IR), λ is often expressed in *micrometers* or microns (1 μm $= 10^{-6}$m). Radiation frequency is commonly expressed in s^{-1} or Hz and wavenumber in cm^{-1}. Table 4.1 also provides typical values for the magnitude of solar variability in each spectral region, and brief comments on how radiation interacts with the atmosphere.

As discussed in Chapter 2, atmospheric molecules are characterized by discrete rotational and vibrational energy states, and by their electronic configurations (see Figure 4.1). The absorption of photons can induce transitions between ground and excited states. The difference between rotational energy levels are much smaller than those of the vibrational

Table 4.1 Regions of the Electromagnetic Spectrum (Thomas and Stamnes, 1999)

Subregion	*Range*	*Solar Variability*	*Comments*
X rays	$\lambda < 10$ nm	10-100%	Photoionizes all thermosphere species.
Extreme UV	$10 < \lambda < 100$ nm	50%	Photoionizes O_2 and N_2. Photodissociates O_2.
Far UV	$100 < \lambda < 200$ nm	7-80%	Dissociates O_2. Discrete electronic excitation of atomic resonance lines.
Middle UV, or UV-C	$200 < \lambda < 280$ nm	1-2%	Dissociates O_3 in intense Hartley bands. Potentially lethal to biosphere.
UV-B	$280 < \lambda < 320$ nm	$< 1\%$	Some radiation reaches surface, depending on O_3 optical depth. Responsible for skin erythema.
UV-A	$320 < \lambda < 400$ nm	$<1\%$	Reaches surface. Benign to humans. Scattered by clouds, aerosols, and molecules.
Visible	$400 < \lambda < 700$ nm	$\leq 0.1\%$	Absorbed by ocean, land. Scattered by clouds, aerosols, and molecules. Primary energy source for biosphere and climate system.
Near IR	$0.7 < \lambda < 3.5$ μm		Absorbed by O_2, H_2O, CO_2 in discrete vibrational bands.
Thermal IR	$3.5 < \lambda < 100$ μm		Emitted and absorbed by surfaces and IR-active gases.

states. The separation between electronic levels is in general much larger than the separation between vibrational levels. For processes which do not result in continuum ionization or photodissociation of the molecule, only the photons of the specific frequencies corresponding to transitions between energy states of the molecule can be absorbed; the corresponding spectrum therefore appears as a series of distinct lines which are often part of absorption bands.

Due to the relatively high energies needed to dissociate or ionize atmospheric gases, photochemistry is mainly initiated by less than one per cent of the solar photons, more specifically, those whose characteristic wavelength is in the X-ray, ultraviolet, or, for certain molecules, in the visible region.

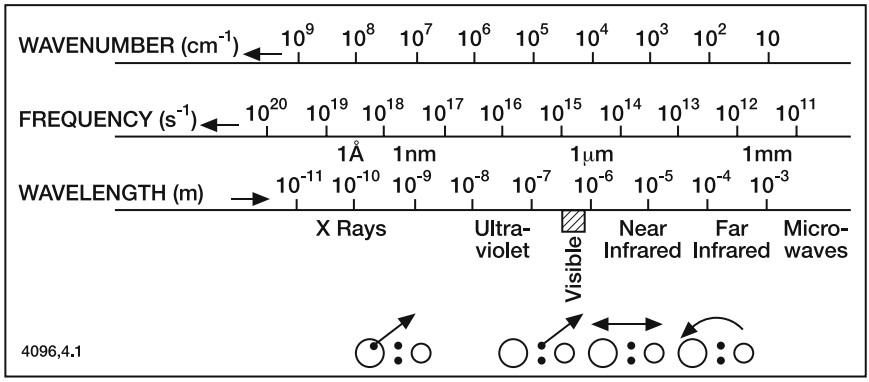

Figure 4.1. Spectral regions and their effect on molecules: from left to right: ionization, dissociation, vibration, and rotation.

Solar radiation also produces thermal effects. Solar energy is absorbed primarily by ozone in the stratosphere and mesosphere, and by molecular oxygen in the upper mesosphere and lower thermosphere. Photolysis of ozone yields some thermal energy directly (through formation of translationally hot products), along with some chemical energy. The latter is converted to thermal energy through chemical reactions (*e.g.*, recombination of atomic oxygen in the presence of a third body) which follow the photodissociation of O_2 and O_3. CO_2 also plays an important role, rivaling O_3 and O_2 in the mid-mesosphere by absorbing solar radiation in the near-infrared bands at 2.0, 2.7, and 4.3 μm. This heating by absorption of solar ultraviolet radiation is balanced by cooling related to infrared emission by CO_2 (15 μm band), and, to a limited extent, by ozone (9.6 μm band) and H_2O (6.7 μm band and rotational bands). Thus, the thermal structure depends on an equilibrium between these processes as well as other phenomena such as the production of latent heat in the troposphere and the dissipation of atmospheric waves in the mesosphere and thermosphere.

In the study of radiation affecting the middle atmosphere it is often convenient to distinguish between two distinct spectral regions (Figure 4.2): (1) wavelengths shorter than 3.5 μm, which represent radiation of solar origin; and (2) wavelengths longer than 3.5 μm, which is made of radiation of both terrestrial and atmospheric origin. For wavelengths longer than 3.5 μm, the solar flux can be neglected relative to the radiation emitted by the Earth's surface. This regime is therefore quite different from shorter wavelengths because of the sharp limit imposed by the spectral function of the terrestrial emission temperature.

The penetration of solar radiation into the Earth's atmosphere depends on atmospheric absorption. Since the absorption coefficients of

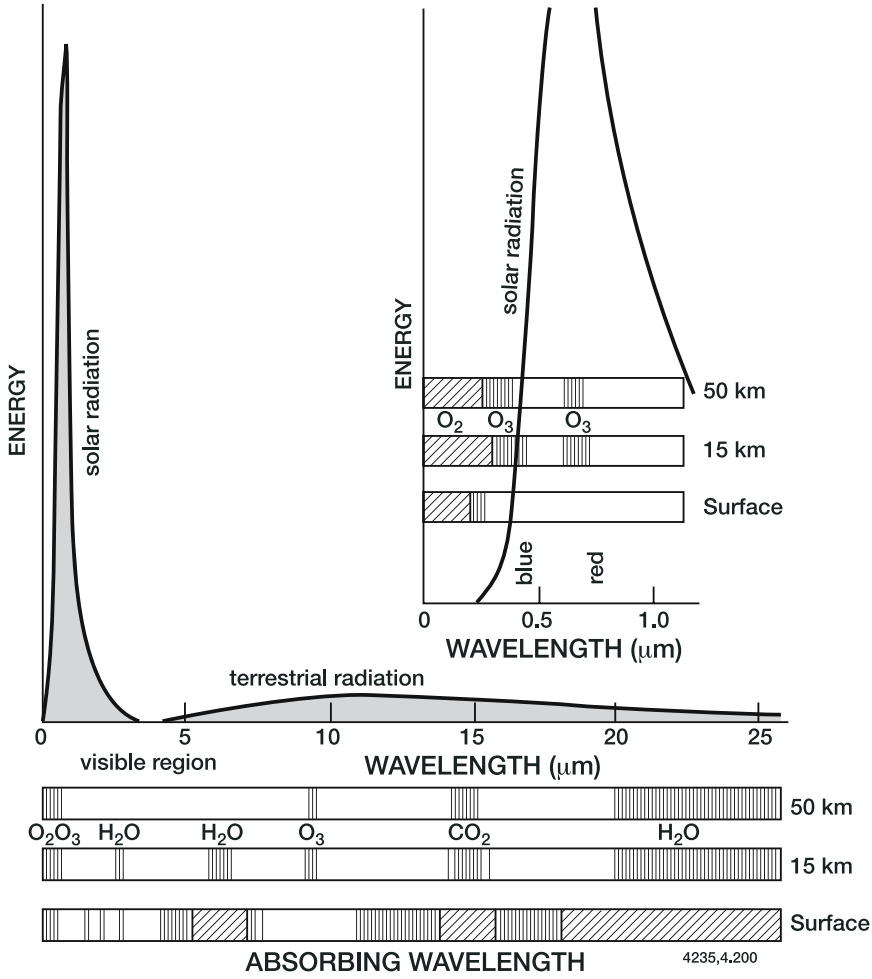

Figure 4.2. Spectral distribution of solar and terrestrial radiation. Atmospheric absorption at different wavelengths. After Iribane and Cho (1980).

minor constituents are functions of wavelength, the penetration depth varies according to the shape of the absorption spectrum (Figure 4.3).

For wavelengths below 100 nm, radiation is almost completely absorbed above 100 km by molecular and atomic oxygen and to a lesser extent by molecular nitrogen. X-rays of wavelength less than 1 nm can, however, penetrate to the middle atmosphere. These X-rays mainly photoionize, or indirectly dissociate the major species, N_2 and O_2, and are responsible for certain sporadic ionospheric perturbations. These aspects of the photochemistry will be discussed in Chapter 7.

At wavelengths longer than 100 nm, solar ultraviolet radiation photodissociates atmospheric molecules. The solar Lyman-α line at

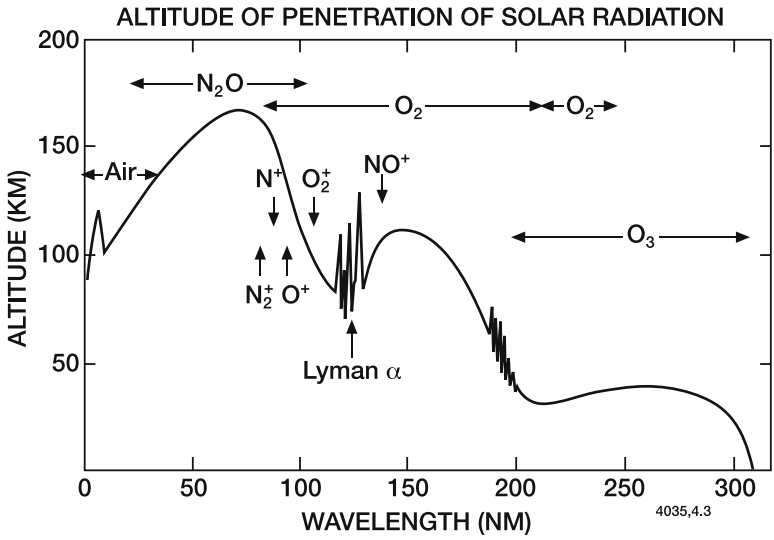

Figure 4.3. Depth of penetration of solar radiation as a function of wavelength. Altitudes correspond to an attenuation of 1/e. The principle absorbers and ionization limits are indicated.

121.6 nm is very intense and is situated in an optical window, that is, a spectral region where absorption by the atmosphere is relatively weak. Therefore, it can penetrate into the upper part of the middle atmosphere, where it effectively dissociates water vapor, carbon dioxide, and methane. Further, it photoionizes nitric oxide, providing the principal source of ionization in the D-region (see Chapter 7). Finally, the Lyman-α line is a significant source of heat in the mid-mesosphere. At longer wavelengths, the solar spectrum is subdivided into regions of absorption by the principal absorbing species, O_2 and O_3. The first of these molecules absorbs only the radiation at wavelengths shorter than about 240 nm. The latter, abundant in the stratosphere, absorbs primarily between 200 and 300 nm, but also to some extent in the visible and even in the infrared. Even so, in the visible (wavelengths greater than 310 nm), the greater part of the solar photons reach the troposphere and the surface. Thus, in this region the effects of molecular scattering and cloud and surface albedo must be considered. Table 4.2 indicates the different spectral regions which must be considered when addressing the photochemical effects of solar radiation on the neutral atmosphere.

Detailed treaments of radiative transfer in the Earth's atmosphere are given by Chandrasekhar (1950), Goody (1964), Liou (1980, 2002), Andrews *et al.* (1987), Goody and Yung (1989), and Thomas and Stamnes (1999). An excellent treatment of non-local thermodynamic

equilibrium (non-LTE) radiative transfer in the atmosphere is provided by Lopez-Puertas and Taylor (2001).

Table 4.2 Spectral Regions of Photochemical Importance in the Atmosphere

Wavelength	*Atmospheric Absorbers*
121.6 nm	Solar Lyman α line, absorbed by O_2 in the mesosphere; no absorption by O_3.
130 to 175 nm	O_2 Schumann Runge continuum. Absorption by O_2 in the thermosphere. Can be neglected in the mesosphere and stratosphere.
175 to 200 nm	O_2 Schumann Runge bands. Absorption by O_2 in the mesosphere and upper stratosphere. Effect of O_3 can be neglected in the mesosphere, but is important in the stratosphere.
200 to 242 nm	O_2 Herzberg continuum. Absorption by O_2 in the stratosphere and weak absorption in the mesosphere. Absorption by the O_3 Hartley band is also important; both must be considered.
200 to ≈310 nm	O_3 Hartley band. Absorption by O_3 in the stratosphere leading to the formation of O (^{1}D).
≈310 to 400 nm	O_3 Huggins bands. Absorption by O_3 in the stratosphere and troposphere leads to the formation of O (^{3}P).
400 to 850 nm	O_3 Chappuis bands. Absorption by O_3 in the troposphere induces photodissociation even at the surface.

4.2 Definitions

Before examining in detail the specific effects of solar and terrestrial radiation on the middle atmosphere, we present a few definitions relative to radiative transfer in the atmosphere.

The radiation field is defined by the monochromatic *radiance* L_ν, which represents the amount of energy dE in frequency interval $d\nu$ traversing a surface dS per time dt in a pencil of solid angle $d\boldsymbol{\omega}$ inclined at an angle θ relative to the normal to the surface (see Figure 4.4a). We can then write

$$L_\nu(\mathbf{r}, \boldsymbol{\omega}) = \frac{dE}{d\nu\, dt\, dS\, d\omega\, \cos\theta} \tag{4.2}$$

This quantity is often expressed in $Wm^{-2}sr^{-1}Hz^{-1}$, and is defined at each point $\mathbf{r}$ in space and for each direction $\boldsymbol{\omega}$ of the pencil of light.

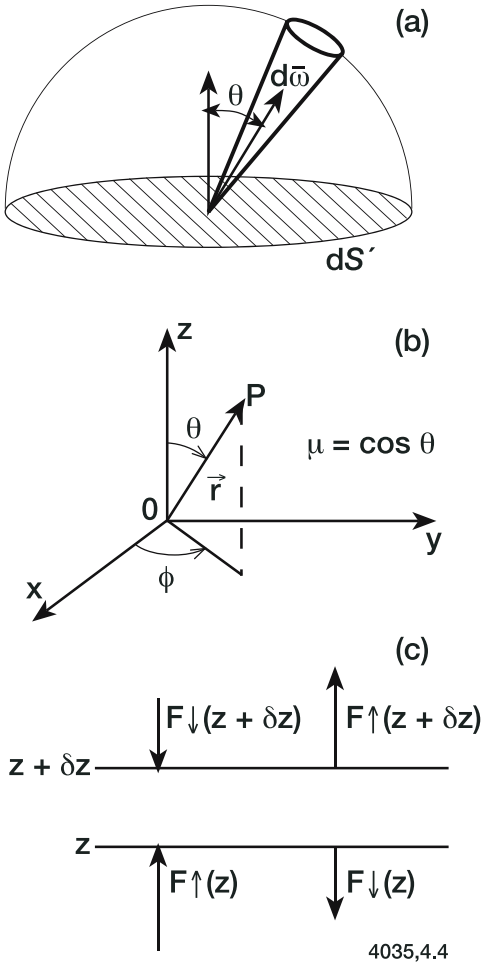

Figure 4.4. (a) Geometry of a pencil of light in solid angle dω traversing a unit of surface dS′. θ is the inclination of the beam relative to the surface. (b) Definition of the azimuthal (ϕ) and zenith (θ) angles. (c) Balance of energy fluxes for a thin layer between altitude z and z + δz.

If L_ν is not a function of direction, the field of radiance is said to be *isotropic*; if L_ν is not a function of position in space, the field is said to be *homogeneous*.

In order to evaluate the rate of radiative heating due to absorption of energy by a unit volume, the net flux density traversing the surface must be determined. The energy flux density (W $m^{-2}Hz^{-1}$) across the surface at angle $\boldsymbol{\omega}$ due to all the pencils of light of direction $\boldsymbol{\omega}'$, called

the *irradiance*, is given by the integral:

$$\mathrm{F}_\nu(\mathbf{r},\boldsymbol{\omega}) = \int_{4\pi} \mathrm{L}_\nu(\mathbf{r},\boldsymbol{\omega}')\cos(\boldsymbol{\omega},\boldsymbol{\omega}')\mathrm{d}\boldsymbol{\omega}' \tag{4.3}$$

In atmospheric problems, we are most often concerned with the energy transfer between horizontal layers, and can therefore write:

$$\mathrm{F}_\nu(\mathrm{z}) = \int_0^{2\pi} \mathrm{d}\phi \int_{-1}^{1} \mu \mathrm{L}_\nu(\mu,\phi)\mathrm{d}\mu \tag{4.4}$$

where $\mu = \cos\theta$, and ϕ are the parameters describing the zenith and azimuthal directions, respectively, of the propagation (see Figure 4.4b).

In the case of a plane parallel atmosphere at altitude z, the net irradiance can be separated into its upward propagating and downward propagating components:

$$\mathrm{F}_\nu \uparrow (\mathrm{z}) = \int_0^{2\pi} \mathrm{d}\phi \int_0^{1} \mu \mathrm{L}_\nu(\mathrm{z};\mu,\phi)\mathrm{d}\mu \qquad (\mu > 0) \tag{4.5}$$

$$\mathrm{F}_\nu \downarrow (\mathrm{z}) = \int_0^{2\pi} \mathrm{d}\phi \int_0^{-1} \mu \mathrm{L}_\nu(\mathrm{z};\mu,\phi)\mathrm{d}\mu \qquad (\mu < 0) \tag{4.6}$$

such that the net irradiance is given by

$$\mathrm{F}_\nu(\mathrm{z}) = \mathrm{F}_\nu \downarrow (\mathrm{z}) - \mathrm{F}_\nu \uparrow (\mathrm{z}) \ . \tag{4.7}$$

The radiance L ($\mathbf{r}$, $\boldsymbol{\omega}$) and irradiance F ($\mathbf{r}$, $\boldsymbol{\omega}$) over a frequency interval $\Delta\nu$ is derived by integration over the frequency

$$\mathrm{L}\,(\mathbf{r},\boldsymbol{\omega}) = \int_{\Delta\nu} \mathrm{L}_\nu\,(\mathbf{r},\boldsymbol{\omega})\ d\nu \tag{4.8}$$

$$\mathrm{F}\,(\mathbf{r},\boldsymbol{\omega}) = \int_{\Delta\nu} \mathrm{F}_\nu\,(\mathbf{r},\boldsymbol{\omega})\ d\nu \tag{4.9}$$

where L ($\mathbf{r}$, $\boldsymbol{\omega}$) and F ($\mathbf{r}$, $\boldsymbol{\omega}$) are expressed in W $\mathrm{m}^{-2}\mathrm{sr}^{-1}$ and W m^{-2}, respectively.

To determine the heating rate at the layer between altitude z and z + δz, the energy balance at each boundary of the layer must be solved (see Figure 4.4c). As the thickness δz approaches zero, the energy absorbed per unit volume is given by the net flux divergence dF/dz. Therefore, the *diabatic heating rate* (expressed as the variation of the temperature in the layer per unit time) is given by

$$\mathrm{Q} = \frac{-1}{\rho \mathrm{c_p}} \frac{\mathrm{dF}}{\mathrm{dz}} = \frac{\mathrm{g}}{\mathrm{c_p}} \frac{\mathrm{dF}}{\mathrm{dp}} \tag{4.10}$$

where c_p is the specific heat at constant pressure, ρ is the total air density, g is the acceleration of gravity and p is the pressure. Q is often expressed in units of K/s or K/day.

In order to study the photochemical effects of radiation, we define the *actinic flux* Φ (r) as the amount of energy (W $m^{-2}Hz^{-1}$) penetrating a unit volume of space at point **r** with

$$\Phi_\nu(\mathbf{r}) = \int_{4\pi} L_\nu(\mathbf{r};\boldsymbol{\omega})d\boldsymbol{\omega} \tag{4.11}$$

$\Phi(\mathbf{r})$ is therefore 4π times the so-called *mean radiance*. Thus, in this definition, each photon arriving at point **r** is given equal weight regardless of the direction of propagation. The dissociation or ionization of atmospheric molecules occurs regardless of the direction of the incident photon, and its value is therefore proportional to the actinic flux (not the irradiance). In the case of a plane stratified atmosphere, one obtains:

$$\Phi_\nu(z) = \int_0^{2\pi} d\phi \int_{-1}^{1} L_\nu\,(z;\mu,\phi)\,d\mu \tag{4.12}$$

The *actinic flux* can also be expressed as the number of photons penetrating a unit volume of space at point **r** per unit time (photons $m^{-2}s^{-1}Hz^{-1}$). In this case, it is given by

$$q_\nu(\mathbf{r}) = \frac{\Phi_\nu(\mathbf{r})}{h\nu} \tag{4.13}$$

Note that the spectral density of any quantity X can be expressed not only as a function of frequency $X_\nu = dX/d\nu$ but also as a function of wavelength $X_\lambda = dX/d\lambda$ or of wavenumber $X_{\overline{\nu}} = dX/d\overline{\nu}$ where $\lambda = c/\nu$ and $\overline{\nu} = 1/\lambda = \nu/c$.

4.3 Extraterrestrial Solar Radiation

4.3.1 The Solar Atmosphere

The production of radiation by the Sun depends strongly on the physical and chemical structure of the solar atmosphere. Therefore, in order to understand the nature and variations of the radiation incident on the Earth, we briefly present some of the important aspects of the Sun's atmosphere, whose structure is schematically represented in Figures 4.5 and 4.6.

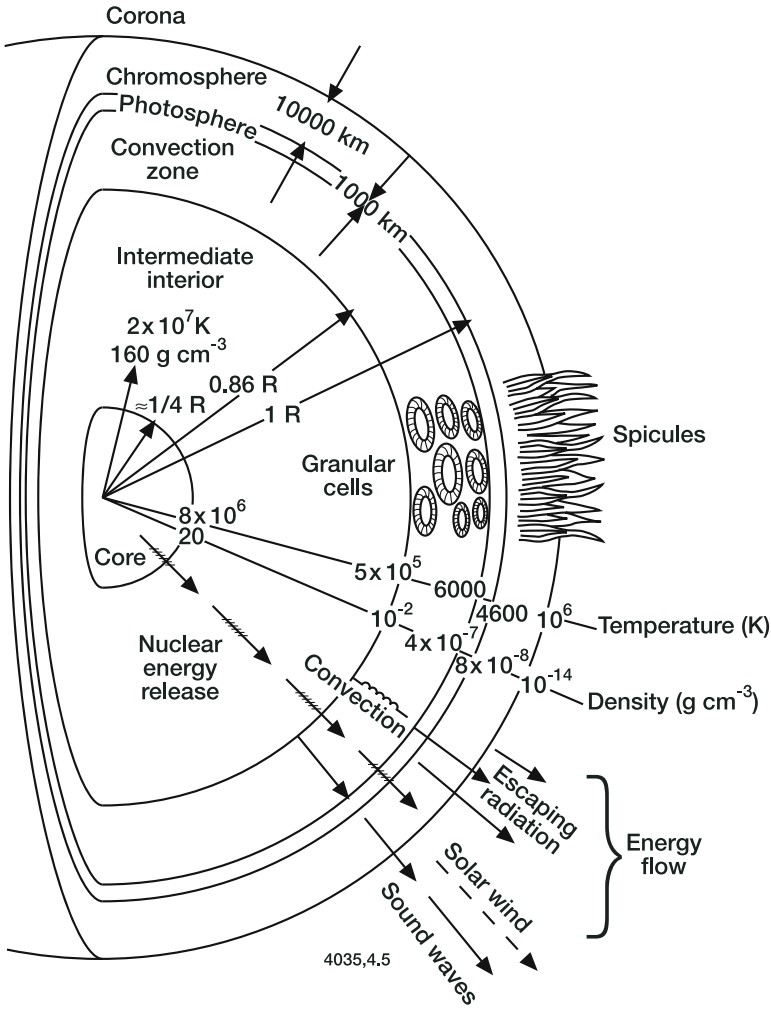

Figure 4.5. Schematic diagram of the solar atmosphere with its different layers and physical characteristics.

The Sun is primarily composed of hydrogen and helium, along with smaller amounts of heavier elements such as calcium, iron, magnesium, aluminum, nickel, etc. The temperature in its interior is believed to be as high as 2×10^7 K, due to a chain of nuclear reactions which convert H into He. This energy is radiated to the upper convective levels, undergoing a series of absorption and emission processes.

Most of the energy reaching the Earth's atmosphere originates from a relatively thin layer (about 1000 km thick) called the *photosphere*. This layer defines the visible volume of the Sun, and although the entire star is

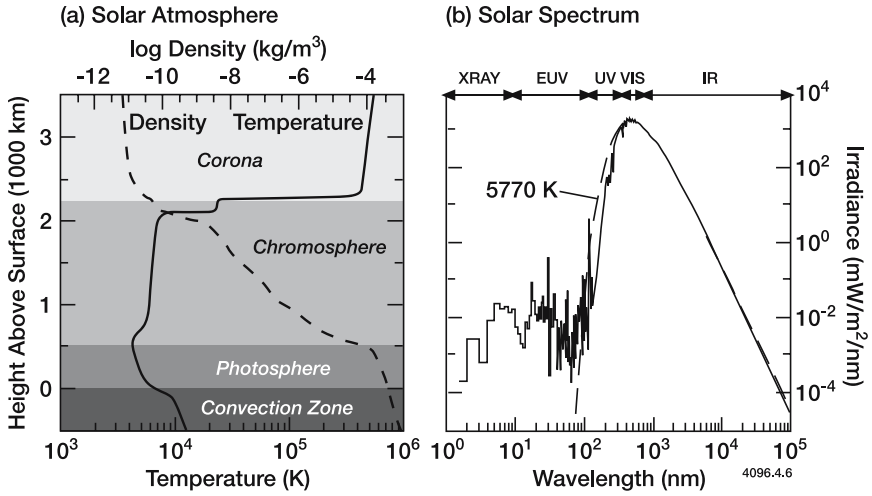

Figure 4.6. Vertical distribution of temperature (T) and density (ρ) at the Sun's surface and its atmosphere (left), which determines the solar irradiance spectrum (right) between 1 and 10^5 nm. From Lean, 1997.

in the gaseous state, the base of the photosphere is generally considered to be the "surface" of the Sun. Its effective temperature is about 5800 K. Observations indicate that the brightness of the photosphere is not continuous, but is characterized by granules which are uniformly distributed over the solar disk. These granules are probably associated with strong convective processes in and below the photosphere.

Transient phenomena such as sunspots and faculae appear in the photosphere, and influence the variability in solar emission at short wavelengths. Sunspots are relatively dark regions with a temperature of about 3000 K and a typical diameter of under 50000 km. These spots are usually grouped in certain places, called *active regions* on the solar disk. The lifetime of a sunspot is variable (from a few days to a few months). Faculae are bright events generally associated with active regions, at least at middle and low solar latitudes. They also appear independently of active regions at high solar latitudes. Observations indicate a fairly regular variation in the occurrence of active regions, with a periodicity of about 11 years, which is called the *solar cycle*. The Sun's rotation on its own axis takes place on an apparent timescale of 27 days, so that the exposure of the Earth to the sunspots also has a 27 day cycle.

The emission of the photosphere is a continuum, superimposed with relatively dark lines called the *Fraunhofer lines*. These are produced by selective absorption and reemission of radiation in the upper photosphere where the temperature is as low as 4000 to 5000 K. Some of these lines

also originate from higher levels, but their effective emission temperature is lower than the kinetic temperature.

The layer above the photosphere extends to 5000 to 10000 km, and is called the *chromosphere*. This layer can sometimes be seen during total solar eclipses. Its temperature is 10^5 – 10^6 K at the upper levels. Radiation originating from the chromosphere is composed predominantly of emission lines (H, He, Ca), and the visible emission is weak.

The region above the chromosphere is called the *corona*, which extends outward for several solar diameters. Its temperature is about 10^6 K. Several emission lines are associated with this region. Its free electrons scatter photospheric light.

Active regions in these upper layers are characterized by variations in chromospheric plages, spicules, prominences, solar flares, and enhanced coronal emission. *Plages* are bright areas in the chromosphere, and are usually observed by their intense calcium K line emission. They usually precede sunspots and last after the sunspots disappear. *Spicules* are small protuberances which appear continuously at the top of the chromosphere, even in quiet regions. Their lifetime is only a few minutes. *Prominences* are large, rather stable clouds of bright gas in the upper part of (and sometimes above) the chromosphere. *Solar flares* are intense eruptive phenomena occurring in the active regions of the chromosphere. They are accompanied by a rapid increase in brightness and an intense enhancement in the emission of ionizing radiation (EUV and X-rays). Flares last from a few minutes to more than an hour, and are divided into different classes in order of increasing importance to the Earth's atmosphere (class 1 or 3). The most intense flares are accompanied by ejection of large quantities of high energy particles (*e.g.*, protons, electrons, and alpha particles).

The Sun is also a source of radio waves. These emissions vary with the solar cycle, and are enhanced (radio burst) during chromospheric or coronal events. Since these emissions can easily be recorded (*e.g.*, at 10.7 cm or 2.8 GHz), they are often used as an indicator of solar activity.

4.3.2 The Solar Constant

The *solar constant* is defined as the total radiative energy flux outside the Earth's atmosphere. This parameter is used to characterize the total solar radiation input. The magnitude of this constant is estimated by Brusa and Frohlich (1982) to be 1367 W m^{-2}, at 1 AU (astronomical unit), which corresponds to an effective solar temperature of 5780 K.

4.3.3 The Sun as a Black Body

If we assume for the purpose of illustration that the Sun behaves as a black body, the energy flux M_E (W m^{-2}) emerging from the surface of the sun is proportional to the fourth power of the temperature, as indicated by the Stefan-Boltzmann law:

$$M_E = \sigma T^4 \tag{4.14}$$

where $\sigma = 5.67 \times 10^{-8}$W $m^{-2}K^{-4}$. The theoretical value of the solar constant is obtained by multiplying the solar emission by a dilution factor β_s which accounts for the Earth-Sun distance:

$$S_C = \beta_s M_E \tag{4.15}$$

with

$$\beta_s = \frac{R_s^2}{r_s^2} \tag{4.16}$$

Here R_s represents the radius of the Sun and r_s the Sun-Earth distance. Due to the annual variation of r_s, the mean dilution factor β_s is 2.164×10^{-5}, while the maximum value attained in January $\beta_{s_{max}}$ is 2.235×10^{-5} and the minimum value occurring in July is $\beta_{s_{min}}$ is 2.093×10^{-5}. The energy input to the Earth from the Sun thus varies annually by 6.6 percent.

The spectral distribution of the exitance emitted by a black body, M_ν is given by Planck's law:

$$M_\nu = \frac{2\pi h\nu^3}{c^2} \frac{1}{e^{h\nu/kT} - 1} \left(\text{W m}^{-2} \text{ Hz}^{-1}\right) \tag{4.17a}$$

where $k = 1.38 \times 10^{-23}$J K^{-1} is Boltzmann's constant and $h = 6.63 \times 10^{-34}$J s is Planck's constant. It is also often expressed in terms of wavelength (μm) as

$$M_\lambda = \frac{c_1}{\lambda^5} \frac{1}{e^{c_2/\lambda T} - 1} \left(\text{W m}^{-2} \ \mu\text{m}^{-1}\right) \tag{4.17b}$$

where $c_1 = 2\pi hc^2 = 3.74 \times 10^8 \text{Wm}^{-2}\mu\text{m}^4$ and $c_2 = hc/k = 1.44 \times 10^4 \mu$m K are the first and second radiation constants, respectively. Thus, if one approximates the Sun as a black body, the number of photons of frequency between ν and $\nu + d\nu$ (the *actinic flux*) impinging on the top of the atmosphere per unit surface and per unit time is

$$q_\nu d\nu = \frac{\beta_s M_\nu d\nu}{h\nu} = \frac{2\pi\beta_s\nu^2}{c^2} \frac{d\nu}{e^{h\nu/kT} - 1} \tag{4.18a}$$

The corresponding flux of photons between wavelength λ and $\lambda + d\lambda$ (expressed for example in photons $\text{cm}^{-2}\text{s}^{-1}\mu\text{m}^{-1}$) is

$$q_\lambda d\lambda = \frac{c_1{}'\beta_s}{\lambda^4} \frac{d\lambda}{e^{c_2/\lambda T} - 1} \tag{4.18b}$$

where $c_1' = 2\pi c = 1.88 \times 10^{23} cm^{-2} s^{-1} \mu m^3$. The total number of photons of frequencies between ν_1 and ν_2 is therefore given by:

$$q(\nu_1 - \nu_2) = \frac{2\pi\beta_s}{c^2} \int_{\nu_1}^{\nu_2} \frac{\nu^2}{e^{h\nu/kT} - 1} d\nu \tag{4.19}$$

In the ultraviolet where the factor $(h\nu/kT)$ is much greater than one:

$$q(\nu_1 - \nu_2) = \frac{2\pi\beta_s}{c^2} \left(\frac{kT}{h}\right)^3 \left\{ e^{-h\nu/kT} \left(\left(\frac{h\nu}{kT} + 1 \right)^2 + 1 \right) \right\}_{\nu_2}^{\nu_1} \tag{4.20}$$

A better description of the solar spectrum is obtained by adopting an equivalent temperature which varies with frequency. Such an equivalent temperature corresponds to the temperature of an effective emission layer in the solar atmosphere at the frequency. A complete description has to account for the solar emission lines in the visible, near ultraviolet, and far ultraviolet regions (see below).

4.3.4 The Observed Solar Spectrum

Since this volume focuses on the terrestrial atmosphere below 100 km, we shall concern ourselves only with the radiation penetrating to or below that level (*i.e.*, the ultraviolet, visible and infra-red, as well as X-rays of wavelengths shorter than 1 nm).

The visible and infrared portion of the solar spectrum is essentially a continuum with the highest emission taking place near 500 nm. Emission lines superimposed on the continuum become increasingly more pronounced in the ultraviolet at wavelengths less than 300 nm. At wavelengths shorter than 208 nm, a sharp decrease in the solar flux occurs. This feature is associated with the Al I ionization edge. Other less pronounced edges with their related continua are due to other ionized elements in the solar atmosphere, such as H, Mg, Si, Fe, and C. Below the aluminum edge, the importance of the solar emission lines increases rapidly, while the absorption lines disappear from the spectrum below 150 nm. At wavelengths shorter than 140 nm, the emission by chromospheric and coronal lines begins to dominate the emission in the continuum. The source of the solar emission thus changes from the photosphere to the chromosphere as the wavelength decreases from 300 to 120 nm. As shown in Figure 4.7, the effective emitting layer of the radiation moves up with shorter wavelength while the absorption in the solar atmosphere increases. The minimum in the brightness temperature between 180 and 150 nm characterizes the transition region between the photosphere and the chromosphere. The variation in the brightness

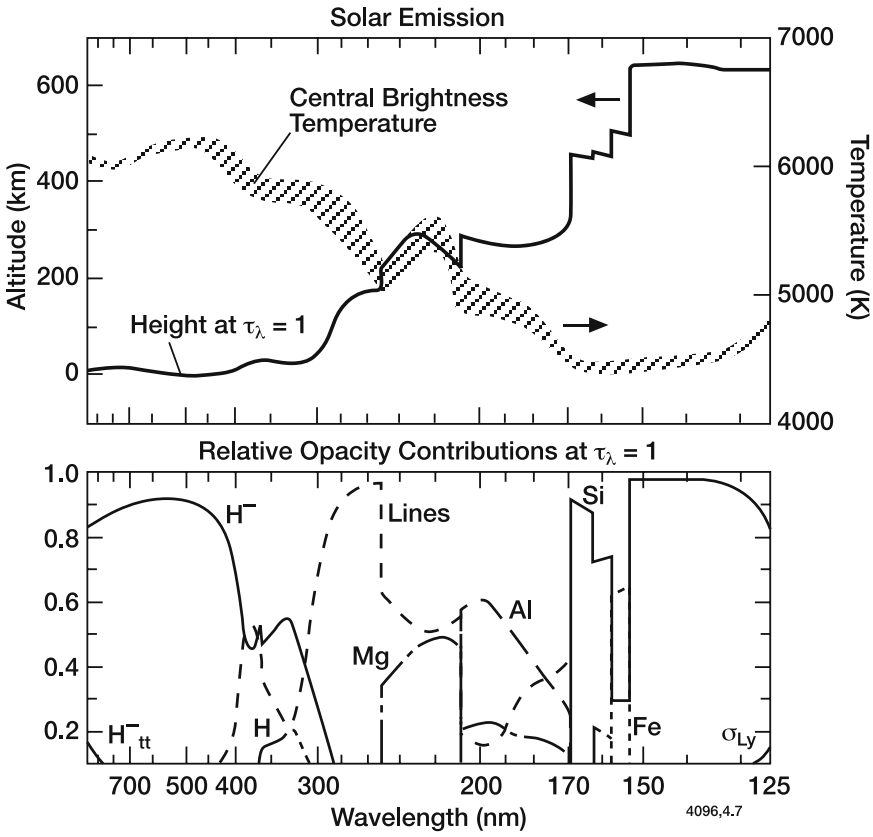

Figure 4.7. Observed continuum brightness temperature of the sun as a function of wavelength and corresponding relative height above $\tau_{500\mathrm{nm}} = 1$ of the solar emission layers (upper panel). Relative contributions to the opacity at this height (lower panel). After Vernazza *et al.*(1976).

temperature (6000 K above 300 nm, 5000 K at 200 nm, 4500 K between 170 and 130 nm) is reflected in the flux values at different wavelengths.

The solar spectrum has been the subject of numerous rocket experiments undertaken since the 1940s. The first spectrum measured above the ozone layer by a V-2 rocket dates from October 1946 (Baum *et al.*, 1946), and not until the 1950s was a solar spectrum observed from an altitude of 100 km (Johnson *et al.*, 1952). Today the solar irradiance is routinely observed by spectrometers on board balloons, aircraft, or spacecraft. During the 1990s, for example, the solar UV flux was measured almost continuously between 120 and 400 nm by the Solar Ultraviolet Spectral Irradiance Monitor (SUSIM) and the Solar/Stellar Irradiance Comparison Experiment (SOLSTICE), both on board the

Upper Atmosphere Research Satellite (UARS) (see *e.g.*, Woods *et al.*, 1996; 1998).

The flux generated by the nuclear burning core of the Sun changes significantly as a function of time. Variations in the solar irradiance, as well as changes in sunspots, faculae and plages, are associated with the 11-year solar cycle, and hence with periodic changes in the magnetic field of the Sun (see *e.g.*, Nesme-Ribes *et al.*, 1996). Over the last 2 solar cycles, the variation in the Sun's total radiative energy has been of the order of 0.1% (Willson and Hudson, 1991; Lee *et al.*, 1995). Variations as a function of wavelength are more difficult to estimate because they rely primarily on intermittant measurements by instruments that are difficult to calibrate. Variability has been shown to be largest at shortest wavelengths, corresponding to the emission from the corona and the upper chromosphere. Large increases in the solar flux at short wavelengths are associated with solar flares.

X-rays of wavelengths shorter than 1 nm constitute an important source of ionization in the D-region, becoming the dominant source during high levels of solar activity. The value of the corresponding flux varies considerably: between 0.1 and 0.8 nm, it has been noted that variations as large as a factor of 1000 may occur over the solar cycle. Similarly, important fluctuations are observed over a solar rotation (27 days) and substantial differences occur from one solar rotation to another. During a solar flare, the X-ray irradiance may become 10000 times greater than that observed during quiet periods.

The flux in the Extreme Ultraviolet (EUV) portion (10-100 nm) of the solar spectrum (see Figure 4.8a) directly affects the chemistry and dynamics of the thermosphere. Its value, and hence the ionization rate in the upper atmosphere, varies substantially with solar activity. Richards *et al.* (1994) have developed a model that provides the extra-terrestrial solar actinic flux from 5 to 105 nm as a function of a solar proxy P which is the average between the instantaneous radiowave flux $F_{10.7}$ emitted by the Sun at 10.7 cm and its average value $F_{10.7A}$ over 81 days. The 10.7 cm flux is routinely monitored and reported in units of 10^{-22} W $m^{-2}Hz^{-1}$; its value ranges typically from 70 (solar minimum) to 200 (solar maximum), and is highly correlated with other indicators of solar activity (*e.g.*, sunspot number).

In the spectral region near 120 nm, the solar hydrogen emission line at Lyman α represents an important source of ionization and dissociation. During quiet periods, it contains more energy than the rest of the spectrum at shorter wavelengths. The total flux of this line as well as its shape vary with solar activity. The actinic flux varies between a minimum of about 3.0×10^{11} photons $cm^{-2}s^{-1}$ for quiet solar activity and a maximum of about 6.0×10^{11} during high solar activity.

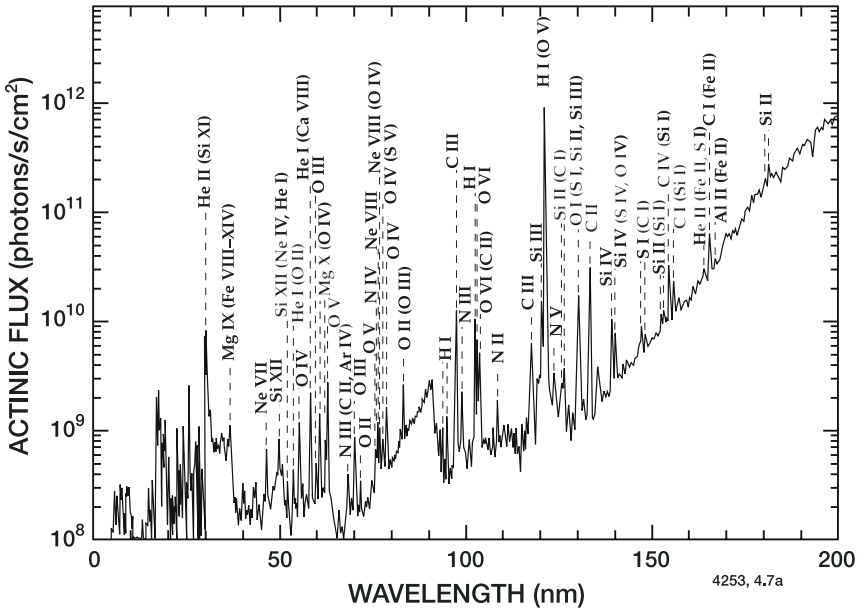

Figure 4.8a. Solar irradiance spectrum at wavelengths less than 200 nm measured on 3 November 1994 with emphasis on the Extreme and Far Ultraviolet regions. The solar bright lines are labeled. From Woods *et al.*(1998).

The solar flux in the 120-420 nm spectral interval plays a key role in the photochemistry of the middle atmosphere. It contains radiation emitted from the chromosphere (temperature of 10^4 to 10^6 K) and photosphere (temperature of approximately 5700 K) in both lines and continuum. Figure 4.8b presents the solar spectrum measured on 29 March 1992 by SUSIM with a 1.1 nm spectral resolution (Brueckner *et al.*, 1993) and by SOLSTICE at 0.1 to 0.25 nm spectral resolution (Rottman *et al.*, 1993).

Analyses of observed data suggest that, over the 11-year solar cycle, the solar flux varies by a factor of 2 at Lyman-α (see Figure 4.9), 20% at 140-155 nm, 15% at 160 nm, 10% at 170-190 nm, and 8% at 200 nm. The variability above the Al I edge at 208 nm is extremely difficult to measure since its magnitude is smaller than instrumental error. It is at most a few percent between 210 and 300 nm, (3-4% at 250 nm, 0.5-1% at 270 nm), and an estimate by Lean (1997) of the 11-year variability in the Sun's spectral irradiance between 0 and 400 nm is given in Figure 4.10.

Changes in the solar irradiance with a 27-day period (apparent rotation period of the Sun) are also observed. The amplitude of the variability decreases with wavelength in a manner similar to that shown in Figure 4.10., but with reduced amplitudes.

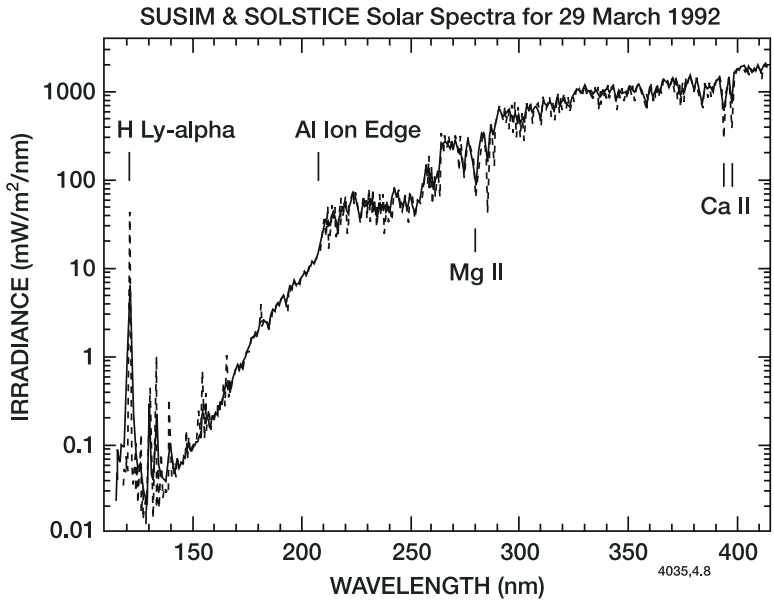

Figure 4.8b. Solar irradiance spectrum between 119 and 420 nm measured on March 29, 1992 by the SUSIM and SOLSTICE spaceborne spectrometers on board the Upper Atmosphere Research Satellite (UARS). From Woods *et al.* (1996).

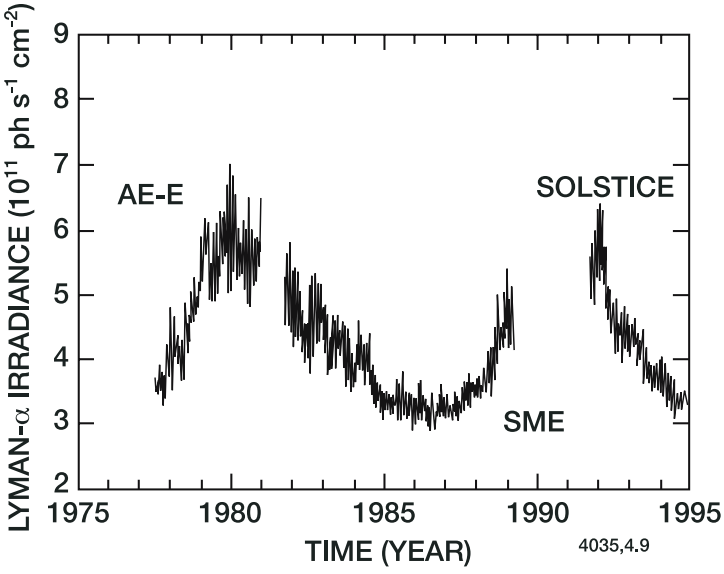

Figure 4.9. Evolution with time of the solar irradiance at Lyman α, based on measurements by the Atmospheric Explorer-E, the Solar Mesosphere Explorer, and the SOLSTICE instrument on board the Upper Atmosphere Research Satellite (UARS), after correction by Woods and Rottman (1997).

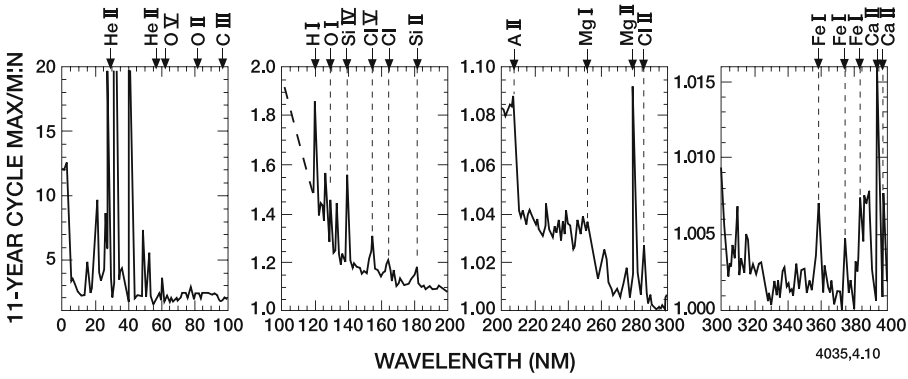

Figure 4.10. Ratio between the solar irradiance at solar maximum and minimum activity conditions (11-year solar cycle) as a function of wavelength (10-400 nm), as estimated by Lean (1997).

4.4 The Attenuation of Solar Radiation in the Atmosphere

4.4.1 Absorption

As solar photons penetrate into the earth's atmosphere, they undergo collisions with atmospheric molecules and are progressively absorbed and scattered. The probability of absorption by a molecule depends on the nature of the molecule and the wavelength of the incoming photon. An effective absorption *cross section*, $\sigma_a(\lambda)$, can be defined for each photochemical species. This quantity is expressed in cm^2, and is independent of the concentration of the species under consideration.

The Beer-Lambert law describes the absorption of a ray of incident intensity I_λ passing through an infinitesimally thin layer ds (see Figure 4.11). The variation of intensity is given by

$$d\,I_\lambda = -k_a(\lambda)\,I_\lambda ds \tag{4.21}$$

where k_a is the absorption coefficient (expressed for example in cm^{-1}). This coefficient is proportional to the concentration n (cm^{-3}) of the absorbing medium (gas or particles) and is related to the effective absorption cross section σ_a (cm^2) by the expression

$$k_a(\lambda) = \sigma_a(\lambda)n \tag{4.22}$$

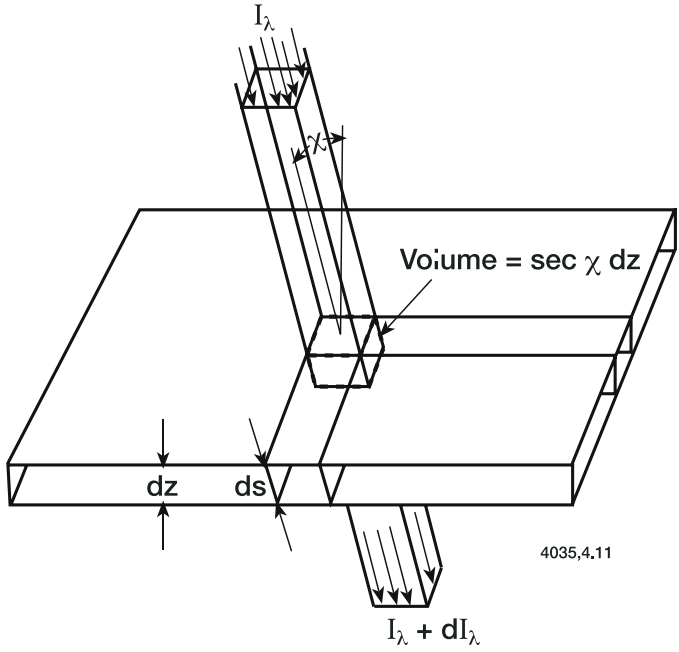

Figure 4.11. Absorption of solar radiation in an atmospheric layer of unit area.

Integrating (4.21) and substituting (4.22) we find

$$I_\lambda(s) = I_{0,\lambda} \exp\left(-\int_s \sigma_a(\lambda) n(s) ds\right) \tag{4.23}$$

where $I_{0,\lambda}$ is the flux at s = 0. The *optical thickness* or *optical depth* over the length s is defined as

$$\tau_a(\lambda, s) = \int_s \sigma_a(\lambda) n(s) ds = \int_s k_a(\lambda, s) ds \tag{4.24}$$

and the corresponding transmission is

$$T_r(\lambda, s) = \exp\left(-\tau_a(\lambda, s)\right) \tag{4.25}$$

(Note that the optical depth is defined here along the line of sight, and not, as in some texts, as the vertical thickness.)

Solar radiation penetrates the atmosphere at an angle of incidence which depends on the local time, season, and latitude. The cosine of the local *solar zenith angle* (χ) is given by

$$\cos(\chi) = \cos(\phi)\cos(\delta)\cos(\mathcal{H}) + \sin(\phi)\sin(\delta) \tag{4.26}$$

where ϕ is the latitude, δ is the solar declination angle, which depends on season ($\pm 23.5^\circ$ for solstice conditions, 0° for equinox, for example), and $\mathcal{H}$ is the hour angle, which is 0° for local noon, and increments

by 15° for each hour from noon. The infinitesimal distances along the optical path ds and along the vertical dz are related by

$$\mathrm{ds} = \mathrm{dz}\ \sec\chi = \mathrm{dz}/\mu_0 \tag{4.27}$$

where $\mu_0 = \cos\chi$. Further, the concentration n(z) is often assumed to vary exponentially with altitude z according to a scale height H (n_0 is the concentration at z = 0; see Chapter 3):

$$\mathrm{n(z)} = \mathrm{n_0}\exp\left(-\mathrm{z/H}\right) \tag{4.28}$$

such that, for a medium containing only one well-mixed absorbing gas (*e.g.*, O_2), the variation of monochromatic solar radiation with altitude in a plane-parallel atmosphere (neglecting the curvature of the Earth) can be written (omitting the index λ):

$$\mathrm{I\,(z)} = \mathrm{I\,(\infty)}\exp\left(-\sec\chi\int_{\mathrm{z}}^{\infty}\sigma_{\mathrm{a}}\mathrm{n_0e^{-z/H}dz'}\right) \tag{4.29}$$

$$= \mathrm{I\,(\infty)}\exp\left(-\sec\chi\sigma_{\mathrm{a}}\mathrm{n_0H\ e^{-z/H}}\right) \tag{4.30}$$

where I (∞) represents the solar intensity outside the earth's atmosphere. The rate of formation of ions, the rates of photodissociation and production of heat, are all directly linked to the rate of energy deposition in the atmosphere by absorption. This last quantity can be written as

$$\mathrm{r} = -\frac{\mathrm{dI}}{\mathrm{ds}} = \frac{\mathrm{dI}}{\mathrm{dz}}\cos\chi \tag{4.31}$$

$$= \sigma_{\mathrm{a}}\mathrm{n_0I\,(\infty)}\exp\left(-\left(\frac{\mathrm{z}}{\mathrm{H}} + \tau_0\exp(-\mathrm{z/H})\right)\right) \tag{4.32}$$

where

$$\tau_0 = \sigma_{\mathrm{a}}\mathrm{n_0H}\sec\chi \tag{4.33}$$

represents the optical depth of the entire atmosphere for zenith angle χ. The rate of energy deposited in the atmosphere exhibits a maximum at the altitude

$$\mathrm{z_m} = \mathrm{H}\ln\tau_0 = \mathrm{H}\ln(\sigma_{\mathrm{a}}\mathrm{n_0H}\sec\chi). \tag{4.34}$$

For an overhead sun, this maximum is located at the altitude:

$$\mathrm{z_0} = \mathrm{H}\ln(\sigma_{\mathrm{a}}\mathrm{n_0H}) \tag{4.35}$$

The rate of energy deposited at altitude

$$\mathrm{z_m} = \mathrm{z_0} + \mathrm{H}\ln\ \sec\chi \tag{4.36}$$

is thus equal to

$$\mathrm{r_m} = \sigma_{\mathrm{a}}\mathrm{n_0I\,(\infty)}\cos\chi\exp\left(-1 - \frac{\mathrm{z_0}}{\mathrm{H}}\right)\ . \tag{4.37}$$

For an overhead sun, one obtains

$$r_0 = r_m(\chi = 0) = \sigma_a n_0 I(\infty) \exp\left(-1 - \frac{z_0}{H}\right) \tag{4.38}$$

Making use of the dimensionless variable

$$Z = \frac{z - z_0}{H} \tag{4.39}$$

the rate of energy deposition in a medium whose concentration decreases exponentially with height, becomes

$$\frac{r}{r_0} = \exp(1 - Z - \sec\chi \exp(-Z)) \tag{4.40}$$

which is represented in Figure 4.12. It should be noted that the penetration of solar radiation and its interaction with the atmosphere leads to the formation of layers whose characteristic altitude z_m is independent of the intensity of the radiation, but strongly dependent on the physical characteristics of the atmospheric medium (nature and concentration of the absorbing gas), the solar zenith angle, and the wavelength of the radiation (because of the spectral distribution of the absorption coefficient). Thus for polychromatic radiation for which

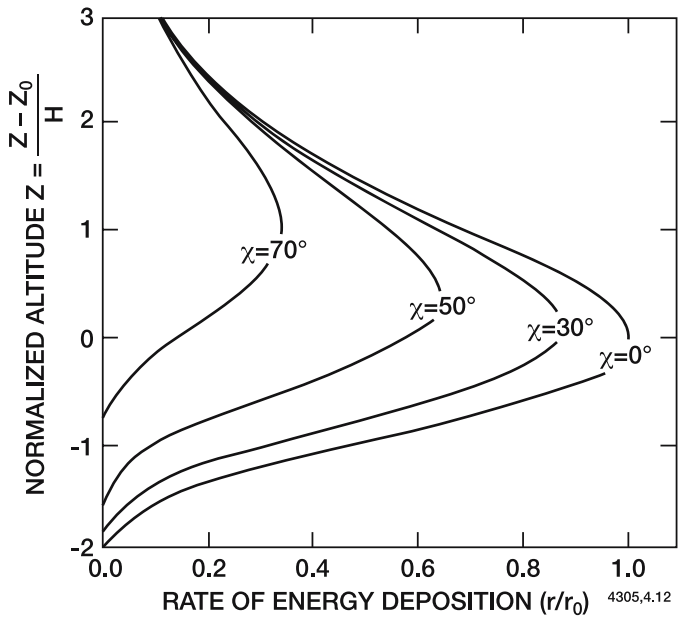

Figure 4.12. Appearance of a characteristic layer due to absorption of solar energy. Distribution obtained by Chapman theory for different values of the solar zenith angle.

regions of strong absorption by one or more absorbing gases occur at different wavelengths, several absorbing layers are found at different altitudes.

The theoretical framework just presented was first suggested by Chapman (1931). This theory provides an explanation for the behavior of the layers of ionization in the thermosphere or of photodissociation in the middle atmosphere. The production of ozone through photodissociation of molecular oxygen exhibits a maximum near 45 km dependent on the insolation. The rate of heating through absorption of ultraviolet radiation by ozone similarly leads to a maximum near the stratopause. Numerous examples of such layers can be found in the neutral and ionized atmosphere.

In practice, however, the analytic calculations by Chapman should be replaced by an expression that accounts for the combined effects of multiple absorbing gases. The Beer-Lambert law for the actinic flux q_λ can also be written:

$$\mathrm{q}_\lambda(\mathrm{z},\chi) = \mathrm{q}_\lambda(\infty)\exp\left(-\tau_\mathrm{a}(\lambda,\mathrm{z},\chi)\right) = \mathrm{q}_\lambda(\infty)\mathrm{T}_\mathrm{r}(\lambda,\mathrm{z},\chi) \tag{4.41}$$

where $\mathrm{T_r} = \exp\left(-\tau_\mathrm{a}\right)$ is the *transmission function*, but in this case the value of the optical depth results from the sum of several terms which vary with the wavelength of incident radiation and the column amount of absorbing gases. For example, in the middle atmosphere, ultraviolet radiation is absorbed by molecular oxygen, or ozone, or both (see Table 4.1), such that one generally writes:

$$\tau_\mathrm{a}(\lambda,\mathrm{z},\chi) = \sec\chi\left[\int_\mathrm{z}^\infty \sigma_\mathrm{a}(\mathrm{O}_2,\lambda)(\mathrm{O}_2)\mathrm{dz} + \int_\mathrm{z}^\infty \sigma_\mathrm{a}(\mathrm{O}_3,\lambda)(\mathrm{O}_3)\mathrm{dz}\right] \tag{4.42}$$

When the solar zenith angle exceeds 75 degrees (sunrise or sunset), the effect of the earth's curvature can no longer be neglected and the secant must be replaced by a more complicated function (Chapman function), which depends not only on solar zenith angle χ but also on the altitude where the absorption occurs (see Box 4.1). The effect of refraction may also be important, especially for long optical paths and for radiation penetrating deep into the atmosphere. Figure 4.13b provides an estimate of the relative contributions of absorption by $\mathrm{O_2}$ and $\mathrm{O_3}$ for different wavelengths. The cross sections of each of these gases must be multiplied by their respective column abundances to compare their absorption effects. The effect of molecular oxygen dominates for wavelengths less than 220 nm but ozone absorption dominates near 250 nm and in the visible.

Box 4.1 Atmospheric Sphericity

The calculation of the optical depth

$$\tau(\mathrm{s}) = \int_{\mathrm{s}} \sigma_{\mathrm{a}} \mathrm{n}(\mathrm{s}) \mathrm{ds} \tag{1}$$

requires an integration of the absorption along the optical path s. In contrast to the troposphere, where inhomogeneities (*e.g.*, clouds) are often large, the middle atmosphere is generally stratified and more homogeneous. In this case, the plane-parallel approximation is generally satisfied, except for direct solar radiation at larger zenith angles. Under twilight conditions ($\chi > 75°$), the sphericity of the Earth must be taken into account by noting that the local solar zenith angle or its cosine value μ_0 vary along the optical path. Thus, under these conditions, the optical depth between a point at altitude z and the top of the atmosphere (∞) along the oblique path must be computed using the more complete expression

$$\tau(\mathrm{z}, \infty) = \int_{\mathrm{z}}^{\infty} \frac{\sigma_{\mathrm{a}} \mathrm{n}(\mathrm{z}') \mathrm{dz}'}{\mu_0(\mathrm{z}')} \tag{2a}$$

if

$$\frac{1}{\mu_0(\mathrm{z}')} = \frac{\mathrm{a} + \mathrm{z}'}{\left[(\mathrm{a} + \mathrm{z}')^2 - (\mathrm{a} + \mathrm{z})^2 \sin^2 \chi\right]^{1/2}} \tag{2.b}$$

where a is the Earth's radius and χ the solar zenith angle at altitude z. For the derivation of Eq. (2.b), see Figure 4.13a below.

Expressions similar to (4.42), in which the $\sec \chi$ factor is replaced by the *Chapman function* Ch(z,χ) are often used to account for the Earth's curvature. If the absorption cross section σ_{a} does not vary along the optical path,

$$\mathrm{Ch}(\mathrm{z}, \chi) = \frac{\int_{\mathrm{z}}^{\infty} \mathrm{n}(\mathrm{z}') \mathrm{dz}' / \mu_0(\mathrm{z}')}{\int_{\mathrm{z}}^{\infty} \mathrm{n}(\mathrm{z}') \mathrm{dz}'} \tag{3}$$

This function, also called the *airmass factor* represents the ratio of the total amount of absorbant along the optical path versus the amount of total absorbant in the vertical. For an isothermal atmosphere in which light refraction can be neglected, and assuming that the absorbing gas has a constant scale height H, the value of the Chapman function can be estimated by the following expressions (Smith and Smith, 1972):

$$\mathrm{Ch}(\mathrm{x}, \chi \leq \frac{\pi}{2}) \simeq \left[\frac{\pi \mathrm{x}}{2}\right]^{\frac{1}{2}} \exp\left(\mathrm{y}^2\right) \mathrm{erfc}\ (\mathrm{y})$$

$$\mathrm{Ch}(\mathrm{x}, \chi > \frac{\pi}{2}) \simeq \left[\frac{\pi \mathrm{x}}{2}\right]^{\frac{1}{2}} \left\{(\sin \chi)^{\frac{1}{2}} \exp\left[\mathrm{x}\,(1 - \sin \chi)\right]\right. \tag{4a}$$

$$\left. - \frac{1}{2} \exp\left(\mathrm{y}^2\right) \mathrm{erfc}\ (\mathrm{y})\right\} \tag{4b}$$

Box 4.1 (Continued)

where $x = (a + z)/H$, a is the Earth's radius, z the altitude and H is the atmospheric scale height, and where $y = [x/2]^{1/2}|\cos\chi|$ and erfc (y) = 1 − erf (y) is the complimentary error function. For $\chi = \frac{\pi}{2}$, (sunrise or sunset), Ch $(x, \frac{\pi}{2}) = (\frac{\pi x}{2})^{\frac{1}{2}}$. This function is equal to about 38 in the middle atmosphere. An empirical approximation to the Chapman function is given by the following expression:

$$\mathrm{Ch}\,(\chi > 85^\circ) \approx \frac{35}{\sqrt{1224 \cdot \cos^2\chi + 1}} \tag{5}$$

For absorbants whose distribution is not horizontally homogeneous, or do not vary exponentially with height, or if the absorption coefficient is not constant, the approximations discussed above are not valid. In this case, the calculation of the the optical depth must consider the full geometry of the problem.

- For solar zenith angles smaller than 90°, the optical depth can be computed by Eqs. (2a) and (2b)

- For solar zenith angles larger than 90°, the optical depth is given by

$$\tau(z, \infty) = 2\int_{z_0}^{z} \frac{\sigma_a n(z')}{\mu_0(z')} dz' + \int_{z}^{\infty} \frac{\sigma_a n(z')}{\mu_0(z')} dz' \tag{6}$$

  where $1/\mu_o(z)$ is given by (2b) and where

$$z_0 = a(\sin\chi - 1) + z\sin\chi \tag{7}$$

  is the lowest altitude encountered by the optical beam. Note that in expression (6), the dependence of the density n with latitude and longitude, which can be important, has been omitted.

- For a zenith angle of 90°, because of a discontinuity in expression (2b) when values of z' become close to the altitude z, the integration is performed along the optical path by noting that the increment Δs within a vertical layer $\Delta z'$ is given by (see Figure 4.13a within the box):

$$\begin{aligned} \Delta s = &\left[(a + z' + \Delta z')^2 - (a + z)^2 \sin^2\chi\right]^{1/2} \\ - &\left[(a + z')^2 - (a + z)^2 \sin^2\chi\right]^{1/2} \end{aligned} \tag{8}$$

Limb sounding retrievals use the approach to perform integrations along the line of sight.

Box 4.1 (Continued)

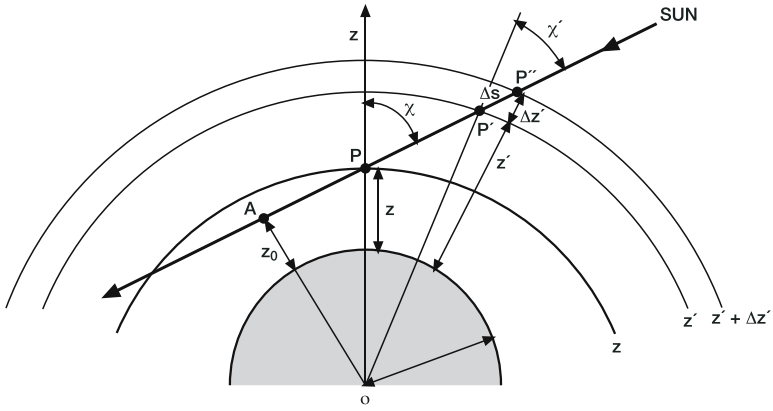

Figure 4.13a. Geometry for calculating the path length in a spherical atmosphere. Factor $\mu_0(z') = \cos\chi'$ is given by the ratio between the distances AP′ and OP′, with $AP' = \left[(a+z')^2 - (a+z)^2 \sin^2\chi\right]^{1/2}$ and $OP' = a+z'$, if a is the Earth's radius, χ and χ' the solar zenith angle at altitudes z and z′, respectively. The path length increment Δs is the difference between distances AP″ and AP′. The value of AP′ is given above. The value of AP″ is given by the same expression in which z′ is replaced by $z' + \Delta z'$. Adapted from Lopez-Puertas and Taylor (2001)

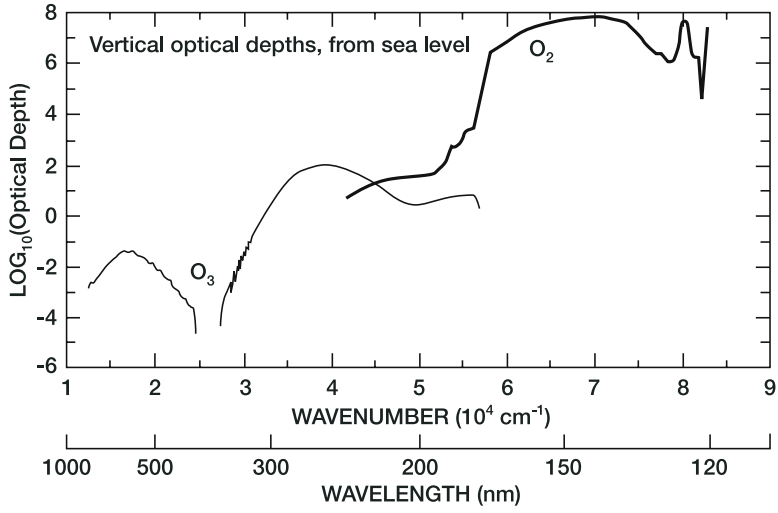

Figure 4.13b. Relative contributions of ozone and molecular oxygen to the vertical optical depth of the atmosphere. Courtesy of Sasha Madronich (NCAR).

In the visible region, the absorption by nitrogen dioxide can also contribute to the optical depth, especially in the lower stratosphere and troposphere. Moreover, molecular oxygen has two weak bands in the red region of the solar spectrum near 0.7 μm.

In the near infrared, the absorption of solar radiation is due chiefly to vibrational and rotational transitions of several atmospheric molecules. The most important absorber is water vapor with several absorbing bands between 0.8 and 3.2 μm. Carbon dioxide also exhibits absorption bands such as the 2.0 μm band, the 2.7 μm band (which overlaps with the 2.7 μm band of water vapor) and the 4.3 μm band, located in a spectral region where both solar and terrestrial radiation is weak. Since these bands consist of many narrow lines, the transmission function corresponding to a given spectral interval cannot be described in terms of the Beer-Lambert law and empirical formulas must be used in practical applications.

4.4.2 Scattering by Molecules and Aerosol Particles

In the optically denser layers of the atmosphere, solar radiation undergoes multiple scattering due to the presence of large concentrations of air molecules and aerosol particles. Scattering is a physical process by which a particle in the path of an electromagnetic wave abstracts energy from this incident wave and re-radiates that energy in all directions. The optical depth describing the attenuation of radiation is thus the result of two contributions (absorption and scattering):

$$\tau(\lambda, \mathrm{z}, \chi) = \tau_{\mathrm{a}}(\lambda, \mathrm{z}, \chi) + \tau_{\mathrm{s}}(\lambda, \mathrm{z}, \chi) \tag{4.43}$$

where

$$\tau_{\mathrm{s}}(\lambda, \mathrm{z}, \chi) = \sec\chi \int_{\mathrm{z}}^{\infty} \mathrm{k_s}(\lambda, \mathrm{z}')\mathrm{dz}' \tag{4.44}$$

or, in the case of scattering by air molecules M,

$$\tau_{\mathrm{s}}(\lambda, \mathrm{z}, \chi) = \sec\chi\, \sigma_{\mathrm{s}}(\lambda)\, \mathrm{n}(\mathrm{M};\mathrm{z})\, \mathrm{H}$$

$\mathrm{k_s}$ being the scattering coefficient, $\sigma_{\mathrm{s}}(\lambda)$ being the corresponding effective cross section, n(M;z) is the total concentration at altitude z and H is the atmospheric scale height. The albedo for single scattering can be defined as

$$\Omega = \frac{\mathrm{k_s}}{\mathrm{k_a} + \mathrm{k_s}} = \frac{\mathrm{k_s}}{\mathrm{k}} \tag{4.45}$$

which describes the relative importance of scattering versus the total attenuation. The parameter k is called the extinction coefficient. The

atmospheric particles responsible for scattering cover a range of sizes from gas molecules ($\approx 10^{-8}$cm) to large raindrops and hail particles ($\approx$cm). The relative intensity of the scattered light depends strongly on the ratio of the particle size to the wavelength of the incident radiation. When this ratio is small, the scattered light is distributed equally into the forward and backward directions (Rayleigh scattering).

The scattering of unpolarized light by air molecules is generally described by Rayleigh theory. In this case, the scattering coefficient is expressed as a function of wavelength λ by (see *e.g.*, Penndorf, 1957)

$$\mathrm{k_s} = \frac{8\pi^3}{3}\frac{(\mathrm{n}_\lambda^2 - 1)^2}{\lambda^4 \mathrm{n(M)}}\mathrm{D} \tag{4.46}$$

where n_λ represents the index of refraction of air and D is the depolarization factor which expresses the influence of molecular anisotropy. For air, a value of D of 1.06 is recommended (Penndorf, 1957; Elterman, 1968), although the depolarization is dependent on wavelength (Bates, 1984). Adopting an analytic expression for the wavelength dependence of the refractive index, the Rayleigh scattering cross section can be written as (adapted from Nicolet, 1984):

$$\sigma_\mathrm{s} = \frac{4.02 \times 10^{-28}}{\lambda^{3.677+0.389\lambda+0.094/\lambda}} \ \mathrm{cm}^2 \tag{4.47}$$

where λ is in μm.

Aerosols (solid or aqueous particles in the atmosphere) also interact with the radiation field. However, Rayleigh theory can no longer be applied to these particles, because the size of the aerosols is of the same order of magnitude or larger than the wavelength of the incident light.

The basic theory for the study of the scattering of light by aerosols was presented by Mie (1908). This theory generally assumes an ensemble of identical spherical particles and requires considerable computing resources for its solution. Modifications to allow for cylindrical and ellipsoidal particles have also been developed. In practice, simplified formulas are often used (see, *e.g.*, Van de Hulst, 1957). The total extinction coefficient at a particular wavelength can be determined by integration over all particle radii r

$$\mathrm{k}(\lambda) = \int_0^\infty \pi \mathrm{r}^2 \, \mathrm{Q_E}\,(\lambda, \mathrm{r}, n_\lambda)\, \frac{\mathrm{dn}}{\mathrm{dr}}\, \mathrm{dr} \tag{4.48}$$

where dn/dr (particles cm^{-3} μm^{-1}) represents the size distribution of the particles, and $\mathrm{Q_E}(\lambda, \mathrm{r}, n_\lambda)$ is the efficiency factor for attenuation of radiation at wavelength λ by a particle of radius r and index of refraction n_λ. $\mathrm{Q_E}$ is often expressed as the sum of an absorption and a scattering efficiency factor. An example of a stratospheric particle size distribution measured at Laramie, Wyoming, by Dehsler *et al.* (1993) on October 2,

1991 (22 km altitude) is shown in Figure 4.14a. In this case, most of the particles are believed to be sulfate aerosol with a peak in the size distribution near 0.07 μm.

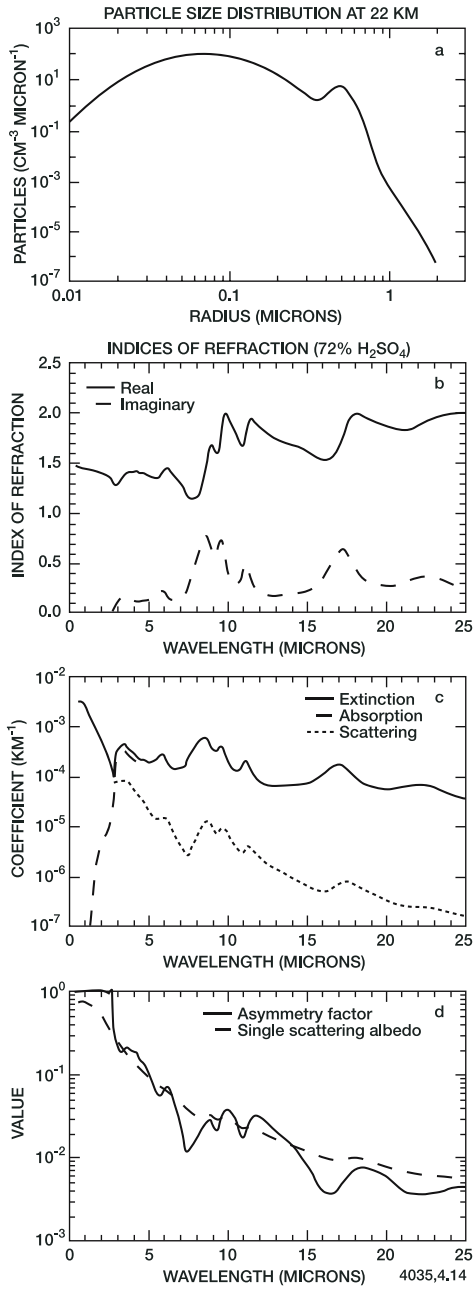

Figure 4.14. (a) Size distribution of aerosols measured on October 2, 1991 at 22 km over Laramie, Wyoming (Dehsler *et al.*, 1993). (b) Real and imaginary parts of the refraction index as a function of wavelength (0-25 μm) for sulfate aerosols (72% H_2SO_4 by weight). (c) Extinction, absorption, and scattering coefficients (km^{-1}) of aerosols for the particle size distribution shown as a function of wavelength in Panel a and the indices of refraction displayed in Panel b. (d) Single scattering albedo and asymmetry factor shown as a function of wavelength for aerosols as described in the previous panels. Courtesy of S. Massie, NCAR.

Another type of particle is also present as shown by the secondary peak near 0.5 μm. Note that atmospheric particles such as those present in polar stratospheric clouds, and ice crystals in the tropical lower stratosphere, have large radii and/or non-spherical shapes.

The real and imaginary parts of the index of refraction calculated for the sulfate aerosols (72% H_2SO_4 by weight) are shown as a function of wavelength in Figure 4.14b. (The real part of the refractive index determines the phase speed of a wave in a given medium while the imaginary part is a measure of the attenuation of the wave by this medium.) For wavelengths less than 3 μm, the imaginary part of the index is negligible, suggesting that the stratospheric sulfate aerosol primarily scatters light in the visible. The extinction, absorption, and scattering coefficients (expressed in km^{-1}) for the particle size distribution given in Figure 4.14a and for the indices of refraction given in Figure 4.14b are presented in Figure 4.14c (assuming that the particles are spherical and applying Mie theory). The total extinction is primarily due to absorption for wavelengths greater than 3 μm, and primarily due to scattering for wavelengths shorter than 2 μm. Also notice that the extinction at visible wavelengths (less than 1μm) is 10 to 30 times larger than the extinction in the infrared. Finally, Figure 4.14d shows the wavelength dependence of the single scattering albedo (see Eq. 4.45) and of the asymmetry factor g defined by

$$g = \int_{-1}^{+1} p(\Theta) \cos\Theta \, d\cos\Theta \tag{4.49}$$

where Θ is the angle between the direction of the incident light beam and the direction of the scattered beam. The phase function $p(\Theta)$ measures the intensity pattern of light scattered off of the aerosol particle for each angle Θ. When the asymmetry factor is negative, most of the light is scattered in the backward direction, while particles with positive g scatter light primarily in the forward direction.

4.5 Radiative Transfer

4.5.1 The Radiative Transfer Equation

The radiation field in the atmosphere is determined from the equation of radiative transfer (Chandrasekhar, 1950; Kourganoff, 1952; Sobolev, 1963; Lenoble, 1977), which is an expression of the energy balance in each unit volume of the atmosphere, including absorption, scattering, and emission. In the case of a horizontally stratified medium, the following expression can be used to describe the radiative transfer in

a layer bounded by two infinite parallel planes (Lenoble, 1977):

$$\frac{\mu \mathrm{dL}_\nu(\mathrm{z};\mu,\phi)}{\mathrm{dz}} = -\mathrm{k}_\nu(\mathrm{z})\left[\mathrm{L}_\nu(\mathrm{z};\mu,\phi) - \mathrm{J}_\nu(\mathrm{z};\mu,\phi)\right] \tag{4.50}$$

where L_ν $(\mathrm{z};\mu,\phi)$ is the spectral density of the radiance, $\mathrm{k}_\nu(\mathrm{z})$ is the extinction coefficient and $\mathrm{J}_\nu(\mathrm{z};\mu,\phi)$ is called the source function at altitude z and for the direction μ,ϕ. J_ν expresses the incoming radiation due either to scattering from all other directions (μ',ϕ') of solar radiation, or to thermal emission by atmospheric molecules. The importance of these contributions varies with the spectral domain under consideration. When the source function can be neglected ($\mathrm{J}_\nu = 0$), a simple exponential extinction expression is obtained. It should also be noted that in many studies, the altitude variable z is replaced by the equivalent variable τ_ν, which represents the optical depth for vertically incident radiation ($\mathrm{d}\tau_\nu = -\mathrm{k}_\nu \mathrm{dz}$). In this case, the radiative transfer equation can be written as:

$$\frac{\mu \mathrm{dL}_\nu(\tau_\nu;\mu,\phi)}{\mathrm{d}\tau_\nu} = \mathrm{L}_\nu(\tau_\nu;\mu,\phi) - \mathrm{J}_\nu(\tau_\nu;\mu,\phi) \tag{4.51}$$

When the atmosphere is assumed to be stratified and plane-parallel, it is common to introduce the radiance $\mathrm{L}_\nu \uparrow$ and $\mathrm{L}_\nu \downarrow$ describing upward and downward propagating photons, as was presented previously for the flux (see Eqs. 4.39 and 4.40). In this case, integrating (Eq. 4.51), we obtain:

$$\begin{aligned}\mathrm{L}_\nu \uparrow (\tau_\nu;\mu,\phi) =& \mathrm{L}_\nu \uparrow (\tau_{\nu,1};\mu,\phi)\, \mathrm{e}^{(\tau_{\nu,1}-\tau_\nu)/\mu} \\ &- \frac{1}{\mu}\int_{\tau_\nu}^{\tau_{\nu,1}} \mathrm{J}_\nu(\tau'_\nu;\mu,\phi)\, \mathrm{e}^{(\tau'_\nu-\tau_\nu)/\mu}\mathrm{d}\tau'_\nu\end{aligned} \tag{4.52}$$

for $\mu > 0$, and

$$\begin{aligned}\mathrm{L}_\nu \downarrow (\tau_\nu;\mu,\phi) =& \mathrm{L}_\nu \downarrow (0;\mu,\phi)\, \mathrm{e}^{-\tau_\nu/\mu} \\ &+ \frac{1}{\mu}\int_{0}^{\tau_\nu} \mathrm{J}_\nu(\tau'_\nu;\mu,\phi)\, \mathrm{e}^{(\tau'_\nu-\tau_\nu)/\mu}\mathrm{d}\tau'_\nu\end{aligned} \tag{4.53}$$

for $\mu < 0$ where the source function J_ν depends on the radiance L_ν, at least when scattering cannot be neglected (see Section 4.5.2). To solve these equations, certain boundary conditions must be specified. For example, outside of the atmosphere one can assume that the only downward propagating radiation is that emitted by the Sun. At lower altitudes (surface or clouds) ($\tau_\nu = \tau_{\nu,1}$) one can assume that short wavelength incident radiation is isotropically reflected by the surface of albedo A ($0.0<\mathrm{A}<1.0$). A more accurate treatment allows for an angular dependence of A. For long wave radiation, it is usually assumed that the Earth's surface emits approximately as a black body at temperature $\mathrm{T_s}$.

Note that the Earth's surface infrared and microwave emissivity is a function of vegetation, snow cover, soil moisture, sea conditions, etc.

4.5.2 Solution of the Equation of Radiative transfer for Wavelengths Less than 3.5 μm: Multiple Scattering

As indicated previously, shortwave radiation below 3.5 μm originates from the Sun. When the direct flux penetrates into the atmosphere, it is progressively attenuated by absorption (τ_{a}) and scattering (τ_{s}). In this case, the source function must account for the diffuse radiation scattered into the beam from other directions (μ', ϕ') as well as the direct sunlight scattered into the direction of the pencil of radiation. If $\Phi_\nu(\infty)$ is the solar irradiance at the top of the atmosphere and (μ_o, ϕ_o) the direction of the sun, the source function is given by (Lenoble, 1977):

$$\mathrm{J}_\nu(\tau_\nu;\mu,\phi) = \frac{\Omega_\nu(\tau_\nu)}{4\pi}\int_0^{2\pi}\mathrm{d}\phi'\int_{-1}^{1}\mathrm{p}_\nu(\tau_\nu;\mu,\phi;\mu',\phi')\mathrm{L}_\nu(\tau_\nu;\mu',\phi')\mathrm{d}\mu' + \frac{\Omega_\nu(\tau_\nu)}{4\pi}\mathrm{p}_\nu(\tau_\nu;\mu,\phi;\mu_o,\phi_o)\Phi_\nu(\infty)\mathrm{e}^{-\tau_\nu/\mu_o} \tag{4.54}$$

where $\Omega(\tau_\nu)$ is the albedo for single scattering (see Eq. 4.45) and $\mathrm{p}_\nu(\tau_\nu;\mu,\phi;\mu',\phi')$ is the phase function defining the probability that a photon propagating in the direction (μ', ϕ') is scattered in the direction (μ, ϕ). Thus, the first term in equation (4.54) represents multiple scattering effects, while the second term represents the contribution of first-order scattering.

If the atmosphere is perfectly clear (neglecting the presence of solid and liquid particulates), the scattering is due only to air molecules and Rayleigh theory can be applied. The corresponding attenuation coefficient is given by the equation (4.46), and the phase function is given by:

$$\mathrm{p}(\Theta) = \frac{3}{4}(1+\cos^2\Theta) \tag{4.55}$$

where

$$\cos\Theta = \mu\mu' + (1-\mu^2)^{\frac{1}{2}}(1-\mu'^2)^{\frac{1}{2}}\cos(\phi-\phi') \tag{4.56}$$

Θ being the angle between incident and scattered light.

The scattering by solid and liquid particulates constitutes a more difficult problem (see, *e.g.*, McCartney, 1976; Bohren and Huffman, 1983). If the particles may be assumed spherical, Mie theory can be invoked. In this case, for aerosols of radius r, the phase function is given

by

$$p(r,\Theta) = \frac{\lambda^2}{2\pi k_s(r)}(S_1 S_1^* + S_2 S_2^*) \tag{4.57}$$

where the coefficients are given by the following expressions:

$$S_1(\Theta) = \sum_{n=1}^{\infty} \frac{2n+1}{n(n+1)} \left(\frac{a_n dP_n^1}{d\Theta} + b_n \frac{P_n^1}{\sin\Theta} \right) \tag{4.58a}$$

$$S_2(\Theta) = \sum_{n=1}^{\infty} \frac{2n+1}{n(n+1)} \left(a_n \frac{P_n^1}{\sin\Theta} + b_n \frac{dP_n^1}{d\Theta} \right) \tag{4.58b}$$

P_n^1 is the associated Legendre polynomial and a_n and b_n are coefficients depending on the index of refraction and on the Mie parameter $\alpha_a = 2\pi r/\lambda$. S^* is the complex conjugate of S and k_s is the scattering coefficient

$$k_s(r) = \frac{2\pi r^2}{\alpha_a^2} \sum_{n=1}^{\infty} (2n+1)(a_n^2 + b_n^2) \tag{4.59}$$

The number of significant terms in this series is of the order of $2\alpha_a + 3$.

In the presence of an ensemble of aerosols characterized by a distribution function $f(r_a)$, the phase function $p(\Theta)$ is deduced from a function related to a specific radius r_a by the relation

$$p(\Theta) = \frac{\int_0^{\infty} p(r_a,\Theta)\sigma(r_a) f(r_a)\, dr_a}{\int_0^{\infty} \sigma(r_a) f(r_a)\, dr_a} \tag{4.60}$$

Mie theory can be extended to non-spherical particles (such as ice crystals, for example) but it is often sufficient to assume that randomly oriented irregular particles scatter light in the same way that spherical particles do.

Several analytic methods have been proposed to solve the equation of radiative transfer in an absorbing and scattering atmosphere, but they can only be applied for the most simple cases. To obtain quantitative solutions, numerical methods are generally used, such as the Monte-Carlo method, DART method, iterative Gauss, discrete ordinate method, etc. A complete summary of these techniques is provided by Lenoble (1977), and a detailed discussion of multiple scattering processes in plane parallel atmospheres is given in the book by Liou (2002).

Because multiple scattering, surface reflection, clouds, and aerosols have a significant effect on radiative intensities at photodissociative wavelengths and consequently on the composition of the middle atmosphere (see, *e.g.*, Luther *et al.*, 1978), simplified radiative transfer

schemes are often used in photochemical models. In the two-stream methods, for example, (Meador and Weaver, 1980; Toon *et al.*, 1989), the diffuse radiation is divided into upward-propagating and downward-propagating components. One commonly-used example is the delta-Eddington method (Joseph *et al.*, 1976). These methods allow for at least approximate representations of the non-isotropic scattering by aerosol and cloud particles, and are typically accurate to about 5% or better in the stratosphere, and to about 10-20% in the troposphere (Petropavlóvskikh, 1995). Multi-stream methods, in which the angular distribution of the diffuse radiation is computed in greater detail (*e.g.*, the discrete ordinates method of Stamnes *et al.*, 1988) are more accurate, but also considerably more computationally intensive.

The model of Meier *et al.* (1982) and Nicolet *et al.* (1982) solves a form of the radiative transfer equation in which the radiance is integrated over all solid angles, and provides the solar actinic flux Φ at wavelength λ or the enhancement factor or source function. The latter is defined by $S = \Phi/\Phi_\infty$, where Φ_∞ is the solar actinic flux at the top of the Earth's atmosphere. A schematic diagram of their model (which assumes that the phase function for scattering is isotropic) is presented in Figure 4.15. It can be shown that the calculated source function S at altitude z results from four contributions: 1) the direct solar flux, 2) the multiply-scattered flux, 3) the ground reflection of

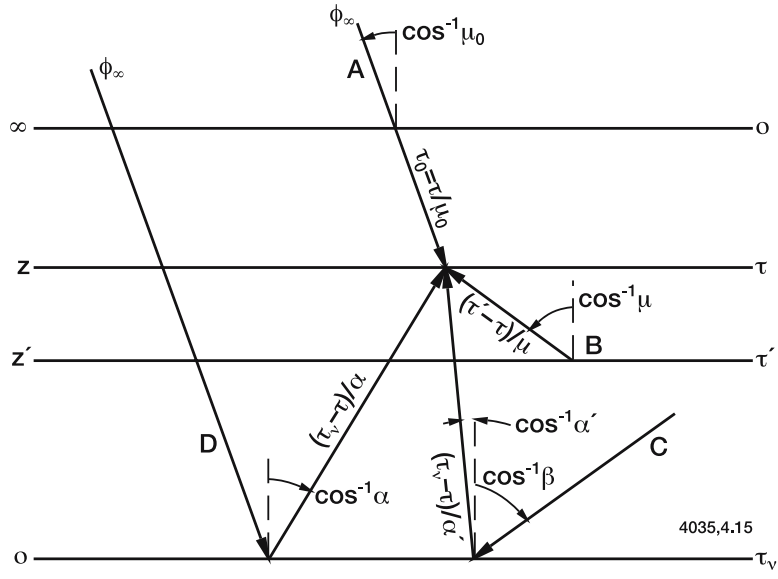

Figure 4.15. Schematic diagram of the scattering model by Meier *et al.*(1982).

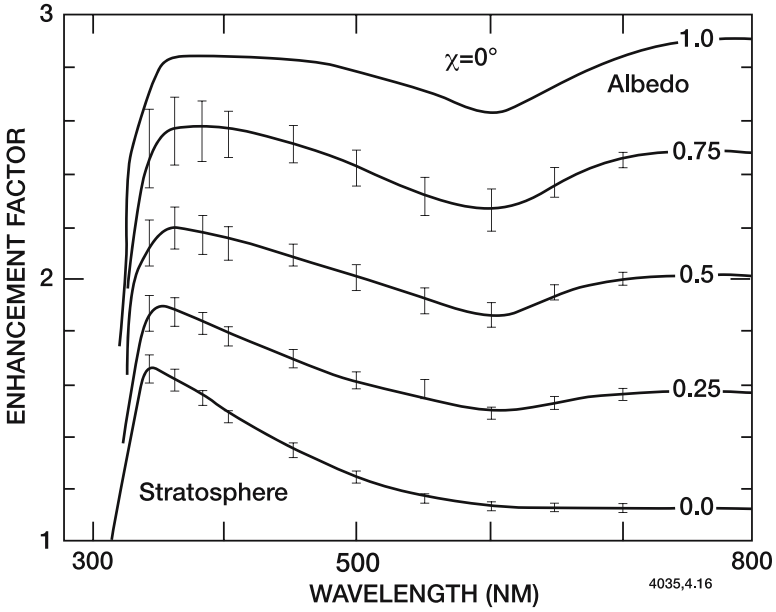

Figure 4.16. Stratospheric enhancement factor calculated by Meier *et al.*(1982) for different values of the albedo.

the multiply-scattered flux, and 4) the ground reflection of the direct flux. The mean enhancement factor in the stratosphere between 300 and 800 nm for different values of the albedo and for an overhead sun is shown in Figure 4.16. The "error bars" indicate the variability of the S factor between the tropopause and the stratopause, suggesting that for $\lambda > 400$ nm a single enhancement factor can be applied to the entire atmosphere with a good accuracy. The S factor as a function of altitude for wavelength intervals from 240 to 700 nm is shown in Figure 4.17a, b, and c for different cases. Figure 4.17a shows the results ignoring the effect of multiple scattering and reflection at ground level. In this case, the enhancement factor is simply the transmission factor which characterizes the attenuation by absorption as well as by Rayleigh and Mie scattering. In the visible part of the spectrum, the attenuation occurs near ground level, while in the UV region, the flux is reduced by the presence of ozone at higher altitudes. The effect of multiple scattering, neglecting ground albedo, appears in Figure 4.17b. The contribution of the scattered light to the radiation field is large except at short wavelengths where pure absorption is strong. At 350 to 400 nm, for example, the scattering provides an additional irradiance of about 50 percent. Finally, Figure 4.17c shows the S factor when both multiple scattering and ground albedo (A = 0.5) are taken

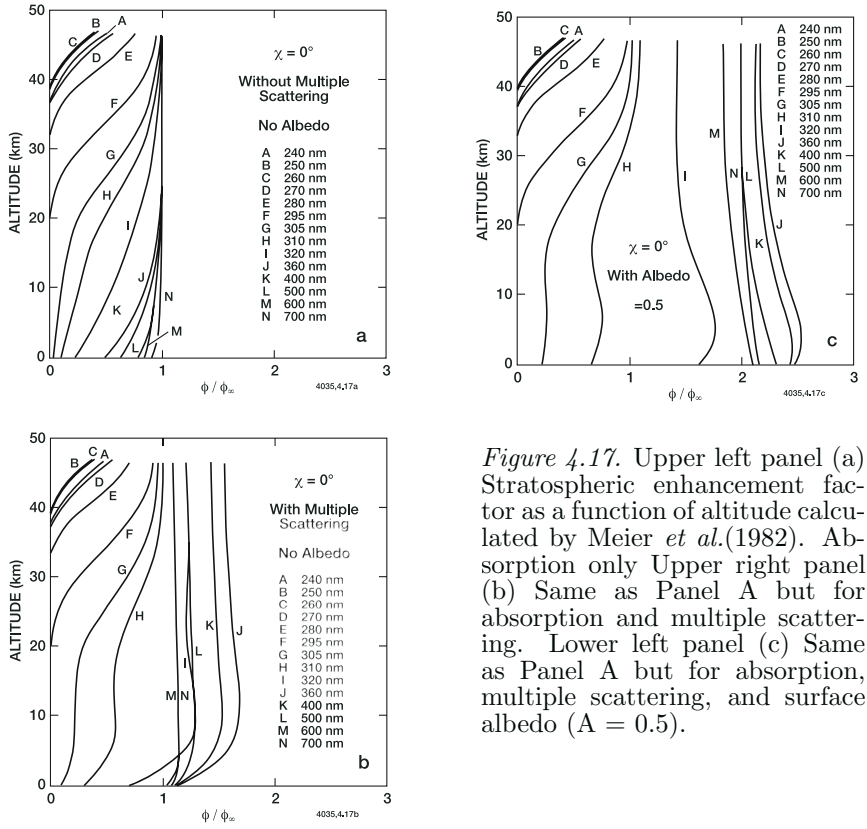

Figure 4.17. Upper left panel (a) Stratospheric enhancement factor as a function of altitude calculated by Meier *et al.*(1982). Absorption only Upper right panel (b) Same as Panel A but for absorption and multiple scattering. Lower left panel (c) Same as Panel A but for absorption, multiple scattering, and surface albedo (A = 0.5).

into account. The enhancement factor is now greater than 2 even at higher altitudes for radiation of wavelength longer than 320 nm. The multiple scattering and albedo will therefore considerably affect the photodissociation of molecules whose absorption cross sections are large above 300 nm (O_3, NO_2, N_2O_5, NO_3, $ClONO_2$). Figure 4.18 shows the scattered radiance measured in the upper stratosphere between 175 and 325 nm for two viewing elevation angles. The actinic flux spectrum recorded above the atmosphere by the spaceborne SUSIM instrument is also shown. The effects of ozone absorption in the ozone Hartley band (220-290) and of O_2 absorption in the Schumann-Runge bands below 200 nm are clearly seen in the observed radiance. Radiances measured at negative viewing elevation angles are larger in spectral regions with small absorption optical depths (195-220 nm and > 285 nm) and smaller in regions where absorption dominates. Scattered solar ultraviolet radiation is an essential component of stratospheric photochemistry

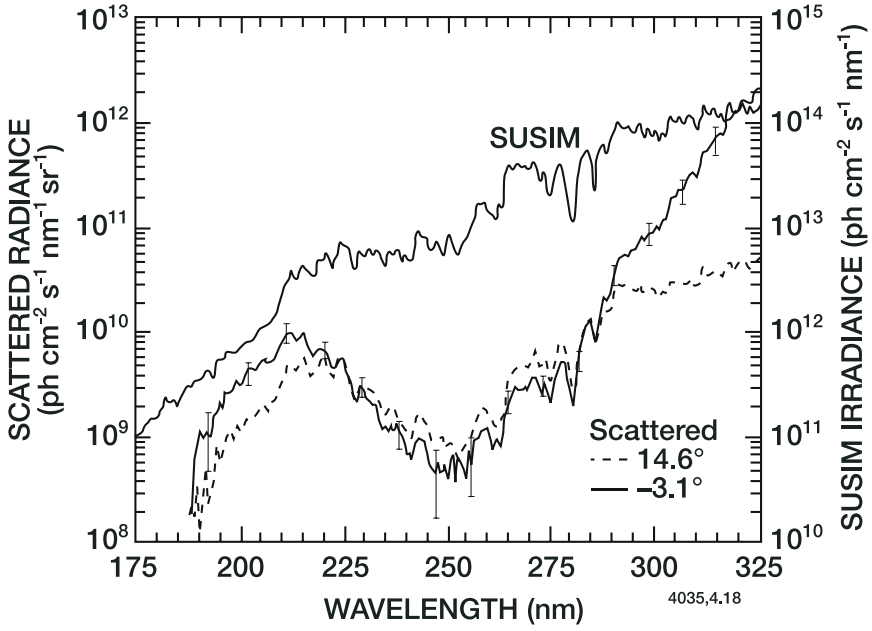

Figure 4.18. Observed scattered radiance at 46.3 km for viewing elevation angles at 14.6° and −3.1° along with SUSIM measurements of the solar irradiance above the atmosphere by the Solar Ultraviolet Spectral Irradiance Monitor (SUSIM; van Hoosier *et al.*, 1988). The solar zenith angle at the time of the scattered radiance measurements during a 1983 balloon flight over Palestine, Texas, is 28°. From Minschwaner *et al.* (1995).

(Herman and Mentall, 1982a; Kylling *et al.*, 1993; Minschwaner *et al.*, 1995) as scattered radiation in many cases dominates the actinic flux and has an important effect on the photolysis of key chemical species (*e.g.*, O_3, NO_2, HNO_3). The measurement of scattered and absorbed solar radiation can provide information on the abundance of several chemical compounds (*e.g.*, ozone, aerosols in the atmosphere) (see Box 4.2).

The presence of clouds in the troposphere modifies somewhat the radiation field in the stratosphere (Lacis and Hansen, 1974) by altering the albedo and introducing a highly scattering medium. Because the reflectance properties of clouds vary considerably with cloud type, numerical models dealing with this problem have to define statistical properties of the cloud distribution.

Box 4.2 Space Observations of Atmospheric Compounds by Solar Absorption Techniques

The atmospheric abundance of some chemical compounds that absorb solar radiation (*e.g.*, ozone) can be measured from space through different techniques.

In the *solar occultation* method a space-borne detector (*e.g.*, photomultiplier tube, photolytic array detector, Fourrier transformed interferometer) points towards the Sun, and during brief periods (sunrise, sunset), when the optical path penetrates into the atmosphere (see Figure 4.19a), measures the attenuation of the solar radiation by the absorbing compounds. The intensity at frequency ν detected by the spacecraft is

$$\mathrm{I}_\nu = \mathrm{I}_{\infty,\nu} \exp\left[-\sigma_\nu \int_{-\infty}^{+\infty} \mathrm{n(s)}\,\mathrm{ds}\right] \qquad (4.61)$$

if $\mathrm{I}_{\infty,\nu}$ is the intensity of the exo-atmospheric solar radiation (measured by the spacecraft when the optical path of the detected radiation does not penetrate into the atmosphere), σ_ν is the (known) absorption cross section of the absorbant at frequency ν, and n(s) is the number density of the absorbing compound along optical paths. (For simplicity, we consider only one absorbing gas).

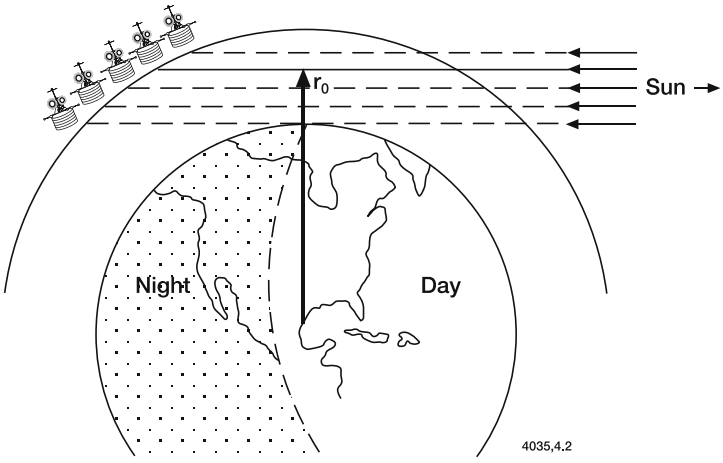

Figure 4.19a. Geometry of solar occultation. McCormick *et al.*(1979)

Assuming that this absorbant is uniformly distributed in each atmospheric layer (and hence that its concentration varies only with height), the integrated concentration N along the optical path with tangent height r_0 (slant column density) can be derived from the observation of I_ν and $\mathrm{I}_{\nu,\infty}$ through Eq. (4.61), when

Box 4.2 (Continued)

$$N(r_0) = \int_{-\infty}^{+\infty} n(s)\,ds = 2\int_{r_0}^{\infty} \frac{r\,n(r)dr}{\sqrt{r^2 - r_0^2}} \tag{4.62}$$

if n(r) represents the vertical profile of the concentration (note that r and r_0 are defined from the center of the earth). The inversion of Equation (4.62) to derive the vertical profile n(r) is often performed using an "onion peeling" method in which the atmosphere is divided into a finite number of vertical layers, and the concentration of the absorbing compound is calculated successively from the top of the atmosphere to the bottom layer. Note that in some cases absorbing constituents are not uniformly distributed in the layers, especially if their concentrations are strongly affected by photochemical conditions. In this case, a correction must be applied (see *e.g.*, Newchurch *et al.*, 1996).

One of the advantages of the solar occultation method is that the concentrations are derived from the measurement of a ratio of 2 fluxes, and therefore are not substantially affected by instrument calibration errors or solar spectral features. Because of the observing geometry involved, this technique provides good vertical resolution. The major limitation results from the limited number of observations due to the sunrise or sunset contraints. Better coverage can be obtained by considering, in addition, lunar and stellar occultations.

Assuming that the column N(z) above altitude z is proportional to the pressure at level z,

$$N(z) = c\,p(z) \tag{4.63}$$

and noting that further attentuation occurs as the scattered light propagates towards the top of the atmosphere, the radiance I_ν measured by the spacecraft is proportional to

$$I_\nu = I_{\nu,\infty} \int_0^{\infty} p(z) \exp\left[-2\sigma_\nu c\,p(z)\right] dz \tag{4.64}$$

It can easily be shown that the largest contribution to this integral is provided by the atmospheric layer at pressure

$$p = [2\sigma_\nu c]^{-1} \tag{4.65}$$

Thus, by choosing a set of wavelengths for which the cross section σ_ν is notably different, the mole fraction of the absorbant (proportional to c) can be retrieved at different altitudes. This method is commonly used to measure the vertical distribution of ozone in the stratosphere on the global scale. The vertical resolution, however, is not better than several kilometers.

The total ozone column abundance can be obtained by measuring the differential absorption of reflected near-UV radiance at two distinct wave-

Box 4.2 (Continued)

lengths (corresponding to strong and weak absorption by ozone, respectively) (see Bhartia *et al.*, 1984).

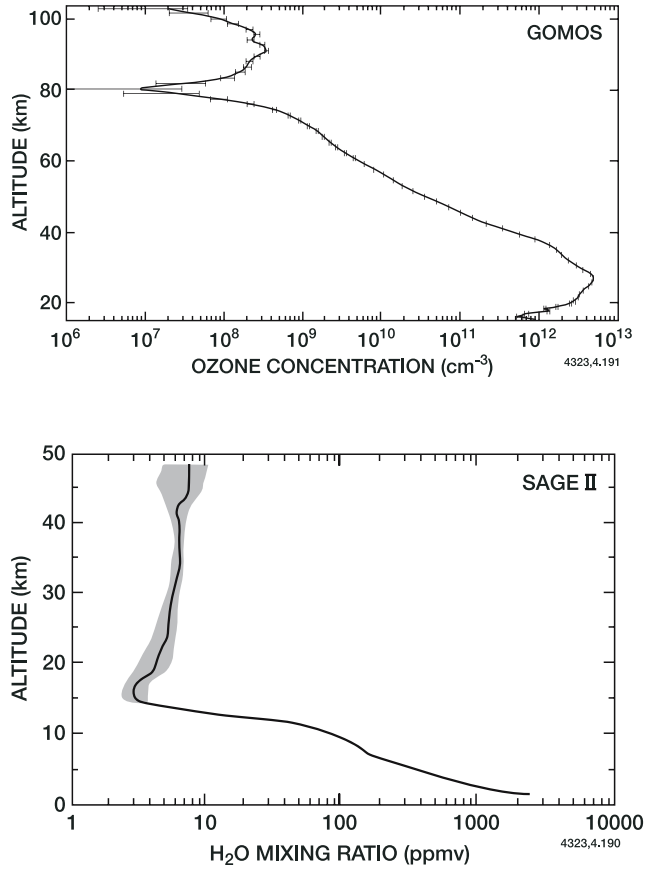

Figure 4.19b. Vertical profiles of chemical compounds retrieved from satellite observations based on occultation methods. Upper Panel: Nighttime ozone number density (cm^{-3}) measured on 24 March 2002 from the tropopause to the mesopause levels (15°N, 115°E) by the GOMOS instrument on board the ENVISAT spacecraft (stellar occultation). Courtesy of J.L. Bertaux and A. Hauchecorne, Service d'Aéronomie du CNRS, France. Lower Panel: Water vapor mixing ratio (ppmv) between the surface and 50 km altitude (33°N, 125°W) measured by SAGE II on 11 January 1987 (solar occultation). Courtesy of M. Geller, State University of New York.

4.5.3 Solution of the Radiative Transfer Equation at Wavelengths Longer than 3.5 μm: Absorption and Emission of Infrared Radiation

In the infrared region above 3.5 μm, the contribution from terrestrial radiation dominates the solar input. Significant thermal emission and absorption by atmospheric gases and aerosols take place in this spectral region. Scattering can usually be neglected. The detailed study of radiative transfer requires complete knowledge of the important bands and a compilation of a large body of spectroscopic data (see, *e.g.*, Rothman *et al.*, 1998, and references therein).

Figure 4.20 shows the infrared emission spectrum recorded by a down-looking spaceborne instrument. Also shown are the black body curves for several temperatures. The deviations in the observed spectrum from black body behavior can be attributed to the nonisothermal character of the atmosphere and the variation of the atmospheric opacity with wavelength (or wavenumber). Highest emissions correspond to infrared fluxes originating from the warm surface of the Earth in quasi-transparent spectral regions (called *windows*). Lowest spectral emissions correspond to spectral regions where absorption by atmospheric molecules is strong, and hence the observed radiation originates from the cold layers of the upper troposphere.

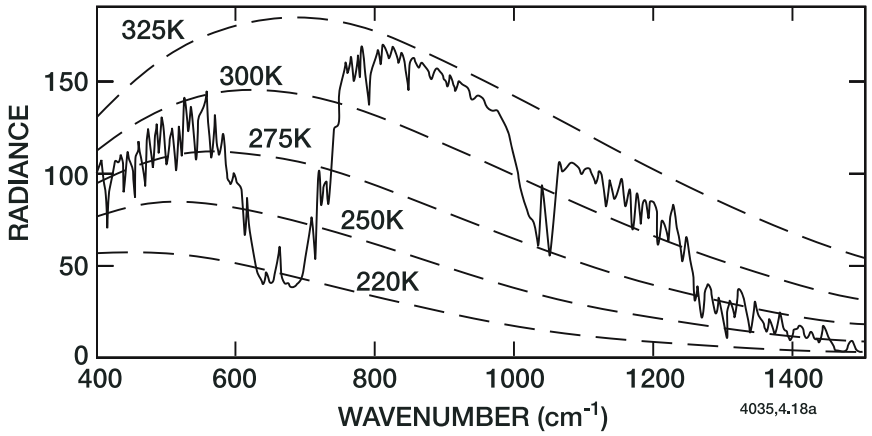

Figure 4.20. Thermal emission spectrum of the Earth recorded by the IRIS Michelson interferometer on board the Nimbus 4 satellite over the Sahara region. Strong absorption by CO_2 (15 μm or 667 cm^{-1}), and ozone (9.6 μm or 1041 cm^{-1}) and water bands are clearly visible. From Hanel and Courath (1970).

The radiatively active trace gases, which contribute most to atmospheric absorption, and hence play a key role in the energy budget of the middle atmosphere, are carbon dioxide, ozone, and water vapor. Other gases, whose sources are partly related to anthropogenic activity (such as CH_4, N_2O, and chlorofluorocarbons) also contribute to the radiation budget.

Carbon dioxide is a linear molecule which has a relatively simple absorption spectrum. One of the strongest bands is the ν_2 fundamental at 15 μm, which contributes significantly to the energy budget of the atmosphere. The ν_3 band at 4.3 μm is also strong and rivals heating by ozone in the middle mesosphere. Additional weak bands centered in the 12-18 μm, 10 μm, and 7.6 μm regions must be considered in the CO_2 climate problem, as discussed by Kiehl and Dickinson (1987).

Ozone is a non-linear molecule, and possesses strong rotational structure as well as 3 fundamental vibration bands, ν_1, ν_2, and ν_3 at 9.066, 14.27, and 9.597 μm, respectively. The ν_2 band overlaps the 15 μm CO_2 band, but the ν_1 and ν_3 transitions form the important 9.6 μm band. Another strong ozone band at 4.7 μm is located in a spectral region with weak solar and terrestrial irradiances.

Water vapor is a non-linear molecule with a complex vibration-rotation spectrum. The ν_2 fundamental band centered at 6.25 μm is overlaid with a series of rotational transitions to make a broad intense band centered at 6.3 μm. A wide pure rotation band extends from about 18 to beyond 100 μm with varying intensity. The ν_1 and ν_3 fundamentals at 2.74 and 2.66 μm absorb a significant amount of solar energy, particularly in the troposphere. Table 4.3 lists the principal spectral bands which are important for climate studies, including the bands from radiatively active constituents which play a secondary role in the radiation budget. Figure 4.21 shows the absorption of radiant energy by the gases which contribute significantly to radiative transfer in the atmosphere (see also Plate 6). This figure shows that each gas has a particular absorption signature which is wavelength dependent. The observation of absorbed or emitted terrestrial radiation in these wavelength bands can yield important information about the distributions of these gases in the atmosphere.

Throughout most of the middle atmosphere, the primary energy loss occurs via radiative emission in the ν_2 band of CO_2 at 15 μm. The contribution of this band to the total cooling has been studied in detail below 100 km (López-Puertas *et al.*, 1992; Mertens *et al.*, 1999; Mlynczak *et al.*, 1999). Dickinson (1973) and Ramanathan (1976) indicated the importance of the CO_2 hot bands in the calculation of the cooling rate. In the region of the atmosphere where the conditions of local thermodynamic equilibrium (LTE) apply, (that is when collisions

Table 4.3 Important infrared atmospheric bands (From WMO, 1982)

Trace gas	Band	Band center cm^{-1}	Band intensity cm^{-2} atm^{-1} (296K)
CO_2	ν_2 (15 μm)	667	≈220
CO_2	ν_3 (4.3 μm)	2348	≈2440
O_3	ν_3 (9.6 μm)	1041	312
H_2O	rotation	0–1650	1306
H_2O	ν_2 (6.3 μm)	640–2800	257
CH_4	ν_4 (7.66 μm)	1306	134
N_2O	ν_1 (7.78 μm)	1285	218
N_2O	ν_2 (17 μm)	589	24
$CFCl_3$	ν_4 (11.8 μm)	846	1813
$CFCl_3$	$\nu_1 + 2\nu_2$	1085, 2144	679
CF_2Cl_2	ν_8 (10.9 μm)	915	1161
CF_2Cl_2	ν_1 (9.13 μm)	1095	1141
CF_2Cl_2	ν_6 (8.68 μm)	1152	777

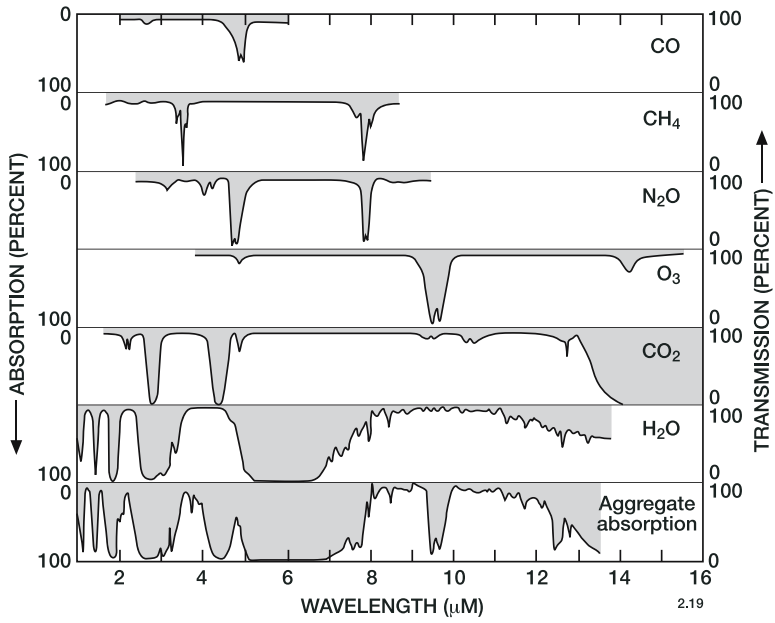

Figure 4.21. Spectral distribution of the absorption by several radiatively active gases (from the Earth's surface to infinity). The aggregate spectrum due to all atmospheric gases is shown in the bottom panel (adapted from Shaw, 1953).

are sufficiently frequent that the energy levels are populated according to a Boltzmann distribution, see Eq. 2.44) then the source function is:

$$\mathrm{J}_\nu(\tau_\nu) = \mathrm{B}_\nu(\mathrm{T}(\tau_\nu)) \tag{4.66}$$

where B_ν (T (τ_ν)) is given by Planck's law:

$$\mathrm{B}_\nu(\mathrm{T}(\tau_\nu)) = \frac{2\mathrm{h}\nu^3}{\mathrm{c}^2}\frac{1}{\mathrm{e}^{\mathrm{h}\nu/\mathrm{kT}} - 1} \tag{4.67}$$

The radiance over most of the middle atmosphere (below 75 km) can thus be derived from the transfer equation (called Schwarzchild's equation, see *e.g.*, Liou, 2002):

$$\mu\frac{\partial \mathrm{L}_\nu(\tau_\nu;\mu,\phi)}{\partial\tau_\nu} = \mathrm{L}_\nu(\tau_\nu;\mu,\phi) - \mathrm{B}_\nu(\tau_\nu) \tag{4.68}$$

In other words, assuming azimuthal symmetry (no dependence of the radiance on ϕ) and making use of equations (4.52) and (4.53), the upward and downward components of the radiance will be evaluated from equations of the following type:

$$\mathrm{L}_\nu \uparrow (\mathrm{z};\mu) = \mathrm{B}_\nu(\mathrm{T_s})\mathrm{T}_{\mathrm{r},\nu}(\mathrm{z},0;\mu) + \int_0^{\mathrm{z}} \mathrm{B}_\nu(\mathrm{z}')\frac{\partial \mathrm{T}_{\mathrm{r},\nu}(\mathrm{z}',\mathrm{z};\mu)}{\partial \mathrm{z}'}\mathrm{dz}' \tag{4.69a}$$

and

$$\mathrm{L}_\nu \downarrow (\mathrm{z};\mu) = -\int_{\mathrm{z}}^{\infty} \mathrm{B}_\nu(\mathrm{z}')\frac{\partial \mathrm{T}_{\mathrm{r},\nu}(\mathrm{z}',\mathrm{z};\mu)}{\partial \mathrm{z}'}\mathrm{dz}' \tag{4.69b}$$

where $\mathrm{T_s}$ is the temperature of the Earth's surface and z is the altitude, while

$$\mathrm{T}_{\mathrm{r},\nu}(\mathrm{z},\mathrm{z_o};\mu) = \exp\left(-\int_{\mathrm{z_o}}^{\mathrm{z}} \mathrm{k}_\nu \mathrm{dz}'/\mu\right) = \exp\left(-\sigma_\nu \mathrm{N}\right) \tag{4.70}$$

is the transmission function at frequency ν (see Eq. 4.25) for an optical path from $\mathrm{z_o}$ to z with inclination μ. The quantity N represents the integrated amount of absorbing gas between altitudes $\mathrm{z_0}$ and z, and σ_ν is the effective absorption cross section at frequency ν. Equation (4.69a) provides the formalism that is central to infrared remote sounding of the atmosphere from space (see Box 4.3).

The solution of equations (4.69a,b) is complex since the absorption spectrum exhibits structure characterizing the numerous rotation and vibration-rotation lines of atmospheric molecules. The absorption coefficient or the transmission function $\mathrm{T}_{\mathrm{r},\nu}$ varies therefore considerably over small regions of frequency (or wavenumber) and in principle a line-by-line integration is required. Figure 4.22 shows, for example, the vertical transmittance through the atmosphere at the edge of the strong 15 μm CO_2 bands (Edwards, 1992).

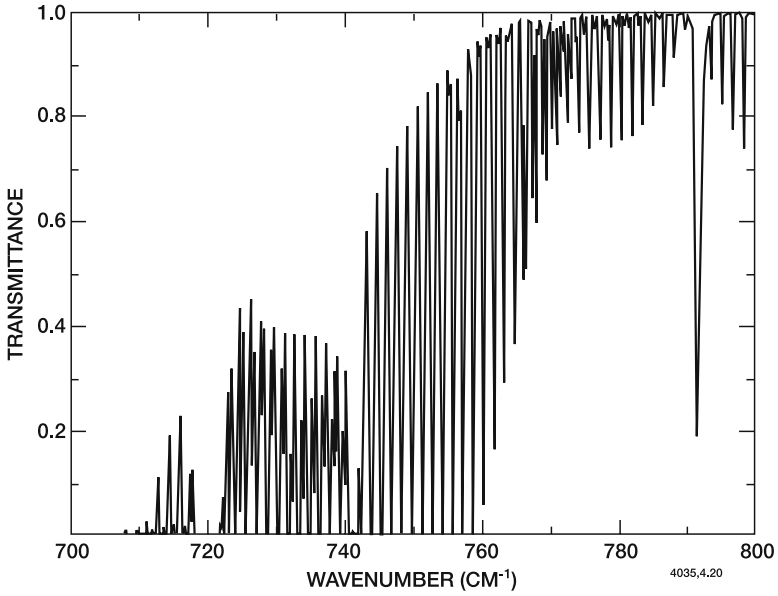

Figure 4.22. An illustration of the spectral fine structure found in atmospheric absorption bands. This example shows a line-by-line calculation of the vertical transmittance through the atmosphere at the edge of the strong 15 μm CO_2 bands (Edwards, 1992).

Box 4.3 Remote Sounding of Atmospheric Temperature and Chemical Composition from Space

By measuring the spectral distribution of the upwelling infrared radiation emitted by the Earth and its atmosphere, spaceborne sensors can provide information on the vertical temperature profile and on the atmospheric abundance of radiatively active trace gases. When local thermodynamic equilibrium conditions apply, the radiance received by a detector with spectral response function φ_ν over frequency interval $\Delta\nu$ and viewing vertically downwards is given by (see Eq. 4.69a)

$$L_{\Delta\nu} = B_{\Delta\nu}\,(\mathrm{T_s})\;\mathrm{T_{r,\Delta\nu}}\,(0,\infty) + \int_0^\infty \mathrm{B_{\Delta\nu}(z)\,w_{\Delta\nu}(z)\,dz} \qquad (4.71)$$

where $T_{\mathrm{r},\Delta\nu}(\mathrm{z_1},\mathrm{z_2})$ is the optical transmission (for frequency interval $\Delta\nu$) between levels $\mathrm{z_1}$, and $\mathrm{z_2}$, $\mathrm{B_{\Delta\nu}}$ $(\mathrm{T_s})$ is the Planck function in the same spectral interval corresponding to the surface temperature $\mathrm{T_s}$ and $\mathrm{B_{\Delta\nu}}$ (z) is the Planck function calculated at each atmospheric altitude z for air temperature profile T(z). The *weighting function*

$$\mathrm{w_{\Delta\nu}(z)} = \int_{\Delta\nu} \varphi_\nu \,\frac{\partial \mathrm{T_{r,\nu}(z,\infty)}}{\partial \mathrm{z}}\,\mathrm{d}\nu \qquad (4.72)$$

Box 4.3 (Continued)

determines the contribution of the emission by different atmospheric layers to the radiance measured at the top of the atmosphere in the spectral interval $\Delta\nu$. The response function of the instrument is such that

$$\int_{\Delta\nu} \varphi_\nu \, \mathrm{d}\nu = 1 \tag{4.73}$$

Thus, in principle if the atmospheric abundance of the absorbing constituents, the response function of the instrument and the surface temperature are known, the temperature profile can be retreived by inverting equation (4.71). Similarly, the concentration of the absorbing species can be derived for a known temperature profile. If the absorption results from a uniformly mixed compound such as CO_2 (constant mixing ratio X), the monochromatic transmission can be expressed as

$$\mathrm{T_{r,\nu}(z,\infty)} = \exp\left[-\sigma_\nu \mathrm{Xn(z)H}\right] \tag{4.74}$$

where σ_ν is the absorption cross section at frequency ν, n(z) is the altitude-dependent air density and H is the atmospheric scale height (assumed to be constant). The corresponding weighting function at frequency ν (assuming $\varphi_\nu = 1$)

$$\mathrm{w_\nu(z)} = \sigma_\nu \mathrm{Xn(z)} \exp\left[-\sigma_\nu \mathrm{Xn(z)H}\right] \tag{4.75}$$

reaches a maximum at the altitude $\mathrm{z_{max}}$ where $\sigma_\nu \mathrm{Xn(z_{max})H} = 1$, and the radiance observed at this frequency by the nadir-viewing spaceborne sensor will be representative of the atmospheric conditions (*e.g.*, temperature) in the vicinity of this altitude. The vertical profile of the temperature or of radiatively active gases can therefore be obtained by measuring the upwelling radiance at different frequencies (using, for example, a multi-channel radiometer). The vertical resolution of these profiles is, however, severely limited by the width of the weighting function (usually more than one atmospheric scale height). It can be somewhat improved by adding observing channels, but remains constrained by the fact that overlapping weighting functions do not provide independent information. In the case of chemical compounds in trace quantities, nadir soundings provide in most cases only the column abundance, and very little information on the vertical distribution. Increased vertical resolution can be obtained by using radiometers with narrow fields of view scanning through the limb of the planet. Limb observations of atmospheric emissions against the cold space background have provided unique information (high vertical resolution, near global coverage) on the abundance of many chemical species in the stratosphere and mesosphere.

The determination of the transmission function versus wavenumber depends strongly on knowledge of the detailed structure of the

absorption spectrum, and in particular, the shape of the absorption lines. (For reviews on the subject, see Mitchell and Zemansky, 1934; Penner, 1959; Goody, 1964; Kondratyev, 1969; Liou, 2002; Gordley *et al.*, 1994; Marshall *et al.*, 1994.) In the absence of molecular collisions and molecular motions, the natural width of a spectral line is very narrow and is determined by the radiative lifetime of the excited state. This width is called the "natural line broadening" and is a direct consequence of the Heisenberg uncertainty principle. It is considerably smaller than the Doppler and Lorentz broadening due, respectively, to the thermal motion of the molecules and the collisions between them. In the troposphere and lower stratosphere the width of the lines of the absorbing molecules such as carbon dioxide and water vapor is determined essentially by collision. In this case, one can assume a Lorentz line shape:

$$\sigma_{\bar{\nu}} = \frac{\mathrm{S}\gamma_{\mathrm{L}}}{\pi\left((\bar{\nu}-\bar{\nu}_{\mathrm{o}})^2+\gamma_{\mathrm{L}}^2\right)} \tag{4.76}$$

where $\sigma_{\bar{\nu}}$ represents the effective absorption cross section and $\bar{\nu}$ is the wavenumber, following the convention of spectroscopists. γ_{L} indicates the half width at half maximum of the line (expressed in wavenumber), $\bar{\nu}_o$ is the midpoint of the line and

$$\mathrm{S} = \int_0^\infty \sigma_{\bar{\nu}} \mathrm{d}\bar{\nu} \tag{4.77}$$

is the integrated intensity of the line. Since the molecular collision frequency varies with pressure and temperature, one may write, (see, *e.g.*, Tiwari, 1978):

$$\gamma_{\mathrm{L}} = \gamma_{\mathrm{L,o}} \frac{\mathrm{p}}{\mathrm{p_o}} \left(\frac{\mathrm{T_o}}{\mathrm{T}}\right)^{\alpha} \tag{4.78}$$

where $\gamma_{\mathrm{L,o}}$ represents the width of the line at standard pressure $\mathrm{p_o}$ and temperature $\mathrm{T_o}$. For most gases, $\gamma_{\mathrm{L,o}}$ is of the order of 0.1 cm^{-1}. The exponent α is approximately equal to 0.75 for CO_2, 0.64 for H_2O, and 0.76 for O_3. At very high altitudes, collisions become much less frequent, and the effect of pressure can be neglected, which results essentially in a Doppler linewidth. In this case, the profile can be represented as a Gaussian:

$$\sigma_{\bar{\nu}} = \frac{\mathrm{S}}{\gamma_{\mathrm{D}}\sqrt{\pi}} \exp\left(-\left[\frac{\bar{\nu}-\bar{\nu}_{\mathrm{o}}}{\gamma_{\mathrm{D}}}\right]^2\right) \tag{4.79}$$

where γ_{D} is the half width of the line measured at 1/e of the maximum intensity. (Note the difference in the definition of γ_{D} and γ_{L}.) A typical value of γ_{D} (which is independent of pressure, though dependent on temperature and wavenumber) is $10^{-3}\mathrm{cm}^{-1}$. In the transition region between the Lorentz and Doppler regimes, the lineshape is determined

by both broadening processes. If these are assumed to be independent, they may be combined to give the Voigt profile (Mitchell and Zemansky, 1934; Penner, 1959; Armstrong, 1967):

$$\sigma_{\bar{\nu}} = \frac{a}{\gamma_D}\frac{S}{\pi^{3/2}}\int_{-\infty}^{+\infty}\frac{\exp(-y^2)}{a^2+(v-y)^2}\,dy \tag{4.80}$$

where $a = \gamma_L/\gamma_D$, $v = (\bar{\nu} - \bar{\nu}_o)/\gamma_D$, and $y = (\bar{\nu}' - \bar{\nu}_o)/\gamma_D$. The Voigt profile is a good approximation to the observed line shape. The Voigt function (4.80) has no known analytic solutions, so that numerical techniques are required for its evaluation (see *e.g.*, Humlicek, 1982). At high pressure, when $a \to \infty$, and at low pressure, when $a \to 0$, the Voigt profile approaches the Lorentz and Doppler profiles, respectively. Figure 4.23 shows the different line shapes.

To determine the upward flux $F\uparrow$ and the downward flux $F\downarrow$ in a one dimensional representation, an integration of Eqs. (4.69a,b) must be performed over all solid angles according to Eq. (4.5) and Eq (4.6). It is convenient to introduce the "flux transmissivity"

$$T_r^*(z',z) = 2\int_0^1 T_r(z',z;\mu)\mu d\mu \tag{4.81}$$

which provides a weighted average of the contribution of light

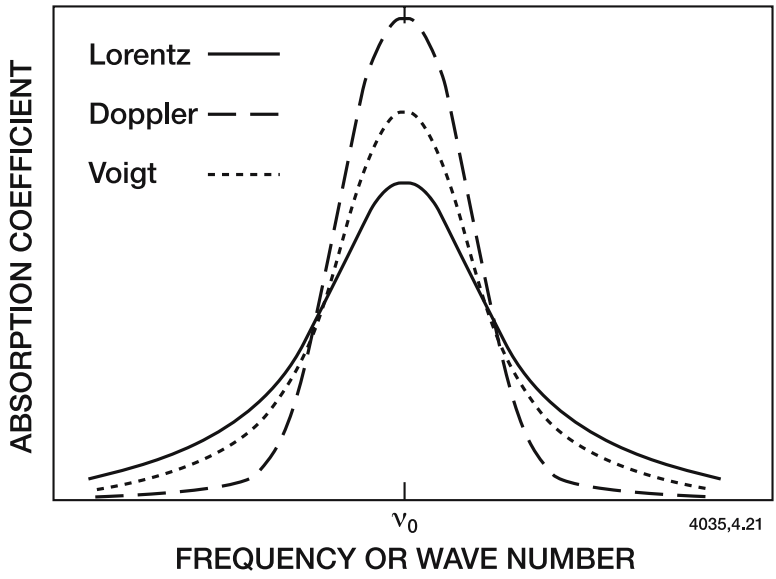

Figure 4.23. Lorentzian, Doppler, and Voigt spectral line profiles for approximately equal half widths and intensities. (From Andrews *et al.*., 1987).

propagating along various inclination angles. It can be shown (see Rodgers and Walshaw, 1966; Goody and Yung, 1989) that the scattered transmission is approximately equivalent to the propagation of a collimated beam at about a 53 degree angle ($\mu = \frac{3}{5}$). In other words, the calculation of $\mathrm{T}_{\mathrm{r}}^{*}$ can be performed with an air mass whose depth is $\frac{5}{3}$ its vertical thickness. Thus

$$\mathrm{T}_{\mathrm{r}}^{*}(\mathrm{z}';\mathrm{z}) \approx \mathrm{T}_{\mathrm{r}}(\mathrm{z}',\mathrm{z};\mu=\frac{3}{5}) \tag{4.82}$$

(Note that Apruzese *et al.* (1982) have shown that a value of 1.81 (versus 1.66) is more relevant for $1/\mu$ in the mesosphere and lower thermosphere.) One then finds

$$\mathrm{F}_{\bar{\nu}} \uparrow (\mathrm{z}) = \pi \mathrm{B}_{\bar{\nu}}(\mathrm{T}_{\mathrm{s}}) \mathrm{T}_{\mathrm{r},\nu}^{*}(\mathrm{z}_{\mathrm{o}},\mathrm{z}) + \int_{0}^{\mathrm{z}} \pi \mathrm{B}_{\bar{\nu}}(\mathrm{z}') \frac{\partial \mathrm{T}_{\mathrm{r},\nu}^{*}(\mathrm{z}',\mathrm{z})}{\partial \mathrm{z}'} \, \mathrm{dz}' \tag{4.83a}$$

$$\mathrm{F}_{\bar{\nu}} \downarrow (\mathrm{z}) = -\int_{\mathrm{z}}^{\infty} \pi \mathrm{B}_{\bar{\nu}}(\mathrm{z}') \frac{\partial \mathrm{T}_{\mathrm{r},\nu}^{*}(\mathrm{z},\mathrm{z}')}{\partial \mathrm{z}'} \, \mathrm{dz}' \tag{4.83b}$$

Thus, in theory, by knowing the location, strength, and shape of all absorption lines, the irradiance at any wavelength (or frequency) can be derived, and the total irradiance corresponding to an entire band could be obtained by a lengthy integration over the spectrum. In order to simplify the computation, and to derive the irradiance over a larger spectral range, the previous equations can be integrated over an interval $\delta\bar{\nu}$ which is sufficiently narrow that the Planck function can be assumed constant ($\delta\bar{\nu} < 50\mathrm{cm}^{-1}$), but containing the largest possible number of emission lines ($\delta\bar{\nu} > 5\mathrm{cm}^{-1}$). In this case, the irradiance for interval i is given by the following expression (after integration by parts of the expression above):

$$\mathrm{F}_{\mathrm{i}} \uparrow (\mathrm{z}) = \pi \mathrm{B}_{\mathrm{i}}(\mathrm{z}) - \int_{0}^{\mathrm{z}} \pi \frac{\mathrm{dB}_{\mathrm{i}}(\mathrm{z}')}{\mathrm{dz}'} \mathrm{T}_{\mathrm{r,i}}^{*}(\mathrm{z}',\mathrm{z}) \mathrm{dz}' \tag{4.84a}$$

$$\mathrm{F}_{\mathrm{i}} \downarrow (\mathrm{z}) = -\pi \mathrm{B}_{\mathrm{i}}(\mathrm{z}=\infty) \mathrm{T}_{r,\mathrm{i}}^{*}(\mathrm{z},\infty) + \pi \mathrm{B}_{\mathrm{i}}(\mathrm{z}) + \int_{\mathrm{z}}^{\infty} \pi \frac{\mathrm{dB}_{\mathrm{i}}(\mathrm{z}')}{\mathrm{dz}'} \mathrm{T}_{\mathrm{r,i}}^{*}(\mathrm{z}',\mathrm{z}) \mathrm{dz}' \tag{4.84b}$$

where $\mathrm{B}_{\mathrm{i}}(\mathrm{z})$ represents the Planck function in the frequency interval i for the temperature of the air and the altitude z, and where

$$\mathrm{T}_{\mathrm{r,i}}^{*}(\mathrm{z}',\mathrm{z}) = \frac{1}{\delta\bar{\nu}} \int_{\delta\bar{\nu}} \mathrm{T}_{\mathrm{r}}^{*}(\mathrm{z}',\mathrm{z}) \mathrm{d}\bar{\nu} \tag{4.85}$$

is an effective transmission function corresponding to interval i. From Eq. (4.10), one can derive that the heating rate corresponding to spectral interval i at altitude z:

$$Q_i = \frac{1}{\rho c_p}\left\{-\pi B_i\,(z=\infty)\,\frac{dT^*_{r,i}}{dz}\,(z,\infty) + \int_0^\infty \pi\,\frac{\partial T^*_{r,i}\,(z',z)}{\partial z}\,\frac{dB_i\,(z')}{dz'}dz'\right\} \tag{4.86}$$

where the first term, called the cool-to-space component, accounts for the emission of radiation from any level z out to space, and the second term accounts for exchange of radiation between any level z and levels above and below this level of interest.

The determination of the effective transmission Eq. (4.85) requires, in principle, a line by line integration including all the complex structures of the various absorbing lines and their overlap. Such a calculation is potentially very accurate and capable of including all the relevant radiative transfer physics, although it may require a considerable amount of computer time. As with all schemes, there remains the uncertainty associated with the underlying spectral line data. However, because they perform the spectral integration directly, line-by-line models may be used as a reference against which the accuracy of more approximate, but faster, techniques may be measured (Ellingson *et al.*, 1991). They can also be used to provide input parameterizations to an approximate method in which the effective transmission function for a band or a portion of a band is expressed in terms of global parameters such as the mean line strength, the mean spacing between the individual lines, and the mean line width. Models have been developed to treat either sections of bands (narrow band models) or entire bands (wide band models). See Tiwari (1978) and Goody and Yung (1989) for excellent reviews of these models. The choice of any particular formulation of the transmission function is dictated by the degree to which the model approximates experimental data. The spectral parameters are usually adjusted to optimize the fit to observed absorption.

Narrow band models parameterize the transmission for wavenumber intervals $\delta\overline{\nu}$ of typically 5 to 20 cm^{-1}. The narrow band model of Elsasser (1942) represents the spectrum by a series of regularly spaced Lorentz lines of the same size and intensity. This model is best applied to linear triatomic molecules such as CO_2 and N_2O. The model by Goody (1964) is based on the idea that the lines are randomly spaced over a particular wavelength interval, with some exponential distribution of line strength. This model can readily be applied to water vapor and to carbon dioxide. If an exponential distribution of the line intensities

is assumed (*i.e.*, the probability of finding a line intensity S_j in a given intensity range decreases exponentially with the value of S_j), the effective transmission function in the spectral interval $\delta\bar{\nu}$ is given by

$$T_{r,\delta\bar{\nu}} = \exp\left(-\left[\frac{S}{d}\right]_{\delta\bar{\nu}} w\left[1+\left(\frac{S}{\pi\gamma}\right)_{\delta\bar{\nu}} w\right]^{-1/2}\right) \tag{4.87}$$

where S (cm^{-2} atm^{-1}) is the mean strength of the lines for the interval $\delta\bar{\nu}$, γ the mean half width (cm^{-1}), and d the mean line spacing, w the amount of absorber (atm cm^{-1}). Malkmus (1967) introduced a distribution of the lines in S_j^{-1}. The statistical model then yields

$$T_{r,\delta\bar{\nu}} = \exp\left(\frac{-(S/d)_{\delta\bar{\nu}}}{2(S\pi\gamma)_{\delta\bar{\nu}}}\left[1+4w\left(\frac{S}{\pi\gamma}\right)_{\delta\bar{\nu}}\right]^{1/2}-1\right) \tag{4.88}$$

Because lines in vibration-rotation bands are arranged neither at regular nor at random intervals, other models have been suggested, such as the random Elsasser model, which is constructed by the random superposition of several different Elsasser bands. Each of the superposed bands may have different average line intensities, line widths, and line spacing. Such a model provides a more accurate representation of the absorption for bands whose lines have relatively constant intensities over a narrow band region, but different intensities from one of these regions to another. These models were originally developed for Lorentz lines, but have also been extended for the Doppler and Voigt line shapes (see Tiwari, 1978).

The above formulations of the effective transmission function have been derived for homogeneous (constant pressure and temperature) optical paths. In the atmosphere, the pressure and the temperature vary with altitude, and the value of the spectral parameters (line width, line strength) should be adjusted accordingly. Curtis (1952) and Godson (1953) presented an approximation in which the transmission of an inhomogeneous atmospheric path is replaced by the transmission of a homogeneous path with an effective line strength

$$\bar{S} = \frac{1}{w}\int_0^w S(T)\,dw' \tag{4.89}$$

and an effective half width of the line

$$\bar{\gamma} = \int_0^w S(T)\gamma(p,T)dw' \Big/ \int_0^w S(T)dw' \tag{4.90}$$

after which the band models for the homogeneous case can be applied. This approximation provides fairly good results for species whose optical mass decreases with pressure (CO_2, H_2O), but is rather poor for

constituents such as ozone, whose molar fraction changes with altitude (Liou, 1980).

There are other techniques that rely on a reordering of the transmittance integrand. As a function of wavenumber, the integrand of

$$\mathrm{T_{r,\delta\overline{\nu}}} = \frac{1}{\delta\overline{\nu}} \int_{\delta\overline{\nu}} \mathrm{e}^{-\mathrm{k}_\nu \mathrm{w}} \mathrm{d}\nu \tag{4.91}$$

shows a fast spectral variation requiring it to be sampled at many wavenumber points. For example, a representative lower stratosphere 15 μm CO_2 Voigt line halfwidth has a value of about 5×10^{-3} cm^{-1}. If we assume that a minimum of two wavenumber points per halfwidth are required to model the line profile, then on the order of 40000 wavenumber points would be needed to cover 100 cm^{-1} over the strong fundamental band and the resulting integration would be computationally expensive. However, if we know the fraction f(k) of the integration range $\delta\overline{\nu}$ in which the absorption coefficient lies between k and k + Δk, it is equivalent to write the band integrated transmittance for a homogeneous path using a k-distribution as

$$\mathrm{T_{r,\delta\overline{\nu}}} = \frac{1}{\delta\overline{\nu}} \int_0^\infty \mathrm{f\,(k)\,e^{-kw}dk}, \tag{4.92}$$

although it is usually more convenient to switch to a cumulative g-distribution function

$$\mathrm{g(k)} = \int_0^\mathrm{k} \mathrm{f\,(k')\,dk'}, \tag{4.93}$$

such that the band transmittance integral may be written

$$\mathrm{T_{r,\delta\overline{\nu}}} = \int_0^1 \mathrm{e}^{-\mathrm{g(k)w}} \mathrm{dg} \tag{4.94}$$

Because g(k) is a monotonically increasing function, it may be evaluated with a few tens of g-points in the range zero to unity, thereby allowing the integral to be evaluated quickly (Lacis and Oinas, 1991).

This method essentially calculates a single equivalent pseudo-line over a pseudo-frequency parameter g from the rapidly varying line spectrum in the wavenumber range $\delta\overline{\nu}$. In this sense, it retains some of the characteristics of a monochromatic line-by-line calculation. If a good correlation exists between the line centers and shapes of spectral lines in different layers of a multi-layered atmosphere, *i.e.*, the mapping of ν to g is essentially the same in all layers, then the g-distributions of several layers may be added together to allow for multi-layer radiative transfer calculations. The conditions under which this *correlated-k* method is valid are discussed by Goody *et al.* (1989) and Fu and Liou (1992). An advantage of the k-distribution technique over band models is that scattering problems can be addressed directly.

Narrow band methods, although reasonably accurate when compared to line-by-line integrations, are still too cumbersome for most climate model applications. *Wide band models* are particularly useful when the spectral variation of the flux is not an important consideration. In this case, the flux equations can be integrated over a whole spectral band $\Delta\nu$ (such as the 15 micron band system of CO_2). A number of approaches exist for constructing the effective transmission $T^*_{\Delta\nu}$ or the corresponding absorptance $A_{\Delta\nu} = 1 - T^*_{\Delta\nu}$ as a function of the optical path (see *e.g.*, Cess and Ramanathan (1972) and Ramanathan (1976)).

Band models are useful for practical applications but have some basic limitations; for example, they are only capable of yielding low spectral resolution and they do not always account for the effects of band wings. Kiehl and Ramanathan (1983) have shown, for example, that in the case of the CO_2 band at 15 μm the Goody and Malkmus formulation can only yield accurate results if the spectral interval $\delta\bar{\nu}$ is less than 10 cm^{-1}, and that the wide band models are probably more suitable for radiative transfer formulations in the middle atmosphere. With the development of fast computer systems, however, band models are becoming obsolete for many applications (*e.g.*, retrieval of temperature and chemical constituents from satellite measurements) and are progressively being replaced by more accurate line-by-line integrations.

The previous discussion is based on the assumption that collisional excitation and de-excitation is the dominant process determining the populations of the vibrational-rotational levels of all radiatively active molecules. This is usually the case in the lower atmosphere, where the pressure is high and molecular collisions are frequent. The relative populations of the upper and lower states of a vibrational-rotational transition are then described by the Boltzmann distribution at the local kinetic temperature T, the gas is considered to be in local thermodynamic equilibrium (LTE), and Kirchoff's law can be applied locally. If we consider a two-level system, then the relative populations of the lower and upper states, n_0 and n_1, respectively, are given by

$$\frac{n_1}{n_0} = \frac{g_1}{g_0} \exp\left(\frac{-h\nu}{kT}\right) \tag{4.95}$$

where g_0 and g_1 are the level statistical weights, and ν is the transition frequency. The source function is then given by Planck's law. In LTE, the relaxation time due to collisions is considerably shorter than the radiative lifetime of the excited vibrational-rotational states. The radiative lifetimes with which we are concerned are of the order of 0.1 sec (0.7 sec for the CO_2 15 μm band, 0.08 sec for the ozone 9.6 μm band, and 0.05 sec for the H_2O 6.3 μm band; (Rothman *et al.*, 1998)). The relaxation time at ground level is determined by thermal collisions with

molecular oxygen and nitrogen, and is considerably shorter. In the case of the CO_2 15 μm band, it is of the order of 2.5×10^{-5} sec in the temperature range 150-210 K with an uncertainty of about 50% (Simpson *et al.*, 1977). Since this relaxation time varies inversely with the pressure, the radiative and relaxation time constants become equal at about 68 km, assuming a scale height of 7 km.

To determine the altitude at which LTE actually breaks down for each state of a given molecule, one must consider all the pumping mechanisms that affect the state in question. These may include; (1) absorption of radiation originating in warmer parts of the atmosphere at lower altitude, (2) absorption of solar radiation in the near-IR, (3) chemical pumping when the molecule is formed in a vibrationally-excited state, (3) collisions where thermal energy produces a transition, and (4) collisions involving exchange of vibrational quanta. Processes (1) and (2) may be particularly important when an absorption band has high optical depth. Breakdown of LTE occurs at about 90 km for the 15 μm CO_2 ν_2 fundamental band, at about 70 km for the 9.5 μm O_3 ν_3 fundamental band, and about 60 km for the 6.3 μm H_2O ν_2 fundamental band. It should be noted that hot bands and isotope bands often depart from LTE much lower down in the stratosphere. Following Kuhn and London (1969), we consider the case of the CO_2 15 μm fundamental band where the partition of population between the upper and lower states is determined by radiative and thermal collisional processes. In the middle atmosphere, these must be considered together in a balance equation to give

$$n_0 B_{01} \overline{L}_{\Delta\nu} - n_1 A_{10} - n_1 B_{10} \overline{L}_{\Delta\nu} + p_t n_1 - l_t n_1 = 0 \tag{4.96}$$

where A_{10}, B_{10}, and B_{01} are the Einstein coefficients for spontaneous emission, induced emission, and absorption, respectively. The thermal collisional deactivation and activation specific loss rates are l_t and p_t, respectively, and the mean radiation field averaged over the band is given by

$$\overline{L}_{\Delta\nu} = \frac{1}{4\pi S} \int_\omega \int_{\Delta\nu} L_\nu k_\nu d\nu d\omega \tag{4.97}$$

This allows us to write the population ratio between the states as

$$\frac{n_1}{n_0} = \frac{B_{01} \overline{L}_\nu + p_t}{A_{10} + B_{10} \overline{L}_\nu + l_t} \tag{4.98}$$

A general form of the source function may be written

$$J_\nu = \frac{2h\nu^3}{c^2} \left(\frac{g_1 n_0}{g_0 n_1} - 1 \right)^{-1} \tag{4.99}$$

which reduces to the Planck function under LTE conditions when n_1/n_0 is given by the Boltzmann equation. The line intensity S can also be

defined in the general case as

$$S = \frac{h\nu}{c^2} B_{01} \frac{n_0}{N} \left(1 - \frac{g_0 n_1}{g_1 n_0}\right) \tag{4.100}$$

Therefore, using the expression for n_1/n_0, we are able to adapt the radiative transfer equations described in the previous sections to the general case where LTE can no longer be assumed (Edwards *et al.*, 1993).

Defining

$$E = \frac{l_t}{A_{10}}[1 - \exp(-h\nu/kT)] \tag{4.101}$$

and making use of the fundamental relations between the Einstein coefficients, and the fact that p_t/l_t must be given by the Boltzmann distribution (because this ratio alone determines n_1/n_0 under LTE conditions), the non-LTE source function may be written

$$J_\nu = \frac{\overline{L}_\nu + EB_\nu}{1 + E} \tag{4.102}$$

The more general, multi-level case, is described by López-Puertas *et al.* (1986). In the lower atmosphere where collisions dominate, $E \to \infty$, $J_\nu \to B_\nu$, and LTE conditions apply. At high altitude where the population of the energy levels is determined by radiative processes only, $E \to 0$, and the source function becomes $J_\nu = \overline{L}_\nu$. This case is referred to as monochromatic radiative equilibrium (MRE) in which, for each frequency, the absorbed radiant energy is balanced by the emitted radiant energy.

The importance of non-LTE processes in stellar atmospheres was first pointed out by Milne (1930), and the first method for treating the problem in the terrestrial mesosphere was presented by Curtis and Goody (1956). Since that time, these questions have been addressed by Houghton (1969), Dickinson (1984), López-Puertas *et al.* (1986), Wintersteiner *et al.* (1992) and Shved *et al.* (1998), among others. Crutzen (1970) pointed out the possible importance of the excitation of the CO_2 ν_2 fundamental band due to collisions with atomic oxygen and the effect that this might have on the cooling of the upper mesosphere and lower thermosphere. Until recently, there was considerable doubt as to the rate constant for this process. López-Puertas *et al.* (1992) obtained a value of between 3 and 6×10^{-12} $cm^3 s^{-1}$ from measurements of the Atmospheric Trace Molecules Spectroscopy (ATMOS) instrument aboard the Spacelab 3 shuttle mission, an order of magnitude faster than previous, widely-used values, and this was supported by the laboratory measurements of Shved *et al.* (1991). This results in a cooling rate at 100 km nearly ten times greater than earlier calculations due to the fact that the higher collision rate helps maintain the population of the upper

level of the fundamental band much closer to LTE. Accuracy in the calculations of heating and cooling rates in the mesosphere and lower thermosphere remains limited by uncertainties in the relaxation rates and their temperature dependencies, together with uncertainties in the kinetic temperature and the concentrations of collision partners.

4.6 The Thermal Effects of Radiation

Figure 4.24 summarizes the different major contributors to solar heating and terrestrial cooling calculated by solving the radiative transfer equations and applying equation (4.10) to derive heating/cooling rates. This figure shows that on the average, the major contribution to solar heating is provided by the absorption of solar ultraviolet radiation by ozone in the stratosphere and mesosphere and by molecular oxygen in the lower thermosphere. Thermal infrared cooling is associated primarily with the presence of carbon dioxide, ozone, and water vapor, and is a strong function of temperature.

The thermal effects of solar and atmospheric radiation have been studied using mathematical models, generally by solving the radiative transfer equations which we have just described (*e.g.*, Ramanathan, 1976). The most elaborate models, particularly those with fine spectral resolution, require rather large computing resources, and cannot be coupled with chemical or dynamical models using present computers unless they are greatly simplified.

In many cases, only the mean vertical temperature distribution is desired. The distribution obtained by assuming local radiative equilibrium between the energy absorbed and the energy emitted at a given altitude yields a very large vertical gradient in the troposphere (Manabe and Moller, 1961). It becomes necessary to consider convection and vertical transport of non-radiative energy. To resolve this problem, one-dimensional *radiative convective models,* such as that first presented by Manabe and Strickler (1964) are widely used. In such models the lapse rate is adjusted to a representative value whenever the computed value exceeds this level. This adjustment is performed until an equilibrium is reached in each atmospheric layer. The net incoming solar energy flux is thus balanced by the net outgoing long wave energy flux at the top of the atmosphere. At the Earth's surface, a balance must exist between the net energy gain by radiation and the loss of heat by convective transfer into the atmosphere. Whenever the lapse rate is subcritical, the model assumes that pure radiative equilibrium is achieved. Such model techniques require an iterative procedure

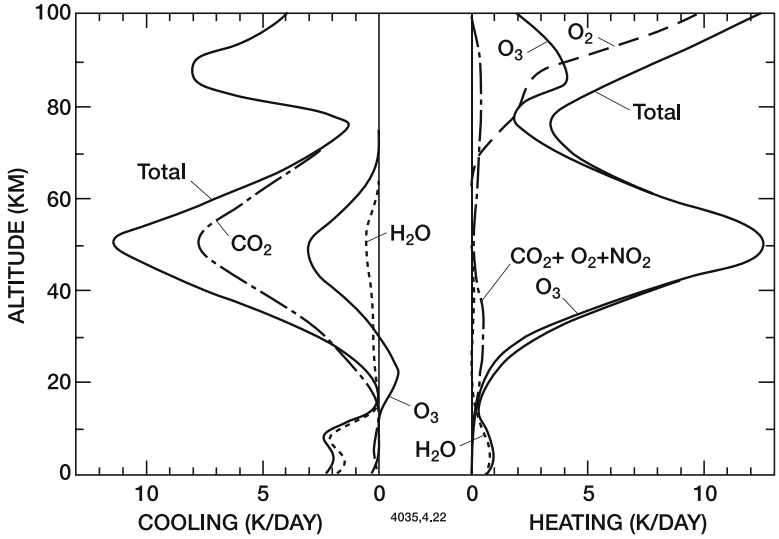

Figure 4.24. Vertical distribution of solar short wave heating rates by O_3, O_2, NO_2, H_2O, CO_2, and of terrestrial long wave cooling rates by CO_2, O_3, and H_2O. From London (1980).

in which the layers of the atmosphere are treated repeatedly until these conditions are satisfied.

Middle atmosphere models calculate the spatial and temporal distribution of the net heating rate Q and the temperature not only as a function of altitude but also as a function of latitude, and even of longitude (local time). Such studies consider the multidimensional transport of heat and the solution of a thermodynamic equation like the one shown in Equation (3.10). The effect of waves should also be considered. Gravity wave dissipation, for example, may play an important role in the mesospheric heat budget. In the multidimensional models, the radiative scheme is often simplified and parameterized; the most simple approach is to assume the "cool-to-space approximation", in which it is assumed that exchange of heat between layers can be neglected in comparison to propagation out to space.

4.6.1 Heating Due to Absorption of Radiation

The absorption of ultraviolet radiation by ozone in the Huggins and Hartley bands constitutes the principal source of heat in the stratosphere and mesosphere. The heating rate reaches 10 K/day near the stratopause on the average, with a maximum of about 15 K/day near the summer pole. The effect of the Huggins bands in the visible region becomes

important in the lower stratosphere, where the resulting heating rate is nearly 1 K/day. These numbers are obviously related to the amount of ozone present, and a change in ozone density would lead to a variation in the stratospheric and mesospheric temperatures, as well as possible changes in the locations of the stratopause and mesopause.

The primary source of heat in the thermosphere is provided by the absorption of solar EUV radiation (10-100 nm). At high latitudes, particle precipitation and Joule heating can become dominant contributions. Above about 75 or 80 km, absorption in the Schumann-Runge continuum of molecular oxygen contributes to the heating of the atmosphere and begins to play the dominant role in the lower thermosphere. At 100 km, the mean heating rate is about 10 K/day, but large variations occur with latitude and season. In the middle and upper mesosphere, the absorption of solar radiation at Lyman α by O_2 also contributes significantly to the heat budget.

The absorption by molecular oxygen in the Herzberg continuum only contributes slightly to the heating rate in the middle atmosphere, and can be neglected relative to the effects of ozone in the stratosphere. There are, however, some O_2 bands at wavelengths as long as 760 nm in the visible. These bands contribute 5-15% of the total heating between 60 and 80 km (Mlynczak and Marshall, 1996).

The meridional distribution of the heating rate due to O_2 and O_3, shown in Figure 4.25, is based on observations by the Upper Atmosphere Research Satellite (UARS) during the period November 19-December 19, 1991 (Mlynczak *et al.*, 1999). The corresponding values are determined by an expression of the form (4.10), *i.e.*,

$$Q = \frac{\cos\chi}{\rho c_p} \int_\nu \frac{dF_{s,\nu}}{dz}\, d\nu \tag{4.103}$$

where the incident solar irradiance is given by

$$F_{s,\nu}(z,\chi) = F_{s,\nu}(\infty) \exp - \left(\sigma(O_3) \int_z^\infty n(O_3) dz' + \sigma(O_2) \int_z^\infty n(O_2)\, dz' \right) \sec\chi \tag{4.104}$$

considering only the effects of absorption by ozone and oxygen. One may then write:

$$Q = \frac{1}{\rho c_p} \left(n(O_3) \int_\nu \sigma(O_3) F_{s,\nu}\, d\nu + n(O_2) \int_\nu \sigma(O_2) F_{s,\nu}\, d\nu \right) \tag{4.105}$$

A parameterization of the atmospheric heating rate by O_3 and O_2 in different spectral regions has been suggested by Schoeberl and Strobel (1978), and is presented in Table 4.4.

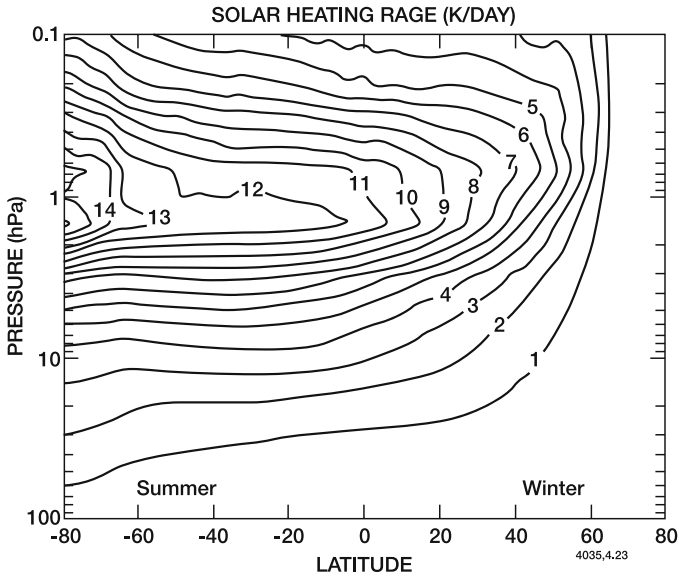

Figure 4.25. Meridional distribution of the atmospheric heating rate (K/day) between 100 and 0.1 mb during November 19-December 19, 1991 as derived from measurements by UARS. Effects of absorption of radiation by ozone and oxygen. After Mlynczak *et al.*(1999).

Relations (4.103) and (4.105) assume that the incoming solar energy absorbed by O_2 and O_3 is entirely converted into heat, and that this process occurs at the location where the photon absorption takes place. In reality, the processes involved are more complex. Absorption of solar radiation often leads to the dissociation of the absorbing molecule, and the release of heat occurs as the photolysis products recombine or react with other chemical species (exothermic reactions). Garcia and Solomon (1983), Apruzese *et al.* (1984), and Brasseur and Offermann (1986) noted that the recombination of atomic oxygen provides an important heating source for the upper mesosphere and lower thermosphere. The hypothesis behind equations (4.103) and (4.105), which is valid in the lower atmosphere where collisions are frequent and recombinations are fast, must therefore be rejected at high altitudes, where the recombination of atomic oxygen can take place several thousands of kilometers away from the location where the original photon was absorbed. In addition, collisions are so infrequent that energy gained by the photolysis products can be partly released by radiative emission rather than through quenching. The primary energy source remains the absorption of solar ultraviolet light by O_2 and O_3. A fraction of the heating is provided (as kinetic energy) through collisions of the photolysis products with other chemical species; it can be quantified

Table 4.4 Parameterization of Atmospheric Heating Rates (from Schoeberl and Strobel, 1978)

Spectral region	*Parameterization*
Chappuis bands	$\frac{Q_c}{(O_3)} = 1.05 \times 10^{-15} \exp(-2.85 \times 10^{-21} N_3)$
Huggins bands	$\frac{Q_{Hu}}{(O_3)} = \frac{1}{N_3}\left[4.66 \times 10^3 - 7.8 \times 10^2 \exp(-1.77 \times 10^{-19} N_3) - 3.88 \times 10^3 \exp(-4.22 \times 10^{-18} N_3)\right]$
Hartley region	$\frac{Q_{Ha}}{(O_3)} = 4.8 \times 10^{-14} \exp(-8.8 \times 10^{-18} N_3)$
Schumann Runge bands	$\frac{Q_{SRB}}{(O_2)} = \frac{1}{0.67 N_2 + 3.44 \times 10^9 (N_2)^{1/2}}$ If $N_2 < 10^{18} cm^2$, $\frac{Q_{SRB}}{(O_2)} = 2.43 \times 10^{-19}$
Schumann Runge continuum	$\frac{Q_{SRC}}{(O_2)} = \frac{1}{N_2}\left[0.98 \exp(-2.9 \times 10^{-19} N_2) - 0.55 \exp(-1.7 \times 10^{-18} N_2) - 0.43 \exp(-1.15 \times 10^{-17} N_2)\right]$

(Note that N_2 and N_3 represent the total slant column abundances (molec cm^{-2}), and (O_2) and (O_3) the number densities (molec cm^{-3}), of O_2 and O_3, respectively. Heating rates are in degrees K/sec.)

as the difference between the energy of the initial incoming photon and the energy required to photodissociate the absorbing molecule (O_2 or O_3). *Chemical heating* is released by exothermic reactions in which the photolysis products are involved. The most important of these reactions as well as their rate constants and heat of reactions are listed in Table 4.5. As noted by Crutzen (1971), Brasseur and Offermann (1986), and Mlynczak and Solomon (1991), in addition to the recombination of oxygen atoms, several reactions involving members of the odd-hydrogen family affect the energy budget of the mesophere.

Table 4.5 Reactions, Rate Constants and Heat of Reactions. (From Mlynczak and Solomon, 1991)

Reaction	*Rate Constant*	*Heat of Reaction* (kcal/mole)
$O + O + M \rightarrow O_2 + M$	$4.7 \times 10^{-33}(300/T)^2$ cm^6 s^{-1}	–119.40
$O + O_2 + M \rightarrow O_3 + M$	$6.0 \times 10^{-34}(300/T)^{2.4}$ cm^6 s^{-1}	–25.47
$O + O_3 \rightarrow O_2 + O_2$	8.0×10^{-12} exp (–2060/T) cm^3 s^{-1}	–93.67
$H + O_2 + M \rightarrow HO_2 + M$	$5.7 \times 10^{-32}(300/T)^{1.6}$ cm^6 s^{-1}	–49.10
$H + O_3 \rightarrow OH^* + O_2$	1.4×10^{-10} exp (–470/T) cm^3 s^{-1}	–76.90
$OH + O \rightarrow H + O_2$	2.2×10^{-11} exp (120/T) cm^3 s^{-1}	–16.77
$HO_2 + O \rightarrow OH + O_2$	3.0×10^{-11} exp (200/T) cm^3 s^{-1}	–53.27

The energy released by chemical heating is generally lower than the energy required to dissociate the absorbing molecules. For example, since the photolysis products of O_2 and O_3 can be excited species including $O(^1D)$ and $O_2(^1\Delta)$, the amount of energy available for heat is reduced by the spontaneous emissions of $O_2(^1\Delta)$ (and of $O_2(^1\Sigma)$ excited by energy transfer from $O(^1D)$). Mlynczak and Solomon (1993) have estimated that the heating efficiency associated with the absorption of solar ultraviolet radiation by ozone is typically 0.95 at 60 km, 0.85 at 70 km, and 0.7 between 70 and 100 km, due to energy loss by $O_2(^1\Delta)$ emission at 1.27 μm. Energy can also be lost by spontaneous emission of the vibrationally excited OH^* radical. A detailed evaluation of the heating efficiency in the middle atmosphere is given by Mlynczak and Solomon (1993). Chemical heating due to exothermic chemical reactions as shown in Table 4.5 is typically 1-15 K/day between 80 and 100 km altitude.

The heating due to absorption in the 2.7 and 4.3 μm bands of carbon dioxide, and the absorption of ultraviolet by water vapor, play minor roles in the heating budget. However, the H_2O bands in the visible and near infrared cannot be neglected in the troposphere, where the water vapor content is much higher than in the middle atmosphere. The absorption of solar radiation by NO_2 in the region between 300 and 600 nm should also be considered. The mean heating rate depends, however, on the distribution of NO_2 concentration and must also include the effects of multiple scattering and reflection by the surface and by clouds. Its contribution can be considerable in the lower stratosphere in summer, where NO_2 is probably present in large amounts. Figure 4.26 shows various contributions to the solar heating rate at equinox (44°N) in the stratosphere and lower mesosphere.

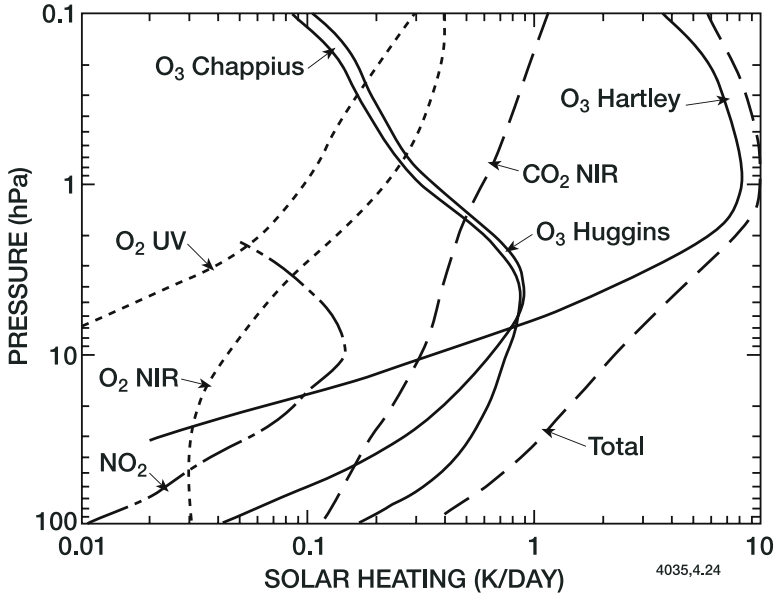

Figure 4.26. Contribution to the stratospheric solar heating (between 100 and 0.1 hPa) of UV and near IR absorption by O_2, ozone absorption (Hartley, Huggins, and Chappuis bands), CO_2 near infrared absorption, and NO_2 absorption. From Mertens *et al.*(1999).

4.6.2 Cooling by Radiative Emission

The radiative infrared cooling produced by atmospheric carbon dioxide, water vapor, and ozone, and obtained by solving the radiative transfer equation (see *e.g.*, Eq. (4.84a,b) and Eq. (4.86)) is represented in Plate 7 as a function of wavenumber and atmospheric pressure (corresponding to an altitude ranging from the surface to approximately 60 km). The calculations (Clough and Iacono, 1995) were made for mid-latitude summer conditions. The 15μm CO_2 band (centered at 667 cm^{-1}) produces a strong stratospheric cooling, which reaches a maximum around 45-50 km (1 hPa pressure level), where the temperature reaches a high value. A local warming, however, associated with this band, is calculated at the tropopause. The 9.6 μm ozone band (centered at 1043 cm^{-1}) also contributes to the cooling of the middle and upper stratosphere, but leads to a warming of the lower stratosphere. Water vapor contributes to upper tropospheric cooling, especially in the spectral region near 300 cm^{-1}. Thermal infrared heating (CO_2, O_3) and cooling (H_2O) near the tropopause tends to largely cancel, so that

changes in greenhouse gas concentrations lead to significant radiative effects in this region of the atmosphere.

Two-dimensional distributions of the radiative cooling rate can be obtained when similar calculations are repeated for different latitudes and seasons. Figure 4.27a shows, for example, the meridional distribution of the 15 μm CO_2 cooling calculated by Mlynczak *et al.* (1999) between 100 and 0.1 hPa, on the basis of measurements by the Upper Atmosphere Research Satellite (UARS) for the period of November 19-December 19, 1991. A precise calculation must include the contribution of different isotopes of CO_2, even those which constitute only 1.5% of the atmospheric abundance of this species. The effect of the fundamental and hot bands of these isotopes is large in the mesosphere and upper stratosphere, where a corresponding cooling rate of about 2 K/day is calculated (Williams and Rodgers, 1972).

An analysis based on the work of Dopplick (1972), Williams and Rodgers (1972), Kuhn and London (1969), and López-Puertas *et al.* (1992a, b), shows that the maximum cooling rate by CO_2 is found at the winter mesopause, where the temperature is relatively high. Flux convergence leads to a slight heating near 80 km in summer, that is, at relatively cold temperatures. The results in the lower thermosphere are subject to some inaccuracy as a result of the uncertainties in the relaxation times of vibrational levels.

The second contribution to infrared energetics of the middle atmosphere is associated with radiative transfer by ozone at 9.6 μm. This contribution leads to substantial cooling near the stratopause, but some significant heating in the lower stratosphere. In the lower stratosphere, the radiative transfer at 9.6 μm leads to a net heating because ozone absorbs some of the terrestrial emission at this frequency at altitudes below the ozone layer. The presence of high clouds in the troposphere can significantly affect the magnitude of ozone longwave heating, however. Figure 4.27b shows the meridional distribution of the cooling by O_3 based on observations by UARS (Mlynczak *et al.*, 1999).

Finally, the meridional distribution of the infrared cooling due to the presence of water vapor in the middle atmosphere is shown in Figure 4.27c (Mlynczak *et al.*, 1999). The longwave emission from the rotational bands of H_2O in the 250-500 cm^{-1} range, including the emission from the upper troposphere (Harries, 1996), is very important in determining the outgoing longwave radiation.

The infrared cooling in the middle atmosphere (*e.g.*, by the 15 μm CO_2 band) can generally be calculated from the "cool-to-space" term of

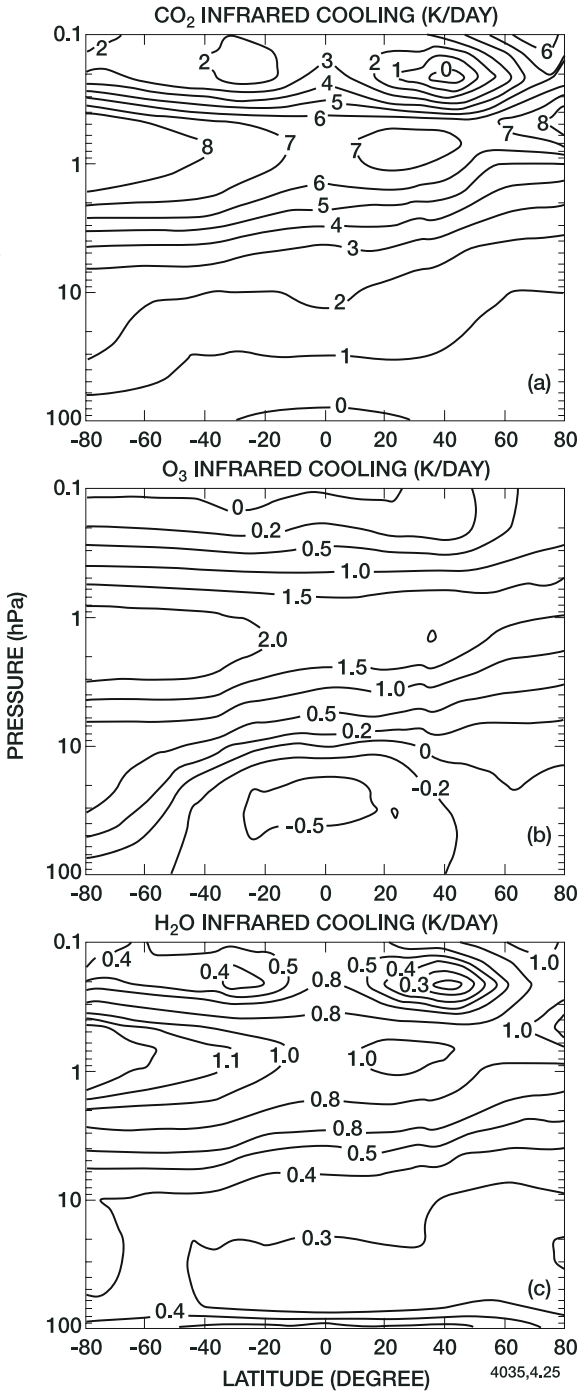

Figure 4.27. (a) Meridional distribution of the atmospheric cooling rate due to infrared emission by CO_2 (15 μm) between 100 and 0.1 mb during November 19-December 19, 1991 as derived from measurements by UARS. (b) Meridional distribution of the infrared cooling rate by ozone at 9.6 μm derived from measurements by UARS during the November 19-December 19, 1991 period. (c) Meridional distribution of infrared cooling by water vapor. Values are in K/day. After Mlynczak *et al.* (1999).

equation (4.86)

$$Q_i = -\frac{1}{\rho c_p} \pi B_i (\infty) \frac{dT_i^*}{dz} (z, \infty) \ . \tag{4.106}$$

If we assume that the temperature T relaxes to some reference temperature T_o, then to a first order

$$B_i (T) = B_i (T_o) + \left. \frac{\partial B_i}{\partial T} \right|_{T_o} (T - T_o) \tag{4.107}$$

and

$$Q(T) = Q(T_o) + \alpha (T - T_o) \ , \tag{4.108}$$

which is the expression for the so-called Newtonian cooling. Coefficient α defined as

$$\alpha = -\rho c_p \left\{ \left. \frac{\partial B}{\partial T} \right|_{T_o} \frac{\partial T^*}{\partial z} (z, \infty) \right\} \tag{4.109}$$

determines a Newtonian relaxation time or a radiative time constant $\tau_{rad} = 1/\alpha$. This time (Figure 4.28) is of the order of 6 days in the upper stratosphere, 20 days near 30 km altitude, and 100 days or more in the lower stratosphere (15-20 km). Mlynczak *et al.* (1999) found that the radiative relaxation time had increased substantially in the lower stratosphere in the early 1990s due to the presence of aerosols produced by the eruption of Mt. Pinatubo. Transport of heat can only occur if the dynamic time constant, τ_{dyn} is less than or comparable to the radiative time constant, τ_{rad}. In the troposphere, where $\tau_{dyn} < \tau_{rad}$, the temperature field is very dependent on transport, while in the middle atmosphere, where $\tau_{rad} << \tau_{dyn}$, the thermal structure is strongly affected by the difference between absorption of ultraviolet radiation and emission in the infrared. Where the radiative lifetime is less than a few days, the diurnal variation in solar energy input produces only small diurnal temperature variations. Variations in the temperature structure induce modifications in the concentration of chemical species, particularly ozone, and as a result, influence the transfer of radiation. Ghazi *et al.* (1979) showed that this effect leads to a reduction in the radiative lifetime in the upper stratosphere, and that the total relaxation coefficient can be written:

$$\alpha = \alpha_{NC} + \alpha_{PH} \tag{4.110}$$

i.e., as the sum of the Newtonian cooling and photochemical relaxation coefficients. Note that the Newtonian cooling approximation requires that the exchange term in Equation (4.86) can be neglected, that the temperature perturbations be small, and the temperature effects in the transmission can be ignored. The approximation is therefore not valid

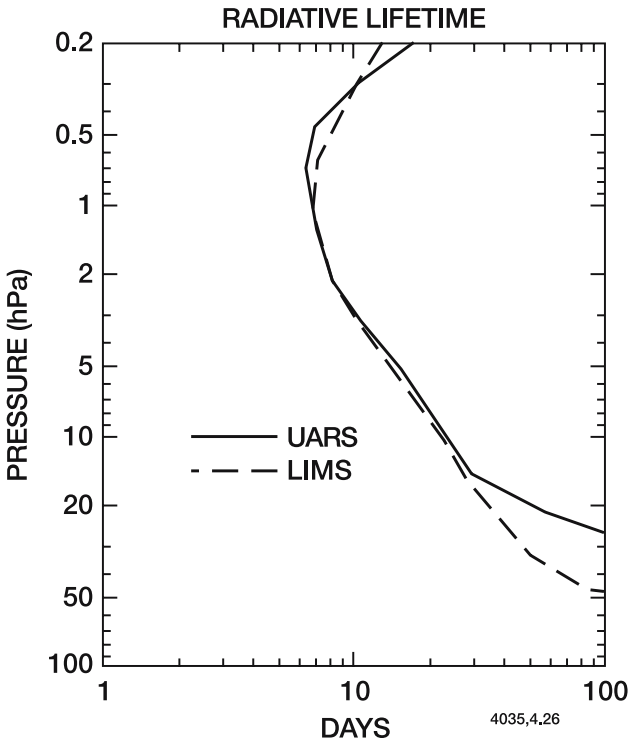

Figure 4.28. Globally averaged infrared radiative relaxation time deduced from data provided by UARS and LIMS. Note the increase in the lower stratospheric relaxation time in response to enhanced aerosol load after the eruption of Mt. Pinatubo (UARS measurements). From Mlynczak *et al.* (1999).

in the lower stratosphere and in the troposphere where the exchange of radiation between layers plays an important role.

4.6.3 Global Energy Budget

Figure 4.25 presents the contribution of the different radiative processes discussed earlier to the globally averaged heating rate between the surface and 100 km altitude. In the stratosphere and lower mesosphere (below 60-70 km), the contribution of radiative processes dominates the global energy budget. Although dynamics can affect the energy budget on the local scale (especially during wintertime), from a global (average) point of view, heating is provided primarily by ozone absorption of solar ultraviolet radiation in the Hartley band, and cooling results from the emission of infrared radiation by carbon dioxide, ozone, and water molecules. Thus, under these conditions,

the globally averaged vertical temperature profile can be determined from radiative equilibrium considerations. In the viscously dominated thermosphere, above approximately 120-130 km, the energy budget is also relatively simple: the solar heating due to EUV absorption by O_2, N_2, and O (with an efficiency depending on the chemical composition) is balanced primarily by molecular thermal conductivity. Dynamical processes provide a significant fraction of the heating above 160 km altitude.

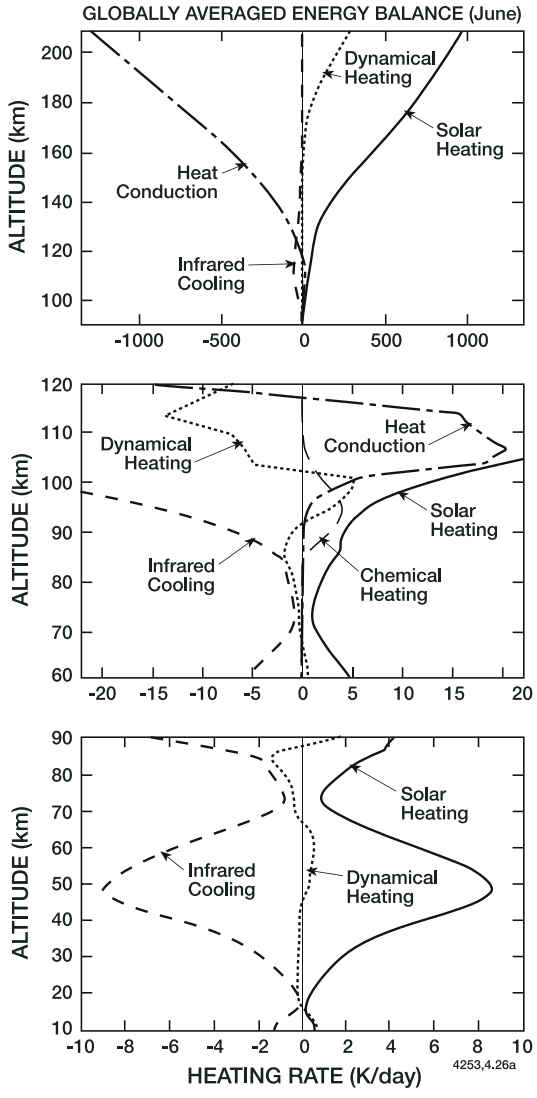

Figure 4.29. Major contribution to the globally averaged energy budget (K/day) in three different regions of the middle and upper atmosphere (from the upper to the lower panel: 90-210 km, 60-120 km, and 10-90 km), as derived for June by the extended Canadian Middle Atmosphere Model (CMAM). The global averaged dynamical heating term represents the sum of heat advection, gravity wave heating eddy mixing, convective adjustment, and other dissipative terms. From Fomichev *et al.* (2002).

In the transition region between the mesosphere and thermosphere (60-130 km), the situation is more complex. Diabatic heating results primarily from the absorption of solar radiation by ozone (Hartley band) and molecular oxygen (Schumann-Runge continuum), and cooling from the emission of infrared radiation (15 micron CO_2 band). Although, on the average, these radiative processes dominate the energy balance in this region of the atmosphere, other mechanisms are also of importance. These include chemical heating (see Section 4.6.1), which provide a significant contribution near the mesopause, heat deposition from the overlying thermosphere by molecular conduction, adiabatic heating by the atmospheric general circulation, conversion of kinetic energy into heat from the dissipation of horizontal winds, heating associated with gravity wave breaking, as well as vertical heat transport by eddy mixing and sporadically by convective adjustment. In the thermosphere, Joule heating (kinetic energy dissipated by ion drag — see Chapter 3) and radiative cooling (which maximizes around 140-150 km) associated with the 5.3 micron emission by nitric oxide (Kockarts, 1980) also play a significant role. The major components of the energy budget in different regions of the atmosphere, as calculated by the model of Fomichev *et al.* (2002), are shown in Figure 4.29.

4.7 Photochemical Effects of Radiation

4.7.1 General

Absorption of ultraviolet and visible photons by atmospheric molecules can induce transitions into electronically excited states, which may then photodissociate (see Chapter 2). The dissociation products play a crucial role in the photochemistry of the atmosphere.

In atmospheric problems, it is necessary to estimate the quantitative value of the photodissociation rate of a molecule A. This is given by:

$$\frac{\mathrm{d}\,(\mathrm{A})}{\mathrm{dt}} = -\mathrm{J_A}\,(\mathrm{A}) \tag{4.111}$$

where n(A) represents the concentration (cm^{-3}) of the molecule and $\mathrm{J_A}$ the photodissociation probability or coefficient. This coefficient is also called the *photodissociation frequency* and is expressed in s^{-1}. The inverse of J represents the lifetime of the molecule against photolysis.

For a wavelength interval $\mathrm{d}\lambda$, the photodissociation coefficient of molecule A is proportional to the actinic flux $\mathrm{q}_\lambda \mathrm{d}\lambda$, the absorption cross section $\sigma_\mathrm{A}(\lambda)$, and the photodissociation quantum efficiency $\epsilon_\mathrm{A}(\lambda)$. The actinic flux $\mathrm{q}_\lambda \mathrm{d}\lambda$ represents the number of photons per unit area and

unit time in the wavelength interval $[\lambda$ to $\lambda + \mathrm{d}\lambda]$ and is related to the energetic flux over the same wavelength interval $\mathrm{d}\Phi = \Phi_\lambda \, \mathrm{d}\lambda$ (where Φ is defined by Equation (4.12)) by

$$q_\lambda = \frac{\Phi_\lambda}{h\nu} = \frac{\lambda \Phi_\lambda}{hc} \tag{4.112}$$

q_λ is expressed, for example, in photons $cm^{-2}s^{-1}nm^{-1}$. When the entire portion of the solar spectrum over which the molecule can dissociate is considered $(\lambda_x - \lambda_y)$, the coefficient is given by (see also Chapter 2):

$$J_A(z;\chi) = \int_{\lambda_x}^{\lambda_y} \epsilon_A(\lambda)\sigma_A(\lambda)\, q_\lambda(\lambda;z;\chi)\, \mathrm{d}\lambda \tag{4.113}$$

The spectral distribution of the absorption cross section and the quantum efficiency of atmospheric molecules is measured in the laboratory and can vary with temperature. In most cases, the quantum efficiency ϵ is nearly unity but may be less, especially near the dissociation limit. This limit (maximum wavelength or minimum frequency) corresponds to the minimum energy required to dissociate the molecule (see, *e.g.*, Eq. (2.18) in the case of O_2 photolysis).

In most cases, the spectral variation of the cross section is sufficiently gradual that one can integrate Equation (4.113) by simple methods. In a few cases (Schumann Runge bands of O_2 and δ bands of NO) the spectrum contains a multitude of narrow lines and more sophisticated methods are needed. A more detailed discussion occurs in Section 4.7.3.

4.7.2 Absorption Cross Sections of the Principal Atmospheric Molecules

In this Section, we present a brief overview of the measured absorption cross sections and photodissociation quantum yields which are used for the calculation of the photolysis rates for the key molecules of the middle atmosphere. More details can be found in the evaluation of chemical and photochemical data periodically published by the Jet Propulsion Laboratory.

4.7.2.1 Molecular Nitrogen

The photodissociation of the most abundant gas in the atmosphere plays very little role in atmospheric chemistry below 100 km because the absorption of dissociating radiation by N_2 is very weak. However, production of atomic nitrogen from N_2 photolysis via predissociation does occur following absorption into the Lyman-Birge-Hopfield bands

($a^1\pi_g - X^1\Sigma_g$ transition). The coefficient of photodissociation is about $5 \times 10^{-12}s^{-1}$ at the top of the atmosphere and decreases rapidly, becoming negligible near the mesopause. The solar CIII line at 97.7 nm plays an important role in this process (see Richards *et al.*, 1981).

4.7.2.2 Molecular Oxygen

The photodissociation of molecular oxygen produces oxygen atoms, which play a central role in middle atmosphere chemistry. A potential diagram for the principal electronic states of the O_2 molecule was presented in Chapter 2, and some of the important transitions between them were mentioned. From the aeronomic viewpoint, the most important transitions are the $X^3\Sigma_g^- - A^3\Sigma_u^+$ which constitutes the Herzberg system (forbidden transition resulting in weak absorption from 185 to 242 nm) and the $X^3\Sigma_g^- - B^3\Sigma_u^-$ which constitutes the Schumann Runge system. The latter is characterized by a banded structure from 175 to 200 nm and a continuum from 137 to 175 nm. The first of these two transitions is a predissociation, that is, a non-radiative transition to a number of repulsive π states; it thus leads to the formation of two oxygen atoms in the ground ^3P state. In the second case ($\lambda < 175$nm) one of the atoms is formed in the excited ^1D state. At shorter wavelengths ($\lambda < 137$nm) some diffuse bands occur, but these are interspersed with a series of windows, which allow some wavelengths to penetrate relatively deeply into the atmosphere. One of these windows coincides with the solar Lyman α line, which plays an important role in atmospheric chemistry. Figure 4.30 shows the general shape of the spectral distribution of the absorption cross section. At wavelengths less than 102.8 nm, photoionization can occur.

The absorption coefficient of molecular oxygen has been the subject of numerous laboratory investigations. In the *Herzberg continuum* (195-242 nm), early laboratory measurements indicated an absorption cross section less than $1.5\times10^{-23}cm^{-2}$, but exhibited significant discrepancies in the absolute value. Part of the difficulty associated with measuring this cross section in the laboratory arises from the formation of the Van Der Waal's molecule, O_4, for which observational evidence has even been found in the atmosphere (Perner and Platt, 1980). Balloon observations of the solar irradiance in the stratosphere led to inferences of the O_2 absorption cross section in-situ (Frederick and Mentall, 1982b; Herman and Mentall, 1982b; Anderson and Hall, 1983), and these have resulted in values somewhat lower than the early laboratory investigations below 210 nm. The lower cross sections (Figure 4.31) have been confirmed by later laboratory measurements (Cheung *et al.*, 1986; Jenouvrier *et al.*, 1986; Yoshino *et al.*, 1988). Note that the Herzberg continuum

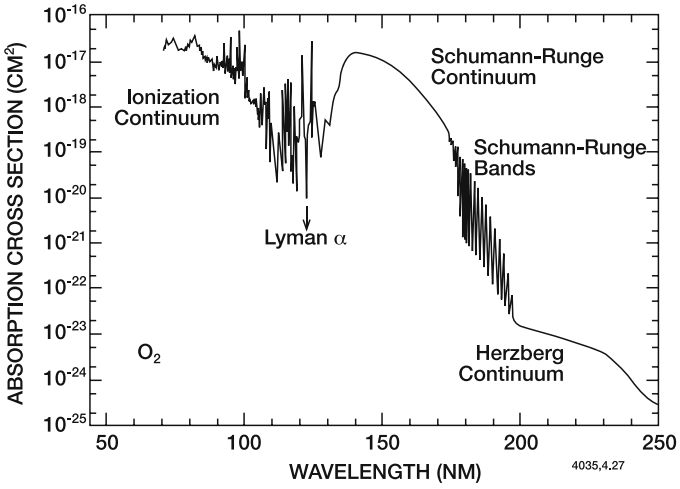

Figure 4.30. Spectral distribution of the absorption cross section of molecular oxygen.

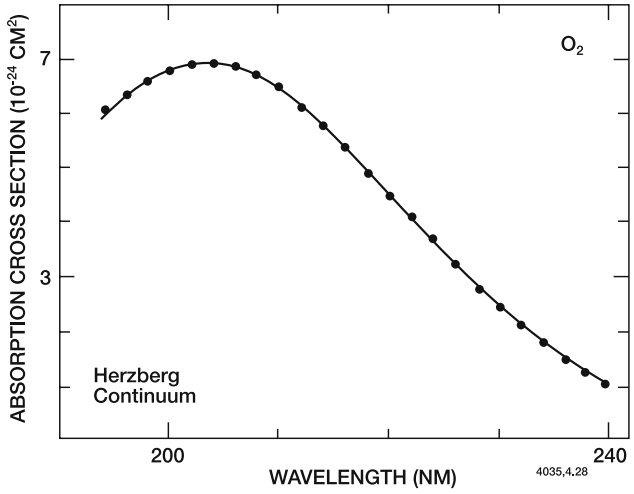

Figure 4.31. Absorption cross section of molecular oxygen in the Herzberg continuum between 194 and 240 nm (From Yoshino *et al.*, 1988).

underlies the Schumann-Runge band region below 205 nm, where it makes an important contribution to the total O_2 cross section (between 195 and 205 nm). The absorption of solar radiation in this spectral region has important implications in middle atmosphere chemistry, particularly for the distributions of N_2O and chlorofluorocarbons in the stratosphere (Froidevaux and Yung, 1982; Brasseur *et al.*, 1983). The O_2

photodissociation frequency corresponding to the Herzberg continuum is about $10^{-9}s^{-1}$ for zero optical depth. In spite of the weakness of this transition, it becomes dominant in the stratosphere (Figure 4.34). The rate of ozone production in the stratosphere, therefore, depends critically on the value of the absorption cross sections in this region.

In the region of the *Schumann-Runge bands* (175-205 nm), molecular oxygen is predissociated and provides an important source of $O(^3P)$. The absorption cross section varies by about 5 orders of magnitude between 175 and 205 nm. The calculation of the photodissociation rate requires a detailed study of the absorption cross section. Experimental results obtained in this region have been applied to the atmospheric problem by several investigators who have proposed various methods to parameterize the solar absorption and the O_2 photolysis in the spectral range corresponding to these bands (*e.g.*, Fang *et al.*, 1974; Kockarts, 1976; Allen and Frederick, 1982; Gijs *et al.*, 1996). Laboratory measurements by Yoshino *et al.* (1983) and Lewis *et al.* (1986; 1994) have led to improved values for Schumann-Runge band spectral parameters, most notably oscillator strengths and predissociation widths of rotational lines. These data have been used by Murtagh (1988), Nicolet and Kennes (1989), Minschwaner *et al.* (1992), and Kockarts (1994) to construct temperature dependent line-by-line representations of the Schumann-Runge bands. Figure 4.32 (right panel) shows the variation of the absorption cross section of O_2 from 175 nm to 205 nm as calculated by Kockarts (1994). Detailed calculations indicate a photodissociation frequency of about $10^{-7}s^{-1}$ at zero optical depth (Nicolet *et al.*, 1989).

The determination of the O_2 photodissociation frequency in the Schumann-Runge bands is obtained from a computation including the complex rotational structure of the band system. A major difficulty in the calculation of Schumann-Runge band photolysis in the middle atmosphere, in addition to requirements for high spectral resolution, arises from the temperature dependence of absorption cross sections. Polynomial expressions have been derived to reproduce the temperature variation provided by the line-by-line calculations (Minschwaner *et al.*, 1992); this kind of approach, however, is generally not feasible to be implemented in detailed middle atmosphere models, but can be used to develop more efficient broad-band parameterizations (see Section 4.7.3).

Because of its strong absorption ($\sigma = 1.5 \times 10^{-17}cm^2$ at 140 nm), the *Schumann-Runge continuum* (130-183 nm; see Figure 4.32, left panel) is only important in the thermosphere, and from the point of view of photolysis, plays a dominant role only above 90 km. Each photolysis event leads to the production of two oxygen atoms, one in the ground ^3P state and the other in the excited ^1D state. As shown by Hudson *et al.* (1966) and by Lean and Blake (1981), the temperature dependence

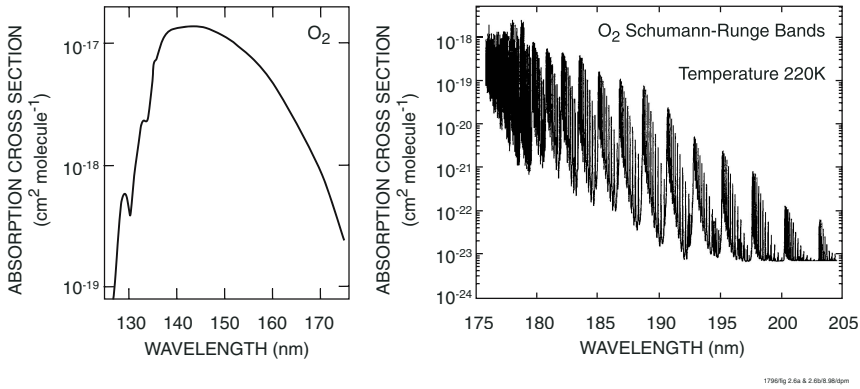

Figure 4.32. Left: Absorption spectrum of O_2 in the Schumann-Runge continuum (from Watanabe *et al.*, 1953). Right: Molecular oxygen absorption cross sections for a temperature of 220 K in the wavelength region of the Schumann-Runge bands (from Kockarts, 1994, using the technique described by Minschwaner *et al.*, 1993). The band structure is clearly visible and the effect of the underlying Herzberg continuum is apparent at wavelengths greater than 190 nm. Kockarts' approximation can be safely used down to a solar attenuation of the order of 10^{-10}.

of the cross section becomes noticeable for wavelengths longer than 160 nm and is mainly due to the redistribution of the population of rotational states. The Schumann-Runge continuum adjoins the Schumann-Runge band system at 175 nm and underlies the bands up to 183 nm. This continuum therefore contributes to the absorption cross section minima in the band system. The photodissociation frequency in the Schumann-Runge continuum at zero optical depth is (2.5-2.8) $\times 10^{-6}\mathrm{s}^{-1}$ (Zhu *et al.*, 1999), but only approximately $1 \times 10^{-8}\mathrm{s}^{-1}$ at 90 km for an overhead sun; this illustrates the large optical depth at these wavelengths even near the top of the middle atmosphere. A parameterization of the photodissociation frequency as a function of the O_2 column abundance is provided by Zhu *et al.* (1999).

At wavelengths less than 130 nm (see Figure 4.33), the most important contribution to oxygen photolysis comes from the *solar Lyman* α line at 121.6 nm ($\sigma = 10^{-20}\mathrm{cm}^2$), which penetrates to the mesosphere. The corresponding photolysis rate at zero optical depth is about $3 \times 10^{-9}\mathrm{s}^{-1}$, but its value can change strongly with solar activity. Figure 4.34 shows the contribution of each spectral region to the photolysis rate of O_2 for an overhead sun. Note the importance of the Herzberg continuum below 65 km (stratosphere and mesosphere), the Schumann-Runge bands from 65 to 90 km (mesosphere), and the Schumann-Runge continuum in the thermosphere. The Lyman α line plays a secondary role in oxygen

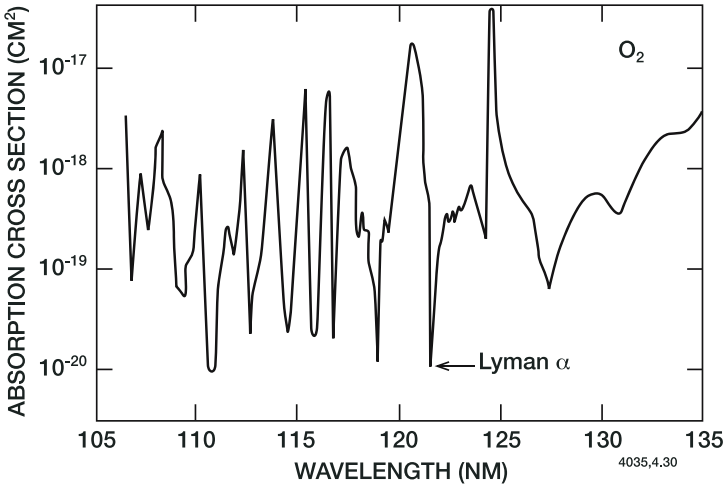

Figure 4.33. Spectral distribution of the absorption cross section of oxygen from 105 to 135 nm. The cross section exhibits a minimum for the wavelength corresponding to the solar Lyman α line. After Watanabe et al., (1953).

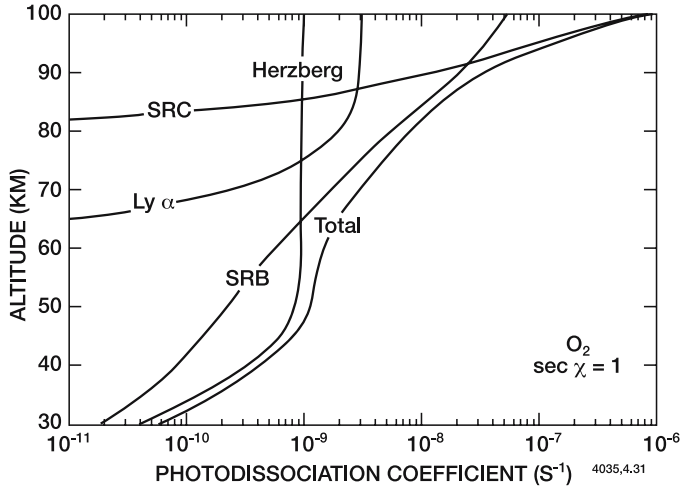

Figure 4.34. Contribution of each spectral region to the photodissociation of molecular oxygen as a function of altitude.

photolysis, but becomes much more important for other atmospheric constituents.

4.7.2.3 Ozone

The energy required to dissociate the ozone molecule being only of 25.4 kcal, (corresponding to a wavelength threshhold of 1180 nm) a large

fraction of the solar radiation from the near infrared to the ultraviolet can, in principle, lead to the photolysis of O_3. It is, however, primarily in 3 specific spectral regions that the absorption by ozone takes place (Figure 4.35): the Hartley band (200-310 nm), the Huggins bands (310-350 nm), and the Chappuis bands (410-750 nm).

The primary absorption by ozone occurs in the *Hartley band*. The absorption cross section maximizes at about 250 to 260 nm, where $\sigma = 10^{-17}\text{cm}^2$. The absorption in this band has been studied since the beginning of the century. The temperature dependence of the absorption is negligible for wavelengths shorter than about 260 nm. Vigroux (1953, 1969), however, observed a weak variation of the cross section with temperature at longer wavelengths, which is probably due to the superposition of strong predissociating bands on the continuum. These bands were observed as early as 1929 by Lambrey and Chalonge.

Around 300 nm, the Hartley band becomes weak, and from 310 to 350 nm it blends with the temperature dependent *Huggins bands*. Figure 4.35 shows the importance of this temperature sensitivity, especially at long wavelengths. A careful calculation is required to account for the details of the spectral structure as a function of temperature.

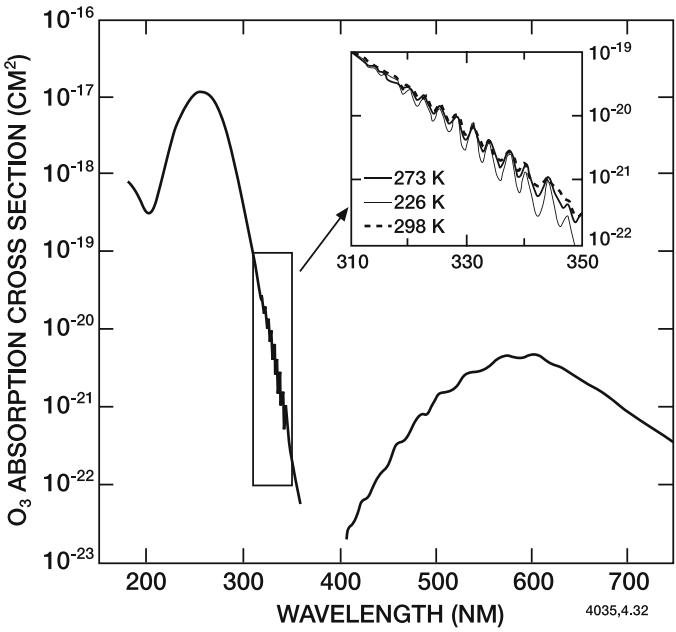

Figure 4.35. Spectral distribution of the ozone cross section in the Hartley band (200-300 nm), Huggins bands (310-350 nm), and Chappuis bands (410-750 nm).

Ozone also absorbs in the visible region via the *Chappuis bands* (Figure 4.35). This spectral regime contributes significantly to the photodissociation of ozone and plays a dominant role in the lower stratosphere and troposphere ($z < 25$ km).

Finally, at wavelengths less than 200 nm, the absorption by ozone is related to the existence of large bands superimposed on a continuum. This spectral region plays a very minor role in the photochemistry of the ozonosphere because these wavelengths are absorbed by molecular oxygen at altitudes far above the ozone layer. It should be noted, however, that in the region of the O_2 Herzberg continuum both ozone and oxygen contribute to absorption of radiation.

A large number of laboratory measurements have been reported for the absorption cross sections of ozone (*e.g.*, Inn and Tanaka, 1953; Vigroux, 1969; Molina and Molina, 1986; Daumont *et al.*, 1992; Yoshino *et al.*, 1993), and are the basis for the recommended values presented by WMO (1985) or JPL (1997). High resolution measurements from 195 to 345 nm, and at different temperatures, have been made by Malicet *et al.* (1995).

Table 4.6 Theoretical Limits Corresponding to Different Photolysis Products (nm)

	$O_2(^3\Sigma_g)$	$O_2(^1\Delta_g)$	$O_2(^1\Sigma_g+)$	$O_2(^3\Sigma_u+)$	$O_2(^3\Sigma_u^-)$
O (^{3}P)	1180	590	460	230	170
O (^{1}D)	410	310	260	167	150
O (^{1}S)	234	196	179	129	108

The photochemistry of ozone is reviewed by Wayne (1987) and Steinfeld *et al.* (1987). The photodissociation products, O and O_2, are found in different energy states depending directly on the energy of the incident photon. Table 4.6 indicates the theoretical limits corresponding to different dissociation products. Some transitions violate the spin rules and therefore play a minor role compared to the allowed transitions in the same spectral region. For wavelengths greater than approximately 320 nm, the following reaction occurs:

$$J_{O_3}; \qquad O_3 + h\nu \rightarrow O(^3P) + O_2(^3\Sigma_g^-) \tag{4.114a}$$

and, for wavelengths less than 305 nm, the spin allowed fragmentation channel

$$J^*_{O_3}; \qquad O_3 + h\nu \rightarrow O(^1D) + O_2(^1\Delta_g) \tag{4.114b}$$

leads mainly to the formation of the electronically excited atom $O(^1D)$. The formation of $O(^1S)$ is possible for $\lambda < 196$ nm.

The calculation of the rate of formation of the $O(^1D)$ atom and the $O_2(^1\Delta g)$ molecule requires exact knowledge of the quantum efficiency for channel (4.114b), especially near the "fall off" region in the vicinity of 310 nm. Several measurements of the quantum yield for O^1D formation as a function of wavelength and temperature have been reported in the literature (*e.g.*, Lin and De More, 1973; Moortgat *et al.*, 1977; Ball *et al.*, 1993; 1995; Takahashi *et al.*, 1996; 1998), suggesting the following picture: At wavelengths less than 305 nm, the $O(^1D)$ yield is approximately constant and equal to 0.9-0.95. In the vicinity of 310 nm, it decreases rapidly with wavelength, but remains different from zero at 335 nm (Silvente *et al.*, 1997; Michelsen *et al.*, 1994). In addition to the spin-allowed photolysis (4.114b) of vibrationally excited ozone molecules, the spin-forbidden dissociation process

$$O_3 + h\nu(\lambda \leq 411\text{nm}) \rightarrow O(^1D) + O_2\left(^3\Sigma_g^-\right) \qquad (4.114c)$$

is believed to contribute to the formation of $O(^1D)$ at wavelengths larger than 310 nm (see Figure 4.36, upper panel, and Takahashi *et al.*, 1998). Figure 4.36 (lower panel) illustrates how the O^1D yield varies with temperature for a number of selected wavelengths in the 305-325 nm range.

Figure 4.37 shows the relative contribution of each band to the ozone photolysis frequency as a function of altitude. It should be noted that the value of the ozone photodissociation coefficient depends critically on the absorption by ozone itself, introducing a nonlinear coupling as a function of altitude. The calculation of J_{O_3} must include the effects of molecular scattering and albedo (see Figure 4.38).

4.7.2.4 Water Vapor

The absorption spectrum of water vapor consists of a continuum from 145 to 186 nm, diffuse bands from 69 to 145 nm, and a continuum below 69 nm. A maximum in the intensity of a diffuse band (121.8 nm) is located in the vicinity of the Lyman-α line (121.6 nm). Figure 4.39 shows the shape of the absorption cross section of water vapor above 120 nm. Measurements of this cross section were reported by Watanabe and Zelikoff, 1953, Thompson *et al.* (1963), Laufer and McNesby (1965), Schurgers and Welge (1968), Yoshino *et al.* (1996b), and Cantrell *et al.* (1997). In particular, the value of $\sigma\,(H_2O)$ at Lyman α has been determined to be about $1.4 \times 10^{-17}\text{cm}^2$. Another noteworthy feature is the rapid decrease in the cross section longward of 175 nm. Beyond this wavelength, the penetration of solar radiation is determined by the O_2

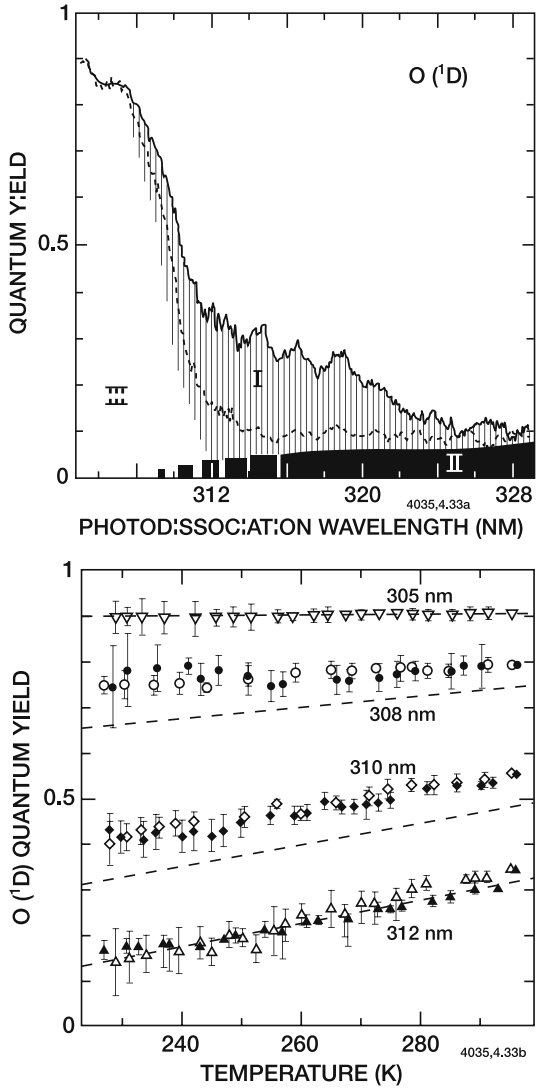

Figure 4.36. Top panel: Contributions of different processes to the $O(^1D)$ quantum yield as a function of wavelengths between 305 and 329 nm. The solid and broken lines represent the quantum efficiencies measured at 295 K and 227 K, respectively. Shaded region I shows the contribution of the hot band excitation process leading to the formation of $O(^1D)$ via Reaction (4.114b) at 295 K. Region II (in black) represents the contribution of the spin-forbidden dissociation (4.114c). Region III corresponds to the $O(^1D)$ formation via Reaction (4.114b) following excitation of ozone at ground vibration state. Bottom panel: $O(^1D)$ quantum efficiency as a function of temperature at 305, 308, 310 and 312 nm. Laboratory measurements are compared to recommendations (dashed lines) by JPL (1997). From Takahashi *et al.* (1998).

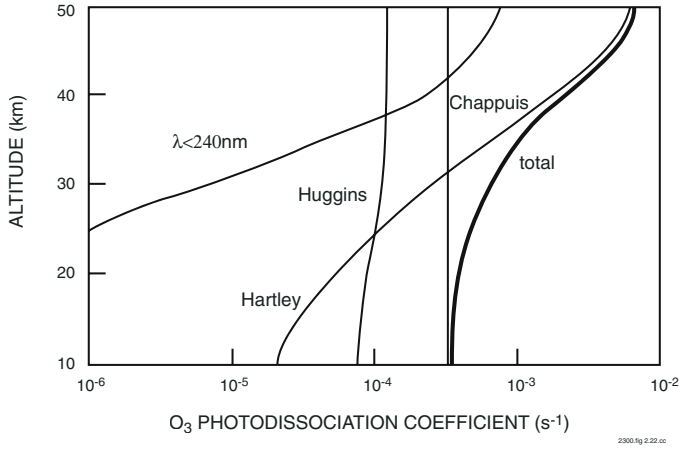

Figure 4.37. Contributions of different absorption bands to the total photodissociation frequency of ozone for overhead sun. Adapted from Nicolet (1980).

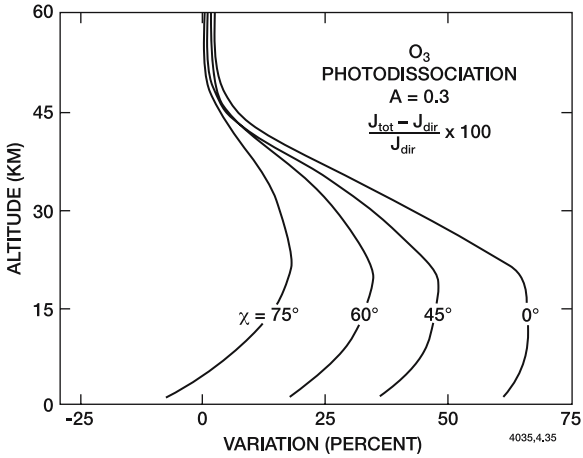

Figure 4.38. Relative effects of scattering on the photolysis rate of ozone from the ground to 60 km for several solar zenith angles. Surface albedo = 0.3.

Schumann-Runge bands. Special attention is therefore required when calculating J_{H_2O} below about 60 km (see Section 4.7.3).

Figure 4.40 shows the contributions of the Lyman α line and the Schumann-Runge bands to the vertical distribution of J_{H_2O}. Photodissociation in the middle atmosphere occurs at wavelengths above about 100 nm, while photoionization occurs for wavelengths less than 98 nm. In the mesosphere and thermosphere, water vapor is photodissociated mainly by the solar Lyman α line, leading to a substantial fraction of the hydrogen atom production at these altitudes.

In the lower mesosphere and upper stratosphere, the continuum absorption of water vapor occurs in the domain of the O_2 Schumann Runge bands. The photolysis frequency at zero optical depth varies from 4.0 to 6.5 $\times 10^{-6} s^{-1}$ depending on the level of solar activity.

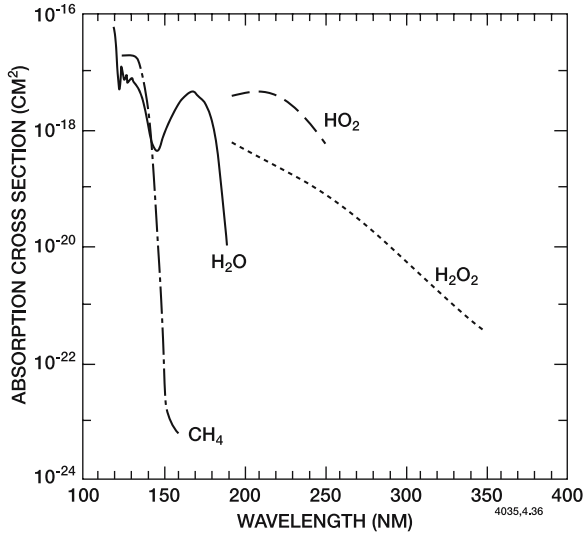

Figure 4.39. Spectral distribution of the absorption cross section of water vapor (H_2O), methane (CH_4), hydrogen peroxide (H_2O_2), and the peroxy radical (HO_2).

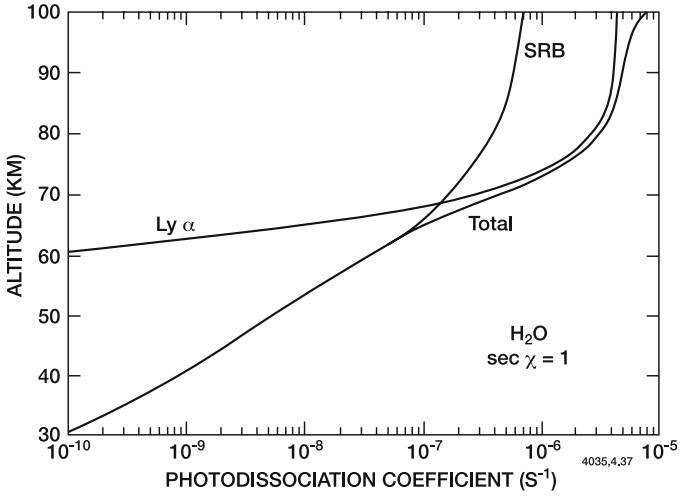

Figure 4.40. Contributions of different spectral regions to the photodissociation of water vapor for an overhead sun.

The products of water photolysis vary with the energy of the incoming radiation. At wavelengths larger than 147 nm (continuum), they are primarily hydrogen atoms and hydroxyl radicals in their fundamental electronic state ($X^2\pi$). At wavelengths shorter than 147 nm (diffuse bands), hydrogen molecules together with oxygen atoms are believed to be produced with a quantum efficiency between 105 and 145 nm which could vary from 2.5 to 23% according to Rebbert *et al.* (1972) and is estimated as 11% according to Stief *et al.* (1975). At wavelengths less than 136 nm, the OH radical produced could also be in its electronically excited $A^2\Sigma^+$ state, with a yield of perhaps 10% (Nicolet, 1978). Thus, one has to consider, in the mesosphere, 3 channels that are initiated by the solar Lyman-α line:

$$H_2O + h\nu\,(\lambda = 121.6\text{ nm}) \rightarrow H + OH\left(X^2\pi\right) \qquad (4.115a)$$

$$\rightarrow H_2 + O\left(^1D\right) \qquad (4.115b)$$

$$\rightarrow H + OH\left(A^2\Sigma^+\right) \qquad (4.115c)$$

with very uncertain quantum efficiencies. In the stratosphere, the major channel is provided by

$$H_2O + h\nu\,(\lambda < 200\text{ nm}) \rightarrow H + OH\left(X^2\pi\right) \qquad (4.115d)$$

4.7.2.5 Hydrogen Peroxide (H_2O_2)

The absorption cross section of hydrogen peroxide is shown in Figure 4.39. In the spectral domain which is important in the stratosphere, absorption cross section measurements have been made by Schurgens and Welge (1968) from 120 to 200 nm, Holt *et al.* (1948) and Holt and Oldenberg (1949) from 185 to 253 nm, and Urey *et al.* (1929) from 215 to 380 nm. More recent measurements include those of Lin *et al.* (1978), Molina and Molina (1981), Nicovich and Wine (1988), and Vaghjiani and Ravishankara (1989). The cross sections vary slightly with temperature. The photodissociation quantum efficiency is believed to be unity.

4.7.2.6 Methane (CH_4)

Methane only photodissociates in the upper part of the middle atmosphere because its absorption cross section becomes very weak at wavelengths longer than 145 nm (Figure 4.39). The most intense part of the spectrum is located below 130 nm, where the cross section is about $1.9 \times 10^{-17}\text{cm}^2$. The Lyman α line dominates the photolysis rate with

a mean value at zero optical depth of about

$$J^{\infty}_{CH_4}(\text{Ly}\alpha) = 5.5 \times 10^{-6}\text{s}^{-1}$$

Like water vapor, the photolysis rate varies over the solar cycle due to the variation in Lyman α flux. The different spin-allowed dissociation pathways after excitation at the Lyman α wavelength are

$$CH_4 + h\nu(\text{Ly}\alpha) \rightarrow CH_3 + H \qquad (39\%) \qquad (4.116a)$$

$$\rightarrow CH_2 + H_2 \qquad (52\%) \qquad (4.116b)$$

$$\rightarrow CH_2 + H + H \qquad (1\%) \qquad (4.116c)$$

$$\rightarrow CH + H + H_2 \qquad (8\%) \qquad (4.116d)$$

with the relative contribution of each channel quoted in parentheses and based on the recommendation by Brownword *et al.* (1997). These quoted efficiencies are different from the values suggested earlier by Slanger and Black (1982).

4.7.2.7 Carbon Dioxide (CO_2)

The spectral distribution of the absorption cross section of CO_2 (Figure 4.41) has been measured by several experimenters (Inn *et al.*, 1953, from 106 to 175 nm; Ogawa, 1971, from 175 to 195 nm; Shemansky, 1972, above 195 nm; Lewis and Carter, 1983, from 120 to 195 nm; Yoshino *et al.*, 1996a, from 118 to 175 nm). Carbon dioxide dissociates only at relatively high altitudes, where solar Lyman α and Schumann Runge continuum radiation is present. The corresponding photolysis rates at the top of the atmosphere are (Nicolet, 1980):

$$\text{J}^{\infty}_{CO_2}(\text{Ly}\alpha) = 2.20 \times 10^{-8}\text{s}^{-1}$$

$$\text{J}^{\infty}_{CO_2}(\text{SRC}) = 9.28 \times 10^{-8}\text{s}^{-1}$$

and, for T = 300K,

$$\text{J}^{\infty}_{CO_2}(\text{SRB}) = 1.90 \times 10^{-9}\text{s}^{-1}$$

These values are also subject to solar activity variations, especially the contribution of Lyman α and the Schumann Runge continuum. The complete calculation of the photolysis rate including absorption by molecular oxygen indicates that CO_2 photolysis is due primarily to Lyman α in the upper mesosphere, and to the Schumann Runge bands in the mesosphere and stratosphere. Due to the strong temperature dependence of the CO_2 cross section in the O_2 Schumann Runge bands region (DeMore and Patapoff, 1972), the value of J_{CO_2} decreases at lower temperatures (see Nicolet, 1980).

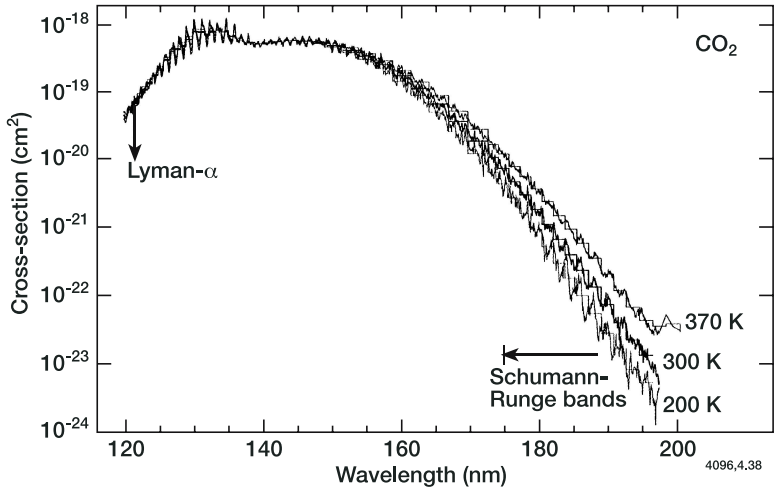

Figure 4.41. Spectral distribution of the absorption cross section of carbon dioxide for three temperatures: 200 K, 300 K, and 370 K. From Lewis and Carter (1983).

4.7.2.8 Formaldehyde (CH_2O)

The absorption cross section of formaldehyde (Figure 4.42) has been studied by several investigators since the experiments of Henri and Schou (1928), in particular by Bass *et al.* (1980), Moortgat *et al.* (1980; 1983), and Cantrell *et al.* (1990). It has long been recognized (Herzberg, 1931; Norrish and Kirkbride, 1932) that the photolysis of CH_2O can lead to two different product paths:

$$(J_{H-CHO}); \qquad CH_2O + h\nu \rightarrow H + CHO \tag{4.117a}$$

$$(J_{H_2-CO}); \qquad CH_2O + h\nu \rightarrow H_2 + CO \tag{4.117b}$$

The relative importance of these processes has been studied by several investigators. According to Moortgat *et al.* (1983), the quantum yield for the production of H_2 and CO is pressure and temperature dependent for wavelengths longer than 330 nm. Figure 4.42 also shows the quantum efficiency associated with each process.

4.7.2.9 Nitric Oxide (NO)

The absorption spectrum of nitric oxide was observed more than a century ago, but the atmospheric importance of this chemical species has been stressed only in recent decades. Cieslik and Nicolet (1973) and Cieslik (1977), for example, used the measurements of Miescher and colleagues at the University of Basel to calculate the photolysis frequency of NO in the middle atmosphere. High resolution measurements of

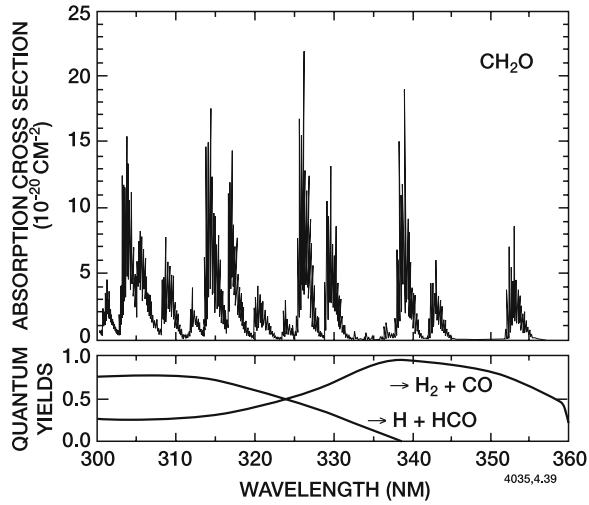

Figure 4.42. Spectral distribution of the formaldehyde cross section and quantum yields for the H + HCO and H_2 + CO channels.

nitric oxide absorption have also been reported by Murray *et al.* (1994). The ultraviolet absorption spectrum of NO exhibits four band systems (Marmo, 1953) defined by the following transitions (cf. Figure 4.43):

$$\gamma \text{ bands}: \quad A^2\Sigma \rightarrow X^2\pi$$
$$\beta \text{ bands}: \quad B^2\Pi \rightarrow X^2\pi$$
$$\delta \text{ bands}: \quad C^2\Pi \rightarrow X^2\pi$$
$$\epsilon \text{ bands}: \quad D^2\pi \rightarrow X^2\pi$$

Calculation of the photolysis rate of nitric oxide must include the predissociation process which occurs at wavelengths less than 192 nm. In particular, predissociation occurs (Figure 4.43) in the δ bands, the β bands ($v' > 6$) and the ϵ bands ($v' > 3$). Callear and Pilling (1970 a,b) indicate that emission dominates predissociation in the ϵ bands. At zero optical depth, the contribution of the γ bands is small compared to those of the δ and β bands.

In the mesosphere and stratosphere, the β bands of quantum number v'' greater than 9, are almost totally attenuated and the other β bands contribute less than 10 percent to the photolysis rate. Thus, only the two bands δ (0-0) at $\lambda \approx 190.9$ nm and δ (1-0) at $\lambda \approx 182.7$ nm need be considered in calculating the photolysis rate in the middle atmosphere. J_{NO} has been studied by Cieslik and Nicolet (1973), Park (1974), Frederick and Hudson (1979), Nicolet and Cieslik (1980), and Minschwaner and Siskind (1993). It should be noted that the derived values are sensitive to the different values assumed for the oscillator

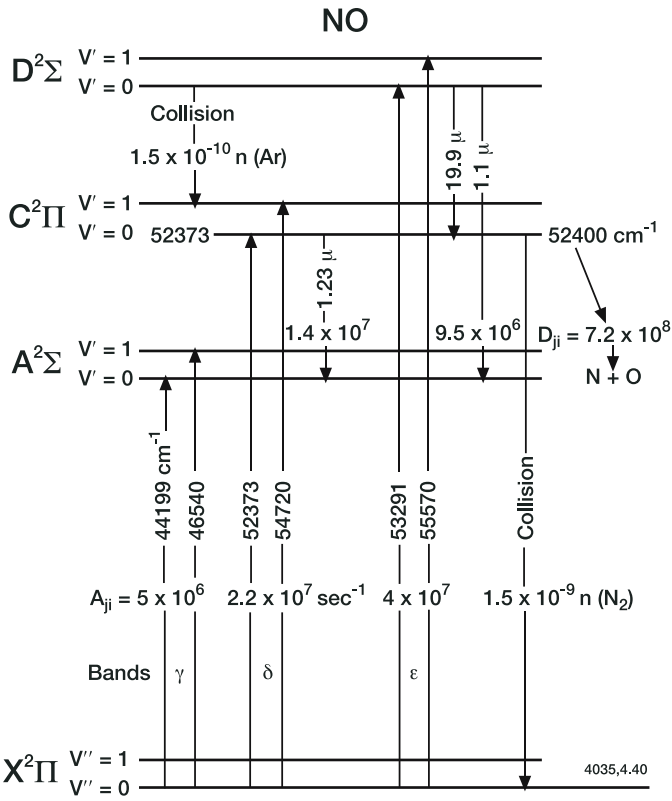

Figure 4.43. Energy levels of nitric oxide and corresponding transitions

strength and the solar flux. Minschwaner and Siskind (1993) indicate that for zero optical depth

$$\mathrm{J_{NO}}\left(\delta\left[0-0\right]\right) = 2.6 \times 10^{-6}\mathrm{s}^{-1}$$

and

$$\mathrm{J_{NO}}\left(\delta\left[1-0\right]\right) = 3.2 \times 10^{-6}\mathrm{s}^{-1}$$

The calculation of the photolysis rate at all atmospheric levels requires detailed knowledge of the solar spectrum. The primary attenuation of the solar flux in the δ (0-0) band is due to the (5-0) Schumann-Runge band of O_2; the attenuation in the δ (1-0) band is due to the (9-0) and (10-0) bands of O_2. Thus, the determination of J_{NO} requires consideration of the ensemble of rotational lines of each NO and O_2 band system. Further, the effect of temperature is important in the intensities of both the NO and O_2 bands. The vertical temperature structure must therefore be considered for aeronomic studies. The attenuation of the δ (1-0) band is more rapid than that of the δ (0-0) band; thus the photolysis rate of NO in the stratosphere and lower mesosphere depends

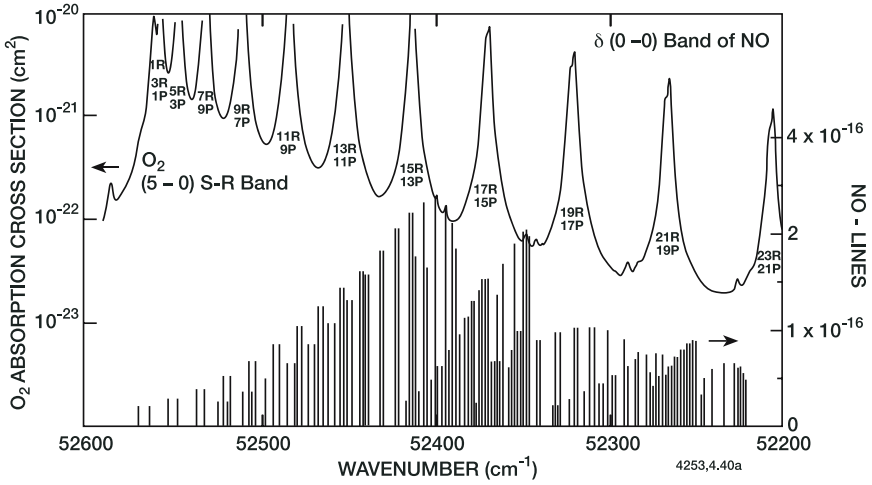

Figure 4.44. Detailed structure of the (5-0) band of the Schumann-Runge system of O_2 in the spectral range of the δ (0-0) band of nitric oxide. From Cieslik and Nicolet (1973).

critically on the behavior of the δ (0-0) band and its attenuation by the (5-0) band of O_2. Figure 4.44 shows the detailed structure of the δ (0-0) band of nitric oxide together with that of the (5-0) band of the O_2 Schumann-Runge system.

Frederick *et al.* (1983) have shown that the inclusion of the opacity provided by nitric oxide itself reduces the calculated dissociation at lower altitude. Since thermospheric NO is known to increase with increasing solar activity, a modulation of the solar penetration with the solar cycle should occur at the wavelengths which photodissociate NO. The direction of this change is, however, opposite to that of the solar irradiance, which increases with solar activity. For example, Minschwaner and Siskind (1993) found that for solar zenith angles greater than 60°, J_{NO} below 100 km may be smaller during solar maximum compared to solar minimum (see Minschwaner and Siskind, 1993). However, the self absorption is sensitive to the δ-band predissociation widths which are highly uncertain.

4.7.2.10 Nitrous Oxide (N_2O)

The absorption spectrum of N_2O has been measured several times (*e.g.*, Selwyn *et al.*, 1977; Hubrich and Stuhl, 1980; Mérienne *et al.*, 1990) since the detection of this molecule by Leifson in 1926. The absorption coefficient above 260 nm has been shown to be very small, which implies that N_2O must be quite inert in the troposphere. The absorption spectrum is shown in Figure 4.45.

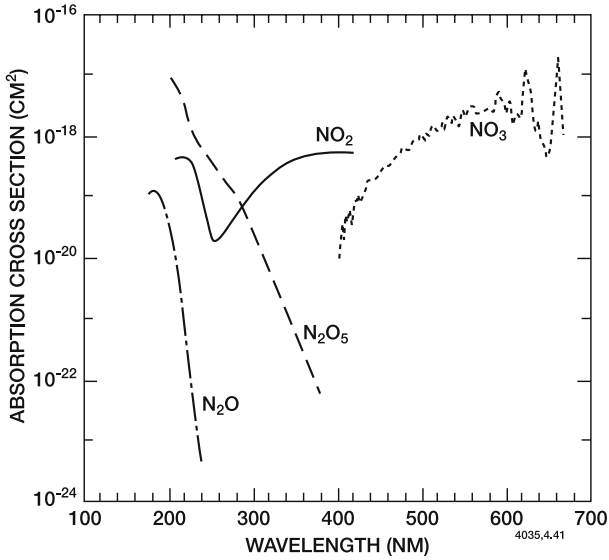

Figure 4.45. Spectral distribution of the absorption cross section for various nitrogen oxides at 220 K.

As shown by Johnston and Selwyn (1975), the cross section of N_2O varies strongly with temperature. The quantum yield for photodissociation is unity, and the products are N_2 and $O(^1D)$. The atmospheric photolysis rate comes predominantly from the absorption of solar radiation in the O_2 Herzberg continuum and Schumann Runge bands. $J^{\infty}_{N_2O} \approx 9 \times 10^{-7} s^{-1}$ for $\lambda > 175$ nm.

4.7.2.11 Nitrogen Dioxide (NO_2)

The absorption spectrum of NO_2 has been studied in various spectral domains since its detection by Bell in 1885 (see, *e.g.*, Bass *et al.*, 1976; Davidson *et al.*, 1988; and Schneider *et al.*, 1987). Figure 4.45 shows the shape of the absorption cross section of NO_2 from 190 to 410 nm. The photolysis quantum efficiency decreases with wavelength near the photolysis limit. JPL (1997) recommends quantum yields of 1.0 at wavelengths less than 285 nm, 0.997 at 300 nm, 0.987 at 350 nm, 0.695 at 400 nm, 0.018 at 420 nm, and 0.0 beyond 424 nm. Because the absorption cross sections vary slightly with temperature, the photodissociation rate decreases by about 10 percent when the temperature changes from 300 to 235 K. It should be noted that this spectral region is quite sensitive to the effects of molecular scattering and albedo (Figure 4.46a,b) so that the precise value of J_{NO_2} depends strongly on geographic conditions and on the albedo of the troposphere.

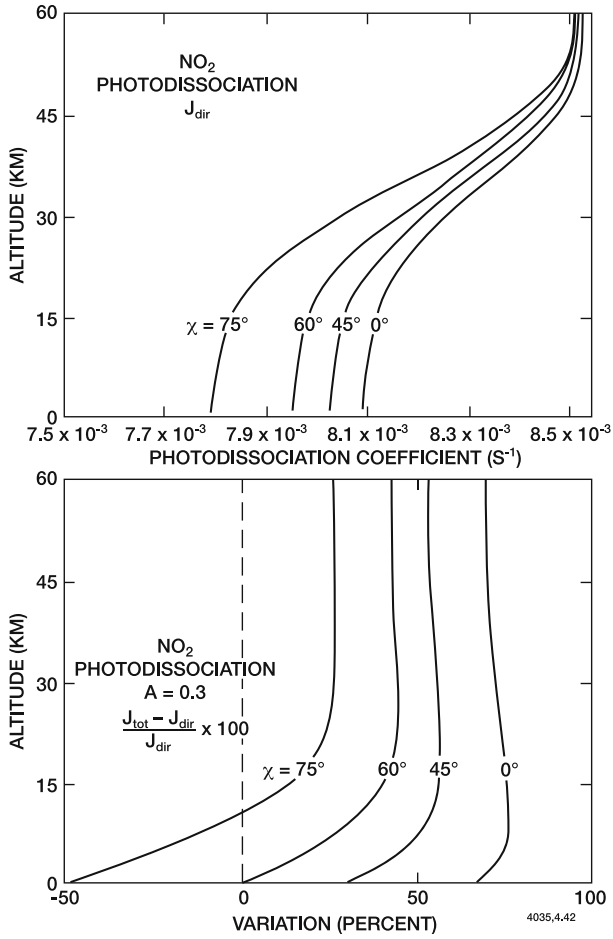

Figure 4.46. (a) Vertical distribution of the NO_2 photolysis rate for several values of the solar zenith angle (absorption of direct solar radiation only). (b) Relative effect of scattering on the photolysis rate of NO_2. Earth albedo = 0.3.

4.7.2.12 Nitrogen Trioxide (NO_3)

The spectroscopy of NO_3 has been reviewed by Wayne *et al.* (1991). The absorption spectrum of this radical (see Figure 4.45) exhibits several predissociating bands first observed in 1962 by Ramsay. Laboratory studies reviewed by Johnston *et al.* (1996) provided quantitative values of the photodissociation parameters. The quantum efficiency for each of the two possible pathways

$$NO_3 + h\nu(\lambda < 580 \text{ nm}) \rightarrow NO_2 + O \qquad (4.118a)$$

and

$$NO_3 + h\nu(\lambda > 580 \text{ nm}) \rightarrow NO + O_2 \qquad (4.118b)$$

is still not completely established, despite measurements by Graham and Johnston (1978), Magnotta and Johnston (1980), and more recently by Orlando *et al.* (1993). Laboratory studies indicate, however, that the first process is dominant and that it may even occur at wavelengths longer than the limit of 580 nm at elevated temperatures. The quantum yield of the second channel is no more than 25 percent from 520 to 640 nm, and is very small at longer wavelengths. The values of the photolysis frequencies determined by Johnston *et al.* (1996) can be used for most atmospheric applications:

$$J^{a}_{NO_3} = 0.156 \text{ s}^{-1}$$

$$J^{b}_{NO_3} = 0.0201 \text{ s}^{-1}$$

4.7.2.13 Dinitrogen Pentoxide (N_2O_5)

The absorption cross sections of N_2O_5 (Figure 4.45) were first measured by Jones and Wulf (1937). Since then, other measurements have been performed by Johnston and Graham (1974), Graham (1975), Yao *et al.* (1982), and by Harwood *et al.* (1993). The latter studies found significant temperature dependence at wavelengths longer than about 280 nm.

4.7.2.14 Nitrous Acid (HNO_2)

The absorption spectrum of HNO_2 (Figure 4.47) has been studied by Stockwell and Calvert (1978), and by Vasudev (1990) and Bongartz *et al.* (1991). More detailed experimental work is needed, but it is clear that the photolysis of HNO_2 is fast, even at low altitudes.

4.7.2.15 Nitric Acid (HNO_3)

The absorption by HNO_3 (Figure 4.47) is a continuum from 220 to 300 nm, and was observed as early as 1943 by Dalmon. Johnston and Graham (1973) and Biaumé (1973) measured the absorption cross section from 180 to 330 nm. The data obtained by these studies are in general agreement between 205 and 300 nm. Burkholder *et al.* (1993) noted that discrepancies remain below 205 nm and above 300 nm. In addition, they recommended that the temperature dependence observed for wavelengths greater than 280 nm be taken into account when calculating J_{HNO_3}. Johnston *et al.* (1974) recommend a quantum yield value of approximately 1 for the OH + NO_2 channel. However, at 193 nm, Turnipseed *et al.* (1992) report this quantum yield to be 0.33 at 193 nm, with the O + HNO_2 channel being important at this wavelength.

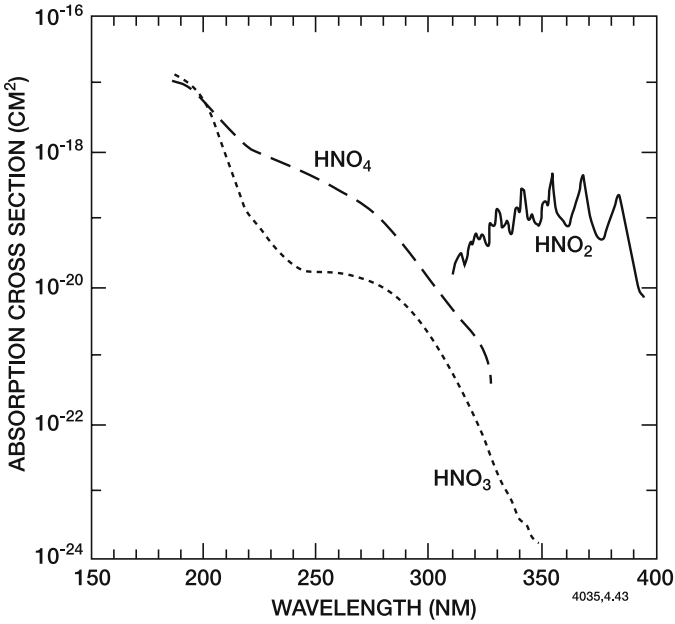

Figure 4.47. Spectral distribution of the absorption cross section for HNO_2, HNO_3, and HNO_4 at 220 K.

The quantum yield for OH production could be as low as 0.75 at 248 nm (Schiffman *et al.*, 1993). More detailed investigations are needed.

4.7.2.16 Peroxynitric Acid (HO_2NO_2 or HNO_4)

The absorption spectrum of HO_2NO_2 (Figure 4.43) was observed by Graham *et al.* (1978) and by Cox and Patrick (1979). These two studies are in good agreements from 205 to 260 nm, but at 195 nm the results of Graham are twice as large as those of Cox and Patrick. Molina and Molina (1981) presented a spectral distribution of the absorption cross section which exhibits much smaller values than the previous studies at all wavelengths. The cross sections are temperature independent between 253 K and 298 K (Singer *et al.*, 1989). The quantum yield of the photolysis was measured at 248 nm by McLeod *et al.* (1988). They report an efficiency of one third for the OH + NO_3 channel and two thirds for HO_2 + NO_2.

4.7.2.17 The Halocarbons

Since the important effects of chlorocarbon compounds on atmospheric ozone were pointed out by Molina and Rowland (1974) and by Rowland and Molina (1975), the absorption spectra of the various chlorocarbons that provide the source of chlorine to the atmosphere have

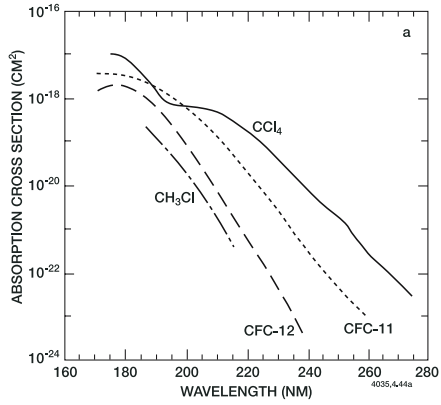

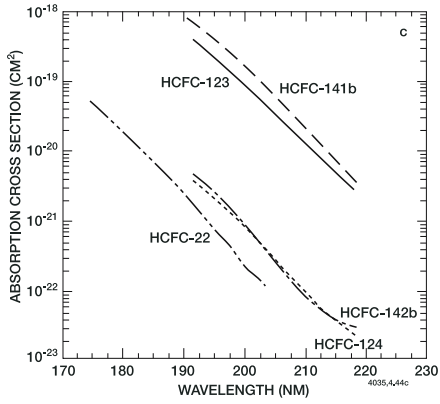

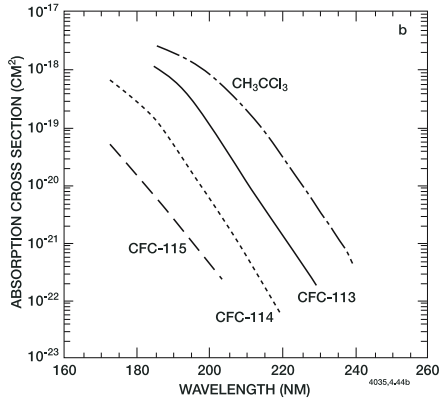

Figure 4.48. Upper left panel (a) Spectral distribution of the absorption cross sections of CCl_4, $CFCl_3$ (CFC-11), CF_2Cl_2 (CFC-12), and CH_3Cl at T=220 K. Lower left panel (b) Spectral distribution of the absorption cross section of CH_3CCl_3, CFC-113, CFC-114, CFC-115 at T=220 K. Upper right panel (c) Spectral distribution of the absorption cross section of several hydrogenated chlorofluorocarbons (HCFC-22, HCFC-123, HCFC-124, HCFC-141b, and HCFC-142b) at T = 220 K.

been measured by several groups, including Rowland and Molina (1975), Hubrich *et al.* (1977), Chou *et al.* (1977; 1978), Van Laethem-Meurée *et al.* (1978a,b), Hubrich and Stuhl (1980), and Simon *et al.* (1988). Spectral distributions of the cross sections for several chlorofluorocarbons (CFCs) and hydrogenated chlorofluorocarbons (HCFCs) are given in Figure 4.48a,b,c.

4.7.2.18 Methyl Bromide (CH_3Br), Bromoform ($CHBr_3$), and Halons

The measurements of the CH_3Br absorption cross sections (Figure 4.49a by Robbins (1976), Molina *et al.* (1982), and Gillotay and Simon (1988) are in very good agreement. In the case of $CHBr_3$, the measurements by Gillotay *et al.* (1989) and Moortgat *et al.* (1993) are in excellent agreement in the spectral region where they overlap. The

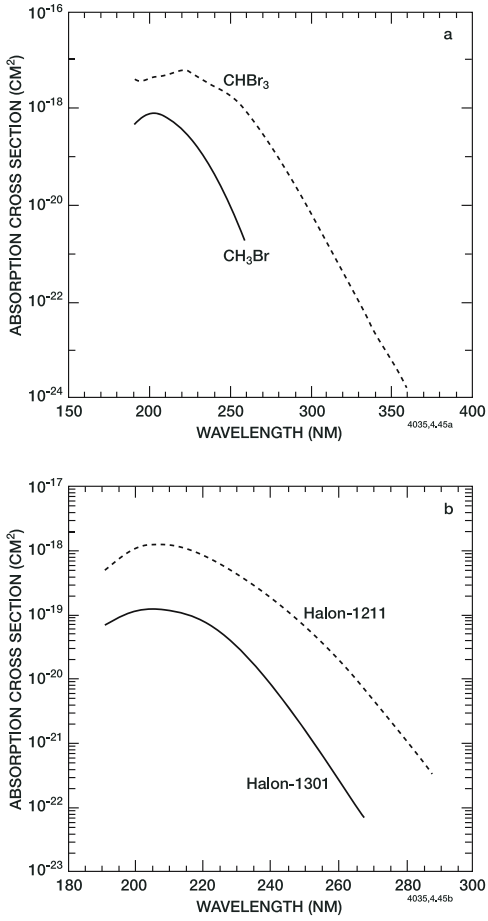

Figure 4.49. (a) Spectral distribution of the absorption cross sections of methyl bromide (CH_3Br) and methyl bromoform ($CHBr_3$) (T=220 K). (b) Spectral distribution of the absorption cross sections of halons–1211 and –1301 (T=220 K).

cross sections for halon 1211 (CF_2ClBr) and halon 1301 (CF_3Br) are given in Figure 4.49b.

4.7.2.19 Chlorine and Bromine Oxides

The absorption cross section of chlorine monoxide ClO is characterized by a continuum (which is independent of temperature) at wavelengths less than 265 nm and by a band structure (which is extremely temperature dependent) at higher wavelengths.

The different laboratory measurements (see *e.g.*, Watson, 1977) are usually in good agreement. A detailed theoretical study of ClO was presented by Langhoff *et al.* (1977a,b). The photodissociation of ClO accounts for 2 to 3 percent of the total chemical destruction of this radical (by atomic oxygen and nitric oxide).

The spectrum of chlorine dioxide (OClO) is characterized by a well developed progression of bands covering parts of the ultraviolet and visible regions (280 to 480 nm). Cross sections were measured by Wahner *et al.*(1987) and by Hubinger and Nee (1994). The lifetime of OClO against photolysis is only a few seconds.

The absorption cross sections of the chlorine peroxyl radical (ClOO) have been measured between 220 and 280 nm by Mauldin *et al.*(1992). The maximum absorption takes place around 246 nm.

The absorption cross section of BrO is represented by a banded spectrum in the 290-380 nm range with the strongest absorption feature around 338 nm (Wahner *et al.*, 1988). Values are temperature dependent. The lifetime associated with the photodecomposition of BrO is of the order of 20 seconds at the Earth's surface (solar zenith angle of 30°) (Cox *et al.*, 1982).

The spectrum of OBrO has a remarkable similarity with that of OClO with highly structured absorption bands. (Rattigan *et al.*, 1994).

4.7.2.20 Dichlorine Peroxide (Cl_2O_2)

The absorption cross sections of Cl_2O_2 (or ClOOCl) have been measured by different investigators (*e.g.*, DeMore and Tschuikow-Roux, 1990; Cox and Hayman, 1988; Permien *et al.*, 1988; Burkholder *et al.*, 1990; Molina *et al.*, 1990; and Huder and DeMore, 1995) between 190 and 450 nm (see Figure 4.50). Values beyond 360 nm, however, are very uncertain. The quantum yield for the photodissociation is unity for the Cl + ClOO channel (Molina *et al.*, 1990).

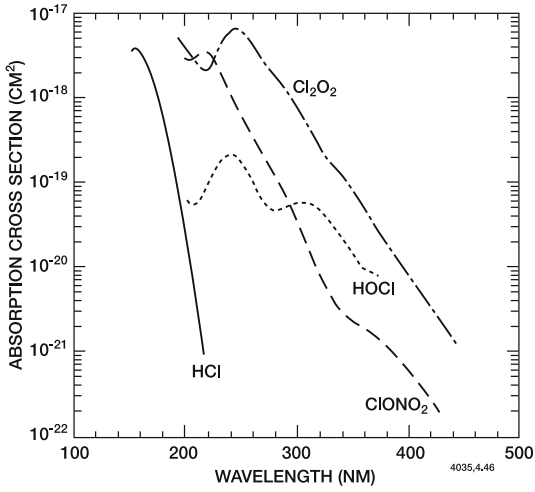

Figure 4.50. Spectral distribution of the absorption cross sections of various inorganic chlorine compounds (T=220 K).

4.7.2.21 Chlorine Nitrate ($ClONO_2$) and Bromine Nitrate ($BrONO_2$)

The absorption cross sections of $ClONO_2$ (Figure 4.50) have been measured by Molina and Molina (1979) and by Burkholder *et al.* (1994). The values are in good agreement and exhibit a temperature variation. The nature of the photo-fragments has been investigated in several laboratory studies. As concluded by JPL (1997), the quantum efficiency Φ_1 for the following channel

$$ClONO_2 + h\nu \rightarrow Cl + NO_3 \qquad (4.119a)$$

is equal to approximately 0.6 for wavelengths less than 308 nm, and to 1.0 for wavelengths longer than 364 nm. Between these two boundaries, the efficiency for this channel is expressed by $7.143 \times 10^{-3}\lambda - 1.60$, if λ is the wavelength expressed in nm. The quantum yield Φ_2 for the second channel

$$ClONO_2 + h\nu \rightarrow ClO + NO_2 \qquad (4.119b)$$

is given by $\Phi_2 = 1 - \Phi_1$.

Bromine nitrate possesses a similar spectrum (Figure 4.51) to that of chlorine nitrate. It is, however, shifted toward slightly longer wavelengths such that the photolysis rate of $BrONO_2$ is faster than that of $ClONO_2$. Like chlorine nitrate, the absorption cross sections are temperature dependent. They have been measured in the laboratory by Spencer and Rowland (1978) and more recently by Burkholder *et al.* (1995). Nickolaisen and Sander (1996) have shown that the quantum yields should be approximately 0.71 for the

$$BrONO_2 + h\nu \rightarrow BrO + NO_2 \qquad (4.120a)$$

channel, and 0.29 for

$$BrONO_2 + h\nu \rightarrow Br + NO_3 \qquad (4.120b)$$

channel.

4.7.2.22 Hydrochloric (HCl), Hydrobromic (HBr), and Hydrofluoric (HF) acids

The absorption cross sections (Figure 4.50) for hydrochloric acid (or hydrogen chloride) HCl were measured by Vodar (1948), Romand and Vodar (1948), and Romand (1949), and later by Inn (1975). The latter measurements extend from 140 to 220 nm, leading to a photodissociation frequency of about $3 \times 10^{-6} s^{-1}$ at zero optical depth. To calculate J_{HCl} in the atmosphere, the Schumann Runge bands and continuum must be considered, as well as the Herzberg continuum.

Measurements of the spectrum of hydrobromic acid or hydrogen bromide HBr have been presented by Goodeve and Taylor (1935), and

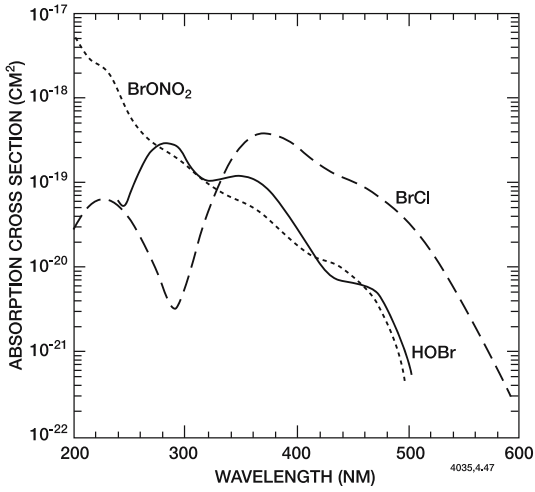

Figure 4.51. Spectral distribution of the absorption cross sections of various inorganic bromine compounds (T=220 K).

Romand (1949). J_{HBr} at zero optical depth is about $5 \times 10^{-6} s^{-1}$, but it is comparable to the rate of reaction with the OH radical in the stratosphere.

The absorption spectrum of hydrofluoric acid or hydrogen fluoride HF indicates that its photolysis can be completely neglected in the middle atmosphere.

4.7.2.23 Hypochlorous (HOCl) and Hypobromous (HOBr) acids

The spectral distribution of the absorption cross section of HOCl was measured by Molina and Molina (1978), Knauth *et al.* (1979), Mishalanie *et al.* (1986), Permien *et al.* (1988), and Burkholder (1993). Discrepancies exist between these measurements, but the values of Burkholder (Figure 4.50) are recommended. The quantum yield for the Cl + OH channel is close to unity.

The absorption cross sections of HOBr were measured by Orlando and Burkholder (1995), Deters *et al.* (1996), Benter *et al.* (1995), and Rattigan *et al.* (1996). The measurements agree reasonably well between 240 and 400 nm, except in the case of Rattigan *et al.*, where the measured cross sections are roughly 50% larger between 300 and 400 nm. Their spectrum (Figure 4.51) also exhibits an absorption tail beyond 400 nm, so that the photolysis rate is a factor 3 higher than if calculated with the cross sections derived from the other studies.

4.7.2.24 BrCl

Absorption cross sections for BrCl (Figure 4.51) have been measured by Maric *et al.* (1994). They vary with temperature. The resulting photolysis rate is very rapid because of the large cross section at visible wavelengths.

4.7.3 Numerical Calculation of Photodissociation Coefficients

The photodissociation frequencies for several important trace species are shown in Figure 4.52 for specific conditions (winter at 40° latitude, solar maximum). The determination of these photolysis rates J at altitude z for solar zenith angle χ is accomplished by the numerical methods described below.

a) When the absorption spectrum is a *continuum*, thus varying slowly with wavelength, the spectrum is divided into discrete intervals and a mean value of σ_i and ϵ_i is assigned to each. Equation (4.113) can then be written as a sum of the intervals i of wavelength $\delta\lambda_i$:

$$J(z,\chi) = \sum_i \epsilon_i \, \sigma_i \, Q_i(z,\chi) \tag{4.121}$$

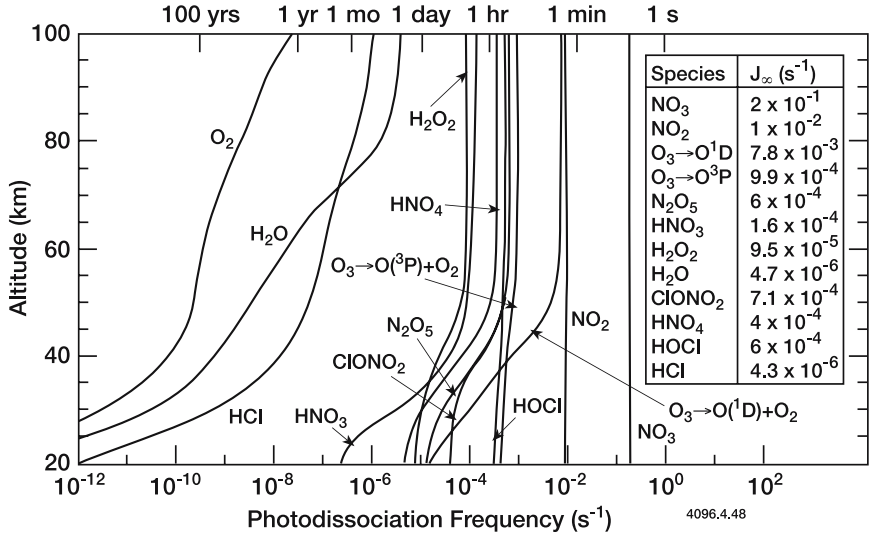

Figure 4.52. Photodissociation rates of several important atmospheric species for winter, solar maximum, 40° latitude. From the model of Garcia and Solomon (1983).

where

$$Q_i = \int_{\delta\lambda_i} q_\lambda \, d\lambda \tag{4.122}$$

is the solar actinic flux within spectral interval i at altitude z and solar zenith angle χ.

b) The absorption spectra of some molecules exhibit a structure of discrete narrow *bands*. Examples include NO and O_2 in the Schumann Runge bands (175-205 nm). In these cases, it is not possible to determine a mean value σ_i of the cross section for use in a broad spectral interval. The generalized expression for atmospheric absorption Eq. (4.113) must then be considered, and an integration performed over spectral intervals smaller than the width of the bands. Such a calculation is often computationally expensive, and approximate methods are often used to reduce computation time. Two aspects must be considered: on one hand, the rate of photolysis of O_2 must be computed, and on the other, the transmission of solar radiation including O_2 absorption must be considered in order to calculate the photodissociation coefficients in the Schumann Runge bands for constituents such as H_2O, CO_2, N_2O, HNO_3, etc. NO must be treated separately because of the very narrow width of its lines (Doppler widths of about 0.1 cm^{-1}). The Schumann Runge region can be analyzed by dividing it into 20 intervals beginning at each O_2 rotational band. The first band, (19–0) is found at 175.345 nm, while the last occurs at 204.08 nm. Other intervals can be adopted, notably the classical division in 500 cm^{-1} bands.

One method which leads to a simple treatment of the penetration of radiation in the Schumann Runge bands and the photolysis rate of O_2 involves establishing an equivalent cross section of O_2 in the interval $\delta\lambda_i$ and then applying the methods for continuum absorption. Thus, for each interval $\delta\lambda_i$ over which the quantum yield is assumed to be unity and the ozone transmission T_{r,O_3} is not varying significantly with wavelength, the O_2 photolysis frequency

$$J_{O_2}(\delta\lambda_i; z, \chi) = \int_{\delta\lambda_i} \sigma_{O_2}(\lambda) \, q_\infty(\lambda) \, T_{r,O_2}(\lambda; z, \chi) \, T_{r,O_3}(\lambda; z, \chi) \, d\lambda \tag{4.123}$$

can be approximated as

$$J_{O_2}(\delta\lambda_i; z, \chi) \simeq \sigma_{\text{eff},i}(\delta\lambda_i; z, \chi) \, Q_{i,\infty}(\delta\lambda_i) \, T^{SRB}_{r,O_2}(\delta\lambda_i; z, \chi) \, T_{r,O_3}(\delta\lambda_i; z, \chi) \tag{4.124}$$

where the effective O_2 cross section for wavelength interval $\delta\lambda_i$ is

$$\sigma_{\text{eff},i}(\delta\lambda_i; z, \chi) = \frac{\int_{\delta\lambda_i} \sigma_{O_2}(\lambda) \, q_\infty(\lambda) \, T_{r,O_2}(\lambda; z, \chi) \, d\lambda}{\int_{\delta\lambda_i} q_\infty(\lambda) \, T_{r,O_2}(\lambda; z, \chi) \, d\lambda} \tag{4.125}$$

the effective O_2 transmission in a $\delta\lambda_i$ Schumann-Runge band interval is

$$T^{SRB}_{r,O_2,i}(\delta\lambda_i; z, \chi) = \frac{\int_{\delta\lambda_i} q_\infty(\lambda)\, T_{r,O_2}(\lambda; z, \chi)\, d\lambda}{\int_{\delta\lambda_i} q_\infty(\lambda)\, d\lambda} \tag{4.126}$$

and the solar actinic flux at the top of the atmosphere, integrated over wavelength interval $\delta\lambda_i$ is

$$Q_{i,\infty}(\delta\lambda_i) = \int_{\delta\lambda_i} q_\infty(\lambda)\, d\lambda \tag{4.127}$$

Note that if the solar flux $q_\infty(\lambda)$ varies slowly within interval $\delta\lambda_i$, the effective O_2 transmission $T^{SRB}_{r,O_2,i}$ is equivalent to the reduction factor R_i introduced by Kockarts (1976).

For compounds X other than O_2 (or NO) for which the absorption cross section varies slowly with wavelength (continuum) over the Schumann-Runge region (*e.g.*, H_2O, CH_4, CO_2), the photodissociation frequency over interval $\delta\lambda_i$ can be derived from

$$J_X(\delta\lambda_i; z, \chi) = \sigma_X(\delta\lambda_i)\, Q_{i,\infty}(\delta\lambda_i)\, T^{SRB}_{r,O_2,i}(\delta\lambda_i; z, \chi)\, T_{r,O_3,i}(\delta\lambda_i; z, \chi) \tag{4.128}$$

The solar flux at altitude z and for solar zenith angle χ, integrated over wavelength interval $\delta\lambda_i$ is simply

$$Q_i(\delta\lambda_i; z, \chi) = Q_{i,\infty}(\delta\lambda_i)\, T^{SRB}_{r,O_2,i}(\delta\lambda_i; z, \chi)\, T_{r,O_3,i}(\delta\lambda_i; z, \chi) \tag{4.129}$$

Since a detailed treatment of radiative transfer in the Schumann-Runge bands is often computationally prohibitive when applied to photochemical models, the effective O_2 cross section σ_{eff} and atmospheric transmission T^{SRB}_{r,O_2} are often pre-calculated through detailed line-by-line integrations, using expressions similar to those shown above. Parameterizations have also been developed (Hudson and Mahle, 1972; Kockarts, 1976; 1994; Allen and Frederick, 1982; Nicolet and Kennes, 1989; Gijs *et al.*, 1997) in which these quantities are expressed as a function of the O_2 slant column

$$N(O_2; z, \chi) = \sec\chi \int_z^\infty (O_2)\, dz' \tag{4.130}$$

if (O_2) is the O_2 number density at altitude z′. Kockarts (1994), for example, expressed effective parameters through polynomial expansions that account for temperature variations, while Gijs *et al.* (1997) express the effective O_2 cross section for each chosen spectral interval by

$$\ln[\sigma_{eff}(N(O_2))] = A(N(O_2))\,[T(N(O_2)) - 220\ K] + B(N(O_2)) \tag{4.131}$$

where $T(N(O_2))$ is the local temperature at the altitude corresponding to the O_2 slant column $N(O_2)$. Parameters A and B are expressed as a function of ln $(N(O_2))$ using Chebeshev polynomial fits. The effective

O_2 transmission is then derived as a function of $N(O_2)$) by noting that

$$\frac{dT^{SRB}_{O_2}}{dN(O_2)} = -\sigma_{eff}\,(O_2) \tag{4.132}$$

An alternative procedure for calculating O_2 transmission and photolysis in the Schumann-Runge bands involves the use of opacity distribution functions (Fang *et al.*, 1974; Minschwaner *et al.*, 1993). The method is analogous to the k-distribution techniques used in infrared radiative transfer (*e.g.*, Lacis and Oinas, 1991). A single set of O_2 cross sections are used for both transmission (or solar actinic flux Q_i) and photolysis frequency for O_2 within a given vibrational band i:

$$Q_i(z,\chi) = Q_i(\infty)e^{-\tau_i(O_3;z,\chi)} \sum_{j=1}^{6} w_j e^{-\sigma_j(O_2)\,N(O_2)} \tag{4.133}$$

$$J_i(O_2;z,\chi) = Q_i(\infty)e^{-\tau_i(O_3;z,\chi)} \sum_{j=1}^{6} w_j \sigma_j(O_2) e^{-\sigma_j(O_2)\,N(O_2)} \tag{4.134}$$

where σ_j are determined by the distribution of cross section magnitudes in each band and w_j are weighting factors. In Zhu *et al.* (1999), the weighting factors are determined by Gauss-Legendre quadratures, which reduces Q_i and J_i to 4-term summations. One advantage of this formulation is that it permits calculation of overlapping of complex spectra, such as occurs in the NO δ bands, through the use of spectral mapping methods (Minschwaner and Siskind, 1993). This method has also been adopted for use in calculating H_2O photolysis in the Schumann-Runge bands (Siskind *et al.*, 1994).

In the spectral intervals close to the solar Lyman-α line, the solar flux as well as the O_2 absorption cross section vary relatively rapidly with wavelength, and parameterizations similar to those used for the Schumann-Runge intervals have been used (Chabrillat and Kockarts, 1997).

References

Allen, M., and J.E. Frederick, Effective photodissociation cross sections for molecular oxygen and nitric oxide in the Schumann-Runge Bands. *J Atmos Sci: 39*, 2066, 1982.

Anderson, G.P., and L.A. Hall, Attenuation of solar irradiance in the stratosphere: Spectrometer measurements between 191 and 207 nm. *J Geophys Res: 88*, 6801-6806, 1983.

Andrews, D.G., J.R. Holton, and C.B. Leovy, *Middle Atmosphere Dynamics*. Academic Press, 1987.

Apruzese, J.P., M.R. Schoeberl, and D.F. Strobel, Parameterization of IR cooling in a middle atmosphere dynamics model, 1. Effects of the zonally averaged circulation. *J Geophys Res: 87*, 8951, 1982.

Apruzese, J.P., D.F. Strobel, and M.R. Schoeberl, Parameterization of IR cooling in the middle atmosphere dynamics model, 2. Non LTE radiative transfer and the globally averaged temperature of the mesosphere and lower thermosphere. *J Geophys Res: 89*, 4917, 1984.

Armstrong, B.H., Spectrum line profiles: The Voigt function. *J Quant Spectrosc Radiat Transfer: 7*, 61, 1967.

Ball, S.M., G. Hancock, I.J. Murphy, and S.P. Rayner, The relative quantum yields of O_2 ($A^1\Delta G$) from the photolysis of ozone in the wavelength range 270 nm $\leq \lambda \leq$ 329 nm. *Geophys Res Lett: 20*, 2063, 1993.

Ball, S.M., G. Hancock, and F. Winterbottom, Product channels in the near-UV photodissociation of ozone. *Faraday Discuss: 100*, 215, 1995.

Bass, A.M., A.E. Ledford, and A.H. Laufer, Extinction coefficients of NO_2 and N_2O_4. *J Res Natl Bur. Stand SecA: 80*, 143, 1976.

Bass, A.M., L.C. Glasgow, C. Miller, J.P. Jesson, and D.L. Filkin, Temperature dependent cross sections for formaldehyde [CH_2O]: The effect of formaldehyde on stratospheric chlorine chemistry. *Planet Space Sci: 28*, 675, 1980.

Bates, D.R., Rayleigh scattering by air. *Planet Space Sci: 32*, 785, 1984.

Baum, W.A., F.S. Johnson, J.J. Obserly, C.C. Rockwood, C.V. Strain, and R. Tousey, Solar ultraviolet spectrum to 88 kilometers. *Phys Rev: 70*, 781, 1946.

Benter, T., C. Feldmann, U. Kirchner, M. Schmidt, S. Schmidt, and R.N. Schindler, UV/VIS absorption spectra of HOBr and CH_3OBr; Br(2P3/2) atom yields in the photolysis of HOBr. *Ber Bunsenges Phys Chem: 99*, 1144, 1995.

Bhartia, P.K., K.F. Klenk, A.J. Fleig, C.G. Wellemeyer, and D. Gordon, Intercomparison of Nimbus 7 Solar Backscattered Ultraviolet ozone profiles with rocket, balloon, and umkehr profiles. *J Geophys Res: 89*, 5227, 1984.

Bhartia, P.K., R.D. McPeters, C.L. Mateer, L.E. Flynn, and C. Wellemeyer, Algorithm for the estimation of vertical ozone profiles from the backscattered ultraviolet technique. *J Geophys Res: 101*, 18,793, 1996.

Biaumé, F., Nitric acid vapour absorption cross section spectrum and its photodissociation in the stratosphere. *J Photochem: 2*, 139, 1973.

Bohren, C.F., and D.R. Huffman, *Absorption and Scattering of Light by Small Particles*. J. Wiley and Sons, 1983.

Bongartz, A., J. Kames, F. Welter, and V. Schurath, Near UV absorption cross sections and trans/cis equilibrium of nitrous oxide. *J Phys Chem: 95*, 1076, 1991.

Brasseur, G., and D. Offermann, Recombination of atomic oxygen near the mesopause: Interpretation of rocket data. *J Geophys Res: 91*, 10,818, 1986.

Brasseur, G., A. De Rudder, and P.C. Simon, Implication for stratospheric composition of a reduced absorption cross section in the Herzberg continuum of molecular oxygen. *Geophys Res Lett: 10*, 20, 1983.

Brownword, R.A., M. Hillenkamp, T. Laurent, R.K. Vasta, H.-R. Volpp, and J. Wolfrum, Quantum yield for H atom formation in the methane dissociation after photoexcitation at the Lyman- α (121.6 nm) wavelength. *Chem Phys Lett: 266*, 259, 1997.

Brueckner, G.E., K.L. Edlow, L.E. Floyd, J.L. Lean, and M.E. van Hoosier, The solar ultraviolet spectral irradiance monitor (SUSIM) experiment on board the Upper Atmosphere Research Satellite. *J Geophys Res: 98*, 10,695, 1993.

Brusa, R.W., and C. Frohlich, Recent solar constant determinations from high altitude balloons, Paper presented at the Symposium on the Solar Constant and the Spectral Distribution of Solar Irradiance, IAMAP Third Scientific Assembly, Published by the Radiation Commission, Boulder, Colo, USA, 1982.

Burkholder, J.B., Ultraviolet absorption spectrum of HOCl. *J Geophy Res: 98*, 2963, 1993.

Burkholder, J.B., J.J. Orlando, and C.J. Howard, Ultraviolet absorption cross section of Cl_2O_2 between 210 and 410 nm. *J Phys Chem: 94*, 687, 1990.

Burkholder, J.B., R.K. Talukdar, A.R. Ravishankara, and S. Solomon, Temperature dependence of the HNO_3 UV absorption cross section. *J Geophys Res: 98*, 22,937, 1993.

Burkholder, J.B., R.K. Talukdar, and A.R. Ravishankara, Temperature dependence of the $ClONO_2$ UV absorption spectrum. *Geophys Res Lett: 21*, 585, 1994.

Burkholder, J.B., A.R. Ravishankara, and S. Solomon, UV visible and IR absorption cross sections of $BrONO_2$. *J Geophys Res: 100*, 16,793, 1995.

Callear, A.B., and M.J. Pilling, Fluorescence of nitric oxide, 6. Predissociation and cascade quenching in NO $D^2\Sigma^+$ ($v = 0$) and NO $C^2\Pi$ ($v = 0$), and the oscillator strengths of the σ (0,0) and (0,0) bands. *Trans Faraday Soc: 66*, 1886, 1970a.

Callear, A.B., and M.J. Pilling, Fluorescence of nitric oxide, 7. Quenching rates of NO C^2 π ($v = 0$), and its rate of radiation to NO A^2 Σ^+, energy transfer efficiencies and mechanisms of predissociation. *Trans Faraday Soc: 66*, 1618, 1970b.

Cantrell, C.A., J.A. Davison, A.H. McDaniel, R.E. Shetter, and J.G. Calvert, Temperature dependent formeldehyde cross sections in the near ultraviolet spectral region. *J Phys Chem: 94*, 3902, 1990.

Cantrell, C., A. Zimmer, and G.S. Tyndall, Absorption cross sections for water vapor from 183 to 193 nm. *Geophys Res Lett: 24*, 2195, 1997.

Cess, R.D., and V. Ramanathan, Radiative transfer in the atmosphere of Mars and that of Venus above the cloud deck. *J Quant Spectrosc Radiat Transfer: 12*, 933, 1972.

Chabrillat, S., and G. Kockarts, Simple parameterization of the absorption of the solar Lyman-α line. *Geophys Res Lett: 24*, 2659, 1997. Correction: *Geophys Res Lett: 25*, 79, 1998.

Chandrasekhar, S., *Radiative Transfer.* Oxford University Press, 1950 (Reprinted by Dover Publ., 1960).

Chapman, S., The absorption and dissociative or ionizing effect of monochromatic radiations in an atmosphere on a rotating earth. *Proc Phys Soc: 43*, 483, 1931.

Cheung, A.S.-C., K. Yoshino, W.H. Parkinson, S.L. Guberman, and D.E. Freeman, Absorption cross section measurements of oxygen in the wavelength region 195-241 nm of the Herzberg continuum. *Planet Space Sci: 34*, 1007, 1986.

Chou, C.C., W.S. Smith, H. Vera Ruiz, K. Moe, G. Crescentini, J.J. Molinar, and F.S. Rowland, The temperature dependence of the ultraviolet absorption cross sections of CCl_2F_2 and CCl_3F, and their stratospheric significance. *J Phys Chem: 81*, 1977.

Chou, C.C., R.J. Milstein, W.S. Smith, H. Vera Ruiz, M.J. Molinar, and F.S. Rowland, Stratospheric photodissociation of several saturated perhalo chlorofluorocarbon

compounds in current technological use (Fluorocarbons –13, –113, –114, and –115). *J Phys Chem: 82*, 1, 1978.

Cieslik, S., Détermination expérimentale des forces d'oscillateur des bandes β, γ, δ, et ξ de la molécule NO. *Bull Cl Sci Acad Roy Belg: 63*, 884, 1977.

Cieslik, S., and M. Nicolet, The aeronomic dissociation of nitric oxide. *Planet Space Sci: 21*, 925, 1973.

Clough, S.A., and M.J. Iacono, Line by line calculation of the atmospheric fluxes and cooling rates: Application to carbon dioxide, ozone, methane, nitrous oxide, and the halocarbons. *J Geophys Res: 100*, 16,519, 1995.

Cox, R.A., and K. Patrick, Kinetics of the reaction $HO_2 + NO_2$ (+ M) $\rightarrow HO_2\ NO_2$ using molecular modulation spectrometry. *Int J Chem Kinetics: 11*, 635, 1979.

Cox, R.A., D.W. Sheppard, and M.P. Stevens, Absorption coefficients and kinetics of the BrO radical using molecular modulation. *J Photochem: 19*, 189, 1982.

Cox, R.A., and G.D. Hayman, The stability and photochemistry of dimers of the ClO radical and implications for the Antarctic ozone depletion. *Nature: 332*, 796, 1988.

Crutzen, P., Comment on paper "Absorption and emission by carbon dioxide in the mesosphere", by J.T. Houghton. *Quart J Roy Meteorol Soc: 96*, 767, 1970.

Crutzen, P.J., Energy conversions and mean vertical motions in the high latitude summer mesosphere and lower thermosphere, in *Mesospheric Models and Related Experiments*. G. Fiocco (ed.), D. Reidel Publishing Co., Dordrecht, Holland, 1971.

Curtis, A.R., Discussion of a statistical model for water vapour absorption. *Quart J Roy Meteorol Soc: 78*, 638, 1952.

Curtis, A.R., and R.M. Goody, Thermal radiation in the upper atmosphere. *Proc Roy Soc: A236*, 193, 1956.

Daumont, D., J. Brion, J. Charbonnier, and J. Malicet, Ozone UV spectroscopy, 1. Absorption cross sections at room temperatures. *J Atmos Chem: 15*, 145, 1992.

Davidson, J.A., C.A. Cantrell, A.H. McDaniel, R.E. Shetter, S. Madronich, and J.G. Calvert, Visible-ultraviolet absorption cross sections for NO_2 as a function of temperature. *J Geophys Res: 93*, 7105, 1988.

DeMore, W.B., and M. Patapoff, Temperature and pressure dependence of CO_2 extinction coefficients. *J Geophys Res: 77*, 6291, 1972.

DeMore, W.B., and E. Tschuikow-Roux, Ultraviolet spectrum and chemical reactivity of the ClO dimer. *J Phys Chem: 94*, 5856, 1990.

Deshler, T., B.J. Johnson, and W.R. Rozier, Baloon-borne measurements of Pinatubo aerosol during 1991 and 1992 at 41°N, vertical profile size distribution and volatility. *Geophys Res Lett: 20*, 1435, 1993.

Deters, B., J.P. Burrows, S. Himmelmann, and C. Blindauer, Gas phase spectra of HOBr and Br_2O and their atmospheric significance. *Ann Geophys: 14*, 468, 1996.

Dickinson, R.E., Method of parameterization for infrared cooling between the altitudes of 30 and 70 km. *J Geophys Res: 78*, 4451, 1973.

Dickinson, R.E., Infrared radiative cooling in the mesosphere and lower thermosphere. *J Atmos Terr Phys: 46*, 995, 1984.

Dopplick, T.G., Radiative heating of the global atmosphere. *J Atmos Sci: 29*, 1278, 1972.

Edwards, D.P., GENLN2: A general line-by-line atmospheric transmittance and radiance model. Version 3.0 description and users guide, *NCAR Technical Note,*

NCAR/TN-367+STR, National Center for Atmospheric Research, Boulder, Colo., USA, 1992.

Edwards, D.P., M. López-Puertas, and M.A. López-Valverde, Non-local thermodynamic equilibrium studies of the 15-μm bands of CO_2 for atmospheric remote sensing. *J Geophys Res: 98*, 14,955, 1993.

Ellingson, R.G., J. Ellis, and S. Fels, The intercomparison of radiation codes used in climate models: Long wave results. *J Geophys Res: 96*, 8929, 1991.

Elsasser, W.M., Heat transfer by infrared radiation in the atmosphere. *Harvard Meteorol. Stud: 6*, Harvard Univ. Press, Cambridge, Mass., USA, 1942.

Elterman, L., *UV, Visible and IR Attenuation for Altitudes to 50 km.* AFCRL Report 68-0153, Environ. Res. Papers, Bedford, Mass, USA, 1968.

Fang, T.M., S.C. Wofsy, and A. Dalgarno, Capacity distribution functions and absorption in Schumann-Runge bands of molecular oxygen. *Planet Space Sci: 22*, 413, 1974.

Fomichev, V.I., W.E. Ward, S.R. Beagley, C. McLandress, J.C. McConnell, N.A. McFarlane, and T.G. Shepherd, Extended Canadian Middle Atmosphere Model: Zonal-mean climatology and physical parameterizations. *J Geophys Res: 107*, DIO, doi:10.1029/2001JD000479, 2002.

Frederick, J.E., and R. D. Hudson, Predissociation of nitric oxide in the mesosphere and stratosphere. *J Atmos Sci: 36*, 737, 1979.

Frederick, J.E., and J.E. Mentall, Solar irradiance in the stratosphere: Implication for the Herzberg continuum absorption of O_2. *Geophys Res Lett: 9*, 461, 1982.

Frederick, J.E., R.B. Abrams, and P.J. Crutzen, A potential mechanism for coupling thermospheric variations to the mesosphere and the stratosphere. *J Geophys Res: 88*, 3829, 1983.

Froidevaux, L., and Y.L. Yung, Radiation and chemistry in the stratosphere: Sensitivity to O_2 cross sections in the Herzberg continuum. *Geophys Res Lett: 9*, 854, 1982.

Fu, Q., and K.N. Liou, On the correlated k-distribution method for radiative transfer in nonhomogeneous atmospheres. *J Atmos Sci: 49*, 2139, 1992.

Garcia, R.R., and S. Solomon, A numerical model for the zonally averaged dynamical and chemical structure of the middle atmosphere. *J Geophys Res: 88*, 1379, 1983.

Ghazi, A.V., V. Ramanathan, and R.E. Dickinson, Acceleration of upper stratospheric radiative damping: Observational evidence. *Geophys Res Lett: 6*, 437, 1979.

Gijs, A., A. Koppers, and D.P. Murtagh, Model studies of the influence of O_2 photodissociation parameterizations in the Schumann-Runge bands on ozone related photolysis in the upper atmosphere. *Ann Geophys: 14*, 68, 1997.

Gillotay, D., and P.C. Simon, Ultraviolet absorption cross sections of methyl bromide at stratospheric temperatures. *Ann Geophys: 6*, 211, 1988.

Gillotay, D., A. Jenouvrier, B. Coquart, M.F. Merienne, and P.C. Simon, Ultraviolet absorption cross sections of bromoform in the temperature range 295-210 K. *Planet Space Sci: 37*, 1127, 1989.

Godson, W.L., The evaluation of infrared radiative fluxes due to atmosphere water vapour. *Quart J Roy Meteorol Soc: 79*, 367, 1953.

Goodeve, C.F., and A.C.W. Taylor, The continuous absorption spectrum of hydrogen bromide. *Proc Roy Soc: A152*, 221, 1935.

Goody, R.M., *Atmospheric Radiation, I. Theoretical Basis.* Oxford at the Clarendon Press, 1964.

Goody, R.M., and Y.L. Yung, *Atmospheric Radiation: Theoretical Basis.* Oxford University Press, 1989.

Goody, R.M., R. West, L. Chen, and D. Crisp, The correlated k-method for radiation calculations in nonhomogeneous atmospheres. *J Quant Spectrosc Radiat Transfer: 42*, 539, 1989.

Gordley, L.L., B.T. Marshall, and D.A. Chu, LINEPAK: Algorithms for modeling spectral transmittance and radiance. *J Quant Spectrosc Radiat Transfer: 52*, 563, 1994.

Graham, R.A., Photochemistry of NO_3 and the kinetics of the N_2O_5 – O_3 system, PhD Thesis, University of California, Berkeley, Calf, USA, 1975.

Graham, R.A., and H.S. Johnston, The photochemistry of NO_3 and the kinetics of the N_2O_5 – O_3 system. *J Phys Chem: 82*, 254, 1978.

Graham, R.A., A.M. Wier, and J.A. Pitts, Ultraviolet and infrared cross section of gas phase HO_2NO_2. *Geophys Res Lett: 5*, 909, 1978.

Hanel, R.A., and B.J. Courath, *Thermal Emission Spectra of the Earth and Atmosphere Obtained from the Nimbus 4 Michelson Interferometer Experiment.* NASA Report X-620-70-244, 1970.

Harwood, M.H., R.L. Jones, R.A. Cox, E. Lutman, and O.V. Rattigan, Temperature-dependent absorption cross sections of N_2O_5. *J Photochem Photobiol A: Chem: 73*, 167, 1993.

Harries, J., The greenhouse earth: A view from space. *Quart J Roy Meteorol Soc: 122*, 799, 1996.

Henri, V., and S.A. Schou, Struktur und Akitivierung der Molekel des Formaldehyds, eine Analyse auf Grund des ultrvioletten Absorption-Spektrums des Dampfes. *Zeit Phys: 49*, 774, 1928.

Herman, J.R., and J.E. Mentall, The direct and scattered solar flux within the stratosphere. *J Geophys Res: 87*, 1319, 1982a.

Herman, J.R., and J.E. Mentall, O_2 absorption cross section (187-225 nm) from stratospheric solar flux measurements. *J Geophys Res: 87*, 8967, 1982b.

Herzberg, G., Ultraviolet absorption spectra of acetylene and formaldehyde. *Trans Faraday Soc: 27*, 378, 1931.

Holt, R.B., and O. Oldenberg, Role of hydrogen peroxide in the thermal combination of hydrogen and oxygen. *J Chem Phys: 17*, 1091, 1949.

Holt, R.B., C.K. McLane, and O. Oldenberg, Ultraviolet absorption spectrum of hydrogen peroxide. *J Chem Phys: 16*, 225, 1948. Erratum: *J Chem Phys: 16*, 638, 1948.

Houghton, J.T., Absorption and emission by carbon dioxide in the mesosphere. *Quart J Roy Meteorol Soc: 95*, 1, 1969.

Hubinger, S., and J.B. Nee, Photoabsorption spectrum for OClO between 125 and 470 nm. *Chem Phys: 181*, 247, 1994.

Hubrich, C., and F. Stuhl, The ultraviolet absorption of some halogenated methanes and ethanes of atmospheric interest. *J Photochem: 12*, 93, 1980.

Hubrich, C., C. Zetsch, and F. Stuhl, Absorptionsspektren von halogenierten Methanen im Bereich von 275 bis 160 nm bei Temperaturen von 298 und 208 K. *Ber Bunsenges Phys Chem: 81*, 437, 1977.

Huder, K.J., and W.B. DeMore, Absoprtion cross sections of the ClO dimer. *J Phys Chem: 99*, 3905, 1995.

Hudson, R.D., and S.H. Mahle, Photodissociation rates of molecular oxygen in the mesosphere and lower thermosphere. *J Geophys Res: 77*, 2902, 1972.

Hudson, R.D., V.L. Carter, and J.A. Stein, An investigation of the effect of temperature on the Schumann-Runge absorption continuum of oxygen, 1580-910 A. *J Geophys Res: 71*, 2295, 1966.

Humlicek, J., Optimized computation of the Voigt and complex probability functions. *J Quart Spectrosc Radiat Transfer: 27*, 437, 1982.

Inn, E.C.Y., Absorption coefficient of HCl in the region 1400 to 2200 A. *J Atmos Sci: 32*, 2375, 1975.

Inn, E.C.Y., and Y. Tanaka, Absorption coefficient of ozone in the ultraviolet and visible regions. *J Opt Soc Amer: 43*, 8760, 1953.

Inn, E.C.Y., K. Watanabe, and M. Zelikoff, Absorption coefficients of gases in the vacuum ultraviolet: 3. CO_2. *J Chem Phys: 21*, 1648, 1953.

Iribarne, J.V., and H.R. Cho, *Atmospheric Physics,* D. Reidel, Dordrecht, The Netherlands, 1980.

Jenouvrier, A., B. Coquart, and M.F. Merienne-Lafore, New measurements of the absorption cross sections in the Herzberg continuum of molecular oxygen in the region between 205 and 240 nm. *Planet Space Sci: 34*, 253, 1986.

Jet Propulsion Laboratory (JPL), *Chemical Kinetics and Photochemical Data for Use in Stratospheric Modeling*, W.B. DeMora, S.P. Sander, D.M. Golden, R.F. Hampson, M.J. Kurylo, C.J. Howard, A.R. Ravishankara, C.E. Kolb, and M.J. Molina, eds., JPL Publication 97-4, 1997.

Johnson, F.S., J.D. Porcell, R. Tousey, and K. Watanabe, Direct measurements of the vertical distribution of atmospheric ozone to 70 km altitude. *J Geophys Res: 57*, 157, 1952.

Johnston, H.S., and R.A. Graham, Gas-phase ultraviolet spectrum of nitric acid vapor. *J Chem Phys: 77*, 62, 1973.

Johnston, H.S., and R.A. Graham, Photochemistry of NO_x compounds. *Canad J Chem: 52*, 1415, 1974.

Johnston, H.S., and G. Selwyn, New cross sections for the absorption of near ultraviolet radiation by nitrous oxide (N_2O). *Geophys Res Lett: 2*, 549, 1975.

Johnston H.S., S.G. Chang, and G. Whitten, Photolysis of nitric acid vapor. *J Phys Chem: 78*, 1, 1974.

Johnston, H.S., H.F. Davies, and Y.T. Lee, NO_3 photolysis product channels: Quantum yields from observed energy thresholds. *J Phys Chem: 100*, 4713, 1996.

Jones, E.J., and O.R. Wulf, The absorption coefficient of nitrogen pentoxide in the ultraviolet and the visible absorption spectrum NO_3. *J Chem Phys: 5*, 873, 1937.

Joseph, J.H., W.J. Wiscombe, and J.A. Weinman, The delta-Eddington approximation for radiative flux transfer. *J Atmos Sci: 33*, 2452, 1976.

Kiehl, J.T., and V. Ramanathan, CO_2 radiative parameterization used in climate models: Comparison with narrow band moels and with laboratory data. *J Geophys Res: 88*, 5191, 1983.

Kiehl, J.T., and R.E. Dickinson, A study of the radiative effects of enhanced atmospheric CO_2 and CH_4 on early earth surface temperatures. *J Geophys Res: 92*, 2991, 1987.

Knauth, H.-D., H. Alberti, and H. Clausen, Equilibrium constant of the gas reaction $Cl_2 + H_2O$ ultraviolet spectrum of HOCl. *J Phys Chem: 83*, 1604, 1979.

Kockarts, G., Absorption and photodissociation in the Schumann-Runge bands of molecular oxygen in the terrestrial atmosphere. *Planet Space Sci: 24*, 589, 1976.

Kockarts, G., Nitric oxide cooling in the terrestrial thermosphere. *Geophys Res Lett: 7*, 137, 1980.

Kockarts, G., Penetration of solar radiation in the Schumann-Runge bands of molecular oxygen, A robust approximation. *Ann Geophys*, 1994.

Kondratyev, K.Y., *Radiation in the Atmosphere.* Academic Press, 1969.

Kourganoff, V., *Basic Methods in Transfer Problems.* Oxford University Press, 1952.

Kuhn, W.R., and J. London, Infrared radiative cooling in the middle atmosphere (30-110 km). *J Atmos Sci: 26*, 189, 1969.

Kylling, A., K. Stamnes, R.R. Meier, and D.E. Anderson, The 200-300 nm radiation field within the stratosphere: Comparison of models with observation. *J Geophys Res: 98*, 2741, 1993.

Lacis, A.A., and J.E. Hansen, A parameterization for the absorption of solar radiation in the earth's atmosphere. *J Atmos Sci: 31*, 118, 1974.

Lacis, A.A., and V. Oinas, A description of the correlated k distribution method for modeling nongray gaseous absorption, thermal emission, and multiple scattering in vertically inhomogeneous atmospheres. *J Geophys Res: 96*, 9027, 1991.

Langhoff, J.R., J.P. Dix, J.O. Arnold, R.W. Nicholls, and L.L. Danylewych, Theoretical intensity parameters for the vibration-rotation bands of ClO. *J Chem Phys: 67*, 4306, 1977a.

Langhoff, S.R., R.L. Jaffe, and J.O. Arnold, Effective cross sections and rate constants for predissociation of ClO in the earth's atmosphere. *J Quant Spectrosc Radiat Transfer: 18*, 227, 1977b.

Laufer, A.M., and J.R. McNesby, Deuterium isotope effect in vacuum ultraviolet absorption coefficients of water and methane. *Canad J Chem: 43*, 3487, 1965.

Lean, J., The sun's variable radiation and its relevance for earth. *Annu Rev Astron Astrophys: 35*, 33, 1997.

Lean, J.L. and A.J. Blake, The effect of temperature on thermospheric molecular oxygen absorption in the Schumann-Runge continuum. *J Geophys Res: 86*, 211, 1981.

Lee, R.B., M.A. Gibson, R.S. Wilson, and S. Thomas, Long-term solar irradiance variability during sunspot cycle 22. *J Geophys Res: 100*, 1667, 1995.

Leifson, S.W., Absorption spectra of some gases and vapors in the Schumann region. *Astrophys J: 63*, 73, 1926.

Lenoble, J., *Standard procedures to compute atmospheric radiative transfer in a scattering atmosphere, I.A.M.A.P.*, National Center for Atmospheric Research, Boulder, Colo., USA, 1977.

Lewis, B.R., and J.H. Carter, Temperature dependence of the carbon dioxide photoabsorption cross section between 1200 and 1700 Å. *J Quant Spectros Radiat Transfer: 30*, 297, 1983.

Lewis, B.R., L. Berzins, and J.H. Carter, Oscillator strengths for the Schumann-Runge bands of O_2. *J Quant Spectrosc Radiat Transfer: 36*, 209, 1986.

Lewis, B.R., S.T. Gibson, and P.M. Dooley, Fine structure dependence of predissociation linewidth in the Schumann-Runge bands of molecular oxygen. *J Chem Phys: 100*, 6993, 1994.

Lin, C.-L., and W.B. DeMore, O(^{1}D) production in ozone photolysis near 3100 A. *J Photochem: 2*, 161, 1973.

Lin, C.L., N.K. Rohatgi, and W.B. Demore, Ultraviolet absorption cross sections of hydrogen peroxide. *Geophys Res Lett: 5*, 113, 1978.

Liou, K.-N., *An Introduction to Atmospheric Radiation,* Academic Press, 1980.

Liou, K.-N., *An Introduction to Atmospheric Radiation*, Second Edition, Academic Press, 2002.

London, J., Radiative energy sources and sinks in the stratosphere and mesophere, Proc of the NATO Advanced Institute on Atmospheric Ozone, A.C. Aikin, ed., *U.S. Dept. of Transportation, FAA-EE-80-20*, FAA, Washington, D.C., USA, 1980.

López-Puertas, M., and F.W. Taylor, *Non-LTE Radiative Transfer in the Atmosphere*, World Scientific, 2001.

López-Puertas, M., R. Rodrigo, A. Molina, and F.W. Taylor, A non-LTE radiative transfer model for infrared bands in the middle atmosphere, I. Theoretical basis and application to CO_2 15-μm bands. *J Atmos Terr Phys: 48*, 729, 1986.

López-Puertas, M., M.A. López-Valverde, C.P. Rinsland, and M.R. Gunson, Analysis of the upper atmosphere $CO_2(\nu_2)$ vibrational temperatures retrieved from ATMOS/Spacelab 3 observations. *J Geophys Res: 97*, 20,469, 1992a.

López-Puertas, M., M.A. López-Valverde, and F.W. Taylor, Vibrational temperatures and radiative cooling of the CO_2 15μm bands in the middle atmosphere. *Quart J Roy Meteorol Soc: 118*, 499, 1992b.

Luther, F.M., D.J. Wuebbels, W.H. Duewer, and J.C. Chang, Effect of multiple scattering on species concentrations and model sensitivity. *J Geophys Res: 83*, 3563, 1978.

Magnotta, F., and H.S. Johnston, Photodissociation quantum yields for the NO_3 free radical. *Geophys Res Lett: 7*, 769, 1980.

Malkmus, W., Random Lorentz band model with exponential-tailed S-1 line intensity distribution function. *J Opt Soc Amer: 57*, 323, 1967.

Malicet, J., D. Daumont, J. Charbonnier, C. Parisse, A. Chakir, and J. Brion, Ozone UV spectroscopy, 2. Absorption cross sections and temperature dependence. *J Atmos Chem: 21*, 263, 1995.

Manabe, S., and F. Moller, On the radiative equilibrium and heat balance of the atmosphere. *Mon Wea Rev: 89*, 503, 1961.

Manabe, S., and R.F. Strickler, Thermal equilibrium of the atmosphere with a convective adjustment. *J Atmos Sci: 21*, 361, 1964.

Maric, D., J.P. Burrows, and G.K. Moortgat, A study of the UV-visible absorption spectra of Br_2 and BrCl. *J. Photochem Photobiol A: Chem: 83*, 179, 1994.

Marmo, F.F., Absorption coefficients of nitrogen oxide in the vacuum ultraviolet. *J Opt Soc Amer: 43*, 1186, 1953.

Marshall, B.T., L.L. Gordley, and D.A. Chu, BANDPAK: Algorithms for modeling broadband transmission and radiance. *J Quant Spectrosc Radiat Transfer: 52*, 581, 1994.

Mauldin III, R.L., J.B. Burkholder, and A.R. Ravishankara, A photochemical, thermodynamic and kinetic study of ClOO. *J. Phys Chem: 96*, 2582, 1992.

McCartney, E.J., *Optics of the Atmosphere: Scattering by Molecules and Particles,* Wiley and Sons, 1976.

McCormick, M.P., P. Hamill, T.J. Pepin, W.P. Chu, T.J. Swissler, and L.R. McMaster, Satellite studies of the stratospheric aerosol. *Bull Am Meteoroleor Soc: 60*, 1038, 1979.

McLeod, H., G. P. Smith, and D. M. Golden, Photodissociation of pernitric acid at 248 nm. *J Geophys Res: 93* 3813, 1988.

Meador, W.E., and W.R. Weaver, Two-stream approximations to radiative transfer in planetary atmospheres: A unified description of existing methods and a new improvement. *J Atmos Sci: 37*, 630, 1980.

Meier, R.R., D.E. Anderson, Jr., and M. Nicolet, Radiation field in the troposphere and stratosphere from 240 to 1000 nm, I. General analysis. *Planet Space Sci: 30*, 923, 1982.

Mérienne, M.F., B. Coquart, and A. Jenouvrier, Temperature effect of the ultraviolet absorption of $CFCl_3$, CF_2Cl_2 and N_2O. *Planet Space Sci: 38*, 617, 1990.

Mertens, C.J., M.G. Mlynczak, R.R. Garcia, and R.W. Portmann, A detailed evaluation of the stratospheric heat budget, 1. Radiation transfer. *J Geophys Res: 104*, 6021, 1999.

Michelsen, H.H., R.J. Salawitch, P.O. Wennberg, and J.G. Anderson, Production of $O(^1D)$ from photolysis of O_3. *Geophys Res Lett: 21*, 2227, 1994.

Mie, G., Beitrage zur optik trueber Medien, Speziell koloidaller metaloesungen *Ann der Phys: 25*, 377, 1908.

Milne, E.A., *Handbuch der Astrophysik,* 3, Part I. 1930 (Reprinted in "Selected Papers on the Transfer of Radiation", Dover, 1966).

Minschwaner, K., and D.E. Siskind, A new calculation of nitric oxide photolysis in the stratosphere, mesosphere, and lower thermosphere. *J Geophys Res: 98*, 20,401, 1993.

Minschwaner, K., G.P. Anderson, L.A. Hall, and K. Yoshino, Polynomial coefficients for calculating O_2 Schumann-Runge cross sections at 0.5 cm^{-1} resolution. *J Geophys Res: 97*, 10,103, 1992.

Minschwaner, K., R.J. Salawitch, and M.B. McElroy, Absorption of solar radiation by O_2: Implications for O_3 and lifetimes of N_2O, $CFCl_3$, and CF_2Cl_2. *J Geophys Res: 98*, 10,543, 1993.

Minschwaner, K., R.J. Thomas, and D.W. Rusch, Scattered ultraviolet radiation in the upper stratosphere, I. Observations. *J Geophys Res: 100*, 11,157, 1995.

Mishalanie, E.A., J.C. Rutkowski, R.S. Hutte, and J.W. Birks, Ultraviolet absorption spectrum of gaseous hypochlorous acid. *J Phys Chem: 90*, 5578, 1986.

Mitchell, A.C.G., and W.M. Zemansky, *Resonance Radiation and Excited Atoms.* Harvard Univ. Press, Cambridge, Mass., USA, 1934 (Reprinted 1961).

Mlynczak, M.G., and B.T. Marshall, A reexamination of the role of solar heating in the O_2 atmospheric and infrared atmospheric bands. *Geophys Res Lett: 23*, 657, 1996.

Mlynczak, M.G., and S. Solomon, On the efficiency of solar heating in the middle atmosphere. *Geophys Res Lett: 18*, 1201, 1991.

Mlynczak, M.G., and S. Solomon, A detailed evaluation of the heating efficiency in the middle atmosphere. *J Geophys Res: 98*, 10,517, 1993.

Mlynczak, M.G., C.J. Mertens, R.R. Garcia, and R.W. Portman, A detailed evaluation of the stratospheric heat budget, 2. Global radiation balance and diabatic circulations. *J Geophys Res: 104*, 6039, 1999.

Molina, M.J., and F.S. Rowland, Stratospheric sink for chlorofluoromethanes: Chlorine atom-catalyzed destruction of ozone. *Nature: 249*, 810, 1974.

Molina, L.T., and M.J. Molina, Ultraviolet spectrum of HOCl. *J Phys Chem: 42*, 2410, 1978.

Molina, L.T., and M.J. Molina, Chlorine nitrate ultraviolet absorption spectrum at stratospheric temperatures. *J Photochem: 11*, 139, 1979.

Molina, L.T., and M.J. Molina, UV absorption cross sections of HO_2NO_2 vapor. *J Photochem: 15*, 97, 1981.

Molina, L.T., and M.J. Molina, Absolute absorption cross sections of ozone in the 185 to 350 nm wavelength range. *J Geophys Res: 91*, 14,501, 1986.

Molina, L.T., M.J. Molina, and F.S. Rowland, Ultraviolet absorption cross sections of several brominated methanes and ethanes of atmospheric interest. *J Phys Chem: 86*, 2672, 1982.

Molina, M.J., A.J. Colussi, L.T. Molina, R.N. Schindler, and T.L. Tso, Quantum yield of chlorine atom formation in the photodissociation of chlorine peroxide (ClOOCl) at 308 nm. *Chem Phys Lett: 173*, 310, 1990.

Moortgat, G.K., E. Kudszus, and P. Warneck, Temperature dependence of $O(^1D)$ formation in the near UV photolysis of ozone. *J Chem Soc, Faraday Trans: 11*, 73, 1216, 1977.

Moortgat, G.K., W. Klippel, K.H. Mobius, W. Seiler, and P. Warneck, Laboratory measurements of photolytic parameters for formaldehyde. Rep. FAA-EE-80-47, Federal Aviation Administration, Washington, D.C., USA, 1980.

Moortgat, G.K., W. Seiler, and P. Warneck, Photodissociation of HCHO in air: CO and H_22 quantum yield at 220 and 300 K. *J Chem Phys: 78*, 1185, 1983.

Moortgat, G.K., R. Meller, and W. Schneider, Temperature dependance (256-296 K) of the absorption cross sections of bromoform in the wavelength range 285-360 nm, in *Proceedings of NATO workshop on "The Tropospheric Chemistry in the Polar Regions", Wolfville, Canada, 23-28 August 1992, NATO ASI Series.* H. Niki and K.H. Becker (eds.), Springer Verlag, Berlin, 359-369, 1993.

Murray, J.E., K. Yoshino, J. R. Esmond, W. H. Parkinson, Y. Sun, and A. Dalgarno, Vacuum ultraviolet Fourier transform spectroscopy of the $\delta(0,0)$ and $\beta(7,0)$ bands of NO. *J Chem Phys: 101*, 62, 1994.

Murtagh, D.P., The O_2 Schumann-Runge system: New calculations of photodissociation cross sections. *Planet Space Sci: 36*, 819, 1988.

Nesme-Ribes, E., S.L. Baliunes, and D. Sokoloff, The stellar dynamo. *Sci Amer: 51*, 1996.

Newchurch, M.J., M. Allen, M.R. Gunson, R.J. Salawitch, G.B. Collins, K.H. Huton, M.M. Abbas, M.C. Abrams, A.Y. Chang, D.W. Fahey, R.S. Gao, F.W. Irion, M. Loewenstein, G.L. Manney, H.A. Michelsen, J.R. Podolske, C.P. Rinsland, and R. Zander, Stratospheric NO and NO_2 abundances from ATMOS solar-occultation measurements. *Geophys Res Lett: 23*, 2373, 1996.

Nickolaisen, S.L., and S.P. Sander, Pressure dependent yields and product branching ratios in the broadband photolysis of chlorine nitrate. *J Phys Chem: 100*, 10,165, 1996.

Nicolet, M., Etude des réactions chimiques de l'ozone dans la stratosphere. *Royal Meteorological Institute of Belgium*, 1978.

Nicolet, M., The chemical equations of stratospheric and mesopheric ozone, Proc of the NATO Advanced Institute on Atmospheric Ozone, A.C. Aikin, ed., *U.S. Dept. of Transportation, FAA-EE-80-20*, FAA, Washington, D.C., USA, 1980.

Nicolet, M., On the molecular scattering in the terrestrial atmosphere: An empirical formula for its calculation in the homosphere. *Planet Space Sci: 32*, 1467, 1984.

Nicolet, M., and S. Cieslik, The photodissociation of nitric oxide in the mesophere and stratosphere. *Planet Space Sci: 28*, 105, 1980.

Nicolet, M., and R. Kennes, Aeronomic problems of molecular oxygen photodissociation, IV. Photodissociation frequency and transmittance in the spectral range of the Schumann-Runge bands. *Planet Space Sci: 37*, 459, 1989.

Nicolet, M., R.R. Meier, and D.E. Anderson, Radiation field in the troposphere and stratosphere, II. Numerical analysis. *Planet Space Sci: 30*, 935, 1982.

Nicolet, M., S. Cieslik, and R. Kennes, Aeronomic problems of molecular oxygen photodissociation, V. Predissociation in the Schumann-Runge bands of oxygen. *Planet Space Sci: 37*, 427, 1989.

Nicovich, J.M., and P.H. Wine, Temperature-dependent absorption cross section of the hydrogen peroxide vapor, *J Geophys Res: 93*, 2417, 1988.

Norrish, R.G.W., and F.N. Kirkbride, Primary photochemical processes, I. The decomposition of formaldehyde, *J Chem Soc: 1*, 1518, 1932.

Ogawa, M., Absorption cross sections of O_2 and CO_2 continua in the Schumann-Runge and far-UV regions, *J Chem Phys Lett: 9*, 603, 1971.

Orlando, J.J., and J.B. Burkholder, Gas phase UV visible absorption spectra of HOBr and Br_2O, *J Phys Chem: 99*, 1143, 1995.

Orlando, J.J., G.S. Tyndall, G.K. Moortgat, and J.G. Calvert, Quantum yields for NO_3 photolysis between 570 and 635 nm, *J Phys Chem: 97*, 10,996, 1993.

Park, J.H., The equivalent mean absorption cross sections for the O_2 Schumann-Runge bands: Application to the H_2O and NO photodissociation rates. *J Atmos Sci: 312*, 1893, 1974.

Penndorf, R., Tables of the refractive index for standard air and the Rayleigh scattering coefficient for the spectral region between 0.2 and 20.0 μm and their application to atmospheric optics. *J Opt Soc Amer: 47*, 176, 1957.

Penner, S.S., *Quantitative Molecular Spectroscopy and Gas Emissivities*. Addison-Wesley, Reading, Mass, USA, 1959.

Permien, T., R. Vogt, and R.N. Schindler, Mechanisms of gas phase-liquid phase chemical transformations. Air Pollution Report 17, R.A. Cox, ed., Environmental Research Program of the CEC, Brussels, 1988.

Perner, D., and U. Platt, Absorption of light in the atmosphere by collision pairs of oxygen $(O_2)_2$. *Geophys Res Lett: 7*, 1053, 1980.

Petropavlóvskikh, I., *Evaluation of Photodissociation Coefficient Calculations for Use in Atmospheric Chemical Models*. Univ. of Brussels and National Center for Atmospheric Research Cooperative Ph.D. Thesis, NCAR/CT-159, 1995.

Ramanathan, V., Radiative transfer within the earth's troposphere and stratosphere: A simplified radiative-convective model. *J Atmos Sci: 33*, 1330, 1976.

Rattigan, O.V., R.L. Jones, and R.A. Cox, The visible spectrum of gaseous OBrO. *Chem Phys Lett: 230*, 121, 1994.

Rattigan, O.V., D.J. Lary, R.L. Jones, and R.A. Cox, UV-visible absorption cross sections of gaseous Br_2O and HOBr. *J Geophys Res: 101*, 23,021, 1996.

Rebbert, R.E., R.L. Lilly, and P. Ausloos, Abstract of papers, 164th National Meeting, Association Chemical Society, New York, August 1972.

Richards, P.G., D.G. Torr, and M.A. Torr, Photodissociation of N_2: A significant source for thermospheric atomic nitrogen. *J Geophys Res: 86*, 1495, 1981.

Richards, P.G., J.A. Fennelly, and D.G. Torr, EUVAC: A solar EUV flux model for aeronomic calculations. *J Geophys Res: 99*, 8981, 1994.

Robbins, D.E., Photodissociation of methyl chloride and methyl bromide in the atmosphere. *Geophys Res Lett: 3*, 213, 1976. Erratum: Ibid, 757, 1976.

Rodgers, C.D., and C.D. Walshaw, The computation of infra-red cooling rate in planetary atmospheres. *Quart J Roy Meteorol Soc: 92*, 67, 1966.

Romand, J., Absorption ultraviolette dans la région of Schumann-Runge, Etude de ClH, BrH et IH gazeux. *Ann Phys, Paris: 4*, 527, 1949.

Romand, J., and B. Vodar, Spectre d'absorption de l'acide chlorhydrique gazeux dans la région de Schumann. *Canad Roy Acad Sci Paris: 226*, 238, 1948.

Rothman, L.S., C.P. Rinsland, A. Goldman, S.T. Massie, D.P. Edwards, J.-M. Flaud, A. Perrin, C. Camy-Peyret, V. Dana, J.-Y. Mandin, J. Schroeder, A. McCann, R.R. Gamache, R.B. Wattson, K. Yoshino, K.V. Chance, K.W. Jucks, L.R. Brown, V. Nemtschinov, and P. Varanasi, The HITRAN molecular spectroscopic data base and HAWKS: 1996 Edition. *J Quant Spectrosc Radiat Transfer: 60*, 665, 1998.

Rottman, G.J., T.N. Woods, and T.P. Sparn, Solar stellar irradiance comparison experiment: Instrument design and operation. *J Geophys Res: 98*, 10,667, 1993.

Rowland, F.S., and M.J. Molina, Chlorofluoromethanes in the environment. *Rev Geophys Space Phys: 13*, 1, 1975.

Schiffman, A., D.D. Nelson, Jr., and D.J. Nesbitt, Quantum yields for OH production from 193 and 248 nm photolysis of HNO_3 and H_2O_2. *J Chem Phys: 98*, 6935, 1993.

Schneider, W.F., A.K. Moortgat, G.S. Tyndall, and J.P. Burrows, Absorption cross sections of NO_2 in the UV and visible region (200-700 nm) at 298K. *J of Photochem Photobiol: 40*, 195, 1987.

Schoeberl, M.R., and D.F. Strobel, The zonally averaged circulation of the middle atmosphere. *J Atmos Sci: 35*, 577, 1978.

Schurgers, M., and K.H. Welge, Absorptionskoeffizient von H_2O_2 und N_2H_4 zwischen 1200 und 2000 A. *Zeit Naturforsch: 23A*, 1508, 1968.

Selwyn, G., J. Podolske, and H.S. Johnston, Nitrous oxide ultraviolet absorption spectrum at stratospheric temperatures. *Geophys Res Lett: 4*, 427, 1977.

Shaw, J., Solar Radiation. *Ohio J Sci: 53*, 258, 1953.

Shemansky, D.E., CO_2 extinction coefficient 1700-3000Å. *J Chem Phys: 56*, 1582, 1972.

Shved, G.M., L.E. Khvorostovskaya, I.Y. Potekhin, A.I. Demyanikov, A.A. Kutepov, and V.I. Fomichev, Measurement of the quenching rate constant of $CO_2(01^10)$-O collisions and its significance for the thermal regime and radiation in the lower thermosphere, *Atmos Oceanic Phys: 27*, 295, 1991.

Shved, G.M., Kutepov, A.A., and Ogivalov, V.P., Non-local thermodynamic equilibrium in CO_2 in the middle atmosphere, I. Input data and populations of the ν_3 mode manifold states. *J Atmos Solar Terr Phys: 60*, 289, 1998.

Silvente, E., R.C. Richter, M. Zheng, E.S. Saltzman, and A.J. Hynes, Relative quantum yields for O^1D production in the photolysis of ozone between 301 and 336 nm: Evidence for the participation of a spin forbidden channel. *Chem Phys Lett: 264*, 309, 1997.

Simon, P.C., D. Gillotay, N. Vanlaethem-Meurée, and J. Wisemberg, Ultraviolet absorption cross sections of chloro- and chlorofluoro-methane at stratospheric temperatures. *J Atmos Chem: 7*, 107, 1988.

Simpson, C.J.S.M., P.D. Gait, and J.M. Simmie, The vibrational deactivation of the bending moe of CO_2 by O_2 and by N_2. *Chem Phys Lett: 47*, 133, 1977.

Singer, R.J., J.N. Crowley, J.P. Burrows, W. Schneider, and G.K. Moortgat, Measurement of the absorption cross section of peroxynitric acid between 210 and 330 nm in the range 253-298 K. *J Photochem Photobiol: 48*, 17, 1989.

Siskind, D.E., K. Minschwaner, and R.S. Eckman, Photodissociation of oxygen and water vapor in the middle atmosphere: Comparison of numerical methods and impact on modeled ozone and hydroxyl. *Geophys Res Lett: 21*, 863, 1994.

Slanger, T.G., and G. Black, Photodissociative channels at 1216 Å for H_2O, NH_3, and CH_4. *J Chem Phys: 77*, 2432, 1982.

Smith, F.L., III, and C. Smith, Numerical evaluation of Chapman's grazing incidence integral Ch (X, χ). *J Geophys Res: 77*, 3592, 1972.

Sobolev, V.V., *A Treatise of Radiative Transfer.* D. Van Nostrand, 1963.

Spencer, J.E., and F.S. Rowland, Bromine nitrate and its stratospheric significance. *J Phys Chem: 82*, 7, 1978.

Stamnes, K., S.C. Tsay, W. Wiscombe, and K. Jayaweera, Numerically stable algorithm for discrete-ordinate-method radiative transfer in multiple scattering and emitting layers. *Appl Opt: 27*, 2502, 1988.

Steinfeld, J. I., S.M. Adler-Golden, and J. W. Gallagher, Critical survey of data on the spectroscopy and kinetics of ozone in the mesosphere and thermosphere. *J Phys Chem: 16*, 911, 1987.

Stief, L.J., W.A. Payne, and R.B. Klemm, A flash-photolysis-resonance fluorescence study of the formation of O (^{1}D) in the photolysis of water and the reaction of O (^{1}D) with H_2, Ar and He. *J Chem Phys: 62*, 4000, 1975.

Stockwell, W.R., and J.C. Calvert, The near ultraviolet absorption spectrum of gaseous HONO and N_2O_4. *J Photochem: 8*, 193, 1978.

Takahashi, K., Y. Matsumi, and M. Kawasaki, Photodissociation processes of ozone in the Huggins band at 308-326 nm: Direct observation of O ($^1D_2$) and O (^{3}Pj) products. *J Phys Chem: 100*, 4084, 1996.

Takahashi, K., N. Taniguchi, Y. Matsumi, M. Kawasaki, and M.N.R. Ashfold, Wavelength and temperature dependence of the absolute O(^{1}D) production yield from the 305-329 nm photodissociation of ozone. *J Chem Phys: 108*, 7161, 1998.

Thomas, G.D., and K. Stamnes, *Radiative Transfer in the Atmosphere and Ocean.* Cambridge University Press, 517 pp., 1999.

Thompson, B.A., P. Harteck, and R.R. Reeves, Jr., Ultraviolet absorption coefficients of CO_2 CO, O_2, H_2O, N_2O, NH_3, NO, SO_2 and CH_4 between 1850 and 4000 A. *J Geophys Res: 68*, 6431, 1963.

Tiwari, S.N., Models for infrared atmospheric radiation. *Adv Geophys: 20*, 1, 1978.

Toon, O.B., C.P. McKay, T.P. Ackerman, and K. Santhanam, Rapid calculation of radiative heating rates and photodissociation rates in inhomogeneous multiple scattering atmospheres. *J Geophys Res: 94*, 16,287, 1989.

Turnipseed, A.A., G.L. Vaghjiani, J.E. Thompson, and A.R. Ravishankara, Photodissociation of HNO_3 at 193, 222, and 248 nm: Products and Quantum Yields. *J Chem Phys: 96*, 5887, 1992.

Urey, H.C., L.C. Dawsey, and F.O. Rice, The absorption spectrum and decomposition of hydrogen peroxide by light. *J Amer Chem Soc: 51*, 1371, 1929.

Vaghjiani, G.L., and A.R. Ravishankara, Absorption cross sections of CH_3OOH, H_2O_2 and D_2O_2 vapors between 210 and 365 nm at 297 K. *J Geophys Res: 94*, 3487, 1989.

Van de Hulst, H.C., *Light Scattering by Small Particles.* Wiley, 1957.

Van Hoosier, M.E., J.-D.F. Bartoe, G.E. Brueckner, and D.K. Prinz, Absolute solar spectral irradiance 120 nm-400 nm (Results from the Solar Ultraviolet Irradiance Monitor — SUSIM — experiment on board Spacelab 2). *Astrophys Lett Commun: 27*, 163, 1988.

Van Laethem-Meurée, N., J. Wisemberg, and P.C. Simon, Absorption des chlorométhanes dans l'ultraviolet: Mesures des sections efficaces d'absorption en fonction de la température. *Bull Acad Roy Belgique Cl Sci: 64*, 34, 1978a.

Van Laethem-Meurée, N., J. Wisemberg, and P.C. Simon, Influence de la température sur les sections efficaces d'absorption des chlorofluorométhanes dans l'ultraviolet. *Bull Acad Roy Belgique Cl Sci: 64*, 42, 1978b.

Vasudev R., Absorption spectrum and solar photodissociation of gaseous nitrous acid in the actinic wavelength region. *Geophys Res. Lett: 17*, 2153, 1990.

Vernazza, J., E.H. Avrett, and R. Loeser, Structure of the solar chromosphere, II. The underlying photosphere and temperature minimum region. *Astrophys J: 30*, 1, 1976.

Vigroux, E., Contribution expérimentale de l'absorption de l'ozone. *Ann Phys, Paris: 8*, 709, 1953.

Vigroux, E. Coefficients d'absorption de l'ozone dans la bande de Hartley. *Ann Geophys: 25*, 169, 1969.

Vodar, M.B., Spectre d'absorption ultraviolet du gaz chlorhydrique et courbe d'energie potentielle de l'état excité de la molecule ClH. *J Phys Rad: 9*, 166, 1948.

Wahner, A., G.S. Tyndall, and A.R. Ravishankara, Absoprtion cross sections for OClO as a function of temperature in the wavelength range 240-480 nm. *J Phys Chem: 91*, 2734, 1987.

Wahner, A., A.R. Ravishankara, S.P. Sander, and R.R. Friedl, Absorption cross section of BrO between 312 and 385 nm at 298 and 223 K. *Chem Phys Lett: 152*, 507, 1988.

Watanabe, K., and M. Zelikoff, Absorption coefficient of water vapor in the vacuum ultraviolet. *J Opt Soc Amer: 43*, 753, 1953.

Watanabe, K., E.C.Y. Inn, and M. Zelikoff, Absorption coefficients of oxygen in the vacuum ultraviolet. *J Chem Phys: 21*, 1026, 1953.

Watson, R.T., Rate constants of ClO of atmospheric interest. *J Phys Chem Ref Data: 6*, 87, 1977.

Wayne, R.P., The photochemistry of ozone. *Atmos Environ: 21*, 1683, 1987.

Wayne, R.P., I. Barnes, P. Biggs, J.P. Burrows, C.E. Canosa-Mas, J. Hjorth, G. LeBras, G.K. Moortgag, D. Perher, G. Poulet, G. Restelli, and J. Sidebottom, The nitrate radical: Physics, chemistry and the atmosphere. *Atmos Environ: 25A*, 1, 1991.

Williams, A.P., and C.D. Rodgers, Radiative transfer by the 15 micron CO_2 band in the mesophere. Proc Intl Radiation Symposium, Sendai, Japan, 26 May-2 June 1972.

Wilson, R.C., and H.S. Hudson, The sun's luminosity over a complete solar cycle. *Nature: 351*, 42, 1991.

Wintersteiner, P.P., R.H. Picard, R.D. Sharma, J.R. Winick, and R.A. Joseph, Line-by-line radiative excitation model for the nonequilibrium atmosphere: Application to CO_2 15 μm emission. *J Geophys Res: 97*, 18,083, 1992.

World Meteorological Organisation (WMO), *The Stratosphere 1981: Theory and Measurements.* Report No. 11, Geneva, Switzerland, 1982.

World Meteorological Organisation (WMO), *Atmospheric Ozone 1985.* Global Ozone Research and Monitoring Project, Report No. 16, Geneva, Switzerland, 1985.

Woods, T.N., and G.J. Rottman, Solar Lyman α irradiance measurements during two solar cycles. *J Geophys Res: 102*, 8769, 1997.

Woods, T.N., D.K. Prinz, G.J. Rottman, J. London, P.C. Crane, R.P. Cebula, E. Hilsenrath, G.E. Brueckner, M.D. Andrews, O.R. White, M.E. VanHoosier, L.E. Floyd, L.C. Herring, B.G. Knapp, C.K. Pankratz, and P.A. Reiser, Validation of the UARS solar ultraviolet irradiances: Comparison with the ATLAS 1 and 2 measurements. *J Geophys Res: 101*, 9541, 1996.

Woods, T.N. G.J. Rottman, S.M. Bailey, S.C. Solomon, and J. Worden, Solar extreme ultraviolet irradiance measurements during solar cycle 22. *Solar Physics: 177*, 133, 1998.

Yao, F., I. Wilson, and H. Johnston, Temperature dependent ultraviolet absorption spectrum for dinitrogen pentoxide. *J Phys Chem: 86*, 3611, 1982.

Yoshino, K., D.E. Freeman, J.R. Esmond, and W.H. Parkinson, High resolution absorption cross section measurements and band oscillator strengths of the (1,0)-(12,0) Schumann-Runge bands of O_2. *Planet Space Sci: 31*, 339, 1983.

Yoshino, K., A.S.-C. Cheung, J.R. Esmond, W.H. Parkinson, D.E. Freeman, and S.L. Guberman, Improved absorption cross sections of oxygen in the wavelength region 205-240 nm of the Herzberg continuum. *Planet Space Sci: 36*, 1469, 1988.

Yoshino, K., J.R. Esmond, D.E. Freeman, and W.H. Parkinson, Measurements of absolute absorption cross sections of ozone in the 185 to 254 nm wavelength region and the temperature dependence. *J Geophys Res: 98*, 5205, 1993.

Yoshino, K., J.R. Esmond, Y. Sun, and W.H. Parkinson, Absorption cross section measurements of carbon dioxide in the wavelength region 118.7-175.5 nm and the temperature dependence. *Spectrosc Ra: 55*, 53, 1996a.

Yoshino, K., J.R. Esmond, W.H. Parkinson, K. Ito, and T. Matsui, Absorption cross section measurements of water vapor in the wavelength region 120 to 188 nm. *Japan Chem Phys: 211*, 387, 1996b.

Zhu, X., J.-H. Yee, S.A. Lloyd, and D.F. Storbel, Numerical modeling of chemical-dynamical coupling in the upper stratosphere and mesosphere. *J Geophys Res: 104*, 23,995, 1999.

Chapter 5

COMPOSITION AND CHEMISTRY

5.1 General

The chemical composition of the atmosphere near the Earth's surface is relatively well known due to numerous measurements of the concentration and variability of many of the important gases. The local surface sources of atmospheric species are related to biological and microbiological activity, volcanic eruptions, and human activities. Some of the species emitted in the troposphere are also destroyed in the troposphere by biological, chemical, and physical processes. Others are transported upward, eventually reaching the stratosphere, where many can undergo chemical transformations. For most constituents, natural sources are larger than those of anthropogenic origin. However, for compounds such as methane (CH_4), carbon monoxide (CO), nitric oxide (NO), sulfur dioxide (SO_2), and nearly all halocarbons, the anthropogenic production has become larger than the natural emissions.

Some minor constituents are produced or destroyed in the atmosphere by photochemical reactions. The altitude at which these processes occur depends on the penetration depth of the solar radiation which initiates the photochemistry.

In this chapter, the chemical and photochemical processes relevant to the principal constituents of the middle atmosphere will be discussed. Knowing the distribution and behavior of the various constituents, global atmospheric budgets can be derived. The budgets of atmospheric methane, carbon monoxide, molecular hydrogen, nitrous oxide, nitrogen oxides, halocarbons, inorganic chlorine, bromine and fluorine, as well as sulfur compounds and ozone, will be discussed in detail. Global perturbations of the chemical composition in the middle atmosphere, including the formation of a springtime ozone hole over Antarctica, will be discussed in Chapter 6. The chemistry of ions will be addressed in Chapter 7.

The terrestrial atmosphere is made up of a multitude of chemical constituents, the most abundant being molecular nitrogen (N_2) and oxygen (O_2). The relative concentrations of these compounds are

essentially constant in the homosphere, as was mentioned in Chapter 3. Noble gases (Argon, Neon, Helium, Krypton, Xenon) are also insensitive to chemical processes. The mean atmospheric mole fraction (also called the mixing ratio) of well-mixed gases and the corresponding total atmospheric mass content for dry air are given in Table 5.1 below:

Table 5.1 Mean Atmospheric Mole Fraction and Total Mass Content

Compound	*Mole fraction*	*Total Mass Content (kg)*
Nitrogen (N_2)	78.084×10^{-2}	3.9×10^{18}
Oxygen (O_2)	20.946×10^{-2}	1.2×10^{18}
Carbon dioxide (CO_2)	370×10^{-6}	7.5×10^{14}
Argon (Ar)	9340×10^{-6}	6.6×10^{16}
Neon (Ne)	18.18×10^{-6}	6.5×10^{13}
Helium (He)	5.239×10^{-6}	3.7×10^{12}
Krypton (Kr)	1.14×10^{-6}	1.7×10^{13}
Xenon (Xe)	0.086×10^{-6}	2.0×10^{12}
Air	1	5.1×10^{18}

In the middle atmosphere, molecular nitrogen is particularly stable since it cannot be photodissociated below the mesopause. On the other hand, the photodissociation of molecular oxygen can occur at altitudes as low as 20 km. Where transport processes can replace the photodissociated molecules, their abundances remain constant, but as photodissociation rates increase at higher altitudes, mixing ratios begin to decline. Oxygen photolysis initiates a series of reactions which determine the chemistry of the "oxygen atmosphere"; these will be the subject of the next section.

The abundance of atmospheric species (see Box 5.1) is variable in space and time, and can be calculated from the continuity equation, which expresses mass conservation in an infinitesimal volume element. For each chemical compound i, continuity can be equivalently expressed by the flux form

$$\frac{\partial \rho_{\mathrm{i}}}{\partial \mathrm{t}} + \boldsymbol{\nabla} \cdot (\rho_{\mathrm{i}} \mathbf{v}) = \tilde{\mathrm{S}}_{\mathrm{i}} \tag{5.1a}$$

or by the advective form

$$\frac{\partial \mu_{\mathrm{i}}}{\partial \mathrm{t}} + \mathbf{v} \cdot \boldsymbol{\nabla} \mu_{\mathrm{i}} = \frac{\tilde{\mathrm{S}}_{\mathrm{i}}}{\rho} \tag{5.1b}$$

where ρ_{i} is the *mass density* (expressed for example as kg of constituent i per cubic meter of air), $\mu_{\mathrm{i}} = \rho_{\mathrm{i}}/\rho$ is the *mass fraction* (expressed for example as kg of constituent i per kg of air), $\mathbf{v}$ is the wind velocity

Box 5.1 Definitions and Units

Number density: Number of particles (*e.g.*, atoms, molecules, or aerosol particles) of substance per unit volume of air expressed, for example, in particles m^{-3} (SI) or particles cm^{-3} (cgs).

Mass density: Mass of substance per unit volume of air expressed, for example, in kg m^{-3} (SI) or in g cm^{-3}.

Mole fraction: Number density of substance divided by number density of air (dimensionless variable). The mole fraction is generally expressed in cmol/mol, mmol/mol, μmol/mol, nmol/mol, and pmol/mol, which corresponds to mole fractions of 10^{-2}, 10^{-3}, 10^{-6}, 10^{-9}, and 10^{-12}, respectively. The terms parts per million by volume (ppmv), parts per billion per volume (ppbv), or parts per trillion per volume (pptv) are often being used to express *mixing ratios by volume*. Volume mixing ratio is equivalent to mole fraction only for an ideal gas.

Mass fraction: Mass density of substance divided by mass density of air (dimensionless variable). The pertinent unit for mass mixing ratio is kg/kg, but this quantity is often expressed as g/kg or g/g. Abundances expressed in μg/g, ng/g, and pg/g correspond to mass fractions of 10^{-6}, 10^{-9}, and 10^{-12}, respectively. The terms ppmm, ppbm, and pptm are often used to characterize *mixing ratios by mass*.

Column abundance: Vertically integrated number density of substance (expressed in particles m^{-2} (SI) or cm^{-2} (cgs)). In the case of ozone, the column abundance is often expressed in Dobson units (DU). One Dobson unit corresponds to the height (in 10^{-3} cm) of an ozone column if the gas were at standard temperature and pressure. It is equivalent to 2.687×10^{16} molecules cm^{-2}.

Particle or mass flux: Number of particles or mass of substance crossing a unit surface per unit time. The appropriate units (SI) are particles $m^{-2}s^{-1}$ or kg $m^{-2}s^{-1}$, but particles $cm^{-2}s^{-1}$ or g $cm^{-2}s^{-1}$ are often used. Total mass flux of a substance (emitted, for example, at the Earth's surface) is often expressed in Tg yr^{-1} (10^{12} g yr^{-1}).

Atmospheric lifetime: Average time that a substance spends in the atmosphere. Atmospheric residence time is a synonymous concept, expressed in days, months, or years. If the removal of the substance is directly proportional to its mass density, the lifetime is also a measure of the time needed to reduce the mass density of the compound by a fraction e(2.718), if there are no sources.

vector, $\tilde{S}_i$ is the net chemical source term (expressed for example by kg of species i per cubic meter of air and per second), ρ is the air mass density (kg m^{-3}) and t is time (s). Noting that the total derivative is

given by

$$\frac{\mathrm{d}}{\mathrm{dt}} = \frac{\partial}{\partial \mathrm{t}} + \mathbf{v} \cdot \boldsymbol{\nabla}$$

equation (5.1b) can also be expressed as

$$\frac{\mathrm{d}\mu_\mathrm{i}}{\mathrm{dt}} = \frac{\tilde{\mathrm{S}}_\mathrm{i}}{\rho} \tag{5.1c}$$

which shows that, in the absence of chemical source or sink, the mass fraction is a conserved quantity. The continuity equation can also be expressed in terms of *number density* $\mathrm{n_i}$ (expressed for example in number of particles i per cubic meter of air):

$$\frac{\partial \mathrm{n_i}}{\partial \mathrm{t}} + \boldsymbol{\nabla} \cdot (\mathrm{n_i}\, \mathbf{v}) = \mathrm{S_i} \tag{5.1d}$$

where $\mathrm{S_i}$ is the net source term, now expressed for example in particles per cubic meter of air and per second. Note that, as the loss term for species i is often proportional to its concentration $\mathrm{n_i}$, the net source term is often expressed as

$$\mathrm{S_i} = \mathrm{P_i} - \mathrm{L_i n_i}$$

where $\mathrm{P_i}$ is the gross production and $\mathrm{L_i}$ is the loss coefficient. In the homosphere (below 90-100 km altitude), Eq. (5.1d) can be written in terms of *mole fraction* or *volume mixing* ratio $\mathrm{X_i} = \mathrm{n_i/n}$, and

$$\frac{\mathrm{dX_i}}{\mathrm{dt}} = \frac{\mathrm{S_i}}{\mathrm{n}} \tag{5.1e}$$

if n is the air number density, Thus, in regions where the mean molecular mass of air is constant, the mole fraction is also a conserved quantity in the absence of chemical conversion processes. When chemical reactions take place, the source terms for species i such as $\mathrm{S_i}$ depend on the concentration of other compounds $\mathrm{n_j}$, and the single continuity equation has to be replaced by a system of N equations, if N is the number of interacting chemical species. The product $\boldsymbol{\phi}_\mathrm{i} = \mathrm{n_i}\mathbf{v}$ represents the flux of constituent i which can be represented in a one-, two-, or three-dimensional space. In numerical models, continuity equations must be solved simultaneously for all of the many species under consideration with appropriate initial and boundary conditions. There are a variety of numerical methods which can be used to provide solutions to this coupled set of equations (see, *e.g.*, Brasseur and Madronich, 1992). Algorithms frequently used to solve a system of nonlinear chemical equations (continuity equations in which the transport terms are neglected) are briefly discussed in Box 5.2.

Box 5.2. Numerical Solutions for Chemical Continuity Equations

A variety of numerical methods can be used to solve the non-linear differential equation

$$\frac{\partial \mathbf{y}}{\partial \mathrm{t}} = \mathbf{S}\ (\mathrm{t}, \mathbf{y}) \tag{5.2}$$

which represents the continuity equation (5.1). In this equation, $\mathbf{y}$, a vector of N elements $(\mathrm{y}_1, \ldots, \mathrm{y}_\mathrm{N})$, represents the density or the mixing ratio of N chemically coupled compounds. Vector $\mathbf{S}\ (\mathrm{t}, \mathbf{y})$ accounts for transport, chemical production and destruction processes at time t, and is called the source term. In many cases, when the chemical lifetimes of the N chemical species (which are provided by the inverse of the eigenvalues λ_i of the Jacobian matrix $\partial \mathbf{S}/\partial \mathbf{y}$) vary by several orders of magnitude, the system is said to be "stiff", and appropriate numerical algorithms must be used.

The performance of numerical methods for chemical continuity equations is generally characterized in terms of accuracy, stability, degree of mass conservation, and computational efficiency. The simplest of such methods is provided by the forward Euler or *fully explicit* scheme, by which the solution $\mathbf{y}^{n+1}$ at time $\mathrm{t_{n+1}}$ is given by

$$\mathbf{y}^{\mathrm{n+1}} = \mathbf{y}^{\mathrm{n}} + \Delta \mathrm{t}\, \mathbf{S}\ (\mathrm{t_n}, \mathbf{y}^{\mathrm{n}}) \tag{5.3}$$

where $\mathrm{t_n} = \mathrm{t_0} + \mathrm{n}\Delta\mathrm{t}$ ($\mathrm{t_0}$ is the initial time), $\Delta \mathrm{t} = \mathrm{t_{n+1}} - \mathrm{t_n}$ is the time step. This solution, in which the source term is evaluated at time $\mathrm{t_n}$, is represented strictly in terms of known quantities. The algorithm is therefore straightforward, but rarely practical (except for long-lived species), because numerical stability requires that the time step Δt be constrained by the following condition:

$$\Delta \mathrm{t} \leq \frac{2}{\lambda_{\max}} = 2\tau_{\min}$$

where $\lambda_{\max}$ is the largest eigenvalue λ_j of the Jacobian matrix, and $\tau_{\min}$ the smallest chemical lifetime of the species involved.

The Eulerian backward or *fully implicit* method

$$\mathbf{y}^{\mathrm{n+1}} = \mathbf{y}^{\mathrm{n}} + \Delta \mathrm{t}\ \mathbf{S}\ \left(\mathrm{t_{n+1}}, \mathbf{y}^{\mathrm{n+1}}\right) \tag{5.4}$$

is unconditionally stable for any Δt, so that the time step may be selected for accuracy considerations. For stiff systems, very small time steps may be required, which introduces a computational constraint that may be as severe as that of explicit methods. Since, in general, the source term $\mathbf{S}$ includes nonlinear terms, the solution cannot be deduced immediately, and equation (5.4) is frequently solved by iterative methods. Prominent among the iterative algorithms is the Newton-Raphson method in which the solution at time $\mathrm{t_{n+1}}$ for iteration $(\mathrm{m}+1)$ is obtained from

Box 5.2 (Continued)

$$\mathbf{y}_{(m+1)}^{n+1} = \mathbf{y}_{(m)}^{n+1} - J^{-1}\mathbf{G}\left(\mathbf{y}_{(m)}^{n+1}\right) \tag{5.5}$$

where $\mathbf{G}$ is an N-valued vector function

$$\mathbf{G}\left(\mathbf{y}^{n+1}\right) = \mathbf{y}^{n+1} - \mathbf{y}^{n} - \Delta t\,\mathbf{S}\left(t_{n+1}, \mathbf{y}^{n+1}\right) \tag{5.6}$$

and J is the Jacobian matrix whose elements are $J_{ij} = \partial G_i/\partial \mathbf{y}_j$. The iteration converges to the solution for time steps smaller than a problem-dependent upper bound.

Another approach is to linearize the source term

$$\mathbf{S}(t, \mathbf{y}) = \mathbf{P}(t, \mathbf{y}) - \mathbf{L}(t, \mathbf{y})\,\mathbf{y} \tag{5.7}$$

where $\mathbf{P}$ represents the production and transport rates and $\mathbf{L}$ the loss coefficient. The solution at time t_{n+1} for iteration $(m+1)$ can easily be derived from

$$\mathbf{y}_{(m+1)}^{n+1} = \mathbf{y}^{n} + \Delta t\left[\mathbf{P}_{(m)}^{n+1} - \mathbf{L}_{(m)}^{n+1}\mathbf{y}_{(m+1)}^{n+1}\right] \quad (m = 0, 1, 2, ...) \tag{5.8}$$

where $\mathbf{P}_{(m)}^{n+1} = \mathbf{P}\left(t_{n+1}, \mathbf{y}_{(m)}^{n+1}\right)$ and $\mathbf{L}_{(m)}^{n+1} = \mathbf{L}\left(t_{n+1}, \mathbf{y}_{(m)}^{n+1}\right)$. This approach is computationally far less expensive than the Newton-Ralpson iteration since only a diagonal, rather than a full matrix needs to be solved at each iteration. In both algorithms, the initial guess for the solution at time t_{n+1} is the solution at time t_n:

$$\mathbf{y}_{(0)}^{n+1} = \mathbf{y}^{n}$$

Another algorithm is provided by the semi-analytic algorithm (Hesstvedt *et al.*, 1978) in which the solution of the ith component of Eq. (5.2) with (5.7) is given by

$$y_i^{n+1} = \left(\frac{P_i}{L_i}\right)^{n} + \left[y_i^{n} - \left(\frac{P_i}{L_i}\right)^{n}\right] \exp\left(-L_i^{n}\Delta t\right) \tag{5.9}$$

where P_i/L_i represents the solution at steady-state. This scheme, which represents the (exact) analytic solution for a scalar linear equation with constant coefficients, is stable. For a system of coupled equations, the accuracy of the solution is improved by an iterative procedure. This computationally efficient algorithm is, however, inherently non-conservative, although rather accurate solutions are obtained in many cases.

Single step methods, such as the Eulerian forward and backward algorithms, can be regarded as particular cases of multistep methods (Byrne and Hindmarsh, 1975). One of them, developed by Gear (1971) is particularly well adapted to "stiff" systems. In this algorithm, the solution to (5.2) is approximated by

Box 5.2 (Continued)

$$\mathbf{y}^{n+1} = \sum_{k=0}^{K} \alpha_k \, \mathbf{y}^{n-k} + \Delta t \beta_0 \, \mathbf{S} \left(t_{n+1}, \mathbf{y}^{n+1} \right) \tag{5.10}$$

where coefficients α_k, β_0, and K, the order of the method (up to 6), are selected to maximize stability and accuracy. Elegant solver packages build around Gear's method continuously and automatically adjust the time step and the order of the method to meet user-specified error tolerances. Gear's method is extremely accurate, robust and stable, but computationally very expensive (since solutions at K previous integration times need to be stored, and numerous iterations and matrix manipulations need to be performed), and hence is not practical for multi-dimensional codes.

The recent application of sparse-matrix techniques combined with computer optimization (vectorization) techniques has, however, improved the speed of Gear's code substantially, so that this advanced algorithm can now be used to study complex problems in multi-dimensional models (see *e.g.*, the SMVGEAR package developed by Jacobson (1995; 1998) and Jacobson and Turco, 1994).

Finally, in order to reduce the "stiffness" of the chemical schemes under consideration in atmosphere models, fast-reacting compounds can be grouped into chemical families whose lifetimes are relatively long. Examples of such families are the odd oxygen, odd hydrogen, odd nitrogen and odd chlorine families discussed in the present chapter. Time-dependent solutions for the concentration of the "families" are found by using simple implicit or even explicit algorithms with relatively large timesteps. When the chemical species belonging to a given family cycle rapidly among each other, the concentrations of individual family members can be computed by assuming photochemical equilibrium conditions between these family members. The advantage of this method is that it is relatively fast since large time steps can be used; the disadvantage is that care must be exercised in choosing the group and assuring that the equilibrium assumptions are valid. In many cases, *e.g.*, during nighttime, the partitioning between family members cannot be derived from equilibrium considerations.

5.2 Oxygen Compounds

Ozone plays a key role in the chemical and radiative budgets of the middle atmosphere. By absorbing solar energy at wavelengths shorter than approximately 320 nm, it protects the biosphere from harmful solar

radiation, and specifically from DNA damage in living cells, from animal and human skin damage, including skin cancer, and from eye cornea and lens damage.

Ozone was discovered in 1839 at the University of Basel, Switzerland, by the German chemist C.F. Schönbein, who had detected the odor of a gas produced in the laboratory without being able to identify its chemical structure. Schönbein named this gas *ozone*, from the Greek word όζειν (ozein, to smell). In 1845, M. de la Rive in Geneva, Switzerland, indicated that this gas was most likely produced by the transformation of oxygen, and in 1863, J.L. Soret, also in Geneva, suggested that ozone was made of 3 oxygen atoms.

Early measurements of atmospheric ozone were provided by chemical analysis (starting in 1853 by Schönbein himself in Vienna, Austria, in 1858 by A. Houzeau in Rouen, France, and systematically from 1877 to 1907 by A. Levy at the Parc Montsouris in Paris). Spectroscopic observations were also made, involving the contributions of A. Cornu (1878 in France), J. Chappuis (1880 in France), W.N. Hartley (1880/81 in the United Kingdom), W. Huggins (1890 in the UK), A. Fowler and R.J. Strutt (1917 in England), C. Fabry and H. Buisson (1920 in France), F.W.P. Götz (1924 in Switzerland), and G.M.B. Dobson (starting in 1924 in the UK). Today, the most accurate measurements of the vertically integrated ozone concentration (also called the ozone *column abundance*) are still provided by UV spectrometers similar to the instrument developed by Dobson in 1928.

The first theory for the formation and destruction of stratospheric ozone involving only oxygen reactions was presented by the British geophysicist S. Chapman at a scientific conference held in France in 1929 (Chapman, 1930). Additional mechanisms were later invoked to account for the destruction of ozone in the mesosphere and stratosphere (see *e.g.*, Nicolet 1975a), including the contribution of hydrogen compounds (Bates and Nicolet, 1950), of nitrogen oxides (Crutzen, 1970; Johnston, 1971), of chlorine species (Stolarski and Cicerone, 1974), and of bromine compounds (Wofsy *et al.*, 1975). The role of industrially produced chlorofluorocarbons as a major source of stratospheric chlorine, and hence as a threat for ozone, was pointed out by Molina and Rowland (1974a,b). In the 1980s, record low ozone concentrations were reported in Antarctica (Chubachi, 1985; Farman *et al.*, 1985) during springtime. The cause of this *ozone hole* was attributed to the presence of anthropogenic chlorine in the stratosphere, enhanced by surface chemistry on polar stratospheric clouds (Solomon *et al.*, 1986; Molina and Molina, 1987).

The next section presents the major photochemical processes affecting the formation and destruction of ozone in a "pure oxygen atmosphere".

The following sections describe the roles of other chemical species in the budget of stratospheric and mesospheric ozone.

5.2.1 Pure Oxygen Chemistry

The photodissociation of molecular oxygen by ultraviolet radiation at wavelengths less than 242.4 nm produces atomic oxygen (Chapman, 1930):

$$(\mathrm{J}_2); \qquad \mathrm{O}_2 + \mathrm{h}\nu \rightarrow \mathrm{O} + \mathrm{O} \tag{5.11}$$

These atoms may recombine in a three body process:

$$(\mathrm{k}_1); \qquad \mathrm{O} + \mathrm{O} + \mathrm{M} \rightarrow \mathrm{O}_2 + \mathrm{M} \tag{5.12}$$

or they may react with molecular oxygen to produce ozone:

$$(\mathrm{k}_2); \qquad \mathrm{O} + \mathrm{O}_2 + \mathrm{M} \rightarrow \mathrm{O}_3 + \mathrm{M} \tag{5.13}$$

Reaction (5.12) plays a significant role only in the thermosphere, where the concentration of atomic oxygen is large (*i.e.*, 10^{12} cm^{-3} at 100 km). Reaction (5.13) is the only known mechanism in the atmosphere that leads to the formation of an ozone molecule. Ozone can recombine with atomic oxygen according to the reaction

$$(\mathrm{k}_3); \qquad \mathrm{O} + \mathrm{O}_3 \rightarrow 2\mathrm{O}_2 \tag{5.14}$$

which leads to the formation of two oxygen molecules. This reaction, which is strongly temperature dependent, provides a loss for O and O_3. The photodissociation of ozone leads to formation of oxygen atoms (see Chapter 4), in either their ground state (^{3}P)

$$(\mathrm{J}_3); \qquad \mathrm{O}_3 + \mathrm{h}\nu\,(\lambda \geq 320 \text{ nm}) \rightarrow \mathrm{O}_2(^3\Sigma_g^-) + \mathrm{O}(^3\mathrm{P}) \tag{5.15}$$

or in their first excited state (^{1}D)

$$(\mathrm{J}_3^*); \qquad \mathrm{O}_3 + \mathrm{h}\nu\,(\lambda \leq 320 \text{ nm}) \rightarrow \mathrm{O}_2(^1\Delta_g) + \mathrm{O}(^1\mathrm{D}) \tag{5.16}$$

In the upper part of the middle atmosphere, some O(^{1}D) atoms can also be produced by molecular oxygen photolysis:

$$(\mathrm{J}_2^*); \qquad \mathrm{O}_2 + \mathrm{h}\nu\,(\lambda < 175.9 \text{ nm}) \rightarrow \mathrm{O}(^1\mathrm{D}) + \mathrm{O}(^3\mathrm{P}) \tag{5.17}$$

When molecular oxygen is in the excited $^1\Delta_\mathrm{g}$ state, it can be deactivated by collision with ground state oxygen molecules O_2 ($^3\Sigma_\mathrm{g}^-$):

$$(\mathrm{k}_6); \qquad \mathrm{O}_2(^1\Delta_\mathrm{g}) + \mathrm{O}_2(^3\Sigma_\mathrm{g}^-) \rightarrow 2\mathrm{O}_2(^3\Sigma_\mathrm{g}^-) \tag{5.18}$$

or it can relax radiatively by emitting a photon in the infrared at $\lambda = 1.27\mu$m

$$(\mathrm{A}_{1.27}); \qquad \mathrm{O}_2(^1\Delta_\mathrm{g}) \rightarrow \mathrm{O}_2(^3\Sigma_\mathrm{g}^-) + \mathrm{h}\nu \tag{5.19}$$

The observation of this emission can be used to deduce the concentration of $O_2(^1\Delta_g)$ and O_3 (see, *e.g.*, Evans *et al.*, 1968; Thomas *et al.*, 1983; Mlynczak and Marshall, 1996; Mlynczak, 1999). $O(^1D)$ is rapidly quenched by collision with N_2 or O_2:

$$(k_{4a}); \qquad O(^1D) + N_2 \rightarrow O(^3P) + N_2 \tag{5.20}$$

$$(k_{4b}); \qquad O(^1D) + O_2 \rightarrow O(^3P) + O_2(^1\Sigma_g^+) \tag{5.21}$$

and, in the thermosphere, by collision with ground state atomic oxygen

$$(k_{4c}); \qquad O(^1D) + O(^3P) \rightarrow 2\ O_2 \tag{5.22}$$

It can also react with ozone

$$(k_5); \qquad O(^1D) + O_3 \rightarrow 2O_2 \tag{5.23}$$

and other chemical compounds, including water vapor and nitrous oxide (see following sections). Because it is produced almost exclusively by photolysis reactions, the concentration of $O(^1D)$ is strongly dependent on local photochemical conditions. Figure 5.1 shows the distribution of $O(^1D)$ calculated for several solar zenith angles.

5.2.2 The Odd Oxygen Family and Oxygen Partitioning

It is useful to examine the photochemistry of the *pure oxygen system* described in the previous section to provide a framework to which other processes may be added and to illustrate the concept of chemical families.

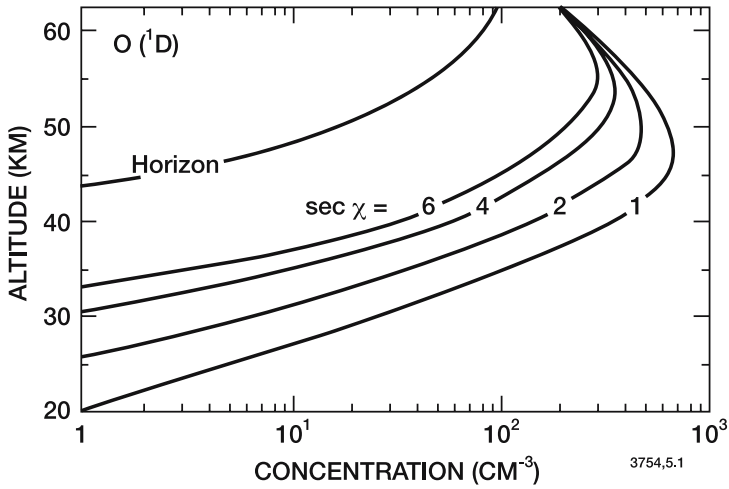

Figure 5.1. Concentration of $O(^1D)$ atoms at various solar zenith angles. From Nicolet (1971).

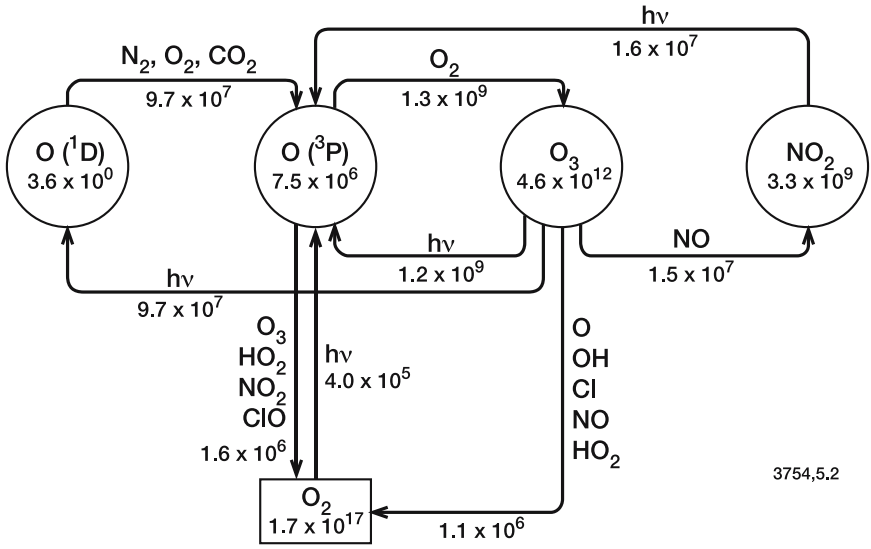

Figure 5.2. Stratospheric chemical cycle affecting odd oxygen species in the stratosphere. The numbers in boxes represent concentrations (cm^{-3}) calculated at 25 km altitude while the numbers associated with the arrows account for the reaction fluxes ($cm^{-3}s^{-1}$) between different compounds (24 hour global average conditions). Note that the figure extends beyond the simple "pure oxygen chemistry" case and that NO_2 is identified as an odd-oxygen reservoir. (See following sections for more details; from Zellner, 1999).

Considering the reactions given in Section 5.2.1, and omitting transport, the continuity equations for O_3, $O(^3P)$, $O(^1D)$, and $O_2(^1\Delta_g)$ can be written as follows:

$$\frac{d(O_3)}{dt} + (J_3 + J_3^*)(O_3) + k_3(O)(O_3) + k_5(O(^1D))(O_3) = k_2(M)(O_2)(O) \quad (5.24)$$

$$\frac{d(O)}{dt} + 2k_1(M)(O)^2 + k_2(M)(O_2)(O) + k_3(O_3)(O) = 2J_2(O_2) + J_2^*(O_2) + J_3(O_3) + k_{4a}(N_2)(O^1D) + k_{4b}(O_2)(O^1D) \quad (5.25)$$

$$\frac{d(O^1D)}{dt} + [k_{4a}(N_2) + k_{4b}(O_2) + k_5(O_3)]\,(O^1D) = J_3^*(O_3) + J_2^*(O_2) \quad (5.26)$$

and

$$\frac{d(O_2\ ^1\Delta_g)}{dt} + A_{1.27}(O_2\ ^1\Delta_g) + k_6(O_2)(O_2\ ^1\Delta_g) = J_3^*(O_3) \quad (5.27)$$

where (O_2) represents the concentration of ground state $O_2(^3\Sigma_g^-)$ and (O) is the density of $O(^3P)$. A similar equation could be written for ground state molecular oxygen, but would not be independent since total oxygen is always conserved:

$$\frac{3d(O_3)}{dt} + \frac{2d(O_2)}{dt} + \frac{2d(O_2\ ^1\Delta_g)}{dt} + \frac{d(O)}{dt} + \frac{d(O^1D)}{dt} = 0 \qquad (5.28)$$

The photochemical lifetimes of these species as determined only by the above reactions are:

$$\tau_{O_3} = \frac{1}{J_3 + J_3^* + k_3(O) + k_5(O\ ^1D)} \approx 2000 \text{ s at 30 km} \qquad (5.29)$$

$$\tau_O = \frac{1}{k_2(O_2)(M) + k_3(O_3) + 2k_1(M)(O)} \approx .04 \text{ s at 30 km} \qquad (5.30)$$

$$\tau_{O^1D} = \frac{1}{k_{4a}(N_2) + k_{4b}(O_2) + k_5(O_3)} \approx 10^{-8} \text{ s at 30 km} \qquad (5.31)$$

$$\tau_{O_2(^1\Delta_g)} = \frac{1}{k_6(O_2) + A_{1.27}} \approx 1 \text{ s at 30 km} \qquad (5.32)$$

The chemical loss of $O_2(^1\Delta_g)$ produces a ground state oxygen molecule. Since O_2 is a permanent gas always present at a constant mixing ratio in the middle atmosphere, this process is not photochemically important. Further, the lifetime of $O_2(^1\Delta_g)$ is never more than its radiative lifetime of about an hour, so that photochemical steady state (see Eqs. (2.37) and (5.27)) may be assumed for this species:

$$(O_2\ ^1\Delta_g) \approx \frac{J_3^*(O_3)}{A_{1.27} + k_6(O_2)} \qquad (5.33)$$

(See also, Thomas *et al.*, 1983, for more details regarding $O_2(^1\Delta_g)$ chemistry).

The O_3, O, and $O(^1D)$ equations are a coupled set of partial differential equations whose time constants differ by many orders of magnitude. Such a set of equations is called a "stiff" system (see Box 5.1). It cannot be easily solved by simple methods, unless a timestep of the order of the smallest lifetime is used for the numerical integration. In view of this problem, it is very useful to define chemical families, whose lifetimes can be very much longer than those of the constituent members. Adding equations (5.24), (5.25), and (5.26) one obtains an equation describing the behavior of the sum of $O(^3P)$, $O(^1D)$, and O_3, which is generally referred to as the *odd oxygen family,* O_x:

$$(O_x) = (O^3P) + (O^1D) + (O_3)\ . \qquad (5.34)$$

One can then write:

$$\frac{d(O_x)}{dt} + 2k_3(O_3)(O) + 2k_5(O(^1D))(O_3) + 2k_1(M)(O)^2$$

$$= 2(J_2 + J_2^*)(O_2) = 2J_{O_2}(O_2) \tag{5.35}$$

where $J_{O_2} = J_2 + J_2^*$ is the total photolysis rate of O_2. The chemical lifetime of the odd oxygen family is then given by

$$\tau_{O_x} \approx \frac{(O_x)}{2k_1(M)(O)^2 + 2k_3(O)(O_3) + 2k_5(O^1D)(O_3)} \tag{5.36}$$
$$\approx \text{weeks at 30 km and 1 year at 20 km}$$

Figure 5.3 presents an altitude profile of the photochemical lifetimes of the O_x family (including important reactions with hydrogen, nitrogen, and chlorine containing species, which will be introduced later), O_3, and O, as well as an estimate of the approximate time constants associated with transport by the winds and a typical vertical diffusive lifetime. In this and other figures involving lifetimes to be presented in this chapter, τ_D represents the vertical diffusive lifetime (mean vertical mixing), assuming a vertical scale height of 5 km. $\tau_{\bar{u}}$, $\tau_{\bar{u}^*}$ and $\tau_{\bar{w}^*}$ represent the time constants for transports by the zonal, meridional,

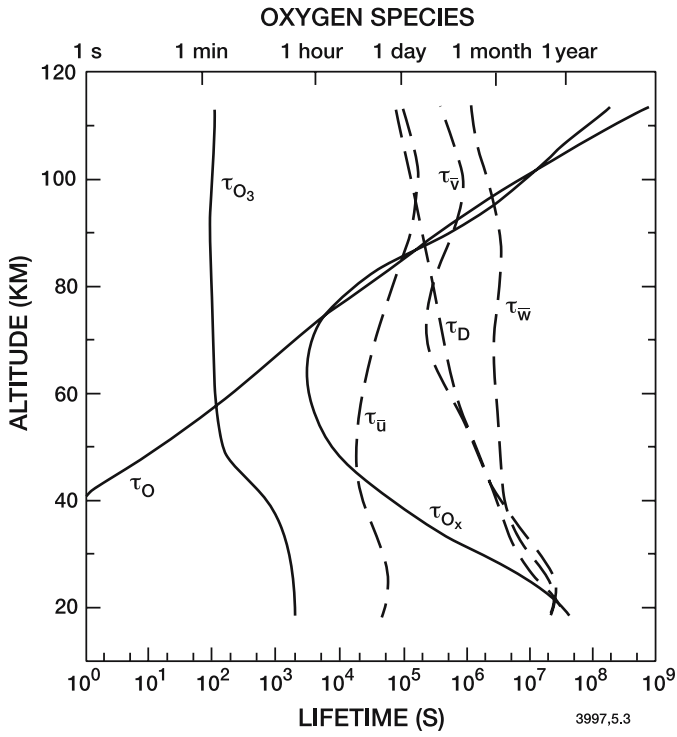

Figure 5.3. Daytime photochemical lifetimes of O_x, O_3, and O, and characteristic transport lifetimes for mid-latitude winter, from the model of Garcia and Solomon (see Garcia and Solomon, 1994, and references therein).

and vertical winds at middle latitudes, assuming characteristic scales of 1000, 1000, and 5 km, respectively. These values are based on an updated version of the model by Garcia and Solomon (1983). We will discuss the implications of the magnitudes of the chemical and dynamical time constants in determining the behavior of these species below.

The definition of the odd oxygen family clearly produces a substantial increment in the photochemical time constant of the equation to be considered, enabling us to solve it more readily. The very fast reactions, such as

$$O_3 + h\nu \rightarrow O(^1D) + O_2 \tag{5.16}$$

$$O(^1D) + O_2 \rightarrow O + O_2(^1\Sigma_g) \tag{5.21}$$

$$O + O_2 + M \rightarrow O_3 + M \tag{5.13}$$

now produce only an exchange, or *partitioning*, among members of the family, but do not appear as production or loss terms in the continuity equation for the family. The use of chemical families is useful, however, only if the time constants characterizing exchange between family members are short compared to the dynamical time constants. Since the net transport of a chemical species depends in part upon its gradient, any species whose lifetime is sufficiently long that transport may play a role in establishing its distribution should be transported according to its own individual gradient. The family definitions may also depend on the problem under consideration. For example, if the detailed photochemistry of the rapidly changing solar illumination found at twilight is of special interest, then the families used may be different from those appropriate to a study of variations on a seasonal time scale.

The use of chemical families allows a clearer distinction to be drawn between reactions which represent *net* and *gross* production and loss terms over the time scale considered. For example, the photolysis of O_3 (Reactions (5.15) and (5.16)) is a gross, but not a net loss term for ozone at altitudes below about 80 km over time scales longer than a few seconds, because nearly all the oxygen atoms which are formed by this reaction rapidly reform ozone (Reaction 5.13), implying no net loss. On the other hand, when ozone reacts with atomic oxygen to form O_2 (Reaction 5.14), a net loss of ozone occurs over an extended time scale. Further, since a typical time scale for meridional transport is of the order of months, it is convenient to consider odd oxygen, rather than ozone or atomic oxygen, since it is only odd oxygen which has a sufficiently long lifetime to be influenced by meridional transport processes. The importance of transport is often more easily seen when families are considered.

This analysis allows us to obtain the concentrations of the odd oxygen family, but it must also be partitioned into its constituent parts. This can be done by examining the photochemical equilibrium expressions for certain members of the family. If the family is composed of N members, we must write photochemical equilibrium expressions for the shortest lived N − 1 members of the family and use these to establish ratios between family members. Below the mesopause, the photochemical time constant for atomic oxygen is relatively short and one can assume that it is essentially in *photochemical equilibrium*. Similar conditions apply to the excited $O(^1D)$ atom. Neglecting minor terms, Eq. (5.26) becomes

$$\frac{d(O^1D)}{dt} \approx 0 \approx J_3^*(O_3) + J_2^*(O_2) - [k_{4a}(N_2) + k_{4b}(O_2)]\,(O^1D) \quad (5.37)$$

or

$$(O^1D) \approx \frac{J_3^*(O_3) + J_2^*(O_2)}{k_{4a}(N_2) + k_{4b}(O_2)} \approx \frac{J_3^*(O_3)}{k_{4a}(N_2) + k_{4b}(O_2)} \quad (5.38)$$

The partitioning between $O(^1D)$ and ozone is thus expressed by the following ratio:

$$\frac{(O^1D)}{(O_3)} \approx \frac{J_3^*}{k_{4a}(N_2) + k_{4b}(O_2)} \quad (5.39)$$

Similarly, Eq. (5.25) becomes

$$\frac{d(O^3P)}{dt} \approx 0 \approx J_3(O_3) + [k_{4a}(N_2) + k_{4b}(O_2)]\,(O^1D) + 2J_{O_2}(O_2) - [k_2(M)(O_2) + k_3(O_3)]\,(O^3P) \quad (5.40)$$

Substituting for $O(^1D)$ from the expression above, the concentration of $O(^3P)$ at equilibrium is

$$(O^3P) \approx \frac{J_{O_3}(O_3) + 2J_{O_2}(O_2)}{k_2(M)(O_2) + k_3(O_3)} \approx \frac{J_{O_3}(O_3)}{k_2(M)(O_2)} \quad (5.41a)$$

and the ratio between $O(^3P)$ and ozone concentration is

$$\frac{(O^3P)}{(O_3)} \approx \frac{J_{O_3}}{k_2(M)(O_2)} \quad (5.41b)$$

The partitioning between the members of the O_x family is given by

$$\frac{(O_3)}{(O_x)} = \frac{1}{\frac{1+(O^3P)}{(O_3)} + \frac{(O^1D)}{(O_3)}} \quad (5.41c)$$

and

$$\frac{(O)}{(O_x)} = \frac{(O_3)}{(O_x)} \times \frac{(O)}{(O_3)} \quad (5.41d)$$

In the stratosphere ozone is much more abundant than atomic oxygen ($O(^3P)$ and $O(^1D)$; see Table 5.2), so that $(O_x) \approx (O_3)$. Neglecting Reaction (k_1) and (k_5) in Eq. (5.35) and assuming that $d(O^3P)/dt$ and $d(O^1D)/dt \approx 0$, the odd oxygen equation can be written (using Eq. 5.41a):

$$\frac{d(O_x)}{dt} + \frac{2k_3 J_{O_3}(O_3)^2}{k_2(M)(O_2)} = 2J_{O_2}(O_2) \tag{5.42}$$

In the upper stratosphere and lower mesosphere, odd oxygen (and ozone) is short-lived, and is approximately in photochemical equilibrium, so that this may be rewritten as:

$$(O_3)_{eq} = \left(\frac{k_2}{k_3}(M)(O_2)^2 \, \frac{J_{O_2}}{J_{O_3}}\right)^{1/2} \tag{5.43}$$

for pure oxygen chemistry. Below about 25 km the photochemical lifetime of odd oxygen becomes comparable to or longer than the transport time scales (as shown in Figure 5.3), so that both chemistry and dynamics influence its concentration. This will be discussed in more detail below. Table 5.2 presents typical values of the daytime distribution of oxygen species in the atmosphere (calculated with hydrogen, nitrogen and chlorine reactions taken into account).

In the upper part of the mesosphere and in the thermosphere, atomic oxygen becomes more abundant than ozone. At these heights, ozone is short-lived due to rapidly increasing photolysis rates, and, during daytime, is in photochemical equilibrium with atomic oxygen. The lifetime of atomic oxygen becomes longer and longer with increasing altitude due to its slower recombination rate (see Eqs. (5.12) and (5.13)) as the air pressure decreases (see Figure 5.3). It can be deduced from Eq. (5.24) that when $d(O_3)/dt=0$,

$$(O_3) = \frac{k_2(M)(O_2)(O)}{J_{O_3} + k_3(O) + k_5(O(^1D))} \approx \frac{k_2(M)(O_2)(O)}{J_{O_3}} \tag{5.44}$$

and from (5.38), setting $d(O_x)/dt \approx d(O)/dt$,

$$\frac{d(O)}{dt} + 2\left(k_1(M) + \frac{k_3 k_2(M)(O_2)}{J_{O_3}}\right)(O)^2 = 2J_{O_2}(O_2) \tag{5.45}$$

The photochemical time constant $\tau(O)$ for atomic oxygen is about 4 hours at 70 km, a day near 80 km and about a week at 100 km. Therefore, the distribution of atomic oxygen above the mesopause is dependent on dynamical conditions. It does not exhibit much diurnal variation above about 85 km, since its lifetime exceeds a day. At lower altitudes, on the other hand, atomic oxygen disappears rapidly after sunset, forming ozone through the recombination reaction (5.13). In

Table 5.2 Example of the Vertical Distributions of Oxygen Compounds in the Middle Atmosphere

Altitude	(O_2)	(O_3)	$(O\,^3P)$	$(O\,^1D)$
(km)	(cm^{-3})	(cm^{-3})	(cm^{-3})	(cm^{-3})
0	5.3 (18)*	8.0 (11)	1.0 (3)	2.7 (–3)
5	3.2 (18)	7.7 (11)	4.6 (3)	9.0 (–3)
10	1.8 (18)	7.5 (11)	1.2 (4)	1.8 (–2)
15	8.8 (17)	2.2 (12)	1.3 (5)	1.2 (–1)
20	3.8 (17)	4.8 (12)	1.6 (6)	8.9 (–1)
25	1.7 (17)	4.9 (12)	8.6 (6)	4.6 (0)
30	7.8 (16)	3.1 (12)	3.3 (7)	2.0 (1)
35	3.6 (16)	1.3 (12)	1.2 (8)	6.7 (1)
40	1.6 (16)	3.9 (11)	3.8 (8)	1.4 (2)
45	8.0 (15)	1.2 (11)	1.1 (9)	2.0 (2)
50	4.2 (15)	4.1 (10)	2.0 (9)	1.9 (2)
55	2.3 (15)	1.5 (10)	2.7 (9)	1.5 (2)
60	1.2 (15)	5.7 (9)	3.3 (9)	1.1 (2)
65	6.3 (14)	2.2 (9)	3.8 (9)	7.5 (1)
70	3.2 (14)	6.0 (8)	3.5 (9)	4.0 (1)
75	1.6 (14)	1.3 (8)	2.8 (9)	1.9 (1)
80	7.1 (13)	9.3 (7)	1.0 (10)	3.0 (1)
85	4.8 (13)	1.7 (8)	1.1 (11)	1.2 (2)
90	2.3 (13)	4.0 (7)	4.5 (11)	1.0 (2)
95	1.0 (13)	5.7 (6)	8.6 (11)	2.0 (2)
100	4.6 (12)	2.5 (6)	1.1 (12)	1.0 (3)

* 5.3 (18) denote 5.3×10^{18} molecules/cm^3.

the middle and lower stratosphere, the abundance of atomic oxygen is very small compared to that of ozone, and the lifetime of ozone is greater than a day. Therefore, relatively small diurnal variations are expected to occur in stratospheric ozone concentrations. In the mesosphere, atomic oxygen densities are comparable to, and even greater than those of ozone (see Table 5.2 and Figure 5.4), so that the recombination reaction leads to ozone increases throughout the mesosphere at the beginning of the night (and decreases after sunrise).

5.2.3 Observations of Ozone

Most of the ozone molecules in a vertical column are found at altitudes ranging from 10 to 35 km (see Table 5.2). Measurements of the total ozone abundance can be performed from the ground using ultraviolet absorption techniques (see *e.g.*, Dobson, 1963) or from space. Total

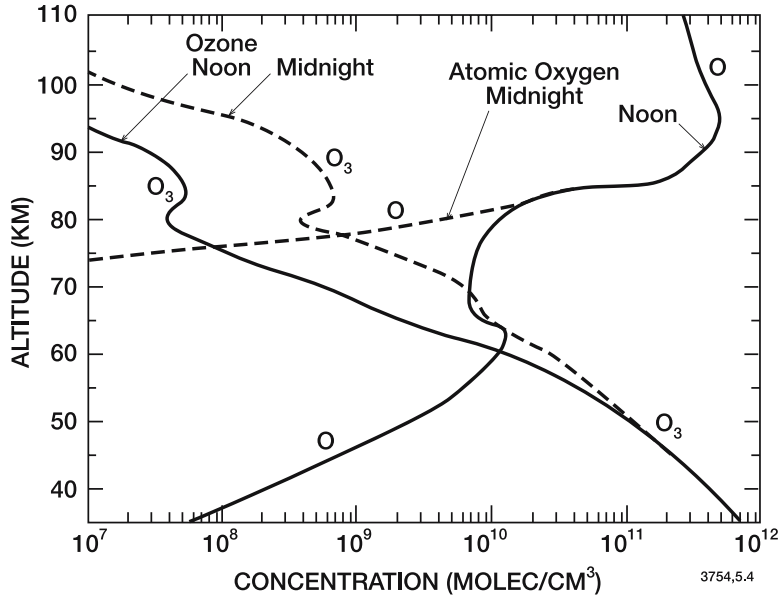

Figure 5.4. Calculated vertical distributions of ozone and atomic oxygen at noon and midnight. From the model of Garcia and Solomon (1983).

ozone has been systematically observed for many years and at numerous locations. Therefore, the general spatial and temporal behavior of this gas in the atmosphere is very well documented (Dütsch, 1970; 1980; London, 1980). For example, it is well known that ozone is characterized by latitudinal and seasonal variations that include a maximum abundance in the region of the least production (see, for example, Dobson, 1963). Figure 5.5 shows the total ozone column versus month for several locations in the northern hemisphere. These values are expressed in Dobson units (DU), which correspond to the height (in millicentimeter) that the ozone column would have if all the gas were at standard temperature and pressure (1 DU = 10^{-3} atm. cm = 2.69×10^{16} molecules cm^{-2}). It should be noted that ozone is most abundant at higher latitudes during most seasons. This increase with latitude is most pronounced in winter and spring. The seasonal variations only become large at latitudes poleward of 30 degrees north. At 80°N, for example, the relative variation in total ozone is about 50 percent over six months.

The global distribution of total ozone as a function of latitude and time deduced from the observations by the Total Ozone Mapping Spectrometer (TOMS) on board the Nimbus 7 satellite is presented in Figure 5.6. This figure shows that the ozone column abundance is typically 260-270 DU in the tropics. The peak total ozone

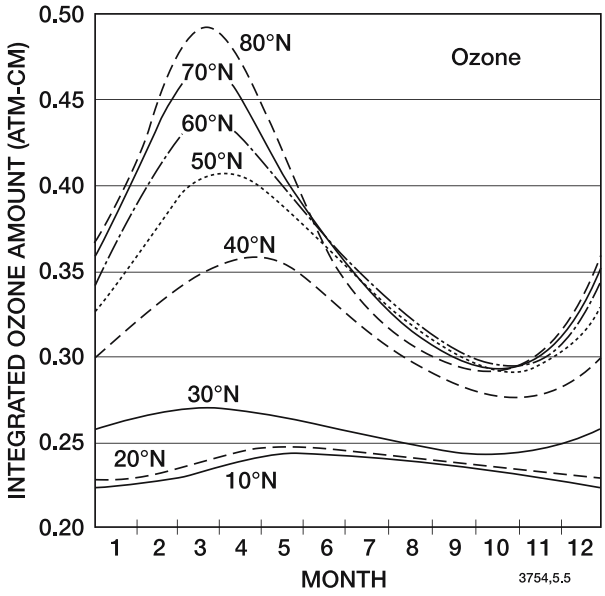

Figure 5.5. Mean seasonal variation of the total ozone abundance at different latitudes in the northern hemisphere. From Dobson (1963).

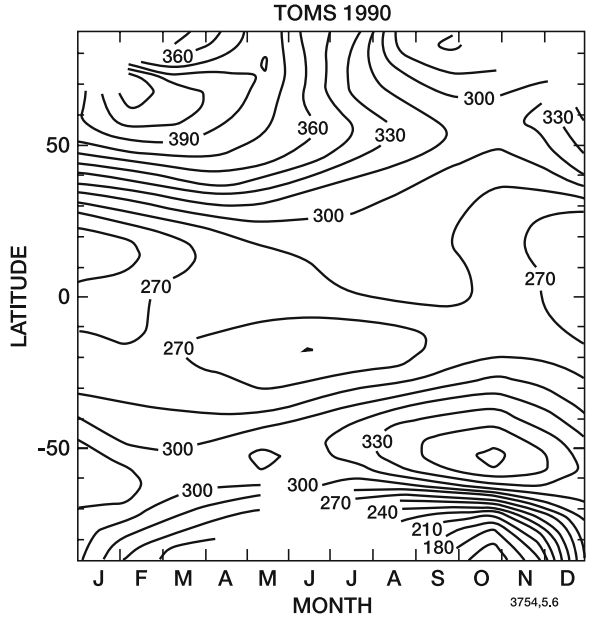

Figure 5.6. Variation of total ozone (DU) with latitude and season in the year 1990, as measured by the TOMS instrument.

abundance (typically 400 DU) appears in the Arctic in late winter. The maximum observed in the southern hemisphere (approximately 360 DU) is somewhat smaller, and located at lower latitudes (60-65°S) and earlier in the season compared to the maximum occurring in the northern hemisphere. The very low ozone column abundance observed from September to November over Antarctica since the late 1970s (see Chapter 6 and Plates 8 and 9) is referred to as the *ozone hole.* Ozone columns as low as 100 DU are observed during the Antarctic springtime. During the 1990s, low ozone concentrations have also been recorded in the Arctic spring. These anomalous ozone levels are associated with cold temperatures in the polar lower stratosphere and the activation of chlorine on surfaces of polar stratospheric cloud particles (see Chapters 2 and 6).

Since the chemical lifetime of odd oxygen in the lower stratosphere is long compared to the time constants associated with transport by the mean meridional circulation (Figure 5.3), transport by mean meridional advection can play an important role in determining the distribution of ozone. Much of the hemispheric asymmetry in total ozone distributions as shown in Figure 5.6 is generally presumed to be due to differences in the stratospheric dynamics of the two hemispheres. As first pointed out based on empirical evidence by Dobson (1930), the primary mechanism accomplishing this transport can be simply understood to a first approximation in terms of the downward and poleward net transport associated with mean motion in the transformed Eulerian or diabatic framework, as discussed in Chapter 3. This implies that the slopes of the mean ozone mixing ratio surfaces are somewhat steeper than the slopes of the isentropic surfaces represented by potential temperatures, as pointed out by Newell (1964), and discussed in more detail by Tung (1982).

A more detailed understanding of the behavior of ozone requires examination of its altitude profile, so that the regions responsible for the observed total column variations can be identified. Figure 5.7 shows some typical vertical distributions of ozone for spring and fall at different latitudes of the Northern Hemisphere (Dütsch, 1980). It is clear that the changes in total column abundance are due to variations found in the ozone concentration between the tropopause and 20 km altitude. Dobson (1963) suggested that this behavior is related to ozone transport in cyclones and anticyclones (*e.g.*, weather systems) that propagate into the lower stratosphere. Experimental support for this view comes from the observation of close correlations between high total ozone abundances and low pressure systems, as shown, for example, in Figure 5.8. As a result of these processes, large local fluctuations in total ozone are often observed, with amplitudes sometimes as large as those

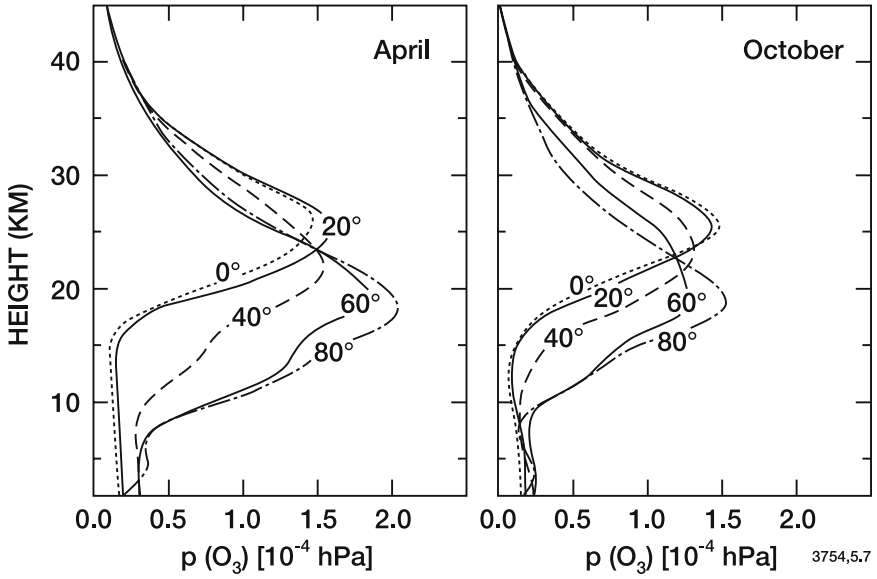

Figure 5.7. Mean vertical distribution of the ozone partial pressure (10^{-4} hPa) for different latitudes of the Northern Hemisphere in April and October (Dütsch, 1980).

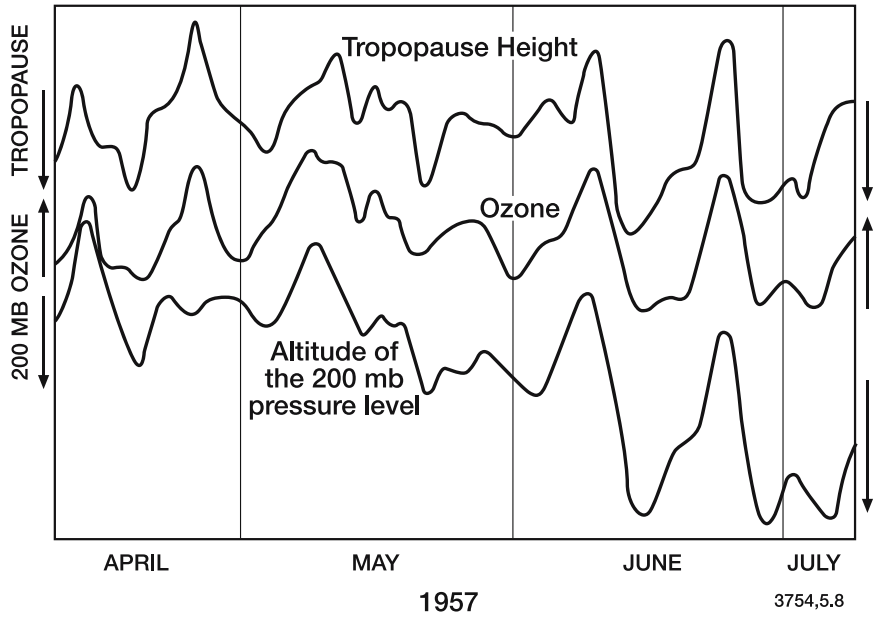

Figure 5.8. Relationship between the variations in total ozone and the altitudes of the tropopause and the 200 hPa level. From Dobson (1963).

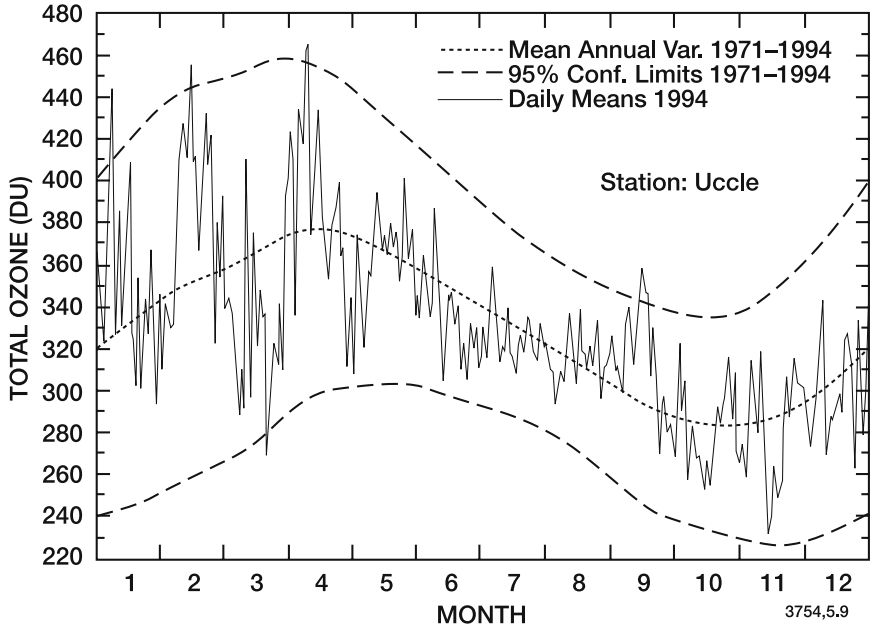

Figure 5.9. Evolution of the total ozone column abundance during 1994 at Uccle, Belgium (De Muer, private communication).

related to the seasonal variations (see Figure 5.9). Dynamical studies suggest that transport above 100 hPa can be broadly understood in terms of a residual Eulerian mean motion in the middle stratosphere (see Section 3.6), but that considerable dispersion related to cyclone propagation dominates the behavior for lower altitudes (see, *e.g.*, Holton *et al.*, 1995).

It is sometimes stated that ozone is produced where its mixing ratio maximizes in the upper stratosphere of the tropics and transported downward and poleward to higher latitudes, thus producing the observed structure in the ozone column. But closer examination reveals a different picture. Figure 5.3 shows that the lifetime of odd oxygen is less than a month above about 30 km in the sunlit atmosphere, decreasing to only about a day near 40 km. The tropical ozone mixing ratio maximum occurs between about 30 and 40 km (see Figure 5.10), in the heart of this region of short lifetime. Under such conditions, ozone is essentially in photochemical equilibrium, with rapid production being balanced by rapid destruction — it does not live long enough to be transported away from this photochemically-controlled zone. Since the time scale for meridional overturning of the stratosphere is slow (order of years) compared to these chemical phenomena, the tropics cannot serve as the source region for the large amounts of total ozone found in

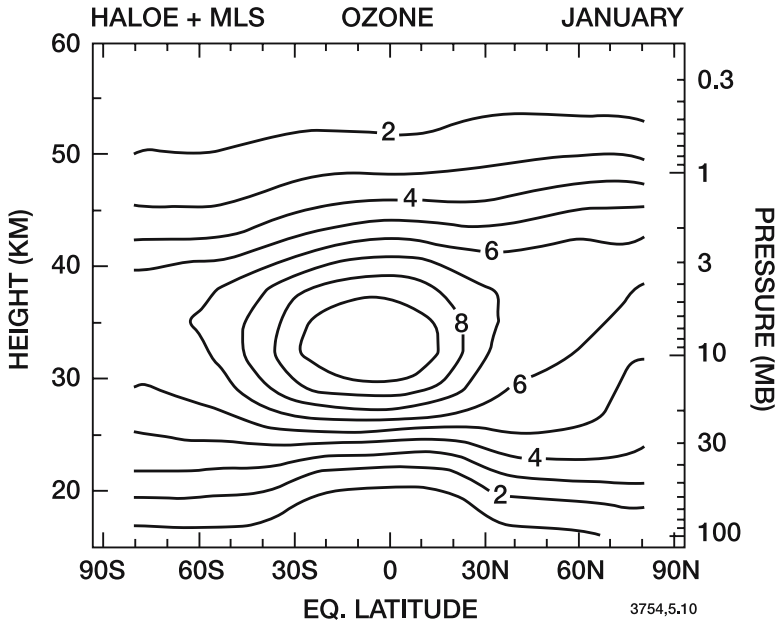

Figure 5.10. Zonally averaged ozone mixing ratio (ppmv) in the stratosphere (15-55 km) in January. Climatological values derived from observations by the Halogen Occultation Experiment (HALOE) and the Microwave Limb Sounder (MLS) on board the Upper Atmosphere Research Satellite (UARS). (Courtesy of W. Randel, NCAR).

the extratropical lower stratosphere, which dominate the total column (see Figure 5.7; also Ko *et al.*, 1989; Perliski *et al.*, 1989).

The primary region that supplies ozone to the extratropical lower stratosphere is a narrow "transition" zone as shown in Figure 5.11. Air flowing across this zone moves through rapidly enough to retain relatively high mixing ratios compared to those found at lower levels. The transition zone slopes upward in the winter hemisphere, due to latitude-dependent changes in the propagation of the solar radiation that drives photochemistry and determines the lifetime. Thus the source for the extratropical ozone column lies not in the tropics, but in the meridional flow poleward and downward from this transition zone — a zone of competition between transport and chemistry.

Satellite observations have added much to our understanding of the morphology of atmospheric ozone, both in terms of its altitude profile and total column density (see Box 5.3). For example, early observations by the Backscatter Ultraviolet Spectrometer (BUV) on board Nimbus 4, as well as by the Limb Infrared Monitor of the Stratosphere (LIMS), and the Solar and Backscatter Ultraviolet Spectrometer (SBUV) on board Nimbus 7 led to the first global view of the distribution of ozone

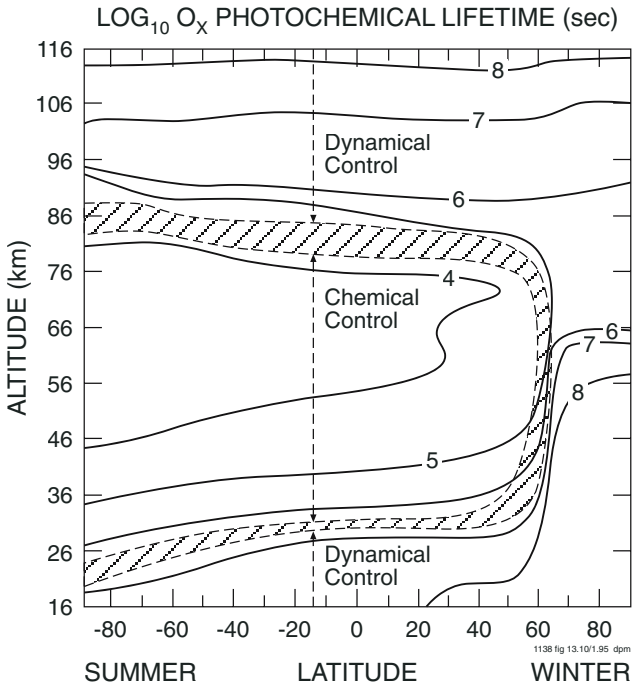

Figure 5.11. Photochemical lifetime of the O_x ($O + O_3$) family (logarithmic scale of values expressed in seconds). In the region of chemical control, the photochemical production and destruction are nearly in balance and steady state conditions can be adopted to derive the concentrations of O_3 and O. In the dynamically controlled regions, photochemical processes play a secondary role and O_x (primarily O_3 in the stratosphere and O in the thermosphere) is primarily influenced by transport processes. In the shaded region, transport and photochemistry play an equally important role. From Garcia and Solomon, 1985.

in the stratosphere. Satellite observations of ozone were also provided by the Stratospheric Aerosol and Gas Experiments (SAGE I and II) and, in the mesosphere, by the Solar Mesospheric Explorer (SME). More recently, an operational version of SBUV (SBUV-2) has been collecting ozone data, while the Upper Atmosphere Research Satellite (UARS) has provided measurements of ozone and a range of related chemical constituents in the stratosphere and mesosphere. Figure 5.10 presents a climatological (zonal mean) distribution of the ozone mixing ratio in January from 100 hPa (approximately 16 km) to 0.3 hPa (55 km) based on the observations of 2 UARS instruments. It is interesting to note that the maximum mixing ratio (9.6 ppmv) is located at 10 hPa (30 km) in the equatorial region, while in the lower stratosphere, the ozone abundance increases with latitude due to poleward transport (as indicated previously in terms of the observed total column abundances).

Box 5.3. Platforms to Observe the Chemical Composition of the Middle Atmosphere

The earliest observations of the chemical composition of the middle atmosphere were performed primarily by balloon-borne (stratosphere) and rocket-borne (mesosphere) instrumentation. In recent decades, however, systematic observations have been made by space-borne sensors, and information on chemical processes in the upper troposphere and lower stratosphere has been provided through chemical measurements made from aircraft platforms (*e.g.*, from high-altitude aircraft such as the ER-2, the WB-57 and the Geofysika). Measurements from ground stations, combined with satellite observations, have provided accurate estimates of long-term ozone trends in the different regions of the world.

Satellite observations provide information on the global distribution and seasonal variation of chemical compounds. Measurements of vertically or horizontally integrated radiances (atmospheric absorption of solar radiation or emission of atmospheric radiation) over a given spectral range (UV-visible, infrared, microwave) are inverted by appropriate algorithms to derive the concentration of selected chemical species. Examples of space instruments include TOMS (Total Ozone Mapping Spectrometer, measuring the ozone column abundances), SBUV (Solar Backscatter Ultraviolet, measuring the ozone column and the vertical distribution of ozone), SAGE (Stratospheric Aerosol and Gas Experiments, measuring the vertical distributions of ozone, nitrogen dioxide, water vapor and aerosols), GOME (Global Ozone Monitoring Experiment, measuring the vertical distribution of ozone, nitrogen dioxide and other minor species). Instruments on board the Upper Atmosphere Research Satellite (UARS) included HALOE (Halogen Occultation Experiment, measuring ozone, NO, NO_2, HCl, HF, CH_4, and H_2O by infrared solar occultation), MLS (Microwave Limb Sounder, measuring ozone, ClO, H_2O, and HNO_3 by a microwave emission technique) and CLAES (Cryogenic Limb Array Etalon Spectrometer, measuring ozone, NO, NO_2, HNO_3, N_2O, N_2O_5, $ClONO_2$, $CFCl_3$, CF_2Cl_2, CH_4, H_2O, and aerosols using an infrared limb emission technique). The vertical distribution of many chemical compounds including key species belonging to the nitrogen and chlorine families was provided by the ATMOS instrument (Fourier Transformed infrared technique for absorbed solar infrared radiation) on board the Space Shuttle. The CRISTA (Cryogenic Infrared Spectrometers and Telescopes for the Atmosphere) and MAHRSI (Middle Atmosphere High Resolution Spectrograph Investigation), also on the Space Shuttle, have provided high-resolution distributions of several chemical compounds in the stratosphere and a near-global distribution of OH in the mesosphere, respectively. Additional information has been obtained from MIPAS (IR limb sounder), SCIAMACHY (UV-visible and near-IR nadir and limb viewer) and GOMOS on board the ENVISAT space platform. Obser-

Box 5.3 (Continued)

vations of important trace constituents at high spatial resolution in the stratosphere and upper troposphere should be provided by HIRDLS (High Resolution Dynamics Limb Sounder), TES (Tropospheric Emission Spectrometer), OMI (Ozone Monitoring Instrument), and an improved version of MLS (Microwave Limb Sounder) on the Aura platform.

One of the great advantages of space observations is that they provide global information on spatial and short-term temporal (*e.g.*, synoptic scale) variations. Figure 5.12, which presents the ozone mixing ratio observed by LIMS at 10 hPa on 24 January 1979, shows that planetary waves, which propagate into the middle atmosphere during winter, perturb significantly the distribution of this chemical compound. The displacement from the North Pole of ozone-poor airmasses, caused by planetary wave disturbances, and the strong poleward flow of subtropical ozone (which propagates counterclockwise around the vortex) are typical of winter situations. If planetary waves break, (for example, during a stratospheric warming event), irreversible transport takes place, and

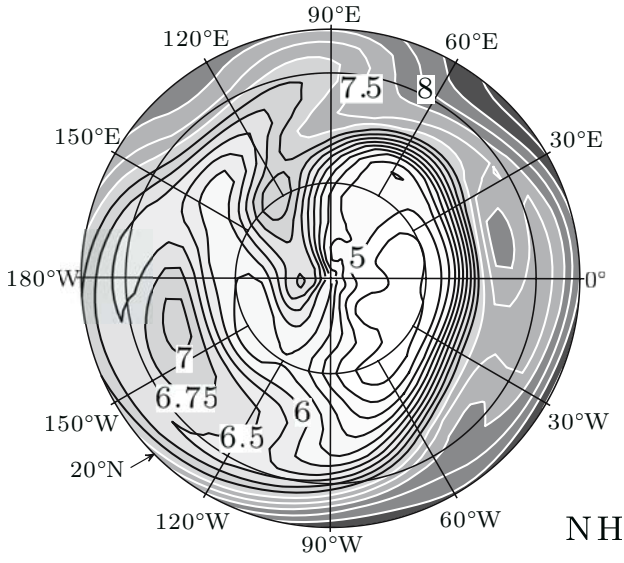

Figure 5.12. Ozone mole fraction (ppmv) on the isobaric surface of 10 hPa measured by the LIMS instrument (Nimbus 7) on 24 January, 1979. Note the intrusion of subtropic ozone into the polar region during a planetary scale wave disturbance. Courtesy of L. Lyjak and J. Gille, NCAR.

contributes to the ozone maximum observed in late winter/early spring at high latitudes. Similar disturbances are less common in the Southern Hemisphere where a minimum in the ozone abundance prevails over the pole during the entire winter. The rapid decrease in the abundance of lower stratospheric ozone observed in September and October is caused by photochemical destruction inside the Antarctic vortex and results from the presence of anthropogenic chlorine compounds (see Chapter 6); it is facilitated by the stability and the strength of the vortex, which does not allow ozone to be easily transported south of 60°S.

Ozone observations near 90 km available from the Solar Mesosphere Explorer are characterized by strong latitudinal gradients and large local variations. Barth *et al.* (1983) suggested that this may result from downward transport of oxygen from the thermosphere because of the long O_x lifetime at these altitudes, as shown in Figure 5.3.

To conclude this discussion, we turn to the question of longer term variations in ozone. Ramanathan (1963), Angell and Korshover (1964; 1973), and Shah (1967) were among the first to note the existence of an oscillatory component in the total ozone abundance which is correlated with the behavior of the zonal winds in the tropical lower stratosphere. These winds change speed and direction with a period between 24 and 33 months; this is the quasi-biennial oscillation (QBO) noted in Chapter 3. Figure 5.13 shows an analysis of ozone QBO based on 13 years of TOMS observations and Plate 6 ozone anomalies associated with QBO in the lower tropical stratosphere. Another question related to long-term variability is that of a possible relationship between

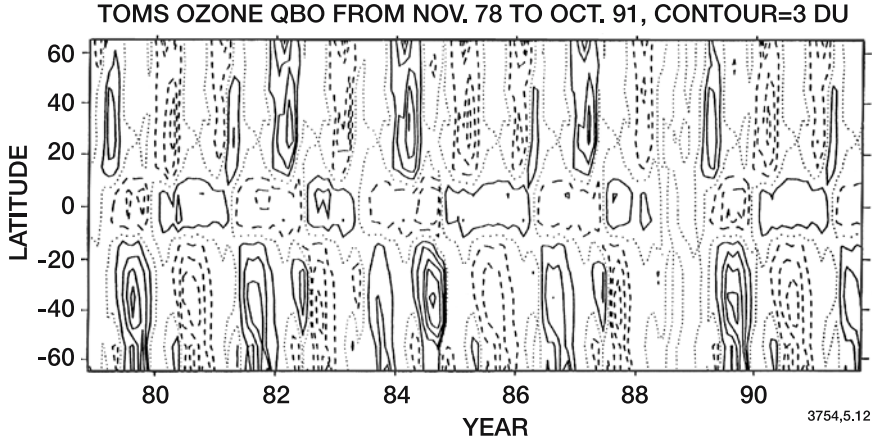

Figure 5.13. Global patterns of ozone QBO deduced from observations by TOMS. Contour intervals correspond to three Dobson units with solid lines for positive anomalies and dashed lines for negative values. From Yang and Tung (1995).

ozone and the 11 year solar cycle. This has long been the subject of vigorous controversy (Willett, 1962; London and Haurwitz, 1963; Willett and Prohaska, 1965; Paetzold *et al.*, 1972; Angell and Korshover, 1973). Observational studies suggest a connection between the chemical and thermal structure of the middle atmosphere and variations in the solar ultraviolet flux. This is certainly true for short-term (27-day) variations (associated with the apparent solar rotation), as revealed by analyses of satellite data (Gille *et al.*, 1984; Hood, 1987; Keating *et al.*, 1987; Hood *et al.*, 1991; Hood and Jirikowic, 1991) and model studies (Eckman, 1986; Brasseur *et al.*, 1987; Summers *et al.*, 1990; Brasseur, 1993). Convincing statistics are more difficult to obtain for the 11-year period, although more recent satellite data analyses suggest a correlation of stratospheric ozone with the solar cycle (Chandra, 1991; Hood and McCormack, 1992; Hood *et al.*, 1993). Model studies (Brasseur, 1993; Huang and Brasseur, 1993) imply that the variation in total ozone over the solar cycle is probably less than two percent. Detection of such a small variation is difficult because of the natural variability in total ozone due to its dependence on dynamical conditions, especially at middle and high latitudes (Figures 5.5 and 5.9).

Finally, and perhaps more importantly, statistical analyses of ground-based and satellite ozone observations suggest that, on the global scale, the abundance of stratospheric ozone has decreased significantly over the 1980s and 1990s. The downward trend is most marked at mid- and high latitudes, and is believed to result largely from the production of industrially manufactured chlorofluorocarbons. This question will be further discussed later in this chapter and in Chapter 6.

5.3 Carbon Compounds

The most abundant carbon-containing compound in the stratosphere and mesosphere is carbon dioxide (CO_2). By interacting with infrared radiation, this gas plays an important role in the thermal budget of the atmosphere, and the 30% increase in its concentration resulting mainly from fossil fuel burning has provided a significant forcing to the climate system of about 1.5 Wm^{-2} (IPCC, 2001). Carbon dioxide does not play any substantial role in the chemistry of the atmosphere except in the lower thermosphere, where its photolysis is an important source of carbon monoxide (CO). This latter gas, which is also released at the Earth's surface by incomplete combustion (pollution) and is partially transported to the stratosphere, is converted to CO_2 by reaction with the hydroxyl radical (OH).

Methane (CH_4), another important carbon-containing species and also a radiatively important gas of the atmosphere, is released at the surface as a result of biogenic processes in oxygen-deficient environments such as wetlands. It is also emitted to the atmosphere in connection with mining activities and natural gas consumption. The oxidation of methane produces a number of partially oxygenated organic compounds such as formaldehyde (CH_2O) and methyl peroxide (CH_3OOH), as well as carbon monoxide and carbon dioxide. This degradation mechanism tends to destroy ozone and OH radicals in NO-poor air masses and to produce ozone and OH in NO-rich environments. The reaction of methane with chlorine atoms converts reactive chlorine atoms into stable hydrogen chlorine (HCl) and hence influences the impact of man-made halocarbons on stratospheric ozone (see Section 5.6.2 and 5.8). Methane is also a source of water vapor in the middle atmosphere, and the increase in its surface emissions associated with agricultural and industrial activities has probably enhanced the abundance of H_2O in the stratosphere and mesosphere.

The following sub-sections present the budget of carbon-containing species and describe the photochemical processes affecting these species in the middle atmosphere.

5.3.1 Methane

The chemistry of atmospheric *methane* in the middle atmosphere was first considered by Bates and Nicolet (1950). Its destruction is due to reactions by the OH radical:

$$(c_2); \qquad CH_4 + OH \rightarrow CH_3 + H_2O \tag{5.46}$$

by excited oxygen $O(^1D)$:

$$(c_{1a}); \qquad CH_4 + O(^1D) \rightarrow CH_3 + OH \tag{5.47a}$$

$$(c_{1b}); \qquad CH_4 + O(^1D) \rightarrow CH_2O + H_2 \tag{5.47b}$$

$$(c_{1c}); \qquad CH_4 + O(^1D) \rightarrow CH_3O\,(\text{or } CH_2OH) + H \tag{5.47c}$$

or by chlorine atoms:

$$(d_5); \qquad CH_4 + Cl \rightarrow CH_3 + HCl \tag{5.48}$$

Branching ratios for (5.47a), (5.47b), and (5.47c) are approximately 75%, 5%, and 20%, respectively. Above the stratopause, it is also necessary to introduce the photolysis of CH_4, particularly by the Lyman α line of the Sun:

$$(J_{CH_4}); \qquad CH_4 + h\nu \rightarrow CH_3 + H \tag{5.49a}$$

$$\rightarrow CH_2 + H_2 \qquad (5.49b)$$

$$\rightarrow CH_2 + H + H \qquad (5.49c)$$

$$\rightarrow CH + H_2 + H \qquad (5.49d)$$

The quantum efficiencies for these different channels vary with wavelength. The values quoted in Chapter 4 (see also Brownsword *et al.*, 1997) for Lyman α excitation need to be confirmed. CH_2 produced by two of these channels reacts rapidly with O_2 to form $CH_2O + O$, $HCO + OH$, $CO + H_2O$ and $CO_2 + H_2$ (or $H + H$). The photolysis of methane produces atomic and molecular hydrogen. However, since the amount of methane in the upper part of the middle atmosphere is small, CH_4 photolysis can generally be neglected in the global atmospheric methane budget.

Since there is no source of methane in the atmosphere, the vertical distribution of CH_4 results from an equilibrium between its photochemical destruction and transport upward from the surface. The continuity equation can therefore be written:

$$\frac{\partial(CH_4)}{\partial t} + \boldsymbol{\nabla} \cdot \boldsymbol{\phi}_{CH_4} + \left[c_1(O^1D) + c_2(OH) + d_5(Cl) + J_{CH_4}\right](CH_4) = 0 \qquad (5.50)$$

where $c_1 = c_{1a} + c_{1b}$.

Figure 5.14 shows the photochemical lifetime for atmospheric methane as a function of altitude along with the time constants associated with transport by the winds and vertical mixing. Since the stratospheric lifetime of this compound against photochemical destruction is the same order of magnitude as the transport time, it provides an excellent tracer to study transport processes.

After the spectroscopic detection of atmospheric methane by Migeotte (1948), methane has been observed many times and its vertical distribution has been characterized at various latitudes by optical methods, or by cryogenic collection and laboratory analysis (balloons, rockets, space shuttle) (see Ehhalt, 1974; Ehhalt *et al.*, 1974; Ackerman *et al.*, 1977; Bush *et al.*, 1978; Fabian *et al.*, 1979; Gunson *et al.*, 1990; and Figure 5.15). These data show that methane is well mixed in the troposphere with a current mixing ratio of approximately 1.75 ppmv, while above the tropopause its concentration decreases rapidly. Methane has also been measured by the Stratospheric And Mesospheric Sounder (SAMS) on board Nimbus 7, and, more recently, by UARS (HALOE and CLAES instruments), so that the global distribution of atmospheric methane can now be characterized, and used to deduce information about transport processes. Figure 5.16 shows the mixing ratio of methane measured in the stratosphere and mesosphere by the HALOE

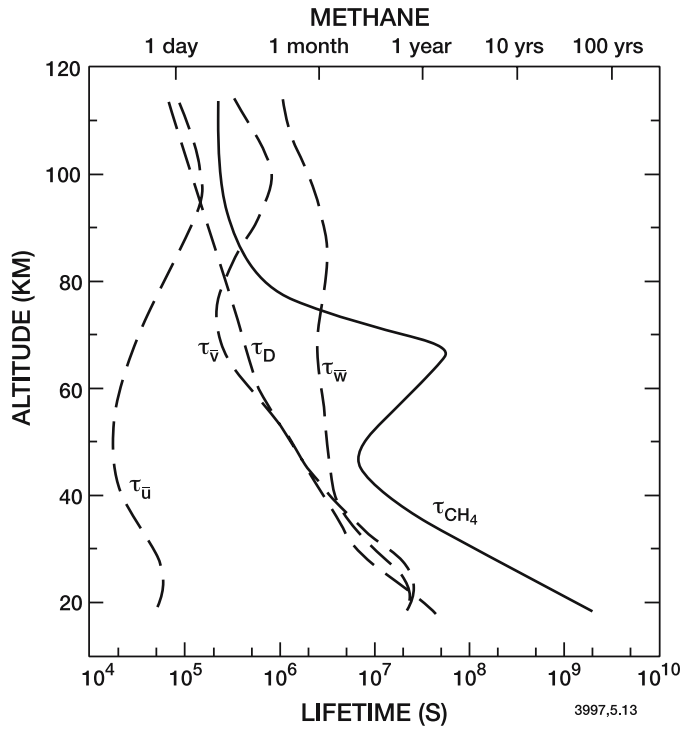

Figure 5.14. Photochemical lifetime of CH_4, and the time constants associated with transport processes.

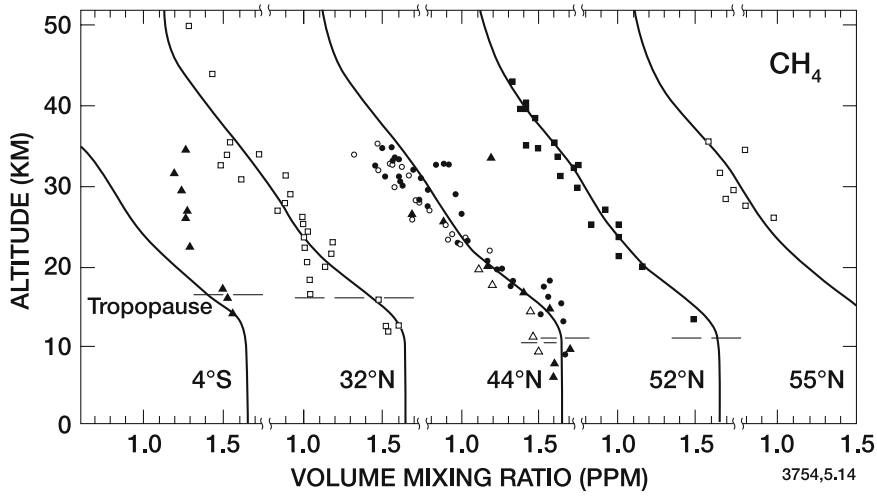

Figure 5.15. Vertical distribution of the methane mixing ratio (ppmv). Observations at various latitudes and one-dimensional model calculations (from Ehhalt and Tonnissen, 1980.)

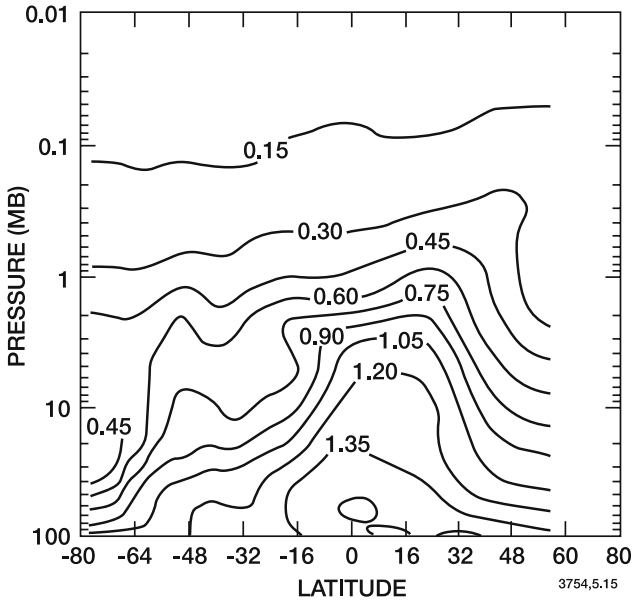

Figure 5.16. Methane mixing ratio (ppmv) measured by HALOE (UARS) during the period 21 September-15 October 1992 and represented as a function of latitude and pressure (Russell *et al.*, 1993).

instrument on board UARS between 21 September and 15 October 1992 (Russell *et al.*, 1993). The high values in the tropical lower and middle stratosphere reflect rapid upward transport from the tropospheric source region in the rising branch of the Hadley cell. The propagation of these high values into the northern hemisphere also indicates the direction of flow (see, *e.g.*, Figure 3.26 and Plate 2).

As we have already noted, CH_4 is not photochemically produced in the atmosphere. Rather, the biosphere and lithosphere provide the natural sources of atmospheric methane. Most of the biological production is attributed to the effects of anaerobic bacteria such as methanobacterium, methanococcus, and methanosarcina. These are primarily found in alkaline regions, of relatively high temperature and enriched in organic materials. Peat bogs, swamps, ponds, rice paddies, and humid tundra produce large amounts of methane. Table 5.3 presents an estimate of the magnitude of these sources, and shows that the most likely natural and anthropogenic sources of methane represent 155 Tg/yr and 360 Tg/yr, respectively. A large fraction of the anthropogenic sources is associated with agricultural processes (cattle, rice cultivation, biomass burning in the tropics) and waste management.

Human production of methane is also associated with industrial and mining activities. Comparison of the methane isotopic ratio ($^{13}C/^{12}C$,

Table 5.3 Global Budget for Methane (Tg/year)[1]

Sources	Range	Likely
Natural		
Wetlands		
Tropics	30-80	60
Northern Latitudes	20-60	40
Others	5-10	10
Termites	10-50	20
Oceans	5-50	10
Freshwater	1-25	5
Others	8-13	10
Total Natural		155
Anthropogenic		
Fossil Fuel Related		100
Coal Mines	15-45	
Natural Gas	25-50	
Petroleum Industry	5-30	
Coal Combustion	7-30	
Waste Management System		
Landfills	20-70	30
Animal Waste	20-30	25
Domestic Sewage Treatment	?	25
Enteric Fermentation	65-100	80
Biomass Burning	20-80	40
Rice Paddies	20-100	60
Total Anthropogenic		360
Total Source		515
Sinks		
Reaction with OH	330-560	445
Removal in Stratosphere	25-55	40
Removal by Soils	15-45	30
Atmospheric Increase	30-40	37
Total Sink		552

[1] 1 Tg = 10^{12} g Source: WMO (1995)

lifetime is given by:

$$\frac{4900 \text{ Tg}}{600 \text{ Tg produced per year}} \approx 8 \text{ years} \tag{5.51}$$

$^{14}C/^{12}C$, and D/H) observed in the atmosphere versus that in organic matter can be used to estimate the magnitude of these non-biological sources (see *e.g.*, Quay *et al.*, 1991; 1999; Lassey *et al.*, 1993; Lowe *et al.*, 1994). Such studies indicate that this latter source must represent about 20 percent of the total production of methane, *i.e.*, between 65 and 170 Tg/yr. Measurement of the isotopic abundance must, however, be considered an upper limit due to the possibility of sample contamination. A more detailed analysis of the methane budget is given, for example, by Crutzen (1983), Crutzen and Gidel (1983), Cicerone and Oremland (1988), and IPCC (1990). IPCC (2001) reports that 60% of the emissions are related to human activities including agriculture, fossil fuel use, and waste disposal. See also the model synthesis of the global methane cycle by Fung *et al.* (1991) and the inverse modeling studies of Hein *et al.* (1997) and Houweling *et al.* (1999).

One may conclude that approximately 600 Tg of methane are produced each year. Since the total atmospheric burden of methane is about 4900 Tg (corresponding to a mean tropospheric mixing ratio of about 1.75 ppmv), a global atmospheric lifetime of 8 years can be derived.

Analyses of air bubbles trapped inside ice cores extracted from Antarctica and Greenland suggest that the concentration of methane has more than doubled over the last 200 years (Etheridge *et al.*, 1998), with a corresponding radiative effect representing a forcing of 0.5 Wm^{-2} (about 20% of the direct radiative forcing due to greenhouse gases since the pre-industrial era; see IPCC, 2001). The growth rate has fluctuated as a function of time: It was as high as 1%/yr in the late 1970s and seems to have declined to 0.5-0.75%/yr in the late 1980s, and to even lower values in the 1990s. The cause of the fluctuations (inter-annual variability) in the methane trends is not entirely clear, but recent changes in the emissions from natural gas (Dlugokencky *et al.*, 1994; 1998) and from tropical biomass burning (Lowe *et al.*, 1994) may have contributed. A positive anomaly in growth rate observed after the eruption of Mt. Pinatubo in 1991 has been attributed to short-term decreases in solar UV radiation and related decrease in OH formation rates in the troposphere (Dlugokencky *et al.*, 1996). Variability in wetland emission rates and fire recurrence associated with climatic anomalies could be additional factors.

5.3.2 Methane Oxidation Chemistry

The oxidation of methane produces a methyl CH_3 radical, which reacts rapidly with molecular oxygen:

$$(c_4); \qquad CH_3 + O_2 + M \rightarrow CH_3O_2 + M \tag{5.52}$$

to produce the methyl peroxy radical. This species can be destroyed by reaction with NO, with itself, with ClO, or with HO_2. The first three processes lead to the formation of the methoxy radical (CH_3O):

$$(c_5); \qquad CH_3O_2 + NO \rightarrow CH_3O + NO_2 \tag{5.53}$$

$$(c_{14b}); \qquad CH_3O_2 + CH_3O_2 \rightarrow 2CH_3O + O_2 \tag{5.54a}$$

$$(c_6); \qquad CH_3O_2 + ClO \rightarrow CH_3O + ClOO \tag{5.55}$$

The $CH_3O_2 + CH_3O_2$ reaction, however, is characterized by several pathways: The major channel (with 55-60% probability at 298 K) leads to the formation of formaldehyde and methanol (CH_3OH)

$$(c_{14a}); \qquad CH_3O_2 + CH_3O_2 \rightarrow CH_2O + CH_3OH + O_2 \ . \tag{5.54b}$$

Methanol is further converted to formaldehyde by

$$(c_{16}); \qquad CH_3OH + OH \rightarrow CH_2O + HO_2 + H_2O \ . \tag{5.56}$$

If Reaction (5.53) is followed by NO_2 photolysis, $NO_2 + h\nu \rightarrow NO + O$, then the net effect is to produce odd oxygen. This reaction is an important source of ozone in the lower stratosphere and upper troposphere (see Crutzen, 1971). Methoxy is in turn destroyed by reaction with molecular oxygen:

$$(c_{15}); \qquad CH_3O + O_2 \rightarrow CH_2O + HO_2 \tag{5.57}$$

to produce formaldehyde.

Reaction

$$(c_7); \qquad CH_3O_2 + HO_2 \rightarrow CH_3OOH + O_2 \tag{5.58}$$

produces methyl peroxide, which either reacts rapidly with OH to reform the methyl peroxy radical

$$(c_{17a}); \qquad CH_3OOH + OH \rightarrow CH_3O_2 + H_2O \ (70\%) \tag{5.59a}$$

or to produce formaldehyde

$$(c_{17b}); \qquad CH_3OOH + OH \rightarrow CH_2O + OH + H_2O \ (30\%) \tag{5.59b}$$

CH_3OOH can also be photolyzed, producing a methoxy and hydroxyl radical

$$(J_{CH_3OOH}); \qquad CH_3OOH + h\nu \rightarrow CH_3O + OH \ , \tag{5.60}$$

and can precipitate in raindrops or aerosols. The primary loss process of CH_3OOH in the stratosphere is, however, the reaction with OH (5.59).

Regardless of the chemical path taken (with the exception of the precipitation process in the troposphere), the carbon atom of the methane molecule must eventually end up as formaldehyde. It should

be noted that the formation of CH_2O also can be accomplished directly via (5.47b). In the mesosphere and lower thermosphere, reaction with atomic oxygen can also play a role:

$$(c_3); \qquad CH_3 + O \rightarrow CH_2O + H \tag{5.61}$$

Formaldehyde was first observed in the stratosphere using infrared absorption (see *e.g.*, Barbe *et al.*, 1979). During daytime, the calculated CH_2O profile results from an equilibrium between the production mechanisms just described and destruction by OH

$$(c_8); \qquad CH_2O + OH \rightarrow CHO + H_2O \tag{5.62}$$

by atomic oxygen

$$(c_9); \qquad CH_2O + O \rightarrow CHO + OH \tag{5.63}$$

by chlorine atoms

$$(d_{10}); \qquad CH_2O + Cl \rightarrow CHO + HCl \tag{5.64}$$

and by photolysis. Photodissociation of CH_2O occurs via two distinct pathways which lead either to the formation of the reactive CHO and H radicals

$$(J_{H-CHO}); \qquad CH_2O + h\nu \rightarrow CHO + H \tag{5.65a}$$

or to the longer-lived species, CO and molecular hydrogen:

$$(J_{H_2-CO}); \qquad CH_2O + h\nu \rightarrow CO + H_2 \tag{5.65b}$$

The CHO radical has a very short lifetime because it is rapidly converted to CO either by photolysis

$$(J_{CHO}); \qquad CHO + h\nu \rightarrow CO + H \tag{5.66}$$

or by reaction with O_2

$$(c_{12}); \qquad CHO + O_2 \rightarrow CO + HO_2 \tag{5.67}$$

Figure 5.17 schematically illustrates the presently understood reaction sequence for carbon compounds in the middle atmosphere. We may now write the continuity equations for the carbon-containing reactive intermediates, which are all sufficiently short-lived that transport may be neglected. Thus,

$$\begin{aligned} \frac{d(CH_3)}{dt} &+ [c_3(O) + c_4(O_2)(M)]\,(CH_3) \\ &= \left[c_{1a}(O^1D) + c_2(OH) + d_5(Cl)\right](CH_4) \end{aligned} \tag{5.68}$$

$$\begin{aligned} \frac{d(CH_3O_2)}{dt} &+ [c_5(NO) + c_7(HO_2) + 2(c_{14a} + c_{14b})(CH_3O_2) \\ &+ c_6(ClO)]\,(CH_3O_2) \\ &= c_4(O_2)(M)(CH_3) + c_{17a}(CH_3OOH)(OH) \end{aligned} \tag{5.69}$$

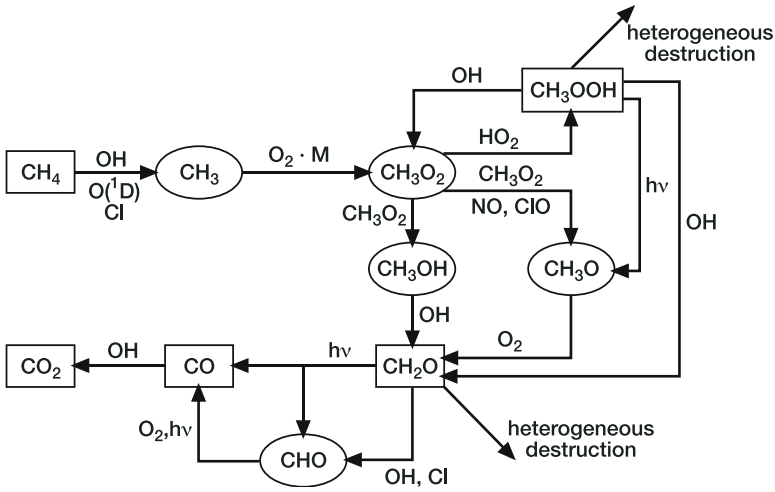

Figure 5.17. Schematic diagram of the methane oxidation scheme in the middle atmosphere.

$$\frac{\mathrm{d(CH_3O)}}{\mathrm{dt}} + \mathrm{c_{15}(O_2)(CH_3O)} = [\mathrm{c_5(NO)} + 2\mathrm{c_{14b}(CH_3O_2)} + \mathrm{c_6(ClO)}]\,(\mathrm{CH_3O_2}) + \mathrm{J_{CH_3OOH}(CH_3OOH)} \tag{5.70}$$

$$\frac{d(\mathrm{CH_3OOH})}{dt} + [\mathrm{J_{CH_3OOH}} + (\mathrm{c_{17a}} + \mathrm{c_{17b}})(\mathrm{OH})]\,(\mathrm{CH_3OOH}) = \mathrm{c_7(CH_3O_2)(HO_2)} \tag{5.71}$$

$$\frac{\mathrm{d(CH_3OH)}}{\mathrm{dt}} + \mathrm{c_{16}(OH)(CH_3OH)} = \mathrm{c_{14a}(CH_3O_2)^2} \tag{5.72}$$

$$\frac{\mathrm{d(CH_2O)}}{\mathrm{dt}} + [\mathrm{c_8(OH)} + \mathrm{c_9(O)} + \mathrm{J_{H-HCO}} + \mathrm{J_{H_2-CO}} + \mathrm{d_{10}(Cl)} + \mathrm{c_{10}(NO_3)}]\,(\mathrm{CH_2O}) = c_{1b}(\mathrm{O^1D})(\mathrm{CH_4}) + \mathrm{c_3(O)(CH_3)} + \mathrm{c_{15}(O_2)(CH_3O)} + \mathrm{c_{14a}(CH_3O_2)^2} + \mathrm{c_{16}(OH)(CH_3OH)} + \mathrm{c_{17b}(OH)(CH_3OOH)} \tag{5.73}$$

$$\frac{\mathrm{d(CHO)}}{\mathrm{dt}} + [\mathrm{J_{CHO}} + \mathrm{c_{12}(O_2)}]\,(\mathrm{CHO}) = [\mathrm{J_{H-HCO}} + \mathrm{c_8(OH)} + \mathrm{c_9(O)} + \mathrm{d_{10}(Cl)} + \mathrm{c_{10}(NO_3)}]\,(\mathrm{CH_2O}) \tag{5.74}$$

Assuming photochemical equilibrium for each species, the daytime concentration of formaldehyde can be approximately estimated from

$$(CH_2O) = \frac{\left[c_1(O\,^1D) + c_2(OH) + d_5(Cl)\right](CH_4)}{J_{H-HCO} + J_{H_2-CO} + c_8(OH) + c_9(O)} \tag{5.75}$$

It should be noted that the methane oxidation chain also results in the production and destruction of the hydrogen compounds H, OH and HO_2:

$$\begin{aligned} &\frac{d(H)}{dt} + \frac{d(OH)}{dt} + \frac{d(HO_2)}{dt} \\ &\quad + \left[c_2(CH_4) + c_8(CH_2O) + c_{17a}(CH_3OOH)\right](OH) \\ &\quad + c_7(CH_3O_2)(HO_2) = (CH_2O)\left[(J_{H-HCO} + c_9(O)\right] \\ &\quad + (HCO)\left[J_{HCO} + c_{12}(O_2)\right] + (CH_3OOH)J_{CH_3OOH} \\ &\quad + c_{1a}(O^1D)(CH_4) + c_{15}(O_2)(CH_3O) + c_3(O)(CH_3) \end{aligned} \tag{5.76}$$

5.3.3 Some End Products of Methane Oxidation: Carbon Monoxide and Carbon Dioxide

The relative efficiency of the two paths of formaldehyde photolysis (Reactions (5.65a) and (5.65b)) is an important parameter because it determines the fraction of methane which ultimately produces molecular hydrogen. Reactions (5.62), (5.63) and (5.64), on the other hand, produce CHO, which in turn yields hydrogen containing radicals through reactions (5.66) and (5.67). As we will see in Section 5.4, these hydrogen radicals recombine to produce water vapor. Therefore, the destruction of methane by this long chain eventually produces water vapor and molecular hydrogen in the stratosphere and mesosphere, such that the sum of the hydrogen mixing ratios

$$4X_{CH_4} + 2X_{H_2O} + 2X_{H_2O}$$

is approximately constant with altitude (neglecting other much less abundant hydrogen species such as OH and H). The increase with height in water vapor abundance observed in the stratosphere (see below) can be qualitatively explained by this mechanism. Each oxidized methane molecule also produces *carbon monoxide* (CO). Noting that the photolysis of CO_2

$$(J_{CO_2}); \qquad CO_2 + h\nu \rightarrow CO + O \tag{5.77}$$

also plays a key role in CO production in the upper mesosphere and in the thermosphere, one may write the production rate for CO in the

middle atmosphere:

$$P_{CO} = \left[c_1(O^1D) + c_2(OH) + d_5(Cl)\right](CH_4) + J_{CO_2}(CO_2) \qquad (5.78)$$

On the global scale, taking into account stratospheric as well as tropospheric processes, the oxidation of methane by the chemical processes just described leads to an annual production of CO of about 400-800 Tg. The contribution of the oxidation of nonmethane hydrocarbons, mostly in the troposphere, is similar in magnitude (200-600 Tg CO/yr). These sources depend directly on the mean value of the OH radical density and constitute about 50 percent of the total CO production. Surface emissions of CO by combustion of gasoline and natural gas represent an injection of about 300-650 Tg/yr through combustion (IPCC, 1996; 2001), with a distribution (more than 90% in the northern hemisphere) that depends on the location of anthropogenic sources. These emissions are comprised of automobile and industrial effluents and are localized in industrial areas. Thus, the direct anthropogenic production of CO is globally of the same order of magnitude as the production via hydrocarbon oxidation. It is, therefore, not surprising that the observed abundance of CO varies greatly with latitude, especially in the troposphere. Observations made at the surface (see *e.g.*, Novelli *et al.*, 1998) show that the mole fraction of carbon monoxide in the "remote" locations typically increases from 50±15 ppbv in the southern polar regions to 140±70 ppbv in the northern hemisphere at high latitudes. The quoted variations around the mean values reflect the seasonal variations. Thus, in the marine boundary layer, the mole fraction of CO reaches a maximum of 200-210 ppbv in the northern winter and a minimum of 35-45 ppbv in the southern summer. In regions affected by urban and industrial pollution, concentrations reach higher values. Tropospheric carbon monoxide has also been observed from space (*e.g.*, from the Space Shuttle, see Reichle *et al.*, 1990, and by the MOPITT instrument on board the EOS/Terra satellite).

Other sources of CO which contribute substantially to the global budget include: domestic combustion of wood for heat, agricultural operations and savanna burning, principally in tropical zones, as well as forest fires and plant respiration (see, Seiler and Crutzen, 1980). CO sources were discussed by Seiler and Conrad (1987), Khalil and Rasmussen (1990), and Crutzen and Zimmermann (1991). A budget based on these estimates is shown in Table 5.4. CO sources have also been derived using model inversion techniques (Manning *et al.*, 1997; Bergamasschi *et al.*, 2000; Pétron *et al.*, 2002). In spite of the uncertainties in the budget figures, it seems likely that the total emissions of CO are between 1250 and 3000 Tg/yr with as much as 2/3 being produced from anthropogenic activities, mainly through

Table 5.4 Global Budget of Carbon Monoxide (Tg CO/yr^{-1}) (Adapted from WMO, 1999)

Sources	Magnitude
Biomass burning	300 – 700
Fossil fuel burning	300 – 500
Methane oxidation	400 – 800
Non-methane oxidation	200 – 600
Vegetation	20 – 200
Oceans	10 – 200
TOTAL	(1230 – 3000)
Sinks	Magnitude
Chemical loss by OH	1400 – 3000
Uptake by soil	100 – 600
Removal in the stratosphere	∼100
TOTAL	1600 – 3700

combustion processes. This explains why northern hemispheric data (see, for example, the data recorded at the Jungfraujoch, Switzerland in 1950-1951 and in the late 1980s; Zander *et al.*, 1989) show a positive trend of 0.9 percent/yr on the average, while no long-term change has been reported in the southern hemisphere. Novelli *et al.* (1998) have deduced from the measurements performed using a distributed air sampling network that the globally averaged CO mixing ratio at the surface over the period 1990-1995 decreased by aproximately 2 ppb/yr.

Carbon monoxide released at the surface is mostly destroyed in the troposphere, but some of the molecules penetrate to the stratosphere. The only important destruction process is provided by reaction with OH:

$$(c_{20} = a_{36}); \qquad CO + OH \rightarrow CO_2 + H \tag{5.79}$$

and the continuity equation for CO in the middle atmosphere may be written:

$$\frac{\partial(CO)}{\partial t} + \boldsymbol{\nabla} \cdot \boldsymbol{\phi}_{CO} + c_{20}(OH)(CO) = P_{CO} \tag{5.80}$$

where P_{CO} is given by expression (5.78).

Figure 5.18 presents the vertical profile of the photochemical lifetime of CO, as well as the time scales for transport. Because of its long

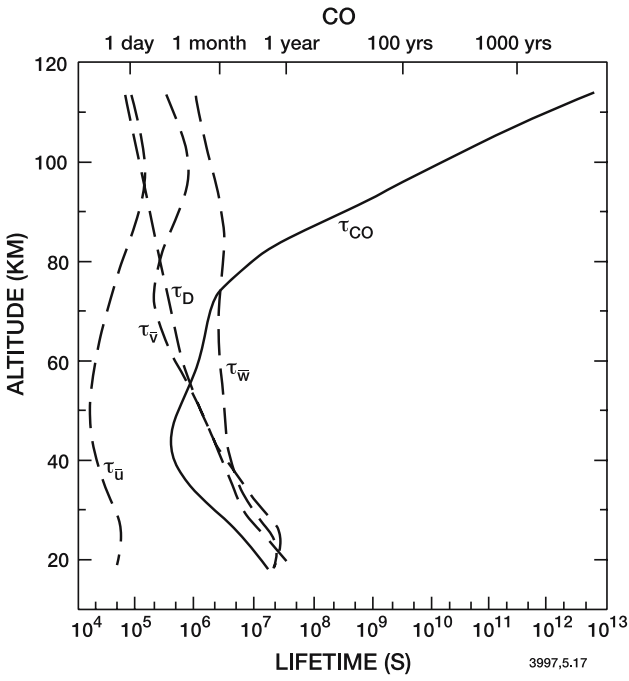

Figure 5.18. Photochemical lifetime of carbon monoxide, and the time constants for transport processes.

chemical lifetime, the distribution of CO is expected to depend strongly on meridional and vertical transport throughout the middle atmosphere. Figure 5.19 shows a number of observations of the vertical distribution of CO in the stratosphere and troposphere. The stratospheric abundances are low and a rapid decrease in mixing ratio is typically observed above the tropopause. This sharp gradient suggests that transport from the troposphere to the stratosphere is limited at middle and high latitudes, as discussed previously (see Chapter 3). The observations display an increase with altitude in the upper stratosphere, as predicted by models. CO profiles have also been measured in the mesosphere, particularly by ground-based microwave methods (*e.g.*, Clancy *et al.*, 1982; Forkman *et al.*, 2003) and from space by the Improved Stratospheric and Mesospheric Sounder (ISAMS) on board UARS (Figure 5.20) and by the Swedish satellite ODIN. Its usefulness as a tracer for mesospheric transport was examined, for example, by Hays and Olivero (1970), and by Allen *et al.* (1981).

Carbon dioxide is another end product of the long chemical methane oxidation chain. The mixing ratio of CO_2 is almost constant with altitude in the homosphere (typically 370 ppmv in year 2000), but

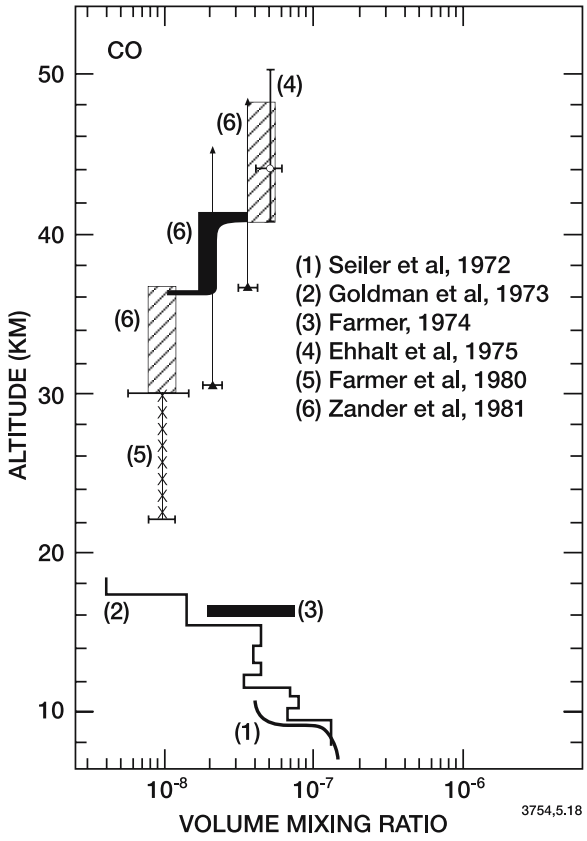

Figure 5.19. Vertical distribution of the CO mixing ratio observed in the stratosphere. (From Zander *et al.*, 1981.)

decreases with height in the upper mesophere and lower thermosphere where it is photolyzed by shortwave ultraviolet radiation. This latter process provides a major source of CO at high altitudes (see *e.g.*, Lopez-Puertas *et al.*, 2000) Downward transport of CO from the thermosphere to the upper stratosphere in the wintertime polar night region (where CO destruction is insignificant) is evident in the ISAMS and the ODIN measurements (see Figure 5.20). In the troposphere, CO_2 exhibits a weak seasonal variation due mainly to biological processes at the surface.

Other carbon containing species, although present in very small amounts, can also provide important information regarding the photochemistry and dynamics of the middle atmosphere. These species will not be presented here in detail, but we note, for example, that measurements of lower stratospheric *ethane* C_2H_6 and *propane* C_3H_8 have been used to deduce atomic chlorine densities there (Rudolph

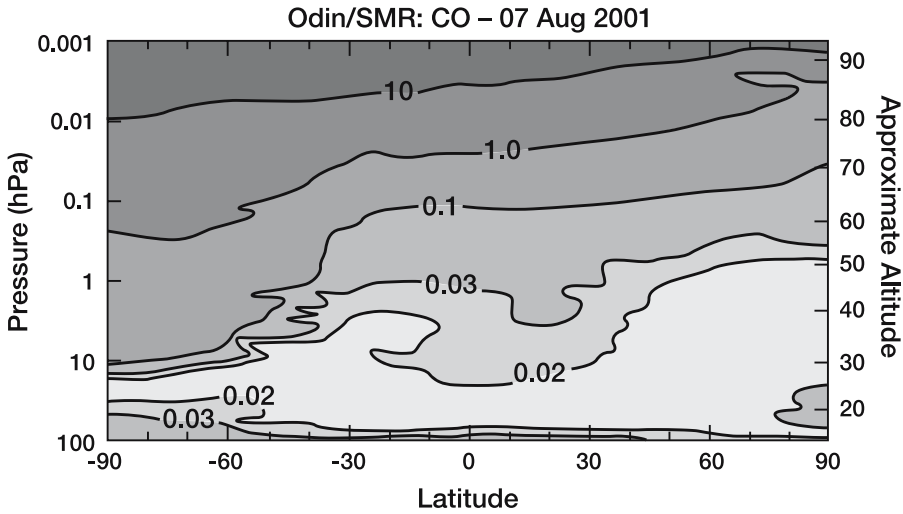

Figure 5.20. Distribution of the zonal mean carbon monoxide mixing ratio (expressed in ppmv) in the stratosphere and mesosphere represented as a function of latitude and atmospheric pressure (or approximate altitude), as measured on 7 August 2001 by the Sub-Millimetre Radiometer on board the Odin satellite. Note the downward transport of CO at high latitudes in the winter hemisphere. From Duprey *et al.*, 2004.

et al., 1981). Ehhalt *et al.*, (1991) have reported a secular trend of 0.9 ± 0.3 percent per year in the tropospheric concentration of ethane over the northern hemisphere, probably in response to anthropogenic activities and biomass burning. Short-lived hydrocarbons, (*e.g.*, isoprene and terpenes released in the atmosphere by vegetation), whose local concentrations may reach 10 ppbv near their sources at the surface, are destroyed before they can reach the stratosphere.

5.4 Hydrogen Compounds

The presence in the middle atmosphere of fast-reacting radicals such as H, OH, and HO_2 (collectively called *odd hydrogen* or HO_x) results from the transport of water vapor (H_2O), methane (CH_4) and molecular hydrogen (H_2) from the troposphere. These source-gases are oxidized by hydroxyl radicals (OH) or by electronically excited oxygen atoms ($O(^1D)$), or are photolyzed by short-wave ultraviolet radiation as they reach increasingly high altitudes. HO_x radicals are efficient catalysts for destroying odd oxygen (ozone and atomic oxygen), particularly in the mesosphere, and in the lower stratosphere and troposphere.

Their atmospheric abundance results from an equilibrium between very rapid photochemical production and destruction mechanisms. The recombination of OH with HO_2 is a loss of HO_x in the middle atmosphere which leads to the formation of water vapor. The reaction of H with HO_2 in the mesosphere and lower thermosphere also produces water, but in addition, can form molecular hydrogen (H_2) which becomes abundant in this region of the atmosphere. Above 100 km, atomic hydrogen becomes a long-lived species whose relative abundance increases with height. The escape of hydrogen to space is a slow but persistent loss process for hydrogen from the Earth system, and may have played a role in the evolution of the atmosphere over geologic timescales.

The following sections provide more quantitative information about the global budget of hydrogen compounds and about the photochemical processes affecting these species.

5.4.1 Water Vapor and Molecular Hydrogen

The effects of hydrogen compounds on the behavior of other chemical species, particularly that of ozone in the mesosphere, were first examined by Bates and Nicolet (1950), and have been the subject of numerous subsequent studies (Hampson, 1966; Hunt, 1966; Hesstvedt, 1968; Crutzen, 1969; Nicolet, 1971). The high reactivity of the hydrogen free radicals, especially OH, makes these species of particular importance in atmospheric chemistry. The compounds that initiate the hydrogen radical chemistry are methane (for which the budget was discussed in Section 5.3), water vapor, and molecular hydrogen.

Water is quite abundant on planet Earth, but is mostly confined to the surface and the interior (see Table 5.5). The atmosphere contains only a very small fraction of the water in the oceans. Water in the oceans represents, however, a small fraction of the vast number of molecules of H_2O contained in hydrated minerals which compose the solid part of the Earth. Clouds contain only a few percent of the water in the atmosphere, although they cover about half of the surface of the globe, so that most of the water in the atmosphere occurs in the vapor phase.

A continuous source of atmospheric water vapor is provided by evaporation at the ocean surface. For this reason, water vapor is quite abundant at low altitudes. Its ground level mixing ratio is variable, changing from about 10^{-2} in the tropics to about 10^{-4} in the desert. Vertical soundings made since 1945 show that the water vapor content decreases with altitude in the troposphere to reach a minimum mixing ratio of a few ppmv a few kilometers above the tropopause.

Table 5.5 Volume of Water in the Earth System

Location	(10^6km^3)
Oceans	1350
Glaciers and ice caps	29
Ground water	8
Freshwater lakes	0.1
Salt lakes and inland seas	0.1
Soil moisture and seepage	0.07
Atmosphere	0.013
Rivers and streams	0.001

Brewer (1949) suggested that water vapor reaches the stratosphere in the ascending branch of the Hadley cell in the tropics (see Chapter 3). The stratosphere is very dry (typically a few ppmv of water vapor) because the tropical tropopause is sufficiently cold (190 to 200K) to "freeze dry" the air and precipitate out much of the water. The relatively dry air penetrating the stratosphere is then transported upwards by the Brewer-Dobson circulation (see Chapter 3) and towards polar regions. The zonally averaged distribution of water vapor measured by LIMS on board the Nimbus 7 satellite (1978-1979) shown in Figure 5.21 (Gille and Russell, 1984) suggests that the extremely low water vapor mixing ratios observed in the tropical lower stratosphere are the result of the freeze-drying mechanism, but the detailed transport processes are still subject to debate. For example, cumulonimbus clouds which penetrate the tropopause have been proposed as a primary mechanism for tropospheric-stratospheric exchanges in the tropics, so that water vapor may be supplied to the stratosphere via these convective systems rather than in a slow large-scale upward transport.

The water budget in the tropical troposphere remains poorly understood, expecially at high altitudes in the vicinity of the tropical tropopause layer (TTL). This region, which extends approximately from 12 km to the level of temperature minimum at about 16 km, can be regarded as the transition zone between the tropospheric Hadley and the stratospheric Brewer-Dobson circulations. In the tropics, the mean vertical humidity profile is shaped like a "C" with high values in the boundary layer (moistened by evaporation from the surface) and in the TTL. The humidity in the TTL is determined by ascent of water in generally concentrated, intense, and nearly vertical convective towers, by detrainment from these convective clouds, by large scale subsidience, by export to the extratropics, and by evaporation of ice crystals or water droplets (see *e.g.*, Newell *et al.*, 1997; Pierrehumbert, 1998; Jensen *et al.*, 1999; Gettleman *et al.*, 2000; Zhu *et al.*, 2000; Vömel *et al.*, 2002). Cirrus

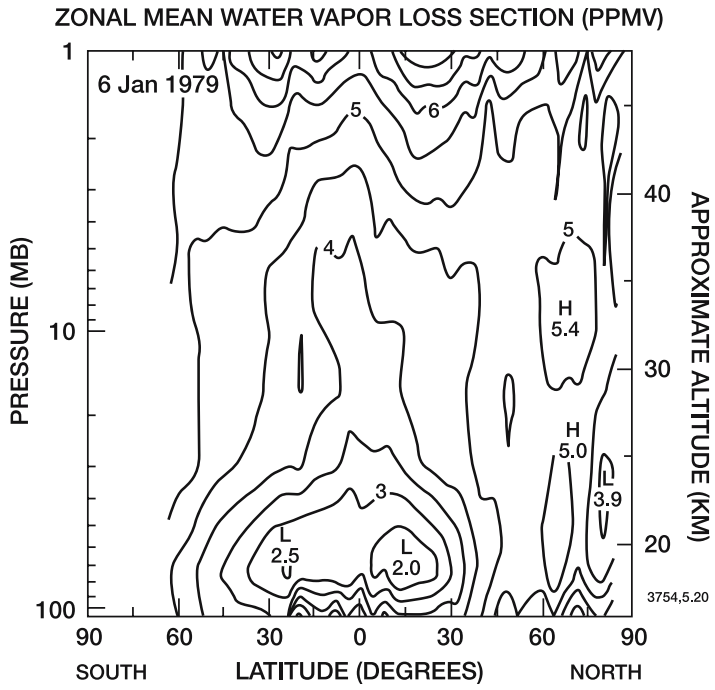

Figure 5.21. Distribution of water vapor observed by the LIMS satellite experiment. From Gille and Russell (1984).

clouds are often present in this layer of the atmosphere. In the absence of ice condensation nuclei, however, supersaturation of air parcels relative to ice is observed (Jensen *et al.*, 1999; Folkins *et al.*, 2002) above the level of zero diabatic heating, where air detrained from convective clouds is transported upward and can penetrate into the stratosphere. Potential long-term changes in the mechanisms (such as convection) that control the humidity of the tropical tropopause layer could have major impacts on the climate system. In the extratropical troposphere, moisture is determined primarily by ascent and descent motions associated with large scale wave motions, although local convection can play a significant role.

In the middle and upper stratosphere, where increasing water vapor mixing ratios are observed, the formation of water vapor results from methane oxidation via the mechanisms discussed in Section 5.3. In the mesosphere, the presence of water vapor leads to the formation of hydrated cluster ions, such as $H^+(H_2O)_n$, which have been commonly observed in the D-region (see Chapter 7). H_2O photolyzes in the thermosphere and upper mesosphere by absorption of shortwave

ultraviolet light (see also Section 4.7.2.4):

$$(\mathrm{J}^{\mathrm{a}}_{\mathrm{H_2O}}); \qquad \mathrm{H_2O} + \mathrm{h}\nu\,(\lambda < 200\ \mathrm{nm}) \rightarrow \mathrm{H} + \mathrm{OH} \qquad (5.81a)$$

$$(\mathrm{J}^{\mathrm{b}}_{\mathrm{H_2O}}); \qquad \mathrm{H_2O} + \mathrm{h}\nu\,(\lambda < 147\ \mathrm{nm}) \rightarrow \mathrm{H_2} + \mathrm{O}(^1\mathrm{D}) \qquad (5.81b)$$

reducing the water vapor mixing ratio and increasing those of the hydrogen free radicals and of molecular hydrogen. Between 175 and 190 nm, the quantum yield for production of OH and H (Reaction 5.81*a*) is equal to 1, while at shorter wavelengths H_2 (Reaction 5.81*b*) is also formed (with a quantum yield of 11% between 105 and 145 nm). In the stratosphere and the lower mesosphere, water vapor reacts with $O(^1D)$:

$$(\mathrm{a}^*_1); \qquad \mathrm{H_2O} + \mathrm{O}(^1\mathrm{D}) \rightarrow 2\mathrm{OH} \qquad (5.82)$$

Upper stratospheric and mesospheric water vapor has been measured by microwave techniques, both from the ground (*e.g.*, Gibbins *et al.*, 1981; Deguchi and Muhleman, 1982; Bevilacqua *et al.*, 1983) and from aircraft (Waters *et al.*, 1980). Measurements by the HALOE instrument on board the Upper Atmosphere Research Satellite (UARS; see Russell *et al.*, 1993; Summers *et al.*, 1997; and Figure 5.22) show that the water vapor mixing ratio in the mesosphere is of the order of 6 ppmv up to 70 km, and that it decreases to values less than 4 ppmv near 75 km. The presence of a local maximum of more than 7.5 ppmv in the tropics detected by the HALOE instrument between 65 and 68 km (Summers *et al.*, 1997) is not understood. If confirmed by independent

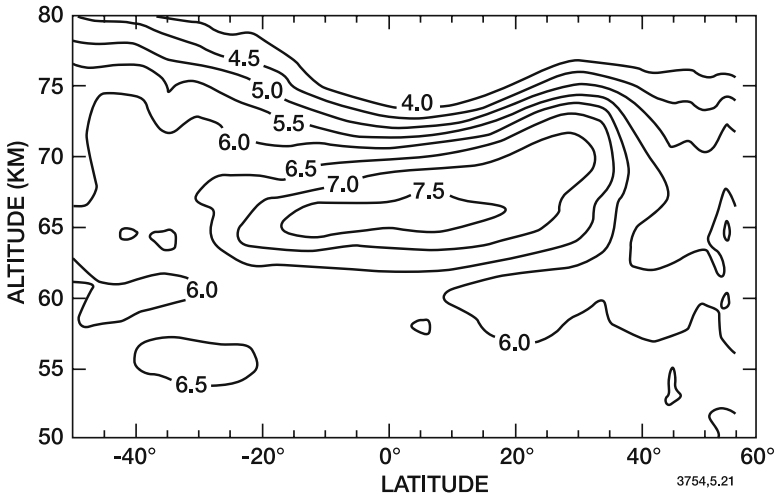

Figure 5.22. Meridional distribution of water vapor (ppmv) measured in the upper stratosphere and mesosphere during October and November 1994 by the HALOE instrument on board the UARS satellite (Summers *et al.*, 1997).

observations, it would imply the existence of a mesospheric source of H_2O, perhaps of extraterrestrial origin. Summers *et al.* (2001) have reported the presence of a narrow layer of enhanced water vapor (10-15 ppmv) in the Arctic summer (82-84 km) coincident with the presence of *noctilucent clouds* (ice particles), suggesting that a high degree of supersaturation is present in this region (see also von Cossart *et al.*, 1999). In the lower thermosphere, the H_2O density has been inferred from ion composition measurements (Arnold and Krankowsky, 1977; Solomon *et al.*, 1982a).

Figure 5.23 shows the photochemical lifetime of water vapor, and the time constants characterizing atmospheric transport. The production of water vapor by methane oxidation is essentially complete by about 50 km. Because the photochemical and vertical transport lifetimes for this gas are comparable above about 50 km, and because there is no known chemical source of water vapor in this region, it provides an excellent tracer for mesospheric transport processes (Allen *et al.*, 1981; Bevilacqua *et al.*, 1983; Le Texier *et al.*, 1988). In addition to

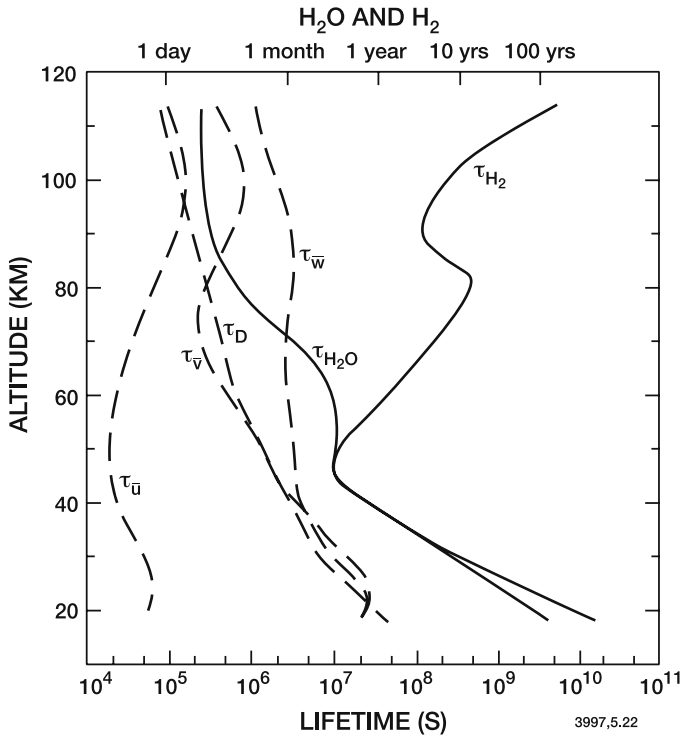

Figure 5.23. Photochemical lifetimes of water vapor and molecular hydrogen, and the time constants for atmospheric transport processes in the middle atmosphere.

its chemical properties, water vapor is radiatively active, and plays an important role in the atmospheric thermal budget through cooling by infrared emission.

Long-term measurements of stratospheric water vapor using a balloon-borne frost point hygrometer have been performed in Boulder, CO (40°N) since 1980 (Oltmans and Hofmann, 1995; Oltmans *et al.*, 2000). A long-term increase in the H_2O concentration, which is larger than expected from the oxidation of increasing concentrations of stratospheric methane, has been reported and may be linked to climate variations, such as a small temperature increase in the troposphere (SPARC, 2000; Rosenlof *et al.*, 2001). Randel *et al.* (2004) showed by analyzing HALOE observations that tropopause temperatures are a primary control for interannual changes in global stratospheric water vapor, but could not detect a long-term trend in H_2O during the 1990s.

Because of its long chemical lifetime in the stratosphere, water vapor should be expected to exhibit variations which are related to atmospheric transport. Early observations, especially those of Kley *et al.* (1979, 1980) suggested that the water vapor profile is highly structured in discrete layers, with a vertical scale of about 1000 m or less (Figure 5.24a). These variations imply a stratified structure in the lower part of the middle atmosphere, and the absence of much vertical mixing in the region of the measurements. The vertical transport of water vapor in the tropical lower stratosphere is characterized by the upward propagation of a succession of wet and dry air masses in response to the seasonal cycle of convective activity in the equatorial troposphere. This so-called "tape-recorder" signal (see Figure 5.24b) has been identified by Mote *et al.* (1996).

Molecular hydrogen (H_2) also provides a source of the free radicals H and OH, because it reacts rapidly with the $O(^1D)$ atom:

$$(a_3^*); \qquad H_2 + O(^1D) \rightarrow H + OH \tag{5.83}$$

The destruction of hydrogen also occurs through the following reactions

$$(a_{19}); \qquad H_2 + OH \rightarrow H_2O + H \tag{5.84}$$

and

$$(a_{24}); \qquad H_2 + O \rightarrow OH + H \tag{5.85}$$

which become significant above 40 km. Mathematical models (see *e.g.*, Hauglustaine *et al.*, 2002) show that these processes lead to a global H_2 loss rate of the order of 15 Tg H_2/yr in the troposphere, and 1 Tg H_2/yr in the stratosphere. In addition to this chemical loss, possible loss of hydrogen at ground level must also be considered, and this is likely to vary with the type of vegetation, temperature, etc. The uptake rate into

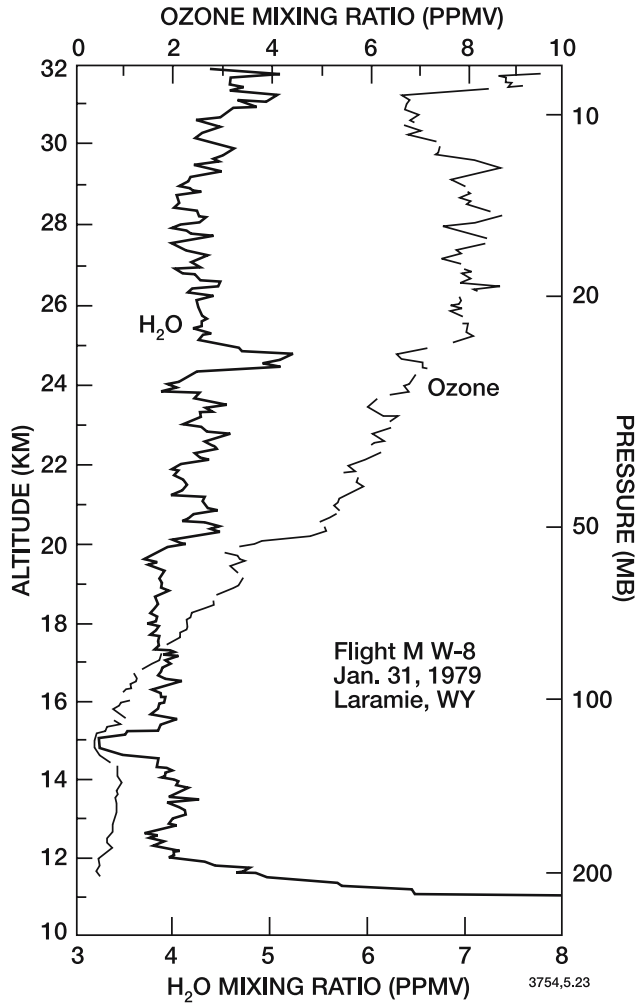

Figure 5.24a. Simultaneous observations of ozone and water vapor by Kley *et al.* (1980).

various soils (see *e.g.*, Ehhalt, 1973; 1999; Novelli *et al.*, 1999) depends primarily on microbial activity in soils, soil texture and soil moisture (Conrad and Seiler, 1985). Estimates of global H_2 uptake range from 40 to 90 Tg H_2/yr.

In the troposphere and in the lower stratosphere, the chemical production of H_2 is due to the photolysis of formaldehyde produced by methane oxidation. About 13 Tg H_2/yr are produced by this mechanism (Schmidt *et al.*, 1980). Oxidation of isoprene and other terpenes in the lower troposphere leads to an additional production of about 10-35 Tg H_2/yr. A precise determination of these quantities requires a

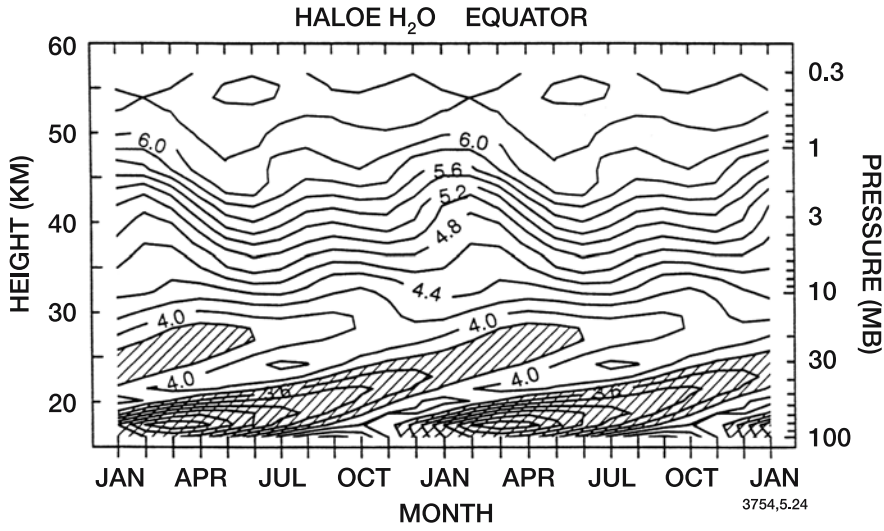

Figure 5.24b. Height-time cross section of the water vapor (ppmv) measured by HALOE during two consecutive years in the equatorial region highlighting the "tape recorder" signal in the annual cycle of H_2O.

better understanding of the spatial distribution of formaldehyde. In the mesosphere, molecular hydrogen can be formed by recombination of the H and HO_2 radicals, which are themselves produced by water vapor photolysis. This mechanism plays a secondary role in the global hydrogen budget, producing large H_2 densities in the mesosphere and lower thermosphere (*e.g.*, Liu and Donahue, 1974).

Formation of H_2 in soils by anaerobic bacteria is possible, but this contribution can be neglected for atmospheric purposes because these hydrogen molecules are rapidly destroyed at ground level by other microorganisms. The oceans are, however, supersaturated in hydrogen, and constitute an important source; this source is more important than that provided by volcanoes. Schmidt *et al.* (1980) estimate that natural ground level production is between 2 and 5 Tg/yr.

Several observations have shown that hydrogen is affected by pollution sources. The hydrogen molecule is an important product of incomplete combustion in several anthropogenic and natural processes. The production of H_2 by industrial combustion and automobiles is estimated to vary from 15 Tg H_2/yr (Novelli *et al.*, 1999) to 25 Tg H_2/yr (Schmidt, 1974). According to Crutzen *et al.* (1979) 9 to 21 Tg H_2/yr are produced by forest and savanna burning, especially for agricultural purposes in tropical regions.

Table 5.6 summarizes the components of the global hydrogen budget. The total amount of hydrogen in the atmosphere is about 200 Tg (170 Tg

Table 5.6 Global Budget of Molecular Hydrogen Based on the estimates of Novelli *et al.* (1999) and Ehhalt (1999)

Production	Tg/yr
Industry and automobile	15
Biomass burning	16
Oceans	3
Nitrogen fixation	3
Photochemical Production	40
Total	77
Loss	Tg/yr
Oxidation by OH	19
Soil uptake	56
Total	75
Mean mixing ratio (ppbv)	530
Burden (Tg H_2)	150
Lifetime (yr)	2-3

in the troposphere and 30 Tg above the tropopause). The global cycling time of hydrogen is of the order of 3±2 years.

Although the atmospheric hydrogen content at ground level was first measured many years ago (Paneth, 1937; Glueckauf and Kitt, 1957), its detection in the stratosphere occurred much later (Ehhalt and Heidt, 1973; Ehhalt *et al.*, 1974; 1975a; Fabian *et al.*, 1979). These observations have mostly been performed by grab sampling, and they have demonstrated that the H_2 mixing ratio is about 0.56 ppmv at the tropopause and in the lower and middle stratosphere. A small decrease in the observed mixing ratio with increasing altitude is indicated by rocket measurements in the upper stratosphere, as shown in Figure 5.25 (Scholz *et al.*, 1970; Ehhalt *et al.*, 1975b). This decrease in mixing ratio is less pronounced at lower latitudes where vertical motion is more intense. Abbas *et al.* (1996a,b) have inferred the vertical profile of H_2 in the upper stratosphere and lower mesosphere based on H_2O and CH_4 mixing ratios observed by the Atmospheric Trace Molecule Spectroscopy (ATMOS) experiment from four Space Shuttle missions. They find a minimum mixing ratio of typically 0.15 ± 0.1 ppmv at 50 km altitude. Model calculations by Le Texier *et al.* (1988) also suggest the existence of a broad minimum in the mid- and upper stratosphere (where

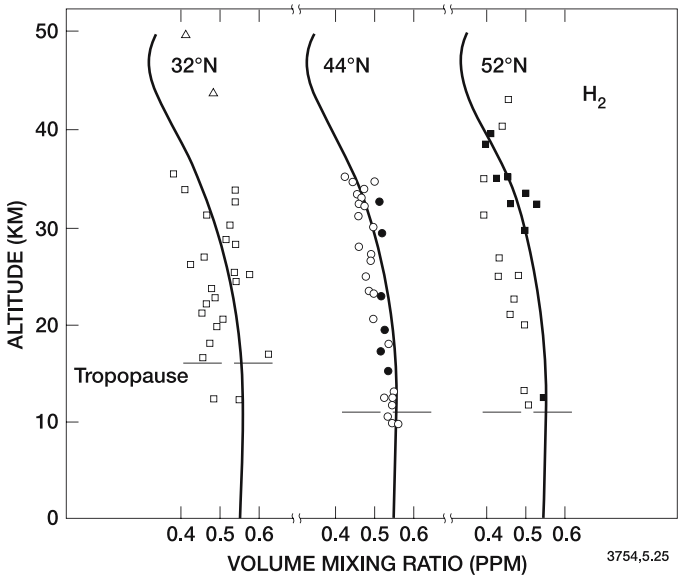

Figure 5.25. Observations of the mixing of molecular hydrogen in the stratosphere, compared to a one-dimensional model. From Ehhalt and Tonnissen (1980).

H_2 oxidation is most rapid) and an increasing mixing ratio at higher altitudes due to the production of H_2 from water vapor photolysis.

5.4.2 Odd Hydrogen Chemistry

The behavior of the hydrogen radicals produced by dissociation of H_2O, H_2 and CH_4 varies strongly with altitude. In the mesosphere and stratosphere, the lifetime of atomic hydrogen is very short because the three body reaction with oxygen rapidly converts H into a hydroperoxy radical, HO_2

$$(a_1); \qquad H + O_2 + M \rightarrow HO_2 + M \tag{5.86}$$

This reaction, however, becomes slow at higher altitudes due to the low air densities found there.

Atomic hydrogen can also react with ozone, and this reaction becomes important in the upper stratosphere and mesosphere:

$$(a_2); \qquad H + O_3 \rightarrow O_2 + OH\dagger(v \leq 9) \tag{5.87}$$

Note that OH formed by this reaction is vibrationally excited (with a vibrational quantum number v less than or equal to 9) and is deactivated either by quenching with air molecules or by photon emission

(Meinel bands observed in the airglow; see Chapter 2). At altitudes above 40 km, the reactions of the OH and HO_2 radicals with atomic oxygen are important:

$$(a_5); \qquad OH + O \rightarrow O_2 + H \tag{5.88}$$

and

$$(a_7); \qquad HO_2 + O \rightarrow O_2 + OH \tag{5.89}$$

On the other hand, in the middle and lower stratosphere and in the troposphere, the reactions of the hydrogen radicals with ozone must be considered:

$$(a_6); \qquad OH + O_3 \rightarrow O_2 + HO_2 \tag{5.90}$$

$$(a_{6b}); \qquad HO_2 + O_3 \rightarrow 2O_2 + OH \tag{5.91}$$

These four reactions provide important loss processes for odd oxygen. Near the tropopause, the OH and HO_2 radicals also react with carbon and nitrogen monoxide:

$$(a_{26}); \qquad HO_2 + NO \rightarrow NO_2 + OH \tag{5.92}$$

$$(c_{20} \equiv a_{36}); \qquad OH + CO \rightarrow CO_2 + H \tag{5.79}$$

In the mesosphere, atomic hydrogen becomes quite abundant and the following reactions (note that molecular hydrogen can be produced) become important:

$$(a_{23a}); \qquad H + HO_2 \rightarrow OH + OH \quad (90 \pm 4\%) \tag{5.93a}$$

$$(a_{23b}); \qquad H + HO_2 \rightarrow H_2 + O_2 \quad (8 \pm 4\%) \tag{5.93b}$$

$$(a_{23c}); \qquad H + HO_2 \rightarrow H_2O + O \quad (2 \pm 2\%) \tag{5.93c}$$

The branching ratios reported here are from the laboratory study of Keyser (1986).

Hydrogen peroxide also plays an important role in oxygen-hydrogen chemistry. It is produced by the HO_2 "self-reaction":

$$(a_{27}); \qquad HO_2 + HO_2 \rightarrow H_2O_2 + O_2 \tag{5.94}$$

which has been shown to have a pressure-independent bimolecular component and a pressure-dependent termolecular component. In the presence of water vapor (*e.g.*, in the troposphere), the rate constant of this reaction varies with the abundance of H_2O (Lii *et al.*, 1981; Kircher and Sander, 1984). H_2O_2 is also formed by the three-body reaction

$$(a_{83}); \qquad OH + OH + M \rightarrow H_2O_2 + M. \tag{5.95}$$

It is destroyed during the day through photolysis:

$$(J_{H_2O_2}); \qquad H_2O_2 + h\nu \rightarrow 2OH \tag{5.96}$$

and to a lesser extent, by reaction with OH:

$$(a_{30}); \qquad H_2O_2 + OH \rightarrow H_2O + HO_2 \tag{5.97}$$

and with atomic oxygen

$$(a_{81}); \qquad H_2O_2 + O \rightarrow OH + HO_2 \tag{5.98}$$

It should be noted that OH is also destroyed by reaction with HO_2:

$$(a_{17}); \qquad OH + HO_2 \rightarrow H_2O + O_2 \tag{5.99}$$

which is faster than the reaction

$$(a_{16}); \qquad OH + OH \rightarrow H_2O + O \tag{5.100}$$

In the lower stratosphere, the presence of large amounts of HNO_3, HO_2NO_2, H_2O_2, and HCl lead to an additional destruction of hydroxyl radical (and odd hydrogen):

$$(b_{27}); \qquad OH + HNO_3 \rightarrow H_2O + NO_3 \tag{5.101}$$

$$(b_{28}); \quad OH + HO_2NO_2 \rightarrow H_2O + O_2 + NO_2 \tag{5.102}$$

$$(a_{30}); \qquad OH + H_2O_2 \rightarrow H_2O + HO_2 \tag{5.103}$$

$$(d_{11}); \qquad OH + HCl \rightarrow H_2O + Cl \tag{5.104}$$

The effect of these reactions is important below about 25 km.

Figures 5.26a and 5.26b present schematic representations of the most important reactions in hydrogen chemistry for the lower and upper portions of the middle atmosphere, respectively. Retaining the most important of these reactions, we may write the continuity equations for the long-lived oxygen-hydrogen species:

$$\begin{aligned} &\frac{\partial(H_2O)}{\partial t} + \boldsymbol{\nabla} \cdot \boldsymbol{\phi}(H_2O) + \left[J_{H_2O} + a_1^*(O^1D)\right](H_2O) \\ &\qquad = a_{16}(OH)^2 + a_{17}(OH)(HO_2) + a_{19}(OH)(H_2) + a_{23c}(H)(HO_2) \end{aligned} \tag{5.105}$$

$$\begin{aligned} &\frac{\partial(H_2)}{\partial t} + \boldsymbol{\nabla} \cdot \boldsymbol{\phi}(H_2) + \left[a_3^*(O^1D) + a_{19}(OH) + a_{24}(O)\right](H_2) \\ &\qquad = a_{23b}(H)(HO_2) + J^b_{H_2O}(H_2O) \end{aligned} \tag{5.106}$$

where $J_{H_2O} = J^a_{H_2O} + J^b_{H_2O}$. Neglecting the formaldehyde and methyl radical reactions discussed above, as well as Reactions (5.101), (5.102), and (5.104), the equations of H, OH, HO_2, and H_2O_2 can be written:

$$\begin{aligned} &\frac{d(H)}{dt} + [a_1(M)(O_2) + a_2(O_3) + a_{23}(HO_2)](H) \\ &\qquad = a_5(O)(OH) + J^a_{H_2O}(H_2O) + a_3^*(O^1D)(H_2) \\ &\qquad + a_{19}(OH)(H_2) + a_{24}(O)(H_2) + a_{36}(CO)(OH) \end{aligned} \tag{5.107}$$

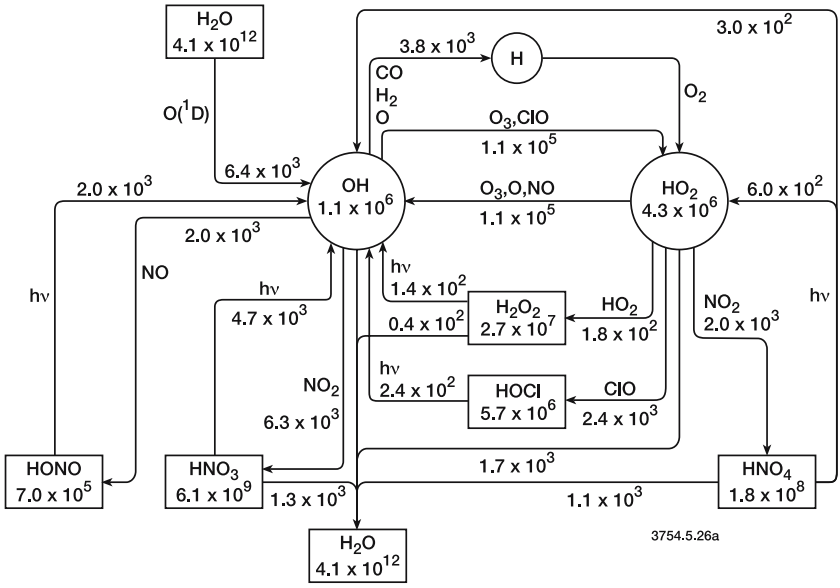

Figure 5.26a. Principal chemical reactions affecting hydrogen compounds in the stratosphere. The numbers in the boxes are concentrations (cm^{-3}) calculated at 25 km altitude (24 h average). The numbers associated with arrows represent fluxes (cm^{-3} s^{-1}) between different compounds. From Zellner (1999).

$$\frac{d(OH)}{dt} + [a_5(O) + a_6(O_3) + 2a_{16}(OH) + a_{17}(HO_2) + a_{19}(H_2) + a_{30}(H_2O_2) + 2a_{83}(M)(OH) + a_{36}(CO)](OH) = J^a_{H_2O}(H_2O) + 2a^*_1(O^1D)(H_2O) + a_2(O_3)(H) + a_{6b}(O_3)(HO_2) + a_7(HO_2)(O) + 2a_{23a}(H)(HO_2) + a_{26}(NO)(HO_2) + 2J_{H_2O_2}(H_2O_2) + a_{81}(O)(H_2O_2) + a_{24}(O)(H_2) + a_{24}(O)(H_2) + a^*_3(O^1D)(H_2) + a^*_2(O^1D)(CH_4) \quad (5.108)$$

$$\frac{d(HO_2)}{dt} + [a_{6b}(O_3) + a_7(O) + a_{23}(H) + a_{26}(NO) + a_{17}(OH) + 2a_{27}(HO_2)](HO_2) = a_1(M)(O_2)(H) + a_6(OH)(O_3) + a_{30}(OH)(H_2O_2) + a_{81}(O)(H_2O_2) \quad (5.109)$$

$$\frac{d(H_2O_2)}{dt} + [J_{H_2O_2} + a_{30}(OH) + a_{81}(O)](H_2O_2) = a_{27}(HO_2)^2 + a_{83}(M)(OH)^2 \quad (5.110)$$

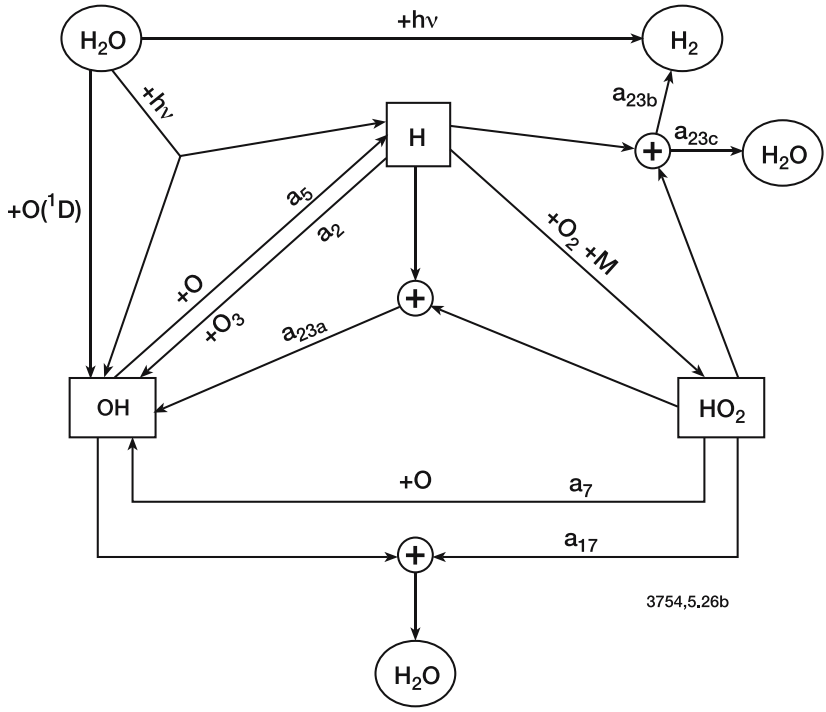

Figure 5.26b. Principal aeronomic reactions of hydrogen compounds in the mesosphere and lower thermosphere.

5.4.3 The Odd Hydrogen Family and Hydrogen Partitioning

Adding together equations (5.107) through (5.109) and introducing a transport term, we obtain an approximate equation for an *odd hydrogen family* defined by $HO_x = H + OH + HO_2$ (neglecting methyl radical and nitrogen reactions):

$$\begin{aligned}\frac{\partial(HO_x)}{\partial t} &+ \nabla \cdot \phi(HO_x) + 2a_{23b+23c}(H)(HO_2) + 2a_{16}(OH)^2 \\ &+ 2a_{17}(OH)(HO_2) + 2a_{27}(HO_2)^2 + 2a_{83}(M)(OH)^2 \\ &= 2J_{H_2O}(H_2O) + 2a_3^*(O^1D)(H_2) + 2a_1^*(O^1D)(H_2O) \\ &+ 2\left[J_{H_2O_2} + a_{81}(O)\right](H_2O_2) + a_2^*(O^1D)(CH_4) \qquad (5.111)\end{aligned}$$

Figure 5.27 presents calculated altitude profiles of the photochemical lifetimes of the HO_x family and its constituent members, as well as H_2O_2, and the time constants for dynamical processes. As in the case of O_x, the lifetime of the family is several orders of magnitude greater than those of

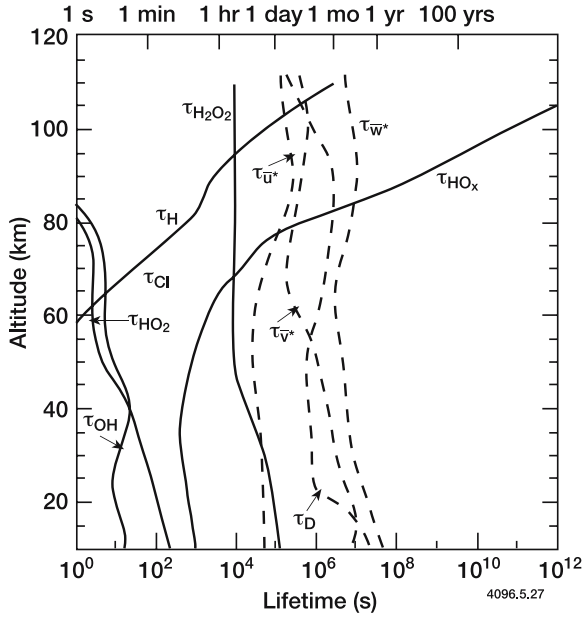

Figure 5.27. Photochemical lifetime of odd hydrogen radicals, as well as the time constants for transport by the zonal and meridional winds, and a one-dimensional diffusive time constant.

some of its members, making the solution of the continuity equation of the HO_x family relatively easy to obtain with simple numerical methods. Even so, the lifetime of the HO_x family is considerably shorter than the transport time scale up to altitudes near 80 km. Therefore, its density will not be directly dependent on transport processes except above this altitude. Throughout the middle atmosphere, the lifetimes of OH and HO_2 are also quite short. Assuming photochemical equilibrium for these species and keeping only the dominant terms in (5.108) and (5.109), one may write:

$$\begin{aligned}[a_5(O) + a_6(O_3) + a_{36}(CO)]\,(OH) \\ \approx a_2(O_3)(H) + a_7(HO_2)(O) + a_{26}(NO)(HO_2)\end{aligned} \quad (5.112)$$

and

$$[a_{6b}(O_3) + a_7(O) + a_{26}(NO)]\,(HO_2) \approx a_1(M)(O_2)(H) + a_6(OH)(O_3) \quad (5.113)$$

The ratio of the concentrations of HO_2 and OH can then be written:

$$\begin{aligned}\frac{(HO_2)}{(OH)} \approx \frac{a_5(O) + a_{36}(CO)}{a_7(O) + a_{26}(NO) + a_{6b}(O_3)} \\ \times \left(\frac{a_1(M)(O_2)}{a_1(M)(O_2) + a_2(O_3)} + \frac{a_6(O_3)}{a_5(O) + a_{36}(CO)}\right)\end{aligned} \quad (5.114)$$

This last expression can be further simplified; in the upper part of the middle atmosphere (z > 40 km), one may assume:

$$\frac{(HO_2)}{(OH)} \approx \frac{a_5}{a_7} \times \frac{a_1(M)(O_2)}{a_1(M)(O_2) + a_2(O_3)} \tag{5.115}$$

In the middle stratosphere, we obtain

$$\frac{(HO_2)}{(OH)} \approx \frac{a_6}{a_{6b}} \tag{5.116}$$

and near the tropopause, it becomes

$$\frac{(HO_2)}{(OH)} \approx \frac{a_{36}(CO) + a_6(O_3)}{a_{26}(NO) + a_{6b}(O_3)} \tag{5.117}$$

In the upper stratosphere and in the mesosphere,

$$(H) \approx \frac{a_5(O)(OH)}{a_1(M)(O_2) + a_2(O_3)} \tag{5.118}$$

so that

$$\frac{(H)}{(OH)} \approx \frac{a_5(O)}{a_1(M)(O_2) + a_2(O_3)} \tag{5.119}$$

These ratios establish the approximate partitioning between members of the HO_x family, as was shown previously for O_x:

$$\frac{(OH)}{(HO_x)} = \frac{1}{\left(1 + \frac{(H)}{(OH)} + \frac{(HO_2)}{(OH)}\right)} \tag{5.120}$$

In the upper stratosphere and in the mesosphere, H_2O_2 is approximately in photochemical equilibrium defined by

$$(H_2O_2) = \frac{a_{27}(HO_2)^2}{J_{H_2O_2} + a_{30}(OH)} \tag{5.121}$$

In the lower stratosphere the H_2O_2 lifetime becomes longer, and the time dependent equation (5.110), must be used with a transport term $\boldsymbol{\nabla} \cdot \boldsymbol{\phi}\,(H_2O_2)$ added. Heterogeneous removal in clouds must also be considered in the troposphere. Figure 5.28 shows calculated vertical distributions of H, OH, HO_2, and H_2O_2 between 10 and 70 km altitude.

In the lower thermosphere, atomic hydrogen becomes the dominant odd hydrogen species. Adding expressions (5.107) through (5.110), assuming $d(OH)/dt = d(HO_2)/dt = d(H_2O_2)/dt = 0$, omitting minor terms and adding a transport term, we find:

$$\frac{\partial(H)}{\partial t} + \boldsymbol{\nabla} \cdot \boldsymbol{\phi}\,(H) + 2(a_{23b} + a_{23c})(HO_2)(H) = 2J_{H_2O}(H_2O) \tag{5.122}$$

Below 75 km, the concentration of H becomes small relative to OH and HO_2, and the addition of equations (5.107), (5.108), and (5.109) leads to the following expression, in which secondary terms are neglected but

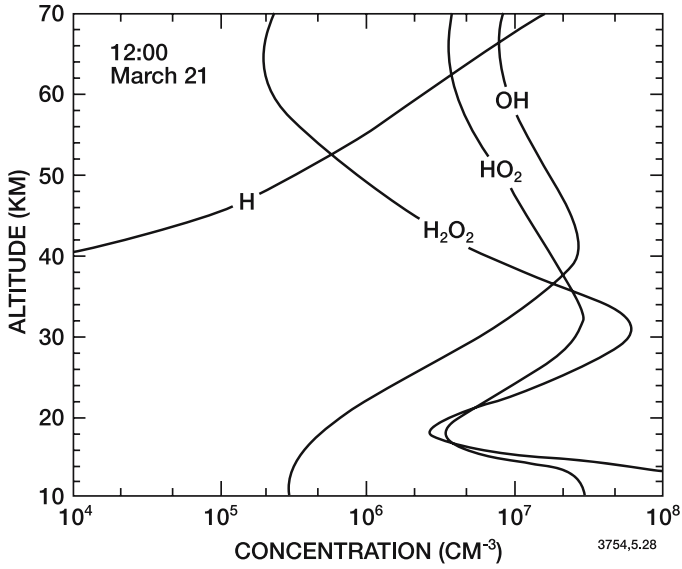

Figure 5.28. Calculated distributions of some hydrogen compounds at mid-latitudes (noon, equinox).

reactions with HNO_3, HO_2, NO_2, and carbon compounds are added:

$$\begin{aligned} 2a_{17}(OH)(HO_2) + 2a_{30}(OH)(H_2O_2) + 2b_{27}(OH)(HNO_3) \\ + 2b_{28}(OH)(HO_2NO_2) + 2c_{17}(CH_3OOH)(OH) \\ = 2J_{H_2O}(H_2O) + 2a_1^*(O\,^1D)(H_2O) \\ + (O\,^1D)(CH_4)\,[2c_{1a}(1+X) + c_{1b}X] \\ + 2c_2X(OH)(CH_4) + 2a_3^*(O\,^1D)(H_2) \end{aligned} \tag{5.123}$$

where X, given by

$$X \simeq \frac{J_{H-HCO} + c_9\,(O)}{J_{H-HCO} + J_{H_2-CO} + c_8(OH) + c_9(O)}$$

is approximately equal to $\frac{1}{2}$. This equation can be simplified in the mesosphere:

$$\begin{aligned} a_{17}(OH)(HO_2) + (a_{23b} + a_{23c})(HO_2)(H) \\ = \left[J_{H_2O} + a_1^*(O\,^1D)\right](H_2O) + a_3^*(O\,^1D)(H_2) \end{aligned} \tag{5.124}$$

and in the stratosphere above 30 km:

$$\begin{aligned} a_{17}(OH)(HO_2) = a_1^*(O\,^1D)(H_2O) + a_3^*(O\,^1D)(H_2) \\ + (1+X)c_{1a}(O\,^1D)(CH_4) + c_2X(OH)(CH_4) \end{aligned} \tag{5.125}$$

while below 30 km,

$$a_{17}(OH)(HO_2) + a_{30}(OH)(H_2O_2) + b_{27}(OH)(HNO_3) + b_{28}(OH)(HO_2NO_2) = (O\,^1D)\,[a_1^*(H_2O) + a_3^*(H_2) + (1 + X)c_{1a}^*(CH_4)] + c_2X(OH)(CH_4) \quad (5.126)$$

5.4.4 Observations of OH and HO_2

OH and HO_2 radicals have been measured in the mesosphere and in the stratosphere by different techniques, including resonance fluorescence, induced fluorescence, as well as remote sensing methods (far-infrared and submillimeterwave) (see, *e.g.*, Anderson, 1971, 1976; Heaps and McGee, 1983; De Zafra *et al.*, 1984; Stimpfle *et al.*, 1990; Wennberg *et al.*, 1990, 1994; Cohen *et al.*, 1994; Park and Carli, 1991; Stachnik *et al.*, 1992; Pickett and Peterson, 1993; 1996; Chance *et al.*, 1996; Jucks *et al.*, 1998). Total column measurements of OH also provide important information about its stratospheric abundance and variability (Burnett and Burnett, 1981; 1982). Figure 5.29 shows the concentration profiles of OH and HO_2 measured by Jucks *et al.* (1998) during mid-morning at 65°N on April 30, 1997, using a balloon-borne Fourier infra-red spectrometer. In the case of OH, the number density

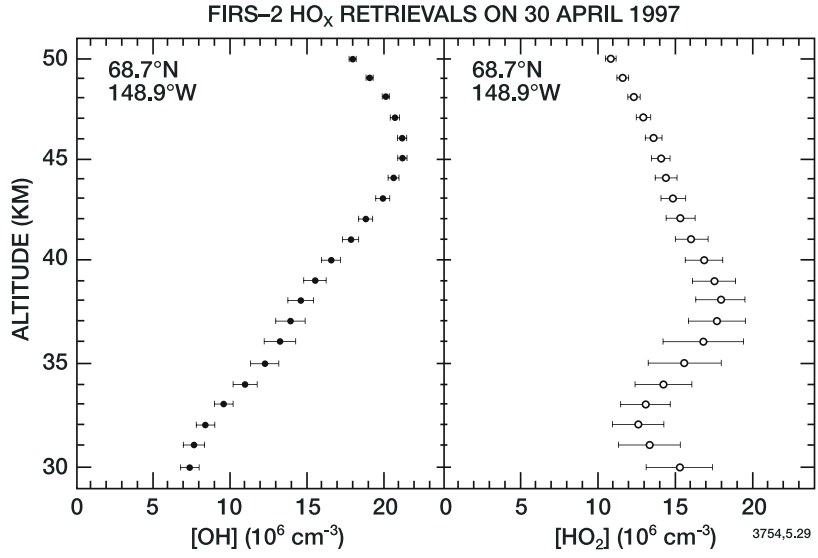

Figure 5.29. Measured concentration of OH and HO_2 on 30 April 1997 at 69°N, 149°W 9:15 local solar time using a balloon-borne thermal emission far-infrared transform spectrometer. From Jucks *et al.* (1998).

increases from 7×10^6 cm^{-3} at 30 km altitude to a maximum value of approximately 20×10^6 cm^{-3} at 46 km. HO_2 densities reach a maximum of about 18×10^6 cm^{-3} at 39 km. At the stratopause, the measured concentrations are 17×10^6 cm^{-3} and 10×10^6 cm^{-3} for OH and HO_2, respectively. The observed $(HO_2)/(OH)$ concentration ratio of 1.7 can be compared with the theoretical values provided by expression (5.115). In the mesosphere, the observations by the Middle Atmosphere High Resolution Spectrograph Investigation (MAHRSI) on board the Space Shuttle (Figure 5.30; Summers *et al.*, 1997) provide daytime concentrations of 11-15 $\times$ 10^6 cm^{-3} at 50 km, (3-8) $\times$ 10^6

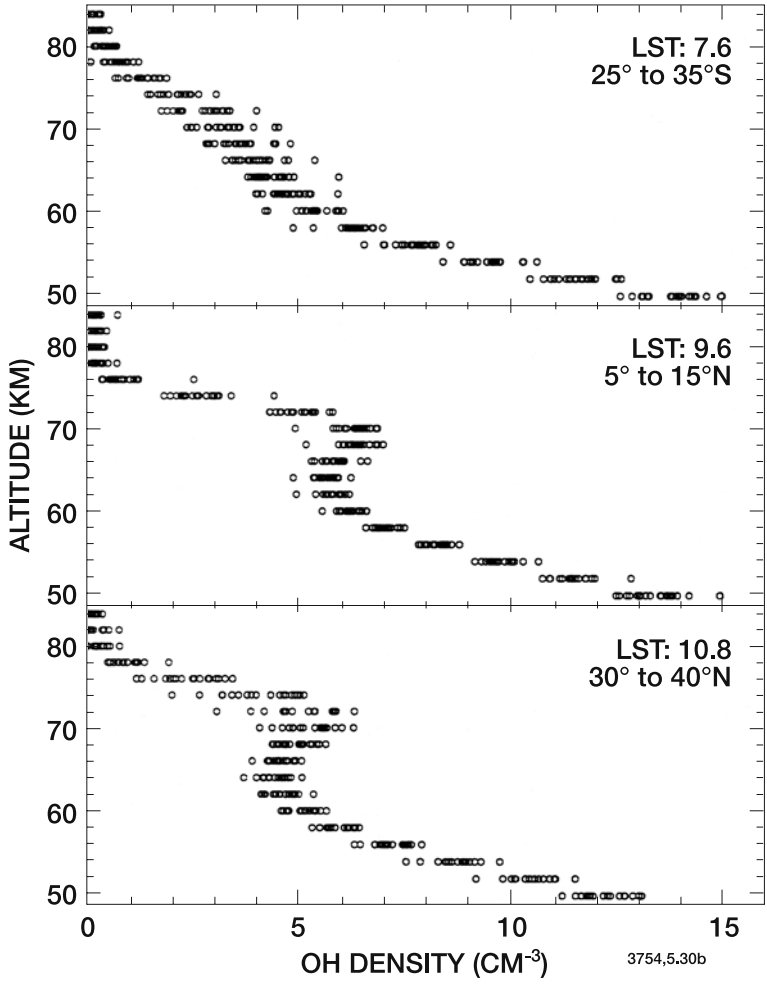

Figure 5.30. Observations of the vertical distribution of the hydroxyl density (cm^{-3}) in the mesosphere (adapted from Summers *et al.* 1997). From top to bottom, the average solar zenith angles for each panel were 62°, 44°, and 53°.

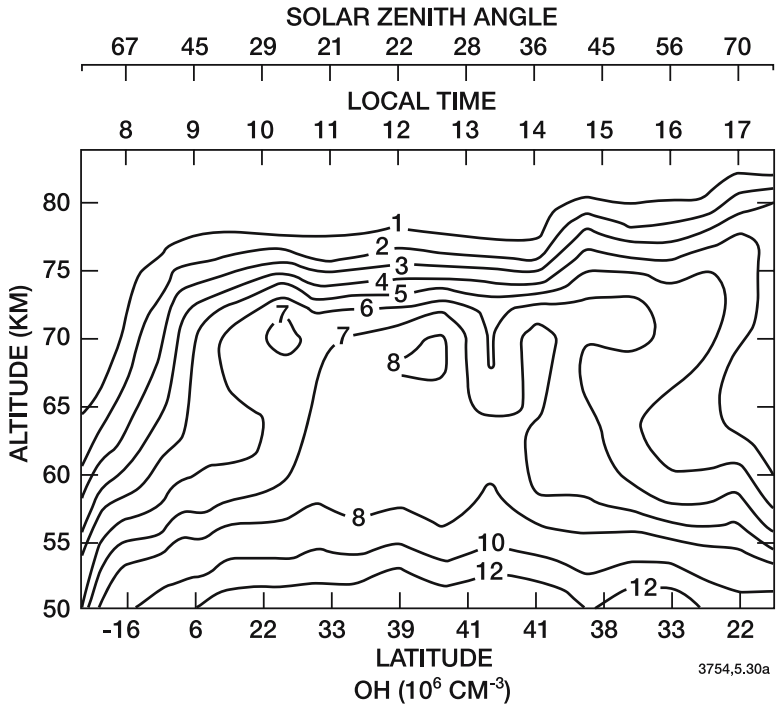

Figure 5.31. Distribution of hydroxl density (cm^{-3}) in the mesosphere observed for different altitudes, latitudes, and local times by the MAHRSI experiment from the CRISTA-SPAS satellite (R.R. Conway, private communication, 1999).

cm^{-3} between 55 and 70 km. Figure 5.31 shows measurements of the OH density by the MAHRSI instrument for different latitudes, altitudes and local times (or solar zenith angles). The stratospheric abundance of hydrogen peroxide, reported by Waters *et al.* (1981), Chance and Traub (1987), Chance *et al.* (1991; 1996), and by Park and Carli (1991), is greater than those of OH and HO_2. Mesospheric atomic hydrogen has also been inferred from observations of the Lyman α and Lyman β emissions (Anderson *et al.*, 1980).

5.5. Nitrogen Compounds

The presence in the middle atmosphere of nitrogen oxides (NO and NO_2 generally called, collectively, NO_x) and related nitrogen compounds such as nitric acid (HNO_3) results from the oxidation of nitrous oxide (N_2O) and, to a lesser extent, from the ionization of molecular nitrogen (N_2) by solar and galactic high energy particles. Nitrogen oxides can also be injected in the lower stratosphere by aircraft engines. Nitric oxide

(NO) and nitrogen dioxide (NO_2) are in photochemical balance during daytime due to fast conversion mechanisms: NO is converted to NO_2 by reaction with ozone, and NO_2 is transformed back to NO either by photolysis or by reaction with atomic oxygen. As these cycles proceed, large amounts of ozone can be catalytically destroyed. The rate for this loss mechanism is, however, limited by the transformation of the nitrogen oxides into less reactive nitrogen compounds. For example, NO_2 reacts with ozone to form nitrogen trioxide (NO_3) which is most abundant during nighttime (when photolytic destruction ceases) and reacts with NO_2 to form dinitrogen pentoxide (N_2O_5). The conversion of nitrogen oxides to a more stable reservoir, nitric acid (HNO_3), occurs either through the reaction between NO_2 and OH or through heterogeneous hydrolysis of N_2O_5 on the surface of aerosol particles. The transport of nitric acid to the troposphere and its removal by precipitation (wet scavenging) removes nitrogen compounds from the middle atmosphere. Other nitrogen reservoirs include pernitric acid (HNO_4 or HO_2NO_2) and chlorine and bromine nitrate ($ClONO_2$ and $BrONO_2$).

In the mesosphere and thermosphere, where the abundance of ozone becomes too low to convert substantial amounts of NO into NO_2 and where the concentration of atomic oxygen is high, reactive nitrogen is mostly in the form of nitric oxide (NO) and atomic nitrogen (N). Substantial production of these chemical species results from ionic processes and N_2 photolysis in the thermosphere. NO is transported downward to the mesosphere where it is destroyed by photolysis and recombination between N and NO to reform stable N_2. The chemical coupling between nitrogen oxides in the thermosphere/upper mesosphere and in the stratosphere is therefore weak, except in the polar night regions where photochemical destruction does not occur and substantial quantities of thermospheric nitrogen compounds are transported to the stratosphere by the general circulation.

Details on the chemical and photochemical processes affecting nitrogen compounds in the middle atmosphere are given in the following sections: Sections 5.5.1-5.5.3 deal with stratospheric nitrogen, while 5.5.4 and 5.5.5 focus on nitrogen compounds in the mesosphere and lower thermosphere.

5.5.1 Sources of Nitrogen Oxides

In the stratosphere, nitric oxide (NO) is produced mostly by dissociation of N_2O by reaction with an excited oxygen atom in the (^1D)

state (Nicolet, 1971; Crutzen, 1971; McElroy and McConnell, 1971):

$$(b_{39}); \qquad N_2O + O(^1D) \rightarrow 2NO \tag{5.127a}$$

The following products are also possible:

$$(b_{38}); \qquad N_2O + O(^1D) \rightarrow N_2 + O_2 \tag{5.127b}$$

The rate of NO production by reaction (5.127a) is given by:

$$P_{NO} = 2b_{39}(N_2O)(O\,^1D) \tag{5.128}$$

and is therefore dependent on the vertical distribution of N_2O. In the stratosphere, N_2O is, in turn, destroyed primarily by photolysis:

$$(J_{N_2O}); \qquad N_2O + h\nu\,(\lambda \leq 200\text{ nm}) \rightarrow N_2 + O(^1D) \tag{5.129}$$

The production reaction

$$(b_0) \qquad N_2 + O(^1D) + M \rightarrow N_2O + M \tag{5.130}$$

is extremely slow, so that the *in situ* production of N_2O in the stratosphere is insignificant.

The equation of continuity for nitrous oxide can thus be written:

$$\frac{\partial(N_2O)}{\partial t} + \boldsymbol{\nabla} \cdot \boldsymbol{\phi}_{N_2O} + (N_2O)\left[J_{N_2O} + (b_{38} + b_{39})(O\,^1D)\right] = 0 \tag{5.131}$$

Nitrous oxide is present throughout the troposphere (and is injected into the lower stratosphere) with a mixing ratio of about 315 ppbv and a global burden of 1510 Tg N. N_2O abundances are about 0.8 ppbv greater in the northern hemisphere, where about 60% of the emissions are located. This compound is produced principally by bacterial processes associated with complex nitrification and denitrification mechanisms in soils (Delwiche, 1978). Thus, as first indicated by Bates and Witherspoon (1952), the biosphere plays a major role in determining the source of N_2O and, hence, the abundance of nitrogen oxides in the stratosphere. In spite of numerous studies, the global budget of atmospheric N_2O remains insufficiently well quantified, because this gas is emitted by several small sources which have large uncertainties. Table 5.7 provides an estimate of the global N_2O sources and sinks. Budget estimates by Mosier *et al.* (1998) and by Kroeze *et al.* (1999) suggest that the total source of N_2O is in the range 6.7-36.6 Tg N/yr with the most likely value close to 17.7 Tg N/yr (9.6 for the natural contribution and 8.1 for the anthropogenic contribution). The global lifetime of nitrous oxide is estimated to be approximately 120 years.

Table 5.7 Estimated Sources and Sinks of Nitrous Oxide (Tg/yr) (From WMO, 1995)

Sources	
A. Natural	
Oceans	1.4-5.2
Tropical Soils	
Wet Forests	2.2-3.7
Dry Savannas	0.5-2.0
Temperate Soils	
Forests	0.05-2.0
Grassland	??
B. Anthropogenic	
Cultivated Soils	1-3
Animal Waste	0.2-0.5
Biomass Burning	0.2-1.0
Stationary Combustion	0.1-0.3
Mobile Sources	0.1-0.6
Adific Acid Production	0.4-0.6
Nitric Acid Production	0.1-0.3
Sinks	
Removal by Soils	?
Photolysis in the Stratosphere	9-17
Atmospheric Increase	3.1-4.7

Figure 5.32 shows the photochemical time constant of N_2O and those appropriate to transport processes. Like CH_4, N_2O is an excellent tracer for transport in the middle stratosphere, where its lifetime is comparable to those for advection by the mean meridional circulation. At higher altitudes in the upper stratosphere and lower mesosphere, the N_2O lifetime remains close to the mean meridional transport lifetimes, making it a more sensitive tracer than CH_4 in this region.

The distribution of N_2O has been measured by cryogenic sampling and gas phase chromatography (Scholz *et al.*, 1970; Ehhalt *et al.*, 1975b; Schmeltekopf *et al.*, 1977) as well as by infrared absorption (Harries, 1973; Farmer, 1974; Farmer *et al.*, 1974, 1980). Figure 5.33a shows the early observations by Schmeltekopf *et al.* at different latitudes. In each case, a decrease in mixing ratio is observed above the tropopause. As was shown previously for CH_4, this decrease is less rapid at the

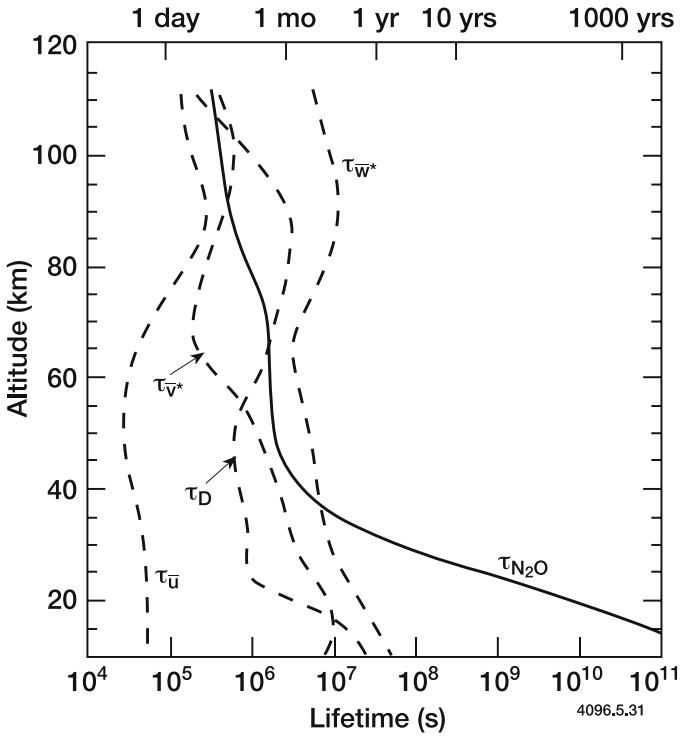

Figure 5.32. Photochemical lifetime of N_2O, as well as the time constants for transport by the zonal and meridional winds, and a one-dimensional diffusive time constant.

equator than at higher latitudes, presumably because of the rapid rate of upward transport associated with the rising branch of the Hadley cell at these latitudes. Space observations were also performed in the late 1970s by the SAMS instrument aboard the Nimbus 7 satellite, and in the 1990s by the CLAES and ISAMS sounders aboard UARS (Figure 5.33b) and by the Cryogenic Infrared Spectrometers and Telescopes for the Atmosphere (CRISTA) experiment on board the Space Shuttle (Offermann *et al.*, 1999 and Plate 3). Like CH_4 (Figure 5.16), large values are obtained in the tropical lower stratosphere. Pre-industrial mole fractions of N_2O were approximately 270 ppbv (Flückinger *et al.*, 1999). The concentration increase during the industrial period has produced a current radiative forcing of 0.15 Wm^{-2} (IPCC, 2001). An analysis of the infrared spectra recorded in the Swiss Alps in 1950-1951 and from 1984-1992 suggests that the column abundance of N_2O has increased by 0.23±0.04%/yr from 1951 to 1984 and by 0.36±0.06%/yr between 1984 and 1992 (Zander *et al.*, 1994). Analyses of data collected during oceanic expeditions (Weiss, 1994) and from a global network of

stations (Swanson *et al.*, 1993) indicate that, on the average, the growth rate in the surface mixing ratio of N_2O was 0.5-0.6 ppbv/yr during 1976-1982, increased to a maximum of 0.8-1.0 ppbv/yr in 1998-1989, and declined to 0.5-0.6 ppbv in the early 1990s.

Figure 5.34 shows the distribution of the nitric oxide production by oxidation of N_2O. This production is directly related to atmospheric dynamics that carries N_2O to its loss region; it reaches a maximum in the mid-stratosphere where its value is about 100 molec $cm^{-3}s^{-1}$. Crutzen and Schmailzl (1983) suggest a global value between 1.1 and 1.9 $\times 10^8$ molec NO $cm^{-2}s^{-1}$, using the N_2O distribution measured by the SAMS satellite.

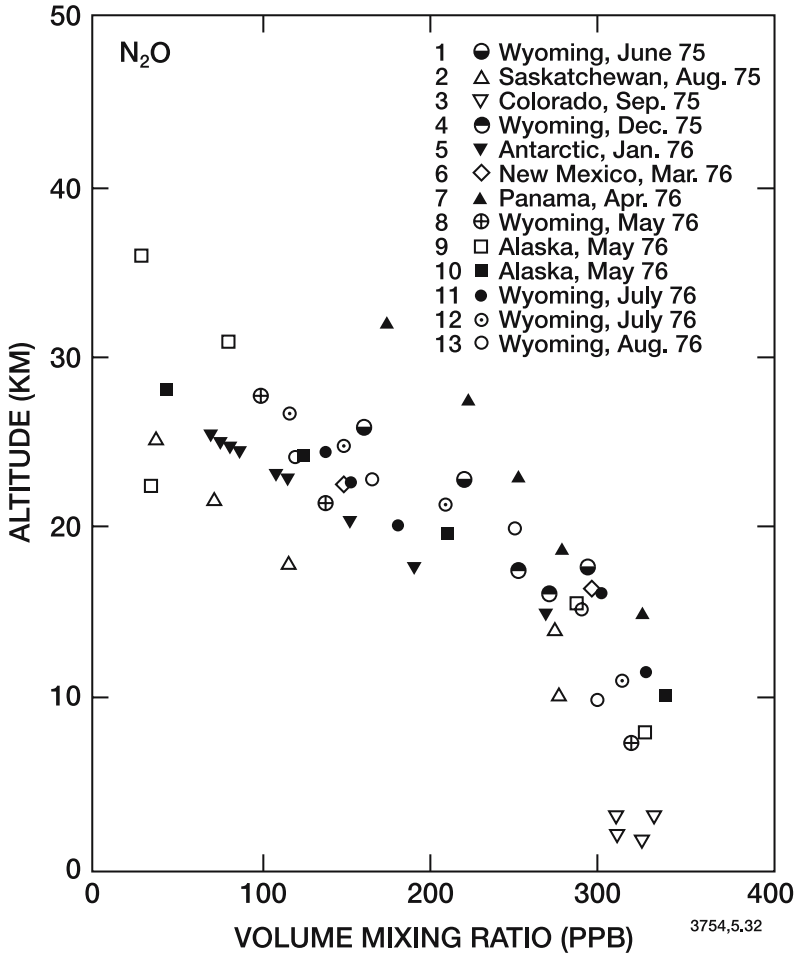

Figure 5.33a. Observations of the mixing ratio of nitrous oxide by Schmeltekopf *et al.* (1977).

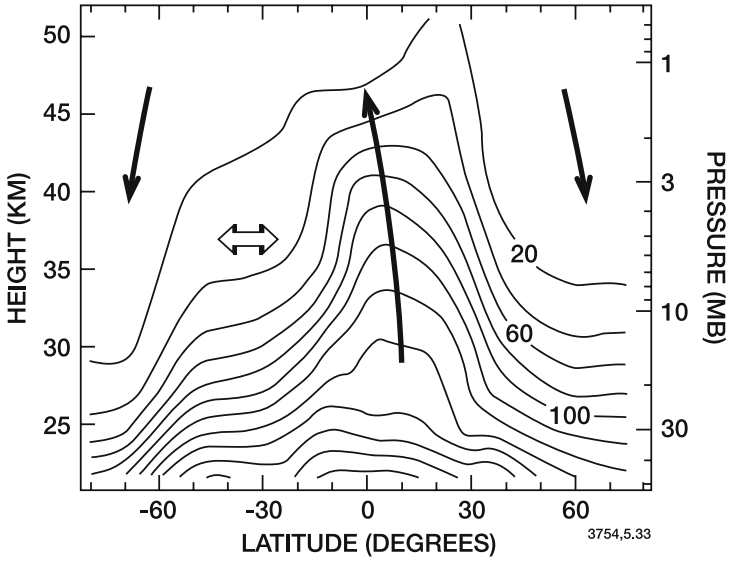

Figure 5.33b. Zonally averaged distribution of the N_2O mixing ratio (in pptv) measured by the CLAES instrument on UARS during 1-20 September, 1992. Courtesy of W. Randel, NCAR.

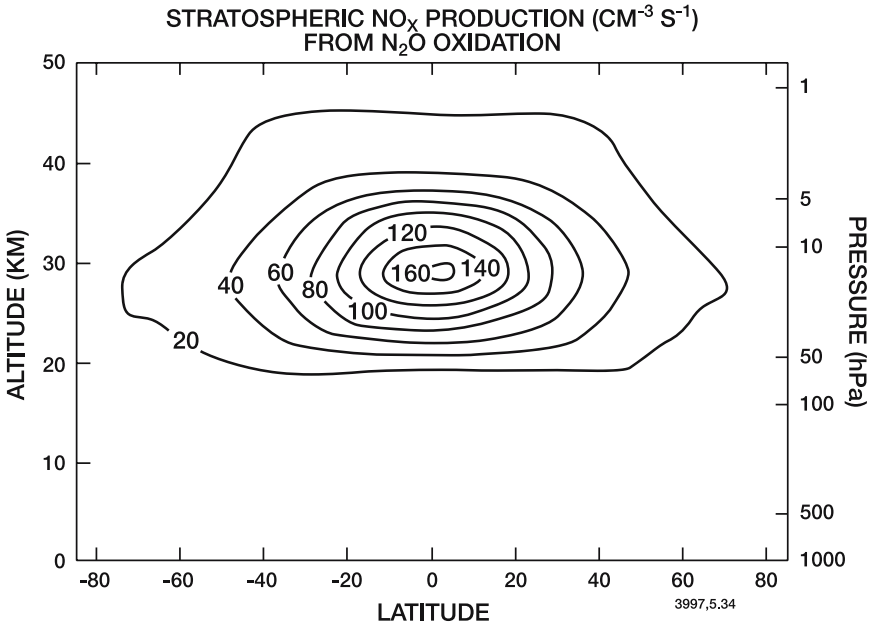

Figure 5.34. Diurnally and annually averaged rate of NO production in the stratosphere through reaction of N_2O with O^1D. From Crutzen and Schmailzl (1983).

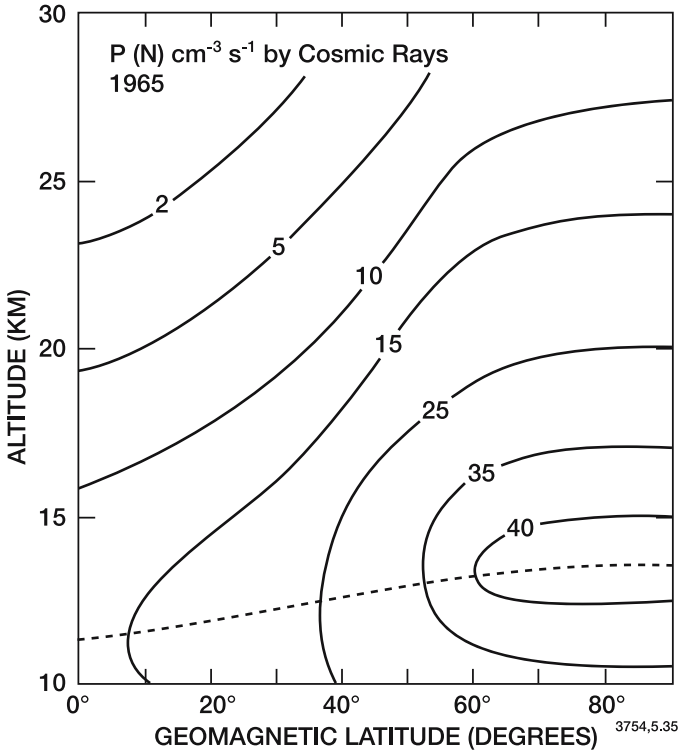

Figure 5.35. Distribution of the rate of production of NO by cosmic rays at solar minimum. Adapted from Nicolet (1975b).

Stratospheric nitrogen atoms can be formed by dissociative ionization and dissociation of molecular nitrogen by galactic cosmic rays. These processes generally occur through secondary electrons ejected by heavy cosmic particles. One ion pair formed by cosmic radiation leads to the production of 1-1.6 atoms of nitrogen (see Chapter 7). Figure 5.35 shows the spatial distribution of P_N for solar minimum (from Nicolet, 1975b) as a function of geomagnetic latitude. In the stratosphere, atomic nitrogen reacts rapidly with molecular oxygen to form nitric oxide. Stratospheric production of nitrogen oxides by cosmic radiation should not be neglected, especially in polar regions where the oxidation of N_2O is slow. Nicolet (1975b) indicated that cosmic radiation leads to an integrated NO production of about $(5 \pm 1) \times 10^7 \mathrm{cm}^{-2}\mathrm{s}^{-1}$ in polar regions and $3 \times 10^7 \mathrm{cm}^{-2}\mathrm{s}^{-1}$ in the tropics.

Crutzen *et al.* (1975) noted that penetration of large amounts of protons into the middle atmosphere during solar proton events would also lead to an intense production of atomic nitrogen. These episodic events can produce enough nitrogen oxide to influence the ozone content,

particularly at high latitudes (see *e.g.*, Jackman, 1991; Jackman *et al.*, 1995). The chemistry of the ionization and odd nitrogen production processes is described in more detail in Chapter 7.

Several other gases released at the Earth's surface carry additional nitrogen into the middle atmosphere. This is the case of hydrogen cyanide (HCN) and methyl cyanide (CH_3CN). In both cases, only limited observations are available and the global budget is not well quantified. The numbers quoted below represent, therefore, orders of magnitude only.

Hydrogen cyanide is believed to be produced primarily as a result of biomass burning (Lobert *et al.*, 1990) with a global release corresponding to 0.5-3.0 Tg N/yr (see also Li *et al.*, 2000). Emissions by fossil fuel consumption appears to be very small (0.04 Tg N/yr) in comparison. The major atmospheric loss of HCN is probably due to ocean uptake (1-2.5 Tg N/yr; see Li *et al.*, 2000). Reactions with OH (0.3 Tg N/yr) and $O(^1D)$ (3×10^{-4}Tg N/yr), as well as photolysis (2×10^{-3}Tg N/yr) are small on the global scale (Li *et al.*, 2000), but should be the major destruction mechanisms in the middle atmosphere. The presence of HCN in the atmosphere has been detected by infra-red spectroscopy (Coffey *et al.*, 1981a; Mahieu *et al.*, 1995; 1997; Rinsland *et al.*, 1999; Zhao *et al.*, 1999). The observed seasonal variation (factor 2-3 at northern mid-latitudes and a factor 5 enhancement in the tropical upper troposphere during the dry season) suggests that the global lifetime of HCN could be as short as 2-4 months (Li *et al.*, 2000). The mixing ratio of HCN appears to be relatively constant with height (100-200 pptv) between the surface and the upper stratosphere with a total atmospheric burden of approximately 0.5 Tg N/yr.

Methyl cyanide (also called acetonitrile) is also produced primarily by biomass burning (0.3-0.4 Tg N/yr; see Lobert *et al.*, 1990; Holzinger *et al.*, 1999). Emissions from automobile exhausts and industrial activities are believed to be small (0.01 Tg N/yr). The ocean is probably a significant sink for atmospheric CH_3CN, but the magnitude of this loss is not yet well quantified. The largest chemical loss is provided by reactions with OH, $O(^1D)$ and Cl, and by photolysis (Arijs and Brasseur, 1985; Hamm and Warneck, 1990). Rainout is another loss process in the troposphere. The high variability in the measured tropospheric concentrations of methyl cyanide suggests that the atmospheric lifetime of this molecule is significantly shorter than predicted when only the photochemical loss processes are taken into account. Since methyl cyanide has a large proton affinity, it plays a major role in the formation of positive ion clusters (called non-proton hydrates) in the stratosphere (see Chapter 7). CH_3CN has been detected in the stratosphere by the MLS instrument on board the Upper Atmosphere Research Satellite

(Livesey *et al.*, 2001). Typical mole fractions of 40-60 ppbv are reported in the tropics between 20 and 30 km altitude. Values are decreasing at higher altitudes (about 10 pptv at 45 km near the equator) and higher latitudes (20 pptv in summer and 10 pptv in winter at 60° latitude and 30 km altitude).

5.5.2 Odd Nitrogen Chemistry in the Stratosphere

In the stratosphere nitric oxide is converted to nitrogen dioxide by reaction with ozone:

$$(b_4); \qquad NO + O_3 \rightarrow NO_2 + O_2 \tag{5.132}$$

by reaction with peroxy radicals ($RO_2 = HO_2$ or CH_3O_2):

$$(a_{26}); \qquad NO + HO_2 \rightarrow NO_2 + OH \tag{5.92}$$

$$(c_5); \qquad NO + CH_3O_2 \rightarrow NO_2 + CH_3O \tag{5.53}$$

and by reactions with ClO and BrO (see Sections 5.6 and 5.7):

$$(d_4); \qquad NO + ClO \rightarrow NO_2 + Cl \tag{5.133}$$

$$(e_4); \qquad NO + BrO \rightarrow NO_2 + Br \tag{5.134}$$

The conversion mechanism by the three-body reaction

$$(b_{82}); \qquad NO + O + M \rightarrow NO_2 + M \tag{5.135}$$

can generally be neglected.

The NO_2 molecule reacts rapidly during the day to reform NO, either by reaction with atomic oxygen:

$$(b_3); \qquad NO_2 + O \rightarrow NO + O_2 \tag{5.136}$$

or by photolysis:

$$(J_{NO_2}); \qquad NO_2 + h\nu(\lambda < 405 \text{ nm}) \rightarrow NO + O(^3P) \tag{5.137}$$

Reaction of NO with O_3 (5.132), followed by reaction of NO_2 with O represents a catalytic cycle which provides the major loss process for odd oxygen in the stratosphere.

In the upper stratosphere and above, nitric oxide is photolyzed in the δ-bands (see Chapter 4)

$$(J_{NO}); \qquad NO + h\nu \rightarrow N\left(^4S\right) + O \tag{5.138}$$

but ground-state atomic oxygen reacts rapidly with O_2 to reform NO

$$(b_7); \qquad N\left(^4S\right) + O_2 \rightarrow NO + O\ . \tag{5.139}$$

However, the reaction of $N(^4S)$ and NO

$$(b_6); \qquad N\left(^4S\right) + NO \rightarrow N_2 + O \tag{5.140}$$

represents a loss of odd nitrogen, which plays a major role in the mesosphere during the daytime.

Additional reactions should also be considered in the stratosphere. These lead to the formation of other nitrogen containing species such as NO_3, N_2O_5, HNO_3, and HO_2NO_2, which represent nitrogen "reservoirs".

The formation of nitrogen trioxide (NO_3) results from the reaction of NO_2 with ozone

$$(b_9); \qquad NO_2 + O_3 \rightarrow NO_3 + O_2 \tag{5.141}$$

and leads to high NO_3 concentrations during nighttime. Other minor sources of NO_3 are provided by Reactions (5.101), (5.156b), (5.159a), and (5.160a), and by reaction

$$(b_{81}); \qquad NO_2 + O + M \rightarrow NO_3 + M \tag{5.142}$$

During the day the NO_3 radical is rapidly photolyzed

$$(J^a_{NO_3}); \qquad NO_3 + h\nu\,(\lambda \leq 620\ \text{nm}) \rightarrow NO_2 + O \tag{5.143a}$$

$$(J^b_{NO_3}); \qquad \rightarrow NO + O_2 \tag{5.143b}$$

According to the laboratory measurements of Orlando *et al.* (1993), the second channel of the NO_3 photolysis (Reaction 5.143b) contributes less than 10% of the total photodissociation. Additional destruction mechanisms for NO_3 include

$$(b_{71}); \qquad NO_3 + O \rightarrow NO_2 + O_2 \tag{5.144}$$

$$(b_{72}); \qquad NO_3 + OH \rightarrow NO_2 + HO_2 \tag{5.145}$$

$$(b_{73a}); \qquad NO_3 + HO_2 \rightarrow NO_2 + OH + O_2 \tag{5.146a}$$

$$(b_{73b}); \qquad \rightarrow HNO_3 + O_2 \tag{5.146b}$$

$$(b_{84}); \qquad NO_3 + NO \rightarrow 2NO_2 \tag{5.147}$$

Dinitrogen pentoxide (N_2O_5), formed by the reaction of NO_2 and NO_3, is produced almost entirely at night, when NO_3 is abundant:

$$(b_{12}); \qquad NO_3 + NO_2 + M \rightarrow N_2O_5 + M \tag{5.148}$$

It is destroyed during the day through photolysis

$$(J^a_{N_2O_5}); \quad N_2O_5 + h\nu\,(\lambda \leq 380\ \text{nm}) \rightarrow NO_3 + NO_2 \tag{5.149a}$$

$$(J^b_{N_2O_5}); \qquad \rightarrow NO_3 + NO + O \tag{5.149b}$$

and by collisional decomposition (the rate of which is highly temperature dependent)

$$(b_{32}); \qquad N_2O_5 + M \rightarrow NO_3 + NO_2 + M \tag{5.150}$$

The quantum yield for process (5.149*b*) decreases with wavelength, and is reported to be 0.72, 0.38, 0.21, and 0.15 at 248, 266, 287, and 289 nm, respectively (Ravishankara *et al.*, 1986).

Another important stratospheric nitrogen containing species is HNO_3. This molecule, which introduces an interaction between nitrogen and hydrogen compounds, is formed by the three body process:

$$(b_{22}); \qquad NO_2 + OH + M \rightarrow HNO_3 + M \tag{5.151}$$

A heterogeneous reaction converting N_2O_5 into HNO_3

$$(h_1); \qquad N_2O_5(g) + H_2O(\ell, s) \rightarrow 2HNO_3 \tag{5.152}$$

occurs on the surface of ice particles [H_2O (solid)], water droplets [H_2O (liquid)], nitric acid ice [$HNO_3 \cdot 3H_2O$ (solid)], sulfate aerosol [H_2SO_4/H_2O] and ternary solution [$H_2SO_4/HNO_3/H_2O$] particles in the lower stratosphere. In the case of sulfate aerosols, the reaction probability γ is close to 0.1 (see *e.g.*, Mozurkiewicz and Calvert, 1988; Hanson and Ravishankara, 1992; Fried *et al.*, 1994; Lovejoy and Hanson, 1995; Hanson, 1997) with only a modest dependence on the H_2SO_4 content and on temperature. For a water ice particle, however, the reaction probability is much less (of the order of 0.01, see Hanson and Ravishankara, 1993). If the ice particle becomes coated with HNO_3, the value of γ drops even further (approximately 0.001). This reaction provides an efficient mechanism to convert nitrogen oxides into nitric acid, especially at high latitudes where the gas-phase conversion of NO_2 to HNO_3 by the OH radical is slow, particularly during wintertime. When particles are present in the stratosphere, Reaction (5.152) is rapid, and the rate of heterogeneous conversion of nitrogen oxides (NO_x) to nitric acid (HNO_3) is limited by the rate at which the gas-phase reaction of NO_2 with ozone (Reaction 5.141) proceeds. Note also that, as the concentration of NO_2 is reduced by Reaction (5.152), the presence of sulfate aerosol particles in the stratosphere, and occasionally of polar stratospheric clouds (PSCs), tends to enhance the levels of ClO and OH in the lower stratosphere. The concentration of ClO is increased mainly because the rate at which this radical recombines with NO_2 (Reaction 5.157) is reduced. The level of OH is enhanced mainly because its gas-phase reaction with NO_2 to form HNO_3 (Reaction 5.151) becomes slower.

The two primary chemical loss processes for HNO_3 are:

$$(J_{HNO_3}); \qquad HNO_3 + h\nu\,(\lambda \leq 310 \text{ nm}) \rightarrow OH + NO_2 \tag{5.153}$$

$$(b_{27}); \qquad HNO_3 + OH \rightarrow NO_3 + H_2O \tag{5.101}$$

HNO_3 molecules are eventually transported from the stratosphere to the troposphere where they are readily incorporated into rain droplets.

Gravitational sedimentation of HNO_3-containing solid or liquid particles can also lead to *denitrification* of the lower polar stratosphere during winter.

The HO_2NO_2 molecule is formed by the reaction:

$$(b_{23a}); \qquad NO_2 + HO_2 + M \rightarrow HO_2NO_2 + M \tag{5.154}$$

and destroyed by unimolecular decomposition at low altitudes:

$$(b_{23b}); \qquad HO_2NO_2 + M \rightarrow HO_2 + NO_2 + M \tag{5.155}$$

as well as by photolysis

$$(J^a_{HO_2NO_2}); \qquad HO_2NO_2 + h\nu\,(\lambda < 325\ \text{nm}) \rightarrow NO_2 + HO_2 \tag{5.156a}$$

$$(J^b_{HO_2NO_2}); \qquad \rightarrow NO_3 + OH \tag{5.156b}$$

and reaction with OH:

$$(b_{28}); \qquad HO_2NO_2 + OH \rightarrow H_2O + O_2 + NO_2 \tag{5.102}$$

At 248 nm, photolysis (Reaction 5.156) yields about one-third OH and NO_3 and two-thirds $HO_2 + NO_2$ (McLeod *et al.*, 1988). The chemistry of HO_2NO_2 is important in both nitrogen and hydrogen chemistries.

Other nitrogen-containing reservoirs $ClONO_2$ and $BrONO_2$ are formed by reactions with chlorine and bromine monoxide, respectively

$$(d_{31}); \qquad ClO + NO_2 + M \rightarrow ClONO_2 + M \tag{5.157}$$

$$(e_{13}); \qquad BrO + NO_2 + M \rightarrow BrONO_2 + M \tag{5.158}$$

Chlorine and bromine nitrate are photolyzed with different possible channels

$$(J^a_{ClONO_2}); \qquad ClONO_2 + h\nu\,(\lambda \leq 320\ \text{nm}) \rightarrow Cl + NO_3 \tag{5.159a}$$

$$(J^b_{ClONO_2}); \qquad \rightarrow ClO + NO_2 \tag{5.159b}$$

$$(J^a_{BrONO_2}); \qquad BrONO_2 + h\nu\,(\lambda \leq 450\ \text{nm}) \rightarrow Br + NO_3 \tag{5.160a}$$

$$(J^b_{BrONO_2}); \qquad \rightarrow BrO + NO_2 \tag{5.160b}$$

Reactions involving halogen atoms will be further discussed in Sections 5.6 and 5.7. Note that these reactions introduce a strong chemical coupling between nitrogen and halogen species in the stratosphere.

The primary reactions of these species are depicted in Figure 5.36. Considering the most important chemical and photochemical processes,

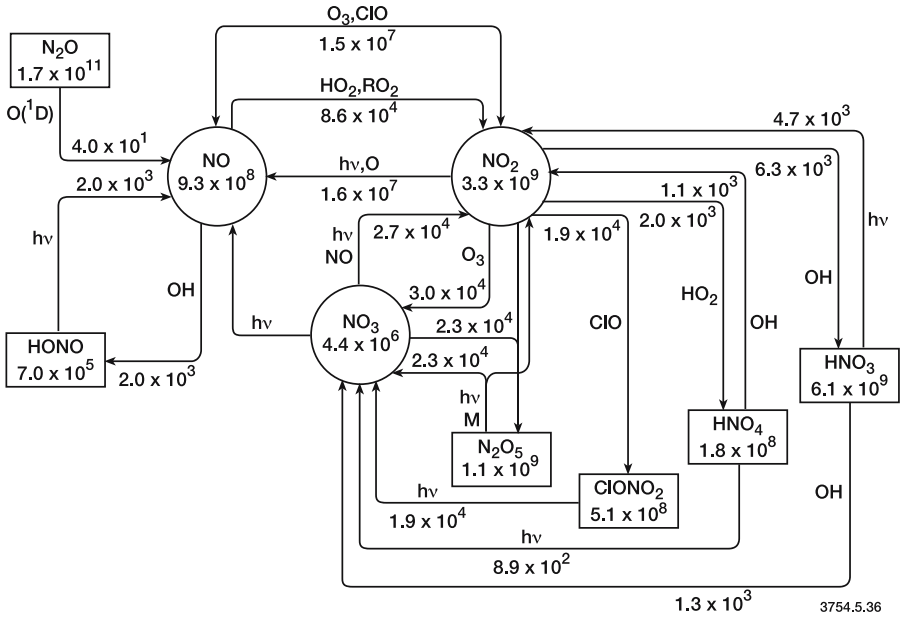

Figure 5.36. Principal chemical reactions affecting nitrogen species in the stratosphere. Concentrations (cm^{-3}) and reaction fluxes ($cm^{-3}s^{-1}$) between different compounds calculated at 25 km altitude (24-hour average) are indicated. After Zellner (1999).

the continuity equations for NO, NO_2, NO_3, N_2O_5, HNO_3, and HO_2NO_2 can be written:

$$\frac{d\,(N)}{dt} + [b_6\,(NO) + b_7\,(O_2)]\,(N) = J_{NO}\,(NO) + P_N \tag{5.161}$$

$$\begin{aligned}\frac{d\,(NO)}{dt} &+ [b_4\,(O_3) + b_6\,(N) + b_{84}\,(NO_3) + a_{26}\,(HO_2)\\ &+c_5\,(CH_3O_2) + d_4\,(ClO) + e_4\,(BrO) + J_{NO}]\,(NO)\\ &= [b_3\,(O) + J_{NO_2}]\,(NO_2) + J^b_{NO_3}\,(NO_3)\\ &+ J^b_{N_2O_5}\,(N_2O_5) + b_7\,(O_2)\,(N) + P\,(NO)\end{aligned} \tag{5.162}$$

$$\begin{aligned}\frac{d\,(NO_2)}{dt} &+ [J_{NO_2} + b_3\,(O) + b_{12}\,(M)\,(NO_3) + b_{22}\,(M)\,(OH)\\ &+ b_{23a}\,(M)\,(HO_2) \;+ b_{81}\,(M)\,(O) + d_{31}\,(M)\,(ClO)\\ &+ e_{13}\,(M)\,(BrO)]\,(NO_2) = [b_4\,(O_3) + a_{26}\,(HO_2)\\ &+ c_5\,(CH_3O_2) + d_4\,(ClO) + e_4\,(ClO)]\,(NO)\\ &+ J_{HNO_3}\,(HNO_3) + [J^a_{NO_3} + b_{71}\,(O) + b_{72}\,(OH)\end{aligned}$$

$$+b_{73a}\,(HNO_2) + 2b_{84}\,(NO)]\,(NO_3)$$
$$+\,[J^{a}_{N_2O_5} + b_{32}\,(M)]\,(N_2O_5)$$
$$+\,[J^{a}_{HO_2NO_2} + b_{23b}\,(M) + b_{28}\,(OH)]\,(HO_2NO_2)$$
$$+\,J^{b}_{ClONO_2}\,(ClONO_2) + J^{b}_{BrONO_2}\,(BrONO_2) \qquad (5.163)$$

$$\frac{d(NO_3)}{dt} + [b_{12}(M)(NO_2) + J_{NO_3} + b_{71}\,(O) + b_{72}\,(OH)$$
$$+\,(b_{73a} + b_{73b})\,(HO_2) + b_{84}\,(NO)]\,(NO_3) = b_9(O_3)(NO_2)$$
$$+\,[J_{N_2O_5} + b_{32}(M)]\,(N_2O_5) + b_{27}(OH)(HNO_3)$$
$$+\,b_{81}\,(M)\,(O)\,(NO_2) + J^{a}_{ClONO_2}\,(ClONO_2)$$
$$+\,J^{a}_{BrONO_2}\,(BrONO_2) \qquad (5.164)$$

$$\frac{d(N_2O_5)}{dt} + (N_2O_5)\,[J_{N_2O_5} + b_{32}(M) + h_1]$$
$$= b_{12}(M)(NO_2)(NO_3) \qquad (5.165)$$

$$\frac{d\,(HNO_3)}{dt} + [J_{HNO_3} + b_{27}\,(OH)]\,(HNO_3)$$
$$= b_{22}\,(M)\,(OH)\,(NO_2) + 2h_1\,(N_2O_5)$$
$$+\,b_{73b}\,(HO_2)\,(NO_3) \qquad (5.166)$$

$$\frac{d(HO_2NO_2)}{dt} + (HO_2NO_2)\,[J_{HO_2NO_2} + b_{28}(OH) + b_{23b}(M)]$$
$$= b_{23a}(NO_2)(HO_2)(M) \qquad (5.167)$$

where P_N and P_{NO} account for all ionic production of N and NO, $J_{NO_3} = J^{a}_{NO_3} + J^{b}_{NO_3}$, $J_{HO_2NO_2} = J^{a}_{HO_2NO_2} + J^{b}_{HO_2NO_2}$, and $J_{N_2O_5} = J^{a}_{N_2O_5} + J^{b}_{N_2O_5}$.

5.5.3 The Odd Nitrogen Family in the Stratosphere and Nitrogen Partitioning

The *odd nitrogen* family (NO_y) is defined as the sum of all nitrogen-containing species except the major atmospheric constituent N_2 and the source gases such as nitrous oxide (N_2O), hydrogen cyanide (HCN) and methyl cyanide (CH_3CN). Thus, in the middle atmosphere, if we include

halogenated nitrates,

$$\mathrm{NO_y} = \mathrm{N} + \mathrm{NO} + \mathrm{NO_2} + \mathrm{NO_3} + 2\,\mathrm{N_2O_5} + \mathrm{HNO_3} + \mathrm{HO_2NO_2} + \mathrm{ClONO_2} + \mathrm{BrONO_2}$$

it is easy to show by adding (5.161) to (5.167) and accounting for the contributions of $\mathrm{ClONO_2}$ and $\mathrm{BrONO_2}$, that

$$\frac{\partial\,(\mathrm{NO_y})}{\partial \mathrm{t}} + \boldsymbol{\nabla}\boldsymbol{\phi}_{\mathrm{NO_y}} + 2\mathrm{b}_6\,(\mathrm{N})\,(\mathrm{NO}) + \beta_{\mathrm{NO_y}}\,(\mathrm{NO_y}) = \mathrm{P_N} + \mathrm{P_{NO}} \quad (5.168)$$

where $\beta_{\mathrm{NO_y}}$ represents an effective loss coefficient accounting for wet scavenging of $\mathrm{HNO_3}$.

In many cases, the $\mathrm{NO_x}$ family is formed as the sum of NO and $\mathrm{NO_2}$, and accounts for the most reactive nitrogen species. The $\mathrm{NO_x}$/$\mathrm{NO_y}$ concentration ratio, which is often reported from field observations, is an indicator of the reactivity of odd nitrogen and its ability to destroy stratospheric ozone (or to affect other chemical families including chlorine and bromine compounds). The value of this ratio increases with altitude above 30 km to reach a value of nearly one in the upper stratosphere and mesosphere. It decreases substantially when the stratospheric aerosol load is enhanced, for example, after large volcanic eruptions (Fahey *et al.*, 1993), and substantial amounts of nitrogen oxides are converted to nitric acid by heterogeneous reaction (5.152). It is also low in the polar regions, especially in air masses processed by polar stratospheric clouds.

Note that $\mathrm{NO_z}$ is sometimes defined as $\mathrm{NO_y}$ – $\mathrm{NO_x}$ (and refers essentially to odd nitrogen reservoirs), and that some authors define $\mathrm{NO_x}$ as the sum of N + NO + $\mathrm{NO_2}$ + $\mathrm{NO_3}$ + 2 $\mathrm{N_2O_5}$ + $\mathrm{HO_2NO_2}$ (all $\mathrm{NO_y}$ compounds except $\mathrm{HNO_3}$), considering thereby all nitrogen compounds which are rapidly converted to $\mathrm{NO_2}$ and NO. This latter definition is adopted in Figure 5.37. In this case, the continuity equation for $\mathrm{NO_x}$ can be written

$$\begin{aligned}\frac{\mathrm{d}\,(\mathrm{NO_x})}{\mathrm{dt}} &+ \mathrm{b}_{22}\,(\mathrm{M})\,(\mathrm{OH})\,(\mathrm{NO_2}) + 2\mathrm{b}_6\,(\mathrm{N})\,(\mathrm{NO}) + 2\mathrm{h}_1\,(\mathrm{N_2O_5}) \\ &= 2\mathrm{b}_{39}\,(\mathrm{N_2O})\left(\mathrm{O}^1\mathrm{D}\right) + \mathrm{P_N} + \mathrm{J}_{\mathrm{HNO_3}}\,(\mathrm{HNO_3}) \\ &+ \mathrm{b}_{27}\,(\mathrm{OH})\,(\mathrm{HNO_3})\end{aligned} \quad (5.169)$$

Figure 5.37 displays the altitude profiles of the photochemical lifetimes of the $\mathrm{NO_y}$ family and its constituent members (gas phase chemistry only), as well as the time constants for transport at middle latitudes. Note that the photochemical lifetimes for $\mathrm{NO_x}$ and $\mathrm{HNO_3}$ are both comparable to the transport lifetimes in the lower stratosphere, so that the distribution of these species will be quite dependent on atmospheric transport. It is important to treat them separately in numerical model

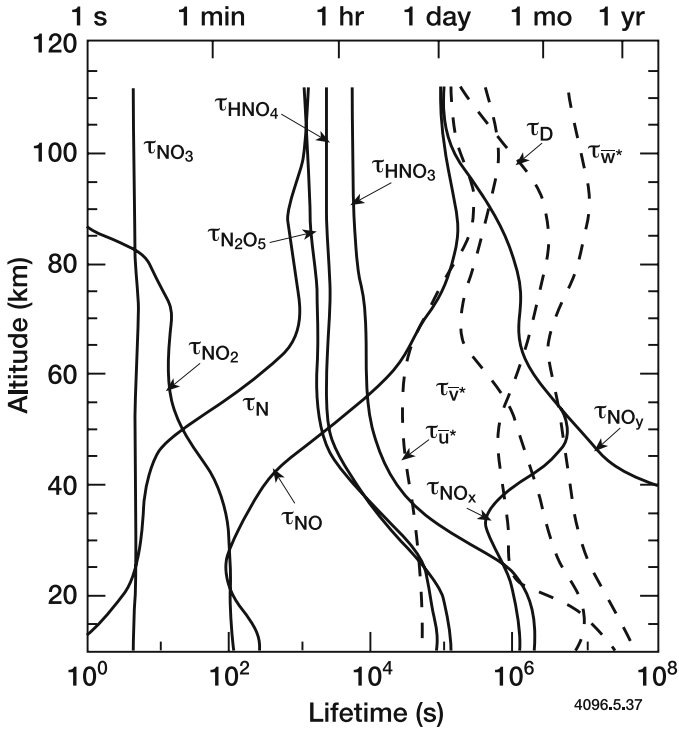

Figure 5.37. Photochemical time constants for NO_y, N, NO, NO_2, NO_3, N_2O_5, HO_2NO_2, and HNO_3, as well as the time constants for transports by the zonal and meridional winds and a one-dimensional eddy diffusion coefficient.

studies. In high latitude winter, it also becomes necessary to treat N_2O_5 separately from the other nitrogen species; this will be discussed in more detail below.

The partitioning of the NO_y family is somewhat more complicated than for the families presented previously. The ratio between N and NO (below 80 km) can be derived from Eq. (5.161) in which b_6 (NO) $\ll$ b_7 (O_2), P_N is neglected, and photochemical conditions (d(N)/dt = 0) are assumed:

$$\frac{(N)}{(NO)} = \frac{J_{NO}}{b_7(O_2)} \tag{5.170}$$

NO_2 is also in equilibrium with NO throughout the sunlit middle atmosphere. Because atmospheric absorption in the 400 nm region is negligibly small, J_{NO_2} is given by its optically thin value of about 1×10^{-2} s^{-1} even at altitudes as low as 15 km, which corresponds to a lifetime of about 2 minutes. NO_2 can therefore be considered to be in immediate photochemical equilibrium with NO during the day, and by conserving the largest terms, we may deduce from (5.163) the following expression

for the ratio of NO to NO_2:

$$\frac{(NO)}{(NO_2)} = \frac{J_{NO_2} + b_3(O)}{b_4(O_3) + a_{26}(HO_2) + c_5(CH_3O_2) + d_4(ClO)} \tag{5.171}$$

The value of this ratio is close to one over most of the stratosphere during daytime, but increases rapidly above 40 km because of increasing atomic oxygen densities. At night, NO is quickly converted to NO_2 up to altitudes of about 60 km. Figure 5.38 shows calculated one-dimensional model distributions of the various nitrogen species. The curves represent a steady state solution for average solar insolation.

Setting NO_3 in photochemical equilibrium in the sunlit stratosphere yields:

$$\frac{(NO_3)}{(NO_2)} \approx \frac{b_9(O_3)}{J_{NO_3}} \tag{5.172}$$

while at night

$$(NO_3)_{night} = \frac{b_9(O_3)}{b_{12}(M)} \tag{5.173}$$

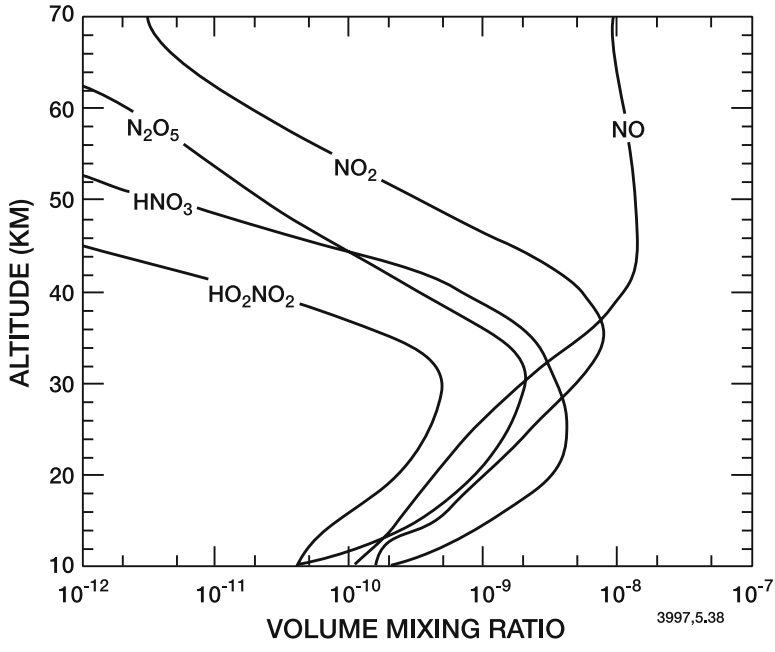

Figure 5.38. Calculated vertical distributions of nitrogen species at mid-latitudes (noon, equinox).

For HO_2NO_2, we obtain

$$\frac{(HO_2NO_2)}{(NO_2)} = \frac{b_{23a}(HO_2)(M)}{J_{HO_2NO_2} + b_{26}(OH)} \tag{5.174}$$

The major difficulty in partitioning the NO_z family is that in the middle atmosphere a simple instantaneous ratio cannot describe the relationship between N_2O_5 and the other family members. This is because N_2O_5 is produced almost entirely at night, when concentrations of NO_3 are large. About 30-50% of the atmospheric NO_x is in the form of N_2O_5 at the end of a typical night in the lower stratosphere. This accumulated N_2O_5 is destroyed primarily during the day by photolysis, which produces a diurnal variation in NO and NO_2. Therefore NO, NO_2, and N_2O_5 are never really in an instantaneous stationary state; rather they achieve a diurnally changing equilibrium over the 24-hour period. A good approximation for the diurnal average steady state ratio can be derived as follows (see also, Crutzen, 1971): First, write the appropriate continuity equation for N_2O_5 averaged over 24 hours:

$$\frac{d(N_2O_5)}{dt} \approx b_{12}(M)(NO_2)_{night}(NO_3)_{night}F_d - J_{N_2O_5}(N_2O_5)F_s \tag{5.175}$$

where F_d and F_s represent the fractions of the day which are dark and sunlit, respectively. We next assume that

$$\begin{aligned}(NO_2)_{night} &= (NO_2)_{day} + (NO)_{day} \\ &\approx \left(1 + \frac{J_{NO_2} + b_3(O)}{b_4(O_3)}\right)(NO_2)_{day}\end{aligned} \tag{5.176}$$

since, as mentioned above, all the nitric oxide in the stratosphere is almost immediately converted to NO_2 at sunset (and using 5.171). Substituting for $(NO_3)_{night}$ and $(NO_2)_{night}$ with the expressions given above, and assuming steady state for N_2O_5, we obtain

$$\frac{(N_2O_5)_{avg}}{(NO_2)_{day}} = \frac{b_9(O_3)\left(1 + \frac{J_{NO_2}+b_3(O)}{b_4(O_3)}\right)F_d}{J_{N_2O_5}F_s} \tag{5.177}$$

An alternate approach is simply to integrate N_2O_5 separately from the other NO_y species. Indeed, this becomes necessary near the polar night region. In the upper stratosphere, where the lifetime of nitric acid becomes relatively short, the HNO_3/NO_2 concentration ratio can be expressed as follows, if the most important reactions are retained and heterogeneous chemical processes are neglected:

$$\frac{(HNO_3)}{(NO_2)} = \frac{b_{22}(M)(OH)}{J_{HNO_3} + b_{27}(OH)} \tag{5.178}$$

In the lower stratosphere, nitric acid is strongly influenced by transport and photochemical equilibrium conditions do not apply.

The NO_y family can be partitioned using the ratios defined above:

$$\frac{(NO_2)}{(NO_y)} = \frac{1}{1 + \frac{(N)}{(NO)} \times \frac{(NO)}{(NO_2)} + \frac{(NO)}{(NO_2)} + \frac{(NO_3)}{(NO_2)} + \frac{(HO_2NO_2)}{(NO_2)} + \frac{2\times(N_2O_5)}{(NO_2)} + \frac{(HNO_3)}{(NO_2)}} \tag{5.179a}$$

and

$$\frac{(NO)}{(NO_y)} = \frac{(NO)}{(NO_2)} \times \frac{(NO_2)}{(NO_y)} \text{ etc.} \tag{5.179b}$$

Figure 5.39 presents a model calculation of the diurnal variation of NO, NO_2, NO_3, N_2O_5, and HNO_3 at 20 and 40 km.

5.5.4 Observations of Nitrogen Species in the Stratosphere

Stratospheric nitrogen species have been measured by balloon-borne instruments since about 1970, and more recently from satellites. Most measurements have been performed by chemiluminescence techniques

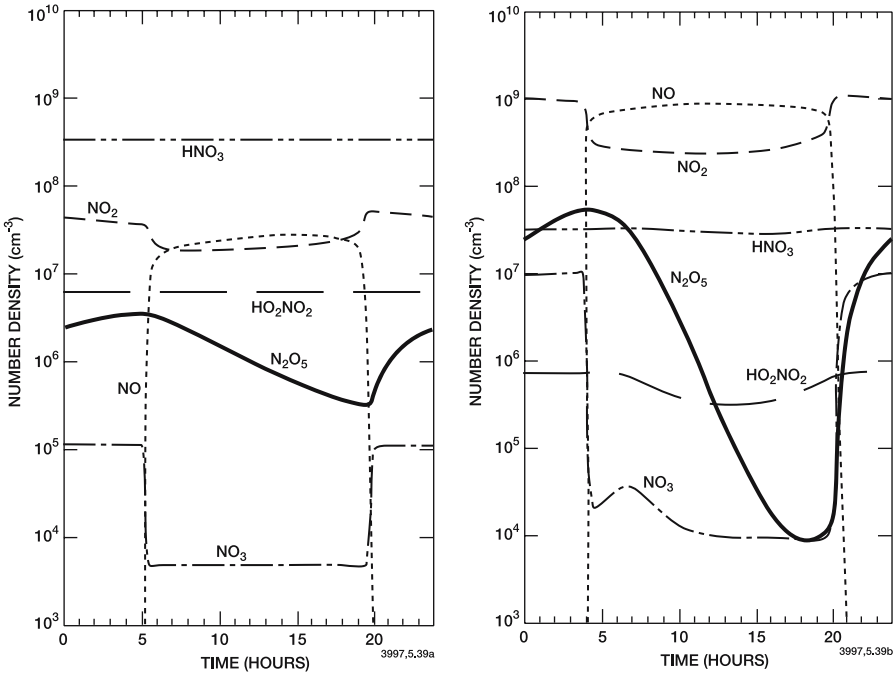

Figure 5.39. Diurnal variation of nitrogen species calculated for May 10 and 65°N at 20 km (left) and 40 km (right).

(in the case of NO, see Ridley *et al.*, 1987; Fahey *et al.*, 1989; Kondo *et al.*, 1992), mass spectroscopy (in the case of HNO_3, see Spreng and Arnold, 1994), UV-visible absorption (in the case of NO_2, see Noxon, 1979; Pommereau and Piquard, 1994; Pfeilsticker and Platt, 1994) and infrared absorption and emission (in the case of NO_2, N_2O_5, HNO_3 and $ClONO_2$, see Oelhaf *et al.*, 1994; Rinsland *et al.*, 1996). Figure 5.40 shows the vertical profile of NO, NO_2, N_2O_5, HNO_3, and $ClONO_2$ observed by a balloon-borne Fourier Transformed Infrared instrument at 35°N in early fall (Sen *et al.*, 1998).

In the case of NO, the mixing ratio increases by a factor of about 100 from 20 to 35 km, and is about 10 ppbv near 40 km. A large degree of variability is also observed, associated with atmospheric dynamics. The rapid increase of the NO mixing ratio after sunrise, as predicted from model calculations (see Figure 5.39), is seen in the measurements made by Ridley *et al.* (1977) (see Figure 5.41).

The observations of nitrogen dioxide reveal an increase in the mixing ratio with increasing altitude up to about 35 km, while above that altitude a progressive decrease is seen, reflecting the changing ratio of NO_2/NO, *e.g.*, Eq. (5.171). More recent satellite observations of NO_2 by LIMS, SAGE and UARS have provided further information, confirming

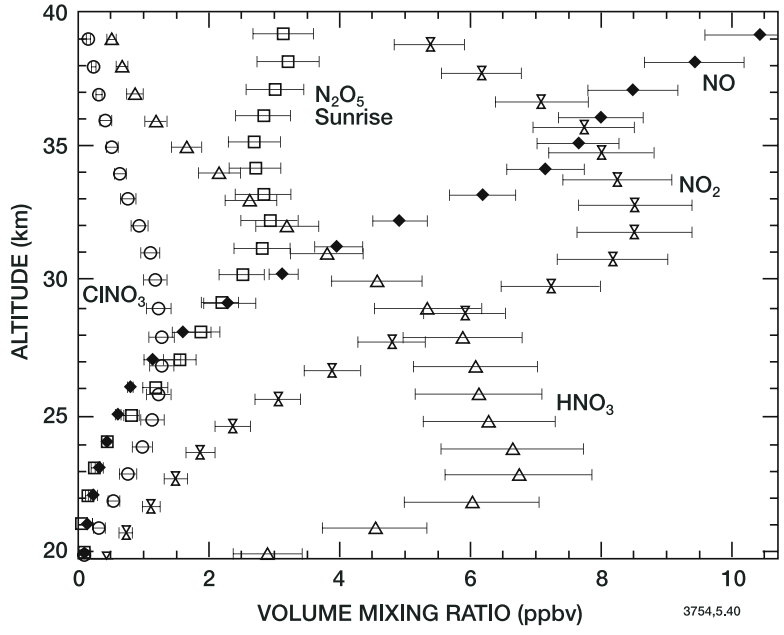

Figure 5.40. Volume mixing ratio (ppbv) of serveral nitrogen-containing species (NO, NO_2, N_2O_5, HNO_3, $ClONO_2$) measured at sunrise by a balloon-borne infrared instrument at 35°N in September 1993. Adapted from Sen *et al.* (1998).

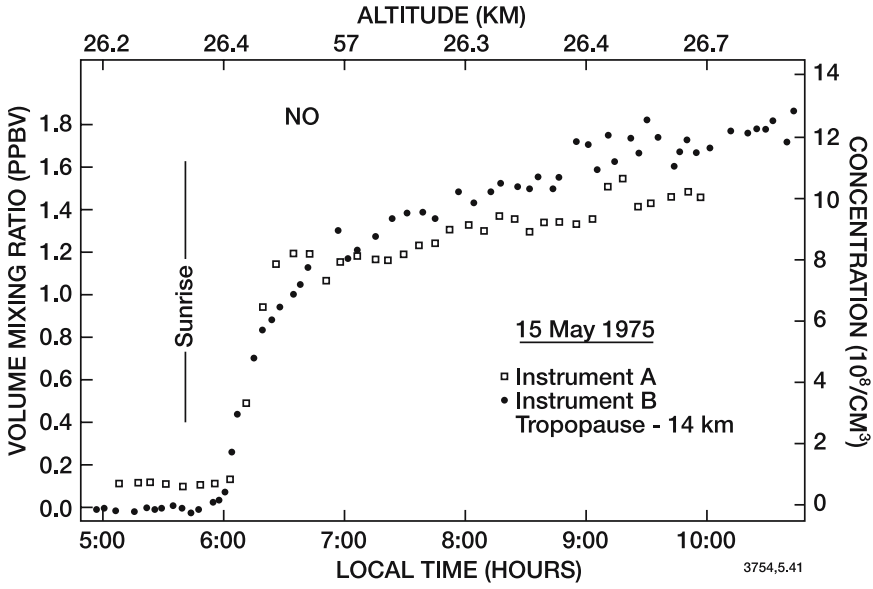

Figure 5.41. Time variation of the NO mixing ratio at about 26.5 km by Ridley *et al.* (1977).

many of the features inferred from earlier studies. Figure 5.42 shows a monthly averaged distribution of nighttime NO_2 measured by LIMS. Note the small abundances observed at low altitudes in the tropics, and the high values found at mid-latitudes in summer; the low densities seen in high latitude winter are related to the formation of N_2O_5 as discussed above. Note the tendency for the altitude of maximum abundance to decrease at higher latitudes, presumably as a result of downward transport by the mean meridional circulation.

The earliest measurements of the NO_2 total column as a function of latitude (Noxon, 1979; Noxon *et al.*, 1979; and Coffey *et al.*, 1981b) showed that the abundance of NO_2 increases with increasing latitude in summer, while in winter the abundance decreases poleward of about 40 or 50 N. As noted by Noxon (1979), very sharp gradients are often observed in the winter hemisphere (about a factor of four in total column in only 5-10 degrees of latitude), particularly at the edge of the winter polar vortex (this is sometimes referred to as the Noxon "cliff"). Plate 10 shows a satellite view of the NO_2 column in the polar region in November.

The behavior of nitrogen compounds in the polar regions and specifically the observed decrease in the abundance of NO_y observed in the vicinity of the winter vortex are the result of complex chemical and physical processes. In the polar night, NO is converted into NO_2

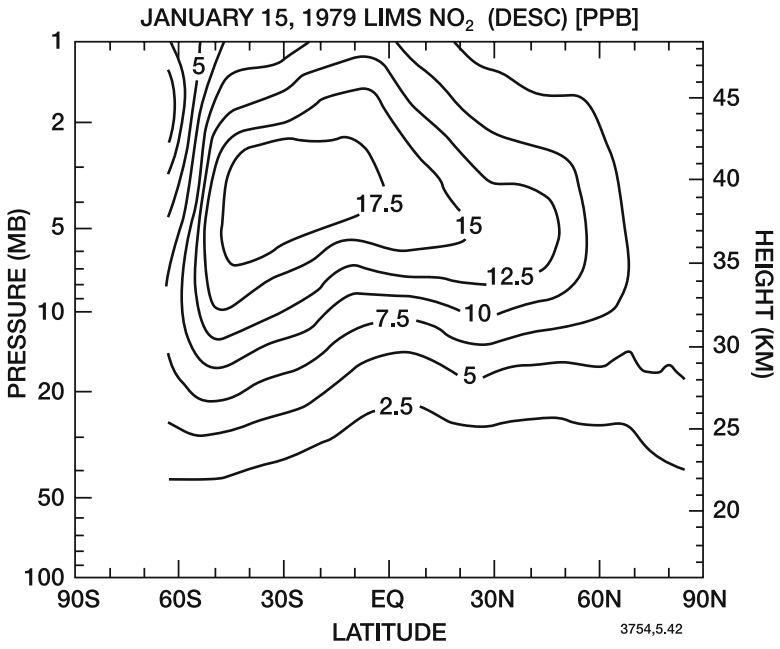

Figure 5.42. Zonally averaged distribution of nighttime NO_2 from the LIMS instrument (Nimbus 7) on 15 January 1979 (Gille, personal communication).

and further into NO_3 by reactions with ozone (see equations (5.132) and (5.141)). NO_3 then combines with NO_2 to form N_2O_5 which provides an important reservoir for nitrogen compounds in the winter hemisphere (see *e.g.*, Evans *et al.*, 1982; Solomon and Garcia, 1983). N_2O_5, however, can be rapidly converted into nitric acid by heterogeneous reaction (5.152) on the surface of sulfate aerosol particles and, if the temperature is sufficiently low, on the surface of polar stratospheric cloud particles. The gravitational sedimentation of these latter particles provides a mechanism to "denitrify" the lower polar stratosphere (*e.g.*, Fahey *et al.*, 1990). Inside the Antarctic vortex during winter and early spring, for example, the abundance of NO_y (and hence of NO, NO_2 and HNO_3) is very low. Denitrification processes are also observed occasionally in the Arctic, but are less frequent than in Antarctica since the temperature is generally somewhat higher during wintertime.

In the sunlit high latitude wintertime lower stratosphere, the photochemical lifetime of N_2O_5 is as large as a few days. This is comparable to the time scale associated with transport. In the presence of planetary wave structure, winds often flow across latitude lines, rapidly moving N_2O_5 from regions where its lifetime is long (*e.g.*, polar night) to sunlit regions where its lifetime is less than a day. Under these circumstances, the N_2O_5 content of a given air parcel is far from

local equilibrium, and carries a "memory" of where it has been traveling (Solomon and Garcia, 1983).

The nighttime distribution of NO_3 has been measured, for example, by Naudet *et al.* (1981) using stellar occultation, and the distribution is close to that predicted by theory. Its total column abundance has also been reported by Noxon *et al.* (1978), Solomon *et al.* (1989a) and by Weaver *et al.* (1996).

Nitric acid constitutes an important reservoir for odd nitrogen, particularly in the lower stratosphere where its density exceeds those of NO and NO_2. Its concentration has been measured by optical methods (for example, Murcray *et al.*, 1975) and by *in-situ* filter sampling (Lazrus and Gandrud, 1974). Recent observations by the Cryogenic Limb Array Etalon Spectrometer (CLAES) on board the UARS satellite (Roche *et al.*, 1993; 1994) are shown in Figure 5.43. The global distribution of HNO_3 has also been measured from the Space Shuttle by the CRISTA instrument (Offermann *et al.*, 1999). Most of the nitric acid is contained in the lower stratosphere, where its photochemical lifetime is relatively long (Figure 5.37), and its distribution is quite sensitive to atmospheric transport. As in the case of ozone, the nitric acid column abundance is greater at high latitudes, where its variability also increases. Note

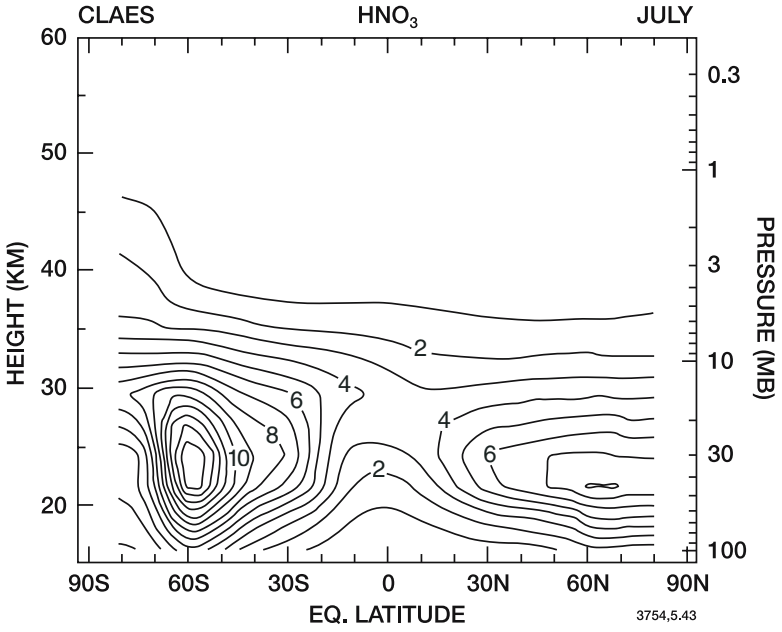

Figure 5.43. Zonally averaged (climatological) distribution of the nitric acid mixing ratio (ppbv) derived from measurements by the CLAES instrument on board UARS for July. (Courtesy of W. Randel, NCAR).

the low concentration of HNO_3 in the winter polar region of the lower stratosphere, where this compound has been removed by sedimentation of particles.

The general tendency for NO_y to increase with latitude can be qualitatively understood in terms of atmospheric transport. Like ozone, NO_y is a long-lived tracer in the lower stratosphere whose source lies in the tropical middle stratosphere. Downward and poleward transport by the meridional circulation (see Chapter 3) leads to increased total NO_y abundances towards higher latitudes, just as is found for O_3. Space observations indicate the importance of planetary waves in establishing odd nitrogen distributions in the middle atmosphere. They also suggest that odd nitrogen transport from the thermosphere to the mesosphere, and even to the stratosphere, occurs during the high latitude polar night period. This subject will be discussed in somewhat more detail in Section 5.5.7.

Figure 5.44 shows the vertical distribution of NO_y at 24°N between 20 and 55 km deduced from space observations. The maximum mixing ratio of approximately 18 ppbv is reached between 35 and 40 km altitude where the production by the oxidation of nitrous oxide is large. The decrease in the mixing ratio near and above the stratopause is associated with the mesosphere destruction through the N + NO reaction.

Simultaneous measurements of NO_y and N_2O provide a useful tool to quantify the budget of odd nitrogen in the stratosphere. Observations (Loewenstein *et al.*, 1993; Kondo *et al.*, 1996) show that there is often a tight linear anticorrelation between these two compounds (see Figure 5.45), confirming that N_2O is the dominant source of NO_y and that there is no efficient removal process for NO_y in most parts of the stratosphere. Deviations from this relationship found, for example, in the lower polar stratosphere suggest that NO_y is removed from this region of the atmosphere by sedimentation of nitrate-containing particles (Fahey *et al.*, 1990). The departure from the linear NO_y-N_2O relationship for low N_2O concentrations (upper stratosphere) is another manifestation of the N + NO reaction (Kondo *et al.*, 1996; Chang *et al.*, 1996).

5.5.5 Odd Nitrogen Chemistry in the Lower Thermosphere and Mesosphere

In the thermosphere, atomic nitrogen can be formed by dissociation of N_2, either through the effects of solar radiation or of energetic particles. The determination of the magnitude of this production (and

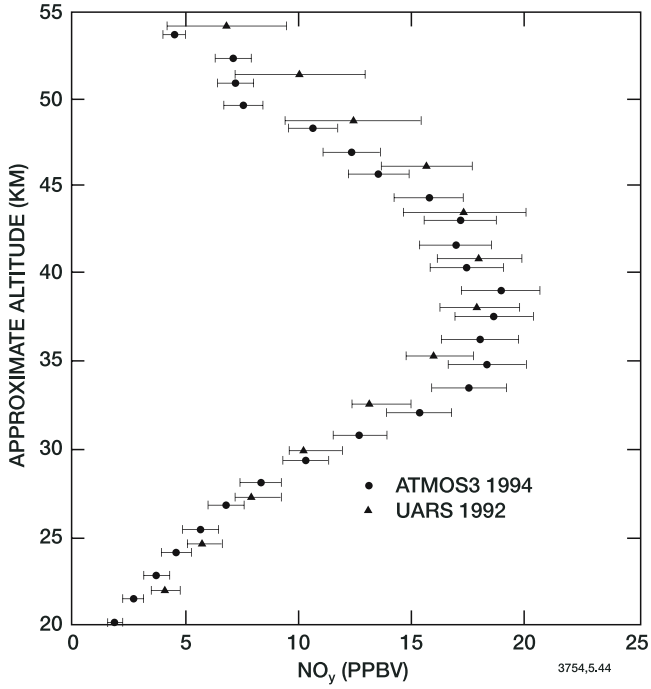

Figure 5.44. Mixing ratio of odd nitrogen (NO_y) as a function of altitude measured in November by ATMOS and UARS instruments at 24°N. The figure illustrates the role of NO photolysis parameterizations (see Nevison *et al.*, 1997).

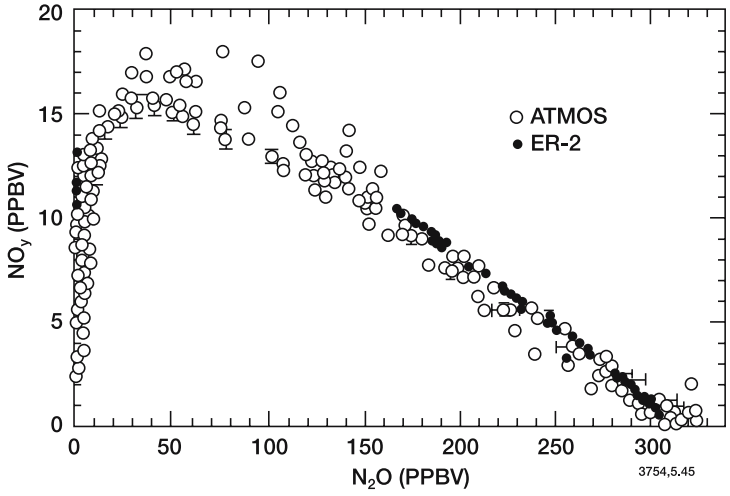

Figure 5.45. Correlations of NO_y with N_2O concentrations measured from ATMOS aboard the Space Shuttle and instruments aboard the ER-2 high altitude aircraft. Adapted from Chang *et al.* (1996).

its variability with solar activity) are presented in Chapter 7. We note here, however, that atomic nitrogen can be produced either in the ground ^{4}S or the excited ^{2}D state by these processes. N(^{2}D) reacts rapidly with molecular oxygen:

$$(b_7^*); \qquad N(^2D) + O_2 \rightarrow NO + O \tag{5.180a}$$

or is de-activated by quenching with atomic oxygen

$$(b_Q); \qquad N(^2D) + O \rightarrow N(^4S) + O \tag{5.180b}$$

while the ground N(^{4}S) state reacts much more slowly, and the rate of its reaction depends strongly on temperature:

$$(b_7); \qquad N(^4S) + O_2 \rightarrow NO + O \tag{5.139}$$

A reaction with OH also converts N(^{4}S) to NO:

$$(b_{7a}); \qquad N(^4S) + OH \rightarrow NO + H \tag{5.181}$$

Photodissociation of nitric oxide mostly in the δ-bands (see Chapter 4), initiates the primary loss process for odd nitrogen in the middle atmosphere:

$$(J_{NO}); \qquad NO + h\nu \rightarrow N(^4S) + O \tag{5.138}$$

because it leads to the formation of an N(^{4}S) atom, which can then react with NO in a so-called "cannibalistic reaction"

$$(b_6); \qquad N(^4S) + NO \rightarrow N_2 + O \tag{5.140}$$

wherein two odd nitrogen particles are destroyed. The following kinetic equations can be written for mesospheric and thermospheric conditions:

$$\frac{d(N^4S)}{dt} + [b_6(NO) + b_7(O_2) + b_{7a}(OH)]\,(N^4S) = J_{NO}(NO) + b_Q(O)(N^2D) + P(N^4S) \tag{5.182}$$

$$\frac{d(N^2D)}{dt} + b_7^*(O_2) + b_Q(O)(N^2D) = P(N^2D) \tag{5.183}$$

$$\frac{d(NO)}{dt} + \Big[b_4(O_3) + a_{26}(HO_2) + c_5(CH_3O_2) + d_4(ClO) + b_6(N^4S) + J_{NO}\Big]\,(NO) = [J_{NO_2} + b_3(O)]\,(NO_2) + b_7^*(O_2)(N^2D) + [b_7(O_2) + b_{7a}(OH)]\,(N^4S) + P(NO) \tag{5.184}$$

or, considering Eq. (5.171),

$$\frac{d(NO)}{dt} + \Big[b_6(N^4S) + J_{NO}\Big]\,(NO) = b_7^*(O_2)(N^2D) + [b_7(O_2) + b_{7a}(OH)]\,(N^4S) + P(NO) \tag{5.185}$$

The rate of production, $P(N^4S)$ and $P(N^2D)$ is discussed in Chapter 7 and involves ionization and dissociation of molecular nitrogen by high energy particles and by shortwave solar radiation. P(NO) is given by Equation (5.128).

5.5.6 The Odd Nitrogen Family in the Lower Thermosphere and Mesosphere

The lifetime of atomic nitrogen is short throughout the middle atmosphere, and steady-state conditions may therefore be assumed for $N(^2D)$ and $N(^4S)$. Thus, for example, the concentration of atomic nitrogen in the ground state (which far exceeds the concentration of N in the electronically excited ^2D state) is given by:

$$(N^4S) = \frac{J_{NO}(NO) + P(N^4S) + b_Q(O)(N^2D)}{b_6(NO) + b_7(O_2) + b_{7a}(OH)} \tag{5.186}$$

This reduces approximately to

$$(N^4S) \approx \frac{J_{NO}(NO) + P(N^4S)}{b_6(NO) + b_7(O_2)} \tag{5.187}$$

If, again, we define the *odd nitrogen* (NO_y) family as

$$(NO_y) = (N^4S) + (N^2D) + (NO) + (NO_2) + (NO_3)$$
$$+ 2(N_2O_5) + (HNO_3) + (HO_2NO_2)$$

which reduces essentially to

$$(NO_y) = (NO) + (NO_2)$$

in the upper stratosphere, and to

$$(NO_y) = (NO) + (NO_2) + (N)$$

in the mesosphere and lower thermosphere, we find by adding the equations of continuity for all of the reactive nitrogen species

$$\frac{d(NO_y)}{dt} + 2b_6(N^4S)(NO) = P(N^2D) + P(N^4S) + P(NO) \tag{5.188}$$

In the lower thermosphere and mesosphere, we may define R as follows:

$$R = \frac{(NO_y)}{(NO)} \approx 1 + \frac{(NO_2)}{(NO)} + \frac{(N^4S)}{(NO)}$$

The value of this factor can be obtained by examination of the continuity equations for each species. Considering transport, and substituting for

$N(^4S)$ with Eq. (5.187), we find

$$\frac{\partial(NO_y)}{\partial t} + \nabla \cdot \boldsymbol{\phi}(NO_y) + \frac{2b_6 J_{NO}(NO_y)^2}{R(b_6(NO_y) + Rb_7(O_2))} = P(NO) + P(N^2D) + \left(\frac{Rb_7(O_2) - b_6(NO_y)}{Rb_7(O_2) + b_6(NO_y)}\right) P(N^4S) \quad (5.189)$$

5.5.7 Observations of Nitric Oxide in the Thermosphere and Mesosphere

Figure 5.46 displays early observations of NO in the thermosphere and mesosphere. The observed variability indicates the strong sensitivity of NO to dynamic processes in the atmosphere, as one might expect based on the comparison between its photochemical lifetime and the time constant for dynamics in this region (see Figure 5.37). The observed minimum near the mesopause is due to the photodissociation of NO and its subsequent recombination with $N(^4S)$. The depth of the minimum depends on the competition between downward transport and this photochemical loss. Its variability as depicted in the figure is probably related to both seasonal and short term temporal variations in mesospheric transport parameters.

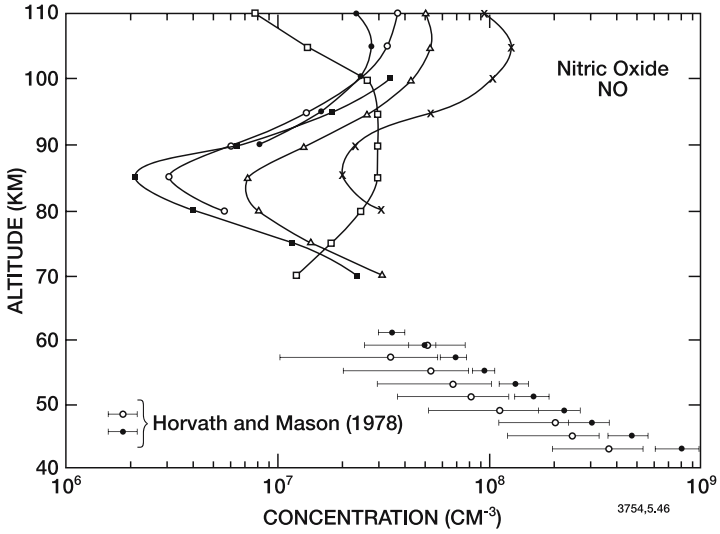

Figure 5.46. Observations of nitric oxide from 40 to 110 km altitude. In the lower part, the values of Horvath and Mason are shown, while at higher altitudes, the observations include those of Meira (1971), Tisone (1973), Tohmatsu and Iwagami (1975, 1976), Witt *et al.* (1976), and Baker *et al.* (1977).

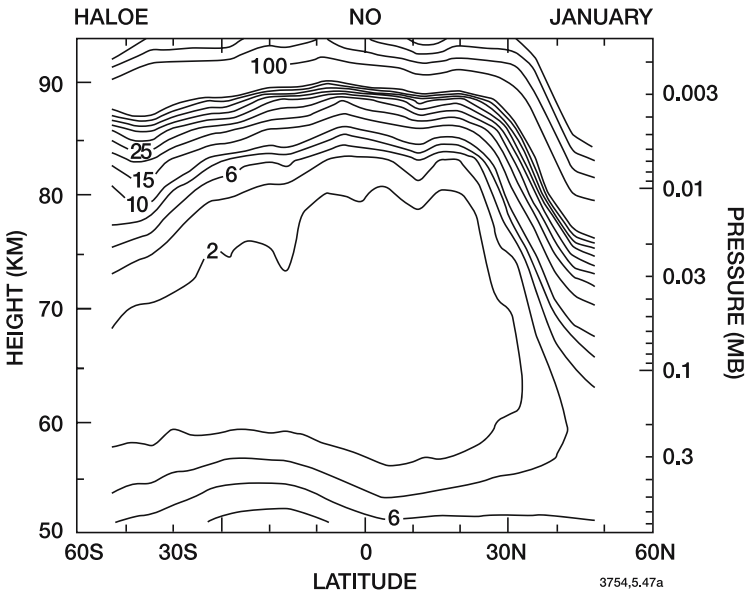

Figure 5.47a. Meridional distribution of the NO mixing ratio (ppbv) derived from the UARS/HALOE instrument in the mesosphere.

In the mesosphere, NO provides the primary source of electrons during geomagnetically quiet conditions, and is responsible for the formation of the ionospheric D-region. This will be discussed in detail in Chapter 7.

Figure 5.47a shows a distribution of NO in the mesosphere and upper stratosphere obtained by HALOE on UARS. The calculated variations with respect to latitude reflect the influence of solar elevation on odd nitrogen destruction, and of spatial variability in transport processes. Note the large NO densities in the high latitude winter stratosphere, particularly near the polar night, where there is virtually no photochemical loss of odd nitrogen (because J_{NO} is zero there). Models show that these high NO concentrations result from the production of odd nitrogen in the thermosphere and its transport down to the mesosphere and stratosphere at these latitudes (see, *e.g.*, Frederick and Orsini, 1982; Solomon *et al.*, 1982; Brasseur, 1982; Siskind *et al.*, 1997; Marsh and Roble, 2002).

Figures 5.47b and c show the concentration of NO observed by the Student Nitric Oxide Explorer (SNOE) in the lower thermosphere on 2 specific days corresponding to low and high auroral activity, respectively (Barth *et al.*, 1999; Solomon *et al.*, 1999). In both cases, the NO density reaches a maximum near 110 km altitude. The value of this maximum in the tropics is correlated with the intensity of solar soft X-rays (2-10 nm) during low geomagnetic activity (Barth *et al.*, 1999). At high latitudes,

the NO density varies considerably (typically a factor 3-5) with auroral activity. Auroral NO is generated by direct particle impact (dissociation of N_2 into excited nitrogen atoms) and by heating resulting from ion-neutral collisions (that accelerates the conversion of N atoms into NO) (Solomon *et al.*, 1999).

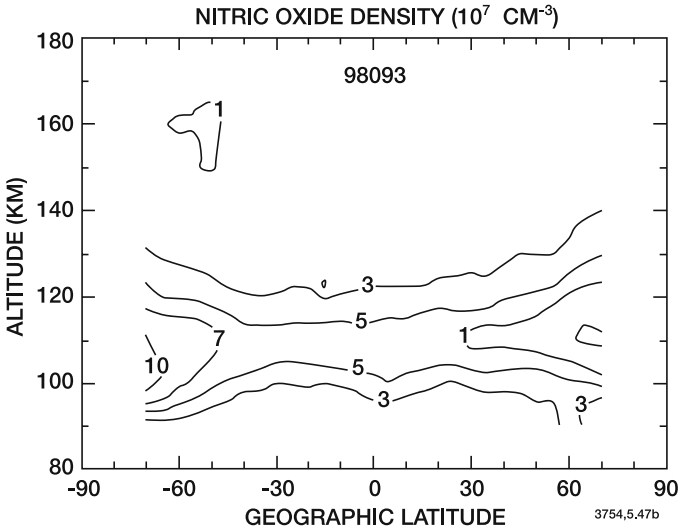

Figure 5.47b. Nitric oxide daily averaged density ($10^7 \mathrm{cm}^{-3}$) measured by the SNOE satellite (Solomon *et al.*, 1999) in the lower thermosphere. Low auroral activity.

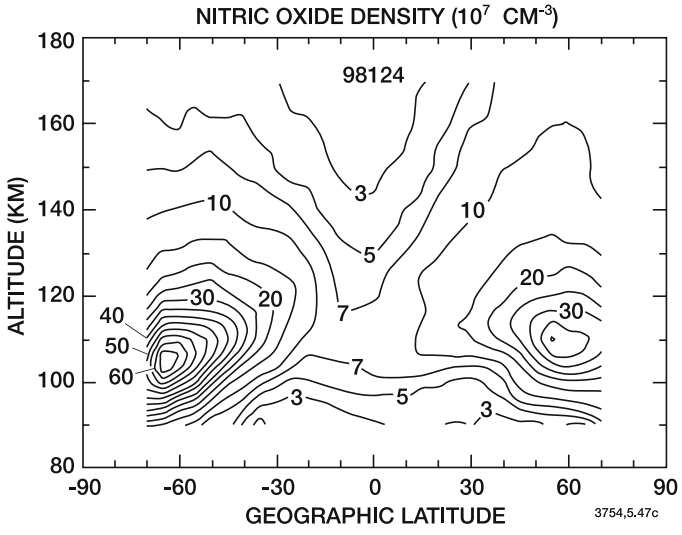

Figure 5.47c. Same as Figure 5.47b but for high auroral activity.

The HALOE and SNOE observations also show the dynamic behavior of the nitrogen oxides at different heights (Plate 11). For example, above 100 km altitude, the NO concentration is characterized by a strong seasonal component associated with solar energy input. At 97 km, the evolution of the NO concentration is primarily influenced by the intensity of the atmospheric tides. The vertical wind produced by the migrating diurnal tides can induce factor 2 changes over 12 hours in the mixing ratio of NO at the equator (Marsh and Russell, 2000).

5.6 Halogen Compounds

The presence of halogens (chlorine, fluorine, bromine and perhaps iodine) in the middle atmosphere results from the upward transport from the troposphere of halocarbons which are released at the Earth's surface as a results of natural or anthropogenic processes. These compounds break up in the stratosphere and release halogen atoms.

Once released in the middle atmosphere, fluorine, chlorine and bromine atoms react rapidly with ozone to form FO, ClO and BrO. Further reactions, which will be presented in the following sections, lead to efficient catalytic destruction of odd oxygen via ClO and BrO.

It is useful to stress that chemical partitioning processes play a major role in halogen-catalyzed ozone destruction that is dramatically illustrated by the contrasts between the gas-phase chemistry of different halogen species shown in simplified form in Figure 5.56. Briefly, the halogen atoms released in the stratosphere from chloro- bromo- and fluorocarbon source gases can form acids (through abstraction of a hydrogen atom) and nitrates (through reaction with NO_2). In the case of fluorine, the acid HF is quickly formed and so tightly bound that essentially all fluorine released from fluorine source gases in the stratosphere is irreversibly and rapidly 'neutralized' as HF (Rowland and Molina, 1975; Stolarski and Rundel, 1975; Sze, 1978). The amount of atomic fluorine and FO available to participate in ozone-destroying catalytic cycles (or, in chemical terms, the catalytic chain length, see Johnston and Podolske, 1978) is therefore extremely low and fluorine has a negligible impact on ozone. Chlorine forms both HCl (Stolarski and Cicerone, 1974) and $ClONO_2$ reservoirs (Rowland *et al.*, 1976). Unlike HF, these gases can be reconverted to chlorine atoms by gas-phase stratospheric chemistry (*i.e.*, by reaction with OH and photolysis, respectively). The amount of Cl and ClO available to participate in ozone-destroying catalytic chemistry therefore is critically dependent on the partitioning of chlorine between these 'active' chlorine radicals

and the non-ozone-destroying 'reservoirs', HCl and $ClONO_2$. The rates of chemical formation and destruction of the reservoirs control this partitioning. Bromine is less tightly bound than chlorine, so that relatively little of the bromine released from bromocarbons is tied up in HBr and $BrONO_2$, rendering this atom quite effective for ozone loss in the lower stratosphere (Wofsy *et al.*, 1975; Yung *et al.*, 1980; Lary, 1996; Daniel *et al.*, 1999), especially in combination with chlorine (Tung *et al.*, 1986; McElroy *et al.*, 1986). Although each bromine atom released in the stratosphere is about 50 times more effective than chlorine, the contemporary abundances of total man-made stratospheric bromine are about 300 times smaller than those of chlorine (*e.g.*, Schauffler *et al.*, 1993; Wamsley *et al.*, 1998). Iodine may also participate in ozone-destroying catalytic cycles with bromine and chlorine (Solomon *et al.*, 1994), but its stratospheric abundance is believed to be much smaller than either those of bromine and chlorine, and its primary sources are believed to be natural rather than largely or partly man-made as in the case of fluorine, chlorine, and bromine.

The effect of the polar stratospheric clouds, which form during winter when the temperature decreases below a threshold of approximately 190 K, is to convert chlorine reservoirs (HCl and $ClONO_2$) back to reactive chlorine through heterogeneous processes that occur on the surface of the cloud particles. This activation of chlorine (and analogous reactions for bromine) leads to rapid ozone depletion at high latitudes after the return of solar light in late winter/early spring. These processes explain the formation of the Antarctic ozone hole in September/October and the large depletion of ozone observed in the Arctic during cold winters. Heterogeneous reactions occurring on the surface of cold sulfate aerosol particles in the stratosphere also lead to chlorine activation and ozone destruction. This effect is considerably amplified after large volcanic eruptions (such as the eruption of Mount Pinatubo in 1991) when the aerosol load in the stratosphere can be enhanced by several orders of magnitude.

The next sections present more details about the photochemical processes affecting halogens in the middle atmosphere, and highlight their relations with other chemical families. Chapter 6 contains a detailed review of ozone depletion by these gases.

5.6.1 Sources of Inorganic Halogens

Numerous chlorine, fluorine, and bromine-containing compounds (halocarbons) are produced at the Earth's surface, both by natural and

industrial processes. Fully halogenated molecules are especially stable, and nearly insoluble in water so they do not rain out to any significant degree. The halocarbons are transported to the stratosphere where they are photo-decomposed (by short-wave solar radiation) and constitute the main source of inorganic halogen species. *Methyl chlorine* (CH_3Cl) is a compound with natural sources, including the oceans, but it is also produced by combustion of biomass, especially in tropical agriculture. Its destruction results mainly from reaction with the hydroxyl radical in the troposphere, but due to its relatively long lifetime (1.5 years), significant amounts of this gas penetrate into the stratosphere, where photolysis becomes another important loss mechanism. Because the anthropogenic contribution to CH_3Cl emissions is small, methyl chloride should be regarded as the largest natural source of inorganic chlorine in the middle atmosphere. Its mixing ratio at the surface is about 600 pptv, while those of the industrial compounds represented about 3 ppbv (3000 pptv) as of 1992 (see Schauffler *et al.*, 1993).

Methyl bromide (CH_3Br), which is also released by the ocean (Singh *et al.*, 1983) and produced by biomass burning (Manõ and Andreae, 1994), is believed to be the largest bromine reservoir in the atmosphere, with surface mixing ratios of typically 9 pptv in the southern hemisphere and 11 pptv in the northern hemisphere. Its lifetime against destruction by OH in the troposphere and uptake by the ocean is of the order of 8 months, so that significant amounts of CH_3Br are transported to the stratosphere where photodecomposition leads to the formation of inorganic bromine. A significant amount of methyl bromide is also produced for agricultural purposes, specifically as a pre-planting and post-harvesting fumigant.

Methyl iodide (CH_3I) is produced by marine algae and phytoplankton in the ocean and probably also by biomass burning. Its lifetime in the atmosphere is only a few days, so that its transport to the stratosphere should occur only during strong convective events (Solomon *et al.*, 1994). The surface mixing ratio of CH_3I is typically a few pptv in the boundary layer with values reaching 10-20 pptv over highly productive regions of the ocean. An estimated budget of natural halocarbons is given in Table 5.8.

While many natural processes produce chlorine at ground level (including for example, sea salt and volcanic emissions of HCl), these compounds are efficiently removed in precipitation (rain and snow) due to high solubility. The removal of HCl emitted, for example, in volcanic plumes (which contain a great deal of water and hence form rain) is extremely efficient (see, *e.g.*, Tabazadeh and Turco, 1993). This renders even the most explosive volcanic plumes ineffective at providing significant inputs of chlorine to the stratosphere. Observations

Table 5.8 Estimated Budgets of CH_3Cl, CH_3Br, and CH_3I (After Brasseur *et al.*, 1999)

	CH_3Cl (Tg yr^{-1})	CH_3Br (Tg yr^{-1})	CH_3I (Tg yr^{-1})
Typical surface mixing ratio (pptv)	650	10	2
Sources			
Biomass burning source	0.7	0.01-0.05	-
Ocean source	0.4	∼0.03	1-2
Terrestrial ecosystems	0.1	-	-
Anthropogenic source	0.05	0.02-0.06	-
TOTAL SOURCES	∼1.2	∼0.05-0.15	∼1.5
Loss to soils	0.1	0.01-0.07	-
Atmospheric loss	≃3	0.06-0.11	≃5
Atmospheric lifetime	1.5 years	1.3 years	5 days

of limited or even unobservable changes in HCl after the eruptions of the El Chichón and Mt. Pinatubo volcanoes in 1981 and 1991 demonstrates this effect (Mankin *et al.*, 1992 and Wallace and Livingston, 1992).

Over recent decades, the global budget of halogens has been considerably modified by the increasingly large industrial production of *chlorofluorocarbons* (CFC's). These chlorine and fluorine-containing compounds, which are generally very stable in the atmosphere (10-100 years lifetime), have been used extensively as refrigerants (CFC-11, -12, -114), solvents (CFC-113), inflating agents (CFC-11, -12) in the manufacturing of foams, and as aerosol propellants. Other organic agents such as *methyl chloroform* (CH_3CCl_3) are also used as solvents, while bromine-containing *halons* (*e.g.*, $CBrClF_2$, $CBrF_3$) are used as fire retardants. It is estimated that, in the mid-1990s, approximately 75-85% of stratospheric chlorine was of anthropogenic origin with a total CFC emission of approximately 1 Tg yr^{-1}. Because of the threat to the ozone layer, CFC's, methyl chloroform, carbon tetrachloride, and the halons have been gradually phased out as a result of international agreements (Montreal Protocol in 1987 and subsequent amendments; see Chapter 6), and replaced by *hydrochlorofluorocarbons* (HCFC's) and *hydrofluorocarbons* (HFC's). The contribution of the HCFC-substitute compounds to ozone depletion is limited by the fact that they are partly destroyed by the OH radical in the troposphere. Observations have

confirmed that the temporal trends in global surface-level abundances of chlorofluorocarbons are consistent with the known industrial emissions (*e.g.*, Montzka *et al.*, 1996a; Prinn *et al.*, 1995; WMO/UNEP, 1985; 1991; 1995; 1999), both in terms of the buildup of these gases in past decades and the slower accumulation in the 1990s following reductions in global use. The HFC's do not contain chlorine atoms at all. However, all organic halogen compounds absorb infrared radiation, and hence contribute to greenhouse warming. Taken together, their current radiative forcing is estimated at 0.34 Wm^{-2} (IPCC, 2001). Table 5.9 provides a list of the major halocarbons with estimated surface concentrations in the 1990s and calculated atmospheric lifetimes, while Figure 5.48 shows a zonally averaged distribution of CFC-12 derived from the observations by CLAES on board UARS (Nightingale *et al.* 1996). Global distributions of CFC-11 observed by the spaceborne CRISTA instrument have been reported by Riese *et al.* (1999). Note that, as a result of measures taken to reduce or phase-out the production of the most harmful halocarbons, the concentration of inorganic chlorine and bromine is expected to decrease in the future. This downward trend, however, should be slow due to the long residence time of these chemical species in the atmosphere. Models suggest that the level of chlorine in the stratosphere should fall below the levels at which ozone depletion first became observable (about 2 ppbv) around the year 2050.

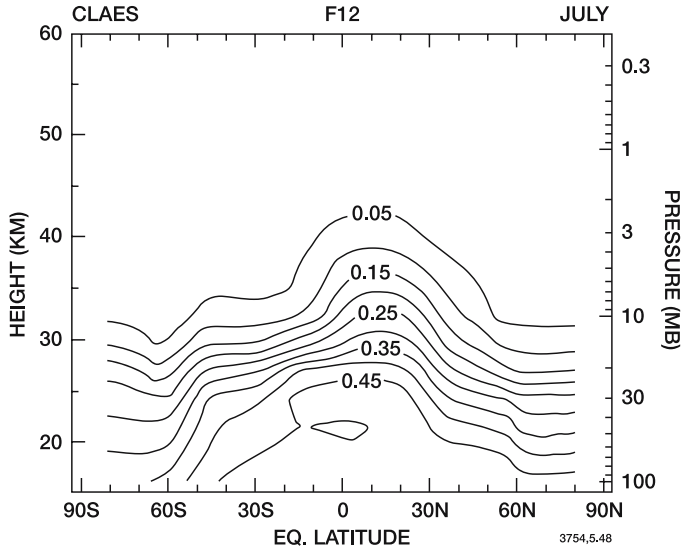

Figure 5.48. Meridional distribution of CFC-12 (CF_2Cl_2) provided by CLAES (on board the UARS satellite). Mixing ratio values (in ppbv) representative of July (Courtesy of W. Randel, NCAR).

Table 5.9 Abundances and Lifetimes of Halogenated Organic Source Gases (Adapted from Brasseur *et al.*, 1999)

Molecule	*Concentration* (ppt) 1990[1]	1992[2]	1995[3]	*Lifetime*[2] *(years)*
CF_2Cl_2 (CFC 12)	474-479	503	532	102
$CFCl_3$ (CFC 11)	254-263	268	272	50±5
$CF_2ClCFCl_2$ (CFC 113)	71-75	82	84	85
CF_2ClCF_2Cl (CFC 114)	15-20	20		300
CF_3CFCl_2 (CFC 114a)	5			≃400
CF_3Cl (CFC 13)	5			640
CCl_4 (CFC 10 or carbon tetrachloride)	107	106[3]	103	42
CH_3CCl_3 (methylchloroform)	140[3]	135[3]	109	5.4±0.4
CHF_2Cl (HCFC 22)	90[5]	102[5]	117	13.3
CH_3Cl (methyl chloride)	600	600	∼550	1.5
$CHCl_3$ (chloroform)	15			0.6
CH_2Cl_2 (dichloromethane)	30			0.4
CCl_2CCl_2 (tetrachloroethane)	10			0.3
CH_2ClCH_2Cl (dichloroethane)	35			
$CHClCCl_2$ (trichloroethane)	2-3			0.01
CH_3Br (methyl bromide)	10-15			1.3
CH_2Br_2 (dibromomethane)	0.5-3			0.5
$CHBr_3$ (bromoform)	0.2-0.3			∼0.06
CH_2ClBr	1-2			
$CHClBr_2$	1			
$CHCl_2Br$	1			
$C_2H_4Br_2$ (ethylene dibromide)	<1			
C_2H_5Br (ethyl bromide)	2-3			
CF_2ClBr (H 1211)	1.2-2.2			20
CF_3Br (H 1301)	1.7-2.5			65
CH_3I (methyl iodide)	≈1-10			0.01
CH_3CFCl_2 (HCFC-141b)		0.3	3.5	9.4
CH_3CF_2Cl (HCFC-142b)		3.5	7.0	19.5
CF_3CH_2F (HFC-134a)		0.3[6]	1.73[6]	14
Total Cl/Br	3800/30			

(1) Kaye *et al.*, 1994
(2) WMO, 1995
(3) Montzka *et al.*, 1996a
(4) WMO, 1992
(5) Montzka *et al.*, 1993
(6) Montzka *et al.*, 1996b

Sulfur hexafluoride (SF_6), a fluorine-containing gas released by high voltage electrical equipment (*e.g.*, powerplants) and emitted by metallurgy facilities, is not a signifcant source of inorganic fluorine in the atmosphere. Its abundance is small (a few pptv), but has been growing rapidly (*i.e.*, 7%/yr) in recent decades. This gas, which is photochemically destroyed only above 70 km altitude and hence has a lifetime of 800 to 3200 years (see Maiss *et al.*, 1996), is of particular interest because it can be used to estimate the mean age of air after it penetrates into the stratosphere (see Chapter 3).

5.6.2 Halogen Chemistry

5.6.2.1 Chlorine

The natural production of chlorine atoms in the stratosphere is provided by the destruction of methyl chloride, either by photolysis

$$(J_{CH_3Cl}) \ ; \qquad CH_3Cl + h\nu \rightarrow CH_3 + Cl \tag{5.190}$$

or by reaction with the hydroxyl radical

$$(d_0) \ ; \qquad CH_3Cl + OH \rightarrow CH_2Cl + H_2O \tag{5.191}$$

A major source of anthropogenic chlorine currently results from the photolysis of chlorofluorocarbons and other chlorocarbons in the stratosphere. In the case of $CFCl_3$ (also called chlorofluorocarbon-11 or CFC-11) the most likely degradation scheme is the following:

$$CFCl_3 + h\nu\,(\lambda < 226 \text{ nm}) \rightarrow CFCl_2 + Cl \tag{5.192a}$$
$$CFCl_2 + O_2 + M \rightarrow CFCl_2O_2 + M \tag{5.192b}$$
$$CFCl_2O_2 + NO \rightarrow CFCl_2O + NO_2 \tag{5.192c}$$
$$CFCl_2O + M \rightarrow COFCl + Cl + M \tag{5.192d}$$
$$COFCl + h\nu \rightarrow FCO + Cl \tag{5.192e}$$

Following this chain, three chlorine atoms are released. Similar reaction paths apply to other chlorofluorocarbons including CFC-12. In this case, the primary destruction mechanism is

$$CF_2Cl_2 + h\nu\,(\lambda < 215 \text{ nm}) \rightarrow CF_2Cl + Cl \tag{5.193}$$

A secondary destruction path is provided by the reaction with the electronically excited oxygen atom $O(^1D)$. For example, in the case of CFC-12,

$$CF_2Cl_2 + O(^1D) \rightarrow CF_2Cl + ClO \tag{5.194}$$

Other channels are possible and could produce Cl or Cl_2. The importance of the degradation of industrially manufactured chloro-

fluorocarbons as a source of stratospheric chlorine (with potential impact on ozone) was first noted by Molina and Rowland (1974a) and Rowland and Molina (1975). Other significant sources of anthropogenic chlorine include the photolysis of carbon tetrachloride

$$(J^{a}_{CCl_4}) \; ; \qquad CCl_4 + h\nu \rightarrow CCl_3 + Cl \tag{5.195a}$$

$$(J^{b}_{CCl_4}) \; ; \qquad CCl_4 + h\nu \rightarrow CCl_2 + Cl_2 \tag{5.195b}$$

and of methyl chloroform

$$(J_{CH_3CCl_3}) \; ; \qquad CH_3CCl_3 + h\nu \rightarrow CH_3CCl_2 + Cl \tag{5.196}$$

This latter compound can also react with the hydroxyl radical

$$(d_1) \; ; \qquad CH_3CCl_3 + OH \rightarrow CH_2CCl_3 + H_2O \tag{5.197}$$

Further processes lead to the release of chlorine atoms.

The increasing use of hydrochlorofluorocarbons could significantly affect the stratospheric budget of chlorine. For example, reactive chlorine is released following the photolysis of HCFC-22

$$(J_{CF_2HCl}); \qquad CF_2HCl + h\nu \rightarrow \text{products} \tag{5.198}$$

and its oxidation by OH

$$(d_{1a}); \qquad CF_2HCl + OH \rightarrow CF_2Cl + H_2O \tag{5.199}$$

Assuming that the intermediate photolysis products are eventually completely dissociated in the stratosphere and neglecting destruction reactions with $O(^1D)$, we can write to a good approximation:

$$\begin{aligned} P_{Cl} = {} & 4J_{CCl_4}(CCl_4) + 3J_{CFCl_3}(CFCl_3) + 2J_{CF_2Cl_2}(CF_2Cl_2) \\ & + [J_{CH_3Cl} + d_0(OH)]\,(CH_3Cl) \\ & + 3\,[J_{CH_3CCl_3} + d_1(OH)]\,(CH_3CCl_3) \\ & + [J_{CF_2HCl} + d_{1a}(OH)]\,(CF_2HCl) \end{aligned} \tag{5.200}$$

When a chlorine atom is produced in the stratosphere, it is converted to chlorine monoxide mainly by ozone:

$$(d_2); \qquad Cl + O_3 \rightarrow ClO + O_2 \tag{5.201}$$

and, to a lesser extent, by HO_2

$$(d_{33}); \qquad Cl + HO_2 \rightarrow ClO + OH \tag{5.202}$$

Chlorine monoxide undergoes two principal reactions during the daytime, one of them with atomic oxygen (mostly in the upper stratosphere and mesosphere)

$$(d_3); \qquad ClO + O \rightarrow Cl + O_2 \tag{5.203}$$

and a second with NO (mostly in the lower stratosphere)

$$(d_4); \qquad ClO + NO \rightarrow Cl + NO_2 \tag{5.133}$$

These reactions reform atomic chlorine. The reaction between ClO and NO represents an important coupling between the chlorine and nitrogen cycles, and the pair of reactions (5.201) and (5.203) constitutes an important catalytic cycle which destroys odd oxygen (primarily in the upper stratosphere).

The photodissociation of ClO

$$(J_{ClO}); \qquad ClO + h\nu \rightarrow Cl + O \tag{5.204}$$

and conversion of ClO to Cl by OH

$$(d_8); \qquad ClO + OH \rightarrow Cl + HO_2 \tag{5.205}$$

play a secondary role. However, this latter reaction has a small efficiency to produce hydrogen chloride HCl (5-7%)

$$(d_{46}); \qquad ClO + OH \rightarrow HCl + O_2 \tag{5.206}$$

This channel reduces significantly the calculated ClO/HCl ratio in the upper stratosphere and, hence, the sensitivity of ozone to chlorine. There are also other slow processes that yield hydrogen chloride. Like HNO_3, HCl provides a relatively inert reservoir which sequesters a photochemically active species and hence reduces the rate of its catalytic reaction with odd oxygen.

$$(d_5); \qquad Cl + CH_4 \rightarrow CH_3 + HCl \tag{5.48}$$

$$(d_6); \qquad Cl + H_2 \rightarrow H + HCl \tag{5.207}$$

$$(d_7); \qquad Cl + HO_2 \rightarrow O_2 + HCl \tag{5.208}$$

$$(d_8); \qquad Cl + H_2O_2 \rightarrow HO_2 + HCl \tag{5.209}$$

$$(d_{10}); \qquad Cl + CH_2O \rightarrow HCO + HCl \tag{5.64}$$

Reaction (5.48) is generally the most important of these, although (5.208) plays a substantial role in the upper stratosphere. HCl can be destroyed by reaction with OH, $O(^1D)$, and $O(^3P)$ to yield a chlorine atom:

$$(d_{11}); \qquad HCl + OH \rightarrow H_2O + Cl \tag{5.210}$$

$$(d_{25}); \qquad HCl + O(^1D) \rightarrow OH + Cl \tag{5.211}$$

$$(d_{12}); \qquad HCl + O(^3P) \rightarrow OH + Cl \tag{5.212}$$

Laboratory studies (Wine *et al.*, 1986) suggest that the reaction between HCl and $O(^1D)$ leads mainly to the formation of OH and Cl, but that a channel producing H and ClO is also significant. Photolysis must also be considered:

$$(J_{HCl}); \qquad HCl + h\nu\,(\lambda < 220nm) \rightarrow H + Cl \tag{5.213}$$

Finally, HCl is soluble in water, and can therefore be removed from the atmosphere in cloud processes.

To end this brief discussion on the reactions of chlorine species, we must consider the formation of other constituents such as ClOO, OClO, $ClONO_2$, HOCl, etc. Chlorine nitrate $ClONO_2$, another important "chemical reservoir" for chlorine, is formed by the reaction of ClO with NO_2:

$$(d_{31}); \qquad ClO + NO_2 + M \rightarrow ClONO_2 + M \tag{5.157}$$

and dissociated in the ultraviolet (Chang *et al.*, 1979)

$$(J^{a}_{ClONO_2}); \qquad ClONO_2 + h\nu \rightarrow Cl + NO_3 \tag{5.159a}$$

with a quantum yield of approximately 0.8. The efficiency of a second channel

$$(J^{b}_{ClONO_2}); \qquad ClONO_2 + h\nu \rightarrow ClO + NO_2 \tag{5.159b}$$

is of the order of 0.15-0.20 while the yield of a third channel

$$(J^{c}_{ClONO_2}); \qquad ClONO_2 + h\nu \rightarrow ClONO + O \tag{5.159c}$$

is less than 0.05. A loss with atomic oxygen, atomic chlorine and the hydroxyl radical should also be mentioned:

$$(d_{32}); \qquad ClONO_2 + O \rightarrow \text{products} \tag{5.214}$$

$$(d_{82}); \qquad ClONO_2 + Cl \rightarrow Cl_2 + NO_3 \tag{5.215}$$

$$(d_{87}); \qquad ClONO_2 + OH \rightarrow HOCl + NO_3 \tag{5.216}$$

This latter reaction leads to the formation of HOCl. The primary production of HOCl, however, is provided by the reaction

$$(d_{33}); \qquad HO_2 + ClO \rightarrow HOCl + O_2 \tag{5.217}$$

HOCl is destroyed mostly by photolysis

$$(J_{HOCl}); \qquad HOCl + h\nu \ (\lambda < 503 \text{ nm}) \rightarrow Cl + OH \tag{5.218}$$

and by reaction with OH:

$$(d_{34}); \qquad OH + HOCl \rightarrow H_2O + ClO \tag{5.219}$$

It can also react with atomic oxygen

$$(d_{35}); \qquad HOCl + O \rightarrow ClO + OH \tag{5.220}$$

and with atomic chlorine

$$(d_{37}); \qquad HOCl + Cl \rightarrow Cl_2 + OH \tag{5.221a}$$

with a possible channel

$$(d_{37a}); \qquad HOCl + Cl \rightarrow HCl + ClO \tag{5.221b}$$

The concentration of inorganic chlorine compounds in the stratosphere can also be affected by heterogeneous reactions on the surface

of solid and liquid particles. For example, hydrolysis of chlorine nitrate

$$(h_2); \qquad ClONO_2(g) + H_2O(\ell, s) \rightarrow HOCl(g) + HNO_3 \qquad (5.222)$$

on the surface of water ice particles, nitric acid ice, supercooled ternary solutions, and liquid sulfuric acid particles (aerosols) leads to the formation of HOCl and of nitric acid. Because HOCl is rapidly photolyzed into Cl and OH, heterogeneous reaction (5.222) provides an efficient mechanism to activate chlorine (*i.e.*, convert a relatively inert chlorine reservoir into a very reactive form of chlorine) in the lower stratosphere. The efficiency of the reaction, and hence the value of the reaction probability, depends strongly on the concentration of sulfuric acid in the solution and hence on the temperature (*e.g.*, Rossi *et al.*, 1987; Tolbert *et al.*, 1988; Hanson and Ravishankara, 1994; Manion *et al.*, 1994; Williams *et al.*, 1994; Robinson *et al.*, 1997; Hanson, 1998). It decreases typically from 0.1 for a H_2SO_4 content of 40% by weight (corresponding to a stratospheric temperature T of 190 K) to 10^{-3} for 60 wt% H_2SO_4 (or T = 205 K), assuming a water partial pressure representative of the lower stratosphere (Figure 2.5 in Chapter 2). The reactivity of $ClONO_2$ is increased when significant quantities of HCl are dissolved in the H_2SO_4/H_2O solution (Hanson, 1998; see Figure 2.6). As the stratospheric temperature decreases and hence the solubility of HCl in a liquid aerosol increases, reaction

$$ClONO_2(g) + HCl(s, \ell) \rightarrow Cl_2(g) + HNO_3 \qquad (5.223)$$

becomes competitive with and even faster than the reaction of chlorine nitrate with water molecules. When the hydrolysis of $ClONO_2$ takes place on water ice, the reaction probability is of the order of 0.3 (Hanson and Ravishankara, 1991); it drops to less than 0.01 when the ice surface contains HNO_3. Note that the nitric acid that is produced by the hydrolysis of N_2O_5 and $ClONO_2$ is partitioned between the gas and the condensed phases according to thermodynamics. For example, at relatively high temperature (T > 190 K), when the particles present in the stratosphere are liquid sulfuric acid aerosols, HNO_3 is released mostly in the gas phase. A similar reaction with dissolved HBr also occurs

$$(h_3'); \qquad ClONO_2(g) + HBr(s, \ell) \rightarrow BrCl(g) + HNO_3 \qquad (5.224)$$

Heterogeneous reactions

$$(h_4); \qquad N_2O_5(g) + HCl(s,\ell) \rightarrow ClNO_2(g) + HNO_3 \qquad (5.225)$$

and

$$(h_5); \qquad HOCl(g) + HCl(s,\ell) \rightarrow Cl_2(g) + H_2O \qquad (5.226)$$

on the surface of particles are responsible for additional chlorine activation. Note that Reaction (5.225) produces $ClNO_2$. This compound

can also be formed by the three-body reaction

$$(d_{36}); \qquad Cl + NO_2 + M \rightarrow ClNO_2 + M \tag{5.227}$$

But the major product (90%) of this reaction is believed to be ClONO:

$$(d_{36a}); \qquad Cl + NO_2 + M \rightarrow ClONO + M \tag{5.228}$$

ClONO is either rapidly photolyzed or converted by isomerization into $ClNO_2$.

In the sunlit atmosphere, the photolysis of Cl_2, HOCl, and $ClNO_2$

$$(J_{Cl_2}); \qquad Cl_2 + h\nu \rightarrow Cl + Cl \tag{5.229}$$

$$(J_{HOCl}); \qquad HOCl + h\nu\,(\lambda < 370\ nm) \rightarrow Cl + OH \tag{5.230}$$

$$(J_{ClNO_2}); \qquad ClNO_2 + h\nu \rightarrow Cl + NO_2 \tag{5.231}$$

produces reactive chlorine atoms.

When high ClO concentrations (0.5-2 ppbv) are present in the stratosphere (*e.g.*, in polar regions during winter when air masses are processed by polar stratospheric clouds), the three-body reaction

$$(d_{60}); \qquad ClO + ClO + M \rightarrow Cl_2O_2 + M \tag{5.232}$$

leads to the formation of significant quantities of the ClO dimer (Cl_2O_2). During nightime, in the springtime polar region, Cl_2O_2 is often the most abundent inorganic chlorine-containing compound in the lower sratosphere. During daytime, Cl_2O_2 is photolyzed

$$(J_{Cl_2O_2}); \qquad Cl_2O_2 + h\nu \rightarrow Cl + ClOO \tag{5.233}$$

producing a chlorine atom and the ClOO radical, which is rapidly photolyzed or is decomposed according to

$$(d_{62}) \qquad ClOO + M \rightarrow Cl + O_2 + M. \tag{5.234}$$

In the PSC processed airmasses of the springtime polar lower stratosphere, ClO becomes the most abundant inorganic chlorine species during daytime. The Cl_2O_2 dimer itself can also be decomposed upon collision with an atmospheric molecule M

$$(d_{61}) \qquad Cl_2O_2 + M \rightarrow ClO + ClO \tag{5.235}$$

at a rate which increases substantially with increasing temperature. Thermal decomposition (5.235) maintains significant levels of ClO in the polar region during the night, if the temperature is sufficiently high (Lefèvre *et al.*, 1994).

The analysis of the termolecular reaction (d_{60}) is complicated by the existence of three bimolecular channels

$$(d_{47}); \qquad ClO + ClO \rightarrow OClO + Cl \tag{5.236a}$$

$$(d_{48}); \qquad \rightarrow Cl_2 + O_2 \tag{5.236b}$$

$$(d_{49}); \qquad \rightarrow ClOO + Cl\ . \tag{5.236c}$$

The reactions between chlorine and bromine monoxide also play an important role in the lower stratosphere, particularly at high latitudes in winter. Three channels must be considered

$$(e_{5a}); \qquad ClO + BrO \rightarrow OClO + Br \tag{5.237a}$$

$$(e_{5b}); \qquad \rightarrow ClOO + Br \tag{5.237b}$$

$$(e_{5c}); \qquad \rightarrow BrCl + O_2 \tag{5.237c}$$

Pathway (a), with an efficiency of approximately 60% of the overall reaction at 200 K, is the major production mechanism for OClO. This latter compound, however, is rapidly photolyzed in the sunlit atmosphere

$$(J_{OClO}); \qquad OClO + h\nu \rightarrow ClO + O \tag{5.238}$$

so that its abundance is greatest during nighttime. BrCl, produced by pathway (*c*), with a yield of approximately 8%, is photodissociated in sunlit regions

$$BrCl + h\nu\,(\lambda < 540\ \text{nm}) \rightarrow Br + Cl\ . \tag{5.239}$$

Retaining the major reactions affecting inorganic chlorine compounds (see also Figure 5.49), the continuity equations for Cl, ClO, HCl, HOCl, $ClONO_2$, Cl_2O_2, OClO, ClOO, BrCl, Cl_2, and $ClNO_2$ can be easily derived:

$$\begin{aligned}\frac{d(Cl)}{dt} &+ (Cl)\,[d_2(O_3) + d_5(CH_4) + d_6(H_2) + d_7(HO_2) + d_8(H_2O_2) \\ &+ d_{10}(CH_2O)] = P_{Cl} + [d_3(O) + d_4(NO) + J_{ClO} + d_8(OH)]\,(ClO) \\ &+ [d_{12}(O) + d_{11}(OH) + J_{HCl}]\,(HCl) + J^{a}_{ClONO_2}(ClONO_2) \\ &+ J_{HOCl}(HOCl) + J_{Cl_2O_2}(Cl_2O_2) + d_{62}(M)(ClOO) \\ &+ (d_{47} + d_{49})(ClO)^2 + 2J_{Cl_2}(Cl_2) + J_{ClNO_2}(ClNO_2) \\ &+ J_{BrCl}(BrCl)\end{aligned} \tag{5.240}$$

where P_{Cl} represents production of chlorine from organo-chlorine molecules.

$$\frac{d(ClO)}{dt} + (ClO)\,[d_3(O) + d_4(NO) + J_{ClO} + (d_8 + d_{46})\,(OH)$$

$$+ d_{31}(M)(NO_2) + 2d_{60}(M)(ClO) + 2(d_{47} + d_{48} + d_{49})(ClO)$$
$$+(e_{5a} + e_{5b} + e_{5c})(BrO)]$$
$$= d_2(O_3)(Cl) + \left[J^b_{ClONO_2} + d_{32}(O)\right](ClONO_2)$$
$$+ 2d_{61}(M)(Cl_2O_2) + J_{OClO}(OClO) \quad (5.241)$$

$$\frac{d(HCl)}{dt} + (HCl)\,[d_{12}(O) + d_{11}(OH) + J_{HCl} + h_3(ClONO_2) + h_4(N_2O_5)$$
$$+h_5(HOCl) + \beta_p] = (Cl)\,[d_5(CH_4) + d_6(H_2) + d_7(HO_2)$$
$$+d_8(H_2O_2) + d_{10}(CH_2O)] + d_{46}(OH)(ClO) \quad (5.242)$$

where β_p represents the pseudo first-order rate (s^{-1}) for wet scavenging of HCl (in the troposphere)

$$\frac{d(HOCl)}{dt} + [J_{HOCl} + d_{34}(OH)$$
$$+h_5(HCl)]\,(HOCl) = d_{33}(HO_2)(ClO) + h_2(H_2O)(ClONO_2) \quad (5.243)$$

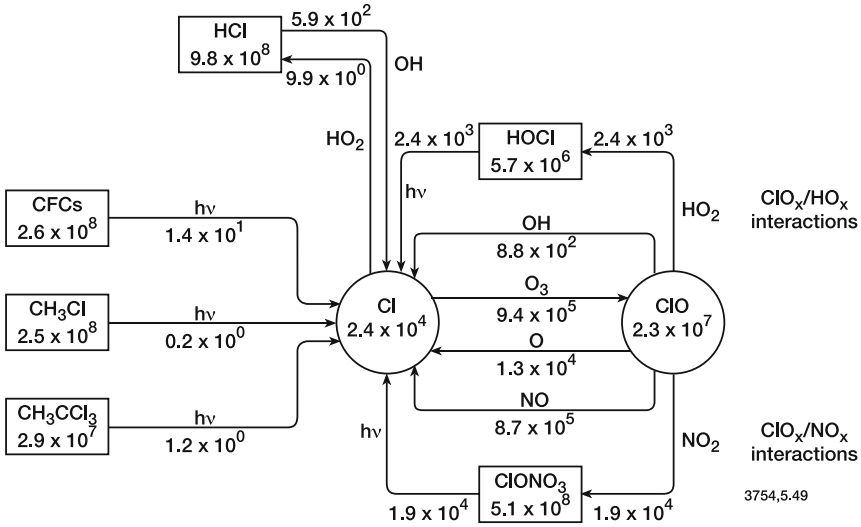

Figure 5.49. Principal chemical reactions affecting chlorine compounds in the stratosphere. Concentrations (cm^{-3}) and reaction fluxes ($cm^{-3}s^{-1}$) between different compounds calculated at 25 km altitude (24-hour average) are indicated. After Zellner (1999).

$$\frac{d(ClONO_2)}{dt} + (ClONO_2)\left[J_{ClONO_2} + d_{32}(O) + h_2(H_2O) + h_3(HCl) + h_3'(HBr)\right] = d_{31}(M)(ClO)(NO_2) \quad (5.244)$$

$$\frac{d(Cl_2O_2)}{dt} + (Cl_2O_2)\left[J_{Cl_2O_2} + d_{61}(M)\right] = d_{60}(M)(ClO)^2 \quad (5.245)$$

$$\frac{d(OClO)}{dt} + J_{OClO}(OClO) = d_{47}\,(ClO)^2 \quad (5.246)$$

$$\frac{d(ClOO)}{dt} + d_{62}(M)(ClOO) = d_{49}\,(ClO)^2 + J_{Cl_2O_2}(Cl_2O_2) \quad (5.247)$$

$$\frac{d(BrCl)}{dt} + J_{BrCl}(BrCl) = e_{5c}\,(ClO)(BrO) \quad (5.248)$$

$$\frac{d(Cl_2)}{dt} + J_{Cl_2}(Cl_2) = h_3\,(ClONO_2)(HCl) + h_5(HOCl)(HCl) + d_{48}(ClO)^2 \quad (5.249)$$

$$\frac{d(ClNO_2)}{dt} + J_{ClNO_2}(ClNO_2) = h_4(HCl)(N_2O_5) \quad (5.250)$$

where J_{ClONO_2} represents the total photolysis coefficient of $ClONO_2$.

One-dimensional model predictions of the theoretical distributions of chlorine compounds are shown in Figure 5.50. The diurnal variations of these species at two specific altitudes are also displayed in Figure 5.51.

5.6.2.2 Fluorine

The dissociation of chlorofluorocarbons such as $CFCl_3$ and CF_2Cl_2, as well as other species such as CF_4, represents a source of atmospheric fluorine. Fluorine atoms react rapidly with molecular oxygen

$$F + O_2 + M \rightarrow FO_2 + M \quad (5.251)$$

to form FO_2, which in turn is rapidly converted back to fluorine atoms:

$$FO_2 + NO \rightarrow FNO + O_2 \quad (5.252)$$

$$FNO + h\nu \rightarrow F + NO\ . \quad (5.253)$$

The F atom also reacts with ozone:

$$(f_2); \qquad F + O_3 \rightarrow FO + O_2 \quad (5.254)$$

to produce fluorine monoxide, which, like chlorine monoxide, can react either with atomic oxygen

$$(f_3); \qquad FO + O \rightarrow F + O_2 \quad (5.255)$$

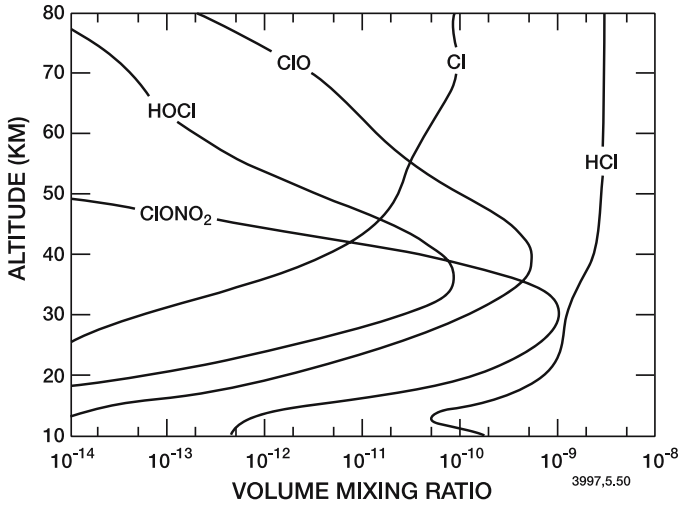

Figure 5.50. Calculated vertical distribution of reactive chlorine species at mid-latitudes equinox conditions, noon values. Total amount of chlorine is assumed to be 3 ppbv.

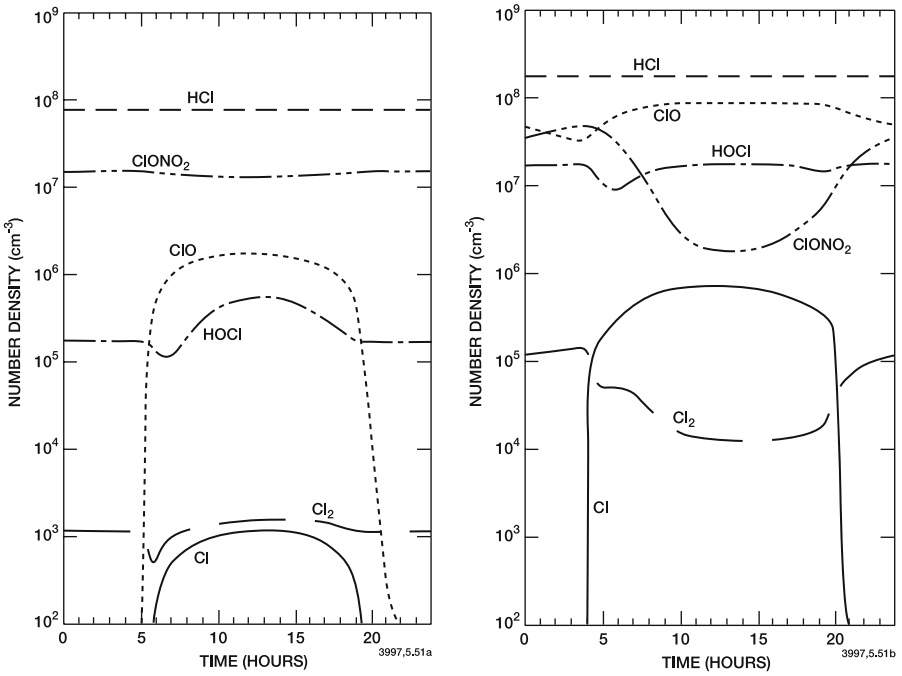

Figure 5.51. Diurnal variation of chlorine species calculated for May 10 and 65°N at 20 km (a) and 40 km (b).

or with nitric oxide:

$$(f_4); \qquad FO + NO \rightarrow F + NO_2 \tag{5.256}$$

Like chlorine, the fluorine atom is also converted into an acid, HF:

$$(f_5); \qquad F + CH_4 \rightarrow HF + CH_3 \tag{5.257}$$

$$(f_6); \qquad F + H_2 \rightarrow HF + H \tag{5.258}$$

$$(f_7); \qquad F + H_2O \rightarrow HF + OH \tag{5.259}$$

Unlike HCl however, hydrogen fluoride does not react appreciably with OH, so that the fluorine atoms, which react with methane, hydrogen, or water vapor, are effectively stabilized as HF. Since the sources of HF and HCl are similar but their loss rates are quite different as a result of the reaction of OH with HCl at low altitudes, the HF/HCl ratio can provide an indication of the abundance of the OH radical (see, *e.g.*, Sze and Ko, 1980).

Because of the stability of HF, the atmospheric densities of F and FO are very small and the effect of fluorine on odd oxygen is insignificant. The reaction of HF with $O(^1D)$ is chemically possible, but is negligible due to the low abundance of this excited atom. The distribution of HF is therefore largely determined by the rates of the surface emission of fluorine containing gases, of photochemical destruction of these gases, and atmospheric dynamics.

5.6.2.3 Bromine

Molecules of the type $C_xH_yBr_z$ produce bromine atoms upon photodissociation and oxidation, like the other halogen atoms just discussed. Unlike fluorine, the chemistry of bromine is broadly similar to that of chlorine (see Yung *et al.* (1980); Poulet *et al.* (1992); Lary (1996) and Figure 5.52) and is therefore capable of affecting the ozone budget. The production of bromine atoms is followed by the reaction

$$(e_2); \qquad Br + O_3 \rightarrow BrO + O_2 \tag{5.260}$$

which produces BrO, the most abundant inorganic bromine compound in the stratosphere below 40 km altitude. In the lower stratosphere, Br is also converted into BrO by

$$(e_{71}); \qquad Br + OClO \rightarrow BrO + ClO \tag{5.261}$$

The main loss of BrO in the upper stratosphere is due to its reaction with atomic oxygen

$$(e_3); \qquad BrO + O \rightarrow Br + O_2 \ , \tag{5.262}$$

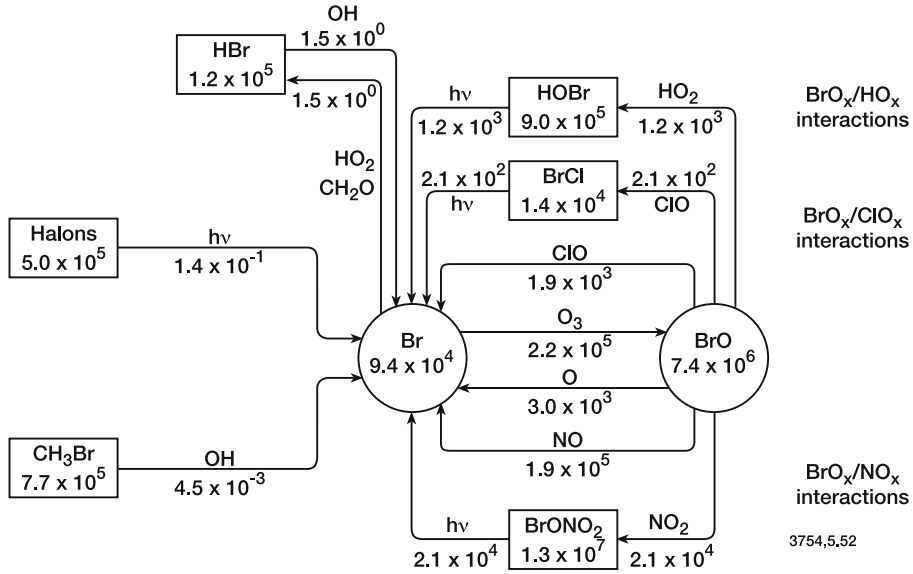

Figure 5.52. Principal chemical reactions affecting bromine species in the stratosphere. Concentrations (cm^{-3}) and reaction fluxes ($cm^{-3}s^{-1}$) between different compounds calculated at 25 km altitude (24-hour average) are indicated. After Zellner (1999).

while, in the lower stratosphere, the major destruction mechanisms are provided by photolysis

$$(J_{BrO}); \qquad BrO + h\nu\,(\lambda < 380\ nm) \rightarrow Br + O \tag{5.263}$$

and the reaction with NO

$$(e_4); \qquad BrO + NO \rightarrow Br + NO_2 \tag{5.134}$$

Conversion of BrO to Br also occurs via

$$BrO + OH \rightarrow Br + HO_2 \tag{5.264}$$

Other reactions such as

$$(e_{5a}); \qquad BrO + ClO \rightarrow Br + OClO \tag{5.237a}$$

$$(e_{5b}); \qquad \rightarrow Br + ClOO \tag{5.237b}$$

$$(e_{5c}); \qquad \rightarrow BrCl + O_2 \tag{5.237c}$$

$$(e_6); \qquad BrO + BrO \rightarrow 2Br + O_2 \tag{5.265}$$

contribute only marginally to the destruction of BrO. Bromine thus plays a role not only through its own catalytic ozone destruction cycle, but can also influence the chlorine cycle through reaction e_5 (see Wofsy *et al.*, 1975). Indeed, the effect of these halogens on the ozone molecule can be

significantly influenced by this "synergy" between the catalytic cycles, wherein both become more effective. Hydrogen bromide (HBr) is formed almost entirely by reactions

$$(e_7); \qquad Br + HO_2 \rightarrow HBr + O_2 \tag{5.266}$$

and

$$Br + H_2CO \rightarrow HBr + HCO \tag{5.267}$$

because Br does not react efficiently with methane or molecular hydrogen, and because the reaction

$$(e_9); \qquad Br + H_2O_2 \rightarrow HBr + HO_2 \tag{5.268}$$

proceeds slowly at middle atmospheric temperatures. The photolysis of HBr in the stratosphere is slow because it involves shortwave ultraviolet light. HBr reacts, however, rapidly with OH, and with $O(^1D)$

$$(e_{11}); \qquad HBr + OH \rightarrow Br + H_2O\ . \tag{5.269}$$

$$(e_{12}^*); \qquad HBr + O(^1D) \rightarrow Br + OH \tag{5.270}$$

The reaction with atomic oxygen $O(^3P)$

$$(e_{12}); \qquad HBr + O(^3P) \rightarrow Br + OH \tag{5.271}$$

becomes important only above 50 km altitude. Finally, BrO can, like ClO, associate with NO_2:

$$(e_{13}); \qquad BrO + NO_2 + M \rightarrow BrONO_2 + M \tag{5.158}$$

and react with HO_2:

$$(e_{15}); \qquad BrO + HO_2 \rightarrow HOBr + O_2 \tag{5.272}$$

to form $BrONO_2$ and HOBr, both of which rapidly photodissociate. By analogy with $ClONO_2$, the photolysis of $BrONO_2$ (at $\lambda < 450$ nm) is believed to produce mainly Br + NO_3 which leads to catalytic ozone destruction (see Burkholder *et al.*, 1995, and cycle (5.337)). The photolysis of HOBr ($\lambda < 425$ nm), which leads to the formation of Br and OH, is the major destruction mechanism for this species in the lower stratosphere, and is also an odd oxygen destruction mechanism. Above approximately 25 km, the main loss of HOBr is provided by the reaction with atomic oxygen

$$(e_{16}); \qquad HOBr + O \rightarrow BrO + OH\ . \tag{5.273}$$

It is important to note that gas-phase $BrONO_2$ can be converted into HOBr by heterogenous reaction on the surface of sulfate aerosol and PSC particles.

$$(h_{10}); \qquad BrONO_2(g) + H_2O(s, \ell) \rightarrow HOBr(g) + HNO_3 \tag{5.274}$$

(see Hanson and Ravishankara, 1994). This reaction provides a significant source of HO_x due to the subsequent photolysis of HOBr. As

a result of the enhanced OH concentration, additional HCl is converted to reactive chlorine (ClO) which leads to increased ozone loss at all latitudes and for all seasons, particularly when high loadings of sulfate aerosols are present in the stratosphere (*e.g.*, Lary *et al.*, 1996).

Finally, as shown by reaction (5.237*c*), the reaction between BrO and ClO leads to the formation of BrCl. Other production mechanisms are provided by heteorogeneous reactions on the surface of aerosol and of PSC particles:

$$(h_{13}); \qquad BrONO_2(g) + HCl(s,\ell) \rightarrow BrCl(g) + HNO_3 \quad (5.275)$$

$$(h_{11}); \qquad HOBr(g) + HCl(s,\ell) \rightarrow BrCl(g) + H_2O \quad (5.276)$$

$$(h_{12}); \qquad HOCl(g) + HBr(s,\ell) \rightarrow BrCl(g) + H_2O \quad (5.277)$$

The loss of BrCl below 30 km is due almost entirely to its photolysis

$$(J_{BrCl}); \qquad BrCl + h\nu\,(\lambda < 540\ nm) \rightarrow Br + Cl\ , \quad (5.278)$$

while, above this altitude, the major destruction mechanism is the reaction with atomic oxygen

$$(e_{17}); \qquad BrCl + O \rightarrow BrO + Cl\ . \quad (5.279)$$

Figure 5.53 presents calculated vertical distributions of a number of bromine compounds, and Figure 5.54 shows the diurnal variation of these species at two selected altitudes. The most abundant bromine species during daytime below 35-40 km is BrO, despite its short chemical lifetime (approximately 10 seconds in the sunlit stratosphere below 35 km). The second most abundant compound in the sunlit atmosphere is HOBr (which represents about 20-30% of odd bromine in the lower stratosphere). Its lifetime during daytime varies from several minutes at 15 km to a few seconds at 50 km. $BrONO_2$ is the most abundant inorganic bromine compound during nighttime in the stratosphere up to 40 km, and is approximately as abundant as HOCl during daytime near 20 km altitude. The lifetime of $BrONO_2$ is of the order of several minutes throughout the sunlit stratosphere, while that of HBr is close to 1 day at 15 km and 1 hour at 50 km. Reactive bromine compounds are thus short-lived, and hence subject to diurnal variations (Figure 5.54).

5.6.2.4 Iodine

Ozone in the lower stratosphere may in principle be affected by iodine chemistry (Solomon *et al.*, 1994). The abundance of total iodine in the troposphere is believed to be of the order of pptv, but the fractional partitioning of iodine free radicals (I and IO) is much higher than in the case of other halogens (chlorine and even of bromine; see Section 5.6.3).

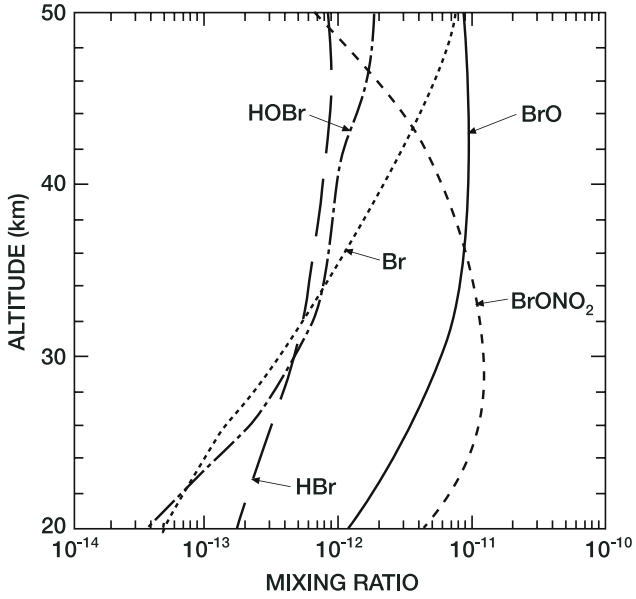

Figure 5.53. Vertical distribution of bromine compounds in the stratosphere (24-hour-average at 30°N equinox). Adapted from McElroy (2002).

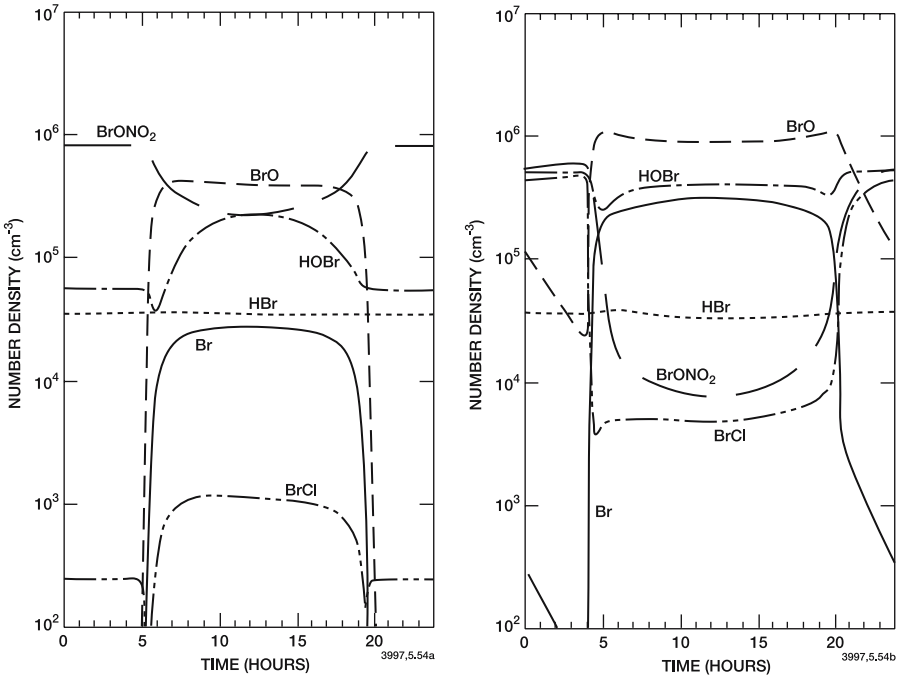

Figure 5.54. Diurnal variation of bromine species calculated for May 10 and 65°N at 20 km (a) and 40 km (b).

Thus, even if limited amounts of iodine penetrated into the stratosphere, they could be very efficient in depleting ozone.

A likely source of active iodine is provided by the photolysis of methyl iodide (CH_3I) and perhaps of other iodocarbons. As the atmospheric lifetime of CH_3I is relatively short (a few days), the tropospheric abundance of this compound is generally lower than 10 pptv (Moyers and Duce, 1972; Singh *et al.*, 1983; Atlas *et al.*, 1993) although local maxima are found over the productive regions of the ocean (Oram and Penkett, 1994). If iodine atoms are released above the tropopause, they react with ozone to form the iodine monoxide radical

$$(g_2); \qquad I + O_3 \rightarrow IO + O_2 \ . \tag{5.280}$$

IO undergoes rapid photolysis

$$(J_{IO}); \qquad IO + h\nu \rightarrow I + O \tag{5.281}$$

and reacts with NO

$$(g_4); \qquad IO + NO \rightarrow I + NO_2 \tag{5.282}$$

or with oxygen atoms

$$(g_3); \qquad IO + O \rightarrow I + O_2 \ . \tag{5.283}$$

Reservoir species (HOI, $IONO_2$ and HI) are produced and destroyed by the following reactions:

$$(g_{15}); \qquad IO + HO_2 \rightarrow HOI + O_2 \tag{5.284}$$

$$(J_{HOI}); \qquad HOI + h\nu \rightarrow I + OH \tag{5.285}$$

$$(g_{13}); \qquad IO + NO_2 + M \rightarrow IONO_2 + M \tag{5.286}$$

$$(J_{IONO_2}); \qquad IONO_2 + h\nu \rightarrow \text{ products} \tag{5.287}$$

$$(g_7); \qquad I + HO_2 \rightarrow HI + O_2 \tag{5.288}$$

$$(g_{11}); \qquad HI + OH \rightarrow I + H_2O \tag{5.289}$$

Finally, inter-halogen reactions such as

$$(g_5); \qquad IO + ClO \rightarrow Cl + I + O_2 \tag{5.290}$$

$$(g_6); \qquad IO + BrO \rightarrow Br + I + O_2 \tag{5.291}$$

which represent rate-limiting steps for ozone destruction, could be significant in the lowermost stratosphere, even if the abundance of total iodine is as low as a few tenths of a pptv (Solomon *et al.*, 1994). Observations by Wennberg *et al.* (1997), and Pundt *et al.* (1998) suggest upper limits close to this value, suggesting a minor or negligible role. However, measurements by Wittrock *et al.* (2000) provide evidence for a greater contribution at high latitudes. Further, the formation and

photolysis of HOI is particularly effective for ozone destruction near the tropopause, even for iodine abundances less than 0.5 pptv (Gilles *et al.*, 1997). On the other hand, formation of iodine reservoirs has been highlighted as a factor in iodine's impact on the atmosphere (Cox *et al.*, 1999). The reaction

$$(g_{16}); \qquad IO + ClO \rightarrow OIO + Cl \tag{5.292}$$

is of particular importance, since photolysis of OIO to re-form odd oxygen as the products IO + O could short-circuit ozone loss via this reaction. However, some studies suggest that OIO photolysis produces I + O_2 (see Ingham *et al.*, 2000) and the photolysis products of this key reaction are not well understood. Tropospheric observations of IO (Friess *et al.*, 2001) and OIO (Allan *et al.*, 2001) suggest that iodine species may play a role in particle formation (Hoffmann *et al.*, 2001). Such processes could reduce iodine's gas-phase role in ozone chemistry, but could be relevant for formation of the stratospheric aerosol layer, particularly if iodine can promote growth of sulfate clusters (Kulmala *et al.*, 2000).

5.6.3 The Halogen Families and Halogen Partitioning

Halogen families are variously defined to account for all chlorine, bromine, iodine, and fluorine atoms attached to inorganic halogen compounds. For example, the *odd chlorine* family Cl_y may be defined as the sum of Cl + ClO + 2 Cl_2O_2 + OClO + ClOO + 2 Cl_2 + HCl + HOCl + $ClONO_2$ + $ClNO_2$ + BrCl. Similarly, *odd bromine* Br_y is provided by the sum of Br + BrO + HBr + HOBr + $BrONO_2$ + BrCl plus any other inorganic form of bromine-containing molecule or radical. Note that a compound like BrCl (whose contribution is generally small except during nighttime in activated air masses of the polar regions) belongs to the odd chlorine as well as the odd bromine family. A similar definition can be provided for *odd iodine* I_y and *odd fluorine* F_y.

A general continuity equation for the halogen families X_y (where X can be Cl, Br, I or F) can be written as

$$\frac{\partial (X_y)}{\partial t} + \boldsymbol{\nabla} \cdot \boldsymbol{\phi}_X + \beta_x (X_y) = P_X \tag{5.293}$$

where β_x represents the loss coefficient (expressed in s^{-1}) accounting for physical removal (*i.e.*, wet scavenging) of X_y, and P_X is the production rate ($cm^{-3}\ s^{-1}$) associated with the photodecomposition of source gases. An expression for this term is given by expression (5.200) in the case

of chlorine ($X_y = Cl_y$). The flux divergence $\boldsymbol{\nabla}\cdot\boldsymbol{\phi}_X$ accounts for the transport of all inorganic compounds of the X_y family.

In some cases, sub-families of the chemical family X_y (representing, for example, the relatively reactive species) can be defined. In the case of chlorine, for example, the most reactive compounds can be grouped into the Cl_x family, defined as the entire odd chlorine family minus the slow-reacting chlorine-containing species HCl and $ClONO_2$:

$$\begin{aligned}\frac{\partial(Cl_x)}{\partial t} &+ \boldsymbol{\nabla}\cdot\boldsymbol{\phi}(Cl_x) + [d_5(CH_4) + d_6(H_2) + d_7(HO_2) \\ &+ d_8(H_2O_2) + d_9(HNO_3) + d_{10}(CH_2O)]\ (Cl) + [d_{31}(M)(NO_2) \\ &+ d_{46}(OH)]\ (ClO) = [d_{11}(OH) + d_{12}(O) + J_{HCl} + h_3(ClONO_2) \\ &+ h_4(N_2O_5) + h_5(HOCl)]\ (HCl) + [J_{ClONO_2} + d_{32}(O) \\ &+ h_2(H_2O) + h_3(HCl) + h_3'(HBr)]\ (ClONO_2)\end{aligned} \tag{5.294}$$

The terms associated with heterogeneous reactions (h_2, h_3, h_3', h_4, h_5) highlight the activation of chlorine when particles are present in the stratosphere.

It is important to underline here the differences between the different halogen families. In the case of bromine (and iodine), all inorganic compounds are fast-reacting species and the concentration of the individual members of the Br_y (and I_y) families can be derived through a simple partitioning procedure assuming photoequilibrium conditions. The abundances of Br_y (and I_y) are obtained by solving an equation of type (5.293). In the case of fluorine, almost all inorganic fluorine is in the form of HF, whose concentration can be obtained by solving (5.293) with $X_y = F_y \approx HF$. In the case of inorganic chlorine compounds, it is generally necessary to solve for HCl and $ClONO_2$ separately from the other members of the odd-chlorine family, because of the relatively long lifetime of hydrogen chloride and chlorine nitrate, especially in the lower stratosphere (see Figure 5.55). Individual species belonging to the Cl_x compounds can be partitioned assuming equilibrium conditions. Retaining the most important terms in (5.240), (5.243), (5.245), and (5.246) and adding terms involving Br and BrO,

$$\frac{(ClO)}{(Cl)} = \frac{d_2(O_3)}{d_3(O) + d_4(NO) + J_{ClO}} \tag{5.295}$$

$$\frac{(HOCl)}{(ClO)} = \frac{d_{33}(HO_2)}{J_{HOCl} + d_{34}(OH)} \tag{5.296}$$

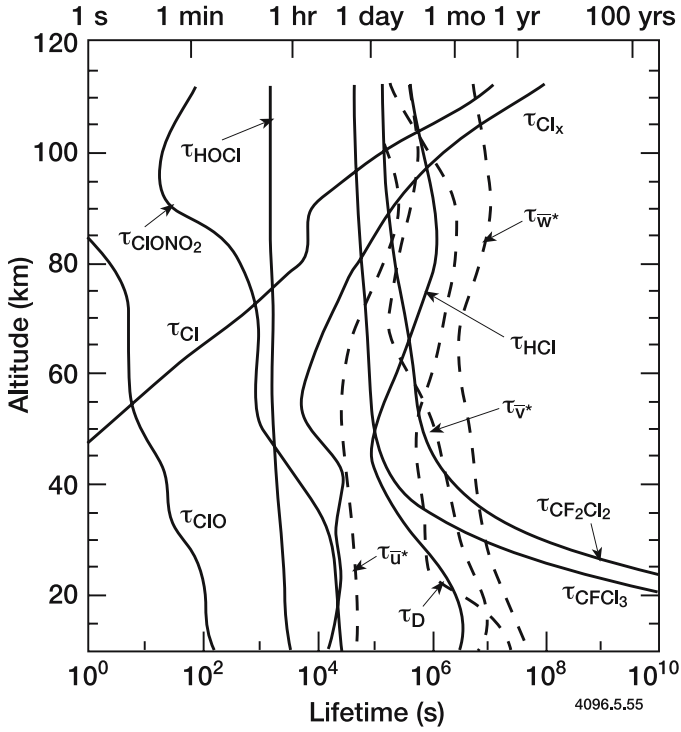

Figure 5.55. Photochemical lifetimes of Cl_x, Cl, ClO, HOCl, $ClONO_2$, HCl, CF_2Cl_2, and $CFCl_3$, as well as the time constants appropriate to atmospheric transport.

$$\frac{(Cl_2O_2)}{(ClO)} = \frac{d_{60}(M)(ClO)}{J_{Cl_2O_2} + d_{61}(M)} \tag{5.297}$$

$$\frac{(OClO)}{(ClO)} = \frac{d_{47}(ClO) + e_{5a}(BrO)}{J_{OClO} + e_{71}(Br)} \tag{5.298}$$

In the upper stratosphere, where the photochemical lifetimes of $ClONO_2$ and HCl become shorter, we may evaluate the equilibrium ratios between these chlorine containing compounds to serve as a rough estimate of their relative abundances. In the absence of heterogeneous processes, using Eq. (5.244),

$$\frac{(ClONO_2)}{(ClO)} = \frac{d_{31}(M)(NO_2)}{J_{ClONO_2} + d_{32}(O)} \tag{5.299}$$

and from Eq. (5.242),

$$\frac{(HCl)}{(Cl)} = \frac{d_5(CH_4) + d_6(H_2) + d_7(HO_2) + d_8(H_2O_2)}{d_{10}(O) + d_{11}(OH) + J_{HCl}} \tag{5.300}$$

or, approximately

$$\frac{(\mathrm{HCl})}{(\mathrm{Cl})} \approx \frac{\mathrm{d}_5(\mathrm{CH_4}) + \mathrm{d}_7(\mathrm{HO_2})}{\mathrm{d}_{11}(\mathrm{OH})} \tag{5.301}$$

These ratios illustrate the importance of the interactions of chlorine chemistry with oxygen, hydrogen and nitrogen species. Figure 5.56 provides an estimate of the partitioning associated with different halogen families.

The above partitioning between halogen species can be dramatically modified when particles (*e.g.*, polar stratospheric clouds, sulfate aerosols) are present in the atmosphere. For example, in air masses processed by polar stratospheric clouds, $\mathrm{ClONO_2}$ and HCl are rapidly converted by heterogeneous reactions to more reactive $\mathrm{Cl_x}$ compounds, and specifically to $\mathrm{Cl_2}$, HOCl, $\mathrm{ClNO_2}$, BrCl. In the presence of solar radiation, these species are photolyzed and high levels of ClO are observed during daytime. ClO recombines with itself and is converted into the $\mathrm{Cl_2O_2}$ dimer, which at night becomes the dominant inorganic

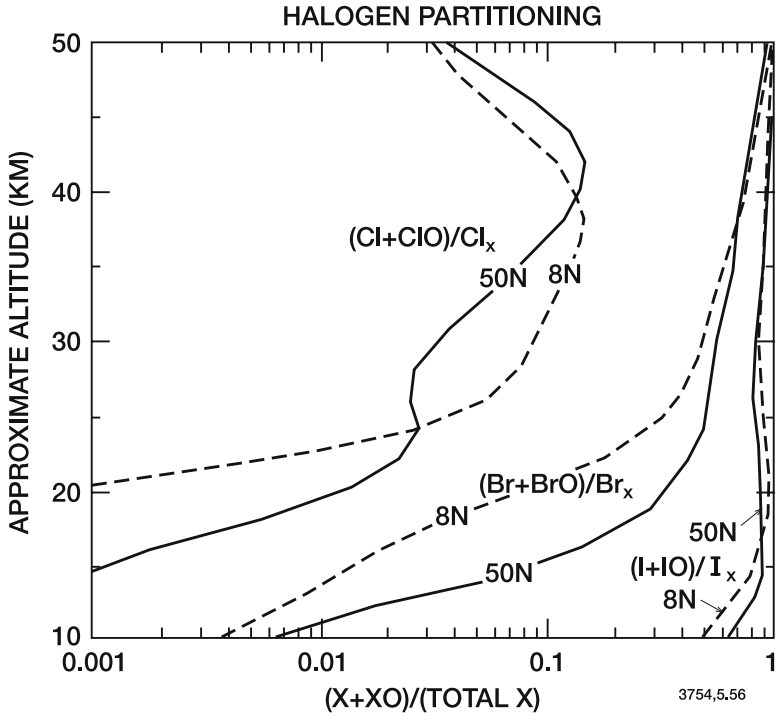

Figure 5.56. Model calculation of the partitioning of free radicals and total halogen content for chlorine, bromine, and iodine at 8°N and 50°N in December. From Solomon *et al.* (1994).

chlorine-containing compound. Thus, in PSC processed airmasses during the springtime, the total abundance of inorganic chlorine is approximately Cly $\simeq$ ClO + 2 Cl_2O_2. ClO can participate in ozone-destroying catalytic cycles, but high concentrations of ClO can only be maintained if the level of nitrogen oxides is very low (to avoid the formation of $ClONO_2$). As indicated above, heterogeneous processes tend to reduce substantially the NO_x/NO_y concentration ratio. With ClO mixing ratios of typically 0.5-2.0 ppbv, in the Antarctic in late winter/early spring, substantial amounts of ozone are depleted over a time period of only a few weeks (see Chapter 6).

5.6.4 Observations of Halogen Compounds

The ClO radical has been directly measured since 1976 using *in-situ* resonance fluorescence techniques and by Menzies (1979), Anderson *et al.* (1980), Waters *et al.* (1981), De Zafra *et al.* (1989), and Stachnik *et al.* (1992) using remote sensing microwave methods. Global observations such as those provided by the MLS instrument aboard UARS (Waters *et al.*, 1993; Figure 5.57) have improved the understanding of the behavior of ClO and the amplitude of its variations. This constitutes an important element in the study of the chlorine-ozone interaction, discussed in more detail in the next chapter.

Infrared spectra of $ClONO_2$ provided the first estimates of the abundance of this key compound (Murcray *et al.*, 1977). Global distributions have also been measured by the CLAES instrument on board UARS (Roche *et al.*, 1993; 1994; Figure 5.58) and by the CRISTA and ATMOS instruments (Zander *et al.*, 1996; Offermann *et al.*, 1999; Riese *et al.*, 1999) on board the Space Shuttle. The largest mixing ratios are found at high latitudes near 25-30 km altitude. The low concentrations observed in the winter polar region below 20 km altitude are due to heterogeneous conversion of $ClONO_2$.

HOCl has been observed by infrared thermal emission (Chance *et al.*, 1996) and by infrared solar absorption (Toon *et al.*, 1992a). The column abundance of OClO has been measured in Antarctica using visible absorption methods, for example, by Solomon *et al.* (1987), and in the Arctic by Wahner and Schiller (1992).

Hydrogen chloride (HCl) has been detected by spectroscopic absorption (Ackerman *et al.*, 1976; Farmer *et al.*, 1976; Raper *et al.*, 1977; Williams *et al.*, 1976; Zander *et al.*, 1996), by absorption radiometry (Eyre and Roscoe, 1977), by *in-situ* filter sampling and chemical analysis (Lazrus *et al.*, 1975, 1976), by submillimeterwave heterodyne techniques

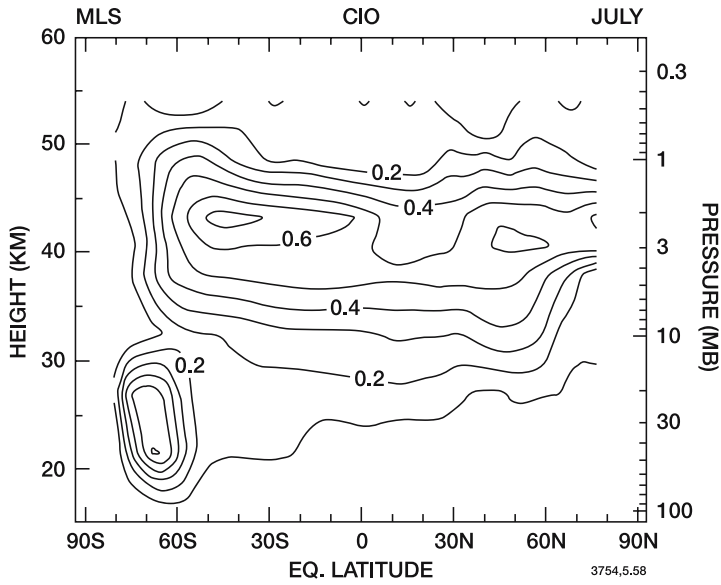

Figure 5.57. Meridional distribution of the ClO mixing ratio (ppbv) in July based on the measurements by the UARS/MLS instrument. Elevated levels in the lower stratosphere in winter at high latitudes (here south of 60°S between 15 and 28 km) are associated with heterogeneous reactions on PSC particles. (Courtesy of W. Randel, NCAR).

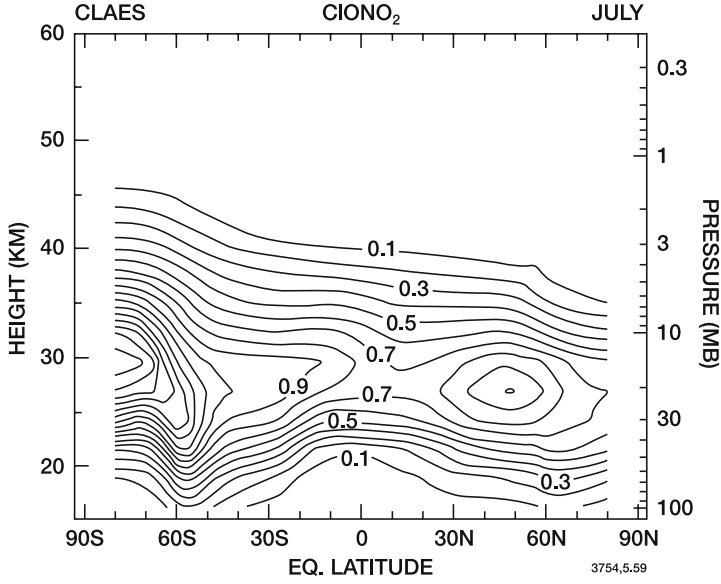

Figure 5.58. Meridional distribution of the $ClONO_2$ mixing ratio (ppbv) in July based on the measurements by the UARS/CLAES instrument (Courtesy of W. Randel, NCAR).

(Stacknik *et al.*, 1992), and by *in-situ* tunable diode laser spectrometry (May and Webster, 1989). In the 1990s, global distributions of this gas were obtained by the HALOE infrared instrument aboard UARS (Russell *et al.*, 1993; Figure 5.59). The distribution and variability of the total column abundances of HCl have been reported, for example, by Mankin and Coffey (1983).

Observations of inorganic bromine, and specifically BrO, have also been reported (see *e.g.*, Brune *et al.*, 1989; Carroll *et al.*, 1989; Toohey *et al.*, 1990; Avallone *et al.*, 1995; Fish *et al.*, 1997). Figure 5.60 shows some measured mixing ratios of BrO at mid-latitudes and in the polar regions. Values range from typically a few pptv at the tropopause to 10-15 pptv in the middle and upper troposphere. The stratospheric column abundance of BrO has been measured at mid-latitudes by Arpag *et al.* (1994), in Antarctica by Solomon *et al.* (1989b), and in the Arctic by Wahner and Schiller (1992).

Observations of bromine-bearing gases show large variations in the abundance of lower stratospheric Br_y, perhaps for both physical reasons (*i.e.*, true variability) and instrumental uncertainty. BrO observations using optical absorption methods (Pfeilsticker *et al.*, 2000) provide a new approach that supports the view that the lower stratospheric Br_y may often be considerably larger than suggested by consideration only of halon and CH_3Br sources. Short-lived molecules such as CH_2Br_2 and even $CHBr_3$ are possible additional sources (see Schauffler *et al.*, 1993) whose origins are largely natural but which may transport bromine to the upper troposphere or even to the stratosphere in convective towers (Ko *et al.*, 1997; Dvortsov *et al.*, 1999).

The impact of fluorine to the stratosphere is reflected in observed abundances of HF, its sole significant stratospheric reservoir. HF is observed mainly by infrared absorption and long records are available from ground-based sites (*e.g.*, Zander, 1981) which confirm its primary origin in anthropogenic sources. Satellite observations from UARS (see Figure 3.26) map its global distribution (Russell *et al.*, 1993), and its long lifetime makes HF a useful tracer for atmospheric motions (Toon *et al.*, 1992b).

5.7 Stratospheric Aerosols and Clouds

The existence of aerosol surfaces in the stratosphere has been known for many decades, but it was not until the discovery of the Antarctic ozone hole that their role in surface chemistry was recognized. Here the stratospheric sulfate layer and polar stratospheric clouds will be

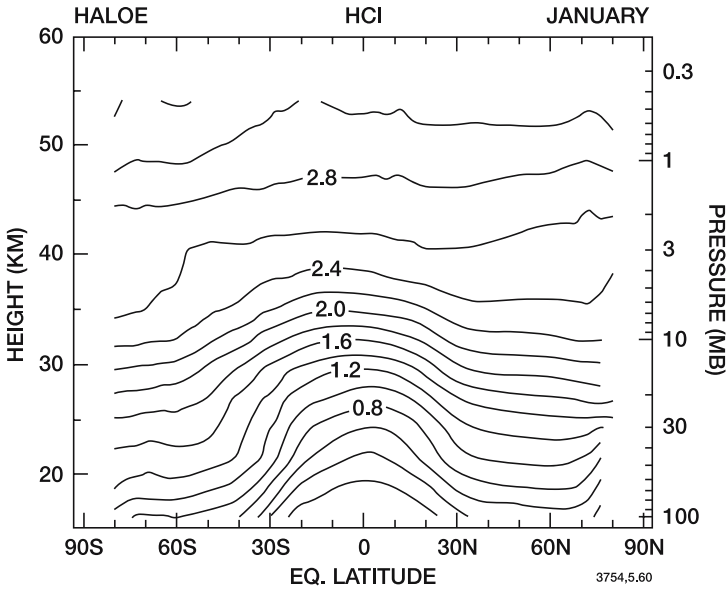

Figure 5.59. Meridional distribution of the HCl mixing ratio (ppbv) in January based on the measurements by the UARS/HALOE instrument (Courtesy of W. Randel, NCAR).

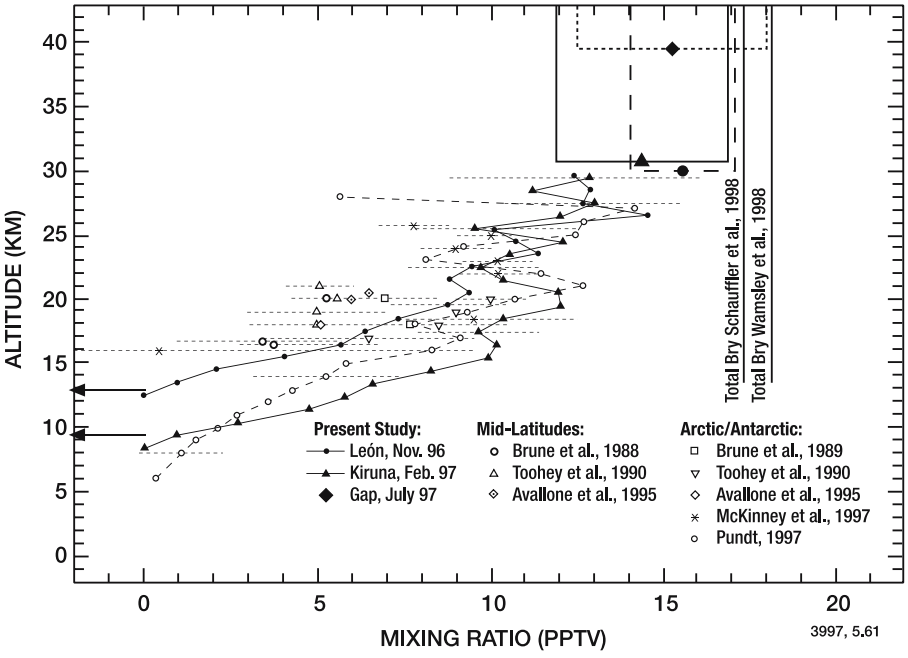

Figure 5.60. Observed stratospheric BrO mixing ratios (pptv) at mid- and high latitudes (Harder *et al.*, 1998).

described. Their critical roles in both mid-latitude and polar ozone depletion are discussed in Chapter 6.

5.7.1 The Sulfate Layer

Atmospheric sulfur is released at the Earth's surface by a number of processes. Some are natural: hydrogen sulfide, H_2S, for example, is a by-product of decomposition of organic matter; dimethyl sulfide (DMS or $(CH_3)_2S$), carbonyl sulfide (COS), and CS_2 are produced by the oceans. DMS is produced from dimethyl sulfide propriothetin (DMSP) by certain species of phytoplankton. COS results from the action of sunlight on dissolved organic compounds. Other sources are related to anthropogenic activities. Industry produces large amounts of sulfur dioxide, particularly through combustion of coal (especially coal fired electric power plants), as well as smaller quantities of H_2S, CS_2 and COS. Sulfur oxides and sulfuric acid vapors are also produced in combustion engines. Finally, volcanoes are responsible for the injection of appreciable amounts of sulfur into the atmosphere (SO_2, H_2S), either continuously through venting or episodically during volcanic eruptions.

Although sulfur is always present in the atmosphere, its density can vary considerably as a result of geophysical or anthropogenic perturbations. Urban regions exhibit large densities of sulfur-containing compounds, while most of the sulfur present above the ocean is of biogenic origin. The density of SO_2 in polluted air is quite variable, and depends on meteorological conditions as well as the source of the air masses, because the tropospheric lifetime of SO_2 is several days. In clean air, the mole fraction of SO_2 at low altitudes ranges from typically 10 to 500 pptv (Friend, 1973; Breeding *et al.*, 1973; Graedel *et al.*, 1974; Maroulis *et al.*, 1980; Nguyen *et al.*, 1983; Herman and Jaeschke, 1984). Values measured over the Pacific Ocean are close to 90 ± 60 pptv in the northern hemisphere and 60 ± 20 pptv in the southern hemisphere (Maroulis *et al.*, 1980). Measurements made in the remote marine atmosphere of the western Atlantic Ocean (Thornton *et al.*, 1987) resulted in median SO_2 mole fractions of 65 pptv in the free troposphere, compared with a value of approximately 1 ppbv in the boundary layer. Measurements by Bandy *et al.* (1993a) show that the mole fraction of SO_2 at 4 km over the coast of Brazil ranges from 15 to 60 pptv. Values close to 700 pptv have, for example, been reported by Boatman *et al.* (1989) in the central United States. Near the tropopause, abundances of about 50 pptv are characteristically observed over continental areas (Jaeschke *et al.*, 1976; Meixner, 1984),

indicating that less than 10% of the molecules typically reach the lower stratosphere. Other sulfur compounds such as H_2S and $(CH_3)_2S$ are short-lived and are therefore rapidly destroyed in the troposphere. On the other hand, COS is very stable and its mole fraction is of the order of 500 pptv throughout the troposphere (Hanst *et al.*, 1975; Sandalls and Penkett, 1977; Maroulis *et al.*, 1977; Friedl *et al.*, 1991; Weiss *et al.*, 1995), even at tropopause levels (Inn *et al.*, 1979; Mankin *et al.*, 1979). The lifetime of tropospheric COS is long, of the order of a year, and only above about 15 km does the mole fraction begin to decrease, reaching about 15 pptv at 30 km. CS_2 possesses an intermediate lifetime, as evidenced by an observed tropospheric variability of about 50% (Sandalls and Penkett, 1977). Its surface mixing ratio is about 100 pptv over polluted areas, but can be as low as 1-5 pptv in remote regions (Bandy *et al.*, 1993b). Therefore, middle atmospheric sulfur is linked in part to transport of COS across the tropopause as first suggested by Crutzen in 1976. COS is primarily produced by biologic, volcanic and anthropogenic sources. Thus, a potential increase in COS, particularly as a result of the use of large quantities of coal, could alter the composition of the atmosphere, increasing the concentration of sulfur aerosols and modifying the terrestrial radiative balance (see Crutzen, 1976; Turco *et al.*, 1980). No trend in COS has, however, been observed (Bandy *et al.*, 1992; Rinsland *et al.*, 1992). Large hemispheric gradients (15-25%), with larger concentrations measured in the Northern hemisphere, have been reported over the North Atlantic (Bingemer *et al.*, 1990; Johnson *et al.*, 1993). Table 5.10 provides an estimate of the global budget of sulfur in the atmosphere and shows that the largest gaseous emissions (approximately 90 Tg/yr) are of anthropogenic origin. However, only a fraction of this reaches the stratosphere. This budget can, however, be perturbed substantially by large volcanic eruptions. It is estimated that after the eruption of El Chichón (Mexico) in 1982 nearly 10 Tg of sulfur were injected into the stratosphere. The eruption of Mt. Pinatubo (the Philippines) in 1991 injected approximately 20 Tg S above the tropopause.

When COS reaches the stratosphere, photolysis occurs:

$$(J_{COS}); \qquad COS + h\nu \rightarrow CO + S \tag{5.302}$$

producing carbon monoxide and atomic sulfur. Sulfur reacts immediately with molecular oxygen:

$$(s_1); \qquad S + O_2 \rightarrow SO + O \tag{5.303}$$

Table 5.10 Global Budget of Sulfur (in Tg S/yr)

Sources		
	Compounds	*Flux*
Volcanoes	SO_2, H_2S, COS	7-10
Vegetation and Soils	H_2S, DMS, COS, CS_2, DMDS	0.4-1.2
Biomass Burning	SO_2, COS, H_2S	2-4
Oceans	DMS, COS, CS_2, H_2S	10-40
Anthropogenic	SO_2, sulfates	88-92
Sinks		
Dry Deposition	SO_2, sulfates	50-75
Wet Deposition	SO_2, sulfates	50-75

to produce sulfur monoxide. This species can also be formed by reaction of COS and atomic oxygen:

$$\mathrm{COS + O \rightarrow CO + SO} \tag{5.304}$$

which, like the slow reaction

$$\mathrm{COS + OH \rightarrow \ products} \tag{5.305}$$

represents an additional destruction mechanism for COS, but these are considerably less important than the direct photolysis process. Sulfur monoxide is in rapid equilibrium with SO_2. Its destruction is dominated by

$$(\mathrm{s_2}); \qquad \mathrm{SO + O_2 \rightarrow SO_2 + O} \tag{5.306}$$

which is more important (Black *et al.*, 1982a,b) than

$$(\mathrm{s_3}); \qquad \mathrm{SO + O_3 \rightarrow SO_2 + O_2} \tag{5.307}$$

and

$$(\mathrm{s_4}); \qquad \mathrm{SO + NO_2 \rightarrow SO_2 + NO} \tag{5.308}$$

Sulfur dioxide is relatively stable and is thus present in fairly large abundance in the stratosphere. It can be photodissociated by radiation in the 200-230 nm region, where its absorption cross section is of the order of 10^{-18} to $10^{-17}\mathrm{cm}^2$.

$$(\mathrm{J_{SO_2}}); \qquad \mathrm{SO_2 + h\nu \rightarrow SO + O} \tag{5.309}$$

or converted to HSO_3 by the following process:

$$(\mathrm{s_5}); \qquad \mathrm{SO_2 + OH + M \rightarrow HSO_3 + M} \tag{5.310}$$

The HSO_3 intermediate is probably destroyed by O_2 (Calvert and Stockwell, 1983; McKeen *et al.*, 1984):

$$(s_6); \qquad HSO_3 + O_2 \rightarrow HO_2 + SO_3 \tag{5.311}$$

Direct conversion of SO_2 to SO_3 by reactions such as

$$(s_7); \qquad SO_2 + HO_2 \rightarrow SO_3 + OH \tag{5.312}$$

$$(s_8); \qquad SO_2 + O + M \rightarrow SO_3 + M \tag{5.313}$$

can be neglected.

Sulfur trioxide can combine with water vapor to form sulfuric acid:

$$(s_9); \qquad SO_3 + H_2O \rightarrow H_2SO_4 \tag{5.314}$$

The acid can be photodissociated

$$(J_{H_2SO_4}); \qquad H_2SO_4 + h\nu \rightarrow HSO_3 + OH \tag{5.315}$$

or can precipitate in water droplets, (as can SO_2 and HSO_3) yielding sulfate aerosols. A complete analysis of sulfur compounds must therefore include heterogeneous processes.

It should be noted that the reaction sequences which convert SO_2 to sulfate do not modify the HO_x budget (McKeen *et al.*, 1984). The intrusion of large amounts of SO_2 in the stratosphere during volcanic eruptions could enhance the short-term amount of ozone in the middle atmosphere by direct chemical effects (Crutzen and Schmailzl, 1983; Bekki *et al.*, 1993) through the following mechanism:

$$\begin{aligned} &SO_2 + h\nu \rightarrow SO + O \\ &SO + O_2 \rightarrow SO_2 + O \\ &2(O + O_2 + M) \rightarrow 2(O_3 + M) \\ &\boxed{\text{Net:} \quad 3\ O_2 \rightarrow 2\ O_3} \end{aligned} \tag{5.316}$$

In the longer-term, and with contemporary loads of chlorine in the stratosphere, the presence of volcanic aerosols causes a reduction in the ozone abundance resulting from the large increase in aerosol surface area available for heterogeneous reactions (Hofmann and Solomon, 1989; Brasseur and Granier, 1992; Michelangeli *et al.*, 1992; Pitari and Rizzi, 1993; Tie *et al.*, 1994). These effects will be further discussed in Chapter 6.

Figure 5.61 shows a schematic diagram of the chemistry of sulfur and Figure 5.62 presents calculated distributions of the gaseous sulfur compounds from the model by Whitten *et al.* (1980). Some observations are also shown for comparison. This model shows that below 30 km

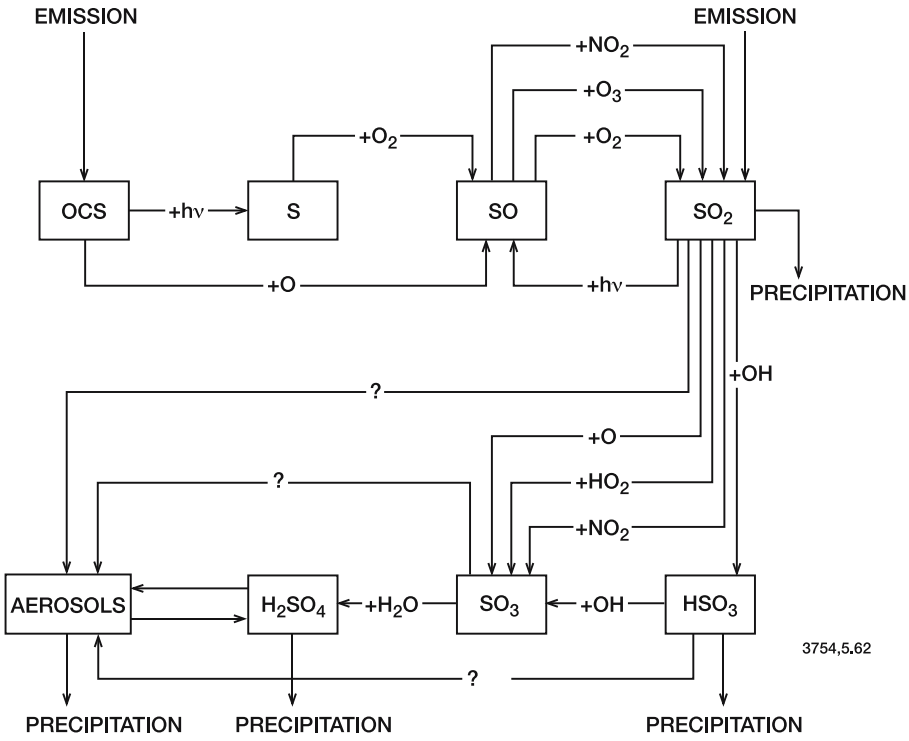

Figure 5.61. Primary sulfur reactions in the middle atmosphere.

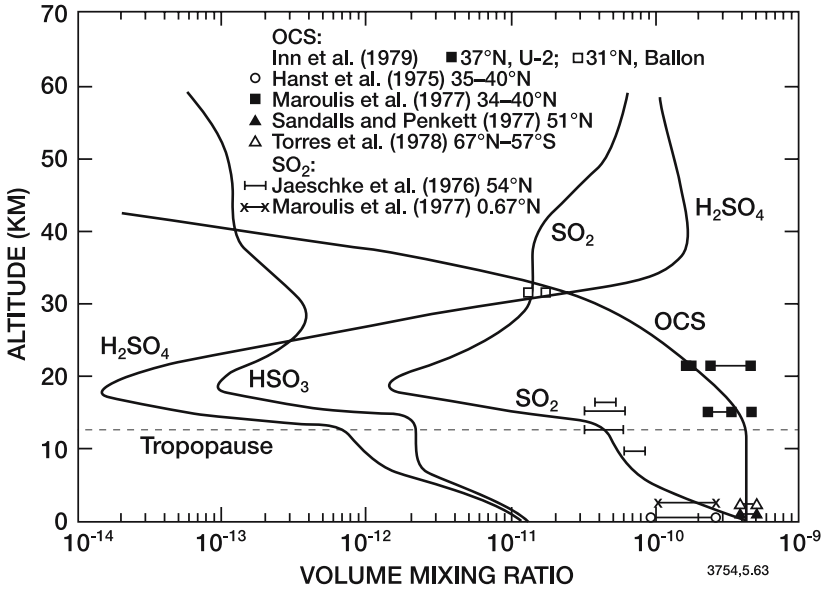

Figure 5.62. Vertical distribution of the primary sulfur compounds, as calculated by Turco *et al.* (1979).

during volcanically quiescent periods, sulfur is mostly in the form of COS, while at higher altitude it is mostly sulfuric acid.

Analyses of observations of negative ion densities can be used to derive the abundance of H_2SO_4, as shown, for example, by Arnold and Fabian (1980), Arijs *et al.* (1981), and Ingels *et al.* (1987). These observations confirm that the gaseous stratospheric H_2SO_4 concentration is largely determined by the equilibrium between the aerosol and vapor phases. The gas and aerosol chemistry of sulfur are discussed in detail in the excellent review by Turco *et al.*, (1982).

The H_2SO_4 molecule plays a major role in the microphysics of nucleation and condensation, and is therefore essential to the formation and growth of aerosols. These sub-micron liquid particles also coagulate, evaporate, or sediment out under the force of gravity. The exact mechanisms of nucleation, especially the initial processes, are poorly known, but it is presently thought that heterogeneous and heteromolecular nucleation of the H_2SO_4-H_2O system around fine Aitken particles (condensation nuclei of radius less than 0.1 μm) is predominant. These Aitken particles are probably transported from the troposphere and perhaps also produced by aircraft engines. Other processes may also be important in aerosol formation, such as homogeneous nucleation (nucleation of polar molecules such as H_2O, HNO_3, H_2SO_4 around ions). Evidence for such a process is implied by the formation of sulfate radicals and complex neutral species during ion-ion recombination.

After nucleation, the droplets grow through heteromolecular condensation, provided that the partial pressure of H_2SO_4 in the surrounding air is greater than the vapor pressure above the droplet. Otherwise, the H_2SO_4 will evaporate and the particles will shrink. The H_2SO_4/H_2O concentration ratio inside an aerosol particle varies significantly with temperature. Under stratospheric conditions, the H_2SO_4 concentration inside an aerosol particle is typically 80% wt at 240 K and 40% wt at 190 K. The concentration of stratospheric sulfate aerosols (SSA) is typically 10-20 particles cm^{-3}. Figure 5.63 presents a schematic diagram of the physical and chemical properties pertaining to stratospheric aerosol. It should be noted that although sulfur enters the stratosphere in gaseous form (essentially COS, CS_2, and SO_2), it leaves the middle atmosphere in the form of particles (sulfate) transported downward by the stratospheric circulation and by gravitational settling, followed by precipitation in tropospheric clouds (see Turco *et al.*, 1982).

An important aerosol property is the size distribution, which is usually expressed in an empirical form (power law, exponential, or log normal function) whose parameters are derived from observations. This size distribution depends on the nature of the particles and varies with

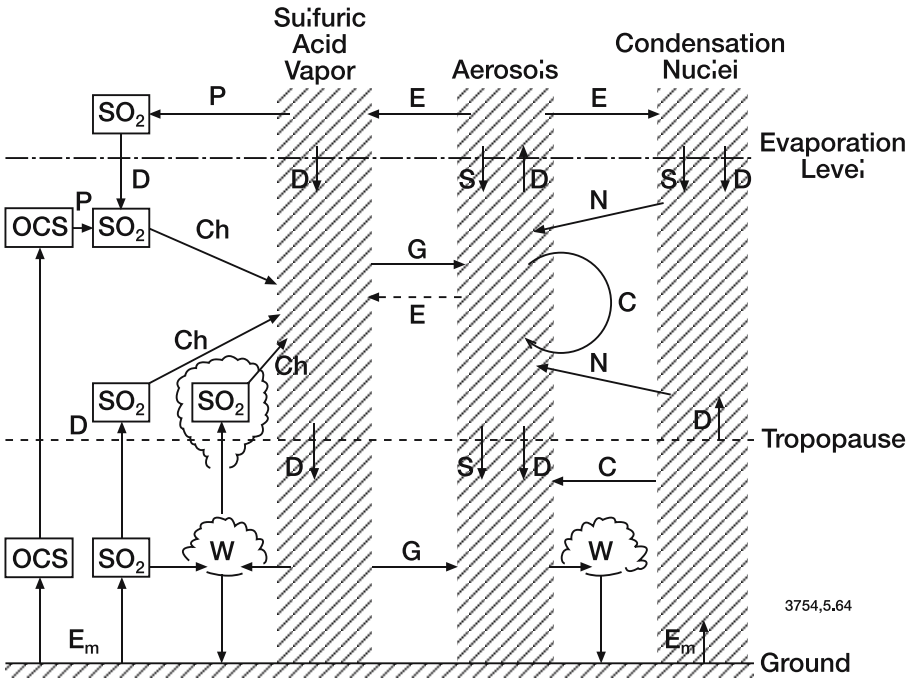

Figure 5.63. Schematic diagram of the physical and chemical processes related to the formation, growth, transport, and destruction of atmospheric aerosols: C = coagulation, Ch = chemistry, D = diffusion, E = evaporation, Em = emission, G = condensation and growth, I = injection, N = nucleation, P = photolysis, S = sedimentation, W = washout and rainout. From Turco *et al.* (1979).

altitude. As shown in Figure 5.64, for example, the concentration of condensation nuclei with radii smaller than 0.01 μm decreases monotoneously with increasing height above the tropopause, while the concentration of the larger particles (radius greater than 0.15μm) exhibits a broad peak in the lower stratosphere. The existence of this aerosol layer (called the *Junge layer*) approximately 5-7 km above the tropopause indicates that these particles grow in-situ in the stratosphere by sulfuric acid formation and by coalescence. Stratospheric sulfate aerosols remain generally liquid, although nonspherical (solid) sulfuric acid hydrate particles have occasionally been observed. They serve as condensation nuclei for the formation of polar stratospheric clouds in the Arctic and Antarctic (see Section 5.8).

Global climatologies of stratospheric aerosols have been produced from observations by satellite instruments. Hitchman *et al.* (1994), for example, have provided meridional distributions of measured extinction ratios based on 9 years of data from the Stratospheric Aerosol and Gas Experiment (SAGE I and II) and the Stratospheric Aerosol

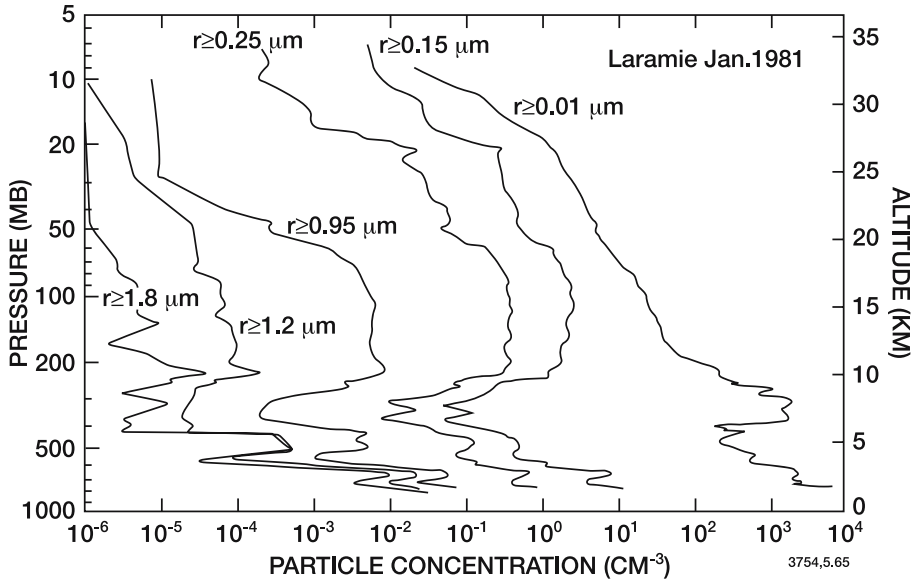

Figure 5.64. Observed particle size distribution with altitude. From Hofmann and Rosen (1981).

Measurement (SAM II) instruments. This climatology has provided insight into the general circulation of the stratosphere, and specifically on the circulation in the tropics associated with the quasi-biennial oscillation. Under background (non-volcanic) situations, the surface area density provided by aerosol particles is typically 0.5-1.0 μm^2 cm^{-3} in the lower stratosphere and less than 0.2 μm^2 cm^{-3} above 25 km altitude. After large volcanic eruptions such as those of El Chichón (Mexico) in April, 1982, and of Mt. Pinatubo (the Philippines) in June, 1991, during which large quantities (1-20 Tg) of SO_2 were injected into the stratosphere, the aerosol surface area increases dramatically (*e.g.*, 1-2 orders of magnitude after the eruption of Mt. Pinatubo). The decay time for such perturbation is typically 2-3 years. Heterogeneous reaction rates are enhanced proportionally, with substantial perturbations in the chemistry of the lower stratosphere (see *e.g.*, Hoffmann and Solomon, 1989; Brasseur and Granier, 1992). Global climatologies of stratospheric aerosol surface area density have been established by Hitchman *et al.* (1994) as well as by Thomason *et al.* (1997) (in this case on the basis of multiwavelength aerosol extinction measurements from space, see Plate 12). The meridional distribution of the aerosol surface area density (annual mean) derived by Thomason *et al.* (1997) is shown in Figure 5.65. Plate 8 shows the evolution of the surface area density at 20.5 km altitude from 1979 to 1995. The spread with latitude

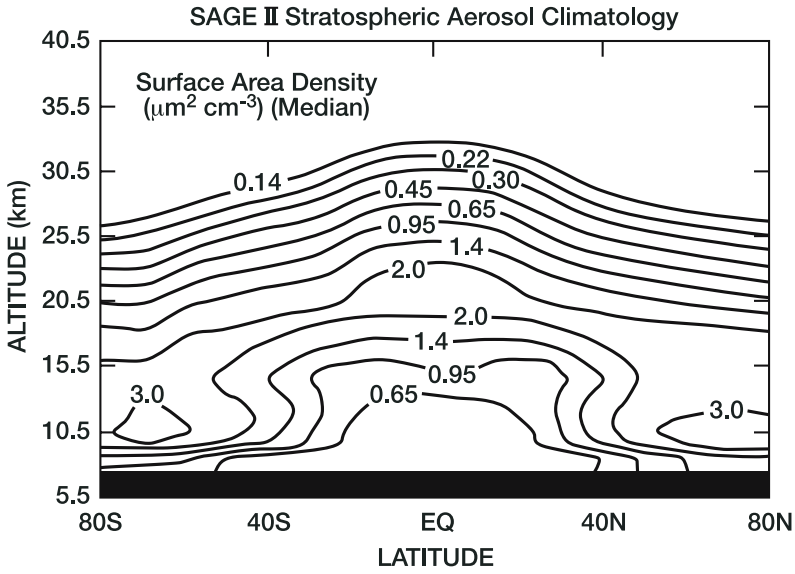

Figure 5.65. Median meridional distribution of the sulfate aerosol surface area density ($\mu m^2 cm^{-3}$) for the period 1985-1994, based on observations by the SAGE II satellite. From Thomason *et al.*, 1997.

of the aerosol perturbation following the eruption of Mt. Pinatubo is visible on this figure. Additional studies of aerosol changes following the Mt. Pinatubo eruption have also been performed by Langford *et al.* (1995), Russell *et al.* (1996), and others.

5.7.2 Polar Stratospheric Clouds

For more than a century, the presence of thin clouds has been reported at high altitudes in the polar regions. Because of their colorful appearances, especially at low solar elevation, these clouds have been named "mother-of-pearl" or nacreous clouds, or–more recently in the context of polar ozone research–*polar stratospheric clouds* (PSCs).

While PSCs form in the winter lower polar stratosphere, there is a second class of high altitude clouds that are formed during summertime at mesopause levels, when the temperature observed at these heights drops below approximately 150 K (see Plate 13). The chemical role of these mesospheric clouds is not yet well understood, but it has been suggested that the frequency of appearance of such clouds could increase in the future in response to human-induced cooling of the middle atmosphere (associated with enhanced levels of CO_2 and other "greenhouse gases" in the atmosphere).

PSCs (see Plate 14) are observed during winter in both the Antarctic and Arctic polar stratosphere (Stanford and Davis, 1974; McCormick *et al.*, 1982), typically from 12 to 26 km altitude (see *e.g.*, Poole and McCormick, 1988; Browell *et al.*, 1990; Gobbi and Adriani, 1993; Godin *et al.*, 1994). The presence of these clouds is associated with cold airmasses ($T < 200$ K). It was originally assumed that these PSCs were composed mainly of water ice (Steele *et al.*, 1983). Such particles are often observed in the Antarctic (*e.g.*, Poole *et al.*, 1988; Fahey *et al.*, 1990) and only occasionally in the Arctic (*e.g.*, Carslaw *et al.*, 1998a,b). Their diameter is typically 1-30 μm and their concentration can vary by several orders of magnitude. Because of their relatively large size, ice particles sediment in the atmosphere by typically 100 m per hour (assuming a diameter of 20 μm), leading to regular dehydration of the lower Antarctic stratosphere and very occasionally also in the Arctic. Such particles, which have been observed, for example, by lidar, can be identified by their optical properties (high depolarization corresponding to nonspherical and therefore solid particles). Early lidar observations made in Antarctica by Poole and McCormick (1988) have shown that, in addition to ice particles (called type II PSCs), optically thinner PSCs were also present at temperatures up to 5-6 K *above* the ice frost point. Crutzen and Arnold (1986) as well as Toon *et al.* (1986) suggested that these small particles could be formed by uptake of nitric acid and water onto pre-existing frozen sulfate aerosols (sulfuric acid tetrahydrate or SAT). The particles, first called Type I PSCs, have been frequently observed in the Antarctic (Fahey *et al.*, 1989; Pueschel *et al.*, 1989; Goodman *et al.*, 1989; 1997) and in the Arctic (Larsen *et al.*, 1996; 1997; Rosen *et al.*, 1997; Enell *et al.*, 1999). Fahey *et al.* (1989) observed that these particles contained considerable amounts of reactive nitrogen, which could possibly be identified as crystals of nitric acid trihydrates ($HNO_3 \cdot 3\ H_2O$ or NAT), which are the most thermodynamically stable solid hydrates under stratospheric conditions (Hanson and Mauersberger, 1988). Final evidence for the existence of NAT in the winter polar stratosphere has been provided by balloon-borne mass spectrometric measurements (Voigt *et al.*, 2000). The presence of nitric acid monohydrate (NAM) (McElroy *et al.*, 1986) and dihydrate (NAD) (Tolbert *et al.*, 1992; Worsnop *et al.*, 1993) has also been considered as a possibility. NAT particles are characterized by low backscatter ratios and high depolarization, and by atmospheric concentrations of generally less than 0.1 particles cm^{-3}. The diameter of these NAT particles ranges typically from 1 to 5 μm, and the volume densities of these particles (typically 1 $\mu m^3 cm^{-3}$) inferred from observations is considerably smaller than for ice particles. Fahey *et al.* (2001) have observed in the Arctic very large HNO_3-containing

particles (probably NAT or NAD). With diameters of 10-20 μm, such particles sediment rapidly (fall speed of 1.5 km day^{-1} for 14 μm spherical particles at 18-19 km), providing an efficient mechanism to denitrify the lower stratosphere.

Recent laboratory studies and field observations have led to a new conceptual picture of the composition and chemistry of PSCs (see Table 5.11). For example, the mechanisms advanced earlier to describe the formation of solid NAT particles appears unlikely to occur in the atmosphere. Lidar measurements by Browell *et al.* (1990) revealed very low depolarization of the backscatter signal, suggesting the presence of liquid particles (Toon *et al.*, 1990). Observations by Dye *et al.* (1992) and their analysis by Carslaw *et al.* (1994), Drdla *et al.* (1994) and Tabazadeh *et al.* (1994) have shown that, in addition to NAT particles (in Lidar terminology also called type Ia particles), liquid supercooled ternary solutions $H_2SO_4/HNO_3/H_2O$ (STS, also called type Ib particles) are often present in the winter stratosphere. These spherical particles have been observed in both polar regions (see *e.g.*, Adriani *et al.*, 1995; Hamill

Table 5.11 Particles in the Stratosphere

Particle type	*Composition/ name*	*Phase*	*Approximate temperature threshold*	*Observational evidence*
Stratospheric sulfate aerosol	H_2SO_4/H_2O	small liquid droplets	T < 261 K	strong
Sulfuric acid tetrahydrate	$H_2SO_4{\cdot}4\ H_2O$ (SAT)	small solid crystals	T < 213 K	weak
Nitric acid trihydrate	$HNO_3 \cdot 3\ H_2O$ (NAT)	solid crystals	T < 196 K	confirmed
Nitric acid dihydrate	$HNO_3 \cdot 2\ H_2O$ (NAD)	solid crystals	T < 193 K	vague
Supercooled ternary solution	$H_2SO_4/HNO_3/H_2O$ (STS)	liquid droplets	T < 192 K	strong
Ice	H_2O	large solid crystals	T < 189 K	strong
Amorphous solution	$H_2SO_4/HNO_3/H_2O$	solid particles	T < 170 K	not confirmed

et al., 1996; Beyer *et al.*, 1997; David *et al.*, 1997; Rosen *et al.*, 1997; Larsen *et al.*, 1997; Carslaw *et al.*, 1998a,b; Steele *et al.*, 1999). They seem to form a few degrees below the stability temperature threshold for NAT. In well developed clouds, STS are submicron particles at concentrations similar to ambient sulfate aerosols, whereby a significant increase in particle volume is observed 3-4 K below the NAT stability temperature.

The formation of PSC particles, as the temperature decreases, can no longer be represented by a "step function" as the stability point for NAT is reached, but should be regarded as a gradual transition from aqueous sulfuric acid aerosols to liquid PSC particles. Carslaw *et al.* (1997) have provided a detailed review of the thermodynamics of ternary solutions. As shown by Figure 5.66, in cold environments ($T < 195$ K), significant quantities of nitric acid are absorbed by sulfate aerosol particles, forming the $H_2SO_4/HNO_3/H_2O$ ternary solution. As the temperature decreases even further ($T < 191$ K), more HNO_3 and H_2O are absorbed from the gas phase, leading to the formation of a

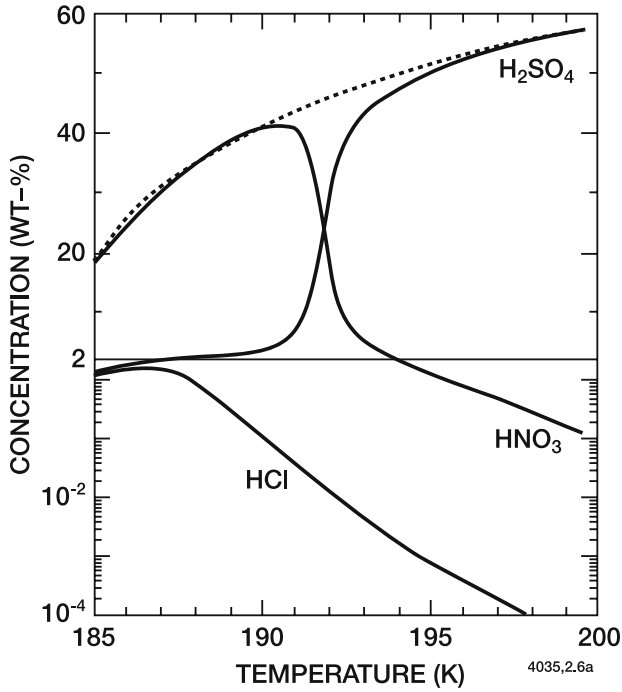

Figure 5.66. Relative mass concentration of H_2SO_4, HNO_3 and HCl dissolved within a liquid aerosol particle as a function of temperature. Note the change from linear to logarithmic scales below 2 wt%. Adapted from Carslaw *et al.* (1994).

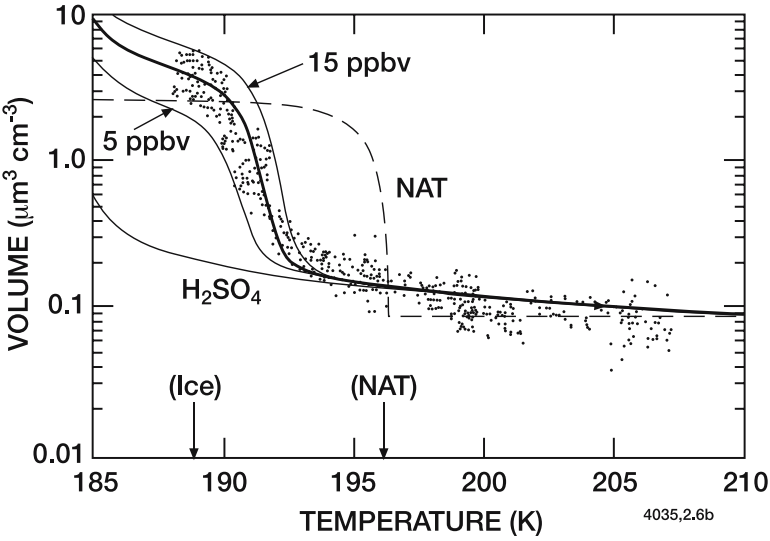

Figure 5.67. Total particle volume density observed by Dye *et al.* (1992) from the high altitude ER-2 aircraft on 24 January 1989, north of Stavanger, Norway, at 19 km altitude. As the temperature decreases, the aerosol particles initially grow as a result of H_2O uptake by the H_2SO_4/H_2O binary solution. At a temperature below 193 K, the volume increase is much more rapid, and suggests combined uptake of H_2O and HNO_3 by a $H_2SO_4/HNO_3/H_2O$ ternary solution. The data points are consistent with mixing ratios of HNO_3 ranging between 5 and 15 ppbv. The light solid line corresponding to the H_2SO_4/H_2O binary aerosol is calculated for a water vapor mixing ratio of 5 ppmv. The dash line corresponds to NAT particle growth without nucleation barrier. From Carslaw *et al.*, (1994).

quasi-binary HNO_3/H_2O solution. At very low temperatures ($T < 188$ K), HCl becomes increasingly soluble in the liquid particle. Shown in Figure 5.67 is the growth of different types of particles (background sulfate aerosols, supercooled ternary solution, NAT) resulting from the uptake of water and nitric acid as the temperature decreases from 210 to 185 K. The interpretation of cloud observations is often complicated due to the fact that different types of particles can co-exist in the same cloud. It seems that type Ib particles (liquid STS) are often observed in air parcels that have encountered temperatures below the SAT melting point during less than a day, while type Ia particles (NAT) are found in air parcels exposed to temperatures below the NAT stability point for several days (see *e.g.*, Tabazadeh *et al.*, 1995; 1996; Toon *et al.*, 2000).

Although the thermodynamics of liquid solutions is rather well understood, the circumstances under which solid PSCs are formed remain unresolved (Peter, 1997; Tolbert and Toon, 2001). It seems unlikely that NAT forms through direct nucleation on SAT because SAT particles become unstable and melt in the presence of gas-phase HNO_3

(Koop and Carslaw, 1996). NAT cannot easily or quickly be produced by direct freezing of the aqueous ternary solutions except, perhaps, if the temperature drops below the ice frost point (189 K) and water precipitates from the solution (Koop *et al.*, 1995). Rapid temperature fluctuations (associated, for example, with lee waves downstream from mountain ridges) may lead to non-equilibrium conditions under which the ternary solution could freeze (Meilinger *et al.*, 1995; Tsias *et al.*, 1997). Tabazadeh *et al.* (1995) have suggested that, under stratospheric conditions, amorphous solid binary or ternary solutions might form and be precursors to the formation of NAT-type crystals. As stressed, however, by Toon *et al.* (2000), it is difficult to establish if such particles have a chemical composition distinct from NAT or if they are just formed with a different nucleation rate. One study suggests that freezing may occur if particles remain cold for more than a day (Salcedo *et al.*, 2001). MacKenzie *et al.* (1995) and Drdla (1994) have suggested that trace impurities in particles may facilitate the freezing process. Further details on the microphysics and heterogeneous chemistry of polar stratospheric clouds can be found in the reviews by Peter (1997) and Carslaw *et al.* (1997). Further discussion on the role of the clouds in the observed ozone depletion in the Arctic and Antarctic is presented in Chapter 6.

5.8 Generalized Ozone Balance

The analysis presented above permits us to establish a generalized ozone and atomic oxygen balance, and to correct the equations derived previously by considering only a pure oxygen atmosphere. Detailed reviews of the ozone balance are provided by Johnston and Podolske (1978), and Crutzen and Schmailzl (1983). A general algorithm for the determination of all significant pathways involved in the ozone budget is provided by Lehmann (2004).

Above 40 km, the catalytic cycles involving hydrogen free radicals represent a very rapid loss process for odd oxygen (Nicolet, 1970):

$$\begin{gathered} \mathrm{OH} + \mathrm{O} \rightarrow \mathrm{H} + \mathrm{O_2} \\ \mathrm{H} + \mathrm{O_2} + \mathrm{M} \rightarrow \mathrm{HO_2} + \mathrm{M} \\ \mathrm{HO_2} + \mathrm{O} \rightarrow \mathrm{OH} + \mathrm{O_2} \\ \boxed{\text{Net: } \mathrm{O} + \mathrm{O} \rightarrow \mathrm{O_2}} \end{gathered} \tag{5.317}$$

or

$$\begin{gathered} OH + O \rightarrow H + O_2 \\ H + O_3 \rightarrow OH + O_2 \\ \boxed{\text{Net: } O + O_3 \rightarrow 2\ O_2} \end{gathered} \tag{5.318}$$

With some algebraic manipulation, the chemistry of these hydrogen catalyzed reactions can be included in the equation for the photochemical equilibrium ozone abundance between about 50 and 80 km to yield the following simple formulas at various altitudes (Allen *et al.*, 1984):

$$(O_3)_{50\ km} \approx \frac{(J_{O_2})^{\frac{2}{3}}(k_{4a}a_{17})^{\frac{1}{3}}\,[k_2(M)]^{\frac{2}{3}}\,(N_2)^{\frac{1}{3}}(O_2)^{\frac{4}{3}}}{(J_{O_3})^{\frac{2}{3}}(J_3^* a_1^* a_5 a_7)^{\frac{1}{3}}(H_2O)^{\frac{1}{3}}} \tag{5.319}$$

$$(O_3)_{70\ km} \approx \frac{J_{O_2}(a_{17})^{\frac{1}{2}}k_2(M)(O_2)^2}{J_{O_3}(J_{H_2O}a_5a_7)^{\frac{1}{2}}(H_2O)^{\frac{1}{2}}} \tag{5.320}$$

$$(O_3)_{80\ km} \approx \frac{(J_{O_2})^2 a_{23}k_2(M)(O_2)^2}{J_{H_2O}a_7a_1(H_2O)(M)\left[J_{O_3} + \frac{a_2}{a_1}\frac{J_{O_2}}{(M)}\right]} \tag{5.321}$$

The important role of odd hydrogen catalyzed destruction of odd oxygen is illustrated by comparing these expressions to Eq. (5.43), which presents the analytic expression for the equilibrium ozone density assuming only pure oxygen chemistry.

The hydrogen radicals also participate in the following cycle:

$$\begin{gathered} OH + O_3 \rightarrow HO_2 + O_2 \\ HO_2 + O_3 \rightarrow OH + 2O_2 \\ \boxed{\text{Net: } 2O_3 \rightarrow 3\ O_2} \end{gathered} \tag{5.322}$$

This process dominates the odd oxygen destruction near the tropopause because it is the most effective catalytic cycle involving only ozone as the reactive odd oxygen species. Most of the other HO_x, NO_x, and ClO_x cycles (see below) also require reaction with atomic oxygen, which is present only in very small amounts at low altitudes. For example, the following cycles are important in the middle and upper stratosphere, and in the mesosphere

$$\begin{gathered} OH + O_3 \rightarrow HO_2 + O_2 \\ HO_2 + O \rightarrow OH + O_2 \end{gathered}$$

$$\boxed{\text{Net: } O + O_3 \rightarrow 2\ O_2} \tag{5.323}$$

or

$$OH + O \rightarrow H + O_2$$

$$H + O_2 + M \rightarrow HO_2 + M$$

$$HO_2 + O_3 \rightarrow OH + 2O_2$$

$$\boxed{\text{Net: } O + O_3 \rightarrow 2O_2} \tag{5.324a}$$

or

$$OH + O \rightarrow H + O_2$$

$$H + O_3 \rightarrow OH + O_2$$

$$\boxed{\text{Net: } O + O_3 \rightarrow 2O_2} \tag{5.324b}$$

The nitrogen compounds can also catalyze the destruction of odd oxygen. This cycle is most efficient near 35-45 km (Crutzen, 1970; Johnston, 1971):

$$NO + O_3 \rightarrow NO_2 + O_2$$

$$NO_2 + O \rightarrow NO + O_2$$

$$\boxed{\text{Net: } O + O_3 \rightarrow 2O_2} \tag{5.325}$$

This cycle must be compared with another cycle that has no effect on odd oxygen:

$$NO + O_3 \rightarrow NO_2 + O_2$$

$$NO_2 + h\nu \rightarrow NO + O$$

$$O + O_2 + M \rightarrow O_3 + M$$

$$\boxed{\text{Net: Null}} \tag{5.326}$$

Thus, the efficiency of the NO_x catalyzed destruction of odd oxygen depends on the competition between photolysis and reaction with atomic oxygen for the NO_2 radical; the rate-limiting step for the destruction of odd oxygen is therefore provided by the $NO_2 + O$ reaction. Other secondary cycles should also be noted:

$$NO + O_3 \rightarrow NO_2 + O_2$$

$$\begin{gathered} NO_2 + O_3 \rightarrow NO_3 + O_2 \\ NO_3 + h\nu \rightarrow NO + O_2 \\ \boxed{\text{Net: } 2\ O_3 \rightarrow 3\ O_2} \end{gathered} \tag{5.327}$$

and

$$\begin{gathered} NO + O_3 \rightarrow NO_2 + O_2 \\ NO_2 + O_3 \rightarrow NO_3 + O_2 \\ NO_3 + NO_2 + M \rightarrow N_2O_5 + M \\ N_2O_5 + h\nu \rightarrow NO_3 + NO_2 \\ NO_3 + h\nu \rightarrow NO + O_2 \\ \boxed{\text{Net: } 2\ O_3 \rightarrow 3\ O_2} \end{gathered} \tag{5.328}$$

Note that these cycles result in ozone destruction only when the photolysis of NO_3 leads to NO + O_2 rather than NO_2 + O. In the latter case, the effect of these cycles is also null.

The catalytic destruction of odd oxygen by chlorine species must also be considered, particularly in the upper stratosphere where this cycle is quite effective (Stolarski and Cicerone, 1974; Molina and Rowland, 1974a):

$$\begin{gathered} Cl + O_3 \rightarrow ClO + O_2 \\ ClO + O \rightarrow Cl + O_2 \\ \boxed{\text{Net: } O + O_3 \rightarrow 2\ O_2} \end{gathered} \tag{5.329}$$

A similar cycle involves bromine compounds:

$$\begin{gathered} Br + O_3 \rightarrow BrO + O_2 \\ BrO + O \rightarrow Br + O_2 \\ \boxed{\text{Net: } \quad O + O_3 \rightarrow 2\ O_2} \end{gathered} \tag{5.330}$$

Below 30 km except in regions where heterogeneous reactions are proceeding rapidly, the densities of Cl and ClO are generally much reduced due to the formation of slow-reacting chlorine reservoirs including HCl and $ClONO_2$. Formation of these reservoirs limits the ozone loss in the lower stratosphere, and the effect of the direct chlorine

catalyzed destruction on odd oxygen is greatly reduced. However, the following cycle is generally important near 20 km:

$$\begin{gathered}
\mathrm{Cl} + \mathrm{O_3} \rightarrow \mathrm{ClO} + \mathrm{O_2} \\
\mathrm{ClO} + \mathrm{HO_2} \rightarrow \mathrm{HOCl} + \mathrm{O_2} \\
\mathrm{HOCl} + \mathrm{h}\nu \rightarrow \mathrm{Cl} + \mathrm{OH} \\
\mathrm{OH} + \mathrm{O_3} \rightarrow \mathrm{HO_2} + \mathrm{O_2} \\
\boxed{\text{Net: } 2\mathrm{O_3} \rightarrow 3\mathrm{O_2}}
\end{gathered} \tag{5.331}$$

Here also similar cycles with bromine must be considered; *e.g.*,

$$\begin{gathered}
\mathrm{Br} + \mathrm{O_3} \rightarrow \mathrm{BrO} + \mathrm{O_2} \\
\mathrm{BrO} + \mathrm{HO_2} \rightarrow \mathrm{HOBr} + \mathrm{O_2} \\
\mathrm{HOBr} + \mathrm{h}\nu \rightarrow \mathrm{Br} + \mathrm{OH} \\
\mathrm{OH} + \mathrm{O_3} \rightarrow \mathrm{HO_2} + \mathrm{O_2} \\
\boxed{\text{Net:} \quad 2\ \mathrm{O_3} \rightarrow 3\ \mathrm{O_2}}
\end{gathered} \tag{5.332}$$

When high concentrations ($\sim$ 1 ppbv) of ClO are present in the lower stratosphere (*e.g.*, in air masses wherein the reservoir's HCl and $\mathrm{ClONO_2}$ have been processed by polar stratospheric clouds), additional cycles must be considered (see Figure 5.68); one of them involves the formation of the $\mathrm{Cl_2O_2}$ dimer which dominates the destruction of polar ozone (*e.g.*, Antarctic ozone hole):

$$\begin{gathered}
\mathrm{ClO} + \mathrm{ClO} + \mathrm{M} \rightarrow \mathrm{Cl_2O_2} + \mathrm{M} \\
\mathrm{Cl_2O_2} + \mathrm{h}\nu \rightarrow \mathrm{Cl} + \mathrm{ClOO} \\
\mathrm{ClOO} + \mathrm{M} \rightarrow \mathrm{Cl} + \mathrm{O_2} + \mathrm{M} \\
2\,(\mathrm{Cl} + \mathrm{O_3} \rightarrow \mathrm{ClO} + \mathrm{O_2}) \\
\boxed{\text{Net: } 2\mathrm{O_3} \rightarrow 3\mathrm{O_2}}
\end{gathered} \tag{5.333}$$

The formation rate of the ClO dimer and the photolysis rate of $\mathrm{Cl_2O_2}$ are critical pieces of information to calculate the ozone loss in the polar regions (Avallone and Toohey, 2001). A second cycle, which introduces an interaction between the chlorine and bromine families also contributes to the destruction of ozone in polar regions, as well as at middle latitudes:

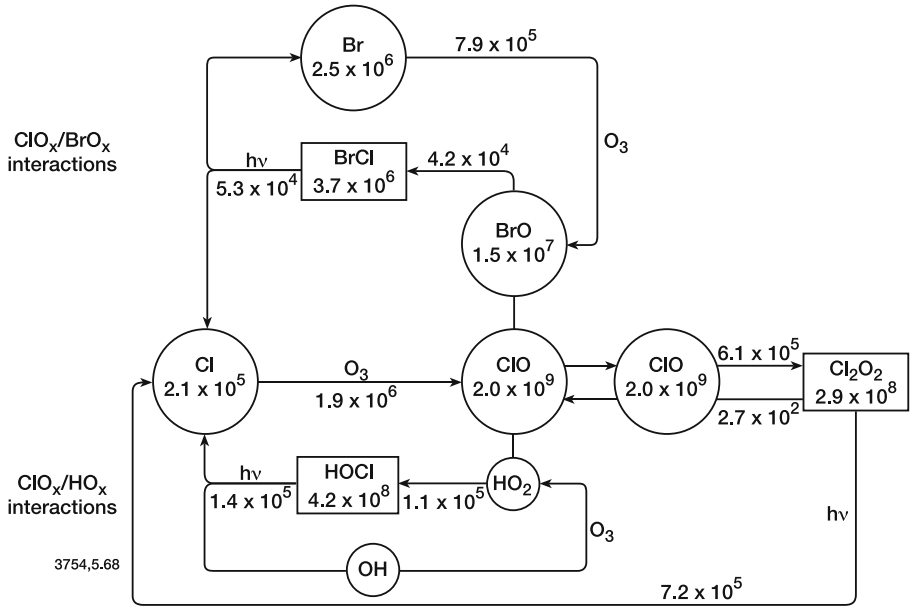

Figure 5.68. Reaction scheme responsible for rapid ozone destruction in polar regions when large amounts of chlorine and bromine are activated by polar stratospheric clouds. Concentrations (cm^{-3}) and fluxes ($cm^{-3}s^{-1}$) associated with chemical reactions are calculated for Antarctic springtime conditions (lower stratosphere). After Zellner (1999).

$$\begin{gathered}
\mathrm{ClO + BrO \rightarrow Br + Cl + O_2} \\
\mathrm{Br + O_3 \rightarrow BrO + O_2} \\
\mathrm{Cl + O_3 \rightarrow ClO + O_2} \\
\boxed{\text{Net: } 2\mathrm{O_3} \rightarrow 3\mathrm{O_2}}
\end{gathered} \tag{5.334}$$

where the $\mathrm{BrO+ClO \rightarrow Br+Cl+O_2}$ reaction, as written here, represents one of the 2 possible processes

$$\begin{gathered}
\mathrm{ClO + BrO \rightarrow Br + ClOO} \\
\mathrm{ClOO + M \rightarrow Cl + O_2 + M}
\end{gathered}$$

or

$$\begin{gathered}
\mathrm{ClO + BrO \rightarrow BrCl + O_2} \\
\mathrm{BrCl + h\nu \rightarrow Br + Cl}
\end{gathered}$$

A similar possible cycle involves an interaction between the bromine and iodine families:

$$\begin{gathered}
\mathrm{BrO} + \mathrm{IO} \rightarrow \mathrm{Br} + \mathrm{I} + \mathrm{O_2} \\
\mathrm{I} + \mathrm{O_3} \rightarrow \mathrm{IO} + \mathrm{O_2} \\
\mathrm{Br} + \mathrm{O_3} \rightarrow \mathrm{ClO} + \mathrm{O_2} \\
\boxed{\text{Net: } 2\mathrm{O_3} \rightarrow 3\mathrm{O_2}}
\end{gathered} \tag{5.335}$$

The importance of chlorine activation in the Antarctic region during winter and spring and the associated ozone destruction by cycles as (5.333) and (5.334) can be seen in Figure 5.69. This diagram shows the chemical changes affecting air masses in the southern polar region, when the temperature becomes so low that polar stratospheric clouds are formed (see Section 5.7.2). Heterogeneous reactions (*e.g.*, (5.222) and (5.223)) occurring on the surface of cloud particles tend to convert chlorine reservoirs into more reactive compounds. These are photolyzed as the Sun returns in the polar region, and the levels of ClO that are produced are sufficiently high to destroy large amounts of ozone in a few weeks. The concentrations of ClO remain high because nitrogen oxides are converted into nitric acid by heterogenous process (see Reaction (5.152)) and therefore cannot react with ClO to form $\mathrm{ClONO_2}$. Note also the denitrification and dehydration of the lower polar stratosphere through sedimentation of the largest cloud particles. As the temperature gradually increases duirng springtime, and the polar stratospheric clouds disappear, nitrogen oxides produced by photolysis of nitric acid survive a sufficiently long time to rapidly convert ClO into $\mathrm{ClONO_2}$. Chlorine atoms react also with methane to form HCl. At that time, the fast catalytic cycles (5.333) and (5.334) cease to be efficient mechanisms to deplete ozone. A more detailed description of the processes affecting polar ozone is given in Chapter 6.

Other reactions affecting ozone in the lower stratosphere must be considered. The following cycle is significant when the photolysis products of $\mathrm{ClONO_2}$ are Cl and $\mathrm{NO_3}$,

$$\begin{gathered}
\mathrm{ClO} + \mathrm{NO_2} \rightarrow \mathrm{ClONO_2} \\
\mathrm{ClONO_2} + \mathrm{h}\nu \rightarrow \mathrm{Cl} + \mathrm{NO_3} \\
\mathrm{Cl} + \mathrm{O_3} \rightarrow \mathrm{ClO} + \mathrm{O_2} \\
\mathrm{NO_3} + \mathrm{h}\nu \rightarrow \mathrm{NO} + \mathrm{O_2} \\
\mathrm{NO} + \mathrm{O_3} \rightarrow \mathrm{NO_2} + \mathrm{O_2} \\
\boxed{\text{Net: } 2\ \mathrm{O_3} \rightarrow 3\ \mathrm{O_2}}
\end{gathered} \tag{5.336}$$

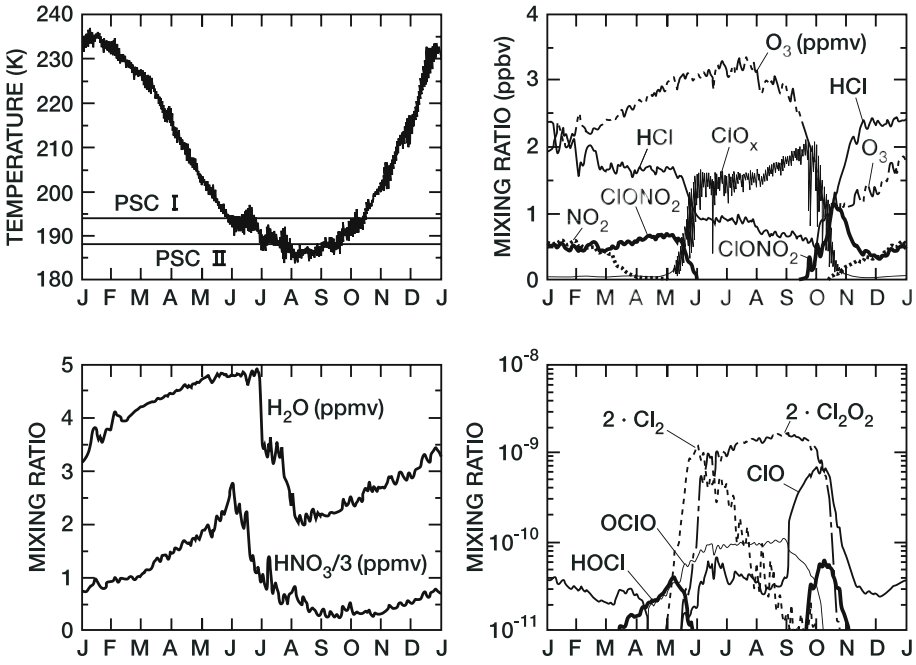

Figure 5.69. Evolution with time of temperature (upper left panel) and chemical composition (other panels) of an airmass situated at 82°S and 20 km altitude, highlighting the activation of halogen compounds in the presence of polar stratospheric clouds. As temperature drops below the threshold for PSC I formation, initial signs of denitrification are seen (June). Dehydration occurs about a month later as the temperature reaches the threshold for water ice formation. The reservoir species (HCl and $ClONO_2$) are converted to reactive chlorine species by heterogeneous reactions on the surface of PSC particles. ClO_x is enhanced throughout the polar night and ozone is destroyed as solar radiation becomes available in the spring. The partitioning between the ClOx species (here defined as Cl + ClO + $2Cl_2O_2$ + OClO + HOCl + $2Cl_2$) is shown in the lower right panel. Ozone recovery takes place in late spring as PSC disappear and reactive chlorine is converted back to $ClONO_2$ and HCl. Values based on the MOZART-3 global chemical/transport model. Courtesy of D. Kinnison (NCAR).

Similarly, $BrONO_2$ photolysis can destroy ozone efficiently in the lower stratosphere (Burkholder, 1995):

$$\mathrm{BrO + NO_2 \rightarrow BrONO_2}$$
$$\mathrm{BrONO_2 + h\nu \rightarrow Br + NO_3}$$
$$\mathrm{Br + O_3 \rightarrow BrO + O_2}$$
$$\mathrm{NO_3 + h\nu \rightarrow NO + O_2}$$
$$\mathrm{NO + O_3 \rightarrow NO_2 + O_2}$$

$$\boxed{\text{Net:} \quad 2\ O_3 \rightarrow 3\ O_2} \tag{5.337}$$

For typical levels of $BrONO_2$, this latter cycle is believed to be more effective at destroying ozone than the similar cycle involving chlorine compounds (Toumi *et al.*, 1993; Lary, 1996). These cycles illustrate the importance of the interactions between various chemical families.

In the ozone destruction cycle presented above, the conversion of NO to NO_2 by direct reactions with ozone can be replaced by other pathways, including the reactions involving the peroxy radical HO_2,

$$NO + HO_2 \rightarrow OH + NO_2$$

$$OH + O_3 \rightarrow HO_2 + O_2$$

or the chlorine oxide radical ClO

$$NO + ClO \rightarrow Cl + NO_2$$

$$Cl + O_3 \rightarrow ClO + O_2$$

It is important to note that certain cycles can lead to ozone formation; this phenomenon is readily observed in the troposphere (see Box 5.4), which is rich in anthropogenic hydrocarbons and nitrogen oxides. In the free troposphere and lower stratosphere, the conversion of NO to NO_2 by peroxy radicals (HO_2 and CH_3O_2) produced by the oxidation of methane and carbon monoxide, followed by the photodissociation of NO_2 leads to the formation of O_3. The complete chains are the following (Crutzen, 1974):

$$CH_4 + OH \rightarrow CH_3 + H_2O$$

$$CH_3 + O_2 + M \rightarrow CH_3O_2 + M$$

$$CH_3O_2 + NO \rightarrow CH_3O + NO_2$$

$$NO_2 + h\nu \rightarrow NO + O$$

$$O + O_2 + M \rightarrow O_3 + M$$

$$CH_3O + O_2 \rightarrow CH_2O + HO_2$$

$$HO_2 + NO \rightarrow NO_2 + OH$$

$$NO_2 + h\nu \rightarrow NO + O$$

$$O + O_2 + M \rightarrow O_3 + M$$

$$CH_2O + h\nu \rightarrow CO + H_2$$

$$\boxed{CH_4 + 4\ O_2 + h\nu \rightarrow H_2\ O + CO + H_2 + 2\ O_3} \tag{5.338}$$

Box 5.4. The Oxidizing Power of the Atmosphere

The influx into the stratosphere of chemical compounds emitted at the surface (*e.g.*, biogenic gases, primarly pollutants) or photochemically produced in the lower atmosphere (*e.g.*, secondary pollutants) depends on the rate at which these compounds are destroyed in the troposphere. The region below the tropopause often acts as a "filter" against species that are transported upwards: soluble molecules are wet-scavenged by precipitation; other species are chemically converted by oxidation processes.

The *oxidation potential* of the atmosphere determines the rate at which most reactive species are destroyed in the atmosphere. Oxidation by molecular oxygen (O_2) is generally slow. The most efficient oxidant is the hydroxyl (OH) radical, although other compounds such as NO_3, H_2O_2 and O_3 play a significant role in certain cases. As in the middle atmosphere, the OH radical in the troposphere is produced primarily during the daytime by the reaction between water vapor (H_2O) and the electronically-excited oxygen atom $O(^1D)$ (see Reaction (5.82) and Engleman, 1965; Levy, 1971) In the upper troposphere, however, especially in the tropics, where the water vapor abundance is relatively low, and molecules released at the surface can be rapidly transported by convective uplift, an additional primary source of hydrogen and radicals (HO_x) is provided by the photolysis of organic molecules, including acetone, aldehydes, and organic peroxides (*e.g.*, Singh *et al.*, 1995; Prather and Jacob, 1997; Müller and Brasseur, 1999).

OH is converted to HO_2 by reactions with carbon monoxide (Reaction (5.79)) and ozone (Reaction (5.90)), and HO_2 is converted back to OH by reactions with nitric oxide (Reaction (5.92)) and ozone (Reaction (5.91)). The loss of HO_x results from the conversion of OH and HO_2 into soluble species like H_2O_2 and HNO_3, followed by wet scavenging of these molecules through precipitation.

Since the presence (in very small quantities) of $O(^1D)$ in the troposphere results from the photolysis of ozone (see Reaction (5.16)), an assessment of the oxidizing power of the atmosphere requires that the global budget of tropospheric ozone be accurately quantified.

Approximately 10% of atmospheric ozone resides in the troposphere. Since solar radiation of wavelengths less than 242 nm that photolyzes molecular oxygen (see Reaction (5.11)) is entirely absorbed above the tropopause, and hence cannot produce ozone in the lower atmosphere, it was believed for a long time that the presence of O_3 in the free troposphere was due to downward transport of ozone-rich air masses from the stratosphere. Dry deposition of O_3 on vegetation was believed to be the only significant loss process.

In the early 1950s, Hagen-Smit (1952) suggested that the high ozone levels frequently observed in urban areas, like Los Angeles during summer-

Box 5.4 (Continued)

time, were associated with the emission of primary pollutants (NO_x, CO, hydrocarbons) by automobiles and power plants. About 20 years later, Crutzen (1973, 1974) and Chameides and Walker (1973) showed that similar processes could provide a substantial photochemical source of ozone in the free troposphere at the global scale. Rather than involving the photolysis of O_2 as in the middle atmosphere, the formation of atomic oxygen (which recombines with O_2 to form ozone) results from the photolysis of NO_2 into O and NO. The process that converts NO back to NO_2 without consuming ozone, and hence "limits" the rate of ozone formation is provided by

$$NO + RO_2 \rightarrow NO_2 + RO \qquad (5.339)$$

where the peroxy radicals RO_2 (which can be a hydroperoxy radical HO_2 or organic peroxy radical such as CH_3O_2, $C_2H_5O_2$, etc.) are produced by the oxidation of the so-called ozone precursors (CO, CH_4, non-methane hydrocarbons). Oxidation of these precursors leads to a net ozone production only for sufficiently high atmospheric levels of nitrogen oxides (see Reactions (5.338) and (5.340)).

The major photochemical losses of tropospheric ozone are provided by reactions of O_3 with OH (Reaction (5.90)) and HO_2 (Reaction (5.91)), as well as by ozone photolysis (Reaction (5.16)), if it is followed by the irreversible loss of $O(^1D)$, for example, by the reaction of this tome with water vapor.

Figure 5.70 shows the number density of OH and HO_2, as well as the net ozone photochemical production as a function of the NO_x mixing ratio, near the surface and in the upper troposphere. These daytime quantities are calculated by a zero-dimensional "box" model for typical values of H_2O, CH_4 CO and nonmethane hydrocarbon concentrations. This figure suggests that the oxidizing properties of the troposphere are strongly affected by the level of tropospheric NO_x. Over the oceans, for example, where the abundance of NO_x is generally very low, the atmosphere acts as a loss for tropospheric ozone and the OH/HO_2 concentration ratio is low. In moderately polluted areas, where NO_x levels are higher, the net ozone production and the OH concentration increase with the NO_x abundance. In highly polluted areas (*e.g.*, urban zones) with very high NO_x concentrations, HO_x radicals are efficiently converted into nitric acid, and the net production of ozone decreases dramatically.

The nitrate radical (NO_3) which is present in the troposphere primarily during nighttime is also a powerful oxidant, and reacts efficiently with many organic compounds (nonmethane hydrocarbons, DMS, etc.). Hydrogen peroxide (H_2O_2) is a major oxidant for SO_2 inside water droplets, and contributes to the formation of sulfate aerosols.

Box 5.4 (Continued)

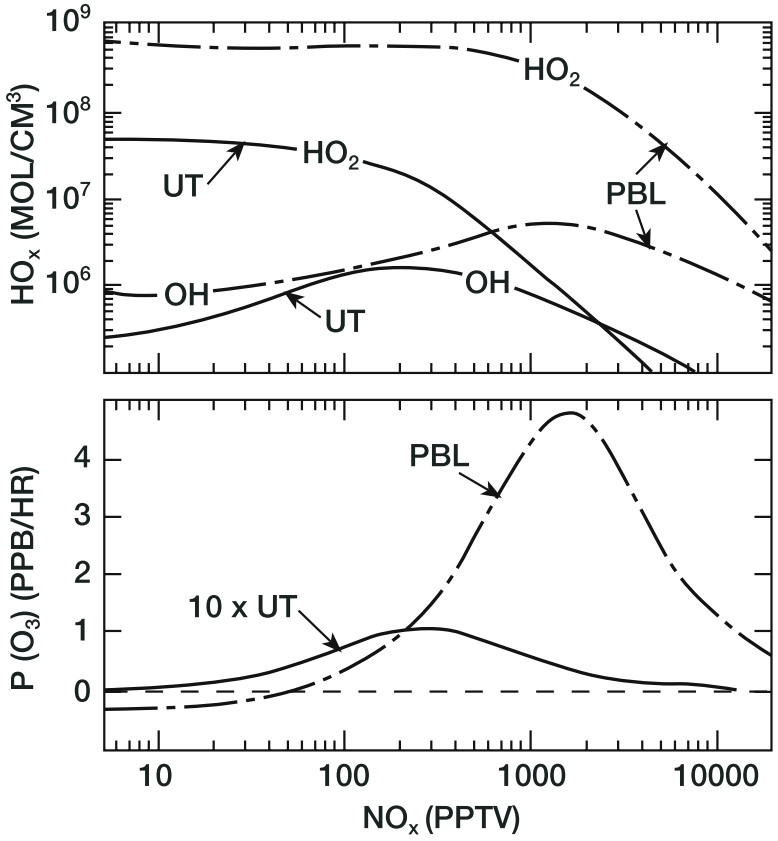

Figure 5.70. Upper panel: Concentration (cm^{-3}) of OH and HO_2 as a function of the NO_x ($NO + NO_2$) mole fraction (pptv) for conditions representative of the upper troposphere (UT-solid line) and planetary boundary layer (PBL-dashed line). Lower panel: Same, but for the net photochemical rate (ppb/hr) of ozone. The values corresponding to the upper troposphere are multiplied by 10. From Brune (2000).

The oxidizing properties of the troposphere have a strong influence on the lifetime of chemical compounds in the atmosphere, and hence on the probability for a molecule to reach the middle atmosphere. Most hydrocarbons, for example, including hydrogenated halocarbons, are efficiently destroyed by the OH radical in the troposphere before they can penetrate into the stratosphere. Compounds that are not oxidized in the troposphere (*e.g.*, chlorofluorocarbons) or weakly oxidized (*e.g.*, methane) reach the stratosphere more easily.

and

$$\begin{gathered}
\mathrm{CO + OH \rightarrow CO_2 + H} \\
\mathrm{H + O_2 + M \rightarrow HO_2 + M} \\
\mathrm{HO_2 + NO \rightarrow OH + NO_2} \\
\mathrm{NO_2 + h\nu \rightarrow NO + O} \\
\mathrm{O + O_2 + M \rightarrow O_3 + M} \\
\boxed{\text{Net: } \mathrm{CO + 2\ O_2 + h\nu \rightarrow CO_2 + O_3}}
\end{gathered} \tag{5.340}$$

If, however, NO is reduced by efficient heterogeneous reactions (*e.g.*, on polar stratospheric clouds), the oxidation of methane becomes catalyzed by ClO, and, rather than producing two ozone molecules per cycle, destroys two ozone molecules for each methane molecule oxidized (Crutzen *et al.*, 1992). The chain is the following (Lary, 1996):

$$\begin{gathered}
\mathrm{CH_4 + OH \rightarrow CH_3 + H_2O} \\
\mathrm{CH_3 + O_2 + M \rightarrow CH_3O_2 + M} \\
\mathrm{CH_3O_2 + ClO \rightarrow CH_3O + Cl + O_2} \\
\mathrm{Cl + O_3 \rightarrow ClO + O_2} \\
\mathrm{CH_3O + O_2 \rightarrow CH_2O + HO_2} \\
\mathrm{HO_2 + ClO \rightarrow HOCl + O_2} \\
\mathrm{HOCl + h\nu \rightarrow OH + Cl} \\
\mathrm{Cl + O_3 \rightarrow ClO + O_2} \\
\mathrm{CH_2O + h\nu \rightarrow CO + H_2} \\
\boxed{\text{Net: } \mathrm{CH_4 + 2\ O_3 + h\nu \rightarrow H_2O + CO + H_2 + 2O_2}}
\end{gathered} \tag{5.341}$$

The complete ozone equation is complex as a result of all these processes. Considering only the most important processes, the general behavior of ozone can be described by the following equations:

$$\begin{aligned}
\frac{\mathrm{d(O_3)}}{\mathrm{dt}} &+ \mathrm{J_{O_3}(O_3) + k_3(O)(O_3) + a_2(H)(O_3) + a_6(OH)(O_3)} \\
&+ \mathrm{a_{6b}(HO_2)(O_3) + b_4(NO)(O_3) + b_9(NO_2)(O_3)} \\
&+ \mathrm{d_2(Cl)(O_3) + e_2(Br)(O_3) = k_2(M)(O_2)(O)}
\end{aligned} \tag{5.342}$$

$$\frac{d(O)}{dt} + 2k_1(M)(O)^2 + k_2(M)(O_2)(O) + k_3(O_3)(O) + a_5(OH)(O) + a_7(HO_2)(O) + b_3(NO_2)(O) + d_3(ClO)(O) + e_3(BrO)(O) = 2J_{O_2}(O_2) + J_{O_3}(O_3) + J_{NO_2}(NO_2) + J_{BrO}(BrO) + J^a_{NO_3}(NO_3) \quad (5.343)$$

where equilibrium has been assumed for $O(^1D)$. Adding Eqs. (5.342) and (5.343), the rate of change for odd oxygen (O_x) becomes

$$\frac{d(O_x)}{dt} + 2k_1(M)(O)^2 + 2k_3(O)(O_3) + a_2(H)(O_3) + [a_5(OH) + a_7(HO_2)](O) + [a_6(OH) + a_{6b}(HO_2)](O_3) + b_3(NO_2)(O) + b_4(NO)(O_3) + b_9(NO_2)(O_3) + d_3(ClO)(O) + d_2(Cl)(O_3) + e_3(BrO)(O) + e_2(Br)(O_3) = 2J_{O_2}(O_2) + J_{NO_2}(NO_2) + J^a_{NO_3}(NO_3) \quad (5.344)$$

This equation still accounts for gross production and destruction rates associated with rapid chemical cycling. To eliminate large, and often compensating terms, it is therefore more appropriate to define the "odd oxygen" as the sum of all chemical compounds that include one or more "odd oxygen" attached to them. If we define O_y as the sum

$$O_y = O(^3P) + O(^1D) + O_3 + NO_2 + 2NO_3 + HNO_3 + HO_2NO_2 + 2N_2O_5 + ClO + 2Cl_2O_2 + 2OClO + 2ClONO_2 + BrO + 2BrONO_2$$

and if we add the continuity equations for all the corresponding species, we obtain, after eliminating the small terms and adding a transport term

$$\frac{\partial(O_y)}{\partial t} + \nabla \cdot \boldsymbol{\phi}(O_y) + 2k_1(M)(O)^2 + 2k_3(O)(O_3) + a_2(H)(O_3) + [a_5(OH) + a_7(HO_2)](O) + [a_6(OH) + a_{6b}(HO_2)](O_3) + 2b_3(NO_2)(O) + 2d_3(ClO)(O) + 2e_3(BrO)(O) + d_{33}(ClO)(HO_2) + e_{15}(BrO)(HO_2) + 2J_{Cl_2O_2}(Cl_2O_2) + 2[d_{48} + d_{49}](ClO)(ClO) + 2e_6(BrO)(BrO) + 2[e_{5b} + e_{5c}](BrO)(ClO) + 2J^b_{NO_3}(NO_3) = 2J_{O_2}(O_2) + a_{26}(HO_2)(NO) + c_5(CH_3O_2)(NO) \quad (5.345)$$

Under this convention, the terms that appear in this general equation for O_y represent the net production and destruction rates of odd oxygen, and correspond to the "limiting rates" in most of the cycles presented above. At all altitudes $(O_y) \approx (O_x)$, so that Eq. (5.345) can be regarded as a form of the odd oxygen equation. In the stratosphere below 50 km,

$$(O_y) \approx (O_x) = (O_3) + (O) \approx (O_3)$$

while, above 70 km

$$(O_y) \approx (O_x) \approx (O).$$

Figure 5.71 shows the relative contribution of the O_x (Chapman cycle), NO_x, HO_x, ClO_x, and BrO_x families to the destruction of ozone in the stratosphere for different latitudes and for two seasons. Note the important role played by NO_x in the mid-stratosphere and by HO_x in the mesosphere and lower stratosphere. Halogen species play a major role at high latitudes (20 km and 45 km). The role of the Chapman reactions is generally small except in the upper stratosphere. In the polar regions during periods of activated chlorine, the major loss in the lower stratosphere results from cycle (5.333) as well as cycle (5.334). This last loss process, which is limited by the rate of reactions between ClO and BrO, plays also a significant role in the lower stratosphere at mid-latitudes, where chlorine and bromine are activated on sulfate aerosol particles. A diagnostic of ozone loss in the lower stratosphere, based on observational data, is given by Lee *et al.* (2002) and Rex *et al.* (2003).

In closing, we remark that although the complete chemistry of the middle atmosphere involves several hundred reactions, most of the important processes can be identified by examining the magnitudes of the photochemical terms in the continuity equations for each species, and the resulting lifetimes. When this information is used to define chemical families, a simple framework is obtained in which the species subject to the influence of transport can be readily identified, and the net versus gross production and loss processes are clearly distinguished from one another. Indeed, the situation is somewhat similar to the difficulties associated with understanding the significance of the net and gross mean meridional and eddy transports in the stratosphere in the classical and residual Eulerian representations, as was described in Chapter 3. Thus, in the photochemistry as well as the dynamics of the middle atmosphere, the occurrence of many simultaneous processes, some of which merely cancel with one another to a great degree, requires careful study to recognize the roles played by each of them. The particular frameworks chosen to accomplish that task in this volume represent one possible choice which may facilitate that study.

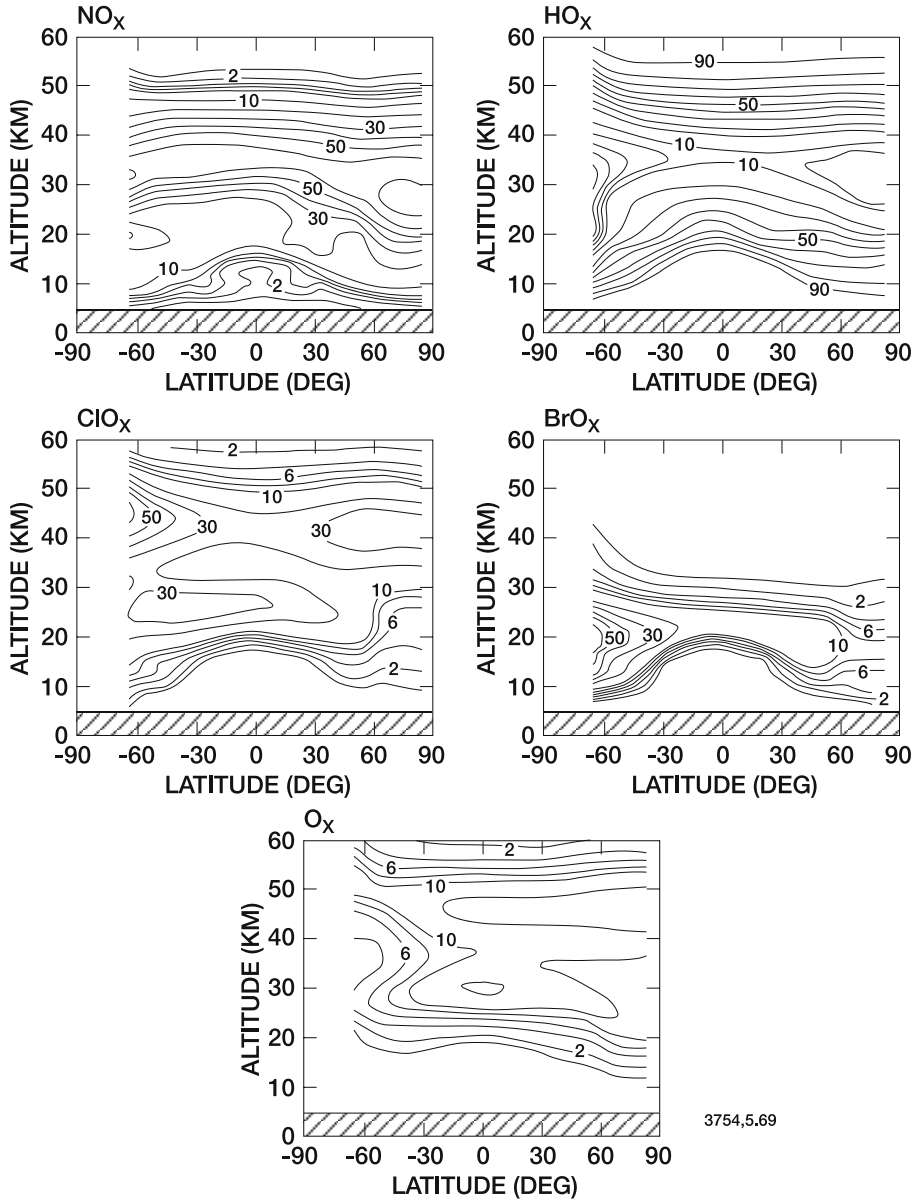

Figure 5.71. Relative contribution (percent) of various chemical families (NO_x, HO_x, ClO_x, BrO_x, and O_x) to the destruction of odd oxygen in the stratosphere in June (based on calculations by the NASA/Goddard 2-D model). Courtesy of C.H. Jackman, NASA.

References

Abbas *et al.* (1996) p. 44 Abbas, M.M., M.R. Gunson, M.J. Newchurch, H.A. Michelsen, R.J. Salawitch, M. Allen, M.C. Abrams, A.Y. Chang, A. Goldman, F.W. Irion, E.J. Moyer, R. Nagaraju, C.P. Rinsland, G.P. Stiller, and R. Zander, The hydrogen budget of the stratosphere inferred from ATMOS measurements of H_2O and CH_4. *Geophys Res Lett: 23*, 2405, 1996a.

Abbas, M.M., H.A. Michelsen, M.R. Gunson, M.C. Abrams, M.J. Newchurch, R.J. Salawitch, A.Y. Chang, A. Goldman, F.W. Irion, G.L. Manney, E.J. Moyer, R. Nagaraju, C.P. Rinsland, G.P. Stiller, and R. Zander, Seasonal variations of water vapor in the lower stratosphere inferred from ATMOS/ATLAS-3 measurements of H_2O and CH_4. *Geophys Res Lett: 23*, 2401, 1996b.

Ackerman, M., D. Frimout, A. Girard, M. Gottignies, and C. Muller, Stratospheric HCl from infrared spectra. *Geophys Res Lett: 3*, 81, 1976.

Ackerman, M., D. Frimout, and C. Muller, Stratospheric CH_4, HCl and ClO and the chlorine ozone cycle. *Nature: 269*, 226, 1977.

Adriani, A., T. Deshler, G. Di Donfranceso, and G.P. Gobbi, Polar stratospheric clouds and volcanic aerosol during spring 1992 over McMurdo Station Actarctica: Lidar and particle counter comparison. *J Geophys Res: 100*, 25,877, 1995.

Allan, P.J., J.M.C. Plane, and G. McFiggans, Observations of OIO in the remote marine boundary layer. *Geophys Res Lett: 28*, 1945, 2001.

Allen, M., Y.L. Yung, and J.W. Waters, Vertical transport and photochemistry in the terrestrial mesosphere and lower thermosphere (50-170 km). *J Geophys Res: 86*, 3617, 1981.

Allen, M., J.I. Lunine, and Y.L. Yung, The vertical distribution of ozone in the mesosphere and lower thermosphere. *J Geophys Res: 89*, 4841, 1984.

Anderson, J.G., Rocket measurement of OH in the mesosphere. *J Geophys Res: 76*, 7820, 1971.

Anderson, J.G., The absolute concentration of OH in the earth's stratosphere. *Geophys Res Lett: 3*, 165, 1976.

Anderson, J.G., Free radicals in the earth's stratosphere: A review of recent results, Proc of the NATO Advanced Institute on Atmospheric Ozone, A.C. Aikin, ed., *U.S. Dept. of Transportation, FAA-EE-80-20*, FAA, Washington, D.C., USA, 1980.

Anderson, J.G., H.J. Grassl, R.E. Shetter, and J.J. Margitan, Stratospheric free chlorine measured by balloon-borne in situ resonance fluorescence. *J Geophys Res: 85*, 2869, 1980.

Angell, J.K., and J. Korshover, Quasi-Biennal variations in temperature, total ozone and tropopause height. *J Atmos Sci: 21*, 5, 479, 1964.

Angell, J.K., and J. Korshover, Quasi-Biennal and long-term fluctuation in total ozone. *Mon Wea Rev: 101*, 426, 1973.

Arijs, E., and G. Brasseur, Acetonitrile in the stratosphere and implications for positive ion composition. *J Geophys Res: 91*, 4003, 1985.

Arijs, E., D. Nevejans, P. Frederick, and J. Ingels, Negative ion composition measurements in the stratosphere. *Geophys Res Lett: 8*, 121, 1981.

Arnold, F., and D. Krankowsky, Water vapour concentrations at the mesopause. *Nature: 268*, 218, 1977.

Arnold, F., and R. Fabian, First measurements of gas phase sulfuric acid in the stratosphere. *Nature: 283*, 55, 1980.

Arpag, K.A., P.V. Johnston, H.L. Miller, R.W. Sanders, and S. Solomon, Observations of the stratospheric BrO column over Colorado, 40°N. *J Geophys Res: 99*, 8175, 1994.

Atlas, E., W. Pollock, J. Greenberg, L. Heidt, and A.M. Thompson, Alkyl nitrates, nonmethane hydrocarbons, and halocarbon gases over the equatorial Pacific Ocean during SAGA 3. *J Geophys Res: 98*, 16,933, 1993.

Avallone, L.M., and D.W. Toohey, Tests of halogen photochemistry using in situ measurements of ClO and BrO in the lower polar stratosphere. *J Geophys Res: 106*, 10,411, 2001.

Avallone, L.M., S.M. Schauffler, W.H. Pollock, L.E. Heidt, E.L. Atlas, and K.R. Chan, In situ measurements of BrO during AASE II. *Geophys Res Lett: 22*, 831, 1995.

Baker, K.D., A.F. Nagy, R.O. Olsen, E.S. Oran, J. Randhawa, D.F. Strobel, and T. Tohmatsu, Measurement of the nitric oxide altitude distribution in the mid-latitude mesosphere. *J Geophys Res: 82*, 3281, 1977.

Bandy, A.R., D.C. Thornton, D.L. Scott, M. Lalevic, E.E. Lewin, and A.R. Driedger III, A time series of carbonyl sulfide in the northern hemisphere. *J Atmos Chem: 14*, 527, 1992.

Bandy, A.R., D.C. Thornton, and A. Driedger III, Airborne measurements of sulfur dioxide, dimethyl sulfide, carbon disulfide, and carbon sulfide by isotope dilution gas chromatography/mass spectrometry. *J Geophys Res: 98*, 23,423, 1993a.

Bandy, A.R., D.C. Thornton, and J.E. Johnson, Carbon disulfide measurements in the atmosphere of the western north Atlantic and the northwestern south Atlantic oceans. *J Geophys Res: 98*, 23,449, 1993b.

Barbe, A., P. Mache, C. Secroun, and P. Jouve, Measurements of tropospheric and stratospheric H_2CO by an infrared high resolution technique. *Geophys Res Lett: 6*, 463, 1979.

Barth, C.A., D.W. Rusch, R.J. Thomas, G.H. Mount, G.J. Rottman, G.E. Thomas, R.W. Sanders, and G.M. Lawrence, Solar mesosphere explorer: Scientific objectives and results. *Geophys Res Lett: 10*, 237, 1983.

Barth, C.A., S.M. Bailey, and S.C. Solomon, Solar-terrestrial coupling: Solar osft X-rays and thermospheric nitric oxide. *Geophys Res Lett: 26*, 1251, 1999.

Bates, D.R., and M. Nicolet, Atmospheric hydrogen. *Publ Astron Soc Pacific: 62*, 106, 1950.

Bates, D.R., and A.E. Witherspoon, The photochemisry of some minor constituents of the earth's atmosphere (CO_2, CO, CH_4, N_2O). *Mon Notic Roy Astron Soc: 112*, 101, 1952.

Bekki, S., R. Toumi, and J.A. Pyle, Role of sulphur photochemistry in tropical ozone changes after the eruption of Mount Pinatubo. *Nature: 362*, 331, 1993.

Bergamaschi, P.R., M. Hein, M. Heinmann, and P.J. Crutzen, Inverse modeling of the global CO cycle, 1. Inversion of CO mixing rations. *J Geophys Res: 105,* 1909, 2000.

Bevilacqua, R.M., J.J. Olivero, P.R. Schwartz, C.J. Gibbins, J.M. Bologna, and D.J. Thacker, An observational study of water vapor in the mid-latitude mesosphere using ground-based microwave technique. *J Geophys Res: 88*, 8523, 1983.

Beyer, K.D., B. Luo, R. Neuber, and T. Peter, Temperature dependence of ternary solution particle volumes as observed by lidar in the Arctic stratosphere during winter 1992/1993. *J Geophys Res: 102*, 3603, 1997.

Bingemer, H.G., S. Bürgermeister, R.L. Zimmermanm, and H.-W. Georgii, Atmospheric OCS: Evidence for a contribution of anthropogenic sources? *J Geophys Res: 95*, 20 617, 1990.

Black, G., R.L. Sharpless, and T.G. Slanger, Rate coefficients for SO reactions with O_2 and O_3 over the temperature range of 230 to 420 K. *Chem Phys Lett: 90*, 598, 1982a.

Black, G., R.L. Sharpless, and T.G. Slanger, Rate coefficients at 198 K for SO reactions with O_2, O_3, and NO_2. *Chem Phys Lett: 90*, 55, 1982b.

Boatman, J.F., D.L. Wellman, C.C. Van Valin, R.L. Gunter, J.D. Ray, H. Sievering, Y. Kim, S.W. Wilkinson, and M. Luria, Airborne sampling of selected trace chemicals above the central United States. *J Geophys Res: 94*, 5081, 1989.

Brasseur, G.P., The response of the middle atmopshere to a long-term and short-term solar variability: A two dimensional model. *J Geophys Res: 98*, 23,079, 1993.

Brasseur, G., and C. Granier, Mount Pinatubo aerosols, chlorofluorocarbons, and ozone depletion. *Science: 257*, 1239, 1992.

Brasseur, G.P., and S. Madronich, Chemistry-transport models, in *Climate System Modeling*. K.E. Trenberth, ed., Cambridge University Press, 1992.

Brasseur, G., A. De Rudder, G.M. Keating, and M.C. Pitts, Response of the middle atmosphere to short-term solar ultraviolet variations, 2. Theory. *J Geophys Res: 92*, 903, 1987.

Brasseur, G.P., J.J. Orlando, and G.S. Tyndall (eds), *Atmospheric Chemistry and Global Change*, Oxford University Press, 1999.

Breeding, R.J., J.P. Lodge, Jr., J.B. Pate, D.C. Sheesley, H.B. Klonis, B. Fogle, J.A. Anderson, T.R. Englert, P. Haagenson, R.B. McBeth, A.L. Morris, R. Pogue, and A.F. Wartburg, Background trace gas concentrations in the central United States. *J Geophys Res: 78*, 7057, 1973.

Brewer, A.W., Evidence for a world circulation provided by the measurements of helium and water vapour distributions in the stratosphere. *Quart J Roy Met Soc: 75*, 351, 1949.

Browell, E.V., C.F. Butler, S. Ismail, P.A. Robinette, A.F. Carter, N.S. Higdon, O.B. Toon, M.R. Schoeberl, and A.F. Tuck, Airborne lidar observations in the wintertime Arctic stratosphere: Polar stratospheric clouds. *Geophys Res Lett: 17*, 385, 1990.

Brownsword, R.A., M. Hillenkamp, T. Laurent, R.K. Vatsa, H.-R. Volpp, and J. Wolfrum, Quantum yield for H atom formation in the methane dissociation after photoexcitation at the Lyman-α (121.6 nm) wavelength. *Chem Phys Lett: 266*, 259, 1997.

Brune, W., OH and HO_2: Sources, interactions with nitrogen oxides, and ozone production. *IGAC Newsletter: 21,* 2000.

Brune, W.H., J.G. Anderson, and K.R. Chan, In situ observations of BrO over Antarctica: ER-2 aircraft results from 54°S to 72°S latitude. *J Geophys Res: 94*, 16,639, 1989.

Burkholder, J.B., A.R. Ravishankara, and S. Solomon, UV/visible and IR absorption cross sections of $BrONO_2$. *J Geophys Res: 100*, 16,793, 1995.

Burnett, C.R., and E.B. Burnett, Spectroscopic measurement of the vertical column abundance of hydroxyl (OH) in the earth's atmosphere. *J Geophys Res: 86*, 5185, 1981.

Burnett, C.R., and E.B. Burnett, Vertical column abundance of atmospheric OH at solar maximum from Fritz Peak, Colorado. *Geophys Res Lett: 9*, 708, 1982.

Bush, J.A., A.L. Schmeltekopf, F.C. Fehsenfeld, D.L. Albritton, J.R. McAffe, P.D. Goldan, and E.E. Ferguson, Stratospheric measurements of methane at several latitudes. *Geophys Res Lett: 5*, 1027, 1978.

Byrne, G.D., and A.C. Hindmarsh, A polyalgorithm for the numerical solution of ordinary differential equations. *ACM Trans. Math Software: 1*, 71, 1975.

Calvert, J.G., and W.R. Stockwell, Acid generation in the troposphere by gas phase chemistry. *Environ Sci Technol: 17*, 428A, 1983.

Carroll, M.A., R.W. Sanders, S. Solomon, and A.L. Schmeltekopf, Visible and near-ultraviolet spectroscopy at McMurdo station, Antarctica, 6: Observations of BrO. *J Geophys Res: 94*, 16,633, 1989.

Carslaw, K.S., B.P. Luo, S.L. Clegg, T. Peter, P. Brimblecombe, and P.J. Crutzen, Stratospheric aerosol growth and HNO_3 gas phase depletion from coupled HNO_3 and water uptake by liquid particles. *Geophys Res Lett: 21*, 2479, 1994.

Carslaw, K.S., T. Peter, and S.L. Clegg, Modeling the composition of liquid stratospheric aerosols. *Rev Geophys: 35*, 125, 1997.

Carslaw, K.S., M. Wirth, A. Tsias, B.P. Luo, A. Dörnbrack, M. Leutbecher, H. Volkert, W. Renger, J.T. Bacmeister, and T. Peter, Particle microphysics and chemistry in remotely observed mountain polar stratospheric clouds. *J Geophys Res: 103*, 5785, 1998a.

Carslaw, K.S., M. Wirth, A. Tsias, B.P. Luo, A. Dörnbrack, M. Leutbecher, H. Volkert, W. Renger, J.T. Bacmeister, and T. Peter, Increased stratospheric ozone depletion due to mountain-induced atmospheric waves. *Nature: 391*, 675, 1998b.

Chameides, W.L., and J.C.G. Walker, A photochemical theory of tropospheric ozone. *J Geophys Res: 78*, 8751, 1973.

Chance, K.V., and W.A. Traub, Evidence for stratospheric hydrogen peroxide. *J Geophys Res: 92*, 3061, 1987.

Chance, K.V., D.G. Johnson, W.A. Traub, and K.W. Jucks, Measurement of the stratospheric hydrogen peroxide concentration profile using far infrared thermal emission spectroscopy. *Geophys Res Lett: 18*, 1003, 1991.

Chance, K.V., W.A. Traub, D.G. Johnson, K.W. Jucks, P. Ciarfallini, R.A. Stachnik, R.J. Salawitch, and H.A. Michelsen, Simultaneous measurements of stratospheric HO_x, NO_x, and Cl_x: Comparison with a photochemical model. *J Geophys Res: 101*, 9031, 1996.

Chandra, S., The solar UV related changes in total ozone from a solar rotation to a solar cycle. *Geophys Res Lett: 18*, 837, 1991.

Chang, A.Y., R.J. Salawitch, H.A. Michelsen, M.R. Gunson, M.C. Abrams, R. Zander, C.P. Rinsland, M. Loewenstein, J.R. Podolske, M.H. Proffitt, J.J. Margitan, D.W. Fahey, R.-S. Gao, K.K. Kelly, J.W. Elkins, C.R. Webster, R.D. May, K.R. Chan, M.M. Abbas, A. Goldman, F.W. Irion, G.L. Manney, M.J. Newchurch, and G.P. Stiller, A comparison of measurements from ATMOS and instruments aboard the ER-2 aircraft: Tracers of atmospheric transport. *Geophys Res Lett: 23*, 2389, 1996.

Chang, J.S., R.R. Barker, J.E. Davenport, and D.M. Goldan, Chlorine nitrate photolysis by a new technique: Very low pressure photolysis. *Chem Phys Lett: 60*, 385, 1979.

Chapman, S., On ozone and atomic oxygen in the upper atmosphere. *Phil Mag: 10*, 369, 1930.

Chubachi, S., A special ozone observation at Syowa station Antarctica from February 1982 to January 1983, in *Atmospheric Ozone*. S. Zerefos and A. Ghazi (eds.), Reidel, Dordrecht, pp. 285, 1985.

Cicerone, R.J., and R.S. Oremland, Biogeochemical aspects of atmospheric methane. *Global Biogeochem Cycles: 2*, 299, 1988.

Clancy, R.T., D.O. Muhlemon, and G.L. Berge, Microwave spectra of terrestrial mesosphere CO. *J Geophys Res: 87*, 5009, 1982.

Coffey, M.T., W.G. Mankin, and R.J. Cicerone, Spectrascopic detection of stratospheric hydrogen cyanide. *Science: 214*, 333, 1981a.

Coffey, M.T., W.G. Mankin, and A. Goldman, Simultaneous spectroscopic determination of the latitudinal, seasonal and diurnal variability of stratosphere N_2O, NO, NO_2 and HNO_3. *J Geophys Res: 86*, 7731, 1981b.

Cohen, R.C., P.O. Wennberg, R.M. Stimpfle, J. Koplow, J.G. Anderson, D.W. Fahey, E.L. Woodbridge, E.R. Keim, R. Gao, M.H. Proffitt, M. Loewenstein, and K.R. Chan, Are models of catalytic removal of O_3 by HO_x accurate? Constraints from in-situ measurements of the OH to HO_2 ratio. *Geophys Res Lett: 21*, 2539, 1994.

Conrad, R., and W. Seiler, Influence of temperature, moisture, and organic carbon on the flux of H_2 and CO between soil and atmosphere: Field studies in subtropical regions. *J Geophys Res: 90*, 5699, 1985.

Cox, R.A., W.J. Bloss, R.L. Jones, and D.M. Rowley, OIO and the atmospheric cycle of iodine. *Geophys Res Lett: 26*, 1857, 1999.

Crutzen, P.J., Determination of parameters appearing in the "dry" and the "wet" photochemical theories for ozone in the stratosphere. *Tellus: 21*, 368, 1969.

Crutzen, P.J., The influence of nitrogen oxide on the atmospheric ozone content. *Quart J Roy Met Soc: 96*, 320, 1970.

Crutzen, P.J., Ozone production rates in oxygen-hydrogen-nitrogen oxide atmosphere. *J Geophys Res: 76*, 7311, 1971.

Crutzen, P.J., A discussion of the chemistry of some minor constituents in the stratosphere and troposphere. *Pure Appl Geophys: 106*, 1385, 1973.

Crutzen, P.J., Photochemical reactions initiated by the influencing ozone in unpolluted tropospheric air. *Tellus: 26*, 47, 1974.

Crutzen, P.J., The possible importance of CSO for the sulfate layer of the stratosphere. *Geophys Res Lett: 3*, 73, 1976.

Crutzen, P.J., Atmospheric interactions: Homogenous gas reactions of C, N and S containing compounds, in *The Major Biochemical Cycles and Their Interactions*. B. Bolin and R.B. Cook (eds.), SCOPE 21, 67-114, Wiley, Chichester, 1983.

Crutzen, P.J., I.S.A. Isaksen, and G.C. Reid, Solar Protons events: Stratospheric sources of nitric oxide. *Science: 189*, 457, 1975.

Crutzen, P.J., and L.T. Gidel, The tropospheric budgets of anthropogenic chlorocarbons, CO, CO_4, CH_3Cl and the effect of various NO_x sources on tropospheric ozone. *J Geophys Res: 88*, 6641, 1983.

Crutzen, P.J., and U. Schmaizl, Chemical budgets of the stratosphere. *Planet Space Sci: 31*, 1009, 1983.

Crutzen, P.J., and F. Arnold, Nitric acid cloud formation in the cold Antarctic stratosphere: A major cause for the springtime 'ozone hole.' *Nature: 324*, 651, 1986.

Crutzen, P.J., and P.H. Zimmermann, The changing photochemistry of the troposphere. *Tellus: 43A-B*, 136, 1991.

Crutzen, P.J., L.E. Heidt, J.P. Krasnec, W.H. Pollock, and W. Seiler, Biomass burning as a source of the atmosphere gases CO, H_2, N_2O, NO, CH_3Cl and COS, *Nature: 282*, 253, 1979.

Crutzen, P.J., R. Müller, C. Brühl, and T. Peter, On the potential importance of the gas phase reaction $CH_3O_2 + ClO \rightarrow ClOO + CH_3O$ and the heterogenous reaction $HOCl + HCl \rightarrow H_2O + CL_2$ in "ozone hole" chemistry. *Geophys Res Lett: 19*, 1113, 1992.

Daniel, J.S., S. Solomon, R.W. Portmann, and R.R. Garcia, Stratospheric ozone destruction: The importance of bromine relative to chlorine. *J Geophys Res: 104*, 23,871, 1999.

David, D., S. Godin, G. Mégie, Y. Emery, and C. Flesia, Physical state and composition of polar stratospheric clouds from airborne lidar measurements during sesame. *J Atmos Chem: 27*, 1, 1997.

Deguchi, S., and O.O. Muhleman, Mesopheric water vapor. *J Geophys Res: 87*, 1343, 1982.

Delwiche, C.C., Biological production and utilization of N_2O. *Pageoph: 116*, 414, 1978.

De Zafra, R.L., A. Parrish, P.M., Solomon and J.W. Barrett, A measurement of stratospheric HO_2 by ground-based nm-wave spectroscopy. *J Geophys Res: 89*, 1321, 1984.

De Zafra, R.L., M. Jaramillo, J. Barrett, L.K. Emmons, P.M. Solomon, and A. Parrish, New observations of large concentration of ClO in the springtime lower stratosphere over Antarctica and its implications for ozone-depleting chemistry. *J Geophys Res: 94*, 11,423, 1989.

Dlugokencky, E.J., L.P. Steel, P.M. Lang, and K.A. Masarie, The growth rate and distribution of atmospheric methane. *J Geophys Res: 99*, 17,021, 1994.

Dlugokencky, E.J., E.G. Dutton, P.C. Novelli, P.P. Tans, K.A. Masarie, K.O. Lantz, and S. Madronich, Changes in CH_4 and CO growth rates after the eruption of Mt. Pinatubo and their link with changes in tropical tropospheric UV flux. *Geophys Res Lett: 23*, 2761, 1996.

Dlugokencky, E.J., K.A. Masarie, P.M. Lang, and P.P. Tans, Continuing decline in growth rate of the atmospheric methane burden. *Nature: 393*, 447, 1998.

Dobson, G.M.B., Observations of the amount of ozone in the earth's atmosphere and its relation to other geophysical conditions. *Proc Roy Soc London: A 129*, 411, 1930.

Dobson, G.M.B., *Exploring the Atmosphere*, Clarendon Press (Oxford), 1963.

Drdla, K., A. Tabazadeh, R.P. Turco, M.Z. Jacobsen, J.E. Dye, C. Twohy, and D. Baumgardner, Analysis of the physical state of one arctic polar stratospheric cloud based on observations. *Geophys Res Lett: 21*, 2475, 1994.

Dupuy, É., J. Urban, P. Ricaud, É. Le Flochmoën, N. Lautié, D. Murtagh, J. De La Noë, L. El Amraoui, P. Eriksson, P. Forkman, U. Frisk, F. Jégou, C. Jiménez, and M. Olberg, Strato-mesospheric measurements of carbon monoxide with the Odin Sub-Millimetre Radiometer: Retrieval and first results. *Geophys Res Lett*, in press.

Dütsch, H.U., Atmospheric ozone: A short review. *J Geophys Res: 75*, 1707, 1970.

Dütsch, H.U., Vertical ozone distribution and tropospheric ozone, Proc of the NATO Advanced Institute on Atmospheric Ozone, A.C. Aikin, ed., *U.S. Dept. of Transportation, FAA-EE-80-20*, FAA, Washington, D.C., USA, 1980.

Dvortsov, V.L., M.A. Geller, S. Solomon, S.M. Schauffler, E.L. Atlas, and D.R. Blake, Rethinking reactive halogen budgets in the midlatitude lower stratosphere. *Geophys Res Lett: 26*, 1699, 1999.

Dye, J.E., D. Baumgardner, B.W. Gandrud, S.R. Kawa, K.K. Kelly, M. Loewenstein, G.V. Ferry, K.R. Chan, and B.L. Gary, Particle size distribution in Arctic polar stratospheric clouds, growth and freezing of sulfuric acid droplets, and implications for cloud formation. *J Geophys Res: 97*, 8015, 1992.

Eckman, R.S., The response of ozone to short-term variations in the solar ultraviolet irradiance, 1. A theoretical model. *J Geophys Res: 91*, 6695, 1986.

Ehhalt, D.H., On the uptake of tritium by soil water and groundwater. *Water Resour Res: 9*, 1073, 1973.

Ehhalt, D.H., The atmospheric cycle of methane. *Tellus: 26*, 58, 1974.

Ehhalt, D.H., Gas phase chemistry in the troposphere, in *Global Aspects of Atmospheric Chemistry*, R. Zellner, ed., Springer Verlag, *Topics in Physical Chemistry: 6*, 21, 1999.

Ehhalt, D.H., and L.E. Heidt, The concentration of molecular H_2 and CH_3 in the stratosphere. *Pageophys: 106*, 1352, 1973.

Ehhalt, D.H., and A. Tonnissen, Hydrogen and carbon compounds in the stratosphere, Proc of the NATO Advanced Institute on Atmospheric Ozone, A.C. Aikin, ed., *U.S. Dept. of Transportation, FAA-EE-80-20*, FAA, Washington, D.C., USA, 1980.

Ehhalt, D.H., L.E. Heidt, R.H. Lueb, and N. Roper, Vertical profiles of CH_4, H_2, CO, N_2O and CO_2 in the stratosphere, in *Proc of the Third Conference on CIAP*. U.S. Dept of Transportation, Washington, D.C., USA, 1974.

Ehhalt, D.H., L.E. Heidt, R.H. Lueb, and W. Pollock, The vertical distribution of trace gases in the stratosphere. *Pageoph: 113*, 389, 1975a.

Ehhalt, D.H., L.E. Heidt, R.H. Lueb, and E.A. Martell, Concentrations of CH_4, CO, CO_2, H_2, H_2O and N_2O in the upper stratosphere. *J Atmos Sci: 32*, 163, 1975b.

Ehhalt, D.H., U Schmidt, R. Zander, P. Demoulin, and C.P. Rinsland, Seasonal cycle and secular trend of the total and tropospheric abundance of ethane above the Jungfraujoch. *J Geophys Res: 96*, 4985, 1991.

Enell, C.-F., A. Steen, T. Wagner, U. Friess, K. Pfeilsticker, and U. Platt, Occurrence of polar stratospheric clouds at kiruna. *Ann Geophys: 17*, 1457, 1999.

Engleman, R., The vibrational state of hydroxyl radicals produced by flash photolysis of water-ozone-argone mixture. *J Am Chem Soc: 87*, 4193, 1965.

Etheridge, D.M., L.P. Steele, R.J. Francey, and R.L. Langenfelds, Atmospheric methane between 1000 AD and present: Evidence of anthropogenic emissions and climate variability. *J Geophys Res: 103*, 15 979, 1998.

Evans, W.J.J., O.M. Hunter, E.J. Lewellyn, and A. Vallance-Jones, Altitude profile of the infrared system of oxygen in the dayglow. *J Geophys Res: 73*, 2885, 1968.

Evans, W.F.J., J.B. Kerr, C.T. McElroy, R.S. O'Brien, and J.C. McConnell, Measurement of NO, NO_2 and HNO_3 during a stratospheric warming at 54°N in February 1979. *Geophys Res Lett: 9*, 493, 1982.

Eyre, J.R., and H.K. Roscoe, Radiometric measurements of stratospheric HCl. *Nature: 266*, 243, 1977.

Fabian, P., R. Borchers, K.H. Weiler, U. Schmidt, L.A. Volz, P.H. Ehhalt, W. Seiler, and F. Muller, Simultaneously measured vertical profiles of H_2, CH_4, CO, N_2O, $CFCl_3$, and CF_2Cl_2 in the mid-latitude stratosphere and troposphere. *J Geophys Res: 84*, 3149, 1979.

Fahey, D.W., K.K. Kelly, G.V. Ferry, L.R. Poole, J.C. Wilson, D.M. Murphy, M. Loewenstein, and K.R. Chan, In situ measurements of total nitrogen, total water, and aerosol in a polar stratospheric cloud in the Antarctic. *J Geophys Res: 94*, 11,299, 1989.

Fahey, D.W., K.K. Kelly, S.R. Kawa, A.F. Tuck, M. Loewenstein, K.R. Chan, and L.E. Heidt, Observations of denitrification and dehydration in the winter polar stratospheres. *Nature: 344*, 321, 1990.

Fahey, D.W., S.R. Kawa, E.L. Woodbridge, P. Tin, J.C. Wilson, H.H. Jonsson, J.E. Dye, D. Baumgardner, S. Borrmann, D.W. Toohey, L.M. Avallone, M.H. Proffitt, J. Margitan, M. Loewenstein, J.R. Podolske, R.J. Salawitch, S.C. Wofsy, M.K.W. Ko, D.E. Anderson, M.R. Schoeberl, and K.R. Chan, In situ measurements constraining the role of sulfate aerosols in mid-latitude ozone depletion. *Nature: 363*, 509, 1993.

Fahey, D.W., R.S. Gao, K.S. Carslaw, J. Kettleborough, P.J. Popp, M.J. Northway, J.C. Holecek, S.C. Ciciora, R.J. McLaughlin, T.L. Thompson, R.H. Winkler, D.G. Baumgardner, B. Gandrud, P.O. Wennberg, S. Dhaniyala, K. McKinney, Th. Peter, R.J. Salawitch, T.P. Bui, J.W. Elkins, C.R. Webster, E.L. Atlas, H. Jost, J.C. Wilson, R.L. Herman, A. Kleinböhl, and M. von König, The detection of large HNO_3-containing particles in the winter arctic stratosphere. *Science: 291*, 1026, 2001.

Farman, J.C., B.G. Gardiner, and J.D. Shanklin, Large losses of total ozone in Antarctic reveal seasonal ClO_x/NO_x interaction. *Nature: 315*, 207, 1985.

Farmer, C.B., Infrared measurements of stratospheric composition. *Canad J Chem: 52*, 1544, 1974.

Farmer, C.B., O.F. Raper, R.A. Toth, and R.A. Schindler, Recent results of aircraft infrared observations of the stratosphere. *Proc Third Conf on the Climatic Impact Assessment Program*, Rep. No. DOT-TSC-OST-74-15, U.S. Dept. of Transportation, Washington, D.C., USA, 234, 1974.

Farmer, C.B., O.F. Raper, and R.H. Norton, Spectroscopic detection and vertical distribution of HCl in the troposphere and stratosphere. *Geophys Res Lett: 3*, 13, 1976.

Farmer, C.B., O.F. Raper, B.D. Robbins, R.A. Toth, and C. Muller, Simultaneous spectroscopic measurements of stratospheric species: O_3, CH_4, CO, CO_2, N_2O, H_2O, HCl and HF at northern and southern mid-latitudes. *J Geophys Res: 85*, 1621, 1980.

Fish, D.J., S.R. Aliwell, and R.L. Jones, Midlatitude observations of the seasonal variation of BrO: 2, Interpretation and modelling study. *Geophys Res Lett: 24*, 1199, 1997.

Flückiger, J.A., T. Dällenbach, T. Blunier, B. Stauffer, T.F. Stocker, D. Raynaud, and J.-M. Barnola, Variations in atmospheric N_2O concentration during abrupt climate changes. *Science: 285*, 227, 1999.

Forkman, P., P. Eriksson, A. Winnberg, R.R. Garcia, and D. Kinnison, Longest continuous ground-based measurements of mesospheric CO. *Geophys Res Lett: 30*, 1532, doi: 10.1029/2003GL016931, 2003.

Frederick, J.E., and N. Orsini, The distribution and variability of mesospheric odd nitrogen: A theoretical investigation. *J Atmos Terr Phys: 44*, 4798, 1982.

Fried, A., B.E. Henry, J.G. Calvert, and M. Mozukewich, The reaction probability of N_2O_5 with sulfuric acid aerosols at stratospheric temperatures and compositions. *J Geophys Res: 99*, 3517, 1994.

Friedl, A., J.R. Drummond, B. Henry, and J. Fox, Versatile integrated tunable diode laser system for ambient measurements of OCS. *Appl Optics: 30*, 1916, 1991.

Friend, J.P., The global sulfur cycle, in *Chemistry of the Lower Atmosphere.* Rasool, I., ed., Plenum Press, 177, 1973.

Friess, U., T. Wagner, I. Pundt, K. Pfeilsticker, and U. Platt, Spectroscopic measurements of troposphere iodine oxide at Neumayer Station, Antarctica. *Geophys Res Lett: 28*, 1941, 2001.

Fung, I., J. John, J. Lerner, E. Matthews, M. Prather, L. Steele, and P. Fraser, Three-dimensional model synthesis of the global methane cycle. *J Geophys Res: 96*, 13,033, 1991.

Garcia, R.R., and S. Solomon, A numerical model of the zonally averaged dynamical and chemical structure of the middle atmosphere. *J Geophys Res: 88*, 1379, 1983.

Garcia, R.R., and S. Solomon, The effect of breaking gravity waves on the dynamics and chemical composition of the mesosphere and lower thermosphere. *J Geophys Res: 90*, 3850, 1985.

Garcia, R.R., and S. Solomon, A new numerical model of the middle atmosphere: 2, Ozone and related species. *J Geophys Res: 99*, 12,937, 1994.

Gear, C.W., *Numerical Initial Value Problems in Ordinary Differential Equations.* Prentice Hall, 1971.

Gettelman, A., J.R. Holton, and A.R. Douglass, Simulations of water vapor in the lower stratosphere and upper troposphere, *J Geophys Res: 105*, 9003, 2000.

Gibbins, C.J., P.R. Schmitz, D.L. Thacher, and R.M. Bevilacqua, The variability of mesospheric water vapor. *Geophys Res Lett: 8*, 1059, 1981.

Gille, J.C., and J.M. Russell, The limb infrared monitor of the stratosphere (LIMS): Experiment description, performance and results. *J Geophys Res: 89*, 5125, 1984.

Gille, J.C., C.M. Smyth, and D.F. Heath, Observed ozone response to variations in solar ultraviolet radiation. *Science: 225*, 315, 1984.

Gilles, M.K., A.A. Turnipseed, J.B. Burkholder, A.R. Ravishankara, and S. Solomon, Kinetics of the IO radical: 2, Reaction of IO with BrO. *J Phys Chem: 101*, 5526, 1997.

Glueckauf, E., and G.P. Kitt, The hydrogen content of air at ground level. *Quart J Roy Met Soc: 83*, 522, 1957.

Gobbi, G.P., and A. Adriani, Mechanisms of formation of stratospheric clouds observed during the Antarctic late winter of 1992. *Geophys Res Lett: 20*, 1427, 1993.

Godin, S., G. Mégie, C. David, D. Haner, C. Flesia, and Y. Emery, Airborne lidar observations of mountain-wave-induced polar stratospheric clouds during EASOE. *Geophys Res Lett: 21*, 1335, 1994.

Goodmann, J., O.B. Toon, R.F. Pueschel, K. Snetsinger, and S. Verma, Antarctic stratospheric ice crystals. *J Geophys Res: 94*, 16,449, 1989.

Goodmann, J., S. Verma, R.F. Pueschel, P. Hamill, G.V. Ferry, and D. Webster, New evidence of size and composition of PSC particles. *Geophys Res Lett: 24*, 615, 1997.

Graedel, T.E., B. Kleiner, and G.C. Patterson, Measurements of extreme concentrations of tropospheric hydrogen sulfide. *J Geophys Res: 79*, 4467, 1974.

Gunson, M.R., C.B. Farmer, R.H. Norton, R. Zander, C.P. Rinsland, J.H. Shaw, and B.-C. Gao, Measurements of CH_4, N_2O, CO, H_2O, and O_3 in the middle atmosphere by the Atmospheric Trace Molecule Spectroscopy experiment on Spacelab 3. *J Geoophys Res: 95*, 13,867, 1990.

Hagen-Smit, A.J., Chemistry and physiology of Los Angeles Smog. *Ind Eng Chem: 44*, 1342, 1952.

Hammill, P., A. Tabazadeh, S. Kinne, O.B. Toon, and R.P. Turco, On the growth of ternary system HNO_3/H_2SO_4 aerosol particles in the stratosphere. *Geophys Res Lett: 23*, 753, 1996.

Hamm, S., and P. Warneck, The interhemispheric distribution and the budget of acetonitrile in the troposphere. *J Geophys Res: 95*, 20,593, 1990.

Hampson, J., Chemiluminescent emissions observed in the stratosphere and mesosphere, in *Les Problemes Meteorologiques de la Stratosphere et de la Mesosphere*. M. Nicolet, ed., Presses Universitaries de France, Paris, 393, 1966.

Hanson, D.R., Reaction of N_2O_5 with H_2O on bulk liquids and on particles and the effect of dissolved HNO_3. *Geophys Res Lett: 24*, 1087, 1997.

Hanson, D.R., Reaction of $ClONO_2$ with H_2O and HCl in sulfuric acid and $HNO_3/H_2SO_4/H_2O$ mixtures. *J Phys Chem: 102*, 4794, 1998.

Hanson, D.R., and K. Mauersberger, The vapor pressures of HNO_3-H_2O solutions. *J Phys Chem: 92*, 6167, 1988.

Hanson, D.R., and A.R. Ravishankara, The reaction probabilities of $ClONO_2$ and N_2O_5 on 40 to 75% sulfuric acid solutions. *J Geophys Res: 96*, 17307, 1991.

Hanson, D.R., and A.R. Ravishankara, Investigation of the reactive and nonreactive processes involving $ClONO_2$ and HCl on water and nitric acid doped ice. *J Phys Chem: 96*, 2682, 1992.

Hanson, D.R., and A.R. Ravishankara, Uptake of HCl and HOCl onto sulfuric acid: Solubilities, diffusivities and reaction. *J Phys Chem: 97*, 12309, 1993.

Hanson, D.R., and A.R. Ravishankara, Reactive uptake of $ClONO_2$ onto sulfuric acid due to reaction with HCl and H_2O. *J Phys Chem: 98*, 5728, 1994.

Hanst, P.L., L.L. Speller, D.M. Watts, J.W. Spence, and F.M. Miller, Infrared measurements of fluorocarbons, carbon tetrachloride, carbonyl sulfide, and other atmospheric trace gases. *Air Pollution Control Assn J: 24*, 12, 1220, 1975.

Harder, H., C. Camy-Peyret, F. Ferlemann, R. Fitzenberger, T. Hawat, H. Osterkamp, D. Perner, U. Platt, M. Schneider, P. Vradelis, and K. Pfeilsticker, Stratospheric BrO profiles measured at different latitudes and seasons: Atmospheric observations. *Geophys Res Lett: 25*, 3843, 1998.

Harries, J.E., Measurements of stratospheric water vapor using infrared techniques, *J. Atmos. Sci.*, 30, 1691, 1973.

Hauglustaine, D.A., and D.H. Ehhalt, A three-dimensional model of molecular hydrogen in the troposphere. *J Geophys Res: 107*, D17, 4330, doi:1029/2001JD001156, 2002.

Hays, P.B., and J.J. Olivero, Carbon dioxide and monoxide above the troposphere. *Planet Space Sci: 18*, 1729, 1970.

Heaps, W.S., and J.J. McGee, Balloon borne lidar measurements of stratospheric hydroxyl radical. *J Geophys Res: 86*, 5281, 1983.

Hein, R., P.J. Crutzen, and M. Heinmann, An inverse modeling approach to investigate the global atmospheric methane cycle. *Global Biogeochem Cycles: 11*, 43, 1997.

Herman, J., and W. Jaeschke, Measurements of H_2S and SO_2 over the Atlantic ocean. *J Atmos Chem: 1*, 111, 1984.

Hesstvedt, E., On the photochemistry of ozone in the ozone layer. *Geophys Publ: 27*, 4, 1968.

Hesstvedt, E., O. Høv, and I.S.A. Isaksen, Photochemistry of mixtures of hydrocarbons and nitrogen oxides in air. *Geophys Norv: 31*, 27, 1978.

Hitchman, M.H., M. McKay, and C.R. Trepte, A climatology of stratospheric aerosol. *J Geophys Res: 99*, 20,689, 1994.

Hoffmann, D.J., and J.M. Rosen, *Balloon-borne Observations of Stratospheric Aerosol and Condensation Nuclei During the Year Following the Mt. St. Helens Eruption.* University of Wyoming Report AP-63, 1981.

Hoffmann, D.J., and S. Solomon, Ozone destruction through heterogeneous chemistry following the eruption of El Chichón. *J Geophys Res: 94*, 5029, 1989.

Hoffman, T., C.D. O'Dowd, and J.H. Seinfeld, Iodine oxide homogeneous nucleation: An explanation for coastal new particle formation. *Geophys Res Lett: 28*, 1949, 2001.

Holton, J.R., P.H. Haynes, M.E. McIntyre, A.R. Douglass, R.B. Rood, and C. Pfister, Stratosphere-troposphere exchange. *Rev Geophys: 33*, 403, 1995.

Holzinger, R., C. Warneke, A. Hansel, A. Jordan, W. Lindinger, D.H. Scharffe, G. Schade, and P.J. Crutzen, Biomass burning as a source of formaldehyde, acetaldehyde, methanol, acetone, acetonitrile, and hydrogen cyanide. *Geophys Res Lett: 26*, 1161, 1999.

Hood, L.L., Solar ultraviolet radiation induced variations in the stratosphere and mesophere. *J Geophys Res: 92*, 876, 1987.

Hood, L.L., and J.L. Jirikowic, Stratospheric dynamical effects on solar ultraviolet variations: Evidence from zonal mean ozone and temperature data. *J Geophys Res: 96*, 7565, 1991.

Hood, L.L., and J.P. McCormack, Components of interannual ozone change based on NIMBUS 7 TOMS data. *Geophys Res Lett: 19*, 2309, 1992.

Hood, L.L., Z. Huang, and S.W. Bougher, Mesospheric effects of solar ultraviolet variations: Further analysis of SME IR ozone and NIMBUS 7 SAMS temperature data. *J Geophys Res: 96*, 12,989, 1991.

Hood, L.L., J.L. Jirikowic, and J.P. McCormack, Quasi-decadal variability of the stratosphere: Influence of long-term solar ultraviolet variations. *J Atmos Sci: 50*, 3941, 1993.

Houweling, S., T. Kaminski, F. Dentener, J. Lelieveld, and M. Heinmann, Inverse modeling of methane sources and sinks using the adjoint of a global transport model. *J Geophys Res: 104*, 26,137, 1999.

Huang, T.Y.W., and G.P. Brasseur, The effect of long-term solar variability in a two-dimensional interactive model of the middle atmosphere. *J Geophys Res: 98*, 20,410, 1993.

Hunt, B.G., Photochemistry of ozone in a moist atmosphere. *J Geophys Res: 71*, 1385, 1966.

Ingels, J.D. Nevejans, P. Frederick, and E. Arijs, Acetonitrile and sulfuric acid concentrations derived from ion composition measurements during the MAP/GLOBUS 1983 Campaign. *Planet Space Sci: 35*, 685, 1987.

Ingham, T., M. Cameron, and J.N. Crowley, Photodissociation of IO (355 nm) and OIO (532 nm): Quantum yields for O^3P and I production. *J Phys Chem: 104*, 8001, 2000.

Inn, E.C.Y., J.F. Vedder, B.J. Tyson, and D. O'Hara, COS in the stratosphere. *Geophys Res Lett: 6*, 191, 1979.

IPCC, *Climate Change: The IPCC Scientific Assessment*, J.T. Houghton, C.J. Jenkins, and J.J. Ephraums, eds., Intergovernmental Panel on Climate Change, Cambridge University Press, Cambridge, UK, 1990.

IPCC, *Climate Change 1995: The Science of Climate Change.* Contribution of Working Group I to the Second Assessment Report of the Intergovernmental Panel on Climate Change, J.T.Houghton, L.G. Meira Filho, B.A. Callander, N. Harris, A. Kattenberg, and K. Maskell, eds., Cambridge University Press, Cambridge, UK, 572 pp., 1996.

IPCC, *Climate Change 2001: The Scientific Basis.* Contribution of Working Group I to the Third Assessment Report of the Intergovernmental Panel on Climate Change, J.T. Houghton, Y. Ding, D.J. Griggs, M. Noguer, P.J. van der Linden, X. Dai, K. Maskell, and C.A. Johnson, eds. Cambridge University Press, Cambridge, UK, 881 pp., 2001.

Jaeschke, W., R. Schmitt, and H.W. Georgi, Preliminary results of stratospheric SO_2 measurements. *Geophys Res Lett: 3*, 517, 1976.

Jackman, C.H., Effects of energetic particles on minor constituents in the middle atmosphere. *J Geomagn Geoelec: 43*, 637, 1991.

Jackman, C.H., M.C. Cerniglia, J.E. Nielsen, D.J. Allen, J.M. Zawodny, R.D. McPeeters, A.R. Douglass, J.E. Rosenfield, and R.B. Rood, 2-Dimensional and 3-Dimensional model simulations, measurements, and interpretation of the influence of the October 1989 solar proton events on the middle atmosphere. *J Geophys Res: 100*, 11,641, 1995.

Jacobson, M.Z., Computation of global photochemistry with SMVGEAR II. *Atmos Environ: 29*, 2541, 1995.

Jacobson, M.Z., Improvement of the SMVGEAR II on vector and scalar machines through absolute tolerance control. *Atmos Environ: 32*, 791, 1998.

Jacobson, M.Z., and R.P. Turco, SMVGEAR: A sparse-matrix vectorized gear code for atmospheric models. *Atmos Environ: 28A*, 273, 1994.

Jensen, E.J., *et al.*, High humidities and subvisible cirrus near the tropical tropopause, *Geophys Res Lett: 25*, 151, 1998.

Johnson, J.E., A.R. Bandy, D.C. Thornton, and T.S. Bates, Measurements of atmospheric carbonyl sulfide during the NASA Chemical Instrumentation Test and Evaluation Project: Implication for the global COS budget. *J Geophys Res: 98*, 23,443, 1993.

Johnston, H., Reduction of stratospheric ozone by nitrogen oxide catalysts from supersonic transport exhaust. *Science: 173*, 517, 1971.

Johnston, H.S., and J. Podolske, Interpretation of stratospheric photochemistry. *Rev Geophys Space Phys: 16*, 491, 1978.

Jucks, K.W., D.G. Johnson, K.V. Chance, W.A. Traub, J.J. Margitan, G.B. Osterman, R.J. Salawitch, and Y. Sasano, Observations of OH, HO_2, H_2O and O_3 in the upper stratosphere, implications for HO_x chemistry. *Geophys Res Lett: 25*, 3935, 1998.

Kaye, J.A., S. Penkett, and F.M. Ormond, (eds.), *Report on Concentrations, Lifetimes and Trends of CFCs, Halons, and Related Species*, NASA Reference Publication 1339, NASA Office of Mission to Planet Earth, 247pp., National Aeronautics and Space Administration, Washington, D.C., USA, 1994.

Keating, G.M., M.C. Pitts, G. Brasseur, and A. De Rudder, Response of middle atmosphere to short-term solar ultraviolet variations: 1, Observations. *J Geophys Res: 92*, 889, 1987.

Keyser, L.F., Absolute rate constant and branching fractions for the $H + HO_2$ reaction from 245 to 300 K. *J Phys Chem: 90*, 2994, 1986.

Khalil, M.A.K., and R.A. Rasmussen, Carbon monoxide in the Earth's atmosphere: Increasing trend. *Science: 224*, 54, 1990.

Kircher, C.C., and S.P. Sander, Kinetics of HO_2 and DO_2 disproportionations. *J Phys Chem: 88*, 2082, 1984.

Kley, D., E.J. Stone, W.R. Henderson, J.W. Drummond, W.J. Harrop, A.L. Schmeltekopf, T.L. Thompson, and R.H. Winkler, In situ measurements of the mixing ratio of water vapor in the stratosphere. *J Atmos Sci: 36*, 2513, 1979.

Kley, D., J.W. Drummond, and A.L. Schmeltekopf, On the structure and microstructure of stratospheric water vapor, in *Atmospheric Water Vapor.* A. Deepak, T.D. Wilkerson, and L.H. Ruhnke, eds., Academic Press, 315, 1980.

Ko, M.K.W., N.D. Sze, and D.K. Weisenstein, Roles of dynamical and chemical processes in determining the stratospheric concentration of ozone in one-dimensional and two-dimensional models. *J Geophys Res: 94*, 9889, 1989.

Ko, M.K.W., N.D. Sze, C.J. Scott, and D.K. Weisenstein, On the relation between stratospheric chlorine/bromine loading and short-lived tropospheric source gases. *J Geophys Res: 102*, 25,507, 1997.

Kondo, Y., P. Aimedieu, M. Koike, Y. Iwasaka, P.A. Newman, U. Schmidt, W.A. Mathews, M. Hayashi, and W.R. Sheldon, Reactive nitrogen, ozone, and nitrate aerosols observed in the Arctic stratosphere in January 1990. *J Geophys Res: 97*, 13,025, 1992.

Kondo, Y., U. Schmidt, T. Sugita, A. Engel, M. Koike, P. Aimedieu, M.R. Gunson, and J. Rodriguez, NO_y correlation with N_2O and CH_4 in the midlatitude stratosphere. *Geophys Res Lett: 23*, 2369, 1996.

Koop, T., and K.S. Carslaw, Melting of $H_2SO_4{\cdot}4H_2O$ particles upon cooling: Implications for polar stratospheric clouds. *Science: 272*, 1638, 1996.

Koop, T., U.M. Biermann, W. Raber, B.P. Luo, P.J. Crutzen, and Th. Peter, Do stratospheric aerosols freeze above the ice frost point? *Geophys Res Lett: 22*, 917, 1995.

Kroeze, C., A. Mosier, and L. Bouwman, Closing the N_2O budget: A restrospective analysis. *Global Biogeochem Cycles: 13*, 1, 1999.

Kulmala, M., L. Pirjola, and J.M. Mäkelä, Stable sulfate clusters as a source of new atmospheric particles. *Nature: 404*, 66, 2000.

Langford, A.O., T.J. O'Leary, M.H. Proffit, and M.H. Hitchman, Transport of the Pinatubo aerosol to a northern midlatitute site. *J Geophys Res: 100*, 9007, 1995.

Larsen, N., B.M. Knudsen, J.M. Rosen, N.T. Kjome, and E. Kyrö, Balloon-borne backscatter observations of type 1 PSC formation: Inference about physical state from trajectory analysis. *Geophys Res Lett: 23*, 1091, 1996.

Larsen, N., B.M. Knudsen, J.M. Rosen, N.T. Kjome, R. Neuber, and E. Kyrö, Temperature histories in liquid and solid polar stratospheric cloud formation. *J Geophys Res: 102*, 23,505, 1997.

Lary, D.J., Gas phase bromine photochemistry. *J Geophys Res: 101*, 1505, 1996.

Lary, D.J., M.P. Chipperfield, R. Toumi, and T. Lenton, Heterogeneous atmospheric bromine chemistry. *J. Geophys Res: 101*, 1489, 1996.

Lassey, K.R., D.C. Lowe, C.A.M. Brenninkmeijer, and A.J. Gomez, Atmospheric methane and its carbon isotopes in the southern hemisphere: Their time series and an instructive model. *Chemosphere–Global Change Science: 26*, 95, 1993.

Lazrus, A.L., and B.W. Gandrud, Distribution of stratospheric nitric acid vapor. *J Atmos Sci: 31*, 1102, 1974.

Lazrus, A.L., B.W. Gandrud, R.N. Woodard, and W.A. Sedlacek, Stratospheric halogen measurements. *Geophys Res Lett: 2*, 439, 1975.

Lazrus, A.L., B.W. Gandrud, R.N. Woodard, and W.A. Sedlacek, Direct measurements of stratospheric chlorine and bromine. *J Geophys Res: 81*, 1067, 1976.

Lee, A.M., R.L. Jones, I. Kilbane-Dawe, and J.A. Pyle, Diagnosing ozone loss in the extratropical lower stratosphere. *J Geophys Res: 107*, 10.1029/2001JD000538, 2002.

Lefèvre, F., G.P. Brasseur, I. Folkins, A.K. Smith, and P. Simon, Chemistry of the 1991-1992 stratospheric winter: Three-dimensional model simulations. *J Geophys Res: 99*, 8183, 1994.

Lehmann, R., An algorithm for the determination of all significant pathways in chemical reaction systems. *J Atm Chem: 47*, 45, 2004.

Le Texier, H., S. Solomon, and R.R. Garcia, The role of molecular hydrogen and methane oxidation in the water vapor budget of the stratosphere. *Quart J Roy Met Soc: 114*, 281, 1988.

Levy II, H., Normal atmosphere: Large radical and formaldehyde concentrations predicted. *Science: 173*, 141, 1971.

Li, Q., D.J. Jacob, I. Bey, R.M. Yantosca, Y. Zhao, Y. Kindo, and J. Notholt, Atmospheric hydrogen cyanide (HCN): Biomass burning source, ocean sink? *Geophys Res Lett: 27*, 357, 2000.

Lii, R.R., M.C. Sauer, Jr., and S. Gordon, Temperature dependence of the gas-phase self reaction of HO_2 in the presence of H_2O. *J Chem Phys: 85*, 2833, 1981.

Liu, S.C., and T.M. Donahue, The aeronomy of hydrogen in the atmosphere of the earth. *J Atmos Sci: 31*, 1118, 1974.

Livesey, N.J., J.W. Waters, R. Khosravi, G.P. Brasseur, G.S. Tyndall, and W.G. Read, Stratospheric CH_3CN from the UARS Microwave Limb Sounder, *Geophys Res Lett: 28*, 779, 2001.

Lobert, J.M., D.H. Scharffe, W.M. Hao, and P.J. Crutzen, Importance of biomass burning in the atmospheric budgets of nitrogen-containing gases. *Nature: 346*, 552, 1990.

Loewenstein, M., J.R. Podolske, D.W. Fahey, E.L. Woodbridge, P. Tin, A. Weaver, P.A. Newman, S.E. Strahan, S.R. Kawa, M.R. Schoeberl, and L.R. Lait. New observations of the NO_y/N_2O correlation in the lower stratosphere. *Geophys Res Lett: 20*, 2531, 1993.

London, J., Radiative energy sources and sinks in the stratosphere and mesophere, Proc of the NATO Advanced Institute on Atmospheric Ozone, A.C. Aikin, ed., *U.S. Dept. of Transportation, FAA-EE-80-20*, FAA, Washington, D.C., USA, 1980.

London, J., and G.M.W. Haurwitz, Ozone and sunspots. *J Geophys Res: 68*, 795, 1963.

Lopez-Puertas, M., M.A. Lopez-Valverde, R.R. Garcia, and R.G. Roble, A review of CO_2 and CO abundancies in the middle atmosphere, in *Atmospheric Science Across the Stratosphere*, Geophysical Monograph 123, American Geophysical Union, 2000.

Lowe, D.C., C.A.M. Brenninkmeijer, G.W. Brailsford, K.R. Lassey, and A.J. Gomez, Concentration and ^{13}C records of atmospheric methane in New Zealand and Antarctica: Evidence for changes in methane sources. *J Geophys Res: 99*, 16,913, 1994.

Lovejoy, E.R., and D.R. Hanson, Measurement of the kinetics of reactive uptake by submicron sulfuric acid particles. *J Phys Chem: 99*, 2080, 1995.

MacKenzie, A.R., M. Kulmala, A. Laaksonen, and T. Vesala, On the theories of type 1 polar stratospheric cloud formation. *J Geophys Res: 100*, 11,275, 1995.

Mahieu, E., C.P. Rinsland, R. Zander, P. Demoulin, L. Delbouille, and G. Roland, Vertical column abundances of HCN deduced from ground-based infrared solar spectra: Long-term trends and variability. *J Atmos Chem: 20*, 299, 1995.

Mahieu, E., R. Zander, L. Delbouille, P. Demoulin, G. Roland, and C. Servais, Observed trends in total vertical column abundances of atmospheric gases from IR solar spectra recorded at the Jungfraujoch. *J Atmos Chem: 28*, 227, 1997.

Maiss, M., L.P. Steele, R.J. Francey, P.J. Fraser, R.L. Langenfelds, N.B.A. Trivelt, and I. Levin, Sulfur hexafluoride, a powerful new atmospheric tracer. *Atmos Environ: 30*, 1621, 1996.

Manion, J.A., C. M. Fittschen, D.M. Golden, L.R. Williams, and M.A. Tolbert, *Israel J Chem: 34*, 355, 1994.

Mankin, W.G., and M.T. Coffey, Latitudinal distributions and temporal changes of stratosphere HCl and HF. *J Geophys Res: 88*, 10,776, 1983.

Mankin, W.G., M.T. Coffey, D.W.T. Griffith, and S.R. Drayson, Spectroscopic measurement of carbonyl sulfide (OCS) in the stratosphere. *Geophys Res Lett: 6*, 853, 1979.

Mankin, W.G., M.T. Coffey, and A. Goldman, Airborne observations of SO_2, HCl, and O_3 in the stratospheric plume of the Pinatubo volcano in July, 1991. *Geophys Res Lett: 19*, 179, 1992.

Manning, M.R., E.A.M. Brenningkmeijer, and W. Allan, The atmospheric carbon monoxide budget of the southern hemisphere. *J Geophys Res: 102*, 10,673, 1997.

Manõ, S., and M.O. Andreae, Emission of methyl bromide from biomass burning. *Science: 263*, 1255, 1994.

Maroulis, P.J., A.L. Torres, and A.R. Bandy, Atmospheric concentrations of carbonyl sulfide in the south-western and eastern United States. *Geophys Res Lett: 4*, 510, 1977.

Maroulis, P.J., A.L. Torres, A.B. Goldberg, and A.R. Bandy, Atmospheric SO_2 measurements on project Gametag. *J Geophys Res: 85*, 7345, 1980.

Marsh, D.R., and J.M. Russell III, A tidal explanation of the sunrise/sunset anomaly in HALOE low-latitude nitric oxide observations. *Geophys Res Lett: 27*, 3197, 2000.

Marsh, D.R., and R. Roble, TIME-GCM simulations of lower-thermospheric nitric oxide seen by the halogen occultation experiment. *J Atmos Terr Phys: 64,* 889, 2002.

May, R.D., and C.R. Webster, In situ stratospheric measurements of HNO_3 and HCl near 30 km using the balloon-borne laser in situ sensor tunable diode laser spectrometer. *J Geophys Res: 94*, 16,343, 1989.

McCormick, M.P., H.M. Steele, P. Hamill, W.P. Chu, and T.J. Swissler, Polar stratospheric cloud sightings by SAM II. *J Atmos Sci: 39*, 1387, 1982.

McElroy, M.B., *The Atmospheric Environment: Effects of Human Activities*. Princeton University Press, 2002.

McElroy, M.B., and J.C. McConnell, Nitrous oxide: A natural source of stratospheric NO. *J Atmos Sci: 28*, 1095, 1971.

McElroy, M.B., R.J. Salawitch, S.C. Wofsy, and J.A. Logan, Reductions of Antarctic ozone due to synergistic interactions of chlorine and bromine. *Nature: 321*, 759, 1986.

McKeen, S.A., S.C. Liu, and C.S. Kiang, On the chemistry of stratospheric SO_2 from volcanic eruptions. *J Geophys Res: 89*, 4873, 1984.

McLeod, H., G.P. Smith, and D.M. Golden, Photodissociation of pernitric acid (HO_2NO_2) at 248 nm. *J Geophys Res: 93*, 3813, 1988.

Meilinger, S.K., T. Koop, B.P. Luo, T. Huthwelker, K.S. Carslaw, U. Krieger, P.J. Crutzen and Th. Peter, Size-dependent stratospheric droplet composition in leewave temperature fluctuations and their potential role in PSC freezing. *Geophys Res Lett: 22*, 3031, 1995.

Meira, L.G., Jr., Rocket measurements of upper atmospheric nitric oxide and their consequences to the lower ionosphere. *J Geophys Res: 76*, 202, 1971.

Meixner, F.X., The vertical sulfur dioxide distribution at the tropopause level. *J Atmos Chem: 2*, 175, 1984.

Menzies, R.T., Remote measurement of ClO in the stratosphere. *Geophys Res Lett: 6*, 151, 1979.

Michelangeli, D.V., M. Allen, Y.L. Yung, R.L. Shia, D. Crisp, and J. Eluszkiewicz, Enhancement of atmospheric radiation by an aerosol layer, *J Geophys Res: 97*, 865, 1992.

Migeotte, M.V., Methane in the earth's atmosphere, *Astrophys J: 107*, 400, 1948.

Mlynzack, M.G., A new perspective on the molecular oxygen and hydroxyl airglow emissions. *J Geophys Res: 104*, 27,535, 1999.

Mlynzack, M.G., and B.T. Marshall, A reexamination of the role of solar heating in the O_2 atmospheric and infrared atmospheric bands. *Geophys Res Lett: 23*, 657, 1996.

Molina, J.S., and F.S. Rowland, Stratospheric sink for chlorofluoromethanes: Chlorine atom-catalyzed destruction of ozone. *Nature: 249*, 810, 1974a.

Molina, J.S., and F.S. Rowland, Predicted present stratospheric abundances of chlorine species from photodissociation of carbon tetrachloride. *Geophys Res Lett: 1*, 309, 1974b.

Molina, L.T., and M.J. Molina, Production of Cl_2O_2 from the self-reaction of ClO radical. *J Phys Chem: 91*, 433, 1987.

Montzka, S.A., R.C. Myers, J.H. Butler, J.W. Elkins, and S.O. Cummings, Global tropospheric distribution and calibration scale of HCFC-22, *Geophys Res Lett: 20*, 703, 1993.

Montzka, S.A., J.H. Butler, R.C. Myers, T.M. Thompson, T.H. Swanson, A.D. Clarke, L.T. Lock, and J.W. Elkins, Decline in the tropospheric abundance of halogen from halocarbons: Implications for stratospheric ozone depletion. *Science: 272*, 1318, 1996.

Mosier, A., C. Kroeze, C. Nevison, O. Oenema, S. Seitzinger, and O. Van Cleemput, Closing the N_2O budget: Nitrous oxide emissions through the agricultural nitrogen cycle — OECD/IPCC/IEA phase II development of IPCC guidelines for national gas inventory methodology. *Nutrient Cycling in Agroecosystems: 52*, 225, 1998.

Mote, P.W., K.H. Rosenlof, M.E. McIntyre, E.S. Carr, J.C. Gille, J.R. Holton, J.S. Kinnersley, H.C. Pumphrey, J.M. Russell III, and J.W. Waters, An atmospheric tape-recorder: The imprint of tropical tropopause temperatures on stratospheric water vapor. *J Geophys Res: 101*, 3989, 1996.

Moyers, J.L., and R.A. Duce, Gaseous and particulate iodine in the marine atmosphere. *J Geophys Res: 77*, 5529, 1972.

Mozurkewich, M., and J.G. Calvert, Reaction probability of N_2O_5 on aqueous aerosols. *J Geophys Res: 93*, 15,889, 1988.

Müller, J.F., and G. Brasseur, Sources of upper tropospheric HO_x: A three-dimensional study. *J Geophys Res: 104*, 1705, 1999.

Murcray, D.G., D.D. Barker, J.N. Brooks, A.Goldman, and W.J. Williams, Seasonal and latitudinal variations of the stratospheric concentration of HNO_3. *Geophys Res Lett: 2*, 223, 1975.

Murcray, D.G., A. Goldman, W.J. Williams, F.H. Murcray, F.S. Bonono, G.M. Bradford, G.R. Cole, P.L. Hanst, and M.J. Molina, Upper limit for stratospheric $ClONO_2$ from balloon-borne infrared measurements. *Geophys Res Lett: 4*, 227, 1977.

Naudet, J.P., D. Hugenin, P. Rigaud, and D. Cariolle, Stratospheric observations of NO_3 and its experimental and theoretical distribution between 20 and 40 km. *Planet Space Sci: 29*, 707, 1981.

Nevison, C.D., S. Solomon, and R.R. Garcia, Model overestimates of NO_y in the upper stratosphere. *Geophys Res Lett: 24*, 803, 1997.

Newell, R. E., The circulation of the upper atmosphere. *Sci Amer: 210*, 62, 1964.

Newell, R.E., Y. Zhu, W.G. Read, and J.W. Waters, Relationship between tropical upper tropospheric moisture and eastern tropical Pacific sea surface temperature at seasonal and interannual time scales. *Geophys Res Lett: 24*, 25, 1997.

Nguyen, B.C., B. Bonsang, and A. Gaudry, The role of the ocean in the global atmospheric sulfur cycle. *J Geophys Res: 88*, 10,903, 1983.

Nicolet, M., Ozone and hydrogen reactions. *Ann Geophys: 26*, 531, 1970.

Nicolet, M., Aeronomic reactions of hydrogen and ozone, in *Mesospheric Models and Related Experiments.* G. Fiocco, ed., D. Reidel Publ., The Netherlands, 1971.

Nicolet, M., Stratospheric ozone: An introduction to its study. *Rev Geophys Space Phys: 13*, 593, 1975a.

Nicolet, M., On the production of nitric oxide by cosmic rays in the mesosphere and stratosphere. *Planet Space Sci: 23*, 637, 1975b.

Nightingale, R.W., A.E. Roche, J.B. Kumer, J.L. Mergenthaler, J.C. Gille, S.T. Massie, P.L. Bailey, D.P. Edwards, M.R. Gunson, G.C. Toon, B. Sen, J.-F. Blavier, and P.S. Connell, Global CF_2Cl measurements by UARS cryogenic limb array etalon spectrometer: Validation by correlative data and a model. *J Geophys Res: 101*, 9711, 1996.

Novelli, P.C., K.A. Masarie, and P.M. Lang, Distributions and recent changes of carbon monoxide in the lower troposphere. *J Geophys Res: 103*, 19,015, 1998.

Novelli, P.C., P.M. Lang, K.A. Masarie, D.F. Hurst, R. Myers, and J.W. Elkins, Molecular hydrogen in the troposphere: Global distribution and budget. *J Geophys Res: 104*, 30,427, 1999.

Noxon, J.F., Stratospheric NO_2, 2. Global behavior. *J Geophys Res: 84*, 5067, 1979.

Noxon, J.F., R.B. Norton, and W.R. Henderson, Observations of atmospheric NO_3. *Geophys Res Lett: 5*, 675, 1978.

Noxon, J.F., E.C. Whipple, Jr., and R.S. Hyde, Stratospheric NO_2, 1. Observational method and behavior at midlatitude. *J Geophys Res: 84*, 5047, 1979.

Oelhaf, H., T.V. Clarmann, H. Fischer, F. Friedl-Vallon, C. Fritzsche, A. Linden, C. Piesch, M. Seefeldner, and W. Volker, Stratospheric $ClONO_2$ and HNO_3 profiles inside the Arctic vortex from MIPAS-B limb emission spectra obtained during EASOE. *Geophys Res Lett: 21*, 1263, 1994.

Offermann, D., K.-U. Grossman, P. Varthol, P. Knieling, M. Riese, and R. Tank, Cryogenic Infrared Spectrometers and Telescopes for the Atmosphere (CRISTA) experiment and middle atmosphere variability. *J Geophys Res: 104*, 16,311, 1999.

Oltmans, S.J., and D.J. Hofmann, Increase in lower stratospheric water vapor at a midlatitude Northern Hemisphere site from 1981 to 1994. *Nature: 374*, 146, 1995.

Oltmans, S.J., H. Volmel, D.J. Hofmann, K. Rosenlof, and D. Kley, The increase in stratospheric water vapor from balloon-borne frost point hygrometer measurements at Washington, DC and Boulder, Colorado. *Geophys Res Lett: 27*, 3453, 2000.

Oram, D.E., and S.A. Penkett, Observations in eastern England of elevated methyl iodide concentrations in air of Atlantic origin. *Atmos Environ: 28*, 1159, 1994.

Orlando, J.J., G.S. Tyndall, G.K. Moortgat, and J.G. Calvert, Quantum yields for NO_3 photolysis between 570 and 635 nm. *J Phys Chem: 97*, 10,996, 1993.

Paetzold, H.K., F. Piscalar, and H. Zschorner, Secular variation of the stratospheric ozone layer over middle Europe during the solar cycles from 1951 to 1972. *Nature: 240*, 106, 1972.

Paneth, F.A., The chemical composition of the atmosphere. *Quart J Roy Meteorol Soc: 63*, 433, 1937.

Park, J.H., and B. Carli, Spectroscopic measurements of HO_2, H_2O_2, and OH in the stratosphere. *J Geophys Res: 96*, 22,535, 1991.

Perliski, L., S. Solomon, and J. London, On the interpretation of seasonal variations in stratospheric ozone. *Planet Space Sci: 37*, 1527, 1989.

Peter, T., Microphysics and chemistry of polar stratospheric cloud particles. *Ann Rev Phys Chem: 48*, 785, 1995.

Pétron, G., C. Granier, B. Khattatov, J.-F. Lamarque, V. Yudin, J.-F. Müller, and J. Gille, Inverse modeling of carbon monoxide surface emissions using Climate Modeling and Diagnostics Laboratory network observations, *J Geophys Res: 107*, D24, 4761, doi:10.1029/2001JD001305, 2002.

Pfeilsticker, K., and U. Platt, Airborne measurements during the Arctic stratospheric experiment: Observations of O_3 and NO_2. *Geophys Res Lett: 21*, 1375, 1994.

Pfeilsticker, K., W.T. Sturges, H. Bösch, C. Camy-Peyret, M.P. Chipperfield, A. Engel, R. Fitzenberger, M. Müller, S. Payan, and B.-M. Sinnhuber, Lower stratospheric organic and inorganic bromine budget for the Arctic winter 1998/99. *Geophys Res Lett: 27*, 3305, 2000.

Pierrehumbert, R.T., Lateral mixing as a source of subtropical water vapor, *Geophys Res Lett: 25*, 151, 1998.

Pickett, H.M., and D.B. Peterson, Stratospheric OH measurements with a far-infrared limb observing spectrometer. *J Geophys Res: 98*, 20,507, 1993.

Pickett, H.M., and D.B. Peterson, Comparison of measured stratospheric OH with prediction. *J Geophys Res: 101*, 16,789, 1996.

Pitari, G., and V. Rizzi, An estimate of the chemical and radiative perturbation of stratospheric ozone following the eruption of Mount Pinatubo. *J Atmos Sci: 50*, 3260, 1993.

Pommerau, J.P., and J. Piquard, Ozone and nitrogen-dioxide vertical distributions by UV-visible solar occulation from balloons. *Geophys Res Lett: 21*, 1231, 1994.

Poole, L.R., and M.P. McCormick, Airborne lidar observations of Arctic polar stratospheric clouds: Indications of two distinct growth stages. *Geophys Res Lett: 15*, 21, 1988.

Poulet, G., M. Pirre, F. Maguin, M. Ramarosson, and G. Le Bras, Role of BrO + HO_2 reaction in the stratospheric chemistry of bromine. *Geophys Res Lett: 19*, 2305, 1992.

Prather, M.J., and D.J. Jacob, A persistent inbalance between HO_x photochemistry of the upper troposphere driven by deep tropical convection. *Geophys Res Lett: 24*, 3189, 1997.

Prinn, R. G., R.F. Weiss, B.R. Miller, J. Huang, F.N. Alyea, D.M. Cunnold, P.J. Fraser, D.E. Hartler, and P.G. Simmonds, Atmospheric trends and lifetime of CH_3CCl_3 and global OH concentrations. *Science: 269*, 187, 1995.

Pueschel, R.F., K.G. Snetsinger, J.K. Goodmann, O.B. Toon, G.V. Ferry, V.R. Oberbeck, J.M. Livingston, S. Verma, W. Fong, W.L. Starr, and K.R. Chan, Condensed nitrate, sulfate, and chloride in Antarctic stratospheric clouds. *J Geophys Res: 94*, 11,271, 1989.

Pundt, I., J.P. Pommereau, C. Phillips, and E. Lateltin, Upper limit of iodine oxide in the lower stratosphere. *J Atmos Chem: 30*, 173, 1998.

Quay, P.D., S.L. King, J. Stutsman, D.O. Wilbur, L.P. Steele, I. Fung, R.H. Gammon, T.A. Brown, G.W. Farwell, P.M. Grootes, and F.H. Schmidt, Carbon isotopic composition of atmospheric CH_4: Fossil and biomass burning source strengths. *Global Biogeochem Cycles: 5*, 25, 1991.

Quay, P., J. Stutsman, D. Wilbur, A. Stover, E. Duglokencky, and T. Brown, The isotopic composition of atmospheric methane. *Global Biogeochem Cycles: 13*, 445, 1999.

Ramanathan, K.R., Bi-annual variation of atmospheric ozone over the tropics, *Quart J Roy Met Soc: 89*, 540, 1963.

Randel, W.J., F. Wu, S.J. Oltmans, K. Rosenlof, and G.E. Nedoluka, Interannual changes of stratospheric water vapor and correlations with tropical tropospause temperatures. *J Atm Sci: 61*, 2133, 2004.

Raper, O.F., C.B. Farmer, R.A. Toth, and B.D. Robbins, The vertical distribution of HCl in the stratosphere. *Geophys Res Lett: 4*, 531, 1977.

Ravishankara, A.R., P.H. Wine, C.A. Smith, P.E. Barbone, and A. Torabi, N_2O_5 photolysis: Quantum yields for NO_3 and $O(^3P)$. *J Geophys Res: 91*, 5355, 1986.

Reichle, H.G., V.S. Connors, J.A. Holland, R.T. Sherrill, H.A. Wallio, J.C. Casas, E.P. Condon, B.B. Gormsen, W. Seiler, The distribution of middle atmosphere carbon monoxide during early October 1984. *J Geophys Res: 95*, 9845, 1990.

Rex, M., R.J. Salawitch, M.L. Santee, J.W. Waters, K. Hoppel, and R. Bevilacqua, On the unexplained stratospheric ozone losses during cold Arctic Januaries. *Geophys Res Lett: 30*, doi: 10.1029/2002GL016008, 2003.

Ridley, B.A., M. McFarland, J.T. Bruin, H.I. Schiff, and J.C. McConnell, Sunrise measurements of stratospheric nitric oxide. *Can J Phys: 55*, 212, 1977.

Ridley, B.A., M. McFarland, A.L. Schmeltekopf, M.H. Proffitt, D.L. Albritton, R.H. Winkler, and T.L. Thompson, Seasonal differences in the vertical distributions of NO, NO_2, and O_3 in the stratosphere near 50°N. *J Geophys Res: 92*, 11,919, 1987.

Riese, M., R. Spang, P. Preusse, M. Ern, M. Jarisch, D. Offermann, and K.-U. Grossmann, Cryogenic Infrared Spectrometers and Telescope for the Atmosphere (CRISTA) data processing and atmospheric temperature and trace gas retrieval. *J Geophys Res: 104*, 16,349, 1999.

Rinsland, C.P., R. Zander, E. Mahieu, P. Demoulin, A. Goldman, D. Ehhalt, and J. Rudolph, Ground-based infrared measurements of carbonyl sulfide total column abundances: Long-term trends and variability. *J Geophys Res: 97*, 5995, 1992.

Rinsland, C.P., M.R. Gunson, R.J. Salawitch, H.A. Michelsen, R. Zander, M.J. Newchurch, M.M. Abbas, M.C. Abrams, G.L. Manney, A.Y. Chang, F.W. Irion, A. Goldman, and E. Mahieu, ATMOS/ATLAS-3 measurements of stratospheric chlorine

and reactive nitrogen partitioning inside and outside the November 1994 Antarctic vortex. *Geophys Res Lett: 23*, 2365, 1996.

Rinsland, C.P., A. Goldman, F.J. Murcray, T.M. Stephen, M.S. Pougatchev, J. Fischman, S.J. David, R.D. Blatherwick, P.C. Novelli, N.B. Jones, and B.J. Connor, Infrared solar spectroscopic measurements of free tropospheric CO, C_2H_5 and HCN above Mauna Loa, Hawaii: Seasonal variations and evidence for enhanced emissions from the southeast Asian tropical fires of 1997-1998. *J Geophys Res: 104*, 18,667, 1999.

Robinson, G.N., D.R. Worsnop, J.T. Jayne, and C.E. Kolb, Heterogeneous uptake of $ClONO_2$ and N_2O_5 by sulfuric acid solutions. *J Geophys Res: 102*, 3583, 1997.

Roche, A.E., J.B. Kumer, J.L. Mergenthaler, G.A. Ely, W.G. Uplinger, J.F. Potter, T.C. James, and L.W. Sterritt, The Cryogenic Limb Array Etalon Spectrometer, CLAES on UARS: Experiment description and performance. *J Geophys Res: 98*, 10,763, 1993.

Roche, A.E., J.B. Kumer, J.L. Mergenthaler, R.W. Nightingale, W.G. Uplinger, G.A. Ely, J.F. Potter, D.J. Wuebbles, P.S. Connell, and D.E. Kinnison, Observations of lower stratospheric $ClONO_2$, HNO_3, and aerosol by the UARS CLAES experiment between January 1992 and April 1993. *J Atmos Sci: 51*, 2877, 1994.

Rosen, J.M., N.T. Kjome, N. Larsen, B.M. Knudsen, E. Kyrö, R. Kivi, J. Karhu, R. Neuber, and I. Benigna, Polar stratospheric cloud threshold temperatures in the 1995-1996 Arctic vortex. *J Geophys Res: 102*, 28,195, 1997.

Rosenlof, K.H., S.J. Oltmans, D. Kley, J.M. Russell III, E.W. Chiou, W.P. Chu, D.G. Johnson, K.K. Kelly, H.A. Michelsen, G.E. Nedoluha, E.E. Remsberg, G.C. Toon, and M.P. McCormick, Stratospheric water vapor increases over the past half century. *Geophys Res Lett: 28*, 1195, 2001.

Rossi, M.J., R. Malhotra, and D.M. Golden, Heterogeneous chemical reaction of chlorine nitrate and water on sulfuric-acid surfaces at room temperatures. *Geophys Res Lett: 14*, 127, 1987.

Rowland, F.S., and M.J. Molina, Chlorofluoromethanes in the environment. *Rev Geophys Space Phys: 13*, 1, 1975.

Rowland, F.S., J.E. Spencer, and M.J. Molina, Stratospheric formation and photolysis of chlorine nitrate. *J Phys Chem: 80*, 2711, 1976.

Rudolph, J., D.H. Ehhalt, and A. Tonissen, Vertical profiles of ethane and propane in the stratosphere. *J Geophys Res: 86*, 7767, 1981.

Russell, J.M., III, L.L. Gordley, J.H. Park, S.R. Drayson, D.H. Hesketh, R.J. Cicerone, A.F. Tuck, J.E. Frederick, J.E. Harries, and P.J. Crutzen, The Halogen Occultation Experiment. *J Geophys Res: 98*, 10,777, 1993.

Russell, P.B., J.M. Livingston, R.F. Pueschel, J.B. Pollack, S. Brooks, P. Hamill, J. Hughes, L. Thomason, L. Stowe, T. Deshler, and E. Dutton, Global to microscale evolution of the Pinatubo volcanic aerosol, derived from diverse measurements and analyses. *J Geophys Res: 101*, 18,745, 1996.

Salcedo, D., L.T. Molina, and M.J. Molina, Homogeneous freezing of concentrated aqueous nitric acid solutions at polar stratospheric temperatures. *J Phys Chem: 105*, 1433, 2001.

Sandalls, F.J., and S.A. Penkett, Measurements of carbonyl sulfide and carbon disulfide in the atmosphere. *Atmos Environ: 11*, 197, 1977.

Schauffler, S.M., L.E. Heidt, W.H. Pollack, T.M. Gilpin, J.F. Vedder, S. Solomon, R.A. Lueb, and E.L. Atlas, Measurements of halogenated organic compounds near the tropical tropopause. *Geophys Res Lett: 20*, 2567, 1993.

Schmeltekopf, A.L., D.L. Albritton, P.J. Crutzen, P.D. Goldan, W.J. Harrop, W.R. Henderson, J.R. McAfee, M. McFarland, H.I. Schiff, T.L. Thompson, D.L. Hofmann, and N.T. Kjome, Stratospheric nitrous oxide altitude profiles at various latitudes. *J Atmos Sci: 34*, 729, 1977.

Schmidt, U., Molecular hydrogen in the atmosphere. *Tellus: 26*, 78, 1974.

Schmidt, U., G. Kulessa, and E. P. Roth, The Atmospheric H_2 cycle, Proc of the NATO Advanced Institute on Atmospheric Ozone, A.C. Aikin, ed., *U.S. Dept. of Transportation, FAA-EE-80-20*, FAA, Washington, D.C., USA, 1980.

Scholz, T.G., D.H. Ehhalt, L.E. Heidt, and E.A. Martell, Water vapor molecular hydrogen, methane, and tritium concentrations near the stratopause. *J Geophys Res: 75*, 3049, 1970.

Seiler, W., and P.J. Crutzen, Estimates of gross and net fluxes of carbon between the biosphere and the atmosphere from biomass burning. *Clim Change: 2*, 207, 1980.

Seiler, W., and R. Conrad, Contribution of tropical ecosystems to the global budget of trace gases, especially CH_4, H_2, CO and N_2O, in *The Geophysiology of Amazonia*, R. Dickinson, ed., John Wiley, pp. 133-160, 1987.

Sen, B., G.C. Toon, G.B. Osterman, J.-F. Blavier, J.J. Margitan, R.J. Salawitch, and G.K. Yue, Measurements of reactive nitrogen in the stratosphere. *J Geophys Res: 103*, 3571, 1998.

Shah, G.M., Quasi-biennial oscillation in ozone. *J Atmos Sci: 24*, 396, 1967.

Singh, H.B., L.J. Salas, and R.E. Stiles, Methyl halides in and over the Eastern Pacific. *J Geophys Res: 88*, 3684, 1983.

Singh, H.B., M. Kanakidou, P.J. Crutzen, and D.J. Jacob, High concentrations and photochemical fate of oxygenated hydrocarbons in the global troposphere. *Nature: 378*, 50, 1995.

Siskind, D.E., J.T. Bacmeister, M.E. Summers, and J.M. Russell III, Two-dimensional calculations of nitric oxide transport in the middle atmosphere and comparison with halogen occultation experiment data. *J Geophys Res: 102*, 3527, 1997.

Solomon, S., and R.R. Garcia, Simulation of NO_x partitioning along isobaric parcel trajectories. *J Geophys Res: 88*, 5497, 1983.

Solomon, S., P.J. Crutzen, and R.G. Roble, Photochemical coupling between the thermosphere and the lower atmosphere, I. Odd nitrogen from 50 to 120 km. *J Geophys Res: 87*, 7206, 1982.

Solomon, S., R.R. Garcia, F.S. Rowland, and D.J. Wuebbles, On the depletion of Antarctic ozone. *Nature: 321*, 755, 1986.

Solomon, S., G.H. Mount, R.W. Sanders, and A.L. Schmeltekopf, Visible spectroscopy at McMurdo Station, Antarctica, 2. Observation of OClO. *J Geophys Res: 92*, 8329, 1987.

Solomon, S., H.L. Miller, J.P. Smith, R.W. Sanders, G.H. Mount, A.L. Schmeltekopf, and J.F. Noxon, Atmospheric NO_3: 1. Measurement technique and the annual cycle at 40°N. *J Geophys Res: 94*, 11,041, 1989a.

Solomon, S., R.W. Sanders, M.A. Carroll, and A.L. Schmeltekopf, Visible and near-ultraviolet spectroscopy at McMurdo Station, Antarctica: 5. Observations of the diurnal variations of BrO and OClO. *J Geophys Res: 94*, 11,393, 1989b.

Solomon, S., R.R. Garcia, and A.R. Ravishankara, On the role of iodine in ozone depletion. *J Geophys Res: 99*, 20,491, 1994.

Solomon, S.C., C.A. Barth, and S.M. Bailey, Auroral production of nitric oxide measured by the SNOE satellite. *Geophys Res Lett: 26*, 1259, 1999.

Spreng, S., and F. Arnold, Balloon-borne mass spectrometer measurements of HNO_3 and HCN in the winter Arctic stratosphere–Evidence for HNO_3-processing by aerosols. *Geophys Res Lett: 21*, 1251, 1994.

Stachnik, R.A., J.C. Hardy, J.A. Tarsala, J.W. Waters, and N.R. Erickson, Submillimeter heterodyne measurements of stratospheric ClO, HCl, and HO_2: First results. *Geophys Res Lett: 19*, 1931, 1992.

Stanford, J.L., and J.S. Davis, A century of stratospheric cloud reports: 1870-1972. *Bull Amer Meteorol Soc: 55*, 213, 1974.

Steele, H.M., P. Hamill, M.P. McCormick, and T.J. Swissler, The formation of polar stratospheric clouds. *J Atmos Sci: 40*, 2055, 1983.

Steele, H.M., K. Drdla, R.P. Turco, J.D. Lumpe, R.M. Bevilacqua, Tracking polar stratospheric cloud development with POAM II and a microphysical model. *Geophys Res Lett: 26*, 287, 1999.

Stimpfle, R.M., P.O. Wennberg, L.B. Lafson, and J.G. Anderson, Simultaneous in situ measurements of OH and HO_2 in the stratosphere. *Geophys Res Lett: 17*, 1905, 1990.

Stolarski, R.S., and R.J. Cicerone, Stratospheric chlorine: A possible sink for ozone. *Canad J Chem: 52*, 1610, 1974.

Stolarski, R.R., and R.D. Rundel, Fluorine chemistry in the stratosphere. *Geophys Res Lett: 2*, 443, 1975.

SPARC (Stratospheric Processes and their Role in Climate), *Assessment of Upper Tropospheric and Stratospheric Water Vapor*, WMO/TD 1043, SPARC Office, Verrieres le Buisson, France, 2000.

Summers, M.E., D.F. Strobel, R.M. Bevilacqua, X. Zhu, M.T. DeLand, M. Allen, and G.M. Keating, A model study of the response of mesopheric ozone to the short-term solar ultraviolet flux variations. *J Geophys Res: 95*, 22,523, 1990.

Summers, M.E., R.R. Conway, D.E. Siskind, M.H. Stevens, D. Offermann, M. Riese, P. Preusse, D.F. Strobel, and J.M. Russell III, Implications of satellite OH observations for middle atmospheric H_2O and ozone. *Science: 227*, 1967, 1997.

Summers, M.E., R.R. Conway, C.R. Englert, D.E. Siskind, M.H. Stevens, J.M. Russell III, L.L. Gordley, and M.J. McHugh, Discovery of a water vapor layer in the Arctic summer mesosphere: Implications for polar mesospheric clouds. *Geophys Res Lett: 28*, 3601, 2001.

Swanson, T.H., J.W. Eltkins, J.H. Butler, S.A. Montzka, R.C. Myers, T.M. Thompson, T.J. Baring, S.O. Cummins, G.S. Dutton, A.H. Hayden, J.M. Lobert, G.A. Holcomb, W.T. Sturges, and T.M. Gilpin, 5. Nitrous oxide and halocarbons division, in *Climate Monitoring and Diagnostics Laboratory Summary Report No. 21, 1992.* J.T. Petersen and R.M. Rosson (eds.), 59-75, NOAA Environ. Res. Labs., Boulder, Colo, USA, 1993.

Sze, N.D., Stratospheric fluorine: A comparison between theory and measurements. *Geophys Res Lett: 5*, 781, 1978.

Sze, N.D., and M.K.W. Ko, Photochemistry of COS, CS_2, CH_3 SCH_3 and H_2S: Implications for the atmospheric sulfur cycle. *Atmos Environ: 14*, 1223, 1980.

Tabazadeh, A., and R.P. Turco, Stratospheric chlorine injection by volcanic eruptions: HCl scavenging and implications for ozone. *Science: 260*, 1082, 1993.

Tabazadeh, A., and O.B. Toon, Freezing behavior of stratospheric sulfate aerosols inferred from trajectory studies. *Geophys Res Lett: 22*, 1725, 1995.

Tabazadeh, A., and O.B. Toon, The presence of metastable HNO_3/H_2O solid phases in the stratosphere inferred from ER-2 data. *J Geophys Res: 101*, 9071, 1996.

Tabazadeh, A., R.P. Turco, and M.Z. Jacobson, A model for studying the composition and chemical effects of stratospheric aerosols. *J Geophys Res: 99*, 12,897, 1994.

Tabazadeh, A., O.B. Toon, and P. Hamill, Freezing behavior of stratospheric sulfate aerosols inferred from trajectory studies. *Geophys Res Lett: 22*, 1725, 1995.

Tabazadeh, A., O.B. Toon, B.L. Gary, J.T. Bacmeister, and M.R. Schoeberl, Observational constraints on the formation of type Ia polar stratospheric clouds. *Geophys Res Lett: 23*, 2109, 1996.

Thomas, R.J., C.A. Barth, G.J. Rottman, D.W. Rusch, G.H. Mount, G.M. Lawrence, R.W. Sanders, G.E. Thomas, and L.E. Clemens, Ozone density in the mesosphere (50-90 km) measured by the SME near infrared spectrometer. *Geophys Res Lett: 10*, 245, 1983.

Thomason, L.W., L.R. Poole, and T. Deshler, A global climatology of stratospheric aerosol surface area density deduced from Stratospheric Aerosol and Gas Experiment II measurements: 1984-1994. *J Geophys Res: 102*, 8967, 1997.

Thornton, D.C., A.R. Bandy, and A.R. Driedger III, Sulfur dioxide over the western Atlantic Ocean. *Glob Biogeochem Cycles: 1*, 317, 1987.

Tie, X., G.P. Brasseur, B. Briegleb, and C. Granier, Two-dimensional simulation of Pinatubo aerosol and its effect on stratospheric ozone. *J Geophys Res: 99*, 20,545, 1994.

Tisone, G.C., Measurements of NO densities during sunrise at Kauai. *J Geophys Res: 78*, 746, 1973.

Tohmatsu, T., and N. Iwagami, Measurement of nitric oxide distribution in the upper atmosphere. *Space Res: 15*, 241, 1975.

Tohmatsu, T., and N. Iwagami, Measurement of nitric oxide abundance in equatorial upper atmosphere. *J Geomagn Geoelec: 28*, 343, 1976.

Tolbert, M.A., and O.B. Toon, Solving the PSC mystery. *Science: 292*, 61, 2001.

Tolbert, M.A., M.J. Rossi, and D.M. Golden, Heterogeneous interactions of chlorine nitrate, hydrogen chloride and nitric acid with sulfuric acid surfaces at stratospheric temperatures. *Geophys Res Lett: 15*, 847, 1988.

Tolbert, M.A., B.G. Koehler, and A.M. Middlebrook, Spectroscopic studies of model polar stratospheric cloud films. *Spectrochimica Acta: 48A*, 1303, 1992.

Toohey, D.W., J.G. Anderson, W.H. Brune, and K.R. Chan, In situ measurements of BrO in the arctic stratosphere. *Geopohys Res Lett: 17*, 513, 1990.

Toon, G.C., C.B. Farmer, P.W. Schafer, L.L. Lowes, and R.H. Norton, Composition measurements of the 1989 Arctic stratosphere by airborne infrared solar absorption spectroscopy. *J Geophys Res: 97*, 7939, 1992a.

Toon, G.C., C.B. Farmer, P.W. Schafer, L.L. Lowes, R.H. Norton, M.R. Schoeberl, L.R. Lait, and P.A. Newman, Evidence for subsidience in the 1989 Arctic winter stratosphere from airborne infrared composition measurements. *J Geophys Res: 97*, 7963, 1992b.

Toon, O.B., P. Hamill, R.F. Turco, and J. Pinto, Condensation of HNO_3 and HCl in the polar stratospheres. *Geophys Res Lett: 13*, 1284, 1986.

Toon, O.B., E.V. Browell, S. Kinne, and J. Jordan, An analysis of Lidar observations of polar stratospheric clouds. *Geophys Res Lett: 17*, 393, 1990.

Toon, O.B., A. Tabazadeh, E.V. Browell, and J. Jordan, Analysis of lidar observations of arctic polar stratospheric clouds. *J Geophys Res: 105*, 20,598, 2000.

Toumi, R., R.L. Jones, and J.A. Pyle, Stratospheric ozone depletion by $ClONO_2$ photolysis. *Nature: 365*, 37, 1993.

Tsias, A., A.J. Prenni, K.S. Carslaw, T.P. Onasch, B.P. Luo, M.A. Tolbert, and T. Peter, Freezing of polar stratospheric clouds in orographically induced strong warming events. *Geophys Res Lett: 24*, 2303, 1997.

Tung, K.K., On the two-dimensional transport of stratospheric trace gases in isentropic coordinates. *J Atmos Sci: 39*, 2330, 1982.

Tung, K.K., M.K.W. Ko, J.M. Rodriguez, and N.D. Sze, Are Antarctic ozone variations a manifestation of dynamics or chemistry? *Nature: 333*, 811, 1986.

Turco, R.P., P. Hamill, O.B. Toon, R.C. Whitten, and C.S. Kiang, A one-dimensional model describing aerosol formation and evolution in the stratosphere, I. Physical processes and mathematical analogs, *J Atmos Sci: 36*, 399, 1979.

Turco, R.P., R.C. Whitten, O.B. Toon, J.B. Pollack, and P. Hamill, OCS, stratospheric aerosols and climate. *Nature: 283*, 283, 1980.

Turco, R.P., R.C. Whitten, and O.B. Toon, Stratospheric aerosols: Observations and theory. *Rev Geophys Space Sci: 20*, 233, 1982.

Voigt, C., J. Schreiner, A. Kohlmann, P. Zink, K. Mauersberger, N. Larsen, T. Deshler, C. Kröger, J. Rosen, A. Adriani, F. Cairo, G. Di Donfrancesco, M. Viterbini, J. Ovarlez, H. Overlez, C. David, and A. Dörnbrack, Nitric acid trihydrate (NAT) in polar stratospheric cloud particles. *Science: 290*, 1756, 2000.

Vömel H. *et al.*, Balloon-borne observations of water vapor and ozone in the tropical upper troposphere and lower stratosphere. *J Geophys Res: 107*, 4210, doi: 10.1029/2001JD000707, 2002.

von Cossart, G., J. Fielder, and V. von Zahn, Size distributions of NLC particles as determined from 3-color observations of NLC by ground-based lidar. *Geophys Res Lett: 26*, 1513, 1999.

Wallace, L., and W. Livingston, The effect of the Pinatubo cloud on hydrogen chloride and hydrogen fluoride. *Geophys Res Lett: 19*, 1209, 1992.

Wamsley, P.R., J.W. Elkins, D.W. Fahey, G.S. Dutton, C.M. Volk, R.C. Myers, S.A. Montzka, J.H. Butler, A.D. Clarke, P.J. Fraser, L.P. Steele, M.P. Lucarelli, E.L. Atlas, S.M. Schauffler, D.R. Blake, F.S. Rowland, W.T. Sturges, J.M. Lee, S.A. Penkett, A. Engel, R.M. Stimpfle, K.R. Chan, D.K. Weisenstein, M.K.W. Ko, and R.J. Salawitch, Distribution of halon-1211 in the upper troposphere and lower stratosphere and the 1994 total bromine budget. *J Geophys Res: 103*, 1513, 1998.

Wahner, A., and C. Schiller, Twilight variation of veritcal column abundances of OClO and BrO in the North Polar region. *J Geophys Res: 97*, 8047, 1992.

Waters, J.W., J.J. Gustincic, and P.N. Swanson, *Atmospheric Water Vapor.* A. Deepak, ed., Academic Press, 1980.

Waters, J.W., J.C. Hardy, R.F. Jarnot, and H.M. Pickett, Chlorine monoxide radical, ozone and hydrogen peroxide: Stratospheric measurements by microwave limb sounding. *Science: 214*, 61, 1981.

Waters, J.W., L. Froidevaux, W.G. Read, G.L. Manney, L.S. Elson, D.A. Flower, R.F. Janot, and R.S. Harwood, Stratospheric ClO and ozone from the Microwave Limb Sounder on the Upper Atmosphere Research Satellite. *Nature: 362* , 597, 1993.

Weaver, A., S. Solomon, R.W. Sanders, K. Arpag, and H.L. Miller, Jr., Atmospheric NO_3, 5. Off-axis measurements at sunrise: Estimates of tropospheric NO_3 at 40°N. *J Geophys Res: 101*, 18,605, 1996.

Weiss, R.F., Changing global concentration of atmospheric nitrous oxide, *Proc. Int. Sym. on Global Cycles of Atmospheric Greenhouse Gases*, Sendai, Japan, 78, 1994.

Weiss, P.S., J.E. Johnson, R.H. Gammon, and T.S. Bates, Re-evaluation of the open ocean source of carbonyl sulfide to the atmosphere. *J Geophys Res: 100*, 23,083, 1995.

Wennberg, P.O., R.M. Stimple, E.M. Weinstock, A.E. Dessler, S.A. Lloyd, L.B. Lapson, J.J. Schwab, and J.G. Anderson. Simultaneous in situ measurements of OH, HO_2, O_3, and H_2O: A test of modeled stratospheric HO_x chemistry. *Geophys Res Lett: 17*, 1909, 1990.

Wennberg, P.O., R.C. Cohen, R.M. Stimpfle, J.P. Koplow, J.G. Anderson, R.J. Salawitch, D.W. Fahey, E.L. Woodbridge, E.R. Keim, R.S. Gao, C.R. Webster, R.D. May, D.W. Toohey, L.M. Avallone, M.H. Proffitt, M. Loewenstein, J.R. Podolske, K.R. Chan, and S.C. Wofsy, Removal of stratospheric O_3 by radicals: In situ measurements of OH, HO_2, NO, NO_2, ClO, and BrO. *Science: 266*, 398, 1994.

Wennberg, P.O., J.W. Brault, T.F. Hanisco, R.J. Salawitch, and G.H. Mount, The atmospheric column abundance of IO: Implications for stratospheric ozone. *J Geophys Res: 102*, 8887, 1997.

Whitten, R.C., O.B. Toon, and R.P. Turco, The stratospheric sulfate aerosol layer: Processes, models observations and simulations. *Pageoph: 118*, 86, 1980.

Willett, H.C., The relationship of total atmospheric ozone to the sunspot cycle. *J Geophys Res: 67*, 661, 1962.

Willett, H.C., and J. Prohaska, Further evidence of sunspot-ozone relationships. *J Atmos Sci: 22*, 493, 1965.

Williams, L.R., J.A. Manion, D.M. Golden, and M.A. Tolbert, Laboratory measurements of heterogeneous reactions on sulfuric acid surfaces. *J Appl Meteorol: 33*, 785, 1994.

Williams, W.J., J.J. Kostus, A. Goldman, and D.G. Murcray, Measurements of the stratospheric mixing ratio of HCl using an infrared absorption technique. *Geophys Res Lett: 3*, 383, 1976.

Wine, P.H., J.R. Wells, and A.R. Ravishankara, Channel specific rate constants for reaction of O (^{1}D) with HCl and HBr. *J Chem Phys: 84*, 1349, 1986.

Witt, G., J.E. Dye, and N. Wilhelm, Rocket-borne measurements of scattered sunlight in the mesosphere. *J Atmos Terr Phys: 38*, 223, 1976.

Wittrock, F., R. Mueller, A. Richter, H. Bovensmann, and J.P. Burrows, Measurements of iodine monoxide (IO) above Spitsbergen. *Geophys Res Lett: 27*, 1471, 2000.

Wofsy, S.C, M.B. McElroy, and Y.L. Yung, The chemistry of atmospheric bromine. *Geophys Res Lett: 2*, 215, 1975.

World Meteorological Organization (WMO), Atmospheric Ozone, Report No. 16, Geneva, 1985.

World Meteorological Organization/United Nations Environment Programme (WMO/UNEP), Scientific assessment of ozone depletion: 1991, Report No. 25, Geneva, 1991.

World Meteorological Organization/United Nations Environment Programme (WMO/UNEP), Scientific assessment of ozone depletion: 1994, Report No. 37, Geneva, 1995.

World Meteorological Organization/United Nations Environment Programme (WMO/UNEP), Scientific Assessment of Ozone Depletion: 1998, Report No. 44, Geneva, 1999.

Worsnop, D.R., L.E. Fox, M.S. Zahniser, and S.C. Wofsy, Vapor-pressures of solid hydrates of nitric-acid. Implications for polar stratospheric clouds. *Science: 259*, 71, 1993.

Yang, H., and K.K. Tung, On the phase propagation of extratropical ozone quasi-biennial oscillation in observational data. *J Geophys Res: 100*, 9091, 1995.

Yung, Y.L., J.P. Pinto, R.T. Watson, and S.P. Sander, Atmospheric bromine and ozone perturbations in the lower stratosphere. *J Atmos Sci: 37*, 339, 1980.

Zander, R., Recent observations of HF and HCl in the upper stratosphere. *Geophys Res Lett: 8*, 413, 1981.

Zander, R., H. Leclercq, and L.D. Kaplan, Concentrations of carbon monoxide in the upper troposphere. *Geophys Res Lett: 8*, 365, 1981.

Zander, R., M.R. Gunson, and C.B. Farmer, Remote sensing of the earth's atmosphere by infrared absorption spectroscopy — An update of the ATMOS program, in: *Advanced Optical Instrumentation for Remote Sensing of the Earth's Surface from Space, Proc. SPIE: 1129*, 10, 1989.

Zander, R., D.H. Ehhalt, C.P. Rinsland, U. Schmidt, E. Mahieu, J. Rudolph, P. Demoulin, G. Roland, L. Delbouille, and A.J. Sauval, Secular trend and seasonal variability of the column abundance of N_2O above the Jungfraujoch station determined from IR solar spectra. *J. Geophys Res: 99*, 16,745, 1994.

Zander, R. E. Mahieu, M.R. Gunson, M.C. Abrams, A.Y. Chang, M. Abbas, C. Aellig, A. Engel, A. Goldman, F.W. Irion, N. Kämpfer, H.A. Michelsen, M.H. Newchurt, C.P. Rinsland, R.J. Salawitch, G.P. Stiller, and G.C. Toon, The 1994 northern midlatitude budget of stratospheric chlorine derived from ATMOS/ATLAS-3 observations. *Geophys Res Lett: 23*, 2357, 1996.

Zellner, R., Chemistry of the stratosphere, in *Global Aspects of Atmospheric Chemistry*. R. Zellner, ed., Springer Verlag, 1999.

Zhao, Y., Y. Kondo, F.J. Murcray, X. Liu, M. Koike, H. Irie, K. Strong, K. Suzuki, M. Sera, and Y. Ikegami, Seasonal variations of HCN over northern Japan measured by ground-based infrared spectroscopy. *Geophys Res Lett: 27*, 2085, 1999.

Zhu, Y., R.E. Newell, and W.G. Read, Factors controlling upper-troposphere water vapor. *J Clim: 13*, 836, 2000.

Chapter 6

OZONE PERTURBATIONS

6.1 Introduction

The previous chapters describe the array of physical and chemical processes that can influence the odd oxygen family (and thereby its most prominent member, ozone). The photochemical lifetime of odd oxygen is less than a day throughout the region from about 35 to 70 km in the sunlit atmosphere (see Figure 5.3). This is much faster than those of the corresponding zonally-averaged transport processes, so that this region provides a testbed for photochemical theory.

Section 6.2 discusses how local temperature, HO_x, NO_x, and ClO_x chemistries affect ozone at chemically-controlled altitudes in the upper stratosphere and mesosphere, providing important constraints on scientific understanding of ozone perturbations. The observation of trends in upper stratospheric ozone has now demonstrated the long-term impact of chlorofluorocarbons on ozone in the upper stratosphere, as was first predicted in the 1970s. The vertical and meridional structure of the observed ozone trends in this region also yield important insights into chlorine-catalyzed ozone destruction. These will be a particular focus of Section 6.2, which discusses how ozone in the chemically controlled regime can be perturbed by changes of temperature, solar radiation, and the chemical families described in Chapter 5.

Below about 25 km, the chemical time scale for odd oxygen increases to months or years in most locations, so that photochemistry is not the only component of the zonally-averaged ozone budget of the lower stratosphere. This dramatic change in lifetime is due largely to the attenuation of the solar radiation field available to drive photochemistry at deeper and deeper altitudes of penetration (see Chapter 4). Where the chemical lifetime of odd oxygen exceeds a month (below about 25 km), it becomes comparable to the time scale characterizing the zonally-averaged transport by the mean meridional circulation. The bulk of the ozone column resides in this dynamically-sensitive region as discussed in Section 5.2.3, so that dynamical processes can play a critical role in modulating the total ozone column not only from day to day, but also on a seasonal and interannual basis. Any chemically-

driven change in ozone at these altitudes depends upon how quickly chemistry can remove the ozone as it flows, *i.e.*, on the potential of chemistry to destroy ozone 'in transit'. If chemistry is negligibly slow compared to dynamics, then ozone will pass through without significant alteration. If chemical processes can remove a portion of the moving ozone flowing through this region, then the column abundance will decrease. Even at altitudes as low as 20 km, chemical processes can sometimes become remarkably fast, for example, when surface chemistry (*e.g.*, on polar stratospheric clouds in Antarctic spring) comes into play. Section 6.3 discusses lower stratospheric ozone depletion. Section 6.3.1 describes the Antarctic ozone hole, focusing on the observations that have shown that chlorine (and, to a lesser extent, bromine) compounds are the primary cause of this spectacular change in ozone's behavior since about 1980. Sections 6.3.2 and 6.3.3 focus on the complex interplays between dynamics and chemistry that affect Arctic and mid-latitude ozone depletion, respectively. Section 6.4 is a summary of the chapter and presents a look ahead to the likely future of the ozone layer to be expected in the 21st century.

6.2 The Photochemically-Controlled Upper Stratosphere and Mesosphere: 25-75 km

Chapter 5 presented the components of the continuity equation for odd oxygen over a range of altitudes. Figure 6.1 shows how each of the rate-limiting steps in the catalytic cycles that affect ozone varies with altitude. The figure illustrates the competing roles of NO_x and ClO_x-driven catalytic loss processes from about 30 to 45 km, the emerging importance of purely O_x-driven loss near 40-55 km, and the domination of ozone chemistry by HO_x-driven catalytic cycles in the mesosphere.

Observations have provided important support for much of the key chemistry controlling upper stratospheric and mesospheric ozone, not only in terms of measurements of, for example, the abundance and distribution of OH, ClO, NO_2, and other trace gases as discussed in Chapter 5 (*e.g.*, Conway *et al.*, 2000; Waters *et al.*, 1983; Anderson *et al.*, 1977; Russell *et al.*, 1996), but also through some direct and dramatic responses to perturbations, detailed in following sections.

6.2.1 Temperature Variability and Ozone Response

It is well known that the primary source of heat in the stratosphere and mesosphere is the absorption of solar ultraviolet radiation by ozone

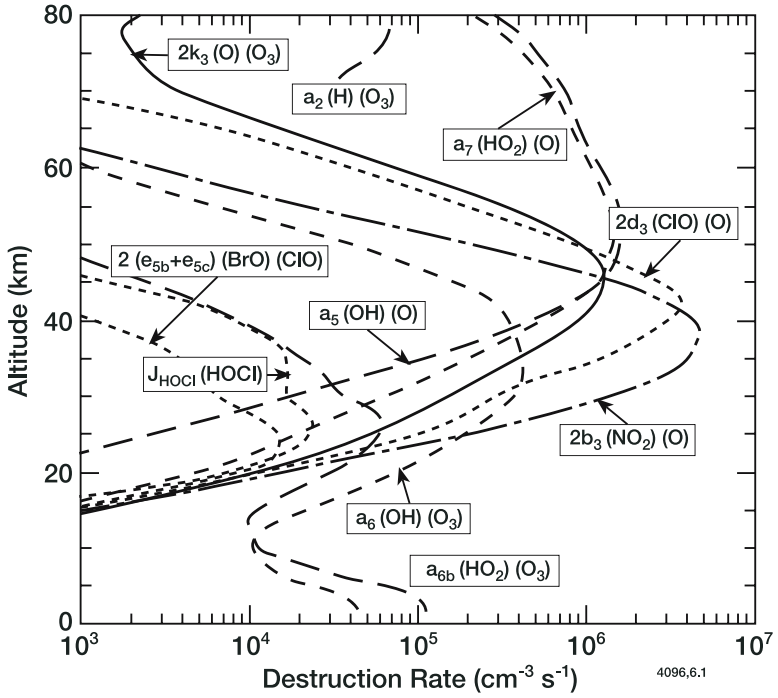

Figure 6.1. Daytime averaged rates of destruction of ozone at 40°N in winter by a range of chemical processes for 1998 levels of reactive chemicals, from the numerical model of Garcia and Solomon (see *e.g.*, Solomon *et al.*, 1998, and references therein).

(see Chapter 3); indeed, if it were not for the presence of ozone, the Earth would not have a stratosphere at all. If the concentration of ozone changes due to some perturbation (such as NO_x increases due to solar proton events, see next section), then the temperature will change in response. A simple, linearized description of this linkage was suggested by Dickinson (1973):

$$\Delta T = \frac{P_H}{\alpha} \cdot \frac{\Delta (O_3)}{(O_3)} \tag{6.1}$$

where P_H is the total gross heating rate, α is the relaxation rate (see Eq. (4.89)) and $\Delta\,(O_3)/(O_3)$ is the relative ozone change. At 50 km, for example, $P_H \approx 10$K/day and $\alpha \approx 0.2$/day, so that for an ozone reduction of 20%, a temperature decrease of about 10°K is expected based on this relationship.

Such a description can serve as a useful guide, but its applicability is limited by several factors. Ozone plays some role in the emission of infrared radiation as well as in absorbing ultraviolet radiation, so that the relaxation rate in the above equation is also linked to ozone change.

Further, a change in temperature will modify all temperature-dependent photochemical rates and hence will feed back to the ozone chemistry. This renders the temperature-ozone relation into a tightly coupled and non-linear system that can be better understood with the aid of some simple chemical arguments. If a pure oxygen atmosphere is assumed (see Chapter 5), the interaction between ozone density and temperature dependent rates is expressed by:

$$\frac{\Delta(O_3)}{(O_3)} = \frac{1}{2}\frac{\Delta(k_2/k_3)}{(k_2/k_3)} \tag{6.2}$$

Based upon the known temperature dependencies of reactions k_2 and k_3, we can write:

$$\frac{\Delta(O_3)}{(O_3)} \approx \frac{-1400}{T^2}\Delta T \tag{6.3}$$

or

$$\frac{d\ln(O_3)}{dT^{-1}} \approx -1400 \text{ K} \tag{6.4}$$

This expression suggests that in a region dominated by pure oxygen chemistry, a temperature decrease of 10°K (imposed for example through a change in circulation) would produce about a 20% increase in ozone.

In the real atmosphere, however, both ozone and temperature change in concert, and there is hence a stabilizing feedback between the two at upper stratospheric altitudes (Luther *et al.*, 1977). As a chemical perturbation occurs, the associated change in temperature assuming a pure oxygen atmosphere and including chemical coupling changes to:

$$\Delta T \approx \frac{P_H/\alpha}{1 + \frac{P_H}{\alpha}(1400/T^2)}\frac{\Delta(O_3)}{(O_3)} \tag{6.5}$$

Let us assume that a perturbation is applied which would produce a 10% ozone decrease in the absence of coupling. As the ozone concentration begins to decrease, the temperature decreases. This decreases the rates of ozone-destroying chemical reactions that have a positive energy of activation (such as the reaction between $O + O_3$ cited above for pure O_x chemistry). The net effect is an equilibrium ozone change that is roughly half as large as that obtained in the uncoupled system. Similarly, the temperature response is also halved.

These considerations lead to an anti-correlation of ozone and temperature above 30 km, first noted by Barnett *et al.* (1975); later studies include those of Krueger *et al.* (1980) and Finger *et al.* (1995). Rood and Douglass (1985), Douglass *et al.* (1985), and Douglass and Rood (1985) noted that there can be substantial phase differences between ozone and temperature changes when dynamical processes are very rapid, due to differences in the local response timescales for

temperature and ozone. However, Finger *et al.* (1996) showed good agreement of observed and calculated anti-correlations between ozone and temperature over much of the upper stratosphere in many cases.

Thus, observations and related theoretical modelling of the anticorrelation between temperature and ozone in the upper stratosphere provide a graphic illustration of the role of temperature-dependent chemistry in modulating ozone, as shown in Figure 6.2.

Eq. (6.5) was derived for a pure-oxygen atmosphere and is therefore only an idealized case. A more realistic analysis includes the temperature

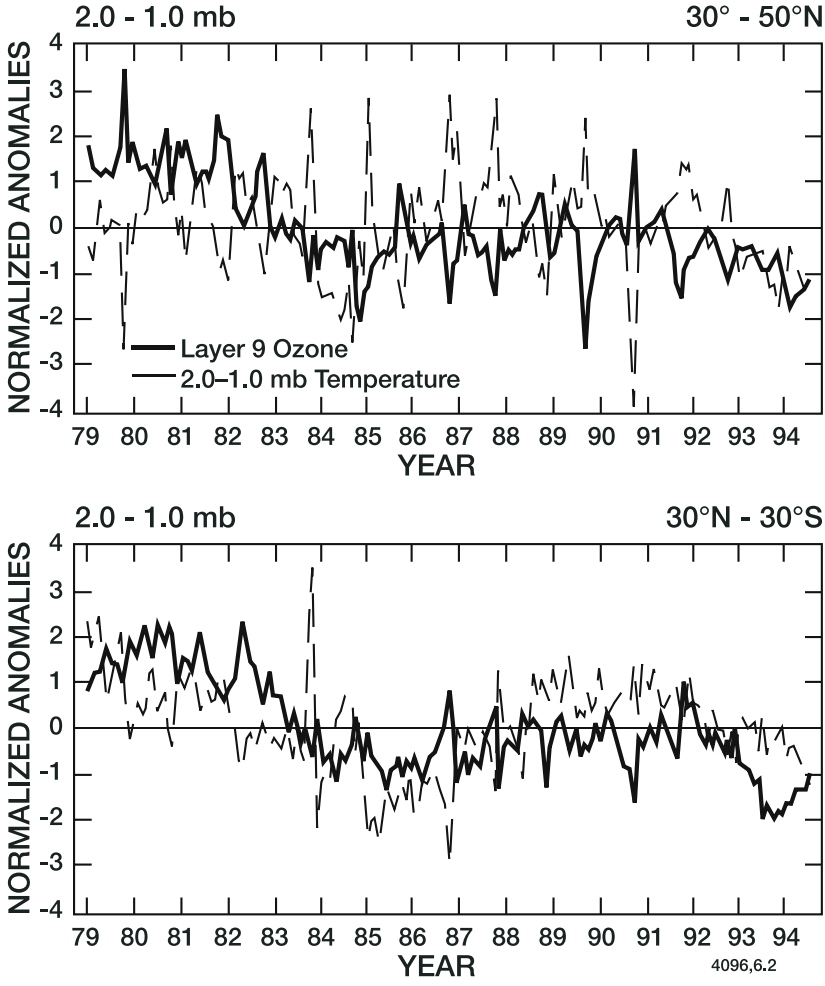

Figure 6.2. Observed variations in ozone and temperature based upon satellite data from 30°N to 50°N (top) and from 30°N to 30°S (bottom), from Finger *et al.* (1995).

effects of hydrogen, nitrogen, and chlorine chemistry. Haigh and Pyle (1982) suggested the following more general expression:

$$\frac{d\ln(O_3)}{dT^{-1}} = \frac{a + b\,f_1 + c\,f_2 + d\,f_3}{2 + f_1 + f_2 + f_3} \tag{6.6}$$

where f_1, f_2, and f_3 are the ratios of the rates of odd oxygen destruction due to HO_x, NO_x, and ClO_x, respectively, compared to the rate of destruction by the pure oxygen reactions. These factors depend on the chemical state of the atmosphere, and, in particular, on the amplitude of the perturbation. The other constants depend only on chemical kinetics and were given by Haigh and Pyle (1982) as a = 2810 K, b = 510 K, c= 1200 K. The value of d is less than 275 K, showing that increasing chlorine should reduce the stabilizing positive feedback between ozone and temperature. Recent kinetic studies suggest that the ClO_x and NO_x catalytic cycles are even less temperature sensitive than earlier calculations, underscoring this aspect of the chemistry.

It should be noted that other chemical species besides odd oxygen also depend upon temperature-dependent chemical reactions, further complicating this coupled picture. For example, the formation of HCl through the reaction of Cl + CH_4 also displays moderately strong temperature sensitivity, so that ozone's full sensitivity to temperature is linked not only to the temperature dependence of those reactions directly involved in ozone destruction, but also those of others that are indirectly linked through other chemicals. In general, these effects are relatively small compared to the direct roles of the competing and temperature-sensitive rate-limiting steps in the odd oxygen chemistry, so that useful information on the competition between chemical mechanisms can be obtained from analyses of ozone-temperature relations in the upper stratosphere.

6.2.2 Particle Precipitation

Perhaps the most striking evidence for the prominent role of the NO_x cycle in influencing ozone was first provided by observations of the changes in ozone following major charged particle precipitation events (see Chapter 7). Protons, electrons, and alpha particles released from the sun are channelled by our planet's magnetic field lines and produce ionization as they enter the Earth's atmosphere. Ionization in turn results in production of NO_x (about 1.5 NO molecules are produced per ionization) and HO_x (about 2 HO_x molecules are produced below 75 km per ionization). Solar disturbances can be associated with input of large quantities of charged particles to the Earth's atmosphere, which

result in the northern and southern lights (the aurorae) due to emissions by excited atoms and molecules. They can also lead to relativistic electron precipitation (REPs) and solar proton events (SPE, also referred to as polar cap absorption or PCA events). While REPs are related mainly to mesospheric ionization and can occur at latitudes as low as about 50°, SPEs and PCA events are characterized by particles with higher energies, some of which can penetrate to the stratosphere, but are generally restricted to high latitudes near the geomagnetic poles.

The possibility that odd nitrogen would be produced by energetic particle precipitation was first advanced by Dalgarno (1971), but the role of odd nitrogen in ozone chemistry was not understood at that time. In the early 1970s Crutzen *et al.* (1975) predicted that particle events could be linked to transient ozone loss. A notable depletion of upper stratospheric ozone was observed following the major solar proton event of August 1972. Ozone dropped by as much as about 20% near 35 km at 75°N on the day after the primary event, and remained low for weeks afterward (see *e.g.*, Heath *et al.*, 1977). A rapid drop in ozone supports the short photochemical lifetime of ozone in this height range, while the continued perturbation is consistent with the long lifetime of the enhanced NO_y in this region (order of months to a year). While dramatic, such events are rare. Major solar proton events are relatively infrequent, and typically occur only near the maximum of the 11-year cycle of solar activity.

More recent work on later solar proton events has benefited from concurrent observations, not only of ozone but also of NO_x compounds (*e.g.*, Jackman *et al.*, 2001), allowing a better link to be drawn between ozone and the enhanced catalytic NO_x concentrations. Figure 6.3 presents a striking illustration of the ability of current models to simulate the general features of observed NO_x and O_3 changes during a solar proton event observed in July 2000 (from Jackman *et al.*, 2001). Note that HO_x also contributes to the observed decreases, especially in the mesosphere. Further, it has been shown that the sensitivity of ozone to increasing NO_x depends upon stratospheric chlorine loading: for the low total chlorine amounts of the early 1970s, upper stratospheric ozone depletion was predicted and observed, but a SPE that occurred in the 1990s actually showed evidence for ozone increases in some regions, due to the much higher chlorine loading present then (Jackman *et al.*, 2000). Thus solar proton events have provided a useful probe not only of the NO_x-catalyzed destruction of ozone, but also of its coupling to chlorine over past decades of change in the ozone layer.

Production of mesospheric and thermospheric NO_x by particle precipitation does provide a possible source of stratospheric NO_y, as illustrated by the data in Figure 6.3. However, its magnitude is

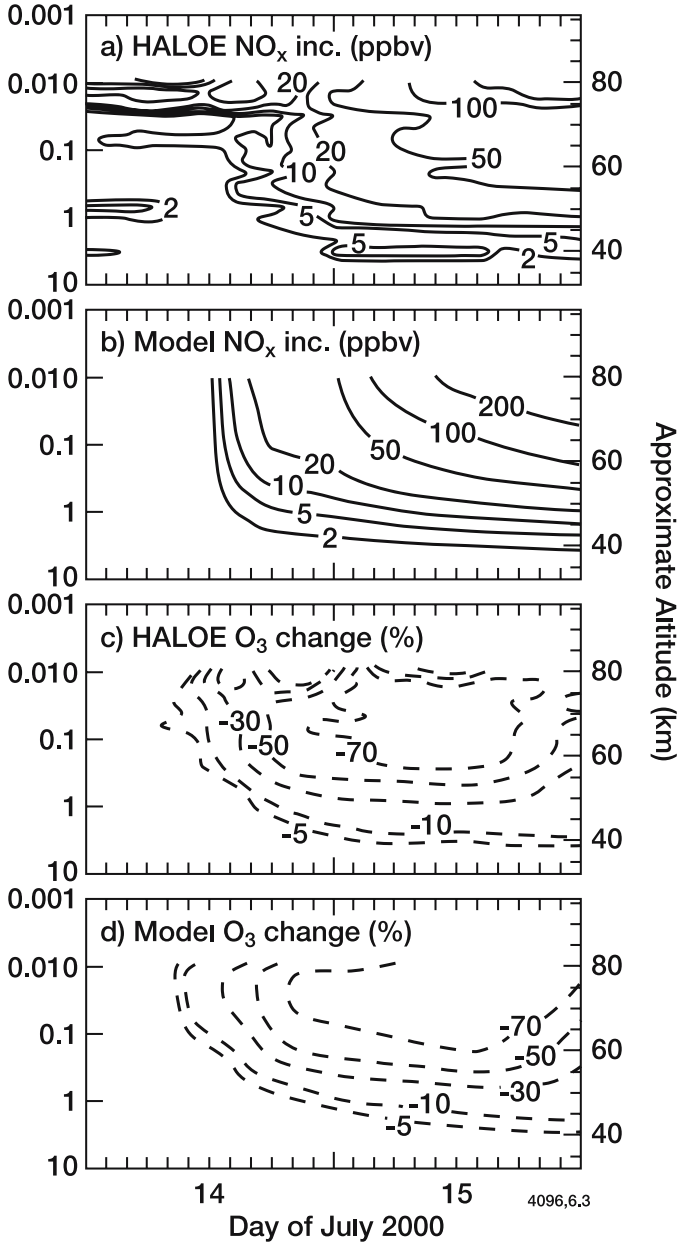

Figure 6.3. Satellite observations from the HALOE instrument of ozone and NO_x changes following the major solar proton event of July 2000, compared to model calculations. From Jackman *et al.* (2001).

critically dependent upon transport from the source region to lower altitudes. Destruction of this potential pool of NO_y is governed mainly

by the reaction of NO with atomic nitrogen (which in turn depends on photochemical processes, particularly the photolysis of NO, see Section 5.5). Mesospheric NO_y, therefore, has a longer lifetime in winter than in summer, and a particularly long lifetime in the dark polar night region. Numerous studies have examined the possible downward transport of this ionization-induced NO_x to the stratosphere, and have shown that there is some contribution but that it is largely confined to high latitudes in winter (see *e.g.*, Solomon *et al.*, 1982; Brasseur *et al.*, 1983; Russell *et al.*, 1984; Siskind *et al.*, 2000; Jackman *et al.*, 2001).

In contrast to NO_x, the depletion of ozone due to HO_x production during particle precipitation events was first observed, and only later understood in terms of theory. The first observations of mesospheric ozone changes related to HO_x production during solar proton events were reported by Weeks *et al.* (1972). Swider and Keneshea (1973) proposed that these unusual though limited rocket measurements might be explained in terms of production of odd hydrogen due to ion chemistry (see Chapter 7). Thomas (1983) presented extensive satellite measurements showing major perturbations (in excess of 60% depletion) to mesospheric ozone during solar proton events, and Solomon *et al.* (1983) demonstrated that these agreed well with theory. Recent studies of solar proton and relativistic electron precipitation (REP) events include those of Jackman and McPeters (1987) and Jackman (2001). While the impact of HO_x production on mesospheric ozone can be quite large and hence sometimes spectacular, it is very short-lived since the lifetime of HO_x is on the order of hours or less everywhere below about 80 km. As might be expected based upon the vertical profile of the HO_x cycle's role in ozone depletion, the impacts of proton events through HO_x chemistry are most pronounced above about 50 km. Nevertheless, particle precipitation events and their associated observable perturbations have provided key tests of scientific understanding of some of the HO_x and NO_x chemistry controlling ozone in the stratosphere and mesosphere.

6.2.3 The Effect of Changes in the Solar Irradiance

Changes in solar irradiance can modify the physical structure, dynamics, and chemical composition of the middle atmosphere. The question of effects of solar activity on the troposphere, particularly the surface climate, has been a subject of scientific and public fascination for many decades. However, it has been stressed that "despite a massive literature on the subject, there is at present little or no evidence of

statistically significant or practically useful correlations between sunspot cycles and the weather or climate" (Pittock, 1978). More recent assessments show that many of the concerns raised by this quotation still apply (see *e.g.*, IPCC, 1994; 2001).

The goal of this section is not to address the Sun's influence on surface climate, but rather to consider its role in variability of ozone in the mesosphere and stratosphere, again with a view towards this perturbation as a test of some components of ozone photochemistry.

The following solar activity variations are known to influence the radiant energy emitted by the Sun:

* Short-term variations (seconds to hours) related to solar flares and disruptive prominences.
* Intermediate-term variations (days to weeks) due to active regions and the solar rotation period (27 days).
* Long-term variations, particularly those over the 11-year cycle of sunspot activity and perhaps the 22-year magnetic field cycle.

Much of the Sun's energy is emitted in the visible, a wavelength range where high-quality observations over the 27-day and 11-year periodicities show very limited variability (less than a percent near 300 nm, see IPCC, 2001). However, at shorter wavelengths in the ultraviolet (see Figure 6.4), the variability is much larger (order of 15-20% over the 11-year solar cycle near 190-200 nm), so that solar activity variations can be expected to alter some of the wavelengths of light that play key roles in stratospheric and mesospheric photochemistry. Changes in the heating rates due to absorption of the same radiation by molecular oxygen and ozone should also be considered. While the major heating is provided by ozone absorption at Hartley band wavelengths (250-300 nm) where the solar variability is small, any change in ozone itself (induced, for example, by solar-driven variability at other wavelengths) will feed back to the radiative budget and temperatures through the mechanisms delineated in Section 6.2.1 above. Finally, we note an indirect effect that can be significant: changes in photolysis rates can modify the ozone column at a given altitude, thereby affecting the penetration of radiation to lower heights and producing a non-local perturbation.

The largest variability in solar output is generally observed at the shortest wavelengths. Extreme ultraviolet radiation varies by a factor of two or more over an 11-year solar cycle, and produces nitric oxide in the thermosphere. As already mentioned, NO can be transported to the mesosphere and, to some extent, in winter even to the upper stratosphere where it can perturb upper stratospheric ozone. This is an indirect mechanism linking solar activity at short wavelengths (which do not penetrate below the lower thermosphere) to chemistry at lower altitudes.

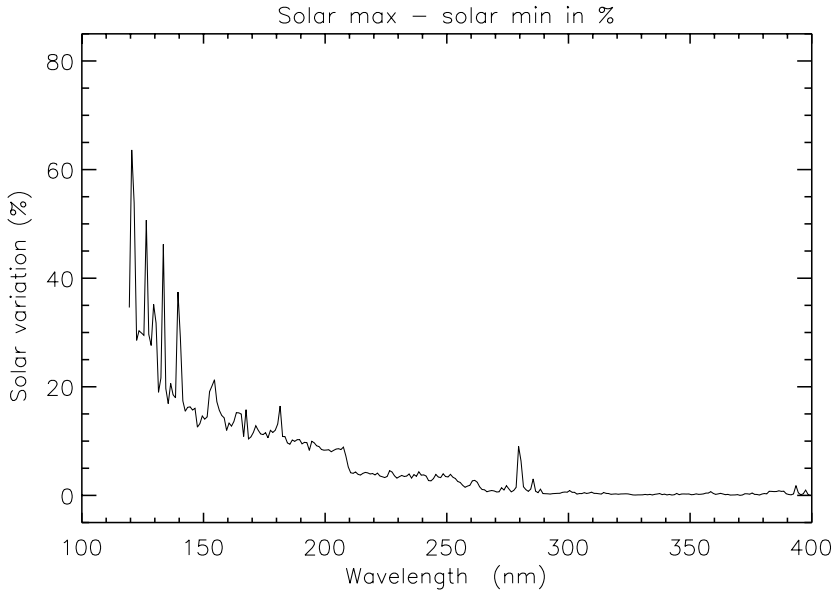

Figure 6.4. Spectral distribution of the variability in the solar flux associated with the 11-year solar cycle. Based on the observations by UARS/SOLSTICE (see also Figure 4.10). Courtesy of G. Rottman, Univ. of Colorado.

The singular role played by the solar Lyman-alpha line at 121.6 nm was discussed in Chapters 4 and 5. This solar emission feature varies by about 30% over the 27-day rotation and by about a factor of 2 over the 11-year solar cycle, and it has a particularly important role in affecting both water vapor and oxygen photolysis in the mesosphere. Thus, solar activity over a solar rotation or an 11-year cycle affects both the loss and production rates of odd oxygen, and the net effect on ozone depends on the balance between competing effects. Furthermore, fast photolysis of water vapor at Lyman-alpha can influence its vertical profile, so that transport cannot be ignored when considering mesospheric solar impacts. However, Lyman-alpha penetrates only to about 65 km. Longer wavelengths are likely to control the solar interactions at lower altitudes. For the lower mesosphere and upper stratosphere, changes in the wavelength range from about 170 to 200 nm can affect photolysis in the Schumann-Runge bands that control production of ozone through the dominant oxygen photolysis process at these altitudes. This acts to increase ozone during periods of high solar activity, although competing effects such as increased photolysis of chlorofluorocarbons in the same wavelength range can provide some compensating effects.

Changes in ozone through any of the above mechanisms can influence temperatures as already noted, and changes in temperature gradients can in turn affect zonal winds, planetary wave propagation, and perhaps even the mean meridional circulation of the stratosphere (see *e.g.*, Geller and Alpert, 1980; Haigh, 1996; Shindell *et al.*, 1999). This possible feedback provides an important mechanism whereby the relatively large changes in solar output at short wavelengths can affect dynamical processes, at least at stratospheric altitudes. Their potential for propagation downward to lower heights (through, for example, reflection of upward-propagating planetary waves) has been a focus of considerable scientific interest (*e.g.*, Haigh, 1996) and provides a possible but as yet unproven mechanism for solar coupling of surface climate through the stratosphere. Further, any change in the mean circulation can affect transport of ozone and related species such as N_2O, CH_4, H_2O, CFCs, etc. Recent studies have focussed on understanding the vertical profile of solar-related coupled changes in both ozone and temperature, and probing the time lags observed between the two (*e.g.*, Chen *et al.*, 1997). Figure 6.5 shows observed and modelled responses of ozone based upon observations of solar variability on the 27-day solar rotation timescale. The figure illustrates good agreement in the upper stratosphere, where local chemistry and chemistry/temperature coupling are both important

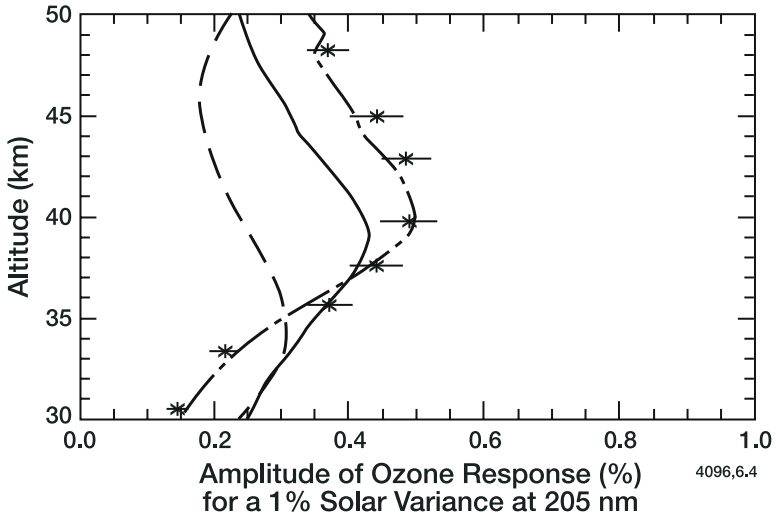

Figure 6.5. Comparison of the observed and calculated ozone sensitivities over 27-day solar rotation timescales, from Chen *et al.* (1997). The dashed line shows a one-dimensional model calculation, while the solid and dot-dashed lines display two-dimensional model estimates using two different prescriptions for the absolute irradiance changes. Observations from Nimbus-7 SBUV are also presented for comparison.

(Chen *et al.*, 1997). Perhaps most important is the ability of models to simulate the overall shapes of the vertical profiles of the responses obtained in both ozone and temperature, since these in turn support the calculation of the penetration of radiation into the atmosphere and hence provide a key test of theory.

6.2.4 Long-term Trends and Halogen Chemistry in the Upper Stratosphere

Section 5.6.3 discussed the chemistries of the halogens chlorine and bromine, and outlined their interactions with one another and with ozone. More than two decades after the pioneering prediction of possible ozone destruction through humankind's use of halogenated chemicals, upper stratospheric ozone observations began to reveal systematic depletion indicative of a changing chemical state (see SPARC, 1998, and references therein).

Chapter 5 described the important role of chemical partitioning processes in modulating ozone destruction by halogen compounds. Observations of HCl, ClO, $ClONO_2$, and other chlorine-bearing gases by infrared spectroscopy onboard the space shuttle (Michelsen *et al.*, 1996; Zander *et al.*, 1996) or from satellites (Dessler *et al.*, 1995; 1998) allow study of how chlorine is chemically partitioned in the middle and upper stratosphere in some detail, as shown in the left-hand side of Figure 6.6. In the uppermost stratosphere above about 45 km, nearly all of the chlorine released from source molecules such as CFCs is sequestered in the HCl reservoir, due largely to the efficacy of the reaction of $Cl + CH_4$ at warm temperatures and high Cl/ClO ratios there. Models (Michelsen *et al.*, 1996), stratospheric observations (Stachnik *et al.*, 1992; Chandra *et al.*, 1993) and laboratory measurements (Lipson *et al.*, 1997; see JPL, 1997; 2000) suggest that a small yield of HCl in the reaction of ClO with OH also affects the HCl/ClO partitioning in this region.

Because nearly all of the chlorine and fluorine released from chlorofluorocarbons resides as HCl and HF in the stratosphere near 50 km, observations of those two gases in this region provide an important verification of their attribution to CFC sources. Global data by Russell *et al.* (1996) display abundances and trends in both HCl and HF near 50 km that are quantitatively consistent with observations of the chlorofluorocarbons at ground level; these observations therefore confirm that CFCs are the key sources for stratospheric chlorine and fluorine. Such observations also suggest that the abundance of reactive chlorine reached its maximum in the late 1990s, while fluorine

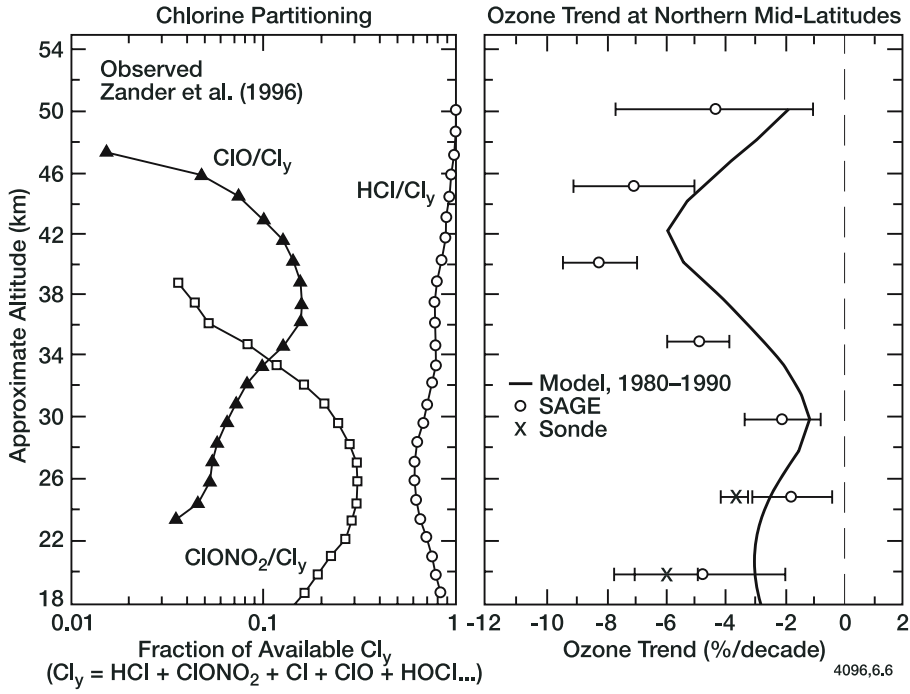

Figure 6.6. Observations of chlorine partitioning as a function of altitude from an instrument on board the space shuttle (Zander *et al.*, 1996) are shown at left. The observed vertical profile of the ozone trend at northern mid-latitudes is shown at the right (SPARC, 1998) together with a model estimate (from Solomon *et al.*, 1997).

continued to increase (Anderson *et al.*, 2000). These observations are broadly consistent with expectations based on global decreases in chlorofluorocarbon emissions, and corresponding increases in substitute compounds such as hydrofluorocarbons that bear fluorine but no chlorine. Taken together, the global measurements of HCl, HF, other chlorine compounds, and the CFC source gases both at the surface and in the tropopause region (*e.g.*, Russell *et al.*, 1993; Zander *et al.*, 1996; Montzka *et al.*, 1996; Schauffler *et al.*, 1993) provide direct evidence that the chlorine content of the stratosphere is greatly perturbed, with about 85% of the 1992 stratospheric chlorine burden attributable to human activities.

Crutzen (1974) and Crutzen *et al.* (1978) carried out some of the first detailed chemical models of chlorine-catalyzed ozone depletion, building upon the studies of Stolarski and Cicerone (1974), Molina and Rowland (1974) and Rowland and Molina (1975) and including the general chemical understanding outlined above. Crutzen (1974) predicted a relative maximum in ClO near 40 km, which was broadly confirmed a

few years later by observations of ClO by Anderson *et al.* (1977), Parrish *et al.* (1981), and Waters *et al.* (1981). The left hand side of Figure 6.6 shows that direct observations of the ClO/Cly profile in the middle and upper stratosphere agree with those early predictions and observations.

Largely because of this relative maximum in ClO, Crutzen (1974) predicted a maximum in ozone depletion in the same region (although other factors such as the availability of atomic oxygen also make some contribution to the vertical profile of ozone depletion). While there were indications of ozone depletion in the upper stratosphere beginning in the 1980s (*e.g.*, Ozone Trends Panel, 1988), it is only within the 1990s that a clear trend could be identified, distinct from natural fluctuations (*e.g.*, Miller *et al.*, 1995; SPARC, 1998). Sample observations of the northern mid-latitude ozone profile trends deduced from satellite and in-situ data as shown in the right-hand side of Figure 6.6 display a maximum near 40 km. The close agreement between the vertical shapes of the observed and predicted ozone changes in the upper stratosphere provides strong evidence for gas-phase chlorine-catalyzed ozone depletion chemistry. Further, the correspondence between the shapes of the vertical profiles of the observed ozone depletion and of the ClO/Cl_y ratio attests to the role of partitioning processes in modulating this chemistry. Indeed, this is the first of several 'fingerprints' that support the role of chlorine in ozone depletion.

Figure 6.7 presents another fingerprint illustrating the role of gas-phase chemistry and chlorine partitioning in ozone depletion, namely the latitudinal gradients observed in upper stratospheric ClO and ozone depletion. In the early 1980s, global measurements of methane by satellite illustrated that the strong upwelling of the Brewer-Dobson circulation in the tropical upper stratosphere (see Chapter 3) gives rise to a maximum in methane there (Jones and Pyle, 1984). The enhanced methane in turn was predicted to lead to a tropical minimum in ClO through its dominant role in ClO/HCl partitioning and hence in ozone depletion (Solomon and Garcia, 1984). Later global satellite observations of ClO (Waters *et al.*, 1993; Waters *et al.*, 1999), as shown in the lower panel of Figure 6.7, indeed display such a latitudinal gradient, with a pronounced minimum in the tropics. Satellite observations of the latitudinal variation of the ozone trends over the period from the early 1980s to the mid-1990s (top panel of Figure 6.7) reveal a similar spatial pattern in the upper stratosphere — again as predicted. Thus, not only the vertical profile but also the latitudinal structure of the ozone depletion in the upper stratosphere parallel the patterns observed in ClO. These spatial variations in ozone depletion point towards gas-phase chlorine chemistry and highlight the role of chemical partitioning in modulating ozone depletion.

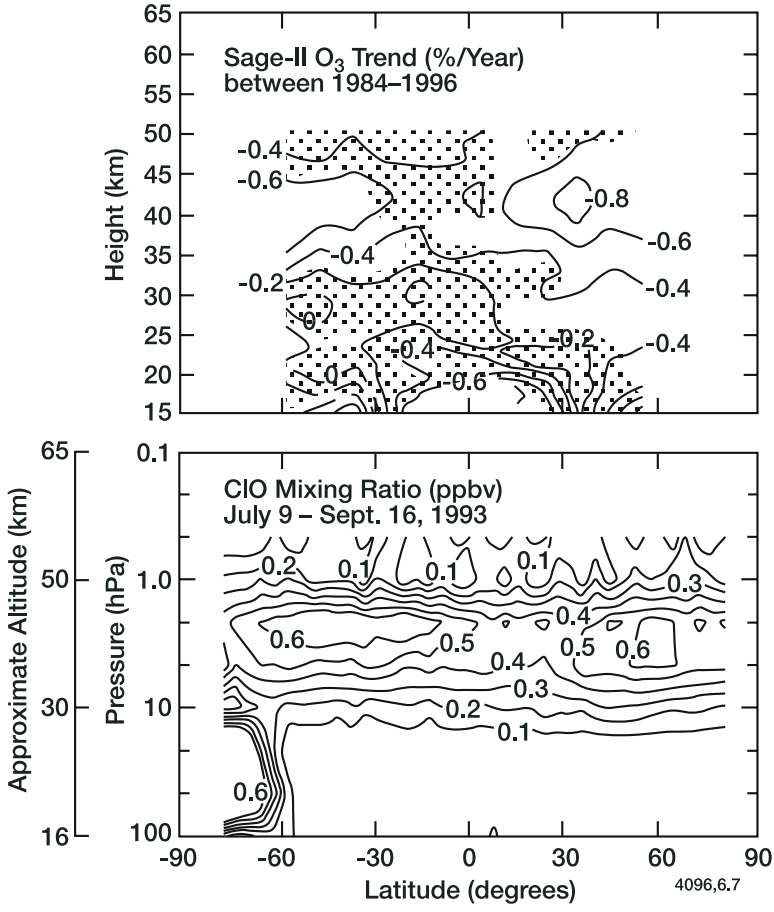

Figure 6.7. Observations of the global distribution of zonally averaged daytime ClO abundance from satellite-based microwave remote sensing (Waters *et al.*, 1999) together with the zonally averaged ozone trend deduced from satellite-based visible spectroscopy (SPARC, 1998; see McCormick *et al.*, 1992). Trends are statistically significant outside the shaded region.

Other processes that could contribute to upper stratospheric ozone changes include trends in methane, nitrous oxide, and water vapor. These source gases can, for example, lead to changes in HO_x and NO_x, which can in turn affect ozone loss rates and the competition between different catalytic cycles. However, the effect of these changes is considerably smaller than the dramatic impact of the five-fold enhancement in chlorine caused by human activities. By the turn of the 21st century, observations and modelling studies showed that chlorine chemistry dominated the trends found in upper stratospheric ozone (see Müller *et al.*, in WMO/UNEP, 1999).

The upper stratosphere was not only depleted in ozone, but was also colder by the 1990s than it had been 20 years earlier (Ramaswamy *et al.*, 1996). The cooling of the upper stratosphere is due in part to the chlorine-driven ozone changes and is hence subject to ozone/temperature feedback as discussed in Section 6.2.1. But much of the upper stratospheric cooling is driven not by ozone itself but by increases in greenhouse gases (mainly carbon dioxide and water vapor). While greenhouse gases warm the planet surface, they cool the stratosphere. Thus, changes in the upper stratospheric thermal structure driven by trends in these gases were believed to be responsible for an average cooling of about 1.5°K near 40 km in 1997 as compared to 1979, and an associated damping of the ozone trend that would otherwise have occurred (see *e.g.*, Forster and Shine, 1999).

6.3 Lower Stratospheric Ozone Depletion: Observations and Explanations

The chemical lifetime of ozone in the sunlit atmosphere increases from the order of days near 35 km to about a year near 20 km. This dramatic change largely reflects slower ozone photolysis rates and increasing air densities that shift the balance between O and O_3 strongly in favor of ozone, thereby reducing the effectiveness of many of the odd oxygen catalytic destruction cycles whose rate-limiting steps involve reactions with O (*e.g.*, the reactions of O with NO_2, ClO, and HO_2). While some chemical cycles involve only ozone, these tend to be slower than those linked to the highly reactive oxygen atom. As chemical processes slow down, dynamical mechanisms play larger relative roles in the odd oxygen budget. Particularly in winter when the mean meridional circulation is relatively fast, chemistry and dynamics both influence ozone abundances (see *e.g.*, Perliski *et al.*, 1989). In summer, reduced wave activity results in a slower circulation, and a detailed analysis of chemical rates is required to determine the balance of competing processes. The hallmark of studies of lower stratospheric ozone changes has been ongoing examination of chemical processes occurring on relatively slow time scales, and the need to understand changes in dynamical processes — both those driven by the ozone changes themselves (*e.g.*, feedbacks from ozone depletion to dynamics) and those perhaps driven by other mechanisms (such as changing greenhouse gas concentrations that can change dynamics or changes in tropospheric meteorology).

Throughout the 1970s and until about the mid-1980s, modelling studies predicted that modest changes in column ozone might someday

occur due to human activities (see Figure 6.8). By the early 1980s, gas-phase photochemical theories predicted that human uses of chlorofluorocarbons would likely produce less than a 5% integrated change in column ozone at steady state as shown in the figure. That steady state would not be achieved until about the middle of the 21st century. The bulk of those changes were predicted to occur in the upper stratosphere, following the arguments regarding chemical partitioning discussed above.

Prior to the discovery of heterogeneous chemistry, models suggested a strong anti-correlation between estimates of the calculated future mid-latitude ozone changes to be expected at steady state due to CFC emissions and that predicted for NO_x emissions from supersonic aircraft, as illustrated in Figure 6.8. For a period of more than a decade (roughly 1974 to the mid-1980s), when the estimated future NO_x impact on ozone increased, the calculated CFC-related ozone depletion decreased. Of particular importance is the reaction:

$$HO_2 + NO \rightarrow NO_2 + OH$$

which has the effect of increasing the net production of odd oxygen

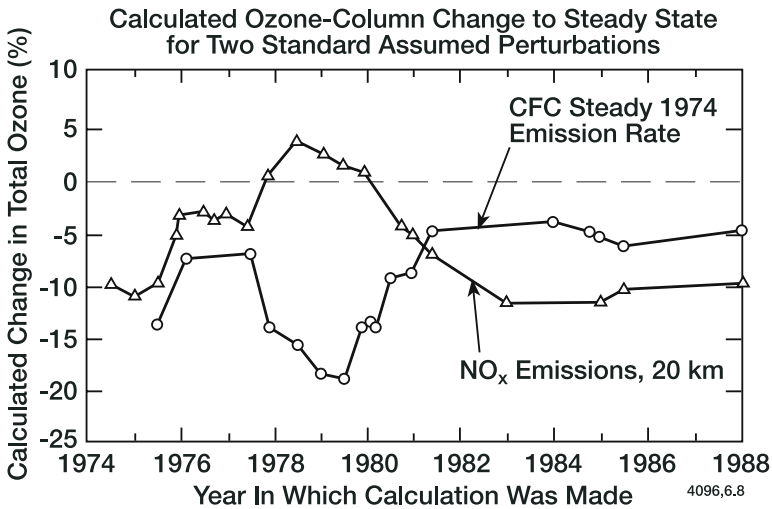

Figure 6.8. Calculated one-dimensional model ozone column change resulting from specific fixed perturbations (increased NO_x emissions at 20 km, simulating possible high altitude aircraft releases, and the steady-state response to 1974 emissions of chlorofluorocarbons), as function of the year in which the calculation was performed. Changes over time reflect changes in the understanding of stratospheric chemistry, not real atmospheric changes. Figure courtesy of D.J. Wuebbles (personal communication).

through methane oxidation chemistry in the lowermost stratosphere. Changes in the early estimates of the rate of this single reaction from laboratory studies (see *e.g.*, Crutzen and Howard, 1978) had large impacts on the estimation of ozone depletion due to emisions of NO_x from supersonic aircraft — note in particular the transition from predictions of ozone depletions due to NO_x input at 20 km to projected increases which occurred around 1979. Other improvements in laboratory kinetics relating to HO_x chemistry (*e.g.*, the rate of OH + $NO_2 \rightarrow HNO_3$) also had significant effects on calculations of the estimated effect of NO_x on stratospheric ozone, for similar reasons. Further, the coupling of the ClO_x and NO_x cycles through, for example, the reactions ClO + $NO_2 \rightarrow ClONO_2$ and ClO + NO $\rightarrow$ Cl + NO_2 are key elements in the competition between NO_x and ClO_x. This balance between chlorine and nitrogen chemistry changed dramatically, however, with the discovery of surface chemistry's large impact on chlorine, nitrogen, and hydrogen radicals in the lower stratosphere (see *e.g.*, Rodriguez *et al.*, 1991). Indeed, Figure 6.8 ends with the last systematic calculation of mid-latitude ozone trends employing gas phase chemistry alone, in 1988. When the first statistically significant ozone changes were observed, they were far larger than model estimates, were found in the lower rather than upper stratosphere, and were located in a region where no one had predicted a special sensitivity: Antarctica.

6.3.1 Antarctic Ozone

Measurable total column ozone depletion was first documented in the Antarctic spring at the British Antarctic Survey station at Halley (Farman *et al.*, 1985). Figure 6.9 presents an updated set of these pioneering measurements, showing a remarkable decline in October average ozone that began near the late 1970s. These findings were quickly confirmed by space-based measurements (Stolarski *et al.*, 1986) and by observations at other Antarctic sites (*e.g.*, Komhyr *et al.*, 1986). Observations of total column ozone using infrared and visible spectroscopy (Farmer *et al.*, 1987; Mount *et al.*, 1987) provided further support for the seasonal depletion of springtime ozone using independent methods. As the satellite measurements confirmed that the depletion extended over roughly the entire continent, the phenomenon became known as the Antarctic ozone 'hole'. Farman *et al.* showed that the ozone hole is confined to particular seasons (*i.e.*, spring) and to south polar latitudes.

6.3.1.1 What is the Ozone Hole?

While not a true 'hole' in the sense that some column ozone remains even in the most extreme depletions observed in the mid 1990s (when October ozone minima were near 100 Dobson Units over the South Pole, or depletion of about two-thirds of the historical levels, see Hofmann *et al.*, 1997), the descriptor captures the fact that the peak depletion is sharply limited to Antarctic latitudes. Dobson (1968 and references therein) noted that there is less ozone naturally present over Antarctica than over the Arctic in winter and much of the spring, but this climatological difference between the natural ozone levels over the poles of the two hemispheres should not be confused with the abrupt decline that began near the mid-1970s as depicted in Figure 6.9. Newman (1994) discusses these and other historical measurements of total ozone and shows that the Antarctic ozone hole began only in the last few decades.

Measurements of the vertical profile of the depletion within the ozone hole were first presented by Chubachi (1984), and were rapidly followed by other data such as that of Hofmann *et al.* (1987), Gardiner (1988), Iwasaka and Kondoh (1987), and satellite studies such as Bevilacqua *et al.* (1997). Hofmann *et al.* (1997) presented a detailed analysis of many years of ozonesonde measurements at the South Pole. Figure 6.10 summarizes a key result of that study, showing that the depletion of the Antarctic ozone column is largely confined to altitudes from about 12-25 km, far below the altitudes where gas-phase chlorine chemistry would predict significant changes. Figure 6.10 also illustrates the shape of the unperturbed ozone 'layer' observed in historical ozone data, and the near-total removal of ozone in the heart of the layer in a typical contemporary sonding for early October. Finally, the figure shows the close correspondence between the region where most of the ozone is depleted and a vertical profile of a typical polar stratospheric cloud (PSC) observed at the South Pole (Collins *et al.*, 1993).

The latitudinal gradients in Antarctic ozone depletion are related to the dynamical structure of the polar winter stratosphere, whose circulation can be viewed as a vortex (see *e.g.*, Schoeberl *et al.*, 1992; Holton *et al.*, 1995). Briefly, the absence of solar illumination in high latitude winter leads to cooling over the poles and hence a large temperature gradient near the polar terminator. This thermal gradient implies rapid zonal (west-east) flow characterizing the 'jet' at the edge of the vortex, while the air within the vortex is relatively isolated compared to surrounding mid-latitude regions, allowing deep depletion to develop. Differences in the pre-1970s ozone abundances in the two polar vortices first noted by Dobson (1968) are related to differences in

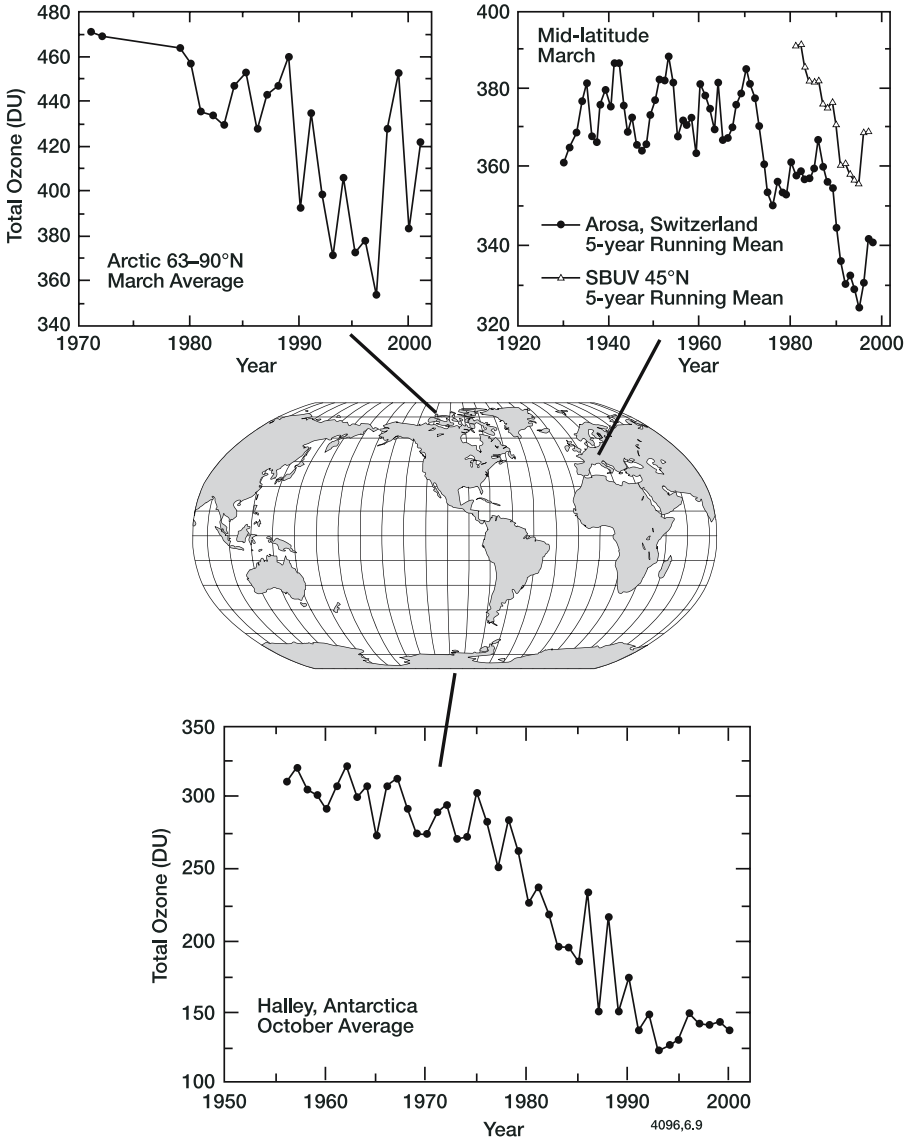

Figure 6.9. Observations of total ozone at various locations. The Antarctic data are from Halley (Farman *et al.*, 1985; Jones and Shanklin, 1995) and updated courtesy of J. Shanklin. The Arctic data are from satellite observations described in Newman *et al.* (1997), updated courtesy of P. Newman. The Arosa, Switzerland, dataset is the longest running in the world (Staehelin *et al.*, 1998a,b). Satellite observations from a slightly higher mid-latitude region are shown for comparison (Hollandsworth *et al.*, 1995), updated courtesy of R. Nagatani. The satellite data are zonally and monthly averaged, while the ground-based data at each site have also been averaged over time as indicated in each case. Adapted from Solomon (1999).

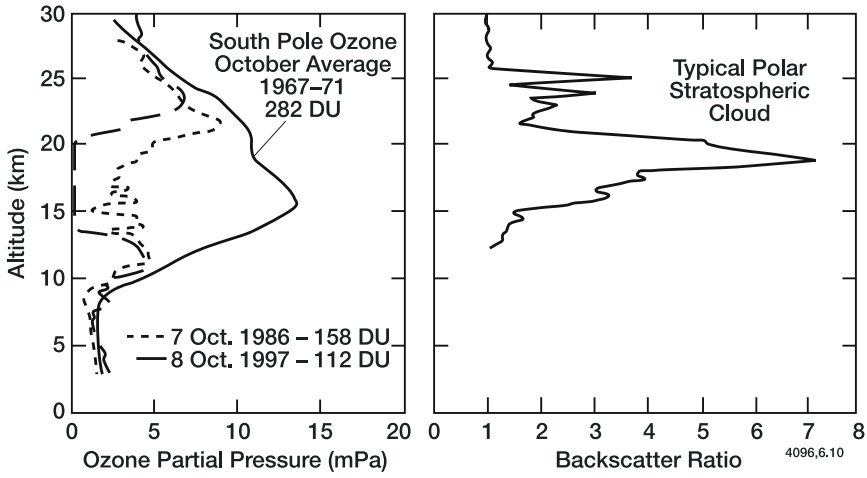

Figure 6.10. Observations of the vertical profile of ozone observed at the South Pole in the Octobers of the late 1960s and early 1970s, contrasted with those of 1986 and 1997. Total ozone (DU) is indicated for each profile, from Hofmann *et al.* (1997). The right hand panel shows a typical polar stratospheric cloud observed at the South Pole from the observations of Collins *et al.* (1993). From Solomon (1999).

atmospheric waves and circulation patterns, which are in turn driven by factors relating to surface topography (*e.g.*, distribution of mountains, oceans, and continents). The north polar vortex is generally more disturbed by atmospheric waves forced from beneath by flow over a more variable surface topography. These lead to greater mixing and faster downward motion which both increases the natural wintertime Arctic ozone abundances (by bringing down ozone-rich air from above) and warms the lower stratosphere (through adiabatic compression). Temperatures in the Antarctic vortex are both colder and less variable than those of the Arctic, which strongly influences the polar ozone depletion in the two hemispheres (see Figure 6.17 below).

Figure 6.11 shows measurements of the seasonal cycle of ozone at Halley in historical and recent data, which show that the depletion occurs only over a limited portion of the year. These observations demonstrate that contemporary observations of ozone at Halley in late August (end of austral winter) are near historical levels, while the bulk of the ozone loss there occurs rapidly during the month of September. In recent years, measurable ozone depletion is also observed in Antarctic summer — in part the result of dilution of the extreme losses in spring.

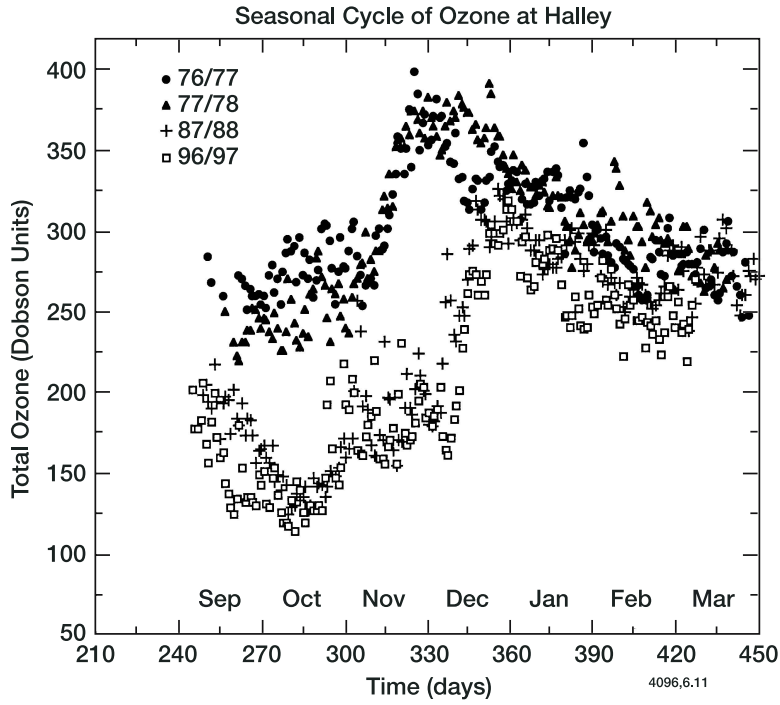

Figure 6.11. Observations of the full seasonal cycle of daily ozone at Halley, Antarctica, in the years before the ozone hole (1976/7 and 1977/8), and in 1987/88 and 1996/7 (courtesy of J. Shanklin). Note the rapid September drop in total ozone in the years displaying the ozone hole. From Solomon (1999).

6.3.1.2 Early Explanations

By the late 1980s, the chemical foundation of the ozone hole in heterogeneous chlorine chemistry was firmly established (WMO, 1989, and references therein). However, the suite of proposals initially advanced to explain its origins prior to that time is of interest both historically and as an illustration of how differing proposals constructively add to and refine scientific debate. Here we briefly summarize the primary explanations advanced to explain the ozone hole following its surprising discovery.

Dynamics. Tung *et al.* (1986) pointed out that the extreme isolation of the Antarctic winter circumpolar vortex leads to very low temperatures approaching radiative equilibrium, in contrast to the Arctic winter vortex, which is much warmer. When radiative equilibrium is achieved, the rate of radiative cooling becomes zero, so the net heating equals the radiative heating alone. Tung *et al.* suggested that the return of sunlight to the Antarctic spring (and the associated radiative heating)

could therefore lead to net upward motion, assuming

$$\overline{Q} = \overline{H} - \overline{C}$$

and

$$\overline{Q} = \frac{d\overline{T}}{dt} + \overline{\Gamma}\ \overline{w}^*$$

where $\overline{Q}$ is the net radiative heating, $\overline{H}$ is the radiative heating rate, $\overline{\Gamma}$ is the static stability and $\overline{w}^*$ is the mean vertical velocity. $\overline{C}$ is the radiative cooling rate, which becomes small as the stratosphere cools in winter. When sunlight returns in spring, $\overline{C}$ is small, but $\overline{H}$ may be large, implying that $\overline{Q}$ could be positive. If the net radiative heating is positive, net upward motion may occur in the mean meridional circulation system. Since the ozone mixing ratio decreases with decreasing altitude below the ozone maximum, upward motion would transport air which is relatively ozone-poor into the lower stratosphere, thereby depleting the ozone column. This type of transport can explain qualitatively the observed decline in spring total ozone, but has a number of quantitative shortcomings. The decadal trend in total ozone can be explained in the context of this theory only if a long-term change in the stratospheric circulation system has occurred. Tung *et al.* (1986) suggested that a long-term trend in Antarctic spring total ozone might be due to changes in the strength of this upward mean circulation over time, possibly because of increased aerosol heating associated with the volcanic aerosol emitted by El Chichón; see also an elegant later paper by Tung (1986). However, observations of conservative tracers that illustrate the direction of dynamical flow, such as aerosols (Hofmann *et al.*, 1987), nitrous oxide (Parrish *et al.*, 1988; Loewenstein *et al.*, 1989) and other long-lived gases (Jaramillo *et al.*, 1989; Toon *et al.*, 1989) quickly demonstrated that the ozone hole could not be caused by such upward motion. Indeed, much as Brewer (1949) deduced the nature of global transport from observations of water vapor as a tracer of atmospheric dynamics, so have observations of a wide variety of chemical tracers shown that transport is directed downwards within the Antarctic stratosphere in spring rather than upwards, although there is still some debate about the strength of this fluid flow and the degree of exchange of air between lower latitudes and polar regions (*e.g.*, Hartmann *et al.*, 1989; Tuck, 1989; Tuck *et al.*, 1997; Schoeberl *et al.*, 1990; 1992; 1995; Manney *et al.*, 1995a,b).

Mahlman and Fels (1986) also considered changes in atmospheric dynamics that might explain the ozone trend through dynamical phenomena. They suggested a reduction in wintertime planetary-scale wave activity in the southern hemisphere troposphere, which would lead to reduced downward transport of ozone into the Antarctic during the winter and spring. However, an explanation relying upon an extended

winter season reduction in ozone transport would imply reduced ozone not only in October, but also earlier in the southern winter (*e.g.*, in August and September). Observations (*i.e.*, earlier versions of the type of data shown in Figure 6.11) demonstrated that the ozone depletion is not a slow process occurring all winter long, but rather a rapid removal that begins around late August as shown above.

Other authors noted that Antarctic stratospheric temperatures differed by 18 K in October at about the 30-mbar level during the years 1979 versus 1985, and pointed out that the colder temperatures appeared well correlated with the total ozone changes observed by TOMS — perhaps indicating a dynamical cause (Newman and Schoeberl, 1986). However, it is important to note that ozone provides the primary source of heat to the stratosphere through its absorption of UV radiation. Shine (1986) suggested that the ozone hole should be expected to lead to a stratospheric cooling (implying that a cooling trend in October could be an effect of the ozone depletion rather than its cause). Observations have since demonstrated that the Antarctic temperature trends indeed occur later in the spring season than the onset of ozone depletion, and thus cannot be the fundamental cause of the ozone hole but rather illustrate one of its effects (*e.g.*, Newman and Randel, 1988). Indeed, the removal of this source of heat has become large enough to influence the warming of the Antarctic stratosphere at the end of the winter-spring season. Jones and Shanklin (1995) demonstrated progressively later warmings over Halley and the ozone observations in Figure 6.11 also illustrate this effect through the delayed austral spring ozone increases (now generally seen in December rather than November).

Solar Activity. Enhanced nitrogen oxides from high solar activity that occurred in the early 1980s were also proposed as a possible cause of the ozone hole (Callis and Natarajan, 1986), drawing upon the well-known catalytic chemistry of NO_x and its enhancement by processes such as solar proton events as discussed in Sections 5.5.2 and 6.2.2. However, the solar theory proved to be in conflict with observations of nitrogen compounds. Measurements of the nitrogen dioxide column by Noxon (1978) and McKenzie and Johnston (1984) displayed reduced rather than enhanced nitrogen oxides over the south polar regions. After the discovery of the ozone hole, similar measurements confirmed those early data using both infrared and visible spectroscopy methods (Coffey *et al.*, 1989; Farmer *et al.*, 1987; Mount *et al.*, 1987). Airborne measurements of the latitudinal gradient of nitric oxide at 20 km (in the heart of the south polar ozone destruction region by Fahey *et al.*, 1989a) using a chemiluminescence method are compared to the data of Noxon (1978) in Figure 6.12. The two datasets both show that the southern high latitude winter/spring stratosphere contains a minimum in nitrogen oxides rather

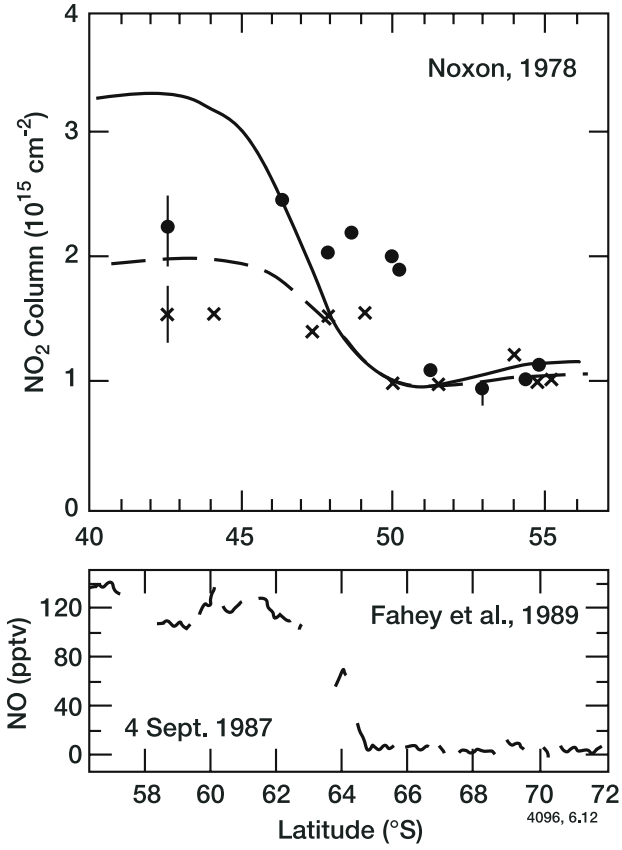

Figure 6.12. Observations of the 'cliff' in NO_2 reported by Noxon (1978). The solid and dashed lines represent Northern Hemisphere measurements while the filled circles and crosses show Southern Hemisphere evening and morning twilight data, respectively. The NO measurements of Fahey *et al.* (1989a) are shown for comparison. The two molecules interchange rapidly with one another in the sunlit atmosphere and hence provide a measure of NO_x. Both datasets show very low NO_x in the high latitude stratosphere. From Solomon (1999).

than a maximum as would be required for the solar theory of Antarctic ozone depletion to operate in the key region displaying the maximum ozone loss. The differences in the location of the steep gradient between the two datasets likely reflect differences in season and local motion of the polar vortex. The observed shape of the profile of ozone depletion is also in conflict with the solar theory, since downward transport of ozone-depleting nitrogen radicals from above would yield greater ozone losses at higher altitudes. This mechanism is therefore inconsistent with the observed ozone removal in a confined range of altitude from about 12-24 km as shown in Figure 6.10.

It is interesting to note that the observations of Noxon (1978; 1979) revealed strong evidence for a 'cliff' in NO_2 in polar regions several years before the Antarctic ozone hole was discovered. The chemistry of this anomaly was not understood and it was called out as one of the key challenges to scientific understanding of stratospheric chemistry of the time (see *e.g.*, WMO, 1985). We now know that the chemistry that produced Noxon's 'cliff' is indeed tied to that of the ozone hole; the relationship between NO_2 and ClO will be discussed further below. Arguably, the ozone hole might have been predicted before it was observed had the Noxon 'cliff' been better understood in the early 1980s. For example, a model calculation with an imposed deficit in polar nitrogen based on the data would have displayed enhanced polar ozone depletion.

Halogen Chemistry on PSCs. The cold temperatures that occur in polar winter can lead to formation of clouds within the stratosphere, and there are visual sightings of such Arctic clouds dating back hundreds of years. In the unpopulated Antarctic, the earliest explorers noted unusually colorful high clouds in winter. The term polar stratospheric clouds (or PSCs) was coined by McCormick *et al.* (1982), who first presented satellite observations of high-altitude clouds in the Antarctic and Arctic stratospheres, but the clouds were considered little more than a scientific curiosity until the ozone hole was discovered.

Solomon *et al.* (1986) suggested that HCl and $ClONO_2$ might react on the surfaces of polar stratospheric clouds, perturbing gas-phase chlorine partitioning in a manner that could greatly accelerate ozone loss in the Antarctic lower stratosphere ($HCl + ClONO_2 \rightarrow HNO_3 + Cl_2$). The Cl_2 formed would photolyze quickly in sunlit air and rapidly form ClO. Solomon *et al.* stressed that this and related heterogeneous reactions would suppress the concentration of NO_2 by forming HNO_3, so that the ClO thereby released could not readily reform the $ClONO_2$ reservoir. They also showed that such changes in NO_x partitioning had the potential to better explain the observed gradients in HNO_3 and NO_2 in polar regions — *i.e.*, providing insight into the then-eight-year-old mystery of the Noxon cliff. Thus it was recognized that rapid ozone loss via chlorine chemistry would require (*i*) the heterogeneous 'activation' of chlorine from both the HCl and $ClONO_2$ reservoirs and (*ii*) the suppression of NO_2 — an essential element in keeping the chlorine active. The production of Cl_2 in this process implies that sunlight would be required to release Cl, so that the ozone depletion would occur when air was not only cold but also sunlit (*i.e.*, largely in spring as observed, rather than in winter when the polar cap is continuously dark or in summer when it is warm). Some ozone loss can take place even in polar winter, however, due to atmospheric waves that move polar air out to

the sunlit atmosphere for brief periods (Tuck, 1989; Sanders *et al.*, 1993; Roscoe *et al.*, 1997).

Observations of PSCs, low NO_2 amounts in polar regions (Figure 6.12), enhanced polar HNO_3 (Murcray *et al.*, 1975; Williams *et al.*, 1982) and the vertical profile of the ozone depletion based upon the Japanese measurements (Chubachi, 1984) were cited in support of heterogeneous chemistry as the primary process initiating Antarctic ozone depletion. Such a mechanism would be most effective in the Antarctic due to colder temperatures and greater PSC frequencies there than in the corresponding seasons in the Arctic (McCormick *et al.*, 1982), a point discussed further below.

As in the discussion of gas-phase chemistry, a complete understanding of ozone depletion requires consideration not only of how much ClO is present (*i.e.*, ClO/Cl_y), but also of the catalytic cycles in which ClO may engage. Solomon *et al.* (1986) emphasized the catalytic ozone destruction initiated by the reaction between HO_2 and ClO. However, this process cannot destroy enough ozone early enough in the spring season to be consistent with the seasonality of the ozone loss process as shown above in Figure 6.11.

Molina and Molina (1987) showed that very rapid ozone depletion can occur through a previously-unrecognized catalytic cycle involving formation and photolysis of a ClO dimer, Cl_2O_2. Following a period of some uncertainty regarding the kinetics and photochemistry of the dimer, laboratory studies confirmed its importance (*e.g.*, Sander *et al.*, 1989; see Rodriguez *et al.*, 1990 for model calculations and JPL, 2000, for a summary of laboratory data). This cycle is now well-recognized as the primary catalytic process responsible for about 75% of the ozone removal in the ozone hole. Note that the reaction of ClO with itself and a third body to form Cl_2O_2 is the rate limiting step in this critical catalytic cycle, implying that measurements of ClO provide a direct measure of the rate of this odd-oxygen loss process.

McElroy *et al.* (1986) and Tung *et al.* (1986) emphasized the role of bromine chemistry in ozone hole formation (in particular, its coupling to chlorine through the reaction between ClO and BrO); this cycle is now known to contribute about 20% to the annual formation of the Antarctic ozone hole (*e.g.*, Anderson *et al.*, 1989). Both McElroy *et al.* (1986) and Tung *et al.* (1986) also emphasized the need for reduced NO_2 in order for ClO to remain active (noting the links to the Noxon 'cliff'), and McElroy *et al.* (1986) also emphasized the Japanese ozonesonde observations, particularly the observation of ozone loss at low altitudes, where bromine can be very effective for ozone destruction.

6.3.1.3 Observations of Chemical Species Involved in Antarctic Ozone Destruction

Foremost among the data that established the cause of the ozone hole are observations of active chlorine species, particularly the ClO that determines ozone loss through Cl_2O_2 formation. De Zafra *et al.* (1987; 1989) presented ground-based microwave emission measurements at McMurdo Station, Antarctica, showing evidence for greatly enhanced ClO in the lower stratosphere. Near 20 km, the observations suggested mixing ratios of about 1 ppbv in September, about 100 times greater than the 10 pptv predicted by gas-phase photochemical theory. Anderson *et al.* (1989) presented in-situ airborne measurements of ClO using a resonance fluorescence method. The latitudinal coverage of the airborne data taken flying south from Chile near 20 km showed a very steep gradient in ClO as the airplane crossed into cold regions within the Antarctic vortex, increasing to about 1 ppbv in mid-September as shown in Figure 6.13. Hence, within a few years after the discovery of the

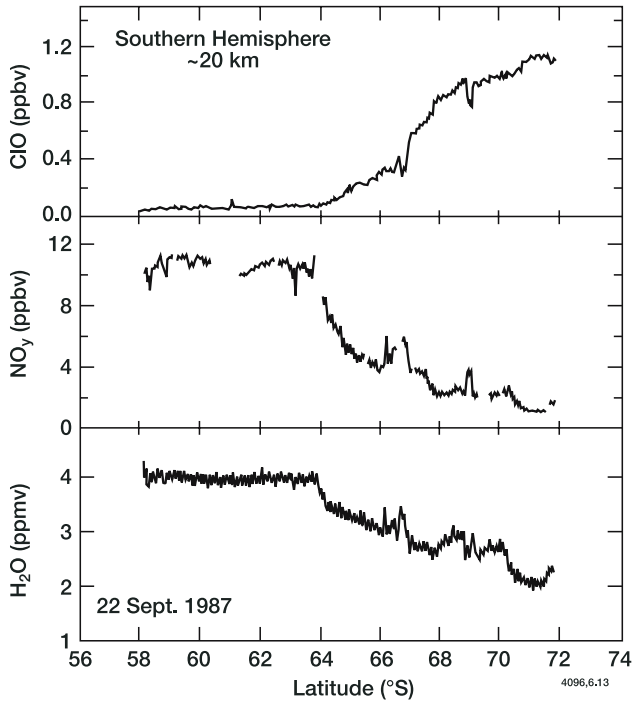

Figure 6.13. Observations of the latitude gradients in ClO, NO_y, and H_2O on a flight of the ER-2 aircraft in September 1987, showing evidence for extremely high ClO in the Antarctic together with substantial denitrification and dehydration (removal of NO_y and H_2O) associated with PSCs. From Solomon (1999).

ozone hole, two independent methods confirmed remarkably elevated ClO abundances in the ozone hole region, which are only possible if chlorine is released from both of the reservoir gases, HCl and $ClONO_2$.

Figure 6.14 shows both ground-based and airborne measurements of ClO in September over Antarctica from 1987, and compares them to gas-phase and heterogeneous photochemical theory. More recently, satellite observations as depicted in Plate 6 have allowed study of the full global distribution of ClO (Waters *et al.*, 1993; 1999) using microwave emission methods which further tie the ozone destruction region with the spatial distribution of enhancements in ClO (Manney *et al.*, 1995b; MacKenzie *et al.*, 1996). The data show that the region of reduced ozone extends over an area larger than the continent beneath, and illustrates the close spatial correspondence between the regions of depleted ozone and those of enhanced ClO (as first emphasized in Anderson *et al.*, 1989). Plate 6 provides a dramatic illustration of the spatial structure of enhanced ClO and depleted ozone over Antarctica.

Observation of chlorine dioxide (OClO) via visible spectroscopy is another independent method of probing the chlorine chemistry that also

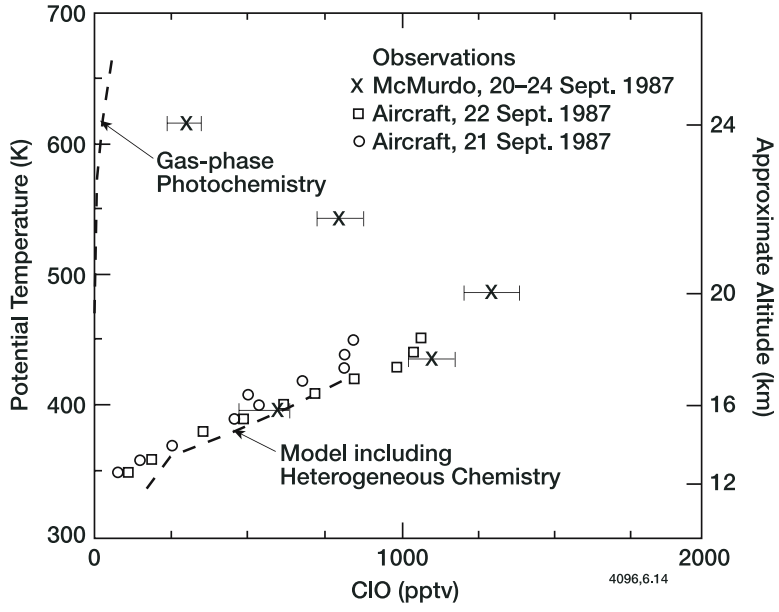

Figure 6.14. Observations of the vertical profiles of ClO in the Antarctic stratosphere in September 1987 from both ground-based microwave remote sensing (de Zafra *et al.*, 1989) and aircraft resonance fluorescence techniques (Anderson *et al.*, 1989). These data are compared to a gas-phase photochemistry model and to the heterogeneous chemistry model of Jones *et al.* (1989), which accounts for air parcel trajectories. From Solomon (1999).

revealed hundred-fold enhancements of active chlorine in the Antarctic vortex (Solomon *et al.*, 1987; Wahner *et al.*, 1989; Kreher *et al.*, 1996). This technique also allowed study of the seasonal changes in Antarctic chlorine activation and its links to PSC chemistry. These showed a seasonal decline of OClO between late August and early October, associated with increasing temperatures in the spring and hence the cessation of PSC chemistry (Solomon *et al.*, 1987).

Observations of the HCl column and, in particular, its ratio to the HF column, strongly suggested that HCl had indeed been converted to active chlorine in the Antarctic spring (Farmer *et al.*, 1987; Toon *et al.*, 1989; Coffey *et al.*, 1989). The recent global satellite data by Russell *et al.* (1993) further demonstrate this behavior on larger spatial scales. The first in-situ measurements of HCl showing evidence for conversion to active chlorine were obtained in Arctic studies by Webster *et al.* (1993); see Section 6.3.2.1. Concurrent global HCl and $ClONO_2$ data from the UARS satellite illustrated the simultaneous chemical conversion of both species where polar stratospheric cloud surfaces were also present (Geller *et al.*, 1995; Yudin *et al.*, 1997). A detailed view of the temperature dependence of chlorine activation is provided from Antarctic in-situ observations of both ClO and HCl, which dramatically illustrate rapid activation at temperatures below about 195 K (Kawa *et al.*, 1997; see earlier studies by Toohey *et al.*, 1993 and Schoeberl *et al.*, 1993a,b), and provide a key demonstration of rapid heterogeneous chemistry under cold conditions.

The combination of simultaneous observations of ClO, HCl, OClO, NO, NO_2, and other gases by a variety of independent chemical methods demonstrates that the springtime Antarctic stratosphere is indeed heavily perturbed compared to expectations from gas-phase chemistry, and in a manner consistent with heterogeneous reactions on PSC particles. Through the resulting enhancements in the ClO/Cl_y ratio, chlorine's effectiveness for ozone destruction is greatly enhanced. For ClO abundances near 1-1.3 ppbv as observed since 1986/7 (and BrO abundances near 7-10 pptv, see Brune *et al.*, 1989), Antarctic ozone is destroyed near 20 km in September at a rate of about 0.06-0.1 ppmv/day, so that within about 40-60 days virtually all of the ozone at this level can be depleted unless rapid dynamical resupply occurs, broadly consistent with Figure 6.10 (see Anderson *et al.*, 1989; Murphy, 1991; MacKenzie *et al.*, 1996). The cold temperatures observed in the Antarctic during September in most years suggest that net downward motion (which would tend to warm the air through adiabatic compression) and horizontal mixing is relatively limited at this time of year. This general picture of relative dynamical isolation in the heart of the ozone depletion region is supported by a number of dynamical

studies (*e.g.*, Hartmann *et al.*, 1989; Manney *et al.*, 1994b; 1995a,b; Schoeberl *et al.*, 1995; 1996).

The observations offer several different spatial and temporal fingerprints that strongly support the identification of chlorine chemistry and its perturbations by heterogeneous processes as the principal cause of the ozone hole. The measurements shown in Figure 6.14 reveal that the enhanced ClO occurs over about the 12-24 km range, the region where PSCs are observed and where the ozone is depleted as shown in Figure 6.10. The airborne data of Anderson and colleagues, as depicted for example in Figure 6.13, demonstrate the steep latitudinal gradient in ClO, consistent with the connection of the ozone hole to cold Antarctic latitudes. A fully three-dimensional view of the same behavior is based upon satellite data (Waters *et al.*, 1993; 1999) is illustrated in Plate 15. Seasonal observations of OClO, ClO, HCl, NO_2, and other gases have been used to show that the large temporal changes in the abundances of these chemical species are consistent with the time evolution of the ozone hole and with heterogeneous chemistry. In short, the vertical, latitudinal, and seasonal behavior observed in active chlorine and a host of related species all provide independent evidence confirming the basic processes that control the occurrence of the ozone hole.

6.3.1.4 The Composition and Chemistry of Polar Stratospheric Clouds

Partly because of limited analysis of Antarctic stratospheric temperatures, early studies that followed the discovery of the ozone hole were not specific about the type of particles of which the observed PSCs were composed. It was generally assumed that the particles were mainly water ice (Steele *et al.*, 1983). Stratospheric ice clouds are frequently optically thick and brilliant in color. Such clouds form when temperatures drop below the temperature at which ice forms (frost point), and are now referred to as Type 2 PSCs. However, sensitive satellite measurements (McCormick *et al.*, 1982) suggested that optically thinner PSCs were also present at warmer temperatures.

As noted in Chapter 5, Toon *et al.* (1986) and Crutzen and Arnold (1986) pointed out that the PSC particles might be composed not only of water ice but also of solid nitric acid trihydrate (NAT). Both studies noted that such composition could affect the impact on ozone in two ways: (*i*) by reducing the amount of nitrogen oxide that could be present (*i.e.*, not only by forming nitric acid but by removing it from the gas phase) and (*ii*) by raising the temperature at which clouds could form, since thermodynamic analyses suggested that NAT could

condense at temperatures well above the frost point. These clouds came to be known as Type 1 PSCs. In addition, Toon *et al.* (1986) suggested that sedimentation of large particles could serve to 'denitrify' the stratosphere. The removal of nitric acid not only from the gas phase but from the stratosphere altogether would have a potential to further reduce NO_2 concentrations, and hence enhance $ClO/ClONO_2$ ratios and attendant chlorine-catalyzed ozone loss. McElroy *et al.* (1986) also considered the possibility of nitric acid/water particles, suggesting that nitric acid monohydrate (NAM) was likely to form.

Figure 6.13 shows evidence for NO_y and H_2O removal in the same region displaying enhanced ClO in the Antarctic stratosphere (poleward of about 64°S in that particular transect) from airborne studies. Later measurements documenting the 'denitrification' and 'dehydration' of the Antarctic lower stratosphere include those of Santee *et al.* (1998, 1999), Voemel *et al.* (1995), and Pierce *et al.*(1994), but see below for a discussion of the roles of denitrification and dehydration in ozone depletion chemistry.

As discussed in Section 5.7.2, observatons have revealed that polar stratospheric clouds are sometimes composed of supercooled liquid solutions, raising important questions about the mechanisms of formation and freezing of various types of PSCs. What is the effect of different surfaces on ozone depletion chemistry? It is extremely important to consider whether the phase and microphysical mechanisms underlying PSC formation are important for ozone depletion. The uptake of condensable vapors enhance surface areas when PSCs are present. This increases the gas-particle collision frequency and hence can enhance the rates of heterogeneous reactions. Background stratospheric aerosols grow into Type 1a (solid) and/or Type 1b (liquid) particles as they cool, then further grow into Type 2 water ice PSCs if temperatures fall below the freezing point. The impact of enhanced surface areas for chemistry depends not only on the frequency with which gases strike these surfaces but also on the reactivity of the surfaces and the availability of those gases.

Let us first consider how reactive the different surfaces are, and where they are to be found in the stratosphere. Laboratory studies have shown that water ice, NAT, and liquid ternary solutions are all effective for activating chlorine heterogeneously, but with differing efficiencies and with different dependencies on temperature, water vapor abundance, and pressure (*e.g.*, Carslaw *et al.*, 1997a; JPL, 1997, and references therein). These dependencies are related to the thermodynamics of the different surfaces, which not only control their surface areas, but also their composition (especially the uptake of HCl onto/into the particles).

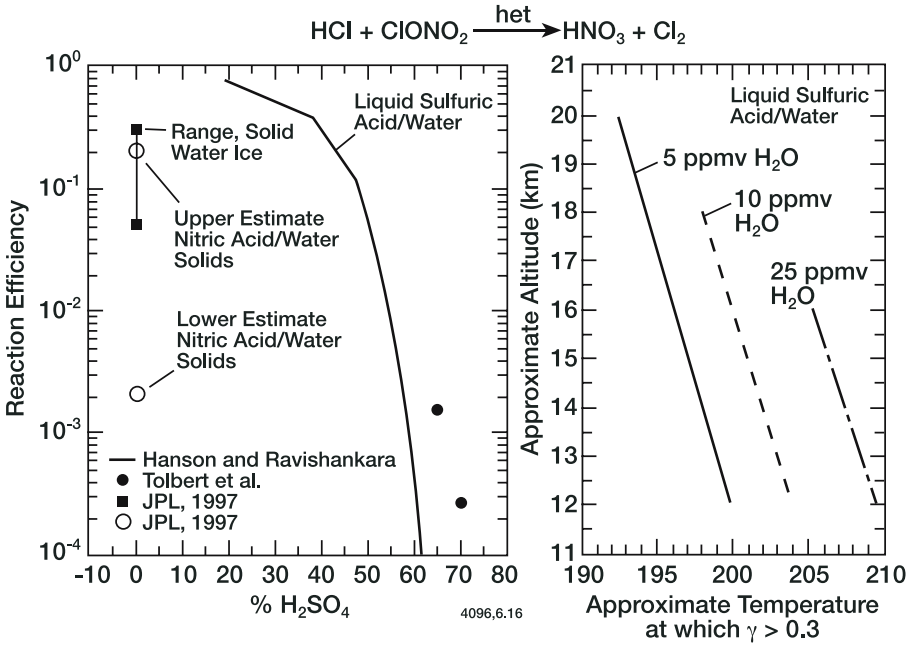

Figure 6.15. The left panel illustrates laboratory data on the efficiency of the reaction between HCl and $ClONO_2$ for ice, nitric acid/water solid surfaces, and liquid sulfuric acid/water solutions. The right panel depicts the altitude variation of the temperature at which the efficiency of this reaction on liquid sulfuric acid/water solutions becomes greater than 0.3 for water vapor mixing ratios that can be observed in the lower stratosphere.

Figure 6.15 summarizes a number of laboratory measurements of the efficiency of the key heterogeneous surface reaction $HCl + ClONO_2 \rightarrow Cl_2 + HNO_3$ (where 1 indicates reaction on every collision of $ClONO_2$ with a surface, 0.1 indicates one reaction in 10 collisions, etc.). Water ice is believed to be highly reactive wherever it can form, but the thermodynamics of ice condensation imply that rather cold temperatures are required to form it in the stratosphere (*e.g.*, below about 188 K near 20 km). There is currently debate about the efficiency of NAT for this reaction (Carslaw and Peter, 1997; JPL, 1997) as well as the conditions under which NAT can form, but from a thermodynamic viewpoint NAT may form near 20 km when temperatures drop below about 195 K, thus allowing reaction on a solid surface at temperatures above the frost point. In the case of liquid solutions, the efficiency of reaction depends strongly on the fraction of water in the particle (*e.g.*, Tolbert *et al.*, 1988; Hanson *et al.*, 1994). The $HCl + ClONO_2$ reaction becomes more efficient for lower percentages of sulfuric acid (and higher water in the liquid particles, which greatly increases the solubility of HCl;

see Robinson *et al.*, 1998 for a detailed recent analysis). This reaction takes place in liquid solutions with an efficiency greater than 1 in one hundred (0.01 as shown in Figure 6.15) for temperatures colder than about 197 K at 20 km, and an efficiency of 1 in ten for temperatures below about 195 K. Ravishankara and Hanson (1996) have emphasized that liquid PSCs can be comparable to or more effective than solid PSCs for many surface reactions at temperatures below about 195 K at 20 km, a point also illustrated in Cox *et al.* (1994), Borrmann *et al.* (1997a), and Del Negro *et al.* (1997).

Because liquid aerosols are present throughout the global stratosphere and because the water vapor pressures available to condense into them increase with increasing total pressure, the temperatures at which effective reactions may occur in liquid particles are higher for lower altitudes (Hofmann and Oltmans, 1992), as is also shown in Figure 6.15. This is an intriguing issue for both the polar and mid-latitude lower stratospheres. Some studies suggest that both liquid and solid surfaces can activate chlorine efficiently near the tropopause (Borrmann *et al.*, 1996; 1997b; Bregman *et al.*, 1997; Solomon *et al.*, 1997). Observations of enhanced ClO and reduced NO close to the tropopause for relatively wet (15 ppmv of H_2O) conditions provide some evidence for such liquid surface chemistry at mid-latitudes (Keim *et al.*, 1996; see also Brune *et al.*, 1990), although there is also evidence for some suppression of such chemistry at the tropopause itself (Smith *et al.*, 2001). Recent work has emphasized that ammonium may play a role along with sulfate in forming aerosols in the upper troposphere and perhaps at the tropopause (see *e.g.*, Tabazadeh and Toon, 1998; Kaercher and Solomon, 1999; Prenni *et al.*, 2001), and the effect of ammonium ions or other impurities such as organics on heterogeneous chemistry is not currently known. Note that Figure 6.15 is based upon the thermodynamic model of Carslaw *et al.* (1997a); its extrapolation to very high water vapor pressures (*e.g.*, greater than 5 ppmv at 200 mbar) is uncertain at present and requires laboratory studies for those conditions (see Robinson *et al.*, 1998); impurities such as ammonium have also not been considered here.

It is useful to note that the HCl + $ClONO_2$ reaction competes with the H_2O + $ClONO_2$ reaction for the available $ClONO_2$ on liquid aerosol surfaces. Thus, if HCl has been depleted, the rate of the latter reaction increases, so that effective heterogeneous activation of chlorine is not dependent upon both HCl and $ClONO_2$ being present. Further, the reactions of HCl with HOCl and HOBr are also quite efficient on liquid aerosol under moderately cold and/or wet conditions (Ravishankara and Hanson, 1996; JPL, 1997), providing additional pathways for chlorine activation.

While there are differences and uncertainties in the reactivity of various surfaces, laboratory data suggest that rather effective chlorine-activating reactions can occur irrespective of particle phase below about 198 K at 20 km and below 200-210 K near 12-14 km. As an air parcel cools and particle reactivities increase, liquid chemistry will occur first. This may be followed by reactions on NAT and ice, depending on factors including microphysics, the minimum temperature reached, and whether or not all of the chlorine activation has already occurred (Turco and Hamill, 1992). This latter point is critical. For example, if effective chemical processing on liquid surfaces has depleted all of the available HCl and/or $ClONO_2$ within an air parcel, then further lowering of temperature and formation of, for example NAT, may have a limited effect on ozone depletion. Moreover, an increased rate of reaction and/or an increased surface area (through, for example, formation of NAT Type 1s or Type 2s) may not enhance ozone depletion in a time averaged sense. If, for example, reactions on sulfate aerosols are sufficient to activate all of the available chlorine within a day, ozone depletion will not be increased if instead reactions on ice activate all of the chlorine in an hour, since the ozone depletion is a process that occurs over a much longer period (weeks) following the activation. Hence, the details of the reactivities and the microphysics that control particle surface areas, while playing a role to some degree, are not critical to formation of the ozone hole (*e.g.*, Portmann *et al.*, 1996; Carslaw *et al.*, 1997b). They are likely to be more important at the margins, particularly regions where temperatures are cold but not extremely cold.

6.3.1.5 The Depth and Area of the Ozone Hole

Current understanding of the key roles of liquid sulfate aerosols, solid PSCs, temperature, and sunlight provides a framework for understanding variations in the depth of the ozone hole (*e.g.*, the minimum possible vertical column) and its spatial area (*i.e.*, the number of square kilometers of depleted ozone).

Primary sources of sulfur to the stratosphere are carbonyl sulfide (Crutzen, 1976; Chin and Davis, 1995) and explosive volcanic eruptions that inject SO_2 gas directly into the stratosphere (*e.g.*, McCormick *et al.*, 1995) which subsequently forms liquid sulfate aerosols (see Section 5.7.1). Observations of PSC extinction show that the major eruptions of El Chichón in 1981 and Pinatubo in 1991 led to large increases in particle surface areas in polar regions (*e.g.*, McCormick *et al.*, 1995; Deshler *et al.*, 1992; Thomason *et al.*, 1997; Hofmann *et al.*, 1992; 1997). Hofmann and Oltmans (1993) showed that enhanced aerosol surface areas due to Pinatubo and Hudson (a South American

volcano) expanded the altitude range of significant Antarctic ozone depletion down to lower, warmer altitudes (*i.e.*, 10-14 km) where solid PSCs do not form. Observations of OClO in the Antarctic fall season (March-April) at temperatures above 200 K in the year immediately following Pinatubo also indicate significant activation of chlorine through sulfate aerosol processing (Solomon *et al.*, 1993). Hence, both ozone and trace gas observations provide support for the role of temperature-dependent heterogeneous chemistry on liquid aerosols and its modulation by volcanic eruptions. Portmann *et al.*, (1996) showed that volcanically enhanced PSC surface areas were likely responsible for the sharp onset of the ozone hole in the early 1980s (due to the El Chichón eruption), and for the very deep ozone holes observed in the early 1990s following the Pinatubo eruption.

The strong sensitivity of heterogeneous chemistry to temperature suggests that warm Antarctic springs, or years of early final warmings, could display less ozone than colder ones. Indeed, the relatively small Antarctic ozone depletions in 1986, 1988, and 2002 were partly due to temperature effects in these warm years — and are qualitatively simulated by numerical models of stratospheric chemistry when constrained by observed temperatures. Since the fundamental cause of warmer and colder years is the propagation of waves into the Antarctic stratosphere, dynamical impacts (*e.g.*, resupply of ozone from other regions) also play a role in dampening the ozone loss in warm years. In 2002, a massive Antarctic wave led to stratospheric temperatures in September that were higher than observed in the previous 50 years, affecting both the area and depth of the ozone hole (as shown in Plate 9; see also Allen *et al.*, 2003). Current models can simulate many key aspects of the onset, growth, and interannual variability in the depth of the Antarctic ozone hole based upon the growth of stratospheric chlorine in past decades along with the modulating effects of known temperature fluctuations and volcanic input of particulates (Portmann *et al.*, 1996; WMO/UNEP, 2003). However, the possibility of changes in dynamics remain incompletely understood, and it is not known whether the unprecedented behavior of the ozone hole of 2002 was a random event related to the chaos of atmospheric flow or the beginning of a more systematic shift (see 6.3.2.3).

The Antarctic ozone hole cannot get very much deeper than it presently is — since virtually all the ozone is now removed each year in those altitudes where PSCs occur. Ozone column minima near 100 DU were observed after the Pinatubo eruption, when the efficiency of heterogeneous chemistry was especially enhanced by very large aerosol amounts over a broad altitude range as noted above. This suggests that the ozone hole could only become deeper in the absence of major

volcanic eruptions if PSCs were to extend to significantly higher or lower altitudes, implying a major change in south polar thermal structure. While substantial changes of this type appear unlikely, the possibility of increases in the horizontal extent of the hole cannot be ruled out. The ozone hole is largely confined to the Antarctic polar vortex, and year-to-year variability in its size can occur. These fluctuations are mainly linked to variability in temperature (*e.g.*, slightly colder or warmer years than average). But changes in exposure to sunlight also play a role, especially in August and early September (*e.g.*, through atmospheric waves that photolyze Cl_2 particularly early in the depletion season). Figure 6.16 shows the growth in size of the ozone hole during the 1980s, and its interannual ups and downs. In general, years of deeper ozone holes are also years of large spatial extent. Several decades will be required before changes in the size or depth of the ozone hole will signal a recovery or a worsening that lies outside of the modulations introduced by temperature, volcanic aerosol content, and wave-driven excursions in sunlight exposure. Some studies suggest that cooling (*e.g.*, that expected from greenhouse gases) may enhance ozone losses in the 'edge' region around the vortex in the future (Lee *et al.*, 2001), perhaps increasing

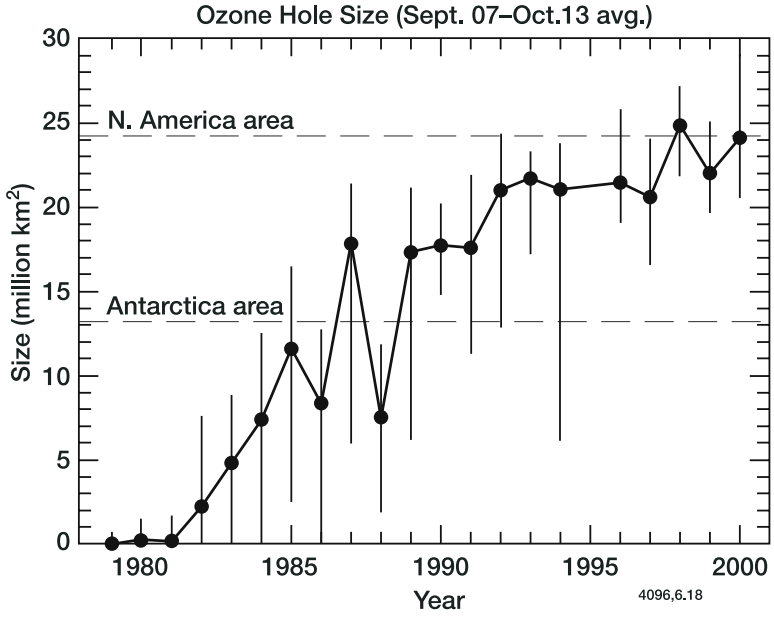

Figure 6.16. Observations of the year-to-year variations in the size of the Antarctic ozone hole based on satellite observations of the region where total ozone drops below 220 Dobson Units. Figure courtesy of P. Newman (personal communication).

the size of the hole. However, as discussed below in the context of the Arctic ozone depletion, the interactions of waves with the mean flow is a complex process that makes a definitive prediction of the future temperatures of the polar and sub-polar stratospheres a challenge.

6.3.1.6 Changes in Understanding

Here we pause for a brief summary of the conceptual picture of Antarctic ozone depletion that emerged in the late 1980s and describe how it has changed. Initial observations of Antarctic chemistry as discussed above showed evidence for both heterogeneous chlorine activation on PSCs and for denitrification. An understanding emerged that chlorine-activating reactions took place on solid PSCs in Antarctic winter, accompanied by denitrification that allowed the depletion to persist in spring, even in the absence of further PSC formation. This picture was simple and very easy to explain in chemical terms. However, the current understanding suggests that denitrification can increase ozone destruction somewhat, but is not required and probably not sufficient on its own for massive polar ozone losses. Even in the Antarctic, denitrification is not 100% effective — some reactive nitrogen remains present (as HNO_3). That HNO_3 will photolyze in spring, reforming $ClONO_2$. Since NO_y abundances are roughly 10 times greater than Cl_y abundances in the lower stratosphere, photolysis of the leftover HNO_3 can neutralize reactive chlorine in the absence of further heterogeneous processing even if denitrification is 80% effective at removing NO_y. A more effective way to drive ozone depletion processes is continued chlorine activation on solid or liquid aerosols in spring. Such reprocessing is sufficient to keep the chlorine active in cold sunlit air whether denitrified or not (Portmann *et al.*, 1996; Chipperfield and Pyle, 1998). This heterogeneous chemistry must occur faster than photolysis of HNO_3 to maintain high ClO levels, but HNO_3 photolysis is not a very rapid chemical reaction and it has been shown that PSC reprocessing can support rapid springtime ozone loss for typical Antarctic conditions. Observations following the eruption of Mt. Pinatubo further support the view that liquid aerosol reprocessing has been a key factor in determining the depth and duration of the ozone hole after major eruptions. More generally, the expansion of heterogeneous chemistry from ice, to NAT, to liquid sulfate aerosols has lessened the expected dependence of the ozone loss on extreme cold to one of relative cold, thereby expanding the height, time and latitude ranges in which ozone depletion may be expected to be enhanced by heterogeneous processes that affect chlorine partitioning. Further, Arctic observations suggest that ozone depletion there is limited mainly by the seasonal cycle of north polar temperatures (*i.e.*, whether

or not temperatures are cold in the spring season when sunlight is also available), and not by denitrification. Gao *et al.* (2001) showed that extensive denitrification, as documented by Fahey *et al.* (2001), did enhance O_3 loss (by about 30%) in a narrow layer in 2000, but Tabazadeh (2001) showed that the more important question may be the depth of such layers. Years of deepest ozone depletion observed in the 1990s were often associated with little or no denitrification (Santee *et al.*, 1998; 1999), and the years of greatest denitrification (*e.g.*, 1999/2000) were not those of greatest Arctic ozone loss. This is the subject of the next section.

6.3.2 Arctic Ozone Depletion

Perhaps ironically in view of the extremely remote nature of the Antarctic, ozone depletion was more readily observed there than in the Arctic. This was due in part to the fact that no correponding 'hole' developed in the Arctic stratosphere in the early 1980s, but also to the paucity of ground-based long-term measurements in the high Arctic and to the greater local variability of Arctic ozone associated with atmospheric waves. As the mechanism for Antarctic ozone depletion began to be elucidated in the latter half of the 1980s, it was understood in general terms that Arctic ozone depletion would likely be smaller due to warmer temperatures (hence, fewer PSCs as already documented in McCormick *et al.*, 1982) and the associated dynamical differences (*i.e.*, a less isolated vortex). The top panel of Figure 6.17 illustrates the climatological differences in the seasonal cycles of temperature for 65°N and 65°S, edge regions of the Arctic and Antarctic. Colder temperatures are typically found at higher latitudes, but this region is shown here in order to illustrate accompanying satellite total ozone data (which is only available in the sunlit atmosphere). Perhaps most importantly, the typical springtime increase in stratospheric temperatures occurs in association with much earlier stratospheric warmings in the north than in the south (*e.g.*, Andrews *et al.*, 1987), suggesting that the overlap between cold temperatures and sunlight must be limited, and the Arctic ozone depletion hence less severe (see *e.g.*, the review by Pyle *et al.*, 1992). However, not all years are typical, and there is some evidence that the Arctic stratosphere may be systematically changing — a point discussed below.

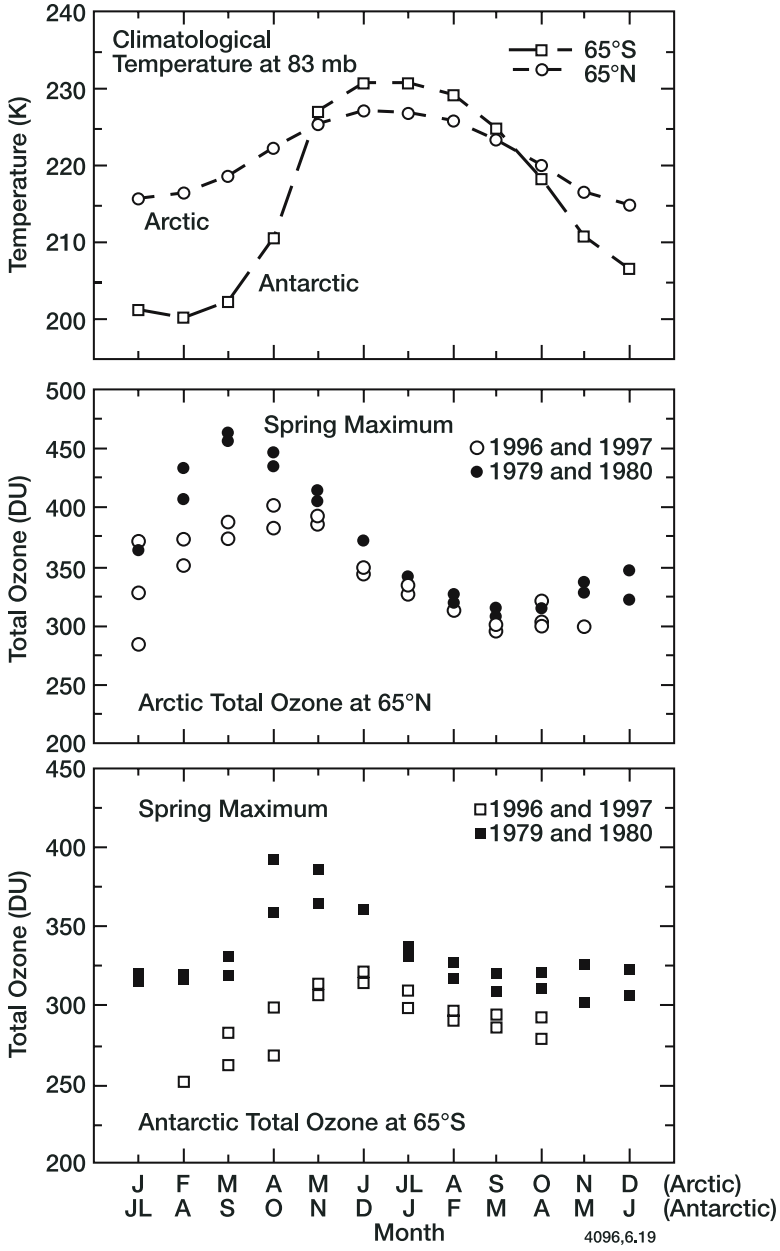

Figure 6.17. Observations of the average temperatures at 65°S and 65°N from the Fleming *et al.* (1990) Cospar International Reference Atmosphere (CIRA) climatology (top). The middle and bottom panels show satellite measurements of the annual cycles of total ozone at 65°N and 65°S in the late 1970s and in 1996 and 1997 (from SBUV/SBUV2, courtesy of R. Nagatani). From Solomon (1999).

6.3.2.1 Chemical Processes in the Arctic

As in the Antarctic, direct observations of a broad range of chemical species have shown that heterogeneous chemistry greatly perturbs the composition of the Arctic vortex. Evidence for effective winter activation of Arctic chlorine was first provided by measurements of enhanced OClO (Solomon *et al.*, 1988) and ClO (Brune *et al.*, 1990). Both gases have since been observed in many other studies (*e.g.*, Schiller *et al.*, 1990; Pommereau and Piquard, 1994a; Perner *et al.*, 1994; Pfeilsticker and Platt, 1994; Brune *et al.*, 1990; 1991; Toohey *et al.*, 1993; Waters *et al.*, 1993; Crewell *et al.*, 1994; Bell *et al.*, 1994; de Zafra *et al.*, 1994; Shindell *et al.*, 1994; Donovan *et al.*, 1997). Decreased NO and NO_2 were also observed with several independent methods (Fahey *et al.*, 1990a; Noxon *et al.*, 1978; Toon *et al.*, 1994; Mankin *et al.*, 1990; Wahner *et al.*, 1990; Pommereau and Piquard, 1994b; Goutail *et al.*, 1994; Pfeilsticker and Platt, 1994; Van Roozendael *et al.*, 1994). The column abundances of HCl and HF further supported the view that chlorine activation on PSCs must be effective in the Arctic (Toon *et al.*, 1994; Mankin *et al.*, 1990; Traub *et al.*, 1994).

In-situ measurements of HCl were particularly important in sharpening the link between enhanced ClO and conversion from HCl, as shown for example in Figure 6.18 (see Webster *et al.*, 1993; Michelsen *et al.*, 1999). Measurements of $ClONO_2$ also displayed evidence for heterogeneous processing on PSCs (*e.g.*, von Clarmann *et al.*, 1993; Roche *et al.*, 1994; Oelhaf *et al.*, 1994; Adrian *et al.*, 1994; Geller *et al.*, 1995; Yudin *et al.*, 1997). Concurrent in-situ and space-based observations of ClO and PSCs together with trajectory studies further linked the activated chlorine to heterogeneous chemistry (Jones *et al.*, 1990b; Yudin *et al.*, 1997; Dessler *et al.*, 1998 and references therein). Thus, the same general fingerprints of heterogeneous chemistry that were first observed in the Antarctic were not only apparent but further strengthened by Arctic data.

Observations of NO_y and water vapor displayed signs of sporadic and limited denitrification and dehydration (compare Figures 6.13 and 6.18), in marked contrast with the pervasive and extensive characteristics of these chemical conditions in the Antarctic (Kawa *et al.*, 1990; Fahey *et al.*, 1990b; see later work by Kondo *et al.*, 1994; Oelhaf *et al.*, 1994; Khattatov *et al.*, 1994; Rinsland *et al.*, 1996; Santee *et al.*, 1998a,b). Denitrification was also observed to occur without accompanying dehydration, suggesting that NAT particles sometimes can become large enough to precipitate without necessarily growing to Type 2 (water ice) proportions (see *e.g.*, Toon *et al.*, 1990; Gandrud

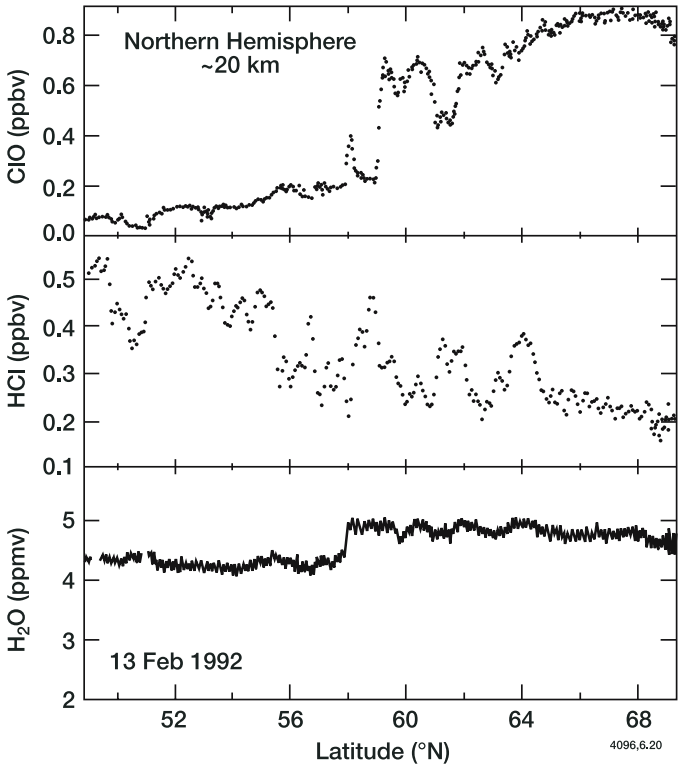

Figure 6.18. Observations of the chemical composition of the Arctic stratosphere from the ER-2 aircraft in February 1992. The data show high ClO abundances associated with reduced HCl abundances as would be expected from heterogeneous conversion. H_2O does not display evidence for dehydration on this Arctic transect. From Solomon (1999).

et al., 1990; Salawitch *et al.*, 1989; Koop *et al.*, 1995; Fahey *et al.*, 2001).

Based on ClO observations (Brune *et al.*, 1990) and related model calculations, observed and calculated rates of ozone loss in February 1989, were shown to be of the order of 20 ppbv/day near 20 km (Schoeberl *et al.*, 1990; Salawitch *et al.*, 1990; McKenna *et al.*, 1990). Further, the BrO observations of Toohey *et al.* (1990) revealed that the ClO-BrO catalytic cycle was probably of particular importance for the Arctic, since ClO enhancements were generally smaller than in the Antarctic and hence the efficiency of the ClO dimer cycle was reduced; note that the rate of the latter depends on the square of ClO density, *e.g.*, Salawitch *et al.*, 1990; 1993). However, the early warming observed, for example, in February 1989, as illustrated in Figure 6.19, prevented extensive total ozone loss in that year. Some early studies suggested that the less extensive denitrification of the Arctic would limit ozone losses

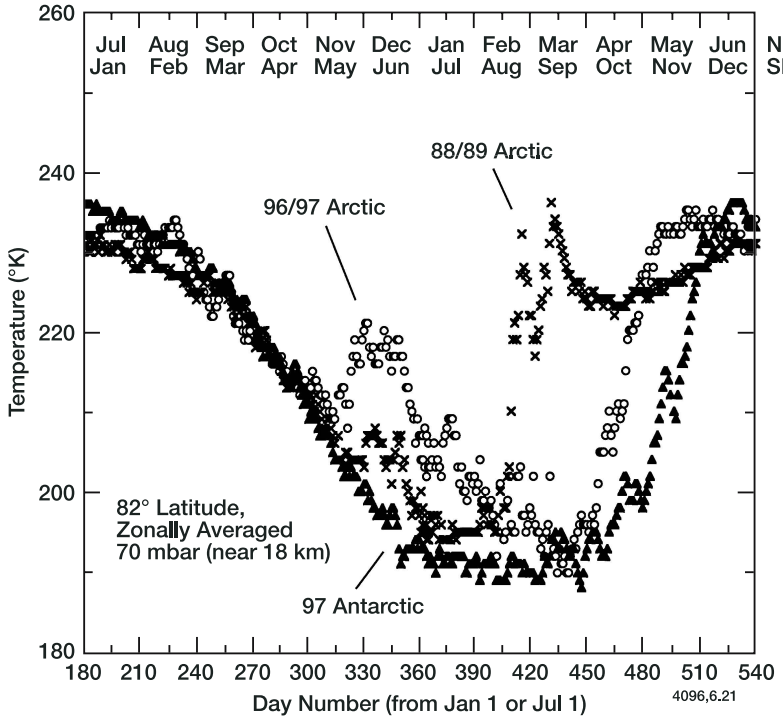

Figure 6.19. Observations of the zonally averaged temperatures in the Arctic for 82°N near 18 km, from the National Center for Environmental Prediction (NCEP) meteorological database for two illustrative recent years, together with Antarctic observations at 82°S in 1997 (shifted by six months for comparison).

there (Brune *et al.*, 1991; Salawitch *et al.*, 1993) through less effective NO_x reduction and hence an early cutoff of the depletion process in spring; the previous section illustrates how new understanding of liquid aerosol chemistry has affected this picture. Thermal decomposition of the Cl_2O_2 dimer (which cuts off the ClO dimer ozone loss cycle) also affects the degree of possible ozone loss as air warms in spring even if denitrified (McKenna *et al.*, 1990; MacKenzie *et al.*, 1996).

6.3.2.2 Quantifying Arctic Ozone Depletion

The more complex dynamics of the Arctic vortex as compared to the Antarctic demand the application of sophisticated tools for analysis of ozone destruction. The greater wave activity of the Northern Hemisphere can enhance ozone losses even in winter by increasing the exposure of polar air to sunlight in the distortions caused by atmospheric waves as compared to the Southern Hemisphere (see *e.g.*, Jones *et al.*, 1990a). However, the same wave activity can warm the air and perhaps

even distort it sufficiently to mix with its surroundings, thus reducing ozone depletion. Detailed methods have been used to evaluate the air parcel trajectories along which ozone and other trace gases are transported (Schoeberl *et al.*, 1990; Manney *et al.*, 1994b; 1995a,b; 1996). These help to quantify the amount of ozone chemically destroyed by revealing that while the time evolution of inert tracers such as N_2O can be well simulated in the Arctic using such approaches, the evolution of ozone shows large departures from conservation that likely reflect chemical loss (Manney *et al.*, 1994a; 1995a,b,c; 1996; 1997). Further, the regions of apparent ozone depletion identified in this manner occur in regions of enhanced ClO as measured by concurrent satellite observations (*e.g.*, Waters *et al.*, 1993; Manney *et al.*, 1994a; 1995c; Lutman *et al.*, 1994a,b; MacKenzie *et al.*, 1996).

Tracer-ozone correlations are another method used to provide insights into polar ozone loss. Briefly, changes in the amount of ozone observed for a given amount of conserved tracer such as N_2O or CH_4 provide a useful (albeit imperfect) diagnostic for ozone loss based upon understanding of ozone-inert tracer relationships and their spatial distributions (Proffitt *et al.*, 1993; Müller *et al.*, 1996; 1997a,b; Plumb and Ko, 1992). Using satellite data for CH_4, O_3, and HCl, for example, Müller *et al.* (1996) suggest that 60 DU of total Arctic ozone was depleted on constant CH_4 surfaces in a manner inconsistent with transport from any other region of the stratosphere in the Arctic winter of 1991/2. The reduced ozone was associated with pronounced HCl depletion observed in the same air, as expected based upon heterogeneous chemistry on PSCs.

Another method of quantifying ozone destruction involves the use of trajectory analyses of airflow together with multiple ozonesondes to find 'matches' wherein the air observed at one site is observed again some days later. Changes in the observed ozone then provide a measure of ozone loss (von der Gaathen *et al.*, 1995). This approach has yielded strong evidence for extensive Arctic ozone depletion that is closely tied to cold temperatures near 195 K (Rex *et al.*, 1997; 1998). Understanding can be further tested by comparing the observed depletion derived from such 'matches' with chemistry calculations along the same trajectories. These studies have shown good agreement in February and March, but some evidence for mid-winter ozone loss that exceeds photochemical theory has also been suggested (Rex *et al.*, 1998; Becker *et al.*, 1998). This intriguing result may suggest dark or twilight chemistry that is not fully understood, or contributions from dynamical phenomena not fully captured in the trajectories.

Fully three-dimensional models driven in some cases by the meteorological data for specific years have also been used to probe the

Arctic ozone losses and test photochemical understanding. These models have succeeded in explaining much of the observed ozone depletion, documenting its connections to chemical processes, and even reproducing much of the observed variability seen from one year to another (see *e.g.*, Chipperfield *et al.*, 1994; 1996; Chipperfield and Pyle, 1998; Deniel *et al.*, 1998; Douglass *et al.*, 1995).

Taken together, these combined approaches to transport analyses using tracers, 'matches', chemical transport models, or Lagrangian calculations along with ozone and trace constituent observations provide strong evidence for a chemically-driven Arctic ozone loss (order of 60-120 DU) in several recent years. Each approach is subject to different sources of quantitative error and uncertainty, such as inaccuracies in temperature data used as input in observationally-based transport studies, incomplete understanding of the factors influencing tracer-tracer correlations, and small scale dynamical processes that are not well represented in modelling studies (*e.g.*, mountain waves). In spite of these shortcomings and in contrast with the Antarctic, there is substantial evidence for a dynamical contribution to recent trends as well — these are discussed in the next section.

6.3.2.3 Variability of Arctic Temperatures

Since Antarctic ozone depletion occurs mainly in September under cold conditions, it is natural to consider whether comparable conditions are ever attained in the Arctic in the analogous month of March. Nagatani *et al.* (1990) pointed out that while Arctic temperatures below about 195 K appeared to be quite rare based on the available record at that time (which extended back to about the 1950s), they are not unknown. For example, the Arctic winter of 1975/6 was a year in which March Arctic temperatures were close to those typically seen in the Antarctic in September, but chlorine loading was small in 1975 and no discernible Antarctic ozone hole was observed at that point (see Figure 6.9). Nagatani *et al.* (1990) noted that extensive Arctic ozone loss might be expected if such meteorological conditions were to be realized in an atmosphere with current chlorine loadings.

There were several unusually cold Arctic winters in the 1990s, with correspondingly large Arctic ozone losses (see Newman *et al.*, 1997; Coy *et al.*, 1997) illustrated in Figure 6.9. Not all the years since 1990 have been cold, as reflected for example in the high spring ozone observed in 1998, for example. Enhanced volcanic aerosol from the Mt. Pinatubo eruption probably contributed to the very low ozone observed in 1992 and 1993 through enhanced PSC chemistry, but the continuing depletions in, for example, 1996 and 1997 suggest a

strong effect of temperature. Figure 6.19 illustrates the full seasonal behavior of temperatures observed in some recent cold years, and contrasts their behavior with the Antarctic. As has already been emphasized, the warmer temperatures generally observed in the winter Arctic stratosphere as compared to the Antarctic reflect adiabatic heating associated with faster downward motion, which also leads to a rapid wintertime increase in Arctic total ozone (from values of around 300 DU in September to as much as 450 DU at the spring maximum in March in 1979 and 1980, for example, as shown in Figure 6.17). In the much colder Antarctic, pre-ozone hole total ozone did not show such a winter increase (remaining instead near 250-300 DU from March through September, see Figures 6.11 and 6.19), suggestive of a much less dynamic vortex. In today's Antarctic atmosphere, an abrupt drop in ozone occurs in September deep in the vortex as shown in Figure 6.11, reflecting rapid chemical removal in sunlit air with limited dynamical resupply as discussed earlier. In the relatively stagnant Antarctic vortex, the total ozone therefore actually decreases in spring to form a 'hole' compared to the surrounding mid-latitude air. In the more dynamic Arctic, transport replaces a substantial portion of the ozone lost, even in the very cold years of the 1990s (see *e.g.*, Manney *et al.*, 1997). Indeed, Figure 6.17 shows that even in 1996 and 1997, Arctic ozone continued to increase at 65°N during spring — it simply did not do so as rapidly as it did in 1979 and 1980. The fact that Antarctic ozone drops rapidly in spring while Arctic ozone does not is one key reason why the depletion in the Arctic is not generally referred to as an ozone hole. Hence, large chemical ozone losses of the order of 60-120 DU do occur in the Arctic, but it is difficult to say that a 'hole' formed since the ozone was apparently being simultaneously resupplied to a major extent (see the detailed analyses by Manney *et al.*, 1997; Müller *et al.*, 1997a,b). The formation of a true Arctic ozone hole according to this definition would require not only cold March temperatures but also very cold temperatures throughout the winter, in order to cause both activation of chlorine in sunlit air and to inhibit the winter buildup of ozone through downward transport. Such conditions did not occur in the 1990s (see Coy *et al.*, 1997; Zurek *et al.*, 1996).

It is important to note that denitrification was observed but was rather limited in degree in the Arctic springs of 1993, 1996, and 1997 (Santee *et al.*, 1998; 1999), so that the observations of ozone depletion of the order of 60-120 DU in each of these years are not associated with extensive denitrification. Rather, as in the Antarctic and consistent with current understanding of liquid aerosol chemistry, the evidence suggests that heterogeneous reactions in the sunlit atmosphere are

mainly responsible for maintaining the high ClO (Santee *et al.*, 1997) that depleted the Arctic ozone in those years (Manney *et al.*, 1997).

Figure 6.11 shows that the Antarctic ozone hole fills in to a substantial degree around December. This increase in ozone is associated with the final stratospheric warming that breaks down the polar vortex and brings in ozone-rich air from lower latitudes. However, it is also important to note that the seasonal increase in Antarctic ozone that marks the warming now occurs systematically later than it did prior to the discovery of the ozone hole — note the ozone seasonal increases observed not in December but in November in the 1970s (see Jones and Shanklin, 1995). Theory suggests that the massive destruction of Antarctic ozone has greatly altered the thermal budget of the Antarctic stratosphere, and is likely to be responsible for this considerable delay in the timing of the Antarctic stratospheric spring warming (*e.g.*, Randel and Wu, 1999). If there were to be a similar delay in the breakdown of the Arctic polar vortex caused by ozone depletion or by another mechanism (such as greenhouse gas changes), then it could have profound implications for Arctic ozone loss in the future. There is some evidence that Arctic stratospheric warmings are tending to occur about 2 weeks later than they did in the past (Zhou *et al.*, 2000). If this trend were to continue, Arctic ozone depletion may deepen in the future, since the spring seasonal overlap between cold temperatures and the amount of sunlight is critical in driving ozone depletion.

In summary, there is abundant evidence for some chemical perturbations and ozone destruction in the Arctic even in relatively warm years, but the degree of ozone depletion depends upon cold temperatures in sunlit conditions, just as in the Antarctic. An unprecedented number of cold years occurred in the Arctic in the 1990s. Each of these was reflected in low ozone in the Arctic record as shown in Figure 6.9. Five of the years from 1991-1998 have been significantly colder than average (Coy *et al.*, 1997; Zurek *et al.*, 1996), and there is evidence that Arctic warmings may be occurring later than before. This series of unusually cold years raises the key question of cause. Randel and Wu (1999) argue that the cooling observed in both the Arctic and the Antarctic is due to the ozone depletion itself. They propose a feedback mechanism as in Shine (1986) wherein ozone losses lead to colder temperatures and hence even greater depletion. The studies by Thompson and Wallace (2000) and Thompson *et al.* (2000) suggest that changes in the dynamics of the north polar vortex may be linked to the underlying tropospheric wave field, particularly the North Atlantic and Arctic Oscillations (NAO, AO) in wave patterns (*i.e.*, the spatial distribution of tropospheric disturbances). These authors suggest a wave-driven systematic linkage between tropospheric waves and stratospheric temperature, which could

reflect ozone changes. Hartley *et al.* (1998) argue for a similar linkage involving the modification of stratospheric dynamics due to the ozone changes, with tropospheric propagation as a key element. Other evidence for downward propagation of stratospheric waves is presented by Baldwin and Dunkerton (2001). However, other studies argue for smaller effects, and suggest mechanisms including greenhouse gases and surface temperatures could account for these changes (see references in Thompson *et al.*, 2000).

As has already been emphasized, the 'greenhouse effect' due to increases in CO_2 and other gases warm the planet surface but cool the stratosphere (*e.g.*, Fels *et al.*, 1980). This effect is predicted to be small (only a few tenths of a degree in today's atmosphere, far less than the recent coolings observed in the Arctic), but dynamical amplification of such changes is also possible. A number of studies have suggested that increased CO_2 and other greenhouse gases could substantially affect stratospheric dynamics, thereby cooling the Arctic stratosphere far more than the radiative effect alone would predict and leading to greater Arctic ozone depletion (*e.g.*, Austin *et al.*, 1992; Shindell *et al.*, 1998). The work of Shindell *et al.* argues for a key role for such a dynamical feedback both in the 1990s and perhaps in future years, with the peak Arctic ozone losses being predicted to occur near 2010, well after the expected peak of chlorine loading (see also Dameris *et al.*, 1998). However, some other three-dimensional models display the opposite effect — those studies suggest that the Arctic stratosphere could warm rather than cool in the future if emissions of CO_2 and other greenhouse gases continue. The different signs of the temperature effects predicted by various models demonstrate great sensitivity to how planetary waves propagate, dissipate, and couple to the mean circulation and temperature fields. At present the possibility that the recent colder Arctic temperatures are simply part of a natural low-frequency cycle that could, for example, induce a series of colder years every fifty years or so cannot be ruled out given the short record of existing global stratospheric temperature data. Hence, while it is clear that there has been significant chemical ozone depletion associated with the cold Arctic winter/spring seasons of recent years, the fundamental reasons for those cold temperatures and their future persistence remain a topic of research.

6.3.3 Mid-Latitude Ozone Depletion

The discovery of the Antarctic ozone hole naturally raised the question of whether mid-latitudes might also display greater ozone depletion than

expected. Within a few years after the ozone hole was discovered, statistically significant trends in ozone were documented at northern mid-latitudes (Ozone Trends Report, 1988, and references therein). By the 1990s, significant trends had been established for both northern and southern mid-latitudes, not only in winter and spring but also in summer (WMO/UNEP, 1991; 2003; Stolarski *et al.*, 1991; McPeters *et al.*, 1996a,b; Harris *et al.*, 1997). Mid-latitude ozone column trends as of the late-1990s were of the order of 5-10%, much smaller than those of the Antarctic (Figure 6.20) but far greater than gas-phase model predictions. Analyses of vertical profiles measured by ozonesondes and satellites suggested that the bulk (at least 2/3) of the northern mid-latitude ozone decline is occurring in the lower stratosphere near 12-20 km (see McCormick *et al.*, 1992; Miller *et al.*, 1995; WMO/UNEP, 1994; Bojkov and Fioletov, 1997; SPARC, 1998). Figure 6.20 depicts the ozone record from Arosa, Switzerland, the sole station in the world where ozone measurements date back to the 1920s. Systematic records were begun at many other stations in the northern hemisphere in the 1950s or 60s (see Ozone Trends Panel Report, 1988), but the length of the record at Switzerland is unique. The figure shows the large seasonal cycle of ozone at mid-latitudes and illustrates that variability in that cycle is one factor that makes observation of a trend difficult. However, when attention is restricted to a single month, such as January for example (shown by the filled circles in the figure), the data do suggest a trend after about 1980. The trend becomes far clearer when the data are averaged over several years, in order to reduce sensitivity to processes such as the quasi-biennial oscillation or the El Niño, which can cause short-term fluctuations of a few years due to dynamical perturbations. Here we present a five-year running mean. The trends in this long-term averaged record are evident; indeed the figure shows evidence for about a 6% maximum trend in mid-latitude ozone and displays considerable similarity to the Antarctic depletion (albeit much smaller in magnitude). We next probe the causes for this striking change — this Antarctica in miniature — observed for mid-latitude ozone.

6.3.3.1 Heterogeneous Chemistry and Mid-Latitude Ozone Depletion

One mechanism that could affect mid-latitude ozone depletion in the lower stratosphere is heterogeneous chemistry. It had long been suspected that some heterogeneous process involving N_2O_5 might be responsible for the Noxon 'cliff' and for anomalously high HNO_3 abundances in middle to high latitudes of the Northern Hemisphere (*e.g.*, Wofsy, 1978; Noxon, 1979; Austin *et al.*, 1986), but it was not

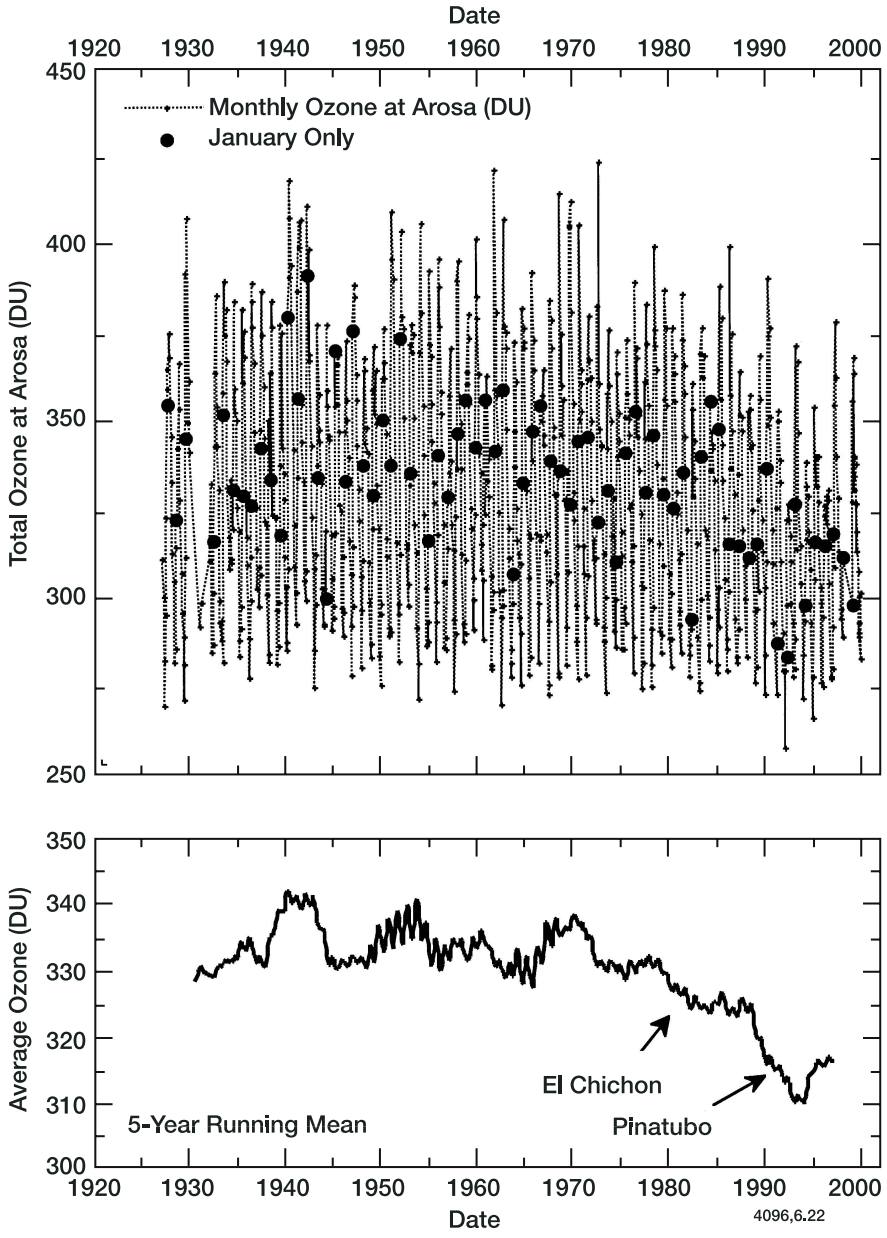

Figure 6.20. Observations of total ozone at Arosa, Switzerland since the 1920s, the world's longest-running total ozone record. The top panel shows monthly mean data for all months and years, illustrating both the large seasonal cycle and its variability. Januaries are indicated by the filled circles, and this month does display a long-term downward trend. The bottom panel presents the 5-year running mean of the same data. Periods when modelling studies suggest volcanic influences due to the El Chichón and Mt. Pinatubo eruptions are indicated.

until the late 1980s that laboratory studies showed that N_2O_5 can hydrolyze rapidly (reaction efficiency of about 0.1) on sulfuric acid/water films (Tolbert *et al.*, 1988) and particles (Mozurkiewicz and Calvert, 1988). Hence the possibility of heterogeneous chemistry on the liquid sulfate layer that is pervasive throughout the stratosphere began to be considered in earnest (but see also Cadle *et al.*, 1975, for an early and interesting exploratory paper).

The hydrolysis of N_2O_5 reduces NO_x and its impact on ozone in the lower stratosphere, and indirectly enhances the effect of ClO through its control of the $ClONO_2$/ClO ratio, as discussed earlier. Recent studies have examined the dependence of the N_2O_5 hydrolysis reaction on temperature and pressure (Robinson *et al.*, 1997) and have probed reaction conditions in extensive detail (JPL, 1997; 2000). This key reaction and the related hydrolysis of bromine nitrate (Hanson *et al.*, 1996) both take place rapidly at virtually all stratospheric conditions, making their influence extremely widespread (and, as shown below, extremely important). In addition to these indirect effects, however, there is evidence for some direct activation of chlorine on liquid sulfate aerosols as well. As noted in connection with polar chemistry, Tolbert *et al.* (1988) suggested that $ClONO_2$ could react with water and with HCl on sulfuric acid/water surfaces, but with a strong dependence on the particle composition, specifically the water content of the particle (hence on the temperature and water vapor pressure).

The laboratory investigations of Tolbert (1988) and Mozurkiewicz and Calvert (1988) prompted Hofmann and Solomon (1989) to study the role of N_2O_5 hydrolysis and chlorine activation on sulfuric acid aerosols at mid-latitudes, particularly under volcanic conditions when such processes would be enhanced. They suggested that this chemistry could be significant for both background and volcanically enhanced conditions, and that the ozone reductions noted by several authors (*e.g.*, Adriani *et al.*, 1987) following the eruption of El Chichón in 1981 might be linked to heterogeneous reactions similar to those occurring in Antarctica, albeit with reduced rates. Observations of marked reductions in NO_2 over New Zealand after the El Chichón eruption (Johnston and McKenzie, 1989) provided some of the first chemical evidence that such processes could be important at mid-latitudes. Several modelling studies further probed the role of this chemistry in determining global ozone trends and related questions of chemical partitioning and odd oxygen destruction cycles studies (*e.g.*, Rodriguez *et al.*, 1991; 1994; Brasseur and Granier, 1992; Prather *et al.*, 1992; McElroy *et al.*, 1992; Pitari *et al.*, 1993; Toumi *et al.*, 1993). Prather *et al.* (1992) pointed out that the hydrolysis of N_2O_5 saturates beyond a certain aerosol load at which N_2O_5 is converted to HNO_3 as fast as

it can be formed, so that further increases in aerosol do not affect NO_x abundances through this process.

Rodriguez *et al.* (1991) and McElroy *et al.*(1992) noted that hydrolysis of N_2O_5 would have the effect of dramatically altering the competition between the various catalytic cycles in the lower stratosphere, enhancing the roles of the odd hydrogen and odd chlorine/bromine destruction mechanisms, even for background aerosol conditions. Direct observations by Wennberg *et al.* (1994) later confirmed this view by providing simultaneous measurements of a suite of key radicals including OH, HO_2, NO, and ClO near 20 km; these data can be related in hindsight to the anomalously low NO mixing ratios reported in the mid-latitude lowermost stratosphere by Ridley *et al.* (1987). Cohen *et al.* (1994) present a detailed chemical argument demonstrating the dominance of HO_x chemistry in the natural lower stratospheric ozone balance based on observations. Taken together, this improved understanding of the balance of terms among chemical cycles of ozone destruction is a key building block for attempts to evaluate ozone loss, which is tied to the competition of chlorine and bromine-catalyzed destruction compared to other chemical processes and to transport. In short, slower rates of ozone loss through other processes (especially NO_x chemistry) result in a larger relative role for human-induced perturbations at mid-latitude due to chlorine and/or bromine increases.

From about 1988 to the early 1990s, the scientific understanding of mid-latitude ozone depletion evolved from a gas-phase picture into the expectation of enhanced ozone depletion at least via the N_2O_5 hydrolysis process, not only for volcanically perturbed conditions but also for background aerosol loading. The eruption of Mt. Pinatubo in June, 1991, was the largest in the 20th century, and occurred near the peak loading of atmospheric chlorine. This geophysical event provided numerous lines of evidence suggesting that heterogeneous chemical reactions on sulfate aerosols play a role in ozone chemistry and its depletion (see the review by Toohey, 1995). Gleason *et al.* (1993) were the first to report record low northern mid-latitude ozone abundances in the following year. Hofmann *et al.* (1994) and McGee *et al.* (1994) demonstrated that substantial ozone losses occurred in the lower stratosphere following Pinatubo, particularly in winter and spring, with peak local depletions near 20 km at 40-50°N as large as about 25%. Randel and Cobb (1994) showed that changes in temperatures relating to aerosol heating can provide an important means of distinguishing ozone losses due to volcanic eruptions from those relating to the QBO, El Niño, or other perturbations in statistical analyses of ozone data (see also Jaeger and Wege, 1990; Bojkov *et al.*, 1993; Zerefos *et al.*,

1994). The high aerosol load present just after the eruption in mid-1991 changed stratospheric heating and hence reduced tropical ozone through dynamical effects (Brasseur and Granier, 1992), but this lasted only a few months and was largely confined to the tropics (see Schoeberl *et al.*, 1992; Tie *et al.*, 1994). For reviews of the many studies establishing the large and persistent mid-latitude ozone changes after Pinatubo, see Toohey (1995) and WMO/UNEP (1994; 1998). Because the stratospheric Brewer-Dobson circulation transports material upward and poleward, major volcanic eruptions that inject material into the tropical stratosphere can have the greatest and longest impacts on global ozone, while volcanic injections at higher latitudes are removed by downward motion. Both El Chichón and Pinatubo are tropical volcanoes.

Chemical measurements after Pinatubo have identified many signatures of heterogeneous reactions on sulfate aerosols at mid-latitudes that are akin to those occurring in the ozone hole region. Observations from New Zealand showed both reduced NO_2 and enhanced HNO_3 column abundances (Johnston *et al.*, 1992; Koike *et al.*, 1994). Aircraft, ground-based, balloon- and shuttle-borne experiments revealed similar large changes in NO_x/NO_y partitioning associated with the roughly thirty-fold increases in aerosol surface observed (*e.g.*, Rinsland *et al.*, 1994; Webster *et al.*, 1994; Fahey *et al.*, 1993; Mills *et al.*, 1993; Coffey and Mankin, 1993; Sen *et al.*, 1998). Figure 6.21 shows direct observations of perturbations in NO_x/NO_y and ClO/Cl_y at 20 km from Fahey *et al.* (1993) associated with the buildup of Pinatubo aerosols at mid-latitudes. NO_x/NO_y decreases follow the behavior broadly predicted by Prather (1992) and expected from the dominance of N_2O_5 hydrolysis. It is important to note that these observations confirm that some of the ozone depletion observed following Pinatubo must have been due to chlorine chemistry, although they do not in themselves establish its magnitude. Randinaya *et al.* (1997) and Slusser *et al.* (1997) used summer polar observations of NO_2 to show evidence for $BrONO_2$ hydrolysis on sulfate aerosols as well. Observations of enhanced OH at sunrise further suggest that the latter process is significant not only in reducing NO_x via heterogeneous chemistry but also as a source of OH (Hanson and Ravishankara, 1995, 1996; Salawitch *et al.*, 1994; Lary *et al.*, 1996).

Turning to the key chlorine-related species, Avallone *et al.* (1993a,b) and Wilson *et al.* (1993) showed post-Pinatubo ClO observations suggesting heterogeneous perturbations in mid-latitude air. HCl observations by Webster *et al.* (1998) provide evidence that not only is ClO enhanced by high volcanic loading at mid-latitudes as an indirect effect through shifts in NO_2, but also is directly affected to some degree

by chlorine activation (as reflected in reduced HCl). Debate on the magnitude of the latter effect in some regions has focussed on both the rates of chlorine activation in liquid aerosols for mid-latitude conditions and on mass-balance among Cl_y species (see Dessler *et al.*, 1996; 1997; 1998; Stimpfle *et al.*, 1994; Smith *et al.*, 2001). While chlorine-activating reactions on liquid sulfate aerosols are thought to be relatively slow at 20 km for the average temperatures that prevail at mid-latitudes, the strongly non-linear dependence of these reactions on temperatures must be considered. Murphy and Ravishankara (1994) showed that the reaction rate averaged over the actual temperatures including cold fluctuations associated with wave motions will substantially exceed the rate computed for the average temperature. In other words, brief exposure to cold temperatures may alter ClO/Cl_y partitioning and hence enhance ozone depletion at latitudes outside of the polar vortex, especially under high aerosol loads (Webster *et al.*, 1998; Solomon *et al.*, 1998).

Figure 6.21 shows that even rather modest changes in aerosol abundances can substantially affect the ClO/Cl_y partitioning near 20 km. Indeed, Figure 6.21 suggests that aerosol surface area increases of a factor of only about 5 (as observed, for example, in northern mid-latitudes following the relatively minor Mount St. Helens eruption; see Thomason *et al.*, 1997) could increase ClO/Cl_y by 50%, thus greatly enhancing the chlorine-driven local ozone destruction reactions. In addition to local depletion, enhanced ozone destruction at higher latitudes may also mix out to mid-latitudes.

As has been emphasized throughout this chapter, processes that enhance ClO partitioning relative to Cl_y are at the heart of ozone depletion. A point of useful comparison may be drawn by noting that if ClO/Cl_y had been constant from 1980 to 1990, then ClO would increase by about 50% over this decade (due to the roughly 50% increase in Cl_y due to chlorofluorocarbon emissions). However, Figure 6.21 demonstrates that far larger changes in ClO can be rapidly induced by volcanic aerosol increases via their effects on chemical partitioning. Solomon *et al.* (1996; 1998) showed that both the long-term ozone trend at northern mid-latitudes and its year-to-year variations in the 1980s and 1990s are highly likely to be closely tied to volcanic aerosol-driven changes in ClO/Cl_y partitioning (see Figure 6.23 below). Jackman *et al.* (1996) and Zerefos *et al.* (1997) reached similar conclusions with their models, and showed that solar cycle contributions to interannual ozone depletion are much smaller. Several authors have shown that the ozone response to volcanic aerosols before humans perturbed stratospheric chlorine (*e.g.*, in the 19th century after the eruption of Krakatoa) would likely be a slight column increase as a result

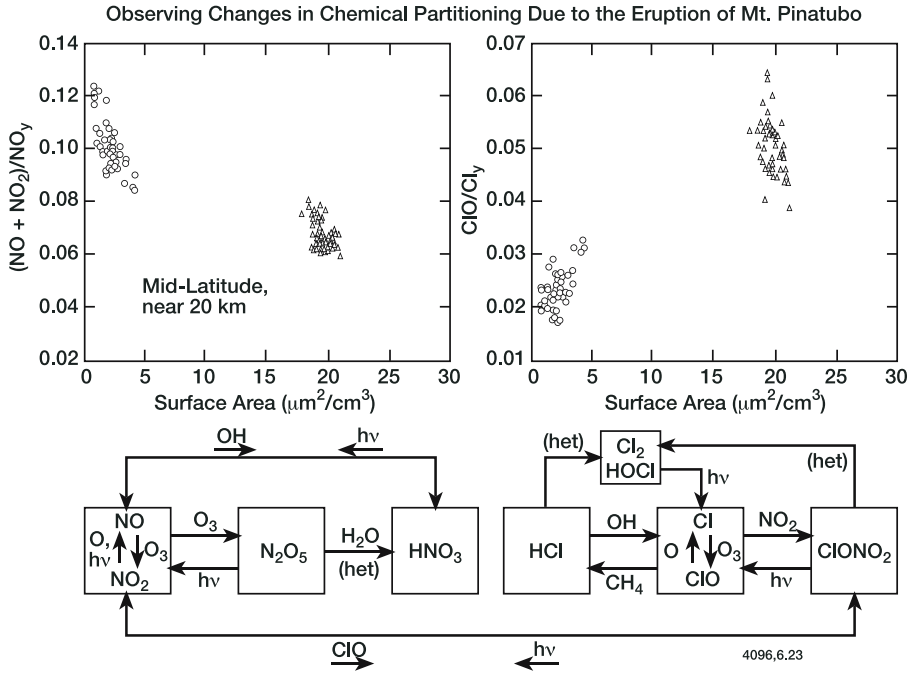

Figure 6.21. Observations of the changes in chemical partitioning as a function of aerosol load after the eruption of Mt. Pinatubo at 20 km at mid-latitudes (Fahey *et al.*, 1993). The primary chemistry responsible for the observed behavior is depicted by the schematic diagram. From Solomon (1999).

of suppression of NO_x-catalyzed destruction as depicted in Figure 6.21 rather than the observed decreases obtained for current chlorine loads (Solomon *et al.*, 1996; Tie and Brasseur, 1995). It is also useful to note that observations such as those at Arosa in Figure 6.20 show no noticeable depletion after a series of large eruptions in the 1960s, most notably the major tropical eruption of Agung in 1963. Observations from many other ground-based sites confirm that the enhancements in aerosol of the 1960s had little effect on ozone (*e.g.*, Bojkov *et al.*, 1995). It is only in the period since about 1980 that chlorine levels have become sufficiently elevated that volcanic perturbations to ClO/Cl_y such as shown in Figure 6.21 result in signficant ozone loss. Hence, the evidence suggests that volcanic particles at mid-latitudes exacerbate halogen-induced ozone depletion in the contemporary stratosphere (much as PSCs do for polar regions, and with some similar chemistry), but cannot on their own significantly destroy stratospheric ozone.

Lary *et al.* (1997) were the first to suggest that soot may also affect northern hemispheric mid-latitude ozone, mainly through possible reactions involving reactive nitrogen species (see Rogaski *et al.*, 1997).

A study by Bekki (1997) further probed this chemistry in some detail, and argued for significant impacts on ozone trends in the vicinity of the tropopause. There is currently debate about the surface area of soot available at stratospheric altitudes, the extent to which it can remain active for chemistry or be quickly 'poisoned', and whether or not chemical data support such perturbations (Gao *et al.*, 1998).

The observation of large mid-latitude ozone depletion following Pinatubo and El Chichón, substantial related changes in chemical species, and a wide range of modelling studies (*e.g.*, Hofmann and Solomon, 1989; Brasseur and Granier, 1992; Michelangeli *et al.*, 1989; Pitari *et al.*, 1993; Bekki and Pyle, 1994; Tie *et al.*, 1997; Solomon *et al.*, 1996; Jackman *et al.*, 1996) provide strong evidence that heterogeneous sulfate aerosol chemistry plays a major role together with manmade chlorine in the processes controlling mid-latitude ozone trends. The observed ClO/Cl_y and NO_x/NO_y dependencies upon volcanic aerosol amounts as shown, for example, in Figure 6.21 may be considered a chemical fingerprint underlying these effects, like the observations of greatly enhanced ClO in the ozone hole region. Another parallel with Antarctic ozone depletion is the observation of a close correspondence in altitude between the region of enhanced Pinatubo aerosol abundances and ozone depletion (as in McGee *et al.*, 1994 and Hofmann *et al.*, 1994, for example). A third fingerprint is the onset and slow relaxation of the ozone depletion after Pinatubo observed at mid-latitudes (see *e.g.*, Solomon *et al.*, 1996; 1998; Jackman *et al.*, 1996) over a period of a few years, mirroring in a slower manner the seasonal depletion of the ozone hole.

6.3.3.2 Dynamical Processes and Mid-latitude Ozone Trends

Several studies examined the extent to which dynamical processes might spread the influence of the ozone hole, either through a one-time 'dilution' at the end of the winter when stratospheric warmings break up the polar vortex or through vortex 'processing' wherein flow of air through the vortex (and hence chemical activation of chlorine) might be transported to lower latitudes (*e.g.*, Tuck, 1989; Tuck *et al.*, 1992; Waugh *et al.*, 1994; 1997; Wauben *et al.*, 1997; Tuck and Proffitt, 1997).

The amount of ozone depletion observed at both northern and southern mid-latitudes is considerably greater than that implied by a one-time end-of-winter dilution process (see *e.g.*, Sze *et al.*, 1989; Prather *et al.*, 1990; Pitari *et al.*, 1992). For the southern hemisphere such one-time dilution likely provides a contribution to the mid-latitude column ozone depletion of about 1-2%. Locally larger but transient dilution effects following the breakup of the Antarctic ozone hole in late spring

have been documented in observations over New Zealand, Australia, Brazil, and Chile (Atkinson *et al.*, 1989; Lehmann *et al.*, 1992; Kirchhoff *et al.*, 1996; 1997a). The city of Punta Arenas, Chile at 53°S occasionally lies just beneath the tip of the Antarctic ozone hole itself for brief periods in October when wave disturbances push the vortex overhead (Kirchhoff *et al.*, 1997a,b). Due to greater dynamical activity, the northern vortex is likely to be subject to a greater degree of processing, and many studies conclude that there is ample evidence for the spread of polar 'filaments' to mid-latitudes at times (Tuck *et al.*, 1992; Gerber and Kampfer, 1994; Pyle *et al.*, 1995; Lutman *et al.*, 1997). However, dynamical analyses and tracer studies suggest that the transport from polar regions alone cannot fully account for the observed ozone losses in mid-latitudes (*e.g.*, Schoeberl *et al.*, 1992; Waugh *et al.*, 1994; Manney *et al.*, 1994; Jones and MacKenzie, 1995; Chipperfield *et al.*, 1996; Wauben *et al.*, 1997; Grewe *et al.*, 1998).

In addition to vortex processing as described above, the notion of PSC processing has also been suggested (wherein PSCs forming outside the vortex provide the sites for heterogeneous reactions), particularly in association with locally cold temperatures that may be related to mountain lee waves and hence of quite small spatial and temporal scale (*e.g.*, Godin *et al.*, 1994; Carslaw *et al.*, 1998). Although the mountain wave clouds themselves are small, air flows through these quasi-stationary clouds, allowing for processing of large quantities of chlorine. All processing mechanisms depend upon heterogeneous chlorine-related chemistry in some fashion and hence connect mid-latitude ozone depletion to chlorine trends, but with important differences in the degree of non-local (*i.e.*, transport-related) linkages. Thus such a mechanism remains tied to chemistry and does not constitute evidence for a purely dynamically-driven effect. Chipperfield (1999) suggests that transport of ozone-depleted air from the Arctic may play a key role in Northern Hemisphere mid-latitude ozone loss. As in the Antarctic, dynamical conditions that modify heterogeneous chemistry should be interpreted as key aspects of setting the stage for ozone loss. However, they can only contribute independently to ozone trends if there is evidence for a trend in those dynamical processes.

Some authors have argued that changes in stratospheric dynamics could have contributed to the observed mid-latitude ozone trends. A review is provided in Ravishankara *et al.* (1999; see references therein). In brief, some studies (*e.g.*, Hood and Zaff, 1995; McCormack and Hood, 1997; Hood *et al.*, 1997; Fusco and Salby, 1999) have argued for a component of purely dynamical change in mid-latitude ozone relating, for example, to changes in the meridional transport of ozone. It is well known that dynamical processes strongly influence ozone variability

from year-to-year, particularly in winter (see for example, Fusco and Salby, 1999). However, evaluation of trends requires long records and analysis of low-frequency changes (*i.e.*, time scales of the order of a decade) rather than a focus on higher frequency (*e.g.*, year-to-year) variations. Some authors suggest that planetary wave activity may indeed have changed in the Northern Hemisphere in particular (*e.g.*, Fusco and Salby, 1999), perhaps in association with the changes in the Arctic Oscillation (AO) noted earlier. Thompson *et al.* (2000) suggest that the systematic changes in the AO could have contributed about 30% to the observed northern mid-latitude ozone depletion. However, the cause of the changes observed in the AO are not well established. They may reflect natural climatic variability, or greenhouse gas coupling to dynamics, or they may be driven at least in part by the ozone change itself through linkage with stratospheric temperature, winds, and/or wave propagation. In the latter case, the dynamical perturbation should be considered a feedback and not a cause. Indeed, changes in ozone can play a major role in temperature gradients, zonal wind and, hence, in stratospheric dynamics, and the feedbacks of ozone loss to dynamics are difficult to distinguish from changes due to other causes (see WMO/UNEP, 2003).

Observations show that about 25% of the observed mid-latitude ozone column depletion occurs above about 25 km, in the altitude range where gas-phase photochemistry is rapid and it is difficult for dynamics to compete (see *e.g.*, SPARC, 1998). A further contribution due to PSC processing and to vortex breakdown is highly likely. Thus, a substantial chemical contribution of at least half of the trend in the column seems difficult to dispute even if locally-driven chemical ozone depletion in the mid-latitude lower stratosphere were to be substantially smaller than suggested by modelling studies and by the post-Pinatubo measurements described above. Thus, the evidence suggests that chlorine chemistry has played an important and very likely dominant role in the observed trends in mid-latitude ozone over the past two decades (for a recent review, see WMO/UNEP, 2003).

6.4 Summary and Outlook

This chapter has outlined the history and conceptual understanding of the processes responsible for ozone depletion by chlorofluorocarbons in the stratosphere. In brief, the long lifetimes of chlorofluorocarbons are reflected in their observed worldwide accumulation in the atmosphere. Their role in stratospheric ozone depletion depends critically on

partitioning processes that follow release of halogen atoms; indeed, the marked contrasts between fluorine (which does not deplete stratospheric ozone), chlorine, and bromine illustrate the central role of partitioning chemistry. Table 6.1 summarizes a series of spatial and temporal fingerprints that connect chlorine chemistry to ozone depletion. Observational evidence for gas-phase chlorine chemistry impacts on ozone is provided, for example, by observations of the ClO/Cl_y and ozone trend profiles above about 25 km at mid latitudes and by the similarities in their observed latitudinal distributions.

The cold conditions of the Antarctic winter and spring stratosphere lead to formation of polar stratospheric clouds. Heterogeneous chemistry involving manmade chlorine takes place on these surfaces and results in the dramatic and unanticipated Antarctic ozone hole. The heterogeneous activation of chlorine from both its HCl and $ClONO_2$ reservoirs and the suppression of the NO_2 (that would otherwise reform $ClONO_2$) alters chlorine partitioning and allows effective ozone loss in cold sunlit air. The close correspondence between observed enhancements in ClO and depleted Antarctic ozone through independent observational methods as functions of altitude, latitude and longitude illustrates the key role of these chemical partitioning processes in producing the ozone hole. A broad range of chemical observations of HCl, HNO_3, NO_2, OClO, and other species support and extend this picture. Quantitative numerical modelling studies that include detailed analyses of transport and chemistry further connect the enhanced ClO produced by heterogeneous chemistry to the formation of the Antarctic ozone hole.

Scientific understanding of PSCs and heterogeneous chemistry has evolved considerably in recent years. The detailed microphysical mechanisms responsible for freezing of PSC particles and for denitrification are subject to debate at present, but these processes appear to be less critical to ozone depletion than once thought. There is evidence from field, laboratory, and modelling studies that PSCs can be composed not only of solid water ice and nitric acid hydrates but also of liquid solutions of water, sulfuric acid, and nitric acid. The chemistry associated with these varying surfaces displays important differences in detail, but has the common feature that all can suppress NO_2 and activate chlorine from the reservoir species, making the ozone depletion process more continuous in temperature and less dependent upon the abrupt temperature thresholds that are associated with formation of solids than previously thought.

Observations of enhanced Antarctic and mid-latitude ozone depletion following the eruption of Pinatubo confirm the impact of liquid aerosol surfaces on chlorine and nitrogen partitioning chemistry. Observations and laboratory studies have demonstrated the efficacy of heterogeneous

processes on such surfaces. As in the Antarctic, concurrent observations of a broad range of chemical species show evidence for surface reactions associated with particles, which work to enhance ClO/Cl_y partitioning at mid-latitudes. Dilution and processing of the polar ozone losses also contribute to mid-latitude ozone depletion. While some studies suggest a role for a purely dynamical trend in mid-latitude ozone depletion, these have not yet succeeded in quantifying a significant independent contribution.

There is abundant evidence for heterogeneous perturbations to Arctic chemistry through observations of ClO, OClO, HCl, and many other key gases. Arctic ozone reached record low values in many years in the 1990s, linked not only with heterogeneous chemistry on Pinatubo aerosols but also with unusually cold spring temperatures. A chemical contribution to these low values has been documented with a variety of methods including trajectory 'matches', chemistry transport modelling, and tracer correlation studies. The fundamental question of the cause or causes of record-low temperatures in many of the Arctic winter/spring seasons of the 1990s remains a topic of debate and a key issue.

In closing, Figures 6.22 and 6.23 are presented to show the impact of changes in global emissions of chlorofluorocarbons and the likely future of the ozone layer based on the conceptual picture developed in this book. Figure 6.22 displays surface observations of CFC-11 and methyl chloroform. The latter gas is the only short-lived industrial chlorofluorocarbon produced in large amounts in the 1970s and 1980s. Because of its five year lifetime, the abundances of methyl chloroform have already begun to decline, due to reduced global emissons. Those of CFC-11 are just passing their peak and are projected to decline slowly in coming decades, reflecting its 50-year lifetime.

Figure 6.23 (top) shows the past and future projections of the total tropospheric chlorine content (which leads the stratosphere by 3-5 years). It was anticipated that the combined effect of all CFCs would lead to a peak stratospheric chlorine loading in the late 1990s. Indeed, observations of stratospheric HCl displayed a pronounced slowing in the late 1990s, and suggest that the stratospheric Cl_y then began to level off (Anderson *et al.*, 2000).

By about 2050, the chlorine will return to levels close to those of the mid- to late 1970s when ozone depletion was first apparent. All other things being equal, the Antarctic ozone hole and mid-latitude ozone depletion will likely disappear around this time. However, the key role of temperature and aerosols in modulating ozone depletion must also be considered. The unusually cold Arctic winter/springs of recent years stand at the time of this writing as a critical challenge to our understanding that could affect the future of polar ozone depletion in

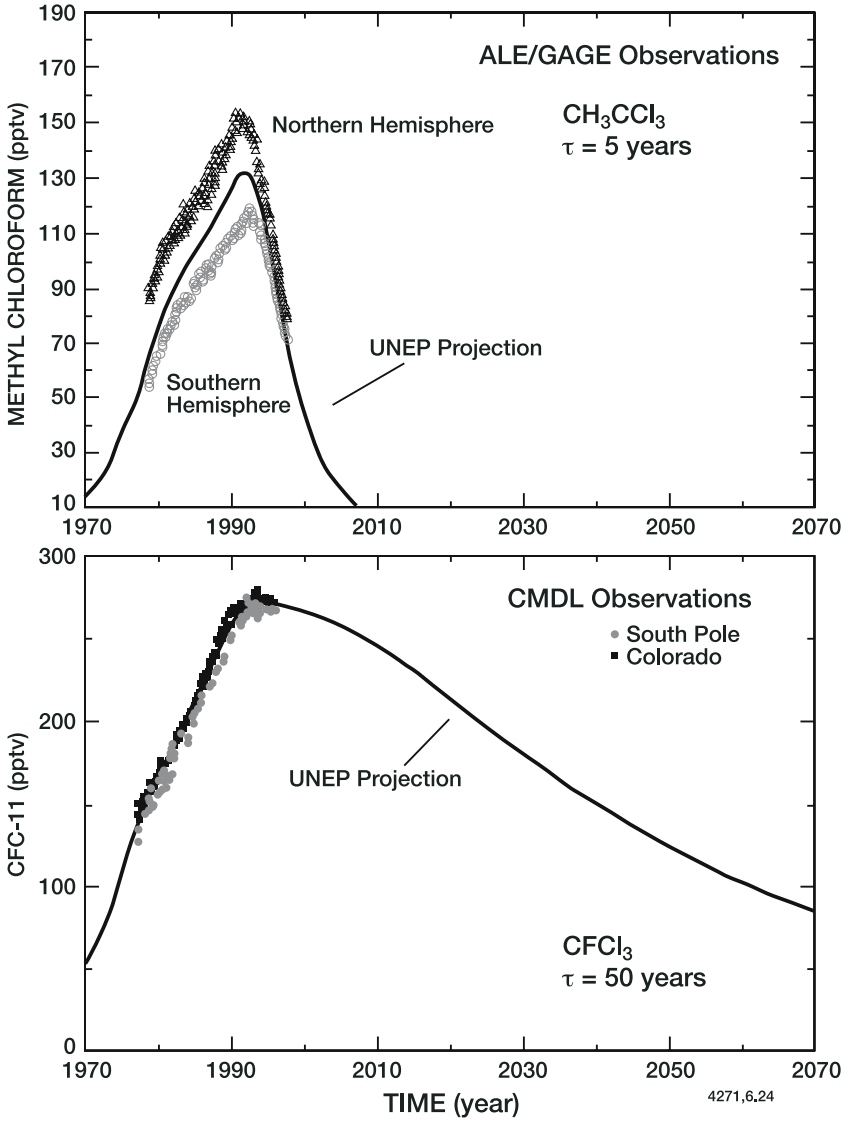

Figure 6.22. Observations of CH_3CCl_3 and CFC-11 from the Atmospheric Lifetime Experiment/ Global Atmospheric Gases Experiment (ALE/GAGE) and Climate Monitoring and Diagnostics Laboratory (CMDL) databases, respectively. The projections from the baseline emission scenario of WMO/UNEP (1998) are shown for comparison. The scenario includes estimated industrial production and emission for each year (including the effects of delayed release in some applications such as refrigeration, see WMO/UNEP, 1998). The methyl chloroform data show a rapid decline observed in recent years due to reduced emissions and the 5-year lifetime of this gas (Prinn *et al.*, 1995; WMO/UNEP, 1998), while the CFC-11 abundances have just passed their peak (Elkins *et al.*, 1993; Montzka *et al.*, 1996; updated courtesy of J. Elkins and S. Montzka) and are projected to decline slowly in the future due to the 50-year lifetime of this gas. From Solomon (1999).

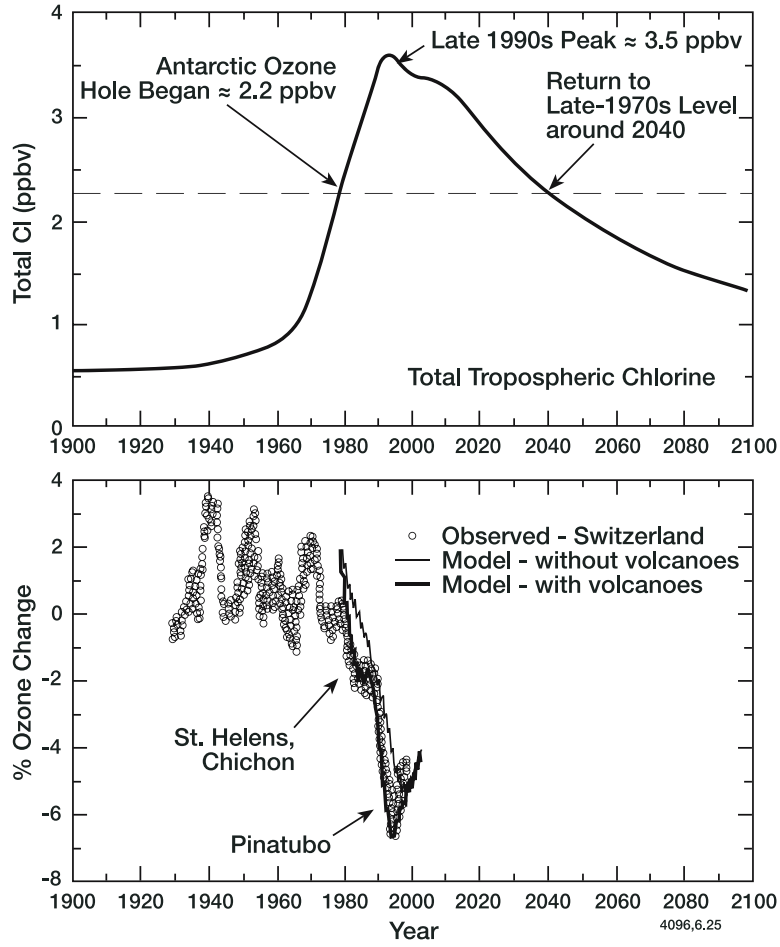

Figure 6.23. The top panel shows the total tropospheric chlorine content estimated from the baseline scenario in WMO/UNEP (1998); this is based on a gas-by-gas analysis like those shown in Figure 6.22. The bottom panel shows the changes in the 5-year running mean ozone observed over Switzerland (Staehelin *et al.*, 1998a,b) compared to a model calculation for 45°N applying the same time averaging, with and without considering the effects of volcanic enhancements in aerosol chemistry (from the model of Solomon *et al.*, 1996; 1998). The major eruptions since 1980 were those of El Chichón in 1982 and Mt. Pinatubo in 1991. Updated from Solomon (1999).

both hemispheres. For example, if the majority of future Arctic winters were to be colder than average, then the Arctic ozone depletion would likely be prolonged. The bottom panel in Figure 6.23 shows the long-running Arosa, Switzerland, ozone record illustrating the onset of mid-latitude ozone depletion, its likely links to heterogeneous chemistry, and its simulation with a current stratospheric chemistry model including

the processes described here. The changes in ozone observed over Arosa are in good agreement with the zonally averaged global satellite data discussed earlier, and the time-averaged trends obtained there appear to be generally representative of northern mid-latitudes. The figure illustrates that the future of mid-latitude ozone depletion is likely to be linked not only to chlorine but also in part to volcanoes for at least several decades. If there were to be an extremely large volcanic eruption such as that of Tamboura (whose 1815 eruption is estimated at about three times the stratospheric impact of Mt. Pinatubo) in coming decades, it is likely that mid-latitude ozone depletion would be increased even though the chlorine content of the stratosphere is expected to be lower than it is today. This illustrates the connection between the accumulation of chlorine in today's atmosphere due to human activities of the industrial era and the unpredictable time scales of geologic phenomena that couple into this altered chemical state.

This book has emphasized many spatial and temporal 'fingerprints' that illustrate the role of chlorine in depleting ozone in the contemporary stratosphere (Table 6.1). Indeed, it is the structure of the ozone loss in space (*e.g.*, in the 40 km region) and time (*e.g.*, in the Antarctic spring and in mid-latitudes in the years following Mt. Pinatubo) that tests and supports scientific understanding, illustrating how gas-phase and heterogeneous modulation of ClO/Cl_y partitioning affects ozone depletion. Through the impacts of this chemistry, the stratospheric ozone layer in the 21^{st} century will continue to reflect the impact of the changes in chlorine enacted in the 20^{th}.

Table 6.1 Summary of Key Fingerprints of Ozone Depletion

Observation	*Method*	*Latitude* (°)	*Altitude* (km)	*Primary Chemistry Linkage*
Profile shapes of upper stratospheric ozone depletion and ClO/Cl_y	Satellite and ground-based	Northern Hemisphere mid-latitude	30-50	Gas-phase chlorine chemistry, particularly partitioning processes
Latitudinal structure of upper stratospheric ozone depletion and ClO	Satellite	Polar, mid-latitude, and tropical	30-50	Gas-phase chlorine chemistry, particularly HCl/ClO
Latitudinal structure of ClO, HCl, NO, NO_2, and ozone loss in polar regions	Airborne and satellite	≈50-85°S; 50-85°N	20	Heterogeneous chlorine activation and NO_2 suppression
Vertical structure of seasonal ozone loss and PSCs in polar regions	Balloon-borne, lidar, and satellite	90°S, 50-85°S, 50-85°N	12-24 km	Heterogeneous chlorine activation
Seasonal changes in PSCs, ozone depletion, OClO, ClO, HCl, and $ClONO_2$	Balloon-borne, lidar, ground-based, and satellite	≈50-90° in both polar regions	≈12-24 km and column	Heterogeneous chemistry
Post-Pinatubo (≈1992-1995) ozone depletion and recovery; contrast with post-Agung (≈1964-1968)	Ground-based and some satellite	Mid-latitudes and polar regions	near 20 km and column	Heterogeneous chemistry
Post-Pinatubo changes in stratospheric chemical state and aerosol content (NO_x, ClO, HNO_3, OClO)	Airborne, ground-based, balloon-borne, and satellite	Mid-latitudes and some polar	near 20 km, near tropopause, and column	Heterogeneous chemistry, particularly N_2O_5 hydrolysis and some chlorine activation

References

Adrian, G.P., M. Baumann, T. Blumenstock, H. Fischer, A. Friedle, L. Gerhardt, G. Maucher, H. Oelhof, W. Scheuerpflug, P. Thomas, O. Trieschmann, and A. Wegner, First results of ground-based FTIR measurements of atmospheric trace gases in north Sweden and Greenland during EASOE. *Geophys Res Lett: 21*, 1343, 1994.

Adriani, A., G. Fiocco, G.P. Gobbi, and F. Congeduti, Correlated behavior of aerosol and ozone contents of the stratosphere after the El Chichón eruption. *J Geophys Res: 92*, 8365, 1987.

Adriani, A., T. Deshler, G. Di Donfrancesco, and G.P. Gobbi, Polar stratospheric clouds and volcanic aerosol during spring 1992 over McMurdo Station, Antarctica: Lidar and particle counter comparisons. *J Geophys Res: 100*, 25,877, 1995.

Allen, D.R., R.M. Bevilacqua, G.E. Nedoluha, C.E. Randall, and G.L. Manney, Unusual stratospheric transport and mixing during the 2002 Antarctic winter, *Geophys Res Lett: 30*, 1599, 2003.

Anderson, J.G., J.J. Margitan, and D.H. Stedman, Atomic chlorine and the chlorine monoxide radical in the stratosphere: Three in-situ observations. *Science: 198*, 501, 1977.

Anderson, J.G., W.H. Brune, and M.H. Proffitt, Ozone destruction by chlorine radicals within the Antarctic vortex: The spatial and temporal evolution of ClO-O_3 anticorrelation based on in situ ER-2 Data. *J Geophys Res: 94*, 11,479, 1989.

Anderson, J., J.M. Russell III, S. Solomon, and L.E. Deaver, Halogen occultation experiment confirmation of stratospheric chlorine decreases in accordance with the Montreal Protocol. *J Geophys Res: 105*, 4483, 2000.

Andrews, D.G., J.R. Holton, and C.B. Leovy, *Middle Atmosphere Dynamics*. Academic Press, Orlando, Fla, USA, 1987.

Atkinson, R.J., W.A. Matthews, P.A. Newman, and R.A. Plumb, Evidence of mid-latitude impact of Antarctic ozone depletion. *Nature: 340*, 290, 1989.

Austin, J., R.R. Garcia, J.M. Russell III, S. Solomon, and A.F. Tuck, On the atmospheric photochemistry of nitric acid. *J Geophys Res: 91*, 5477, 1986.

Austin, J., N. Butchart, and K.P. Shine, Possibility of an Arctic ozone hole in a doubled-CO_2 climate. *Nature: 360*, 221, 1992.

Avallone, L.M., D.W. Toohey, W.H. Brune, R.J. Salawitch, A.E. Dessler, and J.G. Anderson, Balloon-borne in situ measurements of ClO and ozone: Implications for heterogeneous chemistry and mid-latitude ozone loss. *Geophys Res Lett: 20*, 1795, 1993a.

Avallone, L.M., D.W. Toohey, M.H. Proffitt, J.J. Margitan, K.R. Chan, and J.G. Anderson, In situ measurements of ClO at mid-latitudes: Is there an effect from Mt. Pinatubo? *Geophys Res Lett: 20*, 2519, 1993b.

Baldwin, M.P., and T.J. Dunkerton, Stratospheric harbingers of anomalous weather regimes. *Science: 29*, 581, 2001.

Barnett, J.J., J.T. Houghton, and J.A. Pyle, Temperature dependence of the ozone concentration near the stratopause. *Quart J Roy Meteorol Soc: 101*, 245, 1975.

Becker, G., R. Müller, D.S. McKenna, M. Rex, and K.S. Carslaw, Ozone loss rates in the Arctic stratosphere in the winter 1991/92: Model calculations compared with match results. *Geophys Res Lett: 23*, 4325, 1998.

Bekki, S., On the possible role of aircraft-generated soot in the middle latitude ozone depletion. *J Geophys Res: 102*, 10,751, 1997.

Bekki, S., and J.A. Pyle, A two-dimensional modeling study of the volcanic eruption of Mount Pinatubo. *J Geophys Res: 99*, 18,861, 1994.

Bell, W., N.A. Martin, T.D. Gardiner, N.R. Swann, P.T. Woods, P.F. Fogal, and J.W. Waters, Column measurements of stratospheric trace species over Åre, Sweden in the winter of 1991-1992. *Geophys Res Lett: 21*, 1347, 1994.

Bevilacqua, R.M., C.P. Aellig, D.J. Debrestian, M.D. Fromm, K. Hoppel, J.D. Lumpe, E.P. Shettle, J.S. Hornstein, C.E. Randall, D.W. Rusch, and J.E. Rosenfield, POAM II ozone observations in the Anarctic ozone hole in 1994, 1995, and 1996. *J Geophys Res: 102*, 23,643, 1997.

Bojkov, R.D., and V.E. Fioletov, Changes of the lower stratospheric ozone over Europe and Canada. *J Geophys Res: 102*, 1337, 1997.

Bojkov, R.D., C.S. Zerefos, D.S. Balis, I.C. Ziomas, and Z.F. Bais, Record low total ozone during northern winters of 1992-1993. *Geophys Res Lett: 20*, 1351, 1993.

Bojkov, R.D., L. Bishop, and V.E. Fioletov, Total ozone trends from quality controlled ground-based data (1964-1994). *J Geophys Res: 100*, 25,867, 1995.

Borrmann, S., S. Solomon, J.E. Dye, and B. Luo, The potential of cirrus clouds for heterogenous chlorine activation. *Geophys Res Lett: 23*, 2133, 1996.

Borrmann, S., S. Solomon, J.E. Dye, D. Baumgardner, K.K. Kelly, and K.R. Chan, Heterogeneous reactions on stratospheric background aerosols, volcanic sulfuric acid droplets, and Type I polar stratospheric clouds: Effects of temperature fluctuations and differences in particle phase. *J Geophys Res: 102*, 3639, 1997a.

Borrmann, S., S. Solomon, L. Avallone, D. Toohey, and D. Baumgardner, On the occurrence of ClO in cirrus clouds and volcanic aerosol in the tropopause region. *Geophys Res Lett: 24*, 2011, 1997b.

Brasseur, G., The response of the middle atmosphere to long-term and short-term solar variability: A two-dimensional model. *J Geophys Res: 98*, 23,079, 1993.

Brasseur, G., and S. Solomon, *Aeronomy of the Middle Atmosphere.* D. Reidel, Hingham, Mass., 1984.

Brasseur, G., and M.H. Hitchman, Stratospheric response to trace gas perturbations: Changes in ozone and temperature distributions. *Science: 240*, 634, 1988.

Brasseur, G., and C. Granier, Mount Pinatubo aerosols, chlorofluorocarbons, and ozone depletion. *Science: 257*, 1239, 1992.

Brasseur, G., P. DeBaets, and A. de Rudder, Solar variability and minor constituents in the lower thermosphere and in the mesosphere. *Space Sci Rev: 34*, 377, 1983.

Brasseur, G.P., X.X. Tie, P.J. Rasch, and F. Lefevre, A three dimensional simulation of the Antarctic ozone hole: Impact of anthropogenic chlorine on the lower stratosphere and upper troposphere. *J Geophys Res: 102*, 8909, 1997.

Bregman, A., M. van den Broek, K.S. Carslaw, R. Müller, T. Peter, M.P. Scheele, and J. Leieveld, Ozone depletion in the late winter lower Arctic stratosphere: Observations and model results. *J Geophys Res: 102*, 10,815, 1997.

Brewer, A.W., Evidence for a world circulation provided by the measurements of helium and water vapour distribution in the stratosphere. *Quart J Roy Meteorol Soc: 75*, 351, 1949.

Brune, W.H., J.G. Anderson, and K.R. Chan, In situ observations of BrO over Antarctica: ER-2 Aircraft results from 54°S to 72°S Latitude. *J Geophys Res: 94*, 16,639, 1989.

Brune, W.H., D.W. Toohey, J.G. Anderson, and K.R. Chan, In situ observations of ClO in the Arctic stratosphere: ER-2 aircraft results from 59°N to 80°N latitude. *Geophys Res Lett: 17*, 505, 1990.

Brune, W.H., J.G. Anderson, D.W. Toohey, D.W. Fahey, S.R. Kawa, R.L. Jones, D.S. McKenna, and L.R. Poole, The potential for ozone depletion in the arctic polar stratosphere. *Science: 252*, 1260, 1991.

Cadle, R.D., P. Crutzen, and D. Ehhalt, Heterogeneous chemical reactions in the stratosphere. *J Geophys Res: 80*, 3381, 1975.

Callis, L.B., and M. Natarajan, The Antarctic ozone minimum: Relationship to odd nitrogen, odd chlorine, the final warming, and the 11-year solar cycle. *J Geophys Res: 91*, 10,771, 1986.

Carslaw, K.S., B.P. Luo, S.L. Clegg, T. Peter, P. Brimblecombe, and P.J. Crutzen, Stratospheric aerosol growth and HNO_3 gas phase depletion from coupled HNO_3 and water uptake by liquid particles. *Geophys Res Lett: 21*, 2479, 1994.

Carslaw, K.S., and T. Peter, Uncertainties in reactive uptake coefficients for solid stratospheric particles-1. Surface chemistry. *Geophys Res Lett: 24*, 1743, 1997.

Carslaw, K.S., T. Peter, and S.L. Clegg, Modeling the composition of liquid stratospheric aerosols. *Rev Geophys: 35*, 125, 1997a.

Carslaw, K.S., T. Peter, and R. Müller, Uncertainties in reactive uptake coefficients for solid stratospheric particles-2. Effect on ozone depletion. *Geophys Res Lett: 24*, 1747, 1997b.

Carslaw, K.S., M. Wirth, A. Tsias, B.P. Luo, A. Dörnbrack, M. Leutbecher, H. Volkert, W. Renger, J.T. Bacmeister, E. Reimer, and T. Peter, Increased stratospheric ozone depletion due to mountain-induced atmospheric waves. *Nature: 391*, 675, 1998.

Chandra, S., C.H. Jackman, A.R. Douglass, E.L. Fleming, and D.B. Considine, Chlorine catalyzed destruction of ozone: Implications for ozone variability in the upper stratosphere. *Geophys Res Lett: 20*, 351, 1993.

Chen, L., J. London, and G. Brasseur, Middle atmospheric ozone and temperature responses to solar irradiance variations over 27-day periods. *J Geophys Res: 102*, 29,957, 1997.

Chin, M., and D.D. Davis, A reanalysis of carbonyl sulfide as a source of stratospheric background sulfur aerosols. *J Geophys Res: 100*, 8993, 1995.

Chipperfield, M.P., Multi-annual simulations with a three-dimensional chemical transport model. *J Geophys Res: 104*, 1781, 1999.

Chipperfield, M.P., and J.A. Pyle, Model sensitivity studies of Arctic ozone depletion. *J Geophys Res: 103*, 28,389, 1998.

Chipperfield, M.P., D. Cariolle, and P. Simon, A 3D transport model study of chlorine activation during EASOE. *Geophys Res Lett: 21*, 1467, 1994.

Chipperfield, M.P., A.M. Lee, and J.A. Pyle, Model calculations of ozone depletion in the Arctic polar vortex for 1991/92 to 1994/95. *Geophys Res Lett: 23*, 559, 1996.

Chubachi, S., Preliminary result of ozone observations at Syowa Station from February, 1982, to January, 1983. *Mem Natl Inst Polar Res Jap*, Spec Issue 34, 13, 1984.

Coffey, M.T., and W.G. Mankin, Observations of the loss of stratospheric NO_2 following volcanic eruptions. *Geophys Res Lett: 20*, 2873, 1993.

Coffey, M.T., W.G. Mankin, and A. Goldman, Airborne measurements of stratospheric constituents over Antarctica in the austral spring, 1987: 2, Halogen and nitrogen trace gases. *J Geophys Res: 94*, 16,597, 1989.

Cohen, R.C., P.O. Wennberg, R.M. Stimpfle, J. Koplow, J.G. Anderson, D.W. Fahey, E.L. Woodbridge, E.R. Keim, R. Gao, M.H. Proffitt, M. Loewenstein, and K.R. Chan, Are models of catalytic removal of O_3 by HO_x accurate? Constraints from in situ measurements of the OH to HO_2 ratio. *Geophys Res Lett: 21*, 2539, 1994.

Collins, R.L., K.P. Bownan, and C.S. Gardner, Polar stratospheric clouds at the South Pole in 1990: Lidar observations and analysis. *J Geophys Res: 98*, 1001, 1993.

Conway, R.R., M.E. Summers, M.H. Stevens, J.G. Cardon, P. Preusse, and D. Offermann, Satellite observations of upper stratospheric and mesospheric OH: the HO_x dilemma. *Geophys Res Lett: 27*, 2613, 2000.

Cox, R.A., A.R. MacKenzie, R.H. Müller, T. Peter, and P.J. Crutzen, Activation of stratospheric chlorine by reactions in liquid sulphuric acid. *Geophys Res Lett: 21*, 1439, 1994.

Coy, L., E.R. Nash, and P.A. Newman, Meteorology of the polar vortex: Spring 1997. *Geophys Res Lett: 24*, 2693, 1997.

Crewell, S., K. Künzi, H. Nett, T. Wehr, and P. Hartogh, Aircraft measurements of ClO and HCl during EASOE 1991/92. *Geophys Res Lett: 21*, 1267, 1994.

Crutzen, P.J., The influence of nitrogen oxide on the atmospheric ozone content. *Quart J Roy Meteorol Soc: 96*, 320, 1970.

Crutzen, P.J., Ozone production rates in an oxygen-hydrogen-nitrogen oxide atmosphere. *J Geophys Res: 76*, 7311, 1971.

Crutzen, P.J., Estimates of possible future ozone reductions from continued use of fluoro-chloro-methanes (CF_2Cl_2, $CFCl_3$). *Geophys Res Lett: 1*, 205, 1974.

Crutzen, P.J., The possible importance of OCS for the sulfate layer of the atmosphere. *Geophys Res Lett: 3*, 73, 1976.

Crutzen, P.J., and C.T. Howard, Effect of the HO_2 + NO reaction rate constant on one-dimensional model calculations of stratospheric ozone perturbations. *Pure Appl Geophys: 116*, 497, 1978.

Crutzen, P.J., and F. Arnold, Nitric acid cloud formation in the cold Antarctic stratosphere: A major cause for the springtime 'ozone hole'. *Nature: 324*, 651, 1986.

Crutzen, P.J., I.S.A. Isaksen, and G.C. Reid, Solar proton events: Stratospheric sources of nitric oxide. *Science: 189*, 457, 1975.

Crutzen, P.J., I.S.A. Isaksen, and J.R. McAfee, Impact of chlorocarbon industry on the ozone layer. *J Geophys Res: 83*, 345, 1978.

Dalgarno, A., Atmospheric reactions with energetic particles. *Space Res: 7*, 849, 1971.

Dameris, M., V. Grewe, R. Hein, C. Schnadt, C. Brühl, and B. Steil, Assessment of the future development of the ozone layer. *Geophys Res Lett: 25*, 3579, 1998.

Del Negro, L.A., D.W. Fahey, S.G. Donnelly, R.S. Gao, E.R. Keim, R.C. Wamsley, E.L. Woodbridge, J.E. Dye, D. Baumgardner, B.W. Gandrud, J.C. Wilson, H.H. Jonsson, M. Loewenstein, J.R. Podolske, C.R. Webster, R.D. May, D.R. Worsnop, A. Tabazadeh, M.A. Tolbert, K.K. Kelly, and K.R. Chan, Evaluating the role of NAT, NAD, and liquid $H_2SO_4/H_2O/HNO_3$ solutions in Antarctic polar stratospheric cloud aerosol: Observations and implications. *J Geophys Res: 102*, 13,255, 1997.

de Zafra, R.L., M. Jaramillo, A. Parrish, P. Solomon, B. Connor, and J. Barnett, High concentrations of chlorine monoxide at low altitudes in the Antarctic spring stratosphere: Diurnal variation. *Nature: 328*, 408, 1987.

de Zafra, R.L., M. Jaramillo, J. Barrett, L.K. Emmons, P.M. Solomon, and A. Parrish, New observations of a large concentration of ClO in the springtime lower stratosphere

over Antarctica and its implications for ozone-depleting chemistry. *J Geophys Res: 94*, 11,423, 1989.

de Zafra, R.L., L.K. Emmons, J.M. Reeves, and D.T. Shindell, An overview of millimeter-wave spectroscopic measurements of chlorine monoxide at Thule, Greenland, February-March, 1992: Vertical profiles, diurnal variation, and longer-term trends. *Geophys Res Lett: 21*, 1271, 1994.

Deniel, C., R.M. Bevilacqua, J.P. Pommereau, and F. Lefevre, Arctic chemical ozone depletion during the 1994-1995 winter deduced from POAM II satellite observations and the REPROBUS three-dimensional model. *J Geophys Res: 103*, 19,231, 1998.

Deshler, T., A. Adriani, G.P. Gobbi, D.J. Hofmann, G. Di Donfrancesco, and B.J. Johnson, Volcanic aerosol and ozone depletion within the Antarctic polar vortex during the austral spring of 1991. *Geophys Res Lett: 19*, 1819, 1992.

Dessler, A.E., D.B. Considine, G.A. Morris, M.R. Schoeberl, J.M. Russell III, A.E. Roche, J.B. Kumer, J.L. Mergenthaler, J.W. Waters, J.C. Gille, and G.K. Yue, Correlated observations of HCl and $ClONO_2$ from UARS and implications for stratospheric chlorine partitioning. *Geophys Res Lett: 22*, 1721, 1995.

Dessler, A.E., S.R. Kawa, A.R. Douglass, D.B. Considine, J.B. Kumer, A.E. Roche, J.L. Mergenthaler, J.W. Waters, J.M. Russell III, and J.C. Gille, A test of the partitioning between ClO and $ClONO_2$ using simultaneous UARS measurements of ClO, NO_2 and $ClONO_2$. *J Geophys Res: 101*, 12,515, 1996.

Dessler, A.E., D.B. Considine, J.E. Rosenfield, S.R. Kawa, A.R. Douglass, and J.M. Russell, III, Lower stratospheric chlorine partitioning during the decay of the Mt. Pinatubo aerosol cloud. *Geophys Res Lett: 24*, 1623, 1997.

Dessler, A.E., M.D. Burrage, J.-U. Grooß, J.R. Holton, J.L. Lean, S.T. Massie, M.R. Schoeberl, A.R. Bouglass, and C.H. Jackman, Selected science highlights from the first 5 years of the Upper Atmosphere Research Satellite (UARS) Program. *Rev Geophys: 36*, 183, 1998.

Dickinson, R.E., Method of parameterization for infrared cooling between the altitudes of 30 and 70 km. *J Geophys Res: 78*, 4451, 1973.

Dobson, G.M.B., Observations of the amount of ozone in the Earth's atmosphere and its relation to other geophysical conditions. *Proc R Soc London, Ser A.: 129*, 411, 1930.

Dobson, G.M.B., Forty years' research on atmospheric ozone at Oxford: A history. *App Opt: 7*, 387, 1968.

Donovan, D.P., H. Fast, Y. Makino, J.C. Bird, A.I. Carswell, J. Davies, T.J. Duck, J.W. Kaminski, C.T. M^{c}Elroy, R.L. Mittermeier, S.R. Pal, V. Savastiouk, D. Velkov, and J.A. Whiteway, Ozone, column ClO, and PSC measurements made at the NDSC Eureka observatory (80°N, 86°W) during the spring of 1997. *Geophys Res Lett: 24*, 2709, 1997.

Douglass, A.R., and R.B. Rood, Derivation of photochemical information near 1 mbar from ozone and temperature data. *J Geophys Res: 91*, 13,153, 1986.

Douglass, A.R., R.B. Rood, and R.S. Stolarski, Interpretation of ozone temperature correlations. 2, Analysis of SBUV ozone data. *J Geophys Res: 90*, 10,693, 1985.

Douglass, A.R., M.R. Schoeberl, R.S. Stolarski, J.W. Waters, J.M. Russell III, A.E. Roche, and S.T. Massie., Interhemispheric differences in springtime production of HCl and $ClONO_2$ in the polar vortices. *J Geophys Res: 100*, 13,967, 1995.

Elkins, J.W., T.M. Thompson, T.H. Swanson, J.H. Butler, B.D. Hall, S.O.E Cummings, D.A. Fisher, and A.G. Raffo, Decrease in the growth rates of atmospheric chlorofluorocarbons 11 and 12. *Nature: 364*, 780, 1993.

Fahey, D.W., D.M. Murphy, K.K. Kelly, M.K.W. Ko, M.H. Proffitt, C.S.E Eubank, G.V. Ferry, M. Loewenstein, and K.R. Chan. Measurements of nitric oxide and total reactive nitrogen in the Antarctic stratosphere: Observations and chemical implications. *J Geophys Res: 94*, 16,665, 1989a.

Fahey, D.W., K.K. Kelly, G.V. Ferry, L.R. Poole, J.C. Wilson, D.M. Murphy, M. Loewensten, and K.R. Chan, In situ measurements of total reactive nitrogen, total water and aerosol in a polar stratospheric cloud in the Antarctic. *J Geophys Res: 94*, 11,299, 1989b.

Fahey, D.W., S.R. Kawa, and K.R. Chan, Nitric oxide measurements in the arctic winter stratosphere. *Geophys Res Lett: 17*, 489, 1990a.

Fahey, D.W., K.K. Kelly, S.R. Kawa, A.F. Tuck, M. Loewenstein, K.R. Chan, and L.E. Heidt, Observations of denitrification and dehydration in the winter polar stratospheres. *Nature: 344*, 321, 1990b.

Fahey, D.W., S.R. Kawa, E.L. Woodbridge, P. Tin, J.C. Wilson, H.H. Jonsson, J.E. Dye, D. Baumgardner, S. Borrmann, D.W. Toohey, L.M. Avallone, M.H. Proffitt, J. Margitan, M. Loewenstein, J.R. Podolske, R.J. Salawitch, S.C. Wofsy, M.K.W. Ko, D.E. Anderson, M.R. Schoeberl, and K.R. Chan, In situ measurements constraining the role of sulfate aerosols in mid-latitude ozone depletion. *Nature: 363*, 509, 1993.

Fahey, D.W., R.S. Gao, K.S. Carslaw, J. Kettleborough, P.J. Popp, M.J. Northway, J.C. Holecek, S.C. Ciciora, R.J. McLaughlin, T.L. Thompson, R.H. Winkler, D.G. Baumgardner, B. Gandrud, P.O. Wennberg, S. Dhaniyala, K. McKinney, Th. Peter, R.J. Salawitch, T.P. Bui, J.W. Elkins, C.R. Webster, E.L. Atlas, H. Jost, J.C. Wilson, R.L. Herman, A. Kleinböhl, M. von König, The detection of large HNO_3-containing particles in the winter Arctic stratosphere. *Science: 291*, 1026, 2001.

Farman, J.C., B.G. Gardiner, and J.D. Shanklin, Large losses of total ozone in Antarctica reveal seasonal ClO_x/NO_x interaction. *Nature: 315*, 207, 1985.

Farmer, C.B., G.C. Toon, P.W. Shaper, J.F. Blavier, and L.L. Lowes, Stratospheric trace gases in the spring 1986 Antarctic atmosphere. *Nature: 329*, 126, 1987.

Fels, S.B., J.D. Mahlman, M.D. Schwarzkopf, and R.W. Sinclair, Stratospheric sensitivity to perturbations in ozone and carbon dioxide radiative and dynamical response. *J Atmos Sci: 37*, 2265, 1980.

Finger, F.G., R.M. Nagatani, M.E. Gelman, C.S. Long, and A.J. Miller, Consistency between variations of ozone and temperature in the stratosphere. *Geophys Res Lett: 22*, 3477, 1995.

Fleming, E.L., S. Chandra, J.J. Barnett, and M. Corney, Zonal mean temperatures, pressures, zonal winds, and geopotenial heights as a function of latitude. *Adv Space Res: 10*, 1211, 1990.

Forster, P.M., and K.P. Shine, Stratospheric water vapor changes as a possible contributor to observed stratospheric cooling. *Geophys Res Lett: 26*, 3309, 1999.

Fusco, A.C., and M.L. Salby, Interannual variations of total ozone and their relationship to variations of planetary wave activity. *J Clim: 12*, 1619, 1999.

Gandrud, B.W., J.E. Dye, D. Baumgardner, G.V. Ferry, M. Loewenstein, K.R. Chan, L. Sanford, B. Gary, and K. Kelly, The January 30, 1989 Arctic polar stratospheric clouds (PSC) event: Evidence for a mechanism of dehydration. *Geophys Res Lett: 17*, 457, 1990.

Gao, R.S., B. Kaercher, E.R. Keim, and D.W. Fahey, Constraining the heterogneneous loss of O_3 on soot particles with observations in jet engine exhaust plumes. *Geophys Res Lett: 25*, 3323, 1998.

Gao, R.S., E.C. Richard, P.J. Popp, G.C. Toon, D.F. Hurst, P.A. Newman, J.C. Holecek, M.J. Northway, D.W. Fahey, M.Y. Danilin, B. Senh, K. Aikin, P.A. Romashkin, J.W. Elkins, C.R. Webster, S.M. Schauffler, J.B. Greenblatt, C.T. McElroy, L.R. Lait, T.P. Bui, and D. Baumgardner, Observational evidence for the role of denitrification in Arctic stratospheric ozone loss. *Geophys Res Lett: 28*, 2879, 2001.

Gardiner, B.C., Comparative morphology of the vertical ozone profile in the Antarctic spring. *Geophys Res Lett: 15*, 901, 1988.

Geller, M.A., and J.C. Alpert, Planetary wave coupling between the troposphere and the middle atmosphere as a possible sun-weather mechanism. *J Atmos Sci: 37*, 1197, 1980.

Geller, M.A., V. Yudin, A.R. Douglass, J.W. Waters, L.S. Elson, A.E. Roche, and J.M. Russell III, UARS PSC, $ClONO_2$, HCl and ClO measurements in early winter: Additional verification of the paradigm for chlorine activation. *Geophys Res Lett: 22*, 2937, 1995.

Gerber, L., and N. Kämpfer, Millimeter-wave measurements of chlorine monoxide at the Jungfraujoch Alpine Station. *Geophys Res Lett: 21*, 1279, 1994.

Gleason, J.F., P.K. Bhartia, J.R. Herman, R. M^{c}Peters, P. Newman, R.S. Stolarski, L. Flynn, G. Labow, D. Larko, C. Seftor, C. Wellemeyer, W.D. Komhyr, A.J. Miller, and W. Planet, Record low global ozone in 1992. *Science: 260*, 523, 1993.

Godin, S., G. Mégie, C. David, D. Haner, C. Flesia, and Y. Emery, Airborne lidar observations of mountain-wave-induced polar stratospheric clouds during EASOE. *Geophys Res Lett: 21*, 1335, 1994.

Goutail, F., J.P. Pommereau, A. Sarkissian, E. Kyro, and V. Dorokhov, Total nitrogen dioxide at the Arctic polar circle since 1990. *Geophys Res Lett: 21*, 1371, 1994.

Grewe, V., M. Dameris, and R. Sausen, Impact of stratospheric dynamics and chemistry on northern hemisphere midlatitude ozone loss. *J Geophys Res: 103*, 25,417, 1998.

Haigh, J.D., The impact of solar variability of climate. *Science: 272*, 981, 1996.

Haigh, J.D., and J.A. Pyle, Ozone perturbation experiments in a two-dimensional circulation model. *Quart J Roy Meteor Soc: 108*, 551, 1982.

Haigh, J.D., and J.A. Pyle, A two-dimensional calculation including atmospheric carbon dioxide and stratospheric ozone. *Nature: 279*, 222, 1979.

Hampson, J., *Photochemical Behavior of the Ozone Layer.* Tech Note, Can Armament Res and Dev Estab, TN 1627/64, Valcartier, Canada, 1964.

Hanson, D. R., and K. Mauersberger, The vapor pressures of HNO_3-H_2O solutions. *J Phys Chem: 92*, 6167, 1988.

Hanson, D.R., and A.R. Ravishankara, Heterogeneous chemistry of bromine species in sulfuric acid under stratospheric conditions. *Geophys Res Lett: 22*, 385, 1995.

Hanson, D.H., A.R. Ravishankara, and S. Solomon, Heterogeneous reactions in sulfuric acid aerosols: A framework for model calculations. *J Geophys Res: 99*, 3615, 1994.

Hanson, D.R., A.R. Ravishankara, and E.R. Lovejoy, Reactions of $BrONO_2$ and H_2O on submicron sulfuric acid aerosol and the implications for the lower stratosphere. *J Geophys Res: 101*, 9063, 1996.

Harris, N.R.P., G. Ancellet, L. Bishop, D.J. Hofmann, J.B. Kerr, R.D. M^{c}Peters, M. Prendez, W.J. Randel, J. Staehelin, B.H. Subbaraya, A. Volz-Thomas, J. Zawodny,

and C.S. Zerefos, Trends in stratospheric and free tropospheric ozone. *J Geophys Res: 102*, 1571, 1997.

Hartley, D.E., J.T. Villarin, R.X. Black, and C.A. Davis, A new perspective on the dynamical link between the stratosphere and troposphere. *Nature: 391*, 471, 1998.

Hartley, W.N., On the probable absorption of solar radiation by atmospheric ozone. *Chem News: 42*, 268, 1880.

Hartmann, D.L., L.E. Heidt, M. Loewenstein, J.R. Podolske, J. Vedder, W.L. Starr, and S.E. Strahan, Transport into the south polar vortex in early spring. *J Geophys Res: 94*, 16,779, 1989.

Heath, D.F., A.J. Krueger, and P.J. Crutzen, Solar proton event: Influence on stratospheric ozone. *Science: 197*, 886, 1977.

Hofmann, D.J., and S. Solomon, Ozone destruction through heterogeneous chemistry following the eruption of El Chichón. *J Geophys Res: 94*, 5029, 1989.

Hofmann, D.J., and S.J. Oltmans, The effect of stratospheric water vapor on the heterogeneous reaction rate for $ClONO_2$ and H_2O for sulfuric acid aerosol. *Geophys Res Lett: 19*, 2211, 1992.

Hofmann, D.J., and S.J. Oltmans, Anomalous Antarctic ozone during 1992: Evidence for Pinatubo volcanic aerosol effects. *J Geophys Res: 98*, 18,555, 1993.

Hofmann, D.J., J.W. Harder, S.R. Rolf, and J.M. Rosen, Balloon-borne observations of the development and vertical structure of the Antarctic ozone hole in 1986. *Nature: 326*, 59, 1987.

Hofmann, D.J., S.J. Oltmans, J.M. Harris, S. Solomon, T. Deschler, and B.J. Johnson, Observations and possible causes of new ozone depletion in Antarctica in 1991. *Nature: 359*, 283, 1992.

Hofmann, D.J., S.J. Oltmans, W.D. Komhyr, J.M. Harris, J.A. Lathrop, A.O. Langford, T. Deshler, B.J. Johnson, A. Torres, and W.A. Matthews, Ozone loss in the lower stratosphere over the United States in 1992-1993: Evidence for heterogeneous chemistry on the Pinatubo aerosol. *Geophys Res Lett: 21*, 65, 1994.

Hofmann, D.J., S.J. Oltmans, J.M. Harris, B.J. Johnson, and J.A. Lathrop, Ten years of ozonesonde measurements at the south pole: Implications for recovery of springtime Antarctic ozone. *J Geophys Res: 102*, 8931, 1997.

Hollandsworth, S.M., R.D. McPeters, L.E. Flynn, W. Planet, A.J. Miller, and S. Chandra, Ozone trends deduced from combined Nimbus 7 SBUV and NOAA 11 SBUV/2 data. *Geophys Res Lett: 22*, 905, 1995.

Holton, J.R., P.H. Haynes, M.E. McIntyre, A.R. Douglass, R.B. Rood, and L. Pfister, Stratosphere-troposphere exchange. *Rev Geophys: 33*, 403, 1995.

Hood, L.L., and D.A. Zaff, Lower stratospheric stationary waves and the longitude dependence of ozone trends in winter. *J Geophys Res: 100*, 25,791, 1995.

Hood, L.L., J.P. McCormack, and K. Labitzke, An investigation of dynamical contributions to midlatitude ozone trends in winter. *J Geophys Res: 102*, 13,079, 1997.

Intergovernmental Panel on Climate Change (IPCC), *Radiative Forcing of Climate Change: The Scientific Assessment*, Cambridge University Press, 1994.

Intergovernmental Panel on Climate Change (IPCC), *Climate Change: The Scientific Assessment*, Cambridge University Press, 2001.

Iwasaka, Y., and K. Kondoh, Depletion of Antarctic ozone: Height of ozone loss region and its temporal changes. *Geophys Res Lett: 14*, 87, 1987.

Jackman, C.H., and R.D. McPeters, Solar proton events as tests for the fidelity of middle atmosphere models. *Physica Scripta T18*, 309, 1987.

Jackman, C.H., E.L. Fleming, S. Chandra, D.B. Considine, and J.E. Rosenfield, Past, present, and future modeled ozone trends with comparisons to observed trends. *J Geophys Res: 101*, 28,753, 1996.

Jackman, C.H., E.L. Fleming, and F.M. Vitt, Influence of extremely large solar proton events in a changing stratosphere. *J Geophys Res: 105*, 11,659, 2000.

Jackman, C.H., R.D. McPeters, G.J. Labow, E.L. Fleming, C.J. Praderas, and J.M. Russell, Northern Hemisphere atmospheric effects due to the July 2000 solar proton event. *Geophys Res Lett: 28*, 2883, 2001.

Jaeger, H., and K. Wege, Stratospheric ozone depletion at northern midlatitudes after major volcanic eruptions. *J Atmos Chem: 10*, 273, 1990.

Jaramillo, M., R.L. de Zafra, J. Barrett, L.K. Emmons, P.M. Solomon, and A. Parrish, Measurements of stratospheric hydrogen cyanide at McMurdo Station, Antarctica: Further evidence of winter stratospheric susidence? *J Geophys Res: 94*, 16,773, 1989.

Johnston, P.V., and R.L. McKenzie, NO_2 observations at 45°S during the decreasing phase of solar cycle 21, from 1980 to 1987. *J Geophys Res: 94*, 3473, 1989.

Johnston, P.V., R.L. McKenzie, J.G. Keys, and W.A. Matthews, Observations of depleted stratospheric NO_2 following the Pinatubo volcanic eruption. *Geophys Res. Lett: 19*, 211-213, 1992.

Jones, R.L., and A.R. MacKenzie, Observational studies on the role of polar regions in midlatitude ozone loss. *Geophys Res Lett: 22*, 3485, 1995.

Jones, A.E., and J.D. Shanklin, Continued decline of total ozone over Halley, Antarctica, since 1985. *Nature: 376*, 409, 1995.

Jones, R.L., and J.A. Pyle, Observations of CH_4 and N_2O by the NIMBUS 7 SAMS: A comparison with in-situ data and two dimensional numerical model calculations. *J Geophys Res: 89*, 5263, 1984.

Jones, R.L., J. Austin, D.S. McKenna, J.G. Anderson, D.W. Fahey, C.B. Farmer, L.E. Heidt, K.K. Kelly, D.M. Murphy, M.H. Proffitt, A.F. Tuck, and J.F. Vedder, Lagrangian photochemical modeling studies of the 1987 Antarctic spring vortex, 1. Comparison with AAOE observations. *J Geophys Res: 94*, 11,529, 1989.

Jones, R.L., S. Solomon, D.S. McKenna, L.R. Poole, W.H. Brune, D.W. Toohey, J.G. Anderson, and D.W. Fahey, The polar stratospheric cloud event of January 24, 2. Photochemistry. *Geophys Res Lett: 17*, 541, 1990a.

Jones, R.L., D.S. McKenna, L.R. Poole, and S. Solomon, On the influence of polar stratospheric cloud formation on chemical composition during the 1988/89 arctic winter. *Geophys Res Lett: 17*, 545, 1990b.

Jet Propulsion Laboratory (JPL), *Chemical Kinetics and Photochemical Data for Use in Stratospheric Modelling, Evaluation number 12 of the NASA panel for data evaluation*, JPL publication 97-4, 1997.

Jet Propulsion Laboratory (JPL), *Chemical Kinetics and Photochemical Data for Use in Stratospheric Modelling, Evaluation number 13 of the NASA panel for data evaluation*, JPL publication 00-3, 2000.

Kaercher, B., and S. Solomon, On the composition and optical extinction of particles in the tropopause region. *J Geophys Res: 104*, 27441, 1999.

Kawa, S.R., D.W. Fahey, L.C. Anderson, M. Loewenstein, and K.R. Chan, Measurements of total reactive nitrogen during the airborne Arctic stratospheric expedition. *Geophys Res Lett: 17*, 485, 1990.

Kawa, S.R., P.A. Newman, L.R. Lait, M.R. Schoeberl, R.M. Stimpfle, D.W. Kohn, C.R. Webster, R.D. May, D. Baumgardner, J.E. Dye, J.C. Wilson, K.R. Chan, and M. Loewenstein, Activation of chlorine in sulfate aerosol as inferred from aircraft observations. *J Geophys Res: 102*, 3921, 1997.

Keim, E.R., D.W. Fahey, L.A. Del Negro, E.L. Woodbridge, R.S. Gao, P.O. Wennberg, R.C. Cohen, R.M. Stimpfle, K.K. Kelly, E.J. Hintsa, J.C. Wilson, H.H. Jonsson, J.E. Dye, D. Baumgardner, S.R. Kawa, R.J. Salawitch, M.H. Proffitt, M. Loewenstein, J.R. Podolske, and K.R. Chan, Observations of large reductions in the NO/NO_y ratio near the mid-latitude tropopause and the role of heterogeneous chemistry. *Geophys Res Lett: 23*, 3223, 1996.

Kelly, K.K., A.F. Tuck, D.M. Murphy, M.H. Proffitt, D.W. Fahey, R.L. Jones, D.S. McKenna, M. Loewenstein, J.R. Podolske, S.E. Strahan, G.V. Ferry, K.R. Chan, J.F. Vedder, G.L. Gregory, W.D. Hypes, M.P. McCormick, E.V. Browell, and L.E. Heidt, Dehydration in the lower Antarctic statosphere during late winter and early spring, 1987. *J Geophys Res: 94*, 11,317, 1989.

Khattatov, V., V. Yushkov, M. Khaplanov, I. Zaitzev, J. Rosen, and N. Kjome, Some results of water vapor, ozone and aerosol balloon-borne measurements during EASOE. *Geophys Res Lett: 21*, 1299, 1994.

Kirchhoff, V.W.J.H., N.J. Schuch, K.K. Pinheiro, and J.M. Harris, Evidence for an ozone hole perturbation at 30° South. *Atmos Environ: 30*, 1481, 1996.

Kirchhoff, V.W.J.H., C.A.R. Casiccia S., Zamorano B., and F. Zamorano B., The ozone hole over Punta Arenas, Chile. *J Geophys Res: 102*, 8945, 1997a.

Kirchhoff, V.W.J.H., Y. Sahai, C.A.R. Casiccia S., F. Zamorano B., and V. Valderrama V., Observations of the 1995 ozone hole over Punta Arenas, Chile. *J Geophys Res: 102*, 16,109, 1997b.

Knight, J.R., J. Austin, R.G. Grainger, and A. Lambert, A three-dimensional model simulation of the impact of Mt. Pinatubo aerosol on the Antarctic ozone hole. *Quart J Roy Meteor Soc: 124*, 1527, 1998.

Koike, M., N.B. Jones, W.A. Matthews, P.V. Johnston, R.L. McKenzie, D. Kinnison, and J. Rodriguez, Impact of Pinatubo aerosols on the partitioning between NO_2 and HNO_3. *Geophys Res Lett: 21*, 597, 1994.

Komhyr, W.D., R.D. Grass, and R.K. Leonard, Total ozone decrease at South Pole Antarctica, 1964-1985. *Geophys Res Lett: 13*, 1248, 1986.

Kondo, Y., U. Schmidt, T. Sugita, P. Aimendieu, M. Koike, H. Ziereis, and Y. Iwasaka, Total reactive nitrogen, N_2O and ozone in the winter Arctic stratosphere. *Geophys Res Lett: 21*, 1247, 1994.

Koop, T., U.M. Biermann, W. Raber, B.P. Luo, P.J. Crutzen, and T. Peter, Do stratospheric aerosols freeze above the ice frost point? *Geophys Res Lett: 22*, 917, 1995.

Kreher, K., J.G. Keys, P.V. Jonston, U. Platt, and X. Liu, Ground-based measurements of OClO and HCl in austral spring 1993 at Arrival Heights, Antarctica. *Geophys Res Lett: 23*, 1545, 1996.

Krueger, A.J., B.W. Buether, A.J. Fleig, D.F. Heath, E. Hilsenrath, R. M^{c}Peters, and C. Prabakhara, Satellite ozone measurements. *Phil Trans Roy Soc London: A*, 191, 1980.

Lary, D.J., Gas phase bromine photochemistry. *J Geophys Res: 101*, 1505, 1996.

Lary, D.J., M.P. Chipperfield, R. Toumi, and T. Lenton, Heterogeneous atmospheric bromine chemistry. *J Geophys Res: 101*, 1489, 1996.

Lary, D.J., A.M. Lee, R. Toumi, M.J. Newchurch, M. Pirre, and J.B. Renard, Carbon aerosols and atmospheric photochemistry. *J Geophys Res: 102*, 3671, 1997.

Lee, A.M., H.K. Roscoe, A.E. Jones, P.H. Haynes, E.F. Shuckburgh, M.W. Morrey, and H.C. Pumphrey, The impact of the mixing properties within the Antarctic stratospheric vortex on ozone loss in spring. *J Geophys Res: 106*, 3203, 2001.

Lehmann, P., D.J. Karoly, P.A. Newman, T.S. Clarkson, and W.A. Matthews, An investigation into the causes of stratospheric ozone loss in the southern australasian region. *Geophys Res Lett: 19*, 1463, 1992.

Lipson, J.B., M.J. Elrod, T.W. Beiderhase, L.T. Molina, and M.J. Molina, Temperature dependence of the rate constant and branching ratio for the OH+ClO reaction. *J Chem Soc: 93*, Faraday Trans, 2665, 1997.

Loewenstein, M., J.R. Podolske, K.R. Chan, and S.E. Strahan, Nitrous oxide as a dynamical tracer in the 1987 airborne Antarctic ozone experiment. *J Geophys Res: 94*, 11,589, 1989.

Luther, F.M., D.J. Wuebbles, and J.S. Chang, Temperature feedback in a stratospheric model, *J Geophys Res: 82*, 4935, 1977.

Lutman, E.R., R. Toumi, R.L. Jones, D.J. Lary, and J.A. Pyle, Box model studies of ClO_x deactivation and ozone loss during the 1991/92 northern hemisphere winter. *Geophys Res Lett: 21*, 1415, 1994a.

Lutman, E.R., J.A. Pyle, R.L. Jones, D.J. Lary, A.R. MacKenzie, I. Kilbane-Dawe, N. Larsen, and B. Knudsen, Trajectory model studies of ClO_x activation during the 1991/92 northern hemispheric winter. *Geophys Res Lett: 21*, 1419, 1994b.

Lutman, E.R., J.A. Pyle, M.P. Chipperfield, D.J. Lary, I. Kilbane-Dawe, J.W. Waters, and N. Larsen, Three-dimensional studies of the 1991/1992 northern hemisphere winter using domain-filling trajectories with chemistry. *J Geophys Res: 102*, 1479, 1997.

MacKenzie, A.R., M. Kulmala, A. Laaksonen, and T. Vesala, On the theories of type I polar stratospheric cloud formation. *J Geophys Res: 100*, 11,275, 1995.

MacKenzie, I.A., and R.S. Harwood, Arctic ozone destruction and chemical-radiative interaction. *J Geophys Res: 105*, 9033, 2000.

MacKenzie, I.A., R.S. Harwood, L. Froidevaux, W.G. Read, and J.W. Waters, Chemical loss of polar vortex ozone inferred from UARS MLS measurements of ClO during the Arctic and Antarctic late winters of 1993. *J Geophys Res: 101*, 14,505, 1996.

Mahlman, J.D., and S.B. Fels, Antarctic ozone decreases: A dynamical cause? *Geophys Res Lett: 13*, 1316, 1986.

Mankin, W.G., M.T. Coffey, A. Goldman, M.R. Schoeberl, L.R Lait, and P.A. Newman, Airborne measurements of stratospheric constituents over the Arctic in the winter of 1989. *Geophys Res Lett: 17*, 473, 1990.

Mankin, W.G., M.T. Coffey, and A. Goldman, Airborne observations of SO_2, HCl, and O_3 in the stratospheric plume of the Pinatubo volcano in July, 1991, *Geophys Res Lett: 19*, 179, 1992.

Manney, G.L., L. Froidevaux, J.W. Waters, R.W. Zurek, W.G. Read, L.S. Elson, J.B. Kumer, J.L. Mergenthaler, A.E. Roche, A. O'Neill, R.S. Harwood, I. MacKenzie, and R. Swinbank, Chemical depletion of ozone in the Arctic lower stratosphere during winter 1992-93. *Nature: 370*, 429, 1994a.

Manney, G.L, R.W. Zurek, A. O'Neill, and R. Swinbank, On the motion of air through the stratospheric polar vortex. *J Atmos Sci: 51*, 2973, 1994b.

Manney, G.L., R.W. Zurek, W.A. Lahoz, R.S. Harwood, J.C. Gille, J.B. Kumer, J.L. Mergenthaler, A.E. Roche, A. O'Neill, R. Swinbank, and J.W. Waters, Langrangian transport calculations using UARS data. Part I: Passive tracers. *J Atmos Sci: 52*, 3049, 1995a.

Manney, G.L., R.W. Zurek, L. Froidevaux, J.W. Waters, A. O'Neill, and R. Swinbank, Lagrangian transport calculations using UARS data. Part II: Ozone. *J Atmos Sci: 52*, 3069, 1995b.

Manney, G.L., R.W. Zurek, L. Foidevaux, and J.W. Waters, Evidence for arctic ozone depletion in late February and early March 1994. *Geophys Res Lett: 22*, 2941, 1995c.

Manney, G.L., M.L. Santee, L. Froidevaux, J.W. Waters, and R.W. Zurek, Polar vortex conditions during the 1995-96 Arctic winter: Meteorology and MLS ozone. *Geophys Res Lett: 23*, 3203, 1996.

Manney, G.L., L. Froidevaux, M.L. Santee, R.W. Zurek, and J.W. Waters, MLS observations of Arctic ozone loss in 1996-97. *Geophys Res Lett: 24*, 2697, 1997.

McCormack, J.P., and L.L. Hood, Modeling the spatial distribution of total ozone in northern hemisphere winter: 1979-1991. *J Geophys Res: 102*, 13,711, 1997.

McCormick, M.P., H.M. Steele, P. Hamill, W.P. Chu, and T.J. Swissler, Polar stratospheric cloud sightings by SAM II. *J Atmos Sci: 39*, 1387, 1982.

McCormick, M.P., R.E. Veiga, and W.P. Chu, Stratospheric ozone profile and total ozone trends derived from the SAGE I and SAGE II data. *Geophys Res Lett: 19*, 269, 1992.

McCormick, M.P., L.W. Thomason, and C.R. Trepte, Atmospheric effects of the Mt. Pinatubo eruption. *Nature: 373*, 399, 1995.

McElroy, M.B., R.J. Salawitch, S.C. Wofsy, and J.A. Logan, Reductions of Antarctic ozone due to synergistic interactions of chlorine and bromine. *Nature: 321*, 759, 1986.

McElroy, M.B., R.J. Salawitch, and K. Minschwaner, The changing stratosphere. *Planet Space Sci: 40*, 373, 1992.

McGee, T.J., P. Newman, M. Gross, U. Singh, S. Godin, A-M. Lacoste, and G. Mégie, Correlation of ozone loss with the presence of volcanic aerosols. *Geophys Res Lett: 21*, 2801, 1994.

McKenna, D.S., R.L. Jones, L.R. Poole, S. Solomon, D.W. Fahey, K.K. Kelly, M.H. Proffitt, W.H. Brune, M. Loewenstein, and K.R. Chan, Calculations of ozone destruction during the 1988/89 Arctic winter. *Geophys Res Lett: 17*, 553, 1990.

McKenzie, R.L., and P.V. Johnston, Springtime stratospheric NO_2 in Antarctica. *Geophys Res Lett: 11*, 73, 1984.

McPeters, R.D., and G.J. Labow, An assessment of the accuracy of 14.5 years of Nimbus 7 TOMS Version 7 ozone data by comparison with the Dobson network. *Geophys Res Lett: 23*, 3695, 1996a.

McPeters, R.D., S.M. Hollandsworth, L.E. Flynn, J.R. Herman, and C.J. Seftor, Long-term ozone trends derived from the 16-year combined Nimbus 7/Meteor 3 TOMS Version 7 record. *Geophys Res Lett: 23*, 3699, 1996b.

Michelangeli, D.V., M. Allen, and Y.L. Yung, El Chichón volcanic aerosols: Impact of radiative, thermal, and chemical perturbations. *J Geophys Res: 94*, 18,429, 1989.

Michelsen, H.A., R.J. Salawitch, M.R. Gunson, C. Aellig, N. Kämpfer, M.M. Abbas, M.C. Abrams, T.L. Brown, A.Y. Chang, A. Goldman, F.W. Irion, M.J. Newchurch, C.P. Rinsland, G.P. Stiller, and R. Zander, Stratospheric chlorine partitioning: Constraints from shuttle-borne measurements of [HCl], [$ClNO_3$] and [ClO]. *Geophys Res Lett: 23*, 2361, 1996.

Michelsen, H.A., C.M. Spivakovsky, and S.C. Wofsy, Aerosol-mediated partitioning of stratospheric Cl_y and NO_y at temperatures below 200. *Geophys Res Lett: 26*, 299, 1999.

Miller, A.J., G.C. Tiao, G.C. Reinsel, D. Wuebbles, L. Bishop, J. Kerr, R.M. Nagatani, J.J., DeLuisi, and C.L., Mateer, Comparisons of observed ozone trends in the stratosphere through examinations of Umkehr and balloon ozonesonde data. *J Geophys Res: 100*, 11,209, 1995.

Mills, M.J., A.O. Langford, T.J. O'Leary, K. Arpag, H.L. Miller, M.H. Proffitt, R.W. Sanders, and S. Solomon, On the relationship between stratospheric aerosols and nitrogen dioxide. *Geophys Res Lett: 20*, 1187, 1993.

Molina, M.J., and F.S. Rowland, Stratospheric sink for chlorofluoromethanes: Chlorine atom catalyzed destruction of ozone. *Nature: 249*, 820, 1974.

Molina, L.T., and M.J. Molina, Production of Cl_2O_2 from the self-reaction of the ClO radical. *J Phys Chem: 91*, 433, 1987.

Molina, M. J., T-L. Tso, L.T. Molina, and F.C.-Y. Wang, Antarctic stratospheric chemistry of chlorine nitrate, hydrogen chloride, and ice: Release of active chlorine, *Science: 238*, 1253, 1987.

Montzka, S.A., J.H. Butler, R.C. Myers, T.M. Thompson, T.H. Swanson, A.D. Clarke, L.T. Lock, and J.W. Elkins, Decline in the tropospheric abundance of halogen from halocarbons: implications for stratospheric ozone depletion. *Science: 272*, 1318, 1996.

Mount, G.H., R.W. Sanders, A.L. Schmeltekopf, and S. Solomon, Visible spectroscopy at McMurdo Station, Antarctica, 1, Overview and daily variations of NO_2 and O_3 during austral spring, 1986. *J Geophys Res: 92*, 8320, 1987.

Mozurkewich, M., and J.G. Calvert, Reaction probability of N_2O_5 on aqueous aerosols. *J Geophys Res: 93*, 15,889, 1988.

Müller, R., P.J. Crutzen, J-U. Grooß, C. Brühl, J.M. Russell III, and A.F. Tuck, Chlorine activation and ozone depletion in the Arctic vortex: Observations by the halogen occultation experiment on the upper atmosphere research satellite. *J Geophys Res: 101*, 12,531, 1996.

Müller, R., P.J. Crutzen, J-U. Grooß, C. Brühl, J.M. Russell III, H. Gernandt, D.S. McKenna, and A.F. Tuck, Severe chemical ozone loss in the Arctic during the winter of 1995-96. *Nature: 389*, 709, 1997a.

Müller, R., J-U. Grooß, D.S. McKenna, P.J. Crutzen, C. Brühl, J.M. Russell III, and A.F. Tuck, HALOE observations of the vertical structure of chemical ozone depletion in the Arctic vortex during winter and early spring 1996-1997. *Geophys Res Lett: 24*, 2717, 1997b.

Müller, R, R.J. Salawitch, P.J. Crutzen, W.A. Lahoz, G.L. Manney, and R. Tuomi, Upper stratospheric processes, in *Scientific Assessment of Ozone Depletion: 1998*, Rep. 44, pp. 6.1-6.4, World Meteorological Organization/United Nations Environment Programme (WMO/UNEP), Geneva, 1999.

Murcray, D.G., D.B. Barker, J.N. Brooks, A. Goldman, and W.J. Williams, Seasonal and latitudinal variation of the stratospheric concentration of HNO_3. *Geophys Res Lett: 2*, 223, 1975.

Murphy, D.M., Ozone loss rates calculated along ER-2 flight tracks. *J Geophys Res: 96*, 5045, 1991.

Murphy, D.M., and A.R. Ravishankara, Temperature averages and rates of stratospheric reactions. *Geophys Res Lett: 21*, 2471, 1994.

Nagatani, R.M., A.J. Miller, M.E. Gelman, and P.A. Newman, A comparison of Arctic lower stratospheric winter temperatures for 1988-89 with temperatures since 1964. *Geophys Res Lett: 17*, 333, 1990.

Newman, P.A., Antarctic total ozone in 1958. *Science: 264*, 543, 1994.

Newman, P.A., and M.R. Schoeberl, October Antartic temperature and total ozone trends from 1979 to 1985. *Geophys Res Lett: 13*, 1207, 1986.

Newman, P.A., and W.J. Randel, Coherent ozone-dynamical changes during the southern hemisphere spring, 1979-1986. *J Geophys Res: 93*, 12,585, 1988.

Newman, P.A., Antarctic total ozone in 1958. *Science: 264*, 543, 1994.

Newman, P.A., J.G. Gleason, R.D. McPeters, and R.S. Stolarski, Anomalously low ozone over the Arctic. *Geophys Res Lett: 24*, 2689, 1997.

Noxon, J.F., Stratospheric NO_2 in the Antarctic winter. *Geophys Res Lett: 5*, 1021, 1978.

Noxon, J.F., Stratospheric NO_2, 2. Global behavior. *J Geophys Res: 84*, 5067, 1979.

Oelhaf, H., T. von Clarmann, H. Fischer, F. Friedl-Vallon, C. Fritzsche, A. Linden, C. Piesch, M. Seefeldner, and W. Völker, Stratospheric $ClONO_2$ and HNO_3 profiles inside the Arctic vortex from MIPAS-B limb emission spectra obtained during EASOE. *Geophys Res Lett: 21*, 1263, 1994.

Ozone Trends Panel (OTP), *Report of the International Ozone Trends Panel*, WMO Report Number 18, 1988.

Parrish, A., R.L. deZafra, P.M. Solomon, J.W. Barrett, and E.R. Carlson, Chlorine oxide in the stratospheric ozone layer: Ground-based detection and measurement. *Science: 211*, 1158, 1981.

Parrish, A., R.L. de Zafra, M. Jaramillo, B. Connor, P.M. Solomon, and J.W. Barrett, Extremely low N_2O concentrations in the springtime stratosphere at McMurdo Station, Antarctica. *Nature: 332*, 53, 1988.

Perliski, L., S. Solomon, and J. London, On the interpretation of seasonal variations in stratospheric ozone. *Planet Space Sci: 37*, 1527, 1989.

Perner, D., A. Roth, and T. Klüpfel, Ground based measurements of stratospheric OClO, NO_2 and O_3 at Søndre Strømfjord in winter 1991/92. *Geophys Res Lett: 21*, 1367, 1994.

Pfeilsticker, K., and U. Platt, Airborne measurements during the Arctic Stratospheric Experiment: Observations of O_3 and NO_2. *Geophys Res Lett: 21*, 1375, 1994.

Pierce, R.B., W.L. Grose, J.M. Russell III, A.F. Tuck, R. Swinbank, and A. O'Neill, Spring dehydration in the Antarctic stratospheric vortex observed by HALOE. *J Atmos Sci: 51*, 2931, 1994.

Pitari, G., and V. Rizi, An estimate of the chemical and radiative perturbation of stratospheric ozone following the eruption of Mt. Pinatubo. *J Atmos Sci: 50*, 3260, 1993.

Pitari, G., G. Visconti, and M. Verdecchia, Global ozone depletion and the Antarctic ozone hole. *J Geophys Res: 97*, 8075, 1992.

Pitari, G., and V. Rizi, An estimate of the chemical and radiative perturbation of stratospheric ozone following the eruption of Mt. Pinatubo. *J Atmos Sci: 50*, 3260, 1993.

Pittock, A.B., A critical look at long-term sun-weather relationships. *Rev Geophys Space Phys: 16*, 400, 1978.

Plumb, R.A., and M.K.W. Ko, Interrelationships between mixing raitos of long-lived stratospheric constituents. *J Geophys Res: 97*, 10,145, 1992.

Pommereau, J-P., and J. Piquard, Observations of the vertical distribution of stratospheric OClO. *Geophys Res Lett: 21*, 1231, 1994a.

Pommereau, J-P., and J. Piquard, Ozone and nitrogen dioxide vertical distributions by UV-visible solar occultation from balloons. *Geophys Res Lett: 21*, 1227, 1994b.

Portmann, R.W., S. Solomon, R.R. Garcia, L.W. Thomason, L.R. Poole, and M.P. McCormick, Role of aerosol variations in anthropogenic ozone depletion in polar regions. *J Geophys Res: 101*, 22,991, 1996.

Prather, M., Catastrophic loss of stratospheric ozone in dense volcanic clouds. *J Geophys Res: 97*, 10,187, 1992.

Prather, M., M.M. Garcia, R. Suozzo, and D. Rind, Global impact of the Antarctic ozone hole: Dynamical dilution with a three dimensional chemical transport model. *J Geophys Res: 95*, 3449, 1990.

Prenni, A.J., M.E. Wise, S.D. Brooks, and M.A. Tolbert, Ice nucleation in sulfuric acid and ammonium sulfate particles. *J Geophys Res: 106*, 3037, 2001.

Prinn, R.G., R.F. Weiss, B.R. Miller, J. Huang, F.N. Alyea, D.M. Cunnold, P.J. Fraser, D.E. Hartley, and P.G. Simmonds, Atmospheric trends and lifetime of CH_3CCl_3 and global OH concentrations. *Science: 269*, 187, 1995.

Proffitt, M.H., K. Aikin, J.J. Margitan, M. Loewenstein, J.R. Podolske, A. Weaver, K.R. Chan, H. Fast, and J.W. Elkins, Ozone loss inside the northern polar vortex during the 1991-1992 winter. *Science: 261*, 1150, 1993.

Pyle, J.A., G. Carver, J.L. Grenfell, J.A. Kettleborough, and D.J. Lary, Ozone loss in Antarctica: The implications for global change. *Phil Trans R Soc London B: 338*, 219, 1992.

Pyle, J.A., M.P. Chipperfield, I. Kilbane-Dawe, A.M. Lee, R.M. Stimpfle, D. Kohn, W. Renger, and J.W. Waters, Early modelling results from the SESAME and ASHOE Campaigns. *Faraday Discuss: 100*, 371, 1995.

Ramaswamy, V., M.D. Schwarzkopf, and W.J. Randel, Fingerprint of ozone depletion in the spatial and temporal pattern of recent lower-stratospheric cooling. *Nature: 382*, 616, 1996.

Randel, W.J., and J.B. Cobb, Coherent variations of monthly mean total ozone and lower stratospheric temperature. *J Geophys Res: 99*, 5433, 1994.

Randel, W.J., and F. Wu, Cooling of the Arctic and Antarctic polar stratospheres due to ozone depletion. *J Climate: 12*, 1467, 1999.

Randeniya, L.K., P.F. Vohralik, I.C. Plumb, and K.R. Ryan, Heterogeneous $BrONO_2$ hydrolysis: Effect on NO_2 columns and oxone at high latitudes in summer. *J Geophys Res: 102*, 23,543, 1997.

Ravishankara, A.R., and D.R. Hanson, Differences in the reactivity of Type 1 PSC's depending on their phase. *J Geophys Res: 101*, 3885, 1996.

Ravishankara, A.R., and T.G. Shepherd (Lead Authors), M.P. Chipperfield, P.H. Haynes, S.R. Kawa, T. Peter, R.A. Plumb, R.W. Randel, D.W. Waugh, and D.R. Worsnop, Lower Stratospheric Processes, Chapter 7 in *Scientific Assessment of Ozone Depletion: 1998*, Global Ozone Research and Monitoring Project–Report No. 44, World Meteorological Organization/United Nations Environment Programme (WMO/UNEP), Geneva, 1999.

Rex, M., N.R.P. Harris, P. von der Gathen, R. Lehmann, G.O. Braathen, E. Reimer, A. Beck, M.P. Chipperfield, R. Alfier, M. Allaart, F. O'Connor, H. Dier, V. Dorokhov,

H. Fast, M. Gil, E. Kyrö, Z. Litynska, I.S. Mikkelsen, M.G. Molyneux, H. Nakane, J. Notholt, M. Rummukainen, P. Viatte, and J. Wenger, Prolonged stratospheric ozone loss in the 1995-96 Arctic winter. *Nature: 389*, 835, 1997.

Rex, M., P. von der Gathen, N.R.P. Harris, D. Lucic, B.M. Knudsen, G.O. Braathen, S.J. Reid, H. DeBacker, H. Claude, R. Fabian, H. Fast, M. Gil, E. Kyrö, I.S. Mikkelsen, M. Rummukainen, H.G. Smit, J. Stähelin, C. Varotsos, and I. Zaitcev, In situ measurements of stratospheric ozone depletion rates in the Arctic winter 1991/1992: A Lagrangian approach. *J Geophys Res: 103*, 5843, 1998.

Ridley, B.A., M. McFarland, A.L. Schmeltekopf, M.H. Proffitt, D.L. Albritton, R.H. Winkler, and T.L. Thompson, Seasonal differences in the vertical distributions of NO, NO_2, and O_3 in the stratosphere near 50°N. *J Geophys Res: 92*, 11,919, 1987.

Rinsland, C.P., M.R. Gunson, M.C. Abrams, L.L. Lowes, R. Zander, E. Mahieu, A. Goldman, M.K.W. Ko, J.M. Rodriguez, and N.D. Sze, Heterogeneous conversion of N_2O_5 to HNO_3 in the post-Mt. Pinatubo eruption stratosphere. *J Geophys Res: 99*, 8213, 1994.

Rinsland, C.P., M.R. Gunson, R.J. Salawitch, M.J. Newchurch, R. Zander, M.M. Abbas, M.C. Abrams, G.L. Manney, H.A. Michelsen, A.Y. Chang, and A. Goldman, ATMOS measurements of H_2O+2CH_4 and total reactive nitrogen in the November 1994 Antarctic stratosphere: Dehydration and denitrification in the vortex. *Geophys Res Lett: 23*, 2397, 1996.

Robinson, G.N., D.R. Worsnop, J.T. Jayne, C.E. Kolb, and P. Davidovits, Heterogeneous uptake of $ClONO_2$ and N_2O_5 by sulfuric acid solutions. *J Geophys Res: 102*, 3583, 1997.

Robinson, G.N., D.R. Worsnop, J.T. Jayne, C.E. Kolb, E. Swartz, and P. Davidovits, Heterogeneous uptake of HCl by sulfuric acid solutions. *J Geophys Res: 103*, 25,371, 1998.

Roche, A.E., J.B. Kumer, J.L. Mergenthaler, R.W. Nightingale, W.G. Uplinger, G.A. Ely, J.F. Potter, D.J. Wuebbles, P.S. Connell, and D.E. Kinnison, Observations of lower-stratospheric $ClONO_2$, HNO_3, and aerosol by the UARS, CLAES Experiment between January 1992 and April 1993. *J Atmos Sci: 51*, 2877, 1994.

Rodriguez, J.M., M.K.W. Ko, and N.D. Sze, The role of chlorine chemistry in Antarctic ozone loss: Implications of new kinetic data. *Geophys Res Lett: 17*, 255, 1990.

Rodriguez, J.M., M.K.W. Ko, and N.D. Sze, Role of heterogeneous conversion of N_2O_5 on sulphate aerosols in global ozone losses. *Nature: 352*, 134, 1991.

Rodriguez, J.M., M.K.W. Ko, N.D. Sze, C.W. Helsey, G.K. Yue, and M.P. McCormick, Ozone response to enhanced heterogeneous processing after the eruption of Mt. Pinatubo. *Geophys Res Lett: 21*, 209, 1994.

Rogaski, C.A., D.M. Golden, and L.R. Williams, Reactive uptake and hydration experiments on amorphous carbon treated with NO_2, SO_2, O_3, HNO_3, and H_2SO_4. *Geophys Res Lett: 24*, 381, 1997.

Rood, R.B., and A.R. Douglass, Interpretation of ozone temperature correlations, 1. Theory. *J Geophys Res: 90*, 5733, 1985.

Roscoe, H.K., A.E. Jones, and A.M. Lee, Midwinter start to Antarctic ozone depletion: Evidence from observations and models. *Science: 278*, 93, 1997.

Rowland, F.S., and M.J. Molina, Chlorofluoromethanes in the environment. *Rev Geophys: 13*, 1, 1975.

Russell III, J.M., S. Solomon, L.L. Gordley, E.E. Remsberg, and L.B. Callis, The variability of stratospheric and mesospheric NO_x in the polar winter night observed by LIMS. *J Geophys Res: 89*, 7267, 1984.

Russell III, J.M., A.F. Tuck, L.L. Gordley, J.H. Park, S.R. Drayson, J.E. Harries, R.J. Cicerone, and P.J. Crutzen, HALOE Antarctic observations in the spring of 1991. *Geophys Res Lett: 20*, 719, 1993.

Russell III, J.M., M. Luo, R.J. Cicerone, and L.E. Deaver, Satellite confirmation of the dominance of chlorofluorocarbons in the global stratospheric chlorine budget. *Nature: 379*, 526, 1996.

Salawitch, R.J., G.P. Gobbi, S.C. Wofsy, and M.B. McElroy, Denitrification in the Antarctic stratosphere. *Nature: 339*, 525, 1989.

Salawitch, R.J., M.B. M^{c}Elroy, J.H. Yatteau, S.C. Wofsy, M.R. Schoeberl, L.R. Lait, P.A. Newman, K.R. Chan, M. Loewenstein, J.R. Podolske, S.E. Strahan, and M.H. Proffitt, Loss of ozone in the Arctic vortex for the winter of 1989. *Geophys Res Lett: 17*, 561, 1990.

Salawitch, R.J., S.C. Wofsy, E.W. Gottlieb, L.R. Lait, P.A. Newman, M.R. Schoeberl, M. Loewenstein, J.R. Podolske, S.E. Strahan, M.H. Proffitt, C.R. Webster, R.D. May, D.W. Fahey, D. Baumgardner, J.E. Dye, J.C. Wilson, K.K. Kelly, J.W. Elkins, K.R. Chan, and J.G. Anderson, Chemical loss of ozone in the Arctic polar vortex in the winter of 1991-1992. *Science: 261*, 1146, 1993.

Salawitch, R.J., S.C. Wofsy, P.O. Wennberg, R.C. Cohen, J.G. Anderson, D.W. Fahey, R.S. Gao, E.R. Keim, E.L. Woodbridge, R.M. Stimpfle, J.P. Koplow, D.W. Kohn, C.R. Webster, R.D. May, L. Pfister, E.W. Gottlieb, H.A. Michelsen, G.K. Yue, M.J. Prather, J.C. Wilson, C.A. Brock, H.H. Jonsson, J.E. Dye, D. Baumgardner, M.H. Proffitt, M. Loewenstein, J.R. Podolske, J.W. Elkins, G.S. Dutton, E.J. Hintsa, A.E. Dessler, E.M. Weinstock, K.K. Kelly, K.A. Boering, B.C. Daube, K.R. Chan, and S.W. Bowen, The diurnal variation of hydrogen, nitrogen, and chlorine radicals: Implications for the heterogeneous production of HNO_2. *Geophys Res Lett: 21*, 2551, 1994.

Sander, S.P., R.R. Friedl, and Y.L. Yung, Rate of formation of the ClO dimer in the polar stratosphere: Implications for ozone loss. *Science: 245*, 1095, 1989.

Sanders, R.W., S. Solomon, J.P. Smith, L. Perliski, H.L. Miller, G.H. Mount, J.G. Keys, and A.L. Schmeltekopf, Visible and near-ultraviolet spectroscopy at McMurdo Station, Antarctica, 9. Observations of OClO from April to October, 1991. *J Geophys Res: 98*, 7219, 1993.

Santee, M.L., W.G. Read, J.W. Waters, L. Froidevaux, G.L. Manney, D.A. Flower, R.F. Jarnot, R.S. Harwood, and G.E. Peckham, Interhemispheric differences in polar stratospheric HNO_3, H_2O, ClO, and O_3. *Science: 267*, 849, 1995.

Santee, M.L., G.L. Manney, W.G. Read, L. Foidevaux, and J.W. Waters, Polar vortex conditions during the 1995-96 Arctic winter: MLS ClO and HNO_3. *Geophys Res Lett: 23*, 3207, 1996.

Santee, M.L., G.L. Manney, L. Froidevaux, R.W. Zurek, and J.W. Waters, MLS observations of ClO and HNO_3 in the 1996-97 Arctic polar vortex. *Geophys Res Lett: 24*, 2713, 1997.

Santee, M.L., A. Tabazadeh, G.L. Manney, R.J. Salawitch, L. Froidevaux, W.G. Read, and J.W. Waters, UARS Microwave limb sounder HNO_3 observations: Implications for Antarctic polar stratospheric clouds. *J Geophys Res: 103*, 13,285, 1998.

Santee, M.L., G.L. Manney, L. Froidevaux, W.G. Read, and J.W. Waters, Six years of UARS microwave limb sounder HNO_3 observations: Seasonal, interhemispheric, and interannual variations in the lower stratosphere. *J Geophys Res: 104,* 8225, 1999.

Schauffler, S.M., L.E. Heidt, W.H. Pollock, T.M. Gilpin, J.F. Vedder, S. Solomon, R.A. Lueb, and E.L. Atlas, Measurements of halogenated organic compounds near the tropical tropopause. *Geophys Res Lett: 20*, 2567, 1993.

Schiller, C., A. Wahner, U. Platt, H-P. Dorn, J. Callies, and D.H. Ehhalt, Near UV atmospheric absorption measurements of column abundances during airborne arctic stratospheric expedition, January-February 1989, 2. OClO Observations. *Geophys Res Lett: 17*, 501, 1990.

Schmidt, U., and A. Khedim, In situ measurements of carbon dioxide in the winter Arctic vortex and at mid-latitudes: An indicator of the age of stratospheric air. *Geophys Res Lett: 18*, 763, 1991.

Schoeberl, M.R., and D.L. Hartmann, The dynamics of the polar vortex. *Science: 251*, 46, 1991.

Schoeberl, M.R., A.R. Douglass, R.S. Stolarski, P.A. Newman, L.R. Lait, D. Toohey, L. Avallone, J.G. Anderson, W. Brune, D.W. Fahey, and K. Kelly, Stratospheric constituent trends from ER-2 profile data. *Geophys Res Lett: 17*, 469, 1990.

Schoeberl, M.R., and D.L. Hartmann, The dynamics of the polar vortex. *Science: 251*, 46, 1991.

Schoeberl, M.R., L.R. Lait, P.A. Newman, and J.E. Rosenfield, The structure of the polar vortex. *J Geophys Res: 97*, 7859, 1992.

Schoeberl, M.R., P.K. Bhartia, and J.R. Herman, Tropical ozone loss following the eruption of Mt. Pinatubo. *Geophys Res Lett: 20*, 29, 1992.

Schoeberl, M.R., A.R. Douglass, R.S. Stolarski, P.A. Newman, L.R. Lair, D. Toohey, L. Avallone, J.G. Anderson, W. Brune, D.W. Fahey, and K. Kelly, The evolution of ClO and NO along air parcel trajectories. *Geophys Res Lett: 20*, 2511, 1993a.

Schoeberl, M.R., R.S. Stolarski, A.R. Douglass, P.A. Newman, L.R. Lait, J.W. Waters, L. Froidevaux, and W.G. Ready, MLS ClO observations and the Arctic polar vortex temperatures. *Geophys Res Lett: 20*, 2861, 1993b.

Schoeberl, M.R., M. Luo, and J.E. Rosenfield, An analysis of the Antarctic halogen occultation experiment trace gas observations. *J Geophys Res: 100*, 5159, 1995.

Schoeberl, M.R., A.R. Douglass, S.R. Kawa, A.E. Dessler, P.A. Newman, R.S. Stolarski, A.E. Roche, J.W. Waters, and J.M. Russell III, Development of the Antarctic ozone hole. *J Geophys Res: 101*, 20,909, 1996.

Sen, B., G.C. Toon, G.B. Osterman, J.-F Blavier, J.J. Margitan, and R.J. Salawitch, and G.K. Yue, Measurements of reactive nitrogen in the stratosphere. *J Geophys Res: 103*, 3571, 1998.

Shindell, D.T., J.M. Reeves, L.K. Emmons, and R.L. de Zafra, Arctic chlorine monoxide observations during spring 1993 over Thule, Greenland, and implications for ozone depletion. *J Geophys Res: 99*, 25,697, 1994.

Shindell, D.T., D. Rind, and P. Lonergan, Increased polar stratospheric ozone losses and delayed eventual recovery owing to increasing greenhouse-gas concentrations. *Nature: 392*, 589, 1998.

Shindell, D., D. Rind, N. Balachandran, J. Lean, and P. Lonergan, Solar cycle variability, ozone, and climate. *Science: 284*, 305, 1999.

Shine, K.P., On the modelled thermal response of the Antarctic stratosphere to a depletion of ozone. *Geophys Res Lett: 13*, 1331, 1986.

Siskind, D.E., G.E. Nedoluha, C.E. Randall, M. Fromm, and J.M. Russell III, An assessment of Southern Hemisphere stratospheric NO_x enhancements due to transport from the upper atmosphere. *Geophys Res Lett: 27*, 329, 2000.

Slusser, J.R., D.J. Fish, E.K. Strong, and R.L. Jones, Five years of NO_2 vertical column measurements at Faraday (65°S): Evidence for the hydrolysis of $BrONO_2$ on Pinatubo aerosols. *J Geophys Res: 102*, 12,987, 1997.

Smith, J.B., E.J. Hintsa, N.T. Allen, R.M. Stimpfle, and J.G. Anderson, Mechanisms for mid-latitude ozone loss: Heterogeneous chemistry in the lowermost stratosphere. *J Geophys Res: 106*, 1297, 2001.

Solomon, S., The mystery of the Antarctic ozone hole. *Rev Geophys: 26*, 131, 1988.

Solomon, S., Stratospheric ozone depletion: A review of concepts and history. *Rev Geophys: 37*, 275, 1999.

Solomon, S., and R.R. Garcia, On the distributions of long-lived tracers and chlorine species in the middle atmosphere. *J Geophys Res: 89*, 11,633, 1984.

Solomon, S., P.J. Crutzen, and R.G. Roble, Photochemical coupling between the thermosphere and the lower atmosphere, I. Odd nitrogen from 50 to 120 km. *J Geophys Res: 87*, 7206, 1982.

Solomon, S., G.C. Reid, D.W. Rusch, and R.J. Thomas, Mesospheric ozone depletion during the solar proton event of July 13, 1982, Part II. Comparison between theory and measurements. *Geophys Res Lett: 10*, 257, 1983.

Solomon, S., R.R. Garcia, F.S. Rowland, and D.J. Wuebbles, On the depletion of Antarctic ozone. *Nature: 321*, 755, 1986.

Solomon, S., G.H. Mount, R.W. Sanders, and A.L. Schmeltekopf, Visible spectroscopy at McMurdo Station, Antarctica, 2. Observations of OClO. *J Geophys Res: 92*, 8329, 1987.

Solomon, S., G.H. Mount, R.W. Sanders, R.O. Jakoubek, and A.L. Schmeltekopf, Observations of the nighttime abundance of OClO in the winter stratosphere above Thule, Greenland. *Science: 242*, 550, 1988.

Solomon, S., R.W. Sanders, R.R. Garcia, and J.G. Keys, Increased chlorine dioxide over Antarctica caused by volcanic aerosols from Mount Pinatubo. *Nature: 363*, 245, 1993.

Solomon, S., R.W. Portmann, R.R. Garcia, L.W. Thomason, L.R. Poole, and M.P. McCormick, The role of aerosol variations in anthropogenic ozone depletion at northern midlatitudes. *J Geophys Res: 101*, 6713, 1996.

Solomon, S., S. Borrmann, R.R. Garcia, R. Portmann, L. Thomason, L.R. Poole, D. Winker, and M.P. McCormick, Heterogeneous chlorine chemistry in the tropopause region. *J Geophys Res: 102*, 21,411, 1997.

Solomon, S., R.W. Portmann, R.R. Garcia, W. Randel, F. Wu, R. Nagatani, J. Gleason, L. Thomason, L.R. Poole, and M.P. McCormick, Ozone depletion at mid-latitudes: Coupling of volcanic aerosols and temperature variability to anthropogenic chlorine. *Geophys Res Lett: 25*, 1871, 1998.

SPARC (Stratospheric Processes and their Role in Climate), *Assessment of Trends in the vertical distribution of ozone.* WMO Report No. 43, Geneva, Switzerland, 1998.

Stachnik, R.A., J.C. Hardy, J.A. Tarsala, J.W. Waters, and N.R. Erickson, Submillimeter wave heterogyne measurements of stratospheric ClO, HCl, O_3, and HO_2: First results. *Geophys Res Lett: 19*, 1931, 1992.

Staehelin, J., A. Renaud, J. Bader, R. McPeters, P. Viatte, B. Hoegger, V. Bugnion, M. Giroud, and H. Schill, Total ozone series at Arosa (Switzerland): Homogenization and data comparison. *J Geophys Res: 103*, 5827, 1998a.

Staehelin, J., R. Kegel, and N.R.P. Harris, Trend analysis of the homogenized total ozone series of Aroso (Switzerland), 1926-1996. *J Geophys Res: 103*, 8389-8399, 1998b.

Steele, H.M., P. Hamill, M.P. McCormick, and T.J. Swissler, The formation of polar stratospheric clouds. *J Atmos Sci: 40*, 2055, 1983.

Stimpfle, R.M., J.P. Koplow, R.C. Cohen, D.W. Kohn, P.O. Wennberg, D.M. Judah, D.W. Toohey, L.M. Avallone, J.G. Anderson, R.J. Salawitch, E.L. Woodgridge, C.R. Webster, R.D. May, M.H. Proffitt, K. Aiken, J. Margitan, M. Loewenstein, J.R. Podolske, L. Pfister, and K.R. Chan, The response of ClO radical concentrations to variations in NO_2 radical concentrations in the lower stratosphere. *Geophys Res Lett: 21*, 2543, 1994.

Stolarski, R.S., and R.J. Cicerone, Stratospheric chlorine: A possible sink for ozone. *Can J Chem: 52*, 1610, 1974.

Stolarski, R.S., A.J. Krueger, M.R. Schoeberl, R.D. McPeters, P.A. Newman, and J.C. Alpert, Nimbus 7 satellite measurements of the springtime Antarctic ozone decrease. *Nature: 322*, 808, 1986.

Stolarski, R.S., P. Bloomfield, R.D. McPeters, and J.R. Herman, Total ozone trends deduced from Nimbus 7 TOMS data. *Geophys Res Lett: 18*, 1015, 1991.

Swider, W., and T. Keneshea, Decrease of ozone and atomic oxygen in the lower mesosphere during a PCA event. *Planet Space Sci: 21*, 1969, 1973.

Sze, N.D., M.K.W. Ko, D.K. Weisenstein, J.M. Rodriguez, R.S. Stolarski, and M.R. Schoeberl, Antarctic ozone hole: Possible implications for ozone trends in the southern hemisphere. *J Geophys Res: 94*, 11,521, 1989.

Tabazadeh, A., and R.P. Turco, Stratospheric chlorine injection by volcanic eruptions: HCl scavenging and implications for ozone. *Science: 260*, 1082, 1993.

Tabazadeh, A., and O.B. Toon, The role of ammoniated aerosols in cirrus cloud nucleation. *Geophys Res Lett: 25*, 1379, 1998.

Tabazadeh, A., E.J. Jensen, O.B. Toon, K. Drdla, and M.R. Schoeberl, Role of the stratospheric polar freezing belt in denitrification. *Science: 291*, 2591, 2001.

Thomas, R.J., Mesospheric ozone depletion during the solar proton event of July 13, 1982, Part I. Measurement. *Geophys Res Lett: 10*, 253, 1983.

Thomason, L.W., L.R. Poole, and T. Deshler, A global climatology of stratospheric aerosol surface area density deduced from Stratospheric Aerosol and Gas Experiment II measurements: 1984-1994. *J Geophys Res: 102*, 8967, 1997.

Thompson, D.J., and J.M. Wallace, Annular modes in the extratropical circulation, Part I: Month to month variability. *J Clim: 13*, 1000, 2000.

Thompson, D.J., J.M. Wallace, and G.C. Hegerl, Annular modes in the extratropical circulation, Part II: Trends. *J Clim: 13*, 1018, 2000.

Tie, X.X., and G. Brasseur, The response of stratospheric ozone to volcanic eruptions: Sensitivity to atmospheric chlorine loading. *Geophys Res Lett: 22*, 3035, 1995.

Tie, X.X., G.P. Brasseur, B. Briegleb, and C. Granier, Two-dimensional simulation of Pinatubo aerosol and its effect on stratospheric ozone. *J Geophys Res: 99*, 20,545, 1994.

Tie, X.X., C. Granier, W. Randel, and G.P. Brasseur, Effects of interannual variation of temperature on heterogeneous reactions and stratospheric ozone. *J Geophys Res: 102*, 23,519, 1997.

Tolbert, M.A., M.J. Rossi, and D.M. Golden, Heterogeneous interactions of chlorine nitrate hydrogen chloride and nitric acid with sulfuric acid surfaces at stratospheric temperatures. *Geophys Res Lett: 15*, 847, 1988.

Toohey, D.W., A critical review of stratospheric chemistry research in the U.S.: 1991-1994. *Rev Geophys Suppl*, U.S. National Report to International Union of Geodesey and Geophysics 1991-1994, 759, 1995.

Toohey, D.W., J.G. Anderson, W.H. Brune, and K.R. Chan., In situ measurements of BrO in the Arctic stratosphere. *Geophys Res Lett: 17*, 513, 1990.

Toohey, D.W., L.M. Avallone, L.R. Lait, P.A. Newman, M.R. Schoenberl, D.W. Fahey, E.L. Woodbridge, and J.G. Anderson, The seasonal evolution of reactive chlorine in the northern hemisphere stratosphere. *Science: 261*, 1134, 1993.

Toon, G.C., C.B. Farmer, L.L. Lowes, P.W. Schaper, J.-F. Blavier, and R.H. Norton, Infrared aircraft measurements of stratospheric composition over Antarctica during September 1987. *J Geophys Res: 94*, 16,571, 1989.

Toon, G.C., J.-F. Blavier, and J.T. Szeto, Latitude variations of stratospheric trace gases. *Geophys Res Lett: 21*, 2599, 1994.

Toon, O.B., P. Hamill, R.P. Turco, and J. Pinto, Condensation of HNO_3 and HCl in the winter polar stratosphere. *Geophys Res Lett: 13*, 1284, 1986.

Toon, O.B., E.V. Browell, S. Kinne, and J. Jordan, An analysis of lidar observations of polar stratopheric clouds. *Geophys Res Lett: 17*, 393, 1990.

Toumi, R., S. Bekki, and R. Cox, A model study of ATMOS observations and the heterogeneous loss of N_2O_5 by the sulphate aerosol layer. *J Atmos Chem: 16*, 135, 1993.

Traub, W.A., K.W. Jucks, D.G. Johnson, and K.V. Chance, Chemical change in the Arctic vortex during AASE II. *Geophys Res Lett: 21*, 2595, 1994.

Tuck, A.F., Synoptic and chemical evolution of the Antarctic vortex in late winter and early spring, 1987. *J Geophys Res: 94*, 11,687, 1989.

Tuck, A.F., and M.H. Proffitt, Comment on "On the magnitude of transport out of the Antarctic polar vortex" by W.M.F. Wauben *et al.*, *J Geophys Res: 102*, 28,215, 1997.

Tuck, A.F, T. Davies, S.J. Hovde, M. Noguer-Alba, D.W. Fahey, S.R. Kawa, K.K. Kelly, D.M. Murphy, M.H. Proffitt, J.J. Margitan, M. Loewenstein, J.R. Podolske, S.E. Strahan, and K.R. Chan, Polar stratospheric cloud processed air and potential vorticity in the northern hemisphere lower stratosphere at mid-latitudes during winter. *J Geophys Res: 97*, 7883, 1992.

Tuck, A.F., D. Baumgardner, K.R. Chan, J.E. Dye, J.W. Elkins, S.J. Hovde, K.K. Kelly, M. Loewenstein, J.J. Margitan, R.D. May, J.R. Podolske, M.H. Proffitt, K.H. Rosenlof, W.L. Smith, C.R. Webster, and J.C. Wilson, The Brewer-Dobson circulation in the light of high altitude in-situ aircraft observations. *Quart J Roy Meteorol Soc: 123*, 1, 1997.

Tung, K.K., M.K.W. Ko, J.M. Rodriguez, and N.D. Sze, Are Antarctic ozone variations a manifestation of dynamics or chemistry? *Nature: 333*, 811, 1986.

Turco, R.P., and P. Hamill, Supercooled sulfuric acid droplets: Perturbed stratospheric chemistry in early winter. *Ber Bunsenges Phys Chem: 96*, 323, 1992.

Van Roozendael, M., C. Fayt, D. Bolse, P.C. Simon, M. Gil., M. Yela, and J. Cacho, Ground-based stratospheric NO_2 monitoring at Keflavik (Iceland) during EASOE. *Geophys Res Lett: 21*, 1379, 1994.

Von Clarmann, T., H. Fischer, F. Friedl-Vallon, A. Linden, H. Oelhof, C. Piesch, M. Seefeldner, and W. Völker, Retrieval of stratospheric O_3, HNO_3 and $ClONO_2$ profiles from 1992 MIPAS-B limb emission spectra. *J Geophys Res: 98*, 20,495, 1993.

Voemel, H., S.J. Oltmans, D.J. Hofmann, T. Deshler, and J.M. Rosen, The evolution of the dehydration in the Antarctic stratospheric vortex. *J Geophys Res: 100*, 13,919, 1995.

Von der Gathen, P., M. Rex, N.R.P. Harris, D. Lucic, B.M. Knudsen, G.O. Braathen, H. de Backer, R. Fabian, H. Fast, M. Gil, E. Kyrö, I.S. Mikkelsen, M. Rummukainen, J. Stähelin, and C. Varotsos, Observational evidence for chemical ozone depletion over the Arctic in winter 1991-2. *Nature: 375*, 131, 1995.

Wahner, A., R.O. Jakoubek, G.H. Mount, A.R. Ravishankara, and A.L. Schmeltekopf, Remote sensing observations of nighttime OClO column during the airborne Antarctic ozone experiment, September 8, 1987. *J Geophys Res: 94*, 11,405, 1989.

Wahner, A., J. Callies, H-P Dorn, U. Platt, and C. Schiller, Near UV atomospheric absorption measurements of column abundances during airborne Arctic stratospheric expeditions, January-February 1989: 1. Technique and NO_2 observations. *Geophys Res Lett: 17*, 497, 1990.

Waters, J.W., J.C. Hardy, R.F. Jarnot, and H.M. Pickett, Chlorine monoxide radical, ozone, and hydrogen peroxide: Stratospheric measurements by microwave limb sounding. *Science: 214*, 61, 1981.

Waters, J.W., L. Froidevaux, W.G. Read, G.L. Manney, L.S. Elson, D.A. Flower, R.F. Jarnot, and R.S. Harwood, Stratospheric ClO and ozone from the microwave limb sounder on the upper atmosphere research satellite. *Nature: 362*, 597, 1993.

Waters, J.W., W.G. Read, L. Froidevaux, R.F. Jarnot, R.E. Cofield, D.A. Flower, G.K. Lau, H.M. Pickett, M.L. Santee, D.L. Wu, M.A. Boyles, J.R. Burke, R.R. Lay, M.S. Loo, N.J. Livesey, T.A. Lungu, G.L. Manney, L.L. Nakamura, V.S. Perun, B.P. Ridenoure, Z. Shippony, P.H. Siegel, R.P. Thurstans, R.S. Harwood, H.C. Pumphrey, and M.J. Filipiak, The UARS and EOS Microwave Limb Sounder (MLS) experiments. *J Atmos Sci: 56*, 194, 1999.

Wauben, W.M.F., R. Bintanja, P.F.J. van Velthoven, and H. Kelder, On the magnitude of transport out of the Antarctic polar vortex. *J Geophys Res: 102*, 1229, 1997.

Waugh, D.W., R.A. Plumb, R.J. Atkinson, M.R. Schoeberl, L.R. Lait, P.A. Newman, M. Loewenstein, D.W. Toohey, L.M. Avallone, C.R. Webster, and R.D. May, Transport out of the lower stratospheric Arctic vortex by Rossby wave breaking. *J Geophys Res: 99*, 1071, 1994.

Waugh, D.W., R.A. Plumb, J.W. Elkins, D.W. Fahey, K.A. Boering, G.S. Dutton, C.M. Volk, E. Keim, R.S. Gao, B.C. Daube, S.C. Wofsy, M. Loewenstein, J.R. Podolske, K.R. Chan, M.H. Proffitt, K.K. Kelly, P.A. Newman, and L.R. Lait, Mixing of polar vortex air into middle latitudes as revealed by tracer-tracer scatterplots. *J Geophys Res: 102*, 13,119, 1997.

Webster, C.R., R.D. May, D.W. Toohey, L.M. Avallone, J.G. Anderson, P. Newman, L. Lait, M.R. Schoeberl, J.W. Elkins,and K.R. Chan, Chlorine chemistry on polar stratospheric cloud particles in the Arctic winter. *Science: 261*, 1130, 1993.

Webster, C.R., R.D. May, M. Allen, L. Jaegle, and M. P. McCormick, Balloon profiles of stratospheric NO_2 and HNO_3 for testing the heterogeneous hydrolysis of N_2O_5 on sulfate aerosols. *Geophys Res Lett: 21*, 53, 1994.

Webster, C.R., R.D. May, H.A. Michelsen, D.C. Scott, J.C. Wilson, H.H. Jonsson, C.A. Brock, J.E. Dye, D. Baumgardner, R.M. Stimpfle, J.P. Koplow, J.J. Margitan, M.H. Proffitt, L. Jaeglé, R.L. Herman, H. Hu, G.J. Flesch, M. Loewenstein, Evolution

of HCl concentrations in the lower stratosphere from 1991 to 1996 following the eruption of Mt. Pinatubo. *Geophys Res Lett: 25*, 995, 1998.

Weeks, C.H., R.S. Cuikay, and J.R. Corbin, Ozone measurements in the mesosphere during the solar proton event of 2 November 1969. *J Atmos Sci: 29*, 1138, 1972.

Wennberg, P.O., R.C. Cohen, R.M. Stimpfle, J.P. Koplow, J.G. Anderson, R.J. Salawitch, D.W. Fahey, E.L. Woodbridge, E.R. Keim, R.S. Gao, C.R. Webster, R.D. May, D.W. Toohey, L.M. Avallone, M.H. Proffitt, M. Loewenstein, J.R. Podolske, K.R. Chan,and S.C. Wofsy, Removal of stratospheric O_3 by radicals: In situ measurements of OH, HO_2, NO, NO_2, ClO, and BrO. *Science: 266*, 398, 1994.

Williams, W.J., J.J. Kosters, and D.G. Murcray, Nitric acid column densities over Antarctica. *J Geophys Res: 87*, 8976, 1982.

Wilson, J.C., H.H. Jonsson, C.A. Brock, D.W. Toohey, L.M. Avallone, D. Baumgardner, J.E. Dye, L.R. Poole, D.C. Woods, R.J. DeCoursey, M. Osborn, M.C. Pitts, K.K. Kelly, K.R. Chan, G.V. Ferry, M. Loewenstein, J.R. Podolske, and A. Weaver, In situ observations of aerosol and chlorine monoxide after the 1991 eruption of Mount Pinatubo: Effect of reactions on sulfate aerosol. *Science: 261*, 1140, 1993.

WMO (World Meteorological Organization), *Atmospheric Ozone.* Report No. 16, 1985.

World Meteorological Organization/United Nations Environment Programme (WMO/UNEP), *Scientific Assessment of Ozone Depletion: 1989*, Report No. 20, 1989.

World Meteorological Organization/United Nations Environment Programme (WMO/UNEP), *Scientific Assessment of Ozone Depletion: 1991*, Report No. 25, 1991.

World Meteorological Organization/United Nations Environment Programme (WMO/UNEP), *Scientific Assessment of Ozone Depletion: 1994*, Report No. 37, 1994.

World Meteorological Organization/United Nations Environment Programme (WMO/UNEP), *Scientific Assessment of Ozone Depletion: 1998*, Report No. 44, Geneva, 1999.

World Meteorological Organization/United Nations Environment Programme (WMO/UNEP), *Scientific Assessment of Ozone Depletion: 2002*, Report No. 47, Geneva, 2003.

Wuebbles, D.J., F.M. Luther, and J.E. Penner, Effect of coupled anthropogenic perturbations on stratospheric ozone. *J Geophys Res: 88*, 1444, 1983.

Yudin, V.A., M.A. Geller, B.V. Khattatov, A.R. Douglass, M.C. Cerniglia, J.W. Waters, L.S. Elson, A.E. Roche, and J.M. Russell III, A UARS study of lower stratospheric polar processing in the early stages of northern and southern winters. *J Geophys Res: 102*, 19,137, 1997.

Zander, R., E. Mahieu, M.R. Gunson, M.C. Abrams, A.Y. Chang, M. Abbas, C. Aellig, A. Engel, A. Goldman, F.W. Irion, N. Kämpfer, H.A. Michelsen, M.J. Newchurch, C.P. Rinsland, R.J. Salawitch, G.P. Stiller, and G.C. Toon, The 1994 northern mid-latitude budget of stratospheric chlorine derived from ATMOS/ATLAS-3 observations. *Geophys Res Lett: 23*, 2357, 1996.

Zerefos, C.S., K. Tourpali, and A.F. Bais, Further studies on possible volcanic signal to the ozone layer. *J Geophys Res: 99*, 25,741, 1994.

Zerefos, D.S., K. Tourpali, B.R. Bojkov, D.S. Balis, B. Rognerund, and I.S.A. Isaksen, Solar activity-total column ozone relationships: Observations and model studies with heterogeneous chemistry. *J Geophys Res: 102*, 1561, 1997.

Zhou, S., M.E. Gelman, A.J. Miller, and J.P. McCormack, An inter-hemisphere comparison of the persistent stratospheric Polar vortex. *Geophys Res Lett: 27*, 1123, 2000.

Zurek, R.W., G.L. Manney, A.J. Miller, M.E. Gelman, and R.M. Nagatani, Interannual variability of the north polar vortex in the lower stratosphere during the UARS mission. *Geophys Res Lett: 23*, 289, 1996.

Chapter 7

THE IONS

7.1 Introduction

At the end of the 19th century, it was suggested that the presence of an electrically conducting atmospheric layer could explain the observed diurnal variation in the terrestrial magnetic field. In 1901, Marconi established the first radiowave transmission between Europe and North America, and Kennelly and Heaviside independently suggested that this communication was possible only because of the reflection of radio signals by a conducting layer near 80 km altitude. Radiowave methods later led to the first quantitative studies of this layer, through analysis of emitted signals reflected to the surface. Systematic sounding of this type showed that the base of the electrically conducting layer was located at about 50-60 km. Present understanding of chemical processes affecting ions is due primarily to laboratory investigations and to *in situ* mass spectrometric measurements made from balloon and rocket platforms. Such studies have revealed, for example, that electrons are present in very small abundances below the stratopause, and that positive and negative ions dominate the ion composition of the stratosphere while positive ions and electrons dominate the mesosphere and thermosphere. Atmospheric gaseous ions not only affect the electrical properties of the atmospheric medium; they also play an interesting role in the chemistry of the atmosphere.

The *ionosphere* is a weakly ionized fluid of net neutral charge. Atmospheric atoms and molecules can be ionized either by short wavelength solar radiation (UV and X-rays), or by precipitating energetic particles, *e.g.*,

$$\mathrm{X} + \mathrm{h}\nu \rightarrow \mathrm{X}^+ + \mathrm{e} \tag{7.1}$$

$$\mathrm{X} + \mathrm{e}^* \rightarrow \mathrm{X}^+ + 2\mathrm{e} \tag{7.2}$$

where e^* represents an energetic electron. These processes are the starting points for a series of reactions which determine the structure of the ionosphere. Several types of general reactions of importance in ion chemistry should be outlined in order to study the ionosphere.

For example, different ions may be produced from the initial (also called *primary*) particles through charge exchange reactions with neutral molecules:

$$X^+ + Y \rightarrow Y^+ + X \tag{7.3}$$

Negative ions can also be formed by electron attachment on neutral species:

$$e + Z + M \rightarrow Z^- + M \tag{7.4}$$

Electrons can be released from negative ions, either by photodetachment or by collisional detachment:

$$Z^- + h\nu \rightarrow Z + e \tag{7.5}$$

$$Z^- + M \rightarrow Z + M + e \tag{7.6}$$

Positively and negatively charged particles can recombine:

$$X^+ + e \rightarrow \text{neutral products} \tag{7.7}$$

$$X^+ + Y^- \rightarrow \text{neutral products} \tag{7.8}$$

Understanding the formation of the ions requires knowledge of the spectral distribution of solar radiation at short wavelengths, the structure of solar and galactic cosmic rays, as well as the chemical composition of the atmosphere and its physical characteristics such as pressure, temperature, and transport. The variations of solar activity must also be considered.

It is customary to divide the ionosphere into a number of characteristic layers based on the mean vertical profile of electron density.

The *D-region* is located between about 60 km and 90-95 km. In this layer, ionization results mostly from photoionization of NO by Lyman α radiation (121.6 nm). High energy cosmic rays also contribute to the ionization of O_2 and N_2 below 70 km. Radio waves are readily absorbed in the D-region, as will be discussed in Section 7.6.

The *E-region* extends from about 90-95 km to 130 km. It is produced by ionization of molecular and atomic oxygen, and molecular nitrogen, by X-rays and Lyman β radiation (102.6 nm). Although the predominant ions in this layer are O_2^+ and NO^+, relatively large concentrations of Fe^+, Mg^+, Si^+, and Ca^+ are also observed. These latter ions are produced mainly by meteor ablation between 85 and 130 km.

The *F-region* begins above 130 km and is sometimes subdivided into two layers, F_1 and F_2. It is primarily produced by ionization of atomic oxygen and molecular nitrogen by extreme ultraviolet radiation (9-91 nm). The atomic oxygen ion, O^+, dominates. The electron density attains its maximum value of about $10^6 cm^{-3}$ in this layer. The F-region plays an important role in the transmission of certain radio waves, which

can be reflected or refracted if their frequency is less than 5-10 MHz, or transmitted if their frequency is above this limit (television waves).

In the D, E, and F_1 layers, the electron concentration is greatest at maximum solar elevation (local noon). At night, the electrons disappear almost entirely in the D-region, and their density is reduced by a factor of 100 in the E- and F_1-regions. In these layers, the lifetime of the ions is short compared to the transport time scale, and the charged particle concentrations are therefore determined by a photochemical equilibrium between production (by ionization processes) and loss (by recombination of positive ions with electrons or with negative ions). In the F_2-region, on the other hand, the electron density is no longer due to a simple equilibrium between ionization and recombination and the effects of transport by molecular diffusion must be considered, particularly above 300 km. The structure of this part of the ionosphere is complex, and varies considerably with geomagnetic latitude.

Above the F_2 layer, the electron density rapidly decreases. Helium He^+ and then hydrogen H^+ ions dominate, and the effect of the magnetic field on these charged particles becomes more important. As a result, the particles no longer occur in horizontal layers; rather they tend to be aligned by the Earth's magnetic field.

A detailed description of the ionospheric layers is given by Banks and Kockarts (1973) and, more recently, by Hargreaves (1979; 1992). Physical and chemical processes occurring in the upper atmosphere are discussed by Rees (1989) and Kelly (1989).

Electrically charged particles play a substantial role in the middle and upper atmosphere. First, they are directly involved in the occurrence of aurora and airglow, since the formation of energetically-excited molecules or atoms that emit visible radiation are often formed by the recombination of positive ions and electrons. The formation of polar mesospheric clouds near 85 km altitude during summer seems to be facilitated by the presence of condensation nuclei in the form of large proton hydrates. Ions also have an impact on neutral species. As already mentioned in Chapter 5, ionic reactions lead to the formation of odd nitrogen and odd hydrogen compounds with potential impact on mesospheric and stratospheric ozone, especially during solar events. Finally, as the fraction of ionized compounds increases with altitude, air parcels become increasingly affected by electromagnetic forces. The so-called "ion-drag" process (see Chapter 3) becomes a significant force in the thermosphere and needs to be taken into account in the calculation of the winds.

Figure 7.1 shows the shape of the mean vertical distribution of electrons below 1000 km and indicates the dominant ions in each layer. In this chapter, we will discuss only the ions in the middle

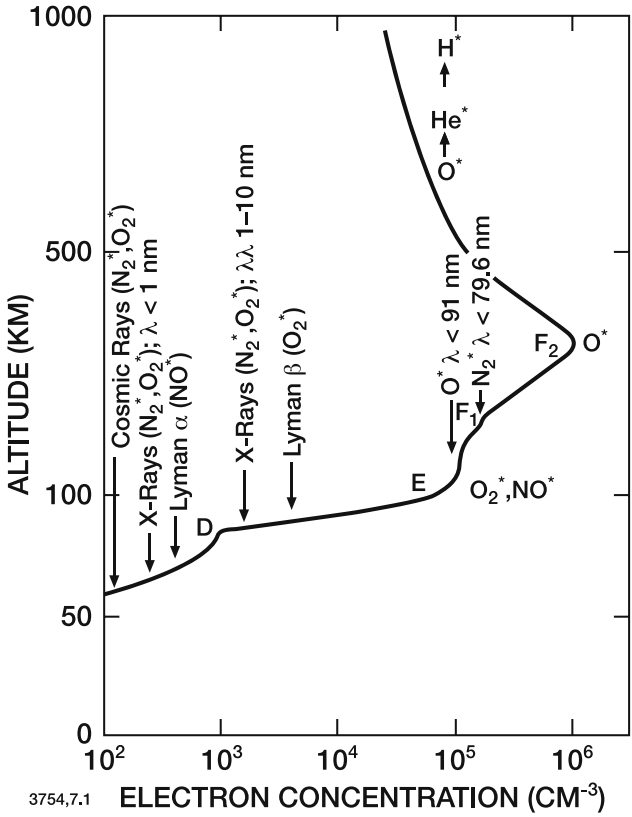

Figure 7.1. Definition of the ionospheric layers based on the vertical distribution of electron density. From Banks and Kockarts (1973).

atmosphere, *i.e.*, those observed in the D-and lower E-regions, and in the stratosphere.

To study the behavior of the ions and electrons in a simple fashion, we first write the following equations of continuity, assuming only a single ion of each type:

$$\frac{dn^+}{dt} = nI - \alpha_D n^+ n_e - \alpha_i n^+ n^- \tag{7.9}$$

$$\frac{dn^-}{dt} = a_e n n_a n_{e^-} n^- (d_p + f_d n + \alpha_i n^+) \tag{7.10}$$

$$\frac{dn_e}{dt} = nI - \alpha_D n^+ n_e - a_e n^2 n_e + n^- (d_p + f_d n) \tag{7.11}$$

where

n = concentration of the neutral species which ionize, attach, and detach electrons (*e.g.*, NO, OH, etc.)

n^+ = concentration of the positive ion
n^- = concentration of the negative ion
n_e = electron concentration
n_a = concentration of main atmospheric molecules (N_2, O_2)
α_D = electron-ion recombination rate
α_i = ion-ion recombination rate
a_e = electron-neutral attachment rate
d_p = negative ion photodetachment rate
f_d = negative ion collisional detachment rate
I = ionization frequency (formation of an electron and a positive ion).

Further, electrical neutrality is assumed:

$$n^+ = n^- + n_e = (1+\lambda)\, n_e \tag{7.12}$$

where

$$\lambda = n^-/n_e \tag{7.13}$$

is the ratio of negative ions to electrons. Expressions (7.9) and (7.10) can now be transformed (assuming $n_a = n$):

$$\frac{dn_e}{dt} = \frac{nI}{1+\lambda} - (\alpha_D + \lambda\alpha_i)n_e^2 - \frac{n_e}{1+\lambda}\frac{d\lambda}{dt} \tag{7.14}$$

$$\frac{dn_e}{dt} = \frac{a_e n^2 n_e}{\lambda} - n_e\,[d_p + f_d n + (1+\lambda)\alpha_i n_e] - \frac{n_e}{\lambda}\frac{d\lambda}{dt} \tag{7.15}$$

eliminating dn_e/dt, we obtain the ratio, λ:

$$\frac{1}{\lambda(1+\lambda)}\frac{d\lambda}{dt} = \left[\frac{a_e n^2}{\lambda} + (d_p + f_d n)\right] - \left[\frac{nI}{(1+\lambda)n_e} + (\alpha_i - \alpha_D)\, n_e\right] \tag{7.16}$$

which is a Riccati differential equation. Analysis of approximate magnitude of the respective terms in Eq. (7.16) shows that it is possible to neglect the contribution of the ionization and recombination terms, so that the equation reduces approximately to

$$\frac{d\lambda}{dt} = (1+\lambda)\, a_e n n_a - (1+\lambda)\,\lambda\,(d_p + f_d n) \tag{7.17}$$

Since the time constant for negative ion formation by attachment (a_e) is at most about an hour at the top of the middle atmosphere (and is much less at lower altitudes), photochemical steady state can be assumed:

$$\lambda = \frac{a_e n n_a}{d_p + f_d n} \tag{7.18}$$

This equation shows that the ratio of the negative ions to electrons depends principally on the rate of attachment of electrons on neutral particles, and on the rate of detachment by solar radiation and collisions.

The continuity equation for electrons in the D-region can be written:

$$\frac{dn_e}{dt} = \frac{nI}{1+\lambda} - (\alpha_D + \lambda\alpha_i)\, n_e^2 \tag{7.19a}$$

but, in the E-region, where $\lambda << 1$,

$$\frac{dn_e}{dt} = nI - \alpha_D n_e^2 \tag{7.19b}$$

A more realistic analysis considers formation of several ions (j), and involves more complex expressions of the type

$$\frac{dn_e}{dt} = \sum_j \frac{n_j I_j}{1+\lambda} - \frac{n_e}{1+\lambda} \sum_j (\alpha_{D,j} + \lambda\alpha_{i,j}) n_j^+ \tag{7.20}$$

with

$$\sum_j n_j{}^+ = (1+\lambda)\, n_e \tag{7.21}$$

An effective recombination rate can then be defined:

$$\alpha_{eff} = \frac{\sum_j (\alpha_{D,j} + \lambda\alpha_{i,j})\, n_j^+}{\sum_j n_j^+} \tag{7.22}$$

such that the equation for electrons becomes

$$\frac{dn_e}{dt} = \sum_j \frac{n_j I_j}{1+\lambda} - \alpha_{eff} n_e^2 \tag{7.23}$$

Because the lifetime of electrons in this part of the atmosphere is quite short, we can assume photochemical equilibrium, and the electron concentration is given by

$$n_e = \left(\frac{\sum_j n_j I_j}{(1+\lambda)\, \alpha_{eff}} \right)^{1/2} \tag{7.24}$$

Figure 7.2.a/7.2.b presents the shape of the vertical distributions of α_{eff} and λ , and Figure 7.3 shows some representative observed electron density profiles in the D- and lower E-regions.

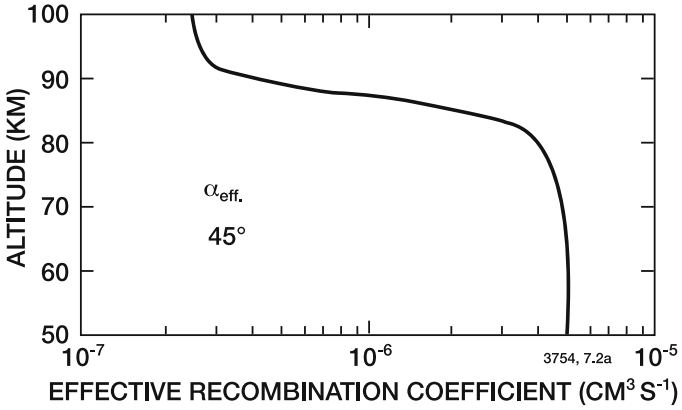

Figure 7.2.a. Vertical distribution of the effective recombination coefficient α_{eff} obtained with a mathematical model. From Brasseur (1982).

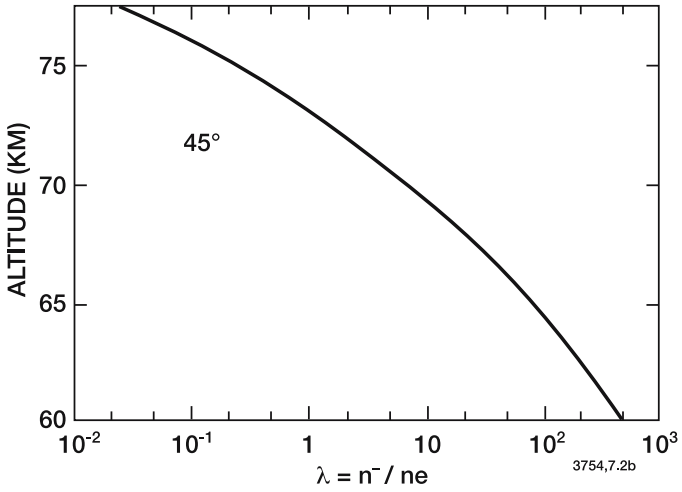

Figure 7.2.b. Ratio λ of negative ions to electrons as a function of altitude as calculated with a mathematical model for low solar activity. From Brasseur (1982).

7.2 Formation of Ions in the Middle Atmosphere

7.2.1 Effect of Solar Radiation

Examination of the photoionization thresholds and absorption cross sections for atmospheric constituents shows that the solar radiation capable of producing ionization is primarily absorbed by O_2, N_2, NO, and O. Table 7.2 presents the photoionization thresholds for various

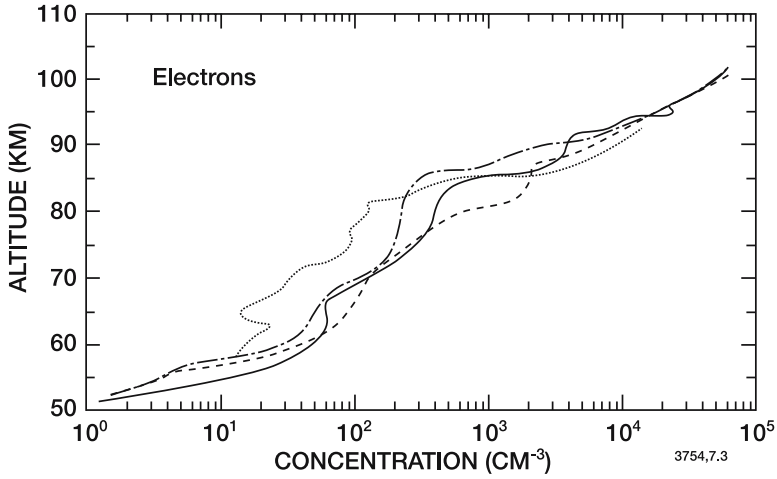

Figure 7.3. Vertical distributions of electron density observed during daytime at Wallops Island, Virginia, during different seasons, for a zenith angle of 60 degrees. Observations in April 1964, June 1965, September 1965, and December 1965. From Mechtly and Smith (1968).

atmospheric molecules. The photoionization limit of molecular oxygen is 102.8 nm, implying that oxygen is ionized by the Lyman β and C III lines and by solar X-rays. On the other hand, molecular nitrogen can only be ionized by wavelengths less than 79.58 nm, and is therefore unaffected by the principal ultraviolet lines which are available below 100 km. Richards *et al.* (1994) present a detailed solar EUV model (5-105 nm) and the sensitivity of the flux to solar activity. Another detailed model of the solar flux is provided by Tobiska *et al.* (2000). Table 7.1 gives some typical values of the incident solar fluxes for different levels of solar activity.

Given the ionization (σ) and absorption (K) cross sections of N_2, O_2, and O for different spectral intervals, the photoionization coefficient can be calculated using the following expression:

$$\mathrm{I(X)} = \sum \sigma_{\mathrm{i}}(\mathrm{X}) \mathrm{q}_{\infty,\mathrm{i}}\, \mathrm{e}^{-\tau} \qquad (\mathrm{X} = \mathrm{N_2}, \mathrm{O_2} \text{ or } \mathrm{O}) \qquad (7.25a)$$

where

$$\tau_{\mathrm{i}} = \mathrm{K_{i,O_2}(O_2) + K_{i,N_2}(N_2) + K_{i,O}(O)} \qquad (7.25b)$$

and where the other symbols have been defined in Chapter 4. Photoionization and photoabsorption cross sections needed to calculate the ion production using 37 wavelength bins are given by Richards *et al.* (1994).

Stewart (1970) suggested analytic expressions which can be used to obtain the photoionization coefficients of N_2, O_2, and O to within 15%

Table 7.1 Flux of ionizing solar radiation ($cm^{-2}s^{-1}$) for different levels of solar activity.

Wavelength Interval (nm)	*Very Quiet Sun*	*Quiet Sun*	*Moderate Solar Activity*	*High solar Activity*
102.6 (L−β)	3.5 (9)	5.0 (9)	8.0 (9)	1.2 (10)
97.7 (C III)	4.4 (9)	5.0 (9)	6.0 (9)	1.0 (10)
91-79.6	7.5 (9)	1.0 (10)	1.3 (10)	1.5 (10)
79.6-73.2	1.0 (9)	1.3 (9)	1.5 (9)	2.0 (9)
73.2-66.5	5.0 (8)	6.0 (8)	8.0 (8)	1.0 (9)
66.5-37.5	4.0 (9)	6.0 (9)	8.0 (9)	1.2 (10)
37.5-27.5	7.5 (9)	1.0 (10)	1.5 (10)	2.0 (10)
27.5-15.0	7.5 (9)	1.0 (10)	1.5 (10)	2.0 (10)
15.0-8.0	5.0 (8)	7.5 (8)	1.0 (9)	2.0 (9)
8.0-6.0	2.5 (7)	5.0 (7)	1.0 (8)	1.5 (8)
6.0-4.1	2.5 (7)	5.0 (7)	1.0 (8)	1.5 (8)
4.1-3.1	7.5 (6)	1.5 (7)	3.0 (7)	4.5 (7)
0.8-0.5	2.9 (2)	2.9 (3)	2.9 (4)	2.9 (5)
0.33-0.5	2.0 (1)	2.0 (2)	2.0 (3)	2.0 (4)
0.15-0.33	1.0 (0)	1.0 (1)	1.0 (2)	1.0 (3)

Table 7.2 Ionization potentials of atoms and molecules (wavelength in nm).

Al	207.1	Fe	157.1	O_3	96.9	CO_2	89.9
Na	241.2	NO	134.0	H_2O	98.5	O	91.0
Ca	202.8	NH_3	122.1	N_2O	96.1	CO	88.5
Mg	162.2	O_2 ($^1\Delta g$)	111.8	CH_4	95.4	N	85.2
Si	152.1	O_2	102.8	OH	94.0	N_2	79.6
C	110.0	SO_2	100.8	H	91.1	Ar	78.7

accuracy. Defining the effective column density as:

$$N^*(z,\chi) = N(N_2,z,\chi) + N(O_2,z,\chi) + 0.8 \times N(O,z,\chi) \qquad (7.26)$$

where N (N_2, z, χ) represents the total column abundance of N_2 (molec cm^{-2}) along the solar ray path, and N (O_2, z, χ) and N (O, z, χ) are defined similarly. Then

$$I_{X^+}^{-1} \approx A_0 + A_1 (N^*(z,\chi) \times 10^{-17}) + A_2 (N^*(z,\chi) \times 10^{-17})^{\alpha} \qquad (7.27)$$

Using this expression, the photoionization frequencies of N_2^+, O_2^+, and O^+ can be estimated for mean solar activity by substituting the appropriate constants given in Table 7.3 below:

Table 7.3 Constants for Photoionization Frequencies

Constituent	A_o	A_1	A_2	α
$I_{N_2^+}$	2.2 (6)	2.2 (6)	6.4 (6)	2.0
$I_{O_2^+}$	1.1 (6)	1.0 (6)	1.3 (6)	2.5
I_{O^+}	2.3 (6)	3.2 (6)	1.0 (6)	2.4

Figure 7.4 shows the ionization rate for four primary ions (O_2^+, N_2^+, O^+, and N^+) between 90 and 120 km altitude. Note that the N^+ ion is produced primarily by dissociative ionization of N_2.

In the D-region, under typical conditions, most of the ionization is due to the effect of the solar Lyman α ray on nitric oxide (Nicolet, 1945). The ionization potential of the NO molecule is only 9.25 eV, which corresponds to a wavelength of 134 nm. In the spectral region of the Lyman α line an atmospheric window exists due to the low absorption cross section of O_2 in this interval, and thus the ionizing radiation can

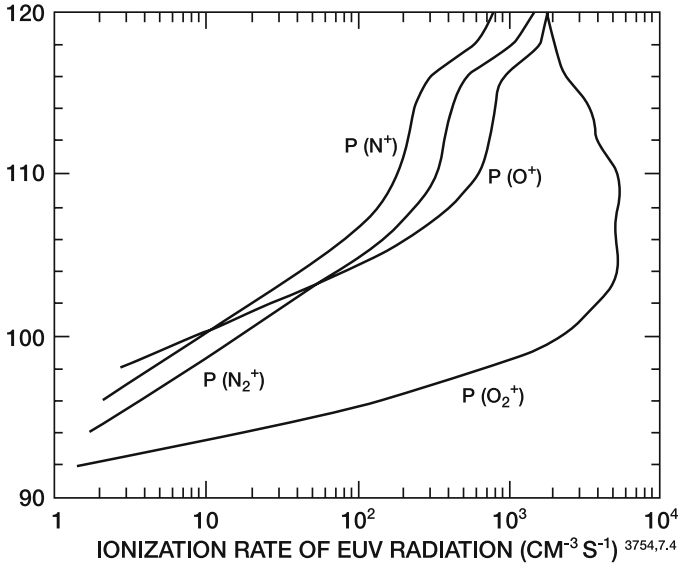

Figure 7.4. Production rate by EUV radiation of primary ions in the E-region of the ionosphere calculated for 50°N at local noon during summertime (from Fritzenwallner, 1997).

penetrate relatively far into the mesosphere. The rate of production of the NO^+ ion is given by

$$P\left(NO^+\right) = I_{NO}\left(NO\right) \tag{7.28}$$

and can be estimated by

$$I_{NO} = 6\left(1 + R\right) \times 10^{-7} \exp\left[-1 \times 10^{-20} N\left(O_2, z, \chi\right)\right] \left(s^{-1}\right) \tag{7.29}$$

where R is a factor that accounts for solar variability and which ranges from 0 (solar minimum) to approximately 0.8 (solar maximum). This expression assumes that the incident flux (q_∞) of Lyman α is $3(1+R) \times 10^{11} cm^{-2} s^{-1}$, $\sigma_{NO} = 2.0 \times 10^{-18} cm^{-2}$, and $\sigma_{O_2} = 1.0 \times 10^{-20} cm^{-2}$. N ($O_2$, z, χ) represents the integrated oxygen abundance along the line of sight, as above. It should be noted that even at night, when the direct incident flux of Lyman α is zero, there is still a considerable flux of scattered Lyman α reflected by the hydrogen geocorona in the uppermost levels of the atmosphere. Its intensity is about 100 to 1000 times weaker than the direct daytime flux. It is, however, a major ion source of the D-region during nighttime. A similar effect occurs for Lyman β, and is important in the E-region, where it is a major source of O_2^+ ions.

The morphology of the D-region is therefore closely related to the distribution of nitric oxide, which is strongly tied to dynamics (Brasseur and Nicolet, 1973; Solomon *et al.*, 1982a,b; Brasseur and De Baets, 1986). Nitric oxide is produced in large amounts in the stratosphere and thermosphere, while in the mesosphere its distribution is heavily dependent on the competition between transport from these neighboring regions and destruction by photochemical processes (see Chapter 5).

The absorption of solar radiation in the spectral region from 102.7 [photoionization limit of $O_2(^1\Sigma_g^-)$] to 111.8 nm [photoionization limit of $O_2(^1\Delta_g)$] represents an additional source of D-region ionization as suggested by Hunten and McElroy (1968). In this region, however, the incident radiation is absorbed both by O_2 and CO_2, so that the rate of formation of the O_2^+ ion

$$P\left(O_2^+\right) = I_{O_2(^1\Delta_g)}\left(O_2(^1\Delta_g)\right) \tag{7.30}$$

is much smaller than the rate of ionization of NO. The rate of production has been determined by Paulsen *et al.* (1972) using the solar fluxes reported by Hall and Hinteregger (1970). The following approximate expression can be applied from 70 to 90 km.

$$\begin{aligned} I_{O_2(^1\Delta_g)} = {} & 0.549 \times 10^{-9} \exp\left[-2.406 \times 10^{-20} N\left(O_2, z, \chi\right)\right] \\ & + 2.614 \times 10^{-9} \exp\left[-8.508 \times 10^{-20} N\left(O_2, z, \chi\right)\right] \left(s^{-1}\right) \end{aligned} \tag{7.31}$$

The effect of solar variability is not accounted for in this expression and needs to be added for detailed calculations.

Hard X-rays ($\lambda < 1$ nm) also penetrate into the D-region. The production of ionization by X-rays is somewhat complex, since it involves the absorption of an X-ray photon by a neutral particle, leading to the production of photoelectrons which are sufficiently energetic to ionize other particles. It thus becomes necessary to distinguish between primary and secondary ionization. The mean number of secondary ion pairs produced depends on the energy of the incident photon. For example, this number has been estimated at about 45 for $\lambda = 0.6$ nm, 75 for $\lambda = 0.4$ nm, and 165 for $\lambda = 0.2$ nm (Nicolet and Aikin, 1960).

For low levels of solar activity, this source of ions is small compared to that produced by the Lyman α line. On the other hand, its contribution becomes more important during disturbed conditions: from 0.1 to 0.8 nm, for example, the solar irradiance is about 1000 times more intense for active conditions, and may increase by an additional factor of 100 during solar flares.

The ionization rate due to X-rays in the D-regions is thus quite variable. During solar flares, the X-ray contribution is reflected in observed changes in ion densities. Because of the relative stability of the dominant ion sources in this region at other times, the variability observed in the electron density (especially in the upper part of the D-region) is believed to be associated with meteorological fluctuations, including planetary wave propagation.

Soft X-rays (1-10 nm) are only important in the upper part of the middle atmosphere (z > 85km). Their flux also varies with solar activity.

7.2.2 The Effect of Energetic Particles

7.2.2.1 General

Energetic charged particles can penetrate into the Earth's atmosphere and ionize atmospheric species. They propagate along helical trajectories following the Earth's geomagnetic field. In polar regions (magnetic latitude $\Lambda > 75°$) the magnetic field lines are open and cosmic particles (*e.g.*, galactic) can easily enter the atmosphere. The depth of penetration of charged particles depends on their mass and energy. When energetic particles collide with neutral gas particles, a small amount of their energy is converted to X-rays as they are rapidly decelerated. This process is called the *bremstrahlung* process. The X-rays can penetrate deeper in the atmosphere than the original particles.

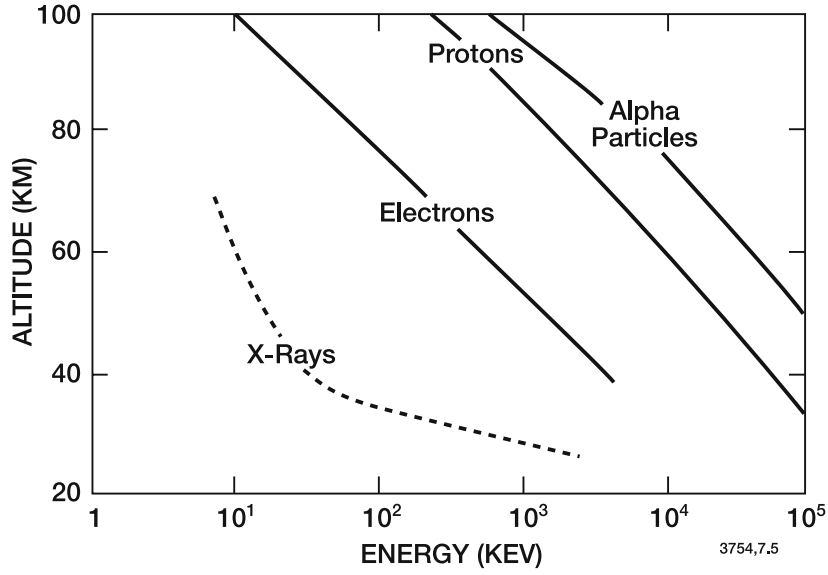

Figure 7.5. Depth of atmospheric penetration for different charged particles and X-rays as a function of energy. Adapted from Potemra (1974) and Thorne (1977a).

Figure 7.5 depicts the approximate depth of atmospheric penetration for different types of charged particles as a function of their energy. This diagram also shows the altitude of bremsstrahlung X-ray penetration produced by precipitation of high energy particles. In the auroral zone ($70^\circ < \Lambda < 75^\circ$), low energy particles (mostly electrons from 1-10 keV) precipitate into the atmosphere from the magnetospheric plasmasheet. These particles provide the optical displays known as the *aurora*, but do not penetrate much below 100 km. In the subauroral zone, ($\Lambda \leq 70^\circ$) particles can be accelerated in the radiation belt, attaining energies as high as a few MeV, and can thus penetrate into the upper stratosphere. Figure 7.6 shows the configuration of the Earth's geomagnetic field and the zones where charged particle precipitation occurs. It should be noted that high energy particles produce substantial fluxes of secondary electrons (energies from 10 to 100 eV) that are responsible for a considerable fraction of the energy transfer from the primary particles to the atmosphere. Knowledge of both the primary and secondary electron fluxes as a function of energy (also called the particle spectrum) and their cross sections for interaction with the principal atmospheric species is thus an important part of evaluating the impact of particle precipitation in aeronomic processes.

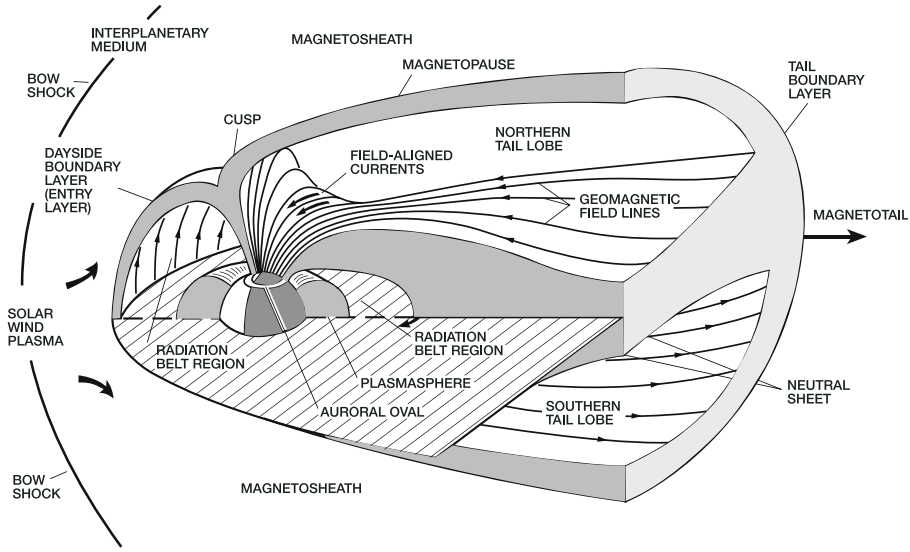

Figure 7.6. Schematic representation of the structure of the magnetosphere. From Kelley (1989) and courtesy of J. Roederer.

7.2.2.2 Cosmic Rays

The ionization of atmospheric constituents by galactic cosmic rays provides the dominant source of ions in the lower mesosphere, stratosphere, and troposphere. The rate of ion pair production increases exponentially with penetration into the atmosphere, *i.e.*, in proportion to the atmospheric density (see Figure 7.7) to reach a maximum near 10 to 15 km (Figure 7.8). The production is larger at high latitude than in the tropics, and is modulated by solar activity (see Eqs. (7.32)-(7.35), below). Galactic cosmic rays are produced outside the solar system, and consist mostly of protons (about 83%) and α particles (about 12%) with energy in the MeV to hundreds of MeV range. They tend to follow the magnetic field lines as they approach the Earth, and to penetrate near the magnetic poles. This is the primary reason for the observed meridional gradient in cosmic ray fluxes, particularly for less energetic particles which are more strongly influenced by the magnetic field. During periods of high solar activity, galactic cosmic rays tend to be removed from the solar system by the intense solar wind. The amplitude of cosmic ray precipitation thus decreases, as does the associated ion pair production. The reverse is true at solar minimum.

Heaps (1978a) derived a convenient parameterization of the rate of ion pair production by cosmic rays Q_{CR} ($cm^{-3}s^{-1}$) as a function of

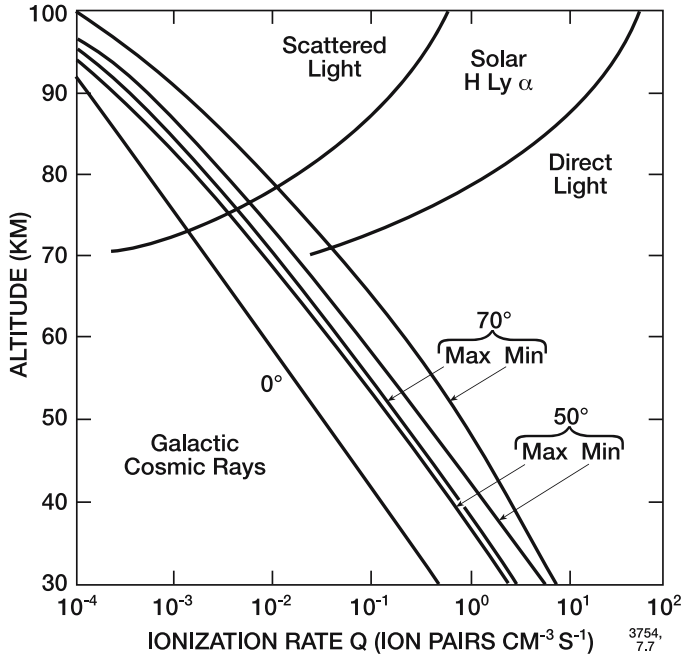

Figure 7.7. Rate of ionization provided by cosmic rays at different geomagnetic latitudes (0, 50, and 70°) and for minimum and maximum levels of solar activity. These values are compared to the ion pair production producted by direct and diffuse Lyman α. From Rosenberg and Lanzerotti (1979).

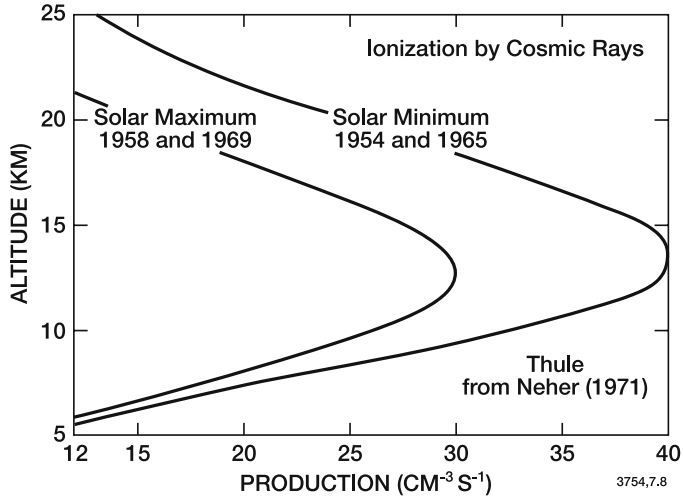

Figure 7.8. Rate of ionization by cosmic rays in the lower stratosphere and troposphere. From Brasseur and Nicolet (1973).

latitude, altitude, and solar activity level. For latitudes less than 53°, the following expressions can be used:

If

$$X_1 = 1.74 \times 10^{-18} \tag{7.32a}$$

$$X_2 = 1.93 \times 10^{-17}\,(\text{solar max}),\ 2.84 \times 10^{-17}\,(\text{solar min}) \tag{7.32b}$$

$$X_3 = 0.6 + 0.8|\cos\phi| \tag{7.32c}$$

then, for total number density (M) greater than 3×10^{17} molec cm^{-3},

$$Q_{CR} = \left(X_1 + X_2\left(|\sin\phi|^4\right)\right)\ 3 \times 10^{17^{(1-X_3)}}(M)^{X_3} \tag{7.33a}$$

while for (M) less than 3×10^{17}cm^{-3},

$$Q_{CR} = \left(X_1 + X_2|\sin\phi|^4\right)(M) \tag{7.33b}$$

where ϕ is the latitude. For latitudes greater than 53° (polar caps)

$$Q_{CR} = X_1(M) \qquad \text{(solar mean)} \tag{7.34a}$$

$$Q_{CR} = (X_1 + X_2)(M)\ \text{(solar min)} \tag{7.34b}$$

$$Q_{CR} = (X_1 - X_2)(M)\ \text{(solar max)} \tag{7.34c}$$

with

$$X_1 = 1.44 \times 10^{-17}\ ;\ X_2 = 4.92 \times 10^{-18} \tag{7.35}$$

The impact of cosmic rays on the chemical composition of the atmosphere has been assessed, for example, by Jackman *et al.* (1993).

7.2.2.3 Magnetospheric Electrons and X-rays Produced by Bremsstrahlung

Electron precipitation from the Earth's radiation belt is sporadically observed to produce ionization at high latitudes. As we have already mentioned, the penetration depth of these electrons depends directly on their energy and knowledge of their corresponding spectrum is thus necessary. The height of maximum ionization is typically 120 km for electron energy of 10 keV, 80 km for 100 keV and 70 km for 500 keV. Significant fluxes at energies exceeding 100 keV are often observed, and their precipitation is generally associated with geomagnetic storms in the subauroral radiation belt. The induced ionization events are generally referred to as relativistic electron precipitation (REP). The lifetime of these electrons is short (a few hours) and the frequency of REP events is not well known. Thorne (1977b) estimated that this phenomenon probably occurs between 1 and 10 percent of the time. Figure 7.9 shows the ionization rate above 60 km altitude due to monoenergetic electrons at various initial energies for an electron flux of 1 cm^{-2}s^{-1}.

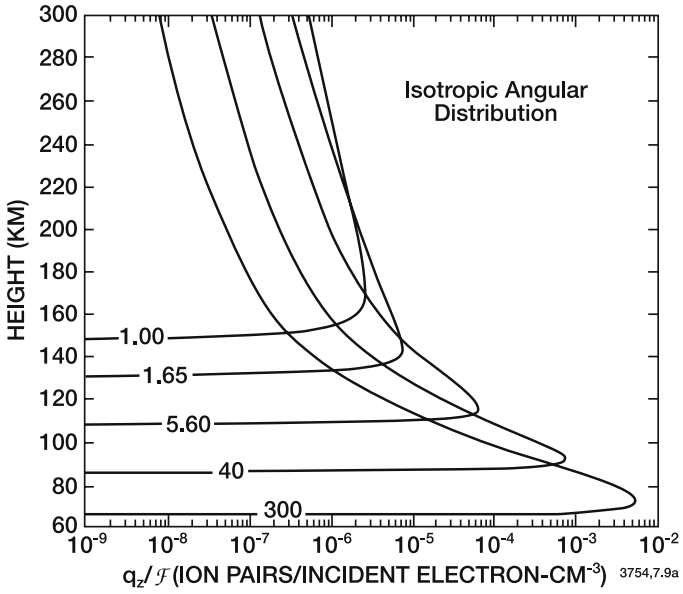

Figure 7.9. Ion production rate ($cm^{-3}s^{-1}$) as a function of altitude due to monoenergetic particles at various initial energies. Production rate due to a normalized flux of 1 electron $cm^{-2}s^{-1}$ at energies ranging from 1 to 300 keV (adapted from Rees, 1963).

Realistic vertical distributions of ion production rates for a given (*e.g.*, observed) energy spectrum of electron precipitation is obtained from the convolution of the monoenergetic ionization rate by this energy spectrum. Figure 7.10 shows an estimate of the average number of ions formed per year by relativistic electron and cosmic ray deposition in the middle atmosphere. The effect of associated bremsstrahlung (X-rays) is also indicated. In any case, in the subauroral zone, this mechanism of ion pair production is of considerable importance. It should be noted, however, that the belt only extends over about 7 percent of the globe. The effect of this process on ionospheric structure and trace neutral species distributions is not yet well established (see *e.g.*, Callis *et al.*, 1991).

7.2.2.4 Solar Proton Events

During large solar flares, heavy particles (mostly protons of energies from 10-500 MeV) can be emitted from the surface of the Sun in substantial amounts. These particles can produce intense ionization in the Earth's D-region, primarily at high latitudes (polar cap). High energy particles also penetrate below the stratopause (E > 10 MeV) and can even reach the tropopause (E $\geq$ 500 MeV). Although this phenomenon

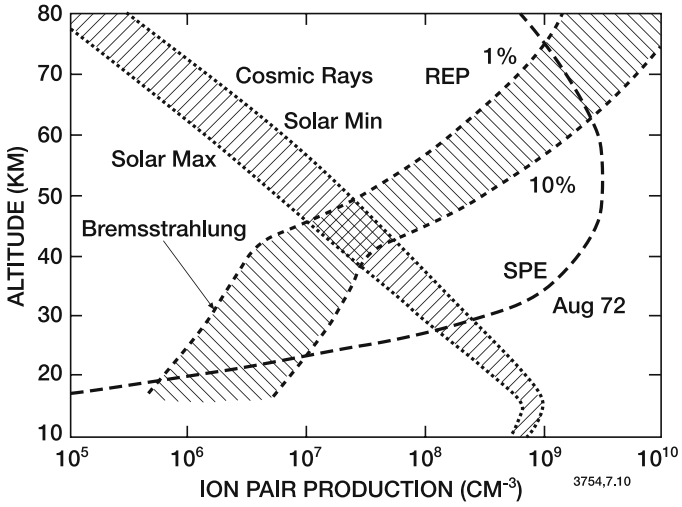

Figure 7.10. Rate of ion pair production by magnetospheric electrons (REP) in the subauroral zone. These values correspond to an annual average, and are compared to the effect of cosmic rays and the total ion pair production associated with the solar proton event (SPE) of August 1972. From Thorne (1977a).

is not frequent, it often lasts for several days. These events can change the ionization rate from its normal value of about 10 $cm^{-3}s^{-1}$ to 10^4 or $10^5 cm^{-3}s^{-1}$. As we shall see below, these events can also alter the composition of the neutral atmosphere (see *e.g.*, Jackman *et al.*, 1990; 1995; Reid *et al.*, 1991). Figure 7.11 presents the vertical distribution of the ion pair production rates associated with some of the solar proton events of recent years. The events of August 1972, July 1982, October 1989, and October 2003 were particularly intense.

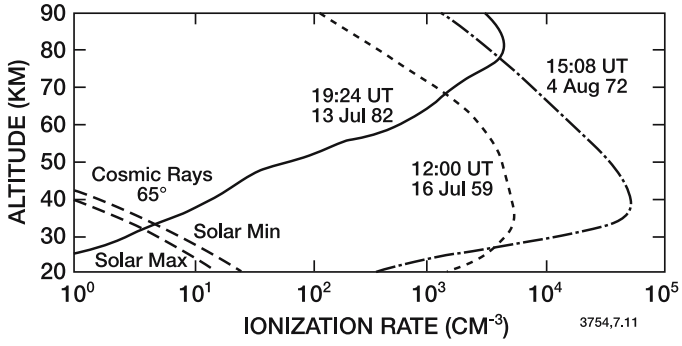

Figure 7.11. Ionization rates associated with some solar proton events, compared to that due to cosmic rays. Adapted from Solomon *et al.* (1983).

7.2.2.5 Ionization Rate Calculation

The calculation of the rate of ion pair production due to corpuscular radiation requires knowledge of the particle energy spectrum and the energy degradation rate in the atmosphere. If j(z,E) dE represents the flux of ionizing particles at altitude z of energies from E to E + dE (the differential flux j(E) is expressed in $cm^{-2}s^{-1}eV^{-1}sr^{-1}$) and if dE/ds is the energy loss per particle in an inelastic collision, then the ionization rate at altitude z is given by (Dubach and Barker, 1971):

$$Q(z) = \frac{\rho(z)}{W} \int_E \int_\Omega \frac{dE}{ds} j(z, E)\, dE\, d\Omega \tag{7.36}$$

where W is the mean energy required per ion pair formation (W ≈ 35 eV), ρ (z) is the air density (g cm^{-3}), and Ω is the solid angle over which Eq. (7.36) is integrated.

The ionization rates of the major species, molecular nitrogen and oxygen, can be determined from the rate of total ion pair production, Q, if it is assumed that the fraction of ionization is proportional to the mass of the target particle (Rusch *et al.*, 1981):

$$Q_{N_2} = Q \frac{.88\,(N_2)}{.88\,(N_2) + (O_2)} \tag{7.37a}$$

$$Q_{O_2} = Q \frac{(O_2)}{.88\,(N_2) + (O_2)} \tag{7.37b}$$

The ion chemistry is initiated by the impact of energetic electrons, e^*, on the nitrogen molecule:

$$e^* + N_2 \rightarrow N_2^+ + 2e \tag{7.38a}$$

$$e^* + N_2 \rightarrow N + N^+ + 2e \tag{7.38b}$$

$$e^* + N_2 \rightarrow N + N + e \tag{7.38c}$$

and on the oxygen molecule:

$$e^* + O_2 \rightarrow O_2^+ + 2e \tag{7.39a}$$

$$e^* + O_2 \rightarrow O + O^+ + 2e \tag{7.39b}$$

The ratio of the peak cross section for simple ionization versus that for dissociative ionization is 0.76:0.24 for N_2 (Eqs. (7.38a,b)), and 0.67:0.33 for O_2 (Eqs. (7.39a,b)) (Rapp *et al.*, 1965). Assuming that the rate of production is proportional to these cross section ratios, we obtain the following approximate expressions (Rusch *et al.*, 1981):

$$P_{N_2^+} = 0.76 \times 0.77Q = 0.585Q \tag{7.40a}$$

$$P_{N^+} = 0.24 \times 0.77Q = 0.185Q \tag{7.40b}$$

$$P_{O_2^+} = 0.67 \times 0.23Q = 0.154Q \quad (7.40c)$$

$$P_{O^+} = 0.33 \times 0.23Q = 0.076Q \quad (7.40d)$$

It should also be noted that the reactions discussed above can also lead to the formation of neutral oxygen and nitrogen atoms, thus initiating processes which can affect the neutral chemistry. These will be discussed in Section 7.5.

7.2.3 Comparison of Different Ionization Processes

Summarizing some of the statements made previously, we note that the ionization above about 90 km is due primarily to the effect of solar ultraviolet radiation (Lyman β and extreme UV) and X-rays on the major species, particularly molecular oxygen. From 60 to 90 km, ionization is produced mainly through the effect of solar Lyman α radiation on nitric oxide, with photoionization of $O_2(^1\Delta_g)$ and hard X-rays ($\lambda < 1$ nm) playing a secondary role under normal conditions. The effect of cosmic rays dominates below about 65 km. Figure 7.12 compares the contributions of each of these terms as a function of altitude during the day (upper panel) and the night (lower panel), for mean solar conditions.

In the absence of solar radiation, the ionization is due primarily to the precipitation of high energy particles (*e.g.*, see Vampola and Gorney, 1983), diffuse Lyman α radiation and cosmic rays. The effect of X-rays emitted by certain stars (Sco XR1, GX333-2.5) plays only a minor role.

As we have already mentioned, sudden perturbations on the Sun (increases in X-ray production, precipitation of energetic protons or electrons) can greatly modify the ionization rate and the morphology of the ionosphere. Table 7.4 presents order of magnitude estimates of the energy penetrating the middle atmosphere, during both quiet and disturbed periods.

7.3 Positive Ion Chemistry

The chemistry of positive ions in the middle atmosphere is relatively well understood. Ions such as O_2^+ and NO^+, which dominate in the lower thermosphere, are rapidly lost below 80 km in a set of clustering reactions ending with stable proton hydrates of the type $H^+(H_2O)_n$. The hydration order n depends on temperature and water vapor concentration. In the stratosphere, water ligands are partly or totally replaced by other molecules such as methyl cyanide (CH_3CN), whose proton affinity is larger than that of water molecules.

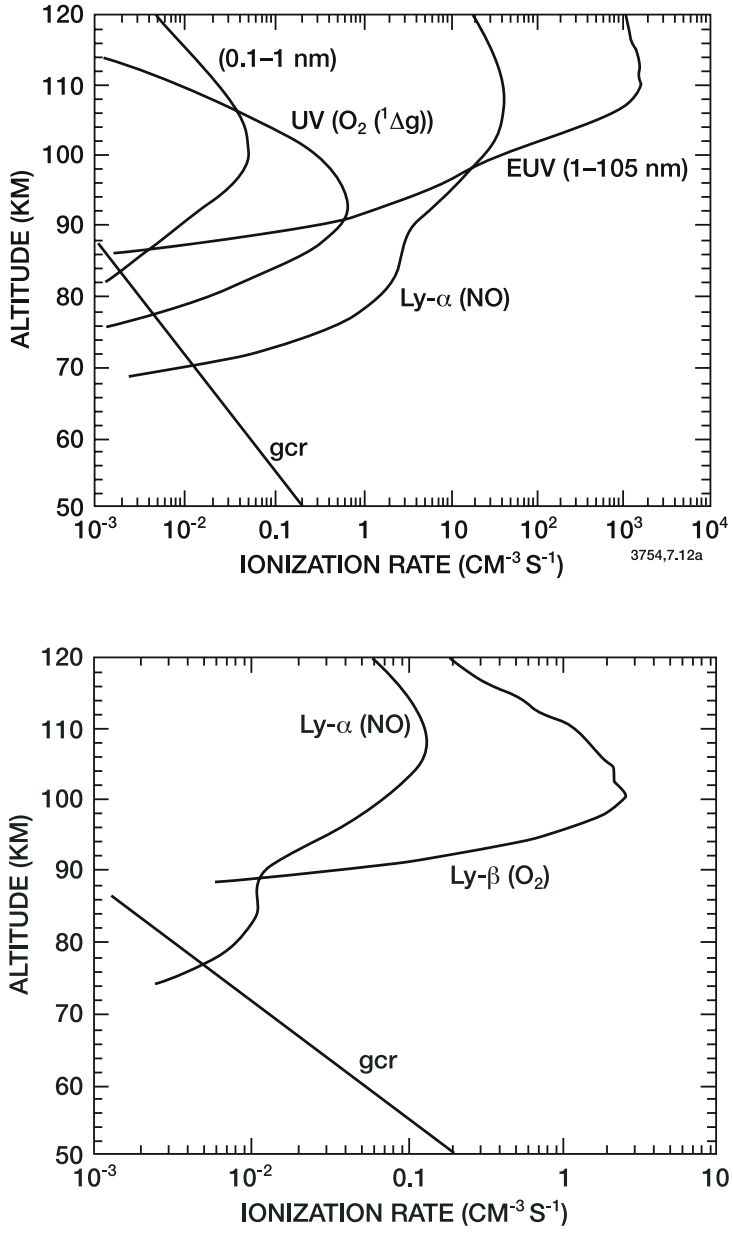

Figure 7.12. Ionization rates produced by various sources in the region from 50 to 100 km at noon (50°) (upper panel) and during the night (50°) (lower panel) in January with mean solar activity. From Fritzenwallner (1997).

Table 7.4 Sources of ionization in the middle atmosphere. (From Rosenberg and Lanzerotti, 1979).

Permanent sources	Flux (ergs $cm^{-2}s^{-1}$)
Galactic cosmic rays	1 (–3) to 1 (–2)
Cosmic X-rays: 0.1 to 1 nm	4 (–9)
Solar X-rays: weak activity, λ 1 nm	1 (–3) to 1 (–1)
Solar X-rays: weak activity, λ 1-10 nm	1 (–1) to 1
Solar H Lyman α: direct	6
Solar H Lyman α: scattered by the geocorona	6 (–3) to 6 (–2)
Magnetospheric electrons: auroral zones	1 (–1) to 1
Magnetospheric electrons: mid-latitudes	1 (–4) to 1 (–3)
Sporadic sources	
Solar cosmic rays (SPE)	1 (–3) to 1 (50 on 8/2/72)
Solar X-rays: solar flares <1 nm	<3
Solar X-rays: solar flares 1-10 nm	<35
Cosmic X-rays: SCO X-1 0.1-1 nm	4 (–7)
Magnetospheric electrons: auroral zones	1 to 1 (3)
Magnetospheric electrons: mid-latitudes	1 (–3) to 1 (–2)

7.3.1 Positive Ions in the E-Region

The primary O_2^+ ion is present in large abundances because its destruction rate by dissociative recombination

$$(\alpha_{O_2^+}); \qquad O_2^+ + e \rightarrow O + O \tag{7.41}$$

and by charge exchange with NO

$$(\gamma_5); \qquad O_2^+ + NO \rightarrow NO^+ + O_2 \tag{7.42}$$

is relatively slow. In contrast, the N_2^+ ion is very short lived because of rapid charge exchange reaction with oxygen:

$$(\gamma_9); \qquad N_2^+ + O_2 \rightarrow N_2 + O_2^+ \tag{7.43}$$

which provides an additional source of O_2^+. N_2^+ also reacts with atomic oxygen, which is present in relatively large amounts in the E-region:

$$(\gamma_3); \qquad N_2^+ + O \rightarrow NO^+ + N \tag{7.44}$$

to produce NO^+. The rates of reactions (7.43) and (7.44) are comparable, implying that the relative importance of each process is dependent on the abundances of O_2 and O. Below about 95-100 km, Reaction (7.43) dominates. The dissociative recombination of NO^+ must also be considered:

$$(\alpha_{NO^+}); \qquad NO^+ + e \rightarrow N\,(^4S, 25\%; ^2D, 75\%) + O \tag{7.45}$$

The equations for the ionic constituents of the E-region can now be written. Neglecting minor reactions and eliminating the density of N_2^+, we can write

$$(O_2^+) = \frac{I_{N_2^+}(N_2) + I_{O_2^+}(O_2)}{\alpha_{O_2^+}(n_e) + \gamma_5(NO)} \tag{7.46}$$

and

$$(NO^+) = \frac{I_{N_2^+}(N_2)\frac{\gamma_3(O)}{\gamma_3(O)+\gamma_9(O_2)} + \gamma_5(NO)(O_2^+)}{\alpha_{NO^+}(n_e)} \tag{7.47}$$

The equation of electrical neutrality must also be considered in ionospheric models. In the E-region, we may write:

$$(n_e) \approx (O_2^+) + (NO^+) \tag{7.48}$$

Figure 7.13 presents a vertical distribution of O_2^+ and NO^+ as observed by Keneshea *et al.* (1970). Figure 7.14 presents a schematic diagram of E-region ion chemistry. For completeness, it should be noted that the O^+ produced by photoionization is destroyed rapidly by reaction with O_2, N_2, and CO_2, and thus plays a negligible role in the middle atmosphere. Its maximum density reaches only about 10 percent of that of O_2^+. All of these polyatomic ions are produced directly by ionization or charge transfer with neutral species, and are referred to as *molecular* ions.

Gas phase metal ions have been observed at mid-latitudes by several investigators and appear to be related to the layers of metallic atoms present in the upper mesosphere and lower thermosphere. Meteoric ablation is believed to be the dominant source of these metals (Plane, 1991). The presence of atomic sodium (Na) was first detected from its noctural emission by Slipher (1929) and is discussed by Chapman (1939). In recent decades several other metallic atoms (*e.g.*, K, Li, Fe, Ca, etc.) and ions (*e.g.*, Mg^+, Fe^+, Al^+, Na^+, Ca^+) have been identified. These species are present in permanent layers from 85 to 110 km, which have been studied in detail using resonance fluorescence lidar techniques (see *e.g.*, Granier *et al.*, 1989; Bills and Gardner, 1990; Qian and Gardner, 1995).

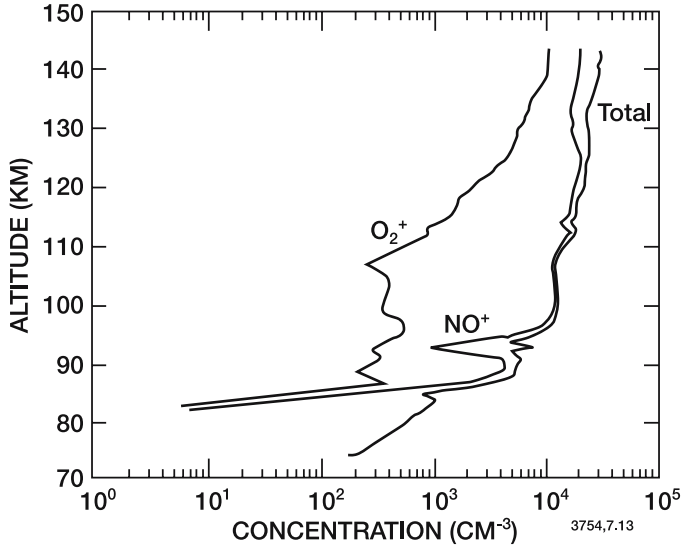

Figure 7.13. Observations of the vertical distributions of O_2^+ and NO^+. From Keneshea *et al.* (1970).

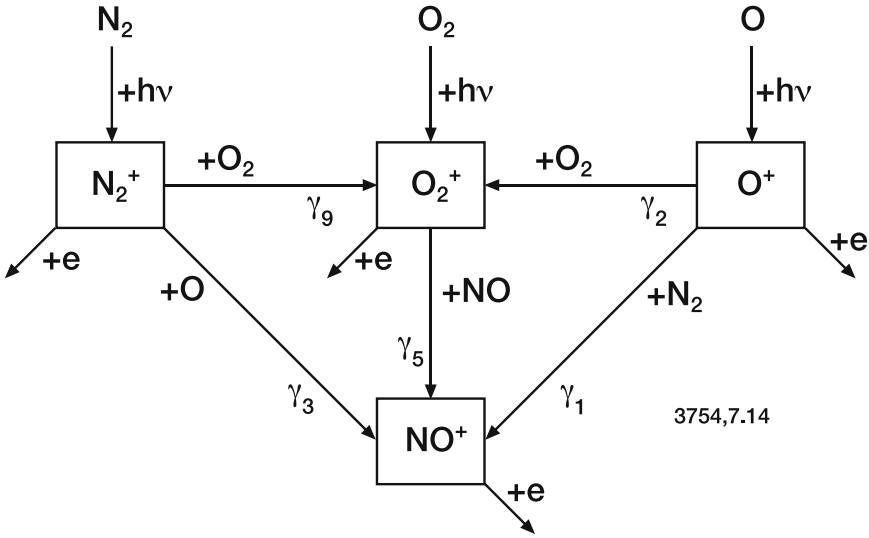

Figure 7.14. Schematic diagram of E-region ion chemistry.

In addition, at altitudes near 100-105 km, thin layers (1-3 km thick) of greatly enhanced metal ion densities are found to extend over horizontal areas of a few hundred kilometers. This phenomenon is called a sporadic E layer, and arises primarily from the effects of wind shears in the presence of a magnetic field, although other mechanisms have also been

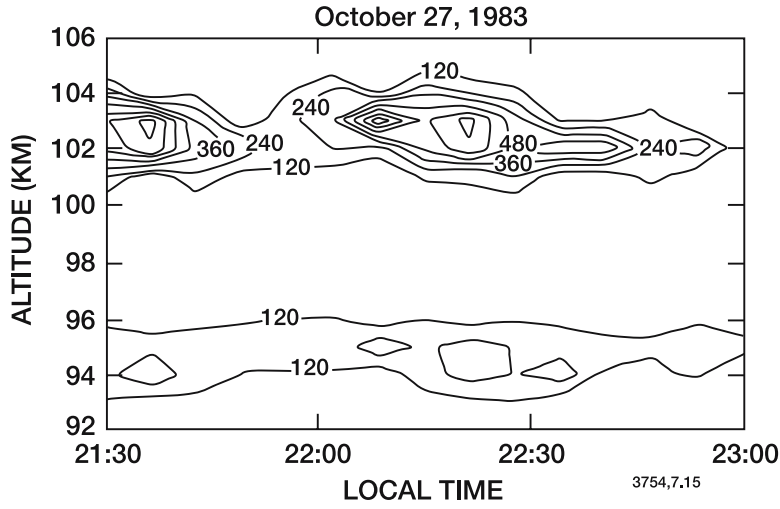

Figure 7.15. Evolution between 21:30 and 23:00 of the Ca^+ density (expressed in number of ions per cubic centimeter) measured by resonant lidar technique between 92 and 106 km on October 27, 1983. The time integration for the lidar observation is 8 minutes. From Granier *et al.*(1989).

proposed. The electron density in these layers is considerably larger than in the nearby regions, leading to enhancement of recombination of O_2^+ and NO^+, reducing their densities relative to those of the metal ions, which have extremely low recombination coefficients. Figure 7.15 shows the evolution of the ionic calcium density (Ca^+) measured in southern France by Granier *et al.* (1989) over a period of 90 minutes. The permanent layer (93-96 km) and a sporadic layer (101-104 km), as detected by the resonant lidar method, are visible.

Part of the ionization of the metallic neutral species X may occur during ablation, but most of the ions are probably produced by photoionization

$$X + h\nu \rightarrow X^+ + e^- \qquad (m_1)$$

and by charge transfer with O_2^+

$$X + O_2^+ \rightarrow X^+ + O_2 \qquad (m_2)$$

and with NO^+

$$X + NO^+ \rightarrow X^+ + NO \qquad (m_3)$$

Similar reactions can, in principle, apply to neutral oxides such as XO or XO_2, leading to the XO^+ and XO_2^+ ions. The major chemical paths leading to the formation of these ions are, however, provided by the

following reactions

$$\mathrm{X^+ + O_3 \rightarrow XO^+ + O_2} \tag{7.49}$$
$$\mathrm{X^+ + O_2 + M \rightarrow XO_2^+ + M} \tag{7.50}$$

Conversion of $\mathrm{XO^+}$ to $\mathrm{X^+}$ occurs through reactions with O, $\mathrm{O_3}$, CO and NO

$$\begin{aligned} &\mathrm{XO^+ + O \rightarrow X^+ + O_2} \\ &\mathrm{XO^+ + O_3 \rightarrow X^+ + 2\,O_2} \\ &\mathrm{XO^+ + CO \rightarrow X^+ + CO_2} \\ &\mathrm{XO^+ + NO \rightarrow X^+ + NO_2} \end{aligned} \tag{7.51}$$

In addition

$$\mathrm{XO_2^+ + M \rightarrow X^+ + O_2 + M} \tag{7.52}$$

Finally, these ions recombine with electrons

$$\begin{aligned} &\mathrm{X^+ + e^- \rightarrow X + h\nu} \\ &\mathrm{XO^+ + e \rightarrow X + O} \\ &\mathrm{XO_2^+ + e \rightarrow X + O_2} \end{aligned} \tag{7.53}$$

Figure 7.16 provides a schematic representation of the most important reactions affecting metal ions in the E-region of the ionosphere. Note, however, that the scheme differs slightly from one metal to another. For example, $\mathrm{Si^+}$ reacts rapidly with water vapor to form the $\mathrm{SiOH^+}$ ion. The reaction of this latter ion with ozone leads to the formation of $\mathrm{SiO_2H^+}$. In the case of sodium (see *e.g.*, Plane *et al.*, 1999), the reaction of $\mathrm{Na^+}$ with ozone is slow, but the following reactions involving water vapor and carbon dioxide are important

$$\begin{aligned} &\mathrm{Na^+ + N_2 + M \rightarrow Na^+N_2 + M} \\ &\mathrm{Na^+N_2 + CO_2 \rightarrow Na^+CO_2 + N_2} \\ &\mathrm{Na^+CO_2 + H_2O \rightarrow Na^+H_2O + CO_2} \end{aligned} \tag{7.54}$$

Additional association reactions could also play a significant role (see Sze *et al.*, 1982; Jégou *et al.*, 1985a,b; Plane, 1991).

Figure 7.17 shows estimates of the vertical distribution of the ion densities for several metals, as calculated by the model of Fritzenwallner (1997; see also Fritzenwallner and Kopp, 1998a).

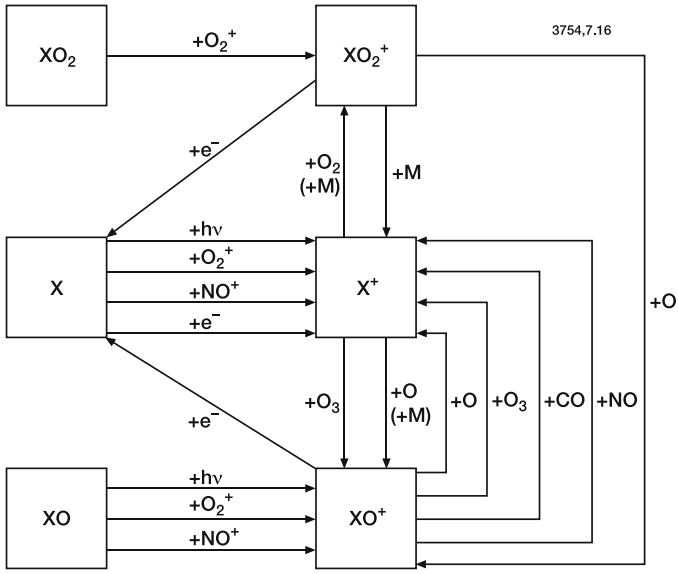

Figure 7.16. Schematic representation of the major chemical processes affecting metal ions (Fe, Mg, Si) in the lower thermosphere and upper mesosphere.

7.3.2 Positive Ions in the D-Region

In 1945 Nicolet suggested that D-region ionization must be due to photoionization of nitric oxide by Lyman α (see Section 7.2). The first theoretical study of the chemistry of this layer by Nicolet and Aikin (1960) led to the expectation that the D-region should be composed primarily of O_2^+ and NO^+. However, the first rocket-borne mass spectrometric measurements by Narcisi and Bailey (1965) revealed that in addition to O_2^+ and NO^+, other species of mass 19 and 37, corresponding to the H_3O^+ and $H_5O_2^+$ ions (hydrated ions of oxonium, commonly named proton hydrates), were present in larger abundances than the primary ions below about 82 km. The presence of relatively large amounts of heavy ions (mass numbers greater than 45) was also established by these measurements. Since the early 1970s, many other "in-situ" measurements of positive ions have confirmed that the transfer of molecular ions (O_2^+ and NO^+) to proton hydrates ($H^+(H_2O)_n$) is a characteristic feature of the lower ionosphere. The altitude profiles of D-region ions observed by the pioneering experiments by Narcisi and Bailey (1965) are shown in Figure 7.18. The formation and stability of these proton hydrates (PH) reflects the large proton affinity of H_2O (170 kcal mole^{-1}) and the strong bonding of H_2O to positive ions in general.

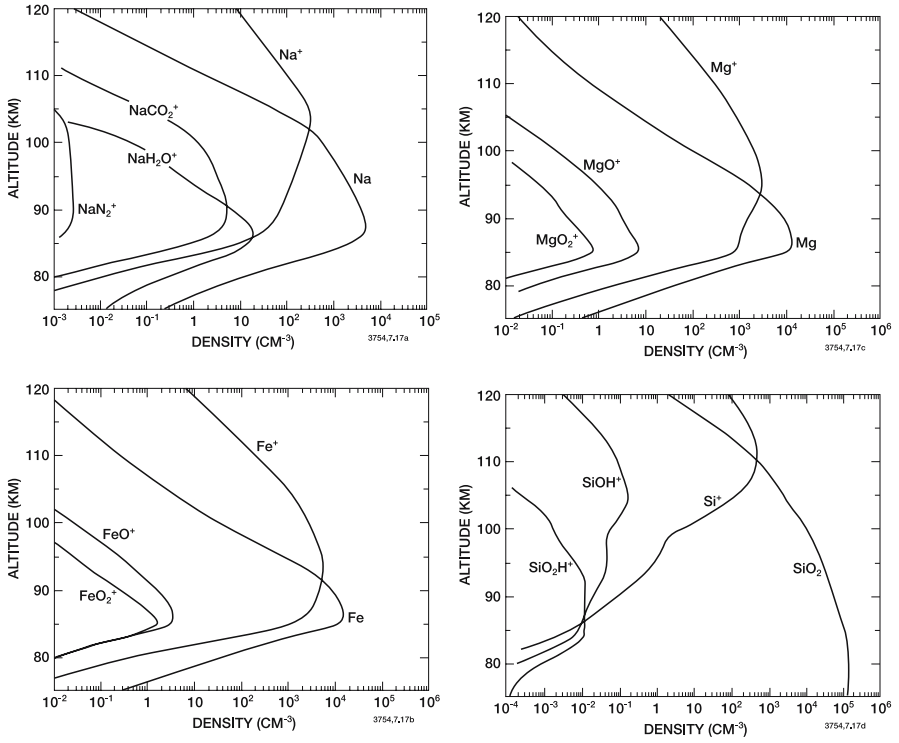

Figure 7.17. Vertical profile of the ion concentration (cm^{-3}) calculated for different metallic species at 50°N for the month of January (noon). The concentration of a corresponding (dominant) neutral species is also shown (from Fritzenwallner, 1997).

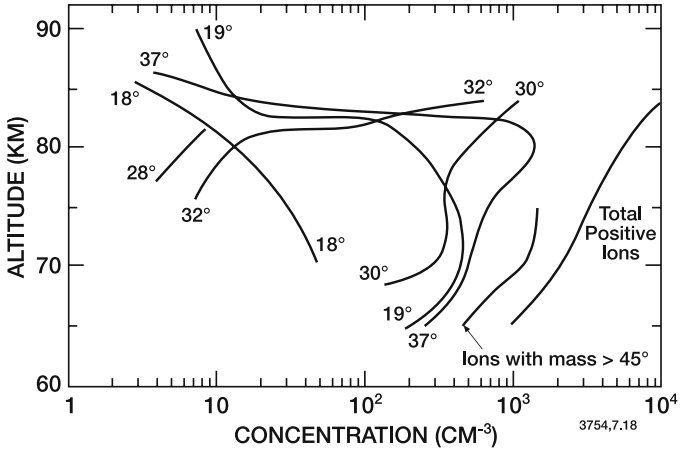

Figure 7.18. First mass spectrometric observations of positive ions from 65 to 90 km (Narcisi and Bailey, 1965).

Other cluster ions such as $NO^+(H_2O)$, $NO^+(CO_2)$, $NO^+(H_2O)_2$, O_4^+, $O_2^+(H_2O)$, etc., are also observed. The altitude (known as the transition height) at which the cross over from proton hydrates to molecular ions (NO^+ and O_2^+) occurs varies from about 70 to 90 km according to season and latitude. The hydration order of the ions (n) is dependent on geophysical conditions (particularly temperature) as well as the atmospheric water vapor content.

Figure 7.19 shows the density profile of the main ions and ion classes measured by Kopp and Herrmann (1984) above Red Lake (Ontario, Canada) on 24 February 1979. As indicated above, NO^+ and O_2^+ are the dominant ions above approximately 80 km, while proton hydrates are the most abundant positive ions below this altitude. The density profiles of each individual proton hydrate (hydration orders 1 to 4), measured during the same experiment, are shown in Figure 7.20.

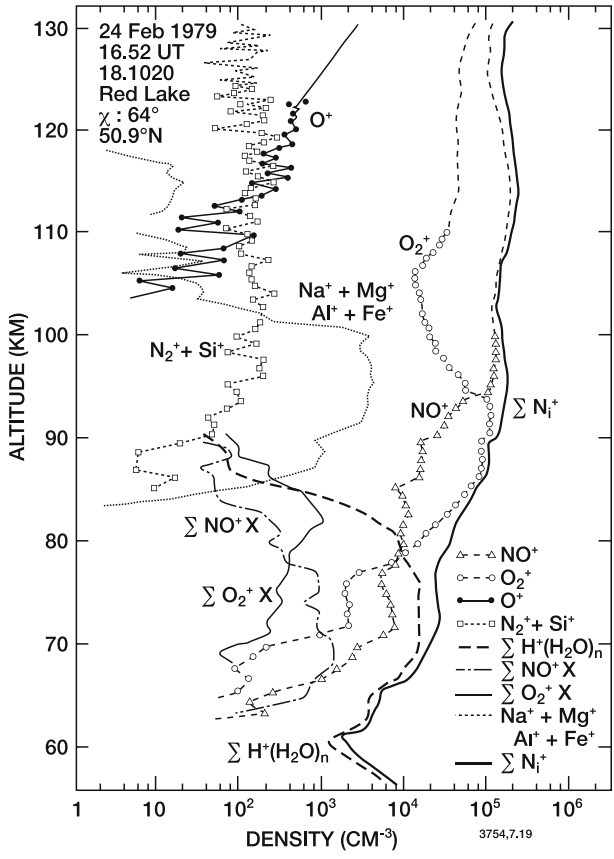

Figure 7.19. Vertical profile of the main ion densities (cm^{-3}) between 60 and 130 km measured by magnetic mass spectrometry above Red Lake (Ontario) on 24 February 1979. From Kopp and Herrmann (1984).

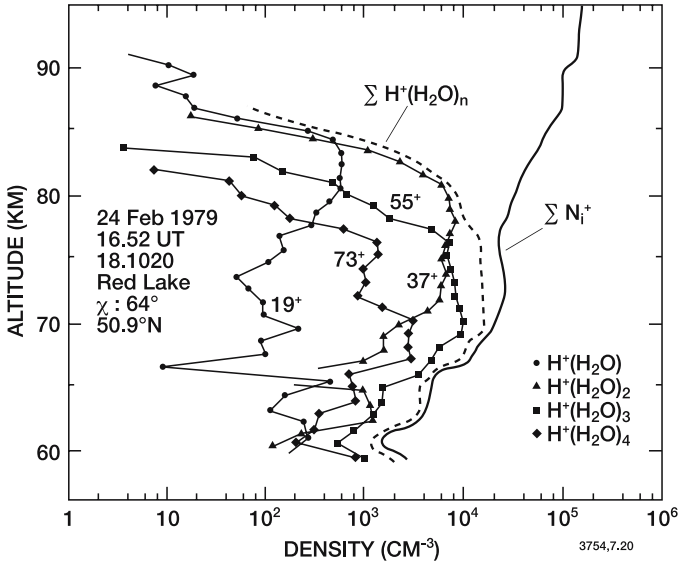

Figure 7.20. Vertical profile of the main proton hydrate densities (cm^{-3}) in the D-region of the ionosphere measured above Red Lake (Ontario) on 24 February 1979. From Kopp and Herrmann (1984).

The most abundant ions generally display hydration orders from 2 to 4, but at cold temperatures near the mesopause hydration orders of 8 or 9 are not uncommon. Björn and Arnold (1981) observed ions as large as $H^+(H_2O)_{20}$ near a very cold summer mesopause at high latitude. These authors also suggest that such ions may be important in the formation of noctilucent clouds.

The transition from a region dominated by NO^+ and O_2^+ ions ($z > 80$ km) to a region dominated by proton hydrates $H^+(H_2O)_n$ results from the fact that three-body reactions affecting O_2^+ and NO^+ become faster at lower altitude than two-body reactions or dissociative electron recombination. The first processes to be considered are the reactions of primary ions (N_2^+, O_2^+, N^+, O^+) with major gases (N_2, O_2) leading to the formation of O_4^+ and NO^+:

$$\begin{aligned} N_2^+ + O_2 &\rightarrow O_2^+ + N_2 \\ N_2^+ + O &\rightarrow O^+ + N_2 \\ N_2^+ + O &\rightarrow NO^+ + N \\ O^+ + O_2 &\rightarrow O_2^+ + O \\ O^+ + N_2 &\rightarrow NO^+ + N \\ O_2^+ + O_2 + M &\rightarrow O_4^+ + M \end{aligned} \qquad (7.55)$$

O_4^+ reacts with atomic oxygen to reform O_2^+ and O_3:

$$O_4^+ + O \rightarrow O_2^+ + O_3 \tag{7.56}$$

and with water vapor to form the first hydrated species:

$$O_4^+ + H_2O \rightarrow O_2^+ \cdot H_2O + O_2 \tag{7.57}$$

The $O_2^+ \cdot H_2O$ ion is very short lived because of the fast hydration reactions

$$O_2^+ \cdot H_2O + H_2O \rightarrow H_3O^+ \cdot OH + O_2 \tag{7.58}$$

$$H_3O^+ \cdot OH + H_2O \rightarrow H^+(H_2O)_2 + OH \tag{7.59}$$

As a result, a proton hydrate of the form $H^+ \cdot (H_2O)_n$ and an OH radical are produced. Successive hydration can occur through the following equilibrium reactions:

$$H^+ \cdot (H_2O)_n + H_2O + M \iff H^+ \cdot (H_2O)_{n+1} + M \tag{7.60}$$

It should be noted that under high atomic oxygen concentrations, the efficiency of O_2^+ hydration is reduced as a result of reaction (7.56). Thus, the rapid decrease in hydrated ions which is observed above 80 km is due at least in part to the rapid increase in the atomic oxygen abundance which occurs in the lower thermosphere. The reaction scheme just described does not completely explain the observed D-region ion distributions, since the primary ion at these altitudes is predominantly NO^+ rather than O_2^+.

Another chain of reactions was found to resolve this discrepancy (Ferguson, 1971; Reid, 1977), explaining how proton hydrate formation occurred starting from NO^+ as the primary ion. Although the direct hydration processes

$$NO^+ + H_2O + M \iff NO^+ \cdot H_2O + M \tag{7.61}$$

$$NO^+ \cdot (H_2O)_n + H_2O + M \iff NO^+ \cdot (H_2O)_{n+1} + M \tag{7.62}$$

were found to be too slow to explain the observations, it was shown that the equivalent reaction can occur via two indirect sequences involving CO_2 and N_2:

$$NO^+ + CO_2 + M \iff NO^+ \cdot CO_2 + M \tag{7.63}$$

$$NO^+ \cdot CO_2 + H_2O \rightarrow NO^+ \cdot H_2O + CO_2 \tag{7.64}$$

and

$$NO^+ + N_2 + M \iff NO^+ \cdot N_2 + M \tag{7.65}$$

$$NO^+ \cdot N_2 + CO_2 \rightarrow NO^+ \cdot CO_2 + N_2 \tag{7.66}$$

followed by

$$NO^+ \cdot CO_2 + H_2O \rightarrow NO^+ \cdot H_2O + CO_2$$

Similar processes occur for higher hydration (*e.g.*, involving $NO^+ \cdot H_2O \cdot CO_2$, see Figure 7.14) until NO^+ is converted to $NO^+ \cdot (H_2O)_3$. This species reacts rapidly with water vapor to produce $H_3O^+ \cdot (H_2O)_2$:

$$NO^+ \cdot (H_2O)_3 + H_2O \rightarrow H^+ \cdot (H_2O)_3 + HNO_2 \qquad (7.67)$$

Higher order clusters can then be formed via reaction (7.60). Most of the equilibria (*e.g.*, Reactions (7.61), (7.62), (7.63) and (7.65)) are strongly temperature sensitive, implying that the composition of the D-region should be quite variable with season and latitude, and that sporadic changes associated with local temperature variations should be observed.

Figure 7.21 presents a schematic diagram of the aeronomy of positive ions in the D-region. Recombination of these ions with negative ions and electrons must also be considered. The recombination coefficient of positive ions with electrons should be between about 10^{-7} and $10^{-5} cm^3 s^{-1}$; the coefficient is faster for clusters than for molecular ions such as NO^+ and O_2^+ (Leu *et al.*, 1973). Models of positive ions in the D-region have been presented by Reid (1977), Thomas (1983), Brasseur and De Baets (1986), Koshelev (1987), Burns *et al.*(1991), Fritzenwallner (1997), Kull *et al.* (1997), and Kazil *et al.*(2003). Figure 7.22 presents model distributions of the principal ions calculated at noon between 50 and 120 km for winter conditions (50°N) (Fritzenwallner, 1997).

7.3.3 Positive Ions in the Stratosphere

In the stratosphere, ionization is produced by cosmic rays. Many of the reaction processes are similar to those occurring in the D-region. The rate of formation of NO^+, however, becomes negligible; the precursor ions are O_2^+ and N_2^+ (which immediately forms O_2^+ by charge exchange with O_2). The reaction chain leading to water vapor clusters is, however, modified by the presence of certain stratospheric neutral species. The reaction of O_4^+ with O_3 must also be mentioned:

$$O_4^+ + O_3 \rightarrow O_5^+ + O_2 \qquad (7.68)$$

and this process competes with reaction with H_2O (Reaction 7.57). The reaction with atomic oxygen is negligible in the stratosphere due to the reduced abundances of this atom there. O_5^+ is almost as abundant as O_4^+ near 25 to 30 km, where ozone densities are greatest. O_5^+ reacts rapidly with H_2O:

$$O_5^+ + H_2O \rightarrow O_2^+ \cdot H_2O + O_3 \qquad (7.69)$$

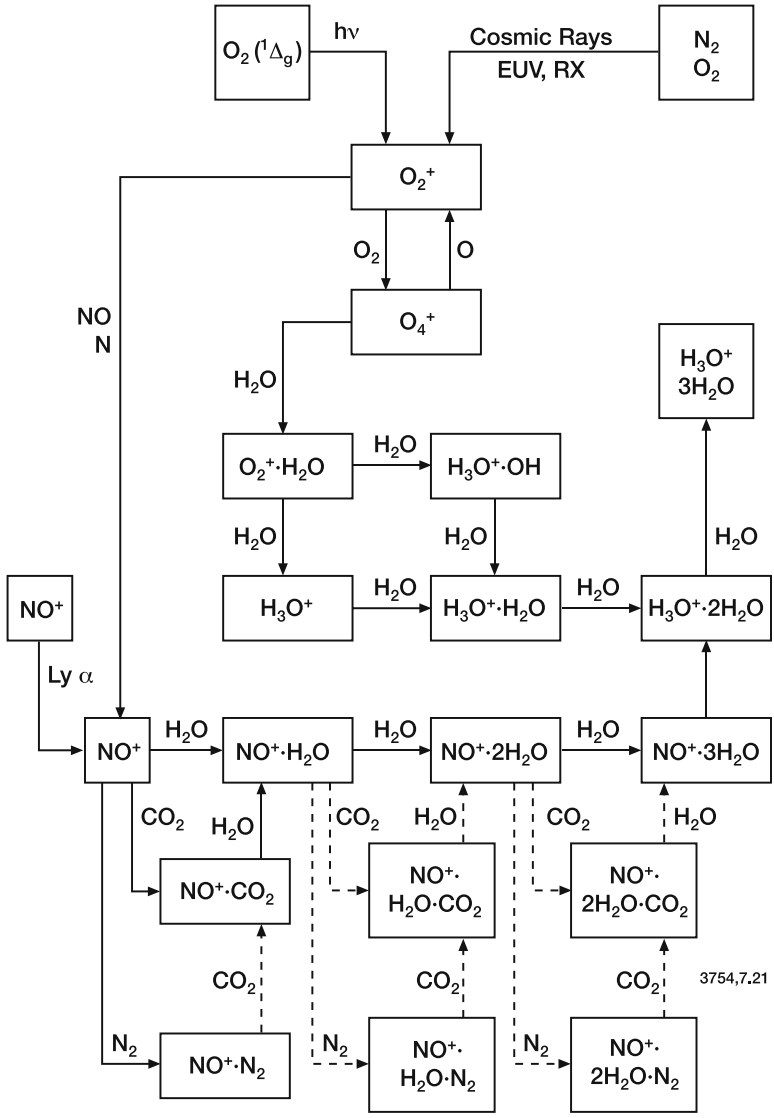

Figure 7.21. Schematic diagram of D-region positive ion chemistry. From Ferguson (1979).

and the ozone molecule destroyed by reaction (7.68) is thus reproduced. The formation chain leading to proton hydrates (PH) can then continue as in the D-region (see Figure 7.23).

The presence of stratospheric species such as HNO_3 and N_2O_5 can alter the chain through reactions of the form:

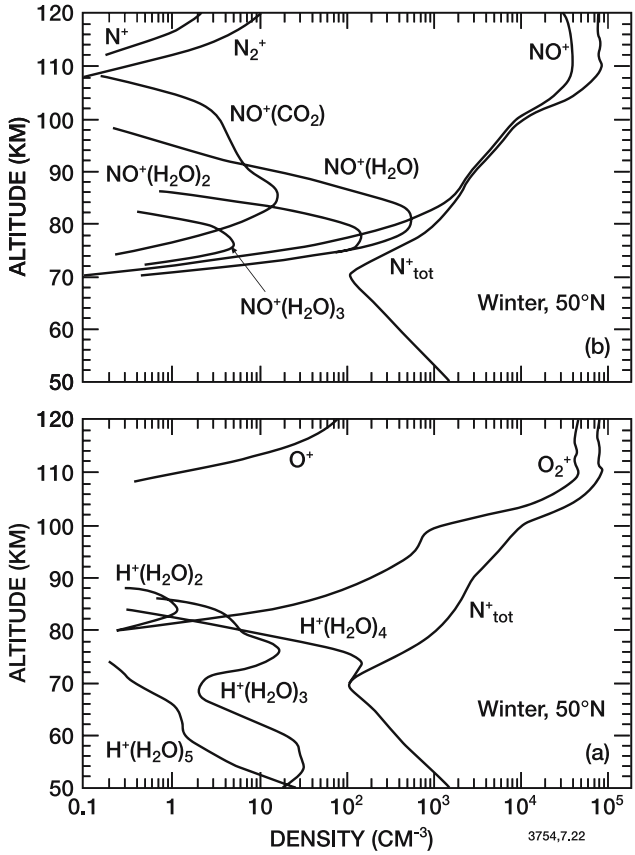

Figure 7.22. Vertical distributions of selected positive ion densities between 50 and 120 km altitude at 50°N calculated for noon conditions in winter. From Fritzenwallner (1997)

$$H_3O^+ + N_2O_5 \rightarrow NO_2^+ \cdot H_2O + HNO_3 \tag{7.70}$$

$$H_3O^+ + HNO_3 \rightarrow NO_2^+ \cdot H_2O + H_2O \tag{7.71}$$

followed by

$$NO_2^+ \cdot H_2O + H_2O + M \rightarrow NO_2^+ \cdot (H_2O)_2 + M \tag{7.72}$$

$$NO_2^+ \cdot (H_2O)_2 + H_2O \rightarrow H^+ \cdot (H_2O)_2 + HNO_3 \tag{7.73}$$

These processes accelerate the conversion of the first hydrated water cluster ion to the second. It should be noted that Reaction (7.70) converts N_2O_5 to HNO_3. Böhringer *et al.* (1983) have shown that this process is probably not fast enough to be important in stratospheric neutral chemistry, however.

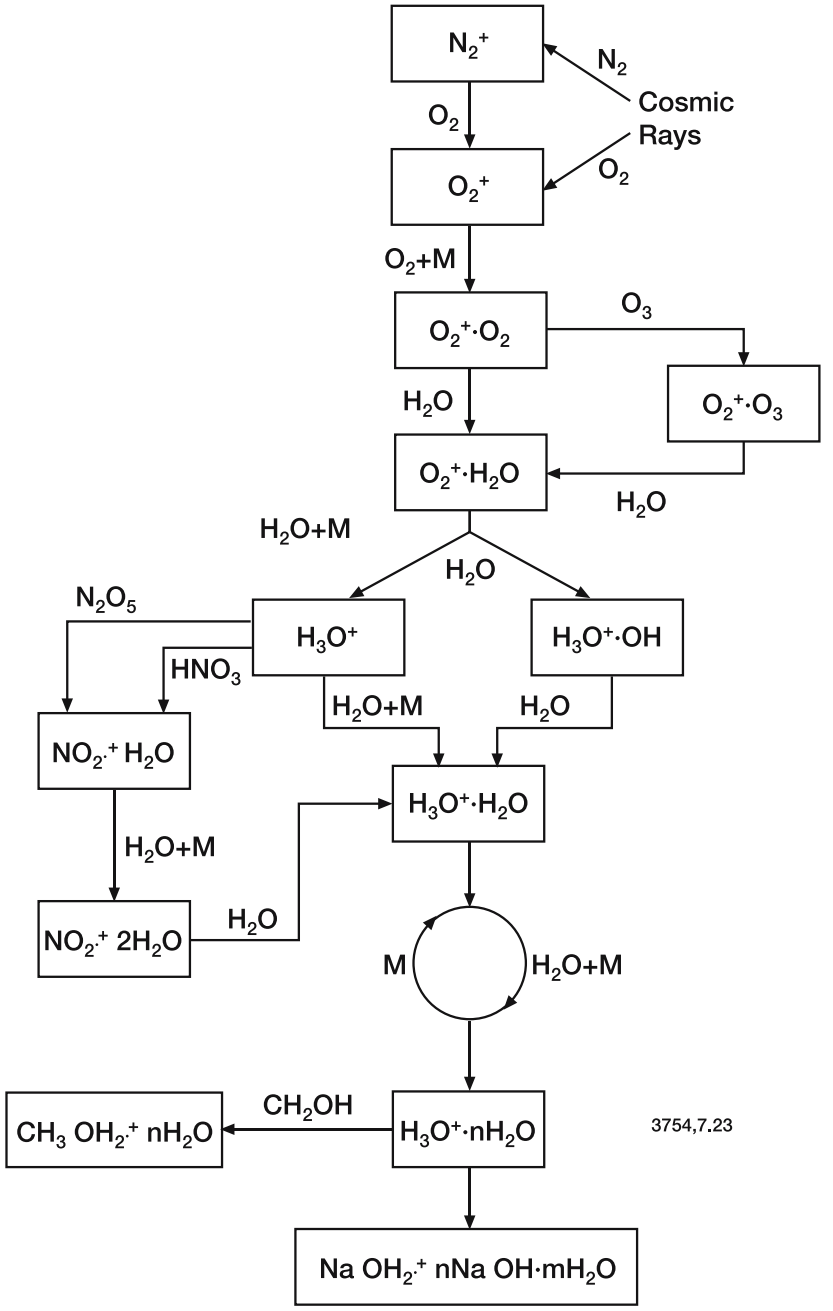

Figure 7.23. Schematic of the aeronomic reactions of positive ions in the stratosphere. From Ferguson (1979).

The first detection of stratospheric positive ions by rocket borne mass spectrometer (Arnold *et al.*, 1977) showed that above 45 km the most abundant ions were proton hydrates ($H^+ \cdot (H_2O)_n$) while below that altitude non-proton hydrates (NPH) of masses 29 ± 2, 42 ± 2, 60 ± 2, and 80 ± 2 were dominant. Arijs *et al.* (1978) also observed ions with a mass number of 96 ± 2.

Arnold *et al.* (1977) proposed that the non-proton hydrates are formed by reactions of proton hydrates with formaldehyde, which possesses a large proton affinity, but this hypothesis was rejected when the reaction of formaldehyde with higher order proton hydrates was found to be endothermic (Fehsenfeld *et al.*, 1978). Ferguson (1978) suggested that proton hydrates might react rapidly with NaOH. If sodium (injected near 90 km by meteor ablation) could reach the stratosphere, it should be present there as NaOH, a species with a large proton affinity.

Other observations by Arnold *et al.* (1978) and Arijs *et al.* (1978; 1980) confirmed the presence of clusters of the form $H^+ X_n (H_2O)_m$, where X was an unidentified molecule. Arijs *et al.* (1980) unambiguously showed that the mass of X was equal to 41, implying that the identity of X could not be NaOH (mass 40). MgOH (mass 41) cannot account for X because the isotopic ratio which would be expected to result from the ^{25}Mg and ^{26}Mg isotopes was not observed.

Theoretical and experimental observations, as well as laboratory studies by Böhringer and Arnold (1981) indicated that the identity of X is almost certainly methyl cyanide CH_3CN (mass 41 and proton affinity of 186 kcal mole^{-1}). This species has been detected in the lower atmosphere (where it is produced by forest fires, automobiles and industrial activities), but the complete budget of its sources and sinks remains poorly quantified (*e.g.*, Becker and Ionescu, 1982; Snider and Dawson, 1984; Arnold and Hauck, 1985; Knop and Arnold, 1987a,b; Hamm *et al.*, 1989; Schneider *et al.*, 1997) (see Chapter 5). Studies of the fractional ion abundances of proton hydrates and non-proton hydrates have been used to infer the profile of CH_3CN from about 15 to 45 km (Arnold *et al.*, 1981; Henschen and Arnold, 1981; Arijs *et al.*, 1982a; Arijs *et al.*, 1983a,b). These profiles have been fitted to model calculations of the neutral chemistry and transport of CH_3CN (Brasseur *et al.*, 1983; Beig *et al.*, 1993a). Figure 7.24 presents a schematic diagram of the key chemical processes believed to affect ion formation and destruction in the stratosphere, while Figure 7.25 shows the relative amount of proton hydrates and non-proton hydrates present in this region of the stratosphere. Using a two-dimensional model, Beig *et al.* (1993b) have shown that the level where the NPH/PH

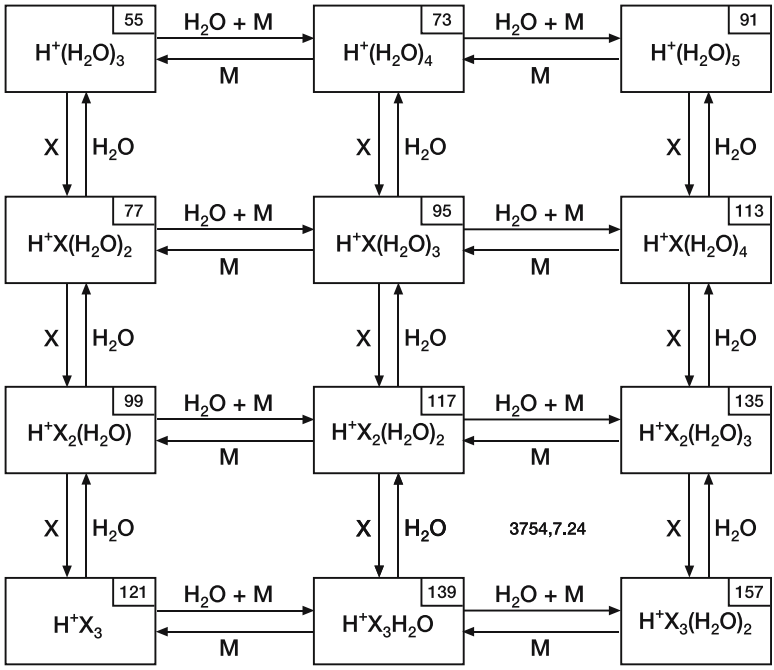

Figure 7.24. Schematic diagram of stratospheric positive ion reactions proposed by Arnold (1980), with X representing a molecule of methyl cyanide (CH_3CN).

concentration ratio is unity varies from approximately 48 km at the equator to about 30 km at the poles.

Especially in the lower stratosphere, other processes can occur, including the reaction with ammonia:

$$H^+ \cdot (H_2O)_n + NH_3 \rightarrow NH_4^+ \cdot (H_2O)_m + (n - m)\, H_2O \qquad (7.74)$$

(where m = 0, 1, 2,...n). This process is quite rapid, particularly for n = 2, 3, and 4 (Fehsenfeld and Ferguson, 1973). However, the stratospheric ammonia abundance is small due to its large solubility and removal in clouds. Reaction (7.74) may be important in the troposphere. The reaction with methanol (proton affinity = 182.2 kcal $mole^{-1}$)

$$H^+ \cdot (H_2O)_n + CH_3OH \rightarrow H^+\, CH_3OH(H_2O)_m + (n - m)\, H_2O \quad (7.75)$$

could play a role, but the vertical distribution of methanol is not well known.

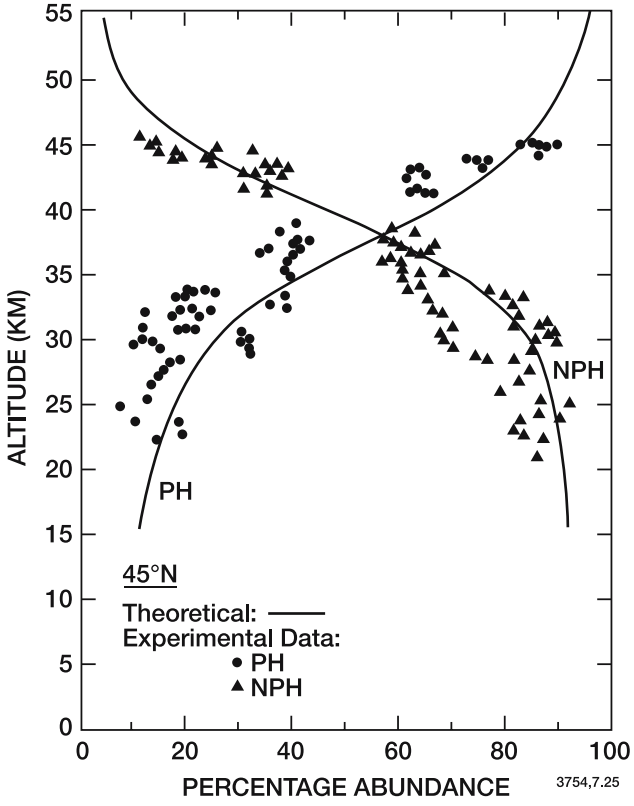

Figure 7.25. Percentage abundance of proton hydrates (PH) and nonproton hydrates (NPH) as a function of altitude at 45°N. The full line indicates model values and dots and triangles are experimental data. From Beig et al. (1993a).

Table 7.5 shows the mass of positive ions measured in the stratosphere by mass spectrometry and the identification of the corresponding ions. Comprehensive reviews of the chemistry and observations of stratospheric positive ions are provided by Arnold (1980), Arijs (1983), and Arijs (1992). Models of positive ions in the stratosphere have been developed by Brasseur and Chatel (1983), Arijs and Brasseur (1986), Beig and Chakrabarty (1988), Beig *et al.* (1993a), etc.

7.4 Negative Ion Chemistry

Negative ions are observed below typically 70–80 km altitude, where the air density is sufficiently high to enable the attachment of electrons to oxygen molecules. A complex set of reactions leads to the formation

Table 7.5 Stratospheric positive ion species detected by balloon-borne mass spectrometers (Arnold, 1986).

Mass	*Ion*	*Mass*	*Ion*
19	H_3O^+	104 ± 1	$H^+CH_3CN(H_2O)_2$
23 ± 1	Na^+	109	$H^+(H_2O)_6$
29 ± 2	H^+HCN	110 ± 1	$H^+CH_3OH(H_2O)_2$
37	$H^+(H_2O)_2$	114 ± 1	$H^+CH_3CN(H_2O)_4$
42	H^+CH_3CN	117 ± 1	
45 ± 1	$H^+HCN{\cdot}H_2O$	119	$H^+(CH_3CN)_2(H_2O)_2$
49 ± 1	$H^+CH_3OH{\cdot}H_2O$	121 ± 1	
55	$H^+(H_2O)_3$	125 ± 1	
58 ± 1	$Na^+(H_2O)_2$	128 ± 1	
60	$H^+CH_3CH{\cdot}H_2O$	134 ± 2	
63 ± 1	$H^+HCN(H_2O)_2$	139 ± 2	
67 ± 1	$H^+CH_3OH(H_2O)_2$	142 ± 1	$H^+H_2O(CH_3CN)_3$
73	$H^+(H_2O)_4$	151 ± 2	
78	$H^+CH_3CN(H_2O)_2$	158 ± 3	
81 ± 1	$H^+HCN(H_2O)_3$	168 ± 3	
83	$H^+(CH_3CN)_2$	179 ± 3	
86 ± 1	$H^+CH_3OH(H_2O)_3$	182 ± 3	
91	$H^+(H_2O)_5$	186 ± 3	
96	$H^+CH_3CN(H_2O)_3$	190 ± 3	
101	$H^+(CH_3CN)_2H_2O$	202 ± 3	

of ions such as NO_3^- and CO_3^-, which can cluster with water molecules. In the stratosphere, NO_3^- and HSO_4^- core ions with H_2O, HNO_3, and H_2SO_4 as ligands become dominant.

7.4.1 Negative Ions in the D-Region

The first studies of the ionosphere using radiowave techniques demonstrated that electrons are nearly absent below 65 or 70 km during the day and 75 or 80 km at night. However, electrical neutrality requires a balance between charged particles. The observation of positive ions implies that equal quantities of a negatively charged particle must be present.

Johnson *et al.* (1958) performed the first observations of negative ions, and suggested that the most abundant negative ion in the D-region is

NO_2^- at mass 46. Since that time, only a very few measurements have been performed. Narcisi *et al.* (1971) and Arnold *et al.* (1971) observed the D-region at night. The presence of a transition zone above which the concentration of negative ions rapidly decreases was established by observation but the altitude of this layer seemed to vary considerably with time (Arnold and Krankowsky, 1977; Arnold, 1980).

This transition zone between electrons and negative ions appears to be located near 70 km during the day, and 5 to 10 km higher at night. But the few available observations are not in agreement as to the composition of the D-region negative ions. Narcisi *et al.* suggested that the dominant ions were hydrated clusters, probably of the type $NO_3^- \cdot (H_2O)_n$, but Arnold *et al.* (1971) found that over Northern Europe (69°N) the most abundant species were CO_3^-, HCO_3^- and Cl^-. Figure 7.26 shows some vertical profiles derived by Arnold *et al.* (1971). Further observations are badly needed.

The chemistry of negative ions has been intensively studied in the laboratory since the 1960s by Ferguson and coworkers. A schematic diagram of the suggested chemistry resulting from their experiments is

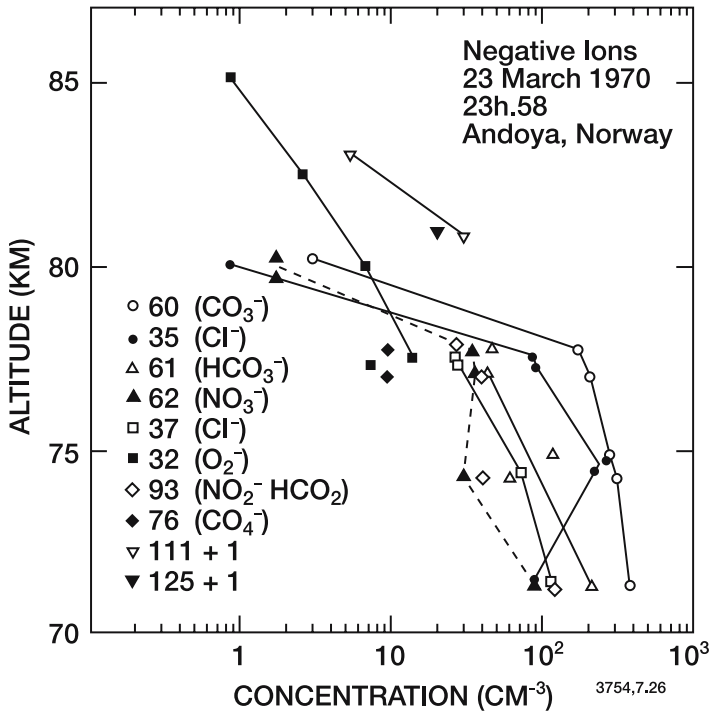

Figure 7.26. Negative ion concentration from 70 to 85 km at Andoya, Norway (March, 1970). (Arnold *et al.*, 1971).

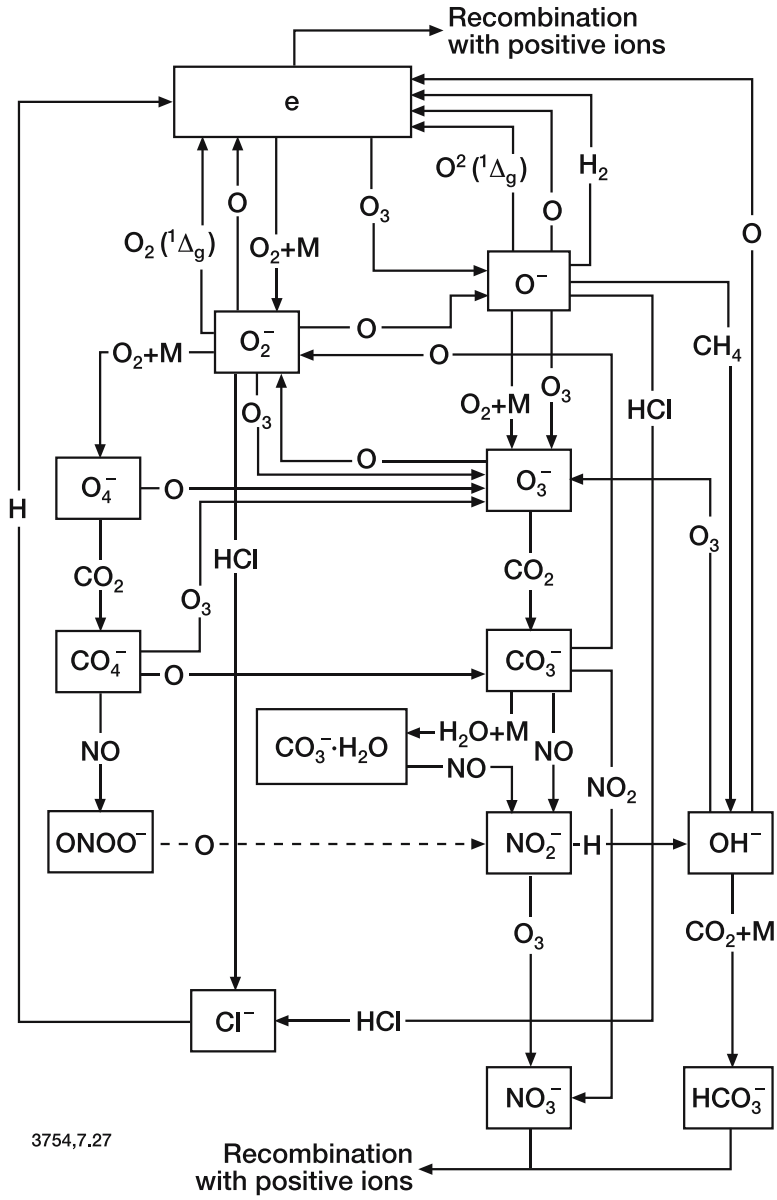

Figure 7.27. Schematic diagram of the negative ion chemistry of the D-region. From Ferguson (1979).

presented in Figure 7.27. The chain of reactions is initiated by electron attachment on an oxygen molecule:

$$\mathrm{e} + \mathrm{O}_2 + \mathrm{M} \rightarrow \mathrm{O}_2^- + \mathrm{M} \tag{7.76}$$

The rate of this reaction varies with the atmospheric density (M), leading to a nearly complete disappearance of free electrons below a certain altitude. The attached electron can be liberated, however, by several reactions:

$$O_2^- + O \rightarrow O_3 + e \tag{7.77}$$

$$\begin{gathered} O_2^- + O_2(^1\Delta_g) \rightarrow 2O_2 + e \\ O_2^- + h\nu \rightarrow O_2 + e \end{gathered} \tag{7.78}$$

These reactions lead to a balance between negative ions and electrons. The increasing densities of atomic oxygen in the upper mesosphere result in increased electron abundances there through Reaction (7.77). The chain leading to stable negative ions occurs through the following sequence:

$$O_2^- + O_3 \rightarrow O_3^- + O_2 \tag{7.79}$$

$$O_3^- + CO_2 \rightarrow CO_3^- + O_2 \tag{7.80}$$

The CO_3^- ion can also be formed by a second sequence:

$$O_2^- + O_2 + M \rightarrow O_4^- + M \tag{7.81}$$

$$O_4^- + CO_2 \rightarrow CO_4^- + O_2 \tag{7.82}$$

$$CO_4^- + O \rightarrow CO_3^- + O_2 \tag{7.83}$$

This last reaction competes with the following processes:

$$CO_4^- + O_3 \rightarrow O_3^- + CO_2 + O_2 \tag{7.84}$$

$$O_3^- + CO_2 \rightarrow CO_3^- + O_2 \tag{7.85}$$

Another source of CO_3^- is provided by the binary formation of O^-

$$e^- + O_3 \rightarrow O^- + O_2 \tag{7.86}$$

followed by a reaction with CO_2

$$O^- + CO_2 + M \rightarrow CO_3^- + M \tag{7.87}$$

The CO_3^- ion is rapidly destroyed by reaction with atomic oxygen

$$CO_3^- + O \rightarrow O_2^- + CO_2 \tag{7.88}$$

which interrupts the formation of negative ions. However, the sequence above can also be followed by:

$$CO_3^- + NO \rightarrow NO_2^- + CO_2 \tag{7.89}$$

$$NO_2^- + O_3 \rightarrow NO_3^- + O_2 \tag{7.90}$$

which leads to the formation of a terminal ion NO_3^-. This species is particularly stable because of its very high electron affinity. If, however,

photodetachment of electrons from NO_3^-

$$NO_3^- + h\nu \rightarrow NO_3 + e \tag{7.91}$$

takes place at the rate suggested by the measurements of Smith *et al.* (1979), the lifetime of NO_3^- could be as small as 20 s, and the concentration of this ion could be considerably smaller than that of major negative ions such as CO_3^-, HCO_3^- and Cl^-. Reaction (7.89) is relatively slow and controls the rate of formation of the NO_3^- ion. Reaction (7.90) is fast, and thus the NO_2^- ion can only be present in small quantities.

The OH^- ion is produced by the following reactions

$$\begin{gathered} O^- + CH_4 \rightarrow OH^- + CH_3 \\ NO_2^- + H \rightarrow OH^- + NO \end{gathered} \tag{7.92}$$

and leads to the eventual formation of HCO_3^-, another terminal ion, through

$$OH^- + CO_2 + M \rightarrow HCO_3^- + M \tag{7.93}$$

if it is not destroyed by these reactions:

$$OH^- + O \rightarrow HO_2 + e \tag{7.94}$$

$$OH^- + H \rightarrow H_2O + e \tag{7.95}$$

In the presence of hydrogen chloride, Cl^- ions are formed as follows:

$$O_2^- + HCl \rightarrow Cl^- + HO_2 \tag{7.96}$$

$$O^- + HCl \rightarrow Cl^- + OH \tag{7.97}$$

$$NO_2^- + HCl \rightarrow Cl^- + HNO_2 \tag{7.98}$$

Cl^- is destroyed by the chemical detachment process:

$$Cl^- + H \rightarrow HCl + e \tag{7.99}$$

In most cases, Figure 7.27 does not indicate the likely formation of ion hydrates $X^- \cdot (H_2O)_n$, where X^- represents, for example, NO_3^-, CHO_3^-, Cl^-, OH^-, NO_2^-, O_3^-, and O_2^-. The formation of such ions by reaction with water vapor has some limited implications for the schematic picture just described (Fehsenfeld and Ferguson, 1974). For example, as suggested by Figure 7.27, the reaction of $CO_3^- \cdot H_2O$ with NO tends to accelerate the conversion of CO_3^- to NO_3^-. The partitioning between ions and their hydrates is a strong function of the temperature and the water vapor concentration. Figure 7.28 shows the relative amount of the four dominant negative ions between 50 and 100 km altitude together with the contribution of the first and second hydrates (n = 1 and 2). This figure shows that, during summer, when the mesospheric temperature is low (see Chapter 3), a substantial fraction

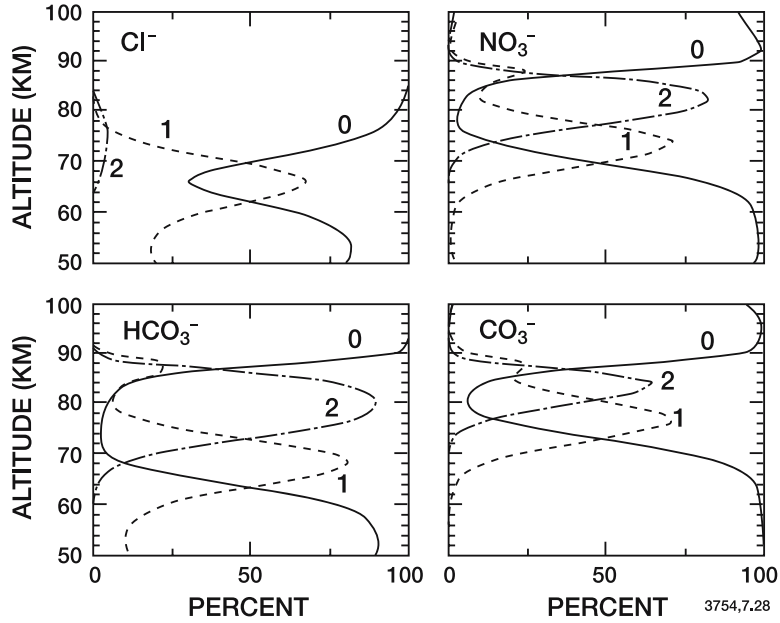

Figure 7.28. Vertical distribution of the 4 dominant negative ions (0) and of their single (1) and doubled (2) hydrated ions in the D-region as modeled by Fritzenwallner (1997) and Fritzenwallner and Kopp (1998b) at 50° (summer).

of the ions are converted to their hydrates near 80 km altitude (67 km in the case of Cl^-). It should be noted that, as in the case of NO^+, the formation of clusters ions with O_2, N_2, CO_2, and H_2O could play an important part in producing ions of the form $X^- \cdot (H_2O)_n$, but these reactions have not yet been studied in the laboratory.

The eventual destruction of negative ions, particularly the terminal ions, occurs by recombination with positive ions. The rate of this reaction has not been measured for all of the species that are actually present in the atmosphere, but a mean rate for reactions of this type, *i.e.*,

$$(\alpha); \qquad X^- + Y^+ \rightarrow \text{neutrals}$$

of $6 \times 10^{-8} \mathrm{cm^3 s^{-1}}$ can be adopted (Smith *et al.*, 1976). Note, however, that this reaction is also believed to exhibit a pressure dependence which may be important in the lower stratosphere (Smith *et al.*, 1981). It should be emphasized that several issues related to the vertical distribution of negative ions in the D-region remain to be solved. Perhaps the main problem is to explain the strong variability in ion and electron concentrations as well as in the λ parameter (see Eq. 7.13) when ion sources are relatively stable (quiet solar conditions). The variability in ionic composition is probably related to fluctuations in the

concentration of neutrals, and hence suggests a strong meteorological control of the D-region.

Models of negative ions in the D-region have been presented by Wisemberg and Kockarts (1980), Thomas and Bowman (1985), Brasseur and De Baets (1986), Burns *et al.* (1991), Kull *et al.* (1997), Fritzenwallner (1997), and Fritzenwallner and Kopp (1998b). Figure 7.29 shows an example of the vertical distributions of negative ions calculated by Fritzenwallner (1997). As in the case of positive ions, the vertical profile of individual negative ion species is strongly related to temperature and minor species concentrations in the mesosphere.

7.4.2 Negative Ions in the Stratosphere

In order to describe the behavior of negative ions in the stratosphere, it is useful to adopt the D-region scheme just described and consider the changes which occur as a result of differences in pressure, temperature, and composition. The chain of reactions leading to NO_3^- from O_2^- can still occur, and is even more efficient because the low densities of

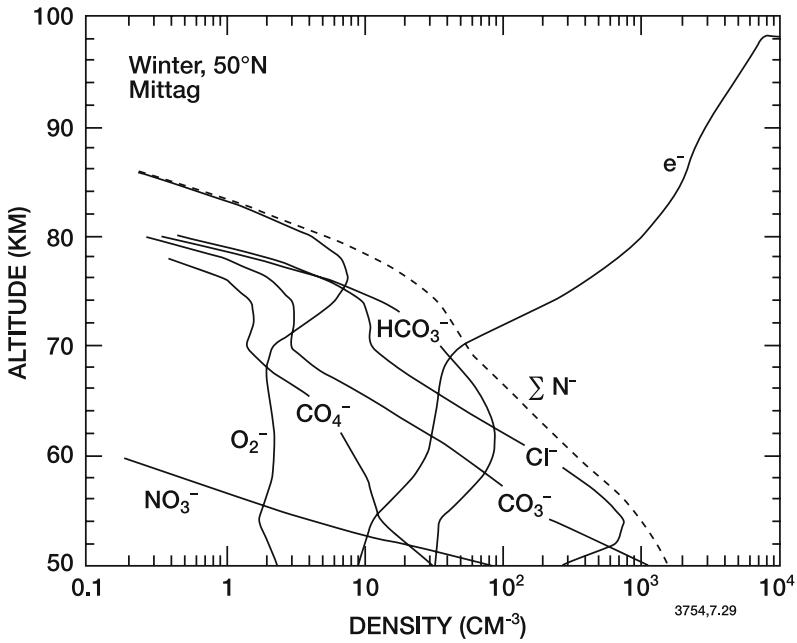

Figure 7.29. Vertical distributions of selected negative ions at 50°N calculated for noon conditions in winter. From Fritzenwallner (1997).

atomic oxygen there decrease the frequency of the interrupting reactions. Further, additional reactions facilitate the formation of NO_3^-:

$$CO_3^- + NO_2 \rightarrow NO_3^- + CO_2 \tag{7.100}$$

This reaction is 20 times faster than (7.89) and becomes dominant in the stratosphere, where the densities of NO and NO_2 are comparable. This mechanism also avoids the chain breaking reactions presented in Section 7.4.1. Further, the rapid reactions of O^-, O_2^-, CO_3^-, NO_2^-, and Cl^- with HNO_3, and the reaction of the latter three species with N_2O_5, lead to additional production of NO_3^-. The formation of hydrated ions, for example by reaction with O_3^-, can reduce the formation rate of NO_3^-, however. Figure 7.30 presents a schematic diagram of these processes.

The possibility of destruction of NO_3^- must also be considered. The hydration of this ion must proceed as in the D-region. Kinetic studies (Fehsenfeld *et al.*, 1975) showed that HNO_3 can substitute for H_2O in a cluster ion. Ions of the form $NO_3^- \cdot (H_2O)_n (HNO_3)_m$ should thus be formed. $NO_3^- \cdot (HNO_3)_n$ reacts rapidly, however, with H_2SO_4 (Viggiano *et al.*, 1980), at least for n = 0, 1, or 2. Thus HSO_4^- or a cluster of the form $HSO_4^- \cdot (H_2SO_4)_m \cdot (HNO_3)_n \cdot (H_2O)_p$ should be the terminal ion in the stratosphere. Figure 7.31 presents a schematic diagram of the corresponding reactions proposed by Arijs *et al.* (1981).

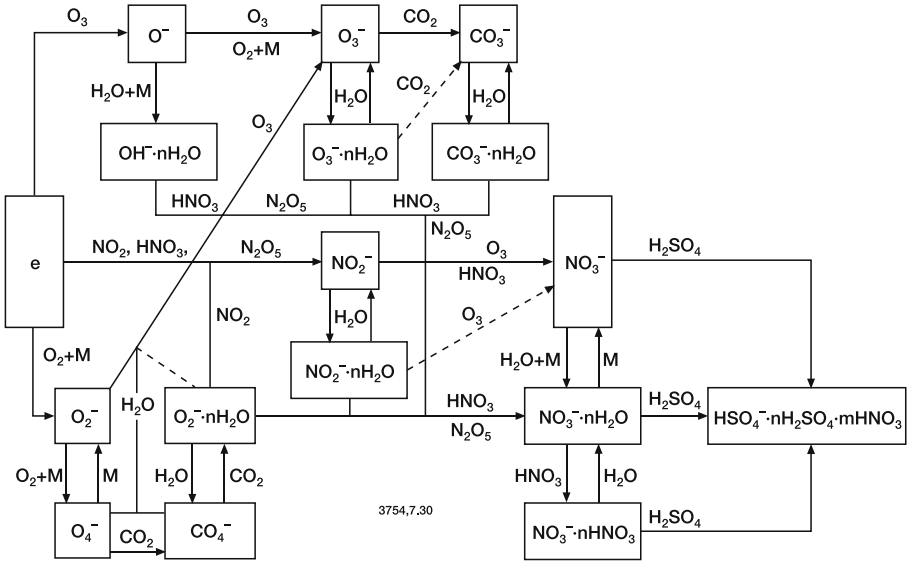

Figure 7.30. Schematic diagram of the negative ion chemistry in the stratosphere. From Ferguson (1979).

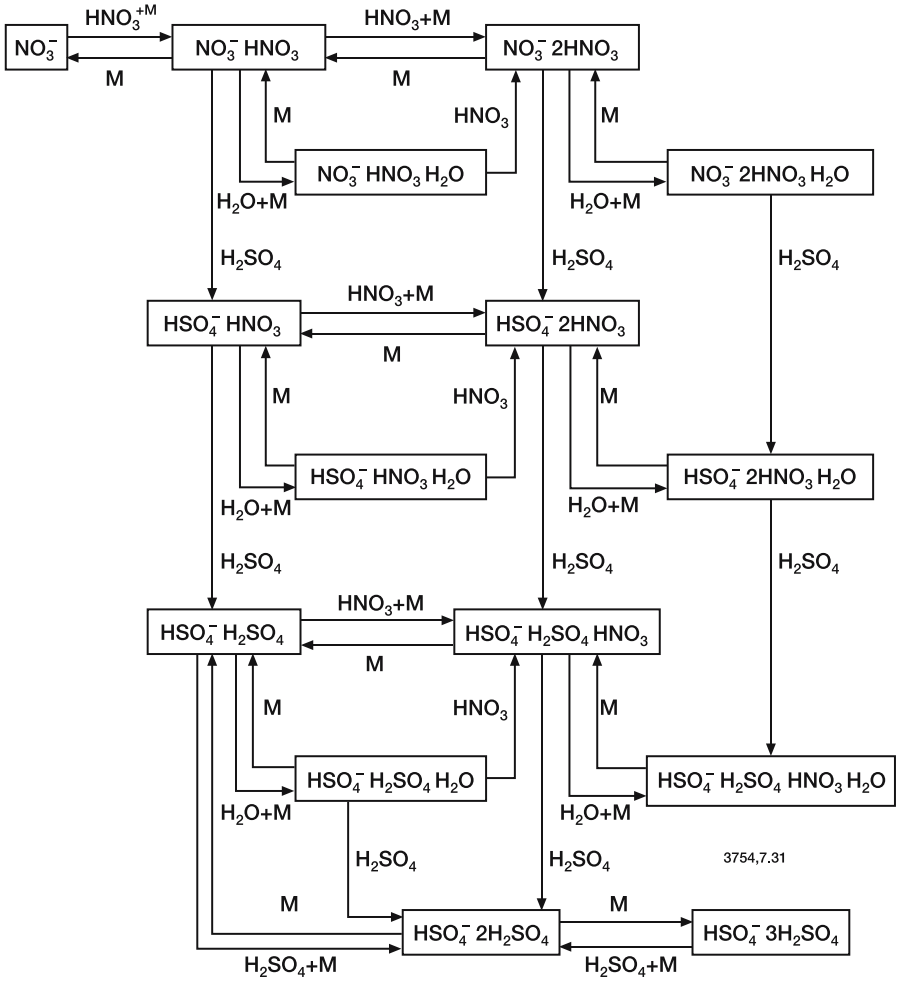

Figure 7.31. Schematic diagram of the negative ion chemistry of the stratosphere suggested by Arijs *et al.* (1981) based on in-situ observations.

The first observations by Arnold and Henschen (1978), and later by Arijs *et al.* (1981) confirmed the presence of some of these cluster ions; the most abundant species observed at 35 km were $HSO_4^- \cdot (H_2SO_4)_3$, $HSO_4^- \cdot (HNO_3)$, $NO_3^- \cdot (HNO_3)_2$, and $HSO_4^- \cdot (H_2SO_4)_2$. Figure 7.32 shows the fractional abundance between 23 and 38 km of major negative cluster ion families containing NO_3^- and HSO_4^- cores (Viggiano and Arnold, 1981). Studies of the fractional abundance of negative ions can be used to infer the vertical profile of neutral H_2SO_4 in the stratosphere, as discussed briefly in Chapter 5.

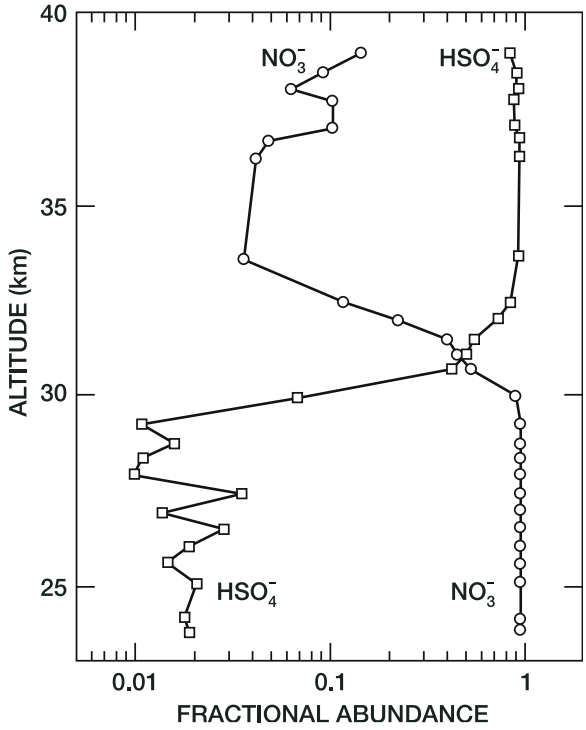

Figure 7.32. Relative abundance of NO_3^- and HSO_4^- core ions observed at mid-latitudes in the stratosphere (September 1980) by Viggiano and Arnold (1981). Note that the NO_3^- $(HNO_3)_n$ ion family dominates below 30 km, while the HSO_4^- $(H_2SO_4)_m$ $(HNO_3)_n$ family is dominant above this altitude.

Other polar molecules are also likely to be important. Investigations of minor mass peaks in negative ion spectra (McCrumb and Arnold, 1981; Arijs *et al.*, 1982a,b) have revealed the presence of ions which may contain other ligands in addition to HNO_3 and H_2SO_4, such as HOCl and HCl. Table 7.6 provides the mass (and the corresponding identification) of negative ions measured by mass spectroscopy in the stratosphere.

Models of the positive and negative ion distributions in the stratosphere were presented by Brasseur and Chatel (1983), Kawamoto and Ogawa (1984, 1985), and by Beig *et al.* (1993a,b). Theoretical studies of both positive and negative ions are hampered by the lack of laboratory data regarding some of the relevant rate constants.

In conclusion, the chemistry of negative ions in both the stratosphere and mesosphere remains at present in a primitive state. Systematic observations as a function of altitude are needed, as well as laboratory kinetic studies, before a deeper understanding can be acquired.

Table 7.6 Negative ion species detected by balloon-borne mass spectrometers in the stratosphere (Arnold, 1986)

Mass	*Ion*	*Mass*	*Ion*
26 ± 2	CN^-	223 ± 1	$HSO_4^-(HNO_3)_2$
43 ± 2	CN^-H_2O	241 ± 1	$HSO_4^-(HNO_3)_2H_2O$
61 ± 1	CO_3^-, NO_3^-	251 ± 1	$NO_3^-(HNO_3)_3$
80 ± 2	$CO_3^-H_2O$, $NO_3^-H_2O$	258 ± 1	$HSO_4^-{\cdot}H_2SO_4{\cdot}HNO_3$
97 ± 1	HSO_4^-	274 ± 1	$HSO_4^-(HNO_3)_2HClO$
109 ± 2	$NO_3^-HNO_2$		$HSO_4^-{\cdot}H_2SO_4{\cdot}HSO_3$
125	$NO_3^-HNO_3$	286 ± 1	$HSO_4^-(HNO_3)_3$
133 ± 1	$HSO_4^-(H_2O)_2$	293 ± 1	$HSO_4^-(H_2SO_4)_2$
	HSO_4^-HCl	374 ± 1	$HSO_4^-(H_2SO_4)_2HSO_3$
143 ± 1	$NO_3^-HNO_3H_2O$	391 ± 1	$HSO_4^-(H_2SO_4)_3$
148 ± 2	HSO_4^-HOCl	409 ± 1	$HSO_4^-(H_2SO_4)_3H_2O$
160	$HSO_4^-HNO_3$	427 ± 1	$HSO_4^-(H_2SO_4)_3(H_2O)_2$
174 ± 1	$NO_3^-HNO_3HNO_2$	454 ± 1	$HSO_4^-(H_2SO_4)_3HNO_3$
188	$NO_3^-(HNO_3)_2$	472 ± 1	$HSO_4^-(H_2SO_4)_3HSO_3$
195	$HSO_4^-H_2SO_4$	489 ± 1	$HSO_4^-(H_2SO_4)_3HSO_3H_2O$
206 ± 1	$NO_3^-(HNO_3)_2H_2O$		

7.5 Effect of Ionic Processes on Neutral Constituents

Reactions between ions and neutral species, can, in principle, affect the budgets of neutral species as mentioned in Chapter 5.

In the stratosphere, the present understanding of the ion composition and chemistry is not adequate to completely describe the possible interactions. The ion production by cosmic rays appears, however, to be too small to modify the neutral composition substantially, except near the tropopause, where the ionization and decomposition of N_2 leads to a small production of nitrogen oxides (Warneck, 1972; Nicolet and Peetermans, 1972; Brasseur and Nicolet, 1973).

During intense solar proton events, the number of ion pairs produced can increase greatly even at relatively low altitudes, perturbing the neutral atmosphere and leading to a considerable increase in the rate of production of nitrogen and hydrogen oxides (see *e.g.*, Swider and Keneshea, 1973; Crutzen *et al.*, 1975; Jackman *et al.*, 1980; 1990; 1995; Reid *et al.*, 1991).

In principle, ions can provide a loss mechanism for species formed at ground level which are long lived in the lower atmosphere. For example,

ion reactions with chlorofluorocarbons which would lead to a lifetime less than a hundred years could be important. However, the most abundant ions, $H^+ \cdot (H_2O)_n$ and $NH_4^+ \cdot (H_2O)_n$ do not react with CF_2Cl_2 and $CFCl_3$.

Only the reaction

$$H_3O^+ + CFCl_3 \rightarrow CCl_3^+ + HF + H_2O \tag{7.101}$$

proceeds rapidly, but H_3O^+ is not present in large enough amounts to be important.

In the stratosphere, positive ions could contribute to the conversion of nitrogen oxides into nitric acid by the following chain:

$$NO_2 + O_3 \rightarrow NO_3 + O_2$$
$$NO_3 + NO_2 + M \rightarrow N_2O_5 + M$$
$$N_2O_5 + H_3O^+ \rightarrow HNO_3 + NO_2^+ \cdot H_2O$$

The importance of this mechanism is also limited by the abundance of the H_3O^+ ion, and should be compared with that of other homogeneous and heterogeneous NO_2 to HNO_3 conversion processes. Another possible mechanism involved in the conversion of NO_x to HNO_3 is the recombination of proton hydrates with NO_3^-

$$H^+ (H_2O)_n + NO_3^- \rightarrow HNO_3 + n(H_2O)$$

In the thermosphere, the effect of the ions in producing neutral nitrogen oxides is very important. In addition to photolysis,

$$(J_{N_2}); \qquad N_2 + h\nu\,(80 < \lambda < 125\ \text{nm}) \rightarrow 2N\,(^2D \text{ or } {}^4S) \qquad [F_0] \tag{7.102}$$

(where F_0 represents the fraction of nitrogen atoms produced in the ^2D state) ionic reactions can lead to the production of nitrogen atoms. The reaction of N_2^+ with atomic oxygen is one such source

$$(\gamma_3); \qquad N_2^+ + O \rightarrow NO^+ + N\,(^2D \text{ or } {}^4S) \qquad [F_1] \tag{7.103}$$

as well as recombination:

$$(\alpha_{N_2^+}); \qquad N_2^+ + e \rightarrow 2N\,(^2D \text{ or } {}^4S) \qquad [F_2] \tag{7.104}$$

The recombination of NO^+

$$(\alpha_{NO^+}); \qquad NO^+ + e \rightarrow N\,(^2D;\ {}^4S) + O \qquad [F_3] \tag{7.105}$$

and the following reactions must also be considered:

$$(\gamma_1); \qquad O^+ + N_2 \rightarrow NO^+ + N\,(^4S) \tag{7.106}$$

$$(\gamma_{12}); \qquad N^+ + O_2 \rightarrow O_2^+ + N\,(^2D;\ {}^4S) \qquad [F_4] \tag{7.107}$$

$$(\gamma_{12}^+); \qquad N^+ + O_2 \rightarrow NO^+ + O \tag{7.108}$$

Fast secondary electrons produced by cosmic and solar particles can dissociate or dissociatively ionize the nitrogen molecule:

$$N_2 + e^* \rightarrow 2N\,(^2D;\ ^4S) + e \qquad [F_5] \qquad (7.109)$$

$$N_2 + e^* \rightarrow N\,(^2D;\ ^4S) + N^+ + e \qquad [F_6] \qquad (7.110)$$

The fractional production of the nitrogen atoms in each electronic state is not yet known with accuracy. This parameter represents an extremely important factor in determining the density of nitric oxide in the E- and D-regions, as discussed below (see also, Norton and Barth, 1970; Rees and Roble, 1979; Solomon, 1983).

Almost all of the atoms which are produced in the ^2D state react with O_2 in the middle atmosphere, producing nitric oxide:

$$(b_7^*); \qquad N\,(^2D) + O_2 \rightarrow NO + O \qquad (7.111)$$

Deactivation by atomic oxygen and electrons play only a minor role below 100 km:

$$N\,(^2D) + O \rightarrow N\,(^4S) + O \qquad (7.112)$$

$$N(^2D) + e \rightarrow N\,(^4S) + e \qquad (7.113)$$

On the other hand, the reaction of the ground state atom with molecular oxygen is relatively slow:

$$(b_7); \qquad N\,(^4S) + O_2 \rightarrow NO + O \qquad (7.114)$$

so that almost all of these nitrogen atoms are destroyed in the lower thermosphere by the rapid reaction with NO:

$$(b_6); \qquad N\,(^4S) + NO \rightarrow N_2 + O \qquad (7.115)$$

Therefore, when dissociation of molecular nitrogen yields one N (^4S) and one N (^2D) atom in the lower thermosphere, the net odd nitrogen production is extremely small: almost every N (^2D) atom produces one NO molecule, but almost every N (^4S) atom immediately destroys one at these altitudes. Net production is provided only by the very small fraction of N (^4S) atoms which react with oxygen rather than with NO. Even very small deviations from a 50%-50% branching ratio can have large effects on lower thermospheric NO densities, making this parameter an extremely important one in NO_x chemistry. Laboratory studies by Kley *et al.* (1997) concerning the state of the product atoms produced in these reactions show that $F_3 = 0.76$, while studies by Zipf and McLaughlin (1978) suggest that $F_5 = 0.5$. To model the effects of these processes, indirect estimates based on airglow studies are often adopted. Rusch *et al.* (1981) adopted, for example, $F_1 = 1$, $F_2 = 0.5$, and $F_4 = 0$. Massie (1979) assumed $F_1 = 1$, $F_2 = 1$, $F_4 = 1$, and $F_5 = 0.75$. Figure 7.33 shows the chemistry of nitrogen compounds in

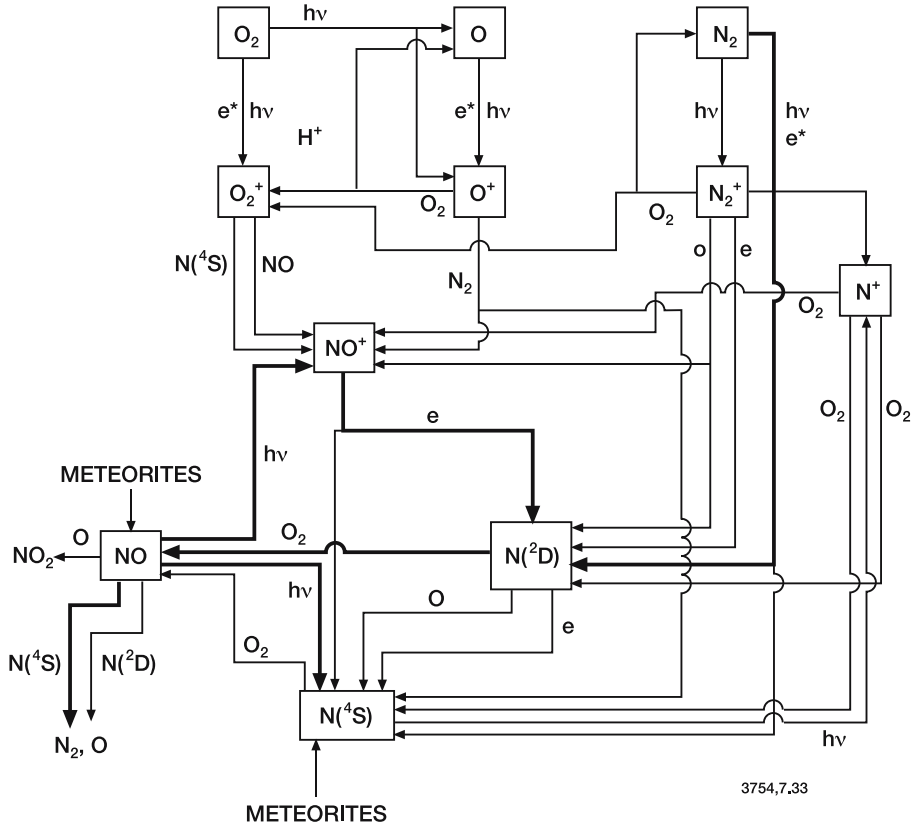

Figure 7.33. Chemistry of nitrogen compounds in the thermosphere and the interactions between neutrals and ions. From Massie (1979).

the thermosphere. We can now evaluate the rates of production P_{NO}, $P_{N\,(^4S)}$, and $P_{N\,(^2D)}$ which were referred to in Eqs. (5.161) and (5.162).

$$P_{N(^2D)} = 2F_0 J_{N_2}(N_2) + F_1\gamma_3(N_2^+)(O) + 2\alpha_{N_2^+}(N_2^+)\,n_e\,F_2 + F_3\alpha_{NO^+}(NO^+)\,n_e + 2P_D F_5 + P_I F_6 \tag{7.116}$$

$$P_{N\,(^4S)} = (1-F_0)2J_{N_2}(N_2) + (1-F_1)\,\gamma_3\,(N_2^+)(O) + 2\alpha_{N_2^+}(1-F_2)(N_2^+)\,n_e + (1-F_3)\alpha_{NO^+}\,(NO^+)\,n_e + \gamma_{12}(N^+)(O_2) + \gamma_1(O^+)(N_2) + 2P_D(1-F_5) + P_I(1-F_6) \tag{7.117}$$

$$P_{NO} = 2b_{39}(N_2O)(O^1D) + P_M(NO) + \gamma_1(O^+)(N_2) \tag{7.118}$$

where P_D is the rate of production of nitrogen atoms due to dissociation of N_2 by energetic electrons (7.109), P_I is the production due to

dissociative ionization (7.110), and P_M is the rate of odd nitrogen production associated with meteors. The rate of production of the nitrogen atom by dissociative ionization is equal to the rate of production of N^+ by the same process (see Eq. (7.40b)):

$$P_I = P_{N^+} = 0.185Q \tag{7.119}$$

where Q is the rate of ion pair production. Note that the N^+ and NO^+ ions formed by these reactions will ultimately yield reactive nitrogen, either by Reaction (7.107) or by Reaction (7.108) followed by (7.104). The relative values of the cross section for dissociation (Winters, 1966; Niehaus, 1967) and dissociative ionization (Rapp *et al.*, 1965) imply a rate for P_D of about 0.85Q (Rusch *et al.*, 1981).

The O^+ ion can also produce nitrogen atoms by reaction (7.106) with nitrogen and dissociative recombination of NO^+. This contribution is only about 0.03Q in the middle atmosphere, however. Below 90 km altitude, each ion pair produced during particle precipitation in the atmosphere (cosmic rays, magnetospheric electrons, and solar proton events) results in a total gross odd nitrogen production

$$P_{NO_x} = P_{N(^2D)} + P_{N(^4S)} + P_{NO}$$

of about 1.25Q (see *e.g.*, Jackman *et al.*, 1979; Rusch *et al.*, 1981). The net production depends on the fractional production of N^4S and N^2D atoms.

Below the mesopause, where water cluster ions are present, the ions can contribute to the formation of hydrogen free radicals (see Figure 7.34). Referring to the reactions in Section 7.3.2, we note that the $O_2^+ \cdot H_2O$ ion can lead to the following chain, producing one H and one OH radical :

$$O_2^+ \cdot H_2O + H_2O \rightarrow H_3O^+ \cdot OH + O_2$$

$$H_3O^+ \cdot OH + e \rightarrow H + OH + H_2O$$

$$\boxed{\text{Net: } H_2O \rightarrow H + OH}$$

or

$$O_2^+ \cdot H_2O + H_2O \rightarrow H_3O^+ \cdot OH + O_2$$

$$H_3O^+ \cdot OH + H_2O \rightarrow H_3O^+ \cdot H_2O + OH$$

$$H_3O^+ \cdot H_2O + nH_2O \rightarrow H_3O^+ \cdot (H_2O)_{n+1}$$

$$H_3O^+ \cdot (H_2O)_{n+1} + e \rightarrow H + (n+2)\,H_2O$$

$$\boxed{\text{Net: } H_2O \rightarrow H + OH}$$

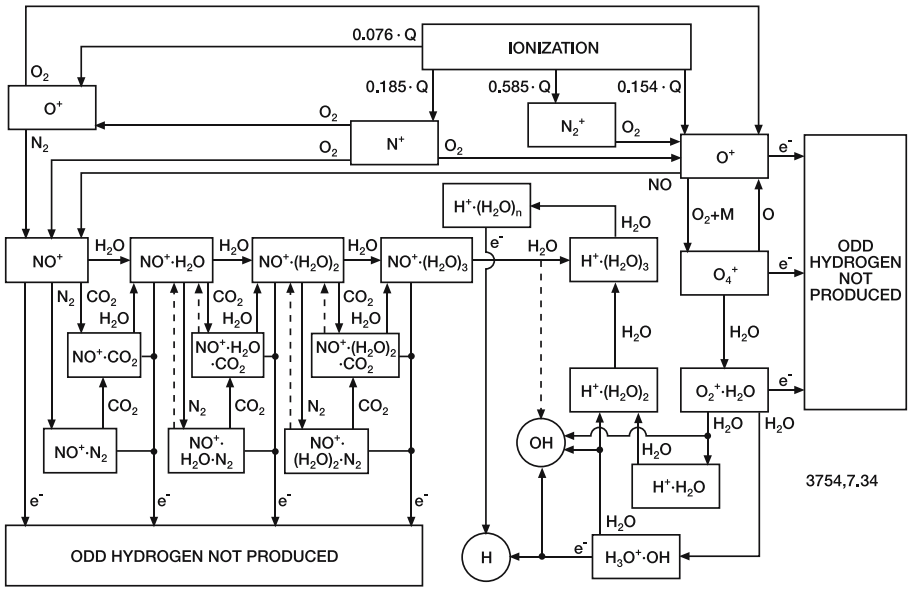

Figure 7.34. Schematic diagram of the ion chemistry leading to odd hydrogen production. From Solomon *et al.* (1981).

Other secondary chains must be considered. The processes and rates of formation of hydrogen radical are described by Frederick (1976), Heaps (1978b), Crutzen and Solomon (1980), and Solomon *et al.* (1981). Below about 75 km, nearly two odd hydrogen particles are formed per O_2^+ ionization; above that altitude, odd hydrogen production depends on the ionization rate and the atomic oxygen and water vapor densities. Figure 7.34 presents a schematic diagram of the positive ion chemistry responsible for odd hydrogen production in the D-region of the ionosphere. Note that odd hydrogen production is much more efficient if the primary ion is O_2^+ than if the primary ion is NO^+ (*i.e.*, during particle precipitation as opposed to quiet times). Figure 7.35 presents a calculated vertical distribution of the rates of production of HO_x and NO_x per ion pair for two values of Q.

7.6 Radio Waves in the Lower Ionosphere

The study of the ionosphere has largely been performed by observation of the properties of radio wave propagation through this medium. In this work we will not attempt to present an exhaustive study of the interaction of electromagnetic waves and a weakly ionized plasma, nor

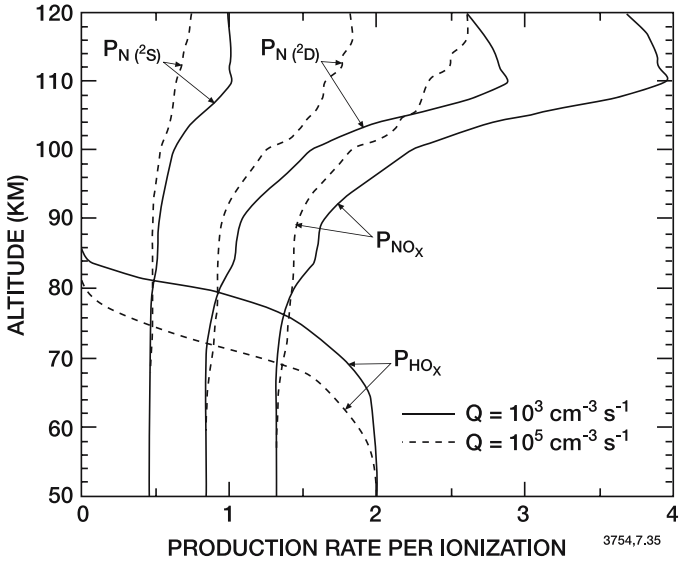

Figure 7.35. Rate of production of nitrogen atoms and odd hydrogen radicals per ion pair as a function of altitude. From Fritzenwallner (1997).

will we review the many techniques used for such studies. The object of this section is to indicate the basic principles which underlie studies of this sort and to present an elementary description of magneto-ionic theory (Appleton, 1937; Hartree, 1931), and finally to show how this approach yields information about the properties of the D-region, particularly in winter.

The conditions of propagation of an electromagnetic wave in the ionospheric medium are determined by the Maxwell and Lorentz equations. These equations determine the properties of the electric (E) and magnetic (H) fields, as well as the displacement (D) and the induction (B) as a function of the electric charge and current densities (J) (see, for example, Budden, 1961; Davies, 1965):

$$\boldsymbol{\nabla} \cdot \mathbf{D} = \rho \tag{7.120}$$

$$\boldsymbol{\nabla} \cdot \mathbf{B} = 0 \tag{7.121}$$

$$\boldsymbol{\nabla} \times \mathbf{H} = \mathrm{J} + \frac{\partial \mathbf{D}}{\partial \mathrm{t}} \tag{7.122}$$

$$\boldsymbol{\nabla} \times \mathbf{E} = -\frac{\partial \mathbf{B}}{\partial \mathrm{t}} \tag{7.123}$$

with

$$\mathbf{D} = \epsilon_0 \mathbf{E} + \mathbf{P} \tag{7.124}$$

$$\mathbf{B} = \mu_0 \mathbf{H} \tag{7.125}$$

where $\mathbf{P}$ is the polarization vector, ϵ_0 is the permitivity of free space, ρ is the space charge density, and μ_0 is the magnetic permeability. The Lorentz equation describes the flow of charge as a function of the electric and induction fields. For electrons, one may write

$$m_e \frac{d\mathbf{V}}{dt} = -e\,(\mathbf{E} + \mathbf{V} \times \mathbf{B}) - m_e\,\nu_c\,\mathbf{V} \tag{7.126}$$

where m_e is the mass of the electron, $\mathbf{V}$ is its speed, -e is the electrical charge and ν_c is the collision frequency between electrons and neutrals.

If one assumes that a plane transverse wave

$$E = E_0 \exp\ i(\omega_r t - kx) \tag{7.127}$$

of amplitude E_o and frequency ω_r propagates as a function of time t in the x direction with a propagation factor $k = 2\pi/\lambda$, λ being the actual wavelength in the medium, then it can be shown (after some mathematical manipulation), that the index of refraction of the ionized medium is given by the Appleton formula:

$$n^2 = 1 - \frac{X}{1 - iZ - \frac{Y_T}{2\,(1-X-iZ)} \pm \left(\frac{Y_T^4}{4(1-X-iZ)^2} + Y_L^2\right)^{1/2}} \tag{7.128}$$

where $X = n_e\,e^2/\epsilon_0\,m_e\,\omega_r^2$, (a dimensionless parameter proportional to the electron concentration n_e), $Y_L = eB_L/m_e\,\omega_r$, and $Y_T = eB_T/m_e\,\omega_r$ represent the effects of the longitudinal (L) and transverse (T) magnetic field components and $Z = \nu_c/\omega_r$ is a dimensionless parameter describing the effect of electron-neutral collisions. This formula shows that the refractive index is a complex number when the collision frequency cannot be neglected compared to the frequency of the wave. The real part of the refractive index describes the refracting and dispersive properties of the medium and the imaginary part its absorption properties. The Appleton formula also shows that if Y_L or Y_T are different from zero, two values can be assigned to n^2, indicating that the presence of a magnetic field introduces anisotropy into the medium, so that two propagation modes exist for each frequency (ordinary and extraordinary wave); this is a phenomenon similar to the optical birefringence of certain crystals.

The most simple form of the Appleton equation is obtained by neglecting the effects of the magnetic field and collisions. This equation is adequate to describe the propagation of high frequency waves (above 30 MHz) in the ionosphere, and can be used to obtain an approximate understanding of the propagation characteristics of lower frequency waves. In this case, one obtains

$$n^2 = 1 - \frac{Kn_e}{f^2} \tag{7.129}$$

where K is a constant which is equal to 80.5 if the wave frequency f is expressed in Hertz. Coupling this expression with Snell's law (which describes the propagation of the electromagnetic radiation), the level of reflection of the wave can be derived. Further, by tuning the wave frequency of the transmitter, information on the vertical profile of electron density can be deduced.

In the D-region, collisions cannot be neglected except for very high frequency propagation. Neglecting the effect of the magnetic field, the refractive index then becomes:

$$n^2 = 1 - \frac{X}{1 - iZ} = 1 - \frac{X}{1 + Z^2} - \frac{iXZ}{1 + Z^2} \tag{7.130}$$

It follows that, to this order of approximation, a wave traveling through an ionized medium with negligible refraction is progressively attenuated with an absorption coefficient given by

$$K = \frac{e^2}{2\epsilon_o \, m_e \, c} \frac{n_e \nu_c}{\omega_r^2 + \nu_c^2} \tag{7.131}$$

which is often expressed in units of nepers per meter (a neper corresponds to 8.69 dB). The Appleton-Hartree theory used to obtain this expression employs an invariant collision frequency for all electrons. However, as pointed out by Phelps and Pack (1959), the cold plasma approximation is not valid in the D-region and the collision frequency should vary with the velocity of the electrons. Sen and Wyller (1960) generalized the Appleton-Hartree theory by assuming a realistic electron energy distribution. In practical applications, however, the above expressions can still be used, provided that ν_c is replaced by an effective collision frequency ν_{eff}, such that the ratio ν_{eff}/ν_c, varies with the radio wave frequency.

Study of the amplitude of waves in the MHz range, reflected in the E- and F-regions, gives a measure of D-region absorption. Techniques involving vertical reflection of pulses (called the A1 method) or oblique reflection of continuous waves (A3 method) provide useful indications of some properties of the D-region, particularly the change in electron concentration with time at a given point for a layer where $\nu_c \approx \omega_r$. Such systematic observations of absorption have established the nature of variations which are related to ionization processes. For example, a variation of the absorption L with solar zenith angle is found, of the form:

$$L = C \cos^a \chi \tag{7.132}$$

where a is typically between 0.6 and 1.0 at mid-latitudes, and C is a constant which varies with season, geomagnetic activity, etc. A variation with solar activity has also been noted (see *e.g.*, Appleton and Piggott,

1954). It has been found that while the absorption varies systematically with the mean zenith angle in summer, abnormally high absorption is observed in winter. In the absence of changes in the atmospheric composition, one would expect to obtain lower absorption in winter than in summer because of the larger wintertime solar zenith angle. However, observations suggest the opposite (winter mean values of the electron concentration are larger than the summertime values, producing the so-called "*smooth winter anomaly*"). During winter, the day-to-day variability in the electron concentration is also higher (typically a factor of 3-4). In addition, unexpected intense absorption events lasting a few days are often observed in winter even under quiet solar conditions (see Figure 7.36). This effect was observed by Appleton as early as 1937, and is often referred to as "*sporadic winter anomaly*". It has been the subject of considerable research. The phenomenon is clearly related to an increase in electron concentration (Mechtly and Shirke, 1968) and NO^+ ion density (Zbinden *et al.*, 1975). Under these conditions, the level at which the water cluster ion densities equal that of the molecular ions (NO^+ and O_2^+) is typically 5 km below normal.

The observations obtained during a measurement campaign at El Arenosillo (37°N) (European winter anomaly campaign 1975/6, see Offermann, 1979) as well as model studies (*e.g.*, Koshelev, 1979; Solomon *et al.*, 1982b) have indicated that the origin of the winter anomaly probably lies in sporadic injection of large amounts of nitric oxide from the thermosphere to the mesosphere in association with changes in atmospheric dynamics. D-region models which include the effects of both chemistry and dynamics (Solomon *et al.*, 1982a,b; Brasseur and De Baets, 1986) show that ionization is more intense in winter than in summer, even under normal conditions, as a result of the greater NO densities in the winter season. The observed changes are consistent with the observations of a "smooth winter anomaly" underlying the sporadic enhancements. Measurements of NO densities during sporadic winter anomaly events (Beran and Bangert, 1979; Beynon *et al.*, 1976; Arnold and Krankowsky, 1979; Aikin *et al.*, 1977) indicate that the NO concentration is greatly elevated during these conditions. The sporadic winter anomaly may be related to atmospheric heating, which decreases the positive ion-electron recombination coefficient because the concentrations of the cluster ions decrease while those of the molecular ions increase (Danilov and Taubenheim, 1983). It is now believed, however, that the NO enhancement and winter anomalous absorption of radio signals is related to transport processes associated with planetary waves (Labitzke *et al.*, 1979; Kawahira, 1982, Garcia *et al.*, 1987).

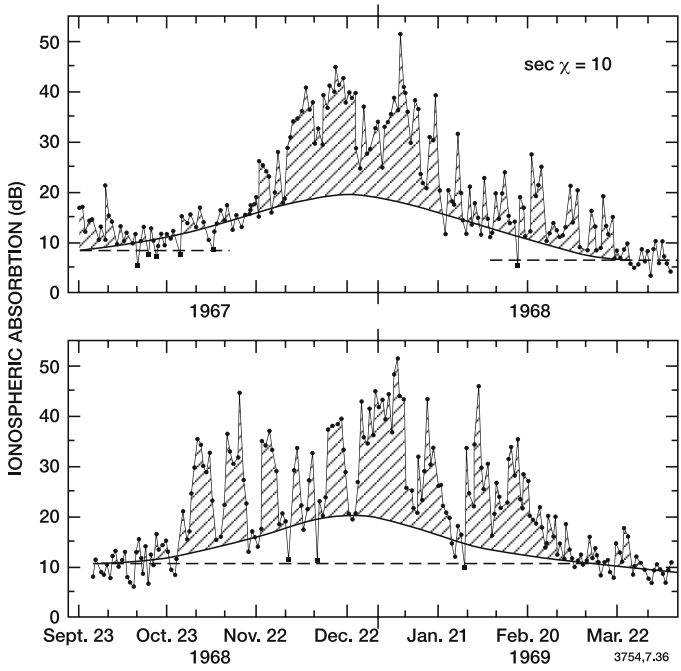

Figure 7.36. Time series of D-region absorption during summer and winter at mid-latitude. From Schwentek (1971).

References

Aikin, A.C., R.A. Goldberg, W. Jones, and J.A. Kane, Observations of the mid-latitude lower ionosphere in winter. *J Geophys Res: 82*, 1869, 1977.

Appleton, E.V., Regularities and irregularities in the ionosphere, 1. *Proc Roy Soc A: 162*, 451, 1937.

Appleton, E., and W.R. Piggott, Ionospheric absorption measurements during a sunspot cycle. *J Atmos Terr Phys: 8*, 141, 1954.

Arijs, E., Positive and negative ions in the stratosphere. *Ann Geophys: 1*, 149, 1983.

Arijs, E., Stratospheric ion chemistry: Present understanding and outstanding problems. *Planet Space Sci: 40*, 255, 1992.

Arijs, E., and G. Brasseur, Acetonitrile in the stratosphere and implication for positive ion composition. *J Geophys Res: 91*, 4003, 1986.

Arijs, E., J. Ingels, and D. Nevejans, Mass spectrometric measurement of positive ion composition in the stratosphere. *Nature: 271*, 642, 1978.

Arijs, E., D. Nevejans, and J. Ingels, Unambiguous mass determination of major stratospheric positive ions. *Nature: 288*, 684, 1980.

Arijs, E., D. Nevejans, P. Frederick, and J. Ingels, Negative ion composition measurements in the stratosphere. *Geophys Res Lett: 8*, 121, 1981.

Arijs, E., D. Nevejans, and J. Ingels, Stratospheric positive ion composition measurements, ion abundances and related trace gas detection. *J Atmos Terr Phys: 44*, 43, 1982a.

Arijs, E., D. Nevejans, P. Frederick, and J. Ingels, Stratospheric negative ion composition measurements, ion abundances and related trace gas detection. *J Atmos Terr Phys: 44*, 681, 1982b.

Arijs, E., D. Nevejans, and J. Ingels, Positive ion composition measurements and acetonitrile in the upper stratosphere. *Nature: 303*, 314, 1983a.

Arijs, E., D. Nevejans, J. Ingels, and P. Frederick, Positive ion composition measurements between 33 and 20 km altitude. *Ann Geophys: 2*, 161, 1983b.

Arnold, F., The middle atmosphere ionized component, in *Proc of the ESA-Symposium on Rocket- and Balloon-Programmes*. Bournemouth, 1980.

Arnold, F., Atmospheric ions. *Studies in Env Sci: 26*, 103, 1986.

Arnold, F., and D. Krankowsky, Ion composition and electron- and ion-loss processes in the earth's atmosphere, pp. 93-127, in *Dynamical and Chemical Coupling Between the Neutral and Ionized Atmosphere*. Grandal, B., and Holtet, J.A., (eds.), D. Reidel Publishing Company, Dordrecht, Holland, 1977.

Arnold, F., and G. Henschen, First mass analysis of stratospheric negative ions, *Nature: 275*, 521, 1978.

Arnold, F., and D. Krankowsky, Mid-latitude lower ionosphere structure and composition measurements during winter. *J Atmos Terr Phys: 41*, 1127, 1979.

Arnold, F., and G. Hauck, Lower stratosphere trace gas detection using aircraft-borne active chemical ionization mass spectrometry. *Nature: 315*, 307, 1985.

Arnold, F., J. Kissel, D. Krankowsky, H. Wieder, and J. Zähringer, Negative ions in the lower ionosphere: A mass spectrometric measurement. *J Atmos Terr Phys: 33*, 1169, 1971.

Arnold, F., D. Krankowsky, and K.H. Marien, First mass spectrometric measurements of positive ions in the stratosphere. *Nature: 267*, 30, 1977.

Arnold, F., H. Böhringer, and G. Henschen, Composition measurements of stratospheric positive ions. *Geophys Res Lett: 5*, 653, 1978.

Arnold, F., G. Henschen, and E.E. Ferguson, Mass spectrometric measurements of fractional ion abundances in the stratosphere — Positive ions. *Planet Space Sci: 29*, 185, 1981.

Banks, P., and G. Kockarts, *Aeronomy.* Academic Press, New York, 1973.

Becker, K.H., and A. Ionescu, Acetonitrile in the lower troposphere. *Geophys Res Lett: 9*, 1349, 1982.

Beig, G., and D.K. Chakrabarty, On modeling stratospheric positive ions, *J Atmos Chem: 6*, 175, 1988.

Beig, G., S. Walters, and G. Brasseur, A two-dimensional model of ion composition in the stratosphere, 1. Positive ions. *J Geophys Res: 98*, 12,767, 1993a.

Beig, G., S. Walters, and G. Brasseur, A two-dimensional model of ion composition in the stratosphere, 2. Negative ions. *J Geophys Res: 98*, 12,775, 1993b.

Beran, D., and W. Bangert, Trace constituents in the mesosphere and lower thermosphere during winter anomaly events, *J Atmos Terr Phys: 41*, 1091, 1979.

Beynon, W.J.G., E.R. Williams, F. Arnold, D. Krankowsky, W.C. Bain, and P.H.G. Dickinson, D-region rocket measurements in winter anomaly absorption conditions. *Nature: 261*, 118, 1976.

Bills, R.E., and C.S. Gardner, Lidar observations of mesospheric Fe and sporadic Fe layers at Urbana, Illinois. *Geophys Res Lett: 17*, 143, 1990.

Björn, L.G., and F. Arnold, Mass spectrometric detection of precondensation nuclei at the arctic summer mesopause. *Geophys Res Lett: 8*, 1167, 1981.

Böhringer, H., and F. Arnold, Acetonitrile in the stratosphere — Implications from laboratory studies. *Nature: 290*, 321, 1981.

Böhringer, H., D.W. Fahey, F.C. Fehsenfeld, and E.E. Ferguson, The role of ion-molecule reactions in the conversion of N_2O_5 to HNO_3 in the stratosphere. *Planet Space Sci: 31*, 185, 1983.

Brasseur, G., *Physique et Chimie de l'Atmosphere Moyenne.* Masson, Paris, 1982.

Brasseur, G., and M. Nicolet, Chemospheric processes of nitric oxide in the mesosphere and stratosphere. *Planet Space Sci: 21*, 939, 1973.

Brasseur, G., and A. Chatel, Modelling of stratospheric ions: A first attempt. *Ann Geophys: 1*, 173, 1983.

Brasseur, G., and P. De Baets, Minor constituents in the mesosphere and lower thermosphere, *J Geophys Res: 91*, 4025, 1986.

Brasseur, G., E. Arijs, A. De Rudder, D. Nevejans, and J. Ingels, Acetonitrile in the atmosphere. *Geophys Res Lett: 10*, 725, 1983.

Budden, K.G., *Radio Waves in the Ionosphere.* Cambridge Univ. Press, 1961.

Burns, C.J., E. Turunen, M. Matveinen, H. Ranta, and J.K. Hargreaves, Chemical modeling of the quiet D- and E-Region using EISCAT electron density profiles. *J Atmos Terr Phys: 53*, 115, 1991.

Callis, L.B., R.E. Boughner, N. Natarajan, J.D. Lambeth, D.N. Baker, and J.B. Blake, Ozone depletion in the high altitude lower stratosphere, 1979-1990. *J Geophys Res: 96*, 2921, 1991.

Chapman, S., Notes on atmospheric sodium. *Astrophys J: 90*, 309, 1939.

Crutzen, P.J., and S. Solomon, Response of mesospheric ozone to particle precipitation. *Planet Space Sci: 28*, 1147, 1980.

Crutzen, P.J., I.S.A. Isaksen, and G.C. Reid, Solar proton events: Stratospheric sources of nitric oxide. *Science: 189*, 457, 1975.

Danilov, A.D., and J. Taubenheim, NO and temperature control of the D-Region. *Space Sci Rev: 34*, 413, 1983.

Davies, K., Ionospheric radio propagation, National Bureau of Standard, *Monograph 80*, 1965 and Dover Publications, New York, 1966.

Dubach, J., and W.A. Barker, Charged particle induced ionization rates in planetary atmospheres. *J Atmos Terr Phys: 33*, 1287, 1971.

Fehsenfeld, F.C., and E.E. Ferguson, Thermal energy positive ion reactions in a wet atmosphere containing ammonia. *J Chem Phys: 59*, 6272, 1973.

Fehsenfeld, F.C., and E.E. Ferguson, Laboratory studies of negative ion reactions with atmospheric trace constituent. *J Chem Phys: 61*, 3181, 1974.

Fehsenfeld, F.C., C.J. Howard, and A.L. Schmeltekopf, Gas phase ion chemistry of HNO_3. *J Chem Phys: 63*, 2835, 1975.

Fehsenfeld, F.C., I. Dotan, D.L. Albritton, C.J. Howard, and E.E. Ferguson, Stratospheric positive ion chemistry of formaldehyde and methanol, *J Geophys Res: 83*, 1333, 1978.

Ferguson, E.E., D-Region ion chemistry. *Rev Geophys Space Phys: 9*, 997, 1971.

Ferguson, E., Sodium hydroxide in the stratosphere. *Geophys Res Lett: 5*, 1035, 1978.

Ferguson, E.E., Ion-molecule reactions in the atmosphere, in *Kinetics of Ion-Molecule Reactions.* Ausloos, P. (ed.), Plenum Press, New York, 1979.

Frederick, J.E., Solar corpuscular emission and neutral chemistry in the Earth's middle atmosphere. *J Geophys Res: 81*, 3179, 1976.

Fritzenwallner, J., *Globales Modell zur Verteilung der Positiven und Negativen Ionen in der Unteren Ionosphären der Erde.* Ph.D. thesis, University of Bern, Switzerland, 1997.

Fritzenwallner, J., and E. Kopp, Model calculations of the silicon and magnesium chemistry in the mesosphere and lower thermosphere. *Adv Space Res: 21*, 859, 1998a.

Fritzenwallner, J., and E. Kopp, Model calculations of the negative ion chemistry in the mesosphere with special emphasis on the chlorine species and the formation of cluster ions. *Adv Space Res: 21*, 891, 1998b.

Garcia, R.R., S. Solomon, G.C. Reid, S.K. Avery, Transport of nitric oxide and the D region winter anomaly. *J Geophys Res: 92*, 977, 1987.

Granier, C., J.P. Jégou, and G. Mégie, Atomic and ionic calcium in the earth's upper atmosphere. *J Geophys Res: 94*, 9917, 1989.

Hall, L.A., and H.E. Hinteregger, Solar radiation in the extreme ultraviolet and its variation with solar rotation. *J Geophys Res: 75*, 6959, 1970.

Hamm, S., G. Helas, and P. Warneck, Acetonitrile in the air over Europe. *Geophys Res Lett: 16*, 483, 1989.

Hargreaves, J.K., *The Upper Atmosphere and Solar-Terrestrial Relations.* Van Nostrand Reinhold, 1979.

Hargreaves, J.K., *The Solar-Terrestrial Environment.* Cambridge Univ. Press, 1992.

Hartree, D.R., The propagation of electro-magnetic waves in a refracting medium in a magnetic field, in *Proc Cambridge Phil Soc: 27*, 143, 1931.

Heaps, M.G., Parameterization of the cosmic ray ion-pair production rate above 18 km. *Planet Space Sci: 26*, 513, 1978a.

Heaps, M.G., *The Effect of a Solar Proton Event on the Minor Neutral Constituents of the Summer Polar Mesosphere.* US Army Atmospheric Sci Lab Report ASL-TR-0012, 1978b.

Henschen, G., and F. Arnold, Extended positive ion composition measurements in the stratosphere — Implication for neutral trace gases. *Geophys Res Lett: 8*, 999, 1981.

Hunten, D.M., and M.B. McElroy, Metastable $O_2(^1\Delta)$ as a major source of ions in the D-region. *J Geophys Res: 73*, 2421, 1968.

Jackman, C.H., Effect of energetic particles on minor constituents in the middle atmosphere. *J Geomagn Geoelect: 43*, 637, 1991.

Jackman, C.H., H.S. Porter, and J.E. Frederick, Upper limits on production rate of NO per ion pair. *Nature: 280*, 170, 1979.

Jackman, C.H., J.E. Frederick, and R.S. Stolarski, Production of odd nitrogen in the stratosphere and mesosphere: An intercomparison of source strengths. *J Geophys Res: 85*, 7495, 1980.

Jackman, C.H., A.P. Douglass, R.B. Rood, R.D. McPeters, and P.E. Maede, Effect of solar events on the middle atmosphere during the past two solar cycles as computed using a two-dimensional model. *J Geophys Res: 95*, 7417, 1990.

Jackman, C.H., J.E. Nielsen, D.J. Allen, M.C. Cerniglia, R.D. McPeeters, A.R. Douglass, and R.B. Rood, The effects of the October 1989 solar proton events on the stratosphere as computed using a 3-Dimensional model. *Geophys Res Lett: 20*, 459, 1993.

Jackman, C.H., M.C. Cerniglia, J.E. Nielsen, D.J. Allen, J.M. Zawodny, R.D. McPeters, A.R. Douglass, J.E. Rosenfield, and R.B. Rood, Two-dimensional and three-dimensional model simulations, measurements, and interpretation of the influence of the October 1989 solar proton events on the middle atmosphere. *J Geophys Res: 100*, 11,641, 1995.

Jégou, J.P., C. Granier, M.L. Chanin, and G. Mégie, General theory of the alkali metals present in the earth's upper atmosphere, 1. Flux model: Chemical and dynamical processes. *Ann Geophys: 3*, 163, 1985a.

Jégou, J.P., C. Granier, M.L. Chanin, and G. Mégie, General theory of the alkali metals present in the earth's upper atmosphere, 2. Seasonal and meridional variations. *Ann Geophys: 3*, 299, 1985b.

Johnson, C.Y., E.B. Meadows, and J.C. Holmes, Ion composition of the arctic ionosphere. *J Geophys Res: 63*, 443, 1958.

Kawahira, K., An observational study of the D-region winter anomaly and sudden stratospheric warmings. *J Atmos-Terr Phys: 44*, 947, 1982.

Kawamoto, H., and T. Ogawa, A steady-state model of negative ions in the lower stratosphere. *Planet Space Sci: 32*, 1223, 1984.

Kawamoto, H., and T. Ogawa, Minor species of negative ions in the lower stratosphere. *Res Lett Atmos Electr: 5*, 1, 1985.

Kazil, J., E. Kopp, S. Chabrillat, and J. Bishop, The University of Bern atmosphere ion model: Time–dependent modeling of the ions in the mesophere and lower thermosphere. *J Geophys Res: 108*, d14, 4432, doi 10.1029/2002JD003024, 2003.

Kelley, M.C., *The Earth's Ionosphere: Plasma Physics and Electrodynamics*. Academic Pres, 1989.

Keneshea, T.J., R.S. Narcisi, and W. Swider, Jr., Diurnal model of the E region. *J Geophys Res: 75*, 845, 1970.

Kley, D., G.M. Lawrence, and E.J. Stone, The yield of N (^2D) atoms in the dissociative recombination of NO^+. *J Chem Phys: 66*, 4157, 1977.

Knop, G., and F. Arnold, Stratospheric trace gas detection using a new balloon-borne ACIMS method: Acetonitrile, acetone and nitric acid. *Geophys Res Lett: 14*, 1262, 1987a.

Knop, G., and F. Arnold, Atmospheric acetonitrile measurements in the tropopause region using aircraft-borne active chemical ionization mass spectrometry. *Planet Space Sci: 35*, 259, 1987b.

Kopp, E., and U. Herrmann, Ion composition in the lower ionosphere. *Ann Geophys: 2*, 83, 1984.

Koshelev, V.V., Variations of transport conditions and winter anomaly in the D-ionospheric region. *J Atmos Terr Phys: 41*, 431, 1979.

Koshelev, V.V., The winter anomaly in the ionospheric D-region – Some numerical calculations. *J Atmos Terr Phys: 49*, 81, 1987.

Kull, A., E. Kopp, C. Granier, and G. Brasseur, Ions and electrons of lower-latitude D region. *J Geophys Res: 102*, 9705, 1997.

Labitzke, K., K. Paetzoldt, and H. Schwentek, Planetary waves in the strato- and mesosphere during the western European winter anomaly campaign 1975/76 and their relation to ionospheric absorption. *J Atmos Terr Phys: 41*, 1149, 1979.

Leu, M.T., M.A. Biondi, and R. Johnsen, Measurements of the recombination of elections with H_3O^+ $(H_2O)_n$ series ions. *Phys Rev: A7*, 292, 1973.

Massie, S.T., *Nitric Oxide Delta Band Absorption Measurements in the Lower Thermosphere.* PhD thesis, University of Colorado, Boulder, Colo, 1979.

McCrumb, J.L., and F. Arnold, High-sensitivity detection of negative ions in the stratosphere. *Nature: 294*, 136. 1981.

Mechtly, E.A., and J.S. Shirke, Rocket electron concentration measurements on winter days of normal and anomalous absorption. *J Geophys Res: 73*, 6243, 1968.

Mechtly, E.A., and L.G. Smith, Seasonal variation of the lower ionosphere at Wallops Island during the IQSY. *J Atmos Terr Phys: 30*, 1555, 1968.

Narcisi, R.S., and A.D. Bailey, Mass spectrometric measurements of positive ions at altitudes from 64 to 112 kilometers. *J Geophys Res: 70*, 3687, 1965.

Narcisi, R.S., A.D. Bailey, L. Della Lucca, C. Sherman, and D.M. Thomas, Mass spectrometric measurements of negative ions in the D- and lower E-regions. *J Atmos Terr Phys: 33*, 1147, 1971.

Nicolet, M., Contribution à l'étude de la structure de l'ionosphère. *Mem Inst Météor Belgique: 19*, 83, 1945.

Nicolet, M., and A.C. Aikin, The formation of the D region of the ionosphere. *J Geophys Res: 65*, 1469, 1960.

Nicolet, M., and W. Peetermans, The production of nitric oxide in the stratosphere by oxidation of nitrous oxide. *Ann Geophys: 28*, 751, 1972.

Niehaus, A., Excitation and dissociation of molecules by electron bombardment. Measurement of the formation probability for neutral fragments as a function of electron energy (in German). *Z Naturf: 22a*, 690, 1967.

Norton, R.B., and C.A. Barth, Theory of nitric oxide in the earth's atmosphere. *J Geophys Res: 75*, 3903, 1970.

Offermann, D., An integrated GBR campaign for the study of the D region winter anomaly in western Europe 1975/76. *J Atm Terr Phys: 41*, 1047, 1979.

Paulsen, D.E., R.E. Huffman, and J.C. Larrabee, Improved photoionization of $O_2(^1\Delta_g)$ in the D region. *Radio Sci: 7*, 51, 1972.

Phelps, A.V., and J.L. Pack, Electron collision frequencies in nitrogen and in the lower ionosphere. *Phys Rev Lett: 3*, 340, 1959.

Plane, J.M.C., The chemistry of meteoric metals in the earth's upper atmosphere. *Int Rev Phys Chem: 10*, 55, 1991.

Plane, J.M.C., C.S. Gardner, J. Yu, C.Y. She, R.R. Garcia, and H.C. Pumphrey, Mesopheric Na layer at 40°N, Modeling and observations. *J Geophys Res: 104*, 3773, 1999.

Potemra, T.A., Ionizing radiation affecting the lower ionosphere, in *ELF-VLF Radio Wave Propagation.* Holtet, J.A. (ed.), Reidel Publishing, Dordrecht, The Netherlands, 21, 1974.

Qian, J., and C.S. Gardner, Simultaneous lidar measurements of mesospheric Ca, Na, and temperature profile at Urbana, Illinois. *J Geophys Res: 100*, 7453, 1995.

Rapp, D., P. Englander-Golden, and D.D. Briglia, Cross sections for dissociative ionization of molecules by electron impact. *J Chem Phys: 42*, 4081. 1965.

Rees, M.H., Aurnal ionization and excitation by incident energetic electrons. *Planet Space Sci: 11*, 1209, 1963.

Rees, M.H., and R.G. Roble, The morphology of N and NO in auroral substorms. *Planet Space Sci: 27*, 453, 1979.

Rees, M.H., *Physics and Chemistry of the Upper Atmosphere*. Cambridge Univ. Press, 1989.

Reid, G.C., The production of water cluster positive ions in the quiet daytime D-region, *J Geophys Res: 25*, 275, 1977.

Reid, G.C., S. Solomon, and R.R. Garcia, Response of the middle atmosphere to the solar proton events of August-December 1989. *Geophys Res Lett: 18*, 1019, 1991.

Richards, P.G., J.A. Fennelly, and D.G. Torr, EUVAC: A solar EUV flux model for aeronomic calculations. *J Geophys Res: 99*, 8981, 1994.

Rosenberg, T.J., and L.J. Lanzerotti, Direct energy inputs to the middle atmosphere, in *Middle Atmosphere Electrodynamics*, N.C. Maynard (ed.), NASA CP-2090, 43, 1979.

Rusch, D.W., J.-C. Gérard, S. Solomon, P.J. Crutzen, and G.C. Reid, The effect of particle precipitation events on the neutral and ion chemistry of the middle atmosphere, 1. Odd nitrogen. *Planet Space Sci: 29*, 767, 1981.

Schneider, J., V. Bürger, and F. Arnold, Methyl cyanide and hydrogen cyanide measurements in the lower stratosphere: Implications for methyl cyanide sources and sinks. *J Geophys Res: 102*, 25,501, 1997.

Schwentek, H., Regular and irregular behavior of the winter anomaly in ionospheric absorption. *J Atmos Terr Phys: 33*, 1647, 1971.

Sen, H.K., and A.A. Wyller, On the generalizations of the Appleton-Hartree magnetoionic formulas. *J Geophys Res: 65*, 3931, 1960.

Slipher, V.M., Emissions in the spectrum of the light of the night sky. *Publ Astron Soc Pac: 41*, 262, 1929.

Smith, D., N.G. Adams, and M.J. Church, Mutual neutralization rates of ionospherically important ions. *Planet Space Sci: 24*, 697, 1976.

Smith, D., N.G. Adams, and E. Alge, Ion-ion mutual neutralization and ion-neutral switching reactions of some stratospheric ions. *Planet Space Sci: 29*, 449, 1981.

Smith, G.P., L.C. Lee, and P.C. Cosby, Photodissociation and photodetachment of molecular negative ions, VIII. Nitrogen oxides and hydrates. *J Chem Phys: 71*, 4464, 1979.

Snider, J.R., and G.A. Dawson, Surface acetonitrile near Tucson, Arizona. *Geophys Res Lett 11*, 241, 1984.

Solomon, S., The possible effects of translationally excited nitrogen atoms on lower thermospheric odd nitrogen. *Planet Space Sci: 31*, 135, 1983.

Solomon, S., D.W. Rusch, J.-C. Gérard, G.C. Reid, and P.J. Crutzen, The effect of particle precipitation events on the neutral and ion chemistry of the middle atmosphere, 2. Odd hydrogen. *Planet Space Sci: 29*, 885, 1981.

Solomon, S., P.J. Crutzen, and R.G. Roble, Photochemical coupling between the thermosphere and the lower atmosphere, 1. Odd nitrogen from 50 to 120 km. *J Geophys Res: 87*, 7206, 1982a.

Solomon, S., G.C. Reid, R.G. Roble, and P.J. Crutzen, Photochemical coupling between the thermosphere and the lower atmosphere, 2. D region ion chemistry and the winter anomaly. *J Geophys Res: 87*, 7221, 1982b.

Solomon, S., G.C. Reid, D.W. Rusch, and R.J. Thomas, Mesospheric ozone depletion during the solar proton cvent of July 13, 1982. 2. Comparison between theory and measurements. *Geophys Res Lett: 10*, 257, 1983.

Stewart, A.I., Photoionization coefficients and photoelectron impact excitation efficiences in the daytime ionosphere. *J Geophys Res: 75*, 6333, 1970.

Swider, W., and T.J. Keneshea, Decrease of ozone and atomic oxygen in the lower mesosphere during a PCA event. *Planet Space Sci: 21*, 1969, 1973.

Sze, N.D., M.K.W. Ko, W. Swider, and E. Murad, Atmospheric sodium chemistry, I. The altitude region 70-100 km. *Geophys Res Lett: 9*, 1187, 1982.

Thomas, L., Modeling the ion composition of the middle atmosphere. *Ann Geophys: 1*, 61, 1983.

Thomas, L., and M.R. Bowman, Model studies of the D-region negative-ion composition during day-time and night-time. *J Atmos Terr Phys: 35*, 397, 1985.

Thorne, R.M., Influence of relativistic electron precipitation on the lower ionosphere and stratosphere, in *Dynamical and Chemical Coupling Between the Neutral and Ionized Atmosphere*. Grandal, B., and J.A. Holtet (eds.), 161, Reidel Publishing, Dordrecht, The Netherlands, 1977a.

Thorne, R.M., Energetic radiation belt electron precipitation: A natural depletion mechanism for stratospheric ozone. *Science: 195*, 287, 1977b.

Tobiska, W.K., T. Woods, F. Eparvier, R. Viereck, L. Floyd, D. Bouwer, G. Rottman, and O.R. White, The SOLAR2000 empirical solar irradiance model and forecast tool. *J Atmos Solar-Terr Phys: 62*, 1233, 2000.

Vampola, A.L., and D.J. Gorney, Electron energy deposition in the middle atmosphere. *J Geophys Res: 88*, 6267, 1983.

Viggiano, A.A., and F. Arnold, The first height measurements of the negative ion composition of the stratosphere. *Planet Space Sci: 29*, 895, 1981.

Viggiano, A.A., R.A. Perry, D.L. Albritton, E.E. Ferguson, and F.C. Fehsenfeld, The role of H_2SO_4 in stratospheric negative-ion chemistry. *J Geophys Res: 85*, 4551, 1980.

Warneck, P., Cosmic radiation as a source of odd nitrogen in the stratosphere. *J Geophys Res: 77*, 6589, 1972.

Winters, H.F., Ionic absorption and dissociation cross section for nitrogen. *J Chem Phys: 44*, 1472, 1966.

Wisemberg, J., and G. Kockarts, Negative ion chemistry in the terrestrial D-region and signal flow graph theory. *J Geophys Res: 84*, 4642, 1980.

Zbinden, P.A., M.A. Hidalgo, P. Eberhardt, and J. Geiss, Mass spectrometer measurements of the positive ion composition in the D- and E-regions of the ionosphere. *Planet Space Sci: 23*, 1621, 1975.

Zipf, E.C., and R.W. McLaughlin, On the dissociation of nitrogen by electron impact and EUV photo-absorption. *Planet Space Sci: 26*, 449, 1978.

Appendix 1

PHYSICAL CONSTANTS AND OTHER DATA

Table A.1.1

General and Universal Constants	
Base of natural logarithms (e)	2.7182818285
π	3.14159265
Molar gas constant ($R = N_A k$)	8.3143 J K^{-1} mol^{-1}
Boltzmann's constant (k)	1.38066×10^{-23} J K^{-1}
Stefan-Boltzmann constant (σ)	5.67032×10^{-8} W m^{-2} K^{-4}
Planck's constant (h)	6.626176×10^{-34} J s
Speed of light (*in vacuo*) (c)	2.9979246×10^{8} m s^{-1}
Gravitational constant (G)	6.67259×10^{-11} m^3 s^{-2} kg^{-1}
Permittivity of free space (μ_0)	8.85×10^{-12} F m^{-1}
Mass of electrons (m_e)	9.1096×10^{-31} kg
Charge of electron (e)	1.6022×10^{-19} C
Atomic mass unit (amu)	$1.6605402 \times 10^{-27}$ kg
Avogadro's number (N_A)	6.022137×10^{23} mol^{-1}
Triple-point temperature of water (T_T)	273.16 K
Energy per unit wavenumber (hc)	1.986445×10^{-25} J m
First radiation constant ($c_1 = 2\pi hc^2$)	3.741832×10^{-16} W m^2
Second radiation constant ($c_2 = hc/k$)	1.438775×10^{-2} m K
Wien displacement constant ($b = \lambda_{max} T$)	2.897769×10^{-3} m K

Sun	
Flux at Sun surface	6.312×10^7 W m^{-2}
Luminosity	3.85×10^{26} W
Mass	1.99×10^{30} kg
Equatorial radius	6.9598×10^8 m
Surface area	6.087×10^{18} m^2
Mean angle subtended by photosphere at Earth	31.988 arc min
Emission temperature	5783 K

Earth	
Average radius	6.371×10^6 m
Equatorial radius	6.378×10^6 m
Polar radius	6.357×10^6 m
Average height of land	840 m
Average depth of oceans	3730 m
Area of Earth's surface	5.10×10^{14} m^2
Area of Earth's continents	1.49×10^{14} m^2
Northern Hemisphere land surface area	1.03×10^{14} m^2
Southern Hemisphere land surface area	0.46×10^{14} m^2
Area of Earth's oceans	3.61×10^{14} m^2
Standard surface gravity	9.80665 m s^{-2}
Mass of Earth	5.973×10^{24} kg
Mass of ocean	1.4×10^{21} kg
Mass of atmosphere	5.136×10^{18} kg
Mass of the biosphere	1.15×10^{16} kg
Eccentricity of orbit	0.016709
Equatorial escape velocity	1.18×10^4 m s^{-1}
Inclination of rotation axis	23.45 deg or 0.409 rad
Mean angular rotation rate	7.292×10^{-5} rad s^{-1}
Earth orbital period	365.25463 days
Length of sidereal day	23.94 hours
Lunar orbital period	27.32 days
Solar constant	1367 ± 2 W m^{-2}
Mean distance from sun (1AU)	1.496×10^{11} m
Furthest Sun-Earth distance (4 July)	1.5196×10^{11} m
Nearest Sun-Earth distance (3 January)	1.4696×10^{11} m
Human population (1987)	5.0×10^9
Earth's mean albedo	0.29

Dry Air	
Average molecular mass	28.97 g mol^{-1}
Specific gas constant	287 J K^{-1} kg^{-1}
Standard surface pressure	1.01325×10^5 Pa
Standard temperature	273.15 K
Mass density at 0°C and 101,325 Pa	1.2928 kg m^{-3}
Molecular density at 0°C and 101,325 Pa	2.68678×10^{25} m^{-3}
Molar volume at 0°C and 101,325 Pa	22.414×10^{-3} m^3 mol^{-1}
Specific heat at constant pressure (c_p)	1005 J K^{-1} kg^{-1}
Specific heat at constant volume (c_v)	717.6 J K^{-1} kg^{-1}
Index of refraction for air	1.000277
Dry adiabatic lapse rate	–9.75 K km^{-1}
Speed of sound in standard, calm air	343.15 m s^{-1}

Water	
Molecular weight	18.016 g mol^{-1}
Gas constant for vapor	461.5 J K^{-1} kg^{-1}
Density of pure water at 0°C	1000 kg m^{-3}
Density of ice at 0°C	917 kg m^{-3}
Density of water vapor at STP	0.803 kg m^{-3}
Specific heat of vapor at constant pressure	1952 J K^{-1} kg^{-1}
Specific heat of vapor at constant volume	1463 J K^{-1} kg^{-1}
Specific heat of liquid water at 0°C	4218 J K^{-1} kg^{-1}
Specific heat of ice at 0°C	2106 J K^{-1} kg^{-1}
Latent heat of vaporization at 0°C	2.501×10^6 J kg^{-1}
Latent heat of vaporization at 100°C	2.25×10^6 J kg^{-1}
Latent heat of fusion at 0°C	3.34×10^5 J kg^{-1}
Index of refraction for liquid water	1.336
Index of refraction for ice	1.312

Appendix 2

CONVERSION FACTORS AND MULTIPLYING PREFIXES

Table A.2.1

International System of Units			
Quantity	*Name of Unit*	*Symbol*	*Definition*
Length	meter	m	
Mass	kilogram	kg	
Time	second	s	
Electrical current	ampere	A	
Temperature	kelvin	K	
	Derived Units		
Force	newton	N	kg m s^{-2}
Pressure	pascal	Pa	N m^{-2}
Energy	joule	J	kg m^2 s^{-2}
Power	watt	W	J s^{-1}
Electric potential difference	volt	V	W A^{-1}
Electrical charge	coulomb	C	A s
Electrical resistance	ohm	Ω	V A^{-1}
Electrical capacitance	farad	F	A s V^{-1}
Frequency	hertz	Hz	s^{-1}

Conversion Factors

Area	1 ha = 10^4 m^2
Volume	1 liter = 10^{-3} m^3
Force	1 N = 10^5 dyn
Pressure	1 bar = 10^5 Pa
	1 atm = 1.01325×10^5 Pa = 760.0 Torr
Energy	1 cal = 4.1855 J
	1 eV = 1.6021×10^{-19} J
Power	1 W = 14.3353 cal min^{-1}
Temperature	T(°C) = T(K) - 273.15
	T(°F) = 1.8 T(°C) + 32
Mixing ratios	1 ppb = 10^{-3} ppm
	1 ppt = 10^{-3} ppb = 10^{-6} ppm
Logarithms	ln x = 2.3026 $\log_{10} x$

Table A.2.2

Multiplying Prefixes

Multiple	*Prefix*	*Symbol*	*Multiple*	*Prefix*	*Symbol*
10^{-1}	deci	d	10	deca	da
10^{-2}	centi	c	10^2	hecto	h
10^{-3}	milli	m	10^3	kilo	k
10^{-6}	micro	μ	10^6	mega	M
10^{-9}	nano	n	10^9	giga	G
10^{-12}	pico	p	10^{12}	tera	T
10^{-15}	femto	f	10^{15}	peta	P
10^{-18}	atto	a	10^{18}	exa	E

The International System of units is used except where usage suggests otherwise. The unit of pressure is the pascal (Pa), but meteorologists commonly use the millibar (mb) or equivalently the hectopascal (hPa). Number densities are often expressed in molecules per cubic centimeter (cm^{-3}). Volume mixing ratios are given in percent, parts per million (ppmv), parts per billion (ppbv), or parts per trillion (pptv). Mass mixing ratios are given in kilograms per kilograms or grams per kilograms. Wavelengths are often expressed in micrometers (μm) or nanometers (nm). Wavenumbers are expressed in inverse centimeters (cm^{-1}).

Table A.2.3

Pressure	Pa	dyn cm^2	atm	torr	hPa
1 Pa	1	10	9.86923×10^{-6}	7.50062×10^{-3}	10^{-2}
1 dyn cm^{-2}	10^{-1}	1	9.86923×10^{-7}	7.50062×10^{-4}	10^{-3}
1 atm	1.01325×10^5	1.01325×10^6	1	760	1.01325×10^3
1 torr	1.33322×10^2	1.33322×10^3	1.31579×10^{-3}	1	1.33322
1 hPa	10^2	10^3	9.86923×10^{-4}	7.50062×10^{-1}	1

Energy	J	eV	erg	cm^{-1}*	K*
1 J	1	6.24151×10^{18}	10^7	5.03412×10^{22}	7.24296×10^{22}
1 eV	1.60218×10^{-19}	1	1.60218×10^{-12}	8.06554×10^3	1.16045×10^4
1 erg	10^{-7}	6.24151×10^{11}	1	5.03412×10^{15}	7.24296×10^{15}
1 cm^{-1}	1.98645×10^{-23}	1.23984×10^{-4}	1.98645×10^{-16}	1	1.43878
1K	1.38065×10^{-23}	8.61734×10^{-5}	1.38065×10^{-16}	6.95036×10^{-1}	1

*Derived from $E = hc\tilde{\nu} = kT$.

Appendix 3

RATE COEFFICIENTS FOR SECOND-ORDER GAS-PHASE REACTIONS[a,b]

Table A.3.1

Reaction	*A Factor*	E_a/R	k_{298}
$O + O_3 \rightarrow O_2 + O_2$	8.0×10^{-12}	2060	8.0×10^{-15}
$O(^1D) + O_2 \rightarrow O + O_2$	3.2×10^{-11}	–70	4.0×10^{-11}
$O(^1D) + O_3 \rightarrow O_2 + O_2$	1.2×10^{-10}	0	1.2×10^{-10}
$\rightarrow O_2 + O + O$	1.2×10^{-10}	0	1.2×10^{-10}
$O(^1D) + H_2 \rightarrow OH + H$	1.1×10^{-10}	0	1.1×10^{-10}
$O(^1D) + H_2O \rightarrow OH + OH$	2.2×10^{-10}	0	2.2×10^{-10}
$O(^1D) + N_2 \rightarrow O + N_2$	1.8×10^{-11}	–110	2.6×10^{-11}
$O(^1D) + N_2O \rightarrow N_2 + O_2$	4.9×10^{-11}	0	4.9×10^{-11}
$\rightarrow NO + NO$	6.7×10^{-11}	0	6.7×10^{-11}
$O(^1D) + CH_4 \rightarrow$ products	1.5×10^{-10}	0	1.5×10^{-10}
$O(^1D) + CCl_4 \rightarrow$ products	3.3×10^{-10}	0	3.3×10^{-10}
$O(^1D) + CH_3Br \rightarrow$ products	1.8×10^{-10}	0	1.8×10^{-10}
$O(^1D) + CH_2Br_2 \rightarrow$ products	2.7×10^{-10}	0	2.7×10^{-10}
$O(^1D) + CHBr_3 \rightarrow$ products	6.6×10^{-10}	0	6.6×10^{-10}
$O(^1D) + CHClF_2 \rightarrow$ products	1.0×10^{-10}	0	1.0×10^{-10}
$O(^1D) + CCl_3F \rightarrow$ products	2.3×10^{-10}	0	2.3×10^{-10}
$O(^1D) + CCl_2F_2 \rightarrow$ products	1.4×10^{-10}	0	1.4×10^{-10}
$O + OH \rightarrow O_2 + H$	2.2×10^{-11}	–120	3.3×10^{-11}
$O + HO_2 \rightarrow OH + O_2$	3.0×10^{-11}	–200	5.9×10^{-11}
$H + O_3 \rightarrow OH + O_2$	1.4×10^{-10}	470	2.9×10^{-11}
$H + HO_2 \rightarrow$ products	8.1×10^{-11}	0	8.1×10^{-11}

[a] The rate constant (cm^3 $molecule^{-1}$ s^{-1}) is expressed by $k = A \exp(-E_a/RT)$, where A, the pre-exponential factor, is given in cm^3 $molecule^{-1}$ s^{-1}, and E_a/R (activation energy of the reaction divided by the gas constant) is given in Kelvin. The value of the rate constant k_{298} at 298 K is given in cm^3 $molecule^{-1}$ s^{-1}.

[b] Sander, S.P., R.R. Friedl, D.M. Golden, M.J. Kurylo, R.E. Huie, V.L. Orkin, G.K. Moortgat, A.R. Ravishankara, C.E. Kolb, M.J. Molina, and B.J. Finlayson-Pitts, *Chemical Kinetics and Photochemical Data for Use in Atmospheric Studies*, Evaluation No. 14, JPL Publication No. 02-25, Pasadena, Calif, USA, 2003.

Reaction	*A Factor*	E_a/R	k_{298}
$OH + O_3 \rightarrow HO_2 + O_2$	1.7×10^{-12}	940	7.3×10^{-14}
$OH + H_2 \rightarrow H_2O + H$	5.5×10^{-12}	2000	6.7×10^{-15}
$OH + OH \rightarrow H_2O + O$	4.2×10^{-12}	240	1.9×10^{-12}
$OH + HO_2 \rightarrow H_2O + O_2$	4.8×10^{-11}	–250	1.1×10^{-10}
$OH + H_2O_2 \rightarrow H_2O + HO_2$	2.9×10^{-12}	160	1.7×10^{-12}
$HO_2 + O_3 \rightarrow OH + 2O_2$	1.0×10^{-14}	490	1.9×10^{-15}
$HO_2 + HO_2 \rightarrow H_2O_2 + O_2$	2.3×10^{-13}	–600	1.7×10^{-12}
$\xrightarrow{M} H_2O_2 + O_2$	1.7×10^{-33} [M]	–1000	4.9×10^{-32} [M]
$O + NO_2 \rightarrow NO + O_2$	6.5×10^{-12}	–120	9.7×10^{-12}
$OH + HNO_3 \rightarrow H_2O + NO_3$	(see Note)		
$OH + HO_2NO_2 \rightarrow$ products	1.3×10^{-12}	–380	4.6×10^{-12}
$HO_2 + NO \rightarrow NO_2 + OH$	3.5×10^{-12}	–250	8.1×10^{-12}
$HO_2 + NO_3 \rightarrow$ products			3.5×10^{-12}
$N + O_2 \rightarrow NO + O$	1.5×10^{-11}	3600	8.5×10^{-17}
$N + NO \rightarrow N_2 + O$	2.1×10^{-11}	–100	3.0×10^{-11}
$N + NO_2 \rightarrow N_2O + O$	5.8×10^{-12}	–220	1.2×10^{-11}
$NO + O_3 \rightarrow NO_2 + O_2$	2.0×10^{-12}	1400	1.8×10^{-14}
$NO + NO_3 \rightarrow 2NO_2$	1.5×10^{-11}	–170	2.6×10^{-11}
$NO_2 + O_3 \rightarrow NO_3 + O_2$	1.2×10^{-13}	2450	3.2×10^{-17}
$OH + CO \rightarrow$ products	$1.5 \times 10^{-13} \times (1 + 0.6\ P_{\mathrm{atm}})$	0	$1.5 \times 10^{-13} \times (1 + 0.6\ P_{\mathrm{atm}})$
$OH + CH_4 \rightarrow CH_3 + H_2O$	2.45×10^{-12}	1775	6.3×10^{-15}
$OH + CH_2O \rightarrow H_2O + HCO$	1.0×10^{-11}	0	1.0×10^{-11}
$OH + CH_3OH \rightarrow$ products	6.7×10^{-12}	600	8.9×10^{-13}
$OH + CH_3OOH \rightarrow$ products	3.8×10^{-12}	–200	7.4×10^{-12}
$OH + HCN \rightarrow$ products	1.2×10^{-13}	400	3.1×10^{-14}
$OH + CH_3CN \rightarrow$ products	7.8×10^{-13}	1050	2.3×10^{-14}
$HO_2 + CH_3O_2 \rightarrow CH_3OOH + O_2$	3.8×10^{-13}	–800	5.6×10^{-12}
$NO_3 + CH_2O \rightarrow HCO + HNO_3$			6.8×10^{-16}
$HCO + O_2 \rightarrow CO + HO_2$	5.2×10^{-12}	0	5.2×10^{-12}
$CH_2OH + O_2 \rightarrow CH_2O + HO_2$			9.1×10^{-12}
$CH_3O + O_2 \rightarrow CH_2O + HO_2$	3.9×10^{-14}	900	1.9×10^{-15}
$CH_3O_2 + CH_3O_2 \rightarrow$ products	2.5×10^{-13}	–190	4.7×10^{-13}
$CH_3O_2 + NO \rightarrow CH_3O + NO_2$	2.8×10^{-12}	–300	7.7×10^{-12}
$O + FO \rightarrow F + O_2$	2.7×10^{-11}	0	2.7×10^{-11}
$F + O_3 \rightarrow FO + O_2$	2.2×10^{-11}	230	1.0×10^{-11}
$F + H_2 \rightarrow HF + H$	1.4×10^{-10}	500	2.6×10^{-11}
$F + H_2O \rightarrow HF + OH$	1.4×10^{-11}	0	1.4×10^{-11}
$F + CH_4 \rightarrow HF + CH_3$	1.6×10^{-10}	260	6.7×10^{-11}
$FO + NO \rightarrow NO_2 + F$	8.2×10^{-12}	–300	2.2×10^{-11}
$FO_2 + NO \rightarrow FNO + O_2$	7.5×10^{-12}	690	7.5×10^{-13}
$CF_3O + O_3 \rightarrow CF_3O_2 + O_2$	2×10^{-12}	1400	1.8×10^{-14}

Reaction	*A Factor*	E_a/R	k_{298}
$CF_3O + NO \rightarrow CF_2O + FNO$	3.7×10^{-11}	–110	5.4×10^{-11}
$CF_3O + CH_4 \rightarrow CF_3OH + CH_3$	2.6×10^{-12}	1420	2.2×10^{-14}
$CF_3O_2 + O_3 \rightarrow CF_3O + 2O_2$			$< 3 \times 10^{-15}$
$CF_3O_2 + NO \rightarrow CF_3O + NO_2$	5.4×10^{-12}	–320	1.6×10^{-11}
$OH + CF_3CH_2F$ (HFC-134a) $\rightarrow H_2O + CF_3CHF$	1.05×10^{-12}	1630	4.4×10^{-15}
$O + ClO \rightarrow Cl + O_2$	3.0×10^{-11}	–70	3.8×10^{-11}
$O + OClO \rightarrow ClO + O_2$	2.4×10^{-12}	960	1.0×10^{-13}
$O + HCl \rightarrow OH + Cl$	1.0×10^{-11}	3300	1.5×10^{-16}
$O + HOCl \rightarrow OH + ClO$	1.7×10^{-13}	0	1.7×10^{-13}
$O + ClONO_2 \rightarrow$ products	2.9×10^{-12}	800	2.0×10^{-13}
$OH + ClO \rightarrow Cl + HO_2$	7.4×10^{-12}	–270	1.8×10^{-11}
$\rightarrow HCl + O_2$	6.0×10^{-13}	–230	1.3×10^{-12}
$OH + OClO \rightarrow HOCl + O_2$	4.5×10^{-13}	–800	6.8×10^{-12}
$OH + HCl \rightarrow H_2O + Cl$	2.6×10^{-12}	350	8.0×10^{-13}
$OH + HOCl \rightarrow H_2O + ClO$	3.0×10^{-12}	500	5.0×10^{-13}
$OH + ClONO_2 \rightarrow$ products	1.2×10^{-12}	330	3.9×10^{-13}
$OH + CH_3Cl \rightarrow CH_2Cl + H_2O$	2.4×10^{-12}	1250	3.6×10^{-14}
$HO_2 + Cl \rightarrow HCl + O_2$	1.8×10^{-11}	–170	3.2×10^{-11}
$\rightarrow OH + ClO$	4.1×10^{-11}	450	9.1×10^{-12}
$HO_2 + ClO \rightarrow HOCl + O_2$	2.7×10^{-12}	–220	5.6×10^{-12}
$Cl + O_3 \rightarrow ClO + O_2$	2.9×10^{-11}	260	1.2×10^{-11}
$Cl + H_2 \rightarrow HCl + H$	3.7×10^{-11}	2300	1.6×10^{-14}
$Cl + H_2O_2 \rightarrow HCl + HO_2$	1.1×10^{-11}	980	4.1×10^{-13}
$Cl + CH_4 \rightarrow HCl + CH_3$	1.1×10^{-11}	1400	1.0×10^{-13}
$Cl + CH_2O \rightarrow HCl + HCO$	8.1×10^{-11}	30	7.3×10^{-11}
$Cl + OClO \rightarrow ClO + ClO$	3.4×10^{-11}	–160	5.8×10^{-11}
$ClO + NO \rightarrow NO_2 + Cl$	6.4×10^{-12}	–290	1.7×10^{-11}
$ClO + ClO \rightarrow Cl_2 + O_2$	1.0×10^{-12}	1590	4.8×10^{-15}
$\rightarrow ClOO + Cl$	3.0×10^{-11}	2450	8.0×10^{-15}
$\rightarrow OClO + Cl$	3.5×10^{-13}	1370	3.5×10^{-15}
$OH + CHF_2Cl$ (HCFC-22) $\rightarrow CF_2Cl + H_2O$	1.0×10^{-12}	1600	4.7×10^{-15}
$OH + CH_3CFCl_2$ (HCFC-141b) $\rightarrow CH_2CFCl_2 + H_2O$	1.25×10^{-12}	1600	5.8×10^{-15}
$OH + CH_3CF_2Cl$ (HCFC-142b) $\rightarrow CH_2CF_2Cl + H_2O$	1.3×10^{-12}	1770	3.4×10^{-15}
$O + BrO \rightarrow Br + O_2$	1.9×10^{-11}	–230	4.1×10^{-11}
$OH + HBr \rightarrow H_2O + Br$	1.1×10^{-11}	0	1.1×10^{-11}
$OH + CH_3Br \rightarrow CH_2Br + H_2O$	2.35×10^{-12}	1300	3.0×10^{-14}
$HO_2 + Br \rightarrow HBr + O_2$	1.5×10^{-11}	600	2.0×10^{-12}
$HO_2 + BrO \rightarrow$ products	3.4×10^{-12}	–540	2.1×10^{-11}

Reaction	*A Factor*	E_a/R	k_{298}
$Br + O_3 \rightarrow BrO + O_2$	1.7×10^{-11}	800	1.2×10^{-12}
$Br + H_2O_2 \rightarrow HBr + HO_2$	1.0×10^{-11}	>3000	$< 5 \times 10^{-16}$
$Br + CH_2O \rightarrow HBr + HCO$	1.7×10^{-11}	800	1.1×10^{-12}
$BrO + O_3 \rightarrow Br + 2O_2$	$\sim 1.0 \times 10^{-12}$	>3200	$< 2 \times 10^{-17}$
$BrO + NO \rightarrow NO_2 + Br$	8.8×10^{-12}	–260	2.1×10^{-11}
$BrO + ClO \rightarrow Br + OClO$	9.5×10^{-13}	–550	6.0×10^{-12}
$\rightarrow Br + ClOO$	2.3×10^{-12}	–260	5.5×10^{-12}
$\rightarrow BrCl + O_2$	4.1×10^{-13}	–290	1.1×10^{-12}
$BrO + BrO \rightarrow 2Br + O_2$	2.4×10^{-12}	–40	2.7×10^{-12}
$\rightarrow Br_2 + O_2$	2.8×10^{-14}	–860	5.0×10^{-13}
$OH + OCS \rightarrow$ products	1.1×10^{-13}	1200	1.9×10^{-15}
$S + O_2 \rightarrow SO + O$	2.3×10^{-12}	0	2.3×10^{-12}
$SO + O_2 \rightarrow SO_2 + O$	2.6×10^{-13}	2400	8.4×10^{-17}
$SO + O_3 \rightarrow SO_2 + O_2$	3.6×10^{-12}	1100	9.0×10^{-14}

Note: The rate coefficient for this reaction is a complex function of temperature and pressure and can be obtained as follows:

$$k(M, T) = k_0 + \frac{k_2 k_3 [M]}{k_2 + k_3 [M]}$$

$$\text{where } k_0 = 7.2 \times 10^{-15} \exp(785/T)$$
$$k_2 = 4.1 \times 10^{-16} \exp(1440/T)$$
$$k_3 = 1.9 \times 10^{-33} \exp(725/T)$$

Appendix 4

RATE COEFFICIENTS FOR GAS-PHASE ASSOCIATING REACTIONS [a,b]

Table A.4.1

Reaction	*Low-Pressure Limit*		*High-Pressure Limit*	
	k_0^{300}	n	k_0^{300}	m
$O + O_2 \overset{M}{\rightarrow} O_3$	6.0×10^{-34}	2.4		
$H + O_2 \overset{M}{\rightarrow} HO_2$	5.7×10^{-32}	1.6	7.5×10^{-11}	0
$OH + NO_2 \overset{M}{\rightarrow} HNO_3$	2.0×10^{-30}	3.0	2.5×10^{-11}	0
$HO_2 + NO_2 \overset{M}{\rightarrow} HO_2NO_2$	1.8×10^{-31}	3.2	4.7×10^{-12}	1.4
$NO_2 + NO_3 \overset{M}{\rightarrow} N_2O_5$	2.0×10^{-30}	4.4	1.4×10^{-12}	0.7
$CH_3 + O_2 \overset{M}{\rightarrow} CH_3O_2$	4.5×10^{-31}	3.0	1.8×10^{-12}	1.7
$FO + NO_2 \overset{M}{\rightarrow} FONO_2$	2.6×10^{-31}	1.3	2.0×10^{-11}	1.5
$ClO + NO_2 \overset{M}{\rightarrow} ClONO_2$	1.8×10^{-31}	3.4	1.5×10^{-11}	1.9
$ClO + ClO \overset{M}{\rightarrow} Cl_2O_2$	1.6×10^{-32}	4.5	2.0×10^{-12}	2.4
$BrO + NO_2 \overset{M}{\rightarrow} BrONO_2$	5.2×10^{-31}	3.2	6.9×10^{-12}	2.9
$OH + SO_2 \overset{M}{\rightarrow} HOSO_2$	3.0×10^{-31}	3.3	1.5×10^{-12}	0

[a] The rate constant (expressed in cm^3 $molecule^{-1}$ s^{-1}) is given by

$$k(M,T) = \left(\frac{k_0(T)[M]}{1 + k_0(T)[M]/k_\infty(T)} \right) 0.6^{\left\{1+[\log_{10}(k_0(T)[M]/k_\infty(T))]^2\right\}^{-1}}$$

where [M] is the air density (molecules cm^{-3}), and T is the temperature (kelvin). k_0 is expressed in cm^6 $molecule^{-2}$ s^{-1}, and k_∞ in cm^3 $molecule^{-1}$ s^{-1}. $k_0(T) = k_0^{300}(T/300)^{-n}$, $k_\infty(T) = k_\infty^{300}(T/300)^{-m}$.

[b] Sander, S.P., R.R. Friedl, D.M. Golden, M.J. Kurylo, R.E. Huie, V.L. Orkin, G.K. Moortgat, A.R. Ravishankara, C.E. Kolb, M.J. Molina, and B.J. Finlayson-Pitts, *Chemical Kinetics and Photochemical Data for Use in Atmospheric Studies*, Evaluation No. 14, JPL Publication No. 02-25, Pasadena, Calif, USA, 2003

Appendix 5

SURFACE REACTION PROBABILITY

Selected surface reaction probabilities (γ) for irreversible reactive uptake of trace gases on condensed surfaces.[a]

Table A.5.1

Reaction	*Surface Type*	*Temp. (K)*	γ	*Uncertainty Factor*
N_2O_5 (g) + H_2O				
$\rightarrow 2HNO_3$	H_2O (s)	188-195	0.02	2
	H_2O (l)	260-295	$\sim$0.05	2
	$HNO_3 \cdot 3H_2O$ (s)	200	4×10^{-4}	3
	$H_2SO_4 \cdot 4H_2O$ (s)	195-207	0.006	2
N_2O_5 (g) + HCl (s)				
$\rightarrow ClNO_2 + HNO_3$	H_2O/HCl (s)	190-220	0.03	
	$HNO_3 \cdot 3H_2O \cdot$ HCl (s)	200	0.003	2
HOCl (g) + HCl (s)				
$\rightarrow Cl_2 + H_2O$	$H_2O \cdot$ HCl (s)	195-200	0.2	2
	$HNO_3 \cdot 3H_2O \cdot$ HCl (s)	195-200	0.1	2
$ClONO_2$ (g) + H_2O (s)				
$\rightarrow$ HOCl + HNO_3	H_2O (s)	180-200	0.3	3
	$HNO_3 \cdot 3H_2O$ (s)	200	0.004	3
	$H_2SO_4 \cdot nH_2O$ (l)	200-265	see *Note 1*	
$ClONO_2$ (g) + HCl (s)				
$\rightarrow Cl_2 + HNO_3$	H_2O (s)	180-200	0.3	3
	$HNO_3 \cdot 3H_2O \cdot$ HCl (s)	185-210	0.2	2
$ClONO_2$ (g) + HBr (s)				
$\rightarrow$ BrCl + HNO_3	H_2O/HBr (s)	200	$>$0.3	
	$HNO_3 \cdot 3H_2O \cdot$ HBr (s)	200	$>$0.3	

[a] Adapted from Sander, S.P., R.R. Friedl, D.M. Golden, M.J. Kurylo, R.E. Huie, V.L. Orkin, G.K. Moortgat, A.R. Ravishankara, C.E. Kolb, M.J. Molina, and B.J. Finlayson-Pitts, *Chemical Kinetics and Photochemical Data for Use in Atmospheric Studies*, Evaluation No. 14, JPL Publication No. 02-25, Pasadena, Calif, USA, 2003.

Note 1: Values of γ are strongly dependent on the H_2SO_4 concentration of the droplet, increasing with decreasing [H_2SO_4].

Table A.5.2

Reaction	*Surface Type*	*Temp. (K)*	γ	*Uncertainty Factor*
HOBr (g) + HCl (s) → BrCl + H_2O	H_2O/HBr (s)	180-228	0.3	3
HOBr (g) + HBr (s) → Br_2 + H_2O	H_2O/HBr (s)	228	0.1	3
$BrONO_2$ (g) + H_2O → HOBr + HNO_3	H_2O (s)	190-200	>0.3	

Appendix 6

ATMOSPHERIC PROFILES

Appendix 6 presents numerical values for several atmospheric quantities as a function of the log-pressure altitude (km). All the variables are represented by zonally, latitudinally and annually averaged values derived from the SOCRATES model (Brasseur *et al.*, *J Geophys Res: 95*, 5639, 1990). The values listed in the Tables should be considered as approximate, and should be used only for crude estimates of physical and chemical parameters of the atmosphere.

The first Table provides an estimate of the geometric height z (km), the atmospheric pressure p (hPa), the absolute temperature T (K), the atmospheric scale height H (km) and the air number density n (cm^{-3}).

The subsequent Tables provide indicative values of the volume mixing ratio (left column) and number density (cm^{-3}, right column) for several chemical constituents of the atmosphere.

Table A.6.1.

log-$p_{alt.}$ *(km)*	*z* *(km)*	*Pressure* *(hPa)*	*Temperature* *(K)*	*H* *(km)*	*Air Dens* *(cm^{-3})*
0	0.0	1.013E+03	290.2	8.6	2.5E+19
5	6.0	4.959E+02	250.5	7.4	1.4E+19
10	11.2	2.428E+02	215.6	6.3	8.2E+18
15	15.7	1.188E+02	198.0	5.8	4.4E+18
20	20.3	5.818E+01	208.0	6.1	2.0E+18
25	25.1	2.848E+01	216.1	6.4	9.6E+17
30	30.1	1.394E+01	221.5	6.5	4.6E+17
35	35.2	6.826E+00	228.1	6.8	2.2E+17
40	40.5	3.341E+00	240.5	7.1	1.0E+17
45	46.2	1.636E+00	251.9	7.5	4.7E+16
50	51.9	8.008E−01	253.7	7.5	2.3E+16
55	57.7	3.920E−01	247.2	7.4	1.2E+16
60	63.2	1.919E−01	235.4	7.0	5.9E+15
65	68.4	9.395E−02	220.6	6.6	3.1E+15
70	73.2	4.599E−02	207.3	6.2	1.6E+15
75	77.8	2.251E−02	198.0	5.9	8.3E+14
80	82.3	1.102E−02	195.3	5.9	4.1E+14
85	86.8	5.396E−03	195.4	5.9	2.0E+14
90	91.3	2.641E−03	192.5	5.8	1.0E+14
95	95.7	1.293E−03	185.2	5.6	5.1E+13
100	99.8	6.330E−04	176.3	5.4	2.6E+13
105	104.0	3.099E−04	177.6	5.5	1.3E+13
110	108.4	1.517E−04	192.5	6.0	5.7E+12

Table A.6.2.a

$log{-}p_{\text{alt.}}$	CH_4		H_2O		CO		HCl		HBr		H_2	
0	1.7E−06	4.3E+13	1.7E−02	4.4E+17	7.5E−08	1.9E+12	1.3E−12	3.2E+07	3.7E−14	9.4E+05	2.7E−07	6.9E+12
5	1.7E−06	2.4E+13	1.2E−03	1.7E+16	5.8E−08	8.4E+11	1.5E−12	2.1E+07	1.9E−14	2.7E+05	2.7E−07	3.9E+12
10	1.7E−06	1.4E+13	3.6E−05	3.0E+14	5.5E−08	4.5E+11	3.2E−12	2.6E+07	2.0E−14	1.7E+05	2.7E−07	2.2E+12
15	1.7E−06	7.3E+12	3.4E−06	1.5E+13	4.6E−08	2.0E+11	5.9E−11	2.6E+08	1.0E−13	4.4E+05	2.7E−07	1.2E+12
20	1.5E−06	3.1E+12	2.1E−06	4.2E+12	2.3E−08	4.7E+10	9.7E−10	2.0E+09	3.1E−13	6.2E+05	3.0E−07	6.0E+11
25	1.4E−06	1.3E+12	2.6E−06	2.5E+12	1.7E−08	1.7E+10	1.3E−09	1.3E+09	3.0E−13	2.8E+05	3.3E−07	3.1E+11
30	1.1E−06	5.0E+11	3.4E−06	1.5E+12	2.2E−08	9.9E+09	1.7E−09	7.9E+08	2.4E−13	1.1E+05	3.6E−07	1.6E+11
35	7.6E−07	1.7E+11	4.1E−06	8.9E+11	2.2E−08	4.9E+09	2.4E−09	5.1E+08	2.4E−13	5.2E+04	3.7E−07	8.0E+10
40	4.4E−07	4.4E+10	4.8E−06	4.8E+11	2.6E−08	2.6E+09	2.6E−09	2.7E+08	2.4E−13	2.4E+04	3.6E−07	3.6E+10
45	2.2E−07	1.0E+10	5.2E−06	2.5E+11	4.8E−08	2.3E+09	2.9E−09	1.4E+08	3.1E−13	1.5E+04	3.3E−07	1.5E+10
50	1.2E−07	2.8E+09	5.4E−06	1.2E+11	8.7E−08	2.0E+09	3.3E−09	7.5E+07	3.5E−13	8.1E+03	3.4E−07	7.8E+09
55	1.0E−07	1.1E+09	5.3E−06	6.1E+10	1.7E−07	1.9E+09	3.4E−09	3.9E+07	3.0E−13	3.4E+03	4.1E−07	4.7E+09
60	9.3E−08	5.5E+08	5.2E−06	3.1E+10	3.1E−07	1.9E+09	3.5E−09	2.1E+07	2.6E−13	1.5E+03	5.1E−07	3.0E+09
65	8.5E−08	2.6E+08	5.0E−06	1.6E+10	5.4E−07	1.7E+09	3.5E−09	1.1E+07	2.5E−13	7.7E+02	6.9E−07	2.1E+09
70	5.9E−08	9.6E+07	4.6E−06	7.4E+09	1.1E−06	1.7E+09	3.5E−09	5.6E+06	2.5E−13	4.0E+02	1.1E−06	1.8E+09
75	2.8E−08	2.3E+07	3.6E−06	3.0E+09	2.2E−06	1.8E+09	3.5E−09	2.9E+06	2.4E−13	2.0E+02	2.0E−06	1.6E+09
80	1.1E−08	4.3E+06	2.3E−06	9.5E+08	4.3E−06	1.8E+09	3.5E−09	1.4E+06	2.0E−13	8.1E+01	2.9E−06	1.2E+09
85	4.0E−09	8.0E+05	1.1E−06	2.2E+08	7.2E−06	1.4E+09	3.0E−09	6.1E+05	2.8E−14	5.6E+00	3.3E−06	6.6E+08
90	1.7E−09	1.7E+05	5.0E−07	5.0E+07	9.9E−06	9.9E+08	2.3E−09	2.3E+05	4.9E−16	4.9E−02	3.3E−06	3.3E+08
95	9.2E−10	4.6E+04	2.7E−07	1.4E+07	1.2E−05	6.1E+08	1.8E−09	9.2E+04	2.0E−17	1.0E−03	3.3E−06	1.7E+08
100	5.7E−10	1.5E+04	1.7E−07	4.4E+06	1.4E−05	3.7E+08	1.5E−09	4.0E+04	1.9E−18	4.9E−05	3.3E−06	8.5E+07
105	2.6E−10	3.3E+03	7.6E−08	9.6E+05	2.0E−05	2.5E+08	1.1E−09	1.4E+04	0.0E+00	0.0E+00	3.1E−06	3.9E+07
110	7.6E−11	4.3E+02	1.8E−08	1.0E+05	4.2E−05	2.4E+08	3.8E−10	2.2E+03	0.0E+00	0.0E+00	2.8E−06	1.6E+07

Table A.6.2.b

log-$p_{\text{alt.}}$	CH_2O		CCl_4		*CFC-11*		*CFC-12*		CH_3CCl_3		CH_3Cl	
0	1.2E−10	3.1E+09	1.1E−10	2.7E+09	2.7E−10	6.8E+09	4.6E−10	1.2E+10	1.5E−10	3.8E+09	6.0E−10	1.5E+10
5	3.2E−11	.6E+08	1.1E−10	1.5E+09	2.7E−10	3.9E+09	4.6E−10	6.7E+09	1.5E−10	2.1E+09	5.8E−10	8.3E+09
10	1.0E−11	8.1E+07	1.1E−10	8.8E+08	2.7E−10	2.2E+09	4.6E−10	3.8E+09	1.5E−10	1.2E+09	5.8E−10	4.7E+09
15	4.8E−12	2.1E+07	1.0E−10	4.5E+08	2.6E−10	1.1E+09	4.5E−10	2.0E+09	1.4E−10	6.2E+08	5.6E−10	2.4E+09
20	9.9E−12	2.0E+07	6.3E−11	1.3E+08	1.7E−10	3.4E+08	3.9E−10	7.8E+08	8.6E−11	1.7E+08	4.6E−10	9.3E+08
25	2.4E−11	2.3E+07	1.3E−11	1.3E+07	5.3E−11	5.1E+07	2.8E−10	2.7E+08	1.8E−11	1.7E+07	3.2E−10	3.1E+08
30	5.6E−11	2.5E+07	1.1E−13	5.2E+04	1.8E−12	8.3E+05	1.4E−10	6.4E+07	2.1E−13	9.6E+04	1.7E−10	7.9E+07
35	8.7E−11	1.9E+07	6.2E−18	1.3E+00	1.2E−15	2.6E+02	2.9E−11	6.3E+06	2.7E−17	5.8E+00	5.0E−11	1.1E+07
40	9.1E−11	9.2E+06					1.8E−12	1.8E+05			6.0E−12	6.0E+05
45	6.2E−11	2.9E+06					5.2E−14	2.4E+03			3.3E−13	1.6E+04
50	3.6E−11	8.3E+05					1.5E−15	3.5E+01			2.2E−14	5.0E+02
55	2.7E−11	3.1E+05					8.5E−17	9.8E−01			4.0E−15	4.6E+01
60	2.1E−11	1.2E+05					7.8E−18	4.6E−02			1.4E−15	8.2E+00
65	1.2E−11	3.7E+04					1.1E−18	3.4E−03			6.4E−16	2.0E+00
70	3.9E−12	6.2E+03									3.3E−16	5.2E−01
75	1.1E−12	9.4E+02									1.7E−16	1.4E−01
80	3.5E−13	1.4E+02									9.3E−17	3.8E−02
85	7.6E−14	1.5E+01									5.4E−17	1.1E−02
90	1.8E−14	1.8E+00									3.5E−17	3.5E−03
95	8.8E−15	4.4E−01									2.5E−17	1.3E−03
100	8.6E−15	2.2E−01									2.0E−17	5.2E−04
105	5.8E−15	7.3E−02									1.3E−17	1.7E−04
110	7.4E−16	4.2E−03									6.7E−18	3.8E−05

Table A.6.2.c

log-$p_{alt.}$	HF		CH_3Br		O_3		$O(^3P)$		$O(^1D)$		H	
0	6.9E−13	1.8E+07	1.0E−11	2.6E+08	3.8E−08	9.5E+11	1.3E−16	3.2E+03				
5	9.8E−13	1.4E+07	9.9E−12	1.4E+08	4.8E−08	6.9E+11	2.9E−16	4.2E+03				
10	1.5E−12	1.2E+07	9.8E−12	8.0E+07	6.5E−08	5.3E+11	9.4E−16	7.7E+03				
15	8.0E−12	3.5E+07	9.3E−12	4.1E+07	2.1E−07	9.0E+11	8.4E−15	3.7E+04				
20	6.8E−11	1.4E+08	5.3E−12	1.1E+07	1.8E−06	3.6E+12	3.9E−13	7.9E+05				
25	1.6E−10	1.6E+08	7.9E−13	7.6E+05	5.2E−06	4.9E+12	6.1E−12	5.9E+06	3.0E−18	2.9E+00		
30	2.7E−10	1.3E+08	2.8E−15	1.3E+03	8.2E−06	3.8E+12	5.5E−11	2.5E+07	2.9E−17	1.3E+01	4.1E−18	1.9E+00
35	3.5E−10	7.6E+07			8.1E−06	1.8E+12	3.5E−10	7.6E+07	1.8E−16	4.0E+01	1.6E−16	3.5E+01
40	3.8E−10	3.9E+07			6.8E−06	6.9E+11	2.7E−09	2.7E+08	1.0E−15	1.0E+02	9.1E−15	9.2E+02
45	4.0E−10	1.9E+07			4.2E−06	2.0E+11	1.8E−08	8.6E+08	3.8E−15	1.8E+02	3.3E−13	1.5E+04
50	4.2E−10	9.5E+06			2.5E−06	5.7E+10	7.8E−08	1.8E+09	8.5E−15	1.9E+02	4.3E−12	9.9E+04
55	4.2E−10	4.8E+06			1.6E−06	1.9E+10	2.3E−07	2.6E+09	1.3E−14	1.5E+02	3.1E−11	3.6E+05
60	4.2E−10	2.5E+06			1.3E−06	7.6E+09	4.9E−07	2.9E+09	1.7E−14	9.8E+01	1.6E−10	9.7E+05
65	4.2E−10	1.3E+06			1.1E−06	3.5E+09	8.4E−07	2.6E+09	1.7E−14	5.2E+01	8.0E−10	2.5E+06
70	4.2E−10	6.8E+05			9.3E−07	1.5E+09	1.3E−06	2.1E+09	1.5E−14	2.4E+01	4.2E−09	6.8E+06
75	4.3E−10	3.5E+05			4.8E−07	4.0E+08	2.3E−06	1.9E+09	1.5E−14	1.3E+01	2.5E−08	2.1E+07
80	4.3E−10	1.8E+05			1.7E−07	6.9E+07	1.3E−05	5.2E+09	3.6E−14	1.5E+01	1.9E−07	7.9E+07
85	4.3E−10	8.6E+04			4.9E−07	9.9E+07	2.5E−04	5.0E+10	1.6E−13	3.3E+01	1.2E−06	2.4E+08
90	4.3E−10	4.3E+04			1.6E−06	1.6E+08	2.0E−03	2.0E+11	7.0E−13	7.0E+01	2.0E−06	2.0E+08
95	4.3E−10	2.2E+04			2.5E−06	1.3E+08	6.6E−03	3.4E+11	1.8E−12	8.9E+01	2.3E−06	1.2E+08
100	4.3E−10	1.1E+04			3.2E−06	8.3E+07	1.5E−02	4.0E+11	5.2E−12	1.4E+02	2.4E−06	6.3E+07
105	4.3E−10	5.5E+03			3.0E−06	3.8E+07	3.9E−02	4.9E+11	2.5E−11	3.2E+02	2.5E−06	3.2E+07
110	4.4E−10	2.5E+03			1.1E−06	6.5E+06	8.0E−02	4.6E+11	1.4E−10	7.8E+02	2.7E−06	1.6E+07

Table A.6.2.d

$log\text{-}p_{alt.}$	OH		HO_2		H_2O_2		Cl		ClO		$HOCl$	
0	1.2E−13	3.0E+06	5.6E−12	1.4E+08	7.8E−11	2.0E+09	1.6E−17	4.0E+02	1.0E−14	2.6E+05	1.7E−13	4.2E+06
5	7.0E−14	1.0E+06	3.4E−12	4.9E+07	2.8E−11	4.0E+08	1.1E−17	1.6E+02	1.2E−14	1.7E+05	8.5E−14	1.2E+06
10	7.0E−14	5.7E+05	1.0E−12	8.3E+06	2.6E−12	2.1E+07	4.0E−17	3.2E+02	6.0E−14	4.9E+05	7.6E−14	6.2E+05
15	9.6E−14	4.2E+05	5.3E−13	2.3E+06	1.4E−12	6.2E+06	1.9E−16	8.3E+02	1.3E−12	5.7E+06	6.9E−13	3.0E+06
20	1.8E−13	3.7E+05	1.5E−12	2.9E+06	1.2E−11	2.4E+07	4.0E−15	8.2E+03	1.7E−11	3.5E+07	8.6E−12	1.7E+07
25	6.9E−13	6.6E+05	6.0E−12	5.7E+06	6.2E−11	5.9E+07	1.5E−14	1.4E+04	6.4E−11	6.2E+07	5.1E−11	4.9E+07
30	3.4E−12	1.6E+06	1.6E−11	7.5E+06	1.2E−10	5.7E+07	8.5E−14	3.9E+04	1.1E−10	5.0E+07	8.8E−11	4.0E+07
35	1.7E−11	3.7E+06	3.2E−11	6.9E+06	1.0E−10	2.2E+07	5.1E−13	1.1E+05	2.2E−10	4.8E+07	1.4E−10	3.0E+07
40	6.7E−11	6.8E+06	5.8E−11	5.9E+06	7.8E−11	7.9E+06	2.1E−12	2.2E+05	4.3E−10	4.4E+07	1.8E−10	1.8E+07
45	1.8E−10	8.5E+06	1.0E−10	4.9E+06	6.2E−11	2.9E+06	1.1E−11	5.1E+05	4.6E−10	2.2E+07	1.4E−10	6.7E+06
50	3.0E−10	6.8E+06	1.7E−10	4.0E+06	5.9E−11	1.4E+06	3.2E−11	7.2E+05	2.3E−10	5.2E+06	7.4E−11	1.7E+06
55	4.0E−10	4.6E+06	2.4E−10	2.7E+06	5.3E−11	6.2E+05	4.9E−11	5.6E+05	1.1E−10	1.2E+06	3.4E−11	3.9E+05
60	5.5E−10	3.2E+06	3.2E−10	1.9E+06	5.4E−11	3.2E+05	6.0E−11	3.5E+05	7.4E−11	4.4E+05	2.3E−11	1.4E+05
65	9.1E−10	2.8E+06	4.9E−10	1.5E+06	8.2E−11	2.5E+05	6.7E−11	2.1E+05	7.1E−11	2.2E+05	1.9E−11	5.7E+04
70	2.0E−09	3.2E+06	9.4E−10	1.5E+06	2.2E−10	3.6E+05	7.1E−11	1.2E+05	7.2E−11	1.2E+05	1.5E−11	2.4E+04
75	4.1E−09	3.4E+06	1.8E−09	1.5E+06	5.3E−10	4.4E+05	8.7E−11	7.2E+04	5.5E−11	4.6E+04	1.1E−11	9.3E+03
80	7.5E−09	3.1E+06	3.0E−09	1.2E+06	9.2E−10	3.8E+05	1.6E−10	6.5E+04	1.0E−11	4.3E+03	4.0E−12	1.6E+03
85	2.4E−09	4.9E+05	6.3E−10	1.3E+05	1.1E−10	2.1E+04	6.5E−10	1.3E+05	3.3E−13	6.7E+01	1.5E−14	3.0E+00
90	5.9E−10	5.9E+04	4.0E−11	4.0E+03	3.6E−12	3.6E+02	1.4E−09	1.4E+05	2.1E−13	2.1E+01	7.7E−17	7.7E−03
95	2.6E−10	1.3E+04	6.5E−12	3.3E+02	3.5E−13	1.8E+01	1.9E−09	9.4E+04	1.2E−13	6.2E+00	2.4E−18	1.2E−04
100	1.3E−10	3.4E+03	1.6E−12	4.0E+01	6.9E−14	1.8E+00	2.1E−09	5.6E+04	7.3E−14	1.9E+00		
105	4.8E−11	6.0E+02	2.3E−13	2.9E+00	8.8E−15	1.1E−01	2.6E−09	3.3E+04	3.2E−14	4.0E−01		
110	1.1E−11	6.5E+01	3.7E−14	2.1E−01	2.2E−16	1.3E−03	3.3E−09	1.9E+04	8.0E−15	4.6E−02		

Table A.6.2.e

$log\text{-}p_{alt.}$	$ClONO_2$		N		NO		NO_2		NO_3		HNO_3	
0	1.3E−12	3.3E+07			1.2E−10	3.1E+09	3.5E−10	8.8E+09	1.3E−11	3.2E+08	1.5E−11	3.8E+08
5	4.0E−13	5.7E+06			1.5E−11	2.2E+08	4.8E−11	6.9E+08	4.0E−13	5.7E+06	1.0E−11	1.5E+08
10	5.0E−13	4.1E+06			4.5E−11	3.7E+08	5.9E−11	4.8E+08	3.0E−14	2.5E+05	2.3E−10	1.9E+09
15	5.9E−12	2.6E+07			6.7E−11	2.9E+08	7.6E−11	3.3E+08	3.5E−14	1.5E+05	3.1E−10	1.3E+09
20	2.2E−10	4.4E+08			9.1E−11	1.8E+08	2.0E−10	4.0E+08	6.5E−13	1.3E+06	2.7E−09	5.5E+09
25	7.3E−10	7.0E+08			2.4E−10	2.3E+08	7.2E−10	6.9E+08	3.9E−12	3.7E+06	4.8E−09	4.6E+09
30	9.8E−10	4.5E+08	1.8E−17	8.3E+00	1.1E−09	5.1E+08	3.3E−09	1.5E+09	1.3E−11	6.0E+06	4.9E−09	2.3E+09
35	6.2E−10	1.4E+08	6.7E−16	1.5E+02	3.5E−09	7.6E+08	7.6E−09	1.7E+09	2.8E−11	6.1E+06	2.6E−09	5.8E+08
40	2.4E−10	2.4E+07	4.6E−15	4.7E+02	5.1E−09	5.1E+08	7.3E−09	7.4E+08	6.3E−11	6.4E+06	5.6E−10	5.7E+07
45	4.1E−11	2.0E+06	1.3E−14	6.1E+02	4.6E−09	2.1E+08	5.1E−09	2.4E+08	6.8E−11	3.2E+06	5.3E−11	2.5E+06
50	4.0E−12	9.3E+04	3.5E−14	8.1E+02	3.3E−09	7.6E+07	4.2E−09	9.6E+07	1.9E−11	4.4E+05	6.8E−12	1.6E+05
55	9.8E−13	1.1E+04	1.2E−13	1.3E+03	2.4E−09	2.8E+07	4.1E−09	4.7E+07	3.6E−12	4.1E+04	2.4E−12	2.8E+04
60	5.6E−13	3.3E+03	4.2E−13	2.5E+03	2.8E−09	1.6E+07	4.2E−09	2.5E+07	2.6E−12	1.6E+04	2.2E−12	1.3E+04
65	3.6E−13	1.1E+03	1.6E−12	4.9E+03	5.0E−09	1.5E+07	5.7E−09	1.8E+07	7.0E−13	2.2E+03	3.8E−12	1.2E+04
70	8.2E−14	1.3E+02	5.8E−12	9.4E+03	1.2E−08	1.9E+07	7.1E−09	1.1E+07	7.0E−14	1.1E+02	5.6E−12	9.1E+03
75	4.5E−15	3.8E+00	3.6E−11	3.0E+04	2.6E−08	2.2E+07	3.1E−09	2.6E+06	3.9E−14	3.2E+01	3.6E−12	3.0E+03
80	6.9E−17	2.8E−02	1.2E−10	5.1E+04	4.9E−08	2.0E+07	2.6E−10	1.1E+05	3.8E−14	1.6E+01	7.0E−13	2.9E+02
85			3.1E−10	6.1E+04	9.3E−08	1.9E+07	2.1E−11	4.3E+03	5.6E−15	1.1E+00	1.1E−13	2.1E+01
90			6.8E−10	6.8E+04	2.0E−07	2.0E+07	2.3E−11	2.3E+03	3.9E−15	3.9E−01	3.9E−14	3.9E+00
95			1.4E−09	7.0E+04	4.8E−07	2.4E+07	3.2E−11	1.6E+03	3.3E−15	1.7E−01	2.4E−14	1.2E+00
100			2.6E−09	6.9E+04	1.3E−06	3.3E+07	4.7E−11	1.2E+03	2.9E−15	7.5E−02	1.9E−14	5.0E−01
105			5.7E−09	7.1E+04	4.7E−06	5.9E+07	8.5E−11	1.1E+03	2.6E−15	3.3E−02	1.4E−14	1.8E−01
110			1.4E−08	7.7E+04	1.4E−05	8.2E+07	1.1E−10	6.3E+02	1.4E−15	7.9E−03	8.6E−15	4.9E−02

Table A.6.2.f

$log\text{-}p_{alt.}$	N_2O_5		HO_2NO_2		Br		BrO		$HOBr$		$BrONO_2$	
0	1.2E−11	3.1E+08	3.6E−13	9.0E+06	9.1E−16	2.3E+04	1.3E−14	3.4E+05	6.6E−14	1.7E+06	1.7E−13	4.3E+06
5	2.3E−11	3.4E+08	9.5E−12	1.4E+08	3.2E−15	4.6E+04	3.0E−14	4.3E+05	6.2E−14	8.8E+05	1.2E−13	1.7E+06
10	1.5E−11	1.2E+08	2.4E−11	2.0E+08	2.0E−14	1.6E+05	6.3E−14	5.1E+05	3.0E−14	2.5E+05	1.6E−13	1.3E+06
15	2.7E−12	1.2E+07	1.5E−11	6.7E+07	6.9E−14	3.0E+05	2.6E−13	1.1E+06	4.3E−14	1.9E+05	4.7E−13	2.0E+06
20	3.6E−11	7.3E+07	7.0E−11	1.4E+08	9.9E−14	2.0E+05	1.7E−12	3.4E+06	4.1E−13	8.3E+05	3.0E−12	6.1E+06
25	2.2E−10	2.1E+08	1.7E−10	1.6E+08	9.9E−14	9.4E+04	3.1E−12	2.9E+06	1.2E−12	1.1E+06	5.2E−12	5.0E+06
30	9.9E−10	4.5E+08	2.0E−10	9.3E+07	1.5E−13	7.0E+04	3.1E−12	1.4E+06	1.3E−12	6.1E+05	5.4E−12	2.5E+06
35	1.1E−09	2.5E+08	7.2E−11	1.6E+07	3.9E−13	8.4E+04	3.3E−12	7.3E+05	1.6E−12	3.4E+05	4.0E−12	8.6E+05
40	5.3E−10	5.4E+07	1.3E−11	1.4E+06	8.8E−13	8.9E+04	3.6E−12	3.6E+05	2.3E−12	2.3E+05	1.9E−12	1.9E+05
45	1.8E−10	8.5E+06	3.5E−12	1.6E+05	2.3E−12	1.1E+05	2.8E−12	1.3E+05	3.1E−12	1.5E+05	4.7E−13	2.2E+04
50	1.1E−10	2.6E+06	1.4E−12	3.2E+04	4.0E−12	9.2E+04	1.7E−12	3.8E+04	3.5E−12	8.0E+04	1.1E−13	2.5E+03
55	5.0E−11	5.7E+05	5.9E−13	6.8E+03	4.8E−12	5.5E+04	1.7E−12	1.9E+04	3.2E−12	3.7E+04	4.0E−14	4.7E+02
60	9.9E−12	5.9E+04	2.8E−13	1.7E+03	5.2E−12	3.1E+04	2.2E−12	1.3E+04	2.8E−12	1.7E+04	2.7E−14	1.6E+02
65	6.2E−13	1.9E+03	1.4E−13	4.4E+02	5.6E−12	1.7E+04	2.7E−12	8.4E+03	2.3E−12	7.0E+03	2.1E−14	6.4E+01
70	9.2E−15	1.5E+01	3.7E−14	6.0E+01	6.8E−12	1.1E+04	2.5E−12	4.1E+03	1.4E−12	2.3E+03	3.3E−15	5.4E+00
75	3.2E−16	2.6E−01	5.9E−15	4.9E+00	9.4E−12	7.8E+03	1.1E−12	8.8E+02	5.0E−13	4.1E+02	1.8E−16	1.5E−01
80	3.1E−17	1.3E−02	8.2E−16	3.4E−01	1.1E−11	4.5E+03	4.4E−14	1.8E+01	5.4E−14	2.2E+01	1.4E−17	5.8E−03
85	5.5E−18	1.1E−03	6.3E−17	1.3E−02	1.1E−11	2.3E+03	2.3E−16	4.6E−02	1.0E−15	2.0E−01	2.6E−18	5.3E−04
90	1.9E−18	1.9E−04	1.8E−17	1.8E−03	1.2E−11	1.2E+03	4.5E−17	4.4E−03	2.4E−16	2.4E−02		
95	1.1E−18	5.3E−05	1.1E−17	5.4E−04	1.2E−11	5.9E+02	1.7E−17	8.7E−04	1.6E−16	7.9E−03		
100			8.5E−18	2.2E−04	1.2E−11	3.1E+02	7.5E−18	1.9E−04	1.3E−16	3.5E−03		
105			6.9E−18	8.8E−05	1.2E−11	1.5E+02	2.7E−18	3.4E−05	1.2E−16	1.5E−03		
110			5.7E−18	3.2E−05	1.2E−11	6.8E+01			9.4E−17	5.4E−04		

Table A.6.2.g

$log\text{-}p_{alt.}$	$BrCl$		CH_3O_2		O_2		$ClOx$		Cly		Bry	
0	3.5E−18	8.9E+01	5.4E−12	1.4E+08	2.1E−01	5.3E+18	1.8E−13	4.6E+06	2.8E−12	7.0E+07	2.9E−13	7.2E+06
5	6.9E−18	9.9E+01	2.3E−12	3.3E+07	2.1E−01	3.0E+18	1.0E−13	1.5E+06	2.0E−12	2.8E+07	2.3E−13	3.3E+06
10	2.4E−16	2.0E+03	2.4E−13	2.0E+06	2.1E−01	1.7E+18	3.0E−13	2.5E+06	4.1E−12	3.3E+07	2.9E−13	2.4E+06
15	2.9E−14	1.3E+05	1.7E−13	7.5E+05	2.1E−01	9.1E+17	4.8E−12	2.1E+07	7.0E−11	3.1E+08	9.7E−13	4.2E+06
20	1.7E−13	3.4E+05	4.4E−13	8.8E+05	2.1E−01	4.3E+17	4.7E−11	9.5E+07	1.2E−09	2.5E+09	5.7E−12	1.2E+07
25	3.3E−13	3.2E+05	6.8E−13	6.5E+05	2.1E−01	2.0E+17	1.5E−10	1.5E+08	2.2E−09	2.1E+09	1.0E−11	9.7E+06
30	1.8E−13	8.3E+04	7.7E−13	3.5E+05	2.1E−01	9.6E+16	2.3E−10	1.1E+08	3.0E−09	1.4E+09	1.0E−11	4.7E+06
35	3.2E−13	7.0E+04	1.0E−12	2.3E+05	2.1E−01	4.6E+16	3.7E−10	8.1E+07	3.4E−09	7.3E+08	9.8E−12	2.1E+06
40	8.2E−13	8.3E+04	2.3E−12	2.3E+05	2.1E−01	2.1E+16	6.2E−10	6.3E+07	3.5E−09	3.5E+08	9.7E−12	9.8E+05
45	7.1E−13	3.3E+04	5.2E−12	2.4E+05	2.1E−01	9.9E+15	6.2E−10	2.9E+07	3.6E−09	1.7E+08	9.7E−12	4.6E+05
50	2.6E−13	6.0E+03	9.0E−12	2.1E+05	2.1E−01	4.8E+15	3.4E−10	7.7E+06	3.6E−09	8.2E+07	9.9E−12	2.3E+05
55	1.1E−13	1.3E+03	1.5E−11	1.7E+05	2.1E−01	2.4E+15	1.9E−10	2.2E+06	3.6E−09	4.2E+07	1.0E−11	1.2E+05
60	7.4E−14	4.3E+02	2.2E−11	1.3E+05	2.1E−01	1.2E+15	1.6E−10	9.3E+05	3.6E−09	2.1E+07	1.1E−11	6.2E+04
65	5.1E−14	1.6E+02	2.5E−11	7.7E+04	2.1E−01	6.5E+14	1.6E−10	4.8E+05	3.6E−09	1.1E+07	1.1E−11	3.4E+04
70	2.3E−14	3.7E+01	1.1E−11	1.8E+04	2.1E−01	3.4E+14	1.6E−10	2.6E+05	3.7E−09	5.9E+06	1.1E−11	1.8E+04
75	3.6E−15	2.9E+00	2.4E−12	2.0E+03	2.1E−01	1.7E+14	1.5E−10	1.3E+05	3.7E−09	3.0E+06	1.1E−11	9.3E+03
80	8.6E−17	3.6E−02	7.1E−13	2.9E+02	2.1E−01	8.6E+13	1.7E−10	7.1E+04	3.7E−09	1.5E+06	1.1E−11	4.7E+03
85	9.6E−18	1.9E−03	4.5E−13	9.0E+01	2.1E−01	4.2E+13	6.5E−10	1.3E+05	3.7E−09	7.4E+05	1.1E−11	2.3E+03
90	3.7E−18	3.7E−04	2.6E−13	2.6E+01	2.1E−01	2.0E+13	1.4E−09	1.4E+05	3.7E−09	3.7E+05	1.2E−11	1.2E+03
95	2.5E−18	1.3E−04	9.6E−14	4.9E+00	2.0E−01	1.0E+13	1.9E−09	9.4E+04	3.7E−09	1.9E+05	1.2E−11	5.9E+02
100	2.3E−18	5.9E−05	4.7E−14	1.2E+00	1.9E−01	5.0E+12	2.1E−09	5.6E+04	3.7E−09	9.6E+04	1.2E−11	3.1E+02
105	2.1E−18	2.6E−05	1.9E−14	2.5E−01	1.7E−01	2.2E+12	2.6E−09	3.3E+04	3.7E−09	4.7E+04	1.2E−11	1.5E+02
110	1.6E−18	9.0E−06	3.0E−15	1.7E−02	1.4E−01	7.7E+11	3.3E−09	1.9E+04	3.7E−09	2.1E+04	1.2E−11	6.8E+01

Table A.6.2.h

log-$p_{\text{alt.}}$	*NOx*		*NOy*		*HOx*	
0	4.7E−10	1.2E+10	5.2E−10	1.3E+10	5.7E−12	1.5E+08
5	6.3E−11	9.1E+08	1.3E−10	1.9E+09	3.5E−12	5.0E+07
10	1.0E−10	8.5E+08	3.9E−10	3.2E+09	1.1E−12	8.9E+06
15	1.4E−10	6.2E+08	4.8E−10	2.1E+09	6.3E−13	2.7E+06
20	2.9E−10	5.9E+08	3.4E−09	6.8E+09	1.6E−12	3.3E+06
25	9.6E−10	9.1E+08	7.1E−09	6.8E+09	6.7E−12	6.4E+06
30	4.4E−09	2.0E+09	1.3E−08	5.7E+09	2.0E−11	9.0E+06
35	1.1E−08	2.4E+09	1.7E−08	3.6E+09	4.9E−11	1.1E+07
40	1.2E−08	1.3E+09	1.4E−08	1.5E+09	1.3E−10	1.3E+07
45	9.6E−09	4.5E+08	1.0E−08	4.8E+08	2.8E−10	1.3E+07
50	7.5E−09	1.7E+08	7.8E−09	1.8E+08	4.8E−10	1.1E+07
55	6.5E−09	7.4E+07	6.6E−09	7.6E+07	6.7E−10	7.7E+06
60	6.9E−09	4.1E+07	6.9E−09	4.1E+07	1.0E−09	6.1E+06
65	1.1E−08	3.3E+07	1.1E−08	3.3E+07	2.2E−09	6.8E+06
70	1.9E−08	3.0E+07	1.9E−08	3.0E+07	7.1E−09	1.2E+07
75	2.9E−08	2.4E+07	3.0E−08	2.4E+07	3.1E−08	2.6E+07
80	5.0E−08	2.0E+07	5.0E−08	2.0E+07	2.0E−07	8.3E+07
85	9.3E−08	1.9E+07	9.3E−08	1.9E+07	1.2E−06	2.4E+08
90	2.0E−07	2.0E+07	2.0E−07	2.0E+07	2.0E−06	2.0E+08
95	4.8E−07	2.4E+07	4.8E−07	2.4E+07	2.3E−06	1.2E+08
100	1.3E−06	3.3E+07	1.3E−06	3.3E+07	2.4E−06	6.3E+07
105	4.7E−06	5.9E+07	4.7E−06	5.9E+07	2.5E−06	3.2E+07
110	1.4E−05	8.2E+07	1.4E−05	8.2E+07	2.7E−06	1.6E+07

FIGURE ACKNOWLEDGEMENTS

Academic Press: Figures 4.12, 4.23, 5.24a, 7.1, 7.6

American Association for the Advancement of Science: Figures 5.22, 5.30

American Geophysical Union: Figures 2.10, 3.4, 3.6, 3.7, 3.11, 3.12, 3.15a,b,c, 3.18, 3.24, 3.25, 3.27, 3.29, 3.32, 3.35, 4.8b, 4.9, 4.18, 4.25, 4.26, 4.27, 4.28, 4.29, 4.42, 5.4, 5.11, 5.13, 5.16, 5.19, 5.20, 5.21, 5.29, 5.40, 5.44, 5.45, 5.47b,c, 5.56, 5.60, 5.65, 5.66, 5.67, 6.2, 6.3, 6.5, 6.9, 6.10, 6.11, 6.12, 6.13, 6.14, 6.17, 6.18, 6.21, 6.22, 6.23, 7.11, 7.13, 7.15, 7.18, 7.25, 7.31. Plate 3.

American Institute of Physics: Figures 4.32, 4.33, 4.36

American Meteorological Society: Figures 3.21, 3.23, 3.31, 3.38, 4.19a, 5.33a, 5.62, 5.63

Birkhäuser Verlag: Figure 3.22

Clarendon Press: Figures 5.5, 5.8

Committee for Space Research (COSPAR): Figure 7.28

Elsevier: Figures 4.15, 4.16, 4.17, 4.31, 4.41, 4.44, 5.34, 5.35, 7.3, 7.8, 7.9, 7.26, 7.32, 7.34, 7.36

European Geophysical Union: Figures 4.32, 7.19, 7.20. Plate 6.

European Space Agency (ESA): Figure 7.24

Federal Aviation Administration (FAA): Figures 3.3, 3.19, 5.7, 5.15, 5.25

Federal Institute of Technology, Zürich, Switzerland: Figures 3.7, 3.9

International Global Atmospheric Chemistry Project (IGAC) of the International Geosphere Biosphere Programme (IGBP): Figure 5.70

National Center for Atmospheric Research (NCAR): Figure 4.22

National Center for Environmental Prediction (NCEP): Figure 6.19

National Research Council of Canada: Figure 5.41

National Space and Aeronautics Administration (NASA): Figures 2.5, 3.2, 3.5, 3.17, 4.20, 5.6, 5.47a, 7.7. Plates 2, 4, 5, 9, 12, 15.

Nature Publishing Group: Figure 3.28

Nonprofit Publisher of *Annual Review of* Series: Figures 2.6, 4.6, 4.10

Ohio Academy of Sciences: Figure 4.21

Plenum Press: Figures 7.21, 7.23, 7.27, 7.30

Princeton University Press: Figure 5.53

Rand Corporation: Figure 2.8

Springer Verlag including Kluwer and Reidel, Publishing Companies: Figures 3.20, 3.37, 4.2, 4.8a, 5.1, 5.2, 5.26a, 5.36, 5.49, 5.52, 5.68, 7.5, 7.10

University of Bern: Figures 7.4, 7.12, 7.17, 7.22, 7.28, 7.29, 7.35

University of Chicago Press: Figure 4.7

University of Colorado: Figure 7.33

University of Wyoming: Figure 5.64

Van Nostrand Publishing Company: Figure 2.1b

World Meteorological Organization (WMO): Figure 3.30

World Scientific: Figure 4.13a

COLOR SECTION

Plate 1. *Aurora photographed on 30 March 2001 at 51°N and 119°W (British Columbia, Canada). Variations in the color arise from the variation in the spectra of the incoming particles. These energetic particles originate from the Sun and are accelerated in the magnetosphere. Green and red light is produced by radiative emissions associated with electronic transitions of atomic oxygen.*
Photo by James W. Hannigan, National Center for Atmospheric Research, Boulder, Colorado.

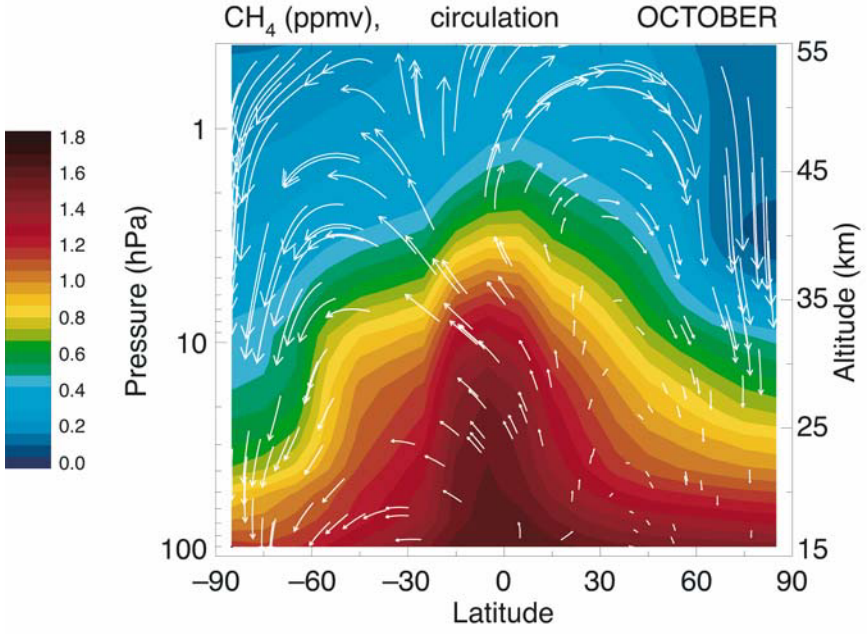

Plate 2. *Zonally averaged methane (CH_4) mixing ratio (ppmv) and the Brewer-Dobson circulation (shown by the arrows) in the middle atmosphere (15-55 km altitude) during October. Methane is released at the Earth surface and is destroyed by chemical reaction with the OH radical, while transported in the troposphere and the stratosphere. The ascending branch of the Brewer-Dobson circulation carries high-methane air from the tropical troposphere into the stratosphere, while the descending branch carries air masses with low methane mixing ratios from the upper stratosphere and mesosphere to the polar troposphere. From NASA/GSFC.*

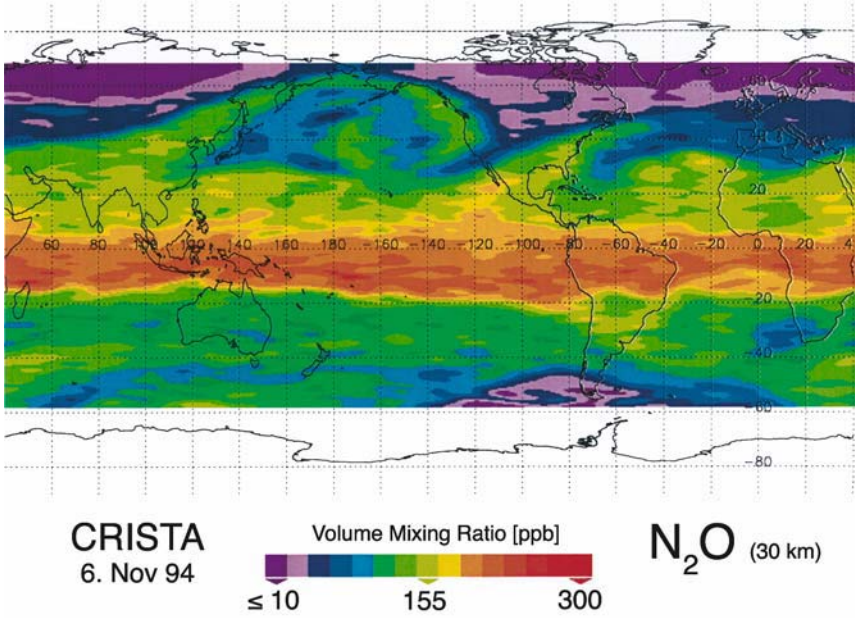

Plate 3. *Distribution of the nitrous oxide (N_2O) mixing ratio (ppbv) on the 10 hPa pressure level or approximately 30 km altitude as measured on November 6, 1994 by the CRISTA instrument on board the Space Shuttle. The data were interpolated by a Kalman filter. N_2O can be regarded as a tracer of dynamical motions: for example a tongue of Arctic air extrudes from the North polar vortex across the United States towards the Pacific Ocean. At the same time a "streamer" of N_2O rich air extends from the tropics across eastern Asia towards the Aleutian Islands and the west cost of Canada and the United States. Another "streamer" propagates along the eastern cost of the North America towards Europe. From Offermann et al., J. Geophys. Res., 104, 16311, 1999.*

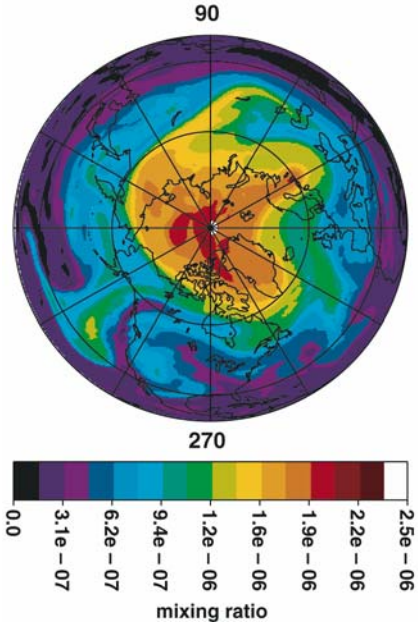

Plate 4. *Ozone volume mixing ratio on the 417 K isentropic surface (approximately 16 km altitude) on 31 December 1991. Filaments of ozone-rich air pulled from the polar region are irreversibly mixed into the mid-latitude surf zone. The net effect is to weaken the latitudinal ozone gradient created by the Brewer-Dobon circulation. From NASA.*

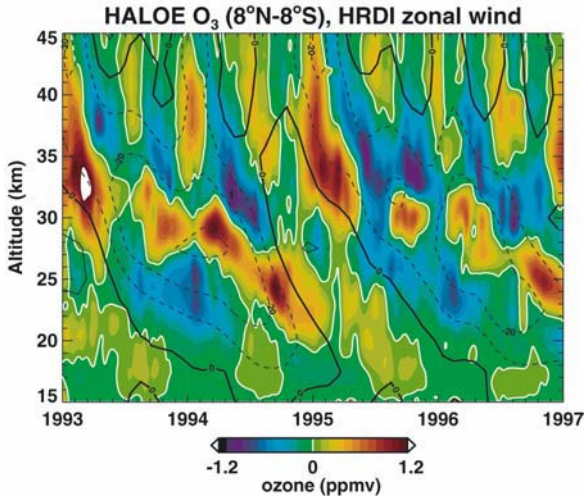

Plate 5. *Ozone anomalies (ppmv) versus altitude (km) and time (years) in the equatorial region (4ºN-4ºS) derived from observations made by the HALOE instrument on board the Upper Altitude Research Satellite (UARS). Superimposed on ozone values are the zonal winds measured by the HRDI instrument on the same satellite. Full lines are eastward winds and dashed lines westward winds with intervals corresponding to 10 m/s. In the 20-30 km altitude range, the positive ozone anomalies are associated with the westerly shear in the quasi-biennal oscillation (QBO), while the negative anomalies are indicative of easterly shears. Above 30 km, ozone variability is associated with temperature variability, which affects the photochemical source terms. Above 35 km, the observed variations are due to temperature effects associated with the QBO and to the semi-annual oscillation. Courtesy of Paul Newman, NASA/GSFC.*

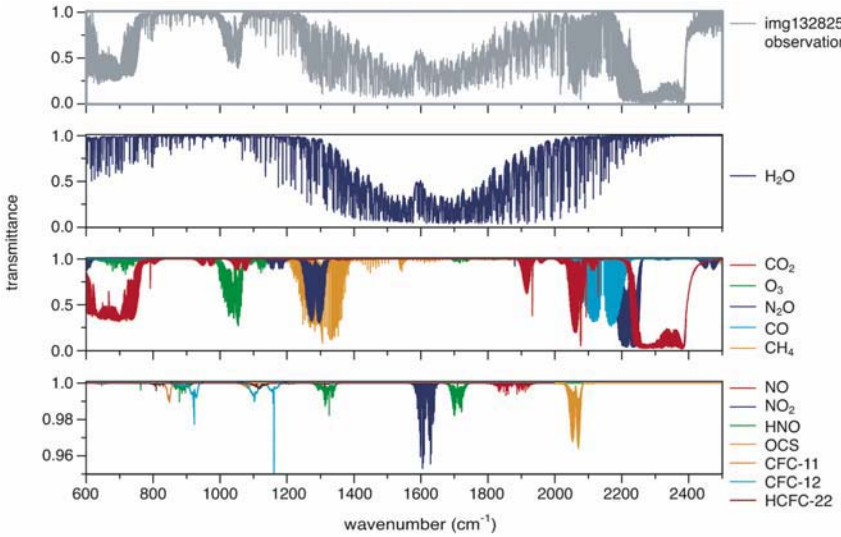

Plate 6. *Atmospheric transmittance in the infrared (600-2500 cm^{-1} or 4-17 μm) observed on 4 April, 1997 over the South Pacific by the Interferometric Monitor for Greenhouse Gases (IMG) on board the Advanced Earth Observing Satellite (ADEOS) (upper panel). The three lower panels show the contributions of water, other strong absorbers (CO_2, O_3, N_2O, CO, CH_4), and weak absorbers (NO, NO_2, OCS, HNO_3, CFC-11 and HCFC-22). Adapted from C. Clerbaux, J. Hadji-Lazaro, S. Turquety, G. Megie, and P.-F. Coheur, Atmos. Chem. Phys., 3, 1495, 2003.*

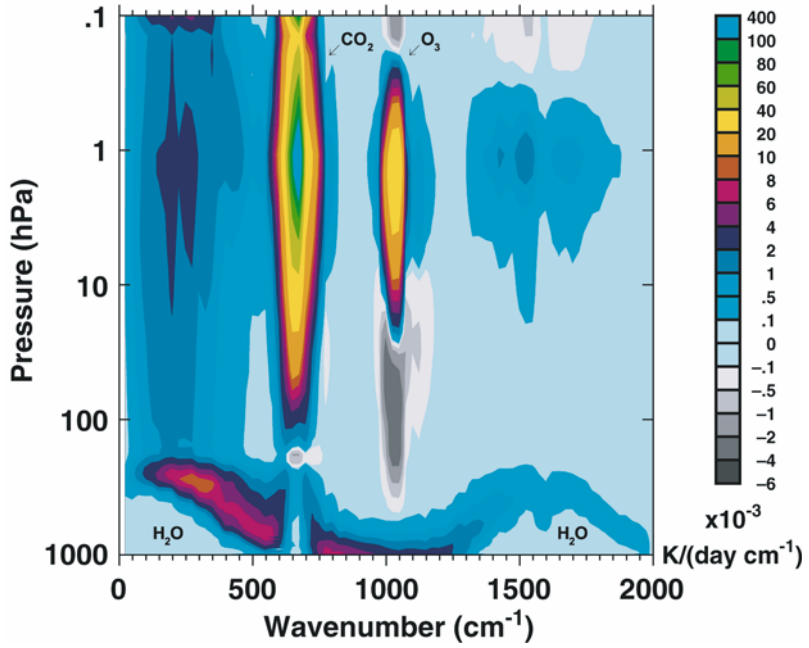

Plate 7. *Thermal infrared cooling rates [10^{-3}K(day)$^{-1}$(cm^{-1})$^{-1}$] by H_2O, CO_2 (355 ppm), and O_3 represented as a function of wavenumber (cm^{-1}) and atmospheric pressure (hPa) for mid-latitude summer conditions. The band centered at 667 cm^{-1} (15 μm) is dominated by CO_2, and exhibits strong stratospheric cooling and a local warming at the tropopause. The band around 1043 cm^{-1} (9.6 μm) is dominated by O_3 and exhibits cooling in the upper stratosphere and warming throughout the lower stratosphere. Water vapor makes a strong contribution to upper tropospheric cooling near 300 cm^{-1}, although its effects are moderated by CO_2. Adopted from Clough and Iacono (1995) with courtesy of WCRP/SPARC.*

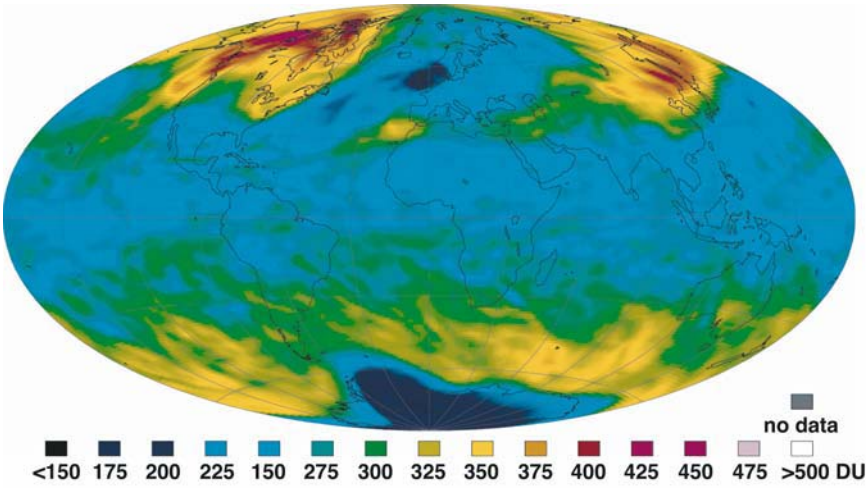

Plate 8. *Global view of the ozone column abundance (Dobson) on 30 November, 1999 as measured by the GOME instrument - Values have been assimilated by the Royal Meteorological Institute of the Netherlands. Note the very low ozone column abundance over Antarctica. Courtesy of Hennie Kelder, KNMI, Netherlands.*

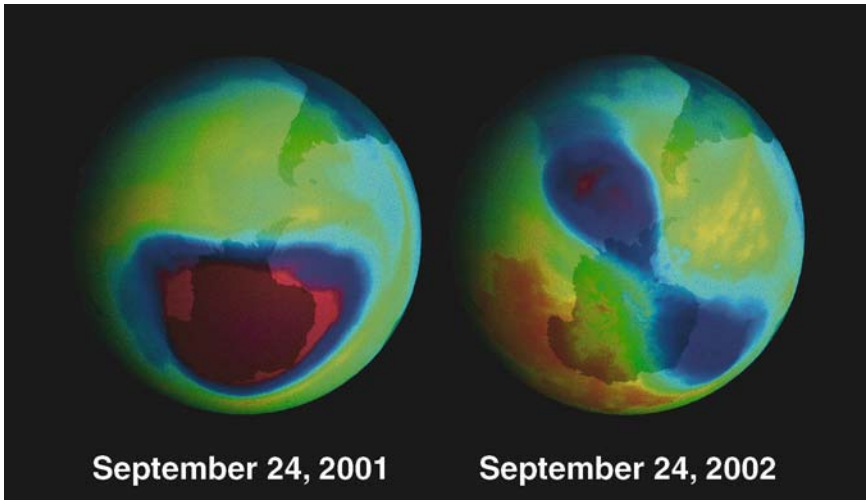

Plate 9. *Interannual variability in the Antarctic ozone hole. The figures compare the ozone column abundance observed on September 24 in 2001 and in 2002. In 2001 as in most previous years of the last 2 decades, the hole was centered approximately over the South Pole with low ozone values over the Antarctic continent. In 2002, a strong wave-2 planetary wave disturbed the polar vortex and produced a very peculiar distribution of the ozone column. The warming associated with this event led to limited ozone depletion and a disappearance of the ozone hole at the end of September. From NASA.*

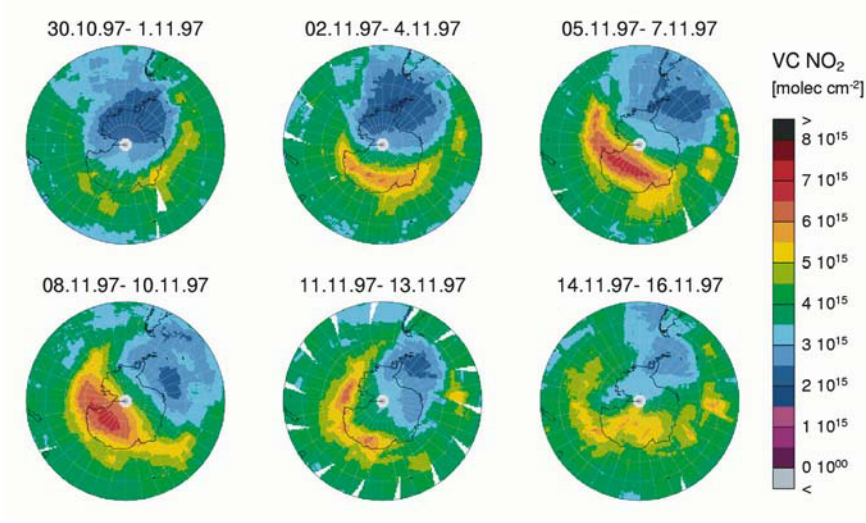

Plate 10. *Vertical column density (molecules cm^{-2}) of nitrogen dioxide (NO_2) measured over Antarctica by the spaceborne GOME instrument between early and mid-November, 1997. The low values (blue) are associated with the polar vortex, which is displaced towards South America as a large planetary wave develops in the region (final warming). Strong latitudinal gradients can be observed in the abundance of NO_2 (called "Noxon Cliff" after J. F. Noxon who discovered them). Courtesy of A. Richter and J. Burrows, Institute of Environmental Physics, University of Bremen, Germany.*

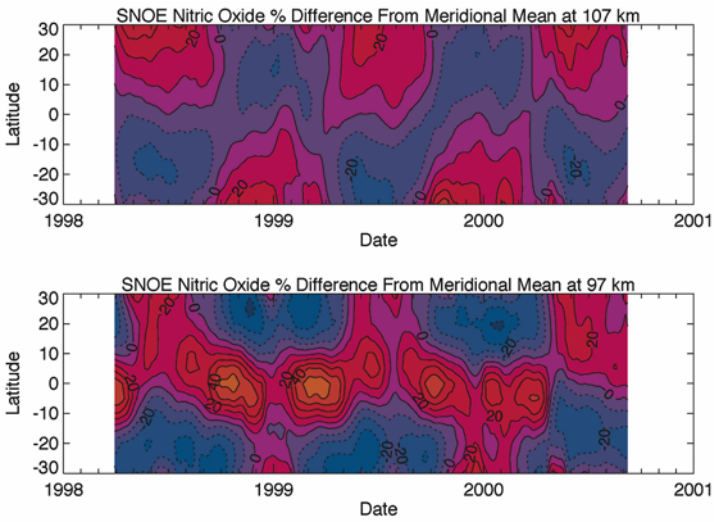

Plate 11. *Nitric Oxide density variation in the lower thermosphere at 107 and 97 km as measured by the Student Nitric Oxide Explorer satellite using the γ-band fluorescence technique. Percent differences from the latitudinal average in the intertropical region at ~11:00 local time are shown. At 107 km, solar control dominates with the peak density shifting to the summer hemisphere. At 97 km, this effect can still be discerned, but the dominant perturbation is now dynamical, as vertical winds driven by middle atmosphere tides control the distribution. The diurnal tide drives changes in the nitric oxide density at the equator, particularly at the equinoxes when tidal forcing tends to be high. Courtesy of Stan Solomon, National Center for Atmospheric Research, Boulder, CO.*

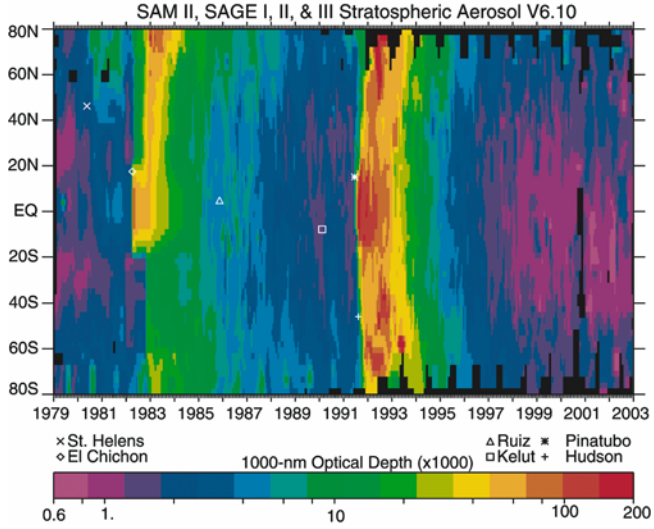

Plate 12. *Evolution between 1979 and 2003 of the zonally averaged aerosol optical depth at 1000 nm represented as a function of latitude. The timing and location of several large volcanic eruptions, which have affected the sulfate aerosol load of the atmosphere, are also shown. The value of the optical depth (typically 10^{-3} during quite periods) increased dramatically after the major eruptions of El Chichon in 1982 and Mt Pinatubo in 1991. The surface area available for heterogeneous processes was also dramatically enhanced. The recovery time following stratospheric perturbations produced by major volcanic eruptions is of the order of 2-3 years. Courtesy of Larry W. Thomason, NASA/Langley.*

Plate 13. *Noctilucent clouds observed over Kühlungsborn, Germany (54°N) on 10 July 1997 at 01:00 GMT. These polar mesospheric clouds are found at approximately 90 km altitude and are illuminated by the Sun, which at that time is located approximately 11 degrees below the horizon. Courtesy of F.-J. Lübken, Leibniz Institute for Atmospheric Physics, Kühlungsborn, Germany.*

Plate 14. *Mother-of-Pearl clouds (also called Polar stratospheric Clouds or PSCs) observed in McMurdo Antarctica. Photo by David J Hofmann.*

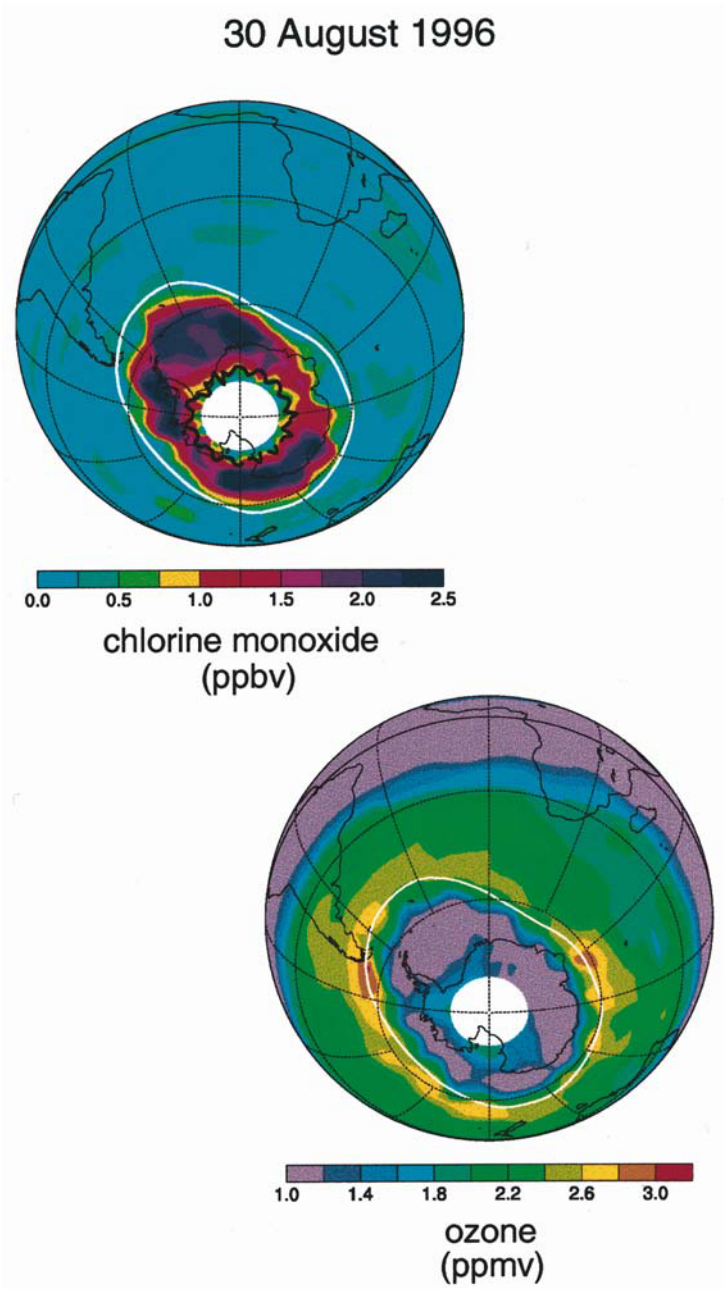

Plate 15. *Satellite observations of chlorine monoxide (ClO) and ozone (O_3) within the lower stratosphere (465 K potential temperature level) of the Southern Hemisphere on 30 August, 1996. The white line delineates the edge of the vortex, while the black line on the chlorine monoxide panel indicates the edge of the dark region over the pole. Chlorine monoxide levels are greatly enhanced in the region between the white and the black lines – that is, in sunlit cold air within the Antarctic polar vortex. The bottom panel shows the corresponding ozone distribution. Ozone abundances have begun to drop inside the vortex where chlorine monoxide is elevated. The region displaying reduced ozone (purple) corresponds very closely to the region of enhanced chlorine monoxide. From NASA.*

INDEX

Absorption cross-sections, 43, 169
Accomodation coefficient, 34
Actinic flux, 159
Activity complex, 29, 31
Adiabatic processes, 59-60
Advection (definition), 51
Aerosol particles
  climatology, 394
  formation of, 393-394
  linkages to polar stratospheric clouds, 396-401
  microphysics, 393
  and multiple scattering, 177-180
  observations of, 394-396
  solubility in, 23
  sulfate layer, 388-396
  and volcanic eruptions, 395
Age of air, 88-90
Age spectrum, 89
Agricultural emissions, 4-5
Airglow, 44
Antarctic ozone depletion
  chemical processes, 407-408, 469-474
  depth and area, 478-481
  observations, 462-465
  role of dynamics, 462-464
  theories, 465-470
Arctic oscillation (AO), 123-125
Arctic ozone depletion
  chemical processes, 484-486
  quantification, 486-488
  role of dynamics, 482-483
  temperature variability, 488-491
Atmospheric sphericity, 174-176

Band models, 200-203
Beer-Lambert Law, 169
Bimolecular reactions, 26, 28-30
BrCl (bromine chloride)
  chemistry of, 370-372, 375-377
  spectrum and photodissociation, 246
Brewer-Dobson circulation, 94-98
BrO (bromine monoxide)
  chemistry of, 374-376
  observations, 386
  spectrum and photodissociation, 243
$BrONO_2$ (bromine nitrate)
  chemistry of, 376-377
  spectrum and photodissociation of, 244
Brunt-Väisälä frequency, 66
Br_y (odd bromine)
  chemistry of, 374-377
  interaction with Clx and O3, 404-406
  partitioning, 380-383

Catalytic cycles, 28
CFCs (chlorofluorocarbons)
  emissions, 361-363
  spectrum and photodissociation of, 241
  trends, 503-504
CH_2O (formaldehyde)
  chemistry of, 298-302
  spectrum and photodissociation of, 233
$CHBr_3$ (bromoform)
  spectrum and photodissociation of, 241-242
CH_3Br (methyl bromide)
  budget, 360-361
  spectrum and photodissociation of,

241-242
CH_3Cl (methyl chloride)
budget, 360-361
spectrum and photodissociation of, 241
CH_3CCl_3 (methylchloroform)
emissions, 361-363
spectrum and photodissociation of, 241
trends, 503-504
CH_3CN (methylcyanide), 335-336
CH_3I (methyliodide)
budget, 360-361, 379
CH_4 (methane)
budget of, 296-298
chemistry of, 298-302
lifetime of, 294-295
observations of, 294-295
oxidation of, 299-302
spectrum and photodissociation of, 231-232
transport of, 294-296
Chapman function, 174-175
Chemical lifetime, 26-27
Chemical-transport models, 131-136
Chemical algorithms, 269-271
Chemical heating, 210-211
Chemiluminescence, 44
Chromosphere, 162
Circulation
diabatic, 99
Eulerian mean, 92-93
Lagrangian mean, 99
transformed Eulerian mean or residual, 99
Cl (atomic chlorine)
chemistry of, 364-372
diurnal variation, 372-373
lifetime of, 381-382
ClO (chlorine monoxide)
chemistry of, 364-372
diurnal variation, 372-373
in Antarctic stratosphere, 472
lifetime of, 381-382
observations of, 384-385
spectrum and photodissociation of, 242-243
Cl_2O_2 (dichlorine peroxide or ClO dimer)
chemistry of, 364-372
spectrum and photodissociation, 243
$ClONO_2$ (chlorine nitrate)
chemistry of, 374-372
in Antarctic stratosphere, 473
lifetime of, 381-382
observations of, 384-385
$ClONO_2$ (*continued*)
spectrum and photodissociation, 244
Cl_x (reactive chlorine)
chemistry of, 364-372
observations of, 384-387
partitioning of, 380-384
Cl_y (odd chlorine)
chemistry of, 364-372
cycle, 6-7
destruction of ozone by, 405-408, 455-459
observations of, 384-387
partitioning of, 380-384
trends, 503-505
CO (carbon monoxide)
budget of, 303-304
chemistry of, 298-303
lifetime of, 304-305
observations of, 305-307
transport of, 305
CO_2 (carbon dioxide)
absorption and emission of IR radiation by, 192
absorption of solar radiation by, 169-177
abundance of, in present atmosphere, 305
chemistry of, 302
effect of industrial activities, 6
non-LTE conditions, 203-206
on geological timescales, 3
spectrum and photodissociation of, 232-233
Column abundance, 267
Continuity equation, 60, 84-85, 266-268
Coriolis force, 59, 67
COS (carbonyl sulfide), 388-390
Cosmic rays
ionization by, 546-548

production of NOx by, 334

D-region of the ionosphere
definition of, 534-535
ionization in, 542-544
negative ion chemistry in, 573-576
positive ion chemistry in, 562-564
Diabatic
circulation, 99
definition, 60
heating rates, 158
Diffusion
eddy, 58, 86, 128
molecular, 127-129
Doppler lineshape, 197
Downward control principle, 113
Dynamical barriers, 106-112

E-region of the ionosphere
definition of, 534-535
ionization in, 539-542
positive ion chemistry in, 554-555
Eddies
definition, 92
diffusion, 58, 86, 128
chemical eddy transport, 102
Electromagnetic spectrum, 151-152
Electronic transitions
term symbols, 18-20
selection rules, 20
Eliassen-Palm flux, 100-101
Endothermicity, 21
Energy budget, 216-218
Energy equation, 59
Energy levels of molecules, 12-20
Energy of activation, 29
Enthalpy of formation, 21
Entropy, 22
Equation of state, 60
Eulerian mean, 92-93
Evolution of the atmosphere, 2-4
Excited species, 44-48
Exothermicity, 21
Extratropical pump, 104-105

F-region of the ionosphere, 534-535
Ferrell cell, 95
Fluorescence, 44
Free radicals, 11
F_y (odd fluorine)
chemistry of, 372-374
partitioning, 380-383

General circulation models, 129-131
Geopotential, 67
Geostrophic approximation, 69-70
Gibbs free energy of reactions, 22
Gravity waves 75-77
Grid-point models, 131

H (atomic hydrogen)
chemistry of, 317-325
lifetime of, 321-322
H_2 (molecular hydrogen)
budget of, 313-316
chemistry of, 313
lifetime of, 316
observations of, 315-316
H_2O (water vapor)
absorption and emission of IR radiation by, 192
chemistry of, 310-311
lifetime of, 312
long-term trends in, 313
observations of, 311-313
spectrum and photodissociation of, 227-231
and transport processes, 313
H_2O_2 (hydrogen peroxide)
chemistry of, 317-325
lifetime of, 321-322
observations of, 325-327
spectrum and photodissociation of, 231
H_2SO_4 (sulfuric acid)
and aerosols, 393-398
chemistry of, 390-391
observations of, 393-396
Halons
spectrum and photodissociation of, 241-243

use of, 361-363
HBr (hydrogen bromide)
chemistry of, 376-377
lifetime of, 321-322
spectrum and photodissociation of, 244-245
HCFCs (hydrochlorofluorocarbons), 361-363
HCl (hydrogen chloride)
chemistry of, 364-372
in Antarctic stratosphere, 473
lifetime of, 321-322
observations of, 384-387
spectrum and photodissociation of, 244-245
HCN (hydrogen cyanide), 335
Heat conduction, 127
Heterogeneous processes, 338, 368, 377, 469
Heterogeneous reactions, 34-40
Heterosphere, 53
HF (hydrogen fluoride)
chemistry of, 372-374
observations of, 386
spectrum and photodissociation of, 244-245
HFCs (hydrofluorocarbons), 361-363
$H^+.(H_2O)_n$ (proton hydrate ions)
formation of, 562-563
observations of, 559-562
production of HO_x bym 585-586
HNO_2 (nitrous acid)
spectrum and photodissociation of, 239
HNO_3 (nitric acid)
chemistry of, 336-341
lifetime of, 342-343
observations of, 350
spectrum and photodissociation of, 239
HNO_4 (peroxynitric acid)
chemistry of, 336-341
lifetime of, 342-343
spectrum and photodissociation of, 240
HO_2 (hydroperoxy radical)
chemistry of, 317-325
lifetime of, 321-322
observations of, 325-327
HOBr (hypobromous acid)
chemistry of, 376-377
spectrum and photodissociation, 245
HOCl (hypochlorous acid)
chemistry of, 364-372
observations of, 384
spectrum and photodissociation of, 245
Homosphere, 53
HO_x (odd hydrogen)
chemistry of, 317-325
destruction of ozone by, 401-403
lifetime of, 321-322
observations, 325-327
partitioning of, 321-325
production of, by ions, 585-586
Hydrostatic approximation, 63
Infrared (IR) radiation
absorption and emission of, 191-206
source of, 191

Ion drag, 114-115
Ionization
by solar radiation, 539-544
by energetic particles, 544-552
Ionosphere, 533-539
Irradiance, 158
Isentropic coordinates, 68
I_y (odd iodine)
chemistry of, 379-380
partitioning, 383

Kelvin waves, 80

Lapse rate, 65
Lifetime, 267

Lorentz line shape, 197

Mass density (definition), 267
Mass fraction (definition), 267
Mean thermal molecular velocity, 29, 34
Mechanistic models, 130
Meridional wind (definition), 57
Mesopause (definition), 53, 116- 117
Mesosphere (definition), 53
Metal ions, 555-559
Mid-latitude ozone depletion
  gas-phase chemistry, 401-407
  heterogeneous chemistry, 492-499
  dynamical processes, 499-501
Mie scattering, 178
Mixed Rossby-gravity waves, 80
Mixing ratio (definition), 84, 267
Molecular diffusion, 127-128
Mole fraction (definition), 267
Momentum equation, 59
Montgomery stream function 68
Montreal protocol, 7

$N(^2D)$ (excited nitrogen atom)
  emissions from, 47
  and thermospheric NO, 351-355
N_2 (molecular nitrogen)
  abundance of, 266
  spectrum and photodissociation of, 219-220
N_2O (nitrous oxide)
  budget of, 329-330
  chemistry of, 328-329
  lifetime of, 330-331
  observations of, 330-332
  production of stratospheric NO from, 329
  spectrum and photodissociation of, 236-237
N_2O_5 (dinitrogen pentoxide)
  chemistry of, 336-341
  diurnal variation of, 346
  lifetime of, 342-343
  observations of, 349
  spectrum and photodissociation of, 239
Negative ions
  in the D-region, 571-577
  observations, 571-572, 579-581
  ratio to electrons, 537-539
  in the stratosphere, 577-581
Newtonian cooling, 215
Nitrogen cycle, 5
NO (nitric oxide)
  chemistry of, 336-341, 353
  diurnal variation of, 346
  and the ionospheric D-region, 542-543
  lifetime of, 342-343
  observations of, 346-347, 355, 358
  spectrum and photodissociation of, 233-236
  in the thermosphere, 351-358
NO_2 (nitrogen dioxide)
  absorption of solar radiation and heating by, 211
  chemistry of, 336-341
  diurnal variation of, 346
  lifetime of, 342-343
  observations of, 347-348
  spectrum and photodissociation of, 237-238
NO_3 (nitrogen trioxide)
  chemistry of, 336-341
  diurnal variation of, 346
  lifetime of, 342-343
  observations of, 350
  spectrum and photodissociation of, 238-239
Noble gases (Ar, Ne, He, Kr, Xe)
  atmospheric mixing ratio, 266
  depletion on Earth relative to cosmic abundance, 2
Non-acceleration theorem, 96
NO_x (reactive nitrogen)
  chemistry of, 336-341
  destruction of ozone by, 403-404
  lifetime of, 342-343

production of, by ions, 582-585
stratospheric sources of, 328-335
NO_y (odd nitrogen)
definition, 341-342
observations of, 351
partitioning of, 341-346
stratospheric sources of, 328-335
Number density (definition), 267

OClO (chlorine dioxide)
in Antarctic stratosphere, 472-473
chemistry of, 364-372
spectrum and photodissociation, 243
$O(^1D)$ (electronically excited oxygen atom)
chemistry of, 273-281
lifetime, 276
production of, 44
production of HOx by, 44, 311
red line emission, 45
$O(^1S)$ (electronically excited oxygen atom)
green line 45
O_2 in the primitive atmosphere, 3
$O(^3P)$ (atomic oxygen)
chemistry of, 273-281
lifetime of, 276
OH (hydroxyl radical)
chemistry of, 317-325
lifetime of, 321-322
Meinel bands of, 46
observations of, 325-327
O_2 (molecular oxygen)
absorption of solar radiation and heating by, 173-208
abundance of, 266
chemistry of, 273-281
emission of O2(1Δg), 46
potential energy curves, 42
spectrum and photodissociation of, 220-224
O_3 (ozone)
absorption of solar radiation and heating by, 173-208
absorption and emission of IR radiation by, 192
and CH4, 413
chemistry of, 273-281
depletion of, 505-506
general equation, 413-416
historical perspective, 272
hole, 462-464
lifetime of, 276-277
observations of, 281-292
and particle precipitation, 448-451
protection of living things by, 1
and the QBO, 291
and solar variability, 292, 451-455
spectrum and photodissociation of, 224-227
and transport processes, 286-287, 290
in the troposphere, 409-413
and volcanic influences, 494-498
O_x (odd oxygen)
chemistry of, 274-281
lifetime of, 277
partitioning of, 279
Optical thickness, 170
Optical transmission, 170
Order of reactions, 25
Oxidizing power of the atmosphere, 410-412

Particle precipitation
effect on neutral species, 581- 586
ionization by, 551-552
penetration depth of, 545
Photodissociation frequency, 43, 218-219
Photolysis, 40-44, 246-249
Photosphere, 160
Planetary waves, 78-79

Polar mesospheric clouds (PMCs), 396
Polar stratospheric clouds (PSCs)
composition and chemistry, 397-399, 474-478
effects on chlorine activation, 469-470
observations, 397
thermodynamics, 399-401
Polar vortex, 107, 462-464
Potential vorticity, 71-74
Positive ions
in the D-region, 559-564
in the E-region, 554-559
in the stratosphere, 564-570
observations, 555-556, 559-562, 568-570
Potential energy curves, 42-43
Potential temperature, 61
Predissociation, 43, 222, 234
Primitive atmosphere, 2-4
Primitive equations, 59-69
Quasi-biennal oscillation
description, 121-123
effect on ozone, 291

Radiance, 156
Radiative-convective models, 206
Radiative equilibrium, 112
Radiative lifetime, 215-216
Radiative transfer
equation 180-181
multiple scattering 182-187
infrared absorption and emission 191-206
Radio waves, 586-589
Rate of chemical reaction, 25-26
Rate-limiting step, 28
Rayleigh friction, 114
Rayleigh scattering, 178
Reaction probability, 34
Recombination, 534, 576
Relativistic electron precipitation (REP), 548-549
Remote sensing of the atmosphere, 188-190, 195-196
Rossby number, 70
Rossby waves, 78-79
Rotational energy, 16

Scale height, 63
Semi-annual oscillation (SAO), 123
SF_6 (sulfur hexafluoride), 364
Single scattering albedo, 177
Solar atmosphere, 159-162
Solar constant, 162
Solar proton events (SPE)
ionization by, 549-550
production of HOx by, 448-451
production of NOx by, 334-335, 448-451
Solar radiation
absorption of, 169-177
heating by, 207-212
scattering of, 177-180
spectral distribution of, 164-168
variation of, 167-169
Solar variability
amplitude, 167-169
effects on middle atmosphere, 451-455
Solar zenith angle, 170
Solubility of gases, 23-24
Sources of ionization, 539-552
Spectral model, 131
Steady (photostationary state), 27
Sticking coefficient, 34
Stratopause (definition), 53
Stratosphere (definition), 53
Structure of the atmosphere, 53-58
Sudden stratospheric warming, 120-121
Sulfur compounds
chemistry of, 389-391
sources of, 388-389
Surface area density, 35

Tape-recorder effect, 106, 313
Temperature

and definition of atmospheric layers, 53
and ozone coupling, 444-448
Termolecular reactions, 26, 32-33
Terrestrial radiation
cooling by, 212-216
absorption and emission of, 191-206
Thermal wind, 70
Thermosphere (definition), 53
Tides 80-83
Time constants
dynamical, 85-88
radiative, 215
photochemical, 26-27, 87-88
Tracer correlations, 90-92
Transport algorithms, 134-135
Tropopause
definition, 53
description, 111-112
Troposphere (definition), 53

Unimolecular reactions, 25-26, 30-32
Uptake coefficient, 34

Vibrational energy, 14-16
Vibration-rotation transitions, 16
Voigt lineshape, 198
Volcanoes
general, 389
and sulfate layer, 395-396
and ozone depletion, 494-499
Vorticity, 71

Waves 74-83
Wave drag
by gravity waves, 117-119
by Rossby waves 119-121
Winter anomaly, 590

Zonal wind (definition), 55

ATMOSPHERIC AND OCEANOGRAPHIC SCIENCES LIBRARY

1. F.T.M. Nieuwstadt and H. van Dop (eds.): *Atmospheric Turbulence and Air Pollution Modelling.* 1982; rev. ed. 1984
   ISBN 90-277-1365-6; Pb (1984) 90-277-1807-5
2. L.T. Matveev: *Cloud Dynamics.* Translated from Russian. 1984
   ISBN 90-277-1737-0
3. H. Flohn and R. Fantechi (eds.): *The Climate of Europe: Past, Present and Future.* Natural and Man-Induced Climate Changes: A European Perspective. 1984
   ISBN 90-277-1745-1
4. V.E. Zuev, A.A. Zemlyanov, Yu.D. Kopytin, and A.V. Kuzikovskii: *High-Power Laser Radiation in Atmospheric Aerosols.* Nonlinear Optics of Aerodispersed Media. Translated from Russian. 1985 ISBN 90-277-1736-2
5. G. Brasseur and S. Solomon: *Aeronomy of the Middle Atmosphere.* Chemistry and Physics of the Stratosphere and Mesosphere. 1984; rev. ed. 1986
   ISBN (1986) 90-277-2343-5; Pb 90-277-2344-3
6. E.M. Feigelson (ed.): *Radiation in a Cloudy Atmosphere.* Translated from Russian. 1984 ISBN 90-277-1803-2
7. A.S. Monin: *An Introduction to the Theory of Climate.* Translated from Russian. 1986
   ISBN 90-277-1935-7
8. S. Hastenrath: *Climate Dynamics of the Tropics*, Updated Edition from *Climate and Circulation of the Tropics.* 1985; rev. ed. 1991
   ISBN 0-7923-1213-9; Pb 0-7923-1346-1
9. M.I. Budyko: *The Evolution of the Biosphere.* Translated from Russian. 1986 ISBN 90-277-2140-8
10. R.S. Bortkovskii: *Air-Sea Exchange of Heat and Moisture During Storms.* Translated from Russian, rev. ed. 1987 ISBN 90-277-2346-X
11. V.E. Zuev and V.S. Komarov: *Statistical Models of the Temperature and Gaseous Components of the Atmosphere.* Translated from Russian. 1987
    ISBN 90-277-2466-0
12. H. Volland: *Atmospheric Tidal and Planetary Waves.* 1988 ISBN 90-277-2630-2
13. R.B. Stull: *An Introduction to Boundary Layer Meteorology.* 1988
    ISBN 90-277-2768-6; Pb 90-277-2769-4
14. M.E. Berlyand: *Prediction and Regulation of Air Pollution.* Translated from Russian, rev. ed. 1991 ISBN 0-7923-1000-4
15. F. Baer, N.L. Canfield and J.M. Mitchell (eds.): *Climate in Human Perspective.* A tribute to Helmut E. Landsberg (1906-1985). 1991 ISBN 0-7923-1072-1
16. Ding Yihui: *Monsoons over China.* 1994 ISBN 0-7923-1757-2
17. A. Henderson-Sellers and A.-M. Hansen: *Climate Change Atlas.* Greenhouse Simulations from the Model Evaluation Consortium for Climate Assessment. 1995
    ISBN 0-7923-3465-5
18. H.R. Pruppacher and J.D. Klett: *Microphysics of Clouds and Precipitation*, 2nd rev. ed. 1997 ISBN 0-7923-4211-9; Pb 0-7923-4409-X
19. R.L. Kagan: *Averaging of Meteorological Fields*. 1997 ISBN 0-7923-4801-X
20. G.L. Geernaert (ed.): *Air-Sea Exchange: Physics, Chemistry and Dynamics*. 1999
    ISBN 0-7923-5937-2
21. G.L. Hammer, N. Nicholls and C. Mitchell (eds.): *Applications of Seasonal Climate Forecasting in Agricultural and Natural Ecosystems*. 2000 ISBN 0-7923-6270-5

ATMOSPHERIC AND OCEANOGRAPHIC SCIENCES LIBRARY

22. H.A. Dijkstra: *Nonlinear Physical Oceanography*. A Dynamical Systems Approach to the Large Scale Ocean Circulation and El Niño. 2000 ISBN 0-7923-6522-4
23. Y. Shao: *Physics and Modelling of Wind Erosion*. 2000 ISBN 0-7923-6657-3
24. Yu.Z. Miropol'sky: *Dynamics of Internal Gravity Waves in the Ocean.* Edited by O.D. Shishkina. 2001 ISBN 0-7923-6935-1
25. R. Przybylak: *Variability of Air Temperature and Atmospheric Precipitation during a Period of Instrumental Observations in the Arctic*. 2002 ISBN 1-4020-0952-6
26. R. Przybylak: *The Climate of the Arctic*. 2003 ISBN 1-4020-1134-2
27. S. Raghavan: *Radar Meteorology*. 2003 ISBN 1-4020-1604-2
28. H.A. Dijkstra: *Nonlinear Physical Oceanography*. A Dynamical Systems Approach to the Large Scale Ocean Circulation and El Niño. 2nd Revised and Enlarged Edition. 2005 ISBN 1-4020-2272-7 Pb; 1-4020-2262-X
29. X. Lee, W. Massman and B. Law (eds.): *Handbook of Micrometeorology*. A Guide for Surface Flux Measurement and Analysis. 2004 ISBN 1-4020-2264-6
30. A. Gelencsér: *Carbonaceous Aerosol*. 2005 ISBN 1-4020-2886-5
31. Soloviev: *The Near-Surface Layer of the Ocean*. Structure, Dynamics and Applications. 2005 ISBN 1-4020-xxxx-x
32. G.P. Brasseur and S. Solomon: *Aeronomy of the Middle Atmosphere*. Chemistry and Physics of the Stratosphere and Mesosphere. 2005 ISBN 1-4020-3284-6; Pb 1-4020-3285-4